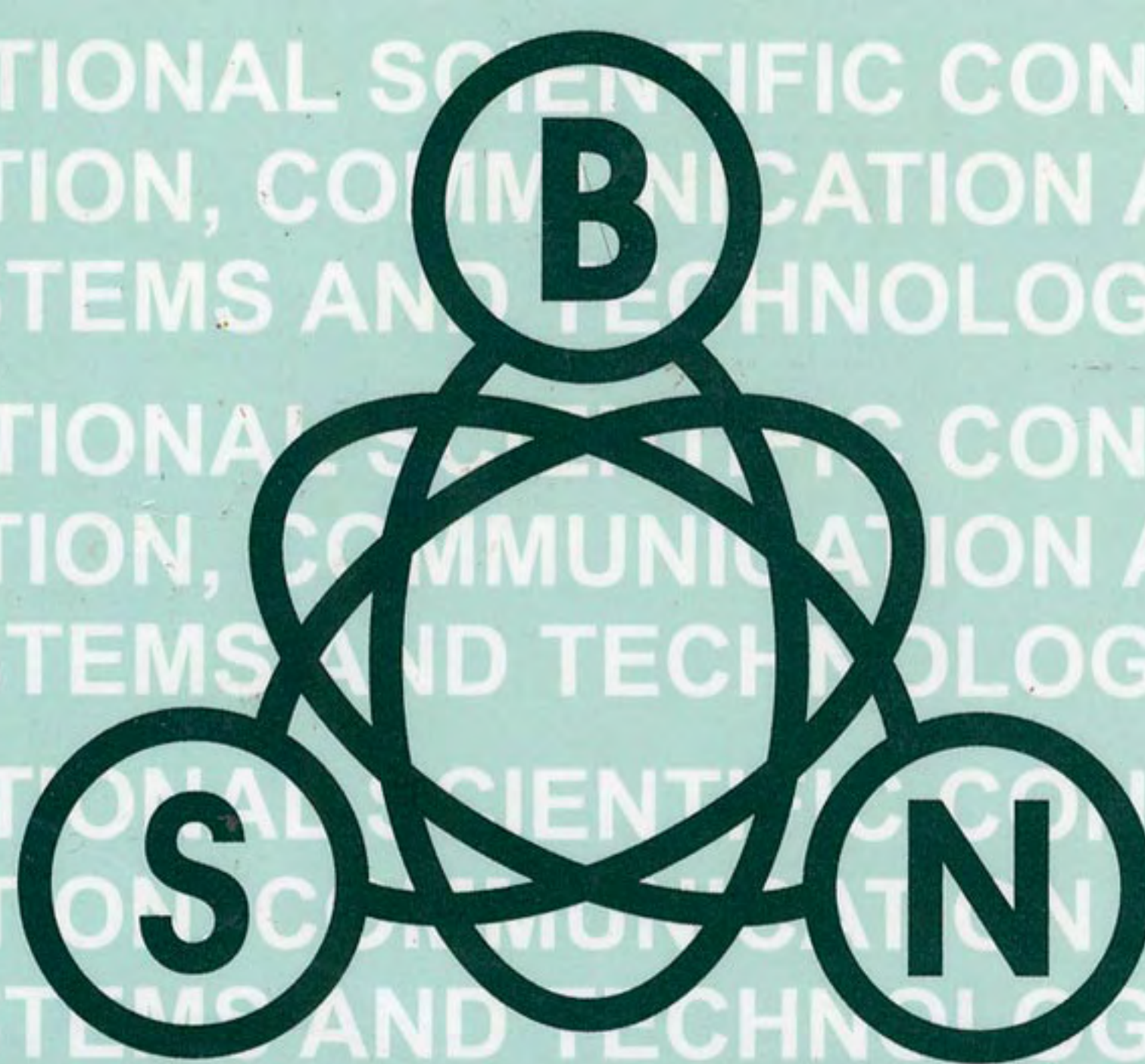


XLII INTERNATIONAL SCIENTIFIC CONFERENCE
ON INFORMATION, COMMUNICATION AND
ENERGY SYSTEMS AND TECHNOLOGIES

XLII INTERNATIONAL SCIENTIFIC CONFERENCE
ON INFORMATION, COMMUNICATION AND
ENERGY SYSTEMS AND TECHNOLOGIES

XLII INTERNATIONAL SCIENTIFIC CONFERENCE
ON INFORMATION, COMMUNICATION AND
ENERGY SYSTEMS AND TECHNOLOGIES



**XLII INTERNATIONAL SCIENTIFIC CONFERENCE
ON INFORMATION, COMMUNICATION AND
ENERGY SYSTEMS AND TECHNOLOGIES**

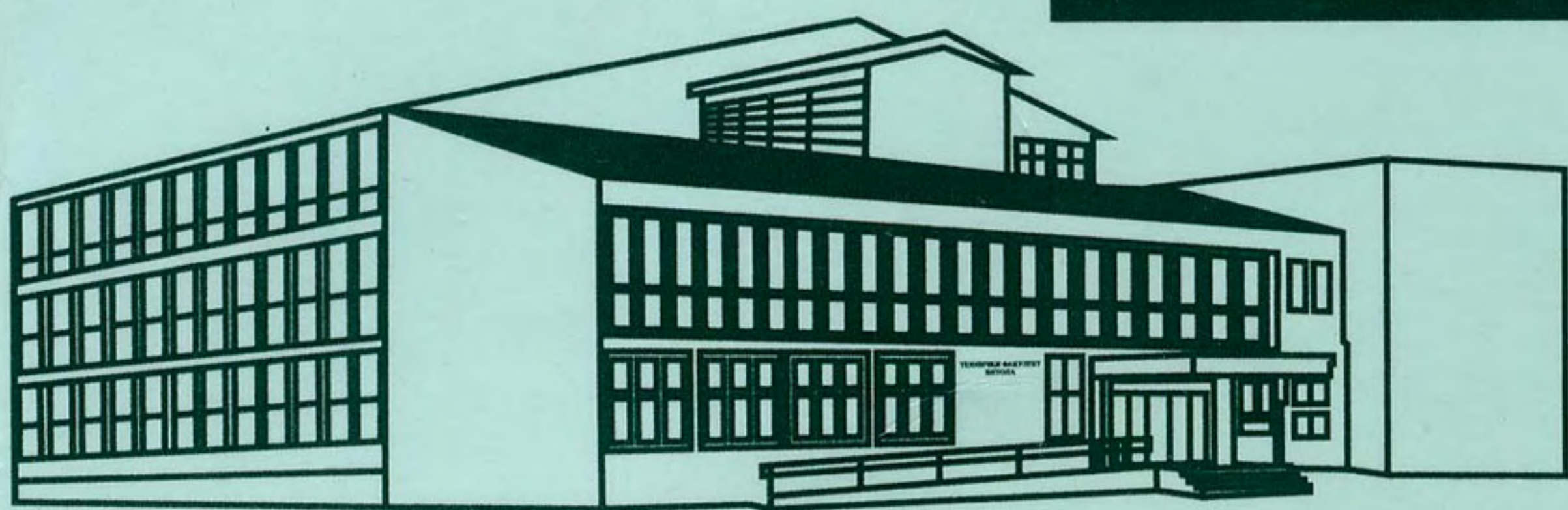


IEEE

ICEST 2007

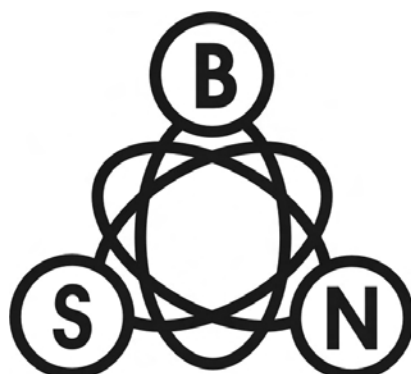


**Proceedings of Papers
Volume 2**



**24 - 27 June, 2007
Hotel Granit, Ohrid, Macedonia**

**XLII INTERNATIONAL SCIENTIFIC CONFERENCE
ON INFORMATION, COMMUNICATION AND
ENERGY SYSTEMS AND TECHNOLOGIES**



IEEE

**ICEST
2007**



Proceedings of Papers

Volume 2

Bitola, 2007

XLII INTERNATIONAL SCIENTIFIC CONFERENCE ON INFORMATION, COMMUNICATION
AND ENERGY SYSTEMS AND TECHNOLOGIES

-ICEST 2007-

Proceedings of Papers – Volume 2 of 2 volumes

Editor: Prof. Dr. Cvetko Mitrovski
Technical Editor: Pargovski Jove
Published by: Faculty of Technical Sciences - Bitola
Printed by: Mikena - Bitola
Total print run: 200

ISBN: 9989 - 786 - 06 - 2

CIP - Каталогизација во публикација
Матична и универзитетска библиотека
"Св. Климент Охридски", Битола

621 . 391 : 004 (063) (082)

007 . 52 (063) (082)

004 . 738 . 52 : 004 . 89 (063) (082)

621 . 397 . 3 : 004 (063) (082)

621 . 396 . 67 (063) (082)

INTERNATIONAL Scientific Conference on Information, Communication and Energy Systems and Technologies
(42 ; 2007 ; Bitola)

ICEST 2007: proceedings of papers / XLII International Scientific Conference on Information, Communication and
Energy Systems and Technologies ; [Editor Cvetko Mitrovski]. - Bitola : Faculty of Technical Sciences, 2007. - 2
св. (XVI , 430 ; XVI, стр. 431 - 860) : илустр. ; 28 см

Фусноти кон текстот. - Библиографија кон трудовите. - Регистри

ISBN 9989 - 786 - 06 - 2

1. Gl. stv. nasl. 2. Mitrovski, Cvetko

а) Електроенергетски системи - Мониторинг - Анализи - Зборници б) Телекомуникациска техника - Сигнали
- Анализи - Зборници в) Автоматски системи - Интелигентни системи - Зборници г) Компјутерски системи -
Системи за менаџмент на бази на податоци - Интернет технологии - Зборници - д) Индустриска електроника
- Контролни системи - Конвертери - Зборници

COBISS.MK - ID 18020161

TABLE OF CONTENTS

VOLUME 2

MEDICAL SYSTEMS

MED.S.1	BCI Mental Tasks Patterns Determination	451
	P. K. Manoilov University of Rousse, Bulgaria	
MED.S.2	An Investigation on Signals in Magnetocardiography	455
	D. Tz. Dimitrov Technical University of Sofia, Bulgaria	
MED.S.3	A Stimulation of Neural Tissue by Pulse Magnetic Signals	459
	D. Tz. Dimitrov Technical University of Sofia, Bulgaria	
MED.S.4	Eye-Blinking Artefacts' Duration Analysis	463
	P. K. Manoilov University of Rousse, Bulgaria	
MED.S.5	The Web Side System for Registration and Processing Medical Data of Urological Department Patients	467
	J. Makal, J. Bilkiewicz and A. Nazarkiewicz* Technical University (BTU), Bialystok, Poland *Provincial Integrated Hospital, Bialystok, Poland	
MED.S.6	Laboratory Stand in Web Browser for Measurements on Distance	469
	J. Makal, A. Idzkowski and A. Krasowski Technical University (BTU), Bialystok, Poland	
MED.S.7	Electronic Identification and Patient Parameters Monitoring	471
	S. Randić, A. Peulić, A. Dostanić and M. Acović Technical Faculty, Sv. Save, Čačak, Serbia	

SIGNAL PROCESSING II

SP II.1	Comparative Analysis of Basic Self-Organizing Map and Neocognitron for Handwritten Character Recognition	477
	I. R. Draganov and A. A. Popova Technical University of Sofia, Bulgaria	
SP II.2	Comparative Analysis of Integral Calculus Algorithms in Magnetic Signals Evaluation	481
	V. Dimitrova Technical University of Sofia, Bulgaria	
SP II.3	Investigation of Maximally Flat Fractional Delay All-pass Digital Filters	483
	K. S. Ivanova and G. K. Stoyanov Technical University of Sofia, Bulgaria	
SP II.4	A Unification of Determined and Probabilistic Methods in Pattern Recognition	487
	G. Kunev, G. Varbanov and C. Nenov Technical University of Varna, Bulgaria	
SP II.5	Complex Input Signal Quantization Noise Analysis for Orthogonal Second-Order IIR Digital Filter Sections	491
	Z. Nikolova Technical University of Sofia, Bulgaria	
SP II.6	Speech Overlap Detection Algorithms Simulation	495
	S. Pleshkova-Bekiarska and D. Damyanov Technical University of Sofia, Bulgaria	
SP II.7	FPGA Implementation of the 2D-DCT/IDCT for the Motion Picture Compression	499
	R. J.R. Struharik and I. Mezei Faculty of Technical Sciences, Novi Sad, Serbia	
SP II.8	Minutiae-based Algorithm for Automatic Fingerprint Identification	503
	E. H. Mulalić, S. S. Cvetković and S. V. Nikolić University of Niš, Serbia	

SP II.9	Performances of The Exponential Sinusoidal Audio Model	507
	Z. N. Milivojević, P. Rajković and S. M. Milivojević*	
	University of Niš, Serbia	
	*Technical Faculty, Cacak, Serbia	
SP II.10	Non-uniform Thresholds for Removal of Signal-Dependent Noise in Wavelet Domain.....	511
	M. Kostov, C. Mitrovski and M. Bogdanov*	
	University of Bitola, Macedonia	
	*University of Skopje, Macedonia	

COMPUTER SYSTEMS AND INTERNET TECHNOLOGIES IV

CSIT IV.1	GUI to Web Transcoding.....	517
	Ts. Filev, J. Pankov and I. Pankov	
	Technical University of Sofia, Bulgaria	
CSIT IV.2	Classification of Classifiers.....	521
	G. Gluhchev, M. Savov and O. Boumbarov*	
	Bulgarian Academy of Sciences	
	*Technical University of Sofia, Bulgaria	
CSIT IV.3	Methods of Graphic Representation of Curves in CAD systems in Knitting Industry.....	523
	E. Iv. Zaharieva-Stoyanova	
	Technical University of Gabrovo, Bulgaria	
CSIT IV.4	Cognitive Model Extension for HCI.....	527
	N. D. Đorđević and D. D. Rančić	
	University of Niš, Serbia	
CSIT IV.5	Performance Analysis of a Suboptimal Multiuser Detection Algorithm.....	531
	I. G. Iliev and M. Nedelchev	
	Technical University of Sofia, Bulgaria	
CSIT IV.6	Realization of Train Rescheduling Software System.....	535
	S. Mladenović and S. Vesković	
	University of Belgrade, Serbia	
CSIT IV.7	Throughput Analysis of EDCA in Multimedia Environment.....	539
	B. Ilievski, P. Latkoski and B. Popovski	
	University of Skopje, Macedonia	
CSIT IV.8	Software Tools and Technologies in Steganography	543
	J. Mirčevski, B. Djokić, M. Srećković*	
	and N. Popović**	
	Informatička škola "Educon", Beograd, Serbia	
	*Elektrotehnički fakultet, Beograd, Serbia	
	**Ministarstvo Inostranih Poslova, Beograd, Serbia	

CONTROL SYSTEMS & ROBOTICS

CS&R.1	Cascade Synchronization of Chaotic Systems on the Basis of Linear-Nonlinear Decomposition.....	549
	D. P. Chantov	
	Technical University of Gabrovo, Bulgaria	
CS&R.2	Sensorless Vector Control of Induction Motors.....	553
	E. Y. Marinov, K. D. Lutskanov and Z. S. Zhekov	
	Technical University of Varna, Bulgaria	
CS&R.3	Genetic Algorithms applied in Parameter Optimization of Cascade Connected Systems.....	557
	B. Danković, D. Antić, Z. Jovanović	
	and M. Milojković	
	University of Niš, Serbia	
CS&R.4	Building 3D Environment Models for Mobile Robots Using Time-Of-Flight (TOF) Laser Scanner	561
	S. Koceski and N. Koceska	
	University of L'Aquila, Italy	
CS&R.5	High-Performance Velocity Servo-System Design Using Active Disturbance Estimator	565
	B. Veselić and Č. Milosavljević*	
	University of Niš, Serbia	
	*Electrical Engineering Faculty, Istočno Sarajevo, Bosnia and Herzegovina	
CS&R.6	Optimal Control Using Neural Networks.....	569
	D. Toshkova and P. Petrov	
	Technical University of Varna, Bulgaria	

CS&R.7	Some Discretizing Problems in Control Theory.....	573
	M. B. Naumović University of Niš, Serbia	

POWER TRANSMISSION AND DISTRIBUTION SYSTEMS I573

PTDS I.1	An Algorithm for Coupled Electric and Thermal Fields in Insulation of the Large Power Cables	579
	I. T. Cârstea and D. P. Cârstea* Faculty of Automatics, Computers and Electronics. Craiova, Romania *Industrial Group of Romanian Railways	
PTDS I.2	Control of the Electrical Field in the Connectors for High-Voltage Cables	583
	I. T. Cârstea and D. P. Cârstea* Faculty of Automatics, Computers and Electronics. Craiova, Romania *Industrial Group of Romanian Railways	
PTDS I.3	Untransposed HV Transmission Line Influence on the Degree of Unbalance in Power Systems.....	587
	Lj. D. Trepzanovski and M. B. Atanasovski University of Bitola, Macedonia	
PTDS I.4	Calculation of GIS 110 kV Insulating Bushing Applying Hybrid BEM-FEM Method	591
	H. Zildžo and H. Matoruga Electrical Engineering Faculty, Sarajevo, Bosna i Hercegovina	
PTDS I.5	Estimation of the Air Power Line Parameters Under the Influence of Lightning Overvoltages	595
	M. G. Todorova and M. P. Vasileva Technical University of Varna, Bulgaria	
PTDS I.6	Calculation Model and Analyses of Grounding of the Fence on Medium Voltage Stations.....	599
	N. Acevski and M. Spirovski University of Bitola, Macedonia	

EDUCATION QUALITY I

EQ I.1	Meaning Making Through e-Learning	605
	B. Gradinarova and Y. Gorvits* Technical University of Varna, Bulgaria *ORACLE 15, Moscow, Russia	
EQ I.2	Software Engineering e-learning Mathematical Software	609
	B. Fetaji, S. Osmani* and M. Fetaji Faculty of Communication Sciences and Technologies, Tetovo, Macedonia *IT center-SEEU, Tetovo, Macedonia	
EQ I.3	Combining Virtual Learning Environment and Integrated Development Environment to Enhance e-learning.....	613
	M. Fetaji, S. Loskovska* and B. Fetaji Faculty of Communication Sciences and Technologies, Tetovo, Macedonia *University of Skopje, Macedonia	
EQ I.4	Software Engineering e-learning Information Retrieval Courseware	617
	B. Fetaji and M. Fetaji Faculty of Communication Sciences and Technologies, Tetovo, Macedonia	
EQ I.5	The Problems in Distant – Learning.....	621
	V. Aleksieva Technical University of Varna, Bulgaria	
EQ I.6	The Roles of Colours in the Multimedia Presentation Building	623
	P. Spalevic, B. Milošević*, K. Kuk** and G. Dimić** Faculty of Technical Sciences, Kosovska Mitrovica, Serbia * University of Niš, Serbia ** <i>High School of Electrical Engineering</i> , Belgrade, Serbia	

ELECTRONIC COMPONENTS, SYSTEMS AND TECHNOLOGIES I

ECST I.1	Synthesis of DCS in Copper Metallurgy.....	629
	D. R. Milivojević, V. Tasić, M. Pavlov and V. Despotović Copper Institute, Bor, Serbia	

ECST I.2	Removal of Power-line Interference from ECG in Case of Non-multiple Even Sampling	633
	G. S. Mihov and I. A. Dotsinsky* Technical University of Sofia, Bulgaria *Bulgarian Academy of Sciences	
ECST I.3	Synthesizing Sine Wave Signals Based on Direct Digital Synthesis Using Field Programmable Gate Arrays.....	637
	H. Z. Karailiev and V. V. Rankovska Technical University of Gabrovo, Bulgaria	
ECST I.4	Negative Impedance Converter Improves Capacitance Converter	641
	V. D. Draganov, Z. D. Stanchev and I. T. Tanchev Technical University of Varna, Bulgaria	
ECST I.5	Fuel Cells and Fuel Cell Power Supply Systems – an Overview	645
	Z. S. Mladenovski*, G. L. Arsov and J. Kosev *COSMOFON – A.D. Skopje, Macedonia University of Skopje, Macedonia	
ECST I.6	Developing and Using Communication Driver for Serial Communication Between PCs and Industrial PLCs	649
	Z. M. Milić, P. B. Nikolić, D. Krstić* and M. Lj. Sokolović* Tigar MH, Pirot, Serbia *University of Niš, Serbia	
ECST I.7	Spice Model of Magnetic Sensitive MOSFET	653
	N. Janković, T. Pesić and D. Pantić University of Niš, Serbia	
ECST I.8	Reduced Data Sample Transmission – Implementation to PIC Microcontroller.....	657
	M. I. Petkovski and C. D. Mitrovski University of Bitola, Macedonia	

POWER TRANSMISSION AND DISTRIBUTION SYSTEMS II & ELECTRICAL MACHINES

PTDS&EM.1	Fast High Voltage Signals Generator for Low Emittance Electron Gun.....	663
	M. Paraliev Paul Scherrer Institut, Villigen, Switzerland	
PTDS&EM.2	Effect of Perforation in High Power Bolted Busbar Connections	667
	R. T. Tzeneva and P. D. Dineff Technical University of Sofia, Bulgaria	
PTDS&EM.3	The Influence of the Supply Voltage Unbalance on the Squirrel Cage Induction Motor Operation.....	671
	G. I. Ganev and G. T. Todorov Technical University of Sofia, Bulgaria	
PTDS&EM.4	Monitoring of the Electric Energy Quality in the Electricity Supply	675
	Tz. B. Tzanev, S. G. Tzvetkova and V. G. Kolev Technical University of Sofia, Bulgaria	
PTDS&EM.5	Algorithm for Efficiency Optimization of the Induction Motor Based on Loss Model and Torque Reserve Control	679
	B. Blanuša, P. Matić, Ž. Ivanović and S. N. Vukosavić* Faculty of Electrical Engineering, Banja Luka, Bosnia and Herzegovina *Faculty of Electrical Engineering, Beograd, Serbia	
PTDS&EM.6	Computation of Electromagnetic Forces and Torques on Overline Magnetic Separator	683
	M. I. Popnikolova Radevska and B. S. Arapinoski University of Bitola, Macedonia	

EDUCATION QUALITY II

EQ II.1	Studying on Frequency Modulation in MATLAB Environment.....	689
	V. M. Georgieva Technical University of Sofia, Bulgaria	
EQ II.2	An Approach of Application Development for the Virtual Laboratory Access	691
	J. Djordjević-Kozarov, M. Jović* and D. Janković University of Niš, Serbia *University of Lugano, Switzerland	
EQ II.3	The Use of Virtual Reality Environments for Training Purposes in Care Settings	693
	E. Maier, M. Donschewa and G. Kempter UCT- Research, FHV, Dornbirn, Austria	

EQ II.4	How to Give a Good Scientific Presentation.....	697
	S. S. Cvetković and S. V. Nikolić University of Niš, Serbia	
EQ II.5	Reevaluation and Replacement of Terms in the Sampling Theory	701
	P. Tz. Petrov Microengineering, Sofia, Bulgaria	
EQ II.6	SWOT Analysis of Method for Automatic Vectorization of Digital Photos Into 3D Model.....	705
	Z. G. Kotevski and I. I. Nedelkovski University of Bitola, Macedonia	

ELECTRONIC COMPONENTS, SYSTEMS AND TECHNOLOGIES II

ECST II.1	Monitoring System of Pulsation Processes in a Milking Machine.....	711
	A. T. Aleksandrov and N. D. Draganov Technical University of Gabrovo, Bulgaria	
ECST II.2	A Method for Improvement Stability of a CMOS Voltage Controlled Ring Oscillators.....	715
	G. Jovanović and M. Stojčev University of Niš, Serbia	
ECST II.3	Load Characteristics under Optimal Trajectory Control of Series Resonant DC/DC Converters Operating above Resonant Frequency.....	719
	N. D. Bankov and Ts. Gr. Grigorova* University of Food Technologies, Plovdiv, Bulgaria *Technical University of Sofia, Branch Plovdiv, Bulgaria	
ECST II.4	Modeling of the Optimal Trajectory Control System of Resonant DC/DC Converters Operating Above Resonant Frequency.....	723
	N. D. Bankov and Ts. Gr. Grigorova* University of Food Technologies, Plovdiv, Bulgaria *Technical University of Sofia, Branch Plovdiv, Bulgaria	
ECST II.5	Comparison of Temperature Dependent Noise Models of Microwave FETs	727
	Z. D. Marinković, V. V. Marković and O. R. Pronić University of Niš, Serbia	
ECST II.6	Power Losses and Applications of Nanocrystalline Magnetic Materials.....	731
	V. C. Valchev, G. T. Nikolov, A. Van den Bossche* and D. D. Yudov** Technical University of Varna, Bulgaria *EELAB EESA Firw08 UGENT, Belgium **Bourgas Free University, Bourgas, Bulgaria	
ECST II.7	Multi level Electronic Transformer	735
	D. D. Yudov, A. Iv. Dimitrov, V. C. Valchev* and D. M. Kovatchev* Bourgas Free University, Bourgas, Bulgaria *Technical University of Varna, Bulgaria	
ECST II.8	An Approach to Effectiveness Increasing of SPICE Macromodels.....	739
	E. D. Gadjeva, B. I. Mihova and V. G. Manchev Technical University of Sofia, Bulgaria	

POSTER SESSIONS

PO I - SIGNAL PROCESSING

PO I.1	Image Filtering and Scaling Algorithms.....	745
	S. G. Mihov and G. S. Zapryanov Technical University of Sofia, Bulgaria	
PO I.2	System for Spectral Investigation of Signals	749
	S. V. Kolev, I. V. Ivanova and Y. S. Velchev Technical University of Sofia, Bulgaria	
PO I.3	Design and Implementation of First Order Sigma-Delta Modulator	751
	S. D. Terzieva, G. T. Tsenov, P. I. Yakimov and V. M. Mladenov Technical University of Sofia, Bulgaria	
PO I.4	Recovering Optical Image Transferred Through Atmospheric Turbulence.....	755
	K. L. Dimitrov Technical University of Sofia, Bulgaria	

PO I.5	CATV systems - Volterra Kernels Identification	757
	O. B. Panagiev and K. L. Dimitrov Technical University of Sofia, Bulgaria	
PO I.6	Comments on the Method “Over Sampling and Averaging for Additional Bits of Resolution”	761
	P. Tzv. Petrov Micro Engineering-Sofia, Bulgaria	

PO II - ELECTRONIC COMPONENTS, SYSTEMS AND TECHNOLOGIES

PO II.1	PSPICE Simulation of Optoelectronic Pulse Circuits	767
	E. N. Koleva and I. S. Kolev Technical University of Gabrovo, Bulgaria	
PO II.2	Temperature Profile of the Impulse Discharge	769
	I. P. Iliev and S. G. Gocheva-Ilieva* Technical University of Sofia, Bulgaria, Branch Plovdiv *University of Plovdiv, Bulgaria	
PO II.3	Simulation Investigation of Frequency Sensitive Digital Phase Detectors	773
	A. H. Yordanov and G. S. Mihov Technical University of Sofia, Bulgaria	
PO II.4	Voltage-Scaling D/A Converters – Analysis and Practical Design Considerations	777
	D. P. Dimitrov Melexis-Bulgaria Ltd, Sofia, Bulgaria	
PO II.5	Mechanical Properties of Thin Electrical Films	781
	S. Letskovska and P. Rahnev Burgas Free University, Burgas, Bulgaria	
PO II.6	An Improved IGBT Behavioral PSpice Macromodel	785
	Ts. Gr. Grigorova and K. K. Asparuhova Technical University of Sofia, Bulgaria	
PO II.7	A Stochastic Model of Gamma-Ray Irradiation Effects on Threshold Voltage of MOS Transistors	789
	M. T. Odalović and D. M. Petković Faculty of Science and Mathematics, Kosovska Mitrovica, Serbia	
PO II.8	Some Geometrical Considerations Connected with the Planetary Movement of the Substrate During Sputtering	793
	S. Pavlov and D. Parashkevov Assen Zlatarov University, Bourgas, Bulgaria	
PO II.9	Program Calculation of Thin Film Thickness in Case of Parallel Arranged Target – Substrate	797
	D. D. Parashkevov Assen Zlatarov University, Bourgas, Bulgaria	

PO III - ELECTRONIC COMPONENTS, SYSTEMS AND TECHNOLOGIES & INDUSTRIAL ELECTRONICS

PO III.1	Automatic Quality Classifiers of Food Products – Rate of the Speed Problems	803
	A. S. Georgiev, L. F. Kostadinova and R. N. Gabrova University of Food Technologies, Plovdiv, Bulgaria	
PO III.2	Computer-Aided Engineering with the help of OrCAD	807
	D. M. Kovatchev, E. Dimitrova and V. C. Valchev Technical University of Varna, Bulgaria	
PO III.3	Magnetron Dielectric Barrier Air Discharge at Low Frequency	811
	P. D. Dineff and D. N. Gospodinova Technical University of Sofia, Bulgaria	
PO III.4	Application of the CFD Method for Heat Transfer Simulation	815
	A. V. Andonova and N. M. Kafadarova Technical University of Sofia, Bulgaria	
PO III.5	Laser Modeling In Q-switch Regime	819
	I. Veselinovic, M. Sreckovic and B. Veselinovic* University of Belgrade, Serbia *Vinča Institute of Nuclear Sciences, Belgrade	
PO III.6	Modeling of Quantum Generators and Amplifiers on Semiconductor Materials	823
	B. Veselinović, M. Srećković*, I. Veselinović* and M. Vlajnić** Vinča Institute of Nuclear Sciences, Belgrade, Serbia * University of Belgrade, Serbia **YUBC System A.D., Belgrade, Serbia	

PO III.7	Analysis of Electrical and Thermal Characteristics of Thermal Cutoffs.....	827
	A. Prijić, Z. Prijić, B. Pešić, D. Pantić and S. Ristić University of Niš, Serbia	
PO III.8	Macromodel for CMOS Analogue Switches Temperature Effects Sensing.....	831
	I. M. Pandiev Technical University of Sofia, Bulgaria	
PO III.9	Microstructure and Optical Properties of ITO Thin Films Investigated for Heat Mirrors in Solar Collectors.....	835
	G. H. Dobrikov, M. M. Rassoovska, S. I. Boiadjiev, K. A. Gesheva*, P. S. Sharlandjiev** and A. Koserkova** Technical University of Sofia, Bulgaria *Bulgarian Academy of Sciences ** Acad. G. Bonchev, Sofia, Bulgaria	

PO IV - COMPUTER SYSTEMS AND INTERNET TECHNOLOGIES

PO IV.1	Automatic Weight Estimation Method for Multiple SVMs in Software Sensors Systems	841
	P. Ts. Andreeva and S. I. Vassileva Bulgarian Academy of Sciences, Sofia, Bulgaria	
PO IV.2	Improving Fairness for Pedestrian Users of CDMA-HDR Networks	845
	V. P. Hristov South West University, Blagoevgrad, Bulgaria	
PO IV.3	Web Application of Traveling Salesman Problem using Genetic Algorithms.....	849
	M. N. Karova, J. P. Petkova and S. P. Penev Technical University of Varna, Bulgaria	
PO IV.4	A Performance Study of Run-time Systems for Distributed Time Warp Simulation.....	853
	H. G. Valchanov, N. S. Ruskova and T. I. Ruskov Technical University of Varna, Bulgaria	
PO IV.5	Genetic Algorithms in Solving Multiobjective Optimization Problems	857
	H. I. Toshev and Ch. D. Korsemov Bulgarian Academy of Sciences, Sofia, Bulgaria	
PO IV.6	Applying Tabu - Search Heuristic for Software Clustering Problem	861
	V. T. Bozhikova and M. Ts. Stoeva Technical University of Varna, Bulgaria	
PO IV.7	A New Approach to Symbol Description of the Spatial Location of Extended Objects in Spatial Databases.....	865
	M. Stoeva and V. Bozhikova Technical University of Varna, Bulgaria	
PO IV.8	A Web-based Course for Development, Implementation and Administration of a Secure Portal within OracleAS Portal 10g.....	869
	V. R. Antonova and P. T. Antonov Technical University of Varna, Bulgaria	
PO IV.9	Models of e-business in Transportation.....	873
	D. D. Marković, B. V. Stanivuković and M. J. Dobrodolac University of Belgrade, Serbia	

PO V - CONTROL SYSTEMS & ROBOTICS

PO V.1	Application of Kalman Filtering Technique to Increase the Probability of Faults Detection in Test Equipment.....	879
	A. D. Tanev and A. Vl. Andonov Higher school of Transport, Sofia, Bulgaria	
PO V.2	Situational Control of RADAR.....	883
	I. E. Korobko Technical University of Sofia, Bulgaria	
PO V.3	Control Systems with Frequency Converters save Energy in Food Industry.....	887
	L. F. Kostadinova, R. N. Gabrova and A. S. Georgiev University of Food Technologies, Plovdiv, Bulgaria	
PO V.4	Multi-channel Wireless ECG System.....	891
	Y. S. Velchev Technical University of Sofia, Bulgaria	
PO V.5	Heart Rate Measurement System.....	895
	Y. S. Velchev Technical University of Sofia, Bulgaria	

PO V.6	Robust Estimators Based on the Two-Stage Method for Closed-Loop Identification	897
	N. R. Atanasov Technical University of Varna, Bulgaria	
PO V.7	Scalable Modular Control Architecture For Walking Machines	901
	M. S. Milushev, N. V. Krantov and V. Zerbe* Technical University of Sofia, Bulgaria *Technical University Ilmenau, Germany	
PO V.8	Evaluation of Fluidic Muscles for a Walking Machine Driver	905
	M. S. Milushev, D. I. Diakov, V. K. Georgieva and N. T. Pavlovic Technical University of Sofia, Bulgaria *University of Niš, Serbia	

SESSION MED. S

Medical Systems

BCI Mental Tasks Patterns Determination

Plamen K. Manoilov

Abstract – Brain computer interface (BCI) is an assistive device, which translates the user's wishes in device's commands. BCI is the only possibility for completely paralysed (locked-in) people to interact with their environment. When the subject performs different mental tasks his brain issues EEG signal with different patterns. Pattern recognition approach based BCIs classify the brain activity to different mental tasks and this way makes a multichannel control. In this paper the unique characteristics finding of 5 groups mental tasks is described.

Keywords – BCI, EEG analysis, mental task, pattern recognition, power spectrum

I. INTRODUCTION

Present day knowledge, about the functioning of the brain does not meet the case to guess the subject's thoughts after analyzing his EEG. BCI prototypes determine the intent of the user from a variety of different electrophysiological signals. They are translated in real time into commands that operate a computer display or other device [5]. Successful operation requires that the user encodes commands in these signals and that the BCI derives the commands from the signals. In some BCIs patterns are in a result of subject's mental load [1]. The subject performs different mental tasks, resulting in changes of the power of different frequencies in different scalp zones. The changes of the power are in large scale when the user is more concentrated. The comparison is made with the power spectrum of the subjects EEG during the performance of so called "Baseline task", task 1. The baseline task is defined like "mentally doing nothing". When the subject does nothing his alpha brain activity power has maximal values.

If the mental tasks are chosen properly, power spectrum changes for each of them are different or are issued by different spaces of the brain. This gives the possibility by the help of a classifier to bound the particular task with its power spectrum alteration (pattern). That type of devices are known as pattern recognition based BCIs. The pattern for each task is formed by the channels (electrodes) and frequencies where the most distinguishable changes occur.

II. EXPERIMENT'S DESCRIPTION

The study continues the work on a project for creating a BCI, started in Delft University of Technology, Delft, The Netherlands in 2004, supervised by professor drs dr Leon Rothkrantz, head of Man-Machine Interaction research group, Faculty of Electrical Engineering, Mathematics and Computer Science.

During the experiments a database with 40 sessions EEG data, around 20 minutes each, recorded from two subjects (male, 25 and 30) was prepared for use together with a tool for a statistical analysis ("R", "MATLAB").

The second stage was processing the EEG from the database and finding (if possible) a specific unique characteristic for every mental task. After classifying the tasks, some of them with more clear and well-expressed characteristics could be chosen for using in BCIs control.

The brain activity of α -range (8 – 13 Hz) was studied. All EEGs were recorded without any biofeedback. In this study only five different groups tasks are examined: "Imaginary figure rotation", task 8, "Hyperventilation", task 9, "Visual presentation of ...", task 3X, "Auditive presentation of ...", task 4X, "Visual and auditive presentation of ...", task 5X. Every two-digit task includes 4 subtasks: presentation of an "yellow triangle", task X0, presentation of a "green dot", task X2, presentation of a "red cross", task X4 and presentation of "blue lines", task X6.

The figures are presented to the subject visually on the computer screen and auditive from the loudspeakers. Every task is performed multiple times per session. Tasks follow each other in a pseudo-random order to avoid a "familiarization" of the subject. The experiment schedule has planned intervals between the tasks, where the subject is allowed to blink.

As a data acquisition system "TruScan 32 EEG" was used in the experiments. It includes EEG cap with 21 silver chloride electrodes, placed according to the international "10-20" system, EEG amplifier and EEG adapter. The needed low resistance between the contact electrodes - skin was improved by the use of an electro technical gel and was controlled during the recording process. The EEG signal was filtered and sampled at 256 Hz.

FireBird DBMS was used. Matlab was used as a data processing application. The connection between them is made by ODBC protocol.

Plamen K. Manoilov is with the Communication Technique and Technologies Department, RU "A. Kanchev", 8 Studentska Str., Rousse, Bulgaria, E-mail: pmanoilov@ecs.ru.acad.bg

III. EEG ANALYSIS

The preliminary selection goal is to determinate the frequencies and channels where the power spectrum changes most during the mental tasks performance according to (1). The comparison is done with the power spectrum of the baseline task.

$$D(k) = P_{av}^B(k) - P_{av}^R(k), \quad (1)$$

where

D - the power spectra difference.

P_{av}^B - the average power spectrum of the base task (task 1 or 2), calculated according to (2)

$$P_{av}^B = \frac{1}{M^B} \sum_{m=1}^{M^B} P^B(k, m) \quad (2)$$

P_{av}^R - average power spectrum of the running task (every task with exception of 1 and 2) according to (3)

$$P_{av}^R = \frac{1}{M^R} \sum_{m=1}^{M^R} P^R(k, m) \quad (3)$$

$P^B(k, m)$ and $P^R(k, m)$ - the power spectra of base and running tasks according to (4)

$$P(k, t) = G_D(k, t)G_D^*(k, t) \quad (4)$$

where

$$G_D(f, t) = \int_{-\infty}^{+\infty} x(t') g_D^*(t' - t) e^{-i2\pi f t'} dt' \quad (5)$$

is Gabor transform.

The time step is a half of the segment length - $0,5 \cdot s_l$.

M^B and M^R - the numbers of the EEG segments for the base and the running task. $M^B \neq M^R$ is possible.

$M = (2l / s_l) - 1$, where l - is the length of the analyzed section;

As the absolute powers differs along the channels, the relative difference between the powers is calculated, (6)

$$D(k)[\%] = \frac{P_{av}^B(k) - P_{av}^R(k)}{P_{av}^B(k)} 100 \quad (6)$$

To assess the electrooculographic (EOG) artefacts, and more precise subjects eye blinks, influence to the chosen frequency range of 8-13 Hz, their power spectrum was examined [2]. It was decided to cut the parts of EEG, containing blinks. Existed database is large enough. No important information might be lost. Selecting clean from EOG artefacts segments was easy to automate, because of the experiments schedule.

Duration of polluted by blink interval is user-dependent [3, 4]. For subject 1 it varies from approximately 0.8-0.2 s before and 1.9-1.5 s after the time of blink's max amplitude. For subject 2 values are respectively 1.1-0.2 s before and 1.9-1.5 s after the blink's max amplitude. This was used to cut properly the polluted sections.

Alpha rhythm amplitude is higher when the subject is in a physical rest state and a relative inactive mental state. It is blocked partially or completely by any mental effort.

Mu-rhythm is blocked partially or completely by the movement or a thought about a movement.

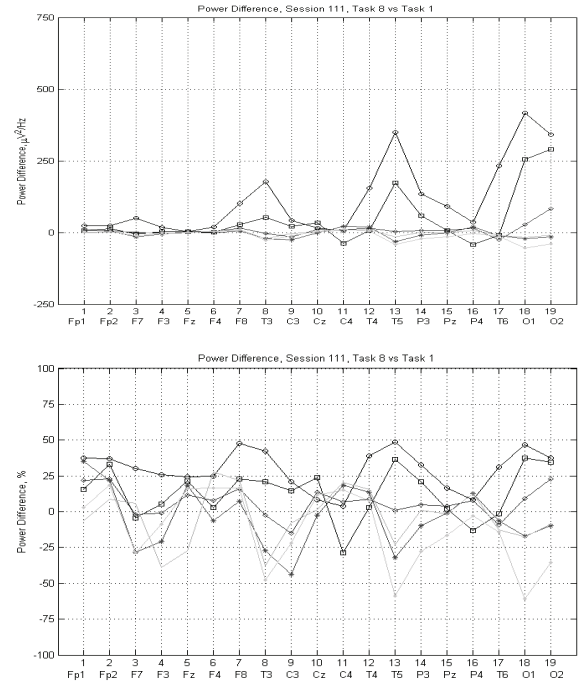


Fig. 1. Graphs of the absolute, $\mu V^2/Hz$, and the relative, %, difference between the power spectra of baseline task, 1, and task 8. Here and everywhere in this paper:

—○— 8 Hz, —□— 9 Hz, —◇— 10 Hz, —*— 11 Hz, —— 12 Hz, —— 13 Hz

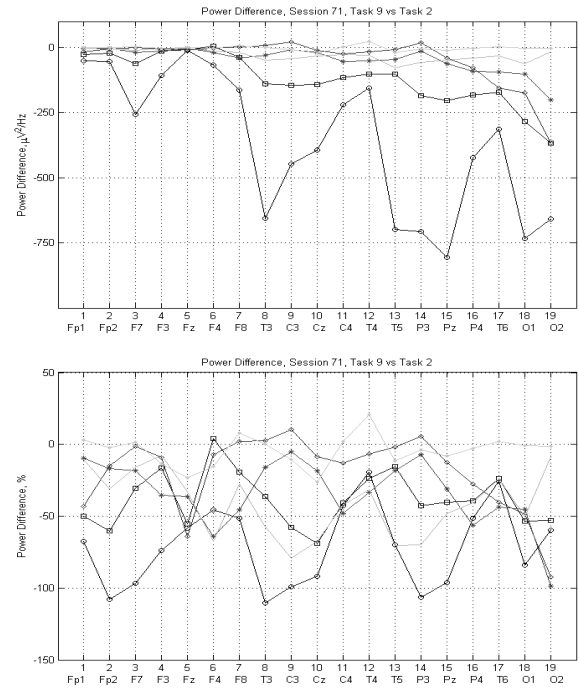


Fig. 2. Graphs of the absolute, $\mu V^2/Hz$, and the relative, %, difference between the power spectra of baseline task, 1, and task 9

Imaginary rotation, task 8, vs. baseline task, 1

Graphs of the power difference for task 8, “Imaginary figure rotation”, are shown in Fig. 1.

From the above graph one could see that the absolute difference between the powers of the baseline task 1 and task 8 rises from the frontal to the occipital parts of the scalp. Characteristic channels with noticeable variations are P3, T4, T5, T6, O1, O2. The graph in Fig.1, below, shows however, that the relative power difference is almost equal.

Results are summarized in Table 1. The characteristics for both subjects differ. The sensitive channels for subject 2 for α -rhythm are moved to the parietal part of the scalp, μ -rhythm appears more in the right part of the scalp.

Hyperventilation, task 9, vs. baseline task, 1

The result from the analysis of task 9 power difference, Fig. 2, is quite different. The variance between the powers of the baseline task 1 and task 9, hyperventilation, is negative. This result comes after a relative long (20-30s) ventilation of the lungs. It is impossible to meet this state in the normal human life, especially in locked-in person, with exception if it is not artificially provoked. The brain activity is clear expressed in the central and parietal parts of the scalp in the lowest frequencies of the range. Alterations above 50% could be noticed. There are differences in the spatial distribution between both subjects.

Visual presentation, tasks 3X, vs. baseline task, 1

The fourth presented objects has a similar influence on the subjects. The decreasing of the power is better expressed for tasks 30 and 34 (Visual presentation of an “yellow triangle” and a “red cross”). The presentation of a “green dot” gives the worst results-1,5 times less than the relative difference for subject 1.

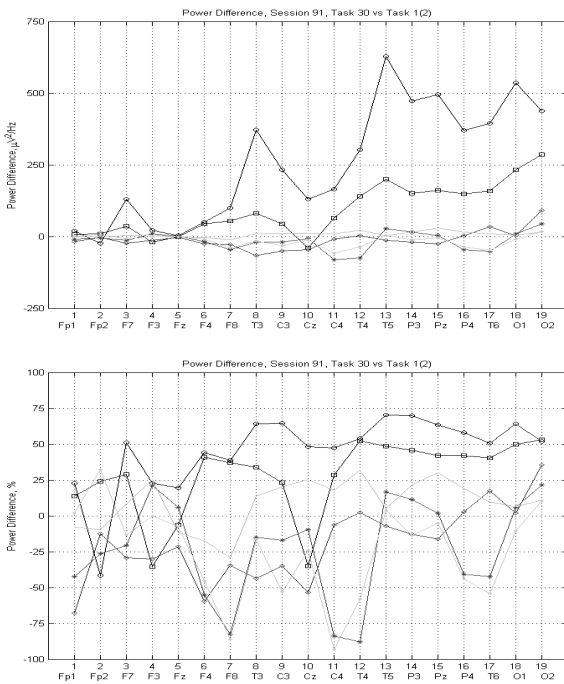


Fig. 3. Graphs of the absolute, $\mu V^2 / Hz$, and the relative, %, difference between the power spectra of baseline task, 1, and task 30

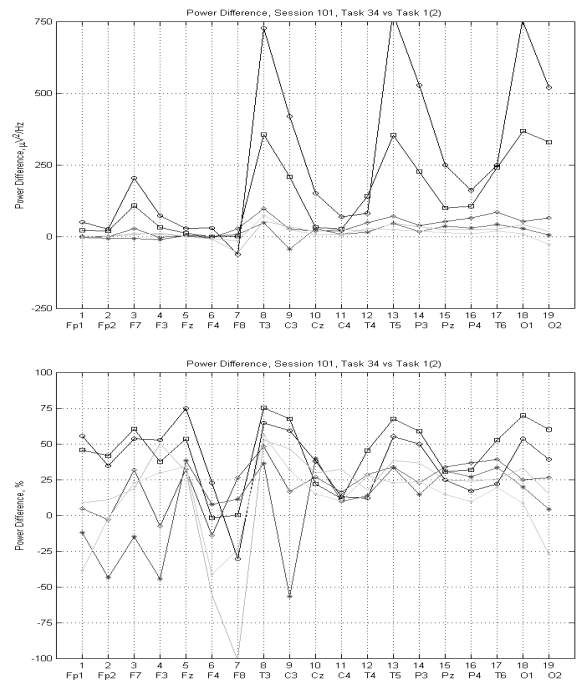


Fig. 4. Graphs of the absolute, $\mu V^2 / Hz$, and the relative, %, difference between the power spectra of baseline task, 1, and task 34

Subject 2 does not show noticeable difference in brain patterns for different presented objects. Sensitive frequencies are 1-2 Hz higher than for subject 1.

Audio presentation, tasks 4X, vs. baseline task, 1

Graphs for task 42 are shown in Fig. 5. The audio-presentation stimulates more slight reactions in both subjects.

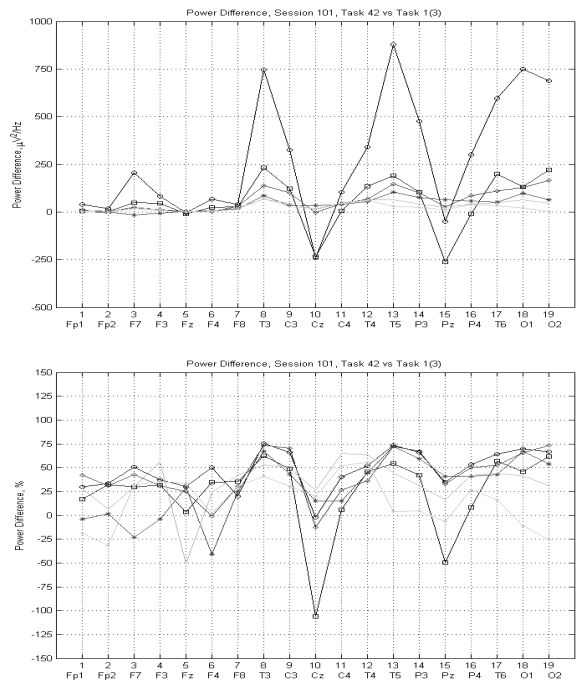


Fig. 5. Graphs of the absolute, $\mu V^2 / Hz$, and the relative, %, difference between the power spectra of baseline task, 1, and task 42

It does not have different characteristics for the different presented objects. An activity in the temporal lobe is noticed in T5 and T6 for subject 1 and in T6 for subject 2.

Audio-visual presentation, tasks 5X, vs baseline task, 1

The audio-visual presentation combines visual- and audio-presentations features. An activity in the temporal and the occipital part of the scalp is noticed.

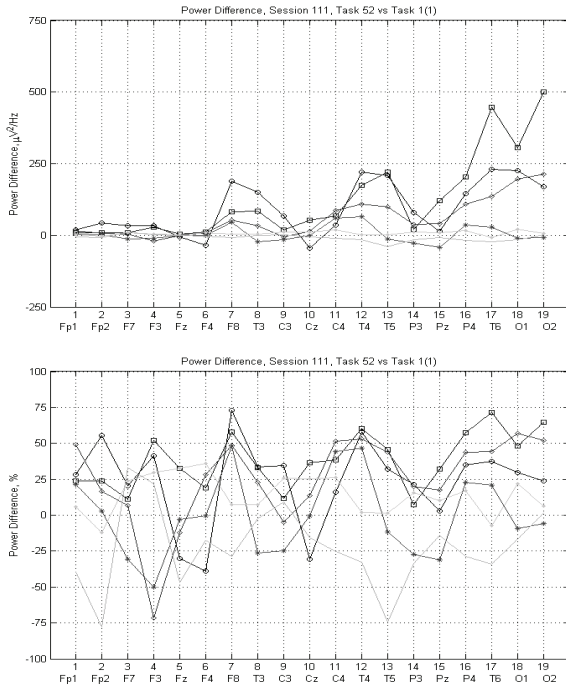


Fig. 6. Graphs of the absolute, $\mu V^2 / Hz$, and the relative, %, difference between the power spectra of baseline task, 1, and task 52

IV. CONCLUSIONS

The following conclusions could be made:

1. Unlike the other tasks, task 8, “Imaginary figure rotation”, alters μ -rhythm and α -rhythm in frontal placed electrodes. It has an unique characteristic. User should use to achieve this state for a short time.
2. In comparison to the other tasks, the “Hyperventilation”, task 9, is not an ordinary one. To achieve the hyperventilation state the subject have to bread deeply a long time. The task is not useful for a trivial control. The well expressed and quite different characteristics of task 9 could be used to switch on/off the BCI. As this state does not exist in the normal life, no errors are possible.
3. Power spectra changes in a result of mental tasks performance are individual for each subject. Control of proper frequencies for every user should be foreseen in the BCI.
4. The presentation of different geometrical figures and colors does not result in different patterns, but has more or less marked patterns for each subject. Signal colors, which tease the subject, give more clear

expressed patterns. Selection of the proper figure and color for every subject is necessary to achieve the best results.

5. From the three group of tasks 3X, 4X, 5X, the “Visual presentation of...” is the most useful for using in BCI. The characteristics could be achieved by self-concentration. No outside assistance is needed.

On the next stage of the work the stability of the characteristics during the performance of each mental task will be studied. After the time interval of the best expressed pattern is determined the final mental task selection could be done.

TABLE I
MENTAL TASKS CHARACTERISTICS SUMMARY

Task	Subj.	Rhythm-Chann:Frequency[Hz]
Imaginary figure rotation, task 8	1	$\alpha - F8, P3, T4, T5, T6, O1, O2 : 8, 9$
	2	$\mu - C3, P3 : 9$
Hyperventilation, task 9	1	$\alpha - F8, P3, Pz, P4, T6 : 9-11$
	2	$\mu - C3, Cz, C4, P3, P4 : 9-11$
Visual presentation, tasks 30, 32, 34, 36	1	$\alpha - Fp2, C3, Cz, P3, Pz, P4, T3 : 8$
	2	$\alpha - Fp1, F3, Fz, F4, C3, Cz, P3, Pz, P4, T6 : 8, 9, 10$
Audio presentation, tasks 40, 42, 44, 46	1	$\alpha - P3, T5, T6, O1, O2 : 8, 9$
	2	$\alpha - O1, O2 : 9, 10$
Audio-visual presentation, tasks 50, 52, 54, 56	1	$\alpha - T5, T6 : 8-11$
	2	$\alpha - T6 : 9-11$

REFERENCES

- [1] Babiloni F., F. Cincotti, L. Lazzarini, J. Millan, J. Mourino, M. Varsta, J. Heikkinen, L. Bianchi, M. G. Marciani, Linear classification of low-resolution EEG patterns produced by imagined hand movements, IEEE Transactions on Rehabilitation Engineering, vol. 8(2), 2000, pp. 186–188.
- [2] Manoilov P. K., EEG Eye-Blinking Artefacts Power Spectrum Analysis, Proceedings of the International Conference on Computer Systems and Technologies CompSysTech’06, V.Tarnovo, Bulgaria, 15-16 June, 2006, pp. IIIA.3-1—IIIA.3-5.
- [3] Manoilov P. K., Electroencephalogram electrooculographic artefacts analysis, Proceedings of the National conference with an International participation, ELECTRONICS’2006, 1-2 June, 2006 pp. 156-161.
- [4] Manoilov P. K., M. P. Iliev, EOG artefacts’ duration analysis, Proceedings of the Fifteenth International Scientific and Applied Science Conference Electronics’2006, September 2006, Sozopol, Bulgaria, pp. 98-103.
- [5] Wolpaw J. R., Brain-computer interface technology: A Review of the First International Meeting, IEEE Transactions on Rehabilitation Engineering, vol. 8, 2000, pp. 164–173.

An Investigation on Signals in Magnetocardiography

Dimiter Tz. Dimitrov

Abstract – The main purpose of this paper is to discuss the lead systems currently being applied in detecting the equivalent magnetic dipole of the heart, and to discuss briefly on the relationship between signals in the cases of ECG-MCG

Keywords– Magnetocardiography, elektrokardiography

I. INTRODUCTION

It's well known that in electrocardiography, the mapping of the distribution of the electric potential on the surface of the thorax has been applied since the first detection of the human electrocardiogram. It's similarly in magnetocardiography. Though the magnetic field is a vector quantity and has therefore three components at each location in space, the mapping method has usually been applied for registering only one component (the x -component) of the magnetic field around the thorax. The mapping has usually been done on a certain grid. In lead field theory, it may be shown that lead systems used in mapping often introduce a distortion of the signal that necessarily originates from the in homogeneities of the volume conductor. (The situation is the same as in mapping the electric potential field.) Some of these magnetic measurements may also be realized with a similar sensitivity distribution by use of electric measurements with a higher signal-to-noise ratio and with easier application (Fig.1).

II. METHODS OF MAGNETOCARDIOGRAPHY

In addition to the analysis of the parameters of the MCG signals, recorded either by determining the equivalent magnetic dipole or by the mapping method, several other techniques have also been applied. Of these the localization of cardiac sources is briefly discussed here. The localization of cardiac electric sources is a highly desired objective since it may enable the localization of cardiac abnormalities including those of abnormal conduction pathways. These may cause dangerous arrhythmias or contribute to a reduction in cardiac performance. Abnormal conduction pathways, for example, conduct electric activity from the atrial muscle directly to the ventricular muscle, bypassing the AV junction. This is called Wolff-Parkinson-White or(WPW)

syndrome.If a retrograde conduction pathway also exists from the ventricular mass back to the atrial mass, this reentry path may result in tachycardia. If the symptoms due to this abnormal conduction do not respond to drugs, then the tissue forming the abnormal pathway must be removed surgically, hence requiring prior localization. In clinical practice the conduction pathways are at present localized invasively with a catheter in an electrophysiological study, which may last several hours. This time may be shortened by first making an initial noninvasive localization of the equivalent source of the conduction pathway from the electric potentials on the surface of the thorax.

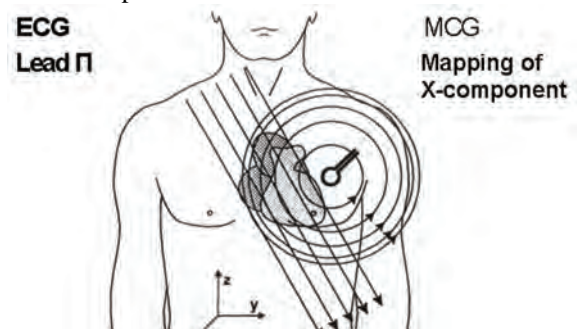


Fig.1 The similarity between the lead fields of certain electric and magnetic leads are illustrated. If the magnetic field is measured in such an orientation (in the x direction in this example) and location, that the symmetry axis is located far from the region of the heart, the magnetic lead field in the heart's region is similar to the electric lead field of a lead, which is oriented normal to the symmetry axis of the magnetic lead. This similarity may also be verified from the similarity of the corresponding detected signals.

In magnetocardiographic localization the goal is to introduce an alternative to the electric localization using the magnetic methods. Utilization of this complementary technique may improve the overall localization accuracy. The magnetocardiographic localization is usually made by mapping the x component of the cardiac magnetic field at 30-40 locations on the anterior surface of the thorax with consecutive measurements using a single-channel magnetometer or simultaneously using a multichannel magnetometer. The dipole model is the most obvious to use as a source model for the localization methods. The accuracy of the magnetocardiographic localization depends to a great extent on the accuracy of the volume conductor model applied. The accuracy of the magnetocardiographic localization of the origin of an abnormal conduction pathway is of the order of 2-3

Dimiter Tz. Dimitrov is from the Faculty of Communication Technique and Technologies ,Technical University of Sofia,Bulgaria,1000 Sofia, 8, Kliment Ohridsky, E-mail: dcd@tu-sofia.bg

cm. Because magnetocardiographic localization has been shown to have greater complexity and costs as compared to the electric method, the magnetic method does not, at present, compete with the electric method in clinical practice

III. METHODS FOR DETECTING OF MAGNETIC HEART VECTOR

It's possible to assume that the heart is a spherical conducting region between the insulating lungs. For the XYZ and ABC lead systems it would be enough to assume cylindrical symmetry for each component, which leads to a spherically symmetric volume conductor for the three orthogonal measurements. The y and z components of the unipositional lead system require, however, an assumption of a conducting spherical heart region inside the insulating lungs. This assumption forces the lead fields to flow tangentially within the heart region. This is called a *self-centering* effect. The magnetic dipole moment of a volume current distribution \vec{J} in an infinite, homogeneous volume conductor with respect to an arbitrary origin can be defined as:

$$\vec{m} = \frac{1}{2} \int \vec{r} \times \vec{J} dv \tag{1}$$

where:

\vec{m} is the magnetic dipole moment;

\vec{J} is the density of volume current distribution

\vec{r} is the radius of an arbitrary current contour

v is the volume of calculation

The lead system that detects this magnetic dipole moment has three orthogonal components. Each component produces, when energized with the reciprocal current, a linear, homogeneous, reciprocal magnetic field \vec{B}_{ML} over the source region. These reciprocal magnetic fields induce lead fields \vec{J}_{LM} in which the lead current is directed tangentially, and its density is proportional to the distance from the symmetry axis (Fig.2).

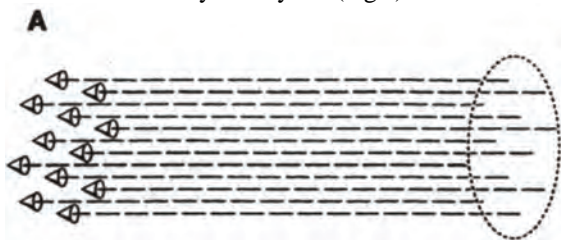


Fig.2A One component of the reciprocal magnetic field \vec{B}_{ML}

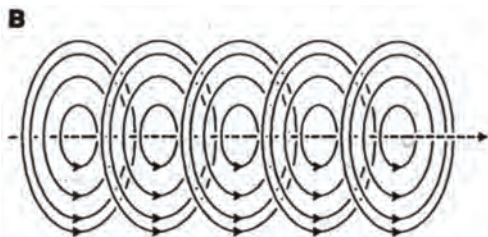


Fig.2(B) One component of the lead field \vec{J}_{LM} of an ideal lead

system detecting the magnetic dipole moment of a volume source. Three such orthogonal components form the complete lead system.

A natural method to realize such a lead system is to make either unipolar or bipolar measurements on the coordinate axes (Fig.3).

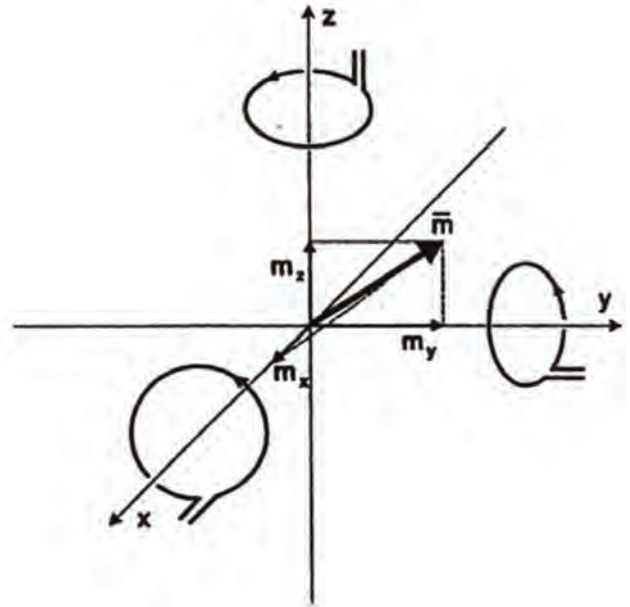


Fig.3. A natural method to measure the magnetic dipole moment of a source locating in the origin is to measure (x, y, z) components of the magnetic field on corresponding coordinate axes.

IV. COMPARISON BETWEEN MCG AND ECG

It can be noted that the bioelectric activity in the heart is responsible for the generation of a source current density, namely $\vec{J}(x, y, z, t)$. As stated before, both the electric and magnetic fields are generated by this same source which, in turn, responds to the electrophysiological phenomenon of depolarization and repolarization of cardiac muscle cells. A logical question arises as to whether any new information might be provided by the magnetic field measurement that is not available from the electric potential field measurement. While it appears, on certain theoretical grounds, that the electric and magnetic fields are not fully independent, other reasons exist for the use of magnetocardiography. These may be divided into *theoretical* and *technical* features. The former ones are based on the universal properties of biomagnetic fields and the latter ones to the technical features of the instrumentation. There are some differences between the plots of potential's curves VMCG and VECG in the cases of MCG and ECG (Fig.4)

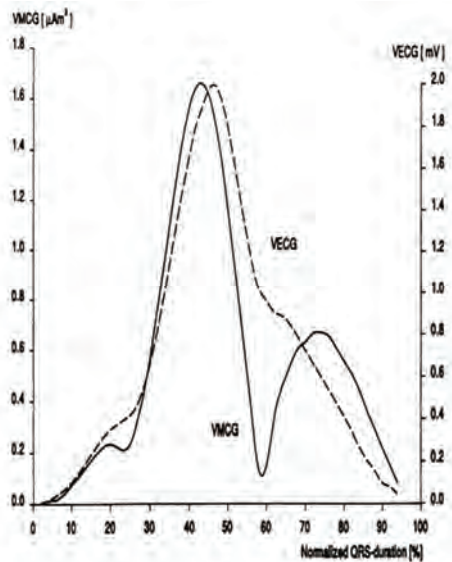


Fig.4 Simultaneous plots of the experimental potential's curves during the QRS complex in the cases of MCG (solid curve) and ECG (dashed curve).

A. Theoretical Advantages of MCG

First, the nature of lead fields of electric and magnetic leads is quite different. Specifically, the ideal magnetic lead is sensitive only to tangential components of activation sources and therefore should be particularly responsive to abnormalities in activation (since normal activation sources are primarily radial). Furthermore, the tangential components are attenuated in the ECG because of the Brody effect. Another factor is that the signal-to-noise ratio for the electrical and magnetic recordings are affected by different factors, so there could be a practical advantage in using one over the other despite their similarities in content.

Second, the magnetic permeability of the tissue is that of free space. Therefore the sensitivity of the MCG is not affected by the high electric resistivity of lung tissue. This makes it possible to record with MCG from the posterior side of the thorax the electric activity of the posterior side of the heart. That is difficult to do with surface ECG electrodes, but is possible to do with an esophageal electrode which is, however, inconvenient for the patient. Another important application of this feature is the recording of the fetal MCG. During a certain phase of pregnancy the fetal ECG is very difficult to record because of the insulating fat layer in the fetus.

B. Technical Advantages of MCG

First, a possibly important distinction is that the magnetic detector is not in contact with the subject. For mass screening, there is an advantage in not requiring skin preparation and attachment of electrodes. (In the case of patients with skin

burns this is a crucial advantage.)

Second, the SQUID (Superconducting QUantum Interference Device) magnetometer is readily capable of measuring DC signals. These are associated with the S-T segment shift in myocardial infarction. Such signals can be obtained electrically only with great difficulty. Although the clinical value has yet to be demonstrated, it should be noted that because of the difficulty in performing electrical measurements, there have been few investigations of DC potentials.

V. CONCLUSION

1. It's clear that application of the MCG-signals in medical diagnostic has many advantages:

a/ The ECG measures the electric potential field, which is a *scalar* field. Therefore, one measurement at each measurement location is enough. The MCG measures the magnetic field, which is a *vector* field. Therefore, MCG measurements should provide a vector description - that is, three orthogonal measurements at each measurement location- to get all available information.

b/ In MCG we are interested in the electric activation of the whole cardiac muscle, not only on its anterior surface. Therefore, to compensate the proximity effect, MCG measurements should be done symmetrically both on the anterior and on the posterior side of the thorax. Actually, the posterior measurement of the MCG increases the information especially on the posterior side of the heart, where the sensitivity of all ECG leads is low due to the insulating effect of the lungs. (As noted earlier, in the measurement of the MEG, we are mainly interested in the electric activation of the surface of the brain, the cortex. Therefore a unipolar measurement is more relevant in measuring the MEG.)

c/ On the basis of the existing literature on the MCG, non symmetric unipositional measurement seems to give the same diagnostic performance as the mapping of the x component of the magnetic field on the anterior side of the thorax.

2. A *combination* of electric and magnetic measurements (i.e., ECG and MCG) gives a better diagnostic performance than either method alone with the same number of diagnostic parameters, because the number of independent measurements doubles.

REFERENCES

- [1] P.Karp P. Cardiomagnetism. In Biomagnetism, Proc. Third Internat. Workshop On Biomagn-tism, Berlin, May 1980, pp. 219-58,
- [2] Hristov, V., and V. Vatchkov, Web based system for microscope observation with structural analyzer EPIQUANT, Engineering Science Magazine, 2006, No 2, pp. 17-24
- [3] Hristov, V. THE ZIGBEE WIRELESS NETWORKS: A REALIZATION, Proc. of the Conference FMNS'05, Blagoevgrad, 9-11 June 2005, vol. 1, pp. 136- 143

This page intentionally left blank.

A Stimulation of Neural Tissue by Pulse Magnetic Signals

Dimiter Tz. Dimitrov

Abstract – In this paper a theoretical and experimental investigation on stimulation of neural tissue by pulse magnetic signals is described. The experimental investigation has been done using appropriate circuit. A comparison between direct electrical stimulation of neural tissue and stimulation of neural tissue by pulse magnetic signals is done with respective conclusions and recommendations. An optimisation of parameters of used pulse magnetic signals for stimulation is done, also.

Keywords – Magnetic stimulation, neural tissue, pulse magnetic signals

I. INTRODUCTION

It's well known that the origin of the biomagnetic field is the electric activity of biological tissue. This bioelectric activity produces an electric current in the volume conductor which induces the biomagnetic field. This correlation between the bioelectric and biomagnetic phenomena is, of course, not limited to the generation of the bioelectric and biomagnetic fields by the same bioelectric sources. This correlation also arises in the stimulation of biological tissue. Magnetic stimulation is a method for stimulating excitable tissue with an electric current induced by an external time-varying magnetic field. It is important to note here that, as in the electric and magnetic detection of the bioelectric activity of excitable tissues, both the electric and the magnetic stimulation methods excite the membrane with electric current. The former does that directly, but the latter does it with the electric current which is induced within the volume conductor by the time-varying applied magnetic field. The reason for using a time-varying magnetic field to induce the stimulating current is, on the one hand, the different distribution of stimulating current and, on the other hand, the fact that the magnetic field penetrates unattenuated through such regions as the electrically insulating skull. This makes it possible to avoid a high density of stimulating current at the scalp in stimulating the central nervous system and thus avoid pain sensation. Also, no physical contact of the stimulating coil and the target tissue is required, unlike with electric stimulation.

II. THE DESIGN OF STIMULATOR COILS

A magnetic stimulator includes a coil that is placed on the surface of the skin. To induce a current into the underlying tissue, a strong and rapidly changing magnetic field must be generated by the coil. In practice, this is generated by first charging a large capacitor to a high voltage and then discharging it with a thyristor switch through a coil. The principle of a magnetic stimulator is illustrated in Fig.1. The magnitude of induced electromotive force (emf) - e is proportional to the rate of change of current, dl/dt and to the inductance of the coil L . The term dl/dt depends on the speed with which the capacitors are discharged; the latter is increased by use of a fast solid-state switch (i.e., fast thyristor) and minimal wiring length. Inductance L is determined by the geometry and constitutive property of the medium. The principal factors for the coil system are the shape of the coil, the number of turns on the coil, and the permeability of the core. For typical coils used in physiological magnetic stimulation, the inductance may be calculated from the following equations.

III. CURRENT DISTRIBUTION IN MAGNETIC STIMULATION

The magnetic permeability of biological tissue is approximately that of a vacuum. Therefore the tissue does not have any noticeable effect on the magnetic field itself. The rapidly changing field of the magnetic impulse induces electric current in the tissue, which produces the stimulation. Owing to the reciprocity theorem, the current density distribution of a magnetic stimulator is the same as the sensitivity distribution of such a magnetic detector having a similar construction. It's necessary to note that in the lead field theory, the reciprocal energization equals the application of stimulating energy. The distribution of the current density in magnetic stimulation may be calculated using the method introduced by Malmivuo (1976) and later applied for the MEG (Malmivuo, 1980). Two cases of application of single coil and quadrupolar coil configuration are described below.

Dimiter Tz. Dimitrov is from the Faculty of Communication Technique and Technologies, Technical University of Sofia, Bulgaria, 1000 Sofia, 8, Kliment Ohridsky, E-mail: dcd@tu-sofia.bg

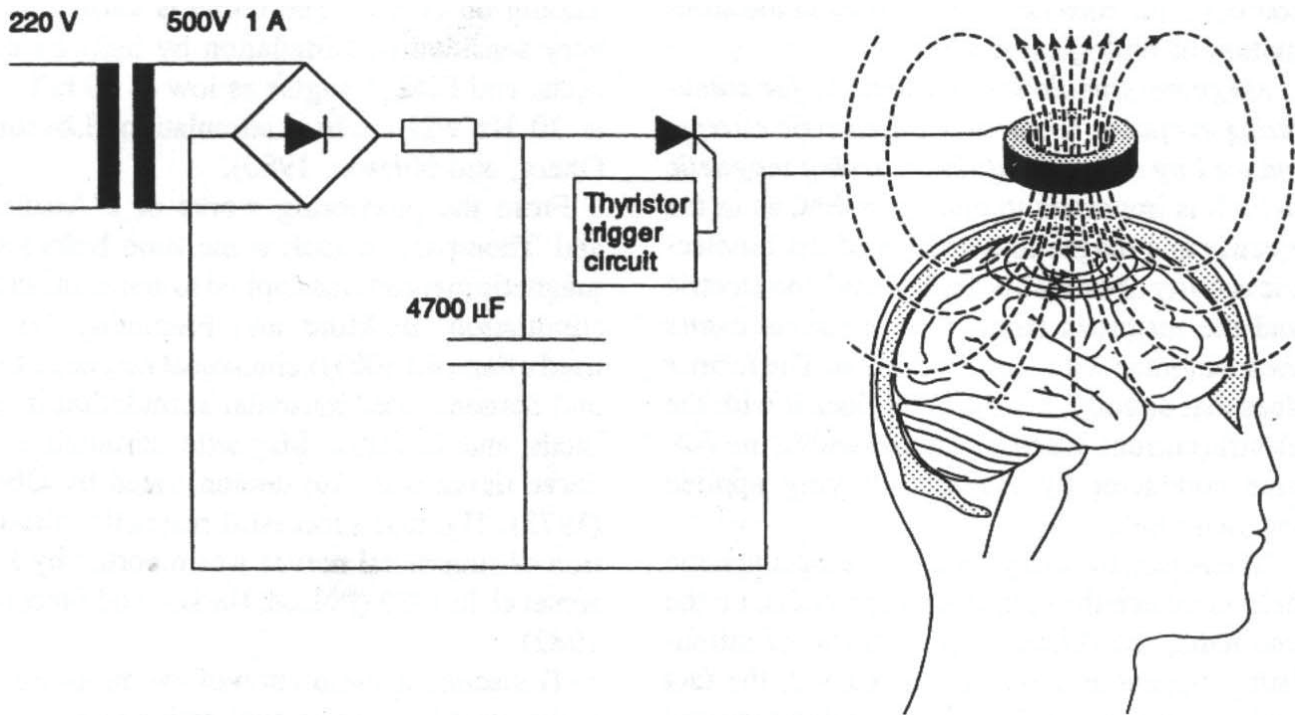


Fig.1 The principle of the magnetic stimulator

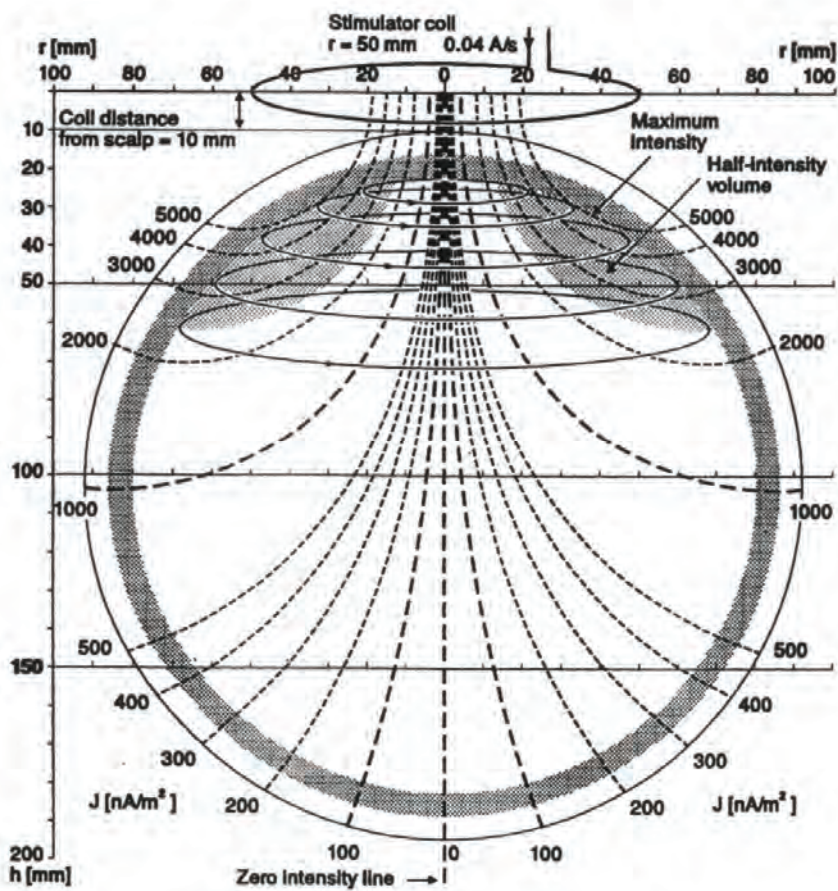


Fig.2. Isointensity lines and half-intensity volume for a stimulation coil with 50mm radius. The distance of the coil plane from the scalp is 10mm

A. Single Coil

The current distribution of a single coil, producing a dipolar field, is presented on fig.2, which illustrates the isointensity lines and half-intensity volume for a coil with a 50 mm radius. The concepts of isointensity line and half-intensity volume are reciprocal to the isosensitivity line and half-sensitivity volume. Because of cylindrical symmetry the isointensity lines coincide with the magnetic field lines.

B. Quadrupolar Coil Configuration

The coils can be equipped with cores of highly permeable material. One advantage of this arrangement is that the magnetic field that is produced is better focused in the desired location. Constructing the permeable core in the form of the letter V results in the establishment of a quadrupolar magnetic field source. With aquadrupolar magnetic field, the stimulating electric current field in the tissue has a linear instead of circular form. In some applications the result is more effective stimulation. On the other hand, a quadrupolar field decreases as a function of distance faster than that of a dipolar coil. Therefore, the dipolar coil is more effective in stimulating objects that are located deeper within the tissue.

IV. STIMULUS PULSE

The experimental stimulator (Fig.1) has a capacitor construction equaling a capacitance of $4760 \mu F$. This was charged to 90-260 V and then discharged by thyristor through the stimulating coil. The result was a magnetic field pulse of 0.1-0.2 T, 5 mm away from the coil. The length of the magnetic field pulse was of the order of 150-300 μs . The energy W which is required to stimulate tissue is proportional to the square of the corresponding magnetic induction B . According to Faraday's induction law, this magnetic field is in turn approximately proportional to the product of the electric field magnitude E and the pulse duration t .

$$W \propto B^2 \propto E^2 t^2 \quad (1)$$

where:

- W is the energy required to stimulate tissue
- B is the magnetic induction
- E is the electric intensity
- t is the pulse duration

The effectiveness of the stimulator with respect to energy transfer is proportional to the square root of the magnetic energy stored in the coil when the current in the coil reaches its maximum value. A simple model of a nerve fiber is to regard

each node as a leaky capacitor that has to be charged. Measurements with electrical stimulation indicate that the time constant of this leaky capacitor is of the order of 150-300 μs . Therefore, for effective stimulation the current pulse into the node should be shorter than this. For a short pulse in the coil less energy is required, but obviously there is a lower limit too.

V. ACTIVATION OF EXCITABLE TISSUE BY TIME-VARYING MAGNETIC SIGNALS

The actual stimulation of excitable tissue by a time-varying magnetic field results from the flow of induced current across membranes. Without such flow a depolarization is not produced and excitation cannot result. Unfortunately, one cannot examine this question in a general sense but rather must look at specific geometries and structures. To date this has been done only for a single nerve fiber in a uniform conducting medium with a stimulating coil whose plane is parallel to the fiber. In the model examined by Roth and Bassar,

the nerve is assumed to be unmyelinated, infinite in extent, and lying in a uniform unbounded conducting medium, the membrane described by Hodgkin-Huxley equations. The transmembrane voltage V_m is shown to satisfy the equation (2):

$$\lambda^2 \frac{\partial^2 V_m}{\partial x^2} - V_m = \tau \frac{\partial V_m}{\partial t} + \lambda^2 \frac{\partial E_x}{\partial x} \quad (2)$$

where:

- V_m is transmembrane voltage
- λ is the membrane space constant
- τ is the membrane time constant
- x is the orientation of the fiber
- E_x is x-component of the magnetically induced electric intensity (proportional to the x component of induced current density)

It is interesting that it is the axial derivative of this field that is the driving force for an induced voltage. For a uniform system in which end effects can be ignored, excitation will arise near the site of maximum changing current and not maximum current itself. In the experimental investigation the coil lies in the xy plane with its center at $x = 0, y = 0$, while the fiber is parallel to the x axis and

at $y = 2,5\text{cm}$ and $z = 1,0\text{cm}$. They consider a coil with radius of 2.5 cm wound from 30 turns of wire of 1.0 mm radius. The coil, located at a distance of 1.0 cm from the fiber, is a constituent of an RLC circuit; and the time variation is that resulting from a voltage step input. Assuming $C = 200\mu\text{F}$ and $R = 3\Omega$ an overdamped current waveform results. From the resulting stimulation it is found that excitation results at $x = 2.0\text{cm}$ (or 2.0 cm, depending on the direction of the magnetic field) which corresponds to the position of maximum $\partial E_x / \partial x$. The threshold applied voltage for excitation is determined to be 30 V. (This results in a peak coil current of around 10A.) These design conditions could be readily realized.

Stimulators with short risetimes ($< 60\mu\text{s}$) need only half the stored energy of those with longer risetimes ($> 180\mu\text{s}$). The use of a variable field risetime also enables membrane time constant to be measured and this may contain useful diagnostic information.

VI.CONCLUSION

It's possible to do the next conclusions after theoretical and experimental investigations described above:

1.The magnetic stimulation can be applied to nervous stimulation either centrally or peripherally.

2.The main benefit of magnetic stimulation is that the stimulating current density is not concentrated at the skin, as in electric stimulation, but is more equally distributed within the tissue. This is true especially in transcranial magnetic stimulation of the brain, where the high electric resistivity of the skull does not have any effect on the distribution of the stimulating current.

3.Another benefit of the magnetic stimulation method is that the stimulator does not have direct skin contact. This is a benefit in the sterile operation theater environment.

4.It may be predicted that the magnetic stimulation can be applied particularly to the stimulation of cortical areas, because in electric stimulation it is difficult to produce concentrated stimulating current density distributions in the cortical region and to avoid high current densities on the scalp.

REFERENCES

- [1] D.Dimitrov, M.Dontschewa „Computer modelling from magnetic field“, 4.Intern.Konferen „Computer Aided Engineering Education“, 13.-15.09.1995, Krakow, 1995
- [2] B D.Dimitrov, M.Dontschewa, M.Nikolova „Computer simulation of 3D-Signals of Nemeks Apparat in Physiotherapie“, 7. Multimedia – Fachtagung, 29.-01.10.1997, Dortmund, 1997
- [3] M.Dontschewa, H.-P. Schade „Leistungsfähiges lowcost multimediales Präsentationssystem. Bestandteile, Voraussetzungen“, 39.IWK, 27.-30.09.1994, Band 1, S. 384, Ilmenau,1994
- [4] Barker AT, Freeston IL, Garnham CW (1990): Measurement of cortical and peripheral neural membrane time constant in man using magnetic nerve stimulation. *J. Physiol. (Land.)* 423: 66.
- [5] Barker AT, Freeston IL, Jalinous R, Merton PA, Morton HB (1985): Magnetic stimulation of the human brain. *J. Physiol. (Land.)* 369: 3P.
- [6] Dimitrov,D.Medical Information Systems, handbook, Technical University of Sofia, 2005

Eye-Blinking Artefacts' Duration Analysis

Plamen Manoilov

Abstract – The artefacts impede the analysis of the electroencephalogram's (EEG) signal and should be handled properly. The most common and characteristic kinds of artefacts are the electrooculographic (EOG) ones, especially subject's eye blinks. In this paper an analysis of the duration of the EEG section, polluted by eye blinking artefacts is described with a connection of using the EEG for brain-computer interface (BCI), working with α - and μ -rhythms (range 8-13 Hz) brain potentials.

Keywords – BCI, blink artefact, EEG analysis, EOG, power spectrum

I. INTRODUCTION

A direct Brain Computer Interface (BCI) is an assistive device that accepts commands directly from the human brain without requiring any physical movement. The ultimate goal of such an interface is to provide effective communication without using the normal neuromuscular output pathways of the brain, but by accepting commands directly encoded in the neurophysiological signals. BCI should be able to detect user's wishes and commands while the user remains silent and immobilized.

For people who are locked-in after having lost all voluntary muscle control due to advanced amyotrophic lateral sclerosis, brainstem stroke or muscular dystrophy, BCI may be their only means of communication with the environment. Obviously, brain-computer communication is vital for people with such severe motor disabilities to increase their quality of life.

BCI may be as useful for people without any disabilities too. In the Alternative Control Technology (ACT) program of the US Air Force Research Laboratory [11] they use EEG to achieve hands free control by US military pilots.

To be as effective as possible, an ideal BCI should allow the user to determine when a command is to be initiated, provide multiple independently controllable channels, and support high information transfer rates. It is unlikely that an ideal BCI will be available in the near future, but a simple reliable interface providing single switch control would also be beneficial for locked-in patients.

The majority of research on human brain-computer communication has been performed using

electroencephalographic [1, 5, 6] (EEG) recordings which are well studied, easily available, and noninvasive. The less widely used electrocorticogram (ECoG) [4] is only available if subjects require electrode implantation on the cortical surface for clinical treatment or evaluation, and research access could be scheduled around clinical activities. Compared to EEG, ECoG recordings have less vulnerability to artefacts, superior spatial resolution, giving ECoG the potential to allow brain-computer communication with greater functionality, although a surgical risk exists at every time.

Designing a BCI system one can choose from a variety of features that may be useful for classifying brain activity, recorded during mental tasks performance. The EEG is measured, sampled, and next used for a communication. Depending on the BCI, particular preprocessing and feature extraction methods are applied to the EEG sample(s) 1-1.5 s of length. It is then possible to detect the task-specific EEG signals or patterns from the EEG samples, with a certain level of accuracy. A classifier that could be Statistical Model Neural Network (SMNN), Hidden Markov Models (HMM) or variations of Linear Discriminant Analysis (LDA) then classifies these features.

EOG stands for electro-oculographic artefacts, which appear in the EEG as a result of subject's eyes moving and blinking. Eye blink artefacts are easy to distinguish. In time domain they show enormous high amplitude relative to the other EEG signal and supposed could have an influence on the control.

II. PROBLEM STATEMENT AND STUDY DESCRIPTION

This study is done during a work on a project for creating a BCI, started in Delft University of Technology, The Netherlands in 2004. Professor drs dr Leon Rothkrantz, head of Man-Machine Interaction research group, Faculty of Electrical Engineering, Mathematics and Computer Science supervised the project.

During the experiments the subjects performed different mental tasks, among them mental rotation, motor imaginary, mathematical calculations, visual presentations etc., issuing different patterns in mu (μ) and alpha (α) rhythmic brain activity frequency ranges, which after a successful classification could be used for building a BCI.

In a result of the experiments a database, which contains 40 sessions EEG data, around 20 minutes each, recorded from two subjects (male, 25 and 30) was prepared for use together with a tool for a statistical analysis ("R", "MATLAB"). Second stage was processing the EEG from the database and

Plamen K. Manoilov is with the Communication Technique and Technologies Department, RU "A. Kanchev", 8 Studentska Str., Rousse, Bulgaria, E-mail: pmanoilov@ecs.ru.acad.bg

finding (if possible) a specific pattern for every mental task. After classifying the tasks, some of them with more clear and well-expressed pattern could be chosen for using for BCIs control. One of the questions to be solved was how to deal with the subject's eyes' blinks caused EOG artefacts.

Sources exist [1], where the researches process the data, containing eye-blinks. From other side, other sources exist [6, 7], where is stated, that eye-blinks could lead to errors in BCIs research and work. The decision was taken to study the power spectrum of the EOG artefacts and define their influence on EEG in connection with the chosen working frequency range.

After this study was done [9], the conclusion was made that the EOG artefacts influence on EEG range 8-13 Hz is significant and they should be eliminated from the data before the feature extraction. For further data processing a decision was taken first to cut the blinks and only after that process the data. Even doing this action by hand, the question about the length of the polluted by the eye-blink segments of data arises.

Some authors [3] simply omit the trials where they discover eye blinks. They achieve this automatically by linearly detrending and removing those time series whose maximum, rectified EOG amplitude, exceeded a threshold. If the blink appears at the end of a trial, its influence could contaminate the next trial. Segments for processing are 1-1.5 s long. Blink influence could last longer. From other side, cutting blindly long segments with blinks will discard useful parts of EEG and slow down BCIs work.

Other author [2], Fig. 1, recognizes and marks the blinks by using parameters of the EEG waveform where it has the highest amplitude. Later the marked EEGs are intended to be used by medical doctors. Study about the length of the polluted by blinks segments is not reported.

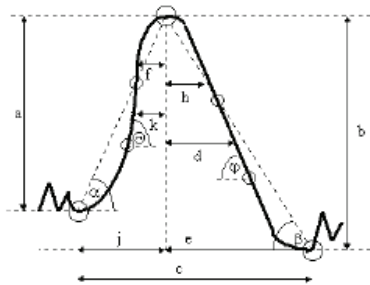


Fig. 1. Parameters, used in [2] to recognize eye blinks

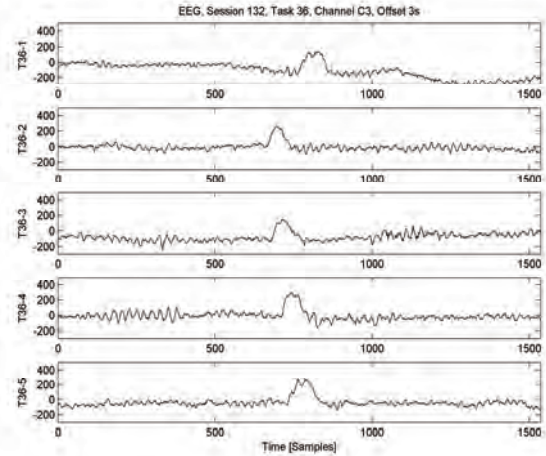
Blinks, recorded during different sessions and tasks are shown in Fig. 2. Except their high amplitude in the low frequency range they do not have any specific and repeated forms. The length of some of them exceeds 1s (256 samples). The duration of their visible part in the time domain is different and subject-dependent. In fact they depend on the subject's emotional stress, fatigue, eye dampness, etc.

The study described in this paper continues the work in [10]. To find the duration of the influence of the blink to the EEG, Gabor transform is used, according to (1)

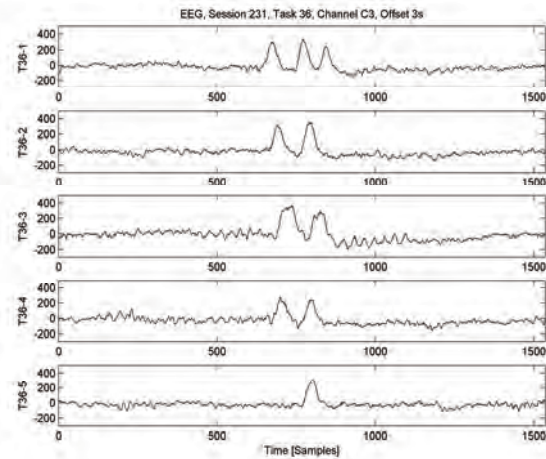
$$P(k,t) = G_N(k,t)G_N^*(k,t), \text{ where} \quad (1)$$

$$G_N(k,t) = \sum_{n=0}^{N-1} x(n,t)H(n)e^{-i2\pi kn/N}, \quad (2)$$

$G_N^*(k,t)$ - complex conjugate,



a)



b)

Fig. 2. Blinks with different forms and durations in time domain

N - number of samples for the analysis,

$H(n)$ - n^{th} sample of Hamming window with length N ,

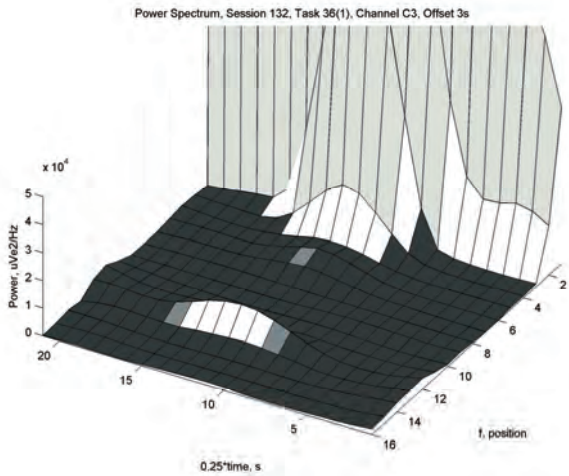
$x(n,t)$ - n^{th} sample of the current segment, with offset t from the beginning of the EEG.

The study uses 6-seconds EEG sections with blinks, to envelop parts before and after the blink. The blink is centered. Every section is divided to segments 1 s each with 0.25 s overlapping. Moving average filter is used along to equal frequencies in neighbour segments after Fourier analysis is done. The results are given as 3D plots in Figs. 3 and 4.

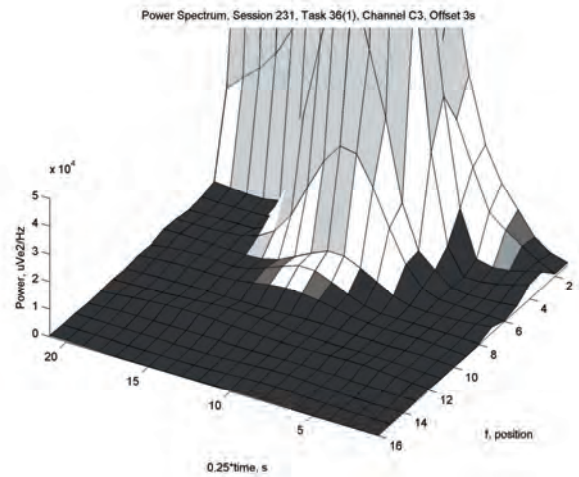
First a similar to Fig. 1 blink's form is chosen - Fig. 2a, session 132, task 36, run 1. The position axis marks in Fig. 3 correspond to the real frequency as (position -1)=frequency, Hz. The distance between the tick marks in time scale is 0.25 s. In all channels amplitude variations of some frequency components in the range of 8-13 Hz are noticed synchronously with 2 Hz-low frequency component, caused by the blink (in C3, Fig. 3a, and P3, Fig. 3b, at 11 Hz, and in O1, Fig. 3c, at 10 and 11 Hz). No matter that the white noise

is slightly filtered, each time in α -range exists a frequency component(s) which amplitude follows caused by the eyelids

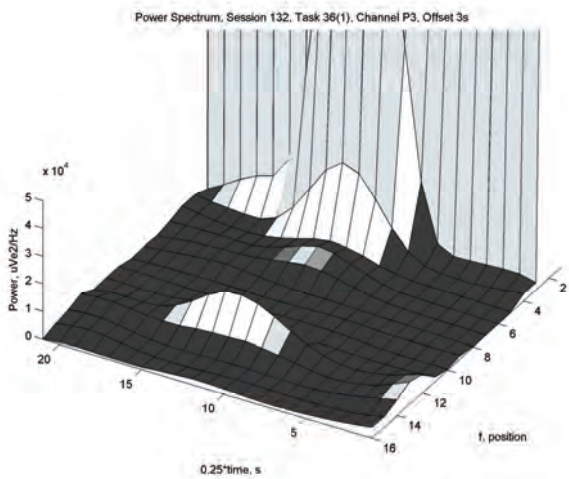
low frequency. The visible part of the eye blink in the time domain, Fig. 2a, is around 128 samples - 0.5 s. Following the 2 Hz component amplitude, the duration where it is rising



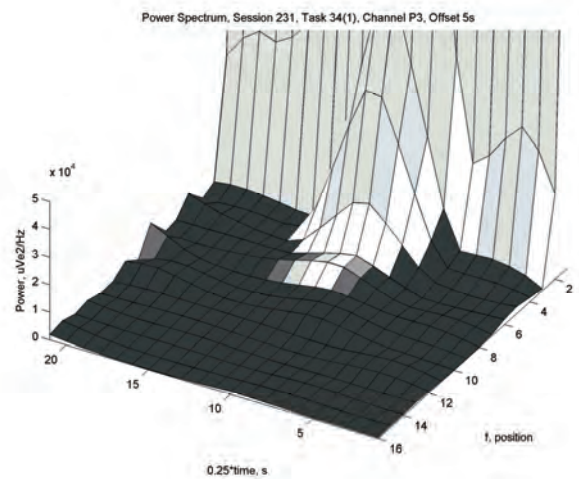
a)



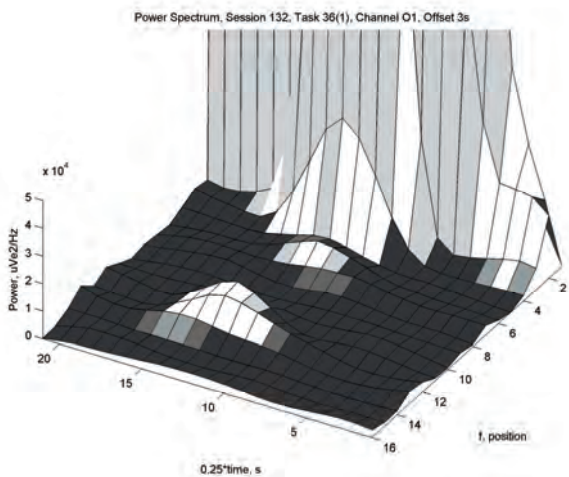
a)



b)

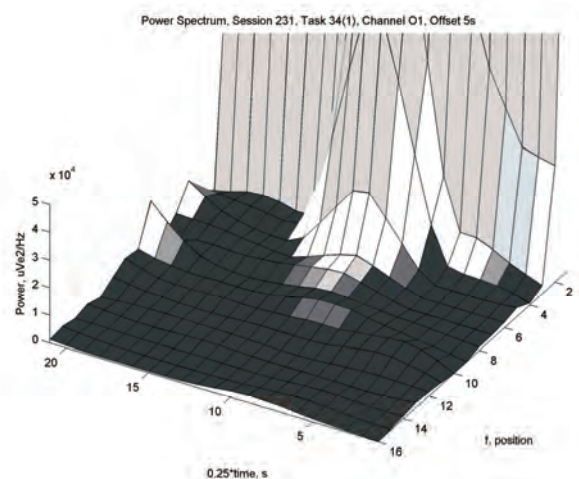


b)



c)

Fig. 3. Spectrogram for C3, P3, O1, session 132



c)

Fig. 4. Spectrogram of a “longlasting” blink, C3, P3, O1, session 231

(comparable to its steady state) is $12 \cdot 0,25 = 3$ s. The changes of 11 Hz frequency amplitude are similar.

The spectrograms of more complex and long lasting blink from Fig. 2b, session 231, task 36, run 1, are shown in Fig. 4. Although three visible periods of the low frequency could be seen there, this is one blink. The visible part in the time domain lasts above 1 s (more than 256 samples). The power is higher in the low frequency part of the range. The 8 Hz part is most affected. Similar to the previous case, the eye blink influence lasts in average 3 s.

The analysis of blinks with different forms and durations in the time domain results in almost equal length of 3 s of the affected section.

Unlike [12], where is stated that average blink duration is 100 ms in our EEG records in the time domain the visible part of the blinks are from 200 to 1100 ms long. Most of them last around 500 ms.

By reason of the different forms (subject-dependent) it is impossible to define eye blinks duration in the time domain. More important characteristic of the blinks is their influence over α -range frequencies. Blinks with different forms in the time domain affect different frequencies between 8 and 13 Hz. These frequencies appear synchronously with the 2 Hz frequency component.

III. CONCLUSIONS

In all channels the blinks amplitude is more than 5 times higher than the amplitude of the blink-free EEG data.

The power of the eye blinks is concentrated up to 3 Hz range.

Eye blinks could be recognized in the time domain by controlling the amplitude of the raw EEG or in the frequency domain by controlling the 2-3 Hz power.

In the range 8-13 Hz in segments, which contain blinks, the power of frequency components is more than 50% more in comparison to blinks-free EEG parts.

When the analyzed segment contains a blink, the power in all channels varies, which lowers the probability of a correct classification of the mental tasks' patterns.

It was decided to omit the EEG segments, which contain eye blinks.

The power of work frequencies (8-13 Hz) could be followed from the spectrograms of all the channels. Depending on the blinks form in the time domain different frequency components change synchronously with the 2 Hz frequency, where the blinks power is concentrated.

According to the study, rejecting 3 s section is quite enough to have blinks free neighbor parts.

REFERENCES

- [1] Blankertz B., G. Curio, K.-R. Müller, Classifying single trial EEG: Towards brain computer interfacing. In T. G. Diettrich, S. Becker, Z. Ghahramani, editors, *Advances in Neural Information Processing Systems (NIPS 01)*, volume 14, 2002, pp. 157-164, <http://ida.first.fhg.de/publications/BlaCurMue02.pdf>.
- [2] Bogacz R., *Blinking Artefact Recognition in EEG Signal Using Artificial Neural Network*, Master thesis, Politechnika Wroclaw, Department of Informatics, Wroclaw, 1998 <http://www.ci.pwr.wroc.pl/~bogacz/artefact> (in Polish).
- [3] Burke D. P., S. P. Kelly, P. Chazal, R. B. Reilly, C. Finucane, A Parametric Feature Extraction and Classification Strategy for Brain-Computer Interfacing, *IEEE Transactions on Neural Systems and Rehabilitation Engineering*, vol. 13, No. 1, March 2005.
- [4] Freeman W. J., L. J. Rogers, M. D. Holmes, D. L. Silbergeld, Spatial Spectral Analysis of Human Electroencephalograms, Including the Alpha and Gamma Bands, *Journal of Neuroscience*, 95, 200, pp. 111-121.
- [5] Hjorth B., An on-line transformation of EEG scalp potentials into orthogonal source derivations, *Electroencephalography and Clinical Neurophysiology*, vol. 39, 1975, pp. 526-530.
- [6] Lauer R. T., P. H. Peckham, K. L. Kilgore, EEG-Based Control of a Hand Grasp Neuroprosthesis, *Neuro-Report*, vol. 10, 1999, pp. 1767-1771.
- [7] Lauer R.T., P. H. Peckham, K. L. Kilgore, W. J. Heetderks, Applications of Cortical Signals to Neuroprosthetic Control: A Critical Review, *IEEE Transactions on Rehabilitation Engineering*, vol. 8, 2000, pp. 205-208.
- [8] Malmivuo J., R. Plonsey, *Bioelectromagnetism, Principles and Applications of Bioelectrical and Biomagnetic Fields*, New York, Oxford, Oxford University Press, 1995, <http://www.tut.fi/~malmivuo/bem/bembook/bembook.zip>.
- [9] Manoilov P. K., EEG Eye-Blinking Artefacts Power Spectrum Analysis, *Proceedings of the International Conference on Computer Systems and Technologies CompSysTech'06*, V.Tarnovo, Bulgaria, 15-16 June, 2006, pp. IIIA.3-1—IIIA.3-5.
- [10] Manoilov P. K., Electroencephalogram eelctrooculographic artefacts analysis, *Proceedings of the National conference with an International participation, ELECTRONICS'2006*, 1-2 JUNE, 2006 pp. 156-161 (in Bulgarian).
- [11] Middendorf M., G. McMillan, G. Calhoun, K. S. Jones, Brain-Computer Interfaces Based on the Steady-State Visual-Evoked Response, *IEEE Transactions On Rehabilitation Engineering*, vol. 8(2), 2000, pp. 211-214.
- [12] Parra L. C., C. D. Spence, A. D. Gerson, P. Sajda, Response Error Correction—A Demonstration of Improved Human-Machine Performance Using Real-Time EEG Monitoring, *IEEE Transactions on Neural Systems and Rehabilitation Engineering*, vol. 11, 2003, pp. 173-177.

The Web Side System for Registration and Processing Medical Data of Urological Department Patients

Jaroslav Makal¹, Jacek Bilkiewicz² and Andrzej Nazarkiewicz³

Abstract – In this paper the functional application for gathering, processing and interpretation of medical data is described. The usage of this data base is possible with the access of internet and with minimal requirements for hardware. Information stored at server can be reviewed and different statistics may be created in depending of medical or epidemiological needs. The future plans of extending this data base with diagnostic module and inference engine are mentioned.

Keywords – internet technology, data base, processing of data, computer aid diagnosis.

I. INTRODUCTION

Computer measuring systems are used in medicine to improve quality and efficiency in health care processes. Personal computers have become inexpensive and relatively easy to use. The Internet technology for data exchange can be utilized from almost any office or doctor's surgery (Fig.1). This technical and socio-economic development has led to a situation when it appears to be appropriate to assume that a large number of doctors is able to access an Internet based information system and collect their medical data for their common or own usage [1]. Every doctors has also the possibility

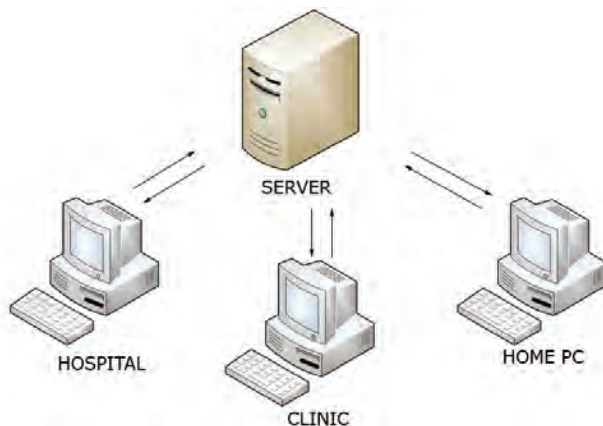


Fig. 1. The users access of database

to review and analyse medical data in their work places: hospital, clinic or home study.

¹Jaroslav Makal is with the Faculty of Electrical Engineering at Bialystok Technical University (BTU), ul. Wiejska 45D, 15-351 Bialystok, Poland, E-mail: jaromaka@pb.edu.pl

²Jacek Bilkiewicz is a student of BTU Faculty of Electrical Engineering, Poland, E-mail: jacek@bilkiewicz.pl;

³Andrzej Nazarkiewicz is with the J.Sniadecki Provincial Integrated Hospital, M.C. Skłodowskiej 26, 15-950 Bialystok, Poland, E-mail: anazar@osiedle.piasta.pl.

II. STRUCTURE OF DATA BASE

The information set is organized in three separate parts (Fig.2): doctors, patients and examinations tables. The table doctors includes the identifications data of all users which allows them to entrance the base. The patients table contains patients personal data and ID of their doctors. The biggest examinations table is composed of the identification part (patient, doctor and examination) and the result table (about 100 rows for every record).

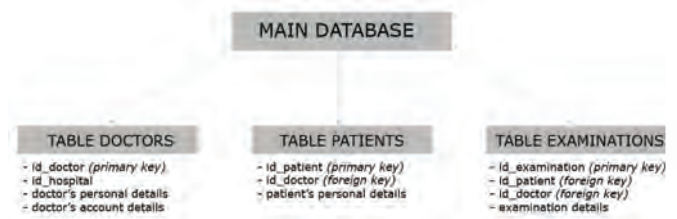


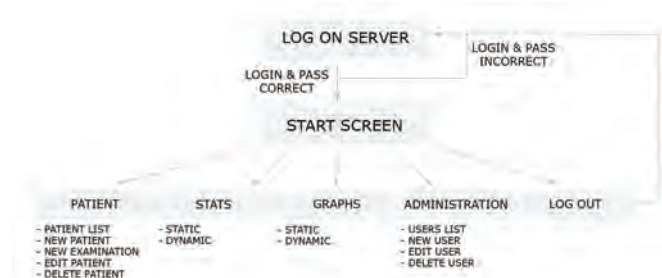
Fig.2. The database structure

Two technologies [2] have been used for establish this base: MySQL –which enables to create any data collection with additional description. It is very popular and wide range used by web-masters also because of its low cost (the licence is not necessary), and

PHP –Type Text -the script language performed in the server allowing to dynamic generation of the web side contents.

The process of database creation is automatized by locating all commands in the file *baza.php* which is placed in the main directory at server. The administrator manages the users status and allows them to make use of all records or only of their own part. User may add/delete the patient or the result of the examination for existing item.

Fig. 3. The process of activating the usage of database



If some results of the patient are observed, the presentation is in the form of a table and all items are sorted according to date (the latest at the beginning). For handy operation the inquiry forms of a new patient is unrolled. The selected parts of

questionnaire data are presented in the Table I (i.e. the part 5. consists of 13 rows; there are near 100 rows in the full version).

TABLE I
THE SELECTED (NOT ALL) PERSONAL AND CLINICAL DATA GATHERED IN DATABASE

1. Personal data:	
Patient`s data (name, second name, surname)	
Examination`s date (year-month-day)	
Code of SD/case history	
2. Anamnesis:	
Diabetes, Hypertension	yes/no
ASC (arteriosclerosis)	yes/no
Sexual activity	yes/no if NO – how many years from/since
Erectile dysfunction	severity: /1-mild; 2-middle; 3-hard
Smoking	yes/no, number of cigarettes/per day
Alcohol	yes/no, 100g drinks/ per week
Physical exercises (jogging, any sport, etc.)	yes/no, how many/per week
3. Ailments	
Chest pain, Intermittent claudication, Orthopnea	yes/no
4. Urination	
IPSS, Quality of Life	number of score
Haematuria, Urinary incontinence	yes/no, number of used sanitary napkins (<i>quantity/per24h</i>)
5. Medicaments:	
Alfa-blockers	yes/no
Blockers of 5-fosfodiesterase /Viagra, Cialis, Levitra/	yes/no
6. Physical examination	
Arterial blood pressure	mmHg
Pulse, Pulse at distal arteries	
Leg ischemia (is there any hair on patient`s legs?)	
DRE (digital rectal examination)	
7. Laboratory tests	
Urine analysis	normal/abnormal
Urine bacteria culture	negative/positive
Glycemia, Cholesterol, LDL, HDL	
Total PSA (last)	ng/ml date
8. USG (ultrasonography) of the low urinary tract	
Urolithiasis/stones at upper urinary tract	yes/no
Prostate volume, Residual volume of urine	cm ³
9. Uroflowmetry	
Qmax	ml/s
Volume of micturition (urine)	ml

III. THE STATISTICS REVIEWING

The pleat *STATS* allows users to form different statistics for particular items of questionnaire and in the future also to make so called intersected statistics. The example of one of simple graph is showed at Fig. 4. All records in the database are clustered for the sake of patients age [3]. There are 74 patients: 40 of them are from 61 to 70 years old. Likewise, the diagram percentage of patients with i.e. Qmax (max urine flow) over 15ml/s can be created in this base.

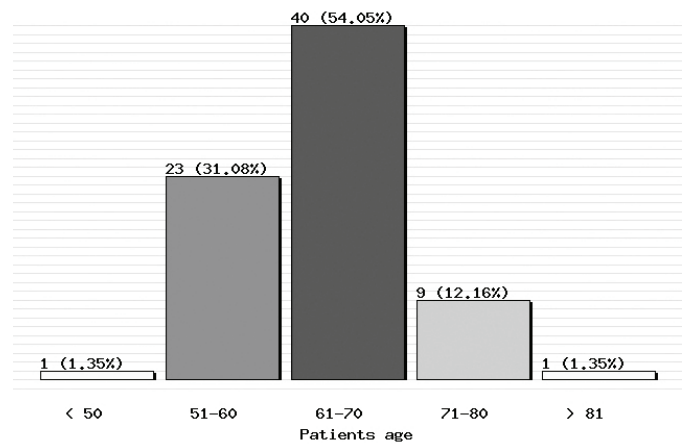


Fig. 4. The histogram of number of patients diversified in the interest of their age

IV. CONCLUSIONS

We have performed the web side system for gathering clinical data. We used the expanded inquiry forms which include all possible data represent patient cases suffering from BPH (Benign Prostatic Hyperplasia), Prostate Cancer and the other causes of lower urinary tract disabilities [4]. So far, only direct statistics are possible in the form of histograms. In near future the answer for the question: how many patients with PSA=4-5 ng/ml have big prostate volume and have BPH as the final diagnosis, can be received from described database.

The long future aim of this system is to help a doctor in a diagnosis. It has the advantage of having a large database of knowledge which can be updated (it can store more knowledge than a person).

ACKNOWLEDGEMENT

This paper is supported by the Ministry of Science and Higher Education (Poland) from the sources assigned for scientific researches in 2005-2008 in the frame of project nr 3 T10C 035 29.

REFERENCES

- [1] Orzechowski P., Makal J.: "Acquisition of Medical Data in the Diagnosis of Benign Prostatic Hyperplasia (BPH)", Proceedings of the 6th School-Conference on Computer Aided Metrology, 2003 Waniewo, Poland; (p. 275-280).
- [2] Ullman L., "About PHP and MySQL for Dynamic Web Sites: Visual QuickPro Guide". 1st Edition 2003 by Peachpit Press.
- [3] Girman C.J.: "Ageing in urology. Population-based studies of the epidemiology of benign prostatic hyperplasia." British Journal of Urology. Supplement, 82 (1998), (p. 34-43).
- [4] "Recognition and treatment of BPH. The actual guidelines of American Urological Association." The Practical Surgery Medicine, nr 5-6, 2003.
- [5] Chang PL, Li YC, Wang TM, Huang ST, Hsieh ML, Tsui KH, "Evaluation of a decision-support system for preoperative staging of prostate cancer", Medical Decision Making 19 (4): 419-427 Oct-Dec 1999.

Laboratory Stand in Web Browser for Measurements on Distance

Jaroslav Makal¹, Adam Idzkowski¹ and Adam Krasowski¹

Abstract –The general description of the Internet laboratory stand and its Web application used in laboratory of metrology and technique of experiment has been presented. Some proposed future improvements to this distance learning system has also been discussed at the end of this paper

Keywords – distance learning, ASP.NET, IEEE-488.2 interface.

I. INTRODUCTION

By means of Internet many real experiments could be done by students in the frame of distance e-learning courses. The most convenient way of the measurements would be the use of a web browser to control the devices and to analyse the results. Such statement was a motivation to create a laboratory stand as a tool in teaching Theory of Circuits at Faculty of Electrical Engineering in Bialystok Technical University.

In this paper the measurements performed on a simple DC circuit has been presented. The supplying current and the voltage in one branch of electrical circuit are measured. Students can use a web browser to manipulate three devices by GPIB (IEEE-488.2) interface. The results are observed in the ordinary webcam and can be saved at request.

II. EQUIPMENT, SOFTWARE AND COMMUNICATIONS

A. Equipment and interfaces

The heart of the laboratory stand is a personal computer with IEEE-488.2 interface board for the PCI bus (model KPCI-488A of Keithley).

The board works as a system controller (Fig. 1) and controls three GPIB instruments (Tektronics P2521G DC power supply, Keithley DMM 2000 multimeter and Motech FG-503 function generator). An internet camera is connected by USB interface to the server and the image is seen in a web browser during the measurements.

B. Server's software

The server runs on Windows XP Professional with IIS

(Internet Information Services) version 5.1 installed. IIS application process model consists of *TCP/IP kernel*, *Inetinfo.exe* which runs in-process applications (low isolation) and multiple *DLLhost.exe* processes which run pooled-process or out-of-process applications (medium or high isolation). Security is assured by Windows authentication, SSL, Kerberos and Web Server Certificate Wizard [1].

The prerecorded video from camera is converted into stream by Microsoft Windows Media Encoder 9. This software uses any camera installed on computer and does not require additional drivers or libraries.

C. Communications

The dynamic website has been created with the use of ASP.NET technology [2-4]. The application is installed on server and a client (student) communicates with it using a web browser. The advantage of this solution is that students, before

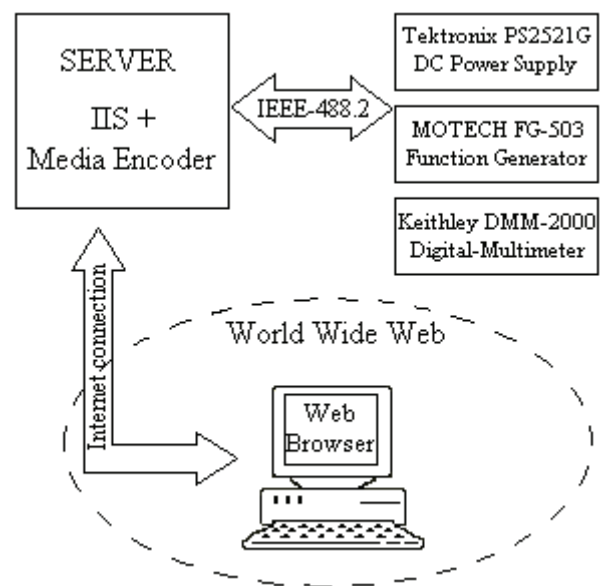


Fig. 1. General outlook on communication.

taking the measurements, do not install any additional software on their own computers which do not have to be modern.

The communications among the devices and the server has been executed by our application, GPIB interface and *iee_32m.dll* library.

GPIB interface board co-operates with the devices using SCPI (Standard Commands for Programmable Instruments) language. Our application sends and receives simple

¹Jaroslav Makal, Adam Idzkowski and Adam Krasowski are with the Faculty of Electrical Engineering, Bialystok Technical University, Wiejska 45D, 15-351 Bialystok, Poland, E-mail: jaromaka@pb.edu.pl

commands and values. As the example of this, to set the voltage 10V on the power supply output, the command "sour:volt 10" is given.

Fig. 2. The panel where the settings of power supply are programmed.

III. USER INTERFACE

The user interface was made with the use of HTML and CSS (Cascading Style Sheets) scripts. The properly created forms like in Fig. 2 serve to input the programming data.

The interface is user friendly. All the settings can be done by choosing a proper point in the list and by filling out any number in the field. Various ways of filling out the numbers are possible, for example the number "10.000.000" can be written as "10000000", "10M", "10000k" or "10^7".

IV. LABORATORY EXERCISE

The aim of laboratory exercise is to find the DC characteristics of P-N junction diode, any other electronic element or circuits.

The results of continuous measurement of current and voltage are shown in special laboratory window in web browser. Default sampling time (the frequency of voltage and current reading) is 500ms. The results, which help to plot I-U characteristic, are presented in the table and can be saved to the file.

The view of the laboratory stand is presented in Fig. 3.



Fig. 3. The view of laboratory stand.

V. CONCLUSIONS

The ASP.NET and IIS technologies allow us to create the server and user application for establish the distance measurements. The CSS technology enables of build-up the project – create new forms and use another (total 14) measuring instruments with GPIB interface (signal generators, oscilloscopes, etc.)

The user's interface looks the best in Internet Explorer because we have used Windows Media Encoder 9 for video streaming and Java applet and ActiveX control for seeing the picture. In other web browsers the image from camera is not visible. Another disadvantage is that the laboratory exercise can be done by exclusively one student at the same time.

Web-based measurements can probably never replace the real contact with the instruments. But the measurements performed in hazardous environments require remote control of the instruments what motivates to do such experiments in the teaching.

ACKNOWLEDGEMENT

This work is prepared within the framework of the project S/WE/3/03. Master's thesis (M.Sc.) which concern this subject are done by Adam Krasowski, the student of Bialystok Technical University.

REFERENCES

- [1] M. Tulloch. *Administering IIS (5)*, McGraw-Hill Osborne Media, 2000.
- [2] S. Worley, *Inside ASP.NET*, New Riders Publishing, 2001.
- [3] D. S. Platt, *Introducing Microsoft .NET, Second Edition*, Washington, Microsoft Press, 2002.
- [4] J. Liberty, D. Hurwitz, Polish translation: R. Górczyński – *ASP.NET. Programming*, Helion, 2006.

Electronic Identification and Patient Parameters Monitoring

Siniša Randić¹, Aleksandar Peulić², Adam Dostanić³ and Marko Acović⁴

Abstract - In this paper has shown different method for wireless monitoring biomedical patient data and safety modes. Our system consists of mobility sensors devices and using wireless transfer for sending measured biomedical data to central computer/data base server in hospital. The proposed health remote control system supports a few levels, a first, level with sensors for monitoring biomedical data, second central level for wireless transfer measured data, third central system for acquisition data and last , fourth level, corresponding application for automatic analysis same, user interface for data access and very important part is hardware protection of data access. Barcode reader and patient's identification card realize hardware protection. This system is convenient for continuous patient monitoring as enhance care of patient's health.

Keywords – Monitoring biomedical patient data, Mobility sensor devices, Wireless transfer measured data

I. INTRODUCTION

To provide human healthcare support with a better quality, we should be able to collect a very large amount of people's vital signs and monitor it efficiently. Current welfare system is based on medical doctor regular consultation, on behalf of our own feeling. The idea is not to replace the current system, but to augment it by an environment using information technologies (IT) and wireless networking, to provide continuous monitoring of one's physiological information, perform simple diagnosis and communicate all that with medical institutions. This case arises when physicians want to monitor individuals whose chronic condition includes risk of sudden acute events or individuals for whom interventions need to be assessed in the home and outdoor environment. If observations over one or two days are satisfactory, ambulatory systems can be utilized to gather physiological data. An obvious example is the use of ambulatory systems for ECG monitoring, which has been part of the routine evaluation of cardiovascular patients for almost three decades. However, ambulatory systems are not suitable when monitoring has to be accomplished over periods of several weeks or months, as is desirable in a number of clinical applications.

Wearable systems are totally no obtrusive devices that

allow physicians to overcome the limitations of ambulatory technology and provide a response to the need for monitoring individuals over weeks or even months. They typically rely on wireless, miniature sensors enclosed in patches or bandages, or in items that can be worn, such as a ring or a shirt. They take advantage of hand-held units to temporarily store physiological data and then periodically upload that data to a database server via a wireless LAN or a cradle that allow Internet connection.

II. SYSTEM DESIGN

On a wearable controller, a software environment allows accumulating data from physiological sensors, recording them into a local database, operating basic data manipulations, and communicating data with the database at medical institutions. These elements compose health remote control systems, which concept shown on Fig 1.

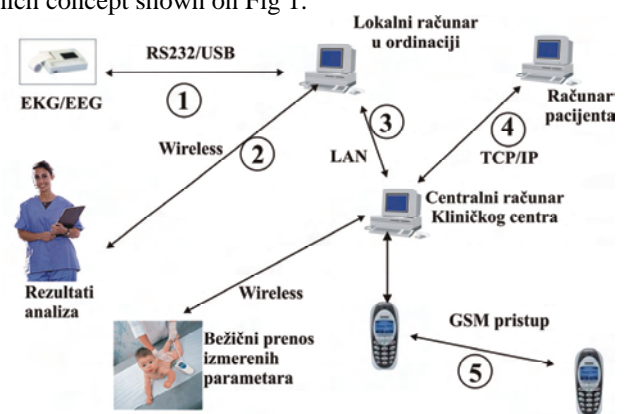


Fig. 1. Health remote control system

The whole system can operate as standalone as well as PC controlled. It can be divided into four parts, radio frequency data transmission network, analogue measurement modules, PC-based base station (including data processing) and programmable, portable recording modules with feedback options. The main goals of the design are lightweight, minimal power consumption, modular design and robust circuitry. The Network in between the measuring modules and the base station is realized as a bi-directional multi-point, single master RF-link, operating in the LPD-frequency range (868MHz) on a single channel. The RF measuring network consists of several measuring (slave) modules (a maximum of 31 slaves is possible) and of one master module. The structure of the network is fully dynamic and in operation reconfigurable and scaleable. The configuration process of the RF-network is fully automatic in conjunction with the control program, running on the PC or the Base station. The

¹Siniša Randić is with the Technical Faculty, Sv. Save 65, 32000 Čačak, Serbia, Email: rasin@tfc.kg.ac.yu.

²Aleksandar Peulić is with the Technical Faculty, Sv. Save 65, 32000 Čačak, Serbia, Email: peulic@tfc.kg.ac.yu.

³Adam Dostanić is with the Technical Faculty, Sv. Save 65, 32000 Čačak, Serbia, Email: adamdostanic@tfc.kg.ac.yu.

⁴Marko Acović is with the Technical Faculty, Sv. Save 65, 32000 Čačak, Serbia, Email: markoacovic@tfc.kg.ac.yu.

initializations process and the required communication in between the master and the module's give the possibility to control the network dynamically. It is therefore necessary to initialize a slave module to a dedicated master. The function of master is slave polling and acquisition of data. The function of slave is recognition of control package and sending data to master. The master acts in direct conjunction with PC by USB or RS232, collecting information from RF link and sending to database by PC application. User action by PC application master translates to slaves by RF link. It is possible to operate several masters in parallel using different channels. The base station collects the data stream of the modules operating in parallel and feed them together. The bandwidth of the whole system is 19200 Baud. The bandwidth of each slave is dynamically controllable by the master. For each slave is also given a back directional configuration channel. Its purpose is to configure the slave and to control hardware functions of measuring device. The channel selection by the master is managed by a collision detection algorithm to ensure the usage of the channel with the minimum radio strength signal. Individual slave (measuring) modules) are controlled by, and communicate with, the master module (PC) using a custom wireless protocol. We use standard 868 MHz RF modules (RF Transceiver TRF6900) because the available Bluetooth technology requires three to five times greater power consumption. In addition, we reduce power consumption by using a custom, power-efficient communication protocol. The core of our wireless modules consists of a low-power Texas Instruments microcontroller MPS430F149. The controller features a 16-bit architecture, ultra-low power consumption (less than 1 mA in active mode and ~1 μ A in standby mode), 60-KB on-chip flash memory, 2-KB RAM, 12-bit A/D converter, and dual UART. Internal microcontroller analog channels monitor battery voltage and temperature. Therefore, slave module is capable of reporting the battery status and temperature to the upper level in the system hierarchy. Master and slave modules form a personal area network, which communication system is wireless, mid-range (up to 40 meters) and consume little energy, for practical usability. Under these requirements, it is constructed transmission circuits using weak radio frequency. On vital data reception, master module automatically records it in a local database. It is designed database architecture centered on measurement sessions and time-based classification. The environment also provides functionalities to display multiple physiological data on graphs, carry out graph manipulation (zoom, slide), and access information about sensors (maker, serial number, picture...). After the data have been saved, it is coupled with sensor information (sensor id number, name) and saved into PC database. It is designed to manage patients' daily monitoring individual data, provide tools to support medical doctor diagnosis process, and a meta-data framework to make easier processes like correlation analysis and data-mining.

WEB Internet service is data transfer is the system extension. Long distances patients monitoring are available and doctors have a possibilities to produce actions from house from example. There is and mobile phone services and figure 2 shows a system design based at Internet and mobile phone services.

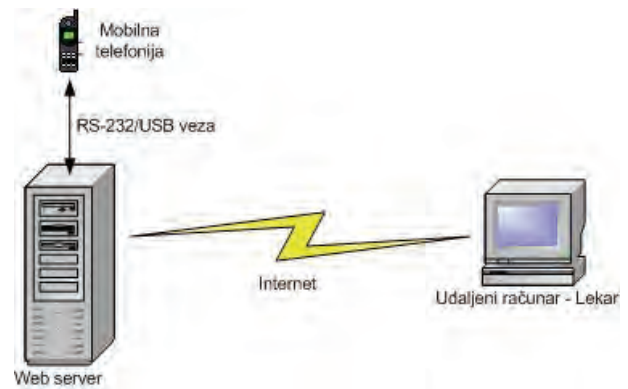


Fig. 2. Internet based patients monitoring system

The hospital web server station has IP (Internet Protocol) address. The symbolic web address is need for directly locations patients data form WEB server.

A mobile phone module is need for Small Message System conected directly to WEB server by a standard RS232 ar USB interface.

III. BAR CODE READER SYSTEM PROTECTION

The realized health remote control system supports a three security levels, a first, lowest patient security level, second a doctor level involved at doctor personal computer and top level at data base server. This chapter describes first security level, realized bar code card reader. Every patient has own identification number and own password implemented in identification card. The identification card has intention to protect external access to health remote control system by unauthorized persons. Second convenience is storage an array of medical date concerning card owner. The Card reader is realized like external device and connected to PC by serial or USB port or wireless, Blue Tooth for example, Figure 3.

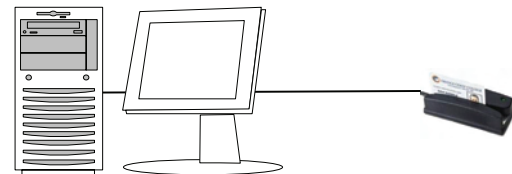


Fig. 3. Bar code reader PC connections

The bar code reader reads personal identification number and password from card memory and sends it to PC. The PC application is realized by Microsoft Visual C++ with intention to establish communication check accepted data form card and permit or deny access to system.

CONCLUSION

Developed system is based to enable continuous monitoring of patient's physiological information. A wearable controller collects measured sensor data. Integrate it into a database, which allow the exchange with medical institutions where a system manages the database for each patient's vital data. Intelligent medical monitors can significantly decrease the number of hospitalizations and nursing visits. In case of medical emergency master module can send an SMS message

to the personal medical doctor. A three security levels are involved in aim to prevent and limit access. A first security level is a bar code reader based realized, and our future work will be focused to improve security capabilities of system.

REFERENCES

- [1] Jovanov, E., Price, J., Raskovic, D., Kavi K, Martin, T., Adhami R.: "Wireless Personal Area Networks in Telemedical Environment" Proceedings of Third International Conference on Information technology in Biomedicine, (ITAB-ITIS2000), pp. 22-27, 2000.
- [2] Jovanov, E., Price J., Raskovic, D, Moore, A., Chapman, J., Krishnamurthy A.: "Patient Monitoring Using Personal Area Networks of Wireless Intelligent Sensors", Biomedical Sciences Instrumentation Vol. 37, in Proc. 38th Annual Rocky Mountain Bioengineering Symposium, RMBS 2001, April 2001, Copper Mountain Conference Center, pp. 373-378.
- [3] Jovanov, E., O'Donnel, A., Morgan A., Priddy, B., Hormigo, R.: "Prolonged Telemetric Monitoring Of Heart Rate Variability Using Wireless Intelligent Sensors And A Mobile Gateway", 2nd Joint EMBS-BMES, Houston, Texas, October 2002.
- [4] Jovanov, E., Price J., Raskovic, D, Moore, A., Chapman, J., Krishnamurthy A.: "Patient Monitoring Using Personal Area Networks of Wireless Intelligent Sensors", Biomedical Sciences Instrumentation Vol. 37, in Proc. 38th Annual Rocky Mountain Bioengineering Symposium, RMBS 2001, April 2001, Copper Mountain Conference Center, pp. 373-378
- [5] Peulic, A., Randjic, S.: "Radio Frequency Measured Data Transmit", ICEST 01.-04. Oct. 2002, Nis, Yugoslavia, CD zbornik, Measurement Technique
- [6] Peulic, A., Randjic, S.: "Computer Based High Radio Frequency Systems Control", TELSIKS 01.-03. October 2003, Nis, Yugoslavia, Proceedings is on CD
- [7] Peulic, A., Randjic, S.: "Computer Based Remote Measuring and Acquisition of Dynamic Data", ICEST 16.-18. October 2003, Sofia, Bulgaria

This page intentionally left blank.

SESSION SP II

Signal Processing II

Comparative Analysis of Basic Self-Organizing Map and Neocognitron for Handwritten Character Recognition

Ivo R. Draganov¹ and Antoaneta A. Popova²

Abstract – In this paper we present a comparative analysis of the performance both as accuracy and time consumption of two neural network classifiers for handwritten character recognition – a basic self organizing map and neocognitron proposed by Kohonen and Fukushima respectively. The results of our study are found useful for characters and pseudo-characters recognition as a certain stage of processing in a whole handwriting recognition system.

Keywords – character, pseudo-character, word, handwriting recognition, self-organizing map, neocognitron.

I. INTRODUCTION

A possible concept used in some systems for handwriting word recognition is splitting words in single characters and pseudo-characters [1]. Thus the separated elements of a word should be recognized at a later stage in these systems using a number of preliminary chosen rules based on common handwriting and language characteristics to form word hypotheses. After confirming or rejecting these hypotheses applying lexicon verification along with language statistics and other techniques we are able to recognize handwritten text word by word.

Considering the large number of methods developed for handwritten character recognition [2,6] and their capability to recognize pseudo-characters (parts of one or more characters) we decide to directly compare a self-organizing map [3] and a neocognitron [4] proposed by Kohonen and Fukushima respectively. These both self-learning neural networks will be compared in their basic form considering recognition accuracy with high quality images of characters free from noise, shifts, etc. Our main goal is to find out to what degree they differ one from another as for their recognition capability based on the different architecture and working principles they have when high quality test data is passed to them.

In the next part we present a description of the structure, preprocessing, learning and recognition algorithms used for both networks in our study. The third part contains the experimental results for different parameters defined in part two. In the last part a conclusion is made which of these

classifiers is more appropriate to be included in a complete handwriting recognition system.

II. COMPARED CLASSIFIERS DESCRIPTION

The architecture of the self-organizing feature map (SOFM) used in our experiments is given in Fig.1.

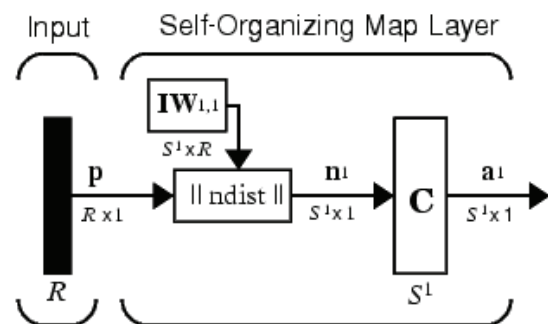


Fig.1. Self-organizing feature map architecture

The input receives consecutively vectors p with dimensions $R \times 1$, where $R=256$, each p represents a character (or pseudo-character). At first a grayscale images for the separate characters are used which we binarize using Otsu algorithm. Afterwards we resize the binary symbol to 256×256 pixels with nearest neighbour interpolation. Then thin or thicken “the width of the pen” used to 12 pixels using erosion or dilation l times:

$$l = \frac{|t-12|}{2}, \quad (1)$$

where t is the initial “width of the pen” found as a maximal value in a histogram representing all “the widths of the pen” (number of ones closed between zeros for each line in the image if an inverted one is used) in the resized binary image. This preprocessing step is needed to make characters as invariant as possible for further forming the learning extract. Finally we divide the result image to 16×16 pixels sized blocks. The number of pixels (ones for example) corresponding to character in each block is calculated and the normalized value (in range $[0,1]$) forms a respective component for the input vector p . The blocks are passed from left to right and from top to bottom.

We use the original Kohonen learning rule defined as:

$$\begin{aligned} w_i(q) &= w_i(q-1) + \alpha[p(q) - w_i(q-1)] = \\ &= (1-\alpha)w_i(q-1) + \alpha p(q) \end{aligned}, \quad (2)$$

¹Ivo R. Draganov is with the Faculty of Communications and Communications Technologies, Technical University, Kliment Ohridski 8, 1000 Sofia, Bulgaria, E-mail: idraganov@abv.bg

²Antoaneta A. Popova is with the Faculty of Communications and Communications Technologies, Technical University, Kliment Ohridski 8, 1000 Sofia, Bulgaria, E-mail: antoaneta.p@komero.net

where i denotes a single neuron; w – the neuron weight; q – current step; α – the learning rate; $N_i(d)$ is the neighbourhood around a winning neuron from which weights of all neurons j should be updated. Here d is the radius of the neighbourhood:

$$N_i(d) = \{j, d_{ij} \leq d\}. \quad (3)$$

$\mathbf{IW}^{l,1}$ from Fig.1 is a weight matrix for all the S input neurons (equal to the number of classes/subclasses for all the characters) with R weights each. \mathbf{n}_i^1 is the result from finding the distance from \mathbf{p} to i -th column of $\mathbf{IW}^{l,1}$:

$$\mathbf{n}_i^1 = -\|\mathbf{IW}_i^{l,1} - \mathbf{p}\|, \quad (4)$$

which is passed to competitive layer C , the output from which \mathbf{a}^l – a $S \times 1$ vector containing one component equal to 1, indicating the recognized character and all the other components equal to 0.

Given the preprocessing steps from above it is clear that our SOFM operates in 256-dimensional space, for each dimension of which a range of 0 to 1 is set. We use midpoint initialization for all the neurons' weights (0.5). The learning rate α and neighbourhood distance d are altered through the learning procedure. It lasts for a given number of steps Q . The neighbourhood distance starts as the maximum distance d_{max} (calculated at first step) between two neurons, and decreases to preliminary defined end neighbourhood distance d_{min} . Similarly the learning rate starts at some initial value α_{init} and decreases until it reaches some smaller one α_{end} – both are preliminary set. As d and α decrease, the neurons of the network typically order themselves in the input space with the same topology in which they are ordered physically.

The neocognitron performs classification of input through a succession of functionally equivalent stages. Each stage extracts appropriate features from the output of the preceding stage and then forms a compressed representation of those extracted features. Fig.2 shows the structure of the neocognitron for a case of recognizing 10 objects (e.g. digits).

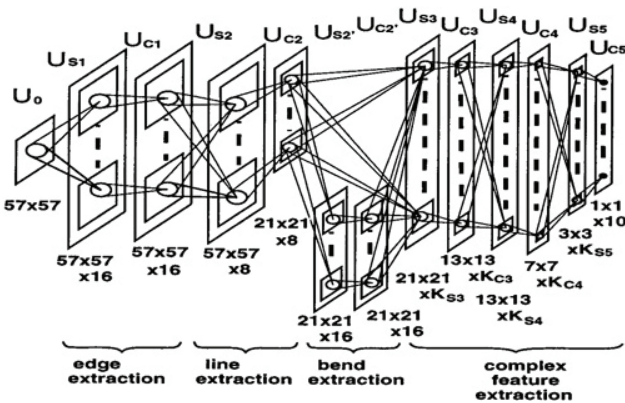


Fig.2. Structure of a neocognitron for 10 objects

The feature extraction is performed by arrays of S -cells that have been trained to respond to certain features that characterize the input patterns U_0 as it is seen from Fig.2. After training the weight vector of an S -cell is equal to the sum of the inputs that have appeared within its receptive field. Each S -cell also receives an inhibitory signal proportional to the *root mean square (rms)* activity present in its receptive

field. The behaviour of an S -cell can be mathematically formulated as a function $\varphi(\cdot)$ of a cell's activation:

$$o(\mathbf{x}) = r_i \varphi(a(\mathbf{x})), \quad (5)$$

$$a(\mathbf{x}) = \frac{1 + \mathbf{x}^T \mathbf{w}}{1 + \frac{r_i}{1 + r_i} b_i \cdot rms(\mathbf{x})} - 1, \quad (6)$$

where \mathbf{x} is the vector of activities present at the receptive field input, \mathbf{w} is the vector of weights learned by the S -cell and r_i is the selectivity parameter found by a separate closed-form training algorithm which we will not discuss. The *rms* activity of the input to the S -cell is defined by:

$$rms(x) = \sqrt{\sum_{i=1}^N c_i x_i^2}, \quad (7)$$

where the vector $\mathbf{c} = [c_1, \dots, c_N]^T$ describes a Gaussian kernel that serves to accentuate inputs towards the centre of the cell's receptive field, as well as implementing the arithmetic mean of the inputs. b_i is a factor set by the learning rule to maximize the cell's response to any training feature.

Interesting here is the S -cell transfer function considered influencing the final recognition accuracy [5]. Originally Fukushima used a threshold linear function of the form:

$$\varphi_{ThreshLin}(a) = \begin{cases} 0, & a < 0 \\ a, & 0 \leq a \end{cases}, \quad (8)$$

but here we will use another two transfer functions in our experiments – the more simple threshold function:

$$\varphi_{Thresh}(a) = \begin{cases} 0, & a < 0 \\ 1, & 0 \leq a \end{cases}, \quad (9)$$

and the sigmoid transfer function:

$$\varphi_{Sig}(a) = \frac{1}{1 + e^{-\beta a}}. \quad (10)$$

Fig.3 shows the structure of an S -cell along with the described transfer functions.

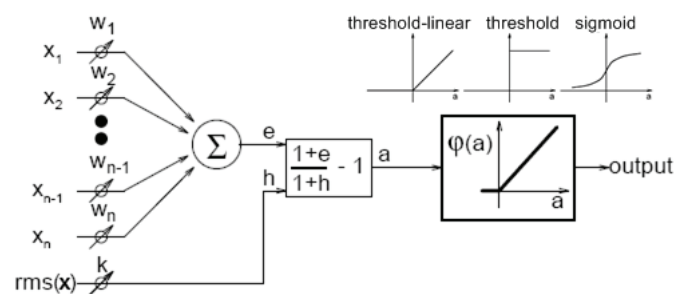


Fig.3. S -cell structure with different transfer functions

C -cells compress the representation – the input to a C -cell from its receptive field is a subsampling of the activity in the preceding S -plane. By subsampling this activity, a compressed representation of the S -plane output is obtained. C -cell also blur the activations of the preceding S -planes by performing a weighted sum of inputs, this time using fixed weights that describe a Gaussian kernel. If we denote the

subsampled input as a vector \mathbf{x} and the Gaussian kernel as \mathbf{w} then the activation of a C-cell in Fukushima's original description of the neocognitron can be written as:

$$a(\mathbf{x}) = \mathbf{w}^T \mathbf{x}. \quad (11)$$

This weighted mean is then passed through a transfer function that limits the output of the C-cell to $[0,1]$:

$$\psi_{Mean}(a) = \frac{a}{1+a}. \quad (12)$$

Here is the second difference from the very original Fukushima's neocognitron. Again in [5] is noted that blurring of S-plane activity by the C-cells is important in allowing the neocognitron to be tolerant of a considerable degree of input distortion. Thus a ranked order filter is incorporated in the very structure of the C-cell. The output of the modified C-cell is given by:

$$\psi_{Max}(x) = \max_i x_i w_i, \quad (13)$$

where $\mathbf{x}=[x_1, \dots, x_N]^T$ is again the subsampled input vector and $\mathbf{w}=[w_1, \dots, w_N]^T$ is the Gaussian kernel. We refer to Eq. (13) as a weighted max operation.

III. EXPERIMENTAL RESULTS

All the experiments are implemented on an IBM® compatible PC® with Pentium®4 Processor working at 1.5 GHz, 256 MB RAM. The operating system is MS® Windows® XP® with SP2 and the working environment is Matlab® 7.0.1 SP1.

Our database collected from different authors contains images of 14502 lower and upper case Latin characters and digits (8-bpp grayscale, 150 dpi). From them we use 8152 preprocessed (filtered by median and range filters) images of lower case characters to train the networks and afterwards 600 additional images which form the test set (for the recognition phase) although a set of 400 is considered to be enough [5].

We use the following parameters for the accuracy comparison:

- relative number of correctly recognized characters:

$$r_c = \frac{m_c}{m} \cdot 100, \%, \quad (14)$$

where m is the number of passed characters for recognition ($m=600$); m_c – the number of correctly recognized ones;

- relative number of wrong classified characters:

$$r_w = \frac{m_w}{m} \cdot 100, \%, \quad (15)$$

where m_w represents the absolute number of wrongly recognized characters;

- relative number of non-classified characters:

$$r_n = \frac{m_n}{m} \cdot 100, \%, \quad (16)$$

where m_n represents the absolute number of non-classified (rejected) characters.

Our first experiment includes finding the optimal value for the minimum learning rate α_{min} of the SOFM. We set $\alpha_{max}=0.9$ and $d_{min} = 0.001$ – a midrange value for the typical working interval $[0.000001,1]$ for the particular case. Before recognition phase we train the network for 10 epochs with 26 classes with 5 subclasses for each present. The so called 'gridtop' topology is used along with Euclidean distance. Rejection criterion is $d > 10^{-6}$. The results are shown in Table I.

TABLE I
FINDING THE OPTIMAL MINIMAL LEARNING RATE FOR SOFM

α_{min}	0.1	0.3	0.6	0.8
Recognition				
$r_c, \%$	26.09	47.83	60.87	56.52
$r_w, \%$	56.52	34.78	21.74	26.09
$r_n, \%$	17.39	17.39	17.39	17.39

The graphical representation of the results from Table I is given in Fig.4.

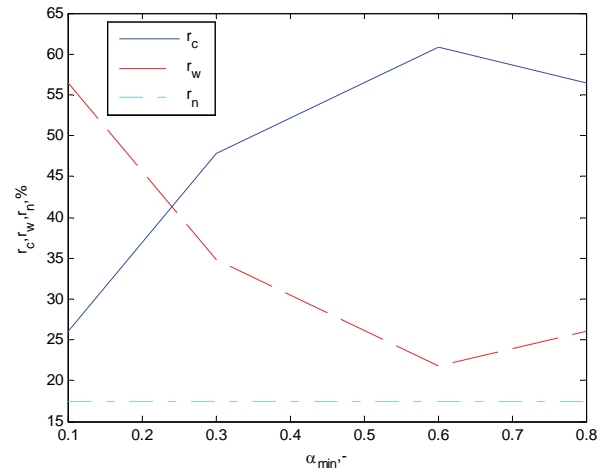


Fig.4. r_c, r_w, r_n as functions of α_{min} for SOFM

Given the above results we choose to use $\alpha_{min}=0.6$ as an optimal value because the number of correctly recognized characters is maximal for it. Thus the next experiment concerns the radius of the neighborhood for fixed α_{min} – we decrease d_{min} from 1 to 10^{-5} by a factor of 10. Again our SOFM is trained for 10 epochs, 26 classes with 5 subclasses. The results are shown in Table II.

TABLE II
FINDING THE OPTIMAL NEIGHBOURHOOD DISTANCE FOR SOFM

d_{min}	10^0	10^{-1}	10^{-2}	10^{-3}	10^{-4}	10^{-5}
Recognition						
$r_c, \%$	39.13	56.52	60.87	56.52	52.17	47.82
$r_w, \%$	60.87	26.09	21.74	26.09	30.43	34.78
$r_n, \%$	0.00	17.39	17.39	17.39	17.39	17.39

The graphical representation of the results from Table I is given in Fig.4.

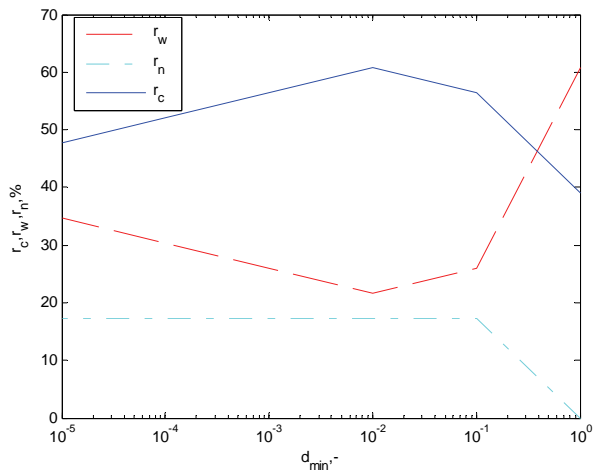


Fig.5. r_c , r_w , r_n as functions of α_{min} for SOFM

Now we have the optimal $\alpha_{min}=0.6$ and $d_{min}=0.01$. How the number of epochs of training the SOFM affects the recognition process, for 26 classes with 5 subclasses, is shown in Table III and graphically in Fig. 6. Training time consumption order is as follows – for 10 epochs – a few minutes, for 100 – about an hour and for 1000 – more than 8 hours.

TABLE III
INFLUENCE OF THE NUMBER OF EPOCHS FOR SOFM

Epochs \ Recognition	10	100	1000
r_c , %	60.87	73.91	82.61
r_w , %	21.74	21.74	17.39
r_n , %	17.39	4.35	0.00

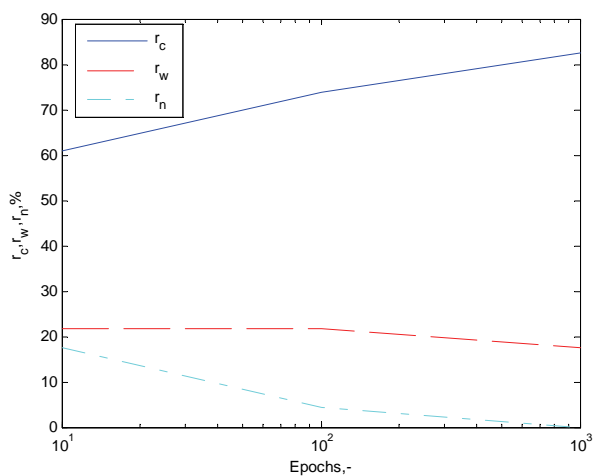


Fig.6. r_c , r_w , r_n as functions of number epochs for SOFM

The results for the neocognitron using the same training and test data are shown in Table IV. The only parameter we change is the S -cell transfer function as seen. The values of the other parameters for this experiment are given in [5].

TABLE IV
RECOGNITION ACCURACY FOR THE NEOCOGNITRON

$\phi(\cdot)$ \ Recognition	Thresh	ThreshLin	Sigmoid
r_c , %	34.75	54.50	65.50
r_w , %	23.00	23.75	34.50
r_n , %	42.25	21.75	0.00

IV. CONCLUSION

It is obvious that the SOFM is equivalent to the neocognitron concerning recognition accuracy when a reasonable amount of time is spent for training (2-10 epochs) and preliminary processed high quality test data is used (small noise levels, shifts, etc.). The last confirms the need and the important role of qualitative preprocessing.

For both - learning rate and neighborhood distance for SOFM should be found appropriate values during training as they highly affect the final recognition accuracy. As neighborhood distance decreases and inclines to 0, the SOFM behaves itself more like a simple competitive neural network which is explainable by its working principle.

As for the S -cell transfer function for the neocognitron it is visible that the sigmoid one is the best option from the three tested ones. In the other two cases the neocognitron drops behind SOFM as for the recognition accuracy.

Depending of the circumstances both of the networks can be applicable in a complete handwriting recognition system.

REFERENCES

- [1] R. Bozinovic and S. Srihari, "Off-Line Cursive Script Word Recognition", IEEE Transactions on Pattern Analysis and Machine Intelligence, vol. 1, pp. 68-83, 1989.
- [2] O. Trier, A. Jain and T. Taxt, "Feature Extraction Methods for Character Recognition – A Survey", Pattern Recognition, vol. 29, no. 4, pp. 641-662, 1996.
- [3] T. Kohonen, "The Self-Organizing Map", Proceedings of IEEE, vol. 78, no. 9, pp. 1467-1480, 1990.
- [4] K. Fukushima, "Neocognitron: A Self Organizing Neural Network Model for a Mechanism of Pattern Recognition Unaffected by Shift in Position", Biological Cybernetics, vol. 36, no. 4, pp. 193-202, 1980.
- [5] K. Fukushima and N. Wake, "Handwritten Alphanumeric Character Recognition by the Neocognitron", IEEE Transactions on Neural Networks, vol. 2, no. 3, pp. 355-365, 1991.
- [6] A. Bekiarski and L. Batchishing, "Choice of structure features for recognition of mongolian letters", Electrotechnics and Electronics, XXXII, no. 1-2, pp. 43-46, 1997.

Comparative Analysis of Integral Calculus Algorithms in Magnetic Signals Evaluation

Virginya Dimitrova¹

Abstract - The article presents three approaches for low-frequency magnetic signals calculation, based on direct integration of the Biot-Savart law using complete elliptic integrals; differences are into the chosen approach for complete elliptic integral calculation. The methods discussed are implemented in C# programming language and the results of their execution are compared both visually and numerically.

Keywords – integral calculus algorithms, complete elliptic integrals, low-frequency-magnetic field

I. INTRODUCTION

The goal of the presented program component is to expose easy-to-use and easy-to-understand approach to evaluate the precision of low-frequency magnetic field calculation when different methods have been used for elliptic integrals solving.

Two ways for precision evaluation are developed:

- Numerical comparison;
- Visual comparison (2D graphs).

Both ways are based on the comparison of the results of low-frequency magnetic field calculation, performed using the *etalon* calculation and *matching* calculation. *Etalon* calculation is performed using the formula for on-axis points [1].

Matching calculation is performed using the formulas for off-axis points based on magnetic field potential that involves complete elliptic integrals of the first and second kind [2]:

$$K = \int_0^{\pi/2} \frac{d\beta}{\sqrt{1 - k^2 \sin^2 \beta}} \quad (1)$$

$$L = \int_0^{\pi/2} \sqrt{1 - k^2 \sin^2 \beta} \cdot d\beta \quad (2)$$

In both cases calculations are performed for the same set of points of **z**-axis that is perpendicular to the plane of the current turn.

The differences into the precision of calculations are caused by the method chosen for elliptic integral calculation:

- Using diagram;
- Using elliptic integral Tables;
- Using Arithmetic-Geometric-Mean.

Magnetic field calculation for different cases of field sources – coils with great number of current turns requires a great deal of computation for large number of points into the area influenced by the field. We need a method that will guarantee a reduced complexity for a large amount of field points, namely with a matrix of points nearly 90000 or more.

The method must guarantee a good precision of calculations too. The main part of field computations is related to complete elliptic integrals evaluation. Consequently, improving the precision, decreasing the complexity of calculations and optimizing memory consumption can be achieved using the best suited method for complete elliptic integrals evaluation.

The first implemented method can be determined as a direct method and uses a diagram to compute the complete elliptic integrals of first and second kind $K(k)$ and $L(k)$ for the corresponding values of k . The main disadvantage of this method is the need to store floating point values into the memory as arrays elements (for example) thus limiting the step of discretization to avoid enlarging of arrays. Besides of errors of discretization this method does not ensure enough precision for the impossibility to obtain real values for $K(k)$ and $L(k)$ with more that two digits after the decimal point from the diagram. The method however has some advantages: relatively small size of the arrays and their static nature allows implementation with static arrays instead of linked lists and thus only two fast indexing operations per k value are needed to obtain $K(k)$ and $L(k)$ values.

Second implemented method is also a direct method as the first one, but is based on calculations (not on the predefined values stored into the memory). This method saves memory but instead of fast indexing operations uses so called modulus $m = 1 - k^2$ and double precision constants into a lot of multiplication and addition operations. (The method is based on FORTRAN subroutine COMELP, rewritten in C# language).

The third implemented method can be determined as an iterative method (starts from a guess and finds successive approximations that converge to the solution) and is effective and numerically stable. This method computes Legendre elliptic integrals $k(k)$ and $L(k)$ by computing the equivalent Carlson elliptic integrals and corresponding RC, RF and RJ routines, originally written in FORTRAN and rewritten in C# language.

Elliptic integrals used in magnetic field calculation are expressed using Legendre's notation.

Numerical comparison is realized in two modes:

- Single values comparison;
- Multiple values comparison.

When the first mode is used the value of the **z**-coordinate of the point into which the magnetic induction **B** should be calculated is entered from the keyboard and the two compared numeric values as well as their difference are displayed.

Under the second mode the magnetic induction **B** is calculated for the predefined set of points and the corresponding compared values are displayed in rows-and-columns form (**DataGrid** Windows Forms control).

¹Virginya T. Dimitrova is with the Faculty of Computer Systems and Control, Technical University, 1000 Sofia, Bulgaria. E-mail: vergv@tu-sofia.bg

In regard to the visual comparison two different graphical representations of the results of precision analysis are supplied:

- 2D graph with z -coordinates of points on X -axis and calculated B -values (using *etalon* method and *matching* method) in different colors on Y -axis;
- 2D graph with z -coordinates of points on X -axis and the difference of the calculated B -values (*etalon* method and *matching* method) on Y axis.

II. DESIGN OF THE PROGRAM

The core of the program is the algorithm shown in fig 1. It supplies all the possibilities needed to satisfy the goal of the program.

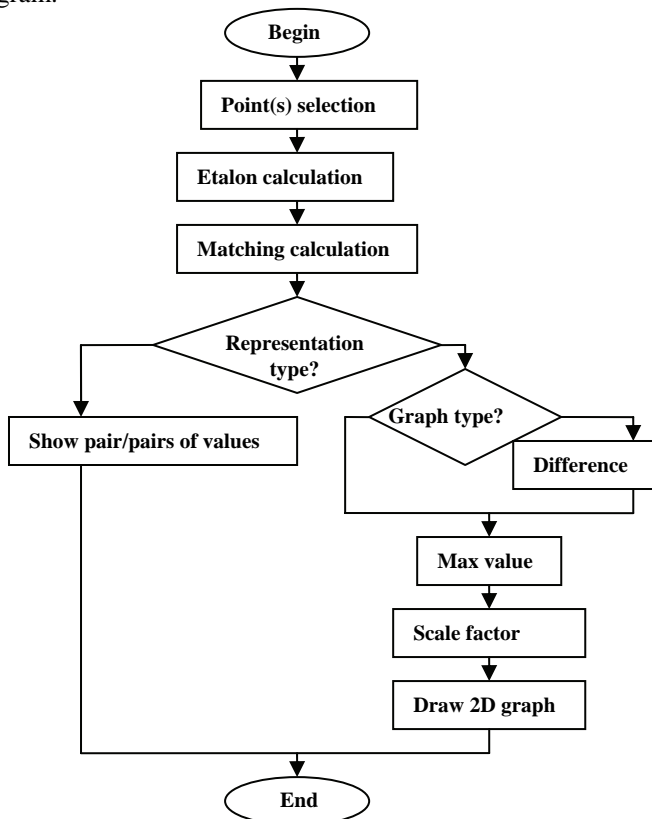


Figure 1. Flow-chart of the program

III. IMPLEMENTATION

Program decision is created using Visual Studio .NET program environment, C# programming language and Windows Forms application template.

Methods for magnetic induction calculation are placed into a separate **FieldCalcs** class. To achieve the universality (ability to calculate magnetic induction for every point into the space) the constructor has two parameters – the values of ρ and z . For the current implementation the value of the first parameter is always 0.0 and only the second parameter changes its value.

Separate instance methods for calculation are supplied:

- **BonZ()** *etalon* method for on-axis points and

- **BEveryWhere()** *matching* method for off-axis points.

The **BEveryWhere()** method has a parameter passed using a .NET delegate mechanism thus allowing to dynamically change the method used for complete elliptic integrals calculation (fig. 2).

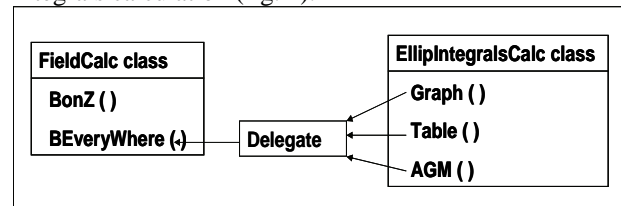


Figure 2. Program components

IV. CONCLUSION

The presented program component has been successfully applied for the evaluation of the effectiveness, numerical stability and precision of the calculations in regard to low-frequency magnetic field generated by different configurations of field sources. The structure and implementation of the program component allows methods for complete elliptic integral calculation, exposed by the **FieldCalc** class, to be replaced, improved or extended with additional methods without changes in the design of the component or applications that reference it.

REFERENCES

- [1] M. P. Zlatev, Theoretical Electrotechnic, Technika, Sofia, 1972
- [2] B. C. Carlson, On computing elliptic integrals and functions, J. Math and Phys., 44 (1965), pp.36-51
- [3] Developing Microsoft .NET Applications for Windows with Visual C# .NET
- [4] V. Todorova, "3D computer simulation of the static magnetic field distribution over the virtual human body", "Information Technologies and Control", ISSN 1312-2622
- [5] V.Dimitrova, Maleshkov St., Methods for 3d surface subdivision in calculation and visualization of static magnetic field distribution, Electronics and Electrotechnics, 2007
- [6] V. Todorova, Maleshkov St., "Geometric Data Exchange in XML format Using .NET Environment", Computer Science'2004, Technical University of Sofia, Bulgaria
- [7] V. Todorova, Maleshkov St., "OpenGL programming in .NET environment: Problems and Solutions", XVIII-Conference SAER-2004, Varna, Bulgaria
- [8] D.Dimitrov, A.Dimitrov, Computer Simulation of Low Frequency Magnetic Field, p.171-175, Proceedings of 17th EAEEIE Annual Conference on Innovation in Education for Electrical and Information Engineering, June, 1-3, 2006, University of Craiova, Romania.
- [9] D.Dimitrov, H.Hristov, Modeling the Moving of Charges in Homogenous Magnetic Field, p.27-31, Proceedings of the First International Conference on Communications, Electromagnetics and Medical Applications (CEMA'06), October,19-21, Sofia, Bulgaria.
- [10] D.Dimitrov, An Investigation on Propagation and Absorption of Electromagnetic Signals Through Biological Media, p.22-26, Proceedings of the First International Conference on Communications, Electromagnetics and Medical Applications (CEMA'06), October,19-21, Sofia, Bulgaria.

Investigation of Maximally Flat Fractional Delay All-pass Digital Filters

Kamelia S. Ivanova¹ and Georgi K. Stoyanov²

Abstract – In this paper the relations between the allpass transfer function poles placement and the fractional delay parameter values are analysed and new closed form expressions are derived. It is shown that the poles are taking very unusual positions compared to other filter realizations. Then, the sensitivities of the most popular allpass sections are investigated and the most appropriate structures for different delay-time values are identified. Using these results it is possible to design high accuracy fractional delay structures over different frequency ranges and in a limited wordlength environment.

Keywords – IIR digital filters, allpass sections, fractional delay, maximally flat approximation, poles position, low sensitivity.

I. INTRODUCTION

Recently, there is a growing interest in developing fractional delay digital filters, which appeared to be very useful in numerous fields of digital signal processing and digital communications (timing adjustment, jitter elimination, digital modems, and speech synthesis) [1].

The theory and the design methods of FIR fractional delay filters are quite well developed [1][2][3] and mature enough to have convenient structures to implement them. There are, however, very few publications about IIR fractional delay filters, probably because of the problems connected to the IIR realizations like possible instabilities, higher level of the round-off noises and worst behavior in a limited wordlength environment due to their higher sensitivities. In general the obtained solution has to be checked so that all poles of the filter remain within the unit cycle in the z-domain. The design of IIR fractional delay is by far more complicated than that of corresponding FIR filters. In this work we choose to investigate allpass based fractional delay IIR filters because they have the best magnitude properties, permitting us to concentrate on the phase response characteristics. We use the approximation procedures proposed by Thiran [4], which appear to be the most appropriate for the design of fractional delay digital structures with a maximally flat group delay.

When designing recursive digital filters in limited wordlength environment, it is very important to develop or choose allpass sections with minimized sensitivities for every given transfer function poles position. But the pole-positions

are varying considerably for different values of the realized fractional delay, so a thorough analysis of the connections between the poles placement and the fractional delay parameter values has been made in this paper. Additionally, we investigate the range of fractional delay parameter values for which the allpass sections are remaining stable as well as the range of values for which the allpass sections have only real poles. We derive analytical relations between the fractional delay parameter values and the poles for second, third and fourth order allpass sections.

The results so obtained are presented analytically and graphically. These results generalize the behavior of the fractional delay allpass sections so they can be used to design high accuracy fractional delay structures in a different frequency range and in a limited wordlength environment.

II. ANALYSES OF ALLPASS BASED FRACTIONAL DELAY FILTERS OF DIFFERENT ORDER

There are several approaches to approximate given phase, group delay, or phase delay response specifications [1][2][3]. To obtain maximally flat group delay responses, we select the method proposed by Thiran because it provides a closed form solution for allpass transfer function coefficients. The coefficients of an allpass filter with a maximally flat group delay response at the zero frequency can be expressed as [4]:

$$a_k = (-1)^k \binom{N}{k} \prod_{n=0}^N \frac{D-N+n}{D-N+k+n}, \text{ for } k=0, 1, 2, \dots, N. \quad (1)$$

This allpass filter is stable when $D > N$ and when $N-1 < D < N$ as it was observed in [2]. We have shown in [7] that the transfer function pole placements are closely related to the fractional delay parameter values. The fractional delay parameter values must be very carefully selected to keep the transfer function poles position inside of the unit circle.

A. Investigation of a second order transfer function

It is easy to obtain the two real poles of the second order fractional delay allpass transfer function when fractional delay parameter value is $1 < D < 2$ and the pair of complex-conjugate decision when $D > 2$. The complex-conjugate poles pair can be expressed as a function of the fractional delay parameter value as follows

¹Kamelia S. Ivanova is with the Faculty of Communications and Communications Technology, Technical University, Kliment Ohridski 8, 1000 Sofia, Bulgaria, E-mail: ksi@tu-sofia.bg

²Georgi K. Stoyanov is with the Faculty of Communications and Communications Technology, Technical University, Kliment Ohridski 8, 1000 Sofia, Bulgaria, E-mail:stoyanov@ieee.org

$$p_{1,2} = \frac{D-2}{D+1} \pm j \sqrt{\frac{3(D-2)}{(D+1)^2(D+2)}} \quad (2)$$

The possible poles positions as a function of increasing fractional delay parameter values from two to infinity are shown in Fig. 1. One could notice that transfer function poles occupy fixed position on the root loci.

The most common requirement for real applications is time delay with small fractional delay parameter values ($N-0.5 < D < N+0.5$, where N is the transfer function order) which means that poles should be positioned near $z = 0$ (more specifically in the range between 0 and 0.2 on both real and imaginary axes in the z plane).

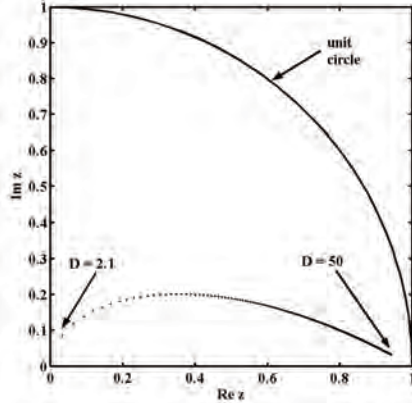


Fig. 1. Possible pole positions of second order allpass transfer function

B. Investigation of a third order transfer function

Similar investigation can be made for third order allpass transfer function. Third order fractional delay allpass filter is stable for fractional delay parameter values $D > 2$. In most of the cases there are one real and a pair of complex-conjugated poles. We identify two distinct situations. In the first one, for $2 < D < 3$, the real pole is negative and the complex-conjugated poles are with positive real parts on the lower root loci. This placement is specific for $N-0.5 < D < N$ fractional delay parameter values. In the second case, for $D > 3$, the real pole and the real part of the complex-conjugated pair are positive. The complex-conjugated poles take values on the upper root loci (Fig. 2). Here one could conclude that poles placement for small fractional delay parameter values are concentrated in the vicinity of $z = 0$.

$$p_1 = \frac{\sqrt[3]{C}}{A(D+1)} - 4 \frac{(D-3)A}{(D+1)(D+2)\sqrt[3]{C}} + \frac{D-3}{D+1}, \quad (3)$$

$$p_{2,3} = -\frac{\sqrt[3]{C}}{2A(D+1)} + 2 \frac{(D-3)A}{(D+1)(D+2)\sqrt[3]{C}} + \frac{D-3}{D+1} \pm j \frac{\sqrt{3}}{2} \left(\frac{\sqrt[3]{C}}{A(D+1)} + 4 \frac{(D-3)A}{(D+1)(D+2)\sqrt[3]{C}} \right), \quad (4)$$

where

$$A = D^3 + 6D^2 + 11D + 6, \quad (5)$$

$$B = \frac{D^3 - 8D^2 + 21D - 18}{D+2} \quad \text{and} \quad (6)$$

$$C = (-4D^2 + 40D - 84 + \sqrt{45BD} + \sqrt{45B})A^2(D+1). \quad (7)$$

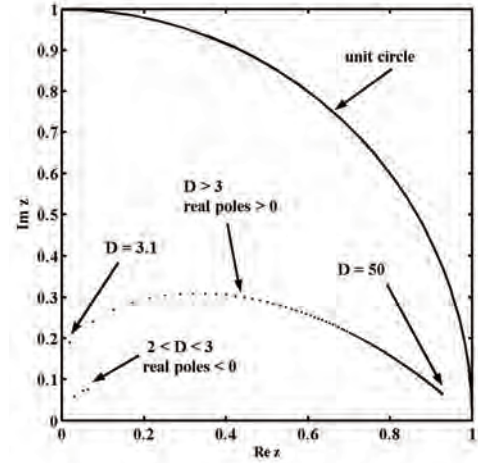


Fig. 2. Possible pole positions of third order allpass transfer function

C. Investigation of a fourth order transfer function

Investigation of fourth order transfer functions leads to similar conclusions, as shown in Fig. 3. One specific distinction of this function is that the upper loci have negative real part for small variation of fractional delay parameter values D .

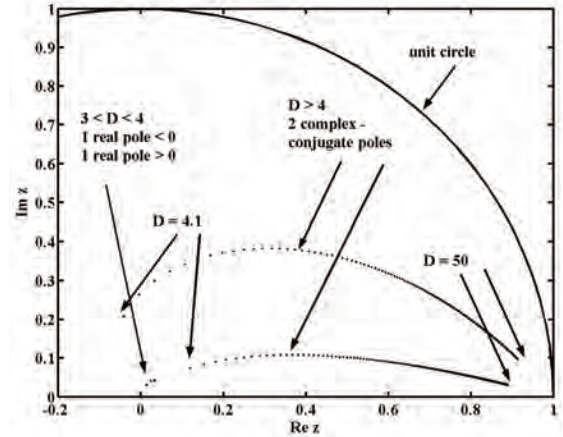


Fig. 3. Possible pole positions of fourth order allpass transfer function

At this point it is easy to make a generalized conclusion for the behavior of N -th order allpass structures: they are stable for $D > N-1$, given that for $D = N$ there exist N solutions in $z = 0$. There are always real poles for the range of values $N-1 < D < N$, and at least one of them is always negative. There are always pairs of complex-conjugated poles for the

case of $D > N$, and increasing of N leads a shift for the bigger part of the loci toward the left half of the z -plane.

III. SECOND ORDER FRACTIONAL DELAY ALLPASS SECTIONS

It is clear from the previous section that the transfer function poles of the allpass circuits with fractional delay are laying in the vicinity of $z=0$ and thus we need realizations with higher pole-density in this region in order to ensure high fractional delay time accuracy. Our extensive search has shown that no such realizations are existing. The most promising candidate is the one based on the famous coupled form having equal pole-density inside the unit circle. Unfortunately, we could not synthesize an allpass section with uniform pole-distribution and because of that we have to investigate and compare the other known allpass sections in order to identify these with lower sensitivity for each pole-positions.

We have shown in [7] that for small values of fractional delay parameter $N - 0.5 < D < N + 0.5$, the phase delay response remains constant over wider range of frequencies and this range is narrowing when increases. In fact realizations with larger D (i.e. transfer function poles near $z = 1$) can be used for implementation of fractional delay filters for very special applications.

When we want to achieve larger non-integer time delay, it is recommendable to use a cascade with the necessary integer number of delay elements and one second order fractional delay allpass structure. This will ensure the largest possible frequency range over which the group delay response will stay flat.

The transfer function of the most popular allpass sections are as follows [5]:

$$H_{MH2A}(z) = \frac{b_1 b_2 - b_1 z^{-1} + z^{-2}}{1 - b_1 z^{-1} + b_1 b_2 z^{-2}}; \quad (8)$$

$$H_{MH2B}(z) = \frac{b_2 - b_1 z^{-1} + z^{-2}}{1 - b_1 z^{-1} + b_2 z^{-2}}; \quad (9)$$

$$H_{KW2A}(z) = \frac{1 + a_1 - a_2 - (a_1 + a_2)z^{-1} + z^{-2}}{1 - (a_1 + a_2)z^{-1} + (1 + a_1 - a_2)z^{-2}}; \quad (10)$$

$$H_{KW2B}(z) = \frac{d_1 + d_2 - 1 - (d_1 - d_2)z^{-1} + z^{-2}}{1 - (d_1 - d_2)z^{-1} + (d_1 + d_2 - 1)z^{-2}}; \quad (11)$$

$$H_{GM2}(z) = \frac{-a_1 - a_2(1 - a_1)z^{-1} + z^{-2}}{1 - a_2(1 - a_1)z^{-1} - a_1 z^{-2}}; \quad (12)$$

$$H_{AL}(z) = \frac{-a_1 + a_2(1 - a_1)z^{-1} + z^{-2}}{1 + a_2(1 - a_1)z^{-1} - a_1 z^{-2}}; \quad (13)$$

$$H_{ST2A}(z) = \frac{1 - 2b - 2(1 - 2a - b + 2ab)z^{-1} + z^{-2}}{1 - 2(1 - 2a - b + 2ab)z^{-1} + (1 - 2b)z^{-2}}; \quad (14)$$

$$H_{ST2B}(z) = \frac{1 - c_2 + (-2 + 2c_1 + c_2)z^{-1} + z^{-2}}{1 + (-2 + 2c_1 + c_2)z^{-1} + (1 - c_2)z^{-2}}. \quad (15)$$

After representing the coefficients of these sections with the coefficients of the Thiran approximation (1), we get the results shown in Table 1-4. With these formulae it is possible to design and realize the corresponding allpass sections for any given delay parameter D .

TABLE I
MH2A AND MH2B FRACTIONAL DELAY FILTER COEFFICIENTS

MH2A		MH2B	
b_1	b_2	b_1	b_2
$\frac{2(D-2)}{(D+1)}$	$\frac{(D-1)}{2(D+2)}$	$\frac{2(D-2)}{(D+1)}$	$\frac{(D-1)(D-2)}{(D+1)(D+2)}$

TABLE II
KW2A AND KW2B FRACTIONAL DELAY FILTER COEFFICIENTS

KW2A		KW2B	
a_1	a_2	d_1	d_2
$\frac{(D^2 - 3D - 4)}{(D+1)(D+2)}$	$\frac{(D^2 + 3D - 4)}{(D+1)(D+2)}$	$\frac{2(D-1)}{(D+2)}$	$\frac{6}{(D+1)(D+2)}$

TABLE III
AL AND GM2 FRACTIONAL DELAY FILTER COEFFICIENTS

AL		GM2	
a_1	a_2	a_1	a_2
$\frac{(D-1)(D-2)}{(D+1)(D+2)}$	$\frac{(D-2)(D+2)}{(D^2+2)}$	$\frac{(D-1)(D-2)}{(D+1)(D+2)}$	$\frac{(D-2)(D+2)}{(D^2+2)}$

TABLE IV
ST2A AND ST2B FRACTIONAL DELAY FILTER COEFFICIENTS

ST2A		ST2B	
a	b	c_1	c_2
$\frac{3}{D^2+2}$	$\frac{3D}{(D+1)(D+2)}$	$\frac{6}{(D+1)(D+2)}$	$\frac{6D}{(D+1)(D+2)}$

IV. SENSITIVITY INVESTIGATIONS

Next we investigate the phase response sensitivities of the fractional delay allpass sections so obtained for two delay parameter D values using the package PANDA [6]. The worst case sensitivities (with transfer function coefficients given in the tables) are shown in Fig. 4 – Fig. 11. Thus it appeared that the Mitra and Hirano (MH2A and MH2B), Gray-Markel (GM2) and Ansari-Liu (AL) structures are the most appropriate for small delay parameter values since they have the lowest phase response sensitivity. For poles near $z = 1$

the low sensitivities sections ST2A and ST2B are behaving much better than all other known sections.

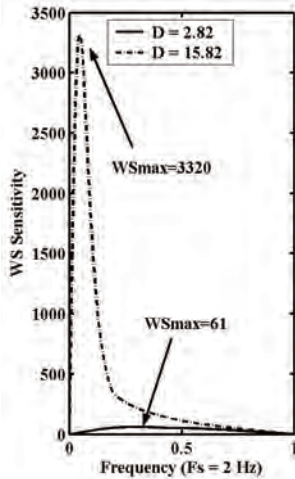


Fig. 4. Worst case sensitivity of MH2A

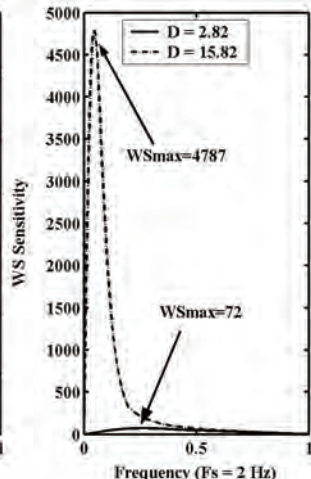


Fig. 5. Worst case sensitivity of MH2B

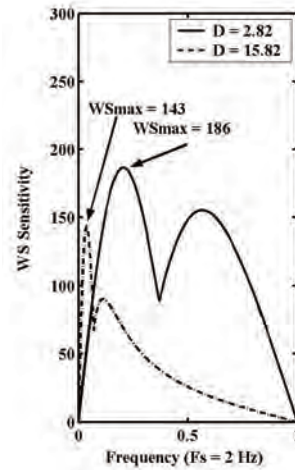


Fig. 10. Worst case sensitivity of ST2A

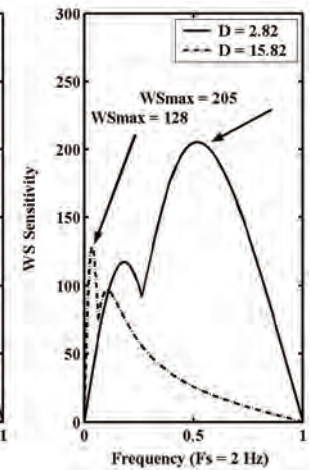


Fig. 11. Worst case sensitivity of ST2B

V. CONCLUSIONS

In this paper we have investigated the behavior of the fractional delay allpass filters with maximally flat group delay response. It was found that transfer function poles of these filters are situated quite differently compared to the ones of the known allpass sections. It was shown that the sections sensitivities depend strongly on the value of the fractional delay parameter D and the most suitable sections for some typical pole-locations have been pointed out. Similar sensitivity analysis for other pole-locations (different values of D) should be conducted and the most proper allpass sections should be selected or synthesized in order to ensure an accurate realization of the fractional delay in a limited wordlength environment.

REFERENCES

- [1] T. Laakso, V. Valimaki, M. Karjalainen and U. Laine, "Splitting the unit delay – tools for fractional delay design", IEEE Signal Processing Mag., vol. 13, no. 1, pp. 30 – 60, Jan. 1996.
- [2] V. Valimaki, "Discrete-Time Modeling of Acoustic Tubes Using Fractional Delay Filters", Dr. Tech. Thesis, Espoo, Finland; Helsinki Univ. of Tech., Faculty of Electrical Eng., Laboratory of Acoustics and Audio Signal Processing, Dec. 1995.
- [3] V. Valimaki, "A new filter implementation strategy for Lagrange interpolation", in Proc. IEEE Int. Symp. Circuits and Systems (ISCAS'95), Seattle, Washington, vol. 1, pp. 361 – 364, April 29–May 3, 1995.
- [4] J.-P. Thiran, "Recursive digital filter with maximally flat group delay", IEEE Trans. Circuit Theory, vol. 18, no. 6, pp. 659 – 664, Nov. 1971.
- [5] G. Stoyanov and A. Nishihara, Very low sensitivity design of digital IIR filters using parallel and cascade-parallel connections of all-pass sections, Bulletin of INCOCSAT, Tokyo Institute of Technology, Vol. 1, pp. 55-64, March 1995.
- [6] N. Sugino and A. Nishihara, "Frequency-domain simulator of digital networks from the structural description", Trans of the IEICE of Japan, Vol. E73, No. 11, pp.1804-1806, Nov.1990.
- [7] K. S. Ivanova, V. I. Anzova, G. K. Stoyanov, "Low sensitivity realizations of allpass based fractional delay filter", Proc. TELECOM'2005, St. Konstantine and Elena, Varna, Bulgaria, pp. 376-382, Oct. 7-9, 2005.

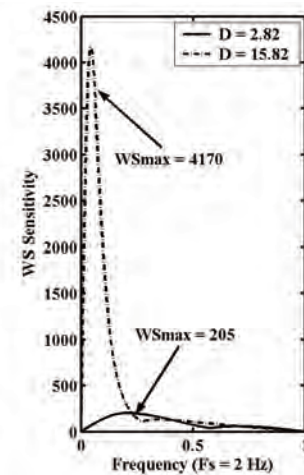


Fig. 6. Worst case sensitivity of KW2A

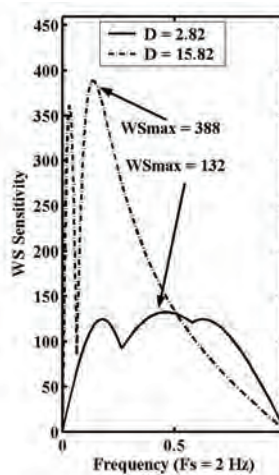


Fig. 7. Worst case sensitivity of KW2B

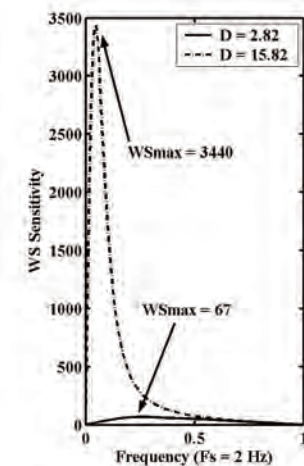


Fig. 8. Worst case sensitivity of AL

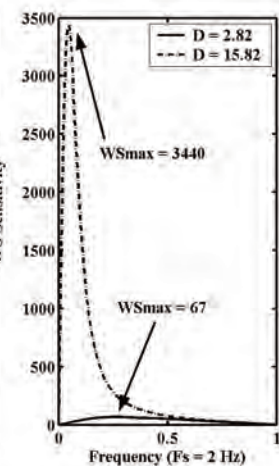


Fig. 9. Worst case sensitivity of GM2

A Unification of Determined and Probabilistic Methods in Pattern Recognition

Geo Kunev¹, Georgi Varbanov² and Christo Nenov³

Abstract – Main goal of the present task is to find possibilities for achieving uniform rules for pattern recognition, regardless of significant difference in initial positions and different methods for achieving the end form of algorithms. We will try to present most used rules for decision making in aggregate of:

- uniform procedure for estimate of state, making a calculation of linear or quadratic form,
- comparing of results with some threshold value.

We can apply this results in KDD (data mining) software.

Keywords – Classification, Bayes, Pattern recognition, KDD

I. INTRODUCTION

By non-concave location of features by class's areas we search dividing function in full quadratic form or in a part:

$$g(x) = c_0 + \sum_{i=1}^d c_i x_i + \sum_{k=1}^d \sum_{j=1}^d c_{ij} x_i x_j(x, \bar{c}) \quad (1)$$

or:

$$g(x) = X^T A X + a^T X + a_0 \quad (2)$$

We search one-type pattern recognition rules for:

1. Algorithms, based on optimal statistical decision making theory,
2. Algorithms, based on dispersion of probabilistic recognition features,
3. Algorithms, based on minimizing of geometric mean recognition error.

II. OPTIMAL STATISTICAL DECISION MAKING

In this well known case [1], pattern recognition task is treat as common statistical task with predefined optimum criteria.

$$R(A/x) = M[I(x\hat{x}/x)] \quad (3)$$

Most used criterion is a loss function $I(x\hat{x})$ for calculation of conditional mean risk, searching the best estimation [4]:

$$R(A) = M[R(A/x)] = M[I(x\hat{x})] \Rightarrow \min \quad (4)$$

Average risk by repeatedly recognition of M classes is:

$$R = \sum_{k=1}^M \sum_{m=1}^M \int_{X_M} c_{km} P_k \cdot f(\bar{y}/x_k) dy \quad (5)$$

Decision rule for M classes ($j=1, M$) is:

$$\bar{y}_i \in X_j, \text{ -if } -c_j \cdot P(x_j) f(y/x_j) \Rightarrow \max \quad (6)$$

Decision rule for two classes is:

$$\begin{aligned} \bar{y}_i \in X_1, \text{ -if } -\frac{f(y_i/x_1)}{f(y_i/x_2)} = \lambda > \lambda_0 = \frac{P_2(c_{21} - c_{22})}{P_1(c_{12} - c_{11})} \\ \bar{y}_i \in X_2, \text{ -if } -\lambda < \lambda_0 \end{aligned} \quad (7)$$

By normal feature dispersion on M classes:

$$\begin{aligned} \bar{y}_i \in X_1, \text{ -if } -g_j(\bar{y}) = -\frac{1}{2} y^T \sum_j y + (\sum_j \mu_j)^T - \\ -\frac{1}{2} \mu_j^T \sum_j \mu_j - \frac{1}{2} \ln |\sum_j \mu_j| + \ln P(x_j) + \ln |c_j| = \\ = Y^T A_j Y + a_j^T y + a_{j0} \Rightarrow \max \end{aligned} \quad (8)$$

By two classes and conditions:

$$\begin{aligned} P(x_1) = P(x_2), \\ (c_{12} - c_{11} = c_{21} - c_{22}), \\ \Sigma_1 = \Sigma_2, \end{aligned} \quad (9a)$$

we have linear recognition rule:

$$\begin{aligned} \bar{y}_i \in X_1, \text{ -if } -y^T \sum^1 (\mu_1 - \mu_2) \\ -\frac{1}{2} (\mu_1 - \mu_2)^T \sum^1 (\mu_1 - \mu_2) < 0 \end{aligned} \quad (9b)$$

Bayesian strategies compare projection of recognized observation (vector) on directions eq.(10), with the mean values vector on the same direction:

$$\begin{aligned} a = \sum^{-1} (\mu_1 - \mu_2) \text{ - by two classes} \\ a = \sum_j^{-1} \mu_j \text{ - by } M \text{ classes.} \end{aligned} \quad (10)$$

¹Geo Kunev is with the Faculty of Computer Sciences, TU Varna, Studentska 1, 9000 Varna, Bulgaria, E-mail: geo_qnew@hotmail.com

²Georgi Varbanov is with the Faculty of Computer Sciences, TU Varna, Studentska 1, 9000 Varna, Bulgaria, E-mail: varbanov@mbox.digsys.bg

³Christo Nenov is with the Faculty of Computer Sciences, TU Varna, Studentska 1, 9000 Varna, Bulgaria, E-mail: chr_nenov@gmail.com

III. RECOGNITION MATRICES STUDY

By limited a priory statistic we search recognition rules, based on sub-areas metrics for different classes. For two classes we can use Fisher's nonzero hypothesis criterion [2]:

$$F = \frac{S_{\Omega}^2}{S_R^2}, \quad : \quad (11a)$$

where:

S_{Ω}^2 - is dispersion estimation (by groups),
 S_R^2 - is dispersion estimation (in group).

As multidimensional analysis we can use Mahalanobis distance between groups with means μ_i and μ_j and common covariance matrix V :

$$V^2 = (\mu_i - \mu_j)^T V^{-1} (\mu_i - \mu_j) \quad (11b)$$

An estimation of dispersion in groups for M classes is:

$$\begin{aligned} S_w &= \sum_{k=1}^M P(x_k) E\{(y - \mu_k)(y - \mu_k)^T / x_k\} = \\ &= \sum_{k=1}^M P(x_k) \sum_k \end{aligned} \quad (12)$$

where:

$P(x_k)$ - every class a priory probability,
 Σ_k - classes covariance matrices,
 y, μ_k - observations and means by classes vectors.

An estimation of dispersion by groups for M classes is:

$$S_B = \sum_{k=1}^M P(x_k) (\mu_k - \mu_0)(\mu_k - \mu_0)^T \quad (13)$$

An estimation based only on statistic:

$$S_{B_{k,m}} = (\mu_k - \mu_m)(\mu_k - \mu_m)^T \quad (14)$$

We search best transformation in form [1]:

$$Z = a^T Y + a_0 \quad (15)$$

like:

$$\begin{aligned} J &= \frac{|S_B^*|}{|S_w^*|} = \frac{\sum_{k=1}^M m_k (\mu_k^* - \mu_0^*)(\mu_k^* - \mu_0^*)^T}{\sum_{k=1}^M \sum_{z \in Z_k} (Z - \mu_0^*)(Z - \mu_0^*)^T} = \\ &= \frac{|A^T (\mu_k - \mu_0)(\mu_k - \mu_0)^T A|}{|\sum_{y \in Y_k} (y - \mu_0)(y - \mu_0)^T|} = \frac{|A^T S_B A|}{|A^T S_w A|} \end{aligned} \quad (16)$$

where:

$y, \mu_k, \mu_0, S_B, S_w$ - are observations, means and dispersion matrixes in initial areas,

and $Z, \mu_k^*, \mu_0^*, S_B^*, S_w^*$ - the same after linear transformation.

By two classes and

$$a^T \Sigma_k a = \sigma_k^{*2}, \quad \text{и} \quad \mu_k^* = a^T \mu_k + a_0 \quad (17)$$

we have:

$$J = \frac{(\mu_k^* - \mu_j^*)^2}{\sigma_k^{*2} - \sigma_j^{*2}} \quad (18)$$

and extremum conditions can be defined:

$$\begin{aligned} \frac{dJ}{da_i} &= \frac{dJ}{d\sigma_k^{*2}} \cdot \frac{d\sigma_k^{*2}}{da_i} + \frac{dJ}{d\sigma_j^{*2}} \cdot \frac{d\sigma_j^{*2}}{da_i} + \\ &+ \frac{dJ}{d\mu_k^*} \cdot \frac{d\mu_k^*}{da_i} + \frac{dJ}{d\mu_j^*} \cdot \frac{d\mu_j^*}{da_i} = 0 \\ \frac{dJ}{da_0} &= \frac{dJ}{d\sigma_k^{*2}} \cdot \frac{d\sigma_k^{*2}}{da_0} + \frac{dJ}{d\sigma_j^{*2}} \cdot \frac{d\sigma_j^{*2}}{da_0} + \\ &+ \frac{dJ}{d\mu_k^*} \cdot \frac{d\mu_k^*}{da_0} + \frac{dJ}{d\mu_j^*} \cdot \frac{d\mu_j^*}{da_0} = 0 \end{aligned} \quad (19a)$$

where:

$$\begin{aligned} \frac{dJ}{d\sigma_k^{*2}} &= -\frac{(\mu_k^* - \mu_j^*)^2}{\sigma_k^{*2} + \sigma_j^{*2}}; \quad \frac{dJ}{d\sigma_j^{*2}} = -\frac{(\mu_k^* - \mu_j^*)^2}{\sigma_k^{*2} + \sigma_j^{*2}} \\ \frac{dJ}{d\mu_k^*} &= -\frac{dJ}{d\mu_j^*} = -\frac{2(\mu_k^* - \mu_j^*)}{\sigma_k^{*2} + \sigma_j^{*2}} \\ \frac{d\sigma_k^{*2}}{da_i} &= -2\Sigma_k a; \quad \frac{d\mu_k^*}{da_i} = \mu_k; \quad \frac{d\sigma_j^{*2}}{da_i} = -2\Sigma_j a; \quad \frac{d\mu_j^*}{da_i} = \mu_j \\ \frac{d\sigma_k^{*2}}{da_0} &= 0; \quad \frac{d\mu_k^*}{da_0} = 1; \quad \frac{d\sigma_j^{*2}}{da_0} = 0; \quad \frac{d\mu_j^*}{da_0} = 1; \end{aligned} \quad (19b)$$

then:

$$2 \left[\frac{(\mu_k^* - \mu_j^*)^2}{\sigma_k^{*2} + \sigma_j^{*2}} \right] \left(\frac{1}{2} \Sigma_k + \frac{1}{2} \Sigma_j \right) a = \mu_k - \mu_j \quad (20)$$

or:

$$a = \left(\frac{1}{2} \Sigma_k + \frac{1}{2} \Sigma_j \right)^{-1} (\mu_k - \mu_j) \quad (21)$$

By equal covariance matrix:

$$a = \Sigma^{-1} (\mu_k - \mu_j) \quad (22)$$

In case of a linear transformation by two classes with equal covariance matrix, the decision is known as Fisher's linear discriminant [2],[3]:

$$S_B \cdot W_i = \lambda \cdot S_w \cdot W_i \quad (23)$$

If S_w is a non-degenerate matrix:

$$S_B \cdot W_i = \lambda \cdot S_w \cdot W_i \quad (24)$$

By dichotomy of two classes and $S_B=S_B'$

$$W = S_w^{-1} \cdot (\mu_k - \mu_i) \tag{25}$$

and this is same as eq.(22).

In multidimensional case:

$$a_k = S_{W_k}^{-1} \cdot (\mu_k - \mu_0) \tag{26}$$

After centering:

$$a_k = S_{W_k}^{-1} \cdot \mu_k \tag{27}$$

IV. MINIMIZING OF GEOMETRIC MEAN RECOGNITION ERROR

This group of methods has goal to develop procedures for finding dividing functions coefficients.

After:

$$y = \begin{vmatrix} 1 \\ x \\ \varphi(x) \end{vmatrix}; a = \begin{vmatrix} c_0 \\ c_i \\ c_{ij} \end{vmatrix} \quad \text{or:} \quad y' = \begin{vmatrix} x \\ \varphi(x) \end{vmatrix}; a' = \begin{vmatrix} c_i \\ c_{ij} \end{vmatrix} \tag{28}$$

we can have eq. (1) in form of linear dividing function [3]:

$$g(x) = a^T Y \tag{29}$$

or:
$$g(x) = a'^T Y' + c_0 \tag{30}$$

Presuming linear class divider:

$$a^T (y_m - y_n) = 0 \tag{31}$$

vector a^T is normal to every vector on dividing surface.

So, every pair of classes (W_i, W_j):

$$\begin{aligned} a^T y_m > 0, & \text{ if } y_m \in W_i \\ a^T y_m < 0, & \text{ if } y_m \in W_j \end{aligned} \tag{32}$$

After transformation:

$$\begin{aligned} y_m &= -y_m; \\ \forall y_m &\in W_j, \end{aligned}$$

decision rule become:

$$a^T y_m < 0; \forall (y_m \in W_i, W_j) \tag{33}$$

Having a decision area supposes non-single decision, therefore it can be used additional limitations, for example, searching minimum weight vector:

$$a^T y_m \geq b > 0; \forall (y_m \in W_i, W_j) \tag{34}$$

In this case a learning task is to find weight vector \bar{a} , matching the best possible equation in form:

$$Ya = b; Y[n,d]; b[n,1]; n > d \tag{35}$$

This system in common case has no exact decision, therefore after setting error vector:

$$e = Ya - b \tag{36}$$

the task can be treated as classical case of minimizing of:

$$J(a) = \|Ya - b\|^2 = \sum_{i=1}^n (a^T y_i - b_i)^2 \tag{37}$$

or:
$$\nabla J(a) = 2Y^T(Ya - b) = \sum_{i=1}^n 2(a^T y_i - b_i) y_i = 0 \tag{38}$$

and:

$$Y^T Ya = Y^T b \tag{39}$$

If the matrix $Y^T Y$ (d.d) is non-degenerate, the vector is:

$$a = (Y^T Y)^{-1} Y^T b = Y^\# \tag{40}$$

where $Y^\# = (Y^T Y)^{-1} Y^T$; $[d,n]$ is well known in theory pseudo-reversed matrix.

In this procedure it can be problems with pseudo-reversing. There are different concrete schemes for applying the least squares method and the best is the Ho-Kashap procedure. This procedure moves in steps to the minimum of eq.(37), keeping gradient directions:

$$\nabla_a J = 2Y^T(Ya - b) \tag{41}$$

$$\nabla_b J = -2(Ya - b) \tag{42}$$

It begins with statistic, grouped in two classes as a generalized normalized observation matrix in form:

$$y = \begin{bmatrix} u_i & x_i \\ -u_j & -x_j \end{bmatrix} \tag{43}$$

where:

x_i and x_j are observations of W_i и W_j , classes, and vector-columns u_i include n_i threshold values, equal to one.

If weight and limitation vectors are:

$$A = \begin{bmatrix} a_0 \\ a \end{bmatrix}; b = \begin{bmatrix} \frac{n}{n_i} u_i \\ \frac{n}{n_j} u_j \end{bmatrix}; n = n_1 + n_2 \tag{44}$$

and according to eq.(39):

$$\begin{bmatrix} u_i^T & -u_j^T \\ x_i^T & -x_j^T \end{bmatrix} \begin{bmatrix} u_i & x_i \\ -u_j & -x_j \end{bmatrix} \begin{bmatrix} a_0 \\ a \end{bmatrix} = \begin{bmatrix} u_i^T & -u_j^T \\ x_i^T & -x_j^T \end{bmatrix} \begin{bmatrix} \frac{n}{n_i} u_i \\ \frac{n}{n_j} u_j \end{bmatrix} \quad (45)$$

After including:

$$\frac{1}{n_i} \sum_{x \in x_i} X = \mu_i$$

$$\sum_{i=1}^2 \sum_{x \in x_i} (X - \mu_i)(X - \mu_i)^T = S_w \quad (46)$$

we have:

$$a_0 = -\mu^T a$$

$$\left[\frac{1}{n} S_w + \frac{n_i n_j}{n^2} (\mu_i - \mu_j)(\mu_i - \mu_j)^T \right] a = \mu_i - \mu_j \quad (47)$$

and:

$$a \frac{1}{n} S_w = (\mu_i - \mu_j) - a \frac{n_i n_j}{n^2} (\mu_i - \mu_j)(\mu_i - \mu_j)^T \quad (48a)$$

As vector direction:

$$a \frac{n_i n_j}{n^2} (\mu_i - \mu_j)(\mu_i - \mu_j)^T \quad (48b)$$

by every a coincide with vector direction $(\mu_i - \mu_j)$:

$$a \frac{1}{n} S_w = \alpha (\mu_i - \mu_j) \quad (49)$$

whence:

$$a = n \alpha \cdot S_w^{-1} (\mu_i - \mu_j) \quad (50)$$

After excluding inessential scalar coefficient $n\alpha$ we have direction that minimizes sum of squares in form:

$$a = S_w^{-1} (\mu_i - \mu_j) \quad (51)$$

V. CONCLUSION

Comparison of eq. (21), (22), (25), (26), (27) gives the conditions, where recognition procedures, based on optimal linear feature area transformation – eq.(15), and linear Fisher’s discriminant has got equal mathematical sense.

In both cases we have projection of observation vector on direction $S_w^{-1} \cdot (\mu_k - \mu_l)$, and comparing the result with some threshold value. So, according to eq.(8), (9), (10),

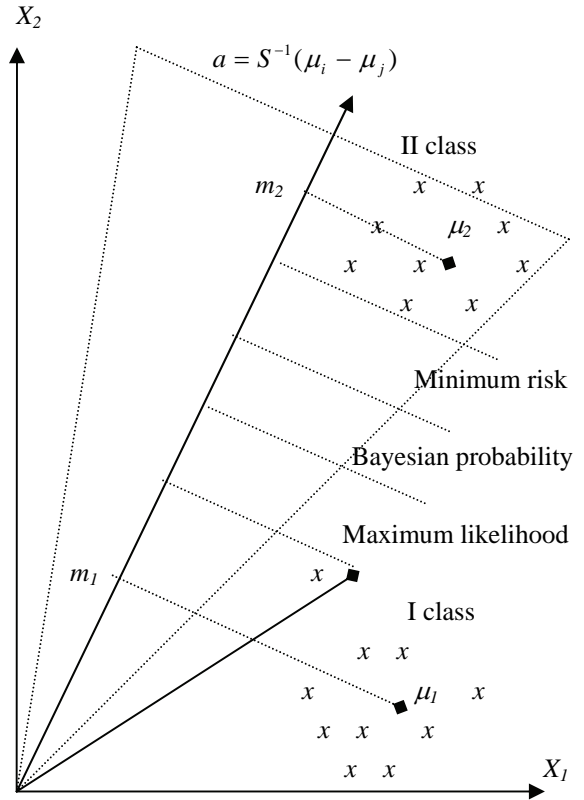


Fig. 1 Classes and classification methods

we can assert about algorithmic equality of recognition procedures.

After comparison of eq.(10), (22), (26), (51) we can see relation between linear parametric and non-parametric, probabilistic and determined methods, and also equivalence conditions of respective recognition procedures.

The fact, that least squares procedure and maximum likelihood procedure approximate by probability to the linear Fisher’s discriminant shows that we have reason to speak not about different, but asymptotic approximate procedures with common computing scheme. The computed value (projection) is compared with threshold valued, which define optimum as decision making in sense of minimizing of risk, maximum conditional or a posteriori probability (Fig. 1).

ACKNOWLEDGEMENT

This paper is a result of a study, with the kind guidance of professor dr Asen Nedev in TU Varna.

REFERENCES

- [1] V. Vapnik, Statistical Learning Theory, J.Wiley, N.Y. 1998
- [2] R.A. Fisher, Contributions to Mathematical Statistics. J.Wiley, N.Y. 1994
- [3] Fukunaga. K, Introduction to statistical pattern recognition. Academ press, N.Y, 1990
- [4] A. Nedev, K. Tenekedjiev, Technical diagnostics and pattern recognition, TU Varna, 1997

Complex Input Signal Quantization Noise Analysis for Orthogonal Second-Order IIR Digital Filter Sections

Zlatka Nikolova

Abstract – In this paper a new method for the estimation of complex output noise variance due to input signal quantization is proposed. The method is applied on very low-sensitivity second-order orthogonal complex IIR filter sections. They are used for the design of higher order narrow-band cascade realizations, which are preferred in many telecommunication applications and are normally implemented with fixed-point arithmetic. It is shown experimentally that the sensitivity of the orthogonal complex structure has a profound impact on its output noise level. The proposed method is applicable to any filter structure and can be used to study the complex signal quantization effects in general.

Keywords – complex orthogonal digital filters, sensitivity, quantization errors, noise analysis.

I. INTRODUCTION

Finite word-length (quantization) effects are important fraction of the parasitic effects group. Initially, all quantization effects have been united together into a single error analysis, but the most useful approach is they to be divided into two categories, requiring different analysis techniques:

- *coefficient quantization* – errors in representing filter coefficients as finite fixed-point numbers;
- *signal quantization* – errors due to the finite-precision arithmetic operations of addition, multiplications and storage.

The filter coefficients are quantized once only and remain constant in the filter implementation. Coefficient quantization effects on filter characteristics perturb them from their ideal forms. If they no longer meet the specifications, the quantization design must be optimized by allocating more bits or choosing more proper filter realization. The structure of the digital filter has a significant effect on its sensitivity to coefficient quantization.

Signal quantization, on the other hand, due to truncation or rounding, is usually best viewed as a random process and can be modeled as producing additive white noise sources in the filter. The effect of signal quantization is to add an error or noise signal to the ideal output of the digital filter, which is composite of one or more of the following error sources: the quantization error of the filter input signal; the errors resulting from the rounding or truncation of multiplication products within the filter; and quantization of the output to refer bits for input to a digital-to-analog converter or another system. Again, as for coefficient quantization, the filter structure affects considerably signal-quantization noise levels.

In this work the attention is restricted to the noise analysis due to input signal quantization. In case of real digital filters there are various good techniques developed long ago [1] [2].

In the last years complex coefficients digital filters are gaining popularity, but their quantization noise theory is still not well developed. Small amount of publications touch the problems barely [3] [4]. Only specific problems are considered so far, and no general technique for quantization noise estimation is proposed.

In this work a new method for complex analytic input signal quantization noise analysis is offered and applied to a very low-sensitivity orthogonal complex second-order section. It is shown experimentally that the low coefficient sensitivity of the circuit escort low output noise variance due to the complex input signal quantization.

II. COMPLEX INPUT QUANTIZATION NOISE ANALYSIS

The input signal quantization is equivalent to a set of uniformly distributed noise samples $e(n)$ added to the actual input signal $x(n)$. In case of fixed-point representation with rounding the quantization noise power (variance) of the random variable $e(n)$ is:

$$\sigma_e^2 = \frac{\delta^2}{12} = \frac{2^{-2B}}{12}, \quad (1)$$

B is the word-length in bits and δ is the quantization step size.

When the quantized input signal $x(n)$ is complex, the originated noise source $e(n)$ must be complex too. Then, the complex output signal $y(n)$ will be mixed with complex output noise $v(n)$. The noise model of complex input signal quantization is shown in Fig. 1.

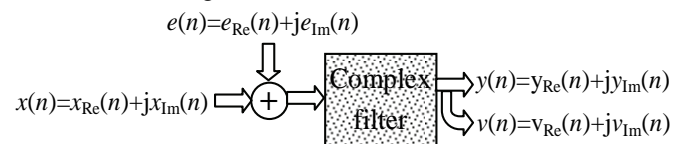


Fig. 1: Noise model due to complex input signal quantization

Analytic signals are processed by a special class complex digital filters named “orthogonal”, which transfer functions can be presented by its real and imaginary parts as follows:

$$H(-jz) = H_{Re}(z) + jH_{Im}(z). \quad (2)$$

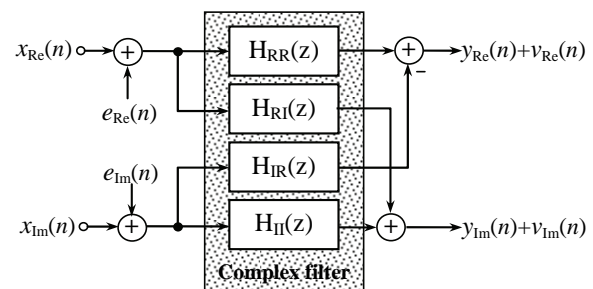


Fig. 2: Block-diagram of the complex digital filter structure - noise representation

¹ Zlatka Nikolova is with the Dept. of Telecommunications, Technical University of Sofia, Bulgaria, e-mail: zvv@tu-sofia.bg

Realized by real elements a complex orthogonal structure (Fig. 2) has got two inputs - real and imaginary and a relevant output couple, producing thereby four real coefficient transfer functions two-by-two equal with \pm sign:

$$H_{Re}(z)=H_{RR}(z)=H_{II}(z); \quad H_{Im}(z)=H_{RI}(z)=-H_{IR}(z). \quad (3)$$

The real $x_{Re}(n)$ and imaginary $x_{Im}(n)$ parts of an analytic signal $x(n)$ are inphase and quadrature components. If their levels are much larger than the quantization step size δ the resulting quantization errors $e_{Re}(n)$ and $e_{Im}(n)$ can be modelled as additive noise sources. The following assumptions can be made:

♦ The quantization errors are uniformly distributed over the range $(-0,5\delta \div 0,5\delta)$. They are stationary white noise sequences (i.e. $e(n)$ and $e(m)$ for $n \neq m$ are uncorrelated);

♦ The error sequence is uncorrelated with the initial signal sequence;

♦ $x_{Re}(n)$ and $x_{Im}(n)$ are orthogonal, i.e. sufficiently different, so that quantization errors $e_{Re}(n)$ and $e_{Im}(n)$ are uncorrelated.

Normally, the real and imaginary parts of the analytic signal are quantized the same word-length. Hence, their noise variances will be identical $\sigma_{e,Re}^2 = \sigma_{e,Im}^2 = \sigma_e^2$ and calculated by Eq. (1).

The assumption that noise signals are statistically independent from source to source leads to the implication that the quantization noise power of their sum is equal to the sum of the respective quantization noise powers. In effect, superposition can be employed and beside the structure from Fig. 2 makes obvious, the real $v_{Re}(n)$ and imaginary $v_{Im}(n)$ components of the complex output noise variance $v(n)$ will be composed respectively as follows: beside

$$\sigma_{v,Re}^2 = \sigma_{v,HRe}^2 - \sigma_{v,HIm}^2 \quad (4)$$

$$\sigma_{v,Im}^2 = \sigma_{v,HRe}^2 + \sigma_{v,HIm}^2. \quad (5)$$

$\sigma_{v,HRe}^2$ and $\sigma_{v,HIm}^2$ are the corresponding output noise variances of the real $H_{Re}(z)$ and imaginary $H_{Im}(z)$ parts of the orthogonal complex transfer function (2):

$$\sigma_{v,HRe}^2 = \sigma_e^2 \frac{1}{2\pi j} \oint H_{Re}(z)H_{Re}(z^{-1})z^{-1} dz, \quad (6)$$

$$\sigma_{v,HIm}^2 = \sigma_e^2 \frac{1}{2\pi j} \oint H_{Im}(z)H_{Im}(z^{-1})z^{-1} dz. \quad (7)$$

III. COMPLEX ORTHOGONAL DIGITAL FILTER CIRCUIT DERIVATION

In order to test the method for complex output noise variance proposed in section II, it is executed on two orthogonal sections – the DF (Direct Form) - and LS2 (Low Sensitivity)-based structures. They are derived after the circuit (poles rotation) transformation in its orthogonal form:

$$z^{-1} = jz^{-1} \text{ or } z = -jz, \quad (8)$$

is applied on the low-pass (LP) second-order real-prototypes [5]. The obtained orthogonal complex coefficients transfer functions have real and imaginary parts of band-pass (BP) type and doubled order. For the DF-based orthogonal complex structure shown in Fig. 3a they are as follow:

$$H_{RR}^{DF}(z)=H_{II}^{DF}(z)=H_{Re}^{DF}(z)=g_0 \frac{1+(-1-g_2+2g_1)z^{-2}+g_2z^{-4}}{1+(g_1^2-2g_2)z^{-2}+g_2^2z^{-4}} \quad (9)$$

$$H_{RI}^{DF}(z)=-H_{IR}^{DF}(z)=H_{Im}^{DF}(z)=g_0z^{-1} \frac{(2-g_1)+(g_1-2g_2)z^{-2}}{1+(g_1^2-2g_2)z^{-2}+g_2^2z^{-4}}; \quad (10)$$

whereas for the LS2-based orthogonal section (Fig.3b) they are:

$$H_{RR}^{LS2}(z)=H_{II}^{LS2}(z)=H_{Re}^{LS2}(z)=0,5a \frac{1+(4a+3b-6)z^{-2}+(1-b)z^{-4}}{1+[(2a+b-2)^2-2(1-b)]z^{-2}+(1-b)^2z^{-4}}; \quad (11)$$

$$H_{RI}^{LS2}(z)=-H_{IR}^{LS2}(z)=H_{Im}^{LS2}(z)=0,5az^{-1} \frac{(4-2a-b)+(2a+3b-4)z^{-2}}{1+[(2a+b-2)^2-2(1-b)]z^{-2}+(1-b)^2z^{-4}}. \quad (12)$$

The orthogonal complex filter structures are with canonical number of elements and preserve some properties of their real prototypes. In order to verify this deduction with respect to the input signal quantization noise assessment, the orthogonal BP filters are turned into the narrow-band realizations which are the most often used in practice. It is shown experimentally that the narrow-band BP LS2-based structure has many times lower coefficient sensitivity than the DF-based orthogonal section in a very short word-length setting [6].

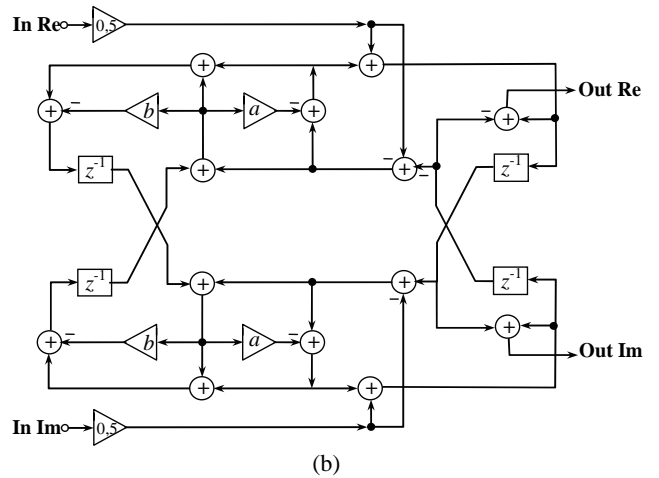
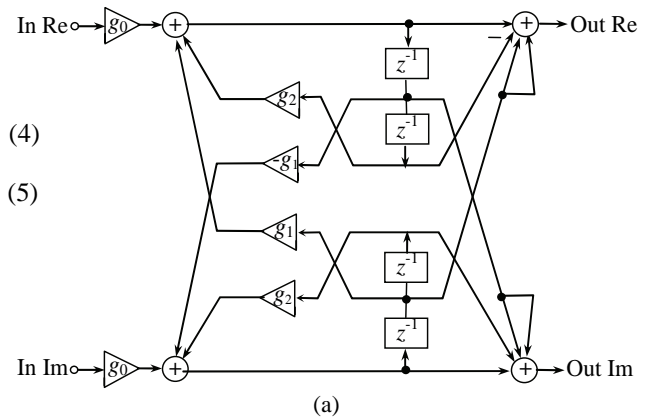


Fig.3: BP orthogonal structure based on (a) DF; (b) LS2 second-order sections

IV. NOISE ANALYSIS OF COMPLEX OUTPUT SIGNAL QUANTIZATION ERRORS

In this section both real and orthogonal structures are investigated in regard to the output errors after analytic input signal quantization.

Initially the real input signal is quantised with a different word-length. The output noise variance for the LS2 and DF real sections is calculated for same pole disposition providing narrow-band LP realizations. Experimental results for input signal quantization from 3 to 8 bits are shown in Fig. 4. Apparently, the low-sensitivity LS2 section output noise variance is significantly lower than this of the DF-section when the input signal is limited to 3 bits only. The numerical results in Table 1 show that the difference comes to be more insignificant as the word-length grows up.

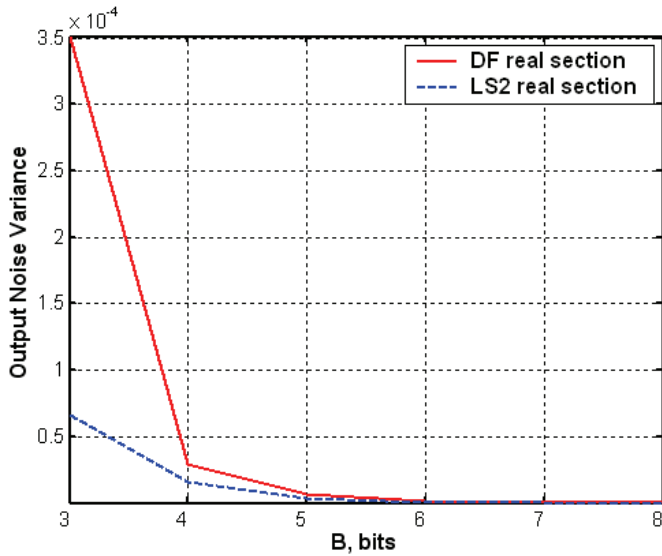


Fig.4: Output noise variance as a function of input signal quantization for LS2 and DF real sections

Table 1

Input signal word-length in bits	Output noise variances of the real sections	
	DF-based (x 10 ⁻²)	
3	0.03510957123100	
4	0.00291925961900	
5	0.00068310479600	
6	0.00016369047700	
7	0.00004088935200	
8	0.00001021082700	
		LS2-based (x 10 ⁻³)
3	0.06610812663435	
4	0.01648302703813	
5	0.00411908868389	
6	0.00102955782586	
7	0.00025738522125	
8	0.00006434590146	

Applying the method proposed in section II, a complex input signal quantization noise analysis is performed. Some experimental results for complex output noise variances for the LS2 and DF orthogonal sections in different complex input signal word-length environment are presented in Table 2.

Table 2

Input signal word-length in bits	Complex output noise variances of the orthogonal complex sections	
	DF-based (x 10 ⁻³)	
3	0.07371185555950 + j 0.07311495898425	
4	0.01852191939397 + j 0.05813840921642	
5	0.00463195749233 + j 0.01567003760465	
6	0.00115823432349 + j 0.00409778278276	
7	0.00028956349204 + j 0.00102688073474	
8	0.00007239109170 + j 0.00025704567665	
		LS2-based (x 10 ⁻⁴)
3	0.04627424248761 + j 0.16527031658588	
4	0.01157974082248 + j 0.04120756759532	
5	0.00289529076001 + j 0.01029772170972	
6	0.00072391264233 + j 0.00257389456465	
7	0.00018097816584 + j 0.00064346305313	
8	0.00004524454240 + j 0.00016086475366	

In order to compare the obtained complex output signal noise variances their complex modulus are graphically presented in Fig. 5. Obviously, the low-sensitivity LS2-based orthogonal complex section demonstrates more than two times lower output noise in case of 3 bits input signal quantization. Let's note that the shorter word-length quantization of the input signal means lower power consumption and faster computation process. For low-sensitivity circuits the resistance to quantization effects provides better signal-to-noise ratio (SNR), i.e. higher quality digital signal processing.

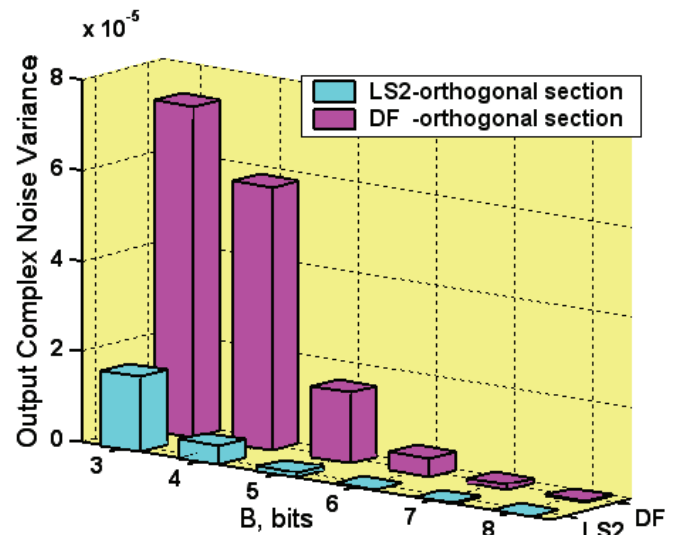


Fig.5: Output noise variances after analytic input signal quantization for LS2 and DF -based orthogonal complex sections

V. EXPERIMENTS

The examined narrowband orthogonal second-order filter sections are tested for limited word-length analytic signal processing. The performed quantized complex input signal is a mixture of white noise and analytic sinusoidal signal. The uniformly distributed white noise samples correspond to the word-length of the input complex signal after its quantization.

In Fig.6a the real part of the complex noise reached to the real output is shown for both DF- and LS2-based orthogonal complex structures. The imaginary output noise signals are presented in Fig. 6b. Apparently, the complex noise at the outputs due to the quantization of the analytic complex input signal is considerably more for the DF-based section than for the LS2-based.

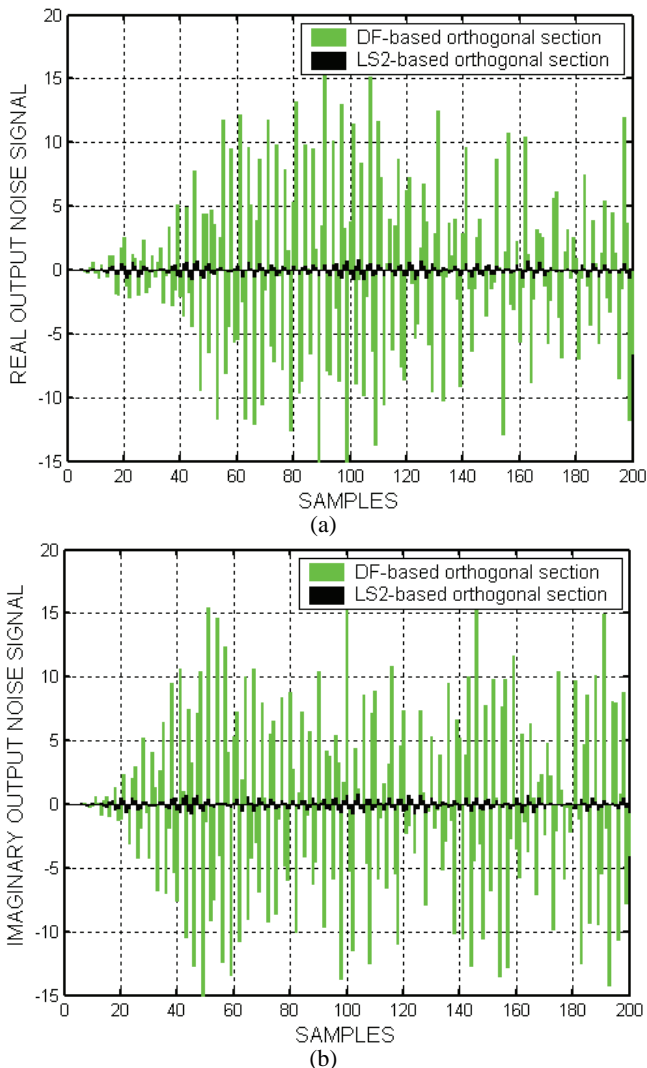


Fig.6: The output noise signals after input quantization to 3 bits for LS2 and DF - based orthogonal complex sections
(a) real output; (b) imaginary output.

The output SNR for the LS2-orthogonal section is about 1,5 times higher in comparison to the DF-based circuit. To achieve the same good result LS2 section demonstrates for 3 bits word-length input signal quantization, the DF orthogonal filter must be employed in minimum 6 bits environment.

It is clear that the level of the output noise as a result of the

input signal quantization and the sensitivity of the system are in a direct relative amount. Therefore, very low-sensitivity complex filter derivation is important to achieve a better noise resistance, improved complex signal filtering and higher quality digital signal processing.

VI. CONCLUSIONS

In this paper a new method for complex noise analysis is proposed. The resulting error signals at the outputs of orthogonal complex second-order digital filter sections after input signal quantization are examined. The proposed method is general enough to be applied for complex filter sections of higher order. After relevant alterations it could be effectively applied for all other types of finite word effects estimation in complex coefficient systems like errors from quantization of multiplication products within the filter.

The expectation that the real prototype properties will be inherited by its complex filter counterpart was confirmed once again with respect to the noise analysis after input signal quantization. It was shown experimentally that both real and orthogonal complex LS2-based filter sections beside very low coefficient sensitivity demonstrate low output noise variance due to input analytic signal quantization. The DF-based real and orthogonal complex circuits keep the same mutual performance even if they have many times higher output noise variance than LS2-based.

Low-sensitivity of complex filters in very limited word-length circumstances for signals and coefficients quantization makes available low computational complexity and provides better quality of the filtering process.

REFERENCES

- [1] K. J. Astrom, E. I. Jury and R. G. Agniel, "A Numerical Method for the Evaluation of Complex Integrals". *IEEE Trans. Automat. Contr.*, vol. AC-15, pp. 468-471, Aug., 1970.
- [2] B. W. Bomar, "Computationally Efficient Low Roundoff Noise Second-Order Digital Filter Sections With No Overflow Oscillations", *IEEE Conference Proceedings Southeastcon '88*, pp:606 – 613, 11-13, April 1988.
- [3] A. Wenzler and E. Luder, "New Structures for Complex Multipliers and Their Noise Analysis", *IEEE International Symposium on Circuits and Systems, (ISCAS'95)*, Vol. 2, pp. 1432 – 1435, 28 April - 3 May 1995.
- [4] P. K. Sim and K. K. Pang, "Quantization Phenomena in a Class of Complex Biquad Recursive Digital Filters", *IEEE Transaction on Circuit and Systems*, vol. CAS-33, No.9, pp. 892-899, Sept. 1986.
- [5] E. Watanabe and A. Nishihara, "A Synthesis of a Class of Complex Digital Filters Based on Circuitry Transformations". *IEICE Trans.*, vol. E-74, No.11, pp.3622-3624, Nov. 1991.
- [6] G. Stoyanov, M. Kawamata, Zl. Valkova, "New first and second-order very low-sensitivity bandpass/ bandstop complex digital filter sections", *Proc. IEEE 1997 Region 10th Annual Conf. "TENCON'97"*, Brisbane, Australia, vol.1, pp.61-64, Dec. 2-4, 1997.

Speech Overlap Detection Algorithms Simulation

Snejana Pleshkova-Bekiarska¹ and Damyan Damyanov²

Abstract – The concern of this paper are different methods of speech overlap detection. Speech overlap is the simultaneous occurrence of speech from more than one speakers. It has some very bad effects in the work of speech recognition systems. Speech overlap detection is one of the main areas in speech and speaker indexing. In speaker indexing, speech signal is partitioned into segments where each segment is uttered by only one speaker. So, parts of speech that include two or more speakers simultaneously should be determined before any following processes. Speaker overlap detection is also useful in some other speech processing applications including speech and speaker recognition. In this paper the method for speech overlap detection Spectral Auto-Correlation Peak Valley Ratio (SAPVR) is shown. At the end of this paper, the results from the work of the methods are plotted. They are the precision rate and the detection rate. The average time for processing for 1 second of speech is also taken under consideration.

Keywords – Spectral Auto-Correlation Peak-Valley Ratio, K nearest neighbour, speech overlap detection.

I. INTRODUCTION

The auto-correlation is a standard method of evaluating how correlated is a signal with a copy of itself, delayed on certain interval d . If we have the series $x(n)$ the auto-correlation of this signal is

$$r = \frac{\sum_i [x(i) - m_x] * [x(i - d) - m_x]}{\sqrt{\sum_i [x(i) - m_x]^2} * \sqrt{\sum_i [x(i - d) - m_x]^2}} \quad (1)$$

where m_x is the mean of the series $x(i)$. If the auto-correlation is computed for delays $d=0,1,2, \dots, N-1$, then we can write the formula of the auto-correlation with a length twice the length of the signal:

$$r(d) = \frac{\sum_i [x(i) - m_x] * [x(i - d) - m_x]}{\sqrt{\sum_i [x(i) - m_x]^2} * \sqrt{\sum_i [x(i - d) - m_x]^2}} \quad (2)$$

The method of Spectral Auto-Correlation Peak-to-Value Ratio (SAPVR) uses spectral auto-correlation function to determine whether a speech frame

is usable or not [1]. A speech segment is "usable" if it contains enough information to identify the target speaker.

The power spectrum of voiced speech can be predicted because of its harmonic structure. If certain input signals are given, like in fig 1,2 3 and consider a frame of speech that is voiced. The frequency spectrum $X(k)$ of such a frame will contain harmonically related pulses. This operation will always result in pulses of decreasing height with increasing lag. If the original magnitude spectrum $X(k)$ contained harmonics at integral multiples of the digital frequency 'p', then the major contribution to the first peak in the spectral autocorrelation, after lag zero, is due to the product of adjacent harmonics, which occurs at lag 'p'. This is shown in figures 4, 5 and 6. That is, the magnitude of the first spectral peak after lag zero for a voiced frame can be approximated as

$$R(p) = X(p)X(2p) + X(2p)X(3p) + \dots \quad (3)$$

Other terms will contain less energy, and will not contribute significantly to this peak. Note that this parameter contains all the information about significant harmonics. The next peak occurs at lag '2p' and its amplitude can be approximated as

$$R(2p) = X(p)X(3p) + X(2p)X(4p) + \dots \quad (4)$$

By the inherent property of the autocorrelation function, this peak has lesser amplitude than $R(p)$. If the segment of speech is unvoiced, the spectral autocorrelation will not contain any prominent peaks other than the one at lag 0. [2]. The behavior of spectral autocorrelation under co-channel condition varied, depending on whether 1.) both the target and interfering speech were voiced, 2.) either one of them were unvoiced or 3.) both of them were unvoiced. When both the speech frames were unvoiced, the spectral autocorrelation did not contain any pulses that were harmonically related to each other. If at least one of the speech frames was voiced, the spectral autocorrelation contained harmonically related pulses as expected. If both the speech frames were voiced, the spectral autocorrelation contained either two distinct trains of pulses that were harmonically related if the speakers' pitches were different by approximately 25%, otherwise there was one train of broad pulses. One important thing is that the ratio of the first local maximum after the one at lag 0, to the local minima between this maximum and the next local minimum, is significantly lower than that of the single speaker case. This is due to the fact that there are significant autocorrelation values for lags that are not harmonically related, due to co-channel conditions. This motivates one to define a spectral autocorrelation ratio, which reflects the extent of corruption of a target speech by the interfering speech.

¹Snejana Pleshkova-Bekiarska is with the Faculty of Telecommunications, Technical University - Sofia, 8 Kliment Ohridski St. Darvenitsa, 1756, Sofia, Bulgaria, E-mail: snegpl@tu-sofia.bg

²Damyan Damyanov is with the Faculty of Telecommunications, Technical University - Sofia, 8 Kliment Ohridski St. Darvenitsa, 1756, Sofia, Bulgaria, E-mail: ellov@abv.bg

The Spectral Autocorrelation Ratio (SAR) parameter is defined as follows:

$$SAR = 20 \log_{10} \{R(p_1) / R(q_1)\} \quad (5)$$

where, R(p1) is the local maximum of spectral autocorrelation other than the one at lag 0 (occurring at lag p1) and R(q1) is the next local maximum that is not harmonically related to the first peak, or the local minimum between p1 and 2p1.

The SAR has to be properly interpreted. If speech of one of the speakers is silent or is unvoiced, a peak that is not harmonically related to the peak due to voicing state of one talker will be substantially lower in amplitude. This is shown in figures 7,8 and 9. This means the SAR will be very high, from which we would conclude that the frame of speech is usable. If, however,

the speech of target and interferer were of comparable magnitude, the SAR ratio would approach zero, which would identify that particular frame as unusable[3]. What if there is a spurious peak of comparable magnitude along with the harmonically related pulses? The SAR will again be low, but the physical interpretation is that, a pure tone is mixed with the speech signal, and if it is of comparable magnitude, that speech frame is definitely unusable.

II. SIMULATION OF ALGORITHMS

The algorithm for evaluating of Spectral Auto-Correlation Peak-to-Value Ratio is as follows:

1. Open and load the wave file in the memory.
2. Create a vector, containing the values of the speech signal.
3. Get the vector length.
4. Create a Hamming window of N points.
5. Evaluate how many windows pass in the vector.
6. For every windowed part of the signal

- Evaluate the Fourier spectrum
- Evaluate the spectral autocorrelation

$$r(d) = \frac{\sum_i [x(i) - m_x] * [x(i-d) - m_x]}{\sqrt{\sum_i [x(i) - m_x]^2} * \sqrt{\sum_i [x(i-d) - m_x]^2}} \quad (6)$$

$$x(n), n = 0, 1, 2, \dots, N-1$$

$$d=0, 1, 2, \dots, N-1$$

- Estimate the first peak and second lag after the first lag.

- Evaluate the SAPVR -

$$SAR = 20 \log_{10} \{R(p_1) / R(q_1)\} \quad (7)$$

- Set a threshold 6.23 dB
- If the SAPVR is above the threshold – the frame is usable
- If not – the frame is unusable – i.e. there is speech overlap and the speaker cannot be identified.

III. QUALITY ESTIMATION AND COMPARISON

For quality estimation purposes:

1. Get an amount of data, for which all of the frames are known (usable and not usable).
2. Use the SAVPR algorithm.
3. With the results from the SAVPR algorithm, evaluate the next formulas

$$DR = \frac{\text{length of truly recognized non-usable segments}}{\text{total length of non-usable segments}} \quad (8)$$

$$FAR = \frac{\text{length of truly recognized usable segments}}{\text{total length of usable segments}} \quad (9)$$

$$PRC = (1 - FAR) * 100 \quad (10)$$

DR - Detection Rate

FAR - False Alarm Rate

PRC - Precision of the recognition approach

TABLE I
DETECTION RATE

Speech of a man	1
Speech of a woman	1
Speech overlap	1

TABLE II
PRECISION OF THE SAVPR ALGORITHM

Speech of a man	0.16667
Speech of a woman	0.71429
Speech overlap	0

In the following figures, simple signals are shown for visualization purposes. The authors have made an extensive search with many male and female voices.

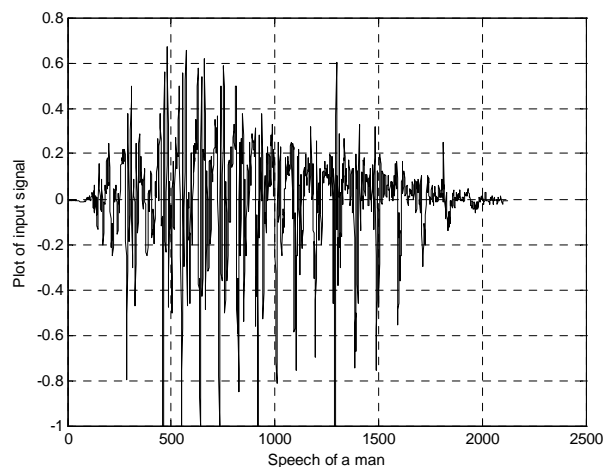


Fig.1. Input signal – speech of a man

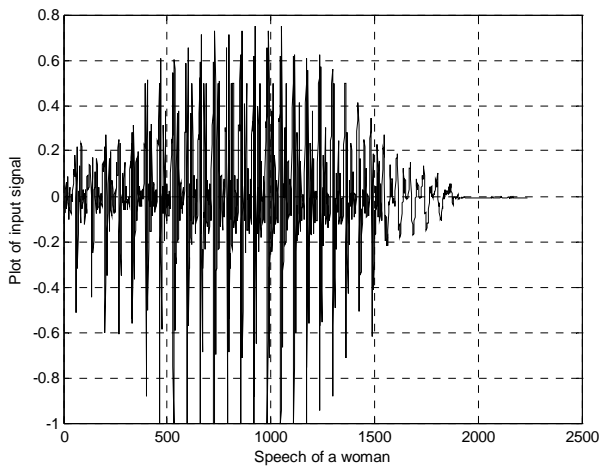


Fig.2. Input signal – speech of a woman

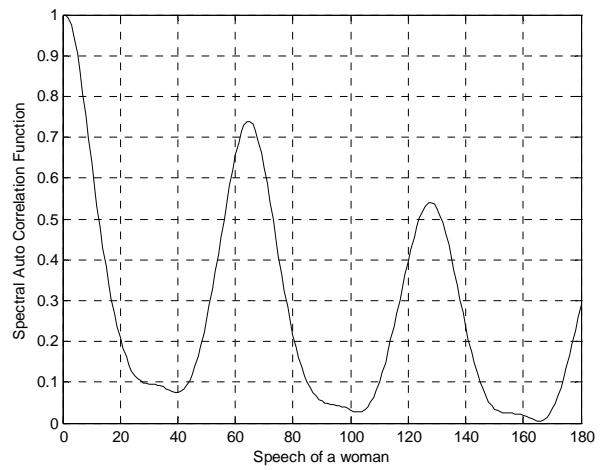


Fig.5. Spectral Auto-correlation – speech of a woman

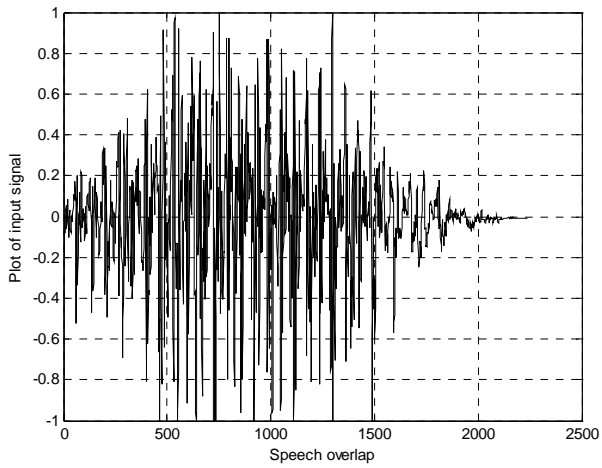


Fig.3. Input signal – speech overlap

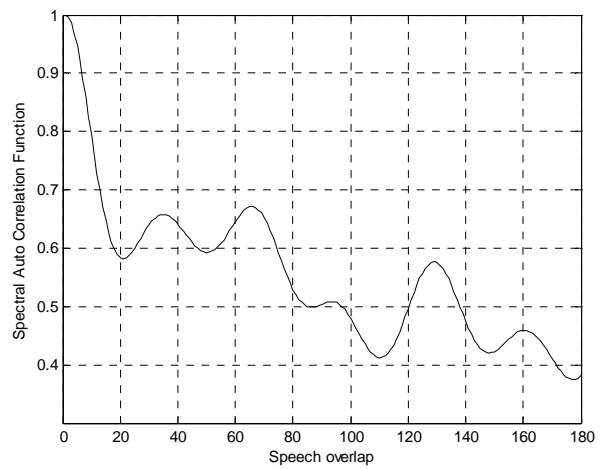


Fig.6. Spectral Auto-correlation – speech overlap

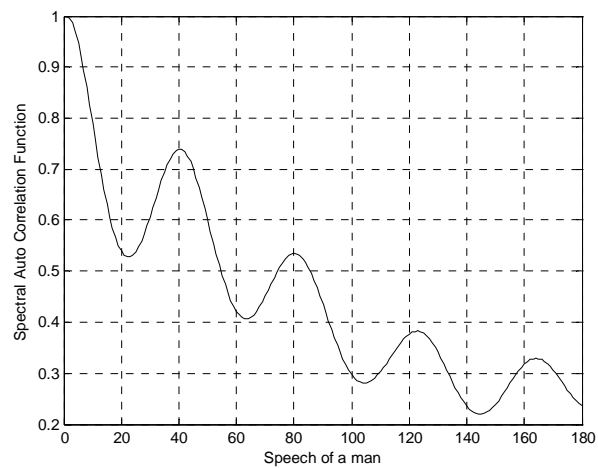


Fig.4. Spectral Auto-correlation – speech of a man

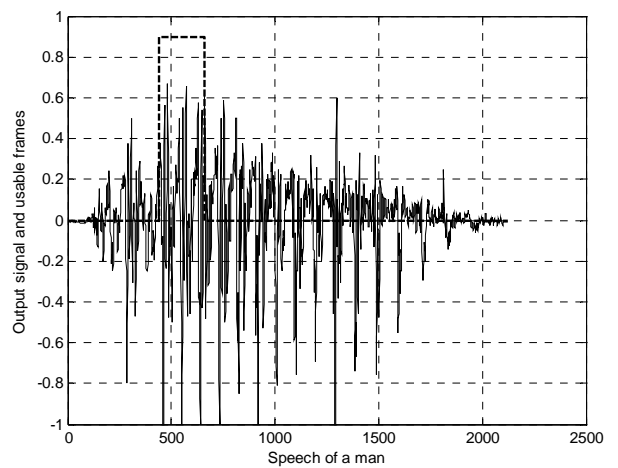


Fig.7. Output signal and usable frames – speech of a man

IV. CONCLUSION

In their future work, the authors have the goal to simulate the other methods, make an appropriate algorithms for them, and show compare the results of the different methods.

REFERENCES

- [1] Katsuri Rangan Krishnamachari, Robert E. Yantoro, Daniel S. Benincasa, Stanlet J. Wenndt "Spectral Autocorrelation ratio as a usability measure of speech segments under co-channel conditions ", IEEE International Symposium on Intelligent Signal Processing and Communication Systems, ISPACS 2000.
- [2] Robert E. Yantoro, "A study of the spectral autocorrelation peak valley ratio (SAVRP) as a method for Identification of usable speech and detection of co-channel speech". AFOSR Rome Labs Summer 2000 Report.
- [3] M. H. Moattar, M.M. Homayounpour "Speech Overlap Detection using Features and its Applications in Speech Indexing" Information and Communication Technologies, 2006. ICTTA '06. 2nd.

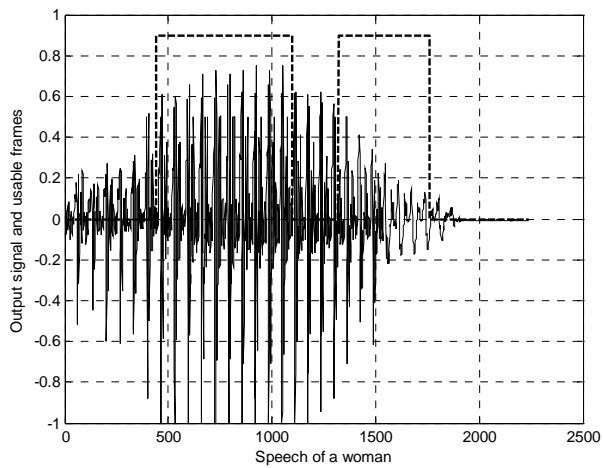


Fig.8. Output signal and usable frames – speech of a woman

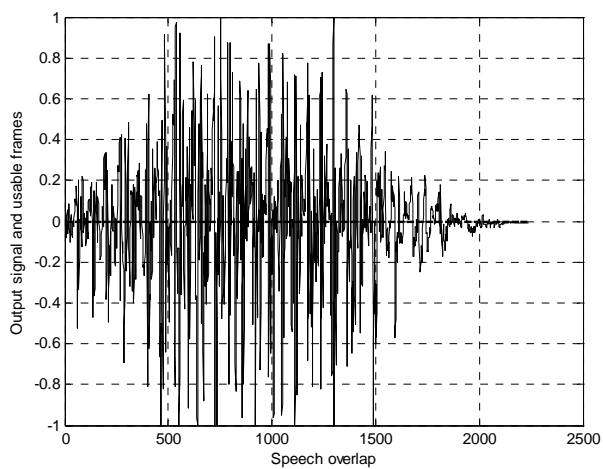


Fig.9. Output signal and usable frames – speech overlap

FPGA Implementation of the 2D-DCT/IDCT for the Motion Picture Compression

Rastislav J.R. Struharik¹ and Ivan Mezei²

Abstract – In this paper architectures for the 2D DCT/IDCT (Discrete Cosine Transform, Inverse Discrete Cosine Transform) are presented. These architectures were developed for the FPGA implementation. First, algorithms for the efficient 2D DCT/IDCT calculation are presented. Using these algorithms micro-architectures for the efficient FPGA implementation are developed. These micro-architectures are then coded in the VHDL and synthesized using Xilinx Foundation ISE development system. Finally, maximum operating frequency and resources needed for the implementation of these cores are reported for the several families of Xilinx's FPGA IC's.

Keywords – Image Compression, JPEG, 2D DCT/IDCT, VHDL, FPGA.

I. INTRODUCTION

Compression is the process of reducing the size of the data sent, thereby, reducing the bandwidth required for the digital representation of a signal. Many inexpensive video and audio applications are made possible by the compression of signals. Compression technology can result in reduced transmission time due to less data being transmitted. It also decreases the storage requirements because there is less data. However, signal quality, implementation complexity, and the introduction of communication delay are potential negative factors that should be considered when choosing compression technology.

Video and audio signals can be compressed because of the spatial, spectral, and temporal correlation inherent in these signals. Spatial correlation is the correlation between neighboring samples in an image frame. Temporal refers to correlation between samples in different frames but in the same pixel position. Spectral correlation is the correlation between samples of the same source from multiple sensors.

There are two categories of compression: lossy and lossless. In medical system applications, image losses can translate into costly medical mistakes; therefore, lossless compression methods are used. Fortunately, the majority of video and image processing applications do not require the reconstructed data to be identical to the original data. In such applications, lossy compression schemes can be used to achieve higher compression ratios.

Discrete Cosine Transform (DCT) [1] is a lossy

compression scheme where an $N \times N$ image block is transformed from the spatial domain to the DCT domain. DCT decomposes the signal into spatial frequency components called DCT coefficients. The lower frequency DCT coefficients appear toward the upper left-hand corner of the DCT matrix, and the higher frequency coefficients are in the lower right-hand corner of the DCT matrix. Because the human visual system is less sensitive to errors in high frequency coefficients than it is to lower frequency coefficients, the higher frequency components can be more finely quantized, or even completely discarded. This operation leads to the significant improvements of the compression ratio, thereby reducing the amount of data that needs to be transmitted or stored, with only moderate degradation of the original picture quality.

For most image compression standards, $N = 8$. An 8×8 block size does not have significant memory requirements, and furthermore, a block size greater than 8×8 does not offer significantly better compression.

DCT is image independent and can be performed with fast algorithms. Examples of standards using DCT:

- Dolby AC2 & AC3: 1-D DCT (and 1-D Discrete Sine Transform)
- JPEG (still images): 2-D DCT spatial compression
- MPEG1 & MPEG2: 2-D DCT plus motion compensation
- H.261 and H.263: moving image compression for video conferencing and video telephony

Much of the processing required to encode or decode video using these standards is taken up by calculating the DCT and/or IDCT. An efficient hardware block dedicated to these functions will improve the performance of the digital video system considerably.

II. EFFICIENT ALGORITHMS FOR THE 2D DCT/IDCT CALCULATION

A. Algorithm for the Efficient 2D DCT Calculation

The algorithm used for the calculation of the 2D DCT is based on the following equation:

$$Y_{pq} = \frac{c(p)c(q)}{4} \sum_{m=0}^{M-1} \sum_{n=0}^{N-1} X_{mn} \cos\left(\frac{\pi(2m+1)p}{2M}\right) \cos\left(\frac{\pi(2n+1)q}{2N}\right) \quad (1)$$

where:

¹Rastislav J.R. Struharik is with the Faculty of Technical Sciences, Trg Dositeja Obradovića 6, 21000 Novi Sad, Serbia, E-mail: rasti@eunet.yu

²Ivan Mezei is with the Faculty of Technical Sciences, Trg Dositeja Obradovića 6, 21000 Novi Sad, Serbia, E-mail: imezei@uns.ns.ac.yu

$$c(p) = \frac{1}{\sqrt{2}} \text{ for } p = 0, c(p) = 1 \text{ otherwise}$$

$$c(q) = \frac{1}{\sqrt{2}} \text{ for } q = 0, c(q) = 1 \text{ otherwise}$$
(2)

Efficient implementation of this equation is possible because 2D DCT can be separated into two 1D DCT [2]. First, the 1D DCT of the rows are calculated and then the 1D DCT of the columns are calculated. The 1D DCT coefficients for the rows and columns can be calculated by separating equation (1) into the row part and the column part. As stated before, for most image compression standards, $M=N=8$. Using vector processing, the output Y of an 8×8 DCT for input X is given by the following equation.

$$Y = C \cdot X \cdot C^t$$
(3)

C is the cosine coefficients and C^t are the transpose coefficients. This equation can also be written as $Y=C \cdot Z$, where $Z = X \cdot C^t$. Coefficients for the C and C^t matrix can be calculated using the following equations.

$$C_{ij} = K \cos \frac{(2i+1)j\pi}{2M}, K = \frac{1}{N} \text{ for } j = 0, K = \frac{\sqrt{2}}{N} \text{ else}$$

$$C_{ij}^t = K \cos \frac{(2j+1)i\pi}{2N}, K = \frac{1}{M} \text{ for } i = 0, K = \frac{\sqrt{2}}{M} \text{ else}$$
(4)

Values for the scaled and rounded coefficients are presented in the following equation.

$$C = \begin{bmatrix} 23170 & 23170 & 23170 & 23170 & 23170 & 23170 & 23170 & 23170 \\ 32138 & 27246 & 18205 & 6393 & -6393 & -18205 & -27246 & -32138 \\ 30274 & 12540 & -12540 & -30274 & -30274 & -12540 & 12540 & 30274 \\ 27246 & -6393 & -32138 & -18205 & -18205 & 32138 & 6393 & -27246 \\ 23170 & -23170 & -23170 & 23170 & 23170 & -23170 & -23170 & 23170 \\ 18205 & -32138 & 6393 & 27246 & 27246 & -6393 & 32138 & -18205 \\ 12540 & -30274 & 30274 & -12540 & -12540 & 30274 & -30274 & 12540 \\ 6393 & -18205 & 27246 & -32138 & -32138 & -27246 & 18205 & -6393 \end{bmatrix}$$

$$C^t = \begin{bmatrix} 23170 & 32138 & 30274 & 27246 & 23170 & 18205 & 12540 & 6393 \\ 23170 & 27246 & 12540 & -6393 & -23170 & -32138 & -30274 & -18205 \\ 23170 & 18205 & -12540 & -32138 & -23170 & 6393 & 30274 & 27246 \\ 23170 & 6393 & -30274 & -18205 & 23170 & 27246 & -12540 & -32138 \\ 23170 & -6393 & -30274 & 18205 & 23170 & -27246 & -12540 & 32138 \\ 23170 & -18205 & -12540 & 32138 & -23170 & -6393 & 30274 & -27246 \\ 23170 & -27246 & 12540 & 6393 & -23170 & 32138 & -30274 & 18205 \\ 23170 & -32138 & 30274 & -27246 & 23170 & -18205 & 12540 & -6393 \end{bmatrix}$$
(5)

Structure of the 2D DCT core using this decomposition is presented on the following figure.



Fig. 1 Efficient 2D DCT Implementation

Let us explain the way the Z matrix is calculated. Each element in the first row of the input matrix X are multiplied by each element in the first column of matrix C^t and added together to get the first value Z_{00} of the intermediate matrix Z . To get Z_{01} , each element of row zero in X is multiplied by each element in the first column of C^t and added and so on. The calculation can be implemented using eight multipliers

and storing the coefficients in ROMs. But, after a closer examination of the coefficients from the C^t matrix there is a way to half the number of multipliers. When the equation $Z = X \cdot C^t$ is written in the scalar form we get following equations.

$$Z_{k0} = 23170(x_{k0} + x_{k1} + x_{k2} + x_{k3} + x_{k4} + x_{k5} + x_{k6} + x_{k7})$$

$$Z_{k1} = 32138(x_{k0} - x_{k7}) + 27246(x_{k1} - x_{k6}) + 18205(x_{k2} - x_{k5}) + 6393(x_{k3} - x_{k4})$$

$$Z_{k2} = 30274(x_{k0} + x_{k7}) + 12540(x_{k1} + x_{k6}) - 12540(x_{k2} + x_{k5}) - 30274(x_{k3} + x_{k4})$$

$$Z_{k3} = 27246(x_{k0} - x_{k7}) - 6393(x_{k1} - x_{k6}) - 32138(x_{k2} - x_{k5}) - 18205(x_{k3} - x_{k4})$$

$$Z_{k4} = 23170(x_{k0} + x_{k7}) - 23170(x_{k1} + x_{k6}) - 23170(x_{k2} + x_{k5}) + 23170(x_{k3} + x_{k4})$$

$$Z_{k5} = 18205(x_{k0} - x_{k7}) - 32138(x_{k1} - x_{k6}) + 6393(x_{k2} - x_{k5}) + 27246(x_{k3} - x_{k4})$$

$$Z_{k6} = 12540(x_{k0} + x_{k7}) - 30274(x_{k1} + x_{k6}) + 30274(x_{k2} + x_{k5}) - 12540(x_{k3} + x_{k4})$$

$$Z_{k7} = 6393(x_{k0} - x_{k7}) - 18205(x_{k1} - x_{k6}) + 27246(x_{k2} - x_{k5}) - 32138(x_{k3} - x_{k4})$$

$$k=0, 1, \dots, 7$$

We can see that for example, input values x_{k0} and x_{k7} are always multiplied by the same coefficient, only the sign can change. This can be efficiently explored to reduce the number of multipliers as shown on the following figure.

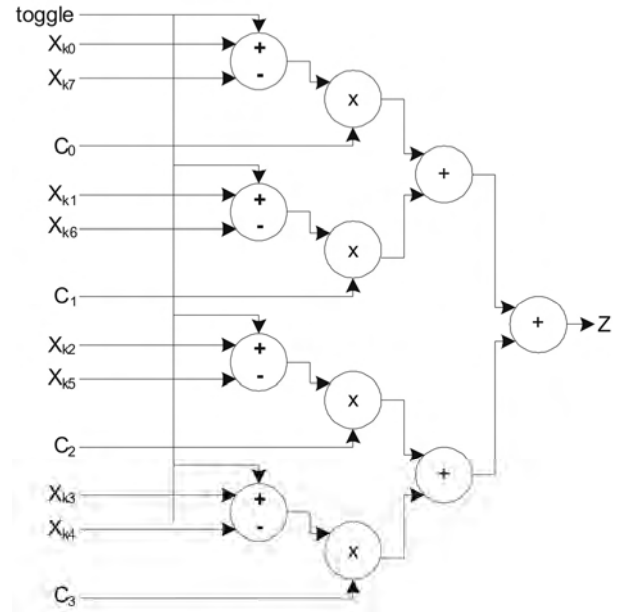


Fig. 2 Efficient 1D DCT Implementation

Using the *toggle* signal the adder/subtractor modules can be configured to operate as adder or as subtractor depending on the current need.

All 64 values for the matrix Z can be calculated in 64 clock cycles. These values are stored in the RAM memory shown between two 1D DCT block on Fig. 1. Using these stored values as input, second 1D DCT is performed resulting in the matrix Y . Structure of this second 1D DCT block is similar to the structure shown on the Fig. 2. Matrix Y holds the values for the 2D DCT transform of the input matrix X .

B. Algorithm for the Efficient 2D IDCT Calculation

Now let us examine the problem of calculating the 2D IDCT. Using the 2D DCT matrix Y , original input matrix X can be calculated in the following way [3].

$$X = C^t \cdot Y \cdot C \quad (7)$$

Matrix C and C^t are identical to those from 2D DCT. We can see that the only difference between Eq. (3) and (7) is in the order by which the matrix C and C^t are applied. Although this seems to be only a minor difference, it turns out to be a significant one, because now we cannot explore the coefficient symmetries like in the case of the 2D DCT. Once more the Eq. (7) can be split into two simpler equations, X=C^t·Z, and Z = Y·C. Because the different order of matrix multiplications, we cannot find the similar symmetry between the coefficients during the 1D IDCT operations. This means that every 1D IDCT block will now use eight multipliers. Structure of the 1D IDCT block is presented on the Fig. 3.

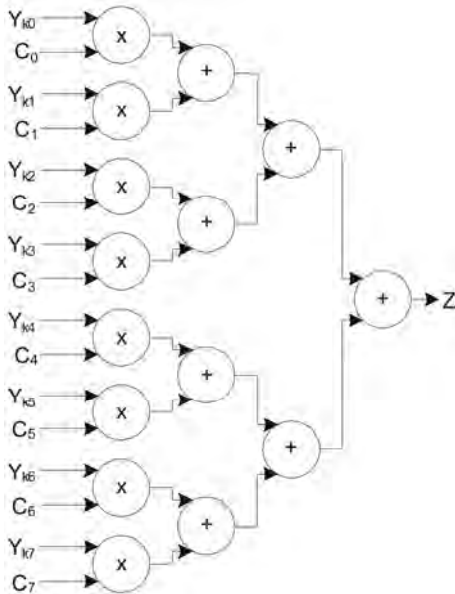


Fig. 3 Structure of the 1D IDCT Module

Basic structure and operation of the 2D IDCT core is identical to that of 2D DCT core presented on Fig. 1.

C. Algorithm for the Quantization/Dequantization Operations

As stated before, to improve the compression ratio it is common practice to perform the quantization of DCT components. Quantization is the process of selectively discarding visual information without a significant loss in the visual effect. Quantization reduces the number of bits needed to store an integer value by reducing the precision of the integer. Each DCT component is divided by a separate quantization coefficient, and rounded to the nearest integer. The larger the quantization coefficient (i.e., coefficient weighting), the smaller the resulting answer and associated bits needed to express the DCT component. In the reverse process, the fractional bits are "rounded" and are recovered as zeros, constituting a precision loss from the original number.

There are several different recommended procedures to perform the quantization. We have opted for the procedure used in the MPEG-2 compression standard [4]. Since we used a 12-bit representation of the DCT components, DC value was

not quantized. For the AC components following formula is used to determine the value of the quantization factor.

$$QDCT_{ij} = \left\lceil \frac{32 \cdot DCT_{ij}}{Qmatrix_{ij} \cdot Qscale} \right\rceil \quad (8)$$

Value of the Qmatrix is the matrix of the quantization coefficients with the following values depending whether we are quantizing luminance or chrominance components.

$$Qmatrix_{luma} = \begin{bmatrix} 16 & 11 & 10 & 16 & 24 & 40 & 51 & 61 \\ 12 & 12 & 14 & 19 & 26 & 58 & 60 & 55 \\ 14 & 13 & 16 & 24 & 40 & 57 & 69 & 56 \\ 14 & 17 & 22 & 29 & 51 & 87 & 80 & 62 \\ 18 & 22 & 37 & 56 & 68 & 109 & 103 & 77 \\ 24 & 35 & 55 & 64 & 81 & 104 & 113 & 92 \\ 49 & 64 & 78 & 87 & 103 & 121 & 120 & 101 \\ 72 & 92 & 95 & 98 & 112 & 100 & 103 & 99 \end{bmatrix} \quad (9)$$

$$Qmatrix_{chroma} = \begin{bmatrix} 17 & 18 & 24 & 47 & 99 & 99 & 99 & 99 \\ 18 & 21 & 26 & 66 & 99 & 99 & 99 & 99 \\ 24 & 26 & 56 & 99 & 99 & 99 & 99 & 99 \\ 47 & 66 & 99 & 99 & 99 & 99 & 99 & 99 \\ 99 & 99 & 99 & 99 & 99 & 99 & 99 & 99 \\ 99 & 99 & 99 & 99 & 99 & 99 & 99 & 99 \\ 99 & 99 & 99 & 99 & 99 & 99 & 99 & 99 \\ 99 & 99 & 99 & 99 & 99 & 99 & 99 & 99 \end{bmatrix}$$

Value of the Qscale parameter enables easy modifications of the quantization factors that will be used during the quantization. Dequantization is performed using the inverse expression of the expression in Eq. (8).

III. ARCHITECTURE OF THE DEVELOPED 2D DCT/IDCT CORES

After reviewing the efficient algorithms for the 2D DCT/IDCT calculations we can now present the basic architecture for the two developed cores, together with their interfaces.

Fig. 4 presents the interfaces for the 2D DCT and 2D IDCT cores.

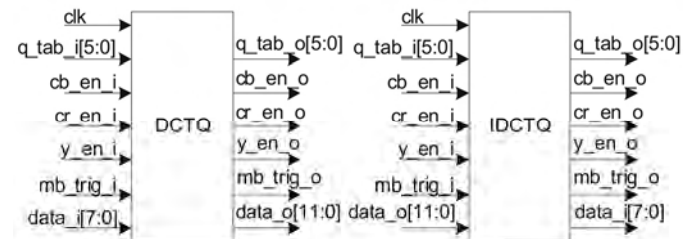


Fig. 4 Interface of the 2D DCT and 2D IDCT Cores

As can be seen from the Fig. 4 interface of both cores is the same. Input signal q_tab_i[5:0] is used to define the required

value of the $Qscale$ parameter in the quantization and dequantization operations. Input signals, cb_en_i , cr_en_i and y_en_i are used to specify the type of the current 8x8 block. Both cores assume that the picture is represented in the YCbCr format. Signal mb_trig_i is a global synchronizing signal used to indicate the start of the next 8x8 block. Input signal $data_i[7:0]$ ($data_i[11:0]$ in the case of 2D IDCT core) holds the pixel values (DCT component values in case of 2D IDCT core). Meaning of every output signal is identical to the input signal with the same name. Fig. 5 presents the basic architecture for the 2D DCT/IDCT cores.

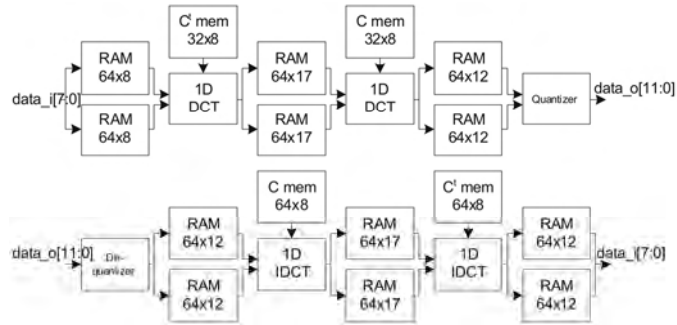


Fig. 5 Interface of the 2D DCT (up) and 2D IDCT (down) Cores

In every core there are three pipeline stages. This enables efficient calculation of the DCT or IDCT values that requires only 64 clock cycles per one 8x8 block. This is the maximum speed at which both cores can operate, but if needed they can work at slower speed. Fig. 6 illustrates the typical waveforms for the characteristic signals.

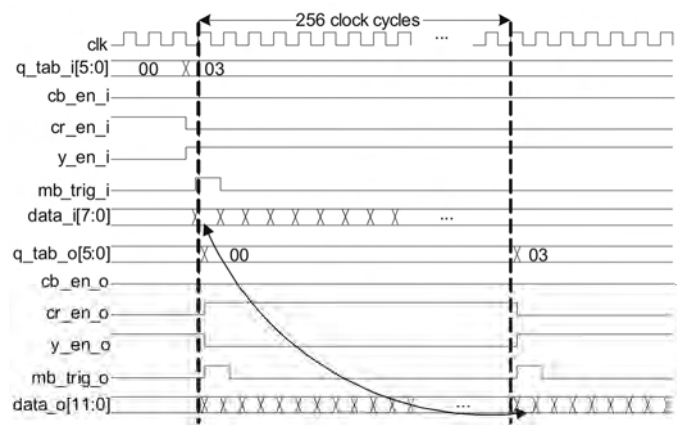


Fig. 6 Typical waveforms of the interface signals for the 2D DCT/IDCT Cores

Previous figure illustrates the interface signal waveforms in case of 256 clock cycle duration of one 8x8 block.

IV. SYNTHESIS RESULTS

Both cores were coded in VHDL and synthesized using Xilinx Foundation ISE 6.2i software. Following table presents the obtained results in terms of core size (number of slices required to implement the core) and maximum operating frequency for several Xilinx FPGA families.

TABLE I
SYNTHESIS RESULTS (OPTIMIZATION GOAL: SIZE)

FPGA Family	2D DCT Core		2D IDCT Core	
	Core Size (# slices)	Core Speed	Core Size (# slices)	Core Speed
SpartanIIE	3777	24.9 MHz	4525	22.7 MHz
SpartanIII	1214	47.8 MHz	1222	43.4 MHz
Virtex	3776	18.8 MHz	4525	17.3 MHz
Virtex2Pro	977	43.7 MHz	971	40.1 MHz

TABLE II
SYNTHESIS RESULTS (OPTIMIZATION GOAL: SPEED)

FPGA Family	2D DCT Core		2D IDCT Core	
	Core Size (# slices)	Core Speed	Core Size (# slices)	Core Speed
SpartanIIE	3794	28.4 MHz	4657	26.0 MHz
SpartanIII	1268	51.1 MHz	1264	47.4 MHz
Virtex	3850	22.3 MHz	4657	21.0 MHz
Virtex2Pro	1036	46.2 MHz	1059	43.5 MHz

Significantly smaller cores sizes in case of the SpartanIII and Virtex2Pro FPGA families are due to the fact that these families have dedicated multipliers that can be used to implement all the multiplications required in the DCT/IDCT calculations. In contrast, SpartanIIE and Virtex families don't have dedicated multipliers embedded on the chip, so every multiplier has to be implemented using the general purpose logic resources, resulting in larger core sizes.

V. CONCLUSION

In this paper hardware implementation of the 2D DCT/IDCT cores was investigated. Efficient algorithms for the calculation of the 2D DCT/IDCT values were proposed. These algorithms were implemented in hardware using the FPGA technology. Using the Xilinx Foundation ISE software synthesis results for several available FPGA families were reported.

REFERENCES

- [1] M. Popović, "Digitalna Obrada Signala", Beograd, Nauka, 1997.
- [2] Xilinx Application Note XAPP610, "Video Compression Using DCT"
- [3] Xilinx Application Note XAPP611, "Video Decompression Using IDCT"
- [4] Xilinx Application Note XAPP615, "Quantization"

Minutiae-based Algorithm for Automatic Fingerprint Identification

Edin H. Mulalić¹, Stevica S. Cvetković² and Saša V. Nikolić³

Abstract - This paper describes a complete fingerprint identification algorithm that uses minutiae for representation and matching of fingerprints. The presented algorithm consists of three main steps: 1) Image enhancement, 2) Minutiae extraction and 3) Minutiae matching. Principal description of each step is given concluded with brief description of developed software with test examples.

Keywords – Fingerprint identification, Image processing.

I. INTRODUCTION

Among all the biometric characteristics, fingerprints are one of the oldest, the most widely used and highly reliable. The most comprehensive explanation of all aspects of fingerprint identification could be found in [1].

The most of the methods for automatic fingerprint identification presented in literature has the similar global structure as our algorithm. At the beginning, image enhancement is applied in order to improve the quality of the input fingerprint image. Then, algorithm extracts local characteristics of the fingerprint – minutiae. Finally, minutiae matching is performed by comparing minutiae form input fingerprint with a set of one or more template fingerprints stored in database. The rest of the paper will give principal description of each step of the algorithm.

II. IMAGE ENHANCEMENT

The performance of minutiae extraction algorithms relies heavily on the quality of the input fingerprint images. Due to skin conditions, sensor noise and incorrect finger pressure, a significant percentage of fingerprint images (approximately 10%) are of poor quality. In general, there are two types of degradation that could be observed in fingerprint images:

- The ridges are not strictly continuous i.e. the ridges have small breaks (gaps),
- Due to the presence of noise which links ridges, parallel ridges are not well separated.

The most widely used technique for fingerprint image enhancement is based on *contextual filters*. In conventional image filtering, only a single filter kernel is used for convolution throughout the image. In contextual filtering, the filter characteristics change according to the local context, where the context is often defined by the local ridge

orientation and local ridge frequency. Appropriate contextual filter should possess the following characteristics:

- It should provide a low pass (averaging) effect along the ridge direction with the aim of linking small gaps and filling impurities due to pores or noise.
- It should have a band pass (differentiating) effect in the direction orthogonal to the ridges in order to increase the discrimination between ridges and valleys and top separate parallel linked ridges.

One of the first using of contextual filters for fingerprint image enhancement was performed by O'Gorman [2] and Mehre [3]. Since then, numerous filtering methods have been proposed in literature, both in spatial and frequency domain. Hong et al. [4] proposed an effective method based on Gabor filters and reported to achieve good performance. In order to improve performances of the previous method Yang et al. [5] modified method described in [4]. Although they reported better accuracy, computational complexity of their algorithm is too high.

Method which is used in this paper is similar in principle to the one described in [4]. The method assumes that parallel ridges and valleys exhibit some ideal sinusoidal plane waves associated with some noise. In other words, the 1-D signal orthogonal to the local orientation is approximately a digital sinusoidal wave. After convolving the image with corresponding Gabor filter which is tuned to a specific local ridge orientation and frequency, image could be efficiently enhanced. An even symmetric two dimensional Gabor filter has the following form in the spatial domain:

$$G_{\theta, f, \delta_x, \delta_y}(x, y) = \exp \left[-\frac{1}{2} \left(\frac{x_{\theta}^2}{\sigma_x^2} + \frac{y_{\theta}^2}{\sigma_y^2} \right) \right] \cos(2\pi f x_{\theta}),$$

$$x_{\theta} = x \cos(90 - \theta) + y \sin(90 - \theta) = x \sin \theta + y \cos \theta,$$

$$y_{\theta} = -x \sin(90 - \theta) + y \cos(90 - \theta) = -x \cos \theta + y \sin \theta \quad (1)$$

where $[x_{\theta}, y_{\theta}]$ are the coordinates of $[x, y]$ after a clockwise rotation of the Cartesian axes by an angle of $(90^{\circ} - \theta)$. The parameters of the previous equation are:

a) θ is the local orientation of the ridges. It is an angle of the ridge with the x -axis computed by examining the gradients of pixel intensities in the x and y directions within the local block (16×16) of the image.

b) f is the local frequency of the sinusoidal plane wave. It corresponds to the reciprocal value of inter-ridge distance in fingerprints images. Although some algorithms in literature

¹Edin H. Mulalić is student at the Faculty of Electronic Engineering, University of Niš, Aleksandra Medvedeva 14, 18000 Niš, Serbia, E-mail: edinmulalic@yahoo.com

²Stevica S. Cvetkovic is PhD student at the Faculty of Electronic Engineering, University of Niš, Aleksandra Medvedeva 14, 18000 Niš, Serbia, E-mail: stevica_cvetkovic@yahoo.com

³Saša V. Nikolić is with the Faculty of Electronic Engineering, University of Niš, Aleksandra Medvedeva 14, 18000 Niš, Serbia, E-mail: 503caci@elfak.ni.ac.yu

calculate f for each block of the image, empirical value can be used [6]. Therefore, the frequency is set to $f = \frac{1}{8}$.

c) σ_x, σ_y are the standard deviations of the Gaussian envelope along the x and y -axes, respectively. Based on empirical data [4], these values were set to $\sigma_x = \sigma_y = 4$.

To apply Gabor filters to an image, the four parameters $\theta, f, \sigma_x, \sigma_y$ must be specified for each pixel. Values of f, σ_x, σ_y are based on empirical data, thus only θ should be calculated for each block of the image. To make the enhancement faster, instead of “online” computing the best-suited contextual filter for each pixel, a set of eight filters (named “filter bank”) for eight discrete values of $\theta_k = k \frac{\pi}{8}$, $k = 0, 1, \dots, 7$ are a priori created and stored. Then, after calculating local orientation which is discretized to the closest value of θ_k , each pixel of the image is convolved with corresponding filter from precomputed Gabor filter bank.

III. MINUTIAE EXTRACTION

Most of proposed minutiae extraction algorithms operate on binary images. The binary images obtained by the binarization process are usually submitted to a thinning phase of algorithm which reduces ridge line thickness to one pixel. Some authors have proposed minutiae extraction approaches that work directly on the gray-scale images, without binarization and thinning, mainly because of following reasons [1]:

- a significant amount of information may be lost during the binarization process;
- binarization and thinning are time consuming;
- thinning may introduce a large number of spurious minutiae;
- in the absence of an a priori enhancement step, most of the binarization techniques do not provide satisfactory results when applied to low-quality images.

But most of these drawbacks can be avoided by using efficient and effective algorithms for image enhancement, binarization, thinning, false minutiae recognition and matching. On the other side, binarization and thinning provide numerous advantages in minutiae recognition phase. Obvious motivation to apply thinning process is to simplify process of recognizing minutiae and minutiae’s position. Method for minutiae extracting presented in this paper is based on images processed by binarization and thinning algorithms. For binarization, global threshold algorithm is used. Among many thinning algorithms described in [7], we chose to implement Nagendraprasad-Wang-Gupta iterative algorithm [8].

The most popular method for minutiae recognition is the Crossing Number (CN) approach. The in a binary image is defined by Arcelli and Baja in 1984. Mathematically, crossing number $CN(p)$ of a pixel p , can be calculated as half the sum of the differences between pairs of adjacent pixels in the 8-neighborhood of p :

$$CN(p) = 0.5 * \sum_{i=0}^7 |val(p_i) - val(p_{(i+1) \bmod 8})| \quad (2)$$

where p is central pixel, p_0, p_1, \dots, p_7 are ordered set of pixels which describes 8-neighborhood of p and $val(p_i) \in \{0, 1\}$. Using $CN(p)$, each pixel can be classified into one of five categories described in Table 1.

CN(p)	Type of pixel
0	Isolated point
1	End of ridge
2	Continuing ridge point
3	Bifurcation point
4	Crossing point

Table 1. Classification of pixels according to its crossing number

False Minutiae Rejection

The presence of noise in poor-quality images and imperfect thinning are two main reasons that cause a large number of extraction errors - dropping of true minutiae and production of false minutiae. Therefore, additional post processing is necessary to filter extracted minutiae and keep only set of true minutiae.

Although the main goal of the filtering process is to remove false minutiae, keeping true minutiae is more important for reliable minutiae matching. There are numerous methods to achieve that goal and most of them are based on set off heuristic rules. Examples of those rules are:

- if the break in the ridges is less than threshold value and no other pixel passes through it, then the break is connected;
- if the angle between the branch and the trunk is greater than 70° and less than 110° , then the branch is removed
- short ridges are removed on the basis of the relationship between the ridge length and the average distance between ridges;
- a ridge ending point that is connected to a bifurcation point, and is below a certain threshold distance is eliminated;
- two bifurcations are eliminated if distance between them is less than threshold value (10-15 pixels).

One effective and efficient method based on set off heuristic rules is presented in [9]. The setting of parameters, mostly some thresholds, should be obtained dynamically. Parameters adaptive to the image usually perform better than fixed values.

Experimental results given in this paper are obtained by using an algorithm for filtering based on examining local neighborhood around potential minutiae point, proposed by Tico and Kousmanen [10].

IV. MINUTIAE MATCHING

Fingerprint matching is a process of comparing an input fingerprint with a set of one or more template fingerprints. The return value is either a degree of similarity (for example, a score between 0 and 1) or a binary decision (matched/not matched). There are three main families of fingerprint matching techniques: correlation based matching, minutiae based matching and ridge-feature based matching [1]. Since it is widely accepted that minutiae set is the most discriminating and reliable feature, in modern systems for automatic fingerprints identification, that approach is the most popular. But, those are not the only reasons for popularity of minutiae based approach. Prior to the matching process, feature information has to be extracted from all the template images. The amount of extracted information from templates has to be low because of saving memory. Also, it has to be possible to efficiently traverse the structure which describes extracted information in order to check for necessary similarities. Those additional demands also favor minutiae based approach. In some applications it is possible to use hybrid approach, combining two or even all three approaches. This paper is focused on minutiae based approach.

Each minutia may be described by a number of attributes, including its location in the fingerprint image, orientation, type (e.g., ridge termination or ridge bifurcation), a weight based on the quality of the fingerprint image in the neighborhood of the minutia, and so on. *Local minutia structure* can be described in many different ways. One simple and most obvious would be a triplet (x, y, Ψ) , where x and y are minutia location coordinates and Ψ is the local ridge direction in given coordinate system. Yang and Verbaauwhede [11] proposed derived local structure as well as an algorithm based on it and experimental results given in this paper are based on implementation of that algorithm. The algorithm is described in the rest of the section.

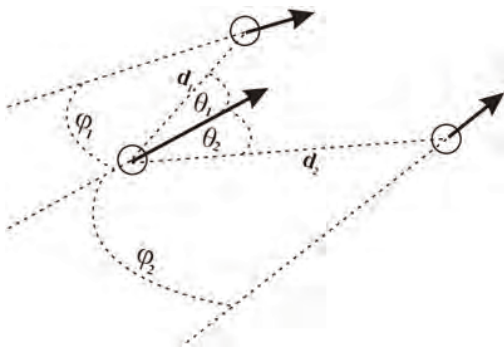


Fig. 1. Example of minutiae local structure

Local structure L_M can be described by Eq. 3:

$$L_M = \{(d_1, \varphi_1, \vartheta_1), (d_2, \varphi_2, \vartheta_2), \dots, (d_N, \varphi_N, \vartheta_N), \Psi\} \quad (3)$$

where N is the number of nearest neighbors of minutiae M , d_i ($i = 1, 2, \dots, N$) describes the distance between the selected minutia M and its i^{th} nearest neighbor, φ_i ($i = 1, 2, \dots, N$) is the

related radial angle between M and its i^{th} nearest neighbor, ϑ_i ($i = 1, 2, \dots, N$) represents the related position angle of the i^{th} nearest neighbor and Ψ is the local ridge direction of minutia M . An example is illustrated in Fig 1.

If (x_M, y_M) denotes x and y coordinates of minutiae M , (x_i, y_i) denotes x and y coordinates of i^{th} nearest neighbor, and $diff(\alpha, \beta)$ calculate the difference between angles α and β and converts the result to range $[0, 2\pi)$, than parameters $(d_i, \varphi_i, \vartheta_i)$ ($i = 1, 2, \dots, N$) can be calculated using following formula:

$$\begin{aligned} d_i &= \sqrt{(x_i - x_M)^2 + (y_i - y_M)^2}, \\ \varphi_i &= diff(\Psi_i - \Psi), \\ \vartheta_i &= diff(\arctan(\frac{y_i - y_M}{x_i - x_M}), \Psi) \end{aligned} \quad (4)$$

Proposed matching algorithm is based on calculating *minutiae similarity factor* and *image similarity factor* using vector of threshold values $(Th_d, Th_\varphi, Th_\vartheta, Th_\Psi, Th_{MSF}, Th_{ISF})$.

Let M be a minutiae from input (query) image with its local structure $L_M = \{(d_1, \varphi_1, \vartheta_1), (d_2, \varphi_2, \vartheta_2), \dots, (d_N, \varphi_N, \vartheta_N), \Psi\}$, and M' be a minutiae from template (database) image described by its local structure $L_{M'} = \{(d'_1, \varphi'_1, \vartheta'_1), (d'_2, \varphi'_2, \vartheta'_2), \dots, (d'_N, \varphi'_N, \vartheta'_N), \Psi'\}$. *Minutiae similarity factor (MSF)* represents degree of similarity between two minutiae M and M' . It can be calculated by observing their local structures L_M and $L_{M'}$. First of all, if $|\Psi - \Psi'| > Th_\Psi$, than $MSF = 0$, M and M' are not matched and another pair of minutiae can be checked. Otherwise, it is necessary to investigate similarity of neighborhoods of minutiae M and M' . If i^{th} neighbor of minutiae M and j^{th} neighbor of minutiae M' satisfy set of conditions described by Eq. 5:

$$\begin{aligned} |d_i - d'_j| &< Th_d \\ |\varphi_i - \varphi'_j| &< Th_\varphi \\ |\vartheta_i - \vartheta'_j| &< Th_\vartheta \end{aligned} \quad (5)$$

than those two neighbors can be marked as "matched neighbors". MSF is equal to the total number of "matched neighbors". If $MSF > Th_{MSF}$, than minutiae M and M' represent "matched minutiae pair". After comparing all minutiae from input image with minutiae from template image, total number of minutiae matched pairs (NUM_{MMP}) is obtained. *Image similarity factor* is calculated using Eq. 6:

$$ISF = \frac{NUM_{MMP}}{\max(NUM_{input}, NUM_{template})} \quad (6)$$

where NUM_{input} and $NUM_{template}$ are total number of minutiae in the input and template images, respectively. Two images are considered to represent the same fingerprint if $ISF > Th_{ISF}$.

V. EXPERIMENTAL RESULTS

For implementation of the presented algorithm we used VS.NET (C#). All experiments have been done on a Pentium IV (3GHz, 1GB RAM) machine. Instead of using images obtained by our own sensors, we used FVC2002 DB_2 database [12]. We used 4, 5 and 6 and 7 nearest neighbors for minutiae matching step of the algorithm. FAR (False Acceptance Rate) and FRR (False Rejection Rate) factors had satisfying values only when 5 and 6-neighborhoods were used. Those results are consistent with results presented in [11]. Figure 2. presents some results of created testing software.

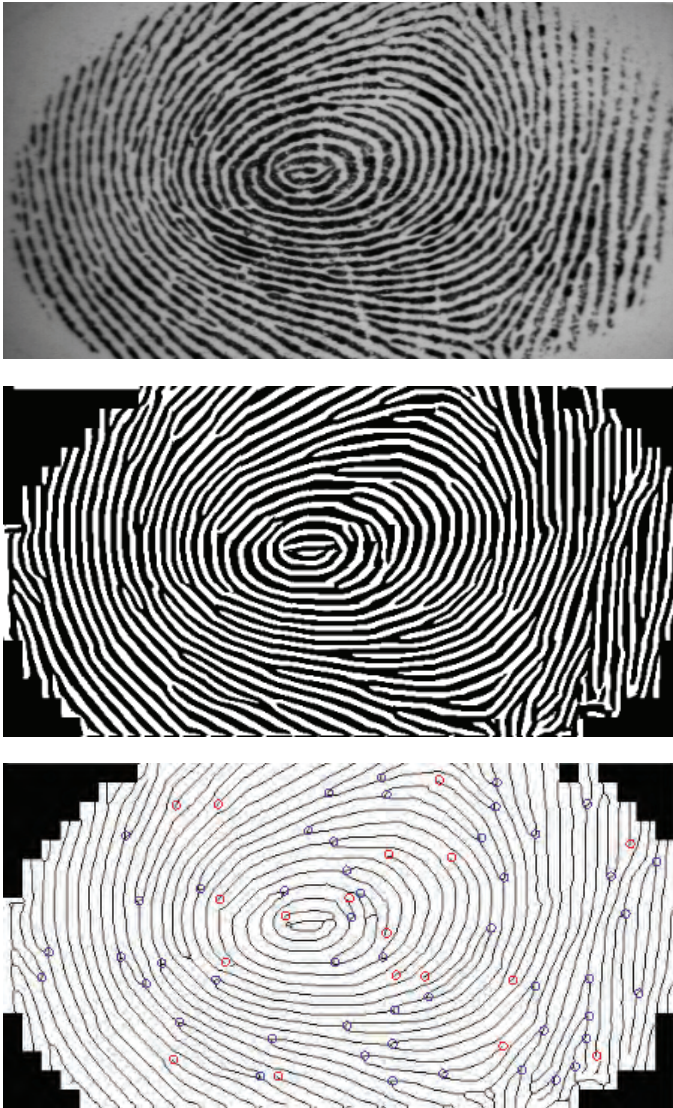


Fig. 2. Example of tested fingerprint image (original, image after enhancement, image after minutiae extraction)

VI. CONCLUSION AND FUTURE WORK

Created software achieved excellent results with images that had good quality, but had some problems in recognizing poor quality images. Those problems were identified and some ideas for their solving are:

- using dynamically calculated frequency improves image enhancement process. Improving this part of the system will allow work with not so good quality images
- grouping images by type of fingerprint improves matching process by reducing number of images which has to be compared with input image. This will improve speed of software.

Mentioned improvements will be focus of our future work.

REFERENCES

- [1] D. Maltoni, D. Maio, A. K. Jain, S. Prabhakar, "Handbook of fingerprint recognition", New York: Springer-Verlag, 2003.
- [2] O'Gorman, L., Nickerson, J.V., "An approach to fingerprint filter design", *Pattern Recognition* 22 (1), 29–38, 1989.
- [3] Mehtre, B.M., "Fingerprint image analysis for automatic identification", *Machine Vision, Appl.* 22 (6), 124–139, 1993.
- [4] L. Hong, Y. Wan, and A. Jain, "Fingerprint Image Enhancement: Algorithm and Performance Evaluation", *IEEE Trans. Pattern Analysis and Machine Intelligence*, Vol. 20, No. 8, pp. 777-789, 1998.
- [5] J. Yang, L. Liu, T. Jiang, and Y. Fan. "A modified gabor filter design method for fingerprint image enhancement", *Pattern Recognition Letters*, 24:1805-1817, 2003.
- [6] A. Ross, A. K. Jain and J. Reisman, "A Hybrid Fingerprint Matcher", *Pattern Recognition*, Vol. 36, No. 7, pp. 1661-1673, 2003.
- [7] M. Couprie, "Note on fifteen 2D parallel thinning algorithms", Internal Report, Institut Gaspard Monge, 2006.
- [8] M.V. Nagendraprasad, P.S.P. Wang, and A. Gupta "Algorithms for thinning and rethickening binary digital patterns", *Digital Signal Processing* 3, 97–102, 1993.
- [9] H. Lu, X. Jiang and Wei-Yun Yau, "Effective and Efficient Fingerprint Image Postprocessing", *Proc. ICARCV2002*, Singapore, pp. 985-989, Dec. 2002.
- [10] Tico, M., and Kuosmanen, P. "An algorithm for fingerprint image postprocessing", in *Proceedings of the Thirty-Fourth Asilomar Conference on Signals, Systems and Computers*, vol. 2, pp. 1735–1739, November 2000.
- [11] S. Yang and I. Verbauwhede, "A secure fingerprint matching technique", *Proc. ACM Workshop on Biometrics: Methods and Applications*, pp. 89-94, November 2003.
- [12] FVC2002 - Fingerprint Verification Competition, <http://bias.csr.unibo.it/fvc2002>

Performances of The Exponential Sinusoidal Audio Model

Zoran N. Milivojevic¹, Predrag Rajkovic² and Sladjana M. Milivojevic³

Abstract – In the first part of this paper TLS and Hankel TLS algorithms for determination of parameters for sinusoidal and exponential sinusoidal model of audio and speech signal are described. In the second part performances of exponential sinusoidal model are determined and a comparative analysis of a model for the case of segment processing with the distinguished and poorly distinguished transiency is performed. In the analysis tabular data and time and frequency diagrams are used.

Keywords – Exponential sinusoidal modeling, TLS algorithm.

I. INTRODUCTION

The sinusoidal model (SM) is suitable for representing the harmonic structure of the speech and audio segments. Special conveniences can be seen in speech analysis/synthesis [1,2], speech modification [3], speech coding [4,5] and audio coding [6,7]. The sinusoidal model for the speech and audio signal $s(n)$ can be presented in the following form:

$$s(n) \approx \sum_{k=1}^K a_k(n) \sin(2\pi f_k(n)n + \phi_k(n)). \quad (1)$$

In the sinusoidal model the signal $s(n)$ is presented as a summary of components with time variable amplitude a_k , frequency f_k and phase ϕ_k . These parameters are often invariable or slowly variable in the time of analysis (duration time of an analyzed sequence, i.e. segment). Depending on the signal the length of the quasi-stationary segment varies from several *ms* to several hundreds *ms* [8].

Speech and audio signals often contain segments with superimposed noise as well as segments with transient sound. In such cases the model described by means of (1) does not give satisfying results. In [9] shows the model for presenting the audio signal created by enlarging the model described with (1) by adding the noise $\eta(n)$ and transient segment $\tau(n)$:

$$s(n) \approx \sum_{k=1}^K a_k(n) \sin(2\pi f_k(n)n + \phi_k(n)) + \eta(n) + \tau(n). \quad (2)$$

In standards for audio signal coding, such as MPEG-1 LI, using of model (2) is not explicitly foreseen. The subcomprehensive coding structure [10] is being used instead. The subcomprehensive coding is efficient for coding signal

with superimposed noise in a wide frequency range. However, when coding signals with transient segments, the efficiency is considerably smaller. Generally seen, transient sound is difficult to model by means of the sinusoidal model. More qualitative modeling can be achieved by enlarging the number of model parameters, which reduces coding efficiency. For that reason in some coding schemes detecting of transient segments and selecting the code structure with enlarged resolutions in time domain is done first.

One way of solving this problem is audio signal modeling and coding by using of superposition of sinusoid with time slow exponential changes of amplitudes and quasistationary noise $\eta(n)$:

$$s(n) \approx \sum_{k=1}^K a_k(n) \cdot e^{-d_k(n)n} \sin(2\pi f_k(n)n + \phi_k(n)) + \eta(n), \quad (3)$$

where d_k is damping factor of the k -th component. The exponential sinusoidal model (ESM) is described in [11]. Its efficiency in modeling transient segments is presented in [12,13]. Determination of model parameters (amplitude a_k , frequency f_k , phase ϕ_k and damping factor d_k) is numerically complex and demands a lot of calculation time.

In this paper algorithms for determining parameters of the exponential sinuous model are described and their performances are determined.

The organization of this paper is as follows. In Section II TLS-ESM algorithm is described. In Section III Hankel TLS algorithm for forming of model parameters is described. In Section IV results of the comparative analysis of the application of SM and ESM models in transient and non-transient sequences are presented.

II. TLS-ESM ALGORITHM

TLS (Total Least Squares) algorithm is used for determining parameters of the exponential sinuous model [14]. For the inlet segment $s(n)$, $n=1, \dots, N$, by TLS algorithm parameters of the model of L order ($b(l)$, $l=1, \dots, L$) are being determined on the condition of minimizing:

$$\sum_{n=1}^N (\hat{s}(n) - s(n))^2 = \sum_{n=1}^N (\Delta s(n))^2, \quad (4)$$

where:

$$\hat{s}(n) = \sum_{l=1}^L b(l)(s(n-l) + \Delta s(n-l)), \quad n = (L+1), \dots, N. \quad (5)$$

¹Zoran N. Milivojevic, Technical College, Aleksandra Medvedeva 20, Nis, Serbia, E-mail: milivojevic@bankerinter.net

²Predrag Rajkovic, Faculty of Mechanical Engineering, Aleksandra Medvedeva 22, Nis, Serbia.

³Sladjana M. Milivojevic, Technical Faculty, Svetog Save 65, Cacak, Serbia, E-mail: milivojevic@bankerinter.net

Equation (5) can be written in the form of:

$$\hat{s}(n) = \sum_{k=1}^K a_k(n) \cdot e^{-d_k(n)n} \sin(2\pi f_k(n)n + \phi_k(n)), \quad (6)$$

where the damping factor d_k can be positive, negative or zero. By comparing of equations (3) and (6) it can be seen that it is possible to apply TLS algorithm for determining parameters of ESM model, i.e. for automatic decomposition of an audio sequence in a certain number of damped sinusoids [15].

III. HANKEL TLS ALGORITHM

Due to its great calculation efficiency, Hankel TLS (HTLS) algorithm is used for solving TLS problems. HTLS algorithm has found its intensive application in nuclear magnetic resonance spectroscopy. In the [15] HTLS algorithm is described that for inlet parameters: a) sequence $s(n)$, $n=1, \dots, N$; and b) model order K_e ; generates parameters of the estimated sinusoids (amplitude \hat{a}_k , frequency \hat{f}_k , phase $\hat{\psi}_k$, damping factors \hat{d}_k). The algorithm consists of the following steps:

Step 1: Out of sequence elements $s(n)$ Hankel matrix H with dimensions $m \times n$ is formed.

Step 2: SVD (singular value decomposition) of matrix H is determined:

$$H = USV^H, \quad (7)$$

Step 3: Shortened matrices of K_e rank are constructed:

$$\hat{H} = U_{K_e} S_{K_e} V_{K_e}^H, \quad (8)$$

where U_{K_e} contains the first K_e columns of the matrix U , V_{K_e} contains the first K_e columns of the matrix V , whereas S_{K_e} is the submatrix ($K_e \times K_e$) of the matrix S .

Step 4: TLS is calculated for the predefined equation system:

$$\bar{U}_{K_e} \approx \underline{U}_{K_e} E, \quad (9)$$

where \bar{U}_{K_e} is obtained from the matrix U_{K_e} after eliminating the first row, \underline{U}_{K_e} is obtained from the matrix U_{K_e} after eliminating the last row. K_e values of E are used for estimation of signal poles:

$$\hat{z}_k = e^{(j2\pi\hat{f}_k - \hat{d}_k)}, \quad k = 1, \dots, K_e. \quad (10)$$

Step 5: The equation of the model is formed on the base of signal poles:

$$\hat{s}(n) = \sum_{k=1}^{K_e} c_k \hat{z}_k^{n-1}, \quad (11)$$

where

$$\hat{c}_k = \frac{\hat{a}_k}{e} e^{j\psi_k}. \quad (12)$$

Taking into consideration that the poles are conjugated complex, the model described with (11) can be presented in a reduced form:

$$\hat{s}(n) = \sum_{k=1}^K \hat{a}_k(n) \cdot e^{-\hat{d}_k(n-1)} \sin(2\pi\hat{f}_k(n-1) + \hat{\phi}_k), \quad (13)$$

where

$$\hat{\phi}_k = \hat{\psi}_k + \pi/2, \quad k = 1, \dots, K. \quad (14)$$

The model described with (13) is equivalent to the ESM model described with (3).

Detailed description of HTLS algorithm can be found in [8, 16].

IV. PERFORMANCES OF ESM MODEL

Performances of ESM model with implemented HTLS algorithm will be determined by means of signal-noise ratio (SNR) that is defined in (8):

$$SNR = 10 \log_{10} \frac{\sum_{n=1}^N s^2(n)}{\sum_{n=1}^N (s(n) - \hat{s}(n))^2}. \quad (15)$$

Thus defined SNR represents a measure of precision of the modeled signal in relation to the original signal.

Further analyses were carried out on the archived speech signal whose sampling frequency is $F_s = 22.050$ kHz, by means of a mathematical packet MatLab. Comparative analyses will be performed by an analysis in time and frequency domains on: a) the original speech signal (s), b) the speech signal modeled by means of an sinusoidal model (s_{SM}) and c) the speech signal modeled by means of an exponential sinusoidal model (s_{ESM}). The following examples relate to two types of sequences: a) with not so outstanding transience (signal sequences where periodicalness is expressed) and b) with an outstanding transience.

IV.A. Sequencies with not so outstanding transience

Examples of sequences of speech and audio signals with not so outstanding transience are presented in Fig. 1 where the original signal s is shown and modeled signals s_{SM} and s_{ESM} for $K_e = 32$. In Fig. 2 the same signals for $K_e = 128$ are shown. In these sequences the signal periodicalness can be seen (pronunciation of vowels, musical signal etc.).

IV.A. Sequences with outstanding transience

Sequences of speech signal with an outstanding effect of transience are modeled for some values of model order K_e ($K_e = 4, 8, 16, 32, 64, 128$). Time forms of signals are presented in

Fig. 3 ($K_e=32$) and Fig. 5 ($K_e=128$). The signal spectra are determined by means of FFT and presented in Fig.4 ($K_e=32$) and Fig. 6 ($K_e=128$).

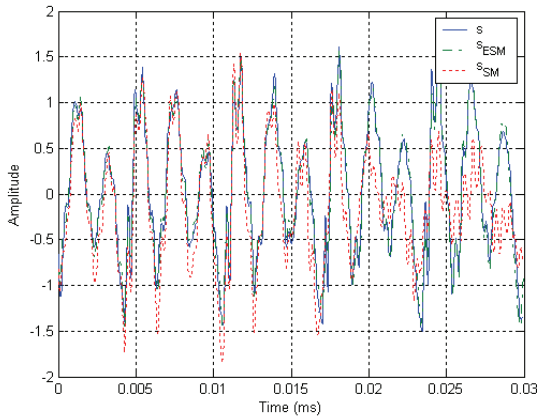


Fig. 1. The sequence of the speech signal for the word 'five' with not so outstanding transience: a) s the original signal, b) s_{ESM} reconstructed signal on the base of the estimated parameters of ESM model and c) s_{SM} reconstructed signal on the base of the estimated parameters of SM model ($F_s=22.050$ kHz, $K_e=32$).

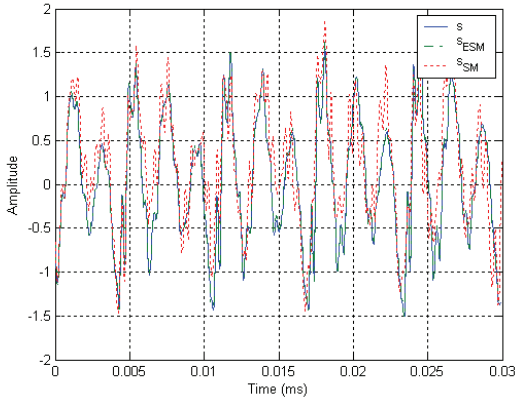


Fig. 2. The sequence of the speech signal for the word 'five' with not so outstanding transience: a) s the original signal, b) s_{ESM} reconstructed signal on the base of the estimated parameters of ESM model and c) s_{SM} reconstructed signal on the base of the estimated parameters of SM model ($F_s=22.050$ kHz, $K_e=128$).

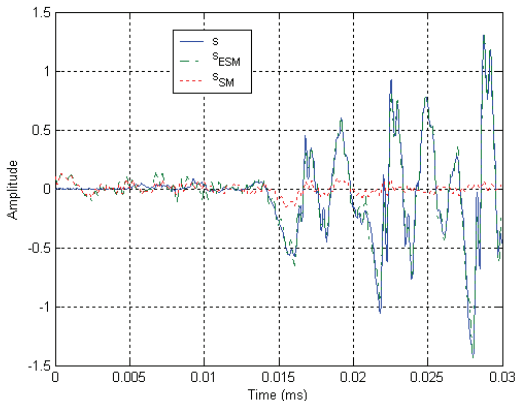


Fig. 3. Transient segment of the speech signal for the word 'five': a) s the original signal, b) s_{ESM} reconstructed signal on the base of the estimated parameters of ESM model and c) s_{SM} reconstructed signal on the base of estimated parameters of SM model ($F_s=22.050$ kHz, $K_e=32$).

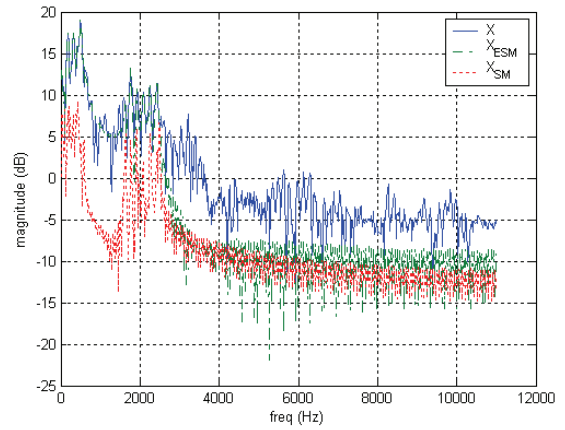


Fig. 4. Spectrum of the transient segment of the speech signal for the word 'five': a) s the original signal, b) s_{ESM} reconstructed signal on the base of the estimated parameters of ESM model and c) s_{SM} reconstructed signal on the base of the estimated parameters of SM model ($F_s=22.050$ kHz, $K_e=32$).

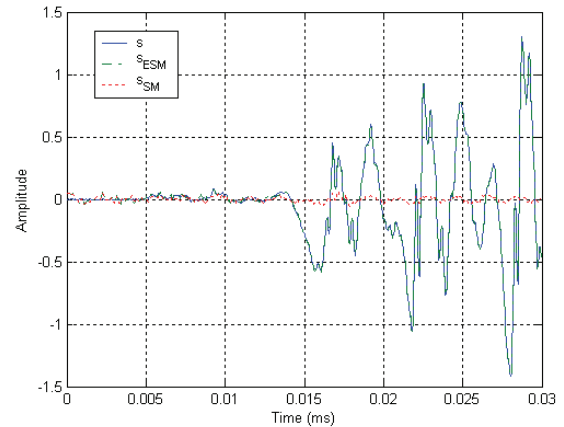


Fig. 5. Transient segment of the speech signal for the word 'five': a) s the original signal, b) s_{ESM} reconstructed signal on the base of the estimated parameters of ESM model and c) s_{SM} reconstructed signal on the base of estimated parameters of SM model ($F_s=22.050$ kHz, $K_e=128$).

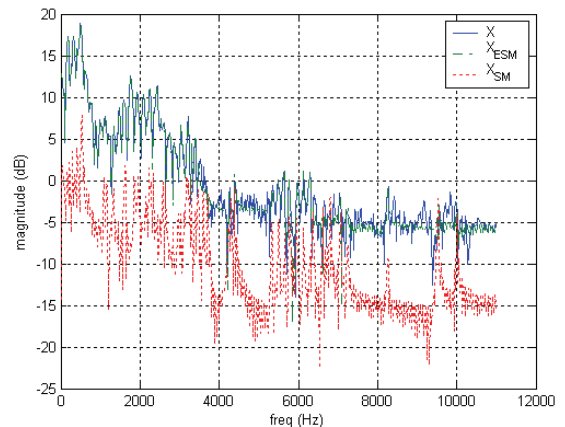


Fig. 6. Spectrum of the transient segment of the speech signal for the word 'five': a) s the original signal, b) s_{ESM} reconstructed signal on the base of the estimated parameters of ESM model and c) s_{SM} reconstructed signal on the base of the estimated parameters of SM model ($F_s=22.050$ kHz, $K_e=128$).

In Table 1 results of SNR at the sinusoidal and exponential model for the transient and weakly present transience are presented.

TABLE I

ADVANTAGES OF SNR FOR A) TRANSIENT AND B) NOT SO OUTSTANDING TRANSIENT SEGMENT FOR THE CASE OF THE APPLICATION OF SINUOUS AND EXPONENTIAL SINUOUS MODEL, DEPENDING ON THE MODEL ORDER

K_e	Transient		Not so outstanding transient	
	SNR_{SM}	SNR_{ESM}	SNR_{SM}	SNR_{ESM}
4	0.1690	3.0173	6.0962	6.2688
8	0.4863	6.3888	9.8830	10.415
16	0.6693	8.3856	6.8996	11.7304
32	0.2837	14.637	4.4636	15.9509
64	0.1115	22.5617	3.5876	19.7519
128	0.1650	27.9215	5.2516	27.8634
mean values	0.3141	13.8186	6.03	15.33

On the base of time and frequency diagrams, as well as on the base of tabular data for SNR it should be concluded that the ESM model is superior in relation to the SM model. Its special advantage is in regard to modeling of signals in transient sequences. In the transient sequence the relation of the mean values is $13.8186/0.311=43.99$, whereas in the sequence with not so outstanding transience the relation is 2.54.

V. CONCLUSION

In this paper the exponential sinusoidal audio model with the implemented HTLS algorithm is described. In the second part of this paper the results of testing the application of the sinusoidal and exponential model in modeling the speech signal are presented. Modeling was performed for various operating parameters of the model. As a measure of successfulness, i.e. of precision of modeling, SNR was used. Analysis of the obtained results points to the greater efficiency of ESM in relation to SM in all the values of the model order. In addition to that, the results demonstrate great efficiency in transient segments, i.e., in the concrete example, 43.99 times in relation to SM model. The results testify that the application of ESM model for the speech and audio signal compression is justified in archiving and transition by communication.

REFERENCES

- [1] E.B. George, M.J.T. Smit, *Speech analysis/synthesis and modification using an analysis-by-synthesis/overlap-add sinusoidal model*, IEEE Trans. Speech Audio Process. 5 (5) (September 1997) 389–406.
- [2] R.J. McAulay, T.F. Quatieri, *Speech analysis-synthesis based on a sinusoidal representation*, IEEE Trans. Acoustics, Speech and Signal Processing 34 (4) (August 1986) 744–754.
- [3] Quatieri, R.J. McAulay, *Speech transformations based on a sinusoidal representation*, IEEE Trans. Acoustics, Speech and Signal Processing 34 (6) (August 1986) 1449–1464.
- [4] R.J. McAulay, T.F. Quatieri, *Speech Coding and Synthesis*, Elsevier, Amsterdam, 1995, pp. 121–173.
- [5] L.B. Almeida, F.M. Silva, *Variable-frequency synthesis: an improved harmonic coding scheme*, in: Proceedings of the International Conference on Acoustics, Speech and Signal Processing, San Diego, CA, 1984, pp. 27.5.1–27.5.4.
- [6] J. Jensen, R. Heusdens, *A comparison of differential schemes for low-rate sinusoidal audio coding*, in: Proceedings of the IEEE Workshop on Applications of Signal Processing to Audio and Acoustics, New Paltz, NY, October 2003, pp. 205–208.
- [7] H. Purnhagen, B. Edler, C. Ferekidis, *Object-based analysis/synthesis audio coder for very low bit rates*, in: Proceedings of the 104th AES Convention, Amsterdam, The Netherlands, May 1998, Convention paper 4747.
- [8] K. Hermus, W. Verhelst, P. Lemmerling, P. Wambacq, S. Huffel, *Perceptual audio modeling with exponentially damped sinusoids*, Signal Processing 85 (2005) 163–176.
- [9] S.N. Levine, *Audio representations for data compression and compressed domain processing*, Ph.D. Thesis, Stanford University, December 1998.
- [10] T. Painter, A. Spanias, *Perceptual coding of digital audio*, Proceedings of the IEEE, vol. 88(4), April 2000, pp. 451–513.
- [11] K. Hermus, W. Verhelst, P. Wambacq, P. Lemmerling, *Total least squares based subband modelling for scalable speech representations with damped sinusoids*, in: Proceedings of the International Conference on Spoken Language Processing, Beijing, China, October 2000, pp. 1129–1132.
- [12] J. Jensen, S.H. Jensen, E. Hansen, *Harmonic exponential modeling of transitional speech segments*, in: Proceedings of the International Conference on Acoustics, Speech and Signal Processing, Istanbul, Turkey, June 2000, pp. 1439–1442.
- [13] P. Lemmerling, I. Dologlou, S. Van Huffel, *Speech compression based on exact modeling and structured total least norm optimization*, in: Proceedings of the International Conference on Acoustics, Speech and Signal Processing, Seattle, WA, May 1998, pp. 353–356.
- [14] S. Van Huffel, J. Vandewalle, *The Total Least Squares Problem: Computational Aspects and Analysis*, Frontiers in Applied Mathematics, vol. 9, SIAM, Philadelphia, PA, 1991.
- [15] K. Hermus, W. Verhelst, P. Wambacq, *Perceptual audio modeling based on Total Least Squares algorithms*, AES 112TH Convention, Munich, Germany, May 10–13, 2002.
- [16] S. Van Huffel, H. Chen, C. Decanniere, P. Van Hecke, *Algorithm for time-domain NMR data fitting based on total least squares*, J. Magn. Reson. A 110 (1994) 228–237.

Non-uniform Thresholds for Removal of Signal-Dependent Noise in Wavelet Domain

Mitko Kostov, Cvetko Mitrovski¹ and Momcilo Bogdanov²

Abstract – This paper presents experimental results obtained using a method that we propose for signal denoising. Noisy signals are processed in a discrete wavelet transform domain with a non-uniform threshold adjusted to the noise level.

Keywords – Denoising, signal-dependent noise, threshold, wavelet domain filtering.

I. INTRODUCTION

There are many methods for noise removal, but very few of them focus on removing varying noise that depends on the local intensity of the signal. This kind of signal-dependent noise is commonly found in nuclear medicine (NM) images. Until now, the offered methods have been based on conventional filtering in time and frequency domain and lately, wavelet transforms. Research to date in wavelet-domain filtering has focused on removing Gaussian noise by using a global threshold that is independent on the signal or by multiscale products of the detail coefficients [1-3]. These methods are inappropriate for denoising signals that contain signal-dependent noise. One simple fix would be to work with the square-root of the image, since this operation is variance stabilizing [1]. Another method for Poisson noise removal in the wavelet domain uses a non-uniform threshold for filtering the noisy wavelet coefficients [4].

In this paper we present results obtained using our method for removal of signal-dependent noise. It is based on generating non-uniform threshold adjusted to the noise level in the signal. It is organized as follows. The standard wavelet shrinkage program is outlined in Section II. In Section III we discuss how to estimate the varying threshold. In Section IV we verify the validity of our approach on 1-D deterministic signal contaminated with artificially added noise proportional to the signal intensity. At the end, Section V concludes the paper.

II. WAVELET DOMAIN FILTERING

In series expansion of discrete-time function f using wavelets

$$f(t) = \sum_{j=1}^J \sum_{k=1}^{2^{-j}M} d_{jk} \psi_{jk}(t) + \sum_{k=1}^{2^{-j}M} a_{Jk} \phi_{Jk}(t), \quad (1)$$

ψ_{jk} and ϕ_{jk} denote wavelet and scaling function, respectively, the indexes j and k are for dilatation and translation, and a_{Jk} and d_{jk} are approximation and detail coefficients.

The most popular form of wavelet-based filtering, wavelet shrinkage [1], is performed by weighting the corresponding detail wavelet coefficient by h_{jk} ($0 \leq h_{jk} \leq 1$) and calculating the inverse wavelet transformation. Conventionally, the filtration is performed either by using “hard threshold” nonlinearity

$$h_{jk}^{(\text{hard})} = \begin{cases} 1, & \text{if } |d_{jk}| \geq \tau_j \\ 0, & \text{if } |d_{jk}| < \tau_j \end{cases} \quad (2)$$

or by using “soft threshold” nonlinearity

$$h_{jk}^{(\text{soft})} = \begin{cases} 1 - \frac{\tau_j \operatorname{sgn}(d_{jk})}{d_{jk}}, & \text{if } |d_{jk}| \geq \tau_j \\ 0, & \text{if } |d_{jk}| < \tau_j \end{cases} \quad (3)$$

where τ_j is a user-specified threshold level.

III. ESTIMATING NON-UNIFORM THRESHOLD

Let \mathbf{y} denotes a noisy signal that consists of a noise-free signal \mathbf{s} and noise \mathbf{n} with zero mean value and energy proportional to the local signal intensity:

$$\mathbf{y} = \mathbf{s} + \mathbf{n}. \quad (4)$$

For this signal the wavelet transform (WT) satisfies

$$\text{WT}(\mathbf{y}) = \text{WT}(\mathbf{s}) + \text{WT}(\mathbf{n}). \quad (5)$$

Let \mathbf{A} and \mathbf{D} denote the approximation and detail wavelet coefficients obtained with wavelet transform of the signal \mathbf{y} . Since the noise is proportional to the local signal intensity, a threshold τ_j for filtering of all the detail wavelet coefficients \mathbf{D} should not be uniform, but it should follow the local signal intensity. Hence, a non-uniform threshold could be determined as $\tau = \alpha|\mathbf{A}|$ where α is a constant parameter which could be determined by equalizing the energy of the approximation and the detail coefficients:

¹Mitko Kostov and Cvetko Mitrovski are with the Faculty of Technical Sciences, I.L.Ribar bb, 7000 Bitola, Macedonia, E-mails: mitko.kostov@uklo.edu.mk, cvetko.mitrovski@uklo.edu.mk

²Momcilo Bogdanov is with the Faculty of Electrical Engineering and Information Technologies, Karpos II b.b., P.O. Box 574, 1000 Skopje, Macedonia, E-mail: bogdanov@etf.ukim.edu.mk

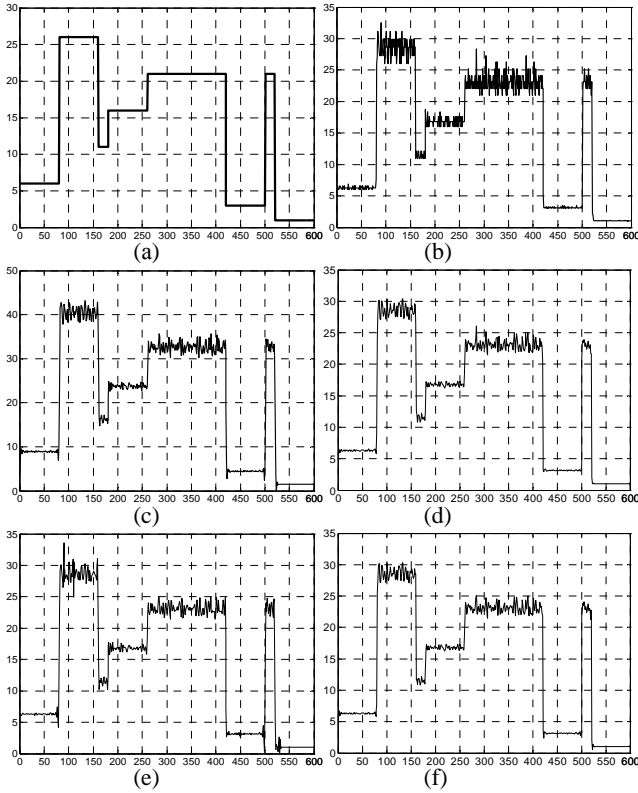


Fig. 1. (a) Deterministic signal; (b) noisy signal; (c) first level approximation coefficients; (d) reconstructed signal using the proposed approach; (e) reconstructed signal using the universal global threshold with db7; (f) reconstructed signal using multiscale product.

$$\sum_i D(i)^2 = \sum_i (\alpha A(i))^2.$$

In this paper we use eq. (6) for the determination of α , based on a set of two new vectors \mathbf{D}_1 and \mathbf{A}_1 (with lower dimension than the initial vectors \mathbf{D} and \mathbf{A}) which are created by using the following.

The detail coefficients \mathbf{D} are like waves and they frequently change their polarity. Therefore, the coefficients between the positive and negative peaks have magnitudes that are close to zero, and we discard their contribution by keeping the local extremes in \mathbf{D} and zeroing the other coefficients:

$$D_1(i) = \begin{cases} D(i) & \text{if } D(i) > \max(D(i-1), D(i+1)) \\ & D(i) < \min(D(i-1), D(i+1)) \\ 0 & \text{otherwise} \end{cases} \quad (7)$$

Similarly, the vector \mathbf{A}_1 is constructed by zeroing the approximation coefficients \mathbf{A} for those indices i where $D_1(i) = 0$:

$$\mathbf{A}_1 = \mathbf{A} \cdot \text{sign}(|\mathbf{D}|)$$

Since the coefficients \mathbf{D}_1 and $\alpha \mathbf{A}_1$ have equal energy and at the same time, the coefficients \mathbf{D}_1 contain narrower and higher peaks compared to the coefficients $\alpha \mathbf{A}_1$, the coefficients $\alpha \mathbf{A}_1$

will be smaller than the coefficients $|\mathbf{D}_1|$ where the signal portion in (5) is bigger, but bigger than coefficients $|\mathbf{D}_{n1}|$ where there is no signal.

In general, since the noise is proportional to the local signal intensity, for the threshold τ the following can be written:

$$\tau(i) = \alpha_n A(i)^n + \dots + \alpha_1 A(i) + \alpha_0, \quad i = 0, \dots, L-1, \quad (9)$$

where L is the length of the vectors \mathbf{A} and τ . The coefficients $\alpha_0, \alpha_1, \dots$ can be obtained by minimizing the square measure E_1 in the smallest squares sense:

$$E_1 = \frac{1}{2} \sum_i \left(|D_1(i)| - (\alpha_n A_1(i)^n + \dots + \alpha_1 A_1(i) + \alpha_0) \right)^2 \quad (10)$$

For the purpose of simplicity, the threshold τ can take the form (6), and in the same time the error function E_1 which is to be minimized is:

$$E_1 = \frac{1}{2} \sum_i \left(|D_1(i)| - \alpha A_1(i) \right)^2. \quad (11)$$

IV. EXPERIMENTAL RESULTS

In this Section, we illustrated our proposal on a deterministic 1-D signal contaminated with artificially generated noise in Fig. 1. The non-decimated wavelet transform [3] is performed using a NPR-QMF prototype filter [5], instead of wavelet filters. We obtained that the approximation coefficients follow the signal contour as it is illustrated in Fig. 1c.

Since the noise is signal dependent, the detail coefficients \mathbf{D} (Fig. 1b) follow the signal level: the signal intensity in the interval 120-160 is higher than the signal intensity in the intervals 160-180 and 180-220, so the noise is highest in the interval 120-160, while lowest in the interval 180-220.

By comparing Fig. 2a and Fig. 2b it can be seen that the coefficients \mathbf{D} contain signal details \mathbf{D}_s with higher intensities around the positions 160 and 180 (jumps in Fig. 2a, i.e. peaks in Fig. 2b); while in the other regions, in the interval 120-220, there is noise. Also, in Fig. 2b it can be noticed that a significant portion of the detail coefficients have values close to zero as a consequence of the fast changing of their polarity.

We experimented with non-uniform thresholds calculated in two ways:

- 1) with eq. (6) by using energy equalizing of the new vectors \mathbf{A}_1 and \mathbf{D}_1 in (8);
- 2) with eq. (9) for different polynomial order n and minimizing of (10).

The thresholds follow the height of the detail peaks as it is illustrated in Fig. 3: the noise level is higher; the thresholds are higher and vice versa. If we make a comparison of two thresholds obtained with 1) and 2), the first threshold is extended and closer to the peaks of the coefficients $|\mathbf{D}|$, which means it is better generated than the second one. This is illustrated in Fig. 3. When a threshold is calculated by using (9), the number of terms (n), have not significant impact on the threshold.

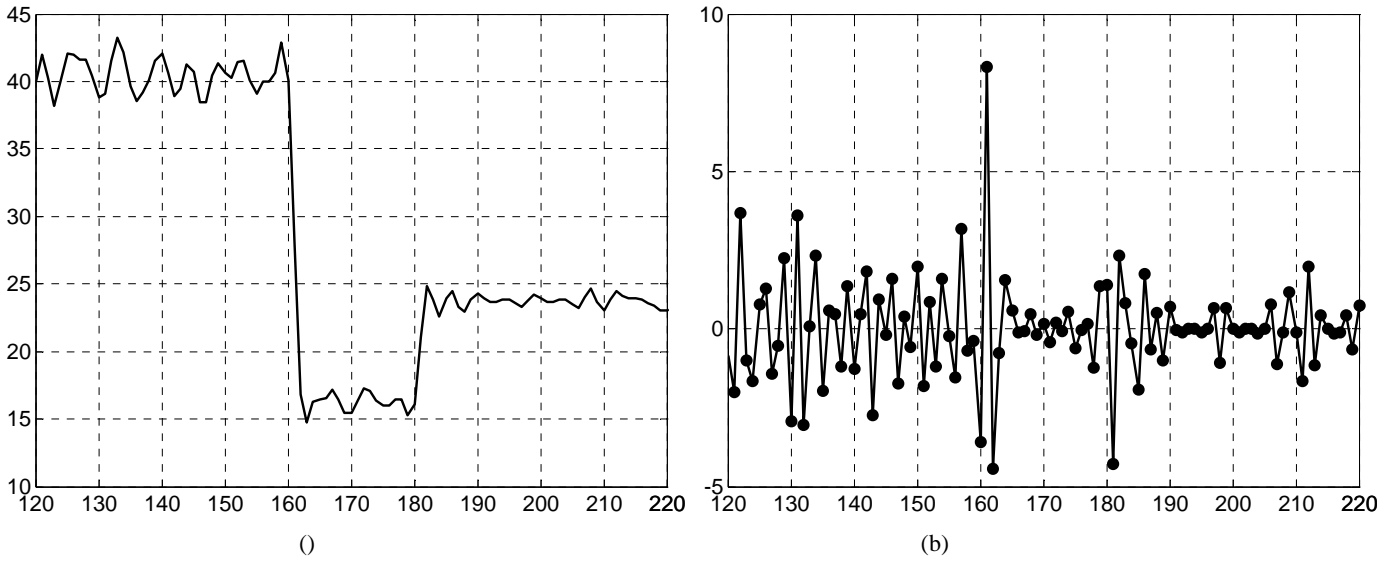


Fig. 2. A part of the first level wavelet coefficients. (a) Approximation coefficients A ; (b) detail coefficients D .

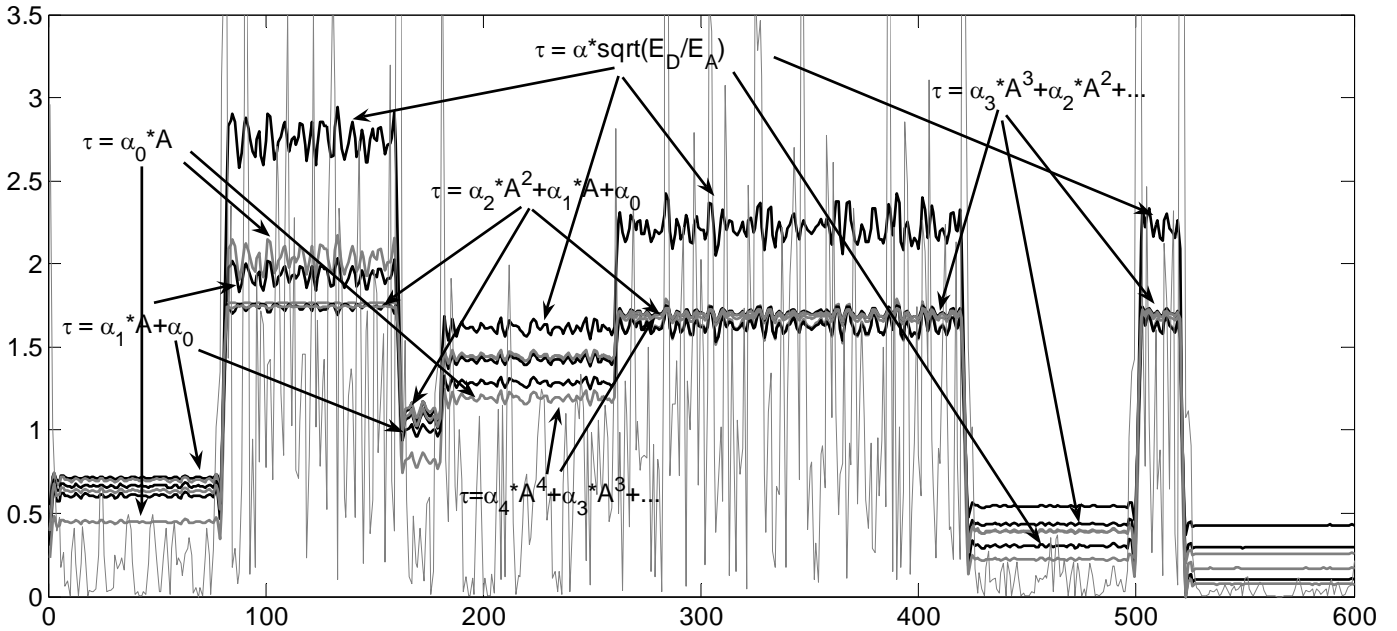


Fig. 3. Details and different estimated non-uniform thresholds: Threshold obtained through energy equalizing when $\tau = \alpha A$ (8) and thresholds obtained through minimization minimization of (10) for different order of the polynomial (9) (for clearer view, the values from 0 to 3.5 are shown only).

Moreover, the experiment illustrates that although the procedure of energy equalizing is simpler than the procedure of minimizing, it yields with better estimated threshold.

Values of these coefficients α_i in (9) obtained with minimization of (10) in the smallest squares sense and the error (10) for different polynomial order are given in Table I.

Using non-uniform threshold preserve the signal coefficients while remove the noise ones. This is shown in Fig. 4 where noise-free detail coefficients and filtrated detail coefficients are given. The coefficients are filtrated with threshold $\tau = \alpha A$ where α is estimated through the coefficients A_1 and D_1 in (8). If a global threshold was used, it was not be possible to reduce noise without removing part of

the signal at the same time. Hence, the reconstructed signals when a global threshold or multiscale product are used, suffer from distortion at the signal jumps positions, while there is no distortion at the signal filtrated with the proposed approach. This distortion appears as a result of removing signal information contained in the detail coefficients when a global threshold is used. This can be seen from Fig. 1d, e and f.

In order to quantitatively compare the proposed method to some known wavelet based methods, we use the energy of the remained noise in the filtrated signal s_1 as a measure:

$$E_n = \sum_i (s(i) - s_1(i))^2 \quad (12)$$

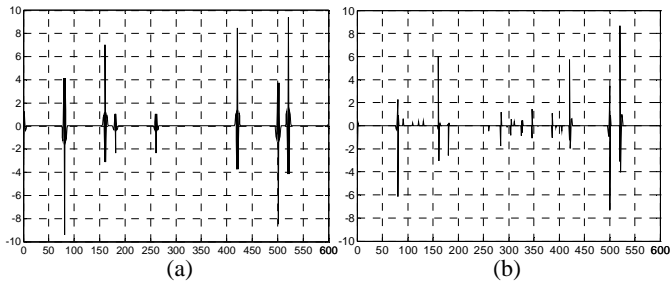


Fig. 4. (a) First level detail coefficients of the noise-free signal; (b) Filtrated coefficients using the threshold $\tau = \alpha \mathbf{A}$ when α is estimated through coefficients \mathbf{A}_1 and \mathbf{D}_1 in (8).

Table 2 contains the results when the signal is reconstructed from the first level approximation and filtrated detail coefficients. It can be seen that when the proposed approach is applied, the noise energy is smaller compared to the other methods that use a global threshold.

V. CONCLUSION

In this paper we give some views and experimental results conducted with our proposed method for denoising signals that contain signal-dependent noise. The experiments give advantage to the proposed method over the known wavelet based methods.

REFERENCES

- [1] D. L. Donoho, "Wavelet Thresholding and W.V.D.: A 10-minute Tour", *Int. Conf. on Wavelets and Applications*, Toulouse, France, June 1992;
- [2] Y. Xu, J. B. Weaver, D. M. Healy, Jr., and J. Lu "Wavelet Transform Domain Filters: A Spatially Selective Noise Filtration Technique", *IEEE Trans. on Image Processing*, vol. 3, no. 6, pp. 747-758, Nov. 1994;
- [3] E. J. Balster, Y. F. Zheng and R. L. Ewing "Feature-Based Wavelet Shrinkage Algorithm for Image Denoising", *IEEE Trans. on Image Processing*, vol. 14, no. 12, pp. 2024-2039, Dec. 2005;
- [4] R. D. Nowak, R. G. Baraniuk, "Wavelet-Domain Filtering for Photon Imaging Systems", *IEEE Trans. on Image Processing*, vol. 8, Iss. 5, p. 666-678, May 1999;
- [5] S. Bogdanova, M. Kostov, and M. Bogdanov, "Design of QMF Banks with Reduced Number of Iterations", *IEEE Int. Conf. on Signal Processing, Application and Technology, ICSPAT '99*, Orlando, USA, Nov. 1999.

TABLE I
COEFFICIENTS α_i IN (9) OBTAINED BY
MINIMIZATION OF (10) AND THE ERROR (10)

Polynomial order n	Coefficients $\alpha_n, \alpha_{n-1}, \dots, \alpha_1, \alpha_0$	Error E in (10)
1 ($\alpha_0 \neq 0$)	0.3714 0.0385	576.2
1 ($\alpha_0 = 0$)	0.0502	585.0
2	0.0484 0.0818 -0.0010	571.1
3	0.2294 0.0422 0.0010 -0.0000	570.9
4	0.2036 0.0315 0.0027 -0.0001 0.0000	571.2
5	0.0643 0.0387 0.0113 -0.0010 0.0000 -0.0000	566.5
6	0.1281 0.0077 0.0043 0.0010 -0.0001 0.0000 -0.0000	560.0
7	0.0035 0.0009 0.0003 0.0001 0.0000 -0.0000 0.0000 -0.0000	600.9
8	1.0e-003 * 0.1347 0.0408 0.0141 0.0047 0.0013 0.0002 -0.0000 -0.0000 0.0000	627.1
9	1.0e-004 * 0.6515 0.2191 0.0848 0.0329 0.0117 0.0033 0.0005 -0.0001 0.0000 -0.0000	607.8
10	1.0e-005 * 0.5918 0.2146 0.0901 0.0387 0.0159 0.0058 0.0017 0.0003 -0.0000 0.0000 -0.0000	634.2

TABLE II
THE ENERGY OF THE REMAINED NOISE IN THE
FILTRATED SIGNAL WITH THE PROPOSED METHOD
AND KNOWN METHODS

Proposed	Known methods				
	wavelet	universal [1]	[4]	sq.root [1]	[2]
1586	sym4	2011	2032	2071	1566
	sym7	2041	2094	2149	1714
	coif3	1958	1964	2076	1753
	coif5	1923	1959	2059	1847
	db2	2017	2040	2091	1614
	db8	1789	1795	1838	1787

SESSION CSIT IV

Computer Systems and Internet Technologies IV

GUI to Web Transcoding

Tsvetan Filev¹, Julian Pankov² and Ivan Pankov³

Abstract - In this paper a transcoding (transformation) scheme of a graphical application working on a server or desktop computer to web environment will be presented. The main working environments and interfaces are listed as well the main graphical environments. A realization scheme is depicted. The main disadvantages of the current approaches are listed, while the advantages of the new approach are shown.

Keywords - transcoding, environments, interfaces, graphical user interface, web interface

I. INTRODUCTION

So far the following approaches for application transformation are used:

- Web remote administration (Remote Desktop, VNC)
- ActiveX controls for IE connecting with remote Office Express Components
- FireFox add-ons: AutoCAD, SolidWorks, etc.
- Flash animations – they act like ActiveX or add-ons

The major minus of the listed methods is the lack of unification. Also the software looks differently on the different systems.

The control is done by JavaScript and Visual Basic scripts – the development is hard, expensive and insecure. A disadvantage is that the different components do not work the same way each time and there is no portability.

In the web administration the control over the system is taken by the new remote user leaving the current user without control.

II. TYPES OF ENVIRONMENTS FOR USER INTERFACE

In more details the environments for user interface and an algorithm for detection are examined in [1]. They are:

¹ Tsvetan V. Filev is with the Faculty of Computer Systems and Control, Technical University, Kliment Ohridski 8, 1000, Sofia, Bulgaria, E-mail: tsvetan.filev@gmail.com

² Julian Pankov is with the Faculty of Mechanical Engineering, Technical University, Kliment Ohridski 8, 1000, Sofia, Bulgaria, E-mail: jpankov@gmail.com

³ Ivan Pankov is with the Faculty of Computer Systems and Control, Technical University, Kliment Ohridski 8, 1000, Sofia, Bulgaria, E-mail: pankov@tu-sofia.bg

Shell environment, Web environment, SOAP query, XML-RPC query, REST query, Pure web query GET or POST, WAP, Graphical environment (GTK), Different mobile devices (PDA, Smart phone)

Of course the list is subject to changes and always more environments can be added like environment for sound control based on VoiceXML which is developed, standardized, documented and supported by W3C[3].

III. TRANSCODING - DEFINITION

The transcoding [2] is found in many areas of content adaptation, but here it will be presented in the area of adaptation of contents generated by computer systems and adopted for PDA or SmartPhone devices.

In the area of mobile devices the data transcoding is obligatory because of the multicolor in order to assure good display.

An example is taking a picture with high resolution and sending it to other phone which displays low resolutions. A transcoding of the image is needed to lower the resolution in order to be displayed properly on the remote device. Except that the image depiction is made better sometimes it is obligatory in order to display the image at all.

The transcoding is reduced to data transformation for one system in a format appropriate for another one.

Besides data transformation it is examined a transformation of computing power of the remote terminal. While showing the result the terminal is taking advantage of the computing power of the computer on which the application was started. In this way the computing power of the remote terminal is increased. One more functionality which it adds is the extension of the functionality of the desktop applications to network applications. In this way even the simple one user applications without networking can be transformed into networked without problems only with the help of a web server.

IV. TYPES OF COMPUTER GRAPHICAL INTERFACES

- Windows – this operating system is fully graphical and it gives up the users a very good developed interface which on its own allows to be developed a great deal of applications like video games, CAD systems, systems for 3 dimensional modeling, text processing, imaging and video.
- Unix/Linux/BSD – these are text based operating systems which have graphical server called X server, allowing the creation of sterling software applications. Of course here exists a full scale of

- applications for all purposes.
- Mac OS – this is the first graphical operating system. And as such it accounts for one of the best developed graphical user interfaces. The latest versions are UNIX based and as such they have integrated X server.

V. TYPES OF WEB SERVERS

- IIS – Internet Information Server was developed by Microsoft. Its beginning is placed like a part of the late versions of the Windows NT operating system with major functionality for its time. In the following Windows products the next versions appear allowing the creation of dynamic pages using ASP, and later on .NET applications.
- Apache – this is a web server developed by Apache Software Foundation and it is fully open source. The first public version was published in 1995. Currently pressing is second generation server with modular structure and good developed possibility for configuration. The servers allows the execution of all kinds of applications including .NET through Common Gateway Interface or through a handler loaded in the server.

VI. TRANSCODING SCHEME

A transcoding scheme is depicted on Fig. 1. On a given desktop computer or server are started in progress web server, transcoder and a given graphical application (for i.e. Windows, Apache, MathLab). Remote web browser executes POST or GET query to the web server using the http protocol sending data from the mouse and the keyboard. The web server receives the query and executes the transcoder passing him the events.

The transcoder through API communicates with the graphical application passing it the events. Next the transcoder generates image which is the current state of the application and returns the result through the web server to the web browser.

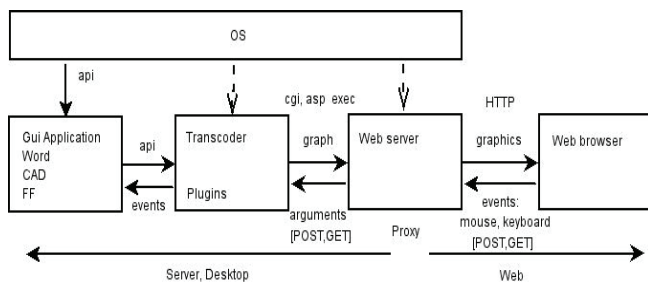


Fig. 1. A transcoding scheme of graphical application from the hosting operating system to web page on the Internet.

On Fig. 2 a modification of the scheme from Fig. 1 is depicted. Here the transcoder and the web server are located on different hosts communicating with each other through

helping server application and web services like SOAP, XML RPC or Windows services.

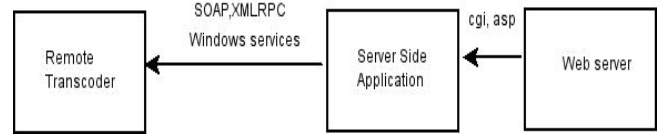


Fig. 2. A modification of the transcoding scheme allowing the execution of graphical applications hosted remotely from the server.

The privilege is that there can be executed applications from many hosts in one local area network only with one web server. This modification is appropriate for the development of administration software.

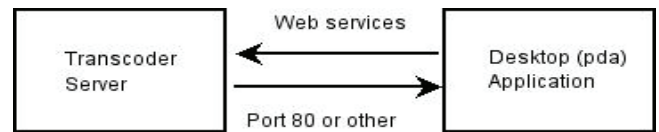


Fig. 3. A modification of the transcoder eliminating the need of web server

On Fig. 3 is depicted a modification of the scheme eliminating the web server while the transcoder is listening directly on port 80 or some other port. In this way remote or desktop PDA applications directly communicate with the graphical applications. This way the transcoding is speeded up and made easier.

VII .NET REALIZATION

On Fig. 4 is depicted a .NET realization. Windows services are used to realize the processes of data exchange.

On Fig. 5 is depicted a realization with included gzip compression.

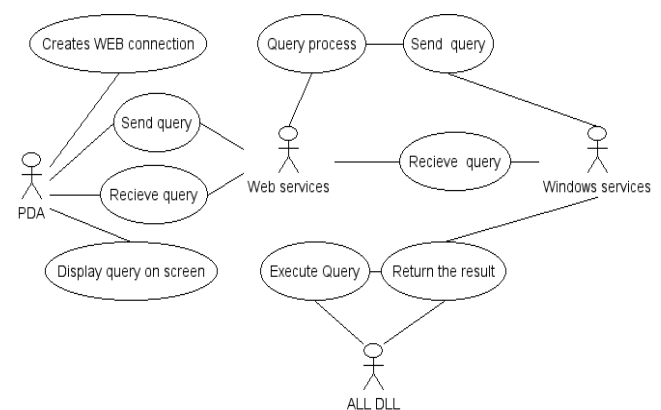


Fig. 4. UML diagram of .NET realization

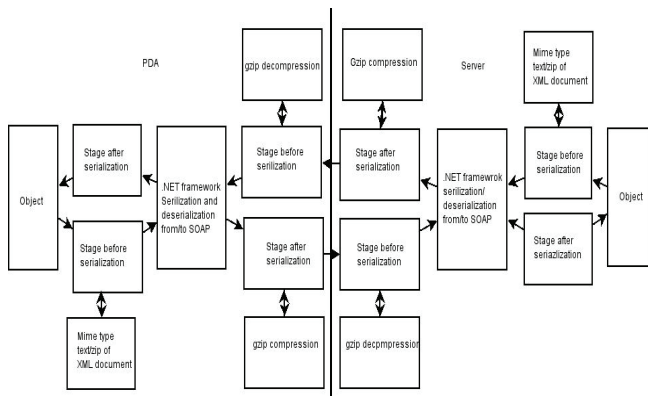


Fig. 5. Scheme with gzip compression

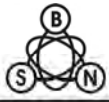
VIII. CONCLUSIONS

The major disadvantages of the current methods for transcoding were shown and a unified and universal method was described. The development can be transformed into middleware for transcoding. In the current realization the graphical interface started on a desktop computer works in background regime and does not interfere with the current

user using the resources. One big area of application of the method is remote and mobile training.

REFERENCES

- [1] T. Filev, Convergence of environments, TU-Sofia, 2006
- [2] <http://en.wikipedia.org/wiki/Transcoding>
- [3] <http://en.wikipedia.org/wiki/VoiceXML>
- [4] A wiki for .NET developers, 2007, <http://pinvoke.net/>
- [5] Nweman M., A controllable Notifying Thread Queue with Generics, 2006, <http://www.codeproject.com/useritems/NotifyingThreadQueue.aspx?df=100&forumid=330069&exp=0&select=1669553>
- [6] Libraries. Pocket PC Developer Network, 2006, <http://www.pocketpcdn.com/libraries/index.html>
- [7] Nikitas, M., Improve XML Web Services' Performance by Compressing SOAP, 2003, <http://www.dotnetjunkies.com/Article/46630AE2-1C79-4D5F-827E-6C2857FF1D23.dcik>
- [8] .NET Zip Library #ziplib (SharpZipLib), 2007, <http://www.icsharpcode.net/OpenSource/SharpZipLib/>



This page intentionally left blank.

Classification of Classifiers

G. Gluhchev¹, M. Savov¹ and O. Boumbarov²

Abstract – In this paper the relationship between three broadly used in practice classifiers – Mahalanobis distance, K nearest neighbors and majority voting, and the optimal classifier in terms of minimum average losses is outlined. Their performance efficiency is experimentally tested on the real problem of signature recognition.

Keywords – Mahalanobis distance, K nearest neighbors, Majority voting.

I. INTRODUCTION

In this paper three of the most popular classifiers are discussed, namely, the Mahalanobis distance based classifier, the K nearest neighbors one and the majority voting. Using the theoretical set-up of the optimal classifier in terms of minimum average losses we make an attempt to show how different classifiers refer to the optimal (Bayesian) one.

The statistical pattern recognition theory assumes that some a priori information is available, including prior probabilities $P(\Omega_1)$ and $P(\Omega_2)$ of the classes, feature density functions $f_1(x)$ and $f_2(x)$, and losses incurred by wrong classification c_{12} and c_{21} respectively. The optimal classifier minimizing the average losses is defined as [1]

$$\begin{aligned} x \in \Omega_1 & \text{ if } P(\Omega_1 | x) \geq P(\Omega_2 | x)c_{12} / c_{21}, \\ x \in \Omega_2 & , \text{ otherwise} \end{aligned} \quad (1)$$

or

$$\begin{aligned} x \in \Omega_1 & \text{ if } f_1(x) \geq f_2(x)P(\Omega_2)c_{12} / P(\Omega_1)c_{21}, \\ x \in \Omega_2 & , \text{ otherwise} \end{aligned} \quad (2)$$

The condition (1) includes a posteriori probabilities of the classes, while the condition two is based on the maximum likelihood ratio. If $P(\Omega_1) = P(\Omega_2)$ and $c_{12} = c_{21}$ the decision is made according to the maximal a posteriori probability or likelihood ratio. Since these are constant we will assume they are equal.

¹Georgi Gluhchev and Mladen Savov are with the Institute of Information Technologies of the Bulgarian Academy of Sciences, 2 Acad. G. Bonchev Str., Sofia 1113, Bulgaria, E-mail: {gluhchev@iinf.bas.bg, ihaiha99@abv.bg}

²Ognyan Boumbarov is with the Technical University in Sofia, 8 Kl. Ohridski Str., Sofia 1000, Bulgaria

II. MAHALANOBIS DISTANCE

In case of normal distributions the inequality (2) will look as follows

$$e^{-[(x-m_1)^t S_1^{-1} (x-m_1) - (x-m_2)^t S_2^{-1} (x-m_2)]} \geq 1 \quad (3)$$

or after taking a logarithm

$$(x-m_1)^t S_1^{-1} (x-m_1) \geq (x-m_2)^t S_2^{-1} (x-m_2) \quad (4)$$

Eq. (4) is actually a comparison of Mahalanobis distance of x to the centers m_1 and m_2 of the classes, and S_1 and S_2 are their covariance matrices.

III. K - NEAREST NEIGHBORS

When no justified assumptions could be made about the priors and class-conditional distributions, non-parametric classifiers are used. One of the most popular among them is the K- nearest neighbor, where a point x is attached to the class Ω_i , provided the ratio κ_i/K of its κ_i representatives among the K nearest neighbors to K is maximal [1]. It is worth to note that without going by the statistical estimations this empirical classifier evaluates the average a posteriori probability $P(\Omega_i | x)$ in a neighborhood of x . Thus, one could conclude that the K – nearest neighbor classifier is an empirical approach to the optimal Bayesian classifier. However, one has to pay attention that this classifier assumes implicitly that the quantity of the training samples corresponds to the prior probabilities of the classes. If this is not the case, the classification error may be too high.

IV. PARZEN WINDOWS

The Parzen window is used for the evaluation of the feature density function in a neighborhood of a point [1]. Therefore, according to inequality (2) the classifier based on Parzen windows could be optimal, as well.

The accuracy of the evaluation depends on the quantity of samples, on the one hand, and on the volume of the neighborhood, on the other hand. This approach resembles to a large extent the K-nearest neighbors one. The difference is that instead of the number K here the volume of the neighborhood is predefined. The advantage consists in its independence from the prior probabilities of the classes, i.e., different size of the training sequences for different classes will not affect the evaluation. Using Parzen windows for the classification actually means that equal prior probabilities are assumed.

V. MAJORITY VOTING

Often in practice a decision is made depending on the number of votes. Such an approach is applicable to the classification problem provided all the features are treated as independent voters of equal importance in the following way.

The interval $[x_{min;ij}, x_{max;ij}]$ is determined for the i^{th} feature and the j^{th} class. All of the feature values of an unknown object x are tested for belonging to the corresponding interval of the classes. If the test result is positive for a particular class, its score is increased by 1. The winner is determined by the maximal score.

This classifier could be treated as a relative to the above mentioned one, provided a Parzen window of size equal to the interval of the corresponding feature is determined for each class. A maximal number of votes could be assigned to more than one class when this approach is used. For some specific problems like signature verification additional samples from the same class may solve the problem.

VI. EXPERIMENTAL COMPARISON

To test how the above reasoning is supported by the practice, the classifiers have been applied to the real problem of signature authentication. For this signings of 14 volunteers has been captured by a TV camera. Every volunteer submitted 10 signatures that have been used for training. The following 8 features have been measured from each signing: 1) d – signing length as a number of frames, 2) α – hand orientation, 3) β – pen azimuth, 4) γ – pen tilt, 5) $\delta = \alpha - \beta$, 6) r_1 / r_2 - ratio of the distances between the pen center and hand contour, 7) P – perimeter of the polygon defined by the characteristic points of the upper hand contour, 8) A – area of the polygon [3].

The classifiers authentication performance has been evaluated in terms of mean, minimal and maximal error. To do this, 1000 signatures of every volunteer have been simulated using the Matlab's random number generator and the assumption of statistically independent features [2]. The classification results are shown in Table 1.

For the Mahalanobis distance an average classification error of 0,2% was obtained (Table 1, line 2, column 2). An absolute result of 0% errors was obtained for 6 volunteers, while the maximal error of 1% was obtained by one of them.

For the K-nearest neighbors classifier an average error of about 1.02% was obtained when one neighbor was used. For three or five neighbors the average error was slightly higher (Table 1, lines 3 и 4).

For the majority vote about 6% of wrong classifications and a maximal error of 19.6% have been observed (Table 1, line 5).

Table 1. Results from the experimental comparison of the classifiers

Classifier	Average error %	Minimal error %	Maximal error %
Mahalanobis	0.2	0	1
1 neighbor	1.02	0	6.2
3 neighbors	1.05	0	5.7
Majority vote	6.01	0.1	19.6

A separate investigation with Parzen windows has not been carried out due to the small number of the training data.

VII. CONCLUSION

In this paper three of the most popular classifiers have been analyzed and compared. The relationship between them was outlined, stemming from the assumptions about the available a priori information. It was shown that the Mahalanobis based classifier was quasi optimal in the sense of minimal losses and normal distribution of features. Empirical estimations of the a posteriori probabilities of the classes are obtained when K-nearest neighbor classifier is applied, provided the volume of the training sequences is proportional to the prior probabilities. Similar behavior could be expected if the class density functions are evaluated using Parzen windows.

The majority vote could be thought as a degenerated variance of the above classifiers. The experimental comparison carried out with real data has confirmed the theoretical analysis.

These results could be taken into account when practical classification problems have to be solved.

ACKNOWLEDGEMENTS

This investigation was supported partly by the Ministry of Education and Sciences in Bulgaria, Contract No BY – TH-202/2006 and BioSecure Network of Excellence, Contract No 507634/2004.

REFERENCES

- [1] R. O. Duda, P. E. Hart, "Pattern Classification and Scene Analysis", Jon Wiley & Sons, N. Y., London, Sydney Toronto, 1999
- [2] M. Savov, G. Gluhchev, O. Bumbarov, "Experiments on Signature Identification with "Hand-pen" System Features", Proc. of the Int. Conference "Automatics and Informatics", Sofia, 2006, pp. 139-141
- [3] M. Savov, G. Gluhchev. "Signature verification via Hand-Pen motion investigation", Proc. Int. Conf. "Recent Advances in Soft Computing", Canterbury, 2006, pp. 490-495

Methods of Graphic Representation of Curves in CAD systems in Knitting Industry

Elena Iv. Zaharieva-Stoyanova¹

Abstract – This paper treats the problems related to curve generation and its application in knitting industry CAD/CAM systems. The methods can be applied for a curve generation in knitting object pattern design. Most commonly used methods are reviewed and some functions for curve generation created. They can be used as programming modules in a CAD system for knitting pattern design.

Keywords – Computer graphics, CAD/CAM systems, parametric cubic curves, Bezier curves, B-splines, FF knitting method.

I. INTRODUCTION

The development of CAD/CAM systems needs a solution of some problems related to graphics representation of designed objects in digital format. Generally, application of computer graphics in knitting industry CAD/CAM systems has two aspects:

- knitting structures design;
- design of knitting pattern shapes.

The second one is related to knitting machine's capacity to make products by fully-fashion (FF) method. It means that the machine knits the cuts of products, or the whole products. This method allows to avoid cutting the materials, reduces the number of the operations and it leads to reducing the waste products to a minimum.

Usually, as designed objects the patterns of knitting products are represented with straight-line polygons. [1],[2] This manner of pattern representation is used because of the following reasons: it is possible for the knitting products size to have a little tolerance within of ± 1 cm; it is easier to process straight-lines than curves; knitting machines are not so precise in material production. This precision depends on a knitting machine performance called fine or gauche. The performance is related to the number of needles per inch or cm. It determines a loop size and a thread thickness, too. All these features distinguish a knitting patterns' presentation from cloths patterns' one.

Because of these reasons the patterns of knitting products are described as straight-lines polygons without curves. If there is a curved section, the workers form it additionally by cutting material.

This paper treats the problems related to curve representation as object in computer graphics. These methods can be applied for a curve's generation in knitting object pattern design. The most commonly used methods are reviewed. Similarly, the methods of curve generation used in cloths patterns representation are given in [3] but as was already mentioned knitting patterns shapes are more flexible. What is aimed here is to apply more methods in the design of knitting pattern objects. Functions drawing curves are created by these methods. Said functions will be used for graphic representation of knitting products' patterns. Their development is strongly related to the requirement of knitting product realization i.e. to obtain a form of knitting pattern which will match the design one. However, it is the main problem of FF knitting method, hence our effort to show some possibilities of usage in CAD/CAM systems in knitting industry automation.

II. CUBIC CURVES REPRESENTATION

Cubic curves are commonly used in computer graphics because they are quite flexible and not so complex as well [4],[5],[6]. These features determined the way the paper reviews the application of said curves.

A. Parametric Cubic Curves

The parametric form of curve representation is more usable:

$$\begin{aligned} x(t) &= a_3 t^3 + a_2 t^2 + a_1 t + a_0 \\ y(t) &= b_3 t^3 + b_2 t^2 + b_1 t + b_0 \end{aligned} \quad (1)$$

Using a vector form, the first equation can be represented as followed:

$$x(t) = [t^3 \quad t^2 \quad t \quad 1] \begin{bmatrix} a_3 \\ a_2 \\ a_1 \\ a_0 \end{bmatrix} \quad (2)$$

Using a vector form equation (1) is transformed into:

$$\begin{aligned} x(t) &= T \cdot A \\ y(t) &= T \cdot B \end{aligned} \quad (3)$$

Where T, A, and B are vectors.

¹Elena Ivanova Zaharieva-Stoyanova is with the Technical University of Gabrovo, 4 H. Dimitar str, 5300 Gabrovo, Bulgaria, E-mail: zaharieva@tugab.bg

The derivatives of the curve with respect to t can be expressed as follows:

$$\begin{aligned} x'(t) &= [3t^2 + 2t + 1 + 0]A \\ y'(t) &= [3t^2 + 2t + 1 + 0]B \end{aligned} \quad (4)$$

Cubic curve definition needs 3 point – two endpoints and one middle point, as well as the tangent vector at the middle point. Let the points P0, P2 fix the endpoints; P1 – the midpoint; and T1 – the tangent at the P1.

The parametric curve can be determined as followed formula:

$$\begin{aligned} x(t) &= T.M.X \\ y(t) &= T.M.Y \end{aligned} \quad (5)$$

Using the first equation, the full formula is obtained as:

$$x(t) = [t^3 \quad t^2 \quad t \quad 1] \begin{bmatrix} -4 & 0 & 4 & 4 \\ 8 & -4 & 6 & -4 \\ -5 & 4 & -2 & 1 \\ 1 & 0 & 0 & 0 \end{bmatrix} \begin{bmatrix} x_2 \\ x_1 \\ x_1 \\ x_0 \end{bmatrix} \quad (6)$$

The product of multiplying T by M is so called basis (or blending) functions:

$$\begin{aligned} f_1(t) &= -4t^3 + 8t^2 - 5t + 1 \\ f_2(t) &= -4t^2 + 4t \\ f_3(t) &= -4t^3 + 6t^2 - 2t \\ f_4(t) &= 4t^3 + 4t^2 - 1 \end{aligned} \quad (7)$$

The basis functions are so called “weighting” function for the points P0, P1, P2, and tangent T1 because they determine how these points exert influence on the curve. The curve will be represented as follows:

$$\begin{aligned} x(t) &= f_1(t)x_0 + f_2(t)x_1 + f_3(t)x_1 + f_4(t)x_2 \\ y(t) &= f_1(t)y_0 + f_2(t)y_1 + f_3(t)y_1 + f_4(t)y_2 \end{aligned} \quad (8)$$

B. Bezier Curves

A Bezier curve in its most common form is a simple cubic equation that can be used in any number of useful ways. Originally, it was developed by Pierre Bezier for CAD/CAM operations.

Bezier curves are also a variation of the parametric cubic curves specified by four control points P0, P1, P2, P3. The expression for the matrix corresponding to formula (6) is:

$$Mb = \begin{bmatrix} -1 & 3 & -3 & 1 \\ 3 & -6 & 3 & 0 \\ -3 & 3 & 0 & 0 \\ 1 & 0 & 0 & 0 \end{bmatrix} \quad (9)$$

The Bezier basis functions are as follows:

$$\begin{aligned} f_1(t) &= -t^3 - 3t^2 - 3t + 1 \\ f_2(t) &= 3t^3 - 6t^2 + 3t \\ f_3(t) &= -3t^3 + 3t^2 \\ f_4(t) &= t^3 \end{aligned} \quad (10)$$

Alternatively, the basis functions are:

$$\begin{aligned} f_1(t) &= (1-t)^3 \\ f_2(t) &= 3t(1-t)^2 \\ f_3(t) &= 3t^2(1-t) \\ f_4(t) &= t^3 \end{aligned} \quad (11)$$

Bezier curve given in parametric format:

$$P(t) = \sum_{i=0}^m C_m^i t^i (1-t)^{m-i} P_i \quad (12)$$

For better graphics interpretation let us transform this formula as:

$$P(t) = (1-t)^m P_0 + \sum_{i=1}^{m-1} C_m^i t^i (1-t)^{m-i} P_i + t^m P_m \quad (13)$$

C. B-splines

A B-spline is a spline-function (part-polynomial function) which equals zero in all sub-segments except in the interval [m, m+1] ([5],[6]).

To represent a B-spline in sub-segment i, the following formula is used:

$$N_{i,0}(x) = \begin{cases} 1, & x_i \leq x \leq x_{i+1} \\ 0, & x \notin (x_i, x_{i+1}) \end{cases} \quad (14)$$

An m-degree B-spline in [x_i, x_{i+m+1}] can be represented as:

$$N_{i,m}(x) = \frac{x - x_i}{x_{i+m} - x_i} N_{i,m-1}(x) + \frac{x_{i+m+1} - x}{x_{i+m+1} - x_{i+1}} N_{i+1,m-1}(x) \quad (15)$$

Normally, square and cubic B-splines are used. Should B-spline can be of higher order, almost cubic B-splines are applied. The cubic B-spline basis functions work over four control points. The basis functions appears below (equation 19, 20). Note that special basis function are needed for the first and last two sections of the B-spline so that it passes through the first and last points.

The basis functions for first section are:

$$\begin{aligned}
 B_1(t) &= (1-t)^3 \\
 B_2(t) &= \frac{21}{12}t^3 - \frac{9}{2}t^2 + 3t \\
 B_3(t) &= -\frac{11}{12}t^3 + \frac{3}{2}t^2 \\
 B_4(t) &= \frac{t^3}{6}
 \end{aligned}
 \tag{16}$$

The basis functions for the second section are:

$$\begin{aligned}
 B_1(t) &= \frac{(1-t)^3}{4} \\
 B_2(t) &= \frac{7}{12}t^3 - \frac{5}{4}t^2 + \frac{t}{4} + \frac{7}{12} \\
 B_3(t) &= -\frac{1}{2}t^3 + \frac{1}{2}t^2 + \frac{1}{2}t + \frac{1}{6} \\
 B_4(t) &= \frac{t^3}{6}
 \end{aligned}
 \tag{17}$$

The basis functions for the middle sections are:

$$\begin{aligned}
 B_1(t) &= \frac{(1-t)^3}{4} \\
 B_2(t) &= \frac{1}{2}t^3 - t^2 + \frac{2}{3} \\
 B_3(t) &= -\frac{1}{2}t^3 + \frac{1}{2}t^2 + \frac{1}{2}t + \frac{1}{6} \\
 B_4(t) &= \frac{t^3}{6}
 \end{aligned}
 \tag{18}$$

III. FUNCTION FOR CURVE GENERATION

Using the formule given in previous section some functions for curve generation are created. Some of them have already been presented in [7], [8]. This paper gives their development and a creation of some new functions.

The following function creates a Bezier curve by using of 3 control points:

```

void CBezierCurvesView::BezierCurves3(CDC *pDC, CPoint *P)
{
    double t, dt, x, y;
    double dx=0, dy=0;
    pDC->MoveTo(P[0]);
    dt=0.01;
    t=0;
    int i = 0;
    while (t<=1)
    {
        x=pow((1-t),3)*P[0].x+3*pow((1-t),2)*t*P[1].x+3*t*t*(1-t)*P[2].x+t*t*t*P[3].x;
        y=pow((1-t),3)*P[0].y+3*pow((1-t),2)*t*P[1].y+3*t*t*(1-t)*P[2].y+t*t*t*P[3].y;
        pDC->LineTo(CPoint((long)x,(long)y));
        t+=dt;
    }
}
    
```

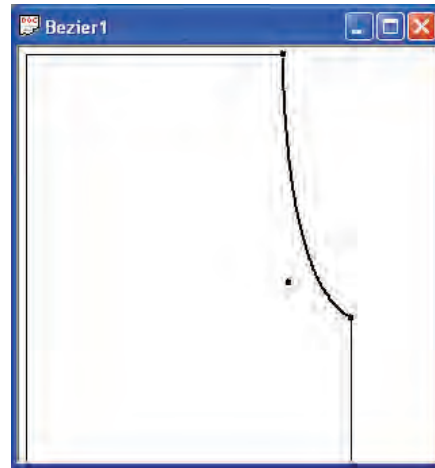


Fig. 1. Curve generation to form sleeve in knitting pattern using 2 control points

A function generating a Bezier curve by using of 2 control points is created, too. These functions are applied in knitting pattern design. Fig. 1 and 2 are examples of their application.

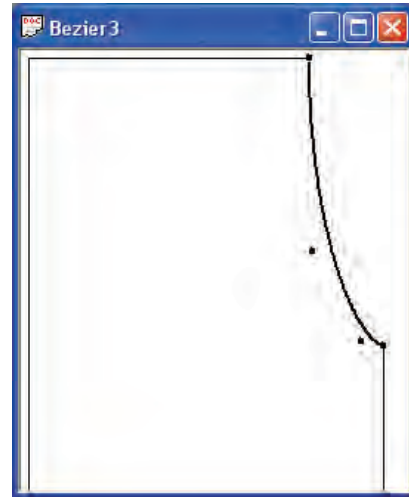


Fig. 2. Curve generation to form sleeve in knitting pattern using 3 control points

To generate a Bezier curve by n control points the following function is created:

```

void CBezierCurvesView::BezierCurvesDraw(CDC *pDC)
{
    double t, dt, x, y;
    double C, xk, yk;
    int i;
    pDC->MoveTo(P[0]);
    dt=0.01;
    t=0;
    while (t<=1)
    {
        xk=0;
        yk=0;
        for (int i=1; i<n-1;i++)
        {
            C = (double)facturiel(n)/(facturiel(i)*facturiel(n-i));
            xk += C*pow(t,i)*pow(1-t,n-i)*P[i].x;
            yk += C*pow(t,i)*pow(1-t,n-i)*P[i].y;
        }
    }
}
    
```

```

x=pow((1-t),n)*P[0].x + xk + pow(t,n)*P[n].x;
y=pow((1-t),n)*P[0].y + yk + pow(t,n)*P[n].y;
pDC->LineTo(CPoint((long)x,(long)y));
t+=dt;
}
}

```

This function can be applied for curve generation of knitting pattern but it has a disadvantage – the curve doesn't go through the control points. To avoid it the function of curve generation splits the control points into some groups and applies the previous function simultaneously. The result is given on fig. 3.

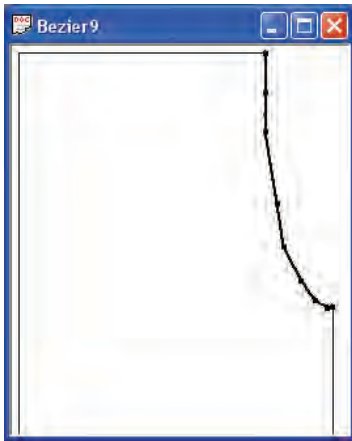


Fig. 3. Curve generation to form sleeve in knitting pattern using Bezier method

The function for curve generation using B-spline method is created, too. It uses the equation 15, 16, 17. The result of its application is represented in fig. 4.

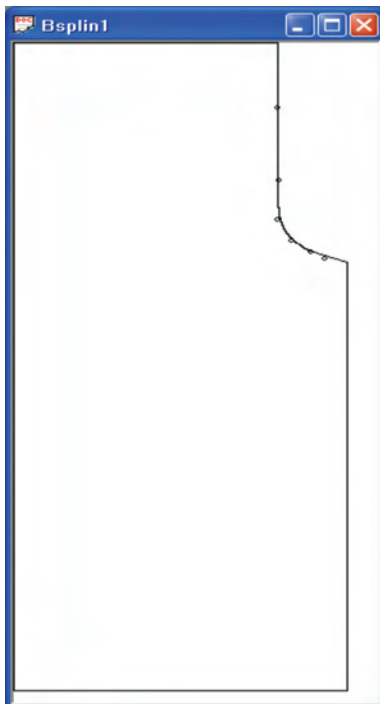


Fig. 4. Knitted pattern generated by using a cube B-spline curve

IV. CONCLUSION

This paper treats the problems related to curve generation and its application in knitting industry CAD/CAM systems. The methods can be applied for a curve's generation in knitting object pattern design. The most commonly used methods are reviewed, especially parametric cubic curve generation, generation of Bezier curves and B-spline method. The paper traces out some methods for curve generation. Some functions for curve generation are created. Their application is as a part of CAD system for knitting pattern design. The development of curve generation functions are strongly related to the algorithm for an accuracy of knitting pattern shape form suggested in [1]. The project is realized as an application in MS Visual C++ 6.00 using MFC.

REFERENCES

- [1] Zaharieva E., J. Angelova, Methodics of Fully Fashioned Knitting on Cotton, *Textil & Obleklo*, 5/1998, pp. 15-17.
- [2] Angelova, J., E. Zaharieva-Stoyanova, Shape Precision at Set Outline Knitting, *Scientific conference EMF'2005*, 22-24. September 2005, Varna, pp. 143-148.
- [3] Rakova R., Hr. Petrov, Methods for Curve Generation of Cloths Patterns by Polynomial Interpolation, *Textil & Obleklo*, 11-12/2000.
- [4] Broucke P., Bézier curves, December 1996.
- [5] Lukipudis E., *Computer Graphics and Geometric Modeling*, Sofia, Tehnika, 1996.
- [6] Pavlidis T., *Algorithms for Graphics and Image Processing*, Bell laboratories, Computer Science Press, 1982.
- [7] Zaharieva-Stoyanova E., Application of Bezier Curves in Knitting Industry CAD/CAM Systems, *International conference ICEST'2005*, 29.06-1.07.2005, Nish, Serbia and Montenegro, pp.687-690.
- [8] Zaharieva-Stoyanova E., Application of Spline Functions in Knitting Products Graphic Design, *International scientific conference UNITECH'05*, 24-25 November 2005, Gabrovo, pp. I-273 – I-276.
- [9] Zaharieva-Stoyanova E., Algorithm for Computer Aided Design Curve Shape Form Generation of Knitting Patterns, *International scientific conference on Automation, Quality and Testing, Robots, AQTR 2006 (THETA15)*, May 25-28 2006, Cluj-Napoka, Romania, pp TI-327-331.

Cognitive Model Extension for HCI

Nebojša D. Đorđević¹ and Dejan D. Rančić²

Abstract – This paper presents research results on Human Computer Interaction (HCI) methodologies. We present an extension of cognitive model for HCI - (XUAN/t), based on decomposition of user dialogue into elementary actions (GOMS). Using this model, descriptions of elementary actions performed by user and system are introduced sequentially, as they will happen. Based on the described model and psychometric concepts, we developed software tool for testing sensorimotor abilities of a user in HCI. Software tool arranges tests into test groups for psychosensorimotor and memory capabilities. User test results are persistently stored in a database and available for further statistical analysis.

Keywords – HCI, User interface.

I. INTRODUCTION

Research results from the past several years indicate significant influence of human-computer interaction (HCI) on computer system development, which, combined with technological development, enabled their application in almost every branch of human activity. HCI can be defined as “a filed of study related to design, evaluation and implementation of interactive computer systems used by humans, which also includes research of the main phenomena that surround it” [1].

Multidisciplinary nature of human-computer interaction requires contribution from different science disciplines; especially from computer science, cognitive psychology, social and organizational psychology, ergonomics and human factors, computer-aided design and engineering, artificial intelligence, linguistics, philosophy, sociology and anthropology.

Main goal of HCI is to improve interaction between the user and the computer in order to make computers more user friendly and designed systems more usable.

Determining the degree of usability is a process in which systems are evaluated in order to determine product-success using methods available to the evaluator.

II. USER INTERFACE

The most important element in HCI is user interface. User articulates his requests to the system via dialogue with the

interface. Interface is the point at which human-computer interaction occurs. Physical interaction with end user is provided using hardware (input and output devices) and software interaction interface elements.

User interface (UI), as an interaction medium of the system, represents “software component of the application which transforms user actions into one or more requests to the functional application component, and which provides the user with feedback about the results of its actions [2].

Key concepts of graphic interfaces were established in the early 70ties. They were based on the WIMP metaphor, which includes key elements of the interface: Window, Icon, Menu and Pointer. Direct manipulation of graphic objects provides object manipulation on the computer screen via pointing devices as standard input devices of modern computer systems.

III. HCI METHODOLOGIES

The importance of human-computer interactions was noticed in the late 70ties. In 1982 this caused a development of an independent research group, which had, in 1992, formed HCI as a special discipline.

The subject of HCI research is human being and everything related to a human being: work, environment and technology. Classification of HCI methodologies was made based on the method by which end user is incorporated into system development [3]:

- *User centered development* - provides system development FOR the user based on feedback information from the user during the entire process of system development.
- *System development WITH users* – development of user participation which promotes system development in user environment (manufacturing facilities, offices, etc.) rather than within software companies.
- *System development based on taking into account the user* - this approach uses cognitive modeling of end users in order to understand user behavior in a certain situation and why one system is better than the other.

IV. COGNITIVE MODEL OF HCI

Cognitive modeling provides a description of user in interaction with the computer system; it provides a model of user’s knowledge, understanding, intentions and mental processing. Description level differs from technique to

¹Mr Nebojša D. Đorđević is with the Faculty of Electronic Engineering, Aleksandra Medvedeva 14, 18000 Nis, Serbia, E-mail: djnebojsa@bankerinter.net

²Dr Dejan D. Rančić is with the Faculty of Electronic Engineering, Aleksandra Medvedeva 14, 18000 Nis, Serbia, E-mail: ranca@elfak.ni.ac.yu

technique and ranges from high-level goals and results regarding thinking about a problem all the way to the level of motor activities of the user such as pressing a key on a keyboard or a mouse click. Research of these techniques is done by psychologists, as well as computer science specialists.

Classification of cognitive models is based on whether the focus is on the user and its task, or on transformation of the task into interaction language [1]:

- Hierarchical presentation of user's tasks and goals (GOMS).
- Linguistic and grammar levels.
- Models of physical level.

GOMS (*Goals, Operators, Methods and Selection*) [4] model consists of the following elements:

Goals – are results of user's task and they describe what the user is trying to accomplish.

Operators – are basic actions which the user must make while working with a computer system. Operators can act on a system (pressing a key) or on the mental state of the user (reading a message). Detail level of the operators is flexible and it varies based on the task, on the user and on the designer.

Methods – are step sequences which need to be performed in order to reach a given goal. A step in the method consists of operators.

Selection rules – provide prediction on which method will be used in reaching a given goal in case there are different possible methods to reach the goal.

Models of the physical level relate to human motor skills and describe user's goals which are realizable in a short time period. An example is KLM model (*Keystroke-Level Model*) [5] used for determining user's performance with a given interface. In this mode, the task of accomplishing a goal is given in two stages:

- *Task acquisition*, during which user makes a mental picture of how to reach a given goal, and
- *Task performance* using the system.

Task acquisition closely connects KLM with GOMS level which gives an overview of the tasks for a given goal. KLM decomposes the phase of task performance into five different physical operators (pressing a key on a keyboard, pressing a mouse button, moving a cursor to a desired position, moving a hand from keyboard to mouse and reverse, and drawing lines using a mouse), one mental operator (mental preparation of user for physical action) and one system response operator (user can ignore this operator unless he is required to wait for system response). Each operator is given a time period for its action. By summing these time periods we get estimated time for completion of those tasks for a given goal. Precision of the KLM model depends on the experience of the designer, because he is required to make a realistic decision about the abilities of end user. Obviously, the development of high quality user interface is impossible without cognitive modeling and techniques. In HCI practice there is no separate cognitive methodology; rather, some cognitive models and techniques are used within other methodologies, usually during evaluation. Cognitive models and techniques

significantly contribute in determining (rationalizing) how acceptable is the designed solution.

V. INTERACTION MODEL

Interaction models are descriptions of user inputs, application actions and result displays. Interaction models are based on formalisms which ensure their implementation within interface development tools.

One of the oldest and most general interaction models is PIE model [1] which describes user inputs (from keyboard or mouse) and output to user (on a screen or a printer).

UAN (*User Action Model*) model [6] was developed by system designers in order to understand the complexity of interactions with regard to the system, rather than the user. UAN model efficiently describes (and identifies) four elements of interaction in a way understandable to all participants in software development. Also, it does not differentiate between text and graphic interfaces, thus supporting every interaction technique. A drawback of this model is its approach to interactions by regarding the system only, without taking into account the other participant, the human being.

This problem was overcome in the XUAN (*Extended User Action Notation*) model, which equally treats both the system and the user. XUAN model treats the user and the system in terms of their visible, in case of the user articulated, internal actions.

XUAN model's advantage is that it includes human mental action. Its drawback is excluding the state of the interface, which can lead to its inconsistency.

VI. EXTENDING XUAN INTERACTION MODEL

In order to evaluate user performance as realistically as possible, we extend the mentioned interaction models (UAN, XUAN). Extended model (XUAN/t – *extended user action notification per time*) treats equally the complexity of interactions, both from the system and from the user. This model is given in table form (Fig. 1) which is divided into two parts.

First part contains two rows in which descriptions of mental or sensory and articulated or motor activities of the user are given. Second part contains three rows in which interface descriptions (visible actions and interface conditions) and internal system actions (core) are given. Separation line dividing these two parts is highlighted in red because it represents a point at which human-computer interaction occurs, and it also represents a time scale. In addition to giving descriptions, activities are presented graphically on the time scale in proportion to time duration. Graphic presentation also provides visual interpretation of position, order and duration of activities.

In order to efficiently estimate the number of actions and time duration of the entire task, a complex dialogue is decomposed into elementary actions using GOMS model. Descriptions of elementary actions by the user and by the

system are entered sequentially in order of occurrence. Each activity is given the time needed for its completion.

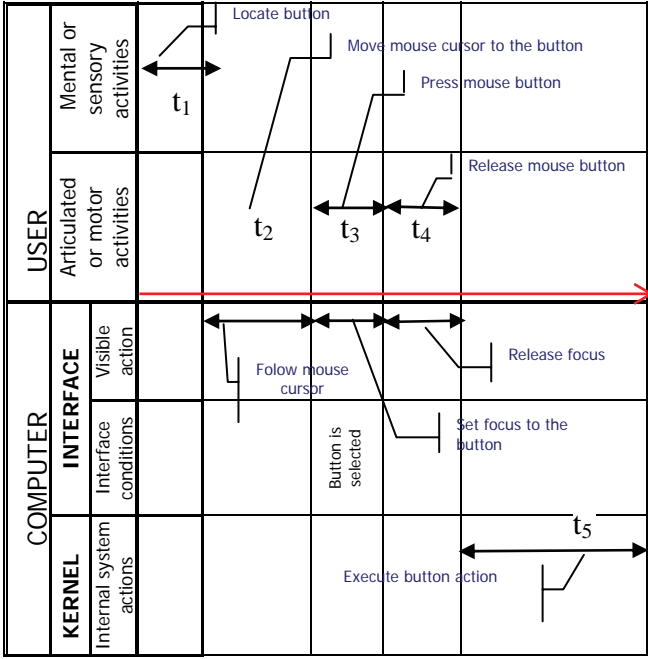


Fig. 1. XUAN/t model of a click-on-a-program-field of the interface

Estimated time is determined by summing the times required for individual activities (see Eq. 1). This way, proposed model provides interpretation of action descriptions with empirical variables which can be evaluated.

$$T = \sum_{k=0}^n t_k \quad (1)$$

In this model time component is based on the duration of individual elementary actions; it is limited by given events as reference points. These events are initiated by the user, but they occur in the system. The system can register them precisely in order to determine the beginning and the end of activity. This model is intuitive and it can be easily supported with available software tools.

VII. TESTING COGNITIVE CHARACTERISTICS

Evaluation of user's cognitive characteristics is done by tests designed for evaluation of certain characteristics and obtaining the user profile. Test construction is based on recognition of activities in user-computer interaction, prominent user characteristics and the method of measurement of individual production results.

There are several steps during user-computer dialogue which we grouped into sensory, intellectual and articulatory activities.

Within sensory activities, we isolated the processes in which human being is gaining knowledge about phenomena and events around him such as:

- Impact of physical and chemical processes from the environment on human senses,

- Initiation of certain physiological processes in nerve cells of the sensory organs,
- Transmission of nerve excitation by neurons to the primary sensor zone in cortex,
- Initiation of a psychological response which enables the human to become aware of the stimuli which acted on the sensory organ.

In order to articulate his demands, user utilizes certain interaction elements of user interface (hardware and software) which enable his physical interaction with the computer. In physical interaction with hardware device, user makes a voluntary activity which is coordinated with visual senses (from the primary sensory zone) and kinesthetic senses (from the motor cortex). Kinesthetic senses provide muscle coordination and development of skills for performing different complex movements while working.

Classification into sensory, intellectual and motor activities is provisional, because they intermix during task performance. In order to investigate senso-motor abilities, based on the described model and psychometric concepts, we developed software CASE tool for evaluation of human cognitive characteristics in interaction with the computer.

Fig. 2. User description input form

Fig. 3. Form for determining the list of tests and defining general and particular test conditions

Software tool provides user identification data input and user characteristics (Fig. 2), determining a test list, and defining general and particular test conditions (Fig. 3).

In order to test all subjects under the same conditions it is necessary to define general conditions (screen resolution, mouse speed, etc.) and determine particular conditions of the micro surrounding (noise, light, temperature, etc.). At the beginning of each test subject is given a test task. During

testing, tests are given in predetermined order and in designed time limits. Testing depends on the choice of tests given on the list.

Test groups related to receiving, information processing and motor activities include tests of memory, sensory and psychomotor abilities.

The goal of *sensory ability tests* (perception) is to determine reaction times of subjects to auditory and visual stimuli. Subject's abilities in domains of seeing, hearing and kinesthetic senses are tested. Test lasts 20 seconds, during which time subject is presented with series of stochastic visual and auditory stimuli. Subject's task is to react as quickly as possible by pressing a certain key (LIGHT-OFF, RINGER-OFF), with which he confirms registration of the tested stimulus. System registers time lapse between giving the stimulus and subject's response, as an evaluation parameter.

The goal of *psychomotor tests* is to determine the precision in object manipulation, psychomotor orientation, reaction time, manipulation aptness and the ability of making visual-motor guesses.

First group of tests, so called "CLICK-A-FIELD", is aimed at probing psychomotor orientation, visual-motor guessing ability and coordinated manipulation of user-computer interaction tools, coordination of individual senses and body parts. Tests last 20 seconds, and subject's task is to click a field (1×1 cm) which cyclically, using random coordinate generator, appears on the screen. During the test, the system *on-line* continually registers times related to certain events (PRESS-MOUSE-BUTTON, RELEASE-MOUSE-BUTTON) and connects them in database with the user and the test. After the event, RELEASE-MOUSE-BUTTON field is erased from the screen and it appears at a new randomly generated coordinates.

In order to determine the influence of different factors on user's psychomotor characteristics we developed four different tests. The goals of these tests are the same, however:

- PM 1 field on the interface is darker shade of gray than the background,
- PM 2 field is highlighted red on the interface,
- in PM 3 test the field is 1×3 cm on the interface,
- in PM 4 test after RELEASE-MOUSE-BUTTON event a beep sound is given in order to provide auditory stimulus.

For determining precision and ability of fast, easy, correct and coordinated manipulation of visual objects with interaction technique of dragging objects on the screen, we developed PM 5 test (so called "DRAG-ME"). Test lasts 20 seconds, and subject's task is to click on a red rectangular object on the screen and drag it into a rectangular window with blue borders. After each attempt the object on the screen appears at a different randomly generated coordinate. System *on-line* registers successful attempts.

The main goal of *memory tests* (TM 1) is to investigate memory span through the ability of immediate reproduction of a series of elements after only one viewing of the series. This test is not time limited; it lasts until the first unsuccessful reproduction is made. Subject is presented, in a certain time interval, with a series of randomly generated numerical signs

of given length. Presentation time of the series is inversely proportional to the length of series. Subject's task is to reproduce the entire series successfully. This step is repeated with each series one sign longer.

We also developed two more tests with the same scenario as TM 1, with a difference:

- TM 2 generated series are made of letter signs, and
- in TM 3 the series are made with alphanumeric signs.

System registers the longest length of successfully reproduced series as a memory span parameter.

VIII. CONCLUSION

In order to evaluate user performance in interaction with interface, we extend the concepts of existing interaction models. Based on the described model and psychometric concepts we developed software tool for testing sensomotor abilities of user in human-computer interaction. Test concept allows program-led testing of the intent-group and precisely quantifies user performance.

In this study we obtained an efficient tool for making user profiles. Differentiation of test users is utilized to determine compatibility of individual interaction models with given intent-groups. Qualitative result analysis provides recommendations for design of individual interface parts which are useful for the intent-group for which it is designed.

REFERENCES

- [1] A. Dix, J. Finlay, G. Abowd and R. Beale, *Human-Computer Interaction*, 2nd ed. Prentice Hall Europe, 1998.
- [2] B. A. Myers, and M. B. Rosson, Survey on user interface programming, In P. Bauersfeld, J. Bennett and G. Lynch, editors, CHI'92 Conference Proceedings on Human Factors in Computing Systems, pp. 195-202, ACM Press, New York, 1992.
- [3] J. Brown, "HCI and Requirements Engineering - Exploring Human-Computer Interaction and Software Engineering Methodologies for the Creation of Interactive Software", SIGCHI Bulletin, vol. 29(1), 1997.
- [4] D. E. Kieras, and A. Arbor, Towards a Practical GOMS Model Methodology for User Interface Design, In M. Helander "Handbook of Human-Computer Interaction", Elsevier Science Publishers B. V. (North Holland), pp. 135-202, 1988.
- [5] S. K. Card, T. P. Moran and A. Newell, "The Keystroke-Level Model for user performance with interactive systems", Communications of the ACM, vol. 23, pp. 396-410, 1980.
- [6] M. D. Harrison and D. J. Duke, "A review of formalisms for describing interactive behaviour, In the Software Engineering and Human-Computer Interaction - Notes in Computer Science, vol. (896), Springer-Verlag, pp. 49-75, 1995.

Performance Analysis of a Suboptimal Multiuser Detection Algorithm

Ilija Georgiev Iliev¹ and Marin Nedelchev²

Abstract – The paper presents a research of the possibilities of an algorithm for MUD, which uses a discrete successive search. The suboptimal methods for MUD in synchronous CDMA systems are prospective class in comparison to the optimal methods, because of the reduced number of calculations and computational complexity. A closed form formula is derived for the number of iteration of the algorithm for obtaining constant error probability. This allows rational use of the computation power of the machine and reduction of the number of the computations in MUD with successive search algorithm.

Keywords – Synchronous CDMA, Multi User Detection, Suboptimal algorithm.

I. INTRODUCTION

CDMA is an effective method for multiple access used in the mobile communications. In CDMA systems multiple users transmit signals in one and the same bandwidth simultaneously. To separate the received signal from a given user, it is required to observe some conditions. In the practice they are not fulfilled. Consequently, the signals from other users become interference – MUI (multi user interference).

As it is well known according to the information theory, the correlation receiver is optimal, when MUI is missing. If MUI exists, it may be considered as a noise with own probability and energy characteristics. Consequently the MUI existence will decrease the noise performance when using a common correlation receiver. For minimizing this drawback, Multi User Detection (MUD) is used. [1]. MUI carries useful information from the other users, that can be processed in a proper way to better the quality of the communication systems.

The optimal receiver for MUD is based on the Maximum Likelihood (ML) criterion [1]. The estimation of optimal decision is connected with verifying of all possible transmitted symbols' combinations. Therefore the great number of computations is the main drawback of ML MUD. The computations increase exponentially with the active users. This seriously complicates its application in the conventional mobile communication systems, nevertheless the high speed and huge computational power of the modern digital signal processors. There are many propositions of methods and algorithms for suboptimal receiving that decrease the

necessary number of computations for detection. In most cases, they are compromise between the computational complexity and the quality of the receiver [2,3].

There exists MUD with parametric optimization. In this case the Maximum A posteriori Probability (MAP) [1] criterion is used as a objective function for optimization. In the MUD case, the objective function is discrete, discontinuous, non differential, non-unimodal, therefore the most appropriate methods for optimization are the random search method, genetic algorithm, Evolutionary strategy etc. [4,5,6]. Their application in comparison to the optimal receiver with ML for MUD, decreases the computation number [6].

The paper presents a research of the possibilities of an algorithm for MUD, which uses a discrete successive search. The initial start point is derived after correlation single detection. The obtained results show that the increasing the number of the iterations leads reaches the theoretical curve for fully compensation the MUI or single detection. A closed form formula is derived for the number of iteration of the algorithm for obtaining constant error probability. This allows rational use of the computation power of the machine and reduction of the number of the computations in MUD with successive search algorithm.

II. OPTIMAL MUD IN SYNCHRONOUS CDMA SYSTEM

System model is shown on Fig.1. The signal processing is done in baseband.

Let the number of the user is K . They transmit synchronously direct spread spectrum (DSS) 2PSK modulated signals. The signal on the receiver input during bit interval T_b is:

$$r(t) = \sum_{k=1}^K \sqrt{E_k} d_k c_k(t) \alpha_k e^{j\theta_k} + n(t) \quad (1)$$

$r(t)$ is represented in a discrete in time matrix form as:

$$r(t) = \mathbf{cAEd} + n(t) \quad (2)$$

where: $\mathbf{d} = [d_1, d_2, \dots, d_K]^T$ is a vector-column, containing the value of the transmitted symbol with duration T_b from the k -th user. The symbols are bipolar NRZ coded $d_k \in \{-1, +1\}$;

¹Ilija Georgiev Iliev – Assoc. Professor, PhD in Dept. of Radiotechnic in Faculty of Communications and Communication Technologies in TU –Sofia E-mail: igiliev@tu-sofia.bg

² Marin Veselinov Nedelchev -Assistant, PhD in Dept. of Radiotechnic in Faculty of Communications and Communication Technologies in TU –Sofia E-mail mnedelchev@tu-sofia.bg

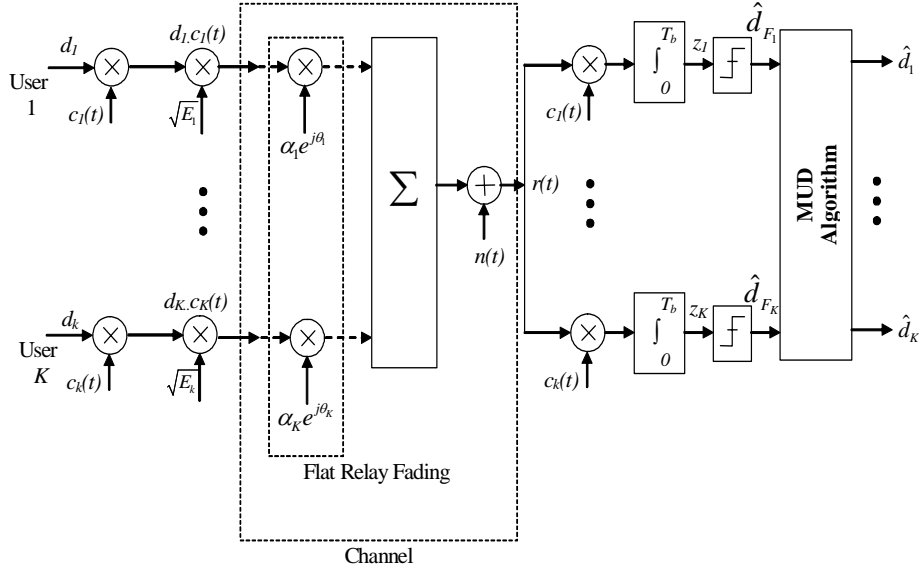


Fig.1 System model of MUD

$\mathbf{A} = \text{diag}[\alpha_1 e^{j\theta_1}, \alpha_2 e^{j\theta_2}, \dots, \alpha_K e^{j\theta_K}]$ is a diagonal matrix and the elements in the main diagonal are the complex channel transmission coefficients of the corresponding user. The amplitudes are Relay distributed and the phases are uniformly distributed in the interval $[0, 2\pi)$. It is assumed that the channels for different users are statistically independent;

$\mathbf{E} = \text{diag}[\sqrt{E_1}, \sqrt{E_2}, \dots, \sqrt{E_K}]$ is a diagonal matrix.

$\sqrt{E_k}$ is the symbol energy of the k-th user;

$\mathbf{c} = [c_1(t), c_2(t), \dots, c_K(t)]$ - is a matrix, each row of it consists of the elements of the spreading sequence for the corresponding use $c_k^{(n)} \in \{-1, +1\}$. The sequences length is N - $N = T_b / T_c$, T_c is the chip duration; $n(t)$ is the realization of complex additive white Gaussian noise (AWGN) with independent real and imaginary components. Each of them has dispersion $\sigma^2 = N_o / 2$ [W/Hz].

MUD is connected with parallel receiving of the symbols from K users. The receiver consists of K single correlation receivers- K receiving channels (Fig.1). Let there exists ideal synchronization and the complex channel transmission coefficients are determined $[\alpha_1 e^{j\theta_1}, \alpha_2 e^{j\theta_2}, \dots, \alpha_K e^{j\theta_K}]$. The vector \mathbf{z} is on the correlator output and it consists of the following elements:

$$\mathbf{z} = [z_1, z_2, \dots, z_K]^T = \mathbf{R}\mathbf{A}\mathbf{E}\mathbf{d} + \mathbf{n} \quad (3).$$

\mathbf{R} is the cross-correlation $K \times K$ matrix, which coefficients are the normalized cross-correlation functions of the spreading sequences:

$$R_{ij} = \frac{1}{N} \int_0^{T_b} c_i(t) c_j(t) dt \quad (4).$$

\mathbf{n} is the AWGN after the correlator, introduced as a vector column $\mathbf{n} = [n_1, n_2, \dots, n_K]^T$ with a covariance matrix equal to: $\mathbf{R}_n = 0.5 N_o \mathbf{R}$. The k-th element is:

$$n_k = \int_0^{T_b} n(t) c_k(t) dt.$$

A. Single detection

In the schematic shown on Fig.1, the decision is made in accordance with the ML criterion separately for each channel - single detection. The received symbols are further used for MUD.

There exists, by definition, a synchronization of the symbol transmitting from multiple active users. Represented in matrix form, the decision device output vector in the single detection case is:

$$\hat{\mathbf{d}}_F = [\hat{d}_{F_1}, \hat{d}_{F_2}, \dots, \hat{d}_{F_K}] = \text{sign} \{ \Re(\mathbf{A}^* \mathbf{z}) \} \quad (5).$$

The variable on the decision device input \mathbf{z} depends on the current transmitted symbol, MUI and the AWGN. This allows determining the noise performance for single detection. For the k-th user and Gaussian approximation of the MUI distribution for flat Relay fading channel, the error probability is:

$$Pe_{k_{MUI}} = 0.5 \left(1 - \sqrt{E_k / \left(N_o + \frac{1}{N} \sum_{i=2}^K E_i + E_k \right)} \right) \quad (6).$$

Eq.6 considers the more difficult case of using of random instead of pseudorandom spreading sequences. The multiplier $1/N$ is connected to the dispersion of the cross-correlation functions of the random sequences.

When the power on the receiver input from all users is equal and using of random sequences, the error probability is:

$$Pe_{k_{MUI}} = 0.5 \left(1 - 1 / \sqrt{N_o + (K-1) / N + 1} \right) \quad (7).$$

If the signal-to-noise ratio (SNR) is much bigger than the signal-to-MUI ratio, therefore the lower bound of the error probability, when MUI exists from K users and single detection is:

$$Pe_{k_{fl}} = 0.5 \left(1 - 1 / \sqrt{1 + (K-1) / N} \right) \quad (8).$$

B. Optimal MUD

Optimal MUD is obtained when MAP criterion is applied. It is searched for the maximum of the received signal correlation with all possible transmit signals. The logarithmic likelihood function is presented in matrix form [1]:

$$\Psi(\mathbf{d}) = 2\Re(\mathbf{d}^T \mathbf{E} \mathbf{A}^* \mathbf{z}) - \mathbf{d}^T \mathbf{E} \mathbf{A} \mathbf{R} \mathbf{A}^* \mathbf{E} \mathbf{d} \quad (9).$$

The symbol $()^*$ means the complex conjugated value and $()^T$ – transpose matrix.

The decision of the transmitted symbols is:

$$\hat{\mathbf{d}} = \arg \left\{ \max_{\mathbf{d}} [\Psi(\mathbf{d})] \right\} \quad (10).$$

The optimal algorithm for MUD leads to eliminating the MUI influence. The error probability for one bit for a given user is equal to the error probability in the case of correlation single detection:

$$Pe_{ko} = 0.5 \left(1 - \sqrt{E_k / [(N_o + E_k)]} \right) \quad (11).$$

III. SUBOPTIMAL DETECTION WITH SUCCESSIVE SEARCH ALGORITHM POSSIBILITIES

A. Algorithm for successive search.

Finding the optimal decision for MUD is considered as optimization task, which objective function is multiparameter, discrete, non-unimodal – (9). One of the possible variants, proposed in [7] is to apply a successive search. The vector for optimization consists of the elements with the user symbols \mathbf{d} . The number of the computations in the algorithm decreases if the start point for optimization is the data from the correlation receivers' outputs. Based on this data, combined with the decision criterion (5), it is obtained a packet of symbols- $\hat{\mathbf{d}}_F$. These criterions do not minimize the errors caused by MUI, just the contrary in the approximation of the error probability with (6), (7), (8), (11), the total interferences are considered as independent Gaussian random value from the noise. The decision criterion (10) at MUD compensates the influence of MUI, and the error probability depends only on the power of the AWGN.

If one bit in the packet is mistaken, it can be corrected using the decision criterion (10). It is necessary to make only $(K+1)$ computations of the objective function (9) with vectors of the set M_d , that have Hamming distance with the vector $\hat{\mathbf{d}}_F$ equal to one:

$$M_d = \left\{ \mathbf{d} : H_d(\hat{\mathbf{d}}_F, \mathbf{d}) = 1 \right\} \quad (12).$$

Then iteration of the algorithm is related to search in a vicinity of the point in the K -dimensional space with Hamming distance of one. This can be realized as each step of the optimization algorithm consecutively changes one element of the vector \mathbf{d} (changes the bit) and evaluates the objective function. After this, it is picked up the bit, which maximizes (9). The decision criterion transforms in:

$$\hat{\mathbf{d}} = \arg \left\{ \max_{\mathbf{d} \in M_d} [\Psi(\mathbf{d})] \right\} \quad (13).$$

The search carries out errors so many times as are the errors number in one vector \mathbf{d} .

A. Parameters of the successive search algorithm.

The receiver output symbols are parallel or the received vector $\hat{\mathbf{d}}$ is a packet, consists of K symbols. Let the channels of the different users are independent and the requirements for the use of Eq.8 are fulfilled. The number of symbol errors m in a given packet is binomial distributed and the probability is given with:

$$P_K(m) = C_K^m (Pe_{k_{fl}})^m (1 - Pe_{k_{fl}})^{K-m} \quad (14).$$

Let's assume that the objective function (9) is decreasing for increasing of the Hamming distance against the optimal decision in (10). If the errors in the packet are more than one, the upper described procedure may be repeated as times as the number of errors is. Each iteration of the successive search reduces only one error in the packet. In this reducing of the error probability, the lower bound of the error probability per bit, for a given user may be obtained with the following equation:

$$P_e = \sum_{m=L+1}^K \frac{m-L}{K} C_K^m (Pe_{k_{fl}})^m (1 - Pe_{k_{fl}})^{K-m} \quad (15),$$

where L is the number of the corrected errors. In fact L defines the minimal number of iterations for successive search. Fig.2 shows the dependence of the error probability against the number of active users (the size of one packet) for a constant number of corrected errors (number of iterations in the criterion (13)). The dashed line shows the lower bound of the error probability in the case of single correlation detection-Eq.8. It is clearly seen that the increase of the number of iterations, decreases the error probability, due to compensation of MUI. Eq. (14) shows that the multiple errors are less probable.

The obtained dependence (15) and Fig.2 make possible for a given error probability and number of active users to compute the minimal number of iterations of the algorithm L . In this way, one may adaptively to change the number of calculations depending on the mobile network loading. It is clear that in the successive search algorithm, the number of calculations of the objective function is significantly reduced.

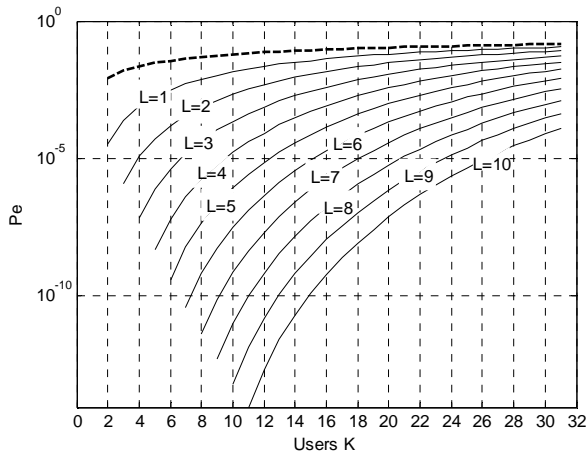


Fig.2

If an optimal algorithm is applied, the number of the computations J of the objective function are obtained by $J=2^K$. If L is used for termination criterion of the search, therefore the number of the computations depends on the number of the iterations and the active users. Furthermore, L may be used for a limit for termination of the search.

IV. SIMULATION RESULTS

The algorithm is simulated in MATLAB. The spectrum is spread with random sequence for each user with length $N=31$. The channel is AWGN with slow Rayleigh fading.

Fig.3 and fig.4 show the measured error probability in dependence of the mean value of E_b/N_0 for $K=10,20$ and different number $L=1,2,3,4$. The results show that the increasing the number of the iterations leads to reach the theoretical curve for fully compensation the MUI or single detection with Eq.11. It is clearly seen from Fig.3 that for $L=4$, the lowest error probability is $Pe=10^{-5}$. In the rest cases for L Pe is bounded below and the value coincides with the value obtained by Eq.15.

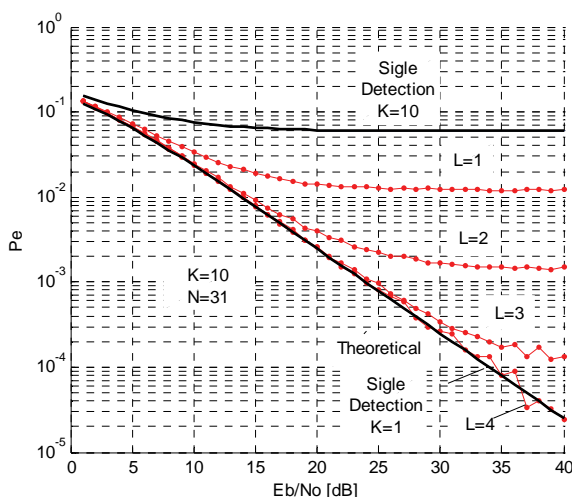


Fig.3 Error probability versus E_b/N_0 for active users $K=10$

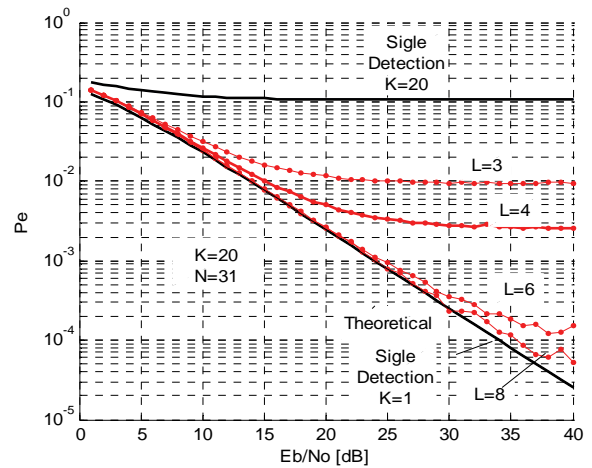


Fig.4 Error probability versus E_b/N_0 for active users $K=20$

V. CONCLUSION

The suboptimal methods for MUD in synchronous CDMA systems are prospective class in comparison to the optimal methods, because of the reduced number of calculations and computational complexity. The results presented in this paper allow changing adaptively the number of the iterations, respectively the number of the calculations of the MUD algorithm in dependence of the number of active users and a constant error probability. Additionally the number of the calculations is reduced because the initial start point for optimization is chosen after single detection.

The obtained results show that the increasing the number of the iterations leads reaches the theoretical curve for fully compensation the MUI or single detection.

REFERENCES

- [1] S. Verdú, *Multiuser Detection*. New York: Cambridge Univ. Press,1998.
- [2] R. Lupas and S. Verdú, Linear multiuser detectors for synchronous code-division multiple-access channels, *IEEE Trans. Inform. Theory*, vol. 35, pp. 123-136, Jan. 1989.
- [3] Z. Xie, R. Short, C. Rushforth, A family of suboptimum detectors for coherent multiuser communications, *IEEE J. on Selected Areas in Commun.*, vol.8, pp. 683-690, May, 1990
- [4] C. Ergun and K. Hacioglu, Multiuser detection using a genetic algorithm in CDMA communications systems, *IEEE Trans. Commun.*, vol. 48, pp. 1374-1383, Aug. 2000.
- [5] M. J. Juntti, T. Schlösser, J. O. Lilleberg, Genetic algorithms for multiuser detection in synchronous CDMA, *IEEE ISIT'97*, (Ulm, Germany), p. 492, 1997.
- [6] K. Yen ,L. Hanzo, Hybrid genetic algorithm based multi-user detection schemes for synchronous CDMA systems, *IEEE Vehicular Techn. Conference*, Tokyo, May 15-18,2000.
- [7] Peng Hui Tan, Lars K. Rasmussen, Multiuser Detection in CDMA—A Comparison of Relaxations, Exact, and Heuristic Search Methods, *IEEE Tr. Wireless Comm.*, Vol. 3, N5, 2004
- [8] Arnaudov Rumen, Rossen Mileteiev - "Analysis of the irregularly sampled signals above the Nyquist limit," *Metrology and Measurement Systems*, Vol.XIII, No. 3, 2006, pp.231-236, Poland.

Realization of Train Rescheduling Software System

Snežana Mladenović¹ and Slavko Vesković²

Abstract - During the past decades numerous methods have been developed, resolving more or less successfully the NP-hard (re)scheduling problems. If, however, there is an ambition to bring into practice one of the scheduling methods, the research must focus on both the development of algorithms and of corresponding software systems. The paper presents the most interesting realization details of the first prototype of train rescheduling system.

Keywords - Train rescheduling, Software system, OPL, CP

I. INTRODUCTION

The train scheduling problem belongs to a category of NP-hard problems of combinatorial optimization, and hence is complex for both modeling and solving. On the other hand, that problem must be solved as a part of tactical planning process in real railway systems.

The assignment of train rescheduling is that on a smaller fragment of railway network, over a shorter planning period an operational reconstruction of timetable is made, in respond to disturbances that have arisen.

The rescheduling in general may be considered to be a more difficult problem than an initial scheduling because additional requirements are imposed to it [1, 2]: to find a solution in a given real time; to have a recovered schedule which will deviate from the initial one as little as possible; the solution if not optimal, to be at least "good enough" with respect to the assigned objective function, etc.

Authors have been agreed that train rescheduling is quite a difficult work. According Norio et al. [3], major reasons of this are as follows:

- it is difficult to decide an objective criterion of rescheduling which is uniformly applicable;
- train rescheduling is a large size combinatorial problem;
- a high immediacy is required;
- no necessary information can be always obtained.

Since train rescheduling is such difficult job, assistance of software systems have been longed for, and nowadays train rescheduling systems are being practically used.

However, only a few published papers deal with train rescheduling software in real time. In fact, the current rescheduling systems test mostly if the solution proposed by the user is feasible one, and they are not doing full schedule regeneration. It also can be noted that authors simplify the scheduling problem in two ways: by simplification of the network structure and omitting and/or approximating constraints that govern the train movement. Thus, the model used by Isaai and Singh in [4] does not allow sequencing on single-track line between two consecutive stations. The first

train must complete its arrival at the next station before the next train departs from the previous station. This rule relaxes problem but leads to a poorer solution, as slower trains can hold up other faster trains while traversing from one station to another.

The design, development and implementation of train rescheduling system are a specific assignment of the software engineering. The paper presents recommendations to be followed as general during design, development and implementation of the rescheduling system. In accordance with these recommendations, the first prototype of train rescheduling system has been realized.

The rest of the paper is organized as follows: Section 2 points to some particularities in the rescheduling software life cycle. Section 3 records the expected design requirements. Section 4 deals with the implementation issues. A special attention must be paid to testing in the incremental software development, and this is discussed in Section 5. An analysis of the first prototype results is a prerequisite for specification of new requirements and development of a new, more perfect prototype, which is discussed in Section 6. Finally, Section 7 presents conclusions.

II. RESCHEDULING SOFTWARE LIFE CYCLE

The spiral model, according to authors' opinion, is the model of the first choice for development of rescheduling applications. The basic assumption is that the specification of users' requirements is not completely finalized before the stages of design and implementation. The software system is developed incrementally, by developing a series of prototypes, that being verified and validated, considering the new user requirements.

A particularity of the proposed spiral model is a risk analysis that must be carried out before design of any new prototype. The risk in developing a rescheduling software system is not low; the prototype may simply "fail", if too tight time limits have been imposed

Herein, only the details of the train rescheduling software life cycle that differentiate from other software systems will be highlighted.

III. DETERMINATION OF REQUIREMENTS

Essential requirements put to the train rescheduling software are:

- interaction with other software systems,
- existence of graphic user interface,
- respect to time limits.

The rescheduling system must receive information from hierarchically higher planning levels. Thus, an initial train timetable and network topology must be accessible to the train rescheduling software. The rescheduling system also must

Authors are with Faculty of Transport and Traffic Engineering
University of Belgrade, Vojvode Stepe 305, 11000 Belgrade, Serbia ,
E-mail's: snezanam@sf.sf.bg.ac.yu; E-mail: veskos@sf.sf.bg.ac.yu

receive the latest information regarding the resources availability, job progress, etc. from the process monitoring system. A general idea is for all data available to be found in the information system **DataBase DB**, wherefrom they will be accessible to the rescheduling software. Usually, a significant effort is required to adapt the real system database for the rescheduling system input. The requirement to make the database correct, consistent and complete often assumes a designing of a series of tests the data must be run through before being used. Since a real database from the railway company was not accessible during the research, a demo MS Access database was created, assuming that it is correct, consistent and complete.

Within the database, it is possible to distinguish the static and dynamic data. The static data are all data on jobs and resources that do not depend on scheduling. E.g., data on train categories belong to static data. Data on resources are relatively static data, as well as on the regular timetable. The job priorities are also static data, not depending on scheduling, either. The priority may be based on the planner's assessment or may be result from the procedure taking into account other data from the information system database. The job priority change may depend on the scheduling period, but also by some external, hardly predictable events; thus suburban and urban trains may temporarily, during the peak hour period, get a higher priority than international trains. In our model, the change of priority procedure takes into consideration the expert assessments in the database made for individual sections and individual periods during the day.

The dynamic base consists of all schedule-dependant data: job start and completion times, current job positions, number of delayed jobs etc. Some data may be considered as both static and dynamic, e.g. resource setup time. Occurrence of unexpected dynamic data in the DB is actually a trigger for the train rescheduling procedure.

The scheduling **Model Base MB** holds an important place in our rescheduling system also. It collects the models that optimize one or the other objective function, imposing or relaxing certain constraints. A special procedure selects a model from the MB, taking into account the user's wish the function wants to optimize.

The architecture of a hypothetical information system with incorporating a train rescheduling system – schedule recovery module, is presented in figure 1 in the form of data flow diagram between the processes. The schedule recovery module should enable the model management: choice, combining, sequencing, running etc.

The user interfaces can determine the scheduling system usability. Obviously, the scheduling visualization must resemble the one the users are accustomed to during their work for many years. Also, since the inference engines and decision-making are hidden from planners–users, the presentation of scheduling results must be such to make him assured quickly and easily on the validity of the "good-enough" solution found.

The scheduling software must have an interface based on "WIMP paradigm" (**W**indow, **I**nteraction, **M**ouse, **P**ointer).

The user interfaces for database modules are in a standardized form and are determined by a used database management package.

The realized schedule recovery module contains 7 models corresponding to different objective functions (maximum tardiness, maximum weighted tardiness, total tardiness, total weighted tardiness, makespan, maximum slack of trains in stations, number of late trains). If we wish to offer the planner–user a possibility of a direct model choice, we must furnish him with a user interface that will enable such manipulation. No other modes of interactive manipulations are necessary because the very objective of the rescheduling system is a full automation that eliminates the user's slow actions.

The literature describes numerous standard user interfaces for presentation of scheduling information [5]. It is interesting that none of the standard graphic interfaces was fully suitable for schedule visualization in the train rescheduling problem for objective and subjective reasons. Objectively, none of the interfaces presents transparently enough the sequencing, overtaking, crossing, waiting and movement of trains. On the other hand, the planners–users are used to visualization known as the train diagram, which is, actually a slightly modified Gantt chart. The modification consists of "touching" the resources on y-axis (in fact, the real infrastructure objects touch each other) and the replacement of bars by their diagonals, which symbolizes the train movement on a resource. Figure 2 represents the realized graphic presentation of a found schedule of the train rescheduling system.

The modified Gantt chart is made automatically by MS Excel. In the graphic presentation, "background" is always a tabular presentation of train diagram, presenting the start and end times of each job activity, along with the information on which resource it will be accomplished.

IV. IMPLEMENTATION

The implementation of the scheduling system is accompanied, from the very beginning by perplexities. Namely, dozens of software companies claim they have developed automatic scheduling generators, that can be applied in different real systems, these being either a choice of a commercially available scheduling generator, development of a "from zero" system, or a combined approach?

In attempts to implement the train rescheduling system solely by scheduling generators available, a series of problems arose: an immensely oversized scheduling problem, difficulties in establishing a link between the scheduling system and the schedule implementation monitoring system, difficulties in coding special cases (e.g. station tracks under specific conditions behave as a single resource, and as separate resources otherwise), timing requirements, ... On the other hand, there was a idea to speed up the stage of implementation by using the scheduling generators available.

The **I**ntegrated **D**evelopment **E**nvironment (IDE) **O**PL Studio [7] enables us to create and modify the **C**onstraint **P**rogramming (**CP**) and scheduling models using the **O**ptimization **P**rogramming **L**anguage (**OPL**), to compose and control models using the procedural language **OPL Script**, to run models by **ILOG Solver** and **ILOG Scheduler** as well as to presentation of results (schedules) in a tabular and graphic form. The **OPL Studio** trial version is available on site

<http://www.ilog.com/products/oplstudio/trial.cfm> and it was used for implementation of the first prototype of train rescheduling system.

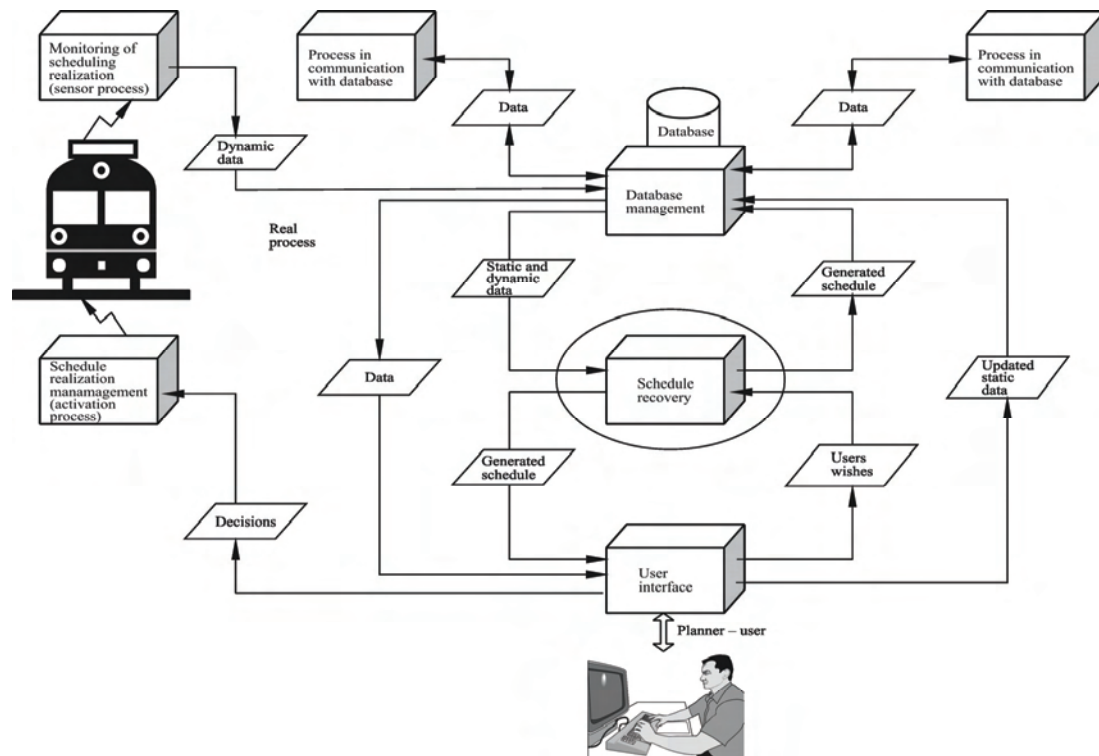


Fig. 1. Position of schedule recovery module in a real information system

In order to improve the time performance the software tools available was added to modules implementing heuristics specific for the train rescheduling problem. By **separation heuristics**, a global problem was split up into a series of smaller size subproblems the ILOG Scheduler is able to solve up to optimality. The **bound heuristics** have initially limited the decision variable domains and objective functions, and the **search heuristics** have directed the search into the space promising good solutions. These heuristics were described in details in [6]. A declarative nature of OPL was used for a simple formulation of the scheduling model. The schedule recovery module itself represents in fact a procedure formulated in the OPL Script with controlling the optimization models in a suitable way constructs "good enough" schedule in the limited time.

V. PROTOTYPE TESTING

The software system testing is traditionally carried out through verification and validation. The prototype verification and validation must be carried out according to the standard criteria for software, these being efficiency: reliability, usability, modifiability, portability, testability, reusability, maintainability, interoperability, and correctness. The first train rescheduling system prototype was assessed for all quality criteria. The specificity of the train rescheduling application imposes to clarify in this point, in particular:

- **efficiency** – the software must work within the envisaged time limit. This is a key property of the rescheduling system. The testing of systems that have to operate within the given time limit is extremely difficult. The idea is to

reiterate each test example for numerous times, and a good direction for support to this idea is the automatic testing. The testing of the first train rescheduling system prototype was made manually, on a large number of input timetables with existing disturbances; each test example, however, was run at least 10 times to determine the mean value of CPU time. It was found during the testing that the variation of CPU time still is not drastic (not more than $\pm 10\%$ of the mean value);

- **reusability** – the property of the software that, as a whole or in parts, it may be used for development of similar systems, thus increasing the development productivity of related systems. E.g., it is known that the train rescheduling is a core of the systems which deal in railway traffic with: timetable preparation, determining of economically acceptable utilization of capacity interval, estimate of costs of stopping and tardiness of trains for operational reasons, forecasting the effects of investments, identification of bottlenecks in infrastructure, choice of possible solution of a conflict point, testing the arrangement and layout of block sections and signals along the railway line etc. Standardization of software modules and their communication is a good direction for upgrading their reuse;
- **modifiability** – expresses a property of easy modifications on the software in case of changed user's requirements. E.g., it is reasonable to expect that the set of constraints be to subject to changes. A declarative nature of CP approach, separation between the constraint

component and search component, available CP tools, offer the programmer fantastic possibilities to achieve the

highest level of modifiability.

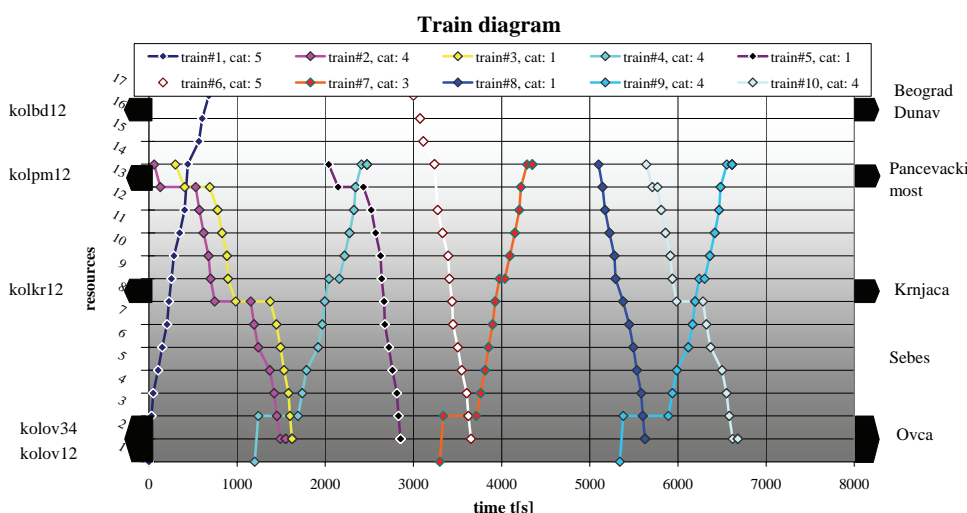


Fig. 2. Realized window of user interface of the first prototype of train rescheduling system – a graph presentation of the recovered train schedule in the form of modified Gantt chart

VI. ANALYSIS OF THE PROTOTYPE RESULTS

The testing of the first train rescheduling system prototype was carried out on a large number of input timetables with existing conflicts. Experiments have been carried out on a fragment of real railway network (a part of Belgrade Railway Junction), with actual train categories operating there, but **with traffic frequency immensely exceeding the real one**. The jobs (trains) are "piled up" on purpose to test the endurance of the method. All seven relevant objective functions participated in the experiment. Each set of jobs suffering disturbances includes trains of different categories and different movement directions. All experiments have been implemented on personal computer Intel (R) Pentium(R) 4 CPU, 2GHz. For example, CPU time needed for generation of schedule, given on figure 2, was 36.65 seconds where objective function was maximum tardiness. From the analysis of experiment results the following conclusion may be drawn:

- CPU time of schedule recovery depends on the number of activities and number of conflicts;
- solving of initial conflicts may bring up additional conflicts;
- in most cases the time performance is satisfactory;
- a heuristic nature of the approach has been demonstrated (in an insignificant number of cases the best-known solution for the given objective function has not been found).

Based on this analysis, we can formulate the proposals the acceptance of which should lead to the improved prototype.

VII. CONCLUSION

A major part of theoretical research carried out during the past decades in the field of scheduling has a limited application in real systems. Therefore, **the research must be concentrated on the development of algorithms, but also on development of software systems**. This paper is one of such attempts.

The rescheduling software system should enable the planner to produce faster a better quality schedule. There are also other reasons for introducing automatic scheduling systems. The scheduling system requires advanced "disciplines" from other subsystems of the real information system. It oblige and ensure the real process to develop according to schedule.

Experiments made on the first train rescheduling system prototype, on a real railway network fragment, with real traffic structure, and possible disturbances, make us believe that the approach proposed in this paper may offer a full support to the railway operational management.

REFERENCES

- [1] Cowling, P. and M. Johansson, "Using real time information for effective dynamic scheduling", *European Journal of Operational Research*, 139(2), pp. 230-244, 2002.
- [2] Vieira, E. G, J. W. Herrmann and E. Lin, "Rescheduling manufacturing systems: a framework of strategies, policies and methods", *Journal of Scheduling*, 6, pp. 39-62, 2003.
- [3] Norio T., Y. Tashiro, T. Noriyuki, H. Chikara and M. Kunimitsu, "Train rescheduling algorithm which minimizes passengers' dissatisfaction", in *Innovations in Applied Artificial Intelligence, Lecture Notes in Artificial Intelligence 3533*, Springer Verlag, pp. 829-838, 2005.
- [4] Isaai, M. T. and M. G. Singh, "An object-oriented, constraint-based heuristic for a class of passenger-train scheduling problems", *IEEE Transactions on Systems, Man and Cybernetics Part C: Applications and Reviews*, 30(1), pp. 12-21, 2000.
- [5] Pinedo, M., *Scheduling: Theory, Algorithms and Systems*, Prentice Hall, 1995.
- [6] Mladenović, S., M. Čangalović, D. Bečejski-Vujaklija and M. Marković, "Constraint programming approach to train scheduling on railway network supported by heuristics", 10th World Conference on Transport Research, CD of Selected and Revised Papers, Paper number 807, Abstract book I, pp. 642-643, Istanbul, Turkey, 2004.
- [7] ILOG OPL Studio <http://www.ilog.com>

Throughput Analysis of EDCA in Multimedia Environment

Blagoj Ilievski, Pero Latkoski and Borislav Popovski

Abstract – This paper addresses issues that arise when end-to-end QoS has to be guaranteed in today’s pervasive heterogeneous wired-cum-wireless networks. The basic IEEE 802.11 standard for local area networks can not cope with the emerging multimedia services such as voice, data and video. On the other hand, the wireless medium is very specific; there is no guarantee for any performances as in the wired medium, especially in the unlicensed spectrum. The new 802.11e MAC which is based on both centrally-controlled and contention-based channel access provides means for needed QoS in such conditions. Here we analyze the .11e’s throughput performance and packet loss for different traffic types, compared with the basic standard, and its dependence of the network conditions.

Keywords – IEEE 802.11e, Network Simulator, performance evaluation.

I. INTRODUCTION

IEEE 802.11 [1] introduces DCF (Distributed Coordination Function) and PCF (Point Coordination Function) on the MAC layer. DCF does not support priority mechanism [2]; all packets are treated using first-come-first-serve philosophy. On the other hand, PCF sustains several resource reservation methods. Although it can support some kinds of time-critical traffic, many inadequacies have been identified, such as unknown transmission duration of polled station, difficulty to predict the amount of frames one wants to send, no management interface defined to build up and control PCF operations. We can summarize that DCF can not provide QoS, and PCF is not capable enough [3].

The 802.11e standard is the result of the WLANs QoS issue. Due to the dynamic nature of these kinds of networks, it is impossible to apply QoS management techniques to negotiate quality between users and network. Nevertheless, it is possible to increase success probability of certain classes of traffic to get appropriate QoS. There are two kinds of QoS:

- Parameterized QoS – A strict QoS requirement expressed quantitatively in terms of data rate, delay bound etc.
- Prioritized QoS – Loose QoS requirement expressed in terms of relative delivery priority.

For different types of traffic, there are different requirements, but in case of WLANs the most common are two: bound delay (for real time traffic) and jitter. On the other hand, certain traffic stream is described by the transmission rate (peak and average), service interval (minimum and maximum) and the burst size of the peak rate.

The term QoS of WLAN refers only to the MAC level. The new standard (IEEE 802.11e) defines “stations with QoS support” - QSTAs, and “access points with QoS support”- QAPs, different from the stations and the access point defined in the original standard (IEEE 802.11). Here, a new method is introduced to support the QoS requirements: Hybrid Coordination Function (HCF). HCF has two main parts. One is HCF Controlled Channel Access (HCCA), for the Integrated Services requirement. The other one is Enhanced Distributed Channel Access (EDCA/EDCF), for the Differential Services requirement. In other words, EDCF is responsible for contention, while HCF for contention free working regime. While the EDCF is appropriate for asynchronous data services, the HCCA provides means of time-bounded services.

In the new IEEE 802.11e standard, acknowledgement (ACK) for successful transmission of the frames sent by stations becomes no obligatory. It means that MAC layer will not send ACK frame after successful receiving of a data frame. This approach decreases the reliability, but the overall traffic transmission efficiency (e.g. VoIP) is upgraded.

II. EDCA FUNCTION

The EDCA function improves the basic DCF function by implementing priorities for different traffic classes. The EDCA defines four access categories (AC), in which the traffic is additionally classified into 8 different traffic classes-user priorities (UP). The traffic in a same class is considered to be of equal priority. Table 1 shows the mapping between access categories and user priorities.

Table 1. Traffic classes (TC) in IEEE 802.11e

Priority	User Priority	802.11D Designation	Access category (AC)	Designation
Lowest	0	BE	AC_BK	Background
.	1	BK	AC_BK	Background
.	2	–	AC_BE	Best Effort
.	3	EE	AC_BE	Video
.	4	CL	AC_VI	Video
.	5	VI	AC_VI	Video
.	6	VO	AC_VO	Voice
Highest	7	NC	AC_VO	Voice

Every AC differs by the parameters variety and has its own queue. The parameters value determinates the AC and the type of the traffic. Three of the parameters are crucial for this standard:

- **CW** - *Contention Window* - A random number is drawn from this interval, or window, for the back off mechanism;

- **AIFS** - *Arbitrary Inter Frame Space* – It is equal to DIFS plus a number of time slots. The value of AIFS differs for every traffic class to enhance the differentiation based on the priority of classes.
- **TXOP Limit** – Maximum allowed time for transmission, of one QSTA. During this period, medium belongs to the station.

A station may implement up to eight transmission queues realized as virtual stations inside a station, with different QoS parameters that determine their priorities [4]. When two or more TCs in a single station start transmitting at the same time, a scheduler inside the station avoids the virtual collision.

Before station starts to transmit, MAC layer classifies the traffic into appropriate AC. Every new MSDU frame finds its place into adequate AC. The frames from different categories compete for the EDCF-TXOP. Each class differs by varying the minimum contention window (CW_{min}) and the interframe space which are used for data transmission. A class with smaller default contention window will result in generating shorter backoff intervals and as a result it gains priority over a station with a larger CW_{min} [5].

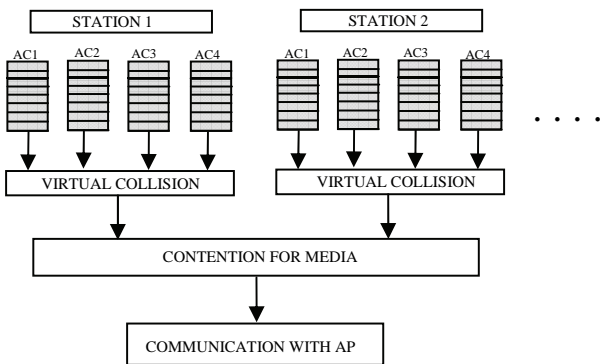


Fig.1. EDCF function

In the IEEE 802.11e EDCA, different ACs use different AIFS values and contention window size when contend for the channel access.

The value of AIFS depends on the AC, and the value of the $aSlotTime$ parameter depends on the used PHY Layer (in our case 802.11b). The number of backoff procedure slots is uniformly distributed random variable between 0 and $CW-1$. The CW is the contention window whose value is between CW_{min} and CW_{max} . After each successful transmission, the CW is reset to CW_{min} , and on each failure packet transmission the backoff procedure doubles the CW value until the value reaches the CW_{max} . In IEEE 802.11e the values of CW_{min} and CW_{max} are different for each AC and used PHY Layer (Table 2).

Table 2. Parameters for three types traffic in IEEE 802.11e

Type	AC	AIFS	CW_{min}	CW_{max}	TXOP Limit
Voice	3	2	7	15	0.003
Video	2	2	15	31	0.006
Data	0	7	31	1023	0

The winner virtual station of the internal competition has right to compete with the rest of the winners of the other stations to transmit over the medium.

The problem of the traffic differentiation is solved by adding field into the MAC header that describes the characteristics of the traffics (Table 3).

Table 3. IEEE 802.11e MAC header

octets: 2	2	6	6	6	2	6	2	n	4
Frame Control	Duration / ID	Address 1	Address 2	Address 3	Sequence Control	Address 4	QoS Control	Frame Body	FSC

There is an option in IEEE 802.11e standard called *packet bursting* - CFB (Contention Free Bursting). This feature, improves the performance of smaller packets (time bounded services) in WLANs [6]. The CFB decreases the overhead and in such a way the delay is decreased and the throughput is increased. The station with included CFB sends multiple small packets as a burst without intermediate contention, as soon as the station gains access to the medium. It is possible to send packets to different destinations in one burst frame. Between an ACK and the following packet only a time interval of SIFS (Short IFS) is required. Therefore the station maintains control over the medium for the whole burst (not longer than TXOP). Sending multiple small packets in a burst avoids contention for each single packet and increases the efficiency. However, the medium access time might be increased because packet bursts occupy the medium for a longer period, therefore the overall network jitter and delay may increase. By adjusting the parameters, especially TXOP Limit one can optimize the network functioning.

III. SIMULATION RESULTS

The network will be analyzed using NS2 (Network Simulator) [7]. In fact, this simulator is the most widely used simulator for analysis of the wireless networks.

The scenario is consisted of one access point (AP) connected with a host via switch and surrounded by six wireless stations (WS) (Fig.2). We assume two directions of the traffic stream: from the station towards the server (uplink) and from the server towards the station (downlink). We shall analyze the uplink throughput performance.

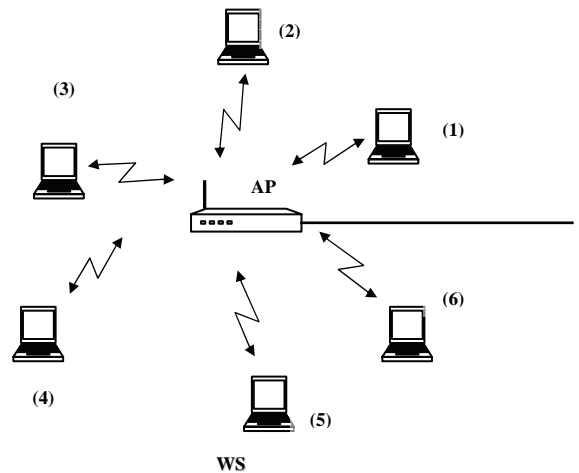


Fig. 2. Simulated WLAN scenario

Table 4 contains the used types of traffic and its parameters. It will be discussed the impact of the “e” standard over these three different types of traffic. All the stations will send packets with included CFB option. In this scenario two stations (5 and 6) generate and receive voice traffic (with the highest priority – AC4), two stations (3 and 4) generate and receive video traffic (AC2); stations 1 and 2 generate and receive data traffic (AC1). The AP transmits three types of traffic generated from the host towards wireless nodes (downlink) and receives also three categories of traffic from wireless nodes (uplink). Voice and video traffic is assumed to be of constant bit rate (CBR). Data traffic is assumed to be FTP traffic.

Table 4. Three types of traffic used in the simulation

Type	Agent/ Application	Frame Size (bytes)	Data Rate (Mbps)
Voice	UDP/CBR	32	0.032
Video	UDP/CBR	1280	1
Data	TCP/FTP	1536	1

We measure the uplink throughput performance and its dependence of the frame size, load and the number of the active stations in the network. First parameter that is changed is packet size. The network is loaded with 40% of its capacity.

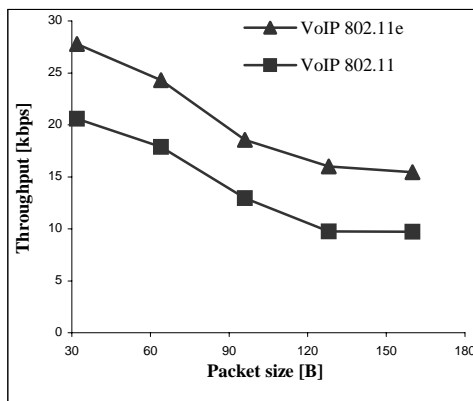


Fig.3. Voice traffic throughput dependence from pck size

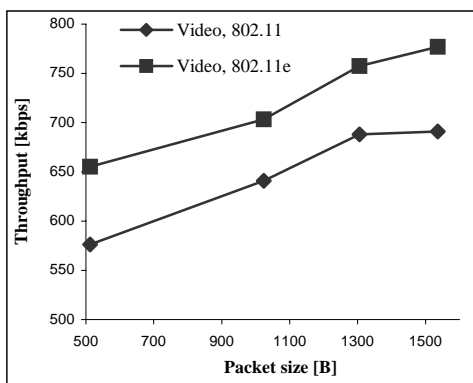


Fig.4. Video traffic throughput dependence from pck size

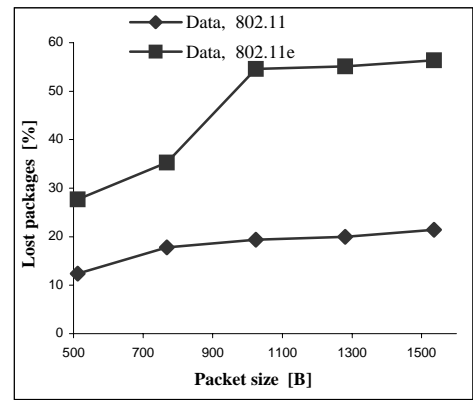


Fig. 5. Lost data packets dependence from pck size

Simulation results show opposite behavior when voice and video traffic are analyzed. The reason is TXOP, which for voice is smaller than the TXOP for video traffic. Data traffic with implemented QoS option is very sensitive of packet size change (Fig.5).

Next three figures will give the dependence from the traffic load parameter.

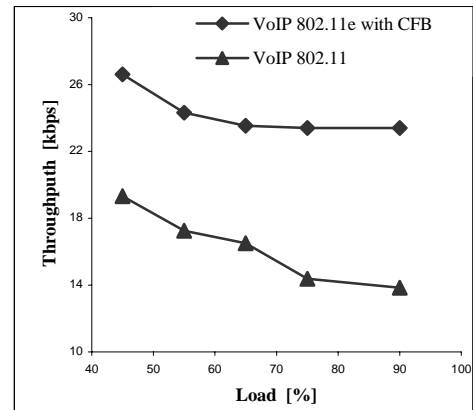


Fig.6. Voice traffic throughput depends from Load

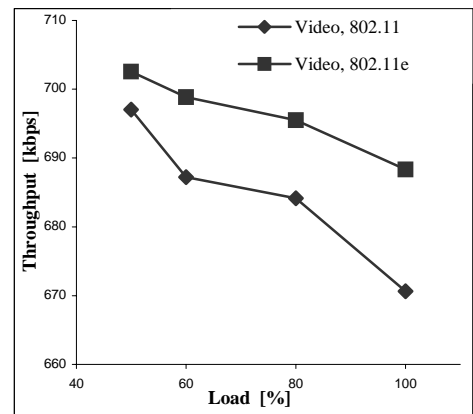


Fig.7. Video traffic throughput depends from Load

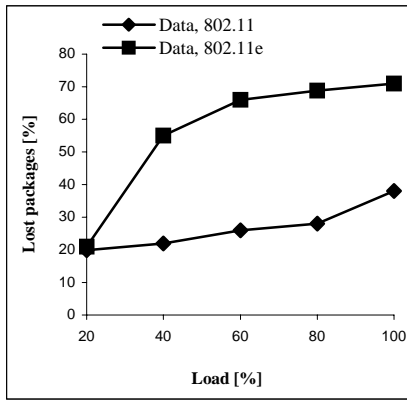


Fig.8. Lost data packages depends from traffic Load

When we discuss the load in the network, the “e” standard shows improvement compared to the basic standard. For voice the throughput is not changing significantly (10% difference in the throughput, for 50% and 90% load – Fig. 6). But the other two categories are very sensitive and deteriorate rapidly compared to the basic standard (Fig. 7, Fig. 8).

The number of the stations in the network is another important parameter. When the number of active stations is large the probability of collision increases as well.

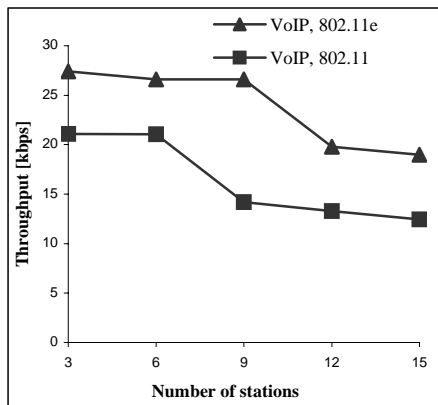


Fig.9. VoIP traffic dependence from number of stations

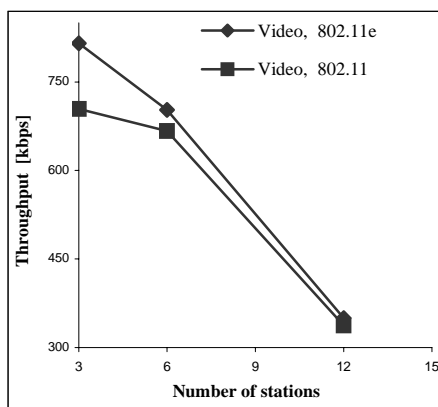


Fig.10. Video traffic dependence from number of stations

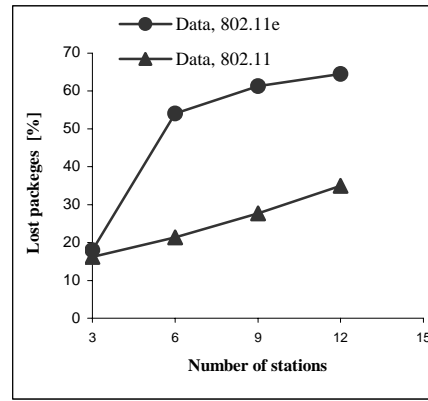


Fig.11. Lost data packages dependence from number of active stations

When the number of the wireless stations in the network is increased, “e” standard gains the voice traffic winning probability over the medium. Video and data has no significant chance when medium is shared by very large number of stations (Fig. 9, Fig. 10, Fig. 11).

IV. CONCLUSION

Our simulator implements the new EDCF function. This function is an upgrade of wireless stations and enables QoS support. By simulations we find that EDCF shows weakness at low-level categories of traffic. It is evidently that the high priority categories of traffic dominantly occupy the medium. The throughput of the different services traffic is very sensitive of the changes in the network (number of the stations, traffic load), or the size of the packets. Also the characteristics of the data traffic deteriorate compared to the basis standard. This implies requirement for further improvements in the 802.11 MAC to increase the quality of the data traffic compared to the basic standard performance.

REFERENCES

- [1] IEEE Standard for Wireless LAN Medium Access Control and Physical Layer Specification, IEEE 802.11.
- [2] P. Latkoski, Z. Hadzi-Velkov, B. Popovski “Extended Model for Performance Analysis of Non-Saturated IEEE 802.11 DCF in Erroneous Channel”, The Third IEEE International Conference on Mobile Ad-hoc and Sensor Systems (MASS 2006), Vancouver, Canada, October 9-12, 2006..
- [3] Qiang Ni , Lamia Romdhani, Thierry Turletti ”A Survey of QoS Enhancements for IEEE 802.11 Wireless LAN”, *Journal of Wireless Communications and Mobile Computing*, Wiley, 2004
- [4] Sameer Mehta and Amit Goel ”Enhancing the 802.11 MAC to incorporate VoWLAN for seamless convergence”, National Symposium on Electronics Technology organized by the IEEE at Kurukshetra University in March 2004.
- [5] Xiang Fan ”Quality of Service Control in Wireless Local Area Networks”, M.T. *University of Twente*, November 2004.
- [6] S.Wietholter, C. Hoene, A. Wolisz ”Perceptual Quality of Internet Telephony over IEEE 802.11e Supporting Enhanced DCF and Contention Free Bursting”, *Berlin*, Sep 27th, 2004.
- [7] “The Network Simulator ”, <http://www.isi.edu/nsnam/ns>.

Software Tools and Technologies in Steganography

Julijana Mirčevski¹, Biljana Djokić², Mileša Srećković³ and Nikola Popović⁴

Abstract: In the paper was exposed the performance estimation of more available program tools for steganographic application and message implementation method. The results were classified and illustrated by the tested procedures. The message creation, implementation and detection was shown in oneself programs tool that operate in Visual Basic environment.

Keywords: steganography, invisible communication, message embedding, steganographic file detection, wavelet transform

I. INTRODUCTION

Steganography as a way of invisible communication is very present in current internet communication. A number of steganographic application available with a various performance in domain of message implementation, system requirements, encoding security and executing reliability.

The digital contents database requires a more complex software tools in order to searching, analysis's, compression and reproduction. Wavelet theory provides the fast discrete algorithms suitable to computer programming application. The clear mathematical theory is a good base to creating a programs environment and a number programs packages. The wavelet transform application are thinkingless without a programming software package but the most used are WaveLab, LastWave, MegaWave i Rice Wavelet Toolbox. Because the mentioned software products belong to free ware software category, it is possible to use that with a registration legality.

Steganography hides the covert message but not the fact that two parties are communicating with each other [1]. The steganography process generally involves placing a hidden message in some transport medium, called the carrier. The secret message is embedded in the carrier to form the steganography medium. The use of a steganography key may be employed for encryption of the hidden message and/or for randomization in the steganography scheme. In summary:

$$\text{steganography_medium} = \text{hidden_message} + \text{carrier} + \text{steganography_key}$$

On the followed figure it is presented scheme of steganography systematization according to [2]. Only the main items would be explained in text.

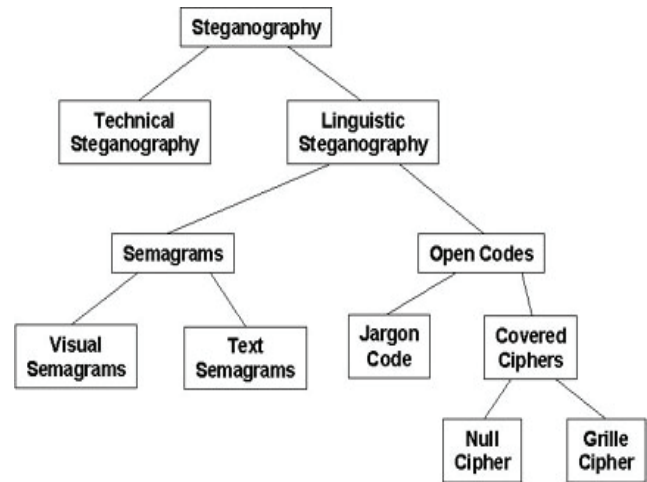


Fig. 1. Classification of Steganography Techniques

- Technical steganography uses scientific methods to hide a message, such as the use of invisible ink or microdots and other size-reduction methods.

- Linguistic steganography hides the message in the carrier in some nonobvious ways and is further categorized as semagrams or open codes.

- Semagrams hide information by the use of symbols or signs.

A visual semagram uses innocent-looking or everyday physical objects to convey a message, such as doodles or the positioning of items on a desk or Website. A text semagram hides a message by modifying the appearance of the carrier text, such as subtle changes in font size or type, adding extra spaces, or different flourishes in letters or handwritten text.

- Open codes hide a message in a legitimate carrier message in ways that are not obvious to an unsuspecting observer. The carrier message is sometimes called the overt communication, whereas the hidden message is the covert communication. This category is subdivided into jargon codes and covered ciphers.

- Jargon code, as the name suggests, uses language that is understood by a group of people but is meaningless to others. Jargon codes include warchalking (symbols used to indicate the presence and type of wireless network signal [3]), underground terminology, or an innocent conversation that conveys special meaning because of facts known only to the speakers. A subset of jargon codes is cue codes, where certain prearranged phrases convey meaning.

- Covered or concealment ciphers hide a message openly in the carrier medium so that it can be recovered by anyone who knows the secret for how it was concealed. A grille cipher employs a template that is used to cover the carrier message.

¹Julijana Mirčevski, Informatička škola "Educon", Beograd, julijana@afrodita.rcub.bg.ac.yu

²Biljana Djokić, Informatička škola "Educon", Beograd, djokicb@eunet.yu

³Mileša Srećković, Elektrotehnički fakultet, Beograd, mileša@afrodita.rcub.bg.ac.yu

⁴Nikola Popović, Ministarstvo inostranih poslova, Beograd

II. FEATURES AND APPLICATIONS

Data-hiding techniques should be capable of embedding [3] data in a host signal with the following restrictions and features:

1. The host signal should be nonobjectively degraded and the embedded data should be minimally perceptible. (The goal is for the data to remain *hidden*. As any magician will tell you, it is possible for something to be hidden while it remains in plain sight; you merely keep the person from looking at it. We will use the words *hidden*, *inaudible*, *imperceptible*, and *invisible* to mean that an observer does not notice the presence of the data, even if they are perceptible.)
2. The embedded data should be directly encoded into the media, rather than into a header or wrapper, so that the data remain intact across varying data file formats.
3. The embedded data should be immune to modifications ranging from intentional and intelligent attempts at removal to anticipated manipulations, such as a channel noise, filtering, resampling, cropping, encoding, lossy compressing, printing and scanning, digital-to-analog (D/A) conversion, and analog-to-digital (A/D) conversion and other.
4. Asymmetrical coding of the embedded data is desirable, since the purpose of data hiding is to keep the data in the host signal, but not necessarily to make the data difficult to access.
5. Error correction coding should be used to ensure data integrity. It is inevitable that there will be some degradation to the embedded data when the host signal is modified.
6. The embedded data should be self-clocking or arbitrarily reentrant [3], [4]. This ensures that the embedded data can be recovered when only fragments of the host signal are available, e.g., if a sound bite is extracted from an interview, data embedded in the audio segment can be recovered. This feature also facilitates automatic decoding of the hidden data, since there is no need to refer to the original host signal.

Trade-offs exist between the quantity of embedded data and the degree of immunity to host signal modification. By constraining the degree of host signal degradation, a data-hiding method can operate with either high embedded data rate, or high resistance to modification, but not both. As one increases, the other must decrease. While this can be shown mathematically for some data-hiding systems such as a spread spectrum, it seems to hold true for all data-hiding systems. In any system, you can trade bandwidth for robustness by exploiting redundancy. The quantity of embedded data and the degree of host signal modification vary from application to application. Consequently, different techniques are employed for different applications [5]. Several prospective applications of data hiding are discussed in this section. An application that requires a minimal amount of embedded data is the placement of a digital water mark.

The embedded data are used to place an indication of ownership in the host signal, serving the same purpose as an author's signature or a company logo. Since the information is of a critical nature and the signal may face intelligent and intentional attempts to destroy or remove it, the coding techniques used must be immune to a wide variety of possible modifications.

A second application for data hiding is tamper-proofing. It is used to indicate that the host signal has been modified from its authored state. Modification to the embedded data indicates that the host signal has been changed in some way.

A third application, feature location, requires more data to be embedded. In this application, the embedded data are hidden in specific locations within an image. It enables one to identify individual content features, e.g., the name of the person on the left versus the right side of an image. Typically, feature location data are not subject to intentional removal. However, it is expected that the host signal might be subjected to a certain degree of modification, e.g., images are routinely modified by scaling, cropping, and tonescale enhancement. As a result, feature location datahiding techniques must be immune to geometrical and other nongeometrical signal modification.

III. DIGITAL CARRIER METHODS

There are many ways to be hidden messages in digital media. The most common steganography method in audio and image files employs some type of least significant bit substitution or overwriting. The least significant bit term comes from the numeric significance of the bits in a byte. The high-order or most significant bit is the one with the highest arithmetic value (i.e., $2^7=128$), whereas the low-order or least significant bit is the one with the lowest arithmetic value (i.e., $2^0=1$).

As a simple example of least significant bit substitution, imagine "hiding" the character 'G' across the following eight bytes of a carrier file (the least significant bits are underlined):

```
10010101   00001101   11001001   10010110
00001111   11001011   10011111   00010000
```

A 'G' is represented in the American Standard Code for Information Interchange (ASCII) as the binary string **01000111**. These eight bits can be "written" to the least significant bit of each of the eight carrier bytes as follows:

```
10010100   00001101   11001000   10010110
00001110   11001011   10011111   00010000
```

In the sample above, only half of the least significant bits were actually changed (shown above in italics and colored). This makes some sense when one set of zeros and ones are being substituted with another set of zeros and ones.

Least significant bit substitution can be used to overwrite legitimate RGB color encodings or palette pointers in GIF and BMP files, coefficients in JPEG files, and pulse code modulation levels in audio files. By overwriting the least significant bit, the numeric value of the byte changes very little and is least likely to be detected by the human eye or ear.

Least significant bit substitution is a simple, albeit common, technique for steganography. Its use, however, is not necessarily as simplistic as the method sounds. Only the most naive steganography software would merely overwrite every least significant bit with hidden data. Almost all use

some sort of means to randomize the actual bits in the carrier file that are modified. This is one of the factors that make steganography detections so difficult.

All steganographic methods are trying to achieve the minimal amount of modification in order to minimize the view changes through introducing detectable artifacts. However, if the cover-image, was initially stored in the JPEG format (as it is frequently the case), message embedding in the spatial domain will disturb but not erase the characteristic structure created by the JPEG compression. It is possible to recover the JPEG format table from stego-image by carefully analyzing the values of DCT coefficients in all blocks. After message embedding, the cover image will become, with a high probability, grather then pure image and, yet not fully compatible with JPEG format. This can be indicated the steganography file.

IV. STEGANOGRAPIC SOFTWARE TOOLS

There are a number of steganographic software tools and steganographic techniques today available on the internet []. They can be ranging from freeware software to commercial products of high price. Most of them are creations of amateur enthusiasts available for free while others are products of private companies and can be purchased for a small fee.

The very important function of steganography detection software is to find possible carrier files. Ideally, the detection software would also provide some clues as to the steganography algorithm used to hide information in the suspect file so that the analyst might be able to attempt recovery of the hidden information.

The detection of steganography software continues to become harder for another reason—the small size of the software coupled with the increasing storage capacity of removable media. S-Tools, for example, requires less than 600 KB of disk space and can be executed directly, without additional installation, from a floppy or USB memory key. Under those circumstances, no remnants of the program would be found on the hard drive.

In text followed bellow, would be present some small and powerful software tools.

ChinCrypt is a small and easy to use textmode programme for crypting data. It can be encrypt a text file, executable file or, image file etc. ChinCrypt is the size of 10kB and work under Windows, Linux and Unix.

Gifshuffle is a command-line-only program for Windows which conceals messages in GIF images by shuffling the colourmap. The picture remains visibly intact, only the order of color within the palette is changed. It works with all GIF images, including those with transparency and animation, and in addition provides compression and encryption of the concealed message. Gifshuffle v2.0 is freeware and requires only 33kB.

JpegX is an encryption program that hides a important information inside standard JPEG image files. The image is left visually unchanged and messages are encrypted and password protected. To decrypt the message, it's need to open the JPEG file that holds it and enter the password if prompted. **JpegX** is a size of 18kB and freeware category.

Shadow is the powerful data encoder/decoder that has the ability to encode/decode everything and anything that fits on/in computer hard disk drive. It can be encoded texts, pictures, movies, music, applications, and so on. Windows is required to Shadow running and the program size is about 56kB.

Hide4PGP v2.0 is a command-line steganographic program for Windows, DOS, OS/2, and Linux that hides data within BMP, WAV, and VOC files. It is designed to be used with both PGP and Stealth, but also works well as a stand-alone program. Version 2.0 has several new features, including a new stego format which is much more robust against format conversions - only lossy compression formats will loose the hidden data. The source is also included and should compile on any platform without major problems. Hide4PGPv2.0 is size of 114kB and freeware.

V. THE HIDDEN MESSAGE EMBEDDING APPROACH IN AN IMAGE

The practical steganography implementation was executed with program which realized in Visual Basic 6 (VB6) environment. Program is very simple application without intention to demonstrate a high programming efficiency. This program is not comparable with the known steganographic tools, in mentioned sense. The significant characteristics of this program are the simple implementation, wide possibility of modification, and very simple using [6]. The program is realized in order to rich the practical approach to understanding of the fundamental processes to hidden message writing in an image.

The following image contents the hidden message: *Breza do hramot, osvetlena od sveki livčinja raga.*



Fig. 2. The JPEG image file containing hidden message

Every pixel of the above image has assigned the adequate color value. The text was embedded in the image through changing of the previous color values. The VB6 functions *SetPixel* and *GetPixel* was used for that. The approach begins with opening new forms in VB6 environment [6], [7]. It is launched a text box and assigned name and then a list box, also. These called the *Textprvi* and *Listaprva*. Further, it introduce a picture box and named as *Prvaslika*. The scalemode of this box must be set on the *pixel* and parameter *autodraw* on the *true* value. It put in program *Common Dialog* control and *Active X* control function. The image reading way was solved by oneself procedure. There are defined commands to image decoding, encoding, writing and reading.

The image was added in Design regime, properties function. During the testing procedures was used the both: a JPEG picture format and a bitmaps files. Especially is written the

program part which makes the data file from picture file. The goal of this subprogram is to convert image file in hexadecimal code date file. These hexadecimal code date file is made for pure image and steganographic image. In comparing these files is clear visible the differences between files because the hexadecimal code of steganography image contain secret information [7]. Although even a trained eye wouldn't know the difference, visually, it will change the statistical properties of the pixel values of the "before" and "after" photo. The data hexadecimal files are different, also.

	Steganography image	Pure image
0	0 FEFEFE FFFFFFFF 65793 F8F8EC F8F8F8 12	FEFEFE FFFFFFFF 65793
1	F4F4E2 F4F4F4 18	F9F9F9 F8F8F8 -65793
2	A2A299 A2A2A2 9	FFFFFF F4F4F4 -723723
3	44432B 444345 26	FFFFFF A2A2A2 -118749
4		CECDCF 444345 -9079434
	2B2A1F 2B2A2C 13	919092 2B2A2C -6710886
5	22210A 222125 27	605F63 222125 -4079166
6	201F19 201F23 10	3E3D41 201F23 -1973790
7	232217 232226 15	535256 232226 -3158064
8	393821 39383C 27	ACABAF 39383C -
9	ABAAA6 ABAAAC 6	7566195
	F9F8E8 F9F8FA 18	FCFBFD ABAAAC -
10	FCFCEF FCFCFC 13	5329233
	FCFCFB FCFCFC 1	FFFEFF F9F8FA -394757
11	F8F9E8 F8F9F7 15	F7F7F7 FCFCFC 328965
12	FDfDE9 FDFDFD 20	FCFCFC FCFCFC 0
13	F8F7F9 FDFDFD 329220	FFFFFF F8F9F7 -460295
14	FAF9E0 FAF9FB 27	
	FDFCEF FDFCFE 15	F7F8F6 FDFDFD 394503
15	FEFDEC FEFDFD 19	F8F7F9 FDFDFD 329220
16	F9F8E4 F9F8FA 22	F6F5F7 FAF9FB 263172
17	FCFBF4 FCFBFD 9	FAF9FB FDFCFE 197379
18	FFFEEB FFEFF 20	FCFBFD FEFDFD 131586
19	FBFAFA FBFAFC 2	F8F7F9 F9F8FA 65793
20	FCFBF4 FCFBFD 9	FBFAFC FCFBFD 65793
21	FCFBF4 FCFBFD 9	FCFBFD FFEFF 197378
22	FCFBF0 FCFBFD 13	F3F2F4 FBFAFC 526344
23	FCFBE2 FCFBFD 27	FAF9FB FCFBFD 131586
24	FCFBEE FCFBFD 15	FAF9FB FCFBFD 131586
25	FCFBF3 FCFBFD 10	FAF9FB FCFBFD 131586
26	FCFBE2 FCFBFD 27	FAF9FB FCFBFD 131586
27	FCFBEA FCFBFD 19	FAF9FB FCFBFD 131586
28	FCFBE7 FCFBFD 22	FAF9FB FCFBFD 131586
29		
30		

Table 1. The data hexadecimal file contents for steganographic image and pure image

The program code is written in *code window*. The user interface is designed very simple and available only with the necessary function. The user interface is shown at the figure 3.

VI. CONCLUSION

Invisible communication is very present in whole internet virtual communication today. Two important uses of data hiding in digital media are to provide proof of the copyright, and assurance of content integrity. Other applications of data hiding, such as the inclusion of augmentation data, need not be invariant to detection or removal, since these data are there for the benefit of both the author and the content consumer.

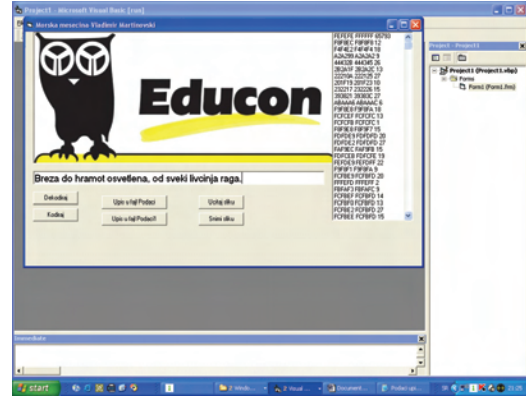


Fig 3. User interface with during embedding message

Thus, the techniques used for data hiding vary depending on the quantity of data being hidden and the required invariance of those data to manipulation [8]. Since no one method is capable of achieving all these goals, a class of processes is needed to span the range of possible applications.

The technical challenges of data hiding are formidable. Any "holes" to fill with data in a host signal, either statistical or perceptual, are likely targets for removal by lossy signal compression. The key to successful data hiding is the finding of holes that are not suitable for exploitation by compression algorithms.

REFERENCES

- [1] Ames Laboratory, Finding Computer Files Hidden In Plain Sight, May 24, 2006, <http://www.fbi.gov/cgi-bin/outside.cgi>
- [2] Gary C. Kessler, An Overview of Steganography for the Computer Forensics Examiner, Forensic Science Communications, July 2004, Volume 6, Number 3, page 1-27
- [3] Bauer, F. L. Decrypted Secrets: Methods and Maxims of Cryptology, 3rd ed. Springer-Verlag, New York, 2002.
- [4] Artz, D. Digital Steganography: Hiding data within data, IEEE Internet Computing, 2001, Vol. 3, pag. 75-80
- [5] Farid, H. Detecting steganographic messages in Digital Images, Technical Report TR2001- 412, Dartmouth College, Computer Science Department, 2001, <http://www.cs.dartmouth.edu/~farid/publications>
- [6] Julijana Mirčevski, Biljana Djokić, Nikola Popović, Moderne softverske tehnike u prepoznavanju proskribovanih kompjuterskih sadržaja, II Konferencija ZITEH, Tara, novembar 2006
- [7] Julijana Mirčevski, Biljana Djokić, Nikola Popović, The wavelet transform based software suitable for a digital contents analyze, V naučno-stručni skup "Nove tehnologije i standardi: digitalizacija nacionalne bastine", 1-3. jun, Beograd
- [8] Steganography, hiding text in images, <http://bapuli.reflectionsindia.org/article32006.htm>

SESSION CS&R

Control Systems & Robotics

Cascade Synchronization of Chaotic Systems on the Basis of Linear-Nonlinear Decomposition

Dragomir P. Chantov¹

Abstract – In this paper a method for cascade synchronization of three or more chaotic systems is proposed. The method is based on the so called Linear-Nonlinear decomposition of the systems. The advantage of this approach is in the possibility for exact analysis of the stability of the synchronization manifold, because the error systems are always linear. The results of the application of the method on a well known continuous chaotic system (the Chua system) are proposed.

Keywords – Chaotic synchronization, Cascade synchronization, Linear-Nonlinear decomposition, One-way coupling.

I. INTRODUCTION

One of the most specific and at the same time one of the most interesting fields of the nonlinear dynamics is the chaos theory. During the last 17 years (after 1990) a great effort is made in two main trends in the chaos theory - the synchronization of chaotic systems and the control of these systems [1]. The primary practical benefit of the chaotic synchronization is in the fact that this interesting phenomenon can be used in the secure communications to protect (hide) the transmitted information from unauthorised access [2].

The cascade synchronization can be considered as a sub-field of the chaos synchronization, by which three or more chaotic systems have to be synchronized by such way that they will evolve identically but at the same time chaotically in the phase space.

Different methods for synchronization of chaotic systems, respectively for cascade synchronization of such systems exist [3]. It is common that because of the fact that all chaotic systems are nonlinear systems, there is no universal synchronization method, which can always be applied and which guarantees the synchronization for a particular system. Therefore the work of searching for new approaches or new modifications of the existing ones, which overcome some of their drawbacks or limitations, continues in the last years.

In this paper the author proposes a modification of the linear-nonlinear decomposition (LND) method for synchronization of chaotic systems, by which in the Slave systems auxiliary driving signal, proportional to the difference function, is lead in. Thus the main limitation of the LND method (only one variant for coupling of the systems, which for most known chaotic systems doesn't guarantee stable synchronization) is overcome by the great variety of auxiliary couplings, which enhance the chance for achieving stable

synchronization. At the same time the proposed approach, called *modified linear-nonlinear decomposition* method (MLND), retains the main advantage of the LND method, being the possibility of exact analysis of the stability of the synchronization manifold. This is conditioned by the fact that the difference system (systems), in contrast to all other synchronization methods, is always linear.

The proposed method is previously tested on simple synchronization of two chaotic systems. In this paper the MLND method is applied for achieving serial cascade synchronization of three or more chaotic systems. The results for the Chua chaotic system are proposed.

II. MODIFIED LINEAR-NONLINEAR DECOMPOSITION METHOD FOR CASCADE CHAOTIC SYNCHRONIZATION

A. Cascade synchronization of chaotic systems

The chaotic synchronization is a phenomenon, by which two identical (most frequently) chaotic systems tune up their dynamics to each other and evolve identically in the phase space. This phenomenon can be used in the communications to secure the transmitted information [2]. For more complex communication systems the receiver and transmitter can be arrays of cascade coupled three or more chaotic systems, or there can exist one or more mediator chaotic systems between the transmitter and receiver. This fact conditions the development of the sub-field of cascade chaotic synchronization.

By the most-frequent type of cascade synchronization three or more identical chaotic systems are coupled sequentially and the proper coupling is searched to achieve stable synchronization between the systems. The first system is called *Master* system, the second one - *Slave1*, but it is also a Master system for the next system of the chain, the third system - *Slave2* and so on. The systems for the most common case of three chaotic systems can be defined as follows:

$$\text{Master} \quad \dot{\mathbf{x}} = \mathbf{f}(\mathbf{x}, t), \quad (1)$$

$$\text{Slave1} \quad \dot{\tilde{\mathbf{x}}} = \tilde{\mathbf{f}}(\tilde{\mathbf{x}}, \mathbf{x}, t), \quad (2)$$

$$\text{Slave2} \quad \dot{\tilde{\tilde{\mathbf{x}}}} = \tilde{\tilde{\mathbf{f}}}(\tilde{\tilde{\mathbf{x}}}, \tilde{\mathbf{x}}, t), \quad (3)$$

where $\mathbf{x} \in \mathfrak{R}^{n_1}$, $\tilde{\mathbf{x}} \in \mathfrak{R}^{n_2}$, $\tilde{\tilde{\mathbf{x}}} \in \mathfrak{R}^{n_3}$ and the initial conditions are $\mathbf{x}(t_0) \neq \tilde{\mathbf{x}}(t_0) \neq \tilde{\tilde{\mathbf{x}}}(t_0)$. For $n_1 = n_2 = n_3$ and

¹Dragomir P. Chantov is with the Faculty of Electrical Engineering, department of Automation, Information and Control Technics, 4 Hadji Dimitar Str., 5300 Gabrovo, Bulgaria, E-mail: dchantov@yahoo.com

$\mathbf{f}(\mathbf{x}) = \tilde{\mathbf{f}}(\tilde{\mathbf{x}}) = \tilde{\tilde{\mathbf{f}}}(\tilde{\tilde{\mathbf{x}}})$ the systems (1)-(3) are identical, which is the most common case. The system (2) is in fact a mediocre system for the synchronization of the systems (1) and (3).

For identical systems, which are considered in this paper, it is called that the three systems are synchronized, if:

$$\lim_{t \rightarrow \infty} \mathbf{e}_a(t) = 0 \quad \wedge \quad \lim_{t \rightarrow \infty} \mathbf{e}_b(t) = 0, \quad (4)$$

where

$$\mathbf{e}_a(t) = \mathbf{x}(t, t_0, \mathbf{x}(t_0)) - \tilde{\mathbf{x}}(t, t_0, \tilde{\mathbf{x}}(t_0)), \quad (5)$$

$$\mathbf{e}_b(t) = \tilde{\mathbf{x}}(t, t_0, \tilde{\mathbf{x}}(t_0)) - \tilde{\tilde{\mathbf{x}}}(t, t_0, \tilde{\tilde{\mathbf{x}}}(t_0)) \quad (6)$$

are the difference functions between the solutions of the first and the second (5), and between the second and the third (6) systems.

The eventual synchronization can also be illustrated directly by observing the difference function between the first and the third systems:

$$\mathbf{e}_c(t) = \mathbf{x}(t, t_0, \mathbf{x}(t_0)) - \tilde{\tilde{\mathbf{x}}}(t, t_0, \tilde{\tilde{\mathbf{x}}}(t_0)). \quad (7)$$

The systems (1) - (3) will be synchronized, if:

$$\lim_{t \rightarrow \infty} \mathbf{e}_c(t) = 0, \quad (8)$$

but in general it is possible the systems (1)-(2) to achieve marginal synchronization, and the systems (2)-(3) - reciprocal to the first marginal synchronization and thus the condition (8) can be fulfilled without the fulfillment of Eq. (4).

B. Modified linear-nonlinear decomposition (MLND) method for cascade chaotic synchronization

One little known decomposition method for synchronization of two identical chaotic systems is the linear-nonlinear decomposition method [4]. The essence of the method is the formal decomposition of the Master system in linear and nonlinear parts:

$$\text{Master} \quad \dot{\mathbf{x}}(t) = \mathbf{f}(\mathbf{x}, t) = \mathbf{A}\mathbf{x}(t) + \mathbf{h}(\mathbf{x}(t), t), \quad (9)$$

where $\mathbf{A}\mathbf{x}(t)$ is the linear part, and $\mathbf{h}(\mathbf{x}(t), t)$ - the nonlinear part of $\mathbf{f}(\mathbf{x}, t)$.

Then the Slave system is constructed in such way, that it is driven with the nonlinear part of Eq.(9):

$$\text{Slave} \quad \dot{\tilde{\mathbf{x}}}(t) = \tilde{\mathbf{f}}(\tilde{\mathbf{x}}, \mathbf{x}, t) = \mathbf{A}\tilde{\mathbf{x}}(t) + \mathbf{h}(\mathbf{x}(t), t). \quad (10)$$

Subtracting Eq. (10) from Eq. (9) one gets the error (difference) system:

$$\dot{\mathbf{e}}(t) = \dot{\mathbf{x}}(t) - \dot{\tilde{\mathbf{x}}}(t) = \mathbf{A}(\mathbf{x}(t) - \tilde{\mathbf{x}}(t)) = \mathbf{A}\mathbf{e}(t). \quad (11)$$

The eventual synchronization between systems (9) and (10) will be stable, if $\lim_{t \rightarrow \infty} \mathbf{e}(t) = 0$, i.e. the point $\mathbf{e}=0$ of the error system (11) is stable. Since Eq. (11) is a linear system, this

analysis is easy to made (the stability is proved from the sign of the eigenvalues of \mathbf{A}), which is the main advantage of the LND method.

However this method has one major limitation - it offers only one variant of coupling of the systems (9) and (10). There is no guarantee, that this variant will give stable synchronization. The more variants of coupling available for any synchronization method, the greater the chance for obtaining stable synchronization. The author suggests the addition of a second coupling, proportional to the error function:

$$\text{Master} \quad \dot{\mathbf{x}}(t) = \mathbf{A}\mathbf{x}(t) + \mathbf{h}(\mathbf{x}(t), t), \quad (12)$$

$$\text{Slave} \quad \dot{\tilde{\mathbf{x}}}(t) = \mathbf{A}\tilde{\mathbf{x}}(t) + \mathbf{h}(\mathbf{x}(t), t) + \alpha \mathbf{E}(\mathbf{x}(t) - \tilde{\mathbf{x}}(t)), \quad (13)$$

where α and \mathbf{E} are the coupling gain and the coupling matrix which defines the exact form of the coupling. Without loss of generality one can choose the so called standard one-way coupling, by which the connecting nonzero element is in the main diagonal of \mathbf{E} . The error system:

$$\dot{\mathbf{e}}(t) = \dot{\mathbf{x}}(t) - \dot{\tilde{\mathbf{x}}}(t) = \mathbf{A}(\mathbf{x}(t) - \tilde{\mathbf{x}}(t)) - \alpha \mathbf{E}(\mathbf{x}(t) - \tilde{\mathbf{x}}(t)) = (\mathbf{A} - \alpha \mathbf{E})\mathbf{e}(t) \quad (14)$$

is again linear and thus retaining the advantage of the LND method one can now choose between great number of coupling variants.

This concept can be applied for the cascade chaos synchronization. In this paper, without loss of generality, cascade synchronization of three identical chaotic systems is considered. Then the Master, the Slave1 and the Slave2 systems, when the modified linear-nonlinear decomposition coupling is applied, are:

$$\text{Master} \quad \dot{\mathbf{x}}(t) = \mathbf{A}\mathbf{x}(t) + \mathbf{h}(\mathbf{x}(t), t), \quad (15)$$

$$\text{Slave1} \quad \dot{\tilde{\mathbf{x}}}(t) = \mathbf{A}\tilde{\mathbf{x}}(t) + \mathbf{h}(\mathbf{x}(t), t) + \alpha_1 \mathbf{E}_1(\mathbf{x}(t) - \tilde{\mathbf{x}}(t)), \quad (16)$$

$$\text{Slave2} \quad \dot{\tilde{\tilde{\mathbf{x}}}}(t) = \mathbf{A}\tilde{\tilde{\mathbf{x}}}(t) + \mathbf{h}(\mathbf{x}(t), t) + \alpha_2 \mathbf{E}_2(\tilde{\mathbf{x}}(t) - \tilde{\tilde{\mathbf{x}}}(t)), \quad (17)$$

where in general $\alpha_1 \neq \alpha_2$ and/or $\mathbf{E}_1 \neq \mathbf{E}_2$.

The two error systems are:

$$\dot{\mathbf{e}}_a(t) = \dot{\mathbf{x}}(t) - \dot{\tilde{\mathbf{x}}}(t) = (\mathbf{A} - \alpha_1 \mathbf{E}_1)\mathbf{e}_a(t), \quad (18)$$

$$\dot{\mathbf{e}}_b(t) = \dot{\tilde{\mathbf{x}}}(t) - \dot{\tilde{\tilde{\mathbf{x}}}}(t) = (\mathbf{A} - \alpha_2 \mathbf{E}_2)\mathbf{e}_b(t). \quad (19)$$

Both systems (18) and (19) are linear, so when designing the two couplings one can easily prove the stability of each of them.

C. Application of the MLND method on particular chaotic systems

Since most of the known chaotic systems are continuous, some 75% of them being of third order, here the results of applying the modified linear-nonlinear decomposition method

for cascade synchronization of one of the well known third-order systems are presented.

The model of the Chua's chaotic electronic circuit is described with the following equations:

$$\begin{aligned} \dot{x}_1 &= \sigma[x_2 - (1+b)x_1 - f(x_1)], \\ \dot{x}_2 &= x_1 - x_2 + x_3, \\ \dot{x}_3 &= -\beta x_2, \end{aligned} \quad (20)$$

where $\sigma = 10$, $\beta = 14.87$, $b = -0.68$. The only nonlinearity is $f(x_1) = bx_1 + \frac{a-b}{2}(|x_1+1| - |x_1-1|)$ with $a = -1.27$.

The typical chaotic attractor of the system is shown in Fig.1. The initial conditions are $\mathbf{x}_0 = [0.1 \ 0.1 \ 0]^T$.

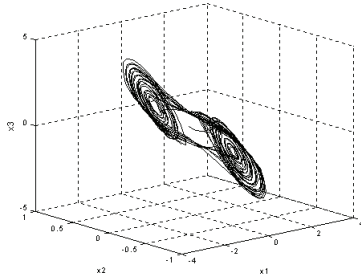


Fig.1. Chua's attractor

If Eq. (20) is considered as a Master system, it can be decomposed in the form of Eq. (9), where:

$$\mathbf{A} = \begin{bmatrix} -\sigma(1+b) & \sigma & 0 \\ 1 & -1 & 1 \\ 0 & -\beta & 0 \end{bmatrix}, \mathbf{h}(\mathbf{x}(t), t) = f(x_1). \quad (21)$$

Two of the eigenvalues of \mathbf{A} are positive - $\lambda_1 = -4.7$, $\lambda_{2,3} = 0.2 \pm 3.2j$ and the synchronization manifold will be unstable, i.e. the basic LND method cannot be applied neither for plain nor for cascade synchronization.

One of the variants of the MLND method (15)-(17) will be shown. Let the Master system is described with Eq. (12) and the two Slave systems are constructed as follows:

$$\begin{aligned} \dot{\tilde{x}}_1 &= \alpha[\tilde{x}_2 - (1+b)\tilde{x}_1 - \underline{f_{nl}}(x_1)], \\ \text{Slave1 } \dot{\tilde{x}}_2 &= \tilde{x}_1 - \tilde{x}_2 + \tilde{x}_3 + \underline{\alpha_1(x_2 - \tilde{x}_2)}, \\ \dot{\tilde{x}}_3 &= -\beta \tilde{x}_2. \end{aligned} \quad (22)$$

$$\begin{aligned} \dot{\tilde{x}}_1 &= \alpha[\tilde{x}_2 - (1+b)\tilde{x}_1 - \underline{f_{nl}}(x_1)] + \underline{\alpha_2(\tilde{x}_1 - \tilde{\tilde{x}}_1)}, \\ \text{Slave2 } \dot{\tilde{x}}_2 &= \tilde{\tilde{x}}_1 - \tilde{\tilde{x}}_2 + \tilde{\tilde{x}}_3, \\ \dot{\tilde{x}}_3 &= -\beta \tilde{\tilde{x}}_2. \end{aligned} \quad (23)$$

The additional coupling between Master and Slave1 systems is obtained by applying the second variant of the standard one-way coupling (OW2) with $\alpha_1 = 10$. The

additional coupling between the Slave1 and Slave2 systems is OW1 with $\alpha_2 = 10$.

The matrixes of the linear error systems (18) and (19) for the chosen coupling schemes are:

$$(\mathbf{A} - \alpha_1 \mathbf{E}_1) = \begin{bmatrix} -\sigma(1+b) & \sigma & 0 \\ 1 & -1 - \underline{\alpha_1} & 1 \\ 0 & -\beta & 0 \end{bmatrix}, \quad (24)$$

$$(\mathbf{A} - \alpha_2 \mathbf{E}_2) = \begin{bmatrix} -\sigma(1+b) - \underline{\alpha_2} & \sigma & 0 \\ 1 & -1 & 1 \\ 0 & -\beta & 0 \end{bmatrix}, \quad (25)$$

with the corresponding eigenvalues:

$$eig(\mathbf{A} - \alpha_1 \mathbf{E}_1) = -10.9, -1.6 \pm 1.3j, \quad (26)$$

$$eig(\mathbf{A} - \alpha_2 \mathbf{E}_2) = -13.9, -0.1 \pm 3.8j. \quad (27)$$

Since all real parts of the eigenvalues (26) and (27) are negative, the necessary conditions for the synchronization stability between each pair of systems are fulfilled. The simulation with Matlab/Simulink confirms the synchronization. The errors $e_{ia} = x_i - \tilde{x}_i$ and $e_{ib} = \tilde{x}_i - \tilde{\tilde{x}}_i$ are shown on Fig.2.

After a period of approximately 30 seconds the three systems, started with different initial conditions each, are completely synchronized. At the same time the chaotic nature of the systems' evolution is retained.

One can confirm the cascade synchronization also by observing the error functions between the Master and the Slave2 systems - $e_{ic} = x_i - \tilde{\tilde{x}}_i$, or by viewing the evolution in the state space (e_{1c}, e_{2c}, e_{3c}) . The latter is shown on Fig.3. After the transient period the error system between the first and the third system is stabilized into the origin (0,0,0), i.e. there is identical synchronization between the first and the third system. Generally it is arguable if this automatically means there is also identical synchronization between the first and the second, and between the second and the third chaotic systems. In some cases it is possible the first pair of systems to exhibit marginal synchronization, where the error after achieving synchronization is a nonzero constant, which depends on the initial conditions. Very unlikely, but not impossible in general, the second pair of chaotic systems can also exhibit marginal synchronization, where the error stabilizes in the same constant with different sign. Then the Master and the Slave2 systems will exhibit identical synchronization without the presence of identical synchronization between Master and Slave1, and between the Slave1 and Slave2 systems.

The influence of the coupling gain α_i is also investigated. By OW1 and OW2 couplings for the Chua system the increasing of α_i leads to decreasing in the transient process, e.g. for $\alpha_1 = \alpha_2 = 20$ the cascade synchronization is almost two times faster. However the conclusion about the influence of the coupling gain cannot be made in general. For other

chaotic systems or even for the OW3 coupling for the Chua system, the increasing of α_i leads to the loss of synchronization. It is also not recommendable to choose very large gain constant, because this will increase the influence of the eventual noise which is always present in the synchronization channel and therefore is included by the couplings in the Slave systems.

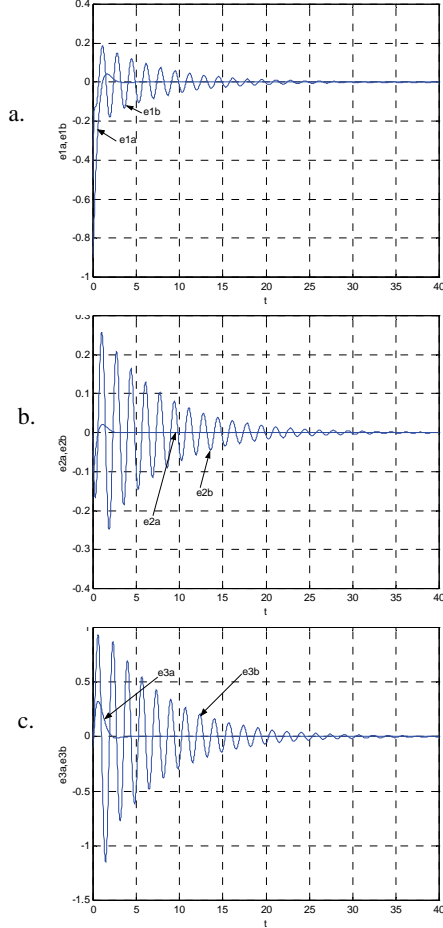


Fig.2. Error functions: a - e_{1a}, e_{1b} ; b - e_{2a}, e_{2b} ; c - e_{3a}, e_{3b}

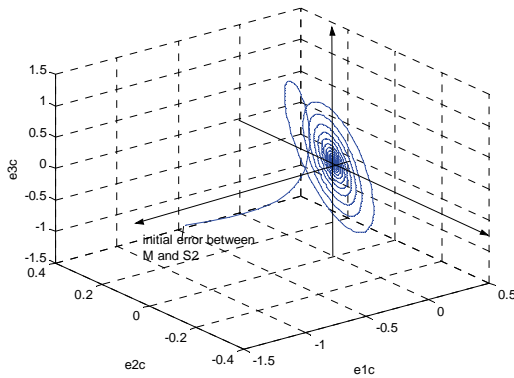


Fig.3. State space (e_{1c}, e_{2c}, e_{3c})

The results for the other possible variants of the MLND method for the Chua system are generalized in Table I. The columns show the additional coupling between the Master and

the Slave 1 systems, the rows show the additional coupling between the Slave 1 and the Slave 2 systems. The coupling constants for all OW1 and OW2 couplings are $\alpha_i = 10$. The coupling constant for the OW3 couplings is $\alpha_i = 2$, because for greater value the error system becomes unstable. The length of the transient before complete identical synchronization between the three systems in simulation seconds is shown. One can see that as long as the basic LND method does not work for the Chua system, all nine possible couplings of the proposed MLND method guarantee stable synchronization. This conclusion however cannot be generalized for all chaotic systems, since each such system as a nonlinear system have its own properties and until now no universal method for chaotic synchronization is proposed.

TABLE I
RESULTS FOR DIFFERENT COUPLINGS

M-S1	OW1	OW2	OW3
S1-S2			
OW1	45s	30s	28s
OW2	32s	5s	9s
OW3	30s	7s	10s

The MLND method is also tested on other chaotic systems. For example for the Rossler system the LND method again does not yield stable synchronization while the OW1 and OW2 additional couplings of the MLND method with properly chosen coupling gains stabilize the error systems and the three Rossler systems exhibit identical synchronization. However the OW3 additional coupling for the Rossler system cannot stabilize the error system for all possible coupling gains, so synchronization is not possible.

III. CONCLUSION

In this paper a new modification of the linear-nonlinear decomposition method was presented by which the standard method is combined with additional coupling, proportional to the error function. Thus retaining the main advantage of the LND method, being the possibility for exact stability analysis, one can choose between different types of couplings so the possibility of finding proper synchronization scheme increases.

REFERENCES

- [1] Boccaletti, S., J. Kurths, G. Osipov, D. Valladares, C. Zhou. The synchronization of chaotic systems. Physics Reports 366 (2002), pp.1-101.
- [2] Carroll, T. Noise-robust synchronized chaotic communications. IEEE Transactions on Circuits and Systems-I, Vol.48, No.12, 2001, pp.1519-1522.
- [3] Pecora, L., T. Carroll, G. Johnson, D. Mar, J. Heagy. Fundamentals of synchronization in chaotic systems, concepts, and applications. Chaos 7(4), 1997, pp.520-543.
- [4] Yu, H., L. Yanzhu. Chaotic synchronization based on stability criterion of linear systems. Physics Letters A preprint (2003), pp.1-7.

Sensorless Vector Control of Induction Motors

Emil Y. Marinov¹, Kosta D. Lutskanov² and Zhivko S. Zhekov³

Abstract – In this paper, two structures based on the partial induction motor model and optimization procedures for speed and flux rotor of the motor are overviewed. Simulation researches of sensorless direct vector control of induction motors using the proposed estimators are accomplished. The researches demonstrate their sufficient performance during motor parameter (rotor resistance) variations, disturbance and wide range variable references input control signals.

Keywords – Sensorless vector control, Induction motor, Flux estimation, Speed estimation.

I. INTRODUCTION

The interest for sensorless induction motor drives has been constantly rising during the last decade. They fill the middle ground between high-performance closed-loop control and simpler open-loop (V/Hz) control of induction motor (IM). The advantages of using these systems are: reduced hardware complexity, reduced size, no sensor cable, increased reliability, less maintenance requirements, lower cost, better noise immunity. Most sensorless AC drives are based on flux vector methods, hence loosely called sensorless vector (SV) control. There are many models of sensorless speed controllers described in the literature based on the extended Kalman filter theory [1,2], linear state Luenberger observer [2,3], neural network [3] and others [4-7]. Basic problem in the area of sensorless control is the estimation of the low speed. Here two structures based on the partial induction motor model and optimization procedures for speed estimation and for flux rotor of the motor, are proposed.

The paper is organized as follows: Section II describes the induction motor model, in Section III are described the proposed structure estimators, Section IV investigates the simulation testing of sensorless vector drive, and Section V summarizes the conclusion about results.

II. INDUCTION MOTOR MODEL

The equations for electrical equilibrium of voltages of the IM with cage rotor in the stationary $\alpha - \beta$ frame, introduced in

a complex form are:

$$\bar{u}_s = R_s \bar{i}_s + \frac{d\bar{\Psi}_s}{dt} \quad (1)$$

$$0 = R_r \bar{i}_r + \frac{d\bar{\Psi}_r}{dt} - j p_p \omega_r \bar{\Psi}_r \quad (2)$$

$$\bar{\Psi}_s = L_s \bar{i}_s + L_m \bar{i}_r \quad (3)$$

$$\bar{\Psi}_r = L_m \bar{i}_s + L_r \bar{i}_r \quad (4)$$

where: $\bar{u}_s, \bar{i}_s, \bar{\Psi}_s, \bar{i}_r, \bar{\Psi}_r$ are representation vectors of the stator variables (voltage, current and flux) and rotor variables (current and flux); ω_r – rotor angular speed; R_s, R_r – stator and rotor phase resistance; L_s, L_r stator and rotor phase inductance; L_m – mutual inductance; p_p – number of the pair poles. For each vector \bar{x} (where x means voltage, current, flux) is valid $\bar{x} = x_\alpha + j x_\beta$ where x_α, x_β are representation vector projections on α and β axes.

After elimination of $\bar{\Psi}_s$ and \bar{i}_r from (1÷4), it is obtained:

$$\bar{u}_s = R_e (T_e p + 1) \bar{i}_s - \frac{R_r L_m}{L_r} \bar{\Psi}_r + j \frac{L_m}{L_r} p_p \omega_r \bar{\Psi}_r \quad (5)$$

$$\bar{i}_s = \frac{1}{L_m} (T_r p + 1) \bar{\Psi}_r - j \frac{T_r}{L_m} p_p \omega_r \bar{\Psi}_r \quad (6)$$

where:

$$R_e = R_s + R_r \frac{L_m^2}{L_r^2}; L_e = \frac{L_s L_r - L_m^2}{L_r}; T_e = \frac{L_e}{R_e}; T_r = \frac{L_r}{R_r}; p = \frac{d}{dt}.$$

For the purpose of vector control system synthesis, electromechanical processes in the IM and the mechanism (for one-mass mechanical part) in orthogonal coordinate system $d-q$, orientated on the rotor flux vector are described by the following equations:

$$u_{sd} = R_e (T_e p + 1) i_{sd} - L_e \omega_g i_{sq} - \frac{R_r L_m}{L_r^2} \Psi_r$$

$$u_{sq} = R_e (T_e p + 1) i_{sq} + L_e \omega_g i_{sd} + \frac{L_m}{L_r} p_p \omega_r \Psi_r$$

$$i_{sd} = \frac{1}{L_m} (T_r p + 1) \Psi_r$$

$$\omega_g = p_p \omega_r + \frac{R_r L_m}{L_r} \frac{i_{sq}}{\Psi_r}$$

$$M_e = k_m \Psi_r i_{sq}$$

$$M_e - M_c = J p \omega_r \quad (7)$$

¹Emil Y. Marinov, Technical University of Varna, Faculty of Computing and Automation, Studentska 1, 9010 Varna, Bulgaria, e-mail: marinov52@mail.bg

²Kosta D. Lutskanov, Technical University of Varna, Faculty of Computing and Automation, Studentska 1, 9010 Varna, Bulgaria, e-mail: lutskanov@abv.bg

³Zhivko S. Zhekov, Technical University of Varna, Faculty of Computing and Automation, Studentska 1, 9010 Varna, Bulgaria, e-mail: fitter@abv.bg

where: $i_{1q}, i_{1d}, u_{1q}, u_{1d}$ - active and excite components of stator current and stator voltage, ω_g - co-ordinate system speed, M_e, M_c - electromagnetic and resistant moments, J - moment of inertia, $k_m = (3p_p L_m / 2L_r) \hat{\Psi}_r$.

III. SPEED END FLUX ESTIMATION

When designing a sensorless direct vector control of IM, there are a few considerable problems: determination of rotor speed, transitory position and magnitude of the support vector, which is most often the rotor flux vector. Two variants for dealing with this problem are proposed. They are based on IM partial model and the optimization procedure us.

A. Estimator 1

Estimator 1 is composed of two partial models of the motor (Model 1, Model 2) and optimization procedure (OP) – fig.1 (with thick line are shown vector variables and with thin line – scalar variables). Model 1 estimates the rotor flux $\hat{\Psi}_r$ and forms $e^{j\theta}$. Model 2 gives estimation of the stator current \hat{i}_s .

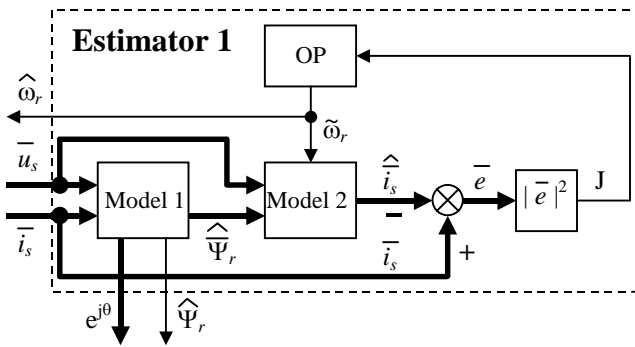


Fig. 1. Structural scheme of Estimator 1

Model 1 is described by the following equations:

$$\hat{\Psi}_r = \frac{L_r \bar{u}_s - R_s \bar{i}_s}{L_m p} - \frac{L_s L_r - L_m^2}{L_m} \bar{i}_s; \quad (8)$$

$$\hat{\Psi}_r = |\hat{\Psi}_r| = \sqrt{\hat{\Psi}_{r\alpha}^2 + \hat{\Psi}_{r\beta}^2}; \quad (9)$$

$$\theta = \arctg \frac{\hat{\Psi}_{r\beta}}{\hat{\Psi}_{r\alpha}}, \quad (10)$$

where θ is the angle between vector $\hat{\Psi}_r$ and axis α .

The equation (8) is a result of (1) after expressing $\bar{\Psi}_s$ by trough $\bar{\Psi}_r$ and \bar{i}_s .

The estimated value of the stator current \hat{i}_s is obtained from Model 2 on the basis of equation (5), as for the purpose is used the measured stator voltage and obtained in Model 1 rotor flux:

$$\hat{i}_s = \frac{\bar{u}_s + \frac{R_r L_m}{L_r^2} \hat{\Psi}_r - j \frac{L_m}{L_r} p_p \omega_r \hat{\Psi}_r}{R_e (T_e p + 1)} \quad (11)$$

The Optimization criterion is:

$$J = |\bar{e}|^2 = \left| \bar{i}_s - \hat{i}_s \right|^2 \quad (12)$$

Through OP $\tilde{\omega}_r$ varies for each sampling period so that the criterion J be minimized and the estimation of the rotor speed $\hat{\omega}_r$ is obtained:

$$\hat{\omega}_r = \tilde{\omega}_r \text{ in case of } J = \min \quad (13)$$

In the simplest case OP may be realized by method of consecutively searching in definite interval. For “ k ” tact $\tilde{\omega}_r(k)$ will be changed in the interval $\hat{\omega}_r(k-1) \pm \Delta\omega_{\max}$.

The determination of $\Delta\omega_{\max}$ is realized on the basis of following reasons. When working with constant flux ($\Psi_r = \text{const}$) and in the presence of current restriction, the maximum value of the electromagnetic torque is $M_{e\max} = k_m \Psi_r I_{sq\max}$, where $I_{sq\max}$ is the maximum permissible value of the active component of stator current with referent current restriction. The result for maximum dynamical torque is $M_{d\max} = |M_{e\max}| + |M_{c\max}| = |M_{e\max}| + M_n$, where M_n is nominal motor torque. From equation of motion (7) is obtained maximum possible change of speed:

$$\Delta\omega_{\max} = \frac{M_{d\max} T_0}{J_{\min}} \quad (14)$$

where T_0 – sampling period, $J_{\min} = J_m$, J_m – inertia moment of motor.

B. Estimator 2

Estimator 2 is composed by one partial model of IM (Model 3) and optimization procedure – fig. 2. The model gives simultaneously estimations for the rotor flux $\hat{\Psi}_r$ and stator current \hat{i}_s and forms $e^{j\theta}$.

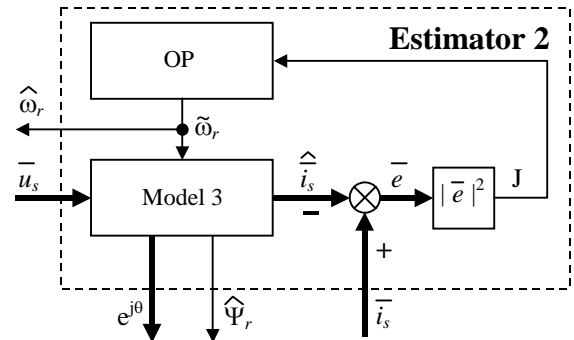


Fig. 2. Structural scheme of Estimator 2

Model 3 is described by equations (5) and (6). The optimization procedure is the same as this one, described in the first variant. Optimization criterion is defined by (12) and the estimation of the rotor speed $\hat{\omega}_r$ is obtained according to (13).

On the basis of the proposed speed and rotor flux estimators is obtained the direct vector control system of the IM – fig. 3. In the figure are used the following symbols: FC – flux controller; SC – speed controller; CCB and CCA – controllers of the active and excite components of the stator current; BC – block for compensation; abc/αβ, αβ/dq, dq/αβ, αβ/abc – coordinate transformers, PC – power converter, IM – induction motor, M – mechanism; ω_{ref} , Ψ_{ref} - referent values of speed and rotor flux; \bar{u}_{dq}^* , $\bar{u}_{\alpha\beta}^*$, \bar{u}_{abc}^* - control signals.

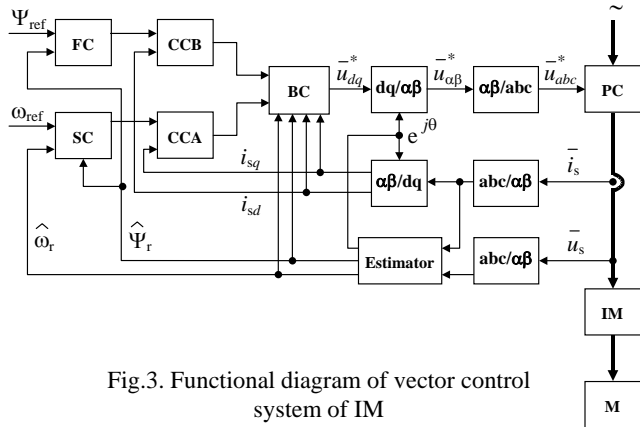


Fig.3. Functional diagram of vector control system of IM

IV. SIMULATION RESEARCH AND REZULTS

The proposed control algorithm has been tested using a 5 kW induction motor with rated torques 36.224Nm and nominal current $I_{sn}=11.2A$. In the simulation model coordinate transformations, non-linear and discrete PC properties are rendered in account. The researches are carried out using variable stator and rotor resistance, without/with noise in the input signals.

A part of the simulation research of the direct vector control system is shown on fig. 4÷7. On the fig.4 and fig.5 is represented the system performance using Estimator 1 and on the fig.6 and fig.7 - using Estimator 2.

Motor speed and rotor flux are compared with the ω_{ref} and Ψ_{ref} (fig.4a÷7a) and with the estimations $\hat{\omega}_r$ and $\hat{\Psi}_r$, derived from the estimators (fig. 4b,c,d,e÷7b,c,d,e). Fig.4,6 are obtained bay using the basis value of the motor electric parameters in absence of noise, fig.5,7 with $R_s=1.2R_{skat}$ and $R_r=1.2R_{rkat}$ (R_{skat} , R_{rkat} basis values of R_s and R_r) and in case of noise addition to the stator currents. The noise addition is simulated by additive white noise, ratio noise/signal=0.05. In all cases the estimators work with the basis values of the motor parameters.

The resistive moment M_c is accepted to be reactive and it changes in range of $(0.1\div 1)M_n$ as follows: $M_c=0.1M_n$ for $t\leq 0.2s$; $M_c=0.5M_n$ for $0.2 < t \leq 1s$; $M_c=M_n$ for $1 < t \leq 1.6s$; $M_c=0.5M_n$ for $1 < t \leq 2s$. Where differences between motor's resistances and basis values exist, a static fault comes out.

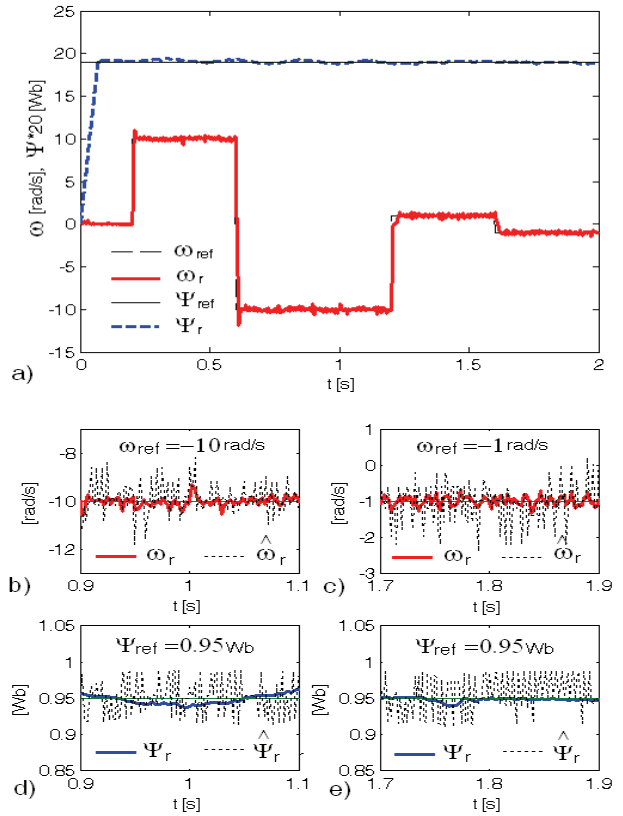


Fig.4. Low speeds in absence of noise and $R_s=R_{skat}$ и $R_r=R_{rkat}$ (with Estimator 1)

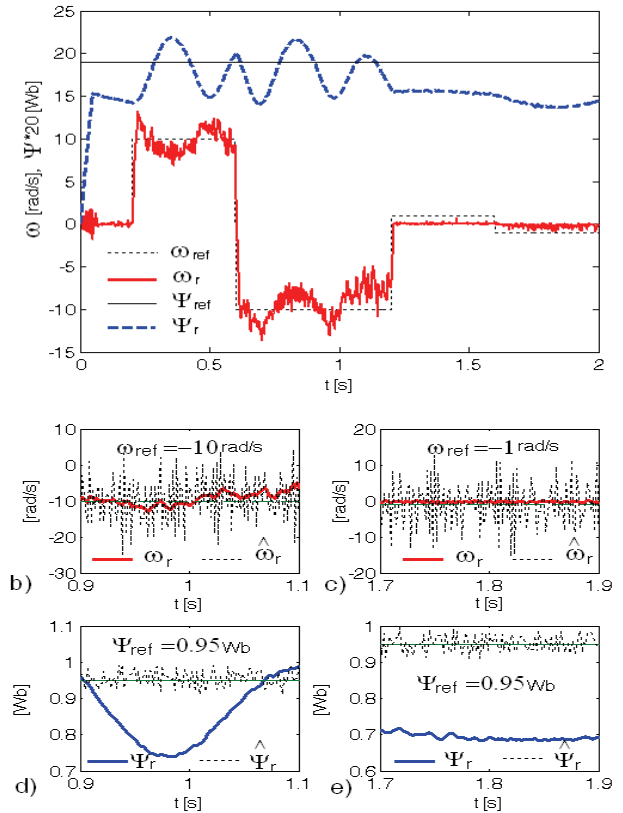


Fig.5. Low speeds in presence of noise and $R_s=1.2R_{skat}$ и $R_r=1.2R_{rkat}$ (with Estimator 1)

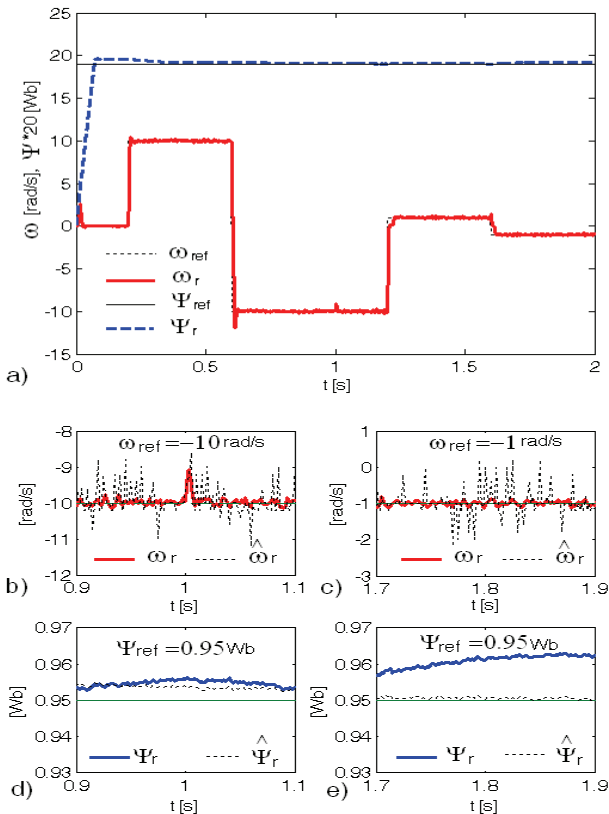


Fig.6. Low speeds in absence of noise and $R_s=R_{skat}$ и $R_r=R_{rkat}$ (with Estimator 2)

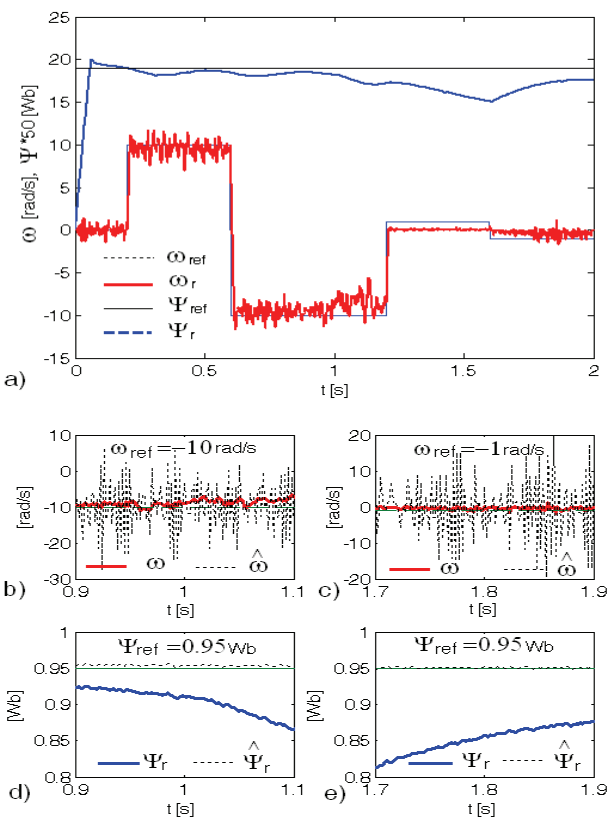


Fig.7. Low speeds in presence of noise and $R_s=1.2R_{skat}$ и $R_r=1.2R_{rkat}$ (with Estimator 2)

When there is difference between motor resistance and their basis values, a static fault occurs. This fault is proportional of the load and of the diversion of the real resistances from the basis values.

The researches accomplished confirm the capability of the system to work with both estimators. The second estimator variant is more robust regarding the parametric and signal disturbances. It makes a filtration of the estimated values of the rotor flux end for this reason it is actually a smooth curve. That is why the estimator from figure 2 is preferable.

V. CONCLUSION

Two structures using partial induction motor model and optimization procedures of speed and rotor flux estimation are proposed. On this basis two structures of direct vector control of IM drive are formed.

Simulation researches are done, confirming the efficiency of the proposed estimators and the vector control systems schemes. The research is carried through under the following conditions: wide range of speed control, variations of motor parameters (rotor end stator resistances), noise implemented in the signals of phase stator currents.

The researches demonstrate sufficient performance of sensorless IM drive control.

REFERENCES

- [1] B. Akin, U. Orguner, A. Ersak and M. Ehsani, "Simple Derivative-Free Nonlinear State Observer for Sensorless AC Drives" Mechatronics, IEEE/ASME Transactions on, Vol. 11, Issue: 5, pp. 634- 643, Oct. 2006.
- [2] V. Bostan, M. Cuiubus, C. Has, and R. Magureanu, "High performance sensorless solutions for induction motor control", Power Electronics Specialist Conference, 2003. PESC '03. 2003 IEEE 34th Annual, Vol. 2, pp. 556 – 561, June 2003.
- [3] M. Cuiubus, V. Bostan, S. Ambrosii, C. Ilas and R. Magureanu, "Luenberger, Kalman and Neural Network Observers for Sensorless Induction Motor Control", Power Electronics and Motion Control Conference, 2000. Proceedings. IPEMC 2000. The Third International, Volume 3, pp. 1256 - 1261, 2000.
- [4] H. Zidan, S. Fujii, T. Hanamoto and T. Tsuji, "A Simple Sensorless Vector Control System for Variable Speed Induction Motor Drives", T.IEE, Japan, Vol. 120-D, No.10, pp.1165-1170, 2000
- [5] G. Edelbaher, K. Jezernik and E. Urlep, "Low-speed Sensorless Control of Induction Machine," Trans. on Industrial Electronics, vol. 53, no. 1, pp. 120- 129, Feb 2006.
- [6] T. Chun, M. Choi and B. Bose, "A Novel Startup Scheme of Stator Flux Oriented Vector Controlled Induction Motor Drive without Torque Jerk", IEEE Transactions on industry applications, Vol. 39, No 3, pp.776-782, May/June, 2003.
- [7] H. Madadi Kojabadi "Simulation and Experimental Studies of Model Reference Adaptive System for Sensorless Induction Motor Drive", Simulation Modelling Practice and Theory, Vol. 13, Issue 6, pp. 451-464, Sep. 2005

Genetic Algorithms applied in Parameter Optimization of Cascade Connected Systems

Bratislav Danković¹, Dragan Antić², Zoran Jovanović³ and Marko Milojković⁴

Abstract – In this paper, rubber cooling system in tyre industry, as a represent of complex, nonlinear, stochastic, cascade-connected systems, is considered. A simple genetic algorithm has been applied in adaptive and optimal control of the system.

Keywords - Genetic algorithms, Nonlinear system, Parameter optimization

I. INTRODUCTION

In every tyre factory in the world, there are one or more tyre thread cooling systems. That tyre thread is used to form external (stripped) part of a tyre. It's estimated that there are about 25000 systems, like that, all over the world, mostly in China, India, USA and Brasil. These systems consist of a large number (4-24) of cascade-connected transporters along which the tyre thread moves, passing from one transporter to another. Thereby, the rubber is cooled by the water which flows in opposite direction. The velocities of individual transporters are adjusted using local controllers which determine the velocity of the next transporter according to the length of rubber between two consecutive transporters. In this manner, a dynamic system with a lot of cascades is obtained (see Fig.1.).

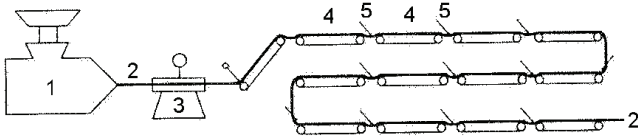


Fig. 1. Cascade system for the rubber strip transportation (1-extruder 2-rubber strip 3-balance 4-transporters 5-transitions)

Following properties of these systems impact dynamics, stability and system quality:

- Tyre thread accumulates at transition places (points 5 at Fig. 1), because of integration of velocities difference.
- Nonlinear dependencies are formed at the cascade transitions, between transporters.

¹ Bratislav Dankovic is with the Faculty of Electronic Engineering, Aleksandra Medvedeva 14, 18000 Nis, Serbia E-mail: dankovic@elfak.ni.ac.yu

² Dragan Antic is with the Faculty of Electronic Engineering, Aleksandra Medvedeva 14, 18000 Nis, Serbia, E-mail: dantic@elfak.ni.ac.yu

³ Zoran Jovanovic is with the Faculty of Electronic Engineering, Aleksandra Medvedeva 14, 18000 Nis, Serbia, E-mail: zoki@elfak.ni.ac.yu

⁴ Marko Milojkovic is with the Faculty of Electronic Engineering, Aleksandra Medvedeva 14, 18000 Nis, Serbia, E-mail: milojkovic@elfak.ni.ac.yu

- During the tyre thread movement along a transporter, rubber runs cold and contracts. Because of that, velocity at transporter's end is smaller than velocity at transporter's beginning, with contraction coefficient μ . Coefficient μ is stochastic because it depends on rubber quality and environment temperature which are stochastic parameters. Influence of stochastic parameters μ_i on cascade systems stability is analyzed in [1].

Due to cascade structure and nonlinearities, the system is prone to oscillations [2],[3]. Under certain conditions, deterministic chaos may appear in the system [4], [5]. Because of the stated properties, the referred system is very complex and difficult to control [6]. The only way for successful control is local control of transporters velocities at every transition (points 5 at Fig. 1) and also a compensation for the entire system using adjustable parameters. Until now, these parameters have been adjusted manually. This paper presents a new method for adjusting parameters using genetic algorithms with optimal control in the sense of the mean square error.

II. CASCADE CONNECTED SYSTEM FOR THE RUBBER STRIP COOLING

Figure 1. shows a cascade connected transporters for the rubber strip cooling. This system in a real factory is given at figure 2.



Fig. 2. Rubber cooling system in tyre industry "Tigar-Michelline", Serbia

The rubber strip comes from extruder (point 1 at Fig. 1.), pass through the balance (point 3 at Fig. 1.) and goes to the cooling system. It's necessary to cool down the rubber strip to the room temperature. When rubber runs through the cooling system, it is being cooled and contracts with contraction coefficient $\mu < 1$. During that contraction, rubber velocities at transporter's ends are not equal to the transporter's velocities,

producing the effect of rubber slipping relatively to transporter.

The length change of the rubber strip between two transporters is described with the following equations:

$$\frac{dl_i}{dt} = V_{g,i-1}^{(2)} - V_{g,i}^{(1)}, i=1,2,\dots,n \quad (1)$$

$$V_{g,i-1}^{(2)} = V_{i-1}, \quad V_{g,i}^{(1)} = \frac{1}{\mu} V_i \quad (2)$$

$$\frac{dl_i}{dt} = V_{i-1} - \frac{1}{\mu} V_i \quad (3)$$

$$\Delta l_i = \frac{1}{s} \left(V_{i-1} - \frac{1}{\mu_i} V_i \right) \quad (4)$$

where:

l_i is the length of rubber strip between i -th and $(i+1)$ -th transporter,

$V_{g,i-1}^{(2)}$ is rubber velocity at the end of the $(i-1)$ -th transporter,

$V_{g,i}^{(1)}$ is rubber velocity at the beginning of the i -th transporter,

n is the number of transporters

Δl_i is length change of rubber strip between two consecutive transporters,

V_{i-1} is the velocity of the $(i-1)$ -th transporter,

V_i is the velocity of the i -th transporter,

μ_i is the rubber compression coefficient for the i -th transporter.

Figure 3. shows a transition between two transporters. To regulate transporter's velocities, it's necessarily to measure the lengths of rubber between transporters (Δl_i). These measurements are being done by special sensors (potentiometers – P at Fig. 3.). Measurer's (potentiometer) angle β_i satisfies the following relation:

$$\beta_i = \Phi(\Delta l_i) \quad (5)$$

where Φ represents nonlinear dependency.

The value of β_i is between 0 and 90 degrees.

Potentiometer voltage is:

$$u_i = K_p \beta_i \quad (6)$$

where K_p is the potentiometer coefficient [V/rad].

Potentiometer's voltage is being amplified and, through tiristor's regulators, the velocities of drive motors are being controlled. Dynamics of i -th transporter with controller and drive motor can be described with following well known equation:

$$T_1 T_2 \frac{dV_i^2}{dt^2} + (T_1 + T_2) \frac{dV_i}{dt} + V_i = u_i \quad (7)$$

where T_1 and T_2 are mechanical and electrical time constants of electromechanical drive.

According to (7), the transfer function for i -th transporter has the following form:

$$W(s) = \frac{V_i(s)}{u_i(s)} = \frac{1}{T_1 T_2 s^2 + (T_1 + T_2) s + 1} \quad (8)$$

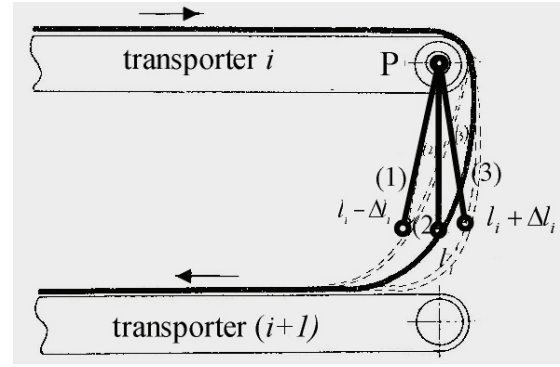


Fig. 3. Measuring the length of the rubber between transporters

Using stated equations (1)-(8), the block diagram of the entire system, given at Figure 4, is obtained.

Integration of velocity between transporters can cause statical error when parameter μ changes (change of used rubber quality or change of ambience temperature). At fig. 3, middle position of the sensor (position (2)) correspondes to normal operating. If μ magnifies, sensor comes in positon (1) and statical error $-\Delta l_i$ occures (the rubber streches). If μ decreases, sensor comes to positon (3) and statical error $+\Delta l_i$ occures (the rubber accumulates). Compensational potentiometers (K_{pi} at fig. 4) are introduced in order to compensate statical errors, so their adjustment bring system back to normal operating (position (2) at fig. 3). Today, these parameters are being adjusted manually (manual system adaptation). This paper presents a new method, based on genetic algorithms for automatic adaptation and optimization of disscused systems.

III. GENETIC ALGORITHMS

The principles of genetic algorithms were first published by Holland in 1962 [7]. Genetic algorithms are optimization techniques based on simulating the phenomena that takes place in the evolution of species and adapting it to an optimization problem.

Genetic algorithms have been used in many areas such as function optimization, image processing, system identification... They have demonstrated very good performances as global optimizers in many types of applications [8], [9].

A brief description of genetic algorithms is given below.

Encoding: The first step in building a genetic algorithm is to choose the parameters of interest in the search space and to encode and concatenate them in order to form a string or chromosome. Thus, each string represents a possible solution to the problem. The genetic algorithm works with a set of strings, called the population. This population then evolves

There are four parameters of interest which should be adjusted by genetic algorithm: K_{r1} , K_{r2} , K_{r3} and K_{r4} . They are encoded binary with five bits each (32 values). In this

way, 20 bits chromosome is obtained. Initial population is generated randomly with population size of 10.

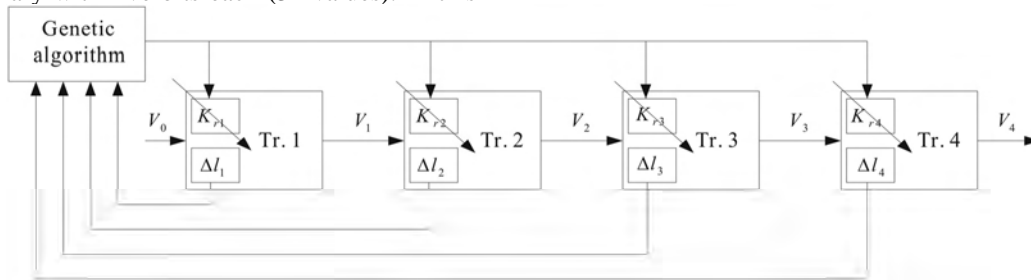


Fig. 7. Block diagram of the laboratory system

Fitness function is the sum of the mean square errors at all transporters (9). Smaller fitness function means lower error and, therefore, better chromosome.

$$f = \sum_{i=1}^4 (\Delta I_i)^2 \quad (9)$$

Selection method is "roulette wheel" with the fittest individual carried forward the next generation in every evolution cycle. Genetic algorithm was performed for 30 generations. To perform the genetic algorithm, Matlab was used in conjunction with the SIMULINK and GAOT toolbox, which is open-source code.

The results for consecutive generations are shown in figure 8. The full line is the fitness function of the best individual, and the dotted line is average fitness function for entire generation. Algorithm converges very fast to the set of K_{ri} parameters which are optimal for the system and give the lowest fitness function.

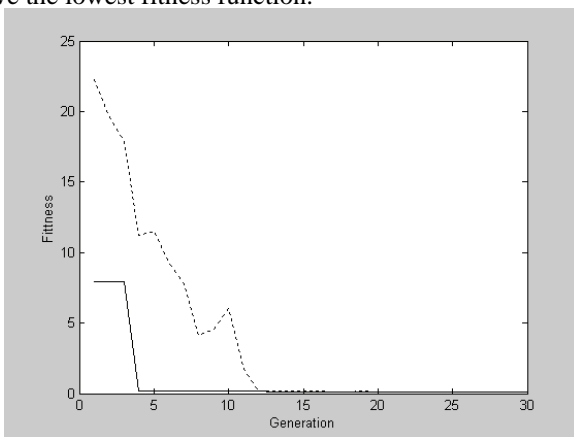


Fig. 8. The best and the average fitness function

V. CONCLUSION

This paper presents the new method for parameter optimization in systems for rubber strip cooling. In this purpose, genetic algorithm is used. Parameters are being adjusted in discrete-time intervals and that gives good results for inert systems like the one considered in this paper. The gained results are better than those which are obtained by classical methods in the sense of better speed and adaptation accuracy.

REFERENCES

- [1] B. Dankovic, Z. Jovanovic, "On the Reliability of Discrete-Time Control Systems with Random Parameters", *Quality Technology and Quantitative Management*, Vol. 2, No 1, March 2005.
- [2] B. Dankovic, "On the Oscilations in the automated cascade systems for rubber thrades transport", Jurema, Zagreb, 1989.
- [3] D. Trajkovic, B. Dankovic, "Analyzing, Modeling and Simulation of the cascade Connected Transporters in Tyre Industry using Signal and Bond Graphs", *Machine Dynamics Problems*, Vol. 29, No3, Warsaw University, 2005.
- [4] B. Dankovic, M. Stankovic, B. Vidojkovic, "On the Appearance of Chaos in the Automatic Control Cascade Systems", *Proc. 7th Symposium of Mathematics and its Applications*, Univ. of Timisoara
- [5] B. Dankovic, B. Vidojkovic, "On the Chaos in Cascade Systems for Rubber Strip Transportation", *Proc. HM 2002, 4th International Conference, Heavy Machinery* (pp. A97-A100)
- [6] B. Dankovic, B. Vidojkovic, Z. Jovanovic, "Dynamical Analysis of the Protector Cooling System in Tyre Industry", *Proc. ICMFMDI 2002, XVII International Conference on Material Flow, Machines and Devices in Industry* (pp. 56-59)
- [7] J. H. Holland, "Outline for a logical theory of adaptive systems," *J. ACM*, vol. 3, pp. 297-314, July 1962; also in A. W. Burks, Ed., *Essays on Cellular Automata*, Univ. Illinois Press, 1970, pp. 297-319.
- [8] Blasco, F.X., M. Martínez, J. Senent and J. Sanchis "An application to control of non-linear process with model uncertainty", In: *Methodology and tools in Knowledge based systems* (Springer, Ed.), 1998.
- [9] T.K. Teng, J.S. Shieh and C.S. Chen, "Genetic algorithms applied in online auto tuning PID parameters of a liquid-level control system", *Transactions of the Institute of Measurement and Control* 25, 5 pp. 433-450, 2003.

Building 3D Environment Models for Mobile Robots Using Time-Of-Flight (TOF) Laser Scanner

Sašo Koceski¹ and Nataša Koceska²

Abstract – In this paper, we present system and an intuitive method to generate visually convincing 3D models of indoor environments from data collected using TOF laser scanner. The method allows line and surface detection and mesh representation of the input data. The method shows accurate 3D environment representation useful for different applications in mobile robotics.

Keywords – TOF Laser Scanner, Environment modelling, Mobile robots, 3D mesh, 3D triangulation.

I. INTRODUCTION

Since standard computers allow efficient processing and visualization of three-dimensional data, the interest of using 3D graphics has increased in numerous fields. Car design, architecture, or the modern movie industry are merely a few examples of fields which are unimaginable nowadays without the use of 3D graphics. The increasing need for rapid characterization and quantification of complex environments has created challenges for data analysis. Mobile systems with 3D laser scanners that automatically perform multiple steps such as scanning, gaging and autonomous driving have the potential to greatly advance the field of environment representation. 3D information available in real-time enables autonomous robots to navigate in unknown environments, e.g., in the field of inspection and rescue robotics.

Autonomous navigation of a mobile robot requires basic capabilities for sensing the environment in order to avoid obstacles and move in a safe way. The problem of the reconstruction can be expressed as a procedure of learning the topology from the data set and reduction of the data set cardinality. We address the problem via the analysis and realistic representation of an unknown indoor environment. Our objective is to build environment models from the real measured data of building interiors using intuitive methods and low-cost data acquisition systems.

Some groups have attempted to build 3D volumetric representations of environments with 2D laser range finders. Thrun et al. [1],[2] and Früh and Zakhor [3] use two 2D laser range finder for acquiring 3D data. One laser scanner is mounted horizontally and one is mounted vertically. The latter one grabs a vertical scan line which is transformed into 3D

points using the current robot pose. But the accuracy in these cases was not satisfactory and also the costs were high.

Our approach is based on 2D Time-Of-Flight (TOF) laser scanner and extended by a low cost rotation module based on a servo command. Combining such an extension with a set of fast algorithms has resulted in good environment representation system.

II. DATA ACQUISITION SYSTEM

A. Main components and connections

The main component of the system is the sensor for data acquisition Laser Radar (LADAR) LD-OEM1000. It is placed in one aluminum carrying construction and attached to the mount with 1 Degree Of Freedom (DOF), so that it can be rotated. On the top of the mount, berth for camera is foreseen (Fig. 1). The rotational axis is horizontal. Annotation: An alternative approach is to rotate the LADAR around the vertical axis. Throughout this paper we will only discuss the approach based on a horizontal rotation, but all presented algorithms can be used in the same way. The differences between both approaches are the orientation of the apex angle and the effects of dynamic objects moving through the scene, e.g. persons. Using vertical scanning, a perturbation either appears with low probability within a few scans making them useless for further data processing, or does not appear at all.



Fig.1. Photo of the created system

For the rotation of the scanner's movable element, a servo command (Hitec HSC 5955TG) was chosen. In order to move the servo command, a PPM (Pulse Position Modulation) was used. It is connected to the main processing unit (Standard

¹Sašo Koceski is with the Applied Mechanics Laboratory, DIMEG, University of L'Aquila, 67040 Roio Poggio (AQ), Italy, E-mail: koceski@yahoo.com

²Nataša Koceska is with the Applied Mechanics Laboratory, DIMEG, University of L'Aquila, 67040 Roio Poggio (AQ), Italy, E-mail: njankova@yahoo.com

PC) via PCI NI 6221 Data Acquisition board (DAQ). For the LADAR, CAN data interface was chosen (instead of a RS-232 which is the standard interface), because it enables high grabbing speed, up to 1 MBit/s, and it can be easily connected via low cost CAN to USB adaptor to an USB port.

B. Working principle

The LADAR measures its environment in two-dimensional polar coordinates. When a measuring beam strikes an object, the position is determined with regard to the distance and direction. The measured data can be transferred in real time to the connected computer for evaluation.

The scan is carried out in a 360° sector. The LADAR ranges on bright; natural surfaces (a white house wall, for example) are approx. 100m. (Fig. 2).

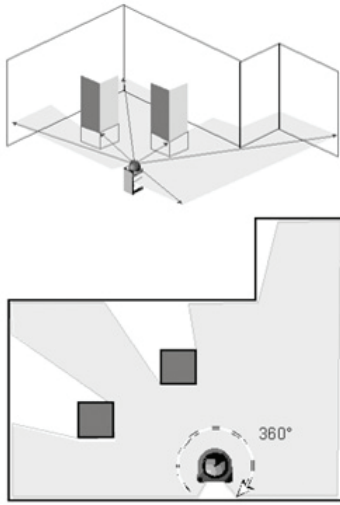


Fig.2. Scanning the environment

The distance to the object is calculated from the propagation time required by the light from the point at which the beam is emitted until the reflection is received by the sensor. The scanner head rotates with a frequency of 5 to 20 Hz (programmable). A laser pulse is emitted in accordance with a variable angle step, thereby triggering a distance measurement. The maximum angular resolution is 0.125° . This is set by the angle encoder at 5,760 steps. The angular resolution can be selected as an integral multiple of 0.125° .

C. Data acquisition and interpretation

Working principle and the given setup determine an intrinsic order of the acquired data. The data coming from the 2D LADAR is ordered counterclockwise. In addition the 2D scans (scanned planes) are ordered due to the rotation. While obtaining horizontal profiles LADAR is sending CAN data packets, with different useful information, among which a pairs of two by two values for distance and corresponding angle. The distance value is represented by a 16-bit binary value with a resolution (step width) of 3.9 mm ($1/256$ m). The angle is also represented by a 16-bit binary value with a

resolution of $1/16^\circ$. Having in mind the vertical rotation of the system (the value for the azimuth angle) as well as the dimension of the structural components of the system (Fig. 3), these values are subsequently transformed into spherical coordinates according to the Eqs. (1) and (2).

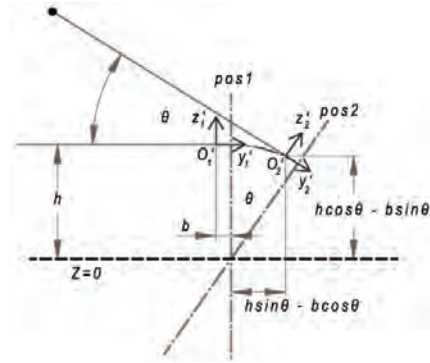


Fig.3. Coordinates transformation

$$\begin{cases} x' = r \cdot \sin \alpha \\ y' = r \cdot \cos \alpha \end{cases} \quad (1)$$

$$\begin{cases} X = -r \cdot \sin \alpha \\ Y = -r \cdot \cos \alpha \cdot \cos \vartheta - h \cdot \sin \vartheta + b \cdot \cos \vartheta \\ Z = -r \cdot \cos \alpha \cdot \sin \vartheta + h \cdot \cos \vartheta + b \cdot \sin \vartheta \end{cases} \quad (2)$$

D. Pre-processing algorithms

Different pre-processing algorithms for line and surface detection were applied to the data. First algorithm is a simple straightforward matching algorithm running in $O(n)$ (n is the number of points), with small constants. The algorithm implements a simple length comparison. The data of the LADAR (points a_0, a_1, \dots, a_n) is ordered counterclockwise so that one comparison per point is sufficient. We assume that the points a_i, \dots, a_j are already on a line. For a_{j+1} we have to check if the condition in Eq. (3) is satisfied.

$$\frac{\|a_i, a_{j+1}\|}{\sum_{t=i}^j \|a_t, a_{t+1}\|} < \varepsilon(j) \quad (3)$$

To obtain better results this algorithm runs on preprocessed data. Data points located close together are joined so the distance from one point to the next point is almost the same. This process minimizes the fluctuations within the data and reduces the points to be processed. Hence this algorithm runs very fast, but the quality of the lines is limited.

The quality could be increased by additional analysis (using Hough transformation for example) of the photos obtained with camera during the scanning process.

After line detection is done the data is converted into 3D. Based on the detected lines, the following algorithm tries to detect surfaces in the 3-dimensional scene.

Scanning a plane surface, the line detection algorithm will return a sequence of lines in successive 2D scans approximate

the shape of this surface. The task is to recognize such structures within the 3D data input and to concatenate these independent lines to one single surface.

The surface detection algorithm proceeds the following steps:

1. The first set of lines - coming from the very first 2D scan - is stored.
2. Every other line is being checked with the set of stored lines. If a matching line is found, these two lines are transformed into a surface.
3. If no such matching line exists, the line may be an extension of an already found surface. In this case, the new line is matching with the top line of a surface. This top line is being replaced by the new line, resulting in an enlarged surface.
4. Otherwise the line is stored as a stand-alone line in the set mentioned above.

To achieve real time capabilities, the algorithm makes use of the characteristics of the data as it comes from the LADAR, i.e. it is the order by the scanned planes. Therefore the lines are sorted throughout the whole scene (with regard to their location within the virtual scene) due to their inherited order. Thus an efficient local search can be realized.

Two criteria have to be fulfilled in order to match lines: On one hand the endpoints of the matching line must be within a ε -area around the corresponding points of the given line. On the other hand the angle between the two lines has to be smaller than a given value. The second constraint is necessary for correct classification of short lines, since they fulfill the distance criterion very easily. These algorithms enables that the robot or a user gets much information about objects in the scenery right during the scan, which is essential for path planning and collision avoiding during the movement of mobile robots inside indoor environments.

E. Post-processing algorithms

Post-processing algorithms were used to create a 3D mesh representation of the room that will give more qualitative information for safe navigation of mobile robots. Despite of the prior algorithms, this step requires information about the whole scene and has to be done after the scan process is finished.

This procedure is based on the Delaunay triangulation algorithm that typically projects the data set onto a plane for finding the most probable connections between close vertices and re-locates in space the connected vertices at the end creating a triangular mesh.

At any stage of the triangulation process one has an existing triangular mesh and sample point to add to that mesh. The process is initiated by generating a supertriangle, an artificial triangle which encompasses all points. At the end of the triangulation process any triangles which share edges with the supertriangle are deleted from the triangle list:

1. All the triangles whose circumcircle encloses to point to be added are identified, the outside edges of those triangles form an enclosing polygon. (The circumcircle

of a triangle is the circle which has the three vertices of the triangle lying on its circumference).

2. The triangles in the enclosing polygon are deleted and new triangles are formed between the point to be added and each outside edge of the enclosing polygon.
3. After each point is added there is a net gain of two triangles. Thus the total number of triangles is twice the number of sample points. (This includes the supertriangles, when the triangles sharing edges with the supertriangle are deleted at the end the exact number of triangles will be less than twice the number of vertices, the exact number depends on the sample point disturbance). The triangulation algorithm may be described in pseudo-code as follows:

subroutine triangular

input: vertex list

output: triangle list

```

initialize the triangle list
determine the supertriangle
add supertriangle vertices to the end of the vertex list
add the supertriangle to the triangle list
for each sample point in the vertex list
  initialize the edge buffer
  for each triangle currently in the triangle list
    calculate the triangle circumcircle center and radius
    if the point lies in the triangle circumcircle then
      add the three triangle edges to the edge buffer
      remove the triangle from the triangle list
    endif
  endfor
delete all doubly specified edges from the edge buffer
this leaves the edge of the enclosing polygon only
add the triangle list all triangles formed between the
point and the edges of the enclosing polygon
endfor
remove any triangles from the triangle list that use the
supertriangle vertices
remove the supertriangle vertices from the vertex list
end
```

The above can be refined in a number of ways to make it more efficient. The most significant improvement is to pre-sort the sample points by one coordinate, the coordinate used should be one with the greatest range of samples. If the X axis is used for pre-sorting then as soon as the x component of the distance from the current point to the circumcircle centre is greater than the circumcircle radius, that triangle need never to be considered for later points. With the above improvement the algorithm presented here should increase with the number of point as approximately $O(N^{1.5})$.

The algorithm does not require a large amount of internal storage. The algorithm only requires one internal array and that is a logical array of flags for identifying those triangles that no longer need to be considered.

III. EXPERIMENTAL RESULTS

The scan shown on Fig. 4 which represents indoor of our laboratory in the form of cloud of points, was obtained by our system, with the following settings: Resolution - $0,25^\circ \times 0,25^\circ$; Frequency - 20 Hz. The scan covers an area of 180(h)x60(v) degrees and includes in total 157976 points. Wired model of the entire scene after triangulation contains 307095 triangles.

Details of one part of the same scene in the form of wired mesh is presented on Fig. 5.

Standard PC with AMD Athlon 64 Processor 2.41GHz and 1GB RAM was used. The software based on the above algorithm was developed in C++ using the Computational Geometry Algorithms Library (CGAL) and VTK (The Visualization Toolkit) which are freely available data processing and visualization libraries.

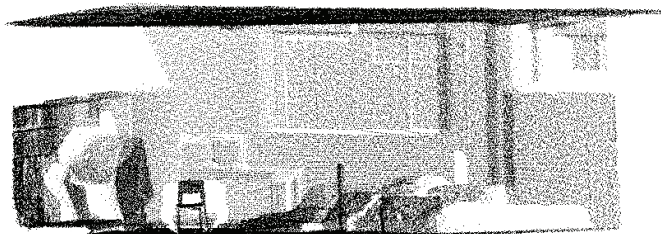


Fig. 4. Point cloud representation of indoor environment

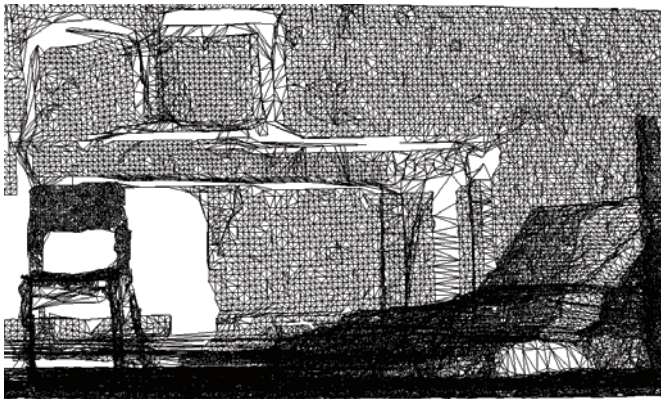


Fig. 5. Details of the environment in the form of wired mesh

IV. CONCLUSION

In this paper low-cost, precise and reliable 3D sensor and methods for environment modeling are presented. With the proposed approach the mobile robot navigation and recognition could be significantly improved. The 3D sensor is built on base of 2D TOF laser scanner, which senses the environment contactless, without the necessity of landmarks. The implemented software, based on presented algorithms, give accurate mesh representation of input data, where particular objects could be easily identified.

V. FUTURE WORK

The future work from one side regards hardware modifications and supplements of the system. First of all, replacement of the current servo command with step motor that could be connected to the PC via CAN bus or USB connection is foreseen. This way we will avoid the usage of the DAQ card and will reduce the cost of the solution. The usage of the camera for photo capturing is also planned. This would lead to efficient texture mapping of the scanned environments and objects. On the other side improvement of the current algorithms and algorithms for terrain maps creation and feature extraction from the scans is planned to be implemented.

REFERENCES

- [1] S. Thrun, D. Fox, W. Burgard, A real-time algorithm for mobile robot mapping with application to multi-robot and 3D mapping, in: Proceedings of the IEEE International Conference on Robotics and Automation (ICRA'00), San Francisco, CA, April 2000.
- [2] D. Hähnel, W. Burgard, S. Thrun, Learning compact 3D models of indoor and outdoor environments with a mobile robot, in: Proceedings of the Fourth European Workshop on Advanced Mobile Robots (EUROBOT'01), Lund, Sweden, September 2001.
- [3] C. Früh, A. Zakhor, 3D model generation for cities using aerial photographs and ground level laser scans, in: Proceedings of the Computer Vision and Pattern Recognition Conference (CVPR'01), Kauai, Hawaii, December 2001.
- [4] G. Guidi, J.-A. Beraldin, C. Atzeni, "High accuracy 3D modeling of Cultural Heritage: the digitizing of Donatello's Maddalena", IEEE Transactions on Image Processing, Vol. 13-3, 2004, pp. 370-380.
- [5] Terzopoulos, D., The Computation of Visible Surface Representation. IEEE Transactions on PAMI, Vol. 10, No 4, 1988.
- [6] G. Guidi, J.-A. Beraldin, S. Ciofi, C. Atzeni, "Fusion of range camera and photogrammetry: a systematic procedure for improving 3D models metric accuracy", IEEE Transactions on Systems Man and Cybernetics Part B-Cybernetics. Vol. 33-4, 2003, pp. 667- 676.
- [7] VTK (www.kitware.com/vtk.html)
- [8] CGAL (www.cgal.org)

High-Performance Velocity Servo-System Design Using Active Disturbance Estimator

Boban Veselić¹ and Čedomir Milosavljević²

Abstract – This paper considers design of digitally controlled high-performance velocity servo-system, featuring fast response without overshoot. The proposed control structure contains main PI controller and active disturbance estimator, to further improve disturbance rejection dynamics. Resulting response meets the high-performance requirements. The designed control system is experimentally verified in induction motor velocity control.

Keywords – Servo-system, Velocity control, Digital PI controller, disturbance estimator.

I. INTRODUCTION

Advanced production technologies have imposed more rigorous demands on servo-systems performances. Velocity servo-systems in high-performance applications must comply with the requirements of fast response without overshoot, high steady state accuracy, good rejection of external disturbances and robustness to parameter perturbations. In general, a servo-system must have at least one pure integrator within the closed loop. Since control plant in a velocity servo-system does not have an integrating property, PI controllers are conventionally used. Such servo-system has no steady-state error on step references and completely rejects constant loads.

Beside standard simple regulation contour, two degrees-of-freedom controllers found their applications in servo-systems [1], in order to improve robustness. Reference and disturbance responses can be separately designed using this control structure. Similar results were obtained using internal model principle and internal model control, combined into IMPACT structure [2]. Another approach in disturbance compensation is introduction of disturbance estimators [3], which may be interpreted as a special case of the above two structures.

This paper deals with the design of a digitally controlled high-performance velocity servo-system. Both pole placement and zero-pole cancellation design methods of PI controller are considered. To further improve disturbance rejection dynamics an active disturbance estimator [4] is introduced. Fast response without overshoot and excellent disturbance rejection properties are ensured. The proposed servo-system is experimentally verified in induction motor velocity control.

II. VELOCITY SERVO-SYSTEM STRUCTURE

Most of velocity servo-systems, regardless of the employed drive, may be described by the simplified generalized block-scheme depicted in Fig. 1. The cascade structure consists of two distinct control loops. Inner current control loop, responsible for adequate torque generation, is enclosed by a main speed control loop. Bandwidth of the inner loop is usually much higher than bandwidth of the speed loop, thus the current control subsystem dynamics may be ignored in the main controller design. Nevertheless, dynamic delay of the inner control subsystem has certain impact on overall system dynamics, acting as an unmodeled dynamics within the speed control loop. The current loop is commonly realized with a bandwidth around 1 kHz, implementing PI controller. Since exogenous disturbances, such as load torque $M_o(t)$, enter directly into the speed control loop, PI speed controller is usually employed in order to eliminate steady-state error in the case of step-like disturbances.

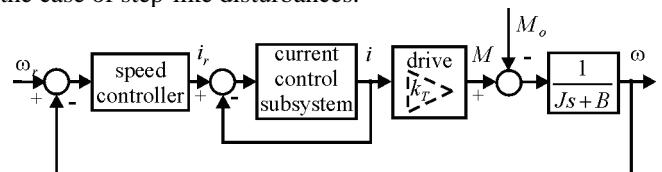


Fig. 1. Generalized velocity servo-system structure

Encouraged by huge technological advance of micro-controllers, digital implementation of control algorithms overcomes analog counterpart. Correct system analysis should be carried out in discrete-time domain. Block diagram of a digitally controlled velocity servo-system is given in Fig. 2. $G_r(z)$ is a discrete-time transfer function of digital controller, $G_{ho}(s)$ is sample and hold transfer function, k_T is a torque constant, J and B are moment of inertia and viscous friction coefficient, respectively. Hence, motor dynamics is described by first order function $G(s) = k_m / (1 + sT_m)$, where $k_m = k_T / B$ is motor gain and $T_m = J / B$ is time constant.

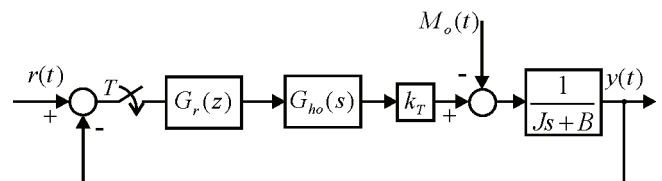


Fig. 2. Digitally controlled velocity servo-system

¹Boban Veselić is with the Faculty of Electronic Engineering, Aleksandra Medvedeva 14, 18000 Niš, Serbia, E-mail: boban.veselic@elfak.ni.ac.yu.

²Čedomir Milosavljević is with the Electrical Engineering Faculty, Vuka Karadžića 30, Lukavica, 71123 Istočno Sarajevo, Bosnia and Herzegovina, E-mail: milosavljevic@elfak.ni.ac.yu.

If load torque is a step function or is slowly varying between two consecutive sampling instants, which is true for small sampling periods, discrete-time model of the closed loop system is given as

$$Y(z) = \frac{G_r(z)G(z)}{1 + G_r(z)G(z)}R(z) - \frac{G(z)}{1 + G_r(z)G(z)}M_{oe}(z), \quad (1)$$

$$G(z) = \mathbf{C}\{\mathcal{Z}^{-1}\{G_{ho}(s)G(s)\}\} = \frac{k_m(1-a)}{z-a}, \quad a = e^{-T_s/T_m},$$

where T_s denotes sample period and $M_{oe} = M_o/k_T$. As mentioned earlier, PI digital controller is employed within speed control loop. Controller transfer function is defined with

$$G_r(z) = k_p + k_i \frac{z}{z-1} = \frac{k_p z - b}{z-1}, \quad b = \frac{k_p}{k_p + k_i}, \quad (2)$$

where k_p , k_i are gains of proportional and integral action.

III. CONTROLLER DESIGN

According to the high-performance requirements, recounted in the introduction, controller (2) parameters should be tuned to provide fast critically aperiodic response. Due to (1) (2), characteristic equation $1 + G_r(z)G(z) = 0$ is of second order, whose roots z_1 , z_2 (poles of the closed loop system (1)) determine system response. As it is well known, second order system dynamics as well as nature of its response is defined by doublet ζ , ω_n , which represents relative damping factor and undamped natural frequency, respectively. Closed loop poles are given by $s_{1,2} = -\zeta\omega_n \pm \omega_n\sqrt{1-\zeta^2}$. In the case of critically aperiodic response, $\zeta = 1$ yielding double real pole $s_1 = s_2 = -\omega_n$. In discrete-time domain these poles are mapped into locations $z_1 = z_2 = e^{-\omega_n T_s}$, $0 < z_1 \leq 1$. To obtain desired closed loop dynamics defined by z_1 using pole placement design technique [5], k_p and k_i of (2) should be

$$k_p = \frac{a - z_1^2}{k_m(1-a)}, \quad k_i = \frac{1 - 2z_1 + z_1^2}{k_m(1-a)}, \quad (3)$$

which results in a closed loop dynamics of the form

$$Y(z) = (1 + a - 2z_1) \frac{z - z_0}{(z - z_1)^2} R(z) - \frac{k_m(1-a)(z-1)}{(z - z_1)^2} M_{oe}(z), \quad (4)$$

showing that the desired poles are ensured. Consequently, a zero $z_0 = (a - z_1^2)/(1 + a - 2z_1)$ arises in the response with respect to reference. Its location depends on the location of the desired pole z_1 , which is plotted in Fig. 3. For zero z_0 not to be dominant, condition $z_0 < z_1$ must hold. According to Fig. 3, valid selection of desired pole z_1 is $a < z_1 < \sqrt{a}$ which gives $T_m < 1/\omega_n < 2T_m$. This indicates that the time constant

of the closed loop system should be larger than motor time constant. This is unacceptable since notion of feedback control is to improve not to degrade system dynamics, so the desired pole must be located inside region $0 < z_1 < a$. This introduces dominant zero, which produces unwanted overshoot. Notice that system response with respect to load torque is free of undesirable zero.

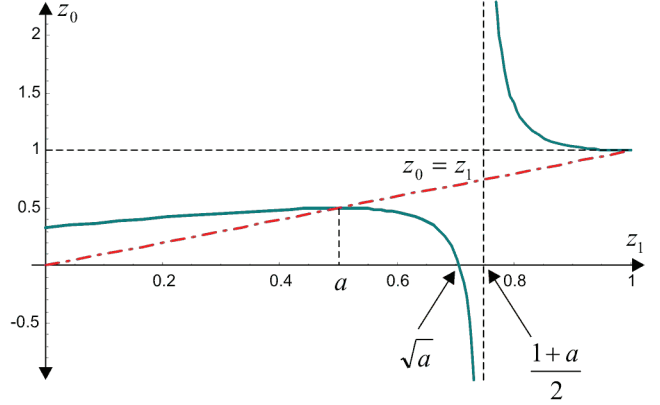


Fig. 3. Location of zero with respect to location of chosen pole

One approach in overshoot elimination is introduction of referent signal filtering, which would slow down the system. This is contradictory to the high-performance requirements.

Another design approach is zero-pole cancellation method, [5]. Namely, controller gains should be set in such manner that controller zero b cancels plant pole a , ($b = a$), and gain k_p determines location of the desired closed loop pole z_3 . Hence, controller parameters are obtained in the form

$$k_p = \frac{a(1-z_3)}{k_m(1-a)}, \quad k_i = \frac{1-z_3}{k_m}. \quad (5)$$

Closed loop system behavior is then described by

$$Y(z) = \frac{1-z_3}{z-z_3} R(z) - \frac{k_m(1-a)(z-1)}{(z-a)(z-z_3)} M_{oe}(z). \quad (6)$$

The system has first order dynamics defined by desired pole z_3 with respect to reference, providing fast response without overshoot. However, complete cancellation does not occur in disturbance related term, which is described by second order dynamics. Furthermore, behavior with respect to disturbance is determined by “slow” pole of the plant $z = a$, which is now dominant. Reference response is quite satisfactory, whereas disturbance rejection dynamics is unacceptable. In order to obtain high-performance servo-system it is necessary to improve disturbance rejection performance.

IV. ACTIVE DISTURBANCE ESTIMATOR

A way to improve system robustness to parameter perturbation and exogenous disturbances is introduction of disturbance estimator. The concept of disturbance estimator is that the external disturbances and model uncertainties, usually regarded as an equivalent disturbance, can be efficiently

With the controllers tuned according to (5) and (9), servo-system dynamics become

$$Y(z) = \frac{1 - z_3}{z - z_3} R(z) - \frac{k_m(1-a)(z-1)}{(z-z_3)(z-z_4)} M_{oe}(z). \quad (10)$$

It is obvious that the proposed structure with active disturbance estimator offers possibility to obtain both responses, with respect to the reference and exogenous disturbances, acceptable for high-performance servo-systems. Overshoot does not arise and system dynamics is completely defined by the freely adopted poles z_3, z_4 .

To completely reject ramp-like exogenous disturbances estimator controller must be of PI type with the parameters defined with eq. (3). System dynamics is then described by

$$Y(z) = \frac{1 - z_3}{z - z_3} R(z) - \frac{k_m(1-a)(z-1)^2}{(z-z_3)(z-z_1)^2} M_{oe}(z). \quad (11)$$

VI. EXPERIMENTAL INVESTIGATION

The effectiveness of the proposed control structure has been investigated by experiments, which have been conducted on a servo-system with a three phase, 50Hz, 0.37kW, Seiber LS71 induction motor with 1.3 Nm nominal torque. Control part of the servo-system is realized by dSPACE DS1104 R&D controller board. Indirect rotor flux oriented vector control of induction motor is employed. The control scheme contains measurement of two line currents and rotor shaft angle position, coordinate transformations, decoupling circuits, electrical angle estimator, two local current control loops with 200 Hz bandwidth and 10 kHz sampling frequency, and a main speed control loop with 1 kHz sampling frequency.

By neglecting current control loops along with other unmodeled dynamics and nonlinearities, present in such complex system, in certain approximation speed control system may be considered as one in Fig. 2. In this representation motor parameters are: $k_T = 0.6481 \text{ Nm/A}$, $J = 3.5 \cdot 10^{-4} \text{ kgm}^2$, $B = 3 \cdot 10^{-4} \text{ Nms/rad}$. Reference signal is given with $r(t) = 100 \cdot h(t - 0.5) \text{ rad/s}$, and the system is subjected to load torque $M_o(t) = 0.65 \cdot h(t - 1.5) \text{ Nm}$, which is 50% of nominal torque.

In the first experiment (Fig. 6., trace (1)), active disturbance estimator is deactivated and the main PI controller is designed using pole placement. Desired dynamics is defined by $\zeta = 1$, $\omega_n = 20 \text{ rad/s}$ ($z_1 = 0.98$). $k_{p1} = 0.0207$, $k_{i1} = 2.118 \cdot 10^{-4}$ are obtained using (3). An unwanted overshoot arises due to the dominant zero $z_0 = 0.99$.

The main controller is then tuned by cancellation method in the second experiment (Fig. 6., trace (2)). Desired bandwidth of 10 Hz results in pole $z_3 = 0.939$, which according to (5) gives $k_{p1} = 0.033$, $k_{i1} = 2.819 \cdot 10^{-5}$. System has good response to reference, but very slow dynamics of disturbance rejection, caused by not cancelled plant pole a .

Finally, active disturbance estimator is activated in the third experiment (Fig. 6. trace (3)). The main PI controller remains unchanged from the previous experiment, while P controller in the estimator is set by applying pole placement under condition $z_4 = z_3$, resulting in $k_{p2} = 0.0324$ by virtue of (9).

The proposed servo system is superior to the other two, with fast velocity response without overshoot and equally fast dynamics in disturbance rejection.

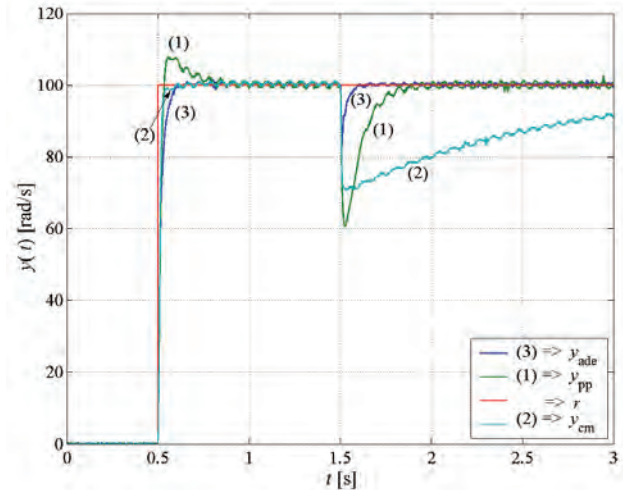


Fig. 6. Velocity servo-system step responses

VII. CONCLUSION

The paper considers design of high-performance velocity servo-system with active disturbance estimator, whose introduction drastically improves system behavior with respect to exogenous disturbances. This ensures fast response without overshoot and system dynamics is completely defined by freely adopted poles. Analytically predicted performance has been experimentally verified in case of induction motor servo-system, in which significant modeling error and parameter uncertainties exist. The proposed servo-system has exhibited excellent exogenous disturbance rejection property as well as robustness to parameter perturbations.

REFERENCES

- [1] T. Umeno, Y. Hori, "Robust speed control of DC servomotors using modern two degrees-of-freedom controller design", IEEE Trans. on Ind. Electronics, Vol. 38, No. 5, pp. 363-368, 1991.
- [2] YA.Z. Tsytkin, U. Holmberg, "Robust stochastic control using the internal model principle and internal model control," Int. J. Control, Vol. 61, No. 4, pp. 809-822, 1995.
- [3] Y. Choi, K. Yang, W.K. Chung, H.R. Kim, H. Suh, "On the robustness and performance of disturbance observers for second-order system", IEEE Trans. Automatic Control, Vol. 48, No. 2, pp. 315-320, 2003.
- [4] B. Veselić, Č. Milosavljević, D. Mitić, "Robust servo-system design based on discrete-time sliding mode control with active disturbance estimator", Transactions on Automatic Control and Computer Science, Vol. 50, No. 1, pp. 5-10, 2005.
- [5] K. Ogata, *Discrete-time control systems*, N. Jersey, Prentice-Hall International, Inc., 1995.

Optimal Control Using Neural Networks

D. Toshkova¹ and P. Petrov²

Abstract – In the present paper a literature review concerning the problem of optimal control synthesis using neural networks is presented.

Key words – neural networks, optimal control

I. INTRODUCTION

During last ten years a large number of papers treating the application of neural networks for optimal control synthesis for plants, whose dynamics is described by linear and nonlinear ordinary and partial differential equations are published. It is determined by the main property of the neural networks to approximate any linear and non-linear function. The most widely used neural networks are feedforward neural networks. Another structure which is also applied is the recurrent neural network. A tendency to start using a broader range of structures emerges which is related to developing of new structures.

II. OPTIMAL CONTROL SYNTHESIS USING NEURAL NETWORKS

In [6] a survey of the possibilities of using neural networks for modeling, identification and control of the systems is presented. Here only the optimal decision control and model prediction control will be mentioned. In the case of model prediction control the plant is modeled through a neural network. By using the neural network model the future plant response are predicted over a specified time horizon. On the basis of predicted future response a specified performance index is minimized to obtain the optimal control. In optimal decision control case the state space is partitioned into separate regions, in which the control action is assumed constant. The control surface is realized through a training procedure of the neural networks.

In [4] model predictive optimal controller for nonlinear discrete systems is considered. A block for system input state realization is used, which transforms the system into quadratic system with equal number of inputs and states in order to develop optima receding horizon controller which leads to decreasing the amount of the calculations in comparison to traditional optimal controllers. A nonlinear feedback law is derived where a neural network in feedback loop is used to generate of optimal input action.

The generated input approximates the solution which is minimal in respect of quadratic cost function with parameters

controlling the final states, the value and variation of the input action for the control purposes. An analysis of the local stability and robustness of the controller is presented.

In [11] the problem of determining optimal controls for nonlinear dynamical systems by using neural networks is considered. Through a few examples the possibilities of the neural networks for on-line solution of the optimal control problems are demonstrated.

In the major part of the publications [2, 3, 10, 12, 13, 14, 15, 16, 17, 18, 21, 22] the optimal control problem is derived by using the dynamic programming method and the obtained solutions are approximated by using neural networks. Although the presented new approaches bear different names – adaptive critic methodology [2, 10, 12, 13, 14, 15, 16], neuro-dynamic programming [3], neural dynamic optimization [20, 21] – they do not differ from each other substantially. Their main advantage is that so called “curse of dimensionality” problem is solved.

The adaptive critic methodology is introduced in [2]. The control law for linear or nonlinear system is determined through consecutive adapting of two neural networks – action network and critic network. The action network captures the relationship between the state and control and the critic neural network captures the relationship between the state and co-state. Through this methodology the control law is determined for a large set of initial conditions. It is not necessary the control law to be determined analytically. The neural network, which is used (multilayered perceptron) do not need external training; it is necessary the functional form of the control law to be known preliminarily. In [10] the necessary conditions for solutions obtained through the adaptive critic methodology to converge are presented and it is shown that the obtained solution is optimal. In [12, 15] the a.m. methodology is developed for distributed parameter systems. In [13] the method is applied for optimal control synthesis for distributed parameter systems, whose dynamics is described by coupled nonlinear partial differential equations. In [14] the proper orthogonal decomposition concept is used for reducing of distributed parameter system to lumped parameter system of low order. The optimal control problem is solved in time through applying the adaptive critic algorithm. Then the control solution is given in the spatial domain by using the same orthogonal functions. In [16] the adaptive critic algorithm is elaborated. It is shown that the necessity of action neural networks drops off.

In [17] three adaptive critic methods, which are used for designing of neural controllers – heuristic dynamic programming, dual heuristic programming and globalized dual heuristic programming are described. Two modifications of the globalized dual heuristic programming as well as generalized training procedure are suggested. The developed approaches do not differ substantially from the methodology

¹Daniela G. Toshkova, Department Production Automatization, Technical University of Varna, 1, Studentska Str., 9010 Varna, Bulgaria, E-mail: daniela_toshkova@abv.bg

²Petar D. Petrov, Department Production Automatization, Technical University of Varna, 1, Studentska Str., 9010 Varna, Bulgaria

suggested in [2]. In both approaches two neural networks are used for approximating the solution for the optimal control – action and critic neural networks. The only difference is that a recurrent neural network is used instead of multilayered perceptron. In [18] the approach is developed for discrete distributed parameter systems. Moreover the algorithm is elaborated and the necessity of action neural networks as in [16] drops off.

In [20, 21] neural dynamic optimization is presented as a method for synthesis of optimal feedback control for nonlinear MIMO systems. The main characteristic of neural dynamic optimization is that the solution for the optimal feedback, whose existence is proved through dynamic programming method is approximated by using neural networks. In [20] the background and motivation for development of neural dynamic optimization is described and in [21] the neural dynamic optimization theory is presented. One major drawback of this approach is the big memory requirements although this requirement is not so severe compared to the classical dynamic programming method.

Another methodology having for a theoretical basis the dynamic programming and using neural networks for approximation is so called neuro-dynamic programming. According to the definition given in [3], neuro-dynamic programming “enables the to learn how to make good decisions by observing their own behavior, and use built-in mechanisms for improving their actions through a reinforcement mechanism”. This methodology is used not only for solving the optimal control problems but for a broader class of problems.

In [9] a recurrent neural network is introduced for the N-stage optimal control problem. The first step of the presented approach is reformulating the N-stage optimal control problem and then the gradient method is used for deriving the dynamics equation of the recurrent neural network. Although the approach enables obtaining real-time solutions it possesses two drawbacks. First, the rigorous mathematical analysis for the stability of the neural network lacks. Second, a neural network which combines the structure of the N-stage optimal control problem and a faster optimization method needs to be explored.

In [22] an approach for synthesis of optimal control for nonlinear systems, which incorporates the N-stage optimal control problem as well as least square support vector machines approach for mapping the state space into action space. SVM with radial basis function kernel are used. The solution is characterized by a set of nonlinear equations. An alternative formulation as a constrained nonlinear optimization problem in less unknowns is given, together with a method for imposing local stability in the LS – SVM control scheme. Advantages of LS – SVM control are that no number of hidden units has to be determined for the controller and that no centers have to be specified for the Gaussian kernels when applying Mercer’s condition. The curse of dimensionality is avoided in comparison with defining a regular grid for the centers in classical radial basis function networks. This is at expense of taking the trajectory of state variables as additional unknowns in the optimization problem, while classical neural network approaches typically lead to parametric optimization

problems. In the SVM methodology the number of unknowns equals the training data, while in the primal space the number of unknowns can be infinite dimensional. A drawback of this approach is the large number of the unknowns.

In [5] the problem of multistage optimal control is considered. The problem is solved by using wavelet neural networks (WNN) as its capability for learning and generalization of functions are bigger. The control law is approximated by using WNN. The Lagrangian is constructed in order to from optimal control problem to come to optimization problem. A weight is introduced to regulate the balance between control system and its good performance by using WNN for mapping of the function from the state space into action space after which the optimal control is achieved. The value of the weight has effect on the simulation result.

In [19] an interactive fuzzy satisfying method for the solution of a multiobjective optimal for a linear distributed parameter system governed by heat conduction equation is suggested. In order to reduce the control problem to an approximate multiobjective linear programming problem a numerical integration formula is used and the suitable auxiliary variables are introduced. By considering the vague nature of the human judgment, the decision maker is assumed to have fuzzy goals for the objective functions. Having elicited the corresponding linear membership functions through the interaction with the decision maker, if the decision maker specifies the reference membership values, the corresponding Pareto optimal solution can be obtained by solving the minimax problems. Then a linear programming based interactive fuzzy satisfying method for deriving a satisfying solution for the decision maker efficiently from a Pareto optimal solution set is presented.

In [23] an approach for optimal control synthesis, in which a fuzzy neural network is used as a controller through simulation of the process of the controlled system is suggested.

In [1] the designing of a neural networks based regulator for nonlinear plants is considered. Both state and output feedback regulators with deterministic and stochastic disturbances have been investigated. A multilayered feedforward neural network has been employed as the nonlinear controller. The training of neural network utilizes the concept of so called “block partial derivatives”. The suggested approach may also be used for optimal control synthesis for plant with state and control constraints. In [7] a neural network based algorithm for a discrete constrained optimal control synthesis for nonlinear systems is presented.

In [25] a recurrent learning algorithm for optimal control synthesis for continuous dynamic systems is suggested. The designed controllers are in the form of unfolded recurrent neural networks. The proposed learning algorithm is characterized by its double–forward–recurrent–loops structure for solving both the temporal recurrent and the structure recurrent problems. The first problem is resulted from the nature of general optimal control problems, where the objective functions are often related (evaluated at) to some specific instead of all time steps or system states only. This causes missing learning signals at some time steps or system states. The second problem is due to the high-order discretization of the continuous systems by the Runge-Kutta

method that is performed to increase the control accuracy. The discretization transforms the system into several identical subnetworks interconnected together, like a recurrent neural network expanded in the time axis. Two recurrent learning algorithms with different convergence properties are derived: the first- and second-order learning algorithms. The stability and the robustness of the designed controllers have to be studied in details.

In [24] a multilayered recurrent neural network is suggested for synthesizing linear quadratic optimal control systems by solving the algebraic matrix Riccati equation in real time. The suggested recurrent neural network consists of four bidirectionally connected layers. It is shown to be capable of solving the algebraic matrix Riccati equations, which enables synthesizing linear quadratic control systems in real time.

In [8] a new alternative for finding of the optimal control for discrete systems, which is based on using the continuous neural network of Hopfield (CNNH) is developed. The quadratic cost function is transformed into energy function of CNNH and the control is the output vector of CNNH. As CNNH works in parallel and in real time, the method may meet all the requirements for control in real time.

III. CONCLUSION

As a conclusion of the survey of the publication considering the optimal control synthesis problem for distributed parameter systems of parabolic type and also those discussing the utilizing neural networks in the optimal control synthesis problems it may be noted the following

- Neural networks enable optimal control synthesis in real time.;
- Important characteristics of the neural networks is their property to be universal function approximators but on the other hand the good approximation is hindered from the possibility of getting trapped in a local minimum;
- The problem for neural networks application for synthesis of optimal control for distributed parameter systems is not investigated entirely (as far as it is known to author only one approach is suggested – adaptive critic [12-16]);
- It is not pointed out definitely in the publications how stable is the suggested controller performance.

REFERENCE

[1] Ahmed, S. and M.A. Al-Dajani, Neural Regulator Design, Neural Networks, 1998, Vol.11, No.9, pp. 1695 – 1709

[2] Balakrishnan, S. N. and V. Biega, Adaptive – critic Based Neural Networks, Proc. Am. Contr. Conf., Seattle, WA, 1995, pp. 335-339

[3] Bertsekas, D.P. and J.N. Tsiklis, Neuro-dynamic programming, Athena Scientific, Belmont, Massachusetts, 1996

[4] Foley, D.C. and N. Sadegh, Short horizon optimal control of nonlinear systems, Proceedings of IEEE Conference on Decision and Control, 2003, Vol. 1, pp. 728 – 733

[5] Hu, X., H. Lue and J. He, Research upon Multistage Optimal Control by Wavelet Neural Network, The Sixth World Congress on Intelligent Control and Automation, 2006, Vol. 1, pp. 2655 - 2658

[6] Hunt, K. J., D. Sbarbaro, R. Zbikowski and P. J. Gawthrop, Neural Networks for Control Systems – A Survey, Automatica, 1992, Vol. 28, No. 6, pp.1083-1112

[7] Irigoyen, E.; Galvan, J.B.; Perez-Illarbe, M.J., Neural networks for constrained optimal control of non-linear systems, Proceedings of

the International Joint Conference on Neural Networks, IEEE, Piscataway, NJ, USA, 2000, Vol. 4, pp. 299-304

[8] Li, Ming-Ai and Ruan Xiao-Gang Optimal control with continuous Hopfield neural network, Proceedings on 2003 IEEE International Conference on Robotics, Intelligent Systems and Signal Processing, 2003, Vol. 2, pp. 758 – 762

[9] Liao, L.-Z., A Reccurent Neural Network for N-stage Optimal Control Problems, Neural Processing Letters, 1999, Vol.10, pp. 195 - 200

[10] Liu, Xin; Balakrishnan, S.N., Convergence analysis of adaptive critic based optimal control, Proceedings of the American Control Conference, IEEE, Piscataway, NJ, USA, 2000, Vol. 3, pp. 1929-1933

[11] Narendra, K. S. and S. J. Brown, Neural Networks for Optimal Control, Proceedings of the 36th Conference on Decision and Control, San Diego, California, USA, 1997, pp. 478 – 480

[12] Padhi, R. and Balakrishnan, S.N., Infinite time optimal neuro control for distributed parameter systems, Proceedings of the American Control Conference, IEEE, Piscataway, NJ, USA, 2000, Vol.6, pp. 3778 – 3782

[13] Padhi, R.; Balakrishnan, S.N., A systematic synthesis of optimal process control with neural networks, Proceedings of the American Control Conference, 2001, Vol. 3, pp. 1910 – 1915

[14] Padhi, Radhakan; Balakrishnan, S.N., Proper orthogonal decomposition based feedback optimal control synthesis of distributed parameter systems using neural networks, Proceedings of the American Control Conference, 2002, Vol. 6, pp. 4389 – 4394

[15] Padhi, R., S.N. Balakrishnan and T. Randolph, Adaptive – Critic Based Optimal Neuro Control Synthesis for Distributed Parameter Systems, Automatica, 2001, Vol. 37, pp. 1223 –1234

[16] Padhi, R., Optimal Control of Distributed Parameter Systems Using Adaptive Critic Neural Networks, Dissertation, University of Missouri – Rolla, 2001

[17] Prokhorov, D.V. and D. Wunsch, Adaptive Critic Designs, IEEE Transactions on Neural Networks, September 1997, pp. 997-1007

[18] Prokhorov, D.V., Optimal Neurocontrollers for Discretized Distributed Parameter Systems, Proceedings of the American Control Conference, 2003, Vol. 1, pp. 549 – 554

[19] Sakawa, M., M. Inuiguchi, K. Kato and T. Ikeda, An Interactive Fuzzy Satisficing Method for Multiobjective Optimal Control Problems in Linear Distributed – Parameter Systems, Fuzzy Sets and Systems, 1999, Vol. 102, pp. 237- 246

[20] Seong, C.-Y. and B. Widrow, Neural Dynamic Optimization for Control Systems – Part I: Background, IEEE Transactions on Systems, Man, and Cybernetics – Part B: Cybernetics, 2001, Vol. 31, No.4, pp. 482 – 489

[21] Seong, C.-Y. and B. Widrow, Neural Dynamic Optimization for Control Systems – Part II: Theory, IEEE Transactions on Systems, Man, and Cybernetics – Part B: Cybernetics, 2001, Vol. 31, No.4, pp. 490 – 501

[22] Suykens, J.A.K., J. Vandewalle and B. De Moor, Optimal Control by Least Squares Support Vector Machines, Neural Networks, 2001, Vol.14, pp. 23 – 35

[23] Tam, Peter K.S.; Zhou, Z.J.; Mao, Z.Y., On designing an optimal fuzzy neural network controller using genetic algorithms, Proceedings of the World Congress on Intelligent Control and Automation (WCICA), 2000, Vol.1, pp. 391 – 395

[24] Wang J. and G. Wu, A Multilayer Reccurent Neural Network for Solving Continuous – time algebraic Riccati Equations, Neural Networks, 1998, Vol.11, pp.939 – 950

[25] Wang, Y.-J. and C.-T. Lin, Reccurent Learning Algorithms for Designing Optimal Controllers of Continuous Systems, IEEE Transactions on Systems, Man, and Cybernetics – Part A: Systems and Humans, 2000, Vol. 30, No.5, pp. 580 – 588



This page intentionally left blank.

Some Discretizing Problems in Control Theory

Milica B. Naumović

Abstract – The methods of obtaining the discrete equivalents for the models of continuous-time objects without and with time delay, as well as some model conversion algorithms, are well-known in the literature. The discretizing and conversing method, presented in this paper, illustrates the use of VAN LOAN's formula for derivation of block triangular matrix exponential [1].

Keywords - Control engineering, discretizing problems, matrix exponential, system with time delay, model conversion.

I. INTRODUCTION

In numerous control applications it is useful to be able to find the matrix exponential in an effective manner. Moreover, computing integrals involving the matrix exponential is necessary, in order to find the cost equivalents in optimal control theory, for example. Notice, that Van Loan's method [1] for computing four characteristic integrals, based on the derivation of block triangular matrix exponential can be in practice in control theory. Matrix exponential is anyhow one of the most frequent computed matrix function [2], and many algorithms, developed for that purpose up to now, have bad numerical performances [3].

A method for computing the exponential of a certain block triangular matrix, due to Van Loan [1], is given as follows:

Theorem 1. Let $n_i, i=1,2,3,4$ be positive integers and set m to be their sum. If the $m \times m$ block triangular matrix \mathbf{C} is defined by

$$\mathbf{C} = \begin{bmatrix} \mathbf{A}_1 & \mathbf{B}_1 & \mathbf{C}_1 & \mathbf{D}_1 \\ \mathbf{0} & \mathbf{A}_2 & \mathbf{B}_2 & \mathbf{C}_2 \\ \mathbf{0} & \mathbf{0} & \mathbf{A}_3 & \mathbf{B}_3 \\ \mathbf{0} & \mathbf{0} & \mathbf{0} & \mathbf{A}_4 \end{bmatrix} \begin{matrix} \} n_1 \\ \} n_2 \\ \} n_3 \\ \} n_4 \end{matrix}, \quad (1)$$

then for $t \geq 0$

$$e^{\mathbf{C}t} = \begin{bmatrix} \mathbf{F}_1(t) & \mathbf{G}_1(t) & \mathbf{H}_1(t) & \mathbf{K}_1(t) \\ \mathbf{0} & \mathbf{F}_2(t) & \mathbf{G}_2(t) & \mathbf{H}_2(t) \\ \mathbf{0} & \mathbf{0} & \mathbf{F}_3(t) & \mathbf{G}_3(t) \\ \mathbf{0} & \mathbf{0} & \mathbf{0} & \mathbf{F}_4(t) \end{bmatrix}, \quad (2)$$

where

$$\mathbf{F}_j(t) = e^{\mathbf{A}_j t}, \quad j=1,2,3,4 \quad (3)$$

$$\mathbf{G}_j(t) = \int_0^t e^{\mathbf{A}_j(t-s)} \mathbf{B}_j e^{\mathbf{A}_{j+1}s} ds, \quad j=1,2,3 \quad (4)$$

$$\mathbf{H}_j(t) = \int_0^t e^{\mathbf{A}_j(t-s)} \mathbf{C}_j e^{\mathbf{A}_{j+1}(s-r)} ds \quad (5)$$

$$+ \int_0^t \int_0^s e^{\mathbf{A}_j(t-s)} \mathbf{B}_j e^{\mathbf{A}_{j+1}(s-r)} \mathbf{B}_{j+1} e^{\mathbf{A}_{j+2}r} dr ds, \quad j=1,2$$

$$\mathbf{K}_1(t) = \int_0^t e^{\mathbf{A}_1(t-s)} \mathbf{D}_1 e^{\mathbf{A}_4 s} ds + \int_0^t \int_0^s e^{\mathbf{A}_1(t-s)} \left[\mathbf{C}_1 e^{\mathbf{A}_3(s-r)} \mathbf{B}_3 + \mathbf{B}_1 e^{\mathbf{A}_2(s-r)} \mathbf{C}_2 \right] e^{\mathbf{A}_4 r} dr ds + \int_0^t \int_0^s \int_0^r e^{\mathbf{A}_1(t-s)} \mathbf{B}_1 e^{\mathbf{A}_2(s-r)} \mathbf{B}_2 e^{\mathbf{A}_3(r-w)} \mathbf{B}_3 e^{\mathbf{A}_4 w} dw dr ds. \quad (6)$$

Corollary to Theorem 1. Let \mathbf{A} , \mathbf{B} and \mathbf{Q}_c be real matrices of dimension $n \times n$, $n \times p$, and $n \times n$, respectively. Assume that matrix \mathbf{Q}_c is symmetric ($\mathbf{Q}_c^\top = \mathbf{Q}_c$) and positive semi-definite ($\mathbf{x}^\top \mathbf{Q}_c \mathbf{x} \geq 0$). Following the previous theorem and combining various submatrices, it can be shown that the

$$\text{integral } \mathbf{Q}(T) = \int_0^T e^{\mathbf{A}^\top s} \mathbf{Q}_c e^{\mathbf{A} s} ds \quad (7)$$

can be calculated as

$$\mathbf{Q}(T) = \mathbf{F}_3(T)^\top \mathbf{G}_2(T), \quad (8)$$

$$\text{where } \exp \left(\begin{bmatrix} -\mathbf{A}^\top & \mathbf{Q}_c \\ \mathbf{0} & \mathbf{A} \end{bmatrix} T \right) = \begin{bmatrix} \mathbf{F}_2(T) & \mathbf{G}_2(T) \\ \mathbf{0} & \mathbf{F}_3(T) \end{bmatrix}. \quad (9)$$

The need for computing integral (7) arises in optimal sampled-data regulation problem, for example.

It is possible to compute the exponential of the matrices of low dimension analytically for an arbitrary sampling interval T . The advantage of an analytical computation is that the result is expressed in terms of different parameters, and it is possible to examine the effect of changing these parameters. Recall that an arbitrary matrix function $f(\mathbf{C})$ can be computed via the wellknown Cayley-Hamilton Theorem. Moreover, if the matrix \mathbf{C} has distinct eigenvalues, the method of eigenvalue decomposition can be used for computing matrix function [2], [4]. In this paper the problems of discretizing the continuous-time systems without and with time delay, as well as the digital model conversion are solved by computing exponential of some special form matrices.

Milica B. Naumović is with the Faculty of Electronic Engineering, University of Niš, Aleksandra Medvedeva 14, 18000 Niš, Serbia, E-mail: nmilica@elfak.ni.ac.yu

II. DISCRETIZING THE MODELS OF ANALOG PLANTS

For simplicity, without loss of generality, consider the n th-order single-input single-output control object. It is convenient to introduce the realization sets as follows [5]:

$$S_c \stackrel{\text{def}}{=} \left\{ (\mathbf{A}_c, \mathbf{b}_c, \mathbf{d}) : G_c(s) = \frac{N_c(s)}{D_c(s)} = \mathbf{d}(s\mathbf{I} - \mathbf{A}_c)^{-1} \mathbf{b}_c \right\}, \quad (10)$$

$$S_q \stackrel{\text{def}}{=} \left\{ (\mathbf{A}_q, \mathbf{b}_q, \mathbf{d}) : G_q(z) = \frac{N_q(z)}{D_q(z)} = \mathbf{d}(z\mathbf{I} - \mathbf{A}_q)^{-1} \mathbf{b}_q \right\}, \quad (11)$$

where

$$\mathbf{A}_q = \Phi(T) = e^{\mathbf{A}_c T}, \quad (12)$$

$$\mathbf{b}_q = \int_0^T e^{\mathbf{A}_c \tau} \mathbf{b}_c d\tau, \quad (13)$$

and
$$G_q(z) = \mathbf{ZL}^{-1} \left\{ \frac{1 - e^{-Ts}}{s} G_c(s) \right\}. \quad (14)$$

Thus, (11) represents ZOH equivalent model for (10) at sampling interval T , that is the so called q-model for the continuous-time system. Note, that \mathbf{A}_q is matrix exponent, and the vector \mathbf{b}_q must be computed by integration as shown in (13). However, it is interesting to note that both \mathbf{A}_q and \mathbf{b}_q can be computed simultaneously using a single matrix exponential.

Define $(n+1) \times (n+1)$ block matrix \mathbf{M} as

$$\mathbf{M} = \left[\begin{array}{c|c} \mathbf{A}_c & \mathbf{b}_c \\ \hline \mathbf{0} & 1 \end{array} \right] \Bigg\}^n, \quad (15)$$

in which the zero in the lower left-hand corner represents an n -dimensional zero row-vector. Then, by using Van Loan's formulas (1)-(6) for matrix exponential of $\mathbf{M}T$ can be found

$$e^{\mathbf{M}T} = \left[\begin{array}{c|c} \mathbf{A}_q & \mathbf{b}_q \\ \hline \mathbf{0} & 1 \end{array} \right]. \quad (16)$$

Thus, the digital model matrices \mathbf{A}_q and \mathbf{b}_q can be computed as follows

$$\left[\mathbf{A}_q \mid \mathbf{b}_q \right] = \left[\mathbf{I} \quad \mathbf{0} \right] \cdot e^{\mathbf{M}T}, \quad (17)$$

whereas

$$\left[\mathbf{A}_c \mid \mathbf{b}_c \right] = \left[\mathbf{I} \quad \mathbf{0} \right] \cdot \mathbf{M}. \quad (18)$$

Example 1. We will use the procedure described in this section to compute continuous-time model plant $(\mathbf{A}_c, \mathbf{b}_c)$ simultaneously on the basis ZOH equivalent model for the plant given by $\left[\mathbf{A}_q \mid \mathbf{b}_q \right] = \left[\begin{array}{c|c} 1 & T & T^2/2 \\ \hline 0 & 1 & T \end{array} \right]$, where T is the sampling period. To use (15)-(18), we create the matrix

$$\mathbf{M}_1 = e^{\mathbf{M}T} = \left[\begin{array}{c|c} \mathbf{A}_q & \mathbf{b}_q \\ \hline \mathbf{0} & 1 \end{array} \right] = \left[\begin{array}{c|c} 1 & T & T^2/2 \\ \hline 0 & 1 & T \\ \hline 0 & 0 & 1 \end{array} \right]$$

that has an eigenvalue $\lambda=1$ with multiplicity $m=3$. The matrix \mathbf{M}_1 is positive-definite, and the 3×3 matrix \mathbf{M} can be written as the matrix logarithm

$$\mathbf{M} = f(\mathbf{M}_1) = (\ln \mathbf{M}_1)/T.$$

To calculate this matrix function, some formulas based on the wellknown Cayley-Hamilton theorem can be used. Namely, the matrix \mathbf{M} can be written as the matrix polynomial of degree 2 as follows

$$\mathbf{M} = \alpha(\mathbf{M}_1) = \alpha_1 \mathbf{M}_1^2 + \alpha_2 \mathbf{M}_1 + \alpha_3,$$

To compute the coefficients $\alpha_i, i=1,2,3$ the scalar function $f(\lambda) = (\ln \lambda)/T$, polynomial $\alpha(\lambda) = \alpha_1 \lambda^2 + \alpha_2 \lambda + \alpha_3$, as well as their first and second derivatives with respect to λ are required. These equations are calculated at the eigenvalue $\lambda=1$ as follows

$$\begin{aligned} f(1) &= 0 & \alpha(1) &= \alpha_1 + \alpha_2 + \alpha_3 \\ f^{(1)}(1) &= 1/T & \alpha^{(1)}(1) &= 2\alpha_1 + \alpha_2 \\ f^{(2)}(1) &= -1/T & \alpha^{(2)}(1) &= 2\alpha_1 \end{aligned}$$

When the values of $\alpha_1 = -1/2T, \alpha_2 = 2/T$ and $\alpha_3 = -3/2T$ are substituted in, the result is

$$\mathbf{M} = -\frac{1}{2T} \begin{bmatrix} 1 & 2T & 2T^2 \\ 0 & 1 & 2T \\ 0 & 0 & 1 \end{bmatrix} + \frac{2}{T} \begin{bmatrix} 1 & T & T^2/2 \\ 0 & 1 & T \\ 0 & 0 & 1 \end{bmatrix} - \frac{3}{2T} \begin{bmatrix} 1 & 0 & 0 \\ 0 & 1 & 0 \\ 0 & 0 & 1 \end{bmatrix} = \begin{bmatrix} 0 & 1 & 0 \\ 0 & 0 & 1 \\ 0 & 0 & 0 \end{bmatrix}$$

Finally, \mathbf{A}_c and \mathbf{b}_c are extracted from the just derived matrix \mathbf{M} according to the partitions shown in (15). So, we get state-space model $(\mathbf{A}_c, \mathbf{b}_c)$, with $\mathbf{A}_c = \begin{bmatrix} 0 & 1 \\ 0 & 0 \end{bmatrix}$ and

$$\mathbf{b}_c = \begin{bmatrix} 0 \\ 1 \end{bmatrix} \text{ for the considered double integrator plant.}$$

III. MODEL CONVERSIONS

Let an integer N denotes the ratio between the slow sampling period T_s and the fast sampling period T , i.e. $N = T_s/T$. Let $(\mathbf{A}_{qs}, \mathbf{b}_{qs}, \mathbf{d})$ represents the slow discrete-time model of the corresponding continuous-time model (10). The commonly used matrix continued-fraction method to convert $(\mathbf{A}_q, \mathbf{b}_q, \mathbf{d})$ to $(\mathbf{A}_c, \mathbf{b}_c, \mathbf{d})$, for example is [6]:

$$\begin{aligned} \mathbf{A}_c &= \frac{1}{T} \ln \mathbf{A}_q \approx \frac{2}{T} \mathbf{F} \\ &\approx \frac{2}{T} \mathbf{F} \left[\mathbf{I}_n - \frac{4}{15} \mathbf{F}^2 \right] \left[\mathbf{I}_n - \frac{3}{5} \mathbf{F}^2 \right]^{-1} \approx \dots \end{aligned} \quad (19)$$

where

$$\mathbf{F} \stackrel{\text{def}}{=} (\mathbf{A}_q - \mathbf{I}_n)(\mathbf{A}_q + \mathbf{I}_n)^{-1}. \quad (20)$$

The vector \mathbf{b}_c can be found by

$$\mathbf{b}_c = \mathbf{A}_c (\mathbf{A}_q - \mathbf{I}_n)^{-1} \mathbf{b}_q. \quad (21)$$

The conversion of the fast-rate digital model $(\mathbf{A}_q, \mathbf{b}_q, \mathbf{d})$ to a slow-rate digital model $(\mathbf{A}_{qs}, \mathbf{b}_{qs}, \mathbf{d})$ with the slow sampling period T_s can be carried out as follows. According to (21), we have $\mathbf{b}_q = (\mathbf{A}_q - \mathbf{I}_n) \mathbf{A}_c^{-1} \mathbf{b}_c$, which gives

$\mathbf{A}_c^{-1} \mathbf{b}_c = (\mathbf{A}_q - \mathbf{I}_n) \mathbf{b}_q$, and $\mathbf{b}_{qs} = (\mathbf{A}_{qs} - \mathbf{I}_n) \mathbf{A}_c^{-1} \mathbf{b}_c$. Thus we obtain $(\mathbf{A}_{qs}, \mathbf{b}_{qs})$ from $(\mathbf{A}_q, \mathbf{b}_q)$ as

$$\mathbf{A}_{qs} = \mathbf{A}_q^N \quad (22)$$

and $\mathbf{b}_{qs} = (\mathbf{A}_{qs} - \mathbf{I}_n) (\mathbf{A}_q - \mathbf{I}_n)^{-1} \mathbf{b}_q$. (23)

Note that the conversion of the fast-rate digital model to a slow-rate one can be obtain in another way by using relation (16), i.e.

$$e^{\mathbf{M}T_s} = \begin{bmatrix} \mathbf{A}_{qs} & \mathbf{b}_{qs} \\ \mathbf{0} & 1 \end{bmatrix} = \begin{bmatrix} \mathbf{A}_q & \mathbf{b}_q \\ \mathbf{0} & 1 \end{bmatrix}^N. \quad (24)$$

By induction it can be shown that

$$\begin{bmatrix} \mathbf{A}_q & \mathbf{b}_q \\ \mathbf{0} & 1 \end{bmatrix}^N = \begin{bmatrix} \mathbf{A}_q^N & \left(\sum_{i=0}^{N-1} \mathbf{A}_q^i \right) \mathbf{b}_q \\ \mathbf{0} & 1 \end{bmatrix}. \quad (25)$$

So, the matrices of the T_s model and T model have the relation

$$\mathbf{A}_{qs} = \mathbf{A}_q^N, \quad \text{and} \quad \mathbf{b}_{qs} = \left(\sum_{i=0}^{N-1} \mathbf{A}_q^i \right) \mathbf{b}_q. \quad (26)$$

IV. DISCRETIZING A CONTINUOUS-TIME SYSTEM WITH TIME DELAY

Consider single-input single-output continuous-time system with time delay described in state-space by

$$\dot{\mathbf{x}}(t) = \mathbf{A}_c \mathbf{x}(t) + \mathbf{b}_c u(t - \tau) \quad (27)$$

$$c(t) = \mathbf{d} \mathbf{x}(t). \quad (28)$$

It is assumed that the time delay is longer than the sampling period T . Let

$$\tau = (d-1)T + \tau', \quad (29)$$

where $0 < \tau' \leq T$ and $d (\geq 1)$ is an integer. Discrete-time transfer functions of systems with a delay that is not an integer times the sampling period are easily obtained by using the modified ZZ transform [7]. The discrete-time state-space model of system (27)-(29) is given in literature [8]-[10], [4] by

$$\begin{bmatrix} \mathbf{x}[(k+1)T] \\ u(kT) \end{bmatrix} = \begin{bmatrix} \Phi & \Gamma_1 \\ \mathbf{0} & 0 \end{bmatrix} \begin{bmatrix} \mathbf{x}(kT) \\ u[(k-1)T] \end{bmatrix} + \begin{bmatrix} \Gamma_0 \\ 1 \end{bmatrix} u(kT) \quad \text{for } d=1, \quad (30)$$

or when $d \geq 2$, the equations are

$$\begin{bmatrix} \mathbf{x}[(k+1)T] \\ u(kT-dT+1) \\ \vdots \\ u(kT-T) \\ u(kT) \end{bmatrix} = \begin{bmatrix} \Phi & \Gamma_1 & \Gamma_0 & 0 & \dots & 0 \\ \mathbf{0} & 0 & 1 & 0 & \dots & 0 \\ \vdots & & & & \ddots & \\ \mathbf{0} & 0 & 0 & 0 & \dots & 1 \\ \mathbf{0} & 0 & 0 & 0 & \dots & 0 \end{bmatrix} \begin{bmatrix} \mathbf{x}(kT) \\ u(kT-dT) \\ \vdots \\ u(kT-2T) \\ u(kT-T) \end{bmatrix} + \begin{bmatrix} 0 \\ 0 \\ \vdots \\ 0 \\ 1 \end{bmatrix} u(kT), \quad (31)$$

where

$$\Phi = e^{\mathbf{A}_c T}$$

$$\Gamma_1 = e^{\mathbf{A}_c(T-\tau')} \int_0^{\tau'} e^{\mathbf{A}_c \lambda} \mathbf{b}_c d\lambda, \quad \text{and} \quad \Gamma_0 = \int_0^{T-\tau'} e^{\mathbf{A}_c \lambda} \mathbf{b}_c d\lambda. \quad (32)$$

The output equation is obtained from (28) to be

$$c(kT) = [\mathbf{d} \ 0 \ \dots \ 0] \begin{bmatrix} \mathbf{x}(kT) \\ u(kT-dT) \\ \vdots \\ u(kT-T) \end{bmatrix}. \quad (33)$$

Notice that the above equations (30) and (31) contain partitioned matrices. Each zero below the matrix Φ in (30) and (31) represents a row vector of n zeros. Recall, that because the signal $u(t)$ is piecewise constant over the sampling interval, the delayed signal $u(t-\tau)$ is also piecewise constant. However, the delayed signal will change between the sampling instants as Fig. 1 visualizes.

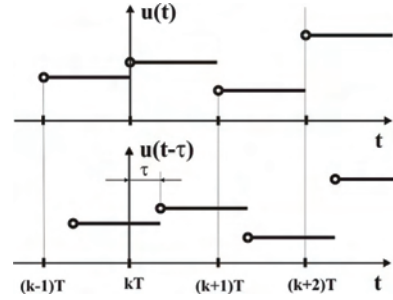


Fig. 1. The piecewise constant signals $u(t)$ and $u(t-\tau)$, $\tau < T$

To integrate the differential equation (27) over one sample period in order to obtain *ZOH* equivalent model, it is convenient to split the integration interval into two parts, so that control signal $u(t-\tau)$ is constant in each part. Hence, the motion of the considered dynamical system (27)-(29) in the interval $kT \leq t < (k+1)T$ is

$$\mathbf{x}(t) = \Phi(t-kT) \mathbf{x}(kT) + \Theta(t-kT) u[(k-1)T], \quad kT \leq t < kT + \tau \quad (34)$$

and

$$\mathbf{x}(t) = \Phi(t-kT-\tau) \mathbf{x}(kT+\tau) + \Theta(t-kT-\tau) u(kT), \quad kT + \tau \leq t < (k+1)T \quad (35)$$

where

$$\Phi(t) = e^{\mathbf{A}c t} \quad \text{and} \quad \Theta(t-\lambda) = \int_{\lambda}^t \Phi(t-\upsilon) \mathbf{b}_c d\upsilon. \quad (36)$$

If we now substitute $t = kT + \tau$ in (34) and $t = (k+1)T$ in (35), we obtain

$$\mathbf{x}(kT + \tau) = \Phi(\tau)\mathbf{x}(kT) + \Theta(\tau)u[(k-1)T], \quad (37)$$

and

$$\mathbf{x}[(k+1)T] = \Phi(T-\tau)\mathbf{x}(kT + \tau) + \Theta(T-\tau)u(kT). \quad (38)$$

It is clear, that the relations (37) and (38) can be expressed as the function of the matrices \mathbf{M} and $e^{\mathbf{M}T}$, given by (15) and (16), as shown below:

$$\begin{bmatrix} \mathbf{x}(T+\tau) \\ u(kT-T) \end{bmatrix} = \begin{bmatrix} \mathbf{A}_{q1} & \mathbf{b}_{q1} \\ \mathbf{0} & 1 \end{bmatrix} \begin{bmatrix} \mathbf{x}(kT) \\ u(kT-T) \end{bmatrix} = e^{\mathbf{M}T} \begin{bmatrix} \mathbf{x}(kT) \\ u(kT-T) \end{bmatrix} \quad (39)$$

and

$$\begin{bmatrix} \mathbf{x}[(k+1)T] \\ u(kT) \end{bmatrix} = \begin{bmatrix} \mathbf{A}_{q2} & \mathbf{b}_{q2} \\ \mathbf{0} & 1 \end{bmatrix} \begin{bmatrix} \mathbf{x}(kT + \tau) \\ u(kT) \end{bmatrix} = e^{\mathbf{M}(T-\tau)} \begin{bmatrix} \mathbf{x}(kT + \tau) \\ u(kT) \end{bmatrix} \quad (40)$$

If we substitute (39) in (40) we obtain

$$\begin{bmatrix} \mathbf{x}[(k+1)T] \\ u(kT) \end{bmatrix} = \begin{bmatrix} \mathbf{A}_{q2} & \mathbf{b}_{q2} \\ \mathbf{0} & 1 \end{bmatrix} \begin{bmatrix} \mathbf{A}_{q1}\mathbf{x}(kT) + \mathbf{b}_{q1}u(kT-T) \\ u(kT) \end{bmatrix} \\ = \begin{bmatrix} \mathbf{A}_{q2}\mathbf{A}_{q1}\mathbf{x}(kT) + \mathbf{A}_{q2}\mathbf{b}_{q1}u(kT-T) + \mathbf{b}_{q2}u(kT) \\ u(kT) \end{bmatrix}. \quad (41)$$

Note that we can compute the product of the matrix exponentials as follows:

$$e^{\mathbf{M}(T-\tau)} e^{\mathbf{M}T} = \begin{bmatrix} \mathbf{A}_{q2} & \mathbf{b}_{q2} \\ \mathbf{0} & 1 \end{bmatrix} \cdot \begin{bmatrix} \mathbf{A}_{q1} & \mathbf{b}_{q1} \\ \mathbf{0} & 1 \end{bmatrix} \\ = \begin{bmatrix} \mathbf{A}_{q2}\mathbf{A}_{q1} & \mathbf{A}_{q2}\mathbf{b}_{q1} + \mathbf{b}_{q2} \\ \mathbf{0} & 1 \end{bmatrix}. \quad (42)$$

Finally, the equations (41)-(42) can be compared with (30)-(32) resulting in

$$\begin{aligned} \Phi &= \mathbf{A}_{q2}\mathbf{A}_{q1} \\ \Gamma_0 &= \mathbf{b}_{q2} \\ \Gamma_1 &= \mathbf{A}_{q2}\mathbf{b}_{q1}. \end{aligned} \quad (43)$$

Example 2. Calculate the ZOH equivalent model for the following continuous-time system with time delay

$$\dot{\mathbf{x}}(t) = \begin{bmatrix} 1 & 0 \\ 1 & 1 \end{bmatrix} \mathbf{x}(t) + \begin{bmatrix} 1 \\ 0 \end{bmatrix} u(t-\tau), \quad \text{where } \tau = 0.2 \text{ and } T = 0.3.$$

The matrix \mathbf{M} defined in (15) is

$$\mathbf{M} = \begin{bmatrix} \mathbf{A}_c & \mathbf{b}_c \\ \mathbf{0} & 0 \end{bmatrix} = \begin{bmatrix} 1 & 0 & | & 1 \\ 1 & 1 & | & 0 \\ \hline 0 & 0 & | & 0 \end{bmatrix}. \quad \text{The matrix exponentials are}$$

$$e^{\mathbf{M}T} = \begin{bmatrix} \mathbf{A}_{q1} & \mathbf{b}_{q1} \\ \mathbf{0} & 1 \end{bmatrix} = \begin{bmatrix} e^{\tau} & 0 & | & e^{\tau}-1 \\ \tau e^{\tau} & e^{\tau} & | & (\tau-1)e^{\tau}+1 \\ \hline 0 & 0 & | & 1 \end{bmatrix},$$

and

$$e^{\mathbf{M}(T-\tau)} = \begin{bmatrix} \mathbf{A}_{q2} & \mathbf{b}_{q2} \\ \mathbf{0} & 1 \end{bmatrix} = \begin{bmatrix} e^{T-\tau} & 0 & | & e^{T-\tau}-1 \\ (T-\tau)e^{T-\tau} & e^{T-\tau} & | & (T-\tau-1)e^{T-\tau}+1 \\ \hline 0 & 0 & | & 1 \end{bmatrix}.$$

Using (43) we get

$$\Phi = \mathbf{A}_{q2}\mathbf{A}_{q1} = \begin{bmatrix} e^T & 0 \\ T e^T & e^T \end{bmatrix} = \begin{bmatrix} 1.350 & 0 \\ 0.405 & 1.350 \end{bmatrix},$$

$$\Gamma_0 = \mathbf{b}_{q2} = \begin{bmatrix} e^{T-\tau}-1 \\ (T-\tau-1)e^{T-\tau}+1 \end{bmatrix} = \begin{bmatrix} 0.105 \\ 0.005 \end{bmatrix},$$

and

$$\Gamma_1 = \mathbf{A}_{q2}\mathbf{b}_{q1} = \begin{bmatrix} e^{T-\tau}(e^{\tau}-1) \\ e^{T-\tau}(1-T+\tau)+e^T(T-1) \end{bmatrix} = \begin{bmatrix} 0.245 \\ 0.050 \end{bmatrix}.$$

V. CONCLUSION

This paper deals with a procedure for simultaneous computing the both matrices of zero-order hold equivalent q-model (\mathbf{A}_q and \mathbf{b}_q) using a single matrix exponential. It is pointed to several applications of this effective approach in some control tasks.

REFERENCES

- [1] C. Van Loan, "Computing Integrals Involving the Matrix Exponential", *IEEE Trans. Automat. Contr.*, Vol. AC-23, No. 3, pp. 395-404, 1978.
- [2] G.H. Golub, C.F. Van Loan, *Matrix Computations*, Johns Hopkins University Press, Baltimore, MD, 1983.
- [3] C.B. Moler, C.F. Van Loan, "Nineteen Dubious Ways to Compute the Exponential of a Matrix", *SIAM Review*, Vol. 20, No. 4, pp. 801-836, 1978.
- [4] R. J. Vaccaro, *Digital Control, A State-Space Approach*, McGraw-Hill, Inc., 1995.
- [5] M.B. Naumović, M.R. Stojić, "Comparative study of finite word length effects in digital filter design via the shift and delta transforms", *Electrical Engineering, Archiv für Elektrotechnik*, Vol. 82, No. 3-4, pp. 213-216, 2000.
- [6] L.S. Shieh, X.M. Zhao, J.W. Sunkel, "Hybrid state-space self-tuning control using dual-rate sampling", *IEE Proc. Control Theory and Applications*, Part D, Vol. 138, No. 1, pp. 50-58, 1991.
- [7] E. I. Jury, *Theory and Application of the z-Transform Method*, New York: Wiley, 1964.
- [8] G.F. Franklin, J.D. Powell, *Digital Control of Dynamic Systems*, Reading, MA: Addison-Wesley, 1980.
- [9] B. Wittenmark, "Sampling of a System with a Time Delay", *IEEE Trans. Automat. Contr.*, Vol. AC-30, No. 5, pp. 507-510, 1985.
- [10] K.J. Åström, B. Wittenmark, *Computer-Controlled Systems - Theory and Design*, Englewood Cliffs, N.J.: Prentice-Hall, 1984.

SESSION PTDS I

Power Transmission and Distribution Systems I

An Algorithm for Coupled Electric and Thermal Fields in Insulation of the Large Power Cables

Ion T. Cârstea¹ and Daniela P. Cârstea²

Abstract – Dielectric heating is caused by losses due to friction of the molecular polarisation process in dielectric materials. A polluted dielectric has a finite resistance so that the leakage current in the dielectric heats the dielectric. The problem of heating is a coupled thermal-electric problem.

The paper presents an algorithm based on a 2D model for coupled fields in the insulation of a large power cable. The heat transfer in insulation is described by the heat conduction equation where the heat sources are both internal sources generated by the leakage current in a resistive dielectric, and the boundary heat sources of the convective and Dirichlet/Neumann type.

Keywords – Coupled fields; Dielectric heatings; Finite element Method.

I. INTRODUCTION

This work deals with the heat generated by ohmic losses generated by the electric field in high-voltage cables. The problem is described by a coupled thermal-electric set of equations. The coupling between the two fields is the thermal effect of the electrical current or a material property as the electrical conductivity. A computation algorithm is presented for coupled problems in two dimensions.

A numerical algorithm based on the finite element method (FEM) is presented describing the solution of two-dimensional systems. In our example we consider only steady-state regime for the electric field although many transient regimes appear in the behaviour of the electromagnetic devices. The assumption is acceptable because the time constants for the electric phenomenon are less than the time constants for the thermal field.

The problem of dielectric heating involves two approaches:

1. The capacitive case. In this case, all the involved insulation media can be assumed to be perfect dielectric without free charges. The mathematical model is given by Laplace's equation, written with the potential V . The conductivity of the medium is zero. In other words the dielectric is assumed to be perfectly insulating so that neither its permittivity nor the voltage frequency mattered.

2. The resistive case. In this case the resistive contribution is not negligible.

We consider a coaxial cable with two insulation layers that can be imperfect dielectrics. Our target example is selected in order to compare the analytical solutions with the numerical solutions. At the application of a voltage U , the field changes from a purely capacitive distribution to a purely resistive field. The field between the initial and final has a time variation.

Generally speaking there is no perfect dielectric insulation so that a leakage current exists. Ohmic losses cause the dielectric heating. A parallel-plane model can be used to compute the electric and thermal fields.

II. MATHEMATICAL MODEL

The electric field distribution can be obtained by approximation of the Maxwell equations. These approximations take different forms in accordance with material properties of the equipment. In modelling of these physical systems we must consider both perfect dielectrics and imperfect (or polluted) dielectrics.

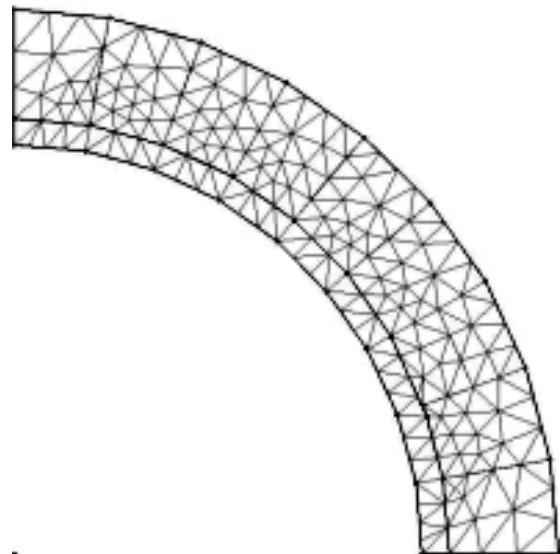


Fig. 1. The analysis domain

In our target example the analysis domain is plotted in the Fig. 1. The mesh with triangular elements is presented.

The static field distribution can be modelled by the following equations:

$$\nabla \times \vec{E} = 0; \quad \vec{E} = \rho \vec{J}$$

with: ρ - the material resistivity, E - the electric strength and J - the current density.

¹Ion T. Cârstea is with the Faculty of Automatics, Computers and Electronics, Craiova, str. Doljului 14, bl. C8c, sc.1, apt.7, judet Dolj, Romania, E-mail: incrst@yahoo.com

²Daniela P. Cârstea is with the Industrial Group of Romanian Railways, Craiova, str. Brâncuși nr. 15, Craiova, Romania, E-mail: danacrst@yahoo.com

A 2D-field model was developed for a resistive distribution of the electric field. An electric vector potential P is introduced by the relation [6]:

$$\vec{J} = \nabla \times \vec{P}$$

Laplace's equation describes the field distribution (for anisotropic materials):

$$\frac{\partial}{\partial x} \left(\rho_x \frac{\partial P}{\partial x} \right) + \frac{\partial}{\partial y} \left(\rho_y \frac{\partial P}{\partial y} \right) = 0 \quad (1)$$

Mathematical model for the thermal field is the conduction equation:

$$\frac{\partial}{\partial x} \left(k_x \frac{\partial T}{\partial x} \right) + \frac{\partial}{\partial y} \left(k_y \frac{\partial T}{\partial y} \right) + q = \gamma c \frac{\partial T}{\partial t} \quad (2)$$

with: $T(x, y, t)$ - temperature in the point with coordinates (x, y) at the time t ; k_x, k_y - thermal conductivities; γ - specific mass; c - specific heating; q - heating source.

It is obviously that there is a natural coupling between electrical and thermal fields. Thus, the resistivity in equation (1) is a function of T , and the heating source q in (2) depend on J . Numerical models for the two field problems can be obtained by the finite element method. An iterative procedure was used for the temperature distribution.

In dielectric applications we consider the dependency of the temperature by the form:

$$\sigma = \sigma_0 \exp(\alpha T) \exp(\gamma E)$$

where: σ_0 stands for the conductivity at a temperature of 0°C and field strength of 0 kV/mm ; α denotes the temperature dependency coefficient and γ denotes the field dependency coefficient.

III. NUMERICAL MODELLING

The differential model can not be solved analytically. A numerical model can be obtained by Galerkin's procedure.

In general the time dependent problems after a spatial discretization can lead to a lumped-parameter model. For example, the heat equation, after spatial discretization, lead to a system of ordinary differential equations by the form:

$$[S] \left\{ \frac{\partial T}{\partial t} \right\} + [R] \{T\} + \{b\} = 0 \quad (3)$$

where $[R]$ and $[S]$ are matrices and b is the vector of the free terms.

The algorithm in pseudo-code has the following structure:

1. Choose the initial value of the temperature

2. Repeat

{Computations for electrical field}

- Compute the resistivity ρ
- Solve the numerical model for electric potential P

{Computations for thermal field}

- Compute the heating source q by (2)
- Solve the numerical model for the temperature

3. Until the convergence_test is TRUE

The convergence test is the final time of the physical process but in the internal loop of the cycle repeat-until we

have an iterative process because the electric conductivity depends highly on temperature T and electric field E .

We present the numerical model for the heat equation. A spatial discretization leads to the ordinary differential equation (3). The time discretization of the temperature can be obtained by a formula of finite difference:

$$\frac{\partial T}{\partial t} = \frac{T^{(k)} - T^{(k-1)}}{\delta t}$$

With this approximation, the heat equation (2) becomes:

$$(\gamma c) T^{(k)} = \nabla(k \nabla T^{(n-1)}) + \frac{(c \gamma) T^{(k-1)}}{\delta t} + q^{(k-1)}$$

A refinement of the numerical algorithm in pseudo-code can have the following form:

1. Put the iteration counter k on 0 and the initial time t_0 .
2. $k = k + 1$
3. Compute the resistivity value.
4. Solve the numerical model for the electric potential P
5. Compute the heat source q in Eqn. 2.
6. Update the numerical model for the temperature
7. Solve the numerical model for the thermal field. The result is the temperature at the moment t_k .
8. Increase the time with the step δt in order to obtain the following step t_k .
9. If the time t_k is less than the imposed limit of the time, then jump to the step 2, else stop.

IV. NUMERICAL RESULTS

Our example is a high-voltage direct-current (HVDC) cable with two insulation layers. The leakage current in dielectric is caused by the finite resistivity of the dielectric insulation.

The geometrical properties of the cable are:

- the internal radius of the first layer is 15 [mm];
- the internal radius of the second layer is 16 [mm];
- the external radius of the second layer is 20 [mm];

The physical electrical properties are:

- The voltage of the cable is $U = 150$ [kV];
- Resistivity of the first layer is $1 \cdot 10^9$ [$\Omega \cdot \text{m}$]
- Resistivity of the second layer is $2 \cdot 10^{10}$ [$\Omega \cdot \text{m}$]

The physical properties are:

- Thermal conductivity of the first layer is 0.271 [W/K.m]
- Specific heat $c = 1800$ [J/Kg.K]
- Specific mass $\gamma = 1300$ [Kg/m³]
- Thermal conductivity of the second layer is 0.17 [W/K.m]
- Specific heat $c = 1600$ [J/Kg.K]
- Specific mass $\gamma = 1200$ [Kg/m³]

At the application of a high voltage the field has a capacitive distribution initially [4]. This distribution is for a short time so that it is not interest for the temperature distribution. Finally the field has a resistive distribution. Between these limits there is an intermediate field that can be computed by an iterative procedure.

The analysis domain is the insulation space. The symmetry of the problem can reduce the analysis domain to a quarter (Fig.1).

The heat source is the thermal effect of the current in the dielectric insulation and the load current of the cable. It is obviously that the ohmic losses in the cable conductor are the most important heat source.

A. Constant heat flux

In our first case we consider that there is a constant heat flux on the interface conductor-insulation. The source of this flux is the Joule-Lenz's effect of the load in the cable. The mathematical model for the heat transfer is the conduction

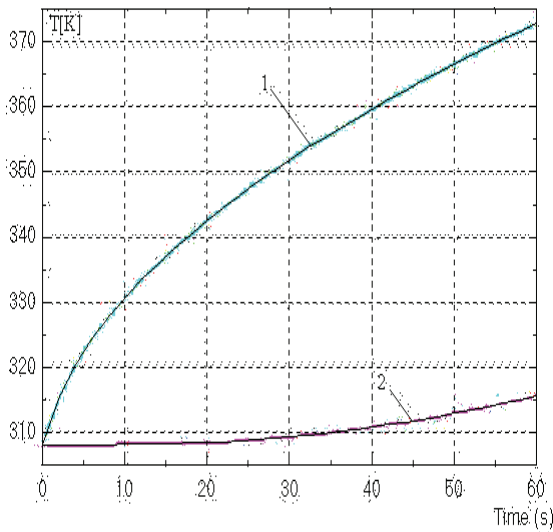


Fig. 2. Temperature versus time

equation (2). The boundary conditions are Neumann's condition at the interface conductor-insulation, and convective condition at the boundary insulation-environment.

The Neumann's condition can be computed by the conductor losses in the case the cable was loaded before switching of the step voltage, that is the current in the cable has been raised long before and the temperature distribution in the cable is stable. In this case the value of the heat flux is computed with the relation [1]:

$$p = \frac{P_{cond}}{2\pi r_0}$$

with P_{cond} - the ohmic losses per cable meter in the inner conductor as Joule-Lenz's effect.

Thus, Neumann's condition is:

$$\frac{\partial T}{\partial n} \Big|_{C_1} = -p$$

with C_1 - the interface of the cable conductor and insulation.

At the interface insulation-environment we consider a convective condition by the form:

$$\frac{\partial T}{\partial n} \Big|_{C_2} = h(T - T_\infty)$$

with h - the convective coefficient, T_∞ - the ambient temperature and C_2 - the boundary of the cable and the external medium.

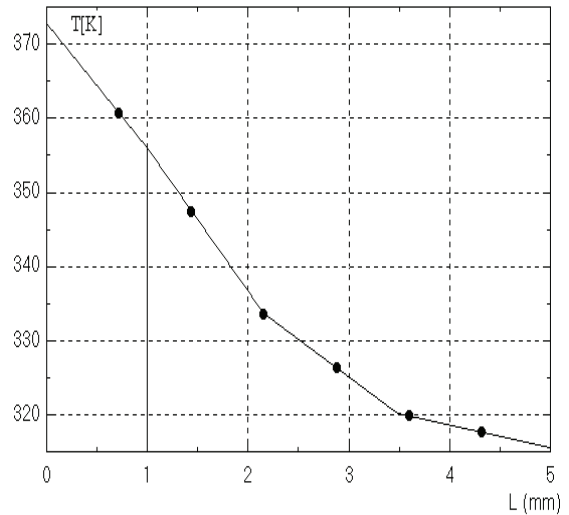


Fig. 3. Final temperature in radial direction

In Fig.2 the temperatures vs. time at external surface of the conductor the curve 1 (green), and environment surface - the curve 2 (red) are plotted. The time interval was 60 [s]. The convection coefficient h was 12 for an environment temperature 308 [K] (35 °C).

In the Fig. 3 the final distribution of the temperature in the radial direction is plotted. The width of the insulation is 5 [mm].

B. Constant temperature

Another practical assumption in electrical engineering is a Dirichlet boundary condition at the interface conductor-insulation. For our target example we considered a constant temperature of the conductor surface and a convective condition at the boundary insulation - environment. In numerical simulation the conductor temperature was considered as 100 °C (373.16 K).

In Fig. 4 the temperature versus time is plotted in two interest points. The first curve denoted 1 (green) is the temperature at the external surface of the first layer. The curve 2 (red) represents the temperature at the external surface of the cable.

From the engineering viewpoint the assumption of Neumann's condition seems more realistic. The heat flux at the conductor surface can be estimated more accurate than the conductor temperature.

An accurate model can be obtained by including the conductor in the analysis domain. This approach increases the computational effort. This case was presented in reference [2].

We presented insulation with two layers. But in advanced technology the first layer at the conductor surface is a

semiconductor. In this way the variation of the electrical field at the interface conductor-insulation is smooth.

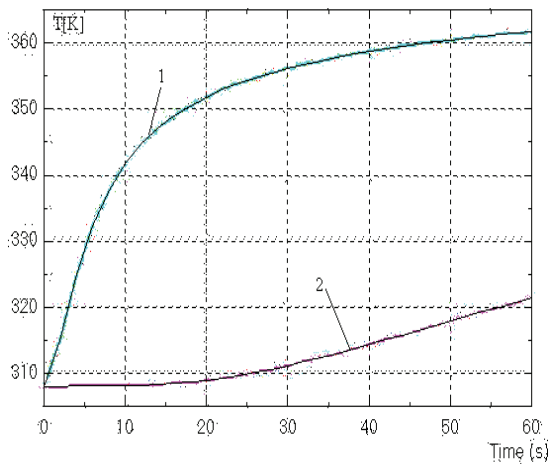


Fig. 4. Temperature versus time for Dirichlet condition

In these two examples we considered a steady-state regime of the electric field. This is a practical situation but there are cases where the voltage has step variations so that a transient regime appears as a natural situation [5].

V. CONCLUSION

In this paper we presented an algorithm for coupled electric and thermal fields in the insulation of the large power cables. A parallel-plane model was considered both for electrical field

and thermal field. The numerical models were obtained by the finite element method in a 2D space.

As target example we considered a cable with two-insulation layer. The resistivity of the insulation was considered as finite value. In this case the ohmic losses of the leakage current in insulation generate supplementary losses. The principal heat source remains the losses in the cable conductor.

As first example we considered a constant heat flux on the interface conductor-insulation. In practice, the heat flux is dependent on the temperature of the cable conductor. By the numerical simulation we can consider all practical cases in the operating regimes of the cable.

In the second example we considered a constant temperature of the conductor.

REFERENCES

- [1] Cârstea, D. "CAD tools for magneto-thermal and electric-thermal coupled fields". Research Report in a CNR-NATO Grant. University of Trento. Italy, 2004
- [2] Cârstea, D., Cârstea, I. *CAD in electrical engineering*. The finite element method. Editor SITECH. 2000. Craiova, Romania.
- [3] *** QuickField program, version 5.3. Year 2004. Page web: www.tera-analysis.com. Company: Tera analysis
- [4] Cârstea, D., Cârstea, I. A finite element technique for HVDC insulation parameters computation. In: *Annals of the University Arad, Romania*. October 2000.
- [5] Cârstea, D., Cârstea, I. Computation models for electrical field in HVDC cables. In: *Papers of the Energy National Conference CNE-M-2000, 19-21 October 2000, Chişinău, Moldova*.
- [6] Bastos, J.P.A., Sadowski, N., Carlson, R. A modelling approach of a coupled problem between electrical current and its thermal effects. In: *IEEE Transactions on Magnetics*, vol.26, No.2, March 1990.

Control of the Electrical Field in the Connectors for High-Voltage Cables

Ion T. Cârstea¹ and Daniela P. Cârstea²

Abstract – The paper presents the analysis and control of electrical field in the mechanical connectors of the high-voltage (HV) cables. In the cable terminals a field enhancement occurs because the core has a sharp edge and the shield is interrupted. A mechanical connector links the cables and controls the electric field using special materials to ensure a homogeneous potential distribution.

We present the analysis of the electric field in connectors and the control of the electrical field using Raychem technology. A semiconductor shield and a control tube can optimise the field distribution in cable connectors and terminals.

Keywords – Numerical analysis; High-voltage cables; Finite element Method.

I. INTRODUCTION

The problem of the analysis and control of the electrical fields in cable terminals is an open problem that involves a multidisciplinary research. The problem of an insulated electrical conductor fitting into a grounded screen is a common configuration in many electromagnetic devices so that the results from our case can be extended in other similar areas.

We consider a high-voltage cable (Fig. 1) where the significances of the components are [1]: 1 – conductor; 2 – phase insulation; 3 – a layer for field control; 4 – a semiconductor shield.

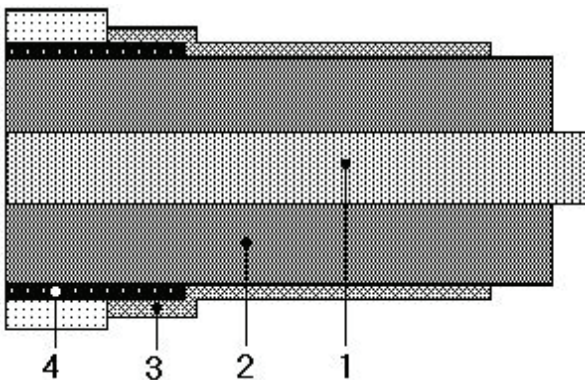


Fig. 1. Cable terminal

The role of the control tube is to do a uniform distribution of the field lines and electrical field in terminal. The material of the tube has a volume resistivity and permittivity controlled rigorously. The tube has a non-linear resistivity with behaviour of a varistor. It has a direct contact with the semiconductor shield of each terminal of the two cables that are connected.

At the joints of two cables the mechanical connectors can be used [1]. In Fig. 2 an axial section of the connection is presented with the following components: 1 – conductor; 2 – phase insulation; 3 – control tube; 4 - muff insulation; 5 – semiconductor layer; 6 – the connector; 7 – a special material for filling (mastic); 8 – semiconductor layer (mantle).

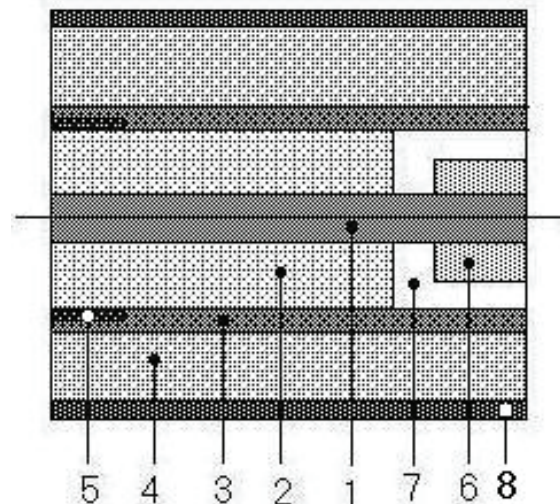


Fig. 2. An axial section in muff

Generally speaking there is no perfect dielectric insulation so that a leakage current exists. Ohmic losses cause the dielectric heating. A parallel-plane model can be used to compute the electric and thermal fields.

The tube for the field control covers the semiconductor shields of each cable terminal of the muff. The mastic has a high permittivity and realises a uniform distribution of the electrical field. In this way the electrical stresses are reduced at the cable terminals. The muff insulation is in direct contact with the external semiconductor and the thick is selected to prevent the partial discharges in the separation zone [1].

II. MATHEMATICAL MODEL

The electric field distribution can be obtained by approximation of the Maxwell equations. These

¹Ion T. Cârstea is with the Faculty of Automatics, Computers and Electronics, Craiova, str. Doljului 14, bl. C8c, sc.1, apt.7, judet Dolj, Romania, E-mail: incrst@yahoo.com

²Daniela P. Cârstea is with the Industrial Group of Romanian Railways, Craiova, str. Brâncuși nr. 15, Craiova, Romania, E-mail: danacrst@yahoo.com

approximations take different forms in accordance with material properties of the equipment. In modelling of these physical systems we must consider both perfect dielectrics and imperfect (or polluted) dielectrics. The control layer of the field has a finite resistivity and controls the electrical stress in the terminals.

The static field distribution can be modelled by the following equations [2]:

$$\nabla \times \vec{E} = 0; \quad \vec{E} = \rho \vec{J}$$

with: ρ - the material resistivity, E - the electric strength and J - the current density.

A 2D-field model was developed for a resistive distribution of the electric field. An electric vector potential P is introduced by the relation:

$$\vec{J} = \nabla \times \vec{P}$$

Laplace's equation describes the field distribution (for anisotropic materials):

$$\frac{\partial}{\partial x} \left(\rho_x \frac{\partial P}{\partial x} \right) + \frac{\partial}{\partial y} \left(\rho_y \frac{\partial P}{\partial y} \right) = 0 \quad (1)$$

Mathematical model for the thermal field is the conduction equation:

$$\frac{\partial}{\partial x} \left(k_x \frac{\partial T}{\partial x} \right) + \frac{\partial}{\partial y} \left(k_y \frac{\partial T}{\partial y} \right) + q = \gamma c \frac{\partial T}{\partial t} \quad (2)$$

with: $T(x, y, t)$ - temperature in the point with coordinates (x, y) at the time t ; k_x, k_y - thermal conductivities; γ - specific mass; c - specific heating; q - heating source.

It is obviously that there is a natural coupling between electrical and thermal fields. Thus, the resistivity in equation (1) is a function of T , and the heating source q in (2) depend on J . Numerical models for the two field problems can be obtained by the finite element method. An iterative procedure was used for the temperature distribution.

The imperfect insulation leads to local heating of the connectors so that a coupled model can be a good approach of the electrical field computation. In our work we consider the electrical properties are constant with the temperature.

III. CONTROL OF THE FIELD DISTRIBUTION

In the real engineering, the designer of an electromagnetic device starts from an imposed performance of the device and tries to reach the performance by a command that can be a distributed or boundary command. In the area of the electrical engineering we can have a parametric optimisation. Practically, there are three possible parameters [3]:

- A physical property as electrical property (for example the permittivity);
- The excitation of the system (voltage or electrical current);
- A geometrical parameter (configuration, dimensions in any direction etc.)

In our target example, there are many regions involving different materials as conductor, semiconductor and dielectrics (insulation). In a synthesis problem we seek the material property - the permittivity that needs to be used in a

certain part of the device. In other words, the optimisation parameter that we seek is the permittivity of those parts so that the object function goes to the extreme value. Gradient techniques can be used to reach the optimum parameter.

Optimisation with respect to geometry of the device is much more complex than with respect to material or excitation.

IV. NUMERICAL RESULTS

We considered the example from the figure 2. Because of the symmetry the analysis domain is limited to a half of the field domain. In the Fig. 3 the meshed domain is plotted with the axis Oz as symmetry axis (the horizontal line).

The finite element method was used for numerical

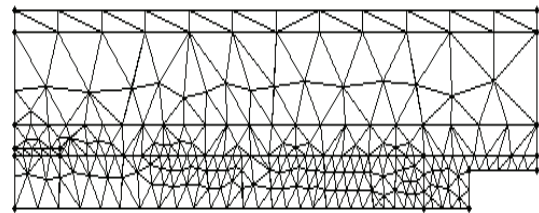


Fig. 3. Meshed domain for a muff

simulation. The program Quickfield [4] uses the triangular elements.

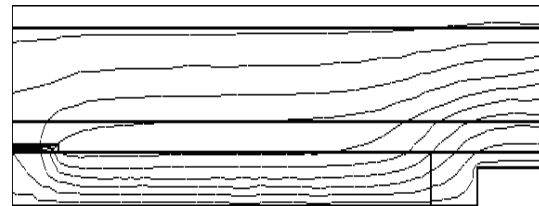


Fig. 4. Equilines of potentials

The geometrical properties of the device are:

- the radius of the conductor is 5 [mm];
- the external radius of the phase insulation is 12 [mm];
- the external radius of the control tube is 16 [mm];
- the external radius of the muff insulation is 28 [mm];
- the external radius of the second semiconductor layer is 31 [mm]
- the width of the internal semiconductor layer is 1 [mm];
- the external radius of the connector is 10 [mm];
- the length of the connector is 15 [mm];

The physical electrical properties are:

- The voltage of the cable is $U=10$ [kV];
- Relative permittivity of the first insulation layer is 3.5
- Relative permittivity of the muff insulation layer is 4
- Relative permittivity of mastic is 6
- Relative permittivity of control tube is 2

In the Fig. 4 the distribution of the field lines are plotted for the data mentioned above.

In our simulation tests we considered many values of the permittivity of the mastic. In Fig. 5 the variation of the electrical field at the external radius of the phase insulation is plotted. If the value of the permittivity of the control tube is

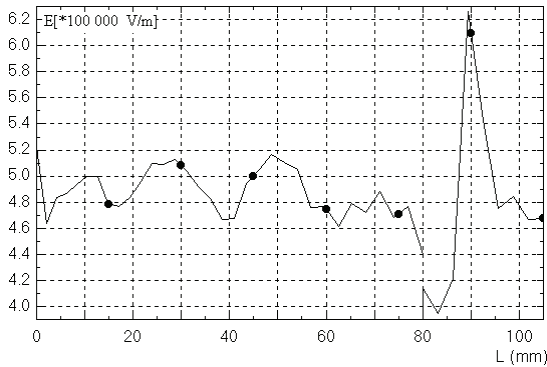


Fig. 5. Strength E versus space ($\epsilon_r=6$)

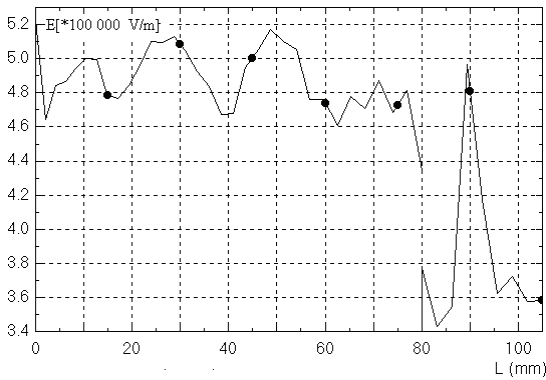


Fig. 6. Strength E versus space ($\epsilon_r=8$)

increased at 8, the distribution of the electrical strength is modified. In the zone of the joint, the electrical field strength is reduced (see Fig. 6).

It is obvious that we can find an optimum value of the material property (in our case the permittivity) so that an objective function can reach a minimum value. In our particular application the objective function is a measure of the deviation of the electrical field from a desired value. The solution of the inverse problem is done iteratively.

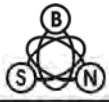
V. CONCLUSION

In this paper we presented some aspects of analysis and control of the electric field in cable connectors. We limited the discussion at the material properties as optimisation parameter. The influence of the material properties on the field distribution in connectors is analysed. The numerical models were obtained by the finite element method in a 2D-space [4].

An optimisation with respect to geometry is an open problem that involves increased computational efforts. At each step of iteration the application software must rebuild the mesh of the finite element program. To simplify the optimisation process, the initial problem is divided into subproblems so that the gradient technique that involves differentiation with respect to geometry is divided into differentiation subproblems.

REFERENCES

- [1] *** Catalog 2001/2002. Tyco (Electronics). *Accesorii pentru cabluri de energie*
- [2] Cârstea, D., Cârstea, I. *CAD in electrical engineering. The finite element method*. Editor SITECH. 2000. Craiova, Romania.
- [3] Hoole, S.R.H., *Finite elements, electromagnetics and design*. 1995, Elsevier, Amsterdam.
- [4] *** QuickField program, version 5.2. Year 2004. Page web: www.tera-analysis.com. Company: Tera analysis



This page intentionally left blank.

Untransposed HV Transmission Line Influence on the Degree of Unbalance in Power Systems

Ljupčo D. Trpezanovski¹ and Metodija B. Atanasovski²

Abstract – In this paper, the untransposed HV transmission line influence on the degree of unbalance in power systems is presented. The model of untransposed HV line with ground wires is given in phase and sequence domain. The proposed model is used for asymmetrical load-flow solution by Newton-Raphson procedure, incorporated in the Neplan 5.0 software. All 400 and 220 kV unbalanced transmission lines in the power system of the Republic of Macedonia are taken with real parameters and asymmetrical state is analyzed. The unbalance factors for negative- and zero-sequence voltages for 400 and 220 kV buses are calculated. Positive-sequence voltages from asymmetrical state are compared with phase voltages from symmetrical state for the same power system, when the transmission lines are treated as balanced.

Keywords – Untransposed HV transmission lines, unbalance factors, asymmetrical load-flow.

I. INTRODUCTION

The three-phase power system consists of several networks with different rated voltages, connected with two or three-winding interconnective transformers. The elements in the power system can be balanced (with equal phase parameters) or unbalanced (with different phase parameters). Practically, all generators, transformers, transposed lines and symmetrical loads can be treated as balanced elements. The untransposed and asymmetrical loads are treated as unbalanced elements. If there is even only one unbalanced element, asymmetrical state in power system is occurred and sequence voltages and currents are present in the power system buses and elements.

The presence of sequence components causes negative influence on the elements correct function. For example: negative-sequence currents at generator terminals rise heating in their rotors; malfunctions of protective relays; zero-sequence currents increase greatly the effect of inductive coupling between parallel transmission lines; higher power system losses; zero-sequence currents in the ground wires and through the ground, etc.

The degree of deviation from the symmetrical state can be valued with the unbalance factors for negative- and zero-sequence voltages or currents. When a system has adverse unbalance factors, the transposition on phase conductors at substations or all through the lines should be applied.

¹Ljupco D. Trpezanovski is with the Faculty of Technical Sciences, University St. Kliment Ohridski, I. L. Ribar bb, 7000 Bitola, Macedonia, E-mail: ljupco.trpezanovski@uklo.edu.mk

²Metodija B. Atanasovski is with the Faculty of Technical Sciences, University St. Kliment Ohridski, I. L. Ribar bb, 7000 Bitola, Macedonia, E-mail: metodija.atanasovski@uklo.edu.mk

It should be noted, that in this research all loads are treated as balanced elements.

The unbalance factors can be calculated from the sequence components (for voltages or currents). If these components are not on disposal, they are obtaining by transformation of the corresponding phase values. Values of phase nodes voltages or elements phase currents for the three-phase power system states, which deviate more or less from symmetrical states, are obtaining with asymmetrical load-flow (ALF) calculations. The solution of ALF problem was successfully performed using methods in phase domain (Newton-Raphson and Fast decoupled procedures) [1] and faster methods in sequence domain [2], [3].

II. UNTRANSPOSED HV TRANSMISSION LINE MODEL IN PHASE AND SEQUENCE DOMAIN

If the HV transmission line has a considerable length, and phase conductors are not transposed, it can causes a significant negative- and zero-sequence components. Usually, because of the great costs for the transposition towers and insulators, line transposition is avoided. Practically, the transposition is recommended if inequality (1) is satisfied:

$$U_n \text{ (kV)} \cdot L_v \text{ (km)} \geq 5000 \text{ (kV} \cdot \text{km)}, \quad (1)$$

where U_n is rated voltage in kV and L_v total line length in km [4]. It is shown that inequality (1) is satisfied for 220 and 400 kV lines, but should be checked for 110 kV lines. For exact unbalance factors calculation, a proper mathematical model of three-phase HV transmission line should be defined. In steady state problems, three-phase transmission line is represented by lumped- π circuit. The series reactance and inductance are lumped between line ends and shunt capacitance of the transmission line is divided into two halves and lumped at line ends [1], [2] and [5].

Let us consider a three-phase unbalanced transmission line with one ground wire.

A. Series Impedance of a Transmission Line

The series impedances of phase conductors and ground wire with earth influence, which are mutually inductive coupled, are illustrated in Fig. 1.

The following equation for the line ends voltage difference can be written for phase a :

$$\begin{aligned} \underline{V}_a - \underline{V}_{a'} = & \underline{I}_a \cdot (R_a + j\omega L_a) + \underline{I}_b \cdot j\omega L_{ab} + \underline{I}_c \cdot j\omega L_{ac} \\ & + j\omega L_{ag} \cdot \underline{I}_g - j\omega L_{an} \cdot \underline{I}_n + \underline{V}_n. \end{aligned} \quad (2)$$

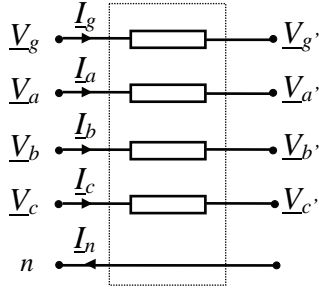


Fig. 1. Series mutually inductive coupled line impedances.

The voltage and current of the fictive earth conductor, signed as n , are given with next equations:

$$\underline{V}_n = \underline{I}_n \cdot (R_n + j\omega L_n) - \underline{I}_a \cdot j\omega L_{na} - \underline{I}_b \cdot j\omega L_{nb} - \underline{I}_c \cdot j\omega L_{nc} - \underline{I}_g \cdot j\omega L_{ng}, \quad (3)$$

$$\underline{I}_n = \underline{I}_a + \underline{I}_b + \underline{I}_c + \underline{I}_g. \quad (4)$$

Substituting Eqs. (3) and (4) in Eq. (2) gives:

$$\Delta V_a = \underline{Z}_{aa-n} \cdot \underline{I}_a + \underline{Z}_{ab-n} \cdot \underline{I}_b + \underline{Z}_{ac-n} \cdot \underline{I}_c + \underline{Z}_{ag-n} \cdot \underline{I}_g \quad (5)$$

Writing similar equations for the other phases and ground wire, the following matrix equation results:

$$\begin{bmatrix} \Delta V_a \\ \Delta V_b \\ \Delta V_c \\ \Delta V_g \end{bmatrix} = \begin{bmatrix} \underline{Z}_{aa-n} & \underline{Z}_{ab-n} & \underline{Z}_{ac-n} & \underline{Z}_{ag-n} \\ \underline{Z}_{ba-n} & \underline{Z}_{bb-n} & \underline{Z}_{bc-n} & \underline{Z}_{bg-n} \\ \underline{Z}_{ca-n} & \underline{Z}_{cb-n} & \underline{Z}_{cc-n} & \underline{Z}_{cg-n} \\ \underline{Z}_{ga-n} & \underline{Z}_{gb-n} & \underline{Z}_{gc-n} & \underline{Z}_{gg-n} \end{bmatrix} \begin{bmatrix} \underline{I}_a \\ \underline{I}_b \\ \underline{I}_c \\ \underline{I}_g \end{bmatrix}. \quad (6)$$

The series impedances line model with only three phase conductors is more convenient and it can be established in few steps. At first, matrix Eq. (6) should be presented in partitioned matrix form as follows:

$$\begin{bmatrix} \Delta \underline{V}_{abc} \\ \Delta \underline{V}_g \end{bmatrix} = \begin{bmatrix} \underline{Z}_A & \underline{Z}_B \\ \underline{Z}_C & \underline{Z}_D \end{bmatrix} \begin{bmatrix} \underline{I}_{abc} \\ \underline{I}_g \end{bmatrix} \quad (7)$$

Multiplying the partitioned matrices results with equations:

$$\Delta \underline{V}_{abc} = \underline{Z}_A \underline{I}_{abc} + \underline{Z}_B \underline{I}_g, \quad (8)$$

$$\Delta \underline{V}_g = \underline{Z}_C \underline{I}_{abc} + \underline{Z}_D \underline{I}_g. \quad (9)$$

Assuming that the ground wire is at zero potential ($\Delta \underline{V}_g = 0$), from Eq. (8) and (9) can be obtained the final three phase conductors model for the transmission line in matrix form:

$$\Delta \underline{V}_{abc} = \underline{Z}_{abc} \underline{I}_{abc}. \quad (10)$$

The \underline{Z}_{abc} impedance matrix includes phase self-impedances and mutual inductive couplings with influence of

earth and ground wire(s). All elements of this matrix can be calculated from the matrix equation:

$$\underline{Z}_{abc} = \underline{Z}_A - \underline{Z}_B \underline{Z}_D^{-1} \underline{Z}_C = \begin{bmatrix} \underline{Z}_{aa} & \underline{Z}_{ab} & \underline{Z}_{ac} \\ \underline{Z}_{ba} & \underline{Z}_{bb} & \underline{Z}_{bc} \\ \underline{Z}_{ca} & \underline{Z}_{cb} & \underline{Z}_{cc} \end{bmatrix}. \quad (11)$$

Usually, instead of impedance matrix, the series admittance matrix $\underline{Y}_{abc}^z = \underline{Z}_{abc}^{-1}$ is applying for the line model.

B. Shunt Capacitance of a Transmission Line

Shunt mutual capacitive couplings for the three phase conductors, ground wire and earth are illustrated in Fig. 2.

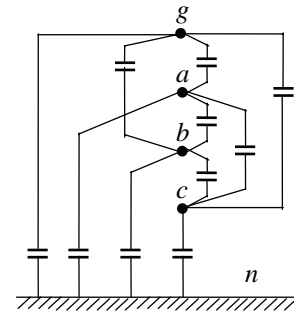


Fig. 2. Shunt mutually coupled line capacitances.

The potentials of the line phase conductors and ground wire are related to the conductor charges by the matrix equation:

$$\begin{bmatrix} V_a \\ V_b \\ V_c \\ V_g \end{bmatrix} = \begin{bmatrix} p'_{aa} & p'_{ab} & p'_{ac} & p'_{ag} \\ p'_{ba} & p'_{bb} & p'_{bc} & p'_{bg} \\ p'_{ca} & p'_{cb} & p'_{cc} & p'_{cg} \\ p'_{ga} & p'_{gb} & p'_{gc} & p'_{gg} \end{bmatrix} \begin{bmatrix} Q_a \\ Q_b \\ Q_c \\ Q_g \end{bmatrix}, \quad (12)$$

where p'_{aa} , p'_{ab} , ..., p'_{gg} are potential coefficients. On the same way, as it was conducted for the series impedances, the only three phase conductors line model for the shunt capacitances could be established. Taking into account the zero potential of the ground wire(s) and Eq. (12), potentials of the line phase conductors with included influences of earth and ground wire(s) in matrix form are:

$$\underline{V}_{abc} = \underline{P}_{abc} \underline{Q}_{abc}. \quad (13)$$

The capacitance matrix can be easy calculated as:

$$\underline{C}_{abc} = \underline{P}_{abc}^{-1} = \begin{bmatrix} C_{aa} & -C_{ab} & -C_{ac} \\ -C_{ba} & C_{bb} & -C_{bc} \\ -C_{ca} & -C_{cb} & C_{cc} \end{bmatrix}. \quad (14)$$

Usually, the shunt admittance matrices Eq. (15) corresponding to the line ends are applying instead of capacitance matrix.

$$\mathbf{Y}_{abc}^s = \frac{1}{2} j\omega \mathbf{C}_{abc}. \quad (15)$$

Finally, the series and shunt admittance lumped- π model of an untransposed transmission line (connected between buses k and j) represented with three-phase compound admittances is shown in Fig. 3.

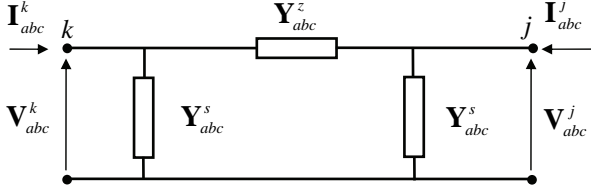


Fig. 3. Lumped- π model of an untransposed transmission line in phase domain.

Following the rules developed for the formation of the admittance matrix using the compound concept [1], the bus k and bus j injected currents can be related to the nodal voltages by the equation:

$$\begin{bmatrix} \mathbf{I}_{abc}^k \\ \mathbf{I}_{abc}^j \end{bmatrix}_{(6,1)} = \begin{bmatrix} \mathbf{Y}_{abc}^z + \mathbf{Y}_{abc}^s & -\mathbf{Y}_{abc}^z \\ -\mathbf{Y}_{abc}^z & \mathbf{Y}_{abc}^z + \mathbf{Y}_{abc}^s \end{bmatrix}_{(6,6)} \begin{bmatrix} \mathbf{V}_{abc}^k \\ \mathbf{V}_{abc}^j \end{bmatrix}_{(6,1)} \quad (16)$$

Above explained procedure can be used for formation the lumped- π model of an untransposed transmission line with more than one ground wire.

Series and shunt admittances can be converted in sequence domain using transformation matrix \mathbf{T}_s and equations:

$$\mathbf{Y}_{dio}^z = \mathbf{T}_s^{-1} \cdot \mathbf{Y}_{abc}^z \cdot \mathbf{T}_s \quad (17)$$

$$\mathbf{Y}_{dio}^s = \mathbf{T}_s^{-1} \cdot \mathbf{Y}_{abc}^s \cdot \mathbf{T}_s. \quad (18)$$

Now, the lumped- π model of an untransposed transmission line in sequence domain can be presented as in Fig. 4.

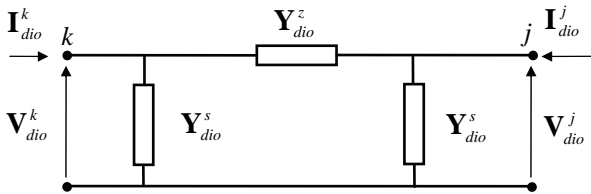


Fig. 4. Lumped- π model of an untransposed transmission line in sequence domain.

Finally, the mathematical model in sequence domain can be presented in matrix form with Eq. (19), similar as it was presented for the phase domain.

$$\begin{bmatrix} \mathbf{I}_{dio}^k \\ \mathbf{I}_{dio}^j \end{bmatrix}_{(6,1)} = \begin{bmatrix} \mathbf{Y}_{dio}^z + \mathbf{Y}_{dio}^s & -\mathbf{Y}_{dio}^z \\ -\mathbf{Y}_{dio}^z & \mathbf{Y}_{dio}^z + \mathbf{Y}_{dio}^s \end{bmatrix}_{(6,6)} \begin{bmatrix} \mathbf{V}_{dio}^k \\ \mathbf{V}_{dio}^j \end{bmatrix}_{(6,1)} \quad (19)$$

Inductive and capacitive mutual couplings among positive-, negative- and zero-sequence circuits are expressed with nonzero off-diagonal elements in matrices \mathbf{Y}_{dio}^z and \mathbf{Y}_{dio}^s .

Instead of mutually admittances, the couplings can be expressed by compensation current sources. Thus, the unbalanced line model can be presented with three decoupled sequence circuits. The mutual couplings are replaced by corresponding controlled sources – current sources. More detailed explanation for the untransposed transmission lines modeling in phase and sequence domain is given in [1, 2], [5].

III. ASYMMETRICAL LOAD-FLOW SOLUTION

The phase voltages for all buses of the entire power system can be obtained performing the ALF solution. Because the sequence voltages are of interest for unbalanced factors definition, it is appropriate to use the ALF methods established in sequence domain. Presented results in this paper are obtained by Newton-Raphson method in sequence domain [2], incorporated in the Neplan 5.0 software [6]. This method is based on the system of three matrix equations each one related to the decoupled positive-, negative- and zero-sequence equivalent circuit of the power system (Eqs. (20), (21) and (22) respectively).

$$\begin{bmatrix} \mathbf{H}_d & \mathbf{N}_d \\ \mathbf{M}_d & \mathbf{L}_d \end{bmatrix} \begin{bmatrix} \Delta \theta_d \\ \Delta \mathbf{V}_d / \mathbf{V}_d \end{bmatrix} = \begin{bmatrix} \Delta \mathbf{P}_d \\ \Delta \mathbf{Q}_d \end{bmatrix}. \quad (20)$$

$$\mathbf{Y}_i \cdot \mathbf{V}_i = \mathbf{I}_i, \quad (21)$$

$$\mathbf{Y}_o \cdot \mathbf{V}_o = \mathbf{I}_o. \quad (22)$$

Actually, the matrix Eq. (20) has the same form as the equations that represent the symmetrical Newton-Raphson load-flow model. The other two supplementary systems given by Eqs. (21) and (22) are systems of linear equations.

IV. STUDY CASES – CALCULATION OF UNBALANCE FACTORS

The influence of untransposed HV transmission lines on the degree of unbalance was studied on the entire power system of the Republic of Macedonia. In the performed analyze are included 50 buses of 400, 220 and 110 kV voltage level, 53 lines, 5 interconnective transformers and 9 equivalent generators with step-up transformers. All 400 and 220 kV lines are untransposed, and real phase arrangements shown in Fig. 5 are taken into account.

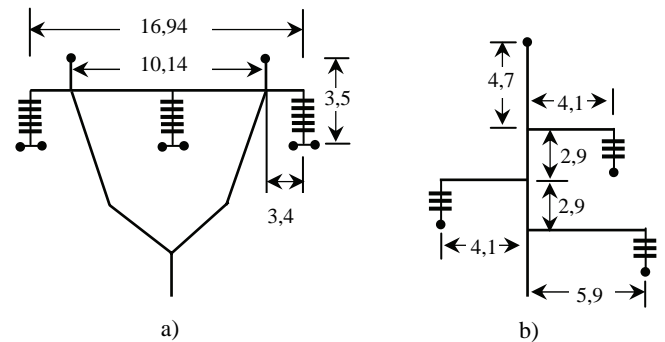


Fig. 5. Phase conductors and ground wire arrangement for untransposed a) 400 kV line and b) 220 kV line (*produced by EMO-Ohrid).

The mentioned power system is shown in Fig. 6, only with buses in which the unbalance factors are calculated. The rest parts of Macedonian power system and connections with neighborhood's power systems are presented with blocks.

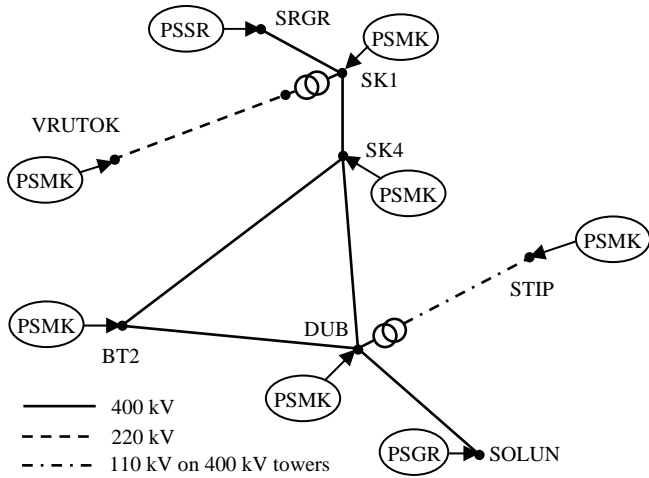


Fig. 6. Untransposed lines and their connections in power system of the Republic of Macedonia - PSMK.

Two cases with all balanced loads were studied. In the first case, all transmission lines are treated as balanced. The solution for voltages in each node of the system buses shows that only positive-sequence voltages exist and they are equal with phase voltages. For this case the voltage in phase (node) a for the bus j is denoted as V_{abal}^j and it is equal with positive-sequence voltage V_d^j . This notation is necessary for definition an unbalanced factor for positive-sequence voltages, when asymmetrical state of the system is compared with the symmetrical state for the same system. In this case total active power loss is $\Delta P_{bal} = 31,22$ MW.

In the second study case, all 400 and 220 kV lines are taken with their real parameters. Presence of six 400 kV lines with total length of 376,7 km, one 220 kV line with 65,2 km and one 110 kV line with length of 40 km (build on 400 kV towers), cause asymmetrical state and appearance of sequence voltages and currents. Because the sequence components have unwanted effects on the power system elements it is desirable to measure the degree of system unbalance. For this purpose the unbalance factors (usually in %) are introduced. Unbalanced factors for positive-, negative- and zero-sequence voltages are given with Eq. (23) respectively.

$$F_d = \frac{V_d}{V_{abal}} \cdot 100; \quad F_i = \frac{V_i}{V_d} \cdot 100; \quad F_o = \frac{V_o}{V_d} \cdot 100. \quad (23)$$

If $F_d = 100\%$ and $F_i = F_o = 0\%$ power system is in symmetrical state. Asymmetrical power system states, which deviate more or less from symmetrical state have greater or smaller unbalanced factors F_i and F_o . Results from study cases are shown in Table I. Although, the unbalanced factors for negative- and zero-sequence voltages are small, the total active power loss in second case is $\Delta P_{unbal} = 37,28$ MW.

TABLE I
RESULTS FOR UNBALANCED FACTORS

bus	V_{abal} (kV)	V_{L1} (kV)	F_d (%)	F_i (%)	F_o (%)
		V_{L2} (kV)			
BT2 400	226.328	226.507	100.003	0.0977	0.1263
		226.697			
DUB 400	224.525	225.039	100.1512	0.1224	0.1363
		225.192			
SK4 400	221.696	222.552	100.2556	0.1481	0.2047
		222.567			
SK1 400	221.446	222.382	100.2816	0.2023	0.1858
		222.394			
STIP 110	59.577	59.829	100.2699	0.2133	0.2371
		59.816			
SK1 220	117.196	117.568	100.2045	0.1942	0.1973
		117.090			
VRU 220	117.604	117.638	100.1659	0.3446	0.5628
		117.896			
		117.477			
		118.084			

V. CONCLUSION

The presence of untransposed HV transmission lines causes asymmetrical states in the power system. These states have unwanted effects on the power system elements and there is a need for their quantification. For evaluation of the unbalance degree, the unbalanced voltage factors are introduced. In this paper, the procedure for untransposed line modeling in phase and sequence domain is presented. Decoupled-sequence line model is applied in the Newton-Raphson method for asymmetrical load flow calculation incorporated in Neplan 5.0 software. Two real state cases of the Macedonian power system are studied. Results from the studies show that in the case with untransposed lines, although the unbalance factors are small, total active power loss growth for 6 MW, against the case when lines are treated as transposed.

REFERENCES

- [1] J. Arrillaga, C.P. Arnold, B.J. Harker, *Computer Modelling of Electrical Power Systems*, John Wiley & Sons Ltd, 1983.
- [2] X.-P. Zhang, "Fast Three Phase Load Flow Methods", IEEE Trans. on PS, Vol. 11, No. 3, pp. 1547-1554, August 1996.
- [3] V. Strezoski, Lj. Trpezanovski, "Three-phase asymmetrical load-flow", International Journal of Electrical Power and Energy Systems, Vol. 22, No. 7, pp. 511-520, October 2000.
- [4] N. Rajaković, *Analiza elektroenergetskih sistema I*, Elektrotehnički fakultet, Akademska misao, Beograd, 2002.
- [5] M.S. Chen, W.E. Dillon, "Power System Modeling", Proc. IEEE, Vol. 62, No. 7, pp. 901-915, July 1974.
- [6] Neplan 5.0 software, BCP Switzerland (Educational version for Faculty of Technical sciences - Bitola).

Calculation of GIS 110 kV Insulating Bushing Applying Hybrid BEM-FEM Method

Hamid Zildžo¹ and Halid Matoruga²

Abstract – This paper elaborates procedure of geometry optimising 110kV SF6 gas insulated bushing with regards to dielectric toils. Iterative Dirichlet-Neumann sequential procedure was applied in frame of modern hybrid BEM/FEM method.

Keywords – Boundary Element Method, Finite Element Method, Method of successive underrelaxation, Galerkin procedure.

I. INTRODUCTION

Finite element method (FEM) is suitable for calculating domains with a number of insulating mediums but with final boundaries. Boundary Element Method (BEM) is suitable for calculating domains with one insulating medium but with final or infinite boundaries. In this paper, hybrid-coupled method of BEM-FEM boundary and final elements is applied which contains best characteristics from both FEM and BEM methods.

II. MATHEMATICAL MODEL

Let us elaborate separately the basic principles of Galerkins procedure of weight residue in FEM method, direct BEM method and iterative sequential Dirichle-Neumanns hybrid BEM-FEM method. With FEM, Laplaces partial differential equation is solved, and with BEM, integral equation of electrostatic field is solved. Potentials on BEM-FEM boundary are iteratively calculated by applying the method of successive sub-relaxation.

III. FINITE ELEMENT METHOD

In the method of final elements, domain of observed physical system in procedure of so called bisection of continuum is divided on final number of parts of certain geometry, which are called final elements. Laplace's partial differential equation of electrostatic field is given with:

$$\frac{\partial}{\partial x} \left(\varepsilon \frac{\partial \varphi}{\partial x} \right) + \frac{\partial}{\partial y} \left(\varepsilon \frac{\partial \varphi}{\partial y} \right) = 0 \quad (1)$$

After applying the Galerkins method of weight residue we can record the solution of electrical potentials distribution in form of linear algebraic equations system:

$$[H]^{FEM} \cdot \{\varphi\}^{FEM} = \{Q\}^{FEM} \quad (2)$$

where:

$[H]^{FEM}$ - Two-dimensional matrix of coefficients that's general clause is given with:

$$h_{ij}^{FEM} = \sum_{e=1}^{n_e} \left[\varepsilon \int_{S_i^e} \left(\frac{\partial N_i^e}{\partial x} \frac{\partial N_j^e}{\partial x} + \frac{\partial N_i^e}{\partial y} \frac{\partial N_j^e}{\partial y} \right) dS \right] \quad (i=1,2,\dots,n_f; j=1,2,\dots,n_f) \quad (3)$$

$\{\Phi\}^{FEM}$ - Column vector matrix of unknown potentials in articulations of one final element of rank $n_f \times 1$.

$\{Q\}^{FEM}$ - Column vector matrix of free clauses containing Neumann's boundary conditions, which's general clause is given with:

$$q_i^{FEM} = \sum_{e=1}^{n_e} \left[\sum_{j=1}^{n_f} \left(\int_{S_i^e} N_i^e \cdot N_j^e \cdot \frac{\partial \varphi_j^{FEM}}{\partial n} dS \right) \right] \quad (4)$$

N_i^e -Functions of configurations which enable that unknown function of potentials is approximated as follows:

$$\varphi = \sum_{j=1}^{n_f} N_j^e \cdot \varphi_j^e \quad (5)$$

$\frac{\partial \varphi_j^{FEM}}{\partial n}$ - Neumann's boundary condition.

IV. DIRECT METHOD OF BOUNDARY ELEMENTS

Mathematical model of direct method of boundary elements is based on Greens symmetrical identity and equations of continuity with which boundary conditions on boundaries between domains with different mediums are entered. Let us observe two special cases of 3-D electrostatic field calculations, with the case when observation point Q is located inside of calculating domain V and second case when point Q is located on domains boundary. General formula for observing potentials within, on the boundary and outside of calculation domain is given with the following formulation:

$$C(Q) \cdot \varphi(Q) + \int_S T(P, Q) \cdot \varphi(P) \cdot dS_P = \int_S G(P, Q) \cdot \frac{\partial \varphi(P)}{\partial n_P} \cdot dS_P \quad (6)$$

¹Hamid Zildžo is with the Electrical Engineering Faculty Zmaja od Bosne bb 71000 Sarajevo, Bosna i Hercegovina
E-mail: hamid.zildzo@etf.unsa.ba

²Halid Matoruga is with the Electrical Engineering Faculty Zmaja od Bosne bb 71000 Sarajevo, Bosna i Hercegovina
E-mail: hmatoroga@etf.unsa.ba, matorogahalid@yahoo.com

where:

$G(P,Q)$ - Greens function,

$T(P,Q)$ - Extraction of Greens function in perpendicular domain on boundary surface,

φ i $\frac{\partial\varphi}{\partial n}$ - Calculated functions of potentials and normal field component on boundary surface,

$C(P,Q)$ - Constant which depends on observation point is given with:

$$C(Q) = \begin{cases} 1 & \text{inside domain V (Poisson formula)} \\ \frac{1}{2} & \text{on smoothly boundary in 2-D and 3-D domain} \\ \frac{\gamma_{3-D}}{4\pi} & \text{on winding boundary in 3-D domain} \\ \frac{\gamma_{2-D}}{4\pi} & \text{on winding boundary in 3-D domain} \\ 0 & \text{out domain V} \end{cases} \quad (7)$$

After application of collocation procedure in point in method of weight residue on Eq. 6 we will get the solution in form of matrix system:

$$[H]^{BEM} \cdot \{\varphi\}^{BEM} = [G]^{BEM} \cdot \left\{ \frac{\partial\varphi}{\partial n} \right\}^{BEM} \quad (8)$$

where:

$[H]^{BEM}$ – Two dimensional matrix of coefficient that’s general clause is given with:

$$h_{i,j}^{BEM} = \sum_{e=1}^{n_e} \int_S N_j^e \cdot T_{i,j}^e \cdot dS_p + \delta_{i,j} \cdot C_i \quad (i=1,2,\dots,n_e \quad j=1,2,\dots,n_e) \dots\dots\dots (9)$$

$[G]^{BEM}$ – Two dimensional matrix of coefficient that’s general clause is given with:

$$g_{i,j}^{BEM} = \sum_{e=1}^{n_e} \int_S N_j^e \cdot G_{i,j}^e \cdot dS \quad (i=1,2,\dots,n_e \quad j=1,2,\dots,n_e) \quad (10)$$

$\{\varphi\}^{BEM}$ i $\left\{ \frac{\partial\varphi}{\partial n} \right\}^{BEM}$ - Column vector matrix of variables.

On domain’s boundary with one medium, in every articulation of boundary elements, the value of variable φ or $\frac{\partial\varphi}{\partial n_p}$ known. So in Eq. 8 calculation is conducted on boundary domain of the variable φ or $\frac{\partial\varphi}{\partial n_p}$ which is not given as boundary condition.

On boundary between two domains with different mediums, unknown are φ and $\frac{\partial\varphi}{\partial n_p}$ as well. In that case, for each domain boundary the system of Eq. 6 is written with consideration of Dirichlet’s and Neumann’s boundary conditions, and on boundaries between two domains with

different mediums additional continuity equations are written for φ and $\frac{\partial\varphi}{\partial n_p}$, which are valid on these boundaries.

V. HYBRID BEM-FEM METHOD

Let us observe example of calculation with related BEM-FEM domain, on Fig. 1.

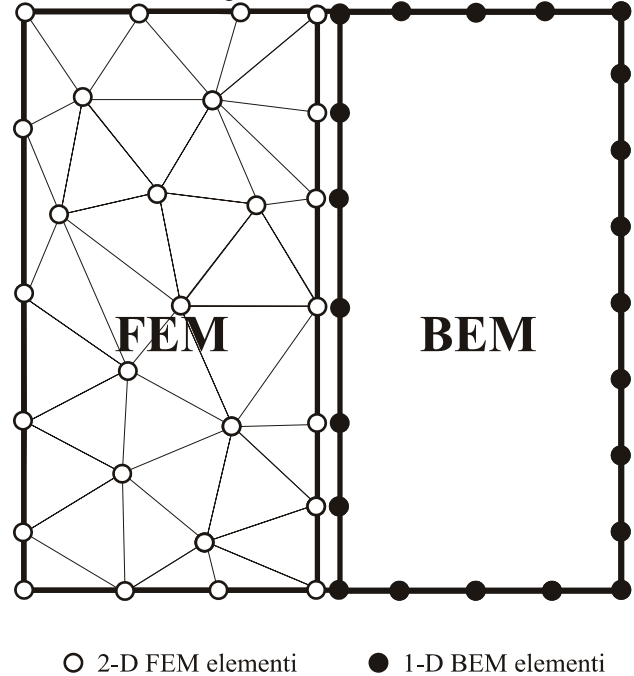


Fig. 1. Example of related BEM-FEM domain calculation

FEM domain is bisected with 2-D FEM final elements whose articulations are marked with white articulations, and BEM domain with 1-D boundary elements whose articulations are marked with black articulations. BEM-FEM boundary from FEM side is connected with 2-D final elements, and from BEM side is connected with 1-D boundary elements.

There are direct and iterative algorithms for connecting the methods of boundary and final elements.

With direct approach, forming of linear system of algebra equations is conducted with the aid of exponent (2) in FEM domain and exponent (8) in BEM domain, and equations of continuity are added on BEM-FEM boundary. This procedure has a large flaw because it is necessary to solve large full equations system.

For the sake of memory saving it is recommended to use some of iterative procedures, and the best known are:

- Robbins’s relaxation algorithm for connecting.
- Neumann – Neumann’s algorithm for connecting.
- Advanced Dirichlet – Neumann’s algorithm.
- Advanced sequential Dirichlet – Neumann’s algorithm.

With iterative BEM-FEM procedures, separated solving of two separated matrix system of linear equations is conducted separately for BEM and separately for FEM domain, and the results of potentials’ distribution or flux on BEM-FEM boundary is iteratively calculated by applying successive sub-relaxation method.

VI. ADVANCED SEQUENTIAL DIRICHLET-NEUMANN'S BEM-FEM ALGORITHM

In this paper advanced [4]sequential Dirichlet-Neumann's BEM-FEM algorithm will be used which consists of following steps .

- Dividing the calculating domain on BEM and FEM domains
- Defining of starting values of potentials on boundary of BEM- FEM
- Starting the iterative cycle which lasts until satisfying the convergence terms:

DO n=0, 1, 2... to convergence

- Solving the field in BEM domain:

On BEM domain boundary other than on BEM-FEM boundary itself, Dirichlet or Neumann's boundary terms are inflicted. Accordingly, in matrix system (8) in matrix $[H]^{BEM}$ and $[G]^{BEM}$ we can write BEM-BEM contributions from pure BEM boundary and BEM-FEM contributions from BEM-FEM boundary.

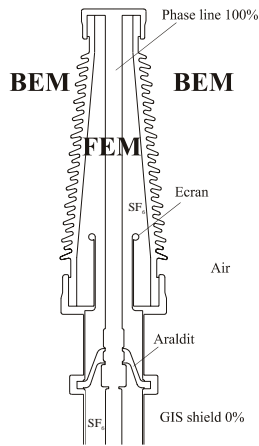


Fig. 2. Example of calculation of 110 kV insulating bushing in SF6 GIS station

$$[H]^{BEM} \begin{Bmatrix} \{\varphi\}_{n+1}^{BEM-BEM} \\ \{\varphi\}_{n+1}^{BEM-FEM} \end{Bmatrix} = [G]^{BEM} \begin{Bmatrix} \left\{ \frac{\partial \varphi}{\partial n} \right\}_{n+1}^{BEM-BEM} \\ \left\{ \frac{\partial \varphi}{\partial n} \right\}_{n+1}^{BEM-FEM} \end{Bmatrix} \quad (11)$$

In the system (11) it is necessary to consider Dirichlet's and Neumann's boundary terms including potential values on BEM-FEM boundary from previous iteration step, as well. Solving the system (11) will give us the values of normal

component of fields on BEM-FEM boundary $\left\{ \frac{\partial \varphi}{\partial n} \right\}_{n+1}^{BEM-FEM}$

- In this step, solving of continuity equation on BEM-FEM boundary is conducted:

$$\begin{aligned} \varepsilon^{FEM} \left\{ \frac{\partial \varphi}{\partial n} \right\}_{n+1}^{FEM-BEM} &= -\varepsilon^{BEM} \left\{ \frac{\partial \varphi}{\partial n} \right\}_{n+1}^{BEM-FEM} \\ \left\{ \frac{\partial \varphi}{\partial n} \right\}_{n+1}^{FEM-BEM} &= -\frac{\varepsilon^{BEM}}{\varepsilon^{FEM}} \left\{ \frac{\partial \varphi}{\partial n} \right\}_{n+1}^{BEM-FEM} \end{aligned} \quad (12)$$

As a result we will get Neumann's boundary terms which are relevant in perpendicular direction on FEM side of BEM-FEM boundary .

- Solving the field in FEM domain:

Solving the field in FEM domain is conducted in this step. On FEM domain boundary except on the BEM-FEM boundary itself, Dirichlet's or Neumann's boundary terms are given. Accordingly, in matrix system (2) in matrix $[H]^{FEM}$ we can write FEM-FEM contributions from pure FEM boundary and contributions from FEM-BEM from BEM-FEM boundary:

$$[H]^{FEM} \cdot \begin{Bmatrix} \{\varphi\}_{n+1}^{FEM-FEM} \\ \{\varphi\}_{n+1}^{FEM-BEM} \end{Bmatrix} = \begin{Bmatrix} \{Q\}_{n+1}^{FEM-FEM} \\ \{Q\}_{n+1}^{FEM-BEM} \end{Bmatrix} \quad (13)$$

where the matrix elements $\{Q\}_{n+1}^{FEM}$ are calculated by applying (4) and (12) formulation. As a result we will get potentials $\{\varphi\}_n^{FEM-BEM}$ on FEM-BEM boundary.

- Correction of calculated potentials on BEM-FEM boundary:

In this step correction of calculated potentials that are calculated on FEM-BEM boundary in previous step is conducted. Correction is conducted by applying the method of successive sub-relaxations:

$$\{\varphi\}_{n+1}^{BEM-FEM} = (1-\theta) \cdot \{\varphi\}_n^{BEM-FEM} + \theta \cdot \{\varphi\}_{n+1}^{FEM-BEM} \quad (14)$$

Sub-relaxation factor θ is given in interval from 0 to 1.

- Checking the convergence of iterative cycle and stopping when suitable punctuality is achieved.

VII. EXAMPLE OF CALCULATION

Fig. 2 presents example of calculation of the electrostatic field on 110kV SF₆ GIS of insulating bushing. Bushing is usually located on top of SF₆ gas insulated station (GIS) and through it an air 110kV phase line is introduced into SF₆ GIS bus bar. It is very important to correctly optimise the geometry of this bushing considering the dielectric tensions.

Copper bus bar goes trough porcelain insulator and goes into the GIS bus bar. Interior of porcelain insulator and GIS bus bar is filled with SF₆ gas. Dielectric permittivity of porcelain is $\varepsilon_r=5$, and SF₆ gas $\varepsilon_r=1$. Araldit support insulator supports bus bar and it has $\varepsilon_r=4$. Permittivity of outside air is $\varepsilon_r=1$. Phase line is located on up thrown 100 % potential, and cover of GIS bus bar is grounded with 0% potential. Various insulating mediums SF₆ gas, araldit and porcelain with final boundaries are bisected with 2 – D final elements. Surrounding air whose boundaries are reaching the infinity represents BEM domain, and is bisected with 1 – D boundary elements.

VIII. CONCLUSION

In this paper modern approach to optimising geometry of conductor bushing is shown regarding the dielectric tensions. Infinite boundaries of air are taken into consideration with establishing BEM-FEM boundary and on outer bushing surface itself. Series of calculations was made and final version of bushing is shown. In final version auxiliary display is built in which serves to stretch optimally the line force fields over the surface of porcelain insulator to satisfy maximum allowed values of normal and tangential components of electric field in all insulating mediums, individually.

REFERENCES

- [1] D. S. Burnett, "FINITE ELEMENT ANALYSIS FROM CONCEPTS TO APPLICATIONS", Addison-Wesley Publishing Company, Massachusetts, 1987.
- [2] Haznadar Z., Štih Ž.: Elektromagnetizam 1,2, Zagreb, 1997.
- [3] Zienkiewicz O. C.: The Finite Element Method, New York, McGraw-Hill, 1977.
- [4] Elleithy, W. M., Al-Gahtani, H. J. and El-Gebeily, M., "Iterative Coupling of BE and FE Methods in Elastostatics", Engineering analysis with Boundary Elements, Vol. 25, No. 8, August 2001, pp. 685-695.

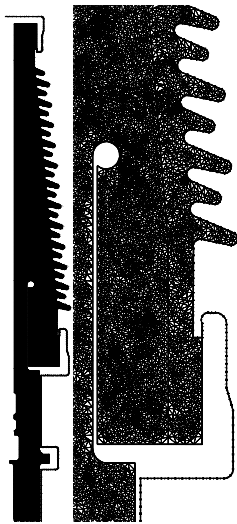


Fig. 3. Generated network of final and boundary elements

Fig. 4 shows the results of calculated distribution of dielectric tensions in observed bushing. Results are derived by applying BEM-FEM computer programme

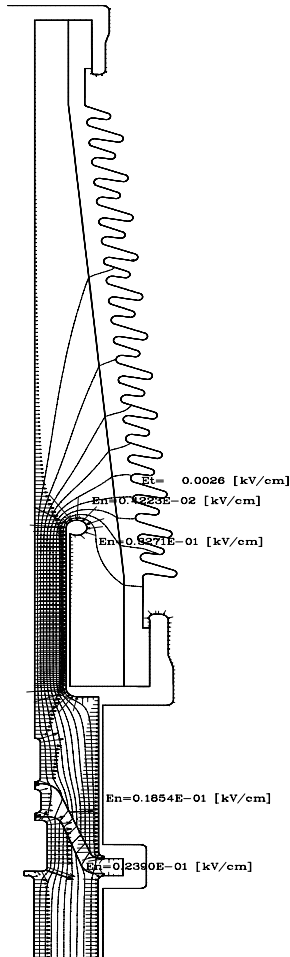


Fig. 4. Calculation results of maximum tangential and normal components of electric field bushing

Estimation of the Air Power Line Parameters Under the Influence of Lightning Overvoltages

Mariana G. Todorova¹ and Margreta P. Vasileva²

Abstract – The overvoltages in the power systems can't be avoided and is necessary to limit them.

There is necessity to know of the power line parameters whit positive, negative and zero sequence (R, L and C). They are used when the power line model is constructed. The aim of this paper is estimation of the line parameters in case of direct lightning stroke over the conductor of air power line by using different number of shifted two-dimensional Haar wavelets.

Keywords – estimation, air power line parameters, shifted two-dimensional Haar wavelets.

I. INTRODUCTION

The overvoltages in the power systems can't be avoided and is necessary to limit them.

There are three main groups of overvoltages – temporary, switching and lightning overvoltages. Lightning overvoltages originate in atmospheric discharges. A direct lightning stroke causes extremely high overvoltages and thus severe faults.

There is necessity of knowing of power line parameters whit positive and zero sequence (R, L and C). They are used when the power line model is constructed.

The detailed models of line elements are known, but there isn't undivided algorithm for commonly description of power system model.

The algorithm based on non-obvious integration is the most universal and easily applied. Program products are also developed for visual programming – package for modeling of dynamic systems SIMULINK, SCILAB etc. Initiating researching system characteristics occurs in dialogue regime. As a result we get a researching system model. Models parameters don't accord to the catalogue data. This needs previous calculations. This is a small defect.

In the present study the parameters of a power line under the influence of lightning overvoltages are estimated via Haar wavelets technique application.

II. MATHEMATICAL EXPRESSIONS FOR DETERMINATION PARAMETERS OF SUBSTITUTE SCHEME OF AIR POWER LINE IN SYMMETRICAL COORDINATES. [2 - 4]

1. Calculation of positive sequence resistance R_1

$$R_1 = \frac{\rho_{20} \cdot \kappa(\omega) \cdot \xi(\theta^0) \cdot \eta}{S}, \quad \Omega/\text{km} \quad (1)$$

where:

ρ_{20} – resistivity of the conductor for 20⁰ C, $\Omega \cdot \text{mm}^2/\text{km}$;

$\kappa(\omega)$ – coefficient, taking into account the change resistance from skin effect;

$$\kappa(\omega) = 1 + 0,0675 \cdot r \cdot \sqrt{\frac{\omega \cdot \mu}{\rho_{20}}}, \text{ if } r \cdot \sqrt{\frac{\omega \cdot \mu}{\rho_{20}}} \leq 4;$$

$$\kappa(\omega) = 1,27 + 0,401 \cdot (r \cdot \sqrt{\frac{\omega \cdot \mu}{\rho_{20}}} - 4), \text{ if } r \cdot \sqrt{\frac{\omega \cdot \mu}{\rho_{20}}} > 4;$$

μ – permeability of the conductor, H/m;

ω – radian frequency, rad;

r – radius of the conductor, mm;

$\xi(\theta^0)$ – coefficient, taking into account the change resistance from temperature;

$$\xi(\theta^0) = 1 + \alpha \cdot (\theta^0 - 20^0);$$

¹Mariana G. Todorova is with the Faculty of Computing and Automation, Technical University, "Studentska" str. № 1, 9010 Varna, Bulgaria, E-mail: mgtodorova@yahoo.com

²Margreta P. Vasileva is with the Faculty of Power engineering, Technical University, "Studentska" str. № 1, 9010 Varna, Bulgaria, E-mail: m.vasileva@tu-varna.acad.bg

α - temperature coefficient of the conductor, $1/^\circ\text{C}$;

θ° - work temperature, $^\circ\text{C}$;

η - coefficient taking into account difference between the real length of the air power line and the conductor length;

$$\eta = 1 + \frac{8}{3} \left(\frac{z}{l_m} \right);$$

z - suspending of the conductor, m; l_m - distance between two poles, m;

S - effective cross - section of the line conductor, mm^2 ;

2. Calculation of zero sequence resistance R_0

$$R_0 = R_1 + 3 \cdot R_3 \quad (2)$$

R_3 - real ground resistance;

$$R_3 = \frac{\mu_0 \cdot \omega}{8}, \Omega / \text{km}; \quad \mu_0 = 4\pi \cdot 10^{-4}, \text{H} / \text{km};$$

$$\omega = 2\pi \cdot f$$

f - frequency, Hz.

3. Calculation of positive sequence inductance L_1

$$L_1 = \frac{\mu_0}{2\pi} \left(\ln \frac{D_{cp}}{r} + \frac{\mu_r}{4} \right), \text{H} / \text{km} \quad (3)$$

μ_r - relative permeability of the conductor;

$D_{cp} = \sqrt[3]{D_{AB} \cdot D_{BC} \cdot D_{AC}}$, m - geometric average distance between two line conductors.

4. Calculation of zero sequence inductance L_0

$$L_0 = \frac{\mu_0}{2\pi} \left(3 \ln \frac{D_3}{\sqrt[3]{r \cdot D_{cp}^2}} + \frac{\mu_r}{4} \right), \text{H} / \text{km} \quad (4)$$

$$D_3 = \frac{640}{\sqrt{f \cdot \gamma_3}}, \text{m}$$

γ_3 - specific conductivity of the soil, $1/\Omega \cdot \text{m}$.

5. Calculation of positive sequence capacitance C_1

$$C_1 \approx \frac{0,241 \cdot 10^{-6}}{\lg \frac{D_{cp}}{r}}, \text{F} / \text{km} \quad (5)$$

6. Calculation of zero sequence capacitance C_0

$$C_0 \approx \frac{0,803 \cdot 10^{-8}}{\lg \frac{S_{cp}}{\sqrt[3]{r \cdot D_{cp}^2}}}, \text{F} / \text{km} \quad (6)$$

$$S_{cp} = 2 \cdot h_{cp};$$

$$h_{cp} = \sqrt[3]{h_A \cdot h_B \cdot h_C};$$

m - average height of the conductors.

Zero sequence inductance and positive and zero sequence resistance depend of the frequency.

III. LIGHTNING CURRENT'S PARAMETERS

High frequency process appears under the lightning influence on the air power line. The frequency depends of the shape and the duration of lightning current. Table 1 shows distribution of the peak value of the lightning current [4].

Table 1
Distribution of the peak value of the lightning current

$P_I, \%$	99	90	75	50	25	10	1
$I_{M, \text{kA}_{\text{max}}}$	3	12	20	30	50	80	130

The lightning current has an aperiodical shape. The front duration is about a few microseconds and the impulse duration is hundreds of microseconds.

The different possibilities for current front duration determine processes with different frequency in air power lines and different parameters for R_1 , R_0 and L_0 .

The aim of this paper is estimation of line parameters in case of direct lightning stroke over the conductor of air power line.

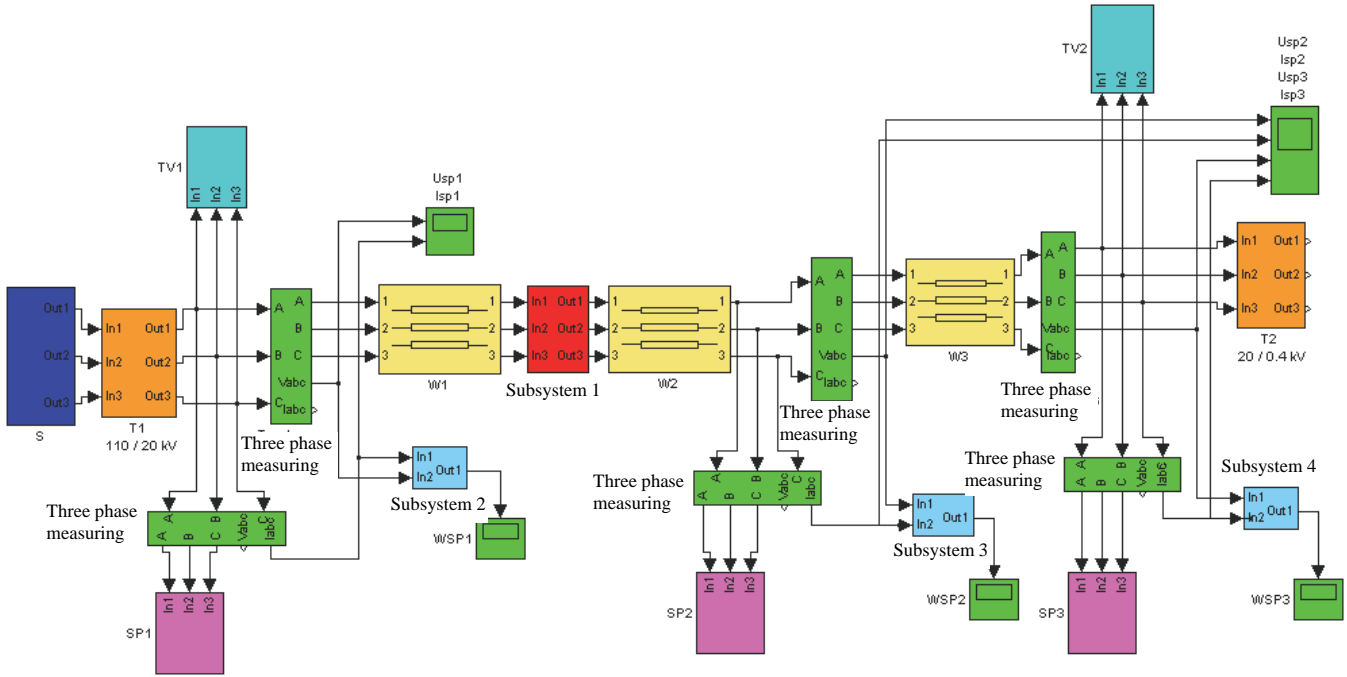


Fig.1 The model of power network 20 kV

The model of power network 20 kV is composed for identification of air power line parameters. Figure 1 shows the model. It unifies description of the following elements: power system (S); power transformer 110-20 kV (T_1); air power line (W_1, W_2) and cable power line (W_3); power transformer 20-0,4 kV (T_2); surge protective devices (SP) – metal oxide surge arresters; voltage measurement transformers (TV).

Standard blocks from Matlab Simulink library [5] are used for modeling of power line, power transformers and surge arresters.

Lightning current parameters are: amplitude 80 kA and shape 1/10 μ s.

The processes in line are described whit a partial differential equations (PDE) system (7).

$$\left\{ \begin{array}{l} -\frac{\partial U(x,t)}{\partial x} = R.I(x,t) + L.\frac{\partial I(x,t)}{\partial t} \\ -\frac{\partial I(x,t)}{\partial x} = C.\frac{\partial U(x,t)}{\partial t} \end{array} \right. \quad (7)$$

The research is in progress whit using of solve method ode23t [5]. This method is an implementation of the trapezoidal rule using a "free" interpolant.

Current and voltage that are needed for identification of air power line parameters are measured in ten points. These points are uniformly distributed through the length of air power line.

IV. PARAMETER IDENTIFICATION

The orthogonal set of Haar functions is a group of square waves with magnitude of $\pm 2^{m/2}$ in some intervals and zeros elsewhere [1]. Since the interval on which Haar functions are defined is not suitable for solving parameter identification problems, suitable transformation is required.

The shifted Haar wavelets are defined [6] as

$$H_m^*(t) = H_1^*(t) \cdot \left(2^j \cdot t - \frac{k}{2^j}\right), \quad (8)$$

where: $j \geq 0$; $m = 2^j + k$; $0 < k \leq 2^j$;

$H_1^*(t)$ -scaling function, pleased during the whole observed interval $[0, T]$.

A function $f(x, t)$ that is square integrable in the regions $t \in [0, T]$, $x \in [0, X]$, can be approximately expanded in a series of two-dimensional shifted Haar wavelets [1, 6].

Table 2
Model parameters, obtained parameters values and relative parameter errors

j	$R_0 = 3568$ \hat{R}_0	$L_0 = 0.0027$ $\hat{L}_0 \cdot 10^{-3}$	$C_0 = 0.45 \cdot 10^{-8}$ $\hat{C}_0 \cdot 10^{-8}$	$R_1 = 15.2$ \hat{R}_1	$L_1 = 0.0012$ $\hat{L}_1 \cdot 10^{-3}$	$C_1 = 0.962 \cdot 10^{-8}$ $\hat{C}_1 \cdot 10^{-8}$	E %
3	3872.0	2.3000	0.4294	13.9770	0.66527	1.0327	8.52
4	3728.1	0.0307	0.4174	20.5979	0.8851	0.7463	4.49
5	3672.4	0.5579	0.3009	18.3197	0.7634	0.5729	2.93
6	3638.8	0.5607	0.2701	22.0923	0.5880	0.4372	1.99
7	3618.7	0.1997	0.1343	23.3584	0.4657	0.3786	1.43
8	3594.8	0.1803	0.1268	25.7336	0.2942	0.2637	0.80
9	3581.6	0.1898	0.1023	26.6987	0.1844	0.1659	0.50

The Haar wavelets implementation reduces the problem of parameter identification to a computationally convenient form. The PDE of system (Eqs.(7)) are transformed into set of algebraic equations, and the algorithm for estimating of the parameters can be derived in a discrete form.

The identification process includes the following fundamental steps: (i) expansion of the functions of PDE into shifted two-dimensional Haar wavelets; (ii) rewriting of the PDE in the matrix form using the Haar wavelets properties and after some well known manipulations [1]; (iii) solving of the obtained matrix equation for the vector of unknown parameters using least – squares technique.

In this section m – file is created in Matlab based on proposed algorithm. The estimation values of the parameters for different number m of shifted two-dimensional Haar wavelets are calculated. The model parameters $R_0, L_0, C_0, R_1, L_1, C_1$, the obtained parameters values $\hat{R}_0, \hat{L}_0, \hat{C}_0, \hat{R}_1, \hat{L}_1, \hat{C}_1$ and the relative parameter errors E are given in Table 2.

V. CONCLUSION

Estimation of the air power line parameters gives a possibility for more precise modeling of processes in power line.

The line parameters in case of direct lightning stroke over the conductor of air power line by using different number of shifted two-dimensional Haar wavelets are estimated. Suitable m – file based on the proposed algorithm for parameter identification is created in Matlab and numerical results are given. The parameters estimations are obtained very accurately when bigger number of Haar wavelets is applied. Compared with the classical methods, the Haar wavelets method is computationally simplest, faster and has low computer memory requirement.

REFERENCES

- [1] Chen C. F., C. H. Hsiao, “Haar wavelet method for solving lumped and distributed parameter systems”, IEEE Proceedings – Control Theory and Applications, vol. 144, no. 1, pp. 87 – 94, 1997.
- [2] Герасимов К. К., Й. Л. Каменов, Моделиране в електроенергийните системи, Авангард Прима, София, 2007.
- [3] Генев Л. Г., Техника на високите напрежения в електроенергийните системи, Техника, София, 1979.
- [4] Hart W. C., Malone E. W., “Lightning and Lightning Protection”, Interference Control Technologies, Gainesville, pp. 3-9, 1988.
- [5] MATPOWER, Power Systems Engineering Research Center, School of Electrical Engineering, Cornell University, Ithaca, www.pserc.cornell.edu / matpower/matpower.html, 1997.
- [6] Todorova M., “Research of the possibilities and application of two dimensional orthogonal functions for dynamic distributed parameters systems identification”, PhD Thesis, Varna (in Bulgarian), 2003.

Calculation Model and Analyses of Grounding of the Fence on Medium Voltage Stations

Nikolce Acevski¹ and Mile Spirovski²

Abstract - Groundings of transformer stations (TS) in power networks with neutral point grounded by small resistively, in the case of single pole fault to ground, may to find on high potential. In such a case considerable potential differences can be registered between some points into and around transformer station and to come to high touch and step voltages. In this paper results of analysis of particular case are introduced, TS MV/MV (medium voltage) 35/10 kV 'Omorane2', near by Veles, which is make to find optimum way for grounding of the fence to satisfied safety criteria's, given in rules and recommendations. The analysis have for purpose not just to answer of the problem which is already described, thus to give some general thinking and recommendations in the general case.

Keywords - grounding, fault to ground, analysis, step and touch voltage, fence of TS, safety criteria's

I. INTRODUCTION

Metal fence of TS HV/MV, TS MV/MV longer time is object of different treatment in projecting practice in relation at type of grounding and abstinence of dangerous step and touch voltages. In this problem it is general approach is one of the following ways:

- fence is grounded with galvanic connection of more places on general grounding grid of TS, figure 1a.
- through special grounding placed from external side of fence on distance of 1 m which can be in galvanic relation with grounding grid, so-called common grounding, or galvanic separated from it, figure 1b.

In first case external electrodes of grounding grid of TS MV/MV usually follows fence of external side on distance of 1 m. with that occupied area is increased with grounder and resistance is decreased of shared parts, but potential of fence is going to be equivalent with grounding grid voltage. Safety criteria's will be satisfied if gradients of potential of both sights of fence are controlled with help of modeling of potential. But that is possible just in case of low specific resistivity on the bottom point ρ , low current of near grounded connection and so on, so in more practical those terms are not fulfilled. In some rube it can be founded some recommendations by which this problematic are examined and in itself includes the way of grounding of neutral point of network.

¹ Nikolce Acevski is with the Faculty of Technical Sciences, Bitola, Macedonia, E_mail: nikola.acevski@uklo.edu.mk

² Mile Spirovski is with the Faculty of Technical Sciences, Bitola, Macedonia, E_mail: mile.spirovski@uklo.edu.mk

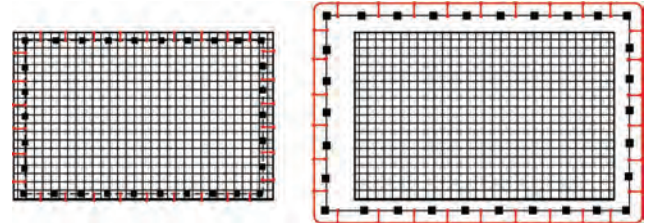


Fig. 1. a) without b) with special grounding placed from external side of fence on distance of 1 m

II. REVIEW TO RECOMMENDATION FOR GROUNDING OF MV TS

According to (10), in phase of projecting of TS 35/10 kV or 35/20 kV it doesn't needs preview or account for grounding, so the project needs just to predict grounding according this recommendation. Therefore it is need connecting of grounding grid of TS 35/10 kV, TS 35/20 kV with annular grounding grid of fence, i.e. it is needed to be used common grounding. Motion of network with isolated neutral point can go on with capacity current of fault to ground is not to be increased more than 10 A in 35 kV network, i.e. 20 A in 10 kV network. Grounding of neutral points of MV networks (35 kV, 20 kV, 10 kV) is obliged when currents of fault to ground will achieve two times higher values than stated above.

Systems of grounding of TS are dimensioned in accordance touch voltage so they are not allowed to over cross voltages shown according phase (1):

$$U_{doz} = \begin{cases} 1000V & T \leq 0,075s \\ \frac{75}{T} V & 0,075s < T \leq 1,153s \\ 65V & T \geq 1,153s \end{cases} \quad (1)$$

where T is duration of fault to ground.

According the same recommendation, safety criteria's of touch voltage will be satisfied if total impedance of grounding has value:

$$Z_u \leq \frac{k_d \cdot U_d}{r \cdot I_k} \quad (2)$$

k_d - attitude of voltage on grounding grid of TS and touch voltage.

U_d - allowed voltage according relation (1)

r - reductive factor of MV overhead line who give a current of TS

I_k - total allowed current of fault to ground of medium voltages network.

In accordance, literary (10) for isolation network when fault to ground has stabile character this values are: $k_d = 2$, $U_d = 65$ V, $I_k = 20$ A. If TS gives current over overhead line the reductive factor amount is $r = 1$. Replacing this values in (2) it gives that safety criteria's will be satisfied only if total impedance of grounding has value lower of $6,5 \Omega$.

According the same recommendation, if network is with grounding natural point over low impedance amplifier with limitation of current of fault to ground on 300 A, total resistance (impedance) of system of grounding on TS 35/10kV or 35/20 kV should be in relation (2) $Z_u \leq 0,7 \Omega$ if it is TS 35/10 kV or TS 35/20 kV connected to the overhead line 35 kV, $k_d = 3$, ($r=1$). In case not to be satisfied over headed condition, it needs, time of disconnection on fault to ground on collectors 35 kV in TS 35/10 kV or TS 35/20 kV to be original for most 0,5s with it disturb to be fraught criteria for security of touch voltage thereated without prove with accountings or measurement or decrease value of voltage grounding on security grounding (for example: with adding of vertical grounding grids, adding for one more annular grounding grid, etc., in order to satisfy overhead term.

According the same recommendation at taking out of grounding to install contour (annular) round fundament grounding grid that is connected with it on more places of distance 1m from wall of building on depth of 0,8 m.

III. MODEL FOR EVALUATION OF THE WAY OF GROUNDING ON FENCE

Often in practice the question is estimated for each other influence on grounding grid for different near placed objects. The answer may be appropriate useful at analyses of secure and work grounding grid of TS MV/LV, at appointment of different metal installation or cable of metal conductive layer near to the grounding grids in basement of housing objects like in case at evaluation is annular grounding grid to fence to be galvanic separate from main grounding grid or linked. And in case of galvanic separated grounding grid of fence of grounding grid of TS it get some potential of fault in TS as a result on that what is found in potential funnel on active grounding grid, (of TS 35/10). Characteristics of both grounding grids can be calculate over below-mentioned mathematics model, based on well-known Maxwell's relation. For two grounding grids a and b with n_a and n_b rectilinear electrodes besides (4), (7) import:

$$\begin{bmatrix} U_a \\ U_b \end{bmatrix} = \begin{bmatrix} r_{aa} & r_{ab} \\ r_{ba} & r_{bb} \end{bmatrix} \cdot \begin{bmatrix} I_a \\ I_b \end{bmatrix} \quad (3)$$

$[U_a], [U_b]$ -vector of voltages on electrodes of grounding grids with dimensions $n_a \times 1$, $n_b \times 1$

$[I_a], [I_b]$ -vector of current of taking away on electrodes on grounding grids, with dimensions $n_a \times 1$ i.e. $n_b \times 1$

$[r_{aa}], [r_{bb}]$ -square symmetrical matrix with dimensions $n_a \times n_a$ i.e. $n_b \times n_b$. On main diagonals with own resistivities on electrodes on grounding grids, and the others members are mutual resistivities of electrodes from the first (second) grounding grid.

$[r_{ab}], [r_{ba}]$ -rectangular matrix with $n_a \times n_b, n_b \times n_a$ members which presents mutual resistivities of elements from grounding grid a with elements from grounding grid b .

At calculation of own and common resistivities to be taken apprehend into consideration and their links on relation of plain on their own discontinuity (land area), one or endless number in dependence on that if the ground is homogeneous or is not homogeneous, and is calculate by method of medium potential literature [2], [3].

During calculation can be omitted failure of voltage because are small on electrode with smaller length and to take in consideration that all elements are on the same potential, i.e.:

$$[U_a] = [1_a] \cdot U_a \text{ and } [U_b] = [1_b] \cdot U_b \quad (4)$$

In the last relation it showed two single vectors with same dimensions like the vectors of voltages. Parameters of two near galvanic separates grounding grids and its mutual influence are analyzed in conditions when from some of them shunt current into fault to ground I_z , for example from grounding grid a , in case fundamental grounding grid. Run a grounding b , annular of fence, doesn't have current of fault to ground.

$$I_z = [1_a]^T \cdot [I_a] \quad (5)$$

$$[1_b]^T \cdot [I_b] = 0 \quad (6)$$

From overhead relation emanate:

$$\begin{bmatrix} U_a \\ U_b \end{bmatrix} = \begin{bmatrix} r_{aa} & r_{ab} \\ r_{ba} & r_{bb} \end{bmatrix} \cdot \begin{bmatrix} I_a \\ I_b \end{bmatrix} \quad (7)$$

From relations (5) and (6) follows:

$$\begin{bmatrix} [1_a]^T & [0_b] \\ [0_a] & [1_b]^T \end{bmatrix} \cdot \begin{bmatrix} I_a \\ I_b \end{bmatrix} = \begin{bmatrix} I_z \\ 0 \end{bmatrix} \quad (8)$$

Relations (7) and (8) can be with one common matrix equations:

$$(9) \quad \begin{bmatrix} [r_{aa}] & [r_{ab}] & -[1_a] & [0_a] \\ [r_{ba}] & [r_{bb}] & [0_b] & -[1_b] \\ [1_a]^T & [0_b]^T & 0 & 0 \\ [0_a]^T & [1_b]^T & 0 & 0 \end{bmatrix} \cdot \begin{bmatrix} [I_a] \\ [I_b] \\ U_a \\ U_b \end{bmatrix} = \begin{bmatrix} [0_a] \\ [0_b] \\ I_z \\ 0 \end{bmatrix}$$

Which solution will be:

$$\begin{bmatrix} [I_a] \\ [I_b] \\ U_a \\ U_b \end{bmatrix} = [C] \cdot \begin{bmatrix} [0_a] \\ [0_b] \\ I_z \\ 0 \end{bmatrix} \quad (10)$$

where $[C] = \{c_{ij}\}$, inverse matrix on square matrix in relation (9) with dimensions $(n_a + n_b + 2) \times (n_a + n_b + 2)$ and $[0_a], [0_b]$ zero vector with dimensions $n_a \times 1, n_b \times 1$.

The systems relations (10) can be presented in progressing form:

$$\begin{aligned} I_a(k) &= c_{kj} \cdot I_z & I_b(k) &= c_{ij} \cdot I_z \\ U_a &= c_{jj} \cdot I_z & U_b &= c_{j+1j} \cdot I_z \end{aligned} \quad (11)$$

where $k = 1, 2, \dots, n_a$ i.e. $k = 1, 2, \dots, n_b$ appropriately,
 $i = k + n_a \quad j = n_a + n_b + 1$

For own self grounding resistively of first grounding at existing of second and mutual grounding resistively of both groundings import:

$$R_a = \frac{U_a}{I_z} = c_{jj}; \quad R_{ab} = \frac{U_b}{I_z} = c_{j+1j} \quad (12)$$

Further it can calculate the potential of any point M of land area like value of potentials which are given as a result of currents on taking away from both groundings:

$$\varphi_M = [r_{aM}] \cdot [I_a] + [r_{bM}] \cdot [I_b] \quad (13)$$

where $[r_{aM}], [r_{bM}]$ is matrix on mutual resistively at all electrodes from both groundings and their links and point M .

If groundings are galvanic linked in that case total current on fault to ground is addition of currents on take away in earth over electrodes on both groundings, and potential of both groundings are equivalent, so equations (4), (5), (6), are modified. Two galvanic linked grounding grids can be solved so as one grounding. Potential who is occur on one grounding like result on

current of fault in near to it grounding can be calculate according to relations, literature [9], and at that the mistake not to be bigger then some %. On this way are avoid matrix equations and potential of passive grounding grid is calculate like potential in its brunt or live medium value potential calculated in middle points of electrodes in annular.

IV. EXAMPLE AND ANALYSES

In base on shown model, who can be generalized like in [7],[8], from sight on authors is made computer program by which help is analyzed the problem of grounding of fence of TS 35/10 kV Omorane, near to Veles. In this example networks on 35 kV and 10 kV sights are with isolation neutral point while network 0,4 kV is directly grounded. All 10 kV drain are airy, and intake is round the same so with one over ground lead. Transformer station is predict to work with isolated natural point with possibility in future to ground, with what it will used medium secure. Because it doesn't exists concrete predictions in which time interval in future can be show need to grounding of neutral point, dimensioned and presentation of grounding is done for real conditions in 35 kV and 10 kV network, but it is tested the variant when network will be grounded over small resistively. Grounding of TS is done by technical recommendation no. 7. The building in which is located complete TS (patch board, command room etc) is predict to have fundamental grounding grid, presented with FeZn clatter 30x4 mm. Fundamental grounding grid is predict on 3 places to be connected with external grounding grid, presented with copper cable Cu 50 mm of distance of 2 m from external wall of object and on depth 0,8 m, because immediately to the fence is made a pavement with width 1 m. Internal of building is present line for equivalence of potential with FeZn clatter 25x3 mm. on which are connected metal construction of 35 kV and 10 kV cells, and all metal parts. Line for equality of potential in object is connected with fundamental grounding grid, grounding grid for modeling of potential and zero point 0,4 kV from transformer station of home needs (with cable PPOO 1x16 mm²), and lighting rod installation.

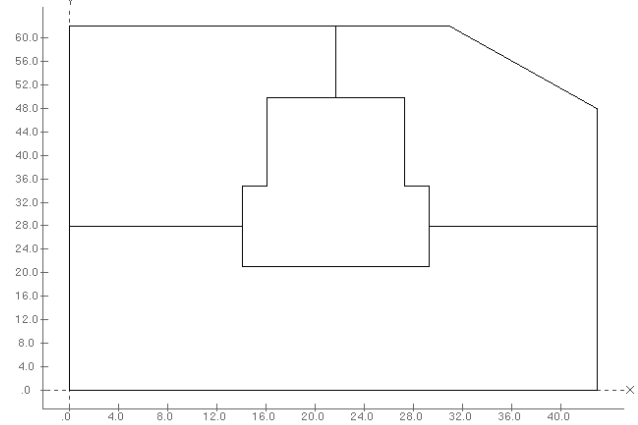


Fig. 2. View of fundamental grounding grid and on grounding of fence of TS 35/10 kV Omorane 2 - Veles

Specific resistively of fundamental in and around transformer station is $\rho = 200 \Omega \text{ m}$.

By analyzing the grounding resistively groundings on TS in two cases (when they are galvanic linked and separated), grounding grid of TS, no. 1, and grounding on fence, no. 2, like and potentials who will find two groundings at fault to ground of 10 kV sight, U_1, U_2 . Also it's calculating touch voltages which are the largest on corner of fence, followed diagonal, from internal and external sight of fence, U_{dv}, U_{dn} . At it is inspect next 4 cases:

1. network is insulate, groundings galvanic separated
2. network is insulate, groundings galvanic linked
3. network is fault to ground over small resistively, groundings galvanic separated
4. network is fault to ground over small resistively, groundings galvanic linked

Results of calculating are shown in table 1:

TABLE 1: CHARACTERISTICS OF THE GROUNDINGS 1 AND 2

case	1	2	3	4
$R(\Omega)$	5,37	2,23	5,37	2,23
$U_1(V)$	107,38	44,61	1610,70	669,15
$U_2(V)$	23,21	44,61	348,15	669,15
$U_2/U_1(\%)$	21,61	100,00	21,61	100,00
$U_{dv}(V)$	5,01	11,63	75,15	174,45
$U_{dn}(V)$	6,36	18,40	95,40	276,00
$U_{dv}/U_2(\%)$	21,59	26,07	21,59	26,07
$U_{dn}/U_2(\%)$	27,41	41,24	27,41	41,24

It shows that in case of insulate network term (2) is satisfied in both cases. But if network is ground over small resistively then grounding resistively is higher of limited $0,7 \Omega$. From table we can see that in cases 2 i.e. 4, grounding resistively is smaller as potential of main grounding grid. However in that case both groundings are proceed on the same potential which is potential of fence and is larger than in cases 1, 3. Like result on that step and touch voltages from internal and external side are larger than in cases when groundings are galvanic separated. This is important in case 4 when they are linked and network is grounded. In that case we get touch voltages higher from limited. If resistively of people body in best case man can be exhibit of voltage of 31,25 % lower from value showed in table 1. For critical case, at touch of external sight of fence this values for cases 3 i.e. 4 will be 119,9 V i.e. 189,75 V.

So in conditions of work with insulate neutral point, terms for secure by recommendation are satisfy in both cases and that is almost indifferent is annular grounding of fence and grounding grid of TS will be galvanic linked or not. But at eventual crossing of network with grounded neutral point safety criteria's is much easier to be satisfied if groundings galvanic are separated. In this case duration

of fault is limited on 0,5 sec. Allowed touch voltage, internal and external of installation for this time by recommendation, relation (1), is 150 V. From here we can give conclusion that in cases of work with grounded natural point safety criteria's are satisfy internal of fence, which is not case out of fence. To be satisfy this conditions in this case its need specific resistively of fundamental around TS to go on, or to add one more ring or vertical elements in poll in annular grounding of fence or drain of TS to do with cables with funeral external layer like on example. IPO 13 which shows that are excellent groundings.

V. CONCLUSION

The analyses shows that projectants working on this problematic shall not roundly to hold to recommendation so they should do some calculating. It shows that technical recommendation no. 7. consistently imports if network is with insulate neutral point. In that case it benefits together grounding. But in eventual crossing of work on neutral point fault to grounded over small resistively, (for which in our country in this moment is convoy comprehensive action), if it proceeded consistently of recommendation, safety criteria's can from most higher step and touch voltages not to be satisfied. In case like this, safety criteria's can be satisfied much easier if galvanic are separated from grounding of fence, from grounding grid of TS HV/MV, TS MV/MV.

REFERENCES

- [1] J. M. Nahman, "Uzemljenje neutralne tacke distributivnih mreza", Naucna knjiga, Beograd 1980.
- [2] J. M. Nahman, "Programi EFD-1 i EFD-2 za proracun uzemljivackih sistema u dvoslojnom i homogenom tlu", XIII Savjetovanje, JUNAKO CIGRE, Bled 1977.
- [3] J. M. Nahman, "Numericki postupak za proracun medjusobnih otpornosti tankih pravolinisnih provodnika", ELEKTROTEHNIKA, ELTHB2, 27 Zagreb ,Maj-Juni 1984, str. 27-32.
- [4] D. Jelovac, "Matematicki modeli za analizu uslova uzemljenja TS 10/0.4 kV", ELEKTROTEHNIKA, ELTHB2, 29, Zagreb, Maj-Juni 1986, pp.149-154.
- [5] I. Zelic, I. Medic, "Analiza utjecaja uzemljivaca ograde postrojenja na raspodelu potencijala u okolnom tlu", ELEKTROTEHNIKA, ELTHB2, 29, Zagreb, str. 79-83.
- [6] Galek, "Analiza dodirnog napona i nacina uzemljenja ograde elektroenergetskog postrojenja", ELEKTROTEHNIKA, ELTHB2, 29, Zagreb, str. 105-108.
- [7] N. Acevski, R. Ackovski, "Determining of galvanically separated gronding grids and grounding systems", MELECON'2000, 10th Mediterranean Electrotehcnical Conference May 29-31 CYPRUS, IEEE Region 8. No, MEL0316.
- [8] N. Acevski, J. Sikoski, " Resavanje na galvanski odvoeni zajemjuvaci i zajemjuvacki sistemi", I Sovetuvawe na ESM, Bitola, 16-18 dekemvri 1999g., str. 166-169.
- [9] N. Acevski, R. Ackovski, " Izvoz na potencijali vo metalnite instalacii i zajemjuvaci na stanbeni objekti", I Sovetuvawe na ESM Bitola, 16-18 dekemvri 1999g., str. 170-173.
- [10] TP-7 na EPS na Srbija (Izvodjenje uzemljenja distributivnih TS 35/10 kV, 35/20 kV, 10/0,4 kV, 20/0,4 kV i 35/0,4 kV, III Izdanje, juni 1996).

SESSION EQ I

Education Quality I



Meaning Making Through e-Learning

B. Gradinarova¹ and Yuri Gorvits²

Abstract – Different approaches have been proposed to add more educational value to e-Learning. One of these views proposes modern pedagogical models that better fit the nature of the unique features of technology. A related approach is to embed modern learning and instructional design theory into new communication and interaction channels provided by information and communication technologies such as Internet. This study presents a model for e-Learning illustrated with a specific case study of in-service teacher training in learning with digital media. Intact e-communities were developed through interaction and communication by using Internet services to share meaning, views, and understanding.

Keywords – e-Learning, e-communities, learning models.

I. INTRODUCTION

Diverse approaches have been offered to add more educational value to distance learning programs. Many e-Learning programs emphasize the “e” side, centering on the learning management system used and searching for new tools to “improve” distance learning [3].

Even though these views are necessary we believe that the central focus is somehow missed. Very few studies concerning pedagogical models for distance learning to fit the particular and unique features of Internet are proposed. Most programs follow a chalk and talk way of teaching without paying much attention to innovation by designing new pedagogical models to fit the unique features new media [5],[6]. We can say that this vision is close to the “old wine in new bottle” view.

Other studies identify learning managing systems as key tools that define the learning methodology and strategies. The software framework forces a way of teaching that reduces the flexibility required by active learning methodologies [3],[12]. Many of them end with a model tailored to the technological framework used instead of a software framework built upon the needs and features given by the pedagogical model assumed.

As a result, we can end up with some e-Learning principles that support any course implementation such as: To promote an active role of learners in the construction of knowledge, to promote meaningful learning, to promote broad and deep learning, to develop skills, attitudes and values, to

allow real experiences through real world activities, to promote collaborative learning, to promote a changing role of teachers/tutors as learning facilitators, to involve learners as co-evaluators, to make learners to reflect on what is doing, to use technology to enrich learning, to enhance action on knowledge objects, to solve cognitive conflicts

These principles emerge from underlying theories and models of learning such as constructivism, understanding as thinking, understanding as a network, social interaction, social distribution, situated learning, generalized learning, and self-regulated learning [1],[8].

This study introduces a model for e-Learning that is built upon these principles, models, and theories. We describe the design, implementation, and evaluation of an e-Learning program. Our pedagogical model is illustrated with a pilot implementation with teachers. We highlight the way teachers construct meaning by reflecting on teaching and learning.

II. DESIGN

We designed a whole e-Learning training program for teachers. We wanted to preserve the academic quality and innovate in the way we deliver education both the technology and model of learning. To do this we followed these steps:

Technology evaluation: We selected a learning management system and evaluated the technical requirements

Team organization: We created a multidisciplinary team to implement the e-Learning program with engineers, educators, and informatics and education specialists.

Model of learning: Once we knew the characteristics of the LMS and content we designed a pedagogical model for e-Learning.

Pilot testing: We designed a pilot testing course on methodologies for using information technologies with a reduced number of teachers. We tested the functioning of the LMS and the pedagogical model. We also evaluated diverse materials, working interfaces, learning strategies, type of interactions, and time spent in different section of the course.

Modeling: We designed and implemented the structure of the LMS by considering the learning model and the structure of the course program. The content of eight courses was modeled. Most of this content was already in digital format facilitating the process content modeling.

Online classes: The students were selected and registered. Then the first week they inspected the platform by following an entrance module. Students also started to virtually communicate and know each other.

Online modules: For learners interaction in each course we designed modules with individual and team activities to

¹Boyka Gradinariva is with Computer Sciences and Technology dep. at TU-Varna 1, Studentska Str., 9010 Varna, Bulgaria, E-mail: Bgradinarova@hotmail.com

²Yury Gorvits is a Business Development Manager Education&Research at ORACLE 15, Savvinskaya Moscow, 119435, Russia E-mail: Yury.Gorvits@oracle.com

design products weekly. They used different interaction tools such as chat and forums to do collective designs and constructions.

Face-to-face modules: We designed three out of eight course modules to be delivered face-to-face. They included content that requires more student-facilitator interaction. Each course was delivered in an intensive week with a day topic and collective works.

Evaluation: We finally evaluated the courses through questionnaires and opinion polls to get ideas, comments, and suggestions concerning online and face-to-face classes. We also implemented a focus group with professors and tutors of the course program to analyze and discuss the attainment of goals and objectives.

A. A model for e-Learning

Our model is based on constructivist principles of learning [8]. We view learning as the process of construction and modification of cognitive structures through learning by experience and collaboration. Each module of the learning cycle is oriented to obtain a contextualized meaningful learning. Learners are required to reflect, apply, criticize, argument, and solve problems and thus allowing them to construct their own representations. We identify five major processes in e-Learning: realizing, approaching, conceptualizing, structuring, and applying.

Realizing implies to identify the educational challenge. This process consists of orienting learners in their studies by identifying the problem and making their point of view. They also understand the objectives of the course work proposed and the starting points. They know what they will learn and the reason why the activities are proposed. The learner has to make representations of the expected products and results, and the rationale for doing this. Realizing involves the process of motivating, problem identification, and pre-concept/concept contrasting.

Approaching consists of constructing a new learning and point of view by learners guided by a group of professionals that design diverse methodological proposals to fit their cognitive styles. The idea is to produce a cognitive conflict to question the learner’s intuitive models and to identify the strengths of the proposed models. It involves the process of reflecting, retention, adapting, exploring, and researching.

Conceptualizing involves identifying the concepts and possible conceptual changes when exploring and approaching to the content. It involves the processes of metacognition, representation, and adaptation.

Structuring implies to construct meaning through didactic strategies such as synthesis, monitoring, and metacognition. This involves processes such as analysis, synthesis, retention, metacognition, and abstraction.

Applying consists of giving the opportunity to students to apply their conceptions to new and different scenarios. It involves evaluation, imaging, adaptation, abstraction, problem solving, contextualizing, and metacognition.

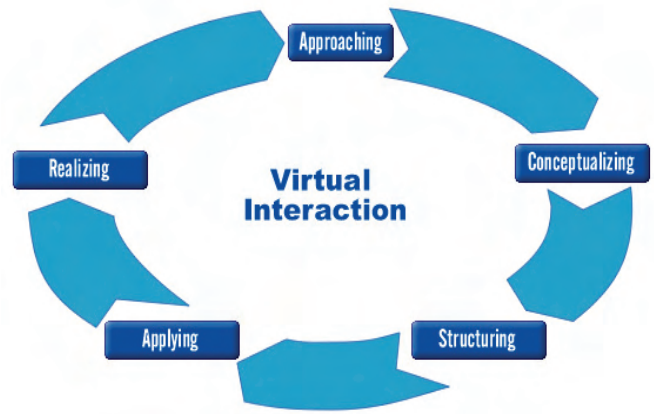


Fig. 1. A model for e-Learning

The virtual interaction triggers a synergic effect on the model by carrying these five processes of knowledge efficiently and thus allowing feedback, confronting ideas, discovering, and collaboration. All these processes are critical in the construction of meaning.

B. Training teachers through e-Learning

Our research took place in the Center for teacher development at Moscow Institute for Open Education. There we have implemented an e-Learning experience in order to design and evaluate the proposed methodological learning model. We also wanted to evaluate the learning management system used and to identify main components and strategies to implement an e-Learning course.

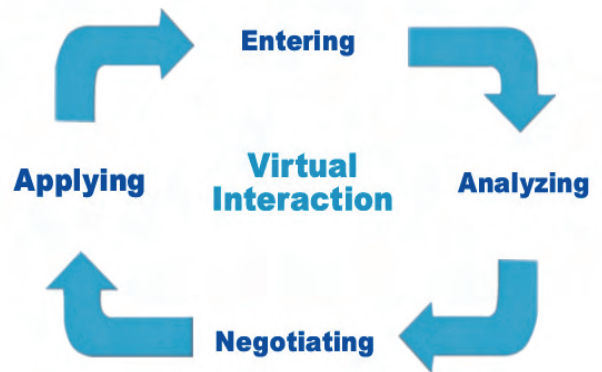


Fig.2. e-Learning cycle

In order to do this we followed five phases: Design, implementation, evaluation, feedback, and redesign. The design of the e-Learning cycle involved processes such as entering to a content unit, analyzing documents, negotiating meaning, and applying what learners have learned through collaborative constructing to end with a group synthesis (see Figure 2).

We have created an interaction virtual space for each content unit to integrate the construction of knowledge around

a topic. Due to the fact that the quality of the interaction among learners was not tacit we implemented an initial strategy to break the initial barriers to communicate and interact. Learners had to introduce themselves to the class by highlighting personal strengths in a playful way and listing their expectancies on the course.

Courses such as the one we are presenting should concentrate in time when teachers work load is not high. The time dedicated by the student to the course is a key to maintain them in the class. The role played by facilitators is very important to foster participation and knowledge construction. The learning management system used can determine the type of activities to be implemented but not necessarily the learning model involved. The follow up strategy is also relevant to the e-Learning experience. Facilitators and administrators should have tools to visualize learner's action within the virtual environment. We also think that the time period dedicated to tutoring and coordinating can determine the quality of the learning experience in online courses. This means time for solving problems, follow up, and to create a working climate to motivate students to actively participate in the learning process.

III. METHODOLOGICAL STRATEGIES

Each online course was divided in five working units during six weeks with a final evaluation. Units were developed in a week basis and ended with an individual or collective product. The last week was dedicated to prepare and take the final evaluation. Each unit consisted of unit description, objectives, general directions, activities, support materials, web links, and online discussions around each activity and working document.

During each module students were involved in activities such as document synthesis, term glossary, abstracts, graphic representations (schemes, concept maps), collective constructions of documents, comparative charts, and case studies.

Each course consisted of a virtual class section, synchronic communication with the professor responsible of the course and diverse discussion forums to implement activities and documents. The course was in charge of a professor, assisted by a coordinator and a teaching assistant facilitator.

IV. MEANING MAKING THROUGH VIRTUAL INTERACTION

We based our observation on meaning construction when learners were interacting within the Virtual Dialog Classroom. There two processes can occur: Presenting and Comparing. Presenting involves posing an opinion, comment, information or knowledge. Comparing includes contrasting beliefs and personal known knowledge with other learners by verifying agreements and disagreements.

This implies three other processes: Falsifying, complementing, and discovering. Falsifying implies to assign

falsity or error to a comment or judgments as a result of disappointing with a belief, comment or knowledge idea. Complementing means that we agree with the comment and accept it as a truth but we believe that it is incomplete. Discovering is new knowledge for learning or new ways of viewing a known knowledge. These processes are grouped within the most general process of comparing and can be externalized or just mentally processed without explicating it.

The idea with our study was to go further of just presenting information. We foster discussions where personal known knowledge is proof tested because of the collective interaction ending with a collaborative social knowledge construction. If we wish to evaluate these processes as triggers for meaningful learning we observed a direct relationship between previous knowledge and the quality of the construction of knowledge. Thus the more knowledge a teacher may have on a specific topic the more probability of falsifying. This is very relevant when assigning a role to content and support materials for the Virtual Dialog Classroom.

V. DISCUSSION

The main goal of this study was to develop a model for e-Learning and test it with a group of teachers by using modern learning theories and principles that better fit e-Learning.

Some of the premises of our design were the enormous potential of collaborative work and virtual interaction in e-Learning as it is mentioned in the literature. However these learning strategies are not tacit and even though they can facilitate learning they can also impede it. To ameliorate this there are some strategies such as teachers sharing their interests in teams and to maintain non formal communication during the course work. This favors confidence among students and group interaction around academic tasks.

One of the key aspects to facilitate collaboration was solving educational problems. Teacher could discuss themes based on their everyday experience by connecting theory and practice, and taking into consideration the teacher's knowledge. A balanced mixture between individual and collaborative strategies is also recommended. e-Learning programs should exploit the unique capabilities of Internet as a communication medium by going further than just student-teacher communication and emphasizing group work among students.

We believe that distance learning programs should exploit the unique features and added value of a powerful medium such as internet. Thus some constructivist theories and principles can be embedded into virtual environments to promote active learning and the construction of meaning.

We have presented an e-Learning model and describe the design, implementation, and evaluation of a training program for school teachers. We analyzed the teacher's construction of knowledge by reflecting on teaching and learning. Through interacting and communicating we have developed electronic communities around pedagogical content. We believe that this

experience reflects a way of knowledge construction from teachers that is not exclusive to e-Learning; rather it can be used in a meaningful way during everyday pedagogical practices in the school.

REFERENCES

- [1] Collis, B. (1997). Pedagogical reengineering: A Pedagogical approach to course enrichment and redesign with the WWW. *Educational Technology Review*, 8, 11-15.
- [2] Dillenbourg, P. (2000). Virtual learning environments. *Proceedings of EUN Conference 2000, Learning in the New Millennium: Building New Education Strategies for Schools. Workshop on Virtual Learning Environments*. Geneva.
- [3] Garrison, D. & Anderson, T. (2003). *E-Learning in the 21st Century: A Framework for Research and Practice*. New York: Routledge/Falmer.
- [4] Haddad, W. (2003). Is instructional technology a must for learning?. *TechKnowLogia*, 5-6, January –March.
- [5] Haavind, S. (2000). Why don't face-to-face teaching strategies work in the virtual classroom? How to avoid the Question Mill. <http://www.concord.org/library/2000fall/face2face.html>
- [6] Harasim, L., S. R. Hiltz, L. Teles, and M. Turoff. (1995). *Learning networks*. Cambridge, MA: MIT Press.
- [7] Harasim, L. (1990). (Ed.). *Online Education: Perspectives on a New Environment*. New York: Praeger.
- [8] Jonassen, D. (1998). The Computer as Mindtools. *TechTrends*, 43(2), 24-32, March.
- [9] Jonassen, D. (1995). Constructivism and computer-mediated communications in distance education. *The American Journal of Distance Education*, 9(2), 7-26.
- [10] Kozma, R., Zucker, A. Espinoza, C., McGhee, R., Yarnall, L., Zalles, D., and Lesis, A. (2000). The online course experience: Evaluation of virtual high school's Third Year of Implementation, 1999-2000 Final Report, <http://vhs.concord.org/Pages/About+Us-project+Evaluation>
- [11] Meyen, E. L., Aust, R.J., Gauch, J.M., Hinton, H.S., Isaacson, R.E., Smith, S.J., Tee, M.Y. (2002). e-Learning: A Programmatic Research Construct for the Future. *Journal of Special Education Technology*, 17(3), 37-46. <http://jset.unlv.edu/17.3/smith/smith.pdf>
- [12] Salomon, G. (1988). Novel constructivist learning environments and novel technologies: Some issues to be concerned with. *Research Dialogue in Learning and Instruction*, (1), 1, 3-12.

Software Engineering e-learning Mathematical Software

Bekim Fetaji¹, Shefik Osmani² and Majlinda Fetaji³

Abstract—The research is proposing a new way of tackling the process of creation of e-learning interactive environments by integrating and undertaking the software engineering approach based on e-learning outcomes. The main research was focused towards creating an e-learning mathematical software solution that will be used in the course “Discrete Mathematics” to learn mathematical operation of different types such as system of linear equations, matrices, determinants, functions etc. This gives the student learners additional advantages in learning and solving equations, and perform matrix operations in a shorter time and have a visual representation of it. It is also an opportunity for the student learners to gain computational experience and to check their results with the software ones. In order to assess e-learning effectiveness we have proposed a methodology called ELUAT (E-learning Usability Attributes Testing) and as measuring instrument the PET (predefined evaluation tasks) inspection technique. It investigates and is modeled to support problem based learning.

I. INTRODUCTION

The software solution developed has evolved as an idea to be a valuable tool for students and others who want to learn mathematical operation of different types such as system of linear equations, matrices, determinants, functions etc. Students complained about course learning content in “Discrete Mathematics” course which involves linear systems solution solving, finding the roots of a function, drawing and evaluating graphic of the function and other mathematical operations. Their opinion was that the learning content was not enough, and they spent to much time solving and calculating mathematical operations such as matrix and system operations with higher range. It means that they spent a lot of time in operations that are second hand and are simple calculations. Therefore we have initiated a research study to design and build software solution that will answer these requirements. The software was envisioned to provide and fulfill the next requirements:

System of linear equation – the software should be able to solve the system independent from the number of unknown variables in that system of equations.

Matrices – as an important part of these mathematical fields are matrices. The solutions of the systems of linear equations will be based on the solutions of the matrices.

The main operations that software will calculate are addition, multiplication, subtraction, inverse of a matrix, transposed matrix, finding their determinants, LU factorization

and adjacent matrices.

Also, the software checks a few matrix properties such is it upper or lower, involuntary, orthogonal, symmetric, asymmetric and diagonal.

The software is able to solve determinants of any range by the same algorithm.

Root of the function – the users can also find the root of the nonlinear function by methods learned in the Numerical Analysis Course at SEEU. Those methods are Bisection, Secant, Newton-Raphson, Regula Falsi, Stephensen and Fixed Point.

Functions – the most challenging part of the developed software system is evaluating and drawing the graph given by a user in a text format. For these algorithms which are very hard to define we have used a Delphi package for evaluating the functions.

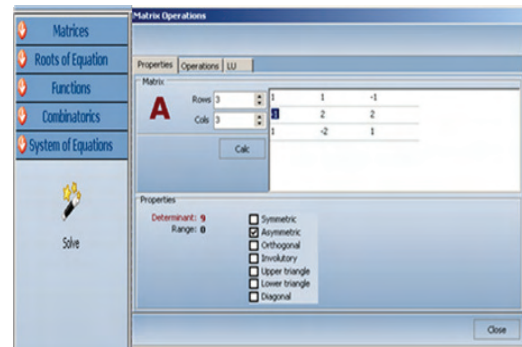


Fig. 1. The Interactive e-learning mathematical interface.

II. RESEARCH METHODOLOGY

We have considered the next learning modeling approaches:

- 1) the content-oriented,
- 2) the tool-oriented, or the
- 3) task-oriented approach [5].

We have decided to use the task-oriented approach. The data were collected throw usability testing, focus groups and interviews with prospective users. The purpose of the research realized is in order: (1) to gather information and asses e-learning interactions between human actors and the developed medium of instruction-the software solution, (intervention strategies and content), (2) determine the distance between learner activities and preconceived scenarios. The observed route of a learner has been used to give feedback information on the effective learning.

In our approach for the software solution we have decided to be modeled and used for Problem Based Learning. In Problem-Based Learning, students think, retrieve information for themselves, search for new ideas and apply them using the software solution.

¹ Bekim Fetaji is with the Faculty of Communication Sciences and Technologies, Ilindenska bb, 1200 Tetovo, Macedonia, E-mail: b.fetaji@seeu.edu.mk

² Shefik Osmani is with the IT center-SEEU, Ilindenska bb, 1200 Tetovo, Macedonia, E-mail: s.osmani@seeu.edu.mk

³ Majlinda Fetaji is with the Faculty of Communication Sciences and Technologies, Ilindenska bb, 1200 Tetovo, Macedonia, E-mail: m.fetaji@seeu.edu.mk

We have used the general principles and guidelines for HCI regarding the software design from [9], and general principles and guidelines for document design and guidelines for online documentation [3]. All this guidelines were closely advised and reviewed when designing the interactive e-learning mathematical tool. In order for the software solution to be successful it should be developed in close consultation and contacts and feedback with users. In the case of technology to support learning that means consulting with both teachers and learners. The matrix form contains three tabs: Properties, Operations and LU. The user can calculate the property of the matrix by following actions: (Note: The matrix should be a square matrix to perform these operations.)

Enter number of rows and columns in textboxes (the numbers should be positive):

1) On the grid enter the matrix values, 2) Click Calc button, 3) As the result users will get the determinant of the matrix, range and the properties in form of checkboxes. Check means that the matrix has that property.

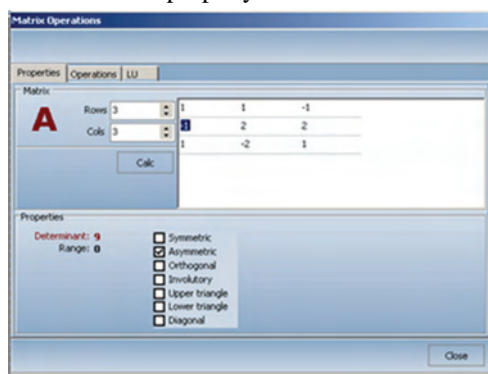


Fig 4. Properties tab of the Matrix Operations

In the operations tab users can calculate few matrix operations, as following: 1) Enter rows and columns of the first matrix, 2) On the grid below input values, 3) On the drop-down list select the action to perform, 4) If operation addition, subtraction or multiplication is selected the enter number of rows and columns of the second matrix the input the values, 5) Click on the Operate button

The result users will see in the result grid, depends on the action selected. In the screenshot there is an example of inverse of matrix.

In the following tab can be calculated the LU factorization as following: 1) As an input here you have one matrix, and output two matrices, 2) Input number of rows and columns of the matrix, 3) Input the values on the grid, 4) Click Factorize button. As a result users have two matrices Lower and Upper matrix (Figure 6.)

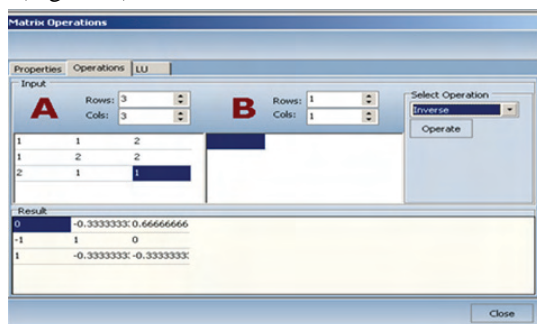


Fig 5. Operations tab of the Matrix Operations

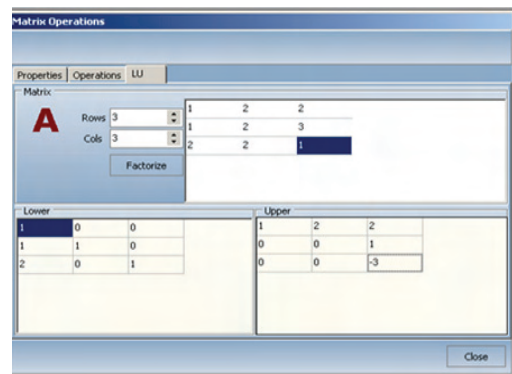


Fig 6. LU tab of the Matrix Operations

Roots of Equation - Bisection

To find the root of equation with method of Bisection users follows these steps: 1) In the $f(x)$ textbox input the function, 2) Enter Tolerance, Endpoint A, Endpoint B and Steps, 3) Click Solve button. The result is displayed in the grid. To see the graph of this function user should click on the graph button (Figure 7).

III. RESEARCH INSTRUMENT DEVELOPMENT

Major challenge for e-learning researchers is to assess e-learning effectiveness.

In order to do that we have proposed a methodology, called ELUAT (E-learning Usability Attributes Testing), which combines an inspection technique with user-testing based on 4 usability attributes we have set. The usability attributes we have set are: 1) Time to learn, 2) Performance speed; 3) Rate of errors; 4) Subjective satisfaction. The e-learning-methodology is necessary for presenting the e-learning in an efficient aspect.

The theoretical basis are pedagogical conceptions defined from [6]:

- Learning according to the constructivist perspective,
- usability of the e-learning environment and
- research about user opinions.

We have based the measuring instrument on the use of predefined evaluation tasks (PET), which precisely describe the activities to be performed during inspection in the form of a predefined tasks, measuring previously assessed usability attributes. We have named it as PET inspection technique and using this technique we evaluated usability attributes using evaluation tasks for a particular scenario. Evaluation tasks in this technique are determined through designing several user scenarios and choosing the scenarios that include the most of the options of the software. This kind of approach using this technique has shown very effective, straightforward and useful in determining the distance between learner activities and preconceived scenarios in several research project we conducted. Using the ELUAT methodology and PET inspection technique we have gathered information on interactions between human actors (intervention strategies and content). Scenario contains at least a collection of components and a method. The components are roles, activities or activity-structures, which role does what (which activity) and at which moment is determined by the method which is made up of one or many plays formed by a series of acts. In an e-learning environment, information obtained from learner activity contain a certain pedagogical semantic. The observed route of

a learner has been used to give feedback information on the level of learning and its effectiveness. We have considered the next learning modeling approaches: the content-oriented, the tool-oriented, and the task-oriented approach, and we have chosen the task oriented approach for which we developed the methodology to suite to our specifics.

Task #	Time for:			M	S	E	R	O	H	F	*
	Task completion	Help search	Recover from errors								
			Time to Learn:	Total:							

Fig. 10. PET inspection technique task based form

The PET inspection technique uses the next measurements: M – Menu Error; R – Repeat task; F- Frustrations; S – Selection error; O – Uses online Help, E – Other errors, H - Help calls, *-Subjective Satisfaction (5-very high, 4-high, 3-average, 2-low, 1-very low).

This methodology and the inspection techniques has been used in several different research projects and it produced valuable information for the design of the subsequent studies and proved as viable methodology and technique.

IV. THE EXPERIMENT

The testing process is divided into three phases [5]: planning, acquisition and execution with evaluation. We have followed these guidelines. The planning phase provides an opportunity for the tester to determine what to test and how to test it. Users are asked to perform tasks while usability experts observe and take note of their actions. The acquisition phase is the time during which the required testing software is manufactured, data sets are defined and collected, and detailed test scripts are written. During the execution and evaluation phase the test scripts are executed and the results of that execution are evaluated to determine whether the product passed the test. The difficult areas that repeat themselves between multiple test participants reveal areas that should be studied and changed by the developers. User testing can often uncover very specific areas needing improvement, where focus groups and task analysis often find more general areas needing improvement. The major output of the planning phase is a set of detailed test plans. In a project that has functional requirements specified by use cases, a test plan should be written for each use case. There are a couple of advantages to this. Since many managers schedule development activity in terms of use cases, the functionality that becomes available for testing will be in use case increments. This facilitates determining which test plans should be utilized for a specific build pf the system. Second, this approach improves the traceability from the test cases back into the requirements model so that changes to the requirements can be matched by changes to the test cases. The specialist/analyst who sits in on the test will almost certainly be a behavioral psychologist, with cognitive psychology skills (the process of learning and understanding) and knowledge of HCI (Human Computer Interaction). They will also be a usability expert, but it's likely that their background will be in psychology rather than site

design. When testing, psychology is far more important than the rational mechanics of good information architecture, though it's clearly desirable to understand both.

V. DATA COLLECTION AND RESULTS

According to the research of [8] for usability testing 5 users are enough, however we have used 10 users. After the usability test we had collected data from the 10 participants we had, were 5 of them were experts while the other 5 novices. In order to handle those data we have used the triangulation technique from [3], were we look at all data at the same time to see how the different data supports each other.

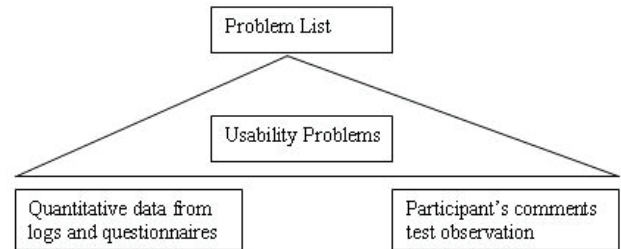


Fig. 4. Triangulation technique[3].

We also tabulated the data for the performance measurements using the next usability attributes: time to learn, speed of performance, rate of errors, Subjective satisfaction, and Frustration for the both classes of users Experts and novices. Please look at the appendix E for the tabulated data sheets and results. Here is the tabulated data sheet for time to learn, and speed of performance as well as the general usability requirements measures.

Usability Attribute	Measuring instrument	Value to be measured	Current Level average	Worst acceptable	Planned target level	Best possible
Time to learn	Task Scenario	Time to complete task	134.7 s	200 s	120 s	90 s
Speed of performance	Task Scenario	Time to complete task	112 s	200 s	110 s	80 s
Rate of errors	Task Scenario	Number of errors	0.63	4	1	0
Subjective satisfaction	Task Scenario	Satisfaction degree of users	3.74	1	3	5
* number. Subject satisfaction scale: very high 5 high 4 average 3 low 2 very low 1						

Table 1. Usability requirements for students

VI. CONCLUSION

The software solution as a new system solution is functioning practically and correctly as defined in its specifications. The experience introduced suggests the positive effects of using the interactive e-learning mathematical tool as our software solution. Randomly assigned treatment groups experienced and worked with the software solution.

Our conclusion regarding the first goal (1) to gather information and assess e-learning level and interactions between human actors and the developed medium of instruction - the software solution. Our analyses have shown that the e-learning interaction based on PET technique is quite high and the learning curve is quite high also. It is obvious that the student learner are faced with a lot of decisions and they need previous knowledge in order to use the software. The high learning curve of the system however is based on student interaction without any previous instructions. If the system is taught and instructed how to be used in classes then the learning curve might drop significantly and therefore the benefit of the usage of the system could be much higher.

Our conclusion regarding the second goal (2) to determine the distance between learner activities and preconceived scenarios, our e-learning research analyses based on EULAT methodology and PET technique as well on focus group, we have seen, evidenced and concluded the next:

- The learners interpret their experiences according to their own perceptions and doing that they construct their own knowledge.

- Active construction demands a high level of independence and self organization.

- Construction of knowledge of the learners and the refinement of the ability to do so do not happen passively and autonomously.

- Learning is situated. The social, motivational and emotional contextual factors of the learning situation decisively control the ways and means of the learning- and retention-process as well as the use of the knowledge and abilities.

Students achieve better results and learn more when they can reflect what they learn. This is especially achieved using our developed software solution where they can reflect what they have learned previously, relate it to past experiences, and apply it practically using the software solution. Generally the software is very much appreciated and well welcomed.

The analysis of numerical methods is very important task in mathematics because it presents the general study of methods for solving complicated problems using the basic operations of arithmetic (addition, subtraction, multiplication, and division).

The contribution of this software solution is that uses a software approach for solving numerical problems that makes the job of the students taking the course "Numerical Analysis" easier as it gives them an opportunity to solve equations, and perform matrix operations in a very short time and learn more in depth and more thoroughly the different mathematical operations..

The speed or let we say the number of steps for finding solutions to equations with one variable will depend rapidly on the interval or the initial approximation points. If we choose closer approximation we will get faster and more accurate results. The reason why we can say that there is no "best" algorithm or there is no "best" method for every case, is just because some of the methods are faster but less accurate, and the others are slower but with a higher accuracy.

The software is easy to use, and is directed not only to students of computer science and mathematics, but to other users that want to perform different mathematical tasks included in the software or just want to test the results gained by hand.

The help file for using the software solution is another opportunity that simplifies the usage of the software as well as giving general information of each method used in its implementation, for those that have no or some knowledge about numerical analysis..

Since there is always room for improvement the study has to move with time, in the sense that it must be continuously improved in design and functionality in order to meet new demands imposed by new technology.

REFERENCES

- [1] Bieber, M., and Vitali, F.(1997), "Toward Support for Hypermedia on the World Wide Web." IEEE Computer, pp. 62-70.
- [2] Campbell, C. (2004), E-effective Writing for E-Learning Environments, NY:Idea Group Publishing
- [3] Dumas, J. S., & Redish J. C. (1999) "A practical guide to Usability Testing" revised edition, Pearson Education Limited, pp.55-62
- [4] Helic, D. Krottmaier, H., Maurer, H., & Scerbakov, N. (2005): Enabling Project-Based Learning in WBT Systems, In International Journal on E-Learning (IJEL), Vol. 4, Issue 4, pages 445-461, 2005.
- [5] Elfriede, D. (2004) "Effective Software Testing: 50 Specific Ways to Improve Your Testing", Addison-Wesley Pub Co
- [6] Klauser, F.; Schoop, E.; Gersdorf, R.; Jungmann, B. & Wirth, K. (2004): The Construction of Complex Internet-Based Learning Environments in the field of Tension of Pedagogical and technical Rationality, Research Report ImpulsEC 10, Osnabrück, 2004.
- [7] Kuhn, D. (1999). A Development model of critical thinking. Educational Research, 28(2), 16-26, 46
- [8] Nielsen, J. (2000). Designing Web Usability: The Practice of Simplicity. New Riders Publishing, Indianapolis, ISBN 1-56205-810-X
- [9] Pressman, R. (2005) "Software Engineering: A practitioners approach 6 Ed" McGraw-HILL, inc, pp.81-117

Combining Virtual Learning Environment and Integrated Development Environment to Enhance e-learning

Majlinda Fetaji¹, Suzana Loskovska² and Bekim Fetaji³

Abstract— The research was undertaken having in consideration two hypothesis. The first hypothesis is that integration of virtual learning environment (VLE) in the form of an e-learning interactive tool and integrated developing environment (IDE) for programming in Java language will contribute in improving the efficiency and quality in learning because of the enhanced graphical user interface and the “hands on approach”. The learners can implement and test what they have learned and further extend their learning at the same time.

The second hypothesis is that the designed graphical user interface of the virtual learning environment will contribute in facilitating its use by improving the results of the learning process, increasing the user-satisfaction and attention during learning that implicates improving the overall efficiency of learning programming in Java. The objective of the research was to investigate what are the possibilities for improving learning Java programming by creating an e-learning interactive tool with enhanced graphical user interface. An analyses of the traditional method of learning programming language and virtual learning environment approach has been realized. Issues have been identified and proposed solutions and recommendations while reviewing the current situations in these fields. The usability of the created virtual environment was reviewed, in order to assess and propose solutions to the identified issues. The outcomes of the research is a Java interactive tool as virtual environment for learning and practicing Java programming language. It provides an integrated help, that the learners need in order to learn Java language without exposing them to the need to leave the application framework. An editor is also provided with compiling option, option for running Java application or applet and capturing and validating the syntax errors from user side. This way we have promoted the Java learning environment as self sufficient to achieve its objective.

I. INTRODUCTION

During the last decades, due to the development of information and communication technology and the raising impact of the Internet, an access to a huge amount of information is enabled world wide. This offers new opportunities to acquire knowledge any time, anywhere regardless to the previous constraints, time and location. More and more information in a daily basis is presented in digital and multimodal form.

In order to use all this information in the process of learning

electronic environments are created and used.

The impact of these technologies is reflected in the increased utilization of e-learning systems and virtual e-learning environments for learning.

However there is a certain skepticism regarding e-learning and virtual environments efficiency lately. This is the reason why we have analyzed e-learning systems and virtual e-learning environments. We are in an opinion that further research needs to be conducted to design a grounded theory that would focus on developing a good and efficient system for learning.

II. ANALYSES OF THE TRADITIONAL METHODS OF TEACHING

Based on our experiences and that of the other colleges from other institutions, related to teaching object oriented programming in a classroom, a conclusion is drawn that teaching and learning object oriented programming is much easier if an electronic environment and if new technologies are used.

Learning to program in object oriented language is difficult for novices in the traditional classroom method.

The instructor must transmit new ideas of programming concepts, writing, debugging and testing a code that is very difficult. The traditional method of learning is instructor-centered and depends on the methods the instructor uses. The method of teaching lectures on the table, even the visual format of the lectures in a computer, is not sufficient. To overwhelm all the elements of the process of learning to program, each element must be practically tested. The traditional method is limited in time, place and time duration of the class. The wide range of experiential background from novices to advanced programmers. Because of the diversity in the level of knowledge and capabilities of students, some might need to do revision on the lectures that is impossible in the traditional way of learning. Using the “hands on approach” that means the learned concepts can be tested and applied immediately, also is impossible in the traditional way of learning. In this method of learning, the students are more passive while offering people the opportunity to be active in the learning process through structuring the context in which problems are presented encourages a more natural style of learning. To outrun these difficulties and to complement the demerits of the traditional method of learning to program, today new methods are developed using the electronic learning environments and developing environments for practical application.

III. VIRTUAL LEARNING ENVIRONMENTS

Over the last years, the education and learning and teaching have been influenced by the rapid technology development.

¹ Majlinda Fetaji is with the Faculty of Communication Sciences and Technologies, Ilindenska bb, 1200 Tetovo, Macedonia, E-mail: m.fetaji@seeu.edu.mk

² Suzana Loskovska is with Electro technical Faculty, Karpos 2, 1000 Skopje, Macedonia, E-mail: suze@etf.ukim.edu.mk

³ Bekim Fetaji is with the Faculty of Communication Sciences and Technologies, Ilindenska bb, 1200 Tetovo, Macedonia, E-mail: b.fetaji@seeu.edu.mk

That is the learning process has been changed towards more interactive learning activities and authentic experiences according to [1].

The new learning environments are technology enhanced and supported and computer based environments called virtual learning environments.

[2] defines virtual learning environments as computer-based environments that are relatively open systems, allowing interactions with other participants and access to a wide range of resources. Such environments foster the “any time/any place” learning model that is not only a different way of delivering knowledge, but also a powerful means of creating knowledge. These new ways potentially have a wide range of advantages over traditional environments (e.g., convenience, flexibility, lower costs, currency of material, increased retention, and transcending geographical barriers) according to [3].

Learning to program is difficult. To help novices to learn programming we have focused our research on developing a virtual environment to facilitate learning to program in a sense of offering an electronic environment that should meet all the users needs and overrun the demerits of the traditional method of learning .

Usually while developing virtual environments pedagogical aspect is left behind without consideration. Therefore, to develop a quality e-learning virtual environment for learning Java we have focused on the pedagogical concept of the e-learning solution.

A research is made on how to design a quality e-learning.

According to [4] to design our e-learning solution we have followed the approach that design and use of e-learning must be grounded in a learning theory approach. “In order to develop the use of e-learning from a pedagogical point of view, it is therefore not enough to study the existing practice. Instead, it is necessary to have an understanding of theoretical principles of the learning process and of the ideal learning environment” [5]. The learning environment is important because it models the learning process of particular course in a technological medium, so we have to ideally model the learning process. That is the interface that the learners interact with and the learning activities are taking place to achieve the learning goals.

This means that the design of e-learning can not be based only in the existing practice, it is necessary to understand the relation between theory and practice to ensure that the design of practice is founded on the learning theory. This concept is shown in the following figure:

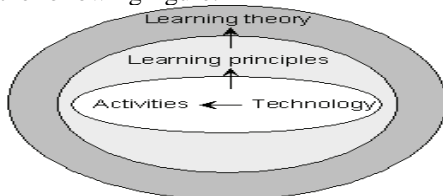


Figure 1 - Theoretically grounded evaluation of technology [2]

We have followed this concept as a pedagogical background of our e-learning solution. It describes that the different learning activities that are driven in the learning environment are supported by the e-learning technologies stated above. The learning principles are formed by the learning activities

to be done to produce the learning outcome. The learning activities are crucial to define the features and abilities the learning environment has to support and are supported by the technology. According to the concept of grounded design in [4] that is “defined as the systematic implementation of processes and procedures that are rooted in established theory and research in human learning” (p. 102), the implementation of the learning activities are rooted in the learning theory and human learning theory.

IV. PEDAGOGICAL CONCEPT ADOPTED

We think that the cognitive and intellectual abilities of learners are crucial in the process of learning to program in an object-oriented programming language.

From the several years teaching experience, we concluded that learning to program in an object-oriented programming language is a complex process where the learning approach is not self sufficient. To support the cognitive learning in the process of learning to program we think that a constructive approach of creating knowledge should be enabled. We think the combination of the two approaches would give a better result on the process of learning. The model of the developed learning environment is founded on the learning activities that depend on the cognitive and intellectual abilities of learners and their abilities to individually construct a knowledge. The pedagogical concept in designing the e-learning virtual environment to learn Java is based on:

- Our e-learning solution for learning programming language Java is grounded on the cognitivist and constructivist learning theory where the learning environment consists of structured learning content integrated as online help content and editing-developing environment which enables creating and finding solution to problems, in the sense that they test different programming concepts of a given example (in the help content) or one created by the user.
- The independent student work supports their individual cognitive abilities to perceive the learning content and process it into knowledge and the individual and subjective construction of knowledge.
- The students work is based on their independent exploration of the learning content where they learn and even more on constructing their knowledge by testing what they have learned and creating new solutions of the given examples or problems or new problems.

V. ADVANTAGES AND DISADVANTAGES IN USAGE COMPARED AGAINST THE TRADITIONAL METHOD OF LEARNING

The virtual learning environment for learning to program in Java will have a simple GUI and will be easy to understand and use, and will be distributed for free download and the more important is the system doesn't need to be installed, meaning we minimize the needed requirements to a simple run of an application. To support the novice programmers our project provides a set of specially designed tools. It includes an editor for editing programs and file manipulation, visual tools for compiling and executing the program and help content that are all presented within a single user-interface

framework. This allows students to move from one activity to another with a minimized effort. All this provides a maximum support to the novice programmers since program construction can be conducted entirely through menu interaction.

It will offer just the essential functions needed to write Java code. This will allow the users to concentrate on the language structure and the principles of coding. The virtual environment offers a developing environment that enables the “hands on approach” that helps students to improve the quality in learning in a sense of immediate testing what they have learned. While the learning content is integrated as a help content, including links to external recourses, multimedia and audio content and the Microsoft avatar as an assistant in learning. This will offer students to learn and practically test the programming concepts, self-pace the process of learning and when and where they want.

To learn programming in Java in the traditional method, we have used the traditional format of lectures in the table or power point presentations that were transmitted by the instructor and were instructor-centered, and not flexible in aspect of time and place.

To write, debug and test a code was very difficult while creating an executive object was impossible with the concept ex-cathedra. Therefore, a simple text editor was used to write the code. To compile and execute the Java code, the Sun Java compiler - Javac was invoked writing a strict syntax-ed command that initiated an increased rate of errors.

In the following table is given the result of comparing learning to program in Java in the traditional method and using the developed learning environment, the same time the advantages of using the developed virtual environment against the traditional method of learning Java:

Variable	Traditional method	Virtual Learning Environment Java
Conducting learning	instructor-paced	self-paced
Flexibility of learning	non	time and place flexibility
Revision of the content	impossible	multiple times
Time duration of the class	limited	unlimited
Writing, testing and debugging	very difficult	easy
Compiling and executing a code	big rate of errors, task scenario 1	low rate of errors, task scenario 2
Learning activity	passive	active

Table 1. Traditional method versus Learning with VLE Java

Disadvantages:

There are still some disadvantages of using the developed virtual environment against the traditional method of learning Java:

1. The acquisition of some skills and concepts of programming depend on direct face-to-face contact with the instructor.
2. The classrooms enable to get an instant feedback from the learners which is very important in the process of learning.
3. The students that can not learn without help are disadvantaged.

The face-to-face training with an instructor leads to greater interaction during learning where the learner may acquire knowledge from the instructor and that leads to greater success

VI. USABILITY TESTING

We conducted usability testing based on performance measurement to quantify usability requirements such as time to complete a task, time to learn, rate of errors and subjective satisfaction defined by task scenario using the traditional method environment and the developed integrated virtual environment Java. Also we made an evaluation by direct observation of users while they were performing different tasks by using the traditional method environment and the developed integrated virtual environment, and users from two different classes were observed.

a. What do we evaluate?

In terms of usability:

- functionalities: can the user perform the requested tasks?
- time: are the tasks performed in a reasonable time?
- satisfaction: is the user satisfied?
- Mistakes: does the user make a lot of mistakes?
- comparison, in particular with text based interface tool.

The research conducted was based on qualitative research were we study the relationships between the study variables and afterwards we use exploratory research to research the factors influencing the graphical user environment and afterwards constructive research to construct the software solution.

We can view the results of the usability testing in the two used environments in the following tables:

Table 1. Usability research for Class-1 in the Traditional method and the developed virtual environment

Usability Attribute	Measuring instrument	Value to be measured	Traditional method environment	Integrated virtual environment
Time to learn	Task Scenario1	Time to complete task	600	400
Speed of performance	Task Scenario1	Time to complete task	600	400
Rate of errors	Task Scenario1	Number of errors	7	2
Subjective satisfaction	Task Scenario1	Satisfaction degree of users	2	5
* number. Subject satisfaction scale: very high high average low very low 5 4 3 2 1				

Table 2. Usability research for Class-2 in the traditional method and the developed virtual environment

Usability Attribute	Measuring instrument	Value to be measured	Traditional method environment	Integrated virtual environment
Time to learn	Task Scenario	Time to complete task	500	300
Speed of performance	Task Scenario	Time to complete task	500	300
Rate of errors	Task Scenario	Number of errors	5	1
Subjective satisfaction	Task Scenario	Satisfaction degree of users	1	5
* number. Subject satisfaction scale: very high high average low very low 5 4 3 2 1				

VII. CONCLUSION

We have tested the viability of the variables chosen for the study of the developed Java Editor e-learning system. It also produced valuable information for the design of the subsequent studies. The conclusions may be summarized as follows:

- The variables provide both qualitative and quantitative and objective and subjective data.

The experiences introduced suggests the positive effects of using the Java Editor in classroom teaching/learning. In these classes, randomly assigned treatment groups experienced the Java Editor assisted learning in different ways, and the data were collected through the class experiences and questionnaires. Those questionnaires have shown positive opinions and high degree of user friendly concept embracement of the developed virtual environment.

Using this kind of user centered approach in building our graphical user interface and involving the users at each stage of the development and evaluation of the interface we have concluded that it resulted in a very user friendly graphical user interface. It is more usable, oriented towards the users and will certainly be used in the future from their side according to the satisfaction rate encountered during the usability testing.

According to the research results we acquired from the empirical study and compared to the previous years of the same java classes when for compiling was used the command based interface and for writing the code the notepad was used, the new developed graphical interface has several advantages. The developed graphical user interface system is easier to use and has better performance rate than the textual command line based interfaces which was usually used previously in java classes for compiling the java code. Also having everything they need in one place the students do not need to leave the application framework at all especially by having the multimedia and virtual assistant help. The option to capture the syntax errors was also welcomed from the users of both type's expert and novice.

In a perspective of learning a programming language, in general, to use a graphical user interface system is less expensive and less time consuming, a greater accuracy in the process of writing the code has been achieved, also compiling and running the code is much easier and linear process than

the use of textual command-line based interface. Users are more involved in using the visual graphical interface and more confident than the previous users using command based textual interface. Our recommendations are to use this kind of structured approach described here to develop similar graphical user interfaces using the user centered approach that will include the users at all the development stages of the graphical interface.

REFERENCES

- [1] Malone, P., Schryer, C. & Rossner-Merrill, V. (2000). Combining Instructional Models and Enabling Technologies to Embed Best Practices in Course Instructional Design. In P. Kommers & G. Richards (Eds.), Proceedings of World Conference on Educational Multimedia, Hypermedia and Telecommunications 2000 (pp. 1685-1686). Chesapeake, VA: AACE.
- [2] Harmon, J. & Marquez-Zenkov, K. (2003). Perpetual Pedagogy: A Critical Deficiency in Modeling Educational Technology to Pre- and In-Service Teachers. In C. Crawford, D. Willis, R. Carlsen, I. Gibson, K. McFerrin, J. Price & R. Weber (Eds.), Proceedings of Society for Information Technology and Teacher Education International Conference 2003 (pp. 3585-3588). Chesapeake, VA: AACE.
- [3] Ahmad R., & Ives B., (1998) "Effectiveness of Virtual Learning Environments in Basic Skills Business Education: A Field Study in Progress.", with. Proceedings of the Nineteenth Annual International Conference on Information Systems (ICIS '98), Helsinki, Finland, December 1998.
- [4] Hannafin, M. J., Hannafin, K. M., Land, S. M. & Oliver, K (1997): Grounded Practice and the Design of Constructivist Learning Environments, Educational Technology Research and Development, 45(3), 1997, p.101-117.
- [5] Hannafin, M., Land, S. & Oliver, K. (1999): Open Learning Environments: Foundations, Methods, and Models. In: Reigeluth, C. M. (Ed.). Instructional-design Theories and Models: A new paradigm of instructional theory, Volume II, 1999, p. 115-141. Lawrence Erlbaum.

Software Engineering e-learning Information Retrieval Courseware

Bekim Fetaji¹ and Majlinda Fetaji²

Abstract— Research studies, practical project activities and real-world implementation experiences were focused on designing and building information retrieval courseware system. The objective of the research was oriented towards creating a courseware system that will be based on assessed, and evaluated e-learning outcomes and previous known concepts to users. It was targeting the computing knowledge level of the users and provides higher level of information for the course content and support for different file formats. The main focus was set on evaluating the e-learning outcomes and based on them designed the information retrieval courseware in compliance with theories of learning and didactical pedagogical approach. The research is proposing a new way of tackling the process of creation of e-learning information retrieval courseware by integrating and undertaking the software engineering approach based on e-learning outcomes and taking into consideration theories of learning pedagogical approach in its development. Also business objective expressed through the cost effectiveness of the entire system was set as priority. We have achieved to have a high cost effectiveness through minimizing maintenance and need for training keeping the learning curve flat. Based on our research survey and user feedbacks it resulted in a courseware system that is cost effective and very usable. We recommend this courseware to departments where the staff computer literacy level is low and there are no financial means for a commercial learning management system.

Keywords – e-learning, information retrieval courseware, education

I. INTRODUCTION

In most of the contemporary universities, the implemented Course Management Systems (CMS) lacks of responsiveness of the well-designed model regarding the specific needs of the institution. Usually these models are complicated and require a lot of additional efforts from the staff and students both for learning and usage. On the other hand they are expensive to maintain and support especially when compared with the level of their usage. A straightforward implementation of an existing commercial tool for Course Management Systems (CMS) in environment of low e-Literacy of teachers and e-Culture of students, slow growth of Internet penetration, inadequate and insufficient IT equipment of the Higher Educational Institutions (e.g., countries of “West Balkans” and other regions in the world with similar economic

environments), can bring only simulations and not a substance for improving the real performances of the learning process.

The proposed model in this project is based on achieving the several parameters: to be in compliance with the learning theories and have a didactical pedagogical approach, e-learning outcomes, simplicity in usage-effecting in low learning curve, minimizing the maintenance and support in order to achieve high cost efficiency.

We also considered as crucial and very important to assess and focus on the computer literacy level, but also of the instructors/teachers' views and ideas with regard to their fields (i.e., their practical knowledge in delivery of course.) Our solution was targeting the academic staff computer literacy current level and adopted to their views and needs as prospective users of the system.

Our main research objective was to create an information retrieval courseware system that we named as Intranet Gateway system that will provide higher accessibility on-campus and off-campus. The aim was to raise the level of accessibility by providing additional e-learning features and options to the end users.

The research study objective was set in finding new and more effective approach in designing and building a course management system that will emulate the approach of the classical “teacher-classroom-content laboratory” and will raise it to the overall level of communication and accessibility to information and e-content.

II. RESEARCH METHOD

Our research methodology was fundamental research of the e-learning outcomes, variables and the findings from our fundamental approach we used in our applied research afterwards based on exploratory and constructive research on several hypermedia development methodologies. A hypermedia application represents a collection of unstructured and multimedia nodes connected through links in an associative way. Since hypermedia systems are highly interactive, the design method has to be user-centered. We have however used a hybrid combination and different interaction mechanisms through active x controls and the hyper document is actually accessed in run time from the user side, while from an administrative perspective it is set as file on a remote server. At all stages of the design and development, prototyping and evaluation were the basic activities in the development process. The data for this research was gathered from research interviews with e-learning specialists and participants, focus group and interviews, as well as web based surveys and printed hard copy surveys with academic staff and students.

Key variables and themes that have been studied are: assessing and measuring e-learning outcomes, students needs

¹Bekim Fetaji is with the Faculty of Communication Sciences and Technologies, Ilindenska bb, 1200 Tetovo, Macedonia, E-mail: b.fetaji@seeu.edu.mk

²Majlinda Fetaji is with the Faculty of Communication Sciences and Technologies, Ilindenska bb, 1200 Tetovo, Macedonia, E-mail: m.fetaji@seeu.edu.mk

analyses, environment of usage feasibility analyses incorporating multicultural and multilinguicity specifics, applications specifics and requirements in correlation with the environment and situation of the University and then broadly generalized for all contemporary Universities, accessibility and learning specifics based on usability testing and evaluation of the environment.

Considering the software development methodology approach, we have used the "spiral" software development life cycle, prototyping, usability expressed in matrix and usability testing; and cross-sectional survey using questioners, in order to find and get the feedback from the users of the system in accordance with the guidelines from [6].

III. REQUIREMENTS ANALYSIS AND THE CONCEPTUAL DESIGN

The mission of the application is established by identifying prospective users and defining the nature of the information base. Also identifying and assessing the e-learning outcomes is set as primary goal. In addition to the customary requirement collection and feasibility assessment tasks, web applications designed for universal access require special care in the identification of human-computer interaction requirements. In order to establish the interaction mode most suitable for each expected category of users, and for each type of output device that users are expected to use to connect to the application based on recommendations from [3].

Speaking to a prospective users and research interviews with e-learning specialists and participants, focus groups we have assessed and defined our users computing literacy level. Our results shown that almost all of them had knowledge of basic Operating System commands, opening , creating, changing, and deleting folders and they know the common operations with using files, as well as they all know MS Word, and notepad. They were all aware of other file formats as: Adobe portable document (pdf), and Windows help file (chm) format. These assessed knowledge level was set as our target and our software was built to target this level of knowledge and use only these operations as well as embed them in our software solution for the courseware.

As far as the conceptualization is concerned the application is represented through a set of abstract models that convey the main components of the envisioned solution. In the Web context, conceptualization focus is on capturing objects and relationships as they will appear to users, rather than as they will be represented within the software system. In our approach in building the Intranet Gateway we have created a Public Folder in a remote server were the entire content of the courses content and subject materials can be placed. Conceptually we have organized the folders to contain all the files inside them and an additional folder to be set up for the web page needs. The lecturer of a particular subject and his assistants have administrative privileges and are allowed to have access to the folder of the subject in the remote folder, were they can add, change, delete, write or read information, change and manage the content. The students are not allowed to have access to these folders. They will access the content from a web interface. To provide a formal user-interface design, the frame concept has been employed.

IV. SYSTEM MODELING

In developing the Intranet Gateway system we have approached using the spiral life cycle model and followed the usability principles recommended by [2], and [5].

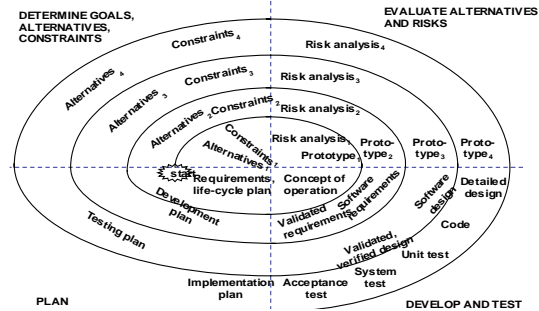


Figure. 1 The Spiral Method, [6]

As a platform we have used Microsoft Active Server Pages-ASP. The spiral methodology reflects the relationship of tasks with rapid prototyping, increased parallelism, and concurrency in design and builds activities. The spiral method should still be planned methodically, with tasks and deliverables identified for each step in the spiral software development life cycle (Figure 1).

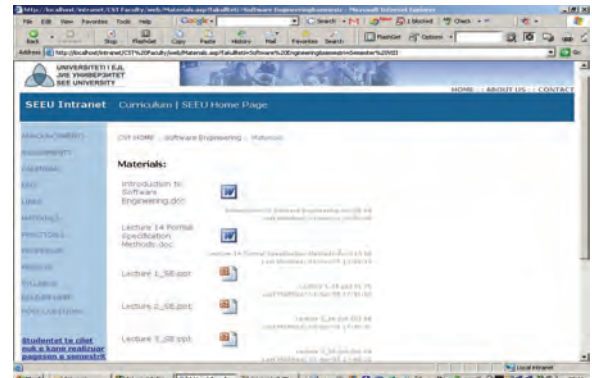


Figure. 2 Intranet Gateway courseware system – Class content materials

An important issue during development was importing the entire content from the remote Public folder and nothing to be hard coded as content.

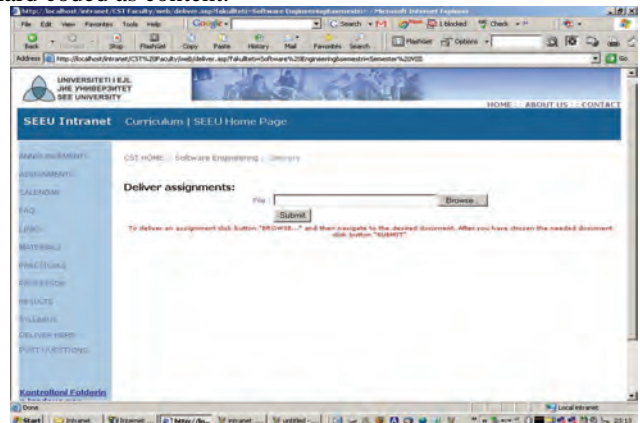


Figure. 3 Intranet Gateway courseware system – Delivery mechanism

This makes it very easy to maintain and manage content. The entire content is loaded in the browser at the moment of accessing the required subject through the web-based interface and the course administrator-lecturer and assistants engaged in the subject are not limited and can offer content in different formats like Word documents, Adobe pdf files, MS chm format and all other available standard formats for content presentation. This is realized through using MS Active X controls.

The course administrator simply using copy-paste functionalities puts the content in the folder from where the students access it. Also, the content shows the attributes when it was created and modified as well as its size together with an icon and description of its format. In defining the initial requirements using this model before building our first prototype, we first anticipated all the requirements and created a project management time table that would involve all anticipated activities like detailed design, needs analyses, development phase, testing the unit, integration and test, evaluation and implementation.

Activity Number	ACTIVITY Name	DURATION (Weeks)	DEPENDS ON (Dependencies)	PT	OT
10	Feasibility study	2		+2	
15	Requirement analyses	6		+1	-1
20	Modeling-Design using UML	9	15	+1	-1
25	Planning activities	2	20		
30	Write data entry software	3	10		
40	Create Data files	5	30		
50	Create multilingual content	3	40		
60	Write Program Specifications	3	10	+1	-1
70	Construct Program	12	60	+3	-2
80	Test System	5	25,40,70		
90	Familiarize users	2	10		
100	Train Staff	6	90		
110	Deployment	2	50,80,100	+1	-1

Table 1: Work breakdown activities with dependencies, duration, pessimistic (PT) and optimistic time (OT)

The project managing team introduced 13 work breakdown activities for the Gateway project.

Then based on our activities using the Critical Path method-CPM in combination with PERT (program evaluation and review technique) we have defined our critical activities and time of delivery (time when the project can be delivered) that was calculated to be in 25 weeks, and we also have done the risk analyses of the system, analyzing all the possible risks. The project had two critical paths (CP) lying between the activities: CP1: 10-60-70-80-110 and the second critical path between the next activities CP2: 15-20-25-80-110. The system was constantly during its all stages critically evaluated first from the development team during meeting sessions and then from the users. Important issue that was highly considered was the news and announcement options. Based on the interviews with students and lecturers it was concluded that students very rarely access announcement and read news regarding the University, Faculty and subject. In order to solve this issue we have implemented news scrolling text developed using JavaScript that according to our survey was highly appreciated. The entire content of the news and announcement will be uploaded from a simple text file, and it will show in each subject page on the left bottom of the screen. The menu content and links are based on a grounded

theory research that included several comparative analyses of course management systems and web-based course systems as well as our experiences and surveys on the users' needs analyses. Following the guidelines from [4] the interface is clear and navigational structure is clearly marked using breadcrumbs allowing the user to orient himself at each point about his position in the content structure hierarchy. Also, a clear exit or shortcut to the other main content groups is provided so the user can easily navigate depending on his preferences and needs, observing the navigational guidelines and not so much the aesthetic perspective of the interface. The aesthetics can be addressed later and has to be sacrificed for the accessibility, content availability and overall functionality since it is not a priority for such a system under development.

V. IMPLEMENTATION ISSUES AND SOLUTIONS

The functionality concerns both training activities and navigational ones, like moving through hypermedia objects and browsing large multimedia structures [1]. The training issues were brought to minimum as it was one of the main goals in the design of the project. The main issue was to develop an interactive system that would support user functionality efficiently and effectively, taking advantage of the new infrastructures currently available. All the users are brought to use a system that is already familiar and based on already used concepts and techniques that they already know how to use the public files. The information provided by the system is presented in a variety of ways, such as interactive simulations demonstrating the use of various Internet tools, hypertext, special sounds, appropriate images and animations, hypermedia object, etc.

VI. CONCLUSION

As a result of the project we have anticipated different outcomes, some positive and some negative aspects. In order to evaluate the outcomes of the Intranet-managed teaching/learning we have based it on the usability testing and evaluation questionnaires that we used as instrument to evaluate the outcomes. The questionnaire was focused on determining the 'level of content' and comparisons between 'old' teaching and 'new-Intranet' approach. Also, a grade average analysis (comparison) of students who attended 'classical' classes and those with using 'Intranet Gateway' is done in the following table for the subjects "Computer Application in Communications 1 and 2 – CAC 1 and 2"; Object Oriented Programming in Java(OOPJ), Web Design and Multimedia (WDM 1). It is very difficult to conclude that this improvement in the performances of student success is only due to the impact of Intranet Gateway, because also other factors can influence it (ex. Methodology of teaching, the evaluative educational aspect of the 'next' generation of students by default for the purpose, etc.), but the notion that the main factor for improvement was this new Course Management System through Intranet after the analysis of the questionnaire is true.

Subject	GPA before Intranet usage	GPA Improvements after usage
CAC 1	6,85	7,40
CAC 2	6,10	6,70
OOPJ	6,72	6,95
WDM	6.05	6.35

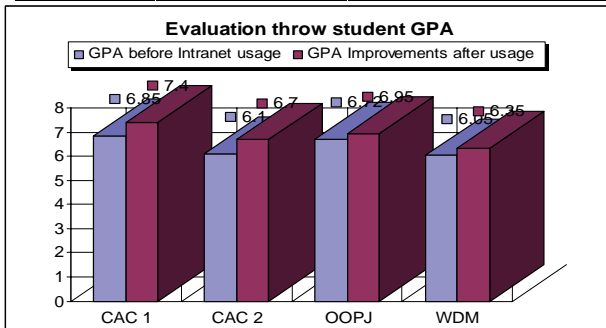


Table.1. Evaluation throw student grade average – GPA

The Intranet gateway was implemented for the courses in the Communication Sciences and Technologies (CST) Faculty - Computers Science Department (CSD) of SEEU. Based on the observations and measuring instruments, the outcomes are as follows:

Positive outcomes:

1. With the use of Intranet, the three classes became more effective. Comparing with the projects from previous years, the quality of the technology tasks were improved, especially the quality of multimedia designs and Web based instruction designs. Some of the projects showed that students accomplished more than they had expected, and even more than the listed course objectives, because they had more opportunities and time to explore the technologies, and to improve learning by team collaboration.

2. Accessibility was substantially increased. The students now had more access to materials and feedback.

3. Student motivation by using the system was also substantially increased. The classes became more interesting for them and they enjoyed learning, requiring new knowledge and technology in the way they felt comfortable, which, to certain extent, motivated their learning. We concluded that learning is substantially more effective when the learners were highly motivated.

4. One of the most important outcomes was that students actively involved through the teaching/learning processes, from which they learned to manage their own studies.

5. Students also learned how to use Intranet to enhance teaching. Their projects reflected not only the technology designs, but also the use of Intranet in teaching. They learned this from the way the classes were organized, and from the way they were taught.

Negative Outcomes:

6. The instructors complained that now their work has been at least doubled and the requirements for a course preparation are more demanding compared to previous years, what effected substantially their motivation in using the system because of the amount of work additionally added to maintain courses.

7. Students were complaining why all of the class materials are not provided electronically-digital format as e-content and why they still have to use only books. They can not take the book everywhere with them while they can access the e-content easily and does not impose any constrain to them.

8. The content provided is of static nature and is simple text and static graphic images which does not effect learning in any other level compared to the previous classes (based on user and instructor survey feedback) and there are no studies that could convey the way of preparing e-content that could substantially increase learning compared to the classical classroom.

9. Based on the user feedbacks, e-learning survey and literature reviews we have concluded that the courseware system at this stage of usage is providing only e-reading and not e-learning since it does not impose any distinct effect on learning, accept on motivation, attention, and accessibility level.

Our observation based on questionnaires, survey and our analyses is that the developed system is very cost effective, with minimized need for a maintenance and staff training since it based on their previously assessed level of knowledge, it proved practical and easy to use, specially having in mind departments were computing knowledge is not a requirement. Future work should involve further research on authentication issues, forum option, links to other University software like library software, SEEU assessment software, central administration, and also should include options for importing and exporting the content into SCORM complement content package that could be easily used in conjunction with the other commercial Course Management Systems.

Because of its cost effectiveness and simplicity of usage and since it is not imposing any previous IT skills and knowledge requirements based on surveys and user feedback it proved practical, useful, and easy to maintain system with highly acceptable cost effectiveness in a broad aspects of usage for different institutions/departments.

REFERENCES

- [1] Challa, C. D., and Redmond, R. T. (1996) "Is it a Lot of Hype? Hypermedia Approach to Document Processing," *Journal of Systems Management* (47:3), pp. 12-21.
- [2] Dumas, J. S., & Redish J. C. (1999) "A practical guide to Usability Testing" revised edition, Pearson Education Limited, pp.55-62
- [3] Helic, D. Krottmaier, H., Maurer, H., & Scerbakov, N. (2005): Enabling Project-Based Learning in WBT Systems, In *International Journal on E-Learning (IJEL)*, Vol. 4, Issue 4, pages 445-461, 2005.
- [4] Maciaszek L. A., & Liang L.L. (2005) *Practical Software Engineering: A case study approach*, Harlow, England: Addison Wesley
- [5] Nielsen, J. (2000). *Designing Web Usability: The Practice of Simplicity*. New Riders Publishing, Indianapolis, ISBN 1-56205-810-X
- [6] Pressman, R. (2005) "Software Engineering: A practitioners approach 6 Ed" McGraw-HILL, inc, pp.81-117

The Problems in Distant - Learning

Veneta Aleksieva¹

Abstract – In this paper are represented the problems in distant- learning. I focus on the feedback in e-learning as a base method for contact between teachers and students, which is considered from two viewpoints: “student – teacher” and “The learning efficiency”.

Keywords – Distant – Learning, Feedback, Final test, Continual assessment tests

The achievements of telecommunication technologies pioneered a way for the new technologies advance as teaching and communication tools, which can provide knowledge without the limitation of the traditional way of teaching. These new technologies help very much for the advance of Distant - Learning, used by a huge number of scientific, cultural and trade companies in some form. Today, the tendency is to apply Distributed Education, in which not only is the student is physically separate from the teachers /and the other students/, but he also learns at his own pace and at a time convenient to him. The opportunity for learning and teaching, independent of the time or the place, is much facilitated by the use of Web-based courses.

E-learning should be a response to some requirements which should be leading, when we will develop E-learning, namely:

- Clearly defined a target group
- Clearly and precisely defined learning goals
- Quality content /reliable, modern, achievable, appropriately represented for the target group/
 - Proper teaching style /the curriculum will be presented or assimilated by the proper teaching methods– active learning, interactive approaches etc./

Effective communication and feed back which are considered from two view points:

- The Feedback “Student –Teacher” – the student’s opportunity to make contact with his teacher /instructor, web- administrator etc./ for various reasons which arise in the learning process
- The Feedback “The learning efficiency” – the teacher’s opportunity to estimate from the students’ results /tests, exams etc. / the success level, his omissions in the presentation of material and the learning efficiency. The analysis of this type feedback offers the chance to correct the mistakes and omissions and to decrease them in the future by adaptive strategy for presentation to a unique target group

Most people have traditional education, from kindergarten to the end of their high school education, so they have their own expectation about the methods and the communication tools in relation Student –Teacher. Perhaps they have some of these problems which must be overcome:

- The change of the teaching role - The teacher is more a consultant and an assistant than a leading figure.
- The change of interaction with the students – distance and time influence the teacher’s control on the learning process.
- The various communication media – The newest communication network tools are more complex, therefore they demand more experience with them. E-learning provides topic-based forums, on-line conversation, e-mail, newsgroups, on-line tutorials and on-line tests of students.
- The students’ isolation – It generates practical and psychological problems and requires the use of new communication network tools, forms and communication skills. There is no competition or contact with other students. The immediate teacher’s support is missing too, so the students have more adaptation time. The student is a social individual and he needs to be a member of a very integrated group, which collaborates and has identical goals and tasks.

The fast feedback opportunity is the essence of E-learning, because it can’t the use benefits of traditional learning – direct relationship with the teacher, discussions about ideas and problems with other students, to teamwork in skills acquisition. Here the accent is on the cognitive learning, namely the acquisition of knowledge by information adoption and revision, but without monitoring and orientation by the teacher of the developed skills and habits. The student’s motivation in E-learning is examined from the teacher’s point of view - the feedback is the only tool, with which the needed results are reached.

These exactly appear to be the reasons for the restrictions on E-learning application areas – in scientific areas which demand basic practical skills accumulation, a mixed learning can be applied, but not only E-learning. /Such professions are those of a dentist, a doctor, a pilot, an army, an underwater diver, a fireman etc. /

It is absurd to expect communication by e-mail equivalent to the communication by audio- or videoconference. This fact exactly determines a necessity of including an alternating different technical feedback decisions, as the proportion between them is defined by the target group, the teaching goals, the expected results of a student’s success, the teaching style included in the E-learning curriculum.

The feedback from students about their opinion of the weak and strong points of the system and the communication is important for a flexible curriculum adaptation and a change of teaching style /as far as possible/. The analysis of this feedback

¹Veneta P. Aleksieva, Technical University, st.”Studentska”1, 9000 Varna, Bulgaria, E-mail: ven7066@abv.bg

provides the opportunity for mistakes correction and their decrease in the future by strategy adaptation for the curriculum presentation according to the characteristics of a target group. It is wrong to search for this feedback at the end of the e-learning course. It is necessary to follow it all through course, because it is a regulator for a maximal student motivation and it tries to meet the student needs and requirements. This feedback traces the personal motivation of each participant. So the number of drop-outs /which at this moment is 30-50%/ is expected to decrease considerably, because the personal motivation has been raised and students' cognitive dissonance will be absent.

In the relationship Teacher-Student the role of grading is important as it is a factor for the student motivation and for his psychological and intellectual advance. At the same time e-learning makes quick and large-scale control in a short time, which necessitates the large application of tests, because tests are the basic form for assessment. This raises the question, "Do tests reflect adequately the present students' skills and knowledge?"

In e-learning test's grading, the form of a question in a test is in the background, but the attention is focused on a correlative relationship among a chosen units. The student's knowledge is assessed on the base of these chosen units, as it analyzes an impartial, indirect, group test for a level of knowledge which is limited in time. It should be kept in mind that grading is an opinion, attitude and assessment of human dignity and insufficient for person. It is a number or verbal expression which measures knowledge or competition of students. Just this fact brings out the impartiality of tests on new ideological level – The impartiality from the viewpoint of ignoring the student's – age, male, race, physical characteristics.

The achievement objectivity depends on the extent to which a subjective estimate of a research-worker is influenced by the test's results, because the test is a method for examination by which in a standard situation reveals personal features. These features are indication for determining a person characteristics and providing the arrangement of a research-person in a classification which is based on a group of comparable persons or based on an ideal standard. In e-learning tests an ideal standard is in a pawn in itself environment which contains a test and is created by a team of teachers to achieve a maximum objectivity assessment.

At the test's base lies suggestive questions which contain in themselves a given alternation. They may be represented in different forms. The test must be formed on the basis of meaningful relations among test items, as it follows a principle of quotas, independent from the question form, their quantity and correlation among separate items in a test.

The continual assessment tests, the grading should be of quantity as well as of quality. It directs the students to the gaps in their learning. Based on this grading, the teacher summarizes for all participants the achieved level and sets up an adequate feedback on two levels:

- Individual – to every participant

- Group - to analyze the tendencies for knowledge gaps in the whole group, which is a basis for additional tasks or directions for self- training

For distinction from continual assessment tests, the final test has a purpose to control the absorption level on whole curriculum. It is single and limited in the time. While continual assessment tests are related with a particular part of curriculum, the final test contents a complex problems which consolidate subject from different lectures. It shows the student's ability to summarize and apply a got knowledge for decision on new practical problems. The structure of a final test is identical with the structure of current tests. The results from final test is estimated, analyzed and reported from the teacher. While by the continual assessment tests the role of rating is only regulative, then by a final test the rating is summarized. We must be made more precise what is the final test. It may be distant when stay question about summary a part of curriculum and a level (Cisco, Microsoft, Sun и др.) or working (a course of foreign language, a course of computer literacy etc.). Working tests are more prestige, because a right participant's identification is on default and is ensured necessary circumstances of test control. In general opinion circulate, that the distant-learning hasn't a same weight as the traditional learning. Therefore exactly working test grows up his notability.

Some education organizations resort to make the final working tests which dislocated in different cities in Test centers. This minimizes a charges as from students as for e-learning sponsors. In this case the student in your initiative and wish takes an examination after his whole training. This test hasn't role of a mandatory final test for hold e-learning course, because is possible a person direct take this exam for certification without participate in any course.

The importance characteristics for effective evaluate by take a test is consistency and trustworthiness - the results of estimation will be same if examination in the different time, the other circumstance, from the different teachers. The evaluate trustworthiness means that the independent teachers will be estimate in same way an answer of one person. Exactly e-learning tests reach in this aspect very high trustworthiness.

The traditional learning models can't to expand to meet the challenge of new generation. In other side distant-learning may be improve /or substitute / the traditional methods and materials /a classroom discussions, a practical occasions, an imprint book/

The last years of globalization demonstrate that learning and teaching from distant, especially when is used the high-speed telecommunication technologies is effective, because the effectivity is measure with the student's achievements, the reversion of an investment, the relationship of the students and the teachers to learning process.

REFERENCES

- [1] B.Collis, J. Moonen, *Flexible Learning in a digital world, experiences and expectations*, London UK, Kogan Page Ltd., 2002
- [2] Т. Элерс, *Методика диагностики мотивации к избеганию неудач*, Украина, Одесса, 2005.

The Roles of Colours in the Multimedia Presentation Building

Petar Spalevic¹, Borivoje Milošević², Kristijan Kuk³ and Gabrijela Dimic⁴

Abstract – This paper describes concept of colours and their usage in the multimedia and Web presentation. Given is explanation of the influence of light on the human eye. Also describes the spectar of colours and the meaning of colours in creating the new Web presentation of High school of electrical engineering in Belgrade.

Keywords – Human eye, light, colour, presentations, meaning of colours, colour scheme.

I. INTRODUCTION

The eye has two main component: the lens and the image sensor. The lens contains part of the light refelected from some objects and polarizes it on the image sensor. The image sensor then changes the light sample into a nerve signal [1].

The eye has two lenses. One of them is the meniscus of the eye which is called the Cornea and the other lens is an adjustable one inside the eye. The cornea does most of the refraction of light [1,2].

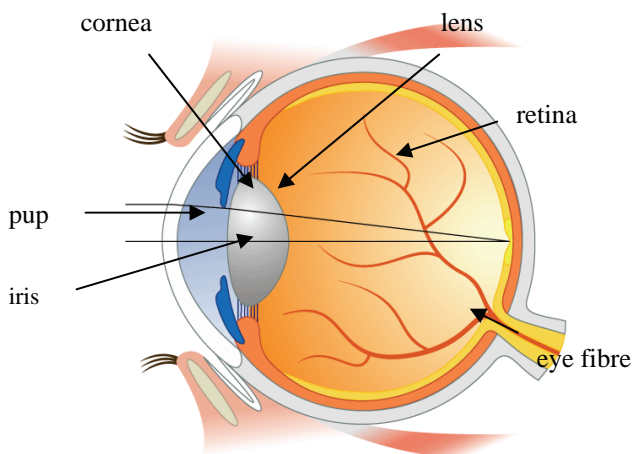


Fig. 1. Human eye

The surface sensitive to light which covers the inner surface of the back of the eye is called the retina. As seen in Fig. 1. the retina can be divided into three main layers of specialized nerve cells: one for changing light into nerv signals, one for processing images and one for transmitting information to the optical nerve found in the brain.

There are two kinds of cells which detect light: wands and cones so called because of the physical shape when seen under the microscope.

The receptor “corks” – Fig. 2. are specialized in colour distinction, but can work only when there is enough light.

There are three kinds of “corks” in the eye: sensitive to red, sensitive to green and sensitive to blue. This sensitivity to different colours occurs because they contain different photopigments that is chemicals which absorb different wavelengths of (colour) light [3].

Fig. 3. shows wavelengths of the light which trigger all three kinds of receptors. This is called RGB coordinating and it shows how the colour information leaves the eye through the optic nerve. Human perception of colour is more complex because of the nerve’s processing at the lower levels of the brain.

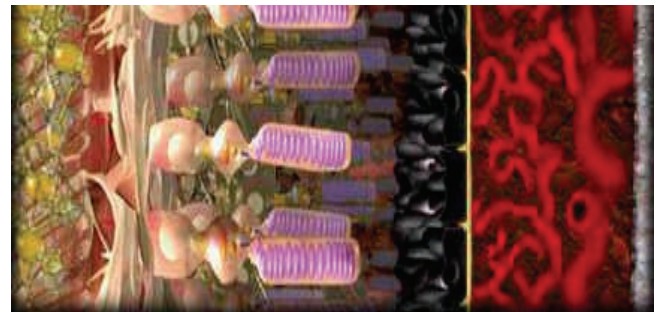


Fig. 2. The receptor “corks”.

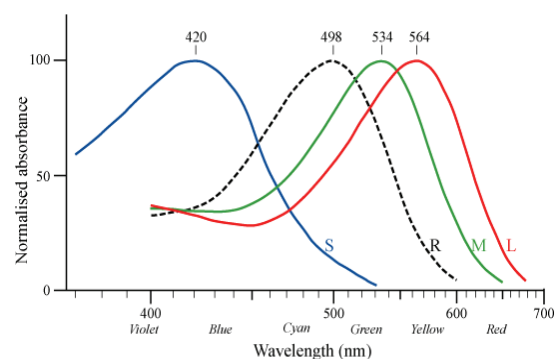


Fig. 3. Wavelength of the light which trigger all three kinds of receptors.

¹Petar Spalevic is with the Faculty of Technical Sciences, Kneza Milosa 7., 38200 Kosovska Mitrovica, Serbia, E-mail: petarspalevic@yahoo.com.

²Borivoje Milošević is with Faculty of Electronics, Aleksandra medvedeva 14, 18000 Niš, Serbia, E-mail: boram@ptt.yu.

³Kristijan Kuk is with *High School of Electrical Engineering*, Vojvode Stepe 283, 11000 Belgrade, Serbia, E-mail: kkristijan@vets.edu.yu.

⁴Gabrijela Dimic is with *High School of Electrical Engineering*, Vojvode Stepe 283, 11000 Belgrade, Serbia, E-mail: gdimic@vets.edu.yu

RGB coordinating is converted into a different coding scheme where colours are classified as: red or green, blue or yellow, light or dark.

RGB coding is an important limit of human eyesight: wavelenghts which exist in the environment are grouped into only three wide categories.

Visible light consists of seven groups of wavelenghts. Those are colours seen in the rainbow: red, orange, yellow, blue, indigo blue and purple. The lights represents one form of the electromagnetic spectar.

The electromagnetic spectar represents a collection of all energies organised into different categories established on wavelenghts for all types of energy.

II. COLOURS

The human eye can recognize only visible light. When we look at the sun it seems colourless or white. White light is not a light that consists of only one colour or frequency, but is made up of many colour frequencies.

The combination of any different colours in the visible spectar produces a light which is coloured or white. For us to be able to see the red colour of an object there must be a source of light for example the sun.

When an object receives a light wave it emmits a light wave red in colour, or it absorbs a spectar of blue or green colour but it reflects a spectar of red colour which we recognise with our eyes.

Red, blue and yellow are called basic colours because together they produce white light. This model of forming colour is called the adaptive model in physics. White and black are not colours because in the absense of any kind of light white becomes black and that is reason why we cannot see anything in the dark.

Our eye registers light and all its components (red, gree and blue) as white. The absense of any source of light the eye registers as black. An the intervals of light of equal intesity of the basic components is registred as gray.

As we can see from combining these three colours will give us any colour from the colour spectar. So where blue and green overlap we got cyan, red and blue become magenta, red and green become yellow.

III. COLOUR SCHEMES FOR MULTIMEDIA PRESENTATION

The first step in making colour schemes for multimedia presentations is defining the target group that watches your presentations.

If they are young , use bright colours. If you are marketing for sales purposes use natural colours like green and blue.

You need to choose a one colour tone to accentuate page allocation. Next choose a colour to complement the first colour to use for titles and subtitles.

Mostly commonly used colour scheme:

- **Warm colours** – Fig. 4. : from red – purple to yellow. Those colours make excellent contrast.

- **Cold colours** – Fig. 5. : from purple to green – yellow. Those colours are excellent for texts.



Figure 4. Warm colours.



Figure 5. Cold colours.

A. Complementary colours

Complementary colours are directly opposite each other on the colour wheel. These colours should be used carefully as they are in direct opposition but providean excellent contrast. For example red is complementary to green on the colour wheel.

When using complementary colours next to each other, vibrations that give a very pleasant feeling and really attract attention, are created. (Fig. 6.)

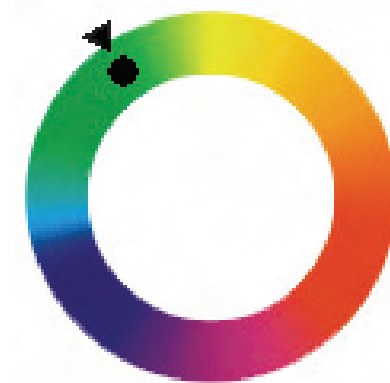


Fig. 6. Colour wheel.

B. Analogue colours

Analogue colours are any three successive colours segments on the colour wheel. These colours produce enough differentiation of elements without stepping away from the union of elements.

C. Monochromatic colours

Monochromatic colour are all variations of the colour segments on the colour wheel (Fig. 6.). You can use these colours without any fear because the represent a variation of one colour but the contrast is weak. They provide harmony because all elements have something in common.

D. Traditional colours

Traditional colours are any three colours found at an angle of 120° one is respect to the other . If the Colour Wheel were a clock the blue would be at 12 o'clock, green at 4 o'clock and red at 8 o'clock. This colour scheme gives presentation a good colour balance.

IV. THE MEANING OF COLOURS

Colours have a direct and intensive influence on humans. To a wide degree, our actions and reactions depend on colours. Lighter colours for example produce emotional responses. When the Blackfriar Bridge, in London, was painted green, the number of suicide jumps was lowered by 34%.

The human eye can see about seven million colours. When our eyes move from one colour to the other it adapts to the change in colour.

Depending on that adaptation we register the so called visual effect. Lighter colours reflect more light which stimulates our eyes [4].

The human eye first registers light colours. The colour first noticed is yellow. Big contrasts between colours blind the human eye so they are hard to look at.

The meaning of colours mainly depends on the culture we were brought up in; for example red does not have the same meaning in U.S.A and in China. Just guess why. The meaning also changes because of our age and gender.

For example women prefer colours from red to blue while men prefer colours that are their opposites. Older people prefer darker colour to light ones [4,5].

The meaning of colours is also very important in creating a Web sites.

The colour scheme of the Web site of High school of electrical engineering in Belgrade (new version which is in creating) is based on three different colours (Fig. 7.)

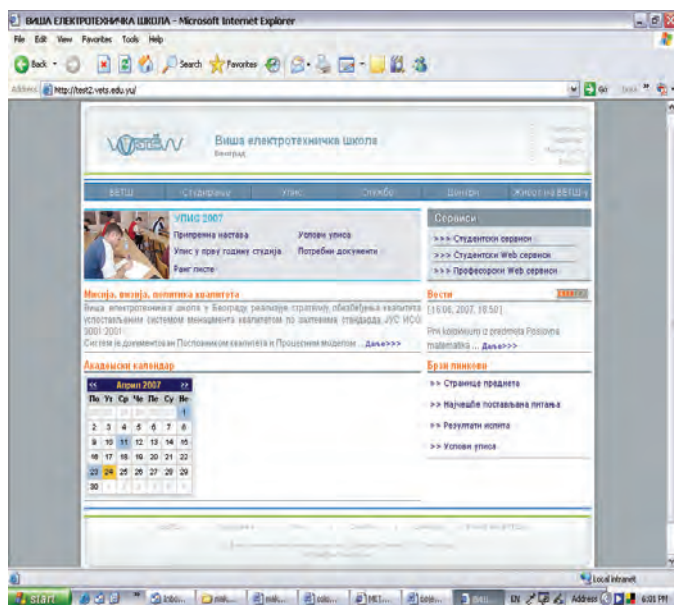


Fig. 7. Web site of High school of electrical engineering in Belgrade.

On the Fig. 8. above, is given the colour scheme into Web site of High school of electrical engineering in Belgrade.

HTML Color Name	Sample		Hex triplet
	(rendered by name)	(rendered by hex triplet)	
lightgrey			#D3D3D3
gray			#808080
darkgray			#A9A9A9
dimgray			#696969
lightslategray			#778899
slategray			#708090
darkslategray			#2F4F4F

Fig. 8. Colour scheme.

V. THE EXPLANATION OF COLOUR SCHEME

A. Blue

Blue is one of most popular colours for presentation. It mirrors quite, harmony, trust and stability. Blue is often a colour used to symbolize honesty and trustworthiness. Blue is associated with water; on coloured maps, oceans, lakes, and streams usually appear blue. This colour agrees with other pastel colours and is perfect with natural colours like green and gray [4,5].

B. Green

Green shows care. It makes positive negative feelings.. Green presents loyalty and intelligence. Green takes up a large portion of the CIE chromaticity diagram because it is in the central area of human color perception[4,5].

C. Grey

Grey looks like a shadow but it represents practicality, safety and credibility when used with cold tones of blue or magenta. Grey symbolizes mediocrity, the background noise. A "grey person" is someone who goes unnoticed, a wallflower [4,5].

D. Orange

Orange is contrasting to blue and highly visible against a clear sky. Therefore, orange is often used for safety. The colour is often used to enhance visibility [4,5].

VI. CONCLUSION

Web colors are colors used in designing web pages, and the methods for describing and specifying those colors. Authors

of web pages have a variety of options available for specifying colors for elements of web documents.

Web colors have an unambiguous colorimetric definition, sRGB, which relates the chromaticities of a particular phosphor set, a given transfer curve, adaptive whitepoint, and viewing conditions. These have been chosen to be similar to many real-world monitors and viewing conditions, so that even without color management rendering is fairly close to the specified values. However, user agents vary in the fidelity with which they represent the specified colors. More advanced user agents use color management to provide better color fidelity; this is particularly important for Web to print applications.

REFERENCES

- [1] N. Chapman and J. Chapman, „*Digital multimedia*”, Chichester, John Wiley & Sons , 2004.
- [2] <http://jendryschik.de/wsdev/farben-auf-webseiten/>
- [3] J.D.Foley, A.Van Dam, "*Fundamentals of interactive computer graphics*", John Wiley & Sons, 2004.
- [4] R.Colvn Clark, C. Lyons, "*Graphics for learning*", John Wiley & Sons , 2000.
- [5] D. Jokanovic and D. Martinovic, „*E- learning- challenges and perspectives, Learning without limits*”, Developing the next 10-th Aniversary Conference of the European Distance Education Network, 10-13 June 2001, Stockholm, Sweden.

SESSION ECST I

Electronic Components, Systems and Technologies I

Synthesis of DCS in Copper Metallurgy

Dragan R. Milivojević¹, Viša Tasić², Marijana Pavlov³ and Vladimir Despotović⁴

Abstract – Many technological processes in production plants demand transfer of information and interaction with the process from remote distances (from control centre, for example). To satisfy these requests, sometimes a complex computer network has to be generated, like a distributed control system (DCS), a type of LAN with local and remote process monitoring and control functions. This paper presents results of development a low cost and easily applied both, hardware and software solutions for process monitoring in Copper Mining and Refining Complex – Bor.

Keywords – monitoring system, process control, computer network, real time

I. INTRODUCTION

Department for Industrial informatics in Copper Institute – Bor produces industrial computer systems. As a core of the developed monitoring and control systems, the third generation of MMS (Microprocessor Measuring Station) is in use. This is a specific industrial PLC (Programmable Logic Controller), which is fully designed and developed in Copper Institute. Classical PC computer is the remote workstation, and allows the interaction between operator and process. On the PC runs the own developed, dedicated software for real time operation, with standard SCADA (Supervisory Control And Data Acquisition) functions, adapted for use in network environment.

The 'Copper production line' is a complex organizational unit of Copper Mining and Refining Complex (RTB) Bor. There are a couple of production plants. The technological equipment at all plants was very old with a poor process control systems. In most of them using the local monitoring systems are quite satisfied. Those systems are based on MMS and interactive PC, and implemented at all key production lines. On this way, technologists can follow the process outline in the plants their own. And the performance was satisfactory. But, the whole copper production process is match complex and very often needed more information's about parameters from some remote plants. This is the main reason why the integration of these partial systems into industrial Local Area Network was carried out.

That's become an industrial distributed control system (IDCS). In such way distributed system for monitoring of all key phases of technological process was formed. The design of the implemented distributed system has been dictated by practical requirements in the concrete application.

II. HARDWARE PLATFORM

To choose the hardware infrastructure to build up the network, it is useful to present basic characteristics of network nodes and the way of it's operation. The system consists of a few couples of industrial automatic measuring stations (PLC, Data Logger etc.) and a couple of PC's. The PC's are used for monitoring and interaction with the process (checking actual state of parameters and remote control). In a general case, for distributed processes a large number of PLC's are required to perform measurement of process parameters, data acquisition, control and transfer to the host computer (PC). Data about status of the process are transferred from the place of origin (PLC) to decision-making place (PC). On PC this data being processed and results presented in proper form on the screen and stored in external memory. If the system performs remote control function, depending on the status of the process, PC sends commands to PLC, which causes appropriate actions and affect the process. Apart from effects on the process, commands have their effects on PLC itself: testing its functionality, time synchronization etc. Designed and implemented network has to satisfy several basic requirements: to provide correct and efficient data transfer from PLC, to execute timely transfer of commands to PLC (while the command is active and actual), to realize supplementary transfer of data from PLC in case that there are any faults in normal transfer [1].

The core of a process control and monitoring system is MMS. It is based on Motorola 68HC11 micro controller. Main characteristics of MMS (standard configuration) are: micro controller Motorola 68HC11E, intern eight channel, 8-bit A/D converter, 64 analog inputs, 64 + 64 digital state signals (input + output) with mutual point (or independent). RS232 communication port, 48 (56) KB for data (RAM), 16 (8) KB for software (EPROM). Local display and functional keyboard gives a possibility of device control, time synchronization and start of measuring. MMS can work independent of monitoring computer (PC based system) and can control the process itself. It can also work like data logger, and memorize over 3000 data messages in local RAM, and later, when connection with the monitoring PC is established, transfer them to PC.

Because of costs, there was a reasonable demand for using the existing private telephone lines like the hardware network infrastructure, as match as possible. This practically means,

¹Dragan R. Milivojević is with the Copper Institute, Zeleni bulevar 35, 19210 Bor, Serbia, E-mail: dane@ibb-bor.co.yu

²Viša Tasić is with the Copper Institute, Zeleni bulevar 35, 19210 Bor, Serbia, E-mail: visa@ibb-bor.co.yu

³Marijana Pavlov is with the Copper Institute, Zeleni bulevar 35, 19210 Bor, Serbia, E-mail: dane@ibb-bor.co.yu

⁴Vladimir Despotović is with the Technical Faculty in Bor, Vojske Jugoslavije 12, 19210 Bor, Serbia, E-mail: dane@ibb-bor.co.yu

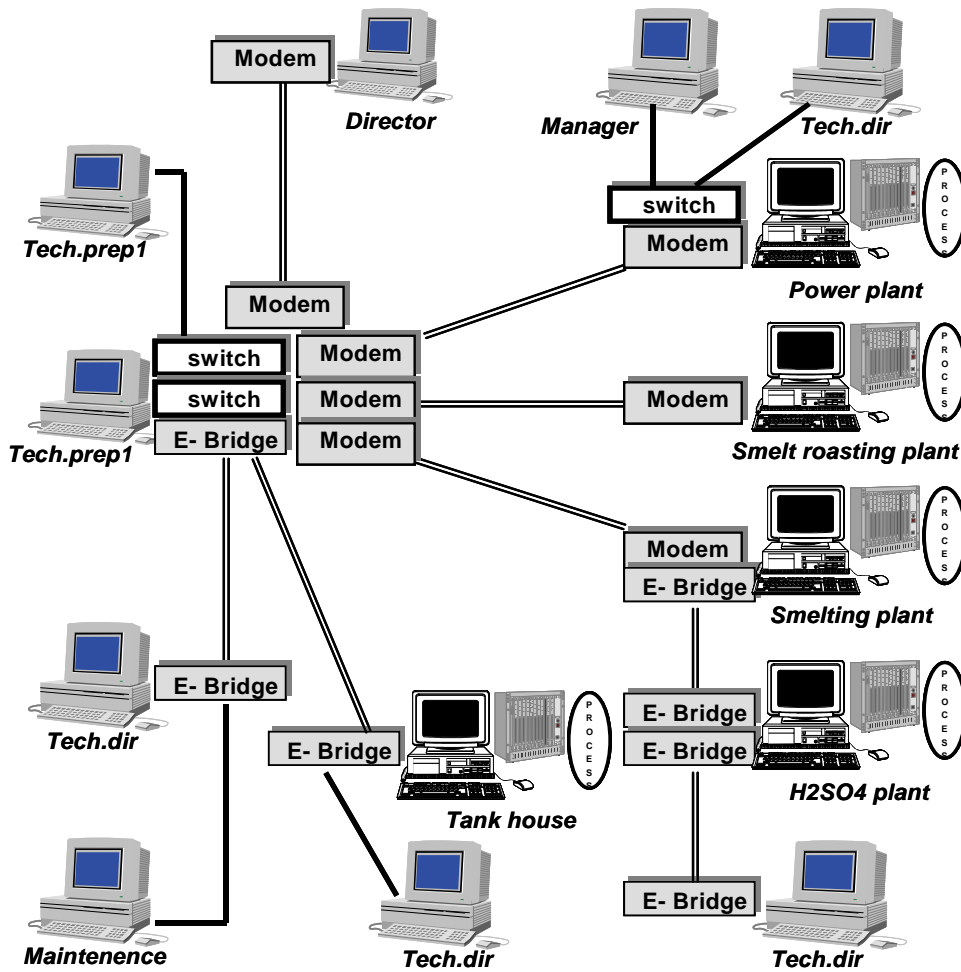
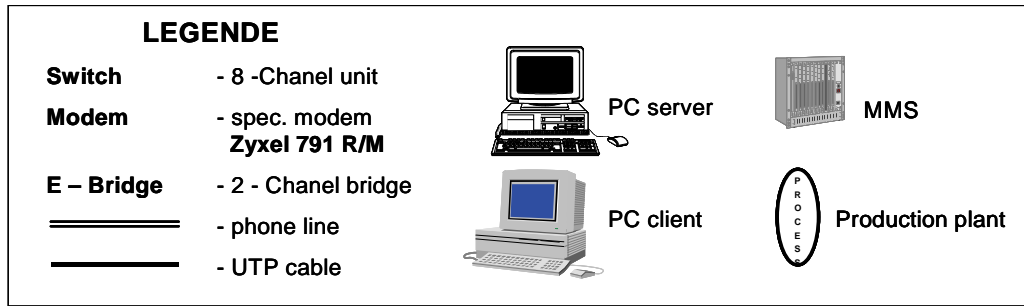


Fig. 1. Block diagram of realized DCS

that some telephone terminals become the computer network nodes. The dynamics of processes request the appropriate response time and this circumstance demands network with satisfactory performances. Building up such network needs a different kind of network equipment: modems, routers, bridges, switches (see Fig. 1.).

III. SOFTWARE ENVIRONMENTS

To control and maintain realized industrial network, the software has to cover the functions on two levels. Regarding

the network structure, it is possible to differentiate software solutions at both levels: PLC and PC. EPROM of MMS holds residential software (firmware), which consists of executable versions of test, control, operational and communication software modules. Operational program module is responsible for measuring of analogue channels and checking states of digital inputs. Type of measuring, sampling rate and other parameters can be changed using local keyboard, or commanded from a monitoring PC. The message is transferred to remote PC, or memorized in local RAM (if PC is disconnected), so it can be transferred later when the

connection is established. MMS can work independently of monitoring computer, so local process control is also possible. If any parameter exceeds given limits, it causes alarm message, or even better, if any parameter shows trend of reaching limit value, it firstly can cause warning message, so the operator, or the system itself can react on time. In MMS control program (executive system) there is a complex communication module. It contains the procedures for handshaking, data transfer, transfer control and recovery, and regular disconnection. That is a kind of protocol, the own developed ASP protocol [3]. Appropriate process control application for a PC based system is developed using Microsoft Visual C++ 6.0 development kit [2], and it's main characteristics are: communication with MMS, data processing, data presentation, process control, data archiving and off-line analysis and interpretation of data.

Interactive SCADA program contains a part (unit) for communication. There are a few procedures writing in assembler and refereeing to the physical port addresses. The monitoring and control program runs very stabile under Windows 98. The client version runs on both Windows 98 and Windows XP OS.

The application communicates with MMS as a secondary network node (PC is a master) using ASP (Asynchronous Serial Protocol). The data can be displayed in real time on dynamic synoptically screens, real-time graphs or in tables. All data are saved in database in three forms, as: daily reports, monthly reports and log files. The history of the process can be displayed in a same manner as in real time. In order to get better performance, user can change process priority, comparing to other active applications on PC, from low to real-time priority. In high or real-time mode, application performances are very stable. Additional facilities are also possible, such as: on line changing of measuring range, changing alarm limits, scaling the axes at the real-time diagram etc.

IV. NETWORK DESIGN

The realized DCS is built up from a couple of sub networks. The sub network is a local plant's monitoring system which contains one, or more MMS and subordinated PC's. This PC can work as local server, workstation, or both. The industrial network is constructed from heterogeneous nodes, PC's and MMS. The PC's in the network can run in different mode: some of them are servers (local), and other is clients (remote monitoring terminals, see Fig. 1.). All of PC's run under Windows OS, and uses its network performances.

The system monitors process at five key plants of the Copper Mining and Refining Complex – Bor: Copper Smelting Plant, Converters Plant, Tank House Plant, Sulphur Acid Plant and Power Plant. The network is decentralized, and servers are sited at all of the plants, connected to corresponding MMS's. One server application can run at the time on one server PC, but all client applications can run in multitasking. This gives a possibility of monitoring processes locally and at remote plants at the same time. Also technologists can easily monitor the process flow. The client applications are restricted to monitoring only, and all control

functions are disabled. As the distances between some network nodes are greater than 3 km, leased telephone lines are used as transmission lines. The second reason is that they already existed, so this solution was cost effective. The next step was integration with system for air quality control, that was carried out successfully. The simultaneous display of process parameters and concentrations of pollution substances is very significant for control of air pollution in town zone.

V. WAY OF OPERATION

The technologists, like a process engineers have to monitor their own plant using local sub networks at local server PC. But, sometimes they really need the information of process parameters from the other (remote) plant, because of interdependence between production lines. In this case on the same PC (local server), the client version of SCADA has to be activated. Now there are two independent programs (local and remote SCADA) like two windows services, running concurrently. If there is a need, it is possible to activate many client programs at every PC, but only one server, and it has to be the appropriate one. There are many differences between server and client programs. The main one is the possibility of interaction and sending commands to MMS and process. Because of decentralized network control, and chance to make some confusion in changing the system configuration and action to the process, the number of functions on client version is significantly decreased. There is shown in practice that the massive data transfer (sometimes it is necessary to take a lot of historical data from remote server) is very slow if PC works under Windows XP OS.

VI. CONCLUSION

The described monitoring system has been implemented for over a year and shown as very efficient. All of local and remote systems give timely quite sufficient useful information, and technologists make the improvements resulting in better productivity. Its significance became even bigger, by integration with air quality monitoring system. As the air pollution in town (imission) is a direct consequence of technological process, interaction between these systems is very useful.

Apart from favorable price/performance ratio, functioning of realized network has shown to be very reliable and especially resistant to poor communication conditions, thanks to solid transfer quality control.

REFERENCES

- [1] D.Milivojevic, "Software elements of MMU", ETRAN 2004, Conference Proceedings CD, Čačak, Serbia, 2004.
- [2] D. Milicev, "Object oriented programming in C++", Mikro Knjiga, Belgrade, 1995.
- [3] D.Milivojevic, V.Tasic, D.Karabasevic, "Communication in realized real-time systems", ETRAN 2003, Conference Proceedings CD, Herceg Novi, Serbia and Montenegro, 2003.



This page intentionally left blank.

Removal of Power-line Interference from ECG in Case of Non-multiple Even Sampling

Georgy S. Mihov¹ and Ivan A. Dotsinsky²

Abstract –This paper deals with some aspects of the subtraction procedure, which removes the power-line interference without affecting the intrinsic to ECG components. The improvement is for the cases of high even non-multiplicity between sampling rate and rated interference frequency.

Keywords –ECG, power-line interference removal, subtraction procedure.

I. INTRODUCTION

The ECG recordings are often contaminated by residual power-line interference despite the high common mode rejection ratio of the amplifiers used [1, 2] and the variety of sophisticated but conceptually traditional digital filters [3, 4], which suppress to different extent the intrinsic to ECG components around the power-line (PL) frequency. This drawback has been overcome some decades ago by the so called subtraction procedure [5]. Its principle consists of: i) applying linear phase digital filter on ‘linear’ ECG segments with near to zero frequency content (usually physiological baseline, low amplitude P-waves and some small parts of T-waves), ii) continuously updating and memorizing the removed phase locked interference components, and iii) subsequent subtracting the corresponding component from the signal wherever non-linear segments are encountered. Later, many improvements of the procedure have been developed to cope with PL amplitude and frequency variations including the cases of non-multiple sampling, which lead to a real (non-integer) number n of samples within one rated PL period [6-8].

The aim of this study is to enhance the accuracy of the PL interference (PLI) elimination when the truncated real number n^* is even and the multiplicity (sampling rate Φ against interference frequency F) is high.

II. THEORETICAL CONSIDERATIONS, EQUATIONS, EXPERIMENTAL RESULTS

According to the generalized structure of the subtraction procedure [7, 8], the phase locked interference B_i to be subtracted from the ongoing contaminated sample Y_i is estimated by means of an interference temporal buffer

$[i-n^*, i-1]$. Its terms $B_{i-1}, B_{i-2}, \dots, B_{i-k}, \dots, B_{i-n}$ represent filtered middle samples of a moving window over the contaminated sequences $X_{i-k-n-1}, X_{i-k-n-2}, \dots, X_{i-k-1}$. When Φ is multiple to F , B_i takes the B_{i-n} value. Otherwise, B_i is estimated by the buffer content, which is processed by additional filter type ‘moving averaging’ with transfer coefficient K_{FB} for $f=F$. The corresponding equations are:

$$\frac{1}{n^*} \sum_{j=-n^*+1}^0 B_{i+j} = B_{mid} K_{FB}; \quad (1)$$

$$K_{FB} = \frac{1}{n^*} \cdot \frac{\sin \frac{n^* \pi F}{\Phi}}{\sin \frac{\pi F}{\Phi}}; \quad (2)$$

$$B_i = B_{mid} n^* K_{FB} - \sum_{j=-n^*+1}^{-1} B_{i+j}. \quad (3)$$

Here $\mathbf{K} \equiv \frac{1}{n^*} \sum_{j=-n^*+1}^0 B_{i+j}$ is the so called *K-filter* [7, 8]. It is

low pass type with coefficient vector $\overline{\mathbf{K}}$ consisting of n^* terms with equal weight $1/n^*$. This filter is transformed in high pass type by subtracting from B_{mid} :

$\mathbf{B} \equiv B_{mid} - \frac{1}{n^*} \sum_{j=-n^*+1}^0 B_{i+j}$. It is called *B-filter* [7, 8] and has

$1 - K_{FB}$ transfer coefficient in $f = F$. The next modification denoted *B*-filter* [7, 8] is expressed by $\mathbf{B}^* \equiv \mathbf{B} / (1 - K_{FB})$ or

$\mathbf{B}^* \equiv \frac{-\frac{1}{n^*} \sum_{j=-n^*+1}^0 B_{i+j} + B_{mid}}{1 - K_{FB}}$ with transfer coefficient equal

to 1 at $f = F$, which is in fact Eq. 1.

When n^* is odd, $n^* = 2m+1$, B_{mid} coincides in time with the real $B_{i-(n-1)/2}$ and Eq. 3 becomes

$$B_i = - \sum_{j=-n^*+1}^{\frac{n^*-1}{2}} B_{i+j} + (n^* K_{FB} - 1) B_{i-(n^*-1)/2} - \sum_{j=\frac{n^*-3}{2}}^{-1} B_{i+j}. \quad (4)$$

Fig. 1 represents the *B*-filter* synthesis for PLI evaluation in case of $\Phi=250$ Hz, and $F=48$ Hz and $F=52$ Hz, both of them with odd multiplicity $n=5$. The traces are obtained in MATLAB environment by the filter vector coefficients:

$$\overline{\mathbf{K}}_{\mathbf{B}} = [1 \ 1 \ 1 \ 1 \ 1]/5; \quad \overline{\mathbf{B}} = [-1 \ -1 \ 4 \ -1 \ -1]/5;$$

¹Georgy S. Mihov is with the Faculty of Electronic Engineering and Technologiess – Technical University of Sofia, E-mail: gsm@tu-sofia.bg

²Ivan A. Dotsinsky is with the Center of Biomedical Engineering – Bulgarian Academy of Sciences, E-mail: iadoc@argo.bas.bg

$$\overline{\mathbf{B}}^* = [-1/5 \quad -1/5 \quad 4/5 \quad -1/5 \quad -1/5] / (1 - K_{FB}).$$

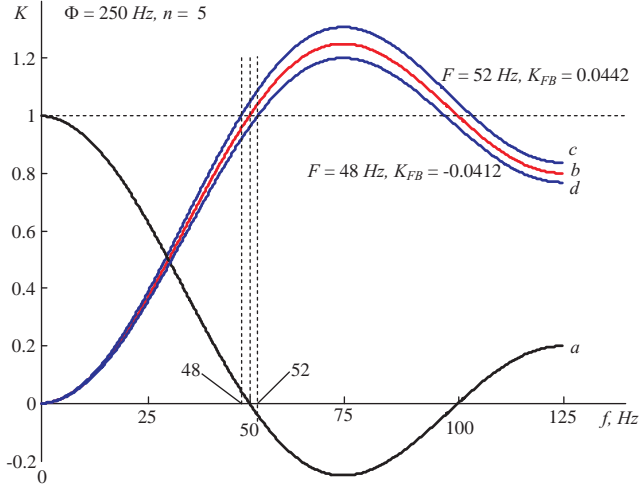


Fig. 1. B^* -filter synthesis: *a*- basic K -filter; *b*- B -filter; *c* and *d*- B^* -filters for $F = 48 \text{ Hz}$ and $F = 52 \text{ Hz}$ ($\Phi = 250 \text{ Hz}$)

The removal of PLI with $F=52 \text{ Hz}$ is shown in Fig. 2. The error does not exceed $\pm 25 \mu\text{V}$.

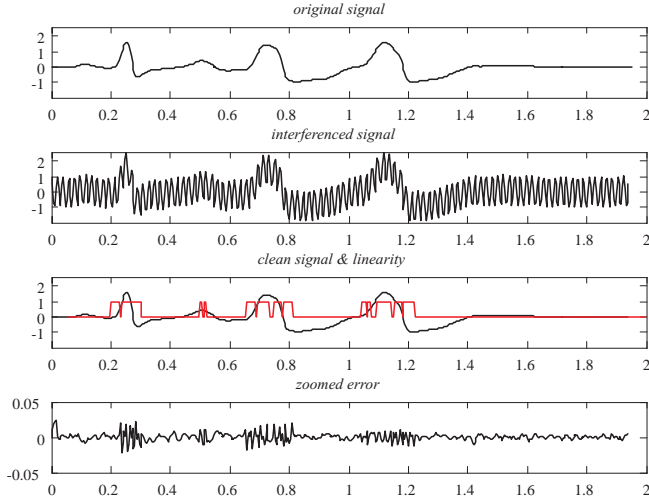


Fig. 2. $\Phi = 250 \text{ Hz}$, $F = 52 \text{ Hz}$, odd multiplicity $n = 5$

If n^* is even, $n^*=2m$, B_{mid} is virtual and does not coincide with a real buffer sample being between $B_{i-n/2}$ and $B_{i-n/2+1}$, which are spaced at $\tau=1/2\Phi$ as shown in Fig. 3.

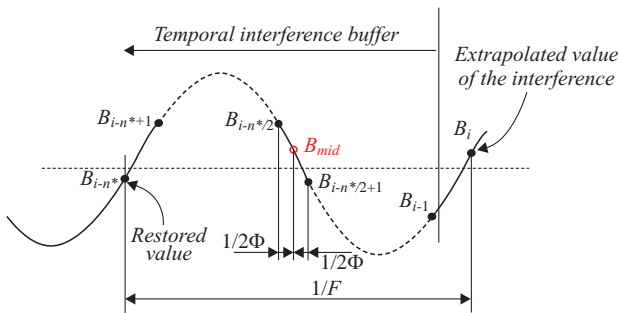


Fig. 3. Content of the temporal buffer in even multiplicity

Since the buffer has no constant component, the next Eqs. are derived assuming the B_{mid} phase is zero.

$$\begin{cases} B_{i-n^*/2} = A \sin \omega(t - \frac{1}{2\Phi}) = A \sin \omega t \cdot \cos \frac{\omega}{2\Phi} - A \cos \omega t \cdot \sin \frac{\omega}{2\Phi} \\ B_{mid} = A \sin \omega t \\ B_{i-n^*/2+1} = A \sin \omega(t + \frac{1}{2\Phi}) = A \sin \omega t \cdot \cos \frac{\omega}{2\Phi} + A \cos \omega t \cdot \sin \frac{\omega}{2\Phi} \end{cases} \quad (5)$$

The following expression is obtained substituting B_{mid} for $A \sin \omega t$ in the sum of the first and third Eqs.:

$$B_{mid} = \frac{B_{i-n^*/2} + B_{i-n^*/2+1}}{2S_C}, \quad S_C = \cos \frac{\pi F}{\Phi}. \quad (6)$$

Eq. 1 becomes $\frac{B_{i-n^*/2} + B_{i-n^*/2+1}}{2S_C} K_{FB} = \frac{1}{n^*} \sum_{j=-n^*+1}^0 B_{i+j}$,

resulting in the following expressions for extrapolated value B_i , B^* -filter and B -filter:

$$\begin{aligned} B_i = & - \sum_{j=-n^*+1}^{i-n^*/2-1} B_{i+j} + B_{i-n^*/2} \left(\frac{n^* K_{FB}}{2 S_C} - 1 \right) + \\ & + B_{i-n^*/2+1} \left(\frac{n^* K_{FB}}{2 S_C} - 1 \right) - \sum_{j=-n^*/2+2}^{-1} B_{i+j} \end{aligned} \quad (7)$$

$$\mathbf{B}^* \equiv \frac{B_{i-n^*/2} + B_{i-n^*/2+1}}{2S_C} = \mathbf{B} / (1 - K_{FB}) \quad (8)$$

$$\begin{aligned} \mathbf{B} \equiv & - \frac{1}{n^*} \sum_{j=-n^*+1}^{-n^*/2-1} B_{i+j} + \left(\frac{1}{2S_C} - \frac{1}{n^*} \right) B_{i-n^*/2} + \\ & + \left(\frac{1}{2S_C} - \frac{1}{n^*} \right) B_{i-n^*/2+1} - \frac{1}{n^*} \sum_{j=-n^*/2+2}^0 B_{i+j} \end{aligned} \quad (9)$$

Fig. 4 represents the B^* -filter synthesis for PLI evaluation according to Eq. 7 in case of $\Phi = 250 \text{ Hz}$ and $F = 60 \text{ Hz}$ (even multiplicity $n^* = 4$). The filter vector coefficients are:

$$\begin{aligned} \overline{\mathbf{K}}_{\mathbf{B}} &= [1 \quad 1 \quad 1 \quad 1] / 4; \\ \overline{\mathbf{B}} &= [-1 \quad 2/S_C - 1 \quad 2/S_C - 1 \quad -1] / 4, \quad S_C = 0,729; \\ \overline{\mathbf{B}}^* &= \left[-1 \quad \frac{2}{S_C} - 1 \quad \frac{2}{S_C} - 1 \quad -1 \right] \frac{1 - K_{FB}}{4}, \quad K_{FB} = 0,0458. \end{aligned}$$

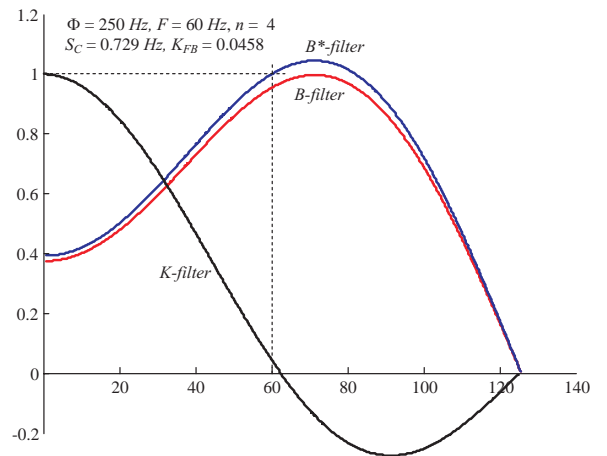


Fig. 4. B^* -filter synthesis for $F = 60 \text{ Hz}$ and $\Phi = 250 \text{ Hz}$

Experimental results with the synthesized B^* -filters of Fig. 4 can be observed in Fig. 5. The traces are as shown in Fig. 2.

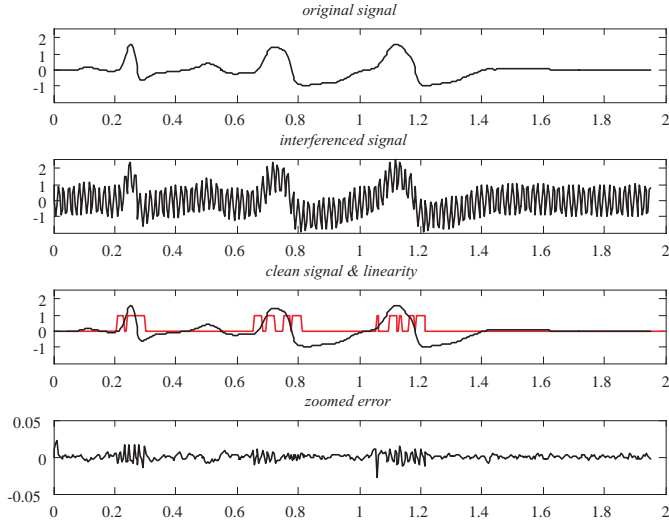


Fig. 5. $\Phi = 250$ Hz, $F = 60$ Hz, even multiplicity $n = 4$

Similar results have been obtained with $\Phi = 500$ Hz and $F = 60$ Hz (even multiplicity $n^* = 8$).

III. INVESTIGATION OF THE SUBTRACTION PROCEDURE STABILITY IN NON-LINEAR ECG SEGMENTS

These investigations are challenged by colleagues of the Cairo University, who experimented PLI removal in case of even multiplicity with very high truncated real number n^* , using even B -filter identical to the K -filter according to publication [8]. It was found that the procedure is prone to autoexcitation if the relative weight of the sample to be compensated in the B -filter equation, is in presence of low frequency components within the temporal buffer. For a longer non-linear segment the B -filter transforms into IIR filter. This process was study in the following way:

1. Low frequency signal epoch of 4 Hz, 200 μ V amplitude and 2 s duration is synthesized.
2. Synthesized PLI with 200 μ V amplitude is added.
3. The subtraction procedure is applied with preset flag for linear segment during the first half of the epoch, this flag being for non-linear segment until the epoch end.
4. The error committed (difference between the free of interference signal and the processed one) is analyzed.

The next figures illustrate the results obtained. All abscissas are in s , the ordinates are scaled in mV . The K -filter is marked as K_B -filter everywhere it is used to build the B^* -filter according to [8].

Experiment 1 (Fig. 6): B_i is calculated using Eq. 7. The applied K -filter is $\bar{\mathbf{K}} = [1/2 \ 1 \ 1 \ 1 \ 1/2]/4$. Another filters are the same for the shown in Fig. 4 synthesis. The traces are the same as in Fig. 5. No autoexcitation can be observed, the filter is stable for infinite duration of the non-linear signal (see the forth trace). Further, Figs. 7-11 consist of filtered signal and zoomed error graphic only.

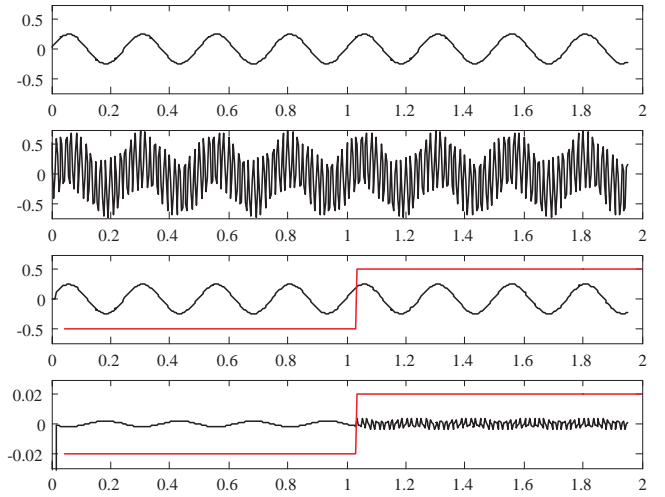


Fig. 6. $\Phi = 250$ Hz, $F = 60$ Hz, even multiplicity $n=4$, B_i is calculated from Eq. 7.

Experiment 2 (Fig. 7): An even K_B -filter is applied which is the same as a K -filter for even multiplicity. B_i is calculated by Eq. 7:

$$B_i = -B_{i-n^*} - 2 \sum_{j=-n^*+1}^{-n^*/2-1} B_{i+j} - 2(1-n^* K_{FB}) B_{i-n^*/2} - 2 \sum_{j=-n^*/2+1}^{-1} B_{i+j} \quad (10)$$

The filter vectors are: $\bar{\mathbf{K}} = [1/2 \ 1 \ 1 \ 1 \ 1/2]/4$; $\bar{\mathbf{K}}_B = [1/2 \ 1 \ 1 \ 1 \ 1/2]/4$; $\bar{\mathbf{B}}^* = [-1/2 \ -1 \ 3 \ -1 \ -1/2]/4/(1-K_{FB})$, $K_{FB} = 0,0334$. Autoexcitation can be observed almost immediately after the nonlinear segment begins. That is due to residual components in the temporal buffer. Additional experiment was made with free of low frequency input signal (the lower graphic). The autoexcitation occurs 300 ms later because of computing error accumulation.

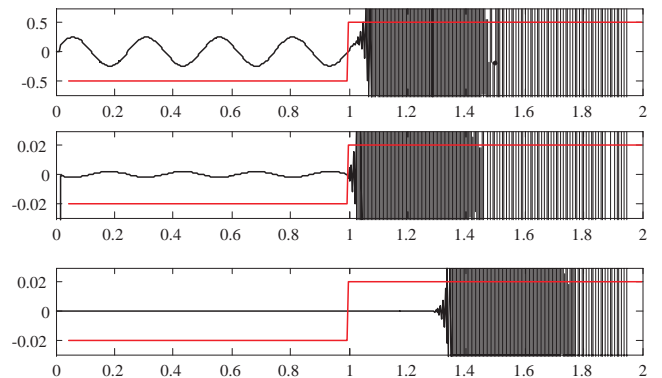
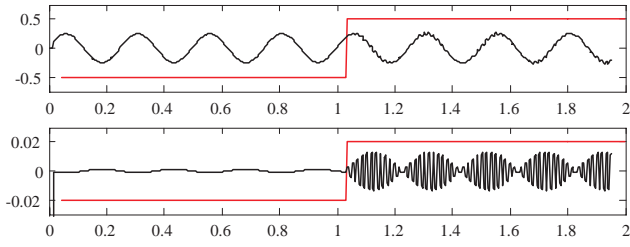
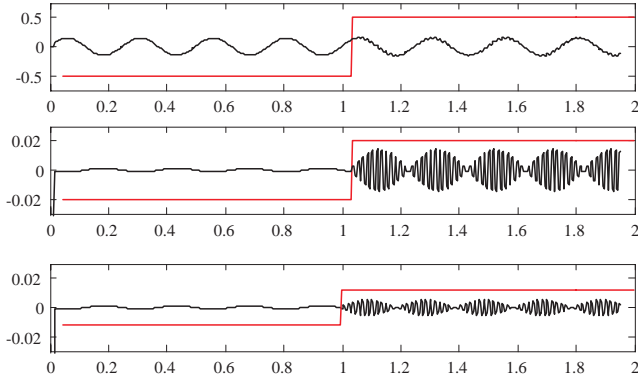


Fig. 7. $\Phi = 500$ Hz, $F = 60$ Hz, even multiplicity $n = 4$

Experiment 3 (Fig. 8): Reduced by 2 even B^* -filter is applied, other data as in **Experiment 2**. The filter vectors are: $\bar{\mathbf{K}} = [1/2 \ 1 \ 1 \ 1 \ 1/2]/4$; $\bar{\mathbf{K}}_B = [1/2 \ 0 \ 1 \ 0 \ 1/2]/2$; $\bar{\mathbf{B}}^* = [-1/2 \ 0 \ 1 \ 0 \ -1/2]/2/(1-K_{FB})$, $K_{FB} = 0,0039$.

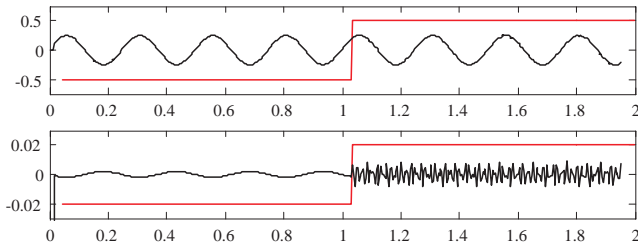

 Fig. 8. Reduced by 2 even B^* -filter

Experiment 4 (Fig. 9): The same as **Experiment 2** but with reduced by 2 even K -filter for linear segments. Filter vectors: $\bar{\mathbf{K}} = [0,5 \ 0 \ 1 \ 0 \ 0,5]/2$; $\bar{\mathbf{K}}_{\mathbf{B}} = [0,5 \ 0 \ 1 \ 0 \ 0,5]/2$; $\bar{\mathbf{B}}^* = [-0,5 \ 0 \ 1 \ 0 \ -0,5]/2/(1 - K_{FB})$, $K_{FB} = 0,0039$.

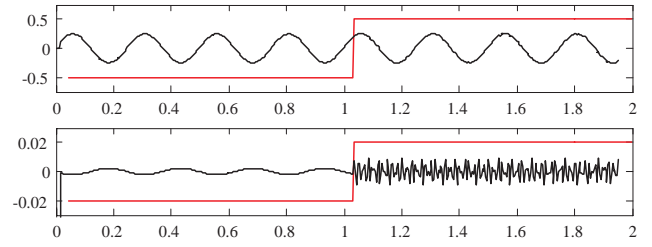

 Fig. 9. Reduced by 2 B^* -filter and reduced by 2 even K -filter.

The lower graphic is obtained setting the flag for non-linear segment when the sinusoid is going through zero (minimum non-linearity). The error is considerably reduced.

Experiment 5 (Fig. 10): The B^* -filter is synthesized by odd K_B -filter. n^* is computed using $n^* = 2 \times \text{floor}\left(\frac{\Phi}{2F}\right) + 1$, where $\text{floor}(a)$ is MATLAB function generating the lower integer of a . Filter vectors: $\bar{\mathbf{K}} = [1/2 \ 1 \ 1 \ 1 \ 1/2]/4$; $\bar{\mathbf{K}}_{\mathbf{B}} = [1 \ 1 \ 1 \ 1 \ 1]/5$; $\bar{\mathbf{B}}^* = [-1 \ -1 \ 4 \ -1 \ -1]/5/(1 - K_{FB})$, $K_{FB} = -0,1717$.


 Fig. 10. Even B^* -filter based on odd K_B -filter.

Experiment 6 (Fig. 11): The same as **Experiment 5** but with even K -filter for linear segments. Filter vectors: $\bar{\mathbf{K}} = [1 \ 1 \ 1 \ 1 \ 1]/5$; $\bar{\mathbf{K}}_{\mathbf{B}} = [1 \ 1 \ 1 \ 1 \ 1]/5$; $\bar{\mathbf{B}}^* = [-1 \ -1 \ 4 \ -1 \ -1]/5/(1 - K_{FB})$, $K_{FB} = -0,1717$.


 Fig. 11. Reduced by 2 even B^* -filter and even K -filter for linear segments.

IV. DISCUSSION AND CONCLUSION

The presented experiments are a significant excerpt only of all carried out. They lead to the following conclusions:

1. Except for the even B -filter used in **Experiment 2**, all other filters are stable for infinite duration of the non-linear ECG signal.

2. The approximation procedure is negligibly influenced by the K -filter type intended for PLI removal from the linear ECG segments. This may be seen comparing the couples '**Experiment 3** – **Experiment 4**' and '**Experiment 5** – **Experiment 6**'

3. The approximation error considerably depends on the residual low frequency components within the temporal buffer (see **Experiment 4**).

4. Out of all analyzed B -filters, the approximation procedure using Eq. 7 is that one that is most efficient for PLI removal from the non-linear ECG segments in case of even multiplicity.

REFERENCES

- [1] J. C. Huhta, J. G. Webster, "60 Hz interference in electrocardiography", IEEE Trans., Biomed Eng 20, pp.91-100, 1973.
- [2] M. van Rijn, A. Peper, and C. A. Grimbergen, "High-quality recording of bioelectrical events", Part 1: Interference reduction, theory and practice, Med. Biol. Eng. Comput., 28, pp. 389-397, 1990.
- [3] S. C. Pei, C. C. Tseng, "Elimination of AC Interference in Electrocardiogram Using IIR Notch Filter with Transient Suppression", IEEE Trans., Biomed. Eng. 42, pp. 1128-1132, 1995.
- [4] P. S. Hamilton, "A comparison of Adaptive and Nonadaptive Filters for Reduction of Power Line Interference in the ECG", IEEE Trans., Biomed. Eng. 43, pp. 105-109, 1996.
- [5] C. Levkov, G. Michov, R. Ivanov, and I. Daskalov, "Subtraction of 50 Hz interference from the electrocardiogram", Med. Biol. Eng. Comput. 22, pp. 371-373, 1984.
- [6] I. Christov, I. Dotsinsky, "New approach to the digital elimination of 50 Hz interference from the electrocardiogram", Med. Biol. Eng. Comput. 26, pp. 431-434, 1988.
- [7] G. Mihov, I. Dotsinsky and Ts. Georgieva, "Subtraction procedure for power-line interference removing from ECG: Improvement for non-multiple sampling", J. Med. Eng. Techn. 29, pp. 238-243, 2005.
- [8] C. Levkov, G. Mihov, R. Ivanov, I. Daskalov, I. Christov and I. Dotsinsky, "Removal of power-line interference from the ECG: a review of the subtraction procedure" BioMed. Eng. OnLine, 4:50, 2005.

Synthesizing Sine Wave Signals Based on Direct Digital Synthesis Using Field Programmable Gate Arrays

Hristo Z. Karailiev¹ and Valentina V. Rankovska²

Abstract – Analysis of the design flow for creating devices and systems based on Altera's Field Programmable Gate Arrays (FPGA) has been made in the present paper. The digital part of the sine wave synthesizer based on FPGA has been designed. The synthesizer is realized using the development system TREX C1 of Terasic Technologies Inc.

Keywords – Field Programmable Gate Arrays - FPGA, Design flow, Direct Digital Synthesis – DDS, Sine wave frequency synthesizer.

Main problems of the report:

- Analysis of the design flow for creating devices and systems based on Altera's FPGA;
- Designing the table, including the values of the sine wave;
- Designing the digital part of the sine wave synthesizer, based on FPGA of Altera;
- Implementation of the synthesizer using the development system TREX C1.

I. INTRODUCTION

The method for direct digital synthesis (DDS) [1] of signals with arbitrary form is well known, but for a long time its wide implementation has been prevented by the low level of the technology development. Various methods for producing arbitrary form output are known – analogue and digital. The DDS method has some advantages: high resolution; it allows an extremely fast transition to another frequency with continuous phase; the digital implementation allows easy realization of microprocessor control. These advantages determine its growing usage in functional generators, various modulations in the communications, etc.

Various digital implementations of DDS synthesizers have been described in the literature: based on discrete components and low scale integrated circuits, such as dividers, counters, etc.; modern application specific integrated circuits, such as AD9851, AD9858, AD9857 and lately based on Field Programmable Gate Arrays (FPGA).

A drawback of the application specific integrated circuits is the fact that they produce output of certain form, for instance AD9851 produces stable frequency and phase-programmable digitized analog output sine wave. They are not so suitable for applications, where signals with arbitrary wave form have to be created, for instance functional generators. That is why in the present work field programmable gate arrays have been used. This approach will allow in a single chip to integrate many functions for creating arbitrary form output [3].

Aim of the report:

Design and implementation of a sine wave synthesizer based on the direct digital synthesis method and field programmable gate arrays.

II. DESIGN FLOW WITH QUARTUS II SOFTWARE

The characteristics, features and resources of FPGA of leading producers have been outlined in [7] and a device of Altera has been chosen. The software of Altera Quartus II Web Edition v.6.1 has been used at the design process.

The main stages of the design flow with Quartus II are shown in Fig 1 [5].

- **Entering the design** of a device or system can be implemented in one of the following ways:

➤ *As a program*, written in one of the following hardware description languages – AHDL, VHDL, Verilog HDL.

The integrated text editor of Quartus II can be used. The software allows using so called MegaWizard Plug-In Manager. It supplies the designer with high level library blocks – megafunctions, which the designer can parameterizes. MegaWizard Plug-In Manager creates automatically the necessary files to include in the project according to the chosen programming language.

➤ *As a block diagram*.

The block editor of Quartus II is used. The block diagram may include library blocks and logic gates entered and parameterized with MegaWizard Plug-In Manager and also user blocks, created with the symbol editor of Quartus II.

- **Defining requirements for the project and settings of Quartus II**

Defining in advance requirements for the project and some settings of the software allows controlling the functions and the features both the software and the created design in order to increase its effectiveness. They are made by some program parts of Quartus II. Some of the assignments and requirements refer to: design files, the device used, timing requirements, etc. Some conditions for the design optimization in relation to the resources of the selected chip, the power consumed, time intervals, maximum frequency, compilation time can be also defined.

¹Hristo Z. Karailiev is with the Technical University of Gabrovo, H. Dimitar 4, 5300 Gabrovo, Bulgaria, E-mail: hkarailiev@gmail.com

²Valentina V. Rankovska is with the Technical University of Gabrovo, H. Dimitar 4, 5300 Gabrovo, Bulgaria, E-mail: rankovska@tugab.bg

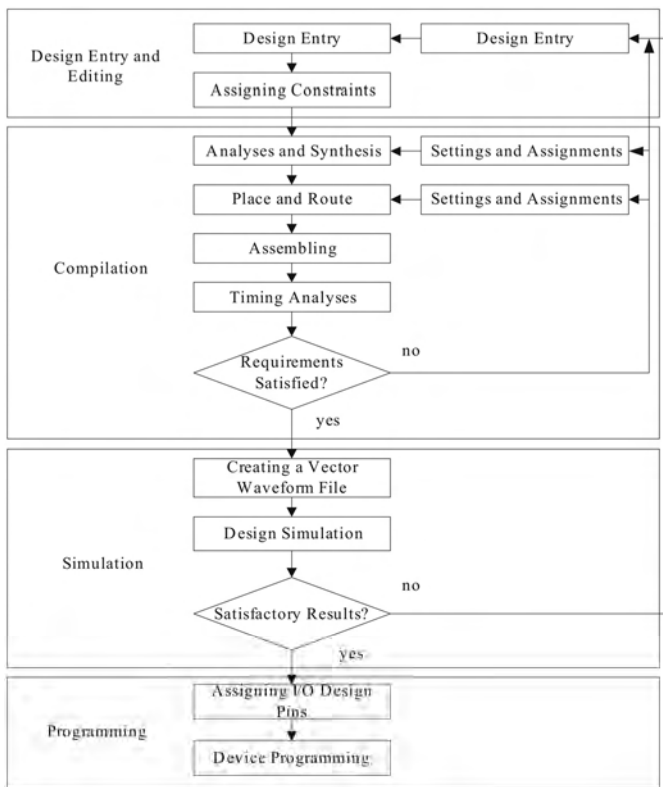


Fig. 1. Design flow with Quartus II

• Design compilation

Several consecutive processes take place at the compilation stage: *analysis and synthesis*, *place and route*, *assembling and timing analysis*. During every of the upper stages the design has been checked for its correctness. This stage is an iteration process – we can return to a previous one if it is necessary (if there are some errors) – till we receive a properly operating design.

At the *Analysis and Synthesis* the design database is created. Analysis & Synthesis performs logic synthesis to minimize the logic of the design, and performs technology mapping to implement the design logic using device resources such as logic elements. It groups register and combinational resources into individual logic cell-sized units in order to use resources efficiently. It examines the logical completeness and consistency of the project, and checks for boundary connectivity and syntax errors. It also optimizes the design for instance making choices that will minimize the number of resources as using functions, which are optimized for Altera devices.

During the *Place and Route* the defined timing and logic requirements are matched to the resources of the selected device. The most suitable place of the logic functions in the device logic cells is found and the most suitable interconnections and pin assignments are selected.

The Assembling completes the design processing, producing files for programming the device and information for the consumed power.

The Timing Analysis is a method of analyzing, debugging, and validating the performance of a design. Timing analysis measures the delay along the various timing paths and verifies the performance and operation of the design. These paths are

the connections between the logic cells in the device as reference signals, data, etc. We can specify constraints and assignments that help the design meet timing requirements. If we specify constraints or assignments, the Fitter optimizes the placement of logic in the device in order to meet those constraints. After that timing analysis calculates the time needed the signals to reach their destination. It can also calculate signal transitions.

• Design simulation

At the simulation test and settings of the logic operations and timing relations in the design is made. First a file with input stimuli for the design input pins is created. Depending on the needed information we can make functional or timing simulation and to test the logical operation and timings in the worst case for the current design. We can estimate the simulation results visually. If the design needs to be corrected that can be made in the design entry. The compilation and the simulation repeat after that.

• Device Programming

At the programming the files produced by the compiler are loaded into the device and it is configured. But first assignment the design pins to the physical device pins is done. The design is compiled again and the device is programmed.

III. ARCHITECTURE OF A DDS SINE WAVE FREQUENCY SYNTHESIZER

An architecture of a frequency synthesizer, used for creating a frequency grid, is shown in [3], based on a study of many references. The presented block diagram can be used for producing arbitrary form signals. In the current design it is used for implementing a sine wave frequency synthesizer (Fig. 2).

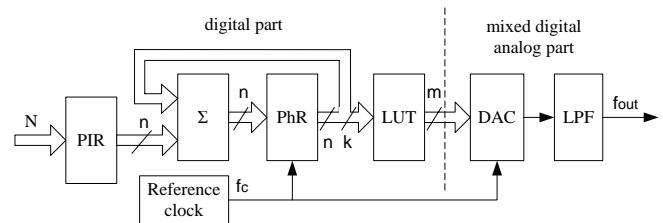


Fig. 2. DDS frequency synthesizer

Briefly the DDS synthesizer operates in the following way: The digital equivalent of the produced frequency is loaded into the phase increment register *PIR*. That value is continuously added to the value, accumulated in the adder Σ .

The most significant *k* bits of the result address the Look-Up Table (*LUT*). In our case the *LUT* includes a set of values defining the form of the sinusoid. The values, derived from the table, are passed to the Digital Analogue Converter (*DAC*) to receive an analogue signal and after that to a low-passed filter (*LPF*) to reject the unwanted components of the signal and its smoothing out.

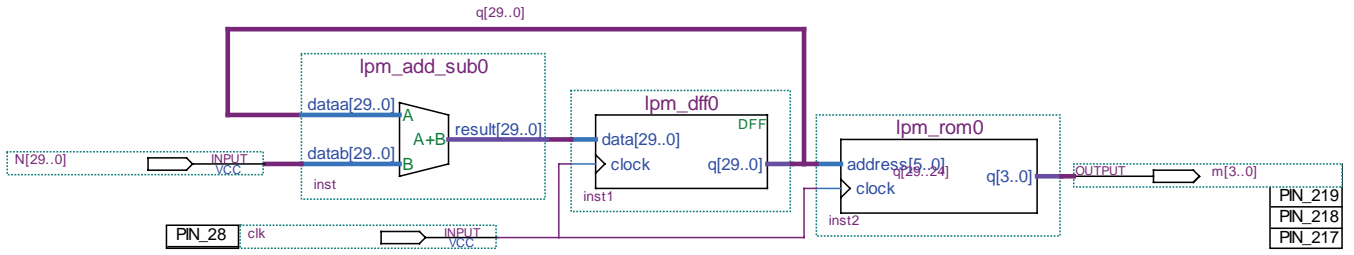


Fig. 3. Functional circuit of the digital part of the sine wave frequency synthesizer

IV. DESIGNING A SINE WAVE FREQUENCY SYNTHESIZER WITH FPGA

- *Creating the project of the sine wave frequency synthesizer*

Fig. 3 shows the functional circuit of the digital part of the sine wave frequency synthesizer, which is implemented in Altera's FPGA Cyclone EP1C6Q240C8 [2]. The registers and the adder are chosen to be 30 bits wide ($n=30$).

The development system TREX C1 of Terasic Technologies Inc. [6] has been used at designing and examining the frequency synthesizer. It has the following resources: $f_{IT}=50\text{ MHz}$, *FPGA Cyclone EP1C6Q240C8*, *three 4-bit DACs*. For the present implementation of the sine wave synthesizer one four-bit DAC (shown in Fig.3) variant and eight-bit DAC variant have been used. A standard three-tap Π -type LC filter has been used.

- *Creating and Filling in the LUT Table*

The output signal Y_{ROM} , passed to the input of the DAC can be expressed by Eq. (1):

$$Y_{ROM} = \{ \sin[\pi \cdot (N \cdot 2^{k-1}) / 2^{k-1}] \} \cdot (-1)^{(2^{m-1}-1) + (2^{m-1}-1)} \quad (1)$$

where: k – the number of the address inputs of LUT; 2^k – the number of the cells in the LUT; 2^{k-1} – the number of the cells for the positive (negative) part of the sinusoid; $N \in 0 \div 2^k - 1$ – the current number of the cell in the LUT, matching the current number of a point of the sinusoid; m – the length of the cells, represented in a number of bits (the resolution of the DAC); $M=2^m$ – a level scaling factor; $2^{m-1}-1$ – an offset of the sinusoid on the ordinate, in order to receive positive values of the function.

The values Y_{ROM} are mixed fractions and can't be loaded in that way into the LUT. That is why they must be rounded and that operation is a source of errors.

The limited number of address inputs k of the LUT and the length p of the cells, define the non-linearity of the output sinusoid. To increase the linearity using the DDS method it is necessary k and m to be relatively big numbers. On the other hand to increase the spurious-free performance it is necessary to take into account the Eq. (2) [6]:

$$k = m + 2 \quad (2)$$

In the case of 4-bit DAC $m=4$, $k=6$, $N_{max}=2^k=64$, $M=2^m=16$. The values received for Y_{ROM} and Y_{ROM}^r in relation to

the current number of the cell $N \in 0-63$, are shown in Fig. 4, and Table I includes the exact and the rounded values, loaded into the MIF file in Quartus II.

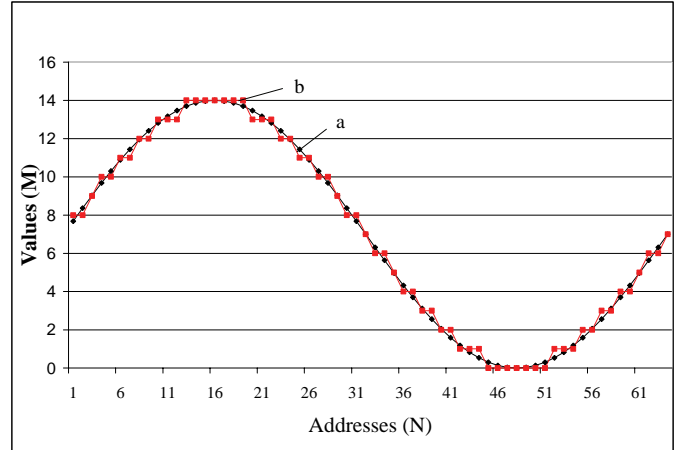


Fig. 4. Output signal, defined by the calculated (a) and rounded (b) values for the amplitude at $N_{max}=64$

In the case of 8-bit DAC $m=8$, $k=10$, $N_{max}=1024$, $M=256$. The values loaded in the MIF file (Fig. 5) are too much that is why they are not shown in a table.

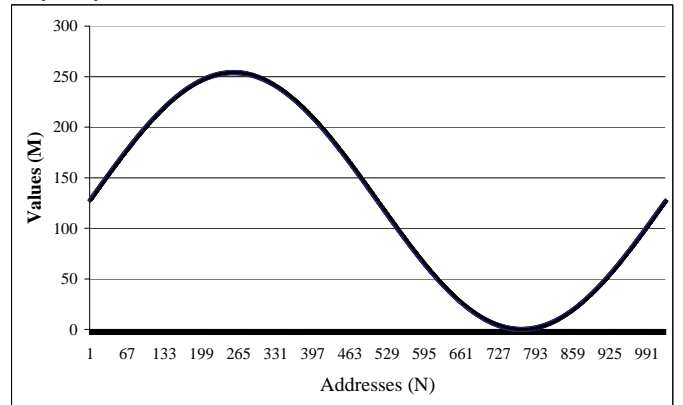


Fig. 5. Output signal, defined by the calculated and rounded values for the amplitude at $N_{max}=1024$

In Quartus II a new file is opened with *File/New/Other Files/Memory Initialization File*. We define the size of the MIF file, in our case 64 addresses, 4-bit cells. An empty MIF

TABLE I
CONTENTS OF THE LUT

N	Y_{ROM}	Y_{ROM}^r	N	Y_{ROM}	Y_{ROM}^r
0	7.68612	8	32	6.31388	6
1	8.365632	8	33	5.634368	6
2	9.031993	9	34	4.968007	5
3	9.678784	10	35	4.321216	4
4	10.29978	10	36	3.700223	4
5	10.88899	11	37	3.111008	3
6	11.44075	11	38	2.559247	3
7	11.94975	12	39	2.050253	2
8	12.41107	12	40	1.588927	2
9	12.82029	13	41	1.179713	1
10	13.17345	13	42	0.826551	1
11	13.46716	13	43	0.532843	1
12	13.69858	14	44	0.301418	0
13	13.8655	14	45	0.134503	0
14	13.96629	14	46	0.033707	0
15	14	14	47	0	0
16	13.96629	14	48	0.033707	0
17	13.8655	14	49	0.134503	0
18	13.69858	14	50	0.301418	0
19	13.46716	13	51	0.532843	1
20	13.17345	13	52	0.826551	1
21	12.82029	13	53	1.179713	1
22	12.41107	12	54	1.588927	2
23	11.94975	12	55	2.050253	2
24	11.44075	11	56	2.559247	3
25	10.88899	11	57	3.111008	3
26	10.29978	10	58	3.700223	4
27	9.678784	10	59	4.321216	4
28	9.031993	9	60	4.968007	5
29	8.365632	8	61	5.634368	6
30	7.68612	8	62	6.31388	6
31	7	7	63	7	7

file appears, in which we fill in the calculated with the program Excel values, and we save the file.

- *Simulation and experiments with the design*

The simulation of the digital part of the design has been made (Fig. 6), and also experimental study of the DDS synthesizer operation as a whole (including DAC and LFP), proving its proper operation.

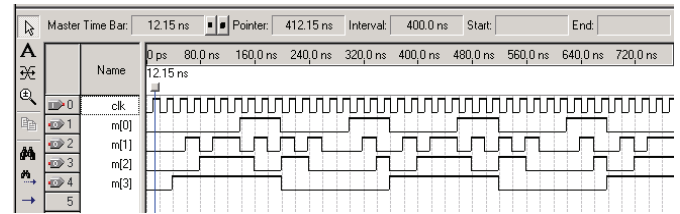


Fig. 6. Output waveforms passed to the DAC

V. CONCLUSION

The contributions of the present work are the following:

- Analysis of the design flow for creating devices and systems, based on FPGA;
- Designing the digital part of the sine wave frequency synthesizer;
- Implementing the synthesizer using the development system TREN C1.

The design is to be expanded as follows:

- Examining the noise sources and reducing their influence [4];
- Producing signals with various modulations – FSK, PSK, I-Q, etc.

REFERENCES

- [1] A Technical Tutorial on Digital Signal Synthesis, Analog Devices, Inc., 1999.
- [2] *Cyclone Device Handbook*, vol. 1, Altera Corp., 2005.
- [3] H. Karailiev and V. Rankovska, "DDS Method for Generating a Frequency Grid at Systems for Test Control and Automated Regulation", ICEST 2006, Conference Proceedings, pp. 300-303, Sofia, Bulgaria, 2006.
- [4] H. Karailiev and V. Rankovska. "Error Sources at Direct Digital Synthesis Signals", ICEST 2007, Conference Proceedings, Ohrid, Macedonia, 2007. (forthcoming)
- [5] *Quartus II Version 5.0 Handbook*. Vol. 1: Design & Synthesis, Altera Corp., 2005.
- [6] *TREN C1 Development Kit Getting Started User Guide*. Terasic Technologies Inc., 2005.
- [7] V. Rankovska, "FPGA Families, Features, Resources, and Devices and Systems Design Technology", Unitech 2006, Conference Proceedings, pp. I-202 – I-207, Sofia, Bulgaria, 2006 (in Bulgarian).

Negative Impedance Converter Improves Capacitance Converter

Ventseslav D. Draganov¹, Zlatko D. Stanchev² and Ilya T. Tanchev³

Abstract - The problem of increasing the frequency output relative sensitivity of the capacitance converter and decreasing the influence of the parasitic capacitances is solved by connecting the Negative Impedance Converter (NIC) into the converter.

An equation of equivalent NIC's capacitance depending on the value of its circuit elements is worked out in this paper. The results are confirmed from investigation by simulation using software, reading the influence of the parasitic capacitances as well as of the input capacitance of the op amp in NIC's circuit.

Key words - Negative Impedance Converter

I. INTRODUCTION

When developing the capacitance converters for measuring of non-electrical quantities a necessity to design converter circuits for registering very small capacity with reduced influence of the parasitic capacitance arises.

A converter "capacitance – DC voltage" consisting of two converters – "capacitance – time interval" and "time interval – DC voltage" is developed. It is capable of compensating the parasitic capacitance of the connected primary capacitance converter to certain extent [1]. This solution provides comparatively low sensitivity (a few pF).

It is suggested a new solution enabling the increasing of the output relative sensitivity of *capacitance converter* when it is needed the comparatively large parasitic capacitance (over 10÷20 pF) to be compensated – by connecting Negative Impedance Converter (NIC).

The use of special schemes for improving then sensitivity of the capacitance converters by decrease of their actual capacitance C_0 is known. Scheme applications are known which:

- connecting of the NIC into the capacitance converter reduces C_0 of the converter to a final capacitance of $C_0 - C_{eq}$ [2].

- improving a capacitive-sensor circuit with a modulator and an RF transmitter by modifying the modulator portion from adding a "negatron" circuit (a configuration that uses equivalent negative capacitance) [3].

The final result of the both cases is higher frequency output relative sensitivity dF/F_0 .

The study of this circuit solution is carried out without reading the influence of the parasitic capacitances as well as of the input capacitance of the used op amp.

The negative impedance converter (NIC) is used to realize negative driving – point impedances. Negative capacitances are applied in gyrator-active C filters [4].

Two floating NIC circuits (FNICs) are now suggested, which can be used to simulate floating negative elements. The dependence of the input impedance of FNIC is defined by the chain matrix. An application of Floating Negative-Impedance Converter (FNIC) for designing of a two directional constant-resistance amplifier is given [5].

II. EXPOSITION

A. Negative Impedance Converter (NIC)

The Negative Impedance Converter (NIC) represents a four-pole (fig.1), for which the following dependences are valid [6]:

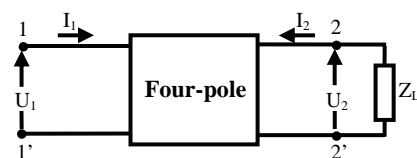


Fig.1. Negative Impedance Converter (NIC)

$$Z_i = \frac{U_1}{I_1} = -k \cdot Z_L \quad (1)$$

$$Z_L = -\frac{U_2}{I_2} \quad (2)$$

$$\frac{U_1}{I_1} = k \cdot \frac{U_2}{I_2} \quad (3)$$

There are two separate boundary cases – the Current Negative Impedance Converter (CNIC) and the Voltage Negative Impedance Converter (VNIC). If the conversion is fulfilled in the respect of the voltages, a VNIC scheme is obtained (fig.2).

¹ Ventseslav D. Draganov is from the Faculty of Electronics at the Technical University - 1, Studentska Str., Varna, Bulgaria, e-mail address: draganov_vd@abv.bg

² Zlatko D. Stanchev is from the Faculty of Electronics at the Technical University - 1, Studentska Str., Varna, Bulgaria, e-mail address: zlatko_stanchev@abv.bg

³ Ilya T. Tanchev is from the Faculty of Electronics at the Technical University - 1, Studentska Str., Varna, Bulgaria, e-mail address: itta@ms3.tu-varna.acad.bg

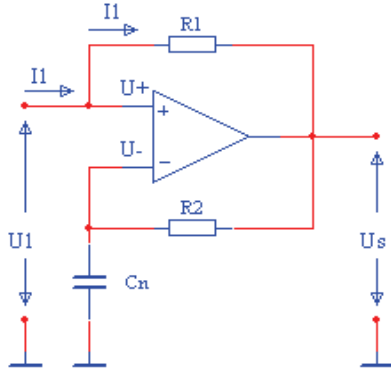


Fig.2. Voltage Negative Impedance Converter (VNIC)

When using ideal elements the dependence is valid:

$$Z_{C_n} = X_{C_n} = \frac{1}{\omega \cdot C_n} \quad (4)$$

$$Z_{C_i} = X_{C_i} = \frac{1}{\omega \cdot C_i} \quad (5)$$

$$U_1 = U_- = U_+ = U_s \cdot \frac{X_{C_n}}{X_{C_n} + R_2} \quad (6)$$

$$U_s = U_1 - R_1 \cdot I_1 \quad (7)$$

From (6) it follows:

$$U_s = \frac{U_1 \cdot (X_{C_n} + R_2)}{X_{C_n}} \quad (8)$$

After substituting of (8) in (7), it is obtained:

$$\frac{U_1 (X_{C_n} + R_2)}{X_{C_n}} = U_1 - R_1 \cdot I_1 \quad (9)$$

After transforming of (9) it is obtained:

$$U_1 = -\frac{R_1 \cdot I_1 \cdot X_{C_n}}{R_2} \quad (10)$$

whence it is determined:

$$Z_i = \frac{U_1}{I_1} = -R_1 \cdot \frac{X_{C_n}}{R_2} \quad (11)$$

From (5) and (11) the input capacity of VNIC is defined:

$$C_i = -\frac{R_2}{R_1} \cdot C_n \quad (12)$$

The Voltage Negative Impedance Converter (VNIC) enables schemes of negative capacitance to be synthesized, taking into consideration the stability since the negative capacitance cannot exist in natural mode, only connected to other elements.

The choice of the element values in the negative impedance realization is usually based on the following general design consideration:

$$R_0 \ll (R_1, R_2, X_C) \ll R_{id} \quad (13)$$

where R_0 is output resistance, R_{id} is input differential resistance of the used operational amplifier [2].

The maximum useful frequency can be increased by making $R_1 = R_2$ [2].

B. Capacitance converter with VNIC, connected into the measured capacitance

For decreasing the influence of the initial capacitance on the primary capacitance converter and of the parasitic capacitances of its connecting conductors with goal - increasing the frequency output relative sensitivity of the capacitance converter, using relaxing generator, to the litter VNIC is connected - fig.3.

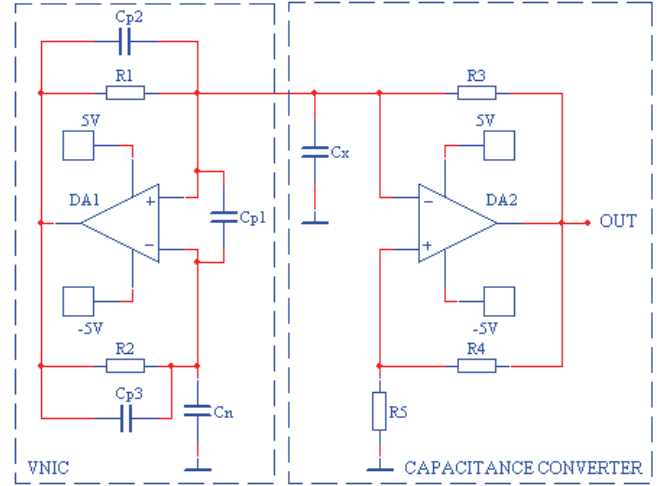


Fig.3. Capacitance converter with VNIC, connected into the measured capacitance

The capacitance converter consists of relaxing generator, which, is realized by the operational amplifier DA2, the resistors R_3 , R_4 , R_5 and the capacitor C_x on the primary capacitance converter. Parallel to the primary capacitance converter is connected VNIC, which is realized by the operational amplifier DA1, the C_n capacitor and the resistors R_1 and R_2 .

The frequency of generated oscillations is defined by the expression [7]:

$$f = \frac{1}{T} = \frac{1}{N \cdot R_3 \cdot C_{eq}} \quad (13)$$

where:

$$C_{eq} = C_x + C_i \quad (14)$$

the coefficient N is defined by values of the resistors R_4 and R_5 as well as of the supply voltage.

After replacing (12) and (14) in (13) following relationship is defined:

$$T = N \cdot R_3 \cdot \left(C_x - \frac{R_2}{R_1} \cdot C_n \right) \quad (15)$$

The period of the generated signal is decreased proportionally to the values of the capacitance C_n and the resistor R_2 and conversely proportionally - to the value of the resistor R_1 in the circuitry of VNIC.

EXPERIMENTAL RESEARCH

The capacitance converter, with *VNIC* connected into the measured capacitance, is studied by simulation with the program product *Electronics Workbench 5.12*. The influence of the value variations of the elements of *VNIC*, connected to the converter on the period of the generated signal *T*, is studied by reading the influence of the input capacitance of the op amp in *NIC*'s circuit as well as of the parasitic capacitances.

1. *The dependence of the period of generated oscillations from the capacitance of the C_n capacitor in *VNIC*'s circuit.*

The dependence is defined by reading also the influence of input capacitance C_{in} on op amp *DA1* in *VNIC*'s circuit. For this purpose, parasitic capacitance C_{p1} is connected to input terminal on *DA1* in parallel, which is a real parasitic capacitance with values from 0 to 5pF; when $C_{p1} = 0$ pF only the input capacitance C_n exercises influence on the op amp, which is smaller than the capacity C_x .

The experimental results are shown graphically in *fig.4*, where value of the resistors $R_1 = R_2 = 15$ k Ω and the *primary capacitance converter* $C_x = 5$ pF.

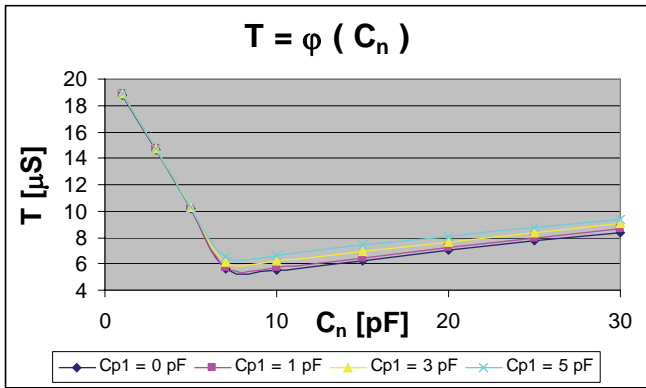


Fig.4. Dependency $T = \varphi (C_n)$, with $C_p = 0 \div 5$ pF

Conclusion: The dependence $T = \varphi (C_n)$ corresponds to this formula from (15) to a considerable degree when the value of the capacitance $C_n < C_x$.

In order to receive an explanation for the radical change of the character of this dependence when the values $C_n > C_x$ the dependence of the current through the parasitic capacitance C_{p1} (*fig.5*) and the voltage between the input terminals of *DA1* (*fig.6*) on the capacitance C_n variation. When $C_n > C_x$ the current through the input capacitance increases, the voltage between the input terminals of *DA1* also increases and the circuitry with *DA1* becomes unstable (it does not correspond to *VNIC*) – the capacitances C_{in} and C_{p1} are connected to C_x in parallel which on its behalf leads to increasing of the total capacitance defining the generator frequency.

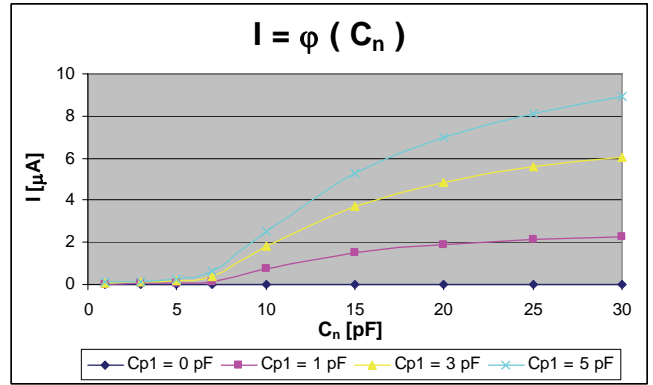


Fig.5. Dependency $I = \varphi (C_n)$, with $C_x = 5$ pF and $C_p = 0 \div 5$ pF

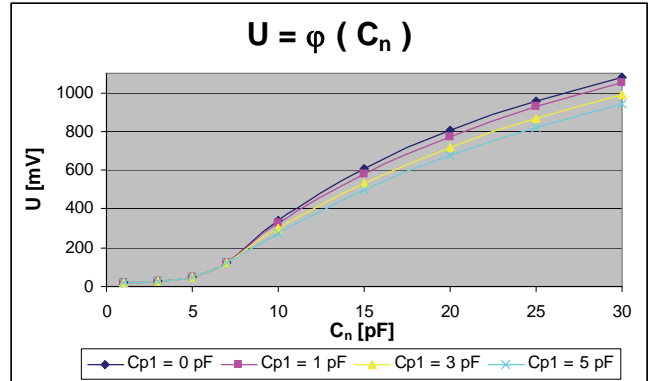


Fig.6. Dependency $U = \varphi (C_n)$, with $C_x = 5$ pF and $C_p = 0 \div 5$ pF

The drawn conclusions are also confirmed when the values of $C_x = 10$ pF (*fig.7*).

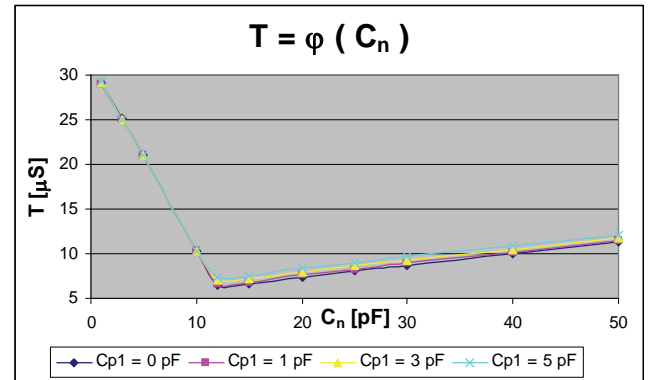


Fig.7. Dependency $T = \varphi (C_n)$, with $C_x = 10$ pF and $C_p = 0 \div 5$ pF

2. *The dependence of the period of generated oscillations from the resistors R_1 and R_2 in *VNIC*'s circuit*

The dependences $T = \varphi (R_2 / R_1)$, at change of the relationship $k = \frac{R_2}{R_1}$, for $R_1 = 15$ k Ω , $C_x = 5$ pF, $C_{p1} = 0$ pF (only the capacitance C_{in} has an effect), are shown graphically in *fig.8*.

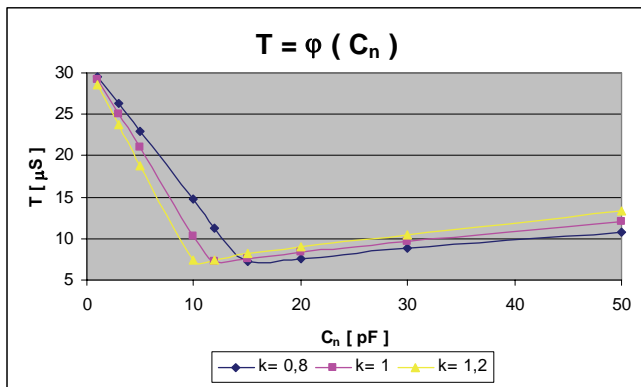


Fig.8. Dependency $T = \varphi(k, C_n)$

Conclusion: The results obtained from the tests show the correctness of the dependency $T = \varphi(C_n, R_2, R_1)$, expression (15), when the capacitance value $C'_n \leq C_x$.

3. The dependence of the parasitic capacitances C_{p2} and C_{p3}

In a real circuitry and the parasitic capacitances C_{p2} and C_{p3} (fig.3) also exists. The experimental results for the dependence of the period of generated signal T on the variation of each of them shown graphically in fig.9 and in fig.10.

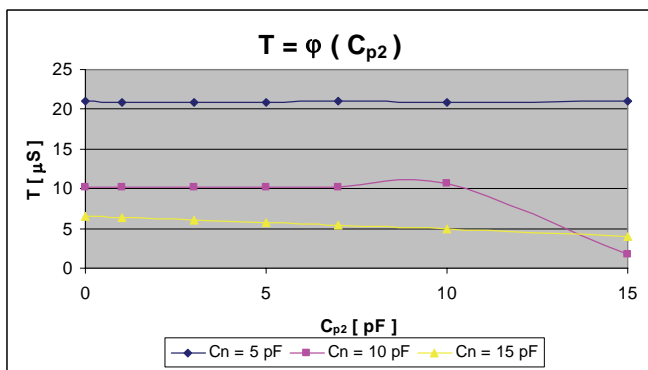


Fig.9. Dependency $T = \varphi(C_{p2})$

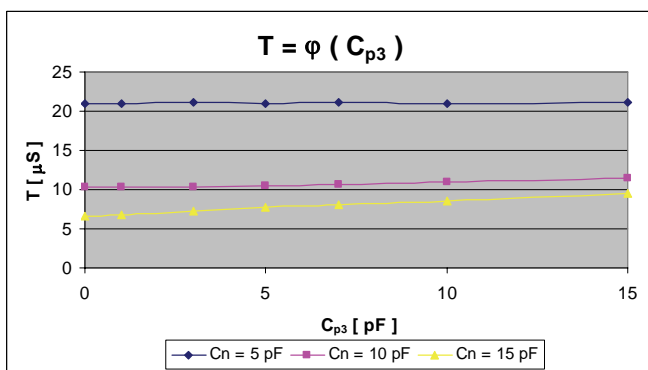


Fig.10. Dependency $T = \varphi(C_{p3})$

In fig.11 the studies of the dependence of the generated signal period T on the simultaneous change of the parasitic capacitances C_{p2} and C_{p3} are depicted.

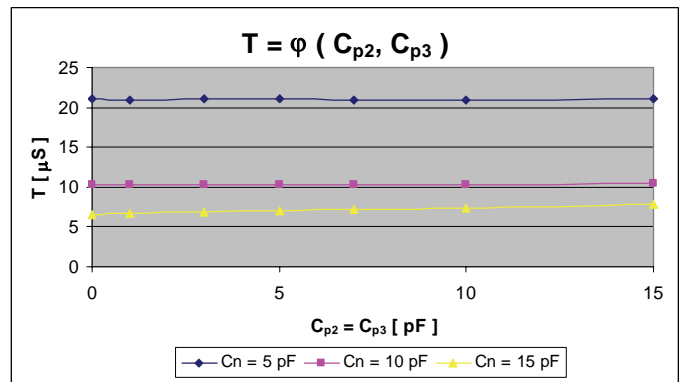


Fig.11. Dependency $T = \varphi(C_{p3})$ with $C_x = 15 \text{ pF}$

Conclusion: When the capacitance $C_n < C_x$ in the circuitry of VNIC the parasitic capacitances C_{p2} and C_{p3} have noticeable effect only just at values over $(5 \div 10) \text{ pF}$, which are greater than the real ones.

III. CONCLUSION

By using the Voltage Negative Impedance Converter (VNIC) the output relative sensitivity of the capacitance converter, constructed on the basis of relaxing generator with connected to it primary capacitance converter is increased. This is due to decreasing of the initial capacitance of the primary capacitance converter as well as to lessening the effect of the parasitic capacitance of the conductors connecting the primary capacitance converter.

The studying the converter carried out through its operating simulation using software confirm the derived theoretical relationships for the effect of the VNIC capacitance variation within a certain range on the frequency of the generated oscillations. The reasons for invalidity of the results outside the range in which the connection of the circuitry of VNIC to the primary capacitance converter decreases its initial capacitance is explained by the results from the studies.

In case of necessity to decrease the effect of the parasitic capacitances in measuring circuits VNIC can be used to increase their sensitivity.

REFERENCE

- [1] Draganov V., И. Танчев, И. Атанасов, С. Георгиева – “Резултати от изследванията на устройство за измерване на малки капацитети” – “Електроника’2006”, София, 2006
- [2] Belousov A. “Negative impedance improves capacitive sensors”, 1995–www.edn.com
- [3] Travis B. “Improved frequency modulator uses “negatron” “ 2002–www.edn.com
- [4] Soundararajan K., K. Ramakrishna – “Nonideal Negative Resistors and Capacitors Using an Operational Amplifier”, IEEE TRANSACTIONS ON CIRCUIT THEORY, September 1975
- [5] Antoniou A. – “Floating Negative-Impedance Converters”, IEEE TRANSACTIONS ON CIRCUIT THEORY, March 1972
- [6] Auvray J. – “Electronique des signaux analogiques”, Borda, Paris, 1980
- [7] Coughlin R.,F. Driscoll – “OPERATIONAL AMPLIFIERS AND LINEAR INTEGRATED CIRCUITS”, Prentice Hall, Inc. Englewood Cliffs 1977

Fuel Cells and Fuel Cell Power Supply Systems – an Overview

Zvonko S. Mladenovski¹, Goce L. Arsov² and Josif Kosev³

Abstract – In this paper general review of the fuel cell as an alternative power supply is given. Fuel cell is an electrochemical power source where internal combustion phase of the fuel is omitted and overall efficiency is two to three times higher compared to conventional power supplies. Fuel cell operation principle, types, advantages and disadvantages are described. At the end a power conditioning subsystem with its components is analysed.

Keywords – Electrochemical power source, Fuel cell, Alternative power supply, Fuel cell power supply systems.

I. INTRODUCTION

At the beginning of the 21st century, fuel cells meet the power needs of variety of applications. The fuel cell (FC) is an electrochemical device that converts the chemical energy into electrical and thermal energy through direct conversion process. The basic features of a FC system are composed of six basic subsystems: a fuel cell stack, a fuel processor, an air, water and thermal management, and power conditioner systems (PCS). The overall system promises to provide a number of advantages, such as diversity of fuels (natural gas, methanol, etc.), high efficiency at full and part load, compatibility of wide range of sizes, and independence of environmental pollution [1] – [3].

Fuel cells as energy source has been present since 1839. They were discovered and developed by the English physicist William Grove. But, since then, for more over one century they were not more than a laboratory curiosity [4]. After the period of 120 years since the fuel cells emerged, NASA demonstrated some of their potential applications in the space flights exploration. Consequently, the industry has started recognizing the commercial aspects of the fuel cells, which due to the technological barriers and their high production costs were not economically profitable at that stage of technology. [5].

However since the mid of the 80's of the 20th century, Office of Transportation Technologies at the U.S. Department of Energy, has started to support fuel cells technology which has aroused the interest of over 100 companies worldwide to

support the R&D of the fuel cells, implementation and economic payoff.

The most common application areas of fuel cell can be classified in five main groups as shown in fig.1 [6].

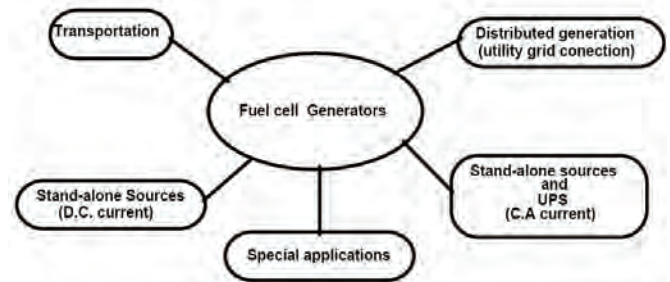
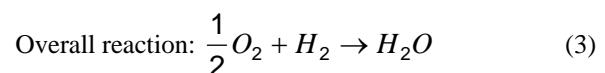
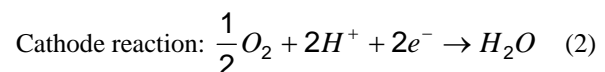


Fig. 1 Classification of fuel cell application

II. DESCRIPTION AND OPERATIONAL PRINCIPLE OF THE FUEL CELLS

The fuel cell is a mini power source generating electrical energy without the combustion stage. The basic physical structure of the fuel cell is consisted of an electrolyte layer (membrane) which in contact with the two porous electrodes (anode and cathode) on its both sides [7]. Porosity of the electrodes enhance the active electrode area hundreds, even thousand times. This fact is very important because electrochemical reactions take place on the electrode surface. Catalyst is incorporated in the electrode microstructure. e.g., platinum, nickel or their alloys which accelerate the speed of electrode's electrochemical reactions [7]. The chemical energy is directly transformed into electrical energy and heat when the hydrogen fuel reacts with the oxygen from the air [4], [5]. Water is the sole byproduct of the reaction. The basic electrochemical reaction is the following one [8]:



Looking at the the previous equations, one can get a wrong impression that this process is very simple, but actually the physical and chemical processes happening on each of the electrodes and membrane are rather complex. A schematic fuel cell representation with flow directions of the fuel, reactant and ion current is given in the Fig. 2 [2].

¹Zvonko S. Mladenovski is with COSMOFON - Mobile Telecommunications Services - A.D. Skopje, Macedonia, E-mail: zvonko.mladenovski@cosmofon.com.mk

²Goce L. Arsov is with the Faculty of Electrical Engineering and Information Technologies, Kaarpos II, b.b. P.O.Box 574, 1001 Skopje, Macedonia, E-mail: g.arsov@iee.org

³Josif Kosev is with the Faculty of Electrical Engineering and Information Technologies, Kaarpos II, b.b. P.O.Box 574, 1001 Skopje, Macedonia, E-mail: j.kosev@iee.org

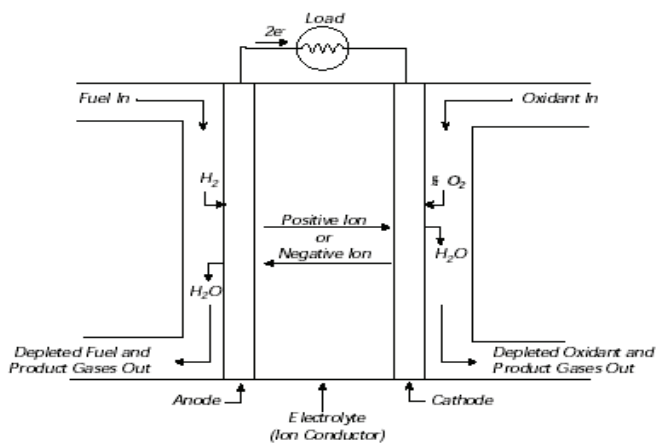


Fig 2. Operational principle of the fuel cell

Single fuel cell at no load (e.g. polymere electrolyte fuel cell - PEFC) in ideal case, generates voltage of 1,16 V at the temperature of 80 °C and gas pressure of 1 bar. Loaded fuel cell at this operational conditions generates 0,7 V. Thereby 60% of the fuel energy is transformed into electrical energy [4]. Maximum emf, E , gained during the hydrogen and air reaction ($H_2 + \frac{1}{2}O_2 \rightarrow H_2O$) at the specified values of temperature and pressure can be determined by the following expression:

$$E = -\frac{\Delta G}{nF} \quad (4)$$

where ΔG is Gibbs free energy, n is number of electrons participating in the reaction, and F is the Faraday constant.

In order to use the fuel cell as energy source practically, a number of single fuel cell has to be serially connected (stacked) to gain the higher output voltage.

When the hydrogen is used as a fuel, the pollutants are not products of the reaction. Hydrogen fuel could be produced by electrolysis process using renewable power sources as sun, hydro, geothermal and wind energy. But the hydrogen could be extracted from any hydrocarbons e.g. petrol, naphtha, biomass, natural and LPG, methanol, ethanol, etc.

The most often classification of the fuel cell is according to the type of the used electrolyte [7]. So there are five types of fuel cell although basically the same electrochemical reaction takes place in all of them [7]:

- Alkaline Fuel Cell - AFC: AFC operating at 250 °C has an electrolyte of highly concentrated potassium hydroxide KOH while those operating at lower temperatures (120 °C) have lowly concentrated KOH. The electrolyte is retained in an asbestos matrix. Wide spectrum of catalysts is used: Ni, Ag etc. The fuel is limited to non-reactive constituents except for hydrogen.
- Polymer Electrolyte Membrane Fuel Cell - PEMFC: Electrolyte in this fuel cell is ionic membrane (Sulfuric acid polymer) which is excellent ionic conductor. Water is the only liquid in the PEMFC and consequently the problem with the corrosion of PEMFC elements are minimal. Water management is a key factor for PEMFC efficient operation. During the operation the PEMFC the humidity of the membrane is critical which determines the operational temperature of the PEMFC in the range of 60-100 °C. The fuel is hydrogen H_2 enriched gas with no presence of CO

(fuel cell poison at low temperatures). Platinum is used as a catalyst

- Phosphoric Acid Fuel Cell - PAFC: Concentrated phosphoric acid (up to 100%) is used in PAFC at operating temperatures in the range of 150 - 250 °C. At lower temperatures, phosphoric acid is bad ionic conductor, and catalyst (Pt) poisoning with CO becomes extremely severe. The relative stability of the phosphoric acid is high compared to the other acids, and that is the reason why this acid is operative at high temperatures with small water quantity which make the water management easy. Electrolyte is put up in silicon matrix while the type of the used catalyst is Pt.
- Molten Carbonate Fuel Cell - MCFC: MCFC's electrolyte is combination of alkali carbonates or combination of Na and K, placed in a ceramic matrix made up of $LiAlO_2$. Operational temperature of the MCFC is in the range of 600 °C to 700 °C at which the alkali carbonates form highly ionian conductive molten salt. Ni (anode) and nickel oxide (cathode) are used to promote reaction.
- Solid Oxide Fuel Cell - SOFC: The membrane electrolyte is solid nonporous metallic oxide usually Y_2O_3 - stabilized ZrO_2 . Operational temperature is in the range from 650 to 1000 °C where ionic conduction of oxygen ions occurs. Typically anode is made of Co-ZrO₂ or Ni-ZrO₂ cermet and cathode is Sr-doped $LaMnO_3$.

Initial use of the fuel cells was in the NASA's space flights, for power generation and production of fresh water for the astronauts. Today the fuel cells might be used in three categories of applications: transport, stationary and portable applications.

AFC is the first modern type of fuel cell developed in the 1960's for the "Apollo" space program. The excellent performances of AFC comparing to the other types of fuel cells, are due to the active O_2 electrode kinetics and its flexibility to use a wide range of electrocatalysts. But, pure H_2 has to be used as fuel because CO_2 in any reformed fuel reacts with KOH electrolyte to form carbonate thus reducing the electrolyte's ion mobility. Purification of the fuel is rather expensive and because of that the use of AFC is limited to the space applications where fuel is pure hydrogen. In the NASA's Space shuttle three 12 kW units have been used for 87 missions with 65 000 hour flight time duration.

PEMFC are used in the transport applications. Exceptionally interesting for this kind of applications is the Direct Methanol Fuel Cell - DMFC. In this type of fuel cell metilacohol (methanol) is directly used as a fuel needing no reformer stage [4]. PEMFC generate electrical energy with high efficiency and power density (180 - 250 mW/cm²) [7]. Also, this type of fuel cells can be used in a small stationary applications for generation of electrical power and heating in the individual houses. The power range is from 2 to 10 kW. This achievement is made by the cost reduction of the materials and manufacturing. Their main advantage is low operating temperatures 60-100 °C and solid electrolyte. Due to the low operational temperature anode catalyst poisoning with CO is significant especially at higher current densities. In this case the output voltage of the fuel cell becomes unstable and fluctuating. Also due to the low operating temperatures, expensive catalysts have to be used for increasing the speed of the electrochemical reactions (platinum).

PAFC are for the time being the only one commercialized type of the fuel cell. It is relatively simple, reliable and quiet power source with 60% efficiency (with cogeneration). As fuel could be used natural gas. 60 MW of this type fuel cells generators are installed worldwide. The power range of the most of the power stations is between 50 and 200 kW, but also they are constructed in the range between 1 and 5 MW. Operational temperature is around 200 °C, and power density reaches values of 310 mW/cm². The PAFC anode is very sensitive to catalyst poisoning even if very small concentrations of contaminants (CO, COS and H₂S) are present. Compromise between the demand for high power density and good operational performances through the life spans of the PAFC should be made. One of the primary targets for the future PAFC development is the extension of the PAFC's life span up to 40 000 hours.

MCFC operates at around 600 °C. At this temperature many of the disadvantages of the lower as well as higher temperature cells can be alleviated with the fact that, for manufacturing MCFC, commonly available materials can be used (utilization of metal sheets reduces fabrication costs), while nickel catalyst is used instead of expensive precious metals. Reforming process takes place within the cell and CO is used directly as a fuel. However, the electrolyte in the MCFC is very corrosive and mobile while the higher temperature influences the mechanical stability and the lifetime of the MCFC materials. An Energy Research Corporation (ERC) in USA has tested a 2MW power supply which operates from 1996 in Santa Clara, Ca.

SOFC electrolyte is solid and cell can be made in tubular, planar or monolithic shape. The solid ceramic construction of the cell alleviates hardware corrosion problems characterized by the liquid electrolyte cells and is impervious to gas cross-over from one electrode to the other. The absence of liquid also eliminates the problem of electrolyte movement and flooding the electrodes. The kinetics is fast while CO is directly usable fuel as in MCFC. Also, as in MCFC, there is no requirement for CO₂ at the cathode. Operational temperature is around 1000 °C which means that the fuel is directly reformed within the cell. Disadvantages of the high operational temperature are the influences on the cell's material properties meaning the different thermal expansion mismatches. Currently two plants (25 kW and 100 kW), produced by Siemens Westinghouse Power Corporation, are installed and they both have cumulative operating time of 9500 hours. The eventual SOFC market is for large stationary fuel cell power supply systems (100 to 300 MW) using natural gas or coal as a fuel.

III. FUEL CELL POWER SUPPLY SYSTEMS

Although fuel cells generate power, power supply system based on fuel cells is a very complex system due to the fact that besides pure hydrogen, fuel cell can operate on diverse conventional fuels generating DC output power. There are many components incorporated in the fuel cell power system in order to enable processing of the fuel and to couple the power supply system to AC distributive network (power grid) as well as utilization of the generated heat in cogeneration to achieve high efficiency. In general the power supply system consists of: fuel processor or reformer, fuel cell and power supply conditioning subsystem.

In the reformer, hydrogen is extracted from the hydrocarbons by a hydrocarbons steam reforming. CO and CO₂ appear as by-

products. The further treatment of CO with steam under high pressure converts it in CO₂.

Fig. 3 shows a simplified diagram of fuel cell power supply system [4]:

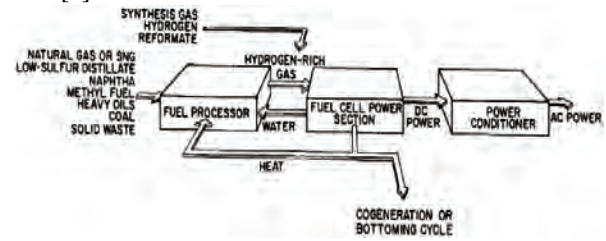


Fig 3. Fuel cell Power Supply System

The quality of the electrical power generated by a fuel cell power supply system is evaluated according to the following three characteristics: efficiency, reliability and quality.

One of the main reasons for the utilization of the fuel cell as power supply is its electrical efficiency (40-57%), and with cogeneration the overall efficiency is even higher (80-85%) [9]. The measured electrical efficiency is the ratio of generated electrical energy and the energy of the fuel used in the fuel cell power supply system. Losses in all the subsystems and the interaction among them influence on the overall efficiency of the power supply system. In order to gain and maintain the high efficiency high level of the coordination among the subsystems is required. The fast response of the power conditioner has the key role in maintaining the high efficiency due to the step load variations.

Reliability is the second key factor in the development of the fuel cell power supply systems. They do not require complex and frequent maintenance. As alternative power supply sources they can substitute the traditional power supply systems in applications such as:

1. **Remote sites applications**, e.g. mobile telephony base stations, where service visit and investment costs for power grid construction are rather expensive,
2. **Critical power supply systems**, e.g. banks and internet servers, where power supply failures could be very expensive.

System's reliability as well as the efficiency is function of the combined subsystem's reliability.

The quality of the generated electrical power is also very important factor influencing the acceptance of the fuel cell power supply systems on the market. High quality of the electrical power demands the shape of the sinusoid of the generated voltage to be close to the shape of ideal sinusoid with a constant frequency and rated value of AC voltage. This characteristics is very essential for the proper operation of the electrical and electronic devices.

The main role of the power conditioner subsystem is to process and control the generated DC power from multiple DC sources and further to generate high quality and reliable AC power maintaining the high efficiency of the power supply system. The AC output of the system should have possibility to interact and to be synchronized with other AC generators including the power grid. [10]. The power conditioner subsystem should comply to the new standard IEEE 1547 referring to the coupling to the power grid and anti-islanding protection.

Usually the power conditioner (Fig. 4 [8]) is composed of two coupled converters: DC-DC converter and AC-DC converter and backup power supply: battery or ultra capacitors. DC-DC converter decouples and isolates the fuel cell and the DC-AC con-

verter and step-up the low output DC voltage of the fuel cell (usually the output voltage of the serially connected fuel cell's is 48 VDC, because the connection of the fuel cells to achieve high voltages, >400 VDC, is complicated related to the reliable functioning of the fuel cell stack [4]). DC-AC converter generates stable and rated AC voltage. The battery serves as a backup during the load transients because the fuel cell dynamics is slower than the converters dynamics, and it enables starting of the fuel cell power supply system.

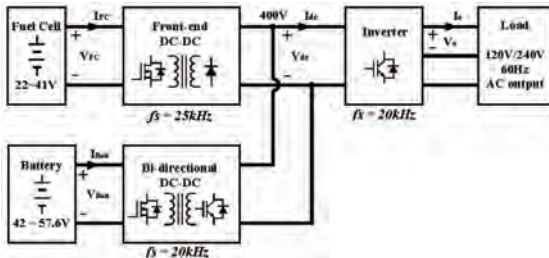


Fig 4. Power conditioner subsystem

DC-DC converter is usually put up between the fuel cell stack DC-AC converter. Different topologies for the DC-DC converter design can be used: classical high frequency hard switching topologies and resonant topologies. Bridge, half-bridge and push-pull topologies may be chosen. The advantage of resonant topologies related to the hard switching converters is avoiding the switching losses but the design and control complexity is greatly increased. Fig. 4 shows different topologies of DC-DC converters for possible use in the power conditioner subsystem are given. [11].

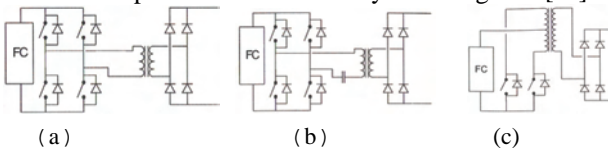


Fig 4. a) bridge, b) serial resonant, c) push-pull converter

DC-AC converter should generate stable and rated AC output voltage. Standard high frequency voltage mode, resonant and resonant with DC link inverters can be used. Some of the considered topologies are given in Fig. 5 [6].

The role of the battery system that is used to prevent voltage transients during the dynamic load variations influences considerably on the topology configuration of the power conditioner subsystem. Most usually the following two methods of the battery connection in the subsystem: 1) the battery is connected on the low DC voltage side or 2) on the high DC voltage side (400 VDC). Both methods have their advantages and drawbacks [6].

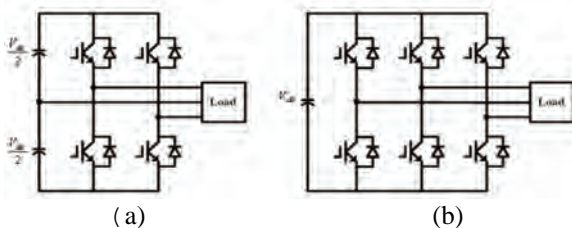


Fig 5. a) Four switch inverter, b) Six switch inverter

IV. CONCLUSION

The use of fuel cells as a power source in stationary and transport applications is the technology of the future. Highly de-

veloped countries, especially USA make great investments in R&D of the fuel cell's technology, production and implementation and power supply systems based on them. For this purpose, for fiscal year 2000, The American Congress provided 117 million USD in fuel cell funding through the Departments of Energy, Transportation and the Environmental Protection Agency. One of the main goals is to decrease the production costs from 3000\$/kW to 1500\$/kW (for cogeneration units) in order to achieve wider commercialization of the fuel cells systems. [5]. Also one of the goals is decreasing the power conditioners subsystems production costs on the value of 40\$/kW [6].

Replacement of the conventional power sources with the new alternative technologies is inevitable in the near future due to the following reasons: 1) depletion of the fossil fuel reserves, especially oil and reduction of its use as a primary power source, 2) reduction of the greenhouse gases and air pollutants in transport and 3) direct influence on the deceleration of the global climate changes.

Application of the fuel cells power systems for the remote telecommunication and critical sites would influence directly on the reduction of the maintenance costs and in the near future on the investment costs for the power grid infrastructure, and indirectly on the global level regarding the previously mentioned three global factors.

Sometimes, instead of connecting in series several fuel cells to obtain the higher output voltage than one cell can give, it may be cheaper and less complex to build a low voltage DC-DC converter and to convert the low voltage of a single cell to some higher levels. Some possibilities using switched capacitor converter are analyzed in [12].

ACKNOWLEDGEMENT

This work has been supported by the Ministry of Education and Science of Republic of Macedonia (project: 13-936/3-05)

REFERENCES

- [1] G. Hoogers, *Fuel Cell Technology Handbook*, CRC Press, 2003
- [2] J. Laramie, and A. Dicks, *Fuel Cell Systems Explained*, pp.25-66, John Wiley and Sons, England, 2000
- [3] M. W. Ellis, M. R. V. Spakovsky, and D. J. Nelson, "Fuel Cell Systems: Efficient, flexible Energy Conversion for 21st Century", Proc. IEEE, vol. 89, no. 12, pp 1808-1818, Dec. 2001
- [4] Sharon Thomas, Marcia Zalowitz, "Fuel Cells – Green Power," *Los Alamos National Laboratory, New Mexico*, 1999.
- [5] "Fuel Cells Fact Sheet," *Environmental and Energy Study Institute, Washington DC*, February 2000.
- [6] "2003 Fuel Cell Seminar Proceedings," Miami, November, 2003.
- [7] J.H. Hirschenhofer, D.B. Stauffer, R.R. Engleman, M.G. Klett "Fuel Cell Handbook, Fourth Edition," *US Department of Energy*, Nov. 1998.
- [8] Andrew R. Balkin, "Modelling a 500 W Electrolyte Membrane Fuel Cell," *University of Technology, Sydney*, June 2002.
- [9] H. Xu, L. Kong, X. Wen, "Fuel Cell Power System and High Power DC-DC converter," *IEEE Transactions on Power Electronics*, vol. 19 No5 September 2004.
- [10] "The Fuel Cell Power Converter –Power Management for Fuel Cell Systems," *Sustainable Energy Technologies*, White Paper, Jan.2001.
- [11] F. Blaabjerg, Z. Chen, S. Baekhoej Kjaer, "Power Electronic as Efficient Interface in Dispersed Power Generation Systems," *IEEE Transactions on Power Electronics*, vol. 19 No5 September 2004.
- [12] G. L. Arsov, J. Kosev, R. Giral, "Low voltage switched capacitor DC-DC converter for fuel-cell applications – Preliminary design considerations", 12th Int. Conf on Power Electronics – Ee 2003, Paper No. T5-1.4, pp. 1-5, Novi Sad, Serbia, 2003

Developing and Using Communication Driver for Serial Communication Between PCs and Industrial PLCs

Zoran M. Milić¹, Petar B. Nikolić², Dragana Krstić³ and Miljana Lj. Sokolović⁴

Abstract – The basic principles of the asynchronous serial communication between PLC controllers and PC based applications are presented in this paper. In order to create HMI interface between operator and the controller at the machine, the Windows based application for visualization and data acquisition was developed. This application is using self-oriented driver for serial communication which was developed and used for purposes of communication and data exchange between industrial controllers working at machines in the plant floor, and PCs. Basic principle of generating communication packets and examples of writing data into PLC's memory registers are given. This driver is also used in self-oriented SCADA programming for data exchange between SCADA application and controllers on the industrial network.

Keywords – PLC, industrial network, network layer.

I. INTRODUCTION

For visualization of the interface between the operator and the machine, it is possible to use different hardware solutions, from the industrial panels, intended only for these purposes and related to a particular PLC type, to the industrial and non-industrial PC's with a proper operating system installed as well as the appropriate user's application program. For the realization, it is suitable to use common personal computer since it enables the enlargement of the system and the integration into the wider information system.

The industrial application specific panels have no ability for multi-tasking work. They need additional communication with PCs or other controllers in the control system where complex calculations are needed. With the respect to those calculations, a change of the data in the registers of the controllers takes place as well as the activation of the appropriate outputs. These panels have neither additional ports, nor the ability to install additional cards (PCI, PCE express) that are obtained as a part of the sensors' and actuators' kits. When the industrial panels are connected to the larger industrial network, and one of the devices blocks its message transmission, this can break the communication of the entire network.

For the communication between the PC and the controller, communicating applications of the controllers' manufacturer can be used, or a specific communication driver can be developed. The communication software enables an easy integration into the application for the machine control, or into the SCADA software, and this decreases the time needed for the entire system realization. Some of these communication software are in the same time OPC servers so that they allow relatively easy integration of the data sources devices from different manufacturers into the unique visualization and acquisition systems.

Writing its own communication driver allows good controller management. It is possible to adjust the operating mode, which is switching between the programs, run and test modes, which is very useful for application testing. Managing the program upload and download to and from the controller is possible to be achieved directly, through the serial interface, or through the network, using the proper network module. In this way, the change of the status registers, control of the restart or switching of the controller, and the memory initialization can be achieved. Direct changing the parameters of the communication link (for example, baud rate, parity bit, stop bit, hardware/software control, BCC/CRC) is possible, and this represents the advantage considering the entire system testing. HMI (Human Machine Interface) applications, which communicate with the controller directly over the driver, perform it in the real time.

This solution has better diagnostics abilities, enables an acceptable real-time response of the machine, gives a bigger independence, but also increases the entire system design and development. Beside the time needed for the design, the important factor in the solution choice is the price. In the case of SCADA application design, the prices of the both system are comparable, since

In the case of SCADA application design, the prices of both systems are similar since the number of the acquisition places, and though the places than need the communication software, relatively small, comparing to the number of PLC's in the system. By the HMI applications, the situation is different. The number of places that need the communication software is the equal as the number of PLC controllers - that is, each machine must have PLC and the particular interface toward the operator, which communicate with that PLC. In this case the price of developing particular driver is much lower than buying a new solution.

¹Zoran M. Milić is with the Tigar MH, Pirot, Serbia E-mail: zronjul@yahoo.com

²Petar Nikolić is with the Tigar MH, Pirot, Serbia E-mail: nikpetar@tigar.com

³Dragana S. Krstić is with the Faculty of Electronic Engineering, University of Niš, Serbia E-mail: dragana@elfak.ni.ac.yu

⁴Miljana Lj. Sokolović is with the Faculty of Electronic Engineering, University of Niš, Serbia E-mail: miljana@venus.elfak.ni.ac.yu

II. NETWORK LAYERS OF THE COMMUNICATION MODEL

Network architecture of the DF1 industrial network has physical layer, data layer, network layer and the application layer [1].

In the case of serial RS232/RS422 communication, physical layer consists of the RS232/RS422 ports at the PC and PLC, RS232/RS422 cable that connects them, voltage values (zeros and ones), number of data bits, number of stop bits, parity bit, bit rate, and the way of establishing and breaking the connection after PC and PLC finish the data transfer [3].

The data connection layer controls the correctness of the data transfer, and the protocol at this layer should provide the mechanism for the acknowledgement of the correct data transmission and reception [2].

The network layer controls the packet transmission to its destination, which is for establishing the connection between the nodes of the network [4].

Application layer in the case of PLC and PC communication contains the commands that are set and executed by the PC and the PLC applications.

III. DF1 LAYER OF THE DATA CONNECTION

DF1 is the Allen Bradley's protocol for the data connection layer, which is based on the ANSI x3.28 specification. The basic principle of the DF1 protocol will be explained at the example of Full Duplex data exchange [1].

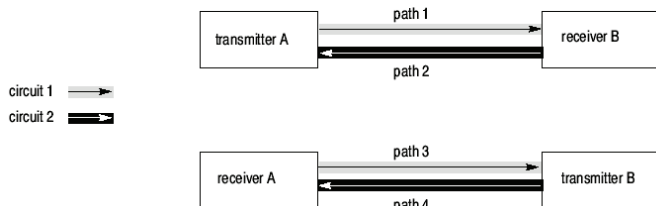


Fig. 1. The data routes for alternating simultaneous communication (Full duplex)

At the Full Duplex protocol (Fig. 1), link uses two physically separated circuits for the simultaneous data exchange. These circuits provide communication at four communication channels.

- In the first circuit the transmitter A sends messages to the receiver B (the route 1) and the receiver A send the returning control messages to the transmitter B (route 3).
- In the second circuit the receiver B sends messages to the receiver A (the route 4) and the receiver B sends the returning control messages to the transmitter A (the route 2).

All messages and the symbols in each of these circuits are transmitted in one direction; from A to B in the first, and from B to A in the second.

- In order to implement 4 logical routes in 2 physically separated circuits a software multiplexer must be used. Its purpose is to combine the command messages (from the transmitter) with the returning messages (from the receiver) as well as with the replies from the transmitter sent in the same direction.

- At the other end of the link, the separator software separates the command messages from the returning reply messages. The separator software should send the command messages to the particular receiver and the returning messages to the corresponding transmitter.
- Although the command and the returning messages in the same circuit exist independently from one another, there is a certain relation between them. For example, the command message in the AB circuit will be delayed if the returning message of the receiver A is inserted into the sequence of the common messages of the transmitter A. Each hardware problem that influences the command symbols in one circuit will also have the influence at the returning symbols in the same circuit [1].

IV. GENERATION AND SEPARATION OF THE DATA FRAME IN THE FULL DUPLEX PROTOCOL

The data frame in the Full Duplex protocol has different forms depending on the observed network layer, and considering the fact that different message parts are generated in different network layer. Fig. 2 illustrates how the particular network layer influences generating the message frame [5]. The influence of the physical layer is not shown.

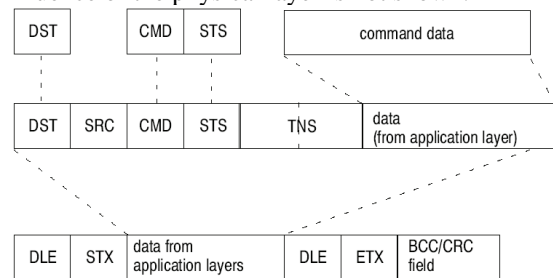


Fig. 2. Data frame: from the top to the bottom: application layer, network layer, data connection layer

The command (for example, read or write) is generated at the application layer, as well as the destination (the address of the PLC controller in the network) and the data related to that command (for example, in the case of reading, this would be the specification of the first memory location and the size of the block to be read).

The network layer is responsible for establishing connection between the communicating nodes, and the address from which the message is transmitted is added here (so that returning message has the correct destination address), transmission status field (which contains the error code for the eventual transmission errors), and the identifier, which is a unique for each message (in order to know which returning message is the reply to the given command).

Data connection layer is intended for the control of the correctness of the transmitted data – one more field is added for the beginning and one for the end of the message as well as the field for the error control.

In order to design the corresponding HMI solution one needs to develop a driver which cover a wide spectrum of communication messages that enable: reading and writing into and from the controllers' registers, changing the content of the status registers, changing the parameters of the

communication link itself, and simultaneous covering relatively large number of communicating devices.

The driver is the application specific for the asynchronous serial communication with the Allen Bradley PLC 5 and the SLC 5 families of the controllers as well as for the Allen Bradley KF2 communicating module [6].

The developed driver supports the following set of commands:

For PLC 5 family of controllers and a KF2 module:

- “Word Range Read” – reading the block of words from the controller’s memory
- “Word Range Write” – writing the block of words into the controller’s memory
- “Typed Read” – reading the block of data from the controller’s memory (this command is also supported for the SLC 5/03 and SLC 5/04 processors from the SLC500 family)
- “Typed Write” – writing the block of data into the controller’s memory (this command is also supported for the SLC 5/03 and SLC 5/04 processors from the SLC500 family)
- “Read – Modify - Write” – bit write command
- “Set Variables” – adjusting the parameter of the serial link – the number of the ENQ packets, the number of the NAK packets and the timeout interval
- “Set CPU Mode” – changing the controllers' operating mode: Test, Program and Run
- “Diagnostic Status” – reading the content of the controllers' status registers

For the SLC 500 and the MicroLogix 1000 family of controllers:

- “Protected Typed Logical Read With Three Address Fields” – reading the block of data from the controllers' memory, starting from the given address
- “Protected Typed Logical Write With Three Address Fields” – writing the block of data into the controllers' memory, starting from the given address
- “Change mode” – changing the controllers' operating mode: Test, Program and Run
- “Diagnostic Status” – – reading the content of the controllers' status registers

V. EXAMPLE

For communication between the PCs and the PLCs in the systems that control machines in the tires industry, asynchronous serial communication is commonly used. The role of the interface between the controller and the operator is given to the applications installed at the industrial PC. The reason for that is the additional processor power that system needs for processing the parameters obtained from the smart sensors, which is the task that most of PLCs cannot satisfy, or the prize of it implementation is to high.

The communication during one working cycle of the different machines is performed in a similar manner. The controller sends a request for the recipe data from the user application over the asynchronous serial communication. The data are read from the particular sensors and according to their content, the application reads some parameters from the data

bases and calculates the parameters of the recipe. According to these data, the machine's parameters are adjusted, and the corresponding machine's operating cycle can begin. During the cycle, several communication sessions between a PC and a PLC can appear. During one session, a certain amount of data needed for the machine control is successively written into, and read from the registers of the controller in order to obtain the data needed for the additional analysis in the PC.

After completing the cycle and the analysis, performed by the user's application, the results of the processing should be written into the data base, and the signal for the initialization of the next cycle should be sent.

The described HMI application is implemented using the Microsoft Visual Basic.NET 2005 developing tool [7].

The example shows writing four integer words (1111, decimal) into the u Allen Bradley PLC 5/20 processor over the serial link, starting from the N8:31 memory location. To do this a command “Word Range Write” was used. In a similar manner, an entire communication over the serial link is performed, where the packets contain all necessary commands, addresses and data. During this procedure the following data exchange takes place (Fig. 3):

- The application sends a data for writing into the driver, that is, it specifies the writing command, all four words of the data and the destination address of the controller
- The driver generates the entire data frame for sending
- The transmitter of the driver sends the packet to the receiver of the PLC
- The receiver of the PLC receives the packet, forwards it for processing to the processor and sends the control message about the successful reception of the packet (DLE ACK) to the link
- After the writing command is successfully completed, PLC processor forwards the message about the successful reception to the transmitter.
- The transmitter of the controller sends the message to the link
- The receiver of the driver receives the message about the successful writing, the application forwards that message and sends the control message about the successful data reception (DLE ACK) to the link.

Command:

DLB	STX	DEF	SRC	CMD	STS	TNS	FNC	PACKET OFFSET	TOTAL TRANS	ADDRESS	DATA	DLB	STX	BCC											
Path 1:	10	02	00	0F	00	05	00	00	00	04	00	06	0E	1F	57	04	57	04	57	04	57	04	30	03	4E

Path 2:

DLB	ACK
10	06

Reply:

DLB	STX	DEF	SRC	CMD	STS	TNS	FNC	DLB	STX	BCC	
Path 4:	10	02	00	4F	00	05	00	00	10	03	A5

Path 3:

DLB	ACK
10	06

Fig. 3. Illustration of the packet exchange over the serial link

A. The driver

The driver was developed as a C#.NET Class Library. Since it represents an interface between the user's HMI application and the physical layer of the network, the following class properties were implemented:

- command – it is a command that forwards the application.

- address – represents the address of the controller in the network
- mem_address - specifies the starting address in the controller's memory where the writing is taking place
- packet_offset – specifies the offset in regard to the of the given mem_address value
- total_trans – specifies the total number of the data words for writing into the controllers' memory during the entire transaction
- sent_data – data, forwarded by the application
- error_check – can have CRC or BCC
- receive_data – the driver forwards these data to the application
- nak – the number of the NAK packets
- enq – the number of the ENQ packets
- time_out – time interval for timeout
- mode – operating mode
- comm_status

- A new object with a dh class is created in the application
- The appropriate class properties are set – depending on the command properties, some of the properties are not necessary
- In order to inflict the controller to send the command, the method "communicate" must be invoked
- Coding the memory address, generating the TNS value, calculating CRC or BCC field and assembling the entire packet is performed within the class frame
- The class itself performs the communication toward the controller
- When class extracts all corresponding data, it sets the "receive_data" property
- After a certain amount of time the application reads the "receive_data" and "comm_status" properties
- If the property "comm_status" is set to "True" value, depending on the program logic, the property "receive_data" is used further
- If the property "comm_status" is set to "False" value, the property "receive_data" is not used further, and depending on the program logic, the command could or could not be repeated.

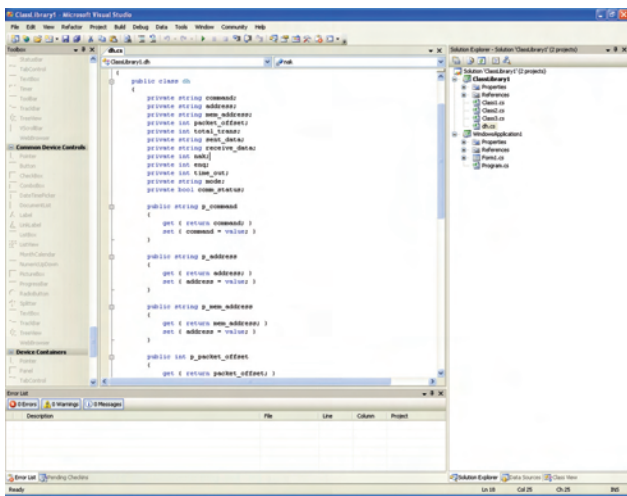


Fig. 4. The example of the class code

The class also contains the method "communicate" that is used by the application for forwarding the request for establishing communication with the controller.

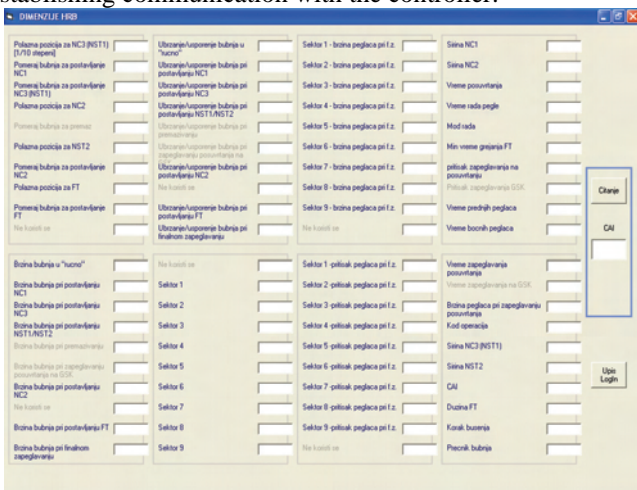


Fig. 5. Writing the dimensions parameters

The procedure in which the class is used for forwarding the data between the HMI application and the controller is given next:

VI. CONCLUSION

Developing the unique own communication driver for the communication between PCs and PLCs in the machine control HMI interface design process enables better diagnostics, good real-time response of the machine and gives larger independence comparing to the use of the communication application offered by the machine manufacturer. The own solution and its integration into the HMI application increases the time needed for the design of the entire system, but at the same time the prize of developing the own driver much lower than the prize for buying the entire solution and no addition license expenses are necessary for each application installed later. The paper describes the communication model that uses asynchronous serial communication, and one practical realization of writing data obtained in a PC and needed for machine control, into the controllers' registers, and reading data needed for additional PC analysis or for updating the data shown on the screen.

REFERENCES

- [1] -, "DF 1 Protocol and command set – Reference Manual", Publication 1770 – 6.5.16, Allen_Bradley, Milwaukee, USA, 1996.
- [2] Andrew S. Tanenbaum, "Computer Networks", London, Prentice Hall PTR, 2002.
- [3] -, "Data Highway or Data Highway Plus Asynchronous (RS-232-C or RS-422-A) Interface Module" User Manual, Allen_Bradley, Milwaukee, USA, March 1989.
- [4] Anthony Chiarella, "Networks in Cisco and Microsoft technology (in Serbian)", Čačak, Computer library, 2005.
- [5] -, "Data Highway Plus and DF1 Communication Protocols", Allen_Bradley, Milwaukee, USA, 2004.
- [6] -, "Allen-Bradley DF1 Serial Communication Interface API", DASTEC Corporation, 2003.
- [7] Michael Halvarson, "Visual Basic.NET Step by Step", CET Computer Equipment and Trade, 2002.

Spice Model of Magnetic Sensitive MOSFET

Nebojsa Jankovic¹, Tajana Pesic² and Dragan Pantic³

Abstract: A new model for a magnetic-sensitive split-drain MOSFET (MAGFET) consisting of only two NMOSTs in the equivalent sub-circuit is described in this paper. The model developed is based on the non-quasi-static (NQS) MOST model of a conventional NMOST, modified to include the effects of the Lorentz force. Based on the results of 3D numerical device simulations, it is shown that the new model can accurately predict the absolute and the relative MAGFET sensitivity for a wide range of the device biasing conditions. Unlike previous models, the new MAGFET model can also predict device dynamic response to time varying magnetic fields more realistically.

Keywords: Magnetic, Sensor, SPICE, Model

I. INTRODUCTION

A magnetic sensor is a transducer which converts a magnetic field into an electric signal. Many integrated magnetic sensor circuits use a split-drain MOSFET (MAGFET) structure as a sensing device. The MAGFET is a long-channel MOSFET with a single gate and two symmetrical drains sharing the total channel current I_D [1]. An imbalance between drain currents occurs due to the influence of the perpendicular magnetic field B_Z . In spite of its large offset, temperature drift and noise [1], the MAGFET remains a popular magnetic field sensing device due to its easy integration with other electronic signal conditioning blocks on silicon chips [2,3]. Hence, the ability to evaluate the performance of magnetic sensors built using MAGFETs prior to chip fabrication is essential to cost-effective development. For the accurate simulation of magnetic sensors, precise MAGFET electrical models are required that are suitable for implementation in circuit simulators such as SPICE. Until now, recent MAGFET models employed in sensor simulations [2,3] were essentially identical to the SPICE Macro Model (SMM) [4]. In the SMM approach, the MAGFET operation is emulated by the parallel connection of two conventional NMOSTs with associated external current-controlled current sources (CCCS) operating in the opposite direction [4]. The CCCS serve to produce the drain current imbalance Δi_D expressed as $\Delta i_D = S \cdot I_D \cdot B_Z$, where S is the relative magnetic sensitivity and I_D is the total MAGFET drain current. A split-drain MAGFET model based on the SMM approach has also been implemented recently in the VHDL-AMS language [5].

¹ N. Jankovic (E-mail: janko@elfak.ni.ac.yu),

² T. Pesic (E-mail: tatjana@elfak.ni.ac.yu), and

³ D. Pantic (E-mail: panta@elfak.ni.ac.yu) are with Faculty of Electronic Engineering Nis, Aleksandra Medvedeva 14, 18000 Nis, Serbia

There are two main drawbacks with the SMM approach. Firstly, the magnetic sensitivity S of the MAGFET is included as an external model parameter and its dependence on the device operating point e.g. the gate and the drain voltages V_{GS} and V_{DS} , respectively, is usually included as a polynomial approximation of measured data. Secondly, since the SMM is a static model, the dynamic MAGFET behavior in the presence of fast varying magnetic fields cannot be simulated. Both drawbacks effectively lower the accuracy of MAGFET modeling and have limited the application of the model.

To overcome these deficiencies, the authors have developed a new MAGFET model that does not involve external CCCS elements. The equivalent sub-circuit consists of only two magnetic-sensitive NMOSTs whose electrical characteristics are simulated by a modified non-quasi-static (NQS) MOST model [6,7] that includes the effects of Lorentz force. Three-dimensional (3D) numerical simulations of a MAGFET device were performed using ISE TCAD [8] to derive and evaluate the new model. The ability of the new model to predict MAGFET dynamic response to the time varying magnetic fields is also presented.

II. 3D NUMERICAL SIMULATIONS

A split-drain MAGFET with $L=125$ nm, $W=100$ μm , $t_{ox}=60$ nm gate oxide, and substrate doping $N_D=10^{15}$ cm^{-3} , is studied in this paper. A concave MAGFET mask layout and standard $1\mu\text{m}$ CMOS technology are adopted for process simulation, yielding $45\mu\text{m}$ wide drain regions separated by a $10\mu\text{m}$ oxide gap. The internal potentials and carrier distributions of the MAGFET in presence of the perpendicular magnetic field B_Z were then obtained using the 3D device simulator ISE DESSIS [8]. Fig. 1 shows the electric field distribution in the channel simulated for $V_{GS}=5\text{V}$, $V_{DS}=1\text{V}$ and $B_Z=100\text{mT}$, where B_Z was orientated in the z-axis direction. It can be seen that the electric field iso-lines are asymmetrical with respect to the (z,x) -plane at $y=0$. This asymmetry is caused by the accumulation of electrons in the upper channel region due to the influence of Lorentz force.

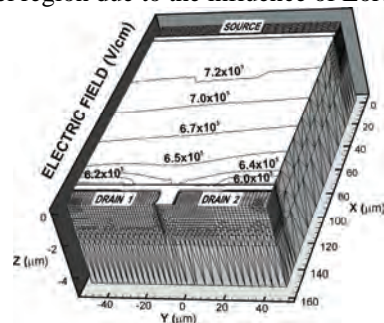


Fig.1 Electric field iso-lines in the MAGFET channel.

Let us define the steady-state excess concentration of electrons Δn (in units of cm^{-3}) that is accumulated along the upper channel edge $y = -50\mu\text{m}$ (Fig.1) as:

$$\Delta n(x, B_Z) = n(x)|_{B_Z} - n_0(x)|_{B_Z=0} \quad (2)$$

where $n(x)|_{B_Z}$ and $n_0(x)|_{B_Z=0}$ are the electron concentrations with and without the presence of magnetic field B_Z , respectively. For constant V_{GS} and V_{DS} , it is assumed that the same amount of electrons have been deflected from the lower channel edge $y=50\mu\text{m}$ (Fig.1). From 3D device simulations, $\Delta n(x, B_Z)$ was extracted at different points along the channel e.g. $x = 30\mu\text{m}$, $60\mu\text{m}$ and $90\mu\text{m}$ corresponding to $L/4$, $L/2$, and $3L/4$, respectively. The variation of $\Delta n(x, B_Z)$ with the magnetic field B_Z extracted for constant channel positions from numerical simulations is shown in Fig. 2.

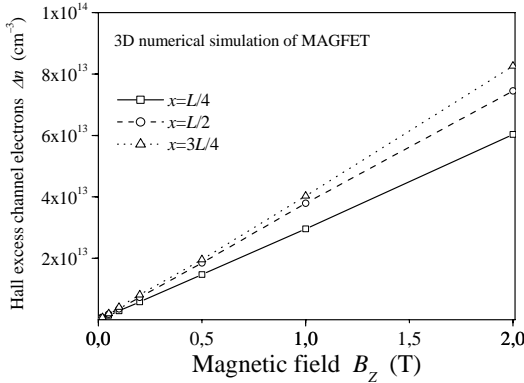


Fig.2 Excess electron concentration Δn versus the magnetic field B_Z extracted for different channel points at $y=-50\mu\text{m}$, $z=0$.

A general linear dependence of $\Delta n(x, B_Z)$ on B_Z is obtained as seen from Fig.2 and the difference $\Delta n(L, B_Z) - \Delta n(0, B_Z)$ is noted to be small even at very high B_Z . Neglecting the latter, we can define an approximate relationship:

$$\Delta n(B_Z) \approx a \cdot B_Z \quad (3)$$

where a is a constant, of units cm^{-3}/T , whose numerical value depends on the geometry and technology of the particular MAGFET. This empirical relationship (3) forms the basis of the development of the new MAGFET model and is explained in more detail in the following section.

III. THE MAGFET MODEL

The operation of a split-drain MAGFET is usually approximated with two identical NMOSTs operating in parallel. It is well known that the carrier transport through conventional MOSTs can be accurately modeled with the equivalent n -segment RC transmission line [6,7]. In the case of a MAGFET device, the channel transport has to be represented with two identical RC chains as illustrated in Fig. 3. Depending on the sign (\pm) of the applied perpendicular magnetic field B_Z , the equivalent resistors R_k in one of channel chains will simultaneously decrease or increase under the action of the Lorentz force due to carrier accumulation or

depletion, respectively. In the expressions underlying the NQS MOST model [16], it can be seen that the magnitude of R_k is inversely proportional to the square root of the substrate

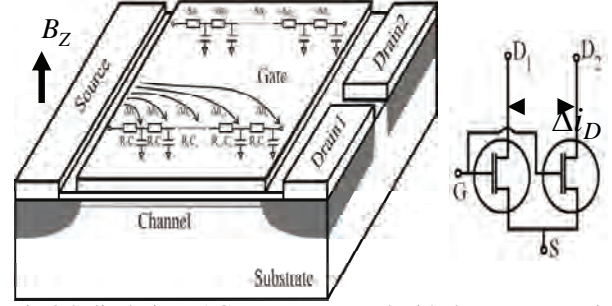


Fig.3 Split-drain MAGFET represented with the two magnetic sensitive NMOSTs

doping concentration e.g. $\sqrt{N_{beff}}$ (see eq. (A4) in Ref [7]). Hence, in order to include magnetic effects into the NQS MOST model [7], we will use an empirical relation (3) assuming that the magnetic field B_Z effectively modulates the parameter N_{beff} by adding or subtracting $\Delta n(B_Z)$. Consequently, the new effective substrate doping variable N'_{beff} will appear instead of the N_{beff} parameter in the NQS MOST model [7] as:

$$N'_{beff} = N_{beff} \pm \Delta n(x, B_Z) = N_{beff} \pm a \cdot B_Z \quad (4)$$

where the $+$ and $-$ signs stand for the different directions of carrier deflection in one of the NMOST channels as illustrated in Fig. 3. The relation (4) is the key modification to the NQS MOST model [7] and its efficiency in the accurate modeling of the MAGFET will be demonstrated in Section IV. The constant a appearing in (4) is a new fitting parameter for magnetic sensitivity used to calibrate the model. When $B_Z=0$, the MAGFET model reverts to the original NQS MOST model [7]. Unlike the SMM approach [4], the relative sensitivity S in the new MAGFET model is calculated a posteriori from simulated electrical characteristics, much the same as it is extracted during experimental MAGFET measurements.

IV. MODELING RESULTS AND DISCUSSION

The new MAGFET model is implemented in SPICE in the form of a sub-circuit with two NMOSTs as illustrated in Fig.3. The magnetic field is represented with a separate voltage generator sourcing a voltage equal in magnitude to B_Z . This voltage source drives a special “magnetic” node in the MAGFET sub-circuit that connects B_Z with the N'_{beff} variable of the modified NQS MOST model following relation (4).

A. Steady-State Analysis

The new model was first calibrated to fit the electrical characteristics of a MAGFET obtained from the 3D device simulator ISE DESSIS for the case of $B_Z=0$. Thus, Fig.4 shows the modeled drain current imbalance $\Delta i_D = I_{D1} - I_{D2}$

versus B_z , together with the numerical results. The experimental data of R. R.-Torres et al. [10] is also included in Fig.4 for reference. In addition, Fig.5(a) and Fig.5(b) show the dependences of the relative magnetic sensitivity S on voltages V_{GS} and V_{DS} , respectively, calculated for $B_z = 100\text{mT}$ from the simulated electrical characteristics of the MAGFET. A good agreement is obtained between the modeling results and the numerical simulations for wide range of MAGFET biasing conditions as shown in Fig.5.

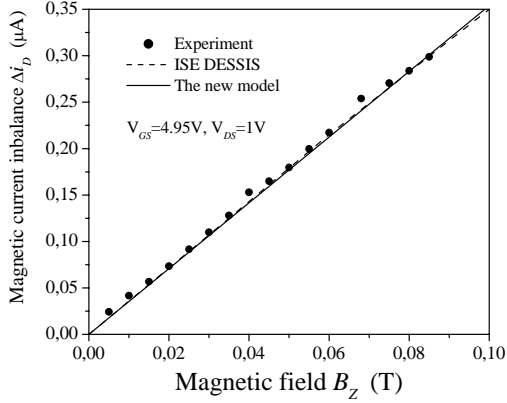
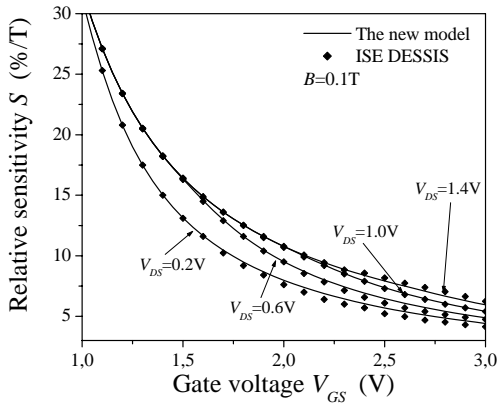
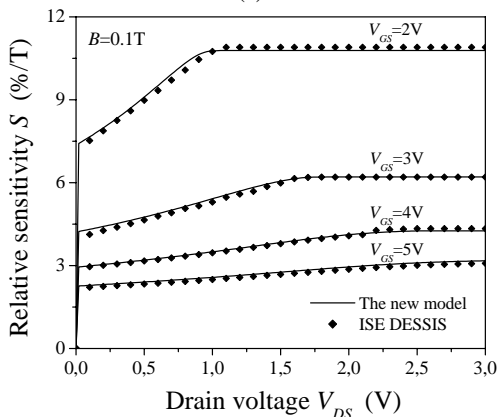


Fig.4 Comparisons of simulated, modeled and experimental MAGFET current imbalance Δi_D versus the magnetic field B_z . The experimental data were taken from Ref. [10].



(a)

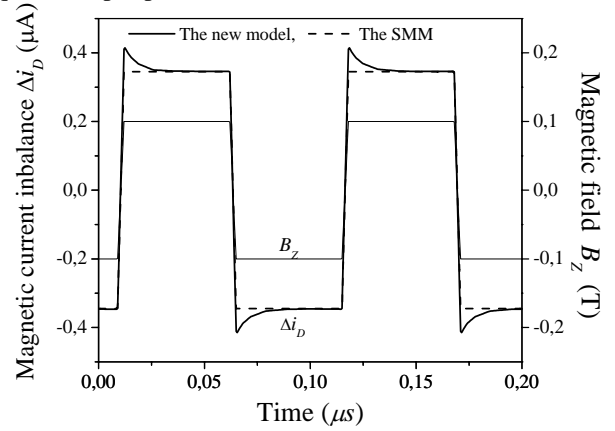


(b)

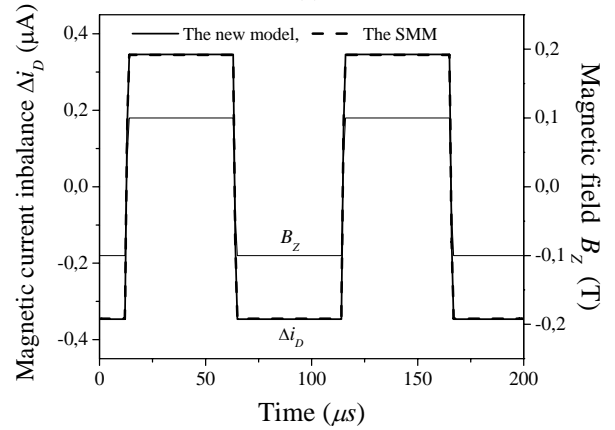
Fig.5 Relative sensitivity S of MAGFET versus: (a) the gate voltage V_{GS} and (b) the drain voltage V_{DS} extracted from 3D device numerical simulations and from the new model

B. The MAGFET dynamic performance

Unfortunately, the present version of ISE DESSIS [8] cannot perform an electrical device simulation for the case of a time varying magnetic field $B_z(t)$. In addition and to the best of our knowledge, only one set of experimental data has been published in relation to the dynamic performance of split-drain MAGFETs under the influence of a pulsed magnetic field [9]. Consequently, we can only demonstrate here the advantages of the new MAGFET model over the SMM approach [4] in predicting MAGFET dynamic behavior. For proper comparison, the NMOSTs of the SMM [4] are taken to be identical to the ones used in the sub-circuit of the new MAGFET model. Also, in order to obtain the same maximal Δi_D response in both models, the relative sensitivity S found for given values of B_z , V_{GS} and V_{DS} in the new MAGFET model simulations were subsequently used as the pre-requested input parameter of the SMM [4].



(a)



(b)

Fig.6 Drain current imbalance Δi_D of MAGFET simulated with the new model and with SSMM in case of pulsed B_z signal with: (a) 3ns rise/fall times and (b) 1 μm rise/fall times.

Let us assume that the MAGFET is subjected to an extremely steep B_z pulsed signal with 3ns rise/fall times. Then, the simulated pulsed response $\Delta i_D(t)$ is as shown in Fig. 6.a. As it can be seen, the new MAGFET model yields transient peaks in the simulated response, whereas these peaks do not appear in the $\Delta i_D(t)$ pulses obtained with the SMM [4]. Note that the $\Delta i_D(t)$ peaks would be expected in reality due to

the transient charging of channel distributed capacitance before reaching steady-state conditions. This conclusion can be indirectly confirmed from the results shown in Fig.6.b. Namely, for substantially slower B_Z pulses, the transient peaks are small, becoming negligible if plotted on a long time-scale. Hence, the device response $\Delta i_D(t)$ from the new MAGFET model to the slow B_Z pulses with $1\mu\text{s}$ rise/fall times and the response of the SMM [4] will be in better agreement as shown in Fig.6.b.

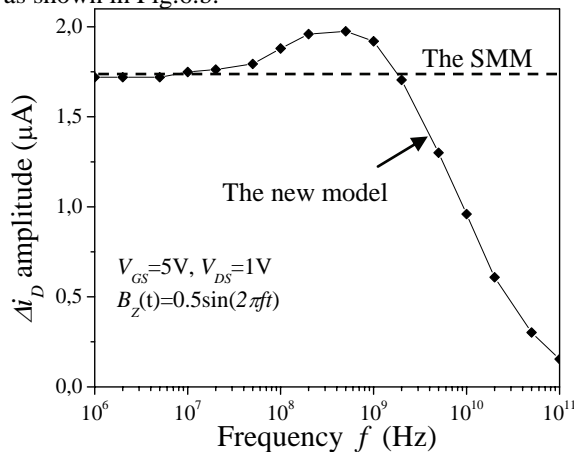


Fig.7 Drain current imbalance amplitude Δi_D of MAGFET versus frequency f in case of the sinewave magnetic signal B_Z simulated with the new model and with SSMM.

Fig.7 shows the simulated frequency characteristics of the $\Delta i_D(t)$ response obtained for $V_{GS}=5\text{V}$ and $V_{DS}=1\text{V}$ from the new MAGFET model. For the purposes of the simulation, a sine-wave magnetic field of $B_Z = 0.5 \cdot \sin(2\pi \cdot f \cdot t)$ in units of Tesla with variable frequency f is assumed. Fig.7 clearly indicates the existence of some limiting frequency f_i for which the MAGFET sensitivity drops to zero. In contrast, the SMM [4] is not able to predict any frequency response limitations of MAGFET sensitivity as illustrated by the dashed line in Fig.7. It is important to emphasize that the limited bandwidth of MAGFET sensitivity is a more natural simulation result, since f_i commonly appears in the sensitivity characteristics of other sensors in different signal domains [12]. A rather high f_i of around 70 GHz is predicted in Fig.7 in the new model, most likely due to the assumption of an ideal MAGFET device. A much lower f_i would be expected due to the influence of the device geometry, noise, and offset [13] as well as the presence of parasitic RC elements in practical MAGFETs. These non-idealities are not included in the present model. The model also predicts a slight increase of $\Delta i_D(t)$ appearing at high frequencies of B_Z as shown in Fig.7. From the Fourier analysis, we found that the $\Delta i_D(t)$ sinewave response of MAGFET in case of large B_Z swing has been distorted at high frequencies by the appearance of additional harmonics which slightly increases the overall output signal amplitude. Since, for small amplitude of B_Z signal the $\Delta i_D(t)$ overshoot is negligible, we can attributed this effect to the highly nonlinear model equations describing the RC elements. Whether the effect exists in practical device frequency characteristics or it

stems from model approximations can be only verified by the experiments.

V. CONCLUSIONS

A new MAGFET model consisting of only two magnetic sensitive NMOSTs in the equivalent sub-circuit is described in this paper. The new model developed is based on the non-quasi-static (NQS) MOST model of conventional NMOSTs, modified to include the effects of Lorentz force. Based on 3D numerical device simulations, it is shown that the new model can accurately predict the absolute and relative MAGFET sensitivity for different biasing conditions of the device. It is also shown that unlike the widely used SMM, the new MAGFET model is able to simulate the device dynamic response to time varying magnetic fields far more realistically.

REFERENCES

- [1] R.S. Popovic, *Hall Effect Devices*, Taylor & Francis; 2nd edition (2003)
- [2] C. Rubio, S. Bota, J.G. Macias, J. Samitier, "Monolithic integrated magnetic sensor in a digital CMOS technology using a switched current interface system", *Proc. IEEE Instrumentation and Measurement Technology Conference*, 2000, pp. 69-73
- [3] C. Rubio, S. Bota, J. G. Macias and J. Samitier, "Modelling, design and test of a monolithic integrated magnetic sensor in a digital CMOS technology using a switched current interface system", *Journal of Analog Integrated Circuits and Signal Processing*, Vol. 29, 2001, pp. 115-126
- [4] Shen-Iuan Liu Jian-Fan Wei Guo-Ming Sung "SPICE macro model for MAGFET and its applications" *IEEE Transactions on Circuits and Systems II: Analog and Digital Signal Processing*, Volume: 46, 1999, pp. 370-375
- [5] M. Zawieja, A. Napieralski, J. J. Charlot, "Application of VHDL-AMS Language for simulation of magnetic sensors", *Proc. TCSET'2002*, Lviv - Slawsko, Ukraine, 2002, pp 345-349
- [6] T. Pesic T, N. Jankovic "Physical-based non-quasi static MOSFET model for DC, AC and transient circuit analysis", *Proc. 24th International Conference on Microelectronics, MIEL'04*, Vol. 1: 2004. pp. 261-264
- [7] T. Pesic T, N. Jankovic, "A compact non-quasi-static MOSFET model based on the equivalent non-linear transmission line", *IEEE Trans. on Computer-Aided Design of Integrated Circuits and Systems*, Vol.24, 2005, pp. 1550-1561
- [8] ISE TCAD – Users Manual, Release 7.0, *Integrated System Engineering AG*, Zurich, Switzerland
- [9] E. A. Gutierrez-D, E. Torres-R, T, R. Torres, "Magnetic sensing as signal integrity monitoring in integrated circuits", *Proc. of Solid-State Device Research Conference (ESSDERC '05)*, Grenoble, France, 2005, pp. 277 – 280
- [10] R. R.-Torres, E. A. G.-D., R. Klima, S. Selberherr, "Analysis of split-drain MAGFETs", *IEEE Trans. Electron Devices*, Vol. 51, No. 12, 2004, pp. 2237-2245
- [11] J. W. Nilsson and J. R. Evans, *PSpice Manual Using Orcad Release 9.2 for Introductory Circuits*. Upper Saddle River, NJ: Prentice-Hall, 2002
- [12] S. Soloman, *Sensors Handbook*, McGraw-Hill Professional (1998)
- [13] G.-M. Sung and S.-I. Liu, "Error correction of transformed rectangular model of concave and convex MAGFETs with AC bias", *IEE Proc.-Circuits Devices Syst.*, Vol. 151, No. 6, 2004, pp.593-600

Reduced Data Sample Transmission – Implementation to PIC Microcontroller

Mile I. Petkovski¹ and Cvetko D. Mitrovski²

Abstract – In this paper, an implementation of simple adaptive sampling algorithm to the general purpose microcontroller is presented. Algorithm is based on the multi-resolution signal analysis using Haar wavelet. As a target system Microchip PIC 16F877A microcontroller on a single chip is used. The algorithm for signal acquisition and adaptive sampling is deployed to the microcontroller's flash memory and tested. Possible applications are explored and studied.

Keywords – Discrete Wavelet Transform, Microcontrollers.

I. INTRODUCTION

The principal problems of signal analysis are analogue signal sampling and their reconstruction (or approximation) on basis of their discrete samples. In the conventional distributed autonomous measuring systems, the common practice is based on the Nyquist sampling theory. This means that the measured signals are converted to the series of equally spaced samples, preprocessed in the distributed measuring system, and passed to the host computer via a serial channel for collecting, storing and for further processing [1].

The available storage capacity and the energy consumption of the distributed measuring systems in some cases are primarily limiting factors [2], which motivate to develop new algorithms based on adaptive sampling [3], and/or sampling and transmission of samples only at instances of time when the signals exhibit nonlinear changes of the slope. The last means reduction of the number of transmitted samples in Nyquist sense, but sufficient for the satisfactory signal reconstruction.

In the paper we propose a design of a system which transmits a subset of the regularly sampled signals, on basis of which the original signal could be satisfactorily reconstructed..

Section II presents theoretical background and basic idea for reduced data transmission. Section III describes the target system for algorithm implementation and section IV graphically presents experimental results.

II. THEORETICAL BACKGROUND

A. Wavelet Packets

Time localization at high frequencies can be enhanced by wavelet packets decomposition. Here approximations as well as detail coefficients are successively decomposed by Mallat's algorithm creating a binary decomposition tree. Each leaf corresponds to a certain frequency. In the orthogonal wavelet decomposition the information lost between successive approximation is captured in the detail coefficients; successive details are never reanalyzed. In the case of wavelet packets each detail coefficient vector is decomposed in two parts using the same approach as in approximation vector splitting (Fig. 1) which offer the richest analysis.

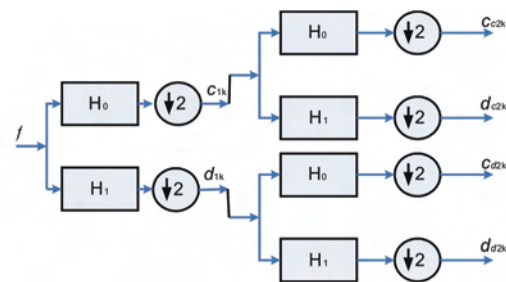


Fig. 1. Wavelet packet decomposition tree.

B. The Adaptive Signal Transmission

The idea of adaptive signal transmission is to transmit only the samples (of the regularly sampled signal) at the instances where the signal exhibits nonlinear changes. Hence the transmitted signal $\mathbf{y} = [y_0 \ y_1 \dots \ y_{P-1}]^T$, is composed from the samples of the uniformly sampled signal $\mathbf{x} = [x_0 \ x_1 \dots \ x_{N-1}]^T$ by omitting samples with indexes that correspond to instances of linear changing of the analogue signal. Although the size of \mathbf{y} is less than the size of \mathbf{x} ($P < N$), The analogue signal could be satisfactorily reconstructed by using first order hold circuit.

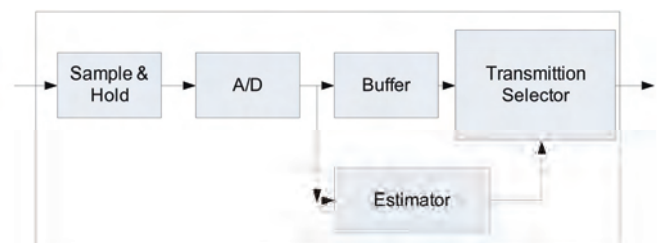


Fig. 2. Adaptive sampling block diagram

¹Mile I. Petkovski is with the Faculty of Technical Sciences, I.L.Ribar bb, 7000 Bitola, Macedonia, E-mail: m.petkovski@ieee.org

²Cvetko D. Mitrovski is with the Faculty of Technical Sciences, I.L.Ribar bb, 7000 Bitola, Macedonia, E-mail: cvetko.mitrovski@uklo.edu.mk

The basic idea is illustrated via the following example. A uniformly sampled signal composed of 32 samples is shown in Fig. 3a.

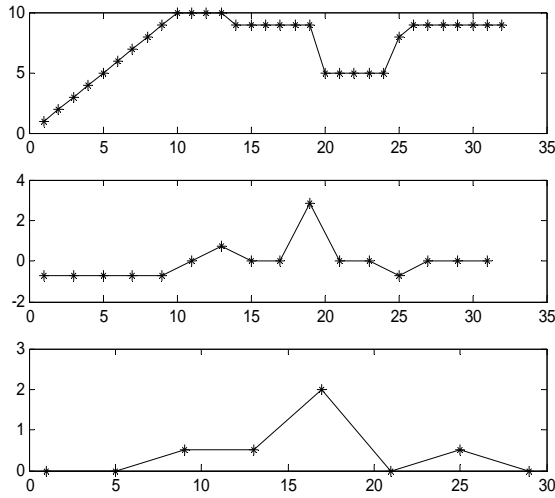


Fig. 3. a)Signal used for algorithm explanation; b) Detail coefficients of DWT; c) Absolute values of detail coefficients of DWT of previously obtained details.

Detail coefficients obtained as a result of discrete Haar wavelet transform of the original signal represent the difference between two successive samples multiplied by a factor of $2^{-1/2}$ (Fig. 3.b).

If the successive samples belong to a linear function the detail result will be a constant. At the second step of decomposition of details coefficients, the two successive constant coefficients will generate zero value coefficients, Fig. 3.c. This leads to the idea, that the decomposition of detail coefficients represents could be used to determine the instances when the transmission of the samples should occur.

The lower the absolute value of the detail coefficients at the second stage of the discrete Haar wavelet transform of the detail coefficients correspond to lower transmission rate of the signal and vice versa..

III. TARGET SYSTEM DESCRIPTION

A. Basic Characteristics of PIC16F877A

In this section we describe the basic features of the microcontroller used for our experiment and the parts of the controller which play the most important rule in this work[4].

Microcontroller basic core features are:

- High Performance RISC CPU
- 35 single word instruction set
- All; single cycle instructions except for program branches which are two cycles
- Operating speed DC – 200ns instruction cycle
- Up to 8k x 14 words of Program Memory
- Up to 368 x 8 bytes of data Memory (RAM)
- Up to 256 x 8 bytes of EEPROM data Memory

- 10 bit multi-channel Analog to Digital (A/D) converter
- Universal Synchronous Asynchronous Receiver Transmitter (USART)

It is important to refer to the fact that the smaller microcontrollers in the same family have the same instruction set. This can be an advantage to contribute to the portability of the source code.

The Analog-to-Digital (A/D) Converter module has eight multiplexed inputs for PIC 16F877A microcontroller, out of which we use only one for the experiment.

Fig. 4 shows an analog input model.

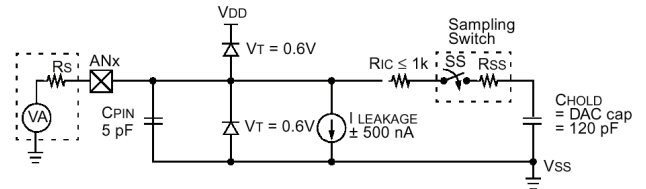


Fig 4. Analog input model.

The A/D conversion as result of successive approximation of the analog input signal corresponds to 10 bit digital number.

The acquisition time which is important to determine the upper sampling frequency can be calculated by the following expressions:

$$T_{ACQ} = (Amplifier\ SettlingTime) + (HoldCapacitorChargingTime) + (TemperatureCoefficient) \tag{2}$$

$$T_{ACQ} = 2\mu s + 16.47\mu s + [(50^\circ C - 25^\circ C)(0.05\mu s / ^\circ C)] = 19.72\mu s$$

The A/D Conversion time per bit is defined as T_{AD} . The A/D conversion requires a minimum $12T_{AD}$ per 10 bit conversion. In our case the internal RC oscillator is used and the typical T_{AD} time is $4\mu s$. [4]

B. Experimental system

The schematic diagram of the input circuitry is presented in Fig. 5. Sensor - potentiometer produce DC voltage signal depending of the measured value. That signal is sent to the microcontroller analog pin for A/D conversion.

Signal generated by the sensor circuit , is in the range of [0 - 5 VDC], and is delivered to the PIC analog port for further A/D conversion. After performing a double level decomposition i.e. discrete wavelet transform, through the High-Pass filtering and down-sampling, transmitting rate estimation and the resulted non-uniformly, adaptive sampled signal is transmitted to the PC for further observing using serial communication port which is supported by the microcontroller hardware and RS232 level converter.

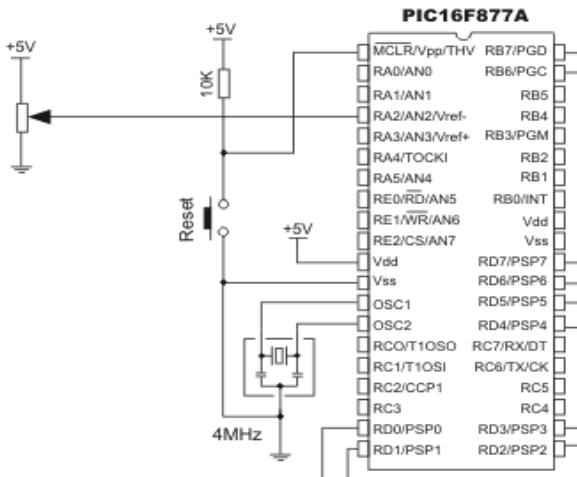


Fig. 5. Schematic Diagram for A/D conversion.

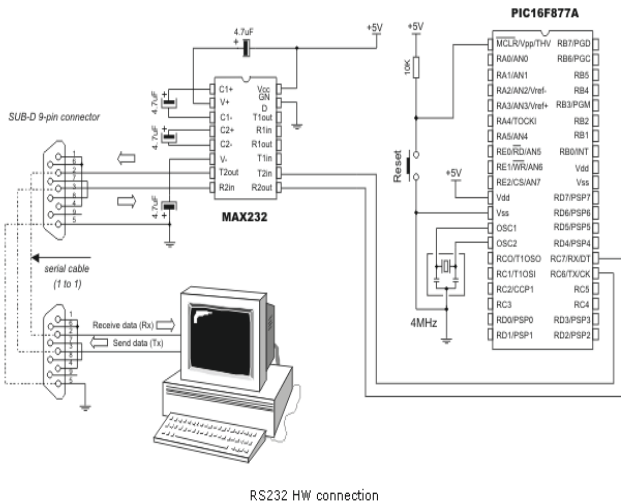


Fig. 6. Schematic Diagram for serial communication.

The system for serial communication is depicted in Fig. 6.

C. The Implemented Algorithm

Program downloaded to the microcontroller non-volatile memory consist of three integral parts as follows: Signal acquiring, where analog signal is converted to digital form and storage the sequence to microcontroller's RAM; Signal processing, where a two successive Haar Discrete Wavelet Transforms are performed, and transmission rate determining according to obtained results; Signal transmission through serial communication port.

The next block diagram graphically describes the Implemented algorithm with enhanced details to second part mentioned above.

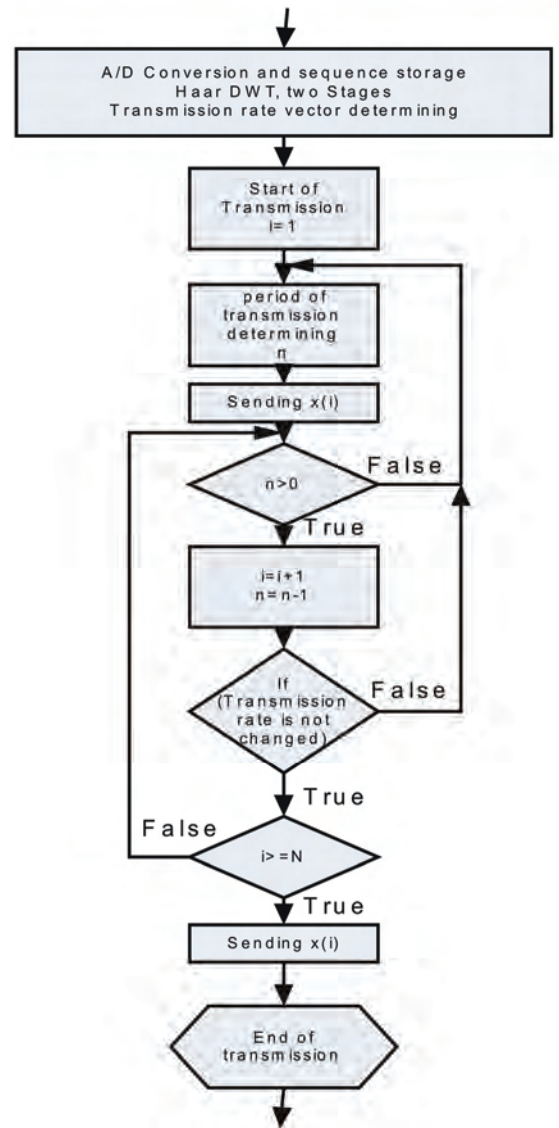


Fig. 7. Block diagram of proposed algorithm

IV. EXPERIMENTAL RESULTS

Analog signal generated by the sensor is uniformly sampled and stored into the microcontroller's RAM. Fig.8 shows 64 bits uniformly sampled signal acquired by the microcontroller. That signal is sent to the host computer for further comparison with reconstructed signal in the latter phase of experiment.

Due to the small amount of storage, only the detail coefficients are calculated in the first stage of discrete Haar wavelet transform (Fig. 9). The further processing and the estimation of the instances at which the samples are permitted (prevented) to be transmitted require another Haar discrete wavelet transform performed to the detail coefficients, as illustrated in Fig. 10.

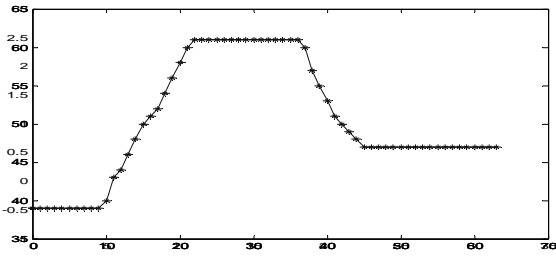


Fig. 8. Uniformly sampled signal generated by the sensor

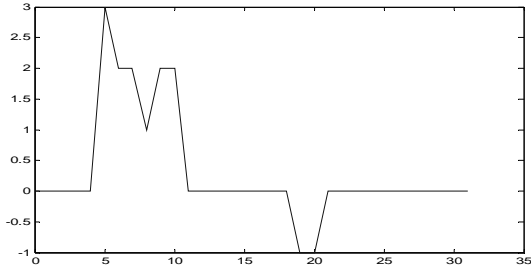


Fig. 9. Detail coefficients of DWT

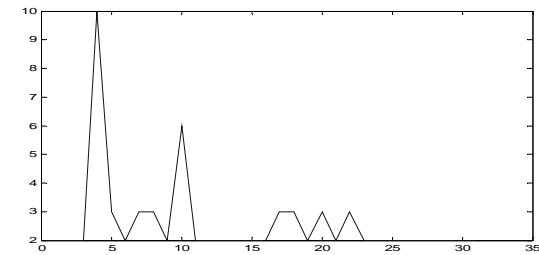


Fig. 10. Absolute value of second stage DWT coefficients

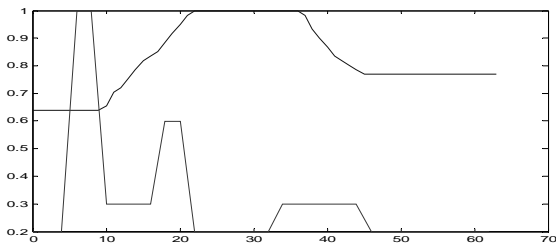


Fig. 11. Transmission rate estimation

According to results illustrated in Fig.11, the transmission rate is estimated. The higher values correspond to shorter sampling period and vice versa. The samples of the transmitted signal are shown in Fig. 12.

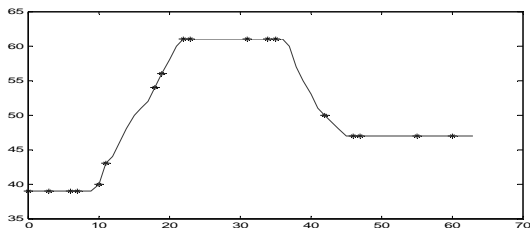


Fig. 12. Adaptive transmitted signal (asterisk) and original signal (solid line)

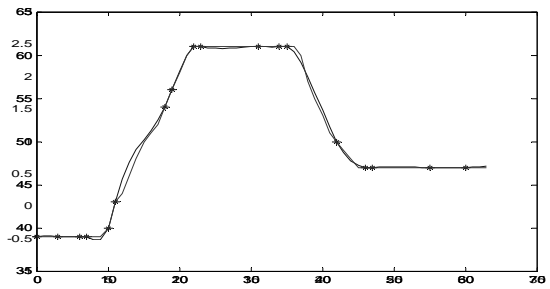


Fig. 13. Reconstructed and original signal

On basis of the transmitted samples the analogue signal could be reconstructed in the host computer either by using first order hold circuit, or by using more complex algorithms for interpolation, such as cubic spline, illustrated in Fig. 13.

V. CONCLUSION

Experimental results shows that the adaptive sampling algorithm is not complex for implementation to the PIC microcontroller. Small storage resources can be exceeded using the same memory locations for the different stages of discrete wavelet transforms.

Possible applications could be extended to wireless sensor subsystems where the reduced number of transmitted samples solution have great impact on energy consumption.

VI. REFERENCES

- [1] J. Gajda, R. Sroka, M. Stencel, A. Wajda, and T. Zeglen, "A Vehicle Classification Based on Inductive Loop Detectors," *IEEE Instrumentation and Measurement Technology Conference*, Budapest, Hungary, May 21 – 23, 2001.
- [2] R. Jaskulke and B. Himmel, "Event-Controlled Sampling System for Marine Research," *IEEE Transactions on Instrumentation and Measurement*, vol. 54, no. 3, June 2005.
- [3] M. Petkovski, S. Bogdanova and M. Bogdanov, "A Simple Adaptive Sampling Algorithm", *14th Telecommunications forum TELFOR 2006*, Serbia, Belgrade, November 21 – 26, 2006.
- [4] DS30292B, *PIC16F87X, 28/40-pin CMOS FLASH Microcontrollers*, 1999 Microchip Technology Inc.

SESSION PTDS&EM

Power Transmission and Distribution Systems II &
Electrical Machines

Fast High Voltage Signals Generator for Low Emittance Electron Gun

Martin Paraliev¹

Abstract – The construction of X-ray Free Electron Lasers (XFEL) requires high brightness, low emittance, monoenergetic, relativistic electron beams. In order to achieve those parameters and to reduce scale of needed accelerator facilities, alternative electron sources should be designed. This article is to describe the progress of the 500kV pulser dedicated to provide HV signals for cold (field) emission based cathodes test bed.

Keywords – High Voltage, Low emittance, 500kV Pulse Generator, High gradient electron acceleration, Tesla coil.

I. INTRODUCTION

To reduce size and cost of XFELs better quality electron sources are needed, capable of producing high brightness, low emittance, monoenergetic electron beams and to preserve those parameters during acceleration. Low Emittance electron Gun (LEG) project at Paul Scherrer Institut (Switzerland) is dedicated to the studies of an alternative low emittance electron sources based on cold (field) electron emission and high gradient acceleration [1]. In order to achieve the needed surface electric field for cold emission, and the necessary acceleration gradient to prevent space charge-driven beam emittance degradation, high voltage (HV) should be applied across anode-cathode gap. To decrease the probability of a vacuum breakdown the HV pulse should be short. The current task is to design and to construct a HV pulse generator to test and to optimize cold emission based electron sources. The next step is, based on this design, to develop a LEG injector for a XFEL.

The behavior of the field emitted current from vacuum-conductor interface is described by Fowler-Nordheim equation (1), [2], [3] and [4]:

$$J(E, \phi) = A \frac{e^{B\phi^{-1/2}}}{\phi} E^2 e^{C\phi^{3/2}/E} \quad (1)$$

where J is emitted current density in A/m^2 , A , B and C are constants ($A = 1.4 \times 10^{-6}$, $B = 9.85$, $C = -6.53 \times 10^9$), E is electric field in V/m (including the field enhancement factor) and ϕ is work function of emitting material in eV. Relative sensitivity of the field emission process $\frac{\Delta J}{J}$ in function of the relative

change of electric field $\frac{\Delta E}{E}$ is given by equation (2). The shot-to-shot voltage stability is set by the requirement emitted current variation to be less than 10%. For the targeted current ($\sim 5A$) emitted by ZrC ($\phi_{ZrC} \approx 3.5 eV$) single tip (emitting area $\approx 0.5 \mu m^2$) the surface electric field (including the field enhancement factor) should be in the range of 7GV/m and the relative voltage shot-to-shot stability should be better than 1%.

$$\frac{\Delta J}{J} = \frac{dJ}{dE} \frac{E}{J} \frac{\Delta E}{E} \quad (2)$$

The electric gradient, for the first phase of the project, was set to 125MV/m (500kV across 4mm anode-cathode gap). A direct connection to the ground potential will be beneficial because it will allow future development including adding a fast gating impulse and testing of multi layer cathode array structures with additional DC focusing.

This HV pulse generator is to be used for testing of different field emitting (FE) structures (single emitting tips, FE arrays, laser-assisted FE cathodes). In addition, operating experience will be used for a design of a higher voltage (1MV) pulse generator for a future XFEL low emittance electron injector facility.

Table 1. Advantages and disadvantages of considered pulsed technologies capable of producing fast HV pulses

Technologies	HV	Stability and load	Short/Single pulse	Scalability	Variable output	Unipolar pulse	Long life	Direct contact	Low cost
Spark gaps	++	--	++	++	--	++	--	no	++
Semiconductor switches	--	++	-	-	++	++	++	no	-
Magnetic voltage adder	++	++	--	-	++	+	++	yes	--
Resonant circuit	+	+	--	++	++	--	++	yes	+
Coupled resonators (k=0.6)	++	+	++	++	++	-	++	yes	-
Transm. line based U adders	+	-	++	+	++	+	++	no	+
Nonlinear transmission lines	-	-	++	--	--	++	++	yes	--
Nonlinear magnetic transf.	++	+	+	--	--	-	++	yes	--

Different pulsed power technologies were considered for the HV pulse generation [5], [6]. Table 1. gives an overview of their advantages and disadvantages.

Critically coupled air-core resonant transformer was chosen to give the best engineering compromise for the particular application.

¹Martin Paraliev, Paul Scherrer Institut, 5232 Villigen PSI, Switzerland

II. RESONANT AIR-CORE TRANSFORMER

A. Critical coupling

In the particular design a rather unusual resonant configuration is used, where the resonant amplitude is built in one cycle only. To achieve this, primary and the secondary resonant circuits are tuned to the same frequencies and the coupling K between them is set to 0.6 (critical coupling). In this condition the transformer resonance is split in two spectral lines, with frequency of one twice the frequency of the other. The voltage of the secondary side (as well as in the primary) is a superposition of fundamental and second harmonic with zero phase difference between them.

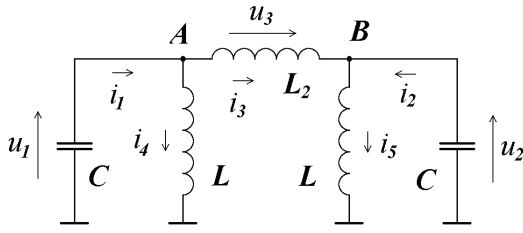


Fig.1. Equivalent circuit of an ideal air-core resonant transformer

The equivalent circuit shown on Fig. 1 is used to study analytically the behavior of the air-core resonant transformer. After referencing the secondary to the primary side the differential equation system (3) was derived. It describes analytically the behavior of the ideal transformer.

$$\begin{cases} \ddot{u}_1 + k_1 u_1 - k_2 u_2 = 0 \\ \ddot{u}_2 + k_1 u_2 - k_2 u_1 = 0 \end{cases} \quad (3)$$

where

$$L_2 = L \frac{1-K^2}{K} \quad (4)$$

$$k_1 = \frac{1}{LC(1-K^2)}, \quad k_2 = \frac{K}{LC(1-K^2)} \quad (5)$$

The solution of the differential system is given below [8]:

$$u_1 = \frac{U}{2} [\cos(\omega_1 t) + \cos(\omega_2 t)] \quad (6)$$

$$u_2 = \frac{U}{2} [\cos(\omega_1 t) - \cos(\omega_2 t)] \quad (7)$$

where

$$\omega_1 = \sqrt{\frac{1}{LC(1+K)}} \quad (8)$$

$$\omega_2 = \sqrt{\frac{1}{LC(1-K)}} \quad (9)$$

and ω_1 and ω_2 are the two resonant lines of the air-core transformer. The critical coupling factor K was analytically calculated for this ideal case using the condition $2\omega_1 = \omega_2$ [7]. The normalized voltage u_1 in the primary side and u_2 in the secondary one are shown on fig.2.

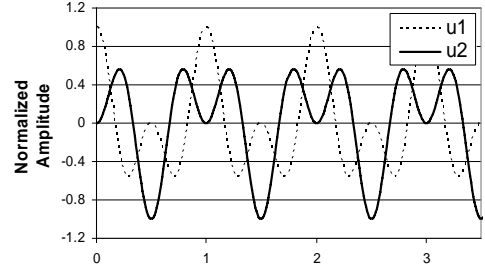


Fig. 2. Primary (u_1) and secondary (u_2) voltage signals of an ideal critically coupled ($K = 0.6$) resonant transformer

The lossy case was simulated (using pSpice®) to find the optimal values for coupling factor and tuning of a real transformer structure [7].

B. Transformer geometry

In order to achieve the necessary coupling without a magnetic core, the transformer geometry was studied. Scaled models and numerical simulations were employed to determine the optimum coil layout. Simulated and measured results from the reference layouts were in a good agreement. A single-turn primary around flat spiral secondary gave the best coupling for given transformer dimensions and coils' conductor cross-sections. An interesting observation was that the coupling factor does not depend much on the conductor's cross-section shape, but rather than the conductor's cross-section perimeter. In general, the larger conductor cross-section perimeter gives better coupling.

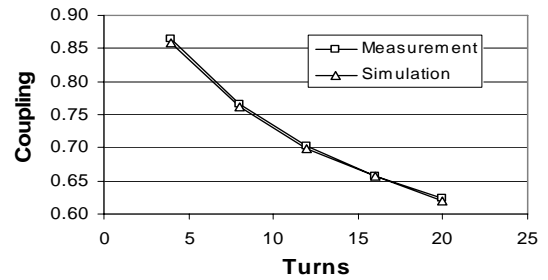


Fig. 3. Measured and simulated coupling factors of reference layouts as a function of secondary number of turns

C. Commutation

In order to keep the transformer pulse response fast the length of its secondary winding was kept as short as possible.

This adversely affects the transformer step-up ratio and requires higher primary voltage. The type of the switching element in the primary side was determined by the operating voltage, speed and life time requirements. There are basically two switch types suitable: thyratrons and spark gaps. In spite of their low cost, the spark gap technology was not used because of short life-time and jitter.

Two air-cooled thyatron switches are used to energize the resonant step-up transformer. They are connected in parallel to decrease the stray inductance. The thyratrons switch the charged primary capacitor to the primary transformer winding. A hollow anode thyatron (CX1725A) was chosen in order to tolerate reverse current. The thyratrons are placed in two electrically sealed aluminum boxes to screen the electromagnetic noise generated during commutation.

D. Construction

To ensure HV performance of the transformer, it is operated inside a pressurized tank with sulfur hexafluoride (SF₆) gas. The secondary coil is fixed in a grove machined on an insulating plastic base. Concentric undulations are machined on the back side of the transformer base to prevent surface discharges. The single-turn primary is 80mm copper strip wound around the secondary coil.

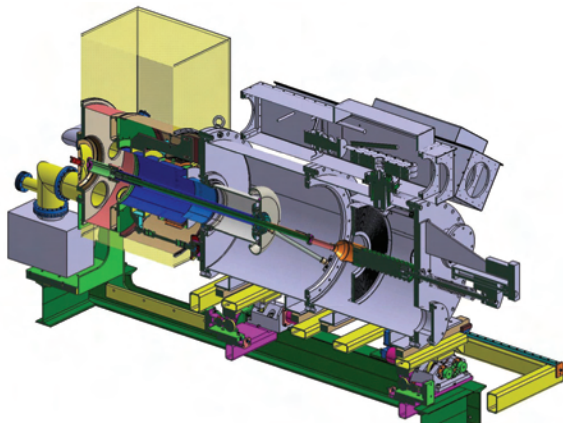


Fig. 4. Cross section of the HV pulse generator.

- a – thyatron, b – capacitor bank, c – feedthrough, d – HV transformer, e – pressure tank, f – vacuum feedthrough, g – middle stalk, h – vacuum chamber with anode and cathode

The primary capacitor is split in two capacitor banks, one in each thyatron box, and it is connected to the primary coil through low inductance gas-tight feedthrough. The secondary HV pulse is conducted by the middle stalk and through a large ceramic feedthrough is applied to the vacuum chamber. A removable cathode electrode is attached to the other end of the stalk. The anode-cathode separation is adjustable (0.30mm). The entire pressure tank is sitting on a precision 5-axes positioning system in order to control the location of the cathode with respect to the anode and the rest of the accelerating structures. Fig. 4. shows a cross section of the pulse generator 3D CAD model.

E. Electrical modelling

A detailed electrical model was made to study the HV pulse generator behavior. Numerical PC based simulator (pSpice®) was used to model the output waveforms and to define the optimum tuning of the resonant transformer.

F. Measured results

The first tests proved the capability of the pulser to deliver an HV pulse to the anode-cathode system. The designed pulse amplitude of -500kV (250ns FWHM) was reached successfully with 20% voltage margin. Fig. 5. shows a very good agreement of the measured and the simulated waveforms.

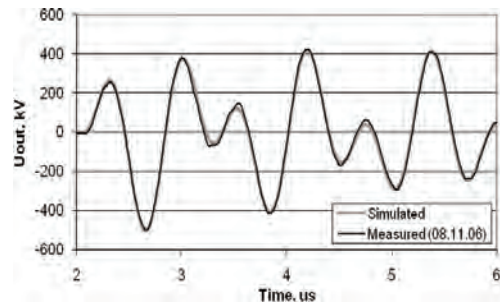


Fig. 5. Simulated and measured output waveforms

Due to mechanical modifications the secondary inductance was higher than the designed value. This shifted the tuning range of the transformer and made the tuning for critical coupling impossible.

To decrease the shot-to-shot variations due to pulsed charging supply voltage fluctuation an active amplitude stabilization system was built. The stability measurements of hundred consequent pulses (Fig. 6.) showed a reduction of shot-to-shot fluctuation from about 1.4% (stabilization off) to less than 0.4% (stabilization on).

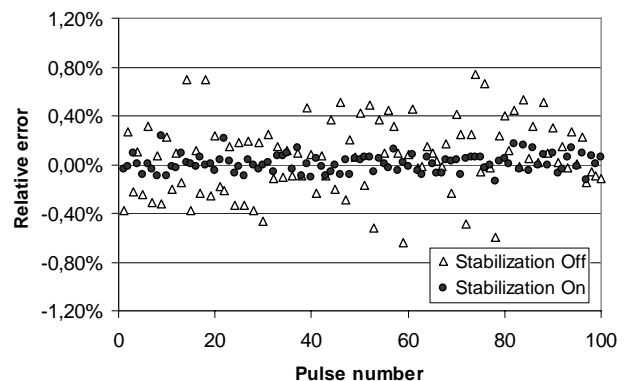


Fig. 6. Shot-to-shot stability measurement with and without active stabilization

G. Radiation safety

Due to HV potentials in the vacuum tank any parasitically emitted electrons are accelerated to high energies and their impact on the vacuum chamber will generate a shower of secondary electrons and high energy photons, including X-rays. In order to ensure the radiation safety for personnel, the HV pulse generator is situated in a bunker with 1m thick concrete walls. A built-in safety interlock system blocks the HV if there are people in the bunker.

The control electronics is placed in two 19" racks – one next to the pulser and the other in the control area. Fig. 7. shows the present position of the HV pulse generator in the bunker.

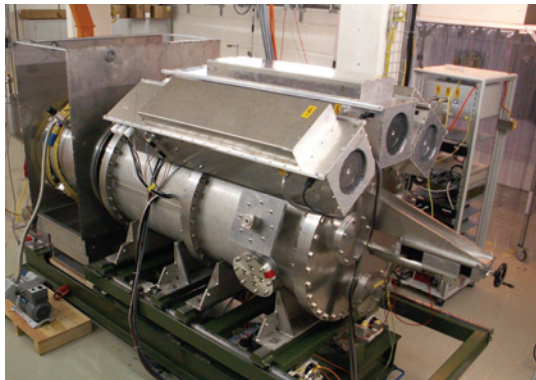


Fig. 7. The HV pulse generator and the control electronics rack in the concrete bunker

III. CURRENT TASKS

The HV transformer is being modified to decrease the secondary inductance. This will make the tuning for critical coupling possible and the positive peaks before and after the main pulse will be with the same amplitude.

There is an ongoing task to add a “tail biter” to cut-off the following oscillations. The electric simulations showed that it is possible to take the energy out of the system after the first cycle. Unlike common resonant systems, in critically coupled one the energy is fully exchanged between the resonators within one cycle. When the primary capacitor has maximum voltage, the currents in the inductors and the voltage over the secondary capacitance are zero. At this moment the entire energy of the system is in the primary side. With an additional switch to discharge quickly the capacitors, the energy is removed and the oscillations stop. A motorized spark gap is being built into the third aluminum box to prove the concept.

Measuring the output voltage of the pulse generator is not a trivial task. The standard RC dividers suitable for this voltage amplitude are large and with limited bandwidth. A capacitive divider is used to measure the HV pulse. It is used to monitor the output from the control area. An optical HV measurement system is being designed to give a second independent measurement of the output pulse. This serves to increase the reliability of the system in case of slow degradation or failure of the voltage monitor.

IV. SUMMARY

An extensive study was done to choose the most suitable technology for generating short HV pulses for cold emission cathode test bed. A critically coupled air-core transformer was chosen to give the best engineering compromise for this particular application. The behavior of coupled resonators was studied analytically and by simulations. The tuning and coupling of the transformer were parametrically optimized. Using scaled physical models and simulations, magnetic coupling of different transformer layouts were examined. The measured results of reference models were in a good agreement with the simulations. Based on these studies, a fast HV pulse generator was successfully designed and constructed. The tests confirmed that it is capable of reaching the designed pulse voltage amplitude of -500kV with pulse length of 250ns (FWHM). The stability studies showed shot-to-shot peak voltage fluctuations within 0.4%. This was utilized by employing an active voltage stabilization subsystem. A detailed equivalent circuit of the pulse generator was created in order to further optimize its performance. The measured output waveforms were in a very good agreement with the numerically generated ones. There is an ongoing task to prepare the pulse generator for the high gradient tests and, as well, to define the possible ways to upgrade the pulser towards 1MV goal.

ACKNOWLEDGEMENT

The constant support of our group leader C. Gough and the other pulsed magnets group's members S. Ivkovic and B. Weiersmueller is highly appreciated. The help provided by the construction department of PSI and especially by W. Pfister was essential for the project advancement.

REFERENCES

- [1] R. Abela, R. Bakker, M. Chergui, L. Rivkin, J. Friso van der Veen, A. Wrulich Ultrafast X-ray Science with a Free Electron Laser at PSI Field emission
- [2] F. Charbonnier, “Developing and using the field emitter as a high intensity electron source”, Applied Surface Science 94/95, 1996, p26-43
- [3] T. J. Levis, “Some Factors Influencing Field Emission and the Fowler-Nordheim Law” Proc. Phys. Soc. (London) 68B 938-43
- [4] K. Li, “Novel Electron Sources for a Low Emittance Gun”, Diploma thesis, institute for Particle Physics, ETH Zurich, 2004
- [5] C. Gough, M. Paraliiev, “Pulsed power techniques for the Low Emittance Gun (LEG)” PSI – Scientific and Technical Report 2003 Vol. VI, p. 76, Villigen PSI, Switzerland
- [6] C. Gough, Audit on High Voltage – High Gradient Generation for the PSI-FEL Project, Villigen PSI, 2007
- [7] M. Paraliiev, C. Gough, S. Ivkovic, Tesla Coil Design for Electron Gun Application, 15th IEEE International Pulsed Power Conference, Monterey, CA USA, 2005, p.1085-1088
- [8] F. L. H. Wolfs, Physics Lecture Notes 2004, University of Rochester, Rochester, NY 14627, USA

Effect of Perforation in High Power Bolted Busbar Connections

Raina T. Tzeneva¹ and Peter D. Dineff²

Abstract -The work reported describes how introducing perforation groups of two or three small holes in a proper way around the bolt holes in high power bolted busbar connections increases significantly the true contact area and therefore reduces contact resistance. The new design is compared with the classical one of bolted busbar connections by the help of several computer models. It has been estimated that the new case leads to a considerable rise of contact pressure and contact penetration in the contact interface between the busbars.

Keywords –Bolted busbar high power connections, Contact penetration, Contact pressure, Contact resistance, Groups of small holes, New hole shape.

I. INTRODUCTION

Steadily increasing energy consumption in densely populated regions imposes severe operation conditions on transmission and distribution systems which have to carry greater loads than in the past and operate at higher temperatures.

Power connections are generally the weak links in electrical transmission and distribution systems – both overhead and underground systems.

Mainly, there are two factors that affect the reliability of a power connection. The first is the design of the connection and the material from which it is fabricated. The second is the environment to which the connection is exposed.

The fundamental requirements for the design of reliable high-power connections used in bare overhead lines are given in [1]. The fundamental design criteria for power connectors are: maximization of electric contact true area, optimization of frictional forces with conductors (buses), minimization of creep and stress relaxation, minimization of fretting and galvanic corrosion, minimization of differential thermal expansion along and normal to interfaces. Summarizing the major connection design criteria, mentioned above it is worthwhile noting that all the criteria can be met simultaneously by working out an outline that achieves a sufficiently large contact load, a large area of metal-to-metal contact and sufficient elastic energy storage in the connection to maintain an acceptable connector's contact load throughout the service life of the connection.

II. THEORETICAL BACKGROUND

All joint surfaces are rough and their surface topography shows summits and valleys. Thus under the joint force F two joint surfaces get into mechanical contact only at their surface summits. Electrical current lines are highly constricted at the contact spots when passing through, as presented schematically in Fig. 1a. This constriction amplifies the electric flow resistance and hence the power loss. Obviously, the more the contact spots, the smaller the power loss at the interface of the conductors. Power connections with superior performance are designed to maximize both the number and the life of the contact spots.

For this reason, it is essential to keep in mind that the load bearing area in an electric joint is only a fraction of the overlapping, known as apparent area. Metal surfaces, e. g. those of copper conductors are often covered with oxide or other insulating layers. As a consequence, the load bearing area may have regions that do not contribute to the current flow since only a fraction of may have metallic or quasi-metallic contact and the real area of electric contact, i.e. the conducting area, could be smaller than the load bearing area (Fig. 1b) [2].

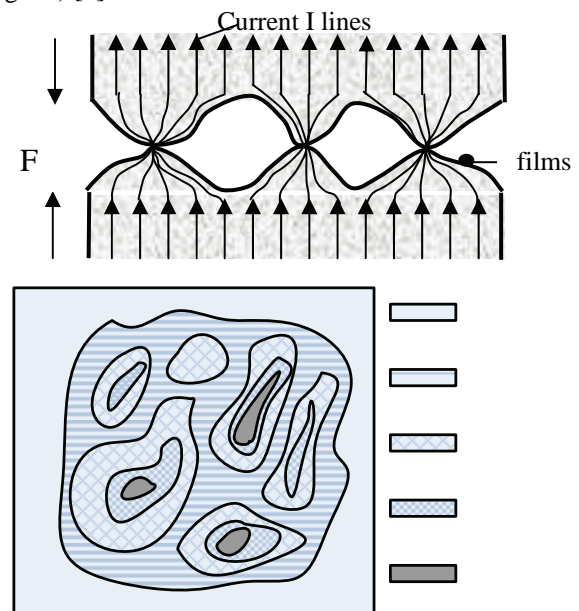


Fig. 1. a) Contact surface and current lines; b) Contact area with α -spots

A conducting area is referred to as quasi-metallic when it is covered with a thin ($< 20 \text{ \AA}$) film that can be tunneled through

¹ Raina T. Tzeneva is with the Department of Electrical Apparatus, Faculty of Electrical Engineering, Technical University of Sofia, 8 Kliment Ohridski, 1000 Sofia, Bulgaria, E-mail: tzeneva@tu-sofia.bg

² Peter D. Dineff is with the Department of Electrical Apparatus, Faculty of Electrical Engineering, Technical University of Sofia, 8 Kliment Ohridski, 1000 Sofia, Bulgaria, E-mail: dineff_pd@abv.bg.

by electrons. This quasi-metallic electric contact results in a relatively small film resistance R_f .

The summits of the two electric joint surfaces, being in metallic or quasi-metallic contact, form the so called α -spots where the current lines bundle together causing the constriction resistance R_c . The number n , the shape and the area of the α -spots are generally stochastic and depend on material parameters of the conductor material, the topography of the joint surfaces and the joint force. For simplicity it is often assumed that the α -spots are circular. Looking at one single circular α -spot its constriction resistance R_c depends on its radius a and the resistivity ρ of the conductor material.

III. MODELLIN BOLTED BUSBAR CONNECTIONS

In this paper, the mechanical changes, associated with the contact penetration depth and the contact pressure, in the contact area between two busbars in a high power bolted busbar connection are studied by the help of the finite elements simulation tool ANSYS Workbench. If a higher contact penetration increases α -spots both in numbers and dimensions, which in turn expands the true contact area and decreases contact resistance, then a new hole-shape could be introduced for this connection.

The new slotted hole shape arises from [3]. Boychenko and Dzekter have shown that changing the connection design can equally be effective in increasing the contact area. In other words, cutting longitudinal slots in the busbar, the actual surface area of a joint can be increased by 1.5 to 1.7 times of that without slots. The contact resistance of joint configuration with slots is 30-40% lower than that without slots and is mechanically and electrically more stable when subjected to current cycling tests [4], [5]. The beneficial effect of sectioning the busbar is attributed to a uniform contact pressure distribution under the bolt, which in turn, creates a larger contact area. This case is investigated in [6].

This idea is developed in [7], [8] and a new slotted hole shape for bolted high power connections is proposed. Fig. 2 shows the hole shape of the investigated 11 cases. Significant rise of the contact pressure and contact penetration is obtained.

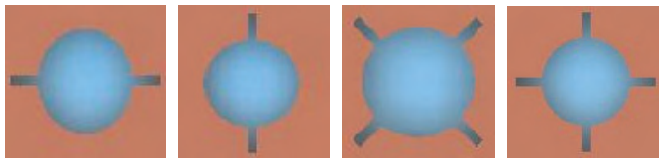


Fig. 2. Hole shape with 2 or 4 slots

Additionally a new shape of slotted holes in which the slots end with small circular holes is raised and investigated in [9] and illustrated in Fig. 3. Positive results for the contact pressure and contact penetration are obtained too.



Fig. 3. Hole shape with slots, ending with small circular holes

But to cut these thin slots in copper or aluminum busbars is a difficult procedure and in this investigation the slots are replaced by groups of two or four small holes.

For that purpose there have been investigated 13 different models.

case 1 – the classical case – copper busbars with 2 bolt holes;

case 2 – two horizontal groups of two holes of diameter $\varnothing 1\text{mm}$ and distance of 0.9mm between the holes, parallel to the busbar axis;

case 3 – two vertical groups of two holes of diameter $\varnothing 1\text{mm}$ and distance of 0.9mm between the holes;

case 4 – mixed – one of the busbars in the connection is of case 2 and the other is of case 3;

case 5 – eight groups of two holes of diameter $\varnothing 1\text{mm}$ and distance of 0.9mm between the holes, displaced at angle of 45 degrees;

case 6 – two horizontal groups of three holes of diameter $\varnothing 0.8\text{mm}$ and distance of 0.2mm between the holes, parallel to the busbar axis;

case 7 – two vertical groups of three holes of diameter $\varnothing 0.8\text{mm}$ and distance of 0.2mm between the holes;

case 8 – four groups (two horizontal and two vertical) of three holes of diameter $\varnothing 0.8\text{mm}$ and distance of 0.2mm between the holes;

case 9 – four groups of three holes $\varnothing 0.8\text{mm}$ and distance of 0.2mm between the holes, laying on two mutually perpendicular axes, rotated at an angle of 45 degrees in relation to the busbar axes;

case 10 – two horizontal groups of three holes of diameter $\varnothing 0.9\text{mm}$ and distance of 0.1mm between the holes ;

case 11 – two vertical groups of three holes of diameter $\varnothing 0.9\text{mm}$ and distance of 0.1mm between the holes;

case 12 - four groups (two horizontal and two vertical) of three holes of diameter $\varnothing 0.9\text{mm}$ and distance of 0.1mm between the holes;

case 13 - four groups of three holes $\varnothing 0.9\text{mm}$ and distance of 0.1mm between the holes, laying on two mutually perpendicular axes, rotated at an angle of 45 degrees in relation to the busbar axes;

Fig. 4 shows the hole shapes of the cases with two groups of small holes (cases 2, 3, 6, 7, 10 and 11).

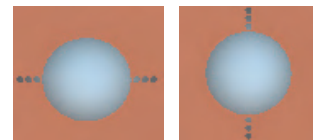


Fig. 4. Hole shape with 2 groups of small holes

Fig. 5 presents the new hole shapes with 4 and 8 groups of small holes (cases 8, 9, 12, 13 and 5).

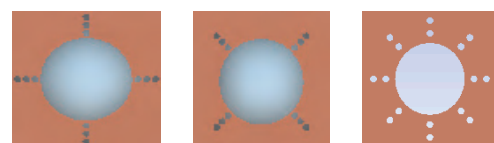


Fig. 5. Hole shape with 4 and 8 groups of small holes

The cases are suggested to: decrease radial loadings on bolts that emerge after the connection is assembled; increase the contact penetration in the busbars near the bolts area; maximize the true area of metal to metal contact in an electrical interface.

The investigated assembly consists of:

- Copper busbars (Young's modulus $E = 1.1 \cdot 10^{11}$ Pa, Poisson's ratio $\mu = 0.34$, width 60mm, height 10mm, length 160mm, busbars' overlap 60mm with 2 holes of $\varnothing 10.5$ mm;
- Fasteners: bolts – Hex Bolt GradeB_ISO 4015 – M10 x 40 x 40 – N, steel $E = 2.10^{11}$ Pa, $\mu = 0.3$; nuts – Hex Nut Style1 GradeAB_ISO 4032 – M10 – W – N, steel $E = 2.10^{11}$ Pa, $\mu = 0.3$; washers – Plain Washer Small Grade A_ISO 7092 – 10, steel $E = 2.10^{11}$ Pa, $\mu = 0.3$. Tension in each bolt $F = 15000$ N.

Models are studied for contact pressure and penetration within the busbars electrical interface.

Fig. 6 shows contact pressure for case 11. It is obvious that the pressure in the surrounding area of the perforation is increased significantly.

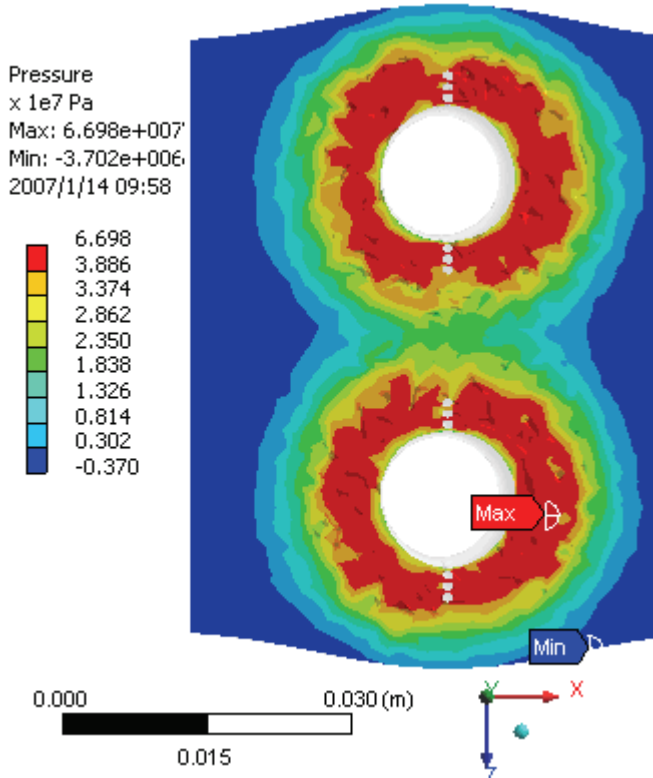


Fig. 6. Contact pressure for case 11 with 2 vertical groups of 3 small holes

Contact penetration for case 12 is shown in Fig.7. When the 4 groups of small holes are introduced the high penetration zone expands covering the region between the perforations.

All the thirteen cases have been evaluated by comparing the max values of pressure and penetration for each one of them as well as the percent participation of the 8 zones according to the legends. With that end in view, all zones are set to have equal upper and lower limits. The zones of highest pressure or penetration are set to equal lower limits while the max values define their upper limits. This comparison procedure is performed by the help of the Adobe Photoshop software,

where each colored zone is identified with a certain number of pixels. The results obtained are summarized in Fig. 9 and Fig. 10.

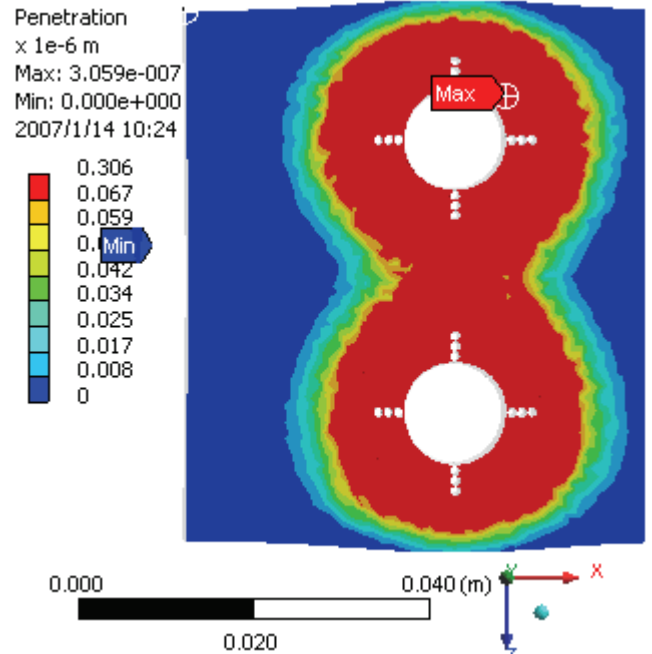


Fig. 7. Contact penetration for case 12 with 4 groups of 3 small holes

The aspect of model meshing is distinguished as a key phase for proper analysis of the problem. This is because on the one hand it is an established certainty that the reason for the good quality of physical space triangulation is closely related to the consistent mapping between parametric and physical space. On the other hand a properly meshed model will present a fairly close-to-reality detailed picture of stress distributions which is a hard task for analytical solution and is usually an averaged value. It is evident from Fig.6 and Fig.7, for the uneven allocation of pressure and penetration, that the perforated cases bring even more complexities.

The meshed model incorporates the following elements: 10-Node Quadratic Tetrahedron, 20-Node Quadratic Hexahedron and 20-Node Quadratic Wedge. Contacts are meshed with Quadratic Quadrilateral (or Triangular) Contact and Target elements.

IV. DISCUSSION AND CONCLUSIONS

When the busbars have groups of small holes around the bolt holes then there emerges a zone of significantly high contact pressure and contact penetration around the perforations. It is confirmed by the models, presented in Fig. 6 and Fig. 7.

Contact pressure data for the thirteen cases are summarized in Fig. 9.

Based on Fig. 9 and Fig. 11 it is obvious that in the extraordinary mixed case 4 the max. pressure is 88.73MPa. This value is 2 times the value of the classical case 1. Additionally the zone of pressure > 38.86 MPa occupies 20.83% of the entire contact area while in the classical case it is 1.75% (12 times larger).

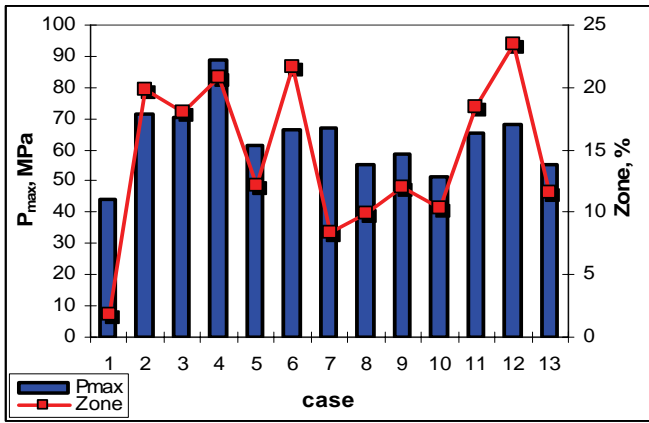


Fig. 9. Max contact pressure and % occupation of the zone of P > 38.86MPa for all cases

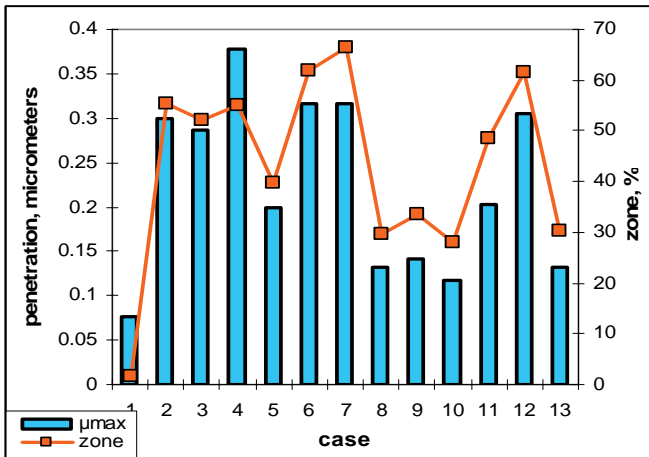


Fig. 10. Max contact penetration and % occupation of the zone of μ > 0.0673μm for all cases

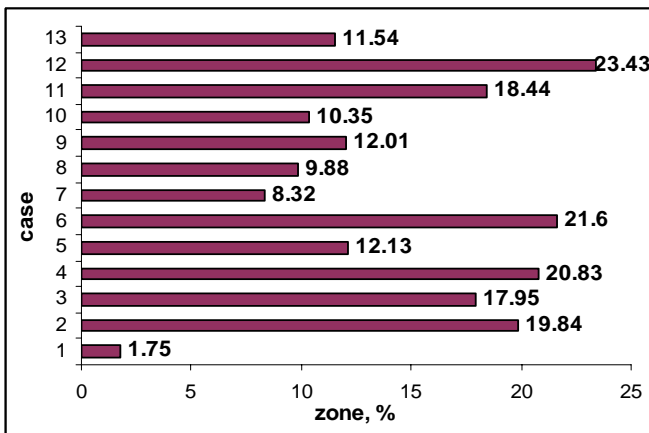


Fig. 11. Percent occupation of the P > 38.86MPa zone for all cases

The other excellent case is 12 with max. contact pressure of 67.92MPa and % occupation of the zone of pressure > 38.86MPa – 23.43% (13.4 times larger than that for the classical case 1).

The results for the contact penetration are summarized in Fig. 10 and Fig. 12.

Again in the best mixed case 4 the contact penetration is 0.37μm. This value is approximately 5 times the penetration of the classical case 1 (Fig. 12). The part of the contact area

with penetration > 0.0673μm occupies 55.04 %, while for the classical case it occupies 1.69% (32.6 times larger) by comparison with the classical case.

Another excellent case 12 has max contact penetration 0.306μm and % occupation of the zone of penetration > 0.0673μm – 61.44% (36.35 times the value for the classical case 1).

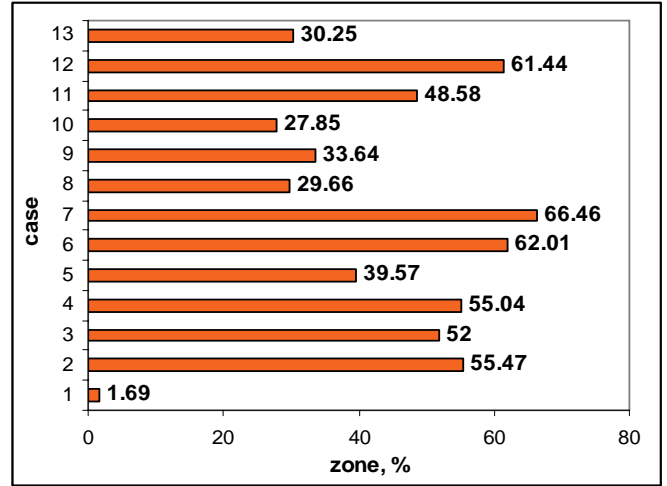


Fig. 12. Percent occupation of the μ > 0.0673μm zone for all cases

REFERENCES

- [1] R. S. Timsit, "The Technology of High Power Connections: A Review", 20-th International Conference on Electrical Contacts, Zurich, Switzerland, p. 526, 2002.
- [2] R. Holm, *Electric Contacts, Theory and Application*, Berlin, Germany, Springer-Verlag, 1976.
- [3] V. I. Boychenko, N. N. Dzekter, *Busbar Connections* (in Russian), Energa, 1978.
- [4] M. Braunovic, "Effect of Connection Design on the Contact Resistance of High Power Overlapping Bolted Joints", IEEE Transactions on Components, Packaging and Manufacturing Technology, vol. 25, Issue 4, pp. 642-650, Dec. 2002.
- [5] M. Braunovich, "Effect of Connection Design on the Performance of Service Entrance Power Connectors", IEEE Transactions on Components, Packaging and Manufacturing Technology, vol. 27, Issue 1, pp.72-78, March 2004.
- [6] R. Tzeneva, P. Dineff and Y. Slavtchev, "Bolted Busbar connections", XIV-th International Symposium on Electrical Apparatus and Technologies SIELA'2005, 2-4 June2005, Proceedings of papers, vol. I, pp. 207-211, Plovdiv, Bulgaria, 2005.
- [7] R. Tzeneva, Y. Slavtchev, N. Mastorakis and V. Mladenov, "Bolted Busbar connections with Slotted Bolt Holes", WSEAS Transactions on Circuits and Systems, Issue 7, vol. 5, pp. 1021-1027, July 2006.
- [8] R. Tzeneva, Y. Slavtchev and V. Mladenov, "Bolted Busbar Connections with Slotted Bolt Holes", Proceedings of the 10-th WSEAS Conference on Circuits, Vouligmani Beach, Athens, pp. 91-95, Greece, July 2006.
- [9] R. Tzeneva, P. Dineff, "Bolted Busbar Connections with Particularly Slotted Bolt Holes", Proceedings of the XLI International Conference on Information, Communication and Energy Systems and Technologies ICEST'06, pp. 371-374, 29-th June-01-st July, Sofia, Bulgaria, 2006.

The Influence of the Supply Voltage Unbalance on the Squirrel Cage Induction Motor Operation

Georgi I.Ganev¹ and George T.Todorov²

Abstract – An influence of the three phase supply voltage unbalance on a squirrel cage induction motor operation is investigated. A method for motor's currents prediction is presented. Experimental investigations are performed and the results are analyzed and compared to the predicted values.

Keywords – squirrel cage induction motor operation, supply voltage unbalance, power quality.

I. INTRODUCTION

Induction motors due to their better characteristics and cost are the most commonly used device that converts alternating current energy to mechanical one. More than one-half of the total electricity is consumed by motor-driving systems. A large part of them are induction motors with small rated power (less than 2kW). Being the induction motors most popular in the industry it is very important to carry out studies about the effect of power quality on the efficiency and reliability of the three-phase motors. On the other side the optimization of induction motor's operation will improve the operation of whole power system.

The two-ax transformation [10] and the symmetrical components transformation [7] are usually applied for induction motors investigation. D-Q transformation is used for investigation of the induction machines' transient processes [8], non-sinusoidal supply voltages influence [5] and induction motors driven by speed-control systems [13]. The Fortesque transformation is commonly used for induction motors steady-state operation studying [1,2,3,4,6,9,11,12], including symmetrical and non-symmetrical behavior. In case of non-symmetrical supply voltage, the three phase voltage system is decomposed into three subsystems – with positive, with negative and zero sequences. This way the induction motor's operation with unbalanced supply voltage is treated as a simultaneously operation of two machines – the first one operates as a motor (produces driving torque) and the second one - as machine breaker (produces torque with opposite direction). The zero sequences currents are neglected. Some disadvantages of this method should be mentioned, in spite of its popularity:

- the induction machine parameters for the positive and the negative sequences are assumed as constants;
- the saturation of induction machine magnetic core is

neglected;

- the superposition principle is used, equalizing the induction machine as a two simple machines with motor and breaker operation, etc.

Most of the papers do not discuss the influence of the voltage unbalance on the motor's currents and efficiency.

An investigation of the influence of the supply voltage unbalance on the operating performance of three-phase squirrel cage induction motor with small power is presented in this paper. An approach for the motor currents prediction is proposed, in case of unbalanced supply with deviation of one-phase voltage.

II. UNBALANCED CURRENT PREDICTION METHOD

A steady-state operation of symmetrical three-phase squirrel cage induction motor is under study in the present paper. An unbalanced three-phase system with variation of the voltage of only one phase supplies the motor. It is assumed that the stator winding is "Y" connected, the motor's parameters are preliminarily known and they remain constant (independent of the magnetic core saturation).

When the squirrel cage induction motor is supplied by three-phase symmetrical voltage system the consumed three-phase currents will form symmetrical system also. Each phase current lags behind the corresponding phase voltage to an angle φ .

Assume that the voltages applied to phases B and C remain constant and the voltage of the phase A decreases. This causes a change in the current drawn by phase A, but some variation in the currents of the other phases also [14].

As it is shown in the Fig.1, the currents I_b and I_c are changed by magnitude and by phases

$$\Delta i_a + \Delta i_b + \Delta i_c = 0 \quad (1)$$

As the voltages U_b and U_c are constant, we can assert that the currents I_b and I_c variation is caused only by the current I_a change and

$$\Delta i_b = \Delta i_c \quad (2)$$

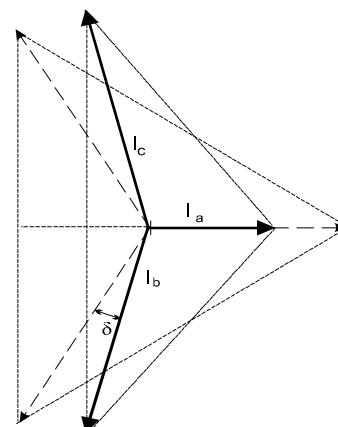


Fig.1. Phasor diagram of the input currents

The current I_b shift is in counter-clockwise direction and the I_c shift – clockwise.

¹ Georgi I.Ganev is with the Technical University – Sofia, branch Plovdiv, Electrical Engineering Department, 25, Tzanko Dustabanov St., 4000, Plovdiv, BULGARIA, E-mail: gganev@tu-plovdiv.bg

² George T.Todorov is with the Technical University – Sofia, Electrical Engineering Department, 8, Kliment Ohridski St., bl.12, 1000, BULGARIA, E-mail: gtto@tu-sofia.bg

As it is seen in Fig.1

$$\cos\left(\delta + \frac{\pi}{3}\right) = \frac{I_a/2}{I_b} = \frac{(1 + \Delta i_a)}{2(1 + \Delta i_b)} \cdot \frac{I}{I} \quad (3)$$

where Δi_a , Δi_b are the changes of the phase A and B currents respectively and δ is the shift of I_b and I_c in relation to the corresponding phasor at symmetrical power supply (the symmetrical currents are shifted at 120° from each other and at angle φ , compared to the phase voltages). As it is seen, the current I_b leads, while I_c lags with an angle δ the corresponding currents at symmetrical conditions.

Let us assume that the torque and power output of the induction motor are unaltered at symmetrical and non-symmetrical supply. Hence

$$U_a I_a \cos \varphi_a + U_b I_b \cos \varphi_b + U_c I_c \cos \varphi_c = 3UI \cos \varphi \quad (4)$$

The variation of the voltages, currents and their phase shift are:

$$\Delta i_a = \frac{\Delta U_a}{U}; \quad \Delta i_b = \frac{\Delta U_b}{U}; \quad \Delta i_c = \frac{\Delta U_c}{U}; \quad \Delta u = \frac{\Delta U}{U};$$

$$U \cdot (1 + \Delta u) \cdot I \cdot (1 + \Delta i_a) \cos \varphi_a + U \cdot I \cdot (1 + \Delta i_b) \cos(\varphi_b + \Delta \varphi_b) + U \cdot I \cdot (1 + \Delta i_c) \cos(\varphi_c + \Delta \varphi_c) = 3UI \cos \varphi$$

Furthermore, $\Delta \varphi_b = +\delta$; $\Delta \varphi_c = -\delta$ (see Fig.1).

Equation (4) can be rearranged, as follows:

$$(1 + \Delta u)(1 + \Delta i_a) + (2 - \Delta i_a) \cos \delta = 3 \quad (5)$$

The predicted changes of the currents Δi_a , Δi_b and the shift angle δ , are:

$$\Delta i_a = -\left(\frac{2\Delta u/3}{1 + 2\Delta u/3}\right)^2 \pm \frac{\sqrt{3\Delta u(\Delta u + 1)}}{(1 + 2\Delta u/3)^2} \quad (6)$$

$$\Delta i_b = \Delta i_a/2 \quad (7)$$

$$\delta = \pm \left(\arccos \frac{1 + \Delta i_a}{2 - \Delta i_a} - \frac{\pi}{3} \right) \quad (8)$$

The predicted values of Δi_a , Δi_b and δ , versus voltage deviation Δu are presented in Fig.2

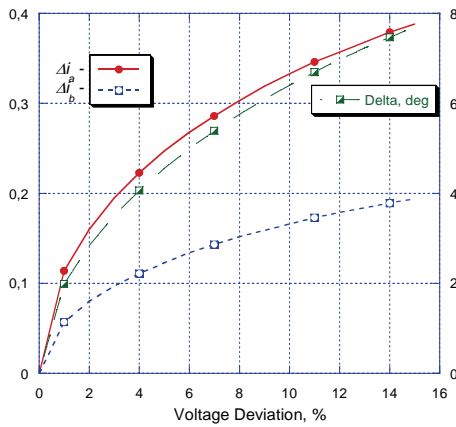


Fig.2. The predicted values of drawn currents' change and the corresponding shift

III. EXPERIMENTAL RESULTS

Series of experiments have been made with an induction motor type AO-71A2, with following parameters: $U_r = 380$ V, $n_r = 2860$ min⁻¹, $I_r = 0.94$ A, $\eta_r = 0.72$, $\cos \varphi = 0.83$, $I_{st}/I_r = 5.2$, $M_{st}/M_r = 2$, $M_{max}/M_r = 2.25$. The motor under test was coupled with DC generator and supplied by three auto-transformers type ATJI-9 with rated current $I_r = 9$ A. Power quality analyzer CA8332, serial number 00200226, produced by Chauven Arnoux have been used to measure the voltages, currents and power of the motor.

The motor's characteristics have been taken under balanced supply voltage and under two cases of unbalanced supply, changing the voltage of one phase (phase A). The same load torque has been applied at the motor shaft for all three cases.

The measured values of the unbalanced factor versus the one-phase voltage deviation (phase A) are shown in Fig.3.

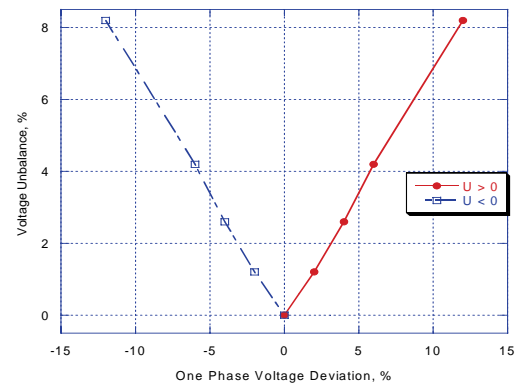


Fig.3. The voltage unbalance versus voltage deviation

Fig.4 shows the three-phase voltage phasors and the three-phase current phasors for three cases. Rated load have been applied to the motor shaft for all three cases. Fig.4(a) and 4(b) show the voltage and current phasors respectively in case of symmetrical supply. In Fig.4(c) and 4(d) the phasors when the supply voltage of phase A is bigger than rated value $U_A = 1.12U_r$ are shown. In Fig.4(e) and 4(f) are shown the phasors at $U_A = 0.88U_r$. All values for the measured current are in mA.

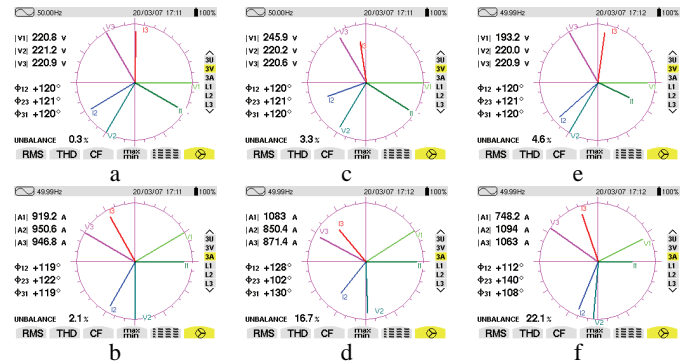


Fig.4. The voltage and current phasors

Test results from measurements performed with variation of the voltage deviation of phase A from -15% to +15% are presented in Fig. 5÷12. The measured quantities for currents, power and rotor speed are referred to the rated values.

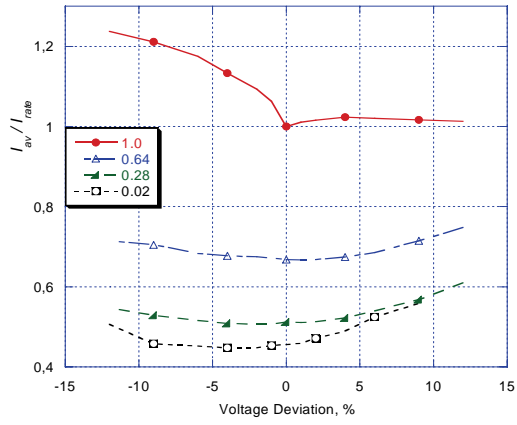


Fig. 5. Average input current

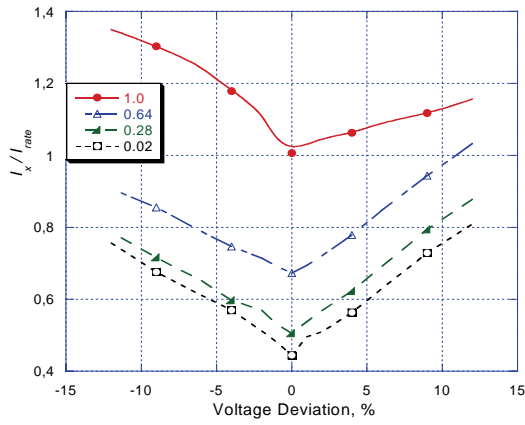


Fig. 6. Over-loaded phase input current

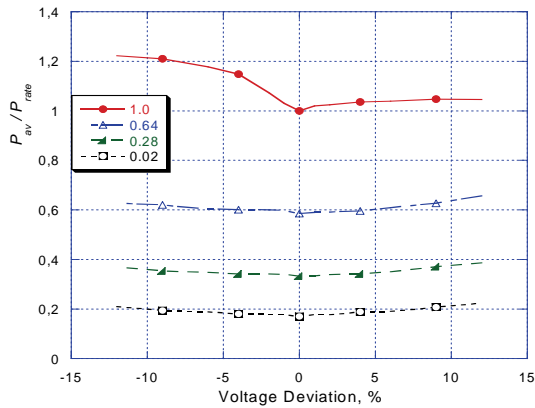


Fig. 7. Average input active power

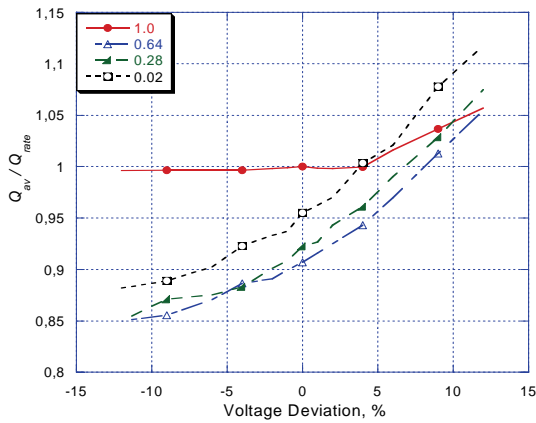


Fig. 8. Average input reactive power

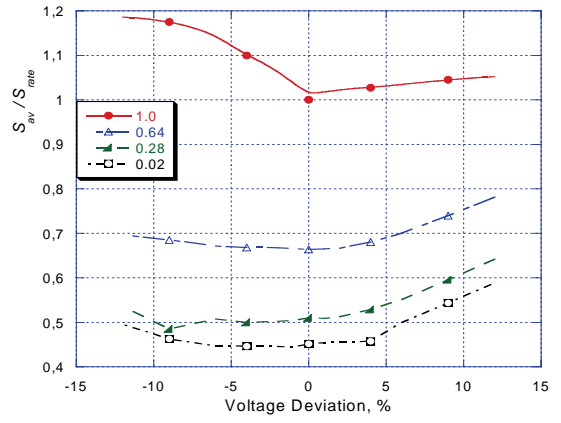


Fig. 9. Average input apparent power

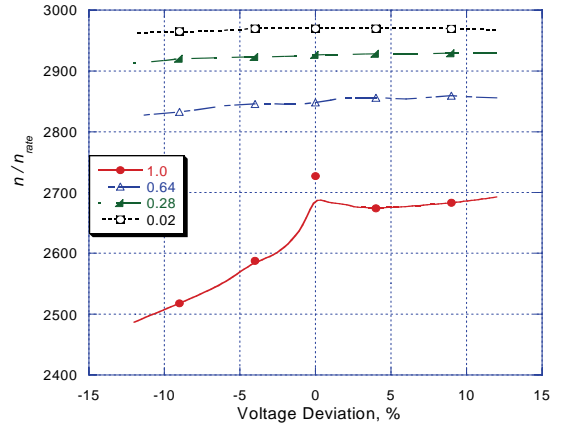


Fig. 10. Induction motor speed

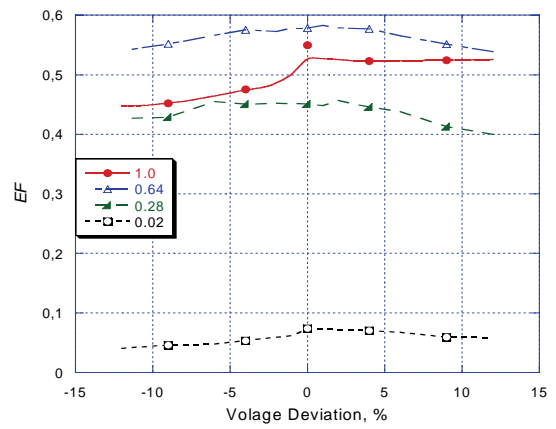


Fig. 11. Induction motor efficiency

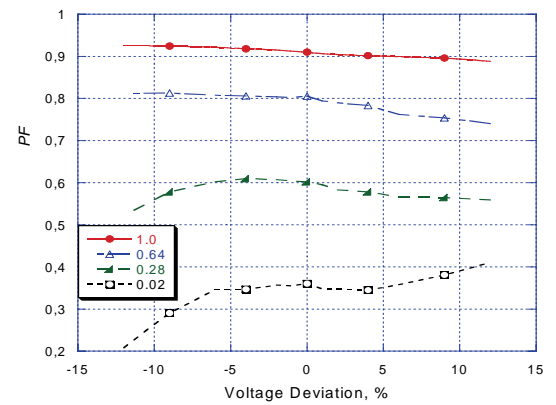


Fig. 12. Induction motor power factor

The characteristics have been taken at four levels of the load applied and four characteristics have been drawn in each figure – at rated load (1.0), at load 64% of the rated (0.64), at load 28% of the rated (0.28) and at 2% of the rated (0.02). All characteristics have been drawn versus the voltage deviation of phase A while the voltage of phases B and C remains equal to the rated value.

The operation of the motor under unbalanced voltage supply could be analyzed by aid of these characteristics. Currents of the overloaded phase of the motor are shown in Fig. 6. When the supply voltage of phase A is over the rated value the current I_A increases too. If the voltage of phase A decreases below the rated value, the induction motor will draw bigger current from the two other phases. Hence, in case of under-voltage the troubles-free phases (phases B and C) are overloaded.

The currents of all three phases are changed not only by magnitude, but by phase too. This means that the active and reactive currents' components are changed and it causes the induction motor active and reactive power varying respectively (see Fig.7, Fig.8 and Fig.9).

Due to the unbalanced supply voltage the magnetic field of the motor is non-symmetrical. As a result the input current and power are bigger and the efficiency is lower (Fig.11), compared to the values at balanced supply voltage. In one-phase over-voltage case, the non-symmetrical magnetic field causes saturation of some sections of the magnetic core and the power factor reduces (see Fig.8 and Fig.12).

Finally a comparison between predicted and measured values of the phase currents and currents' phase shift is given in Fig.13.

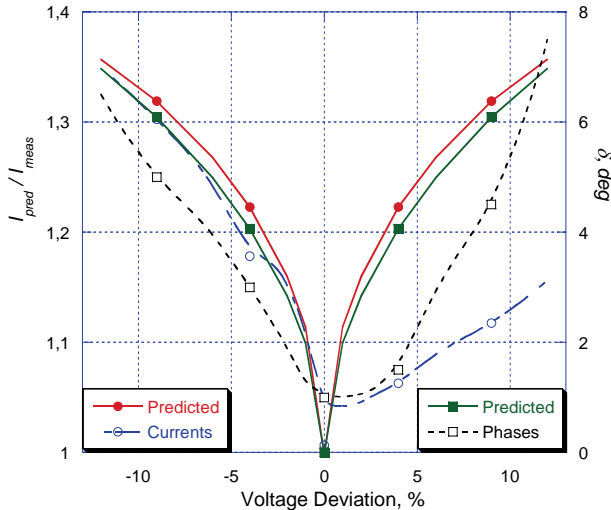


Fig.13. Predicted values and measured values of the phase currents and currents' phase shift

IV. CONCLUSION

1. An approach for motor currents prediction, when the motor is supplied by unbalanced three-phase voltage with deviation of the one-phase voltage, is proposed. The predicted values are close to the measured values. The differences could be caused by the small power of the motor under test.

2. It has been found out that at the same voltage unbalance values, the over-voltages and under-voltages cause different effects on the induction motor performance. This means that unbalance behavior establishment has to render an account of the voltage variation direction.

3. The supply voltage unbalance influence to the squirrel cage induction motor is:

- if the voltage decreases the average input currents will increase, the average input active and apparent power will increase too, the rotor speed will decrease. The efficiency and power factor slightly decrease. In the studied case, the currents' increase reaches to high value - $1,2I_r$ with only 3% unbalanced voltage.

- if the voltage increases over the rated value, the reactive power will increase and it will determine an increase in the apparent power, the rotor speed will remain nearly constant and the power factor and efficiency will decrease slightly.

4. The supply voltage unbalance makes the squirrel cage induction motor performance worst – the current drawn increases and the efficiency decreases, which means an increase in exploitation expenses.

5. Further experimental investigations with induction motors with bigger rated power will be made for verification of the proposed method.

REFERENCES

- [1] Ангелов А., Д.Димитров, Электрически машини, ч.1, Техника, София, 1976
- [2] Динов В., Несиметрични режими и преходни процеси в електрическите машини, Техника, София, 1974
- [3] Иванов-Смоленский, Электрические машины, Энергия, Москва, 1980.
- [4] Сыромятников И.А., Режимы работы асинхронных и синхронных двигателей, Энергоатомиздат, Москва, 1984
- [5] Boucherma M., M.Y.Kaika, A.Khezzer, Park Model of Squirrel Cage Induction Machine Include Space Harmonics Effects, Journal of EE, vol.57., no.4, 2006, pp. 193-199
- [6] Equiluz L.I., Lavandero P., Manana M., Performance Analysis of a Three-phase Induction Motor under Non-sinusoidal and Unbalanced conditions
- [7] Fortescue C.L., Method of Symmetrical Co-ordinates Applied to the Solution of Polyphase Networks, 34th Annual Conv. of A.I.E.E., Atlantic City, N.J., June, 1918.
- [8] Lee R., P. Pillay, R. Harley, D. Q References Frames for the Simulation of the Induction Motors, Electric Power Systems Research, 8 (1984 / 85), pp.15-26.
- [9] McPherson G., R.D.Laramore, An Introduction to Electrical Machines and Transformers, J.Wiley, 1990.
- [10] Park R.H., Two-reaction Theory of Synchronous Machines – Generalized Method of Analysis, part 1, Winter Convention of the AIEE, New York, NY, Jan.28 - Feb.1, 1929
- [11] Pillay P., P.Hoffman, M.Manyage, Derating of Induction Motors Operating with a Combination of Unbalanced Voltages and Over- and Under-voltages, IEEE Trans.on Energy Conversion vol.17, no.4, Dec.2002, pp.485-490
- [12] Quispe E., G.Gonzales, J. Aguado, Influence of Unbalanced and Waveform Voltage on the Performance Characteristics of the Three-phase Induction Motors
- [13] Tamimi J., H.Jaddu, Optimal Vector control of Three-phase Induction Machine, Proc. of the 25th IASTED, 2006, pp.92-96
- [14] Todorov G., G.Ganev, Influence of the Non-symmetrical Three-phase Loads on the Transformer and Supply Grid, ICES'2005, Nis, Serbia and Montenegro, pp.135-138.

Monitoring of the Electric Energy Quality in the Electricity Supply

Tzancho B. Tzanev¹, Svetlana G. Tzvetkova² and Valentin G. Kolev³

Abstract –Ensuring and supporting of the electric energy quality is a basic duty of the electric supplying companies. The consumers have every right to require and to get qualitative electric energy. But they should to have obligations, with their consumers and their work regimes, not to worsen the indexes of electric energy quality in the electric supplying systems.

Results from monitoring of the electric energy quality in distribution installation low voltage on kiosk switchgear supplying administrative building are given in the paper.

Keywords – monitoring, electric energy, quality, low voltage, distribution installation

I. INTRODUCTION

In the last years is observed a tendency of growing numbers and capacity of the consumers that make worse the electric energy quality, but also these that demand great requirements to the quality.

The combination of such characteristics of the supplying system, in which the consumers of electric energy can execute functions deposited in them, is defined by the general term *electric energy quality* [1]. Often the concept of electric energy quality is used to describe the specific characteristics of the supply voltage. The electric energy quality has two basic components – continuity and voltage level.

In 1999, the European organization for standardization in the electromagnetic field approved European standard EN 50160 “*Voltage characteristics of electricity supplied by public distribution systems*“, which reflects the theoretical level, level of the measuring techniques and exploitation practice in the electric energy quality field during the past years. Since March 2006 this standard was introduced as Bulgarian standard BSS EN 50160 and completely replaced BSS 10694-80.

The standard BSS EN 50160 includes the following basic indexes of electric energy quality [2]: frequency deviation; voltage deviation; fast voltage fluctuations; flicker; unbalance; harmonics; interharmonics; voltage dips; transient overvoltages; short-time and long-time interruptions.

¹Tzancho B. Tzanev is with the Faculty of Electrical Engineering, Technical University - Sofia, Kliment Ohridski 8, 1000 Sofia, Bulgaria, E-mail: tzanev@tu-sofia.bg

²Svetlana G. Tzvetkova is with the Faculty of Electrical Engineering, Technical University - Sofia, Kliment Ohridski 8, 1000 Sofia, Bulgaria, E-mail: stzvet@tu-sofia.bg

³Valentin G. Kolev is with the Faculty of Electrical Engineering, Technical University - Sofia, Kliment Ohridski 8, 1000 Sofia, Bulgaria, E-mail: vkolev@tu-sofia.bg

The norms of electric power quality indexes for low and medium voltage electric distribution networks are given in Table I according to BSS EN 50160 [2, 3].

The electric energy quality in the electricity supply system is formed in jointly operation of various electrical installations and equipment, which influence in different way on electric energy indexes. This necessitates audit and estimation of the energy installations in details and introducing of contemporary systems for monitoring and control of the electric energy quality in the exploitation. In this way energy efficient exploitation of the electrical installations will be ensured.

Results from monitoring of the electric energy quality in distribution installation low voltage on kiosk switchgear supplying administrative building are given in the paper.

II. MONITORING OF THE ELECTRIC ENERGY QUALITY IN DISTRIBUTION INSTALLATION LOW VOLTAGE

To be done a complex assessment of the electric energy quality and its influence on the electrical installations operation in given industrial enterprise or administrative building is necessary to be made investigations in different points of the electric supplying system.

Determination of the electric energy quality indexes and theirs influence on the electrical installations operation may be done in the following ways:

- Theoretical – this is possible only if we know all data for electrical installation elements. The method is very labour-consuming and inaccurate;
- By simulation of computer model – this also is possible only if we know all data for electrical installation elements. This method is used very often. It is more accurate in comparison with the theoretical method;
- By measurements with special instruments.

Monitoring of the electric energy quality indexes could be made by using of contemporary fixed or portable measuring instruments. The basic principles in which the measuring instruments have to respond are the following [4]:

- To measure the electric energy quality indexes according to BSS EN 50160;
- To have high accuracy and possibility for data registration in real time;
- To have self-contained power supply;
- To allow data transfer by modem, optical port or computer;
- To have software that allow data processing according to BSS EN 50160;
- To allow the time for averaging of the measured values to be given by the operator;

TABLE I
NORMS OF THE TO ELECTRIC ENERGY QUALITY INDEXES FOR LOW AND MEDIUM VOLTAGE
ELECTRICAL DISTRIBUTION NETWORKS ACCORDING TO BSS EN 50160

Characterization	Low voltage networks	Medium voltage networks
Frequency	49,5-50,5 Hz (for 99,5% from 1 year period) or 47-52 Hz (whole year)	49,5-50,5 Hz (3a 99,5% from 1 year period) or 47-52 Hz (whole year)
Voltage deviation	$U_H \pm 10\%$ (for every period from one week, 95% from the average effective voltage value per 10 min); $U_H +10/-15\%$ (for every period from 1 week, all average effective voltage values per 10 min)	$U_H \pm 10\%$ (for every period from one week, 95% from the average effective voltage value per 10 min)
Fast voltage fluctuations	Less than $5\%U_H$; fluctuations up to $10\%U_H$ with short duration may advent few times per day in some conditions. Flicker: $P_{lt} \leq 1$ (for 95% from period from 1 week)	Less than $4\%U_H$; fluctuations up to $6\%U_H$ with short duration may advent few times per day in some conditions. Flicker: $P_{lt} \leq 1$ (for 95% from period from 1 week)
Voltage unbalance	95% from the average effective voltage value with back sequence per 10 min must be in limits from 0 to $2\%U_H$ from the right sequence for every period of 1 week. In some power network areas may have values up to $3\%U_H$	95% from the average effective voltage value with back sequence per 10 min must be in limits from 0 to $2\%U_H$ from the right sequence for every period of 1 week. In some power network areas may have values up to $3\%U_H$
Harmonics	95% on the average effective voltage value of each harmonic formation of voltage per 10 min for every period of one week must be: $U_3 \leq 5\%$, $U_5 \leq 6\%$, $U_7 \leq 5\%$, $U_{11} \leq 3.5\%$, $U_{13} \leq 3\%$; Total harmonic distortion $\leq 8\%$	95% on the average effective voltage value of each harmonic formation of voltage per 10 min for every period of one week must be: $U_3 \leq 5\%$, $U_5 \leq 6\%$, $U_7 \leq 5\%$, $U_{11} \leq 3.5\%$, $U_{13} \leq 3\%$; Total harmonic distortion $\leq 8\%$
Voltage dip	Expected number may be from few scores to one thousand per one-year period.	Expected number may to be from few scores to one thousand for a year period.
Short-time interruptions	Values: from a few scores to several hundred	Values: from a few scores to several hundred
Long-time interruptions	Values: (interrupting over 3 min) annual frequency from 10 to 50, depending on area	Values: (interrupting over 3 min) annual frequency from 10 to 50, depending on area

- The software have to work under WINDOWS 9X, XP, 2000 and to allow data collection, statistical data processing, data representing by graphics and tables;
- To be convenient for transport and maintenance;
- To respond to all safety requirements;
- To have acceptable price.

The experience show that the determination of the electric energy quality indexes by measurement with special instruments is most accurate and most fast method.

For the aim, an investigation of the electric energy quality in distribution installation low voltage is done. It is supplied from kiosk switchgear 1000 kVA, 20/0,4 kV. The distribution installation supplies administrative building in which the electric energy consumers are mainly electrical heaters for heating (about 90%) and computers (about 10%).

The measurements were done by special instrument for analysis of the electric energy quality indexes *Power Quality Analyser MI2192* production of company *Metrel*. The instrument allows measuring of all electrical quantities and indexes of electric energy quality according to BSS EN 50160. They are following [4]:

- Phase values of voltage (U_{rms});
- Values of the line voltage (U_{xx});

- Frequency;
- Phase values of current (I_{rms});
- Value of current in the neutral conductor (I_{null});
- Total value of current;
- Active power (P);
- Reactive power (Q);
- Apparent power (S);
- Power factor (Pf);
- Total values of active, reactive and apparent power for Ph1 ... Ph3;
- Total value of the power factor;
- Active energy (consumption/ generate);
- Reactive energy (inductive/capacitive);
- Voltage and current harmonics (up to 63th harmonic);
- Voltage and current interharmonics;
- Voltage and current Total Harmonic Distortion;
- Voltage deviation;
- Flicker;
- Determination of the voltage dips and peaks;
- Determination of the voltage interruptions;
- Determination of transient processes;
- Level of pulsations;
- Unbalance.

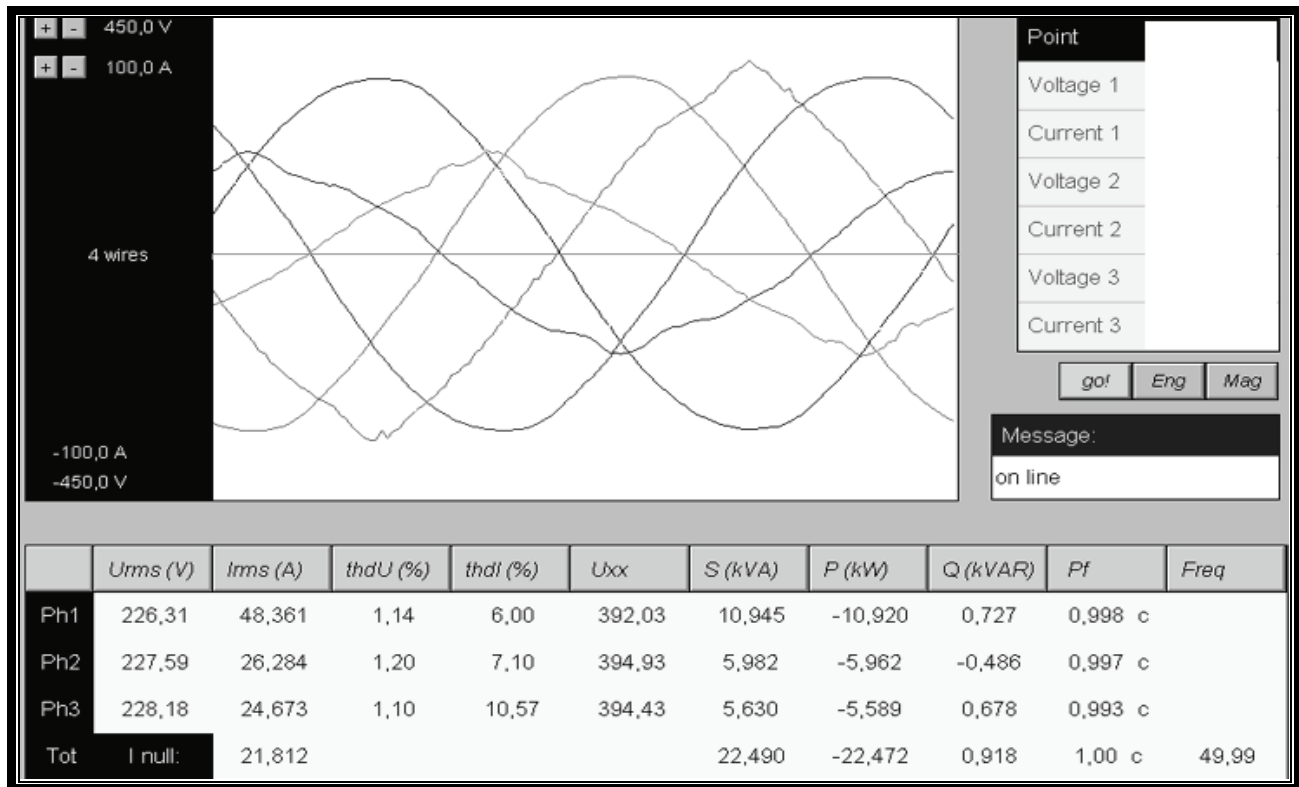


Fig. 1 Currents and voltages in the three phases and table with data for the basic electrical quantities that characterized the load and voltage in distribution installation low voltage on kiosk switchgear 1000 kVA, 20/0,4 kV supplying administrative building

Power Quality Analyzer MI2192 is used in 3-phase networks with or without neutral conductor. It has voltage and current inputs. The current clamps with different sensibility could be turned to the current inputs. The data are measured and recorded in 2048 KB SRAM memory. The measuring and recording data are accessible for reading by the communication port RS232 by software working under WINDOWS. The rate of data transfer is 2400-57600 bit/sec.

The graphics of the currents and voltages in the three phases and the table with data for the basic electrical quantities that characterized the load and voltage in distribution installation low voltage are given on fig. 1. It looks that the load is ohmic load and quite small capacitance is due to the pulse electric supplying blocks of the computers and monitors that is appeared ohmic-capacitive load.

The maximum voltage deviation is +3,9%. It is less than the norm from +10%. The frequency deviation is -0,01 Hz. Therefore, the voltage deviation and frequency deviation are in the admissible norms.

The voltage unbalance is insignificant – around 0,8%. It is less than the norm from 2%. The load of the phases is very unequal. Most loaded is phase 1. Phases 2 and 3 are rather lighter loaded. Current unbalance is 49%. Therefore, redistribution of the loads in the phases must be done.

It is necessary to draw attention that the voltage fluctuations and frequency fluctuations are in very smaller borders from 1% per 1 sec. For this reason we could not speak for any fluctuations of these two indexes. This is due to the fact that investigated distribution installation supply only two lifts and

there are not other more powerful installations with fast changeable operating mode.

From the graphics given on fig. 1 it is clear that the voltage sinusoid is better than current sinusoid.

The voltage and current harmonics for each phase are shown on fig. 2. The odd harmonics predominate. For the voltage these are 3, 5 and 11 harmonics. Their values are very lower than the admissible values given in Table I. Predominate 3, 5, 7 and 9 current harmonics. The maximum value has the third current harmonic - 3,25% per phase 1, 4,5% per phase 2 and 7% per phase 3. The magnitude of 3, 5, 7 and 9 current harmonics according to IEC 61000-3-4 is respectively 23%, 11%, 9% and 5% [5]. Hence, the magnitudes of the measured current harmonics are lower than admissible values.

The voltage total harmonic distortion is 1,14% per phase 1, 1,20% per phase 2 and 1,10% per phase 3. These values of the voltage total harmonic distortion are far under the admissible value from 8% for low voltage networks given in Table I.

The current total harmonic distortion is 6,00% per phase 1, 7,10% per phase 2 and 10,57% per phase 3. These values of the current total harmonic distortion are less than the admissible value from 25% [5].

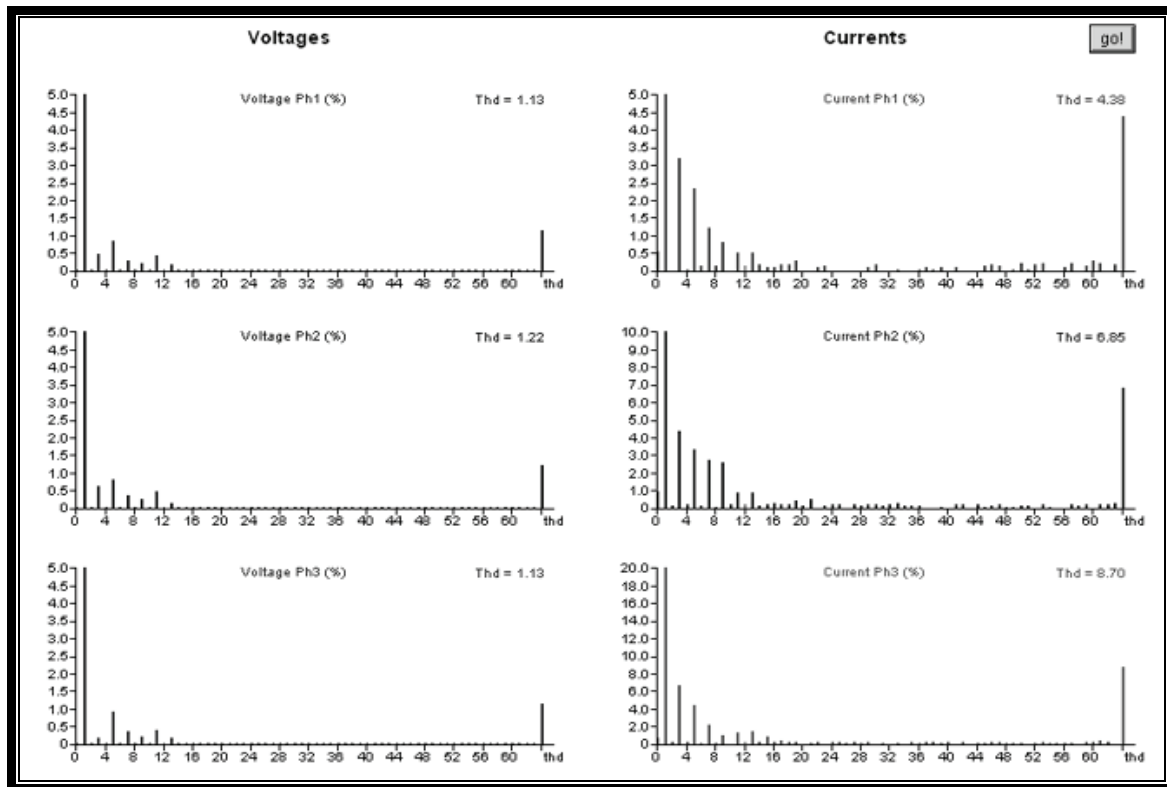


Fig. 2 Voltage and current harmonics measured in distribution installation low voltage on kiosk switchgear 1000 kVA, 20/0,4 kV supplying administrative building

IV. CONCLUSION

Ensuring and supporting electric energy quality is a basic duty of the electric supplying companies. On the other hand, the consumers have right to require and receive qualitative electric energy. But they should to have obligations, with their consumers and their work regimes, not to worsen the indexes of electric energy quality in electric supplying systems.

The measurements in the distribution installation low voltage on kiosk switchgear 1000 kVA, 20/0,4 kV supplying administrative building that were done, show that measured electric energy quality indexes are in the norms. The electric energy could not influence negative on the normal operation of the consumers.

REFERENCES

- [1] Schlabbach J., D. Blume and T. Stephanblome, *Voltage Quality in Electrical Power Systems*, UK, 2001.
- [2] BSS EN 50160 *Voltage characteristics of electricity supplied by public distribution systems*, 2006.
- [3] "Indexes for Electric Supplying Quality", State Energy and Water Regulatory Commission, 2004.
- [4] Tzanev T., S. Tzvetkova, V. Kolev, B. Tzaneva, V. Tzvetkova, "Analisis of the possibilities of instruments for electric energy quality measuring and assessment", Energy Forum'2006, Varna, pp. 224-231, 2006.
- [5] IEC 61000-3-4 *Limits for harmonic currents $I_1 > 16$ A*, 1998.

Algorithm for Efficiency Optimization of the Induction Motor Based on Loss Model and Torque Reserve Control

Branko Blanuša¹, Petar Matic¹, Željko Ivanović¹ and Slobodan N. Vukosavić²

Abstract - New algorithm, based on loss model and torque reserve control, for efficiency optimization of the induction motor drive is presented in this paper. As a result, power and energy losses are reduced, especially when load torque is significant less compared to its nominal value. This algorithm can be used in high performance drive and present good compromise between power loss reduction and good dynamic characteristics. Simulation and experimental tests are performed.

Key words- Efficiency Optimization, Induction Motor Drive, Loss Model, Parameter Identification, Torque Reserve

I. INTRODUCTION

Induction motor is without doubt the most used electrical motor and a great energy consumer [1]. Three-phase induction motors consume 60% of industrial electricity and it takes considerable efforts to improve their efficiency [1]. Most of the motors operate at constant speed although the market for variable speed is expanding. Moreover, induction motor drive (IMD) is often used in servo drive application. Vector control (VC) or Direct Torque Control (DTC) are the most often used control technique in the high performance applications.

There are numerous published papers which treated problem of efficiency optimization in the IMD in the last 20 years. Although, good results are achieved, there is no generally accepted method. There are three strategies which are usually used in the efficiency optimization of the induction motor drive [2]:

- Simple State Control-SSC;
- Loss Model Control-LMC and
- Search Control-SC.

First strategy is based on the control one variable in the drive. This variable must be measured or estimated and its value is used in the feedback control to keep it on predefined reference value. This strategy is simple, but gives good results only for the narrower set of the working conditions. Also, it is sensitive to parameter changes due to parameter variations caused by temperature and saturation.

In the second strategy model of the power losses is used for the optimal control of drive. This is the fastest strategy, because the optimal control is calculated directly from the loss model. However, power loss modeling and calculation of the optimal operating point can be very complex. Also, this strategy is sensitive to parameter variations.

In the search strategy the on-line efficiency optimization control on the basis of search is implemented. Optimization variable, stator or rotor flux is decremented or incremented in steps until the measured input power settles down to the lowest value.

¹Branko Blanus is with the Faculty of Electrical Engineering, Patre 5, 78000 Banja Luka, Bosnia and Herzegovina, E-mail: bbranko@etfbl.net

²Slobodan N. Vukosavic is with the Faculty of Electrical Engineering, Bulevar Kralja Aleksandra 73, 11000 Beograd, Serbia, E-mail: boban@etf.bg.ac.yu

This strategy has an important advantage compared to other strategies. It is completely insensitive to parameter changes. The control does not require knowledge of motor parameters and the algorithm is applicable universally to any motor.

Besides all good characteristics of search strategy methods, there is an outstanding problem in its use. Flux has never reached its nominal value, then in small steps oscillate around it. Sometimes convergence to optimal value can be too slow.

Very interesting problem for any optimization algorithm is its work with low flux level for a light load. When load is low, optimization algorithm settles down magnetization flux to make balance between iron and copper losses and reduce total power losses. In this case drive is very sensitive to load perturbations.

LMC algorithm with on-line parameter identification in the loss model and torque reserve control implemented for indirect vector controlled IMD is proposed in this paper. Parameter identification is based on matrix calculation and Moore-Penrose pseudoinversion. Input power, output power and values of the variables in the loss model must be known. Torque reserve is determined on calculated reference flux from loss model and current and voltage constraints in machine. Algorithm for efficiency optimization is included in the model of IMD and both simulation and experimental studies are performed to validate theoretical development.

Functional approximation of the power losses in the induction motor drive is given in the second Section. Procedure of parameter identification in the loss model and calculation of optimal magnetization current are described in the third Section. Experimental results are presented in the fourth Section.

II. FUNCTIONAL APPROXIMATION OF THE POWER LOSSES IN THE INDUCTION MOTOR DRIVE

The process of energy conversion within motor drive converter and motor leads to the power losses in the motor windings and magnetic circuit as well as conduction and commutation losses in the inverter.

Converter losses: Main constituents of converter losses are the rectifier, DC link and inverter conduction and inverter commutation losses. Rectifier and DC link inverter losses are proportional to output power, so the overall flux-dependent losses are inverter losses. These are usually given by:

$$P_{INV} = R_{INV} \cdot i_s^2 = R_{INV} \cdot (i_d^2 + i_q^2), \quad (1)$$

where i_d, i_q are components of the stator current i_s in d, q rotational system and R_{INV} is inverter loss coefficient.

Motor losses: These losses consist of hysteresis and eddy current losses in the magnetic circuit (core losses), losses in the stator and rotor conductors (copper losses) and stray losses. At nominal operating point, the core losses are typically 2-3 times

smaller than the copper losses, but they represent main loss component of a highly loaded induction motor drives [3]. The main core losses can be modeled by [4]:

$$P_{Fe} = c_h \Psi_m^2 \omega_e + c_e \Psi_m^2 \omega_e^2, \quad (2)$$

where ψ_d is magnetizing flux, ω_e supply frequency, c_h is hysteresis and c_e eddy current core loss coefficient.

Copper losses are due to flow of the electric current through the stator and rotor windings and these are given by:

$$P_{Cu} = R_s i_s^2 + R_r i_q^2, \quad (3)$$

The stray flux losses depend on the form of stator and rotor slots and are frequency and load dependent. The total secondary losses (stray flux, skin effect and shaft stray losses) usually don't exceed 5% of the overall losses [3]. Formal omission of the stray loss representation in the loss function have no impact on the accuracy algorithm for on-line optimization.

Based on previous consideration, total flux dependent power losses in the drive are given by the following equation:

$$P_\gamma = (R_{INV} + R_s) i_d^2 + (R_{INV} + R_s + R_r) i_q^2 + c_e \omega_e^2 \Psi_m^2 + c_h \omega_e \Psi_m^2. \quad (4)$$

Efficiency algorithm works so that flux in the machine is less or equal to its nominal value:

$$\psi_D \leq \psi_{Dn}, \quad (5)$$

where ψ_{Dn} is nominal value of rotor flux. So linear expression for rotor flux can be accepted:

$$\frac{d\psi_D}{dt} = \frac{R_r}{L_r} L_m i_d - \frac{R_r}{L_r} \psi_D, \quad (6)$$

where $\Psi_D = L_m i_d$ in a steady state.

Expression for output power can be given as:

$$P_{out} = d \omega_r \psi_D i_q, \quad (7)$$

where d is positive constant, ω_r angular speed, ψ_D rotor flux and i_q active component of the stator current. Based on previous consideration, assumption that position of the rotor flux is correctly calculated ($\Psi_Q = 0$) and relation $P_{in} = P_\gamma + P_{out}$ output power can be given by the following equation:

$$P_{in} = a i_d^2 + b i_q^2 + c_1 \omega_e^2 \Psi_D^2 + c_2 \omega_e \Psi_D^2 + d \omega_r \psi_D i_q, \quad (8)$$

where $a = R_s + R_{INV}$, $b = R_s + R_{INV} + R_r$, $c_1 = c_e$ and $c_2 = c_h$.

Input power should be measured and exact P_{out} is needed in order to acquire correct power loss and avoid coupling between load pulsation and the efficiency optimizer.

III. DETERMINATION OF THE PARAMETERS IN THE LOSS MODEL AND DERIVATION OF THE OPTIMAL MAGNETIZATION CURRENT

Procedure of the parameter determination in the loss model is shown in Fig. 1. There is a modification in the procedure described in paper [3], so the iron losses is considered separately like hysteresis losses and eddy current losses. The inputs to the algorithms are samples of i_d^2 , i_q^2 , $\omega_e \Psi_D^2$, $\omega_e^2 \Psi_D^2$, $\omega_r \psi_D i_q$ and P_{in} and they are acquired every sample time, usually 100-200 μ s. As the high frequency components do not contribute identification $W = [a \ b \ c_1 \ c_2 \ d]^T$, input parameters and P_{in} are averaged within Q intervals $T = QT_s$. The averaging is implemented as the sum of Q consecutive samples of each signal (Fig.1). Column vectors $P(:,1)$, $P(:,2)$, $P(:,3)$, $P(:,4)$ and $P(:,5)$ of matrix $P_{M \times 5}$ are created from the M successive

values of A_N , B_N , C_{N1} , C_{N2} , D_N , $N=1, \dots, M$ and vector Y_N is formed from the M averaged values of input power

$$\begin{aligned} \int_{nT}^{(n+1)T} P_{IN}(t) dt &= a \int_{nT}^{(n+1)T} i_d^2(t) dt + b \int_{nT}^{(n+1)T} i_q^2(t) dt + \\ c_1 \int_{nT}^{(n+1)T} [\Psi_D^2(t) \omega_e^2(t) dt] &+ c_2 \int_{nT}^{(n+1)T} [\Psi_D^2(t) \omega_e(t) dt] + \\ d \int_{nT}^{(n+1)T} [i_q(t) \psi_D(t) \omega_r(t) dt] & \end{aligned}$$

$$Y_N = aA_N + bB_N + c_1C_{N1} + c_2C_{N2} + dD_N. \quad (9)$$

Calculation of the vector W_g is based on Moore Penrose pseudoinverse of rectangular matrix $P_{M \times 5}$ [3]:

$$W_g = [a \ b \ c_g \ c_g \ d_g]^T = (P^T P)^{-1} P Y, \quad (10)$$

and W_g is approximate solution of matrix equation $PW=Y$, such the value of $\|PW - Y\|$ is minimum.

New vector W_g is usually calculated every 1.5-2s. The choice of Q is essential for the correct parameter identification. Credibility of W_g , relies on the excitation energy contained in the input signals. Hence, in absence of any disturbances, matrix $P^T P$ is getting near or being singular and values obtained from P should be discarded. In that case values of parameters are not changed and parameter determination is continued. For a known operational conditions of the induction motor (ω_r and T_{em}) and parameters in the loss model it is possible to calculate current i_d which gives minimum of the power losses [4].

Based on expression (4) power losses can be expressed in terms related to i_d , T_{em} and ω_s as follows

$$P_\gamma(i_d, T_{em}, \omega_e) = \left(a + c_1 L_m^2 \omega_e^2 + c_2 L_m^2 \omega_e \right) i_d^2 + \frac{b T_{em}^2}{(d L_m i_d)^2}. \quad (11)$$

Assuming absence of saturation and specifying slip frequency:

$$\omega_s = \omega_e - \omega_r = \frac{i_q}{T_r i_d}. \quad (12)$$

power loss function can be expressed as function of current i_d and operational conditions (ω_r , T_{em}):

$$\begin{aligned} P_\gamma(i_d, T_{em}, \omega_r) &= \left(a + c_1 L_m^2 \omega_r^2 + c_2 L_m^2 \omega_r \right) i_d^2 + \\ \frac{(2c_1 \omega_r + c_2) L_m T_{em}}{dT_r} &+ \left(c_1 \frac{T_{em}^2}{(dT_r)^2} + \frac{b T_{em}^2}{(dL_m)^2} \right) \frac{1}{i_d^2}. \end{aligned} \quad (13)$$

Based on equation (13), it is obvious, the steady-state optimum is readily found based upon the loss function parameters and operating conditions. Substituting $\alpha = \left(a + c_1 L_m^2 \omega_r^2 + c_2 L_m^2 \omega_r \right)$

and $\gamma = c_1 \frac{T_{em}^2}{d^2 T_r^2} + \frac{b T_{em}^2}{d^2 L_m^2}$ value of current i_d which gives minimal losses is:

$$i_{dopt} = \left(\frac{\gamma}{\alpha} \right)^{0.25}. \quad (14)$$

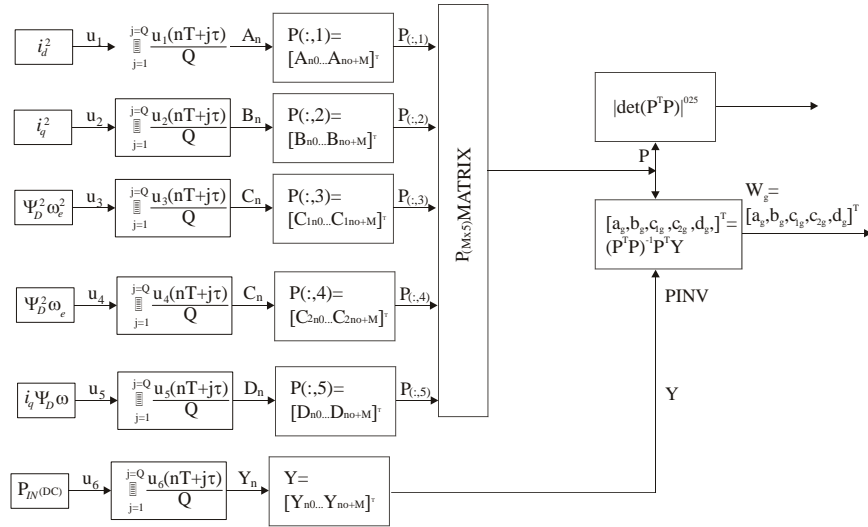


Fig 1. Determination of the parameters in the loss model from input signals.

Presented method is loss model based so it is fast [5]. Optimal value of magnetizing current is directly calculated from the model.

Online procedure of parameter identification is applied, so this method is robust on the parameter variations. One of the greatest problem of *LMC* methods is its sensitivity on load perturbation, especially for light loads when the flux level is low. This is expressed for a step increase of load torque and then two significant problems appear:

1. Flux is far from its value during transient process, so transient losses are big.
2. Insufficiency in the electromagnetic torque leads output speed to converge slow to its reference value with significant speed drops. Also, oscillations in the speed response are appeared.

These are common problem of methods for efficiency optimization based on flux adjusting to load torque. Speed response on the step change of load torque (from 0.5 p.u. to 1.1 p.u.), for nominal flux and when *LMC* method is applied, is presented in the Figs. 2. Speed drops and slow speed convergence to its reference value are more exposed for *LMC* method.

These are reasons why torque reserve control in *LMC* method for efficiency optimization is necessary. Model of efficiency optimization controller with torque reserve control is presented in Fig. 3. Optimal value of magnetization current is calculated from the loss model and for given operational conditions Eq. (14). Increment of magnetizing current (Δi_d) is generated from the fuzzy rules through the fuzzy inference and defuzzification, on the basis of the previously determined torque reserve (ΔT_{em}). Fuzzy logic controller is used in determination of Δi_d . Controller is very simple, and there is one input, one output and 3 rules. Only 3 membership functions are enough to describe influence of torque reserve in the generation of i_{dopt}^* .

If torque reserve is sufficient then $\Delta i_d \approx 0$ and this block has no effect in a determination of i_{dopt}^* . Oppositely, current i_d (magnetization flux) increases to obtain sufficient reserve of electromagnetic torque.

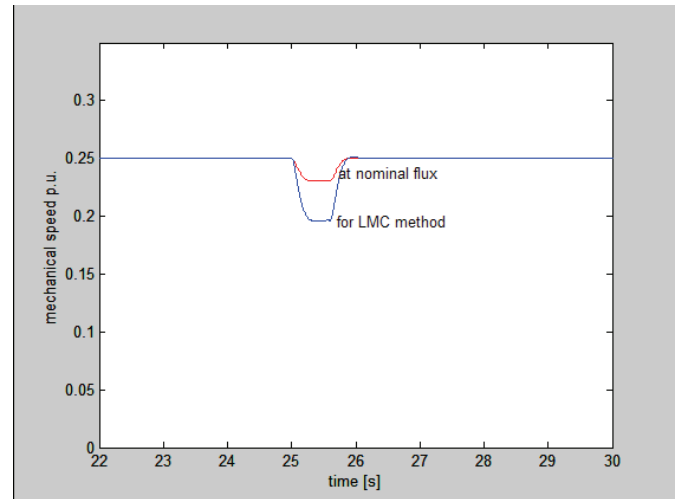


Fig. 2. Speed response on the step load increase for nominal flux and when LMC is applied.

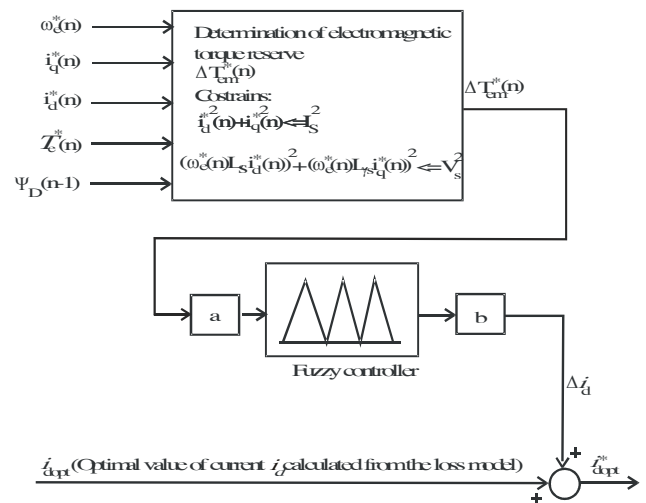


Fig. 3. Block for efficiency optimization with torque reserve control.

Two scaling factors are used in efficiency controller [6]. Factor a is used for normalization of input variable, so same controller can be used for a different power range of machine. Factor b is output scaling factor and it is used to adjust influence of torque reserve in determination of i_{dopt}^* and obtain requested compromise between power loss reduction and good dynamic response.

IV. EXPERIMENTAL RESULTS

Experimental tests were performed on the Laboratory Station for Vector Control of the Induction Motor Drives -Vectra. Basic parts of the Laboratory Station Vectra are:

- induction motor (3 MOT, $\Delta 380V/Y220V$, 3.7/2.12A, $\cos\phi=0.71$, 1400o/min, 50Hz)
- incremental encoder connected with the motor shaft,
- three-phase drive converter (DC/AC converter and DC link),
- PC and dSPACE1102 controller board with TMS320C31 floating point processor and peripherals,
- interface between controller board and drive converter.

Control and acquisition function as well as signal processing are executed on this board, while PC provides comfortable interface toward user.

Algorithms observed in this paper is software realized using Matlab – Simulink, C and real-time interface for dSPACE hardware. Handling real-time applications is done in ControlDesk.

Power losses and speed response of the motor drive with and without applied algorithm for torque reserve control are presented in Figs. 4. and 5. respectively. The load torque step changes in $t_1=25s$ from 0.5 p.u. to 1.0 p.u. and vice versa in $t_2=50s$ at constant reference speed $\omega_{ref}=0.2$ p.u.

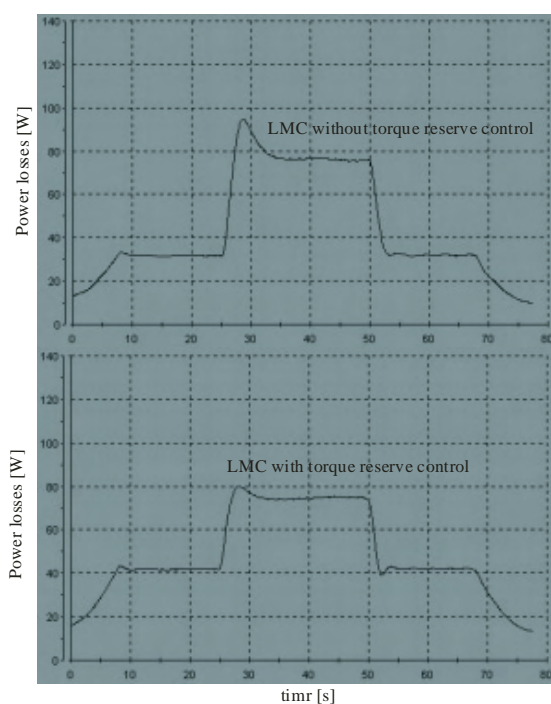


Fig. 4. Graphics of power losses for a step change of load torque.

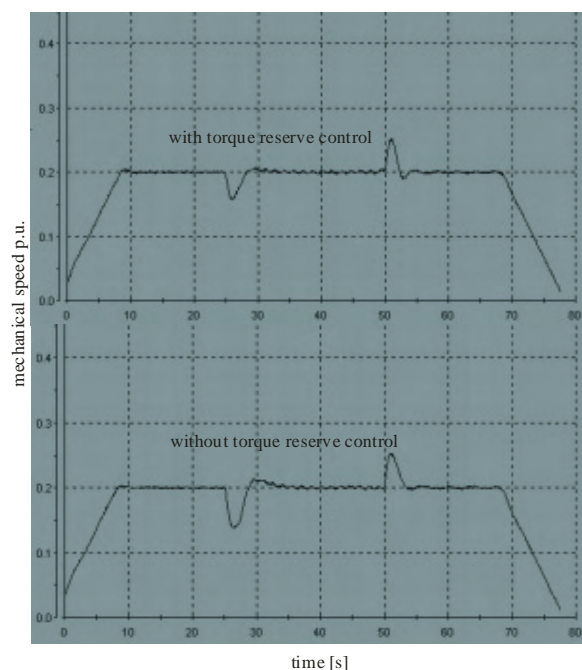


Fig. 5. Graphics of mechanical speed for a step change of load torque.

V. CONCLUSION

By implementation of *LMC* method with torque reserve control next results are reached:

1. Less sensitivity on load perturbation compared to standard *LMC* methods without torque reserve control.
2. Better control characteristics
3. Less transient losses

Algorithm with torque reserve control gives negligible higher losses in a steady state then standard *LMC* methods.

REFERENCES

- [1] S. N. Vukosavić "Controlled Electrical Drives - Status of technology", Proceedings of XLII ETRAN Conf., pp. 3-16, No. 1, 1998.
- [2] F. Abrahamsen, F. Blaabjerg, J. K. Pedersen, P.B. Thogersen, "Efficiency optimized control of medium-size induction motor drives", Industry Applications Conference, pp. 1489 -1496, Vol. 3, 2000.
- [3] S. N. Vukosavić, E. Levi, "Robust DSP-based Efficiency Optimization of Variable Speed Induction Motor Drive", IEEE Transaction of Ind. Electronics, Vol. 50, No. 3, 2003.
- [4] W. A. Roshen, "Magnetic Losses for Non-Sinusoidal Waveforms Found in AC motors", IEEE Tran. on Power Electronics, pp. 1138-1141, Vol. 21, No. 4, 2006.
- [5] C. Chekaborty, "Fast Efficiency Optimization Techniques for the Indirect Vector Controlled Induction Motor Drives", IEEE Trans on Industry Applications, pp. 1070-1076, Vol. 39, No. 4, 2003.
- [6] Emanuele Cerruto, Alfio Consoli, Antonio Testa, "Fuzzy Adaptive Vector Control of Induction Motor Drives", IEEE Transactions on Power Electronics, Vol.12, No.6 November 1999.
- [7] C.A. Hernandez Aramburo, T. C. Green, S. Smith, "Assesment of Power Losses of an Inverter -Driven Induction Machine With Its Experimenta; Validation", IEEE Tran. on Industry Applications, Vol. 39, No. 4, 2003.

Computation of Electromagnetic Forces and Torques on Overline Magnetic Separator

Mirka I. Popnikolova Radevska¹ and Blagoja S. Arapinoski²

Abstract: In this paper will be presented an approach to improved nonlinear magnetic field analyses of the Overline Magnetic Separator (OMS), on the basis of FEM as a represent of the numerical methods. By using the iterative procedure, Finite Element Method, it will be calculated the nonlinear distribution of magnetic field, under rated excitation on the (OMS). The electromagnetic field on the basis of the fluxes and flux densities in the particular domain of the (OMS), will be defined. The electromagnetic forces and torques will be calculated.

Keywords – Overline Magnetic Separator, Finite Element Method, Electromagnetic force, Electromagnetic torque.

I. INTRODUCTION

The rated data of the(OMS) that will be analyzed in this paper are rated data: $I_n = 31.4 \text{ A}$, $U_n = 220 \text{ V}$. The three dimensional cartesian system is used for the analyses.(bide analiziran vo pravoagolen koordinaten system.) Maximum clearance distance is $d = 0.42 \text{ m}$. A nonlinear interactive procedure is applied, calculations are carried out quasistatically, at given transportation line position. Real Overline Magnetic Separator OMS, product of Steinert is presented in Fig. 1, and OMS Model is presented in Fig. 2.

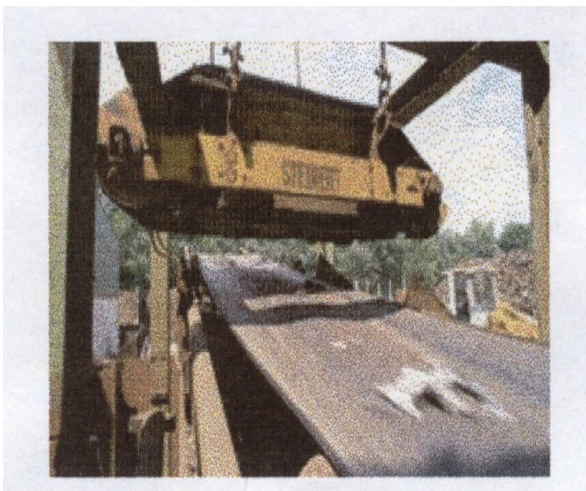


Fig. 1. Overline Magnetic Separator OMS

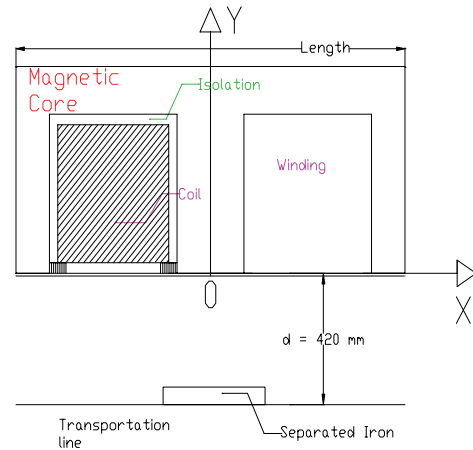


Fig. 2. Model of Overline Magnetic Separator OMS.

II. OMS MODEL IN FEM 4.0

FEM has possibility to solve magnetic vector potential and consequently magnetic flux density by solving relevant set of Maxwell equations for magnetostatic case as well as for time harmonic case. In magnetostatic case field intensity \mathbf{H} and flux density \mathbf{B} must obey:

$$\nabla \mathbf{H} = \mathbf{J} \quad (1)$$

$$\nabla \mathbf{B} = 0 \quad (2)$$

subject to a constitute relation between \mathbf{B} and \mathbf{H} for each material:

$$\mathbf{B} = \mu \mathbf{H} = \frac{1}{\nu} \cdot \mathbf{H} \quad (3)$$

and for nonlinear material permeability μ is actually function of \mathbf{B} .

FEM goes about finding a field that satisfies Eq. 1-Eq. 3 via a magnetic vector potential. Flux density is written in terms of the vector potential \mathbf{A} , as:

$$\mathbf{B} = \nabla \times \mathbf{A} \quad (4)$$

This definition of \mathbf{B} always satisfies Eq. 2. Then Eq.1 can be redefined as:

$$\nabla \times \left(\frac{1}{\mu(\mathbf{B})} \nabla \mathbf{A} \right) = \mathbf{J} \quad (5)$$

¹Mirka I. Popnikolova Radevska is with the Faculty of Technical Sciences, I.L.Ribar bb, 7000 Bitola, Macedonia, E-mail: mirka.radevska@uklo.edu.mk

²Blagoja S. Arapinoski is with the Faculty of Technical Sciences, I.L.Ribar bb, 7000 Bitola, Macedonia, E-mail: blagojarp@mt.net.mk

As first step in program pre-processing part, input is the OMS geometry and material properties for all separators domains are defined. This includes current density and conductivity in both OMS windings as well as magnetic properties, including magnetization curve for non-linear calculations.

In order to be able to solve the problem with FEM, boundary conditions on the outer electromagnets geometry must be defined. For analyzed separator Dirichlet boundary conditions are used.

On Fig. 3 mesh of finite elements is presented which is derived fully automatically and it is consisted of 24975 nodes and 49851 finite elements.

On Fig. 3, mesh of finite elements is presented which is derived fully automatically.

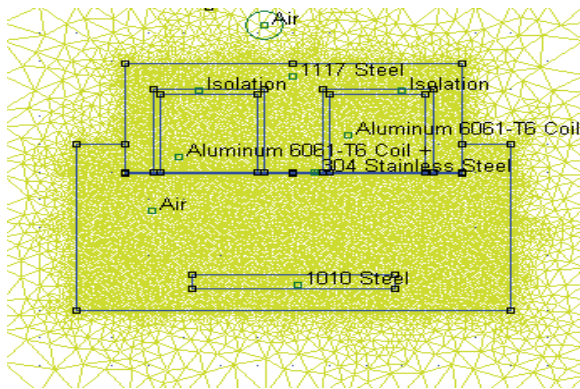


Fig. 3. Finite element mesh in cross section of OMS1.

When a more accurate calculation of the magnetic vector potential is needed, then mesh density should be increased especially on interface between two different materials. In that case contour of integration passes at least two elements away from any interface or boundaries. Greater mesh density increases the computation time. So, the good way to find mesh which is “dense enough” in order necessary accuracy to be achieved and still computation time to be reasonably small is comparison of results from different mesh densities can be picked smallest mesh which gives convergence to the desired digit of accuracy.

In OMS post processing part, we make comparison of electromagnetic characteristics in three cases: OMS1 with super malloy main core, which separates pure iron, OMS2 with 1117 steel main core, which separates 1010 steel and OMS3 with M_45 steel main core, which separates 1006 steel. OMS1, OMS2, are separating materials with one form and OMS3 another. Especially the differences on magnetic field density can be seen on Fig. 4, Fig. 5 and Fig. 6 respectively.

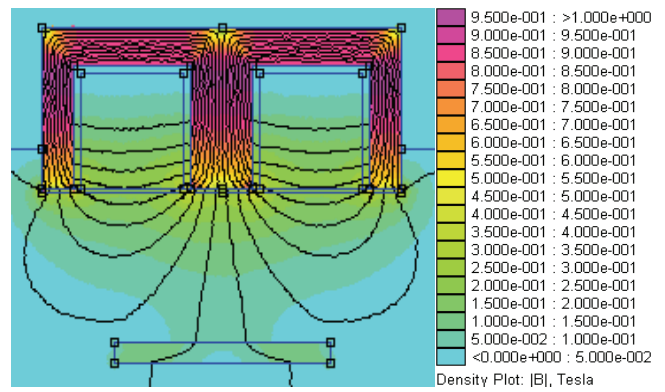


Fig. 4. Magnetic field density on OMS1.

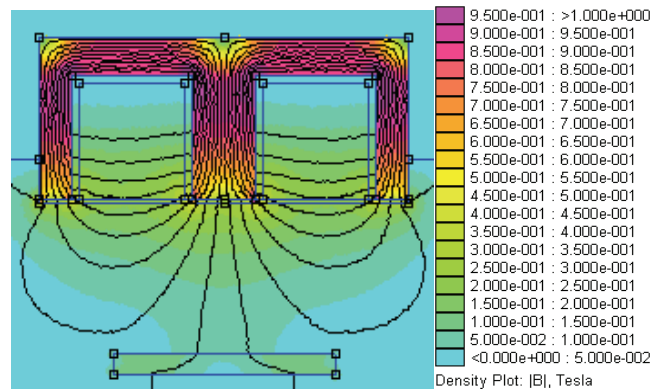


Fig. 5. Magnetic field density on OMS2.

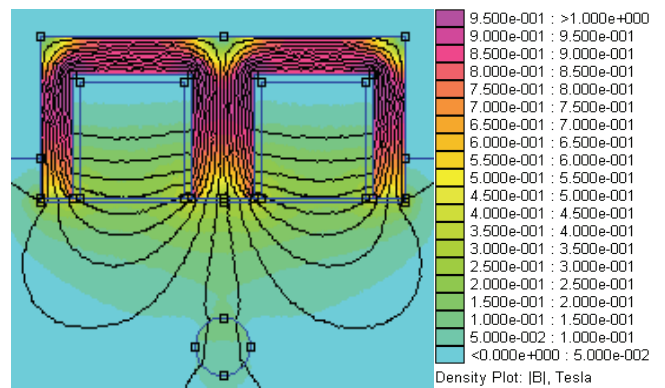


Fig. 6. Magnetic field density on OMS3.

III. ELECTROMECHANICAL CHARACTERISTICS

The knowledge of electromagnetic forces and torque characteristics is very important matter for analysis of OMS. In this paper numerical calculation of electromechanical forces and torques that are calculated on the base of Maxwell’s Stress Tensor and Weighted Stress Tensor are applied on the OMS.

Maxwell’s Stress Tensor prescribes a force per unit area by magnetic field on a surface. The net force on an object is obtained by creating surface totally enclosing the object of interest and integrating the magnetic stress over that surface.

The differential force produced is:

$$dF = \frac{1}{2}(H(B \cdot n) + B(H \cdot n) - (H \cdot B)n) \quad (6)$$

where n denotes the direction normal to the surface at the point of interest.

Weighted Stress Tensor Integral greatly simplifies the computation of forces and torques, as compared to evaluating forces via the stress tensor line integral of differentiation of co-energy. Merely select the blocks upon which force or torque are to be computed and evaluate the integral. No particular “art” is required in getting good force or torque results (as opposed to the Stress tensor line integral), although results tend to be more accurate with finer meshing around the region upon which the force or torque is to be computed. One limitation of the Weighted Stress Tensor integral is that the regions upon which the force is being computed must be entirely surrounded by air/or abutting a boundary. In cases in which the desired region abuts a non-air region, force results may be deduced from differentiation of co-energy.

The forces characteristics on directions x and y axis, versus different clearance distances and rated current for OMS1, OMS 2 and OMS 3 are presented in Fig.7 and Fig. 8.

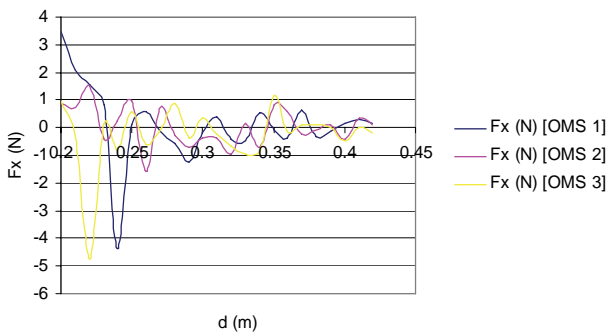


Fig. 7. Forces on direction x-axis, versus different clearance distances for OMS1, OMS2 and OMS3.

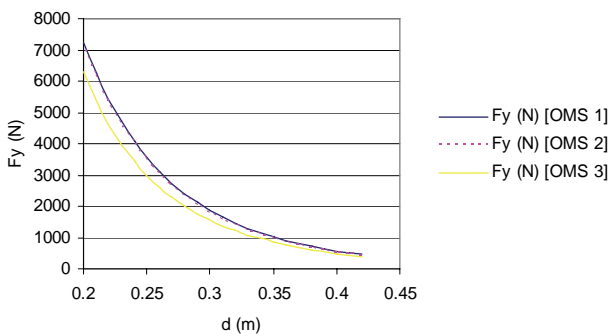


Fig. 8. Forces on direction y-axis, versus different clearance distances for OMS1, OMS2 and OMS3.

The torque characteristics versus different clearance distances and rated current, for OMS1, OMS2 and OMS3 are presented in Fig. 9.

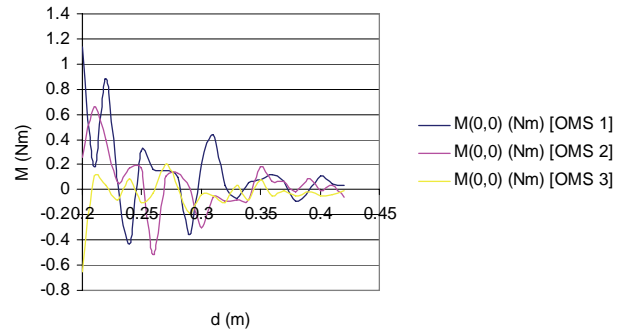


Fig.9. The torque characteristics versus different clearance distances for OMS1, OMS2 and OMS3 .

The forces on directions x and y axis characteristics versus different currents and constant clearance distance $d = 0.37 \text{ mm}$ for OMS1, OMS 2 and OMS 3 are presented in Fig.10 and Fig. 11.

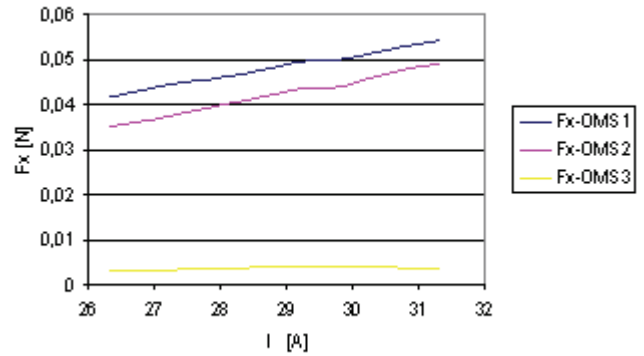


Fig.10 Forces on direction x-axis, versus different currents for OMS1, OMS2 and OMS3.

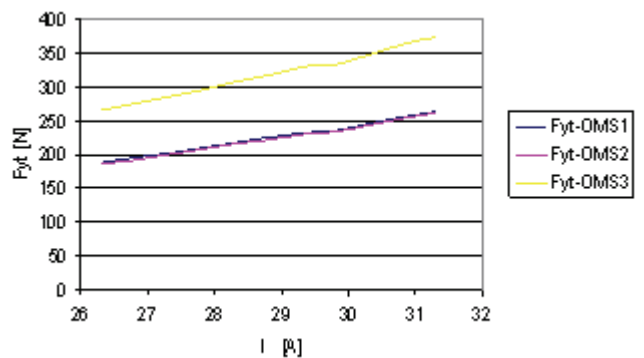


Fig. 11. Forces on direction y-axis, versus different currents for OMS1, OMS2 and OMS3.

The torque characteristics $M_t = f(I); d = const.$, were computed with weighted stress tensor integral for OMS1, OMS2 and OMS3 are presented in Fig. 12.

REFERENCES

- [1] M. Popnikolova Radevska: "Calculation of Electromechanical Characteristics on Overband Magnetic Separator with Finite Elements", ICEST 2006, p.p. 367-370, Sofia, Bulgaria 2006.
- [2] D. Meeker, "Finite Element Method Magnetics Version 4.2", User's Manual, 2006 .
- [3] STEINERT Btriesanweisungen fur Uberbandmagnetscheider und Aushebemagnete, Technische Daten TD UME P, 2002.
- [4] John Wiley & Sons, "ELECTROMAGNETIC DEVICES" New York-London-Sydney.

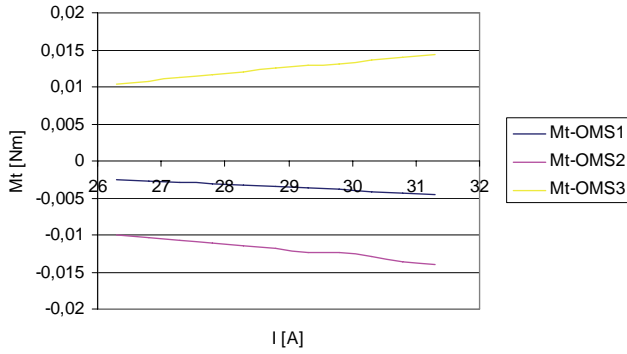


Fig 12. The torque characteristics versus different currents and constant distance clearance for OMS1, OMS2 and OMS3 .

Magnetic field co-energy is defined:

$$W_C = \int \left(\int_0^H B(H') dH' \right) dV \tag{7}$$

On base of the Eq. 7, the magnetic co-energies are computed and their characteristics versus different currents and constant clearance distances for OMS1, OMS2 and OMS3 are presented in Fig. 13:

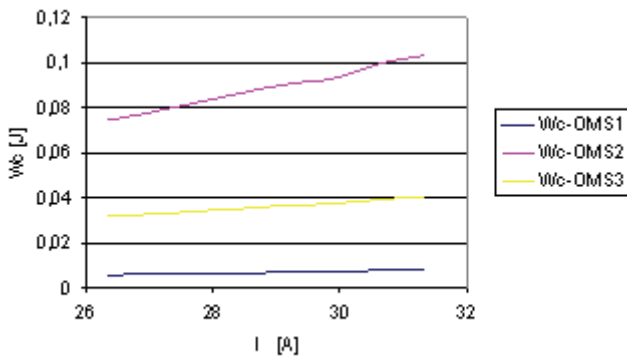


Fig 13. The magnetic co-energy characteristics versus different currents and constant clearance distance for OMS1, OMS2 and OMS3 .

IV. CONCLUSION

In this paper the non-linear magnetic field analyses and computation of electromagnetic and electromechanical characteristics are presented. For this purpose as the most suitable, Finite Element Method is applied. Additionally electromagnetic forces and torque are calculated for rated load current and different clearance distance and for constant clearance distance and different currents. Also in this paper forces and torques are computed via Maxwell's Stress Tensor and Weighted Stress Tensor. Magnetic field co-energy is also computed and presented in this paper.

SESSION EQ

Education Quality II

Studying on Frequency Modulation in MATLAB Environment

Veska M. Georgieva¹

Abstract – Frequency Modulation (FM) is widely used in communication systems. FM is used at VHF radio frequencies for high-fidelity broadcasts of music and speech. A narrowband form is used for voice communications in radio settings. It's made a trial in the paper to present the possibility of the computer simulation in MATLAB environment by deeper studying and analyzing the effect of various factors such as modulations index, the form and amplitude of the modulating signal on the spectrum and spectrum band of the modulated signals. The paper can be used in engineering education in studying this process.

Keywords – Frequency modulation, communication systems, modulations index, narrowband FM, wideband FM, computer simulation.

I. INTRODUCTION

At the university level, the material studied becomes more abstract and more mathematical. It's described in the paper a laboratory exercises for the course on Signals and Systems of students from faculty of communications and from faculty of computer systems.

FM is a form of modulation which represents information as variations in the instantaneous frequency of carrier wave. On the base of theory of the process, with help of computer simulation, the students get deeper insight of effect of various factors such as modulations index, the form and amplitude of the modulating signal. They can investigate their influence on the power spectral density and bandwidth of the modulated signals.

The computer simulation can be realized in the program environment of MATLAB with using the system for visual modelling SIMULINK. A model can be created, which generate the analysed signals and functions. There are 2 methods to create a model in SIMULINK. First it's can be used mathematical formulae for creating building blocks, [1] and second by direct using of blocks for the investigated process [4,5,6,7]. By generation in case of analogue signals can be used functions or blocks from SIMULINK [2]. Digital data can be represented by shifting the carrier frequency among a set of discrete values, a technique known as frequency-shift keying. A program can be made in case of digital signals, so the signals can be choose from the students.

¹Veska M. Georgieva is with the Faculty of Communication, TU-Sofia, Kl.Ohridsky str.8, Sofia, Bulgaria, E-mail: vesg@tu-sofia.bg

II. PROBLEM FORMULATION

The problem on the FM signal analysis can be presented with following features:

- There are 3 kinds of signal in case of FM process: modulating, carrier and FM modulated signal.

- The analogue modulating signals can have different forms such as sinusoidal, rectangular, triangular, saw-tooth, Gaussian. Their parameters can be determinate by the students. Digital signals and their parameters can be determinate totally from the students.

- The sinusoidal signal can be used as carrier.

The mathematical description for the modulated signal is given in Eq.1

$$\begin{aligned}
 a_{FM}(t) &= A_0 \cos \psi_{FM}(t) = \\
 &= A_0 \cos(\omega_0 t + m_\omega \sin \Omega t)
 \end{aligned} \tag{1}$$

where m_ω is the modulation index.

This indicates by how much the modulated variable varies around its unmodulated level. In this case, for FM, it relates to the variations in the frequency of the carrier signal. The modulation index m_ω is depended from the frequency of the modulating signal (Eq.2):

$$m_\omega = \frac{\Delta\omega_m}{\Omega} \tag{2}$$

If $m_\omega \ll 1$, the modulation is called narrowband FM, and it's bandwidth is approximately 2Ω .

If $m_\omega \gg 1$, the modulation is called wideband FM, and it's bandwidth is approximately $2\Delta\omega_m$.

- The frequency spectrum of an actual FM signal has components extending out to infinite frequency, although they become negligibly small beyond a point.

For a simplified case, the harmonic distribution of a sine wave signal modulated by another sine wave signal can be represented with Bessel functions – this provides a basis for a mathematical understanding of frequency modulation in the frequency domain.

So on base of computer simulation we can formulate following problems:

1. To create a model of FM modulation process in case of $m_\omega \ll 1$ and in case of $m_\omega \gg 1$.
2. To analyze the influence of the form of the modulating signal on the power spectral density.
3. To investigate the influence of the modulations index of the spectrum and bandwidth of the modulated signal.

By the simulation we need to see the going processes. The characteristics can be given in graphical mode.

III. EXPERIMENTAL PART

The formulated problems are solved by computer simulation in MATLAB, version 6.5 with using the SIMULINK TOOLBOX [3].

For a model creating are used mathematical formulae for creating building blocks. To generate the analogue signals with different forms such as, sinusoidal, rectangular, triangular, saw-tooth, and Gaussian, the students can use the following blocks: 'Signal Generator', 'Ramp', 'Step', 'Repeating Sequence', 'MATLAB Function', 'Product'. The using blocks can be connected in the model informative and by the control, too. The type of the connection is dependent on the block and on the logic of his work. The running time can be set in constant or variable step. The students can observe a running process by the block 'Scope', which is included in the model, too. They can see the spectrum of the FM signals by the 'Spectrum Scope'. An example for a simulated model is given in Fig.1.

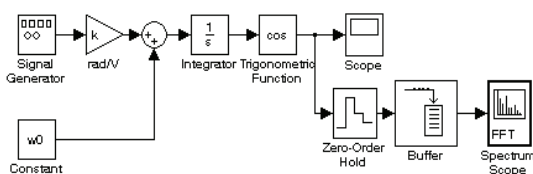


Fig.1 Model for FM process

Fig.2 presents in graphical mode the FM signal. It's generated a saw-tooth as modulating signal for FM. The following parameters are choosen: $A_M=1V$; $A_0=1V$; $F_M=100\text{ Hz}$; $f_0=2000\text{ Hz}$; $K=5000$.

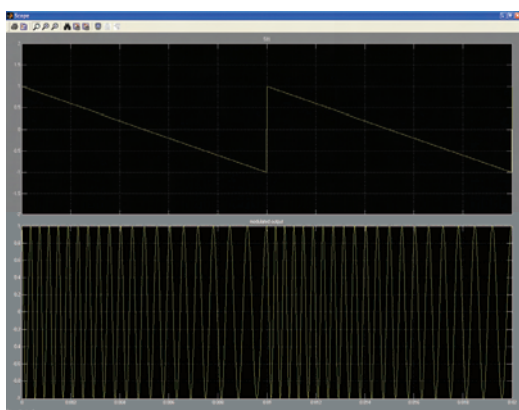


Fig.2 Modulating and modulated signals by FM

The power spectral density of this FM signal is given in Fig.3. It's shown, that the bandwidth of the FM signals, independent of the form of modulating signal.

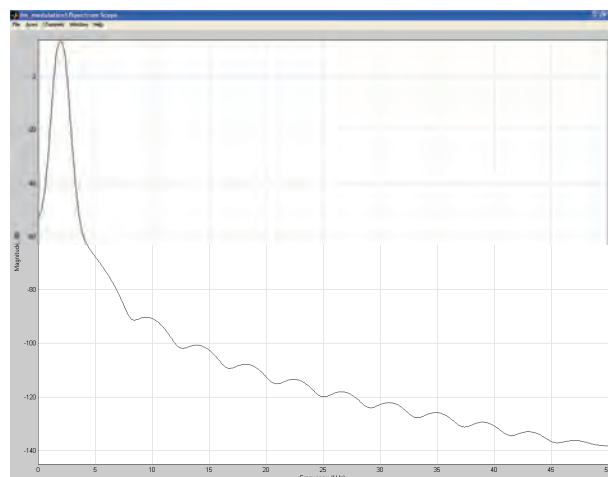


Fig.3. Power Spectral Density of FM signal by $m_{\omega} \gg 1$

IV. CONCLUSION

The frequency modulation is one of the very important problems in the theory of the signals. It's made a trial in the paper to present the possibility of the computer simulation in MATLAB environment to get deeper insight on studying this process, on effect of various factors such as modulations index, the form and amplitude of the modulating signal. It's helpful for the students to create models to generate different signals and to change their parameters. So with the help of the simulation they can investigate the influence of the signal parameters on the FM frequency band and the spectrum type, and observe the running processes in the time domain, too.

REFERENCES

- [1] E. Simeonov, V. Georgieva, D.Dimitrov, Practical Analysis of Signals with Amplitude Modulation, Proceedings ICEST'2003, pp.495-498, Sofia, Bulgaria, 2003
- [2] Ingle Vinay K. & Proakis John G., Digital Signal Processing Using MATLAB, Brooks/Cole Publishing Company, 2000
- [3] MATLAB 6.5, User's Guide, www.mathwork.com
- [4] V. Georgieva, S. Lishkov, D.Dimitrov, Spectrum Signal Analysis in MATLAB Environment, Proceedings ICEST'2005, pp. 738- 740, Nish, Serbia and Montenegro, 2005
- [5] V. Georgieva, D.Dimitrov, S. Lishkov, Correlation Signal Analysis in MATLAB Environment, Proceedings ICEST'2005, pp. 741-742, Nish, Serbia and Montenegro, 2005
- [6] V. Georgieva, S. Lishkov, D.Dimitrov, V. Ivanova, Studying on Digital Filters in MATLAB Environment, Proceedings ICEST'2005, pp. 735-738, Nish, Serbia and Montenegro, 2005
- [7] V. Georgieva, D. Dimitrov, M. Neykova, Pulse Modulation Analysis in MATLAB Environment, Proceedings of CSICE'05, pp. 79-81, Sofia, Bulgaria, 2005

An Approach of Application Development for the Virtual Laboratory Access

Jelena Djordjević-Kozarov¹, Milan Jović² and Dragan Janković³

Abstract – Continuous development and implementation of information and telecommunication technologies based on Internet, as a global network, and on multimedia notes brings us to the new results in the field of measurement as the science discipline. A model used in realization of a measurement laboratory for remote experiments is described in this paper. A way and realization of user access to the measurement system through the Internet is explained into detail.

Keywords – Virtual laboratory, Internet application, remote access.

I. INTRODUCTION

Process control and management are permanent needs in all technic and technical processes. Measurements are usually not located at the same place and it is necessary to acquire them from the different locations, put them in the same database, process and analyze, or use them in the next measurement process. In that case, we can define the measurement system as an set of the measuring features connected in one functional entirety, used for the data acquisition.

Beside the indispensable software, in the modern measuring systems it is necessary to receive the measuring data in digital form. Low price of microprocessor's components and systems, made possible the realization of the systems with distributed data processing. Those systems usually have the autocalibration and electric isolation.

The development of information technologies has opened new possibilities in realization of measurement data acquisition systems. Described measurement systems present the conception in the field of remote measurement laboratories. The laboratory heart usually consists of a group of measuring instruments, connected to the Internet through the appropriate network equipment. Possibility of the data acquisition and their storing into the databases, enable the easy communication between the laboratories which are on geographically distant places.

Distributed architecture of the remote measurement laboratory is described in paper [1]. System is realized as a

hierarchical structure on few levels. Clients can access through application level. Those realization can be classified as a client / server architecture, where the user's computers are clients, and the computers in the measuring laboratories [2] are servers. Basic components of this architecture are: main server, connection with measurement systems (laboratories) and measurement instruments which perform the laboratory.

II. INTERNET APPLICATION AS A PART OF THE LABORATORY SOFTWARE SOLUTION

Laboratory is realized by program language LabVIEW [3], i.e. the LabVIEW application, through which clients can access measuring instruments and acquire data, is realized. It is needed to have input parameters for each measuring instrument in that virtual laboratory in order to carry out the desired measurement by virtual instruments. Input parameters are the parameters which set the start values of the measuring instruments. When the measurement equipment is connected to the computer and all parameters are set, the LabVIEW application carries out the data acquisition and generates the output file. Digitalized values of the acquired data are placed into the output file.

Software solution, which connects the user and the appropriate LabVIEW application, is realized by standard procedure languages. The Internet part of the software solution is written by using the ASP [4] (Active Server Pages) technology in Java Script language and by using the CGI [5] (Common Gate Interface) scripts. The pages for the measuring laboratory access are realized in the same technology. In order to access the laboratory the user has to be logged in. When the user's identification data are checked by the application, the user can access the laboratory recourses. ASP technology allows the work with SQL, which presents the language for the database queries. SQL server is on the main computer in the measurement laboratory. All information about the users who may access the laboratory, and all information about measurements which are made (including the measurement parameters and results) are placed in the database (Fig. 1).

Depending on chosen measuring experiment, the ASP page with the appropriate fields for the start value inputs will appear on the screen. When the user input parameters for the desired measurement, the appropriate CGI script starts (Fig. 2).

All scripts are written in C++ program language. This technology enables a data exchange between the web pages and the classic applications, which are written in standard

¹Jelena Djordjević is with the Faculty of Electronic Engineering, University of Niš, Aleksandra Medvedeva 14, 18000 Niš, Serbia, E-mail: jelenadj@elfak.ni.ac.yu

²Milan Jović is with the Faculty of Informatics, University of Lugano, Switzerland, E-mail: milan.jovic@lu.unisi.ch

³Dragan Janković is with the Faculty of Electronic Engineering, University of Niš, Aleksandra Medvedeva 14, 18000 Niš, Serbia, E-mail: gaga@elfak.ni.ac.yu

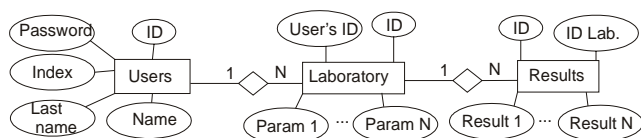


Fig. 1. Virtual laboratory database model

program languages. In that way, the extended functionalities of the web applications up to the real possibilities of the classic applications has been achieved. Through the Internet pages the data, which are needed to make the measurements, are gathered by these scripts. All the data are collected into the input text file in appropriate format demanded by LabVIEW standard. Important functionality of all standard programming languages is a possibility to make an external call of the another program application on the computer. This functionality is used here for the calls of a appropriate LabVIEW application. When the input file is created, the CGI script goes into a waiting state, while the appropriate LabVIEW application is running and the output file is not created. Then, a HTML file is created and transferred to the user.

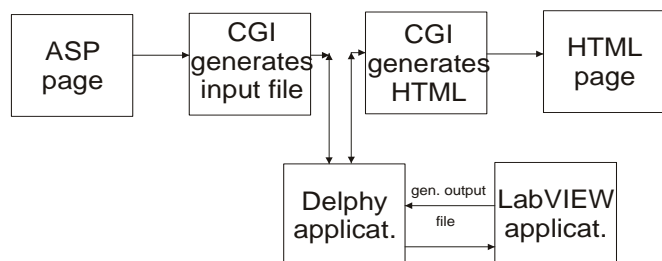


Fig. 2. Virtual laboratory application structure

The beginning of the next phase of this application is a moment when a measurement is done and the data should be collected and showed to the user. This moment is not possible to detect by the CGI script. In another hand, a CGI script generates a HTML page which will be presented to a user as a resulted one. Input file for the LabVIEW application is generated by the CGI script. An application which controls the execution of the appropriate LabVIEW application, as well as it's shut down when a measurement is over and an output file is created, is developed in programming language Delphi [6]. In other words, this application has a position of a trigger of the real physical measurement process for the current equipment configuration. Once a CGI script creates an input file for the appropriate LabVIEW application, the Delphi application detects that input file and starts up a LabVIEW application. When the measurement is done and the output file is created, the Delphi application shuts down the LabVIEW application in order to fulfill demands for the next measurement. In the meanwhile, the CGI script is blocked in the while loop which is aborted when the output file is created and there are no other constrains, and then the HTML file can be created.

In system like this, the concurrence of more measuring requirements on the same measuring system at the same time appears. The first solution of this problem was solved in a trivial manner by not allowing the access to anyone while the

laboratory is occupied by the user who is already logged. New solution is to put all logged clients in a queue and the CGI script does not create an input file for the user until that user is not the next one who should get into the laboratory. In this way, increase of users number increases the waiting time (with linear dependency) in the queue, but it is equal for everyone who is in order to login.

III. CONCLUSION

Nowadays, a computer is an essential tool in a number of areas. They became irreplaceable in the process monitoring, product quality checking, automation, process control and management, realization of the measurement systems, etc. The development of information technologies has opened new possibilities in realisation of measurement data acquisition systems.

Remote measurement system is often accessed through the global Internet network. The laboratory heart consists of a group of specialised and/or general instruments, connected to the Internet through the PC. Within a remote measurement laboratory, clients can cooperate to each other and use all laboratory resources, even they are on geographically distant places.

Suggested system is based on client-server architecture, it is easy to expand and it makes possibilities for distant clients to access the instruments. CGI scripts, written in C++ program language, generate the measurement input file based on the data achieved from the current user's Internet page. Laboratory, which is realized in LabVIEW, is started by application written in program language Delphi, immediately after the input file is created. Delphi application terminate the LabVIEW application when the measurement experiment is done and an output file with the measured data is created. Then, a CGI script generates a HTML file with the results for the user. System expanding can be shown with the increasing number of laboratories, which are connected to the system. Every laboratory needs a different LabVIEW virtual instrument. In the case of increasing the number of connected laboratories, the application has good bases for further development, which is related to easy handling and to the possibility of easy upgrading and interface changing.

REFERENCES

- [1] Jelena Đorđević, Milan Jović, „Development of a Measurement Laboratory for Remote Experiments“, ETRAN 2006, Conference Proceedings, Vol. IV, Belgrade, Serbia, 2006.
- [2] Jelena Đorđević, Miroljub Pešić i Miodrag Arsić, “An Approach for Distributed Measurement Systems Development”, Metrological Congress 2003, Conference Proceedings, Belgrade, Serbia and Montenegro, 2003.
- [3] *Distance-Learning Remote Laboratories using LabVIEW*, User's manuel, National Instruments Corporation, USA, Februar 2002.
- [4] A. Keyton Weissinger, *ASP in a Nutshell - A Desktop Quick Reference*, Second Edition, July 2000.
- [5] Thomas Boutell, *Dynamically Generated Web Pages With CGI Programming*, ISBN: 0-201-42219-0.
- [6] Ivan Hladni, *Inside Delphi 2006*, Wordware ISBN: 1598220039.

The Use of Virtual Reality Environments for Training Purposes in Care Settings

Edith Maier¹, Miglena Dontschewa² and Guido Kempter³

Abstract – In our paper we describe the outline of a project that aims to apply virtual reality (VR) technologies in healthcare education, in particular for learning how to cope with aggression in care settings. We consider a Virtual Learning Environment (VLE) populated by intelligent virtual agents a safe and effective medium. After briefly discussing current VR applications in healthcare and therapy we explore the use of VR for behavioural training and examine the critical factors for implementing effective VLEs. Finally, we discuss how to measure the impact of VLEs.

Keywords – virtual reality, virtual learning environment, aggression, training, emotions in HCI

I. INTRODUCTION

Nurses and caregivers are the most likely to suffer from aggression and violence in healthcare systems. Incidents range from verbal abuse, physical attacks to sexual harassment. Difficulties in coping with such incidents of aggression can lead to increased stress, low job satisfaction and absenteeism which in turn poses a major socio-economic problem.

This is why a 5-day aggression management training programme is offered by the Institute of Nursing Sciences in St. Gallen, which was originally developed in the Netherlands, and has been widely used in the UK and Switzerland in nursing homes, mental health care and disability care settings. It consists of a mixture of theoretical elements, exchange of experience and hands-on training. The participants are encouraged to perceive aggression from an interactional and situative context and to develop their interventions accordingly. It also emphasises the need for a clear institutional policy.

Studies demonstrate that attitudes of nurses influence their behaviour regarding aggression and that training programmes can positively change their attitudes. However, it has proven very difficult to furnish evidence for the effectiveness of such training programmes.

¹ User Centered Technologies Research Institute at the University of Applied Sciences Vorarlberg Hochschulstrasse 1, A-6850 Dornbirn, E-mail: Edith.Maier@fhv.at, and University of Applied Sciences St. Gallen, CH-Tellstrasse 2, 9001 St. Gallen, E-mail: edith.maier@fhsg.ch

^{2 3} User Centered Technologies Research Institute at the University of Applied Sciences Vorarlberg, Hochschulstrasse 1, A-6850 Dornbirn, E-mail: Miglena.Dontschewa@fhv.at and Guido.Kempter@fhv.at

Although participants report a higher degree of confidence in their ability to cope with aggression, a recent study by Hahn et al. [1] did not observe any significant attitude changes. It concluded that this might be due to the impact of the pedagogical quality of training courses, lack of organisational support and/or the fact that the measuring instruments were inadequate.

So even if recent scientific literature suggests the use of more preventive measures, communication and negotiation skills and de-escalation techniques in the management of aggression, the effectiveness of different strategies so far has not been evaluated systematically. Most authors hope that future studies will help dispel some of the uncertainties that exist at present whilst it is conceded that it is very challenging to design appropriate experiments to investigate the comparative success rates of different strategies both for ethical and cost reasons. This is why we propose to use virtual reality (VR) to enhance aggression management training on the one hand and evaluate the impact of different coping strategies on the other.

II. VIRTUAL REALITY ENVIRONMENTS FOR BEHAVIOURAL TRAINING

A. Definitions and concepts related to VR

Virtual reality (VR) is a technology, which allows a user to interact with a computer-simulated environment, or – according to Thalmann -, “it refers to a technology which is capable of shifting a subject into a different environment without physically moving him/her” [2]. According to this definition virtual reality environments (VREs) aim at inducing the immersion of one or more individuals in a virtual environment by creating the illusion that they are in a place, time or situation different from their actual real-world location and/or time.

The technology was first used by Sutherland [3] and advanced rapidly, e.g. with the invention of the head-mounted display or the data glove. Currently, VREs are primarily visual experiences, displayed on a computer screen or through special stereoscopic displays because of people’s binocularity. But more advanced VREs include additional sensory information such as auditive and tactile information, and attempts are currently made to simulate smell.

Users can interact either through the use of standard input devices (i.e. keyboard and mouse) or through multimodal devices such as the above-mentioned data glove. The simulated environment can be similar to the real world,

e.g. simulations for pilot training, or it can differ significantly from reality as in VR games.

B. Current healthcare and therapeutic uses of VR

VREs have been used in a wide range of application domains: engineering, physics, medicine, education, marketing, real estate and many others.

Gradually, VR is also finding its way into the training of healthcare professional. VR technology has been used for anatomy instruction or surgery simulation. In the case of laparoscopy¹, for example, it is important to realistically visualize body parts.

More relevant to our project is the use of VR for treating various phobias. Virtual reality exposure therapy is an evolving technique that has been attracting increasing attention and research interest in a range of disciplines such as human-computer interaction, graphics design, psychiatry, clinical psychology and psychotherapy [4]. Quite basic VR simulation with simple sight and sound models, for example, has proven very effective in treating fear of flying, spider phobia (arachnophobia) or various zoophobias [5].

Another promising development is the application of VR for treating post-traumatic stress disorder (PTSD), e.g. in veterans. The U.S. Office of Naval Research is evaluating VR tools which integrate the sights and sounds of combat as well as smell and other sensory factors to treat PTSD [6].

C. Characteristics of virtual environments

Several psychological factors have come to be regarded as essential in VRE, namely a sense of presence immersion, involvement, interaction, person view (first or third person view) and emotions. The challenge consists in achieving the best balance between those factors.

In behavioural training, the realistic and believable modelling of people's behaviour and their emotional expression is important to evoke real-life reactions in trainee and to create a sense of presence and involvement in the (virtual) situation. There is a large body of research on this topic, but there is little information about emotional expression and visualization in this field. Which emotions can be depicted believably? How realistic does an emotional visualization have to be? What possibilities do we have to represent and evoke emotions? We now briefly discuss the various characteristics:

Immersion

An immersive digital environment is an artificial, interactive, computer-created scene or "world" within which users can immerse themselves. The degree of immersion is influenced by factors like the amount of detail of the 3D scenes, the degree of isolation from the physical environment, perception of self-inclusion in the VRE, natural modes of interaction and control, perception of self-movement or interactive user-input [7]. A high degree of

immersion is important, as it is seen as a prerequisite for a sense of presence (see below).

Involvement

Involvement is a psychological state experienced as a result of focusing one's energy and attention on a coherent set of stimuli or meaningfully related activities and events. Involvement largely depends on the meaning that the individual attaches to the stimuli, activities or events. For many people, high levels of involvement can be obtained with media other than VRE, such as movies, books or video games. Though the factors underlying involvement and immersion may differ, the levels of immersion and involvement experienced in a VRE are interdependent: increased levels of involvement may lead users to experience more immersion in an immersive environment and vice versa [8].

Sense of Presence (SoP)

Both involvement and immersion are necessary for experiencing presence. Presence can generally be defined as the subjective experience of being in one place or environment, even when one is physically situated in another. However, SoP is not a characteristic of a medium but the feeling of the user of "being there" and thus has to be clearly distinguished from immersion.

First person view

In real-life one is able to see one's own limbs, therefore it might be disturbing not to be able to see one's own body in VREs. This perspective is called first person view, as opposed to the third person view in which the on-screen character is seen at a distance from a number of different possible angles. A third person perspective provides for more awareness of one's surroundings and position within it as well as the distances to objects and other characters. In scenarios that are especially arousing or disturbing such as is the case when confronted with aggressive behaviour, the ability to process the scene from a third person view might be very helpful.

Interaction

As already mentioned users can interact with a VR system through a range of devices and channels, e.g. haptic (data gloves), magnetic position/orientation sensors, 3D mouse, voice, gesture or face recognition. Interaction implies that users can (more or less) control the pace, order and (sometimes) occurrence of the events in the VRE. Interactivity enhances the sense of immersion, as humans are used to manipulate objects and engage in interaction with animals or other humans. Being a passive observer can be a choice in behavioural training (e.g. to learn from fixed situations), but an active involvement will be more effective.

Emotions

A factor largely ignored up to now is the expression of affect of virtual characters and the emotions this elicits in a user. Many studies have shown the ability of movies and imaging techniques to elicit emotions. Nevertheless, it is

¹ Laparoscopy is a type of surgical procedure in which a small incision is made, usually in the navel, through which a viewing tube (laparoscope) is inserted.

less clear how to manipulate the content of interactive media to induce specific emotional responses. Besides, we do not yet know which emotions, or more generally, which affective states can be conveyed through the setting or environment itself (as opposed to the virtual characters). It has been shown that humans have an inherent tendency to interact with different kinds of media in a natural and social way, mirroring interactions between humans in social situations [9]. But can a virtual character have and show complex, mixed emotions and affective states? Can, for example, aggression be conveyed convincingly? Is an emotional message transmitted through appearance or behaviour?

Even less is known about the effect of VREs on the user's affective state. Riva [10] found that the interaction with a fear-inspiring VRE produced anxiety, whereas interaction with a pleasant one produced relaxation. Besides, it turned out that a circular interaction existed between presence and emotions, i.e. the feeling of presence was greater in the "emotional" environments and in turn, the emotional state was influenced by the level of presence. The link between presence and emotion enables us to measure the sense of presence by standard psychological methods of emotion measurement.

IV. METHODOLOGY AND IMPLEMENTATION

For the design and development of the virtual learning environment (VLE) and the virtual agents we shall apply a user-centred approach. This implies that potential users are involved right from the start of the project and are consulted at regular intervals on all aspects of the VLE's design. Their comments and suggestions for improvement are then fed back into the design of the VLE. This participatory and iterative approach relies mostly on qualitative and informal methods and will allow developers to gain a more detailed understanding of the users' attitudes and requirements.

The fundamental idea is to allow caregivers to try out various coping strategies without being directly involved themselves, i.e. the usefulness of a coping strategy can be learned safely and vicariously through the victim character's experiences. Apart from characters representing the aggressor(s) and the victim(s), the VLE will also include bystanders and/or assistants as well as locations (nursing home, psychiatric ward) and scenarios that are typical for real-life incidents. To elicit real-life reactions in trainees when faced with particular scenarios, it is important to model people's behaviour and their emotional expressions in a realistic and believable way, i.e. the VLE has to be "ecologically valid".

VR will first of all help to design scenarios that are based on incidents of aggression that have occurred in real life and have been gathered in the course of many in-depth interviews with caregivers as well as experts in the Institute of Nursing Sciences. The interviews also provide the storylines, settings and special characteristics of the intelligent virtual agents to be developed. Since for ethical and privacy concerns it will be impossible to install video cameras in relevant locations such as nursing homes, we

shall have to resort to film clips and actors experienced in this type of work

We shall then investigate to what extent VR can help induce behavioural changes by simulating the effects certain types of behaviour or communication strategies have on the patient or elderly person receiving care. VR will also allow us to combine settings, personality types and coping strategies because we are aware of the fact that the success of a particular strategy is highly dependent on context and the psychological make-up of the people involved. Thus, VR also enables us to adapt training to people's personal preferences or needs.

From previous studies [11] relevant to the aims of our project the following recommendations can be derived for the development of virtual environments in general:

Firstly, agent and environment believability can be improved by ensuring cultural similarity with target users. In our case we shall pay particular attention to professional milieu, i.e. the special characteristics of care settings.

Secondly – and closely related to the first –, the terminology and phraseology used has to reflect the language use prevalent in a particular environment. Besides, a cohesive storyline also contributes to deeper immersion in a virtual environment.

In addition to that, the possibility to interact with the characters has shown to be a major factor in successful immersion. However, since our project is primarily about letting people try out various coping strategies without being directly involved themselves, the inclusion of personal avatars is not foreseen in the design of the VLE. However, we might consider to allow at least superficial interaction – such as selecting physical characteristics of an otherwise unplayable agent, to make users identify more with a given character.

Recent findings [11] have also shown that the graphical design of the characters seem to have limited impact on the user's rating of their believability or on the elicitation of empathy. The results suggested that excellent graphical design is not necessary to create an engaging experience as long as characters act in a believable manner.

IV. MEASURING THE IMPACT OF VIRTUAL LEARNING ENVIRONMENTS (VLE)

Due to technical limitations such as processing power or image resolution problems it is still difficult and time-consuming to create high-fidelity VR experiences. Even though these limitations are likely to be overcome soon, it is still important to evaluate the effectiveness and learning impact of the VLE to be constructed. It has been shown that learning with attributes such as enjoyment, engagement and increased attention does occur in virtual environments. This is also born out by the empirical results from non-educational VR research, e.g. simulations for task training, e.g. in the military/defence industry or the visualisation of large data sets used for exploration, pattern discovery and investigation.

A common measure of the quality or effectiveness of a virtual environment (VE) is the amount of presence it evokes in users. Presence is often defined as the sense of being there in a VRE. There has been much debate about the best way to measure presence, and researchers need, and have sought, a measure that is reliable, valid, sensitive, and objective. We hypothesize that to the degree that a VRE seems real, it would evoke physiological and psychological responses similar to those evoked by real situations or environments.

Rather than measure attitudinal changes as done previously [1], we want to focus on psycho-physiological factors to measure the impact of a VLE. We therefore intend to examine the cognitive judgment of learners by using 10 bipolar rating scales. The ends of each scale comprise opposite adjectives that will be determined in a preceding survey to identify the descriptive features of the synthetic agents.

As pointed out before, the link between presence and emotion allows us to use standard methods of emotion measurement. In our project, we intend to monitor the emotional reactions to the aggression scenarios by taking psycho-physiological measurements. Skin conductance, for example, can be measured at the inner hand, heart-rate activity by means of electrocardiography and breathing movements with the help of a stretching belt round the chest.

V. CONCLUSIONS AND EXPECTED RESULTS

The main benefits of using a VLE for aggression management training can be summarised as follows:

- Users can practice skills safely, without experiencing potentially dangerous real world consequences.
- The stimuli the user receives can be controlled.
- VLEs empower users with disabilities by giving them a sense of control over their environment.
- VLEs allow learners to actively participate and focus on their personal abilities.

Besides, the project is expected to contribute to advancing the following research issues:

- Identify heuristics and guidelines for user interface design to assess the impact of VR applications
- Measure the impact of learning in virtual environments (VE) ; possible indicators are presence, engagement, immersion
- Identify factors that contribute to or distract from the act of learning in a VE (e.g. social, hardware, network, content and curriculum quality issues)
- How can scaffolding be built into the software to guide the users, esp. those with cognitive impairments?
- Examine the impact of emotional models on the learning experience

The project will be implemented in close collaboration between several research organisations including the Institute of Nursing Science at the University of Applied Sciences in St. Gallen, Switzerland, the User-Centred

Technologies Centre and Virtual Reality Lab at the University of Applied Sciences in Vorarlberg, Austria as well as the Institute of Medical Education at the Inselspital in Berne, Switzerland.

REFERENCES

- [1] S. Hahn, I. Needham, C. Abderhalden, JAD Duxbury, RJG Halfens, "The effect of a training course on mental health nurses' attitudes on the reasons of patient aggression and its management", *Journal of Psychiatric and Mental Health Nursing*, vol. 13, pp. 197-204, 2006.
- [2] D. Thalman, *Introduction to Virtual Environments, Teaching Materials*, Virtual Reality Lab, Swiss Federal Institute of Technology, Lausanne, 1998.
- [3] I.E. Sutherland, "The Ultimate Display", *Proceedings of IFIP 65*, vol.2, pp. 506-508, 1965.
- [4] C. van der Mast, "Technological challenges and the Delft virtual reality exposure system", *Proceedings 6th Intl. Conf. Disability, Virtual Reality & Assoc. Tech.*, Denmark, pp. 83-90, 2006.
- [5] P. Emmelkamp, "Technological innovations in clinical assessment and psychotherapy", *Psychotherapy & Psychosomatics*, vol. 74, pp. 336-343, 2005.
- [6] J. Huergo, "Evaluating Virtual Reality Therapy for Treating Acute Post Traumatic Stress Disorder, Press Release, Office of Naval Research, 2005.
- [7] W. Sherman and A. Craig, *Understanding Virtual Reality – Interface, application, and design*, Elsevier Science, 2003.
- [8] B.G. Witmer, M.J. Singer, "Measuring Presence in Virtual Environments: A Presence Questionnaire. Presence: Teleoperators & Virtual Environments, vol. 7, pp. 225-240, 1998.
- [9] B. Reeves and C. Nass, *The Media Equation. How People Treat Computers, Television, and New Media Like Real People and Places*, New York, Cambridge Univ. Press, 1996.
- [10] G. Riva, F. Mantovani, C. Capideville, A. Preziosa, F. Morganti, D. Villani, G. Gaggioli, C. Rotella, "Affective Interactions Using Virtual Reality: The Link between Presence and Emotions", *CyberPsychology & Behavior*, 10:1, pp. 45-56, 2007.
- [11] L. Hall, S. Woods, R. Aylett, L. Newall and A. Paiva, "Achieving empathic engagement through affective interaction with synthetic characters", *Proceedings of ACII 2005: Affective Computing and Intelligent Interaction*, pp. 731-738, 2005.

How to Give a Good Scientific Presentation

Stevica S. Cvetković¹ and Saša V. Nikolić²

Abstract - The major goal of this paper is to serve as a guideline for organization of research presentations. Systematic description of complete process which includes five steps: Constraints considering, Structure planning, Design, Practise and Delivery of presentation is given. This procedure can be used for thesis presentation, as well as for conference, or technical reports to research sponsors, both by graduate students and professional engineers.

Keywords – Scientific presentation, Engineers education.

I. INTRODUCTION

The outline of almost every good talk is the same [1]:

**“Tell them what you’re going to tell them;
Then tell them;
Then tell them what you told them.”**

As a researcher you will have many opportunities to present results of your research. Your presentation may be given in research laboratory, a university course or a conference. The goal of this paper is to provide you with some tools to help you design and deliver your presentation.

Major principles for giving a scientific presentation can be found in numerous literature [2-11]. Inspiration for us to analyze this topic was lack of systematic description of complete process which includes planning, creating and delivering the presentation.

The one thing which is emphasized in everything written about presentations is: **Content is key!** Many speakers forget that the content is the most important issue, not how nice a presentation is. Quite often flashy presentations hide the fact that there is no content. Remember that the discussion after the presentation is when the speaker demonstrates who he really is. This is where many good presentations get blown away.

While the content of the presentation is of primary importance, the presentation style also affects the overall impression of the audience and can enhance or detract from the actual scientific impact of the content presented. Number of quality scientific papers were not adequately evaluated because of their poor presentation. Balance between the quality of content and ability to clearly convey scientific information in an oral presentation is critical to both teaching and research. The best presentations are built on a clear message, supported with well-organized facts and enhanced

with illustrations, charts and graphs. It is always a great pleasure to attend presentation where results are well presented, the flow of the lecture is easy to follow, and the illustrating materials are clear.

An effective presentation depends on five important steps presented in Fig. 1. The rest of the paper will give detailed explanation for each of these steps.

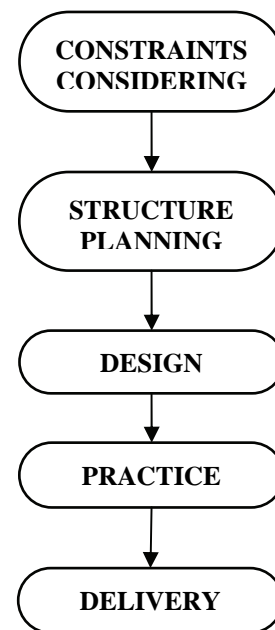


Figure 1. Five steps for effective presentation

II. CONSTRAINTS CONSIDERING

The structure of the presentation is strongly influenced by following constraints:

A. The Audience

Your talk needs to convey information to the audience. It is therefore imperative that you know who your audience is. Knowledge of your audience is an important prerequisite in making decisions about the content, format, language and style of your presentation.

You have to give answers to the following questions:

- Who are the members of your audience?
- How familiar are they with your topic and content?
- What do they already know about your topic?
- What do they want or need to know?

¹Stevica S. Cvetkovic is PhD student at the Faculty of Electronic Engineering, University of Niš, Aleksandra Medvedeva 14, 18000 Niš, Serbia, E-mail: stevica_cvetkovic@yahoo.com

²Saša V. Nikolić is with the Faculty of Electronic Engineering, University of Niš, Aleksandra Medvedeva 14, 18000 Niš, Serbia, E-mail: caci@elfak.ni.ac.yu

Consider your presentation from the audience's point of view. What's in it for them? If you can show them early on that they will benefit in some way from listening to your presentation, you will have a much better chance to achieve your outcome.

It makes no sense to present a complex topic at your level of understanding, you may be the only one who understands it. For example, if you write formula

$$f(x) = \frac{1}{\sqrt{2\pi}\sigma} \exp\left(-\frac{1}{2}\left(\frac{x-\mu}{\sigma}\right)^2\right)$$

to a group of arts students, they will get nothing from it. Therefore, try to gear the presentation to the audience level of understanding.

B. The Time Limit

It is very important to plan your presentation time carefully. In the research environment over-time is considered one of the worst sins. Content of the presentation has to be decided according to provided time. Short talks (10 – 15 min) have a different strategy from long talks (45 – 60 min). Anyway, assume **1 to 2 minutes per slide** depending on complexity.

For a short talk, there is no time to explain analytical analysis, implementation details or formulas. Focus on the "take home message" and the data to support it.

If you give a long talk, lots of time can be used to discuss the methods in detail if they differ from standard protocols.

III. STRUCTURE PLANNING

Structure planning refers to defining of presentation skeleton which includes first level titles and subtitles, as will be described later. Whenever possible, you should first define skeleton and after that, during the design process, you should develop the contents of all paragraphs. Depending on type of your talk, two types of structures are described [2], [3].

A. Research Presentation

Every research presentation should contain at least one slide for each of the following titles:

*Introduction*₂ to include the basic facts needed to tune the reader to the presentation;

*Problem statement*₂ to define precisely the problem being attacked by the research under consideration, and why is that problem important;

*Existing solutions and their criticism*₂ to survey briefly the major existing solutions from the open literature and to underline their deficiencies from the point of view of interest for this research;

*Proposed solution and why it is expected to be better*₂ to give the essence of the proposed solution (i.e., the essence of the idea which is to be introduced), followed by a logical discussion about the expected benefits stemming from the idea;

*Conditions and assumptions of the research to follow*₂ to summarize the environment of interest. The term *conditions* refers to the specifics of the real environment, and the term *assumptions* refers to the simplifications which simplify the

analysis without any negative impacts on the validity and representativeness of the final results.

*Analytical analysis*₂ to show one or more of the following:

- proof of validity of the major idea of the presentation;
- calculation of initial values for simulation analysis to follow;

• rough estimation of the performance and complexity; Analytical analysis will not give the final answers; however, it will help understanding the concept. It will be helpful both to the researcher and the reader.

*Simulational / Implementational results*₂ to show performance and complexity. For some types of research, this one could be the major and the longest part of the paper.

*Conclusion*₂ with the following three major elements:

- revisiting the major contribution from the performance/complexity point of view;
- stating who will benefit from the presented results;
- what are the newly open problems and research avenues.

B. Review Presentation

An important prerequisite for a good research paper is that a good review paper is prepared first, to demonstrate that major solutions for the problem of interest are known.

In the case of a survey paper, the major requirement is to have two main parts:

Concepts part to define the major issues. The concepts part should be preceded by a classification of concepts.

Systems part to define various algorithms and implementations, etc. The systems part should be preceded by a classification of systems. Each system in the systems part should be described using the same template (e.g., origin, environment, essence, advantages, drawbacks, relevant details, performance consideration, complexity consideration, conclusion, trends, etc.). The choice of elements for the template is flexible. What is not flexible is that the same elements must be used in each template.

IV. DESIGN PROCESS

It has been said that we remember 20% of what we hear, 30% of what we see, but between 50% and 75% of what we see and hear [11]. Always have in mind that your audience have a limited attention span i.e. they phase in and out of the presentation. Attention span is actually quite short 10-20 seconds. So how do you keep them with you?

You have to make two certain decisions when designing your presentation:

- What information ?
- What format ?

Because of their overlapping, it is impossible to give separate answers to the previous questions. Review of basic principles of designing presentation is shown next.

A. Content

The basic principle of slide's content design process is: **Minimize the content and keep it simple!** Create simple and clear slides which can be read easily and get back in touch with the presentation. The slide message should be clean and easy to absorb. All content should not be put on the slides because the audience will focus on reading of slide's content and the speaker will be ignored. Only the most important points should be on the slide:

- Maximum of 8 lines per slide.
- No more than 8 words per line.
- 1-2 minutes per slide.

B. Headlines

Each slide should be clearly titled, indicating focus of slide. Use strong headlines that concisely states the idea of the slides. Headlines should:

- Orient the audience.
- Help define presentation's structure.
- Help keep speaker on track.

C. Semantic Splitting

The rule of semantic splitting [2] could be defined as: If a sentence must be spread over more than one line, each line should represent a separate thought. As an illustration, two examples are shown next:

Text without semantic splitting:

- Writes get satisfied on distance or locally, depending on what brings better performance
- Good if reads and writes are interleaved with similar probabilities of occurrence

The previous text with semantic splitting:

- Writes get satisfied on distance or locally, depending on what brings better performance
- Good if reads and writes are interleaved, with similar probabilities of occurrence

D. Visual Aids

General principle for visual aids is to keep them simple and clear. Also, clear explanation of the used variables and how they were measured, is essential.

Equations - Use them only where necessary in cases you give a long presentation (45 – 60 min). If you have enough time to use them, explain clearly every variable. They quite often turn off a non mathematical audience. Instead of using them, a conceptual model may be much useful.

Tables - Complicated tables are not visual aids. They have been described as instruments of torture for the audience. Tables of data suitable for written publication are highly unsuitable for a scientific presentation. Try to summarize the findings without using tables. If you must use them, state why the result is important to your hypothesis.

Graphs - Graphs should replace tables where possible in a visual presentation. They are better than tables in showing relationships. Always follow next principles:

- State the significance of the relationship shown and why it is so important to the issue you are examining;
- Always describe the variables;
- Always show regression statistics;
- Use colors in graphs with multiple relationships;
- Limit relationships to 3 per graph, better to show two graphs than confuse the listener;

E. Text

Text size - You will find some variations in recommendations for the size of body text. However, use the 24 karat rule for "golden presentations" - don't use fonts smaller than 24 points. The size of the room is the key, large rooms require large typeface points no smaller than 30. Text height should be one centimeter for every one meter of distance from your audience.

Font

- Use no more than 2 font styles, too many fonts can be distracting. Most references recommended to use only one font, two is the maximum.
- Try to use clear fonts like Arial or Helvetica.
- Avoid fancy fonts, scripts, fonts with shadow effects and italics because they are difficult to read when projected.

Colors - Although it is possible to change the slide's color scheme, **it is best to use the base palette for the template, developed by design experts.** However, if you want to experiment, high-contrast colors are only wise solution. Light text (yellow, gray or white) on dark background (blue, olive or purple) is always good solution.

Background Colors - Dark colored backgrounds are easiest to read. Blue, black or purple are suggested. For education purposes, use deep forest green, olive or teal. Never use a clear white background, at least apply light color. Remember that color evokes psychological responses. Red is stimulating, it increases excitement, heightens emotion and can cause problems. Brown is also a color to avoid.

Foreground Colors - Yellow is easiest to read on blue background. It is stimulating color, excellent for combination with blue and red text. Gray is neutral, it eliminates bias. Light violet is expansive and open-minded color

V. PRACTISE

Nothing improves a presentation more than one practice talk! This is perhaps one of the most important principle [6]. If you practice your presentation just once, your talk will be infinitely smoother.

A. Actually Practise

This does not mean running through the slides and going "yeah, then that stuff, then the next slide, then the experiment

part, a couple of diagrams, data, conclusions”. Actually stand up and give the talk. Practice improves the flow of the talk. There will be less “um’s” in the talk if you practice. People have a natural tendency when speaking in public to pause and say “um” when they forget what they were going to say for just an instant. By running through the talk you will develop a natural flow. You will come up with phrasings and ways to describe things that you will use when you give your presentation. Most importantly you will discover things that you don’t actually understand. **Explaining something to someone else is the best way to determine if you really understand it.** Don’t fool yourself into thinking you can explain it, try it. If you don’t understand, you have time to figure it out before the talk. Even things you know well might be difficult to explain. Practicing helps you to find the words. Also, giving a presentation can be a nervous business, practice can help alleviate that fear.

B. Memorize the First Few Lines

Starting out is the hardest part of the talk. Once you get going and into a flow things are easier. But that first little bit is nerve racking. One thing you can do is to memorize the first few lines you are going to say. Don’t memorize the entire talk, just first few lines: “Hello, I’m Stevica Cvetkovic. The title of my presentation is How to Give a Good Scientific Presentation. The goal of this paper is to provide you with some tools to help you design and deliver your presentation...”. Wing it from here.

VI. DELIVERY

The challenge to the speaker is to hold the attention of the audience. An important part of delivery is your interaction with the audience through: 1) Voice, 2) Movements, 3) Stage Presence. In order to have effective presentation, you must accept following principles.

Prepare strong wording to emphasize strong points or transitions. Examples for beginnings, middles and endings are shown:

Beginnings: “My name is ... and I will be talking about...”

Middles: “That concludes what I have to say about cross sections. I will now discuss...”

Endings: “To summarize, I would like to show you ...”

Talk to the audience, not the overhead, or the computer. Avoid to read your slides. The audience’s attention should be on the speaker. A paper can never serve as a speech or vice versa.

You are your own best visual aid. Use your body language, facial expression and gestures to add impact to your verbal message.

Deliver dramatically. If you mumble to yourself no one will pay attention. Speak with conviction. Change you voice level as much as possible, monotone puts you to sleep.

Ask the audience questions, whenever possible. Or at least challenge them to think about the issue. Example: “If this worked this way then we would expect this result, but we got this! Why?” Then explain.

Keep it interesting. If you have practical examples, interesting tidbits or humorous asides, people will be less likely to drift off to sleep.

REFERENCES

- [1] Strunk, W., and E. B. White, “The elements of style”, 3rd ed. New York: Macmillan, 1979.
- [2] Milutinović, V., “The Best Method for Presentation of Research Results,” IEEE TCCA Newsletter, pp. 1-6, September 1997.
- [3] Milutinović, V., “A good Method to Prepare and Use Transparencies for Research Presentations,” IEEE TCCA Newsletter, pp. 1-6, March 1997.
- [4] E.Bulska, "Good oral presentation of scientific work", Analytical and Bioanalytical Chemistry, 385, 403-405, 2006.
- [5] Barbara Grimes, “Tips for a Great Presentation”, November 2000, www.mc.vanderbilt.edu/nursing/tools/help/ppttips.pdf
- [6] “Tips For Giving a Scientific Presentation”, www.fw.msu.edu/orgs/gso/documents/GSOWorkshopDocsSp2006/TipsforGivingaScientificPresentation.pdf
- [7] Michael St. John, “How to Give a Good Scientific Seminar: Does, Don’ts and Strategy”, www.biologie.uni.hamburg.de/ihf/de/teaching/How_to_give_a_presentation.pdf
- [8] Samuel B. Silverstein, “The Art of Scientific Presentation” www.physto.se/~silver/presentation/SciPresTalk.pdf
- [9] Smith R, “How not to give a presentation”, British Medical Journal, 321:1570–1571, 2000.
- [10] Jason Harrison, “Planning a Scientific Presentation”, Graduate seminar, October 2002.
- [11] Sorgi M, Hawkins C “Research: How to plan, speak and write about it”, Berlin, Springer-Verlag, pp. 110–135, 1985.

Reevaluation and Replacement of Terms in the Sampling Theory

Petre Tzv. Petrov¹

Abstract – Terms should be short, unique, unambiguous and self-explanatory. Transferring terms from one field of the science to the other should be made with caution. Basic terms of the sampling theory are discussed in the paper. It is shown they are incorrect, misleading or inexact and should be replaced. New terms with definitions and explanations are given for the replacement of the incorrect terms.

Keywords - terms, terminology, sampling theory

I. INTRODUCTION

Each engineering term should as short as possible, unique and self-explanatory. The term should be correct and leading to exact mathematical presentation if possible. The definition of the term should be a logical expansion of the term and not unexpected explanation. The term should be an abbreviation of the definition or an abridged definition.

The signal sampling theory (SST) as explained and applied in [1-10] contains a lot of terms which should be reevaluated, rejected and replaced with new terms explaining better the nature of the signal sampling and reconstruction process. The paper is dealing with that subject. It is intended to help students, researchers and engineers to clarify the SST.

II. OLD, INCORRECT AND MISLEADING TERMS

The terms below are considered incorrect and misleading from engineering (physical) point of view. Some of them are still acceptable from mathematical or another point of view.

Aliasing - a misleading term meaning in most of the cases that the analog signal (AS) is not adequately sampled and filtered. Also the term is used to show that a sinusoid (or co-sinusoid) is changing from one frequency to another. In the second case it is better to use the “coefficient of the change of the frequency” $K_{ch} = F_{it}/F_{rs}$, where F_{it} is the initial frequency and F_{rs} is the resulting frequency. (The word “alias” has a criminal meaning in [11, 12]).

Classical sampling theorem (CST) – is an oversimplified sampling theorem generally stating that two samples are enough to reconstruct “exactly” band limited signals (BLS) with maximal frequency F_{smax} . According to the CST the sampling rate F_s should be selected according to the equation $F_s = F_{smax}$ or $F_s \geq F_{smax}$. The CST is based on Fourier series. It is proved [13] that with CST: 1/ the simplest band limited signal (SBLs) cannot be

reconstructed always and 2/ the amplitude errors cannot be evaluated. The theorem is not taking into account the errors due to non synchronized signal sampling and is pretending for “exact” reconstruction. In general the CST is applicable for synchronized sampling with SSF $N \geq 2$ without errors evaluation and with low pass filtering.

Co-sine wave (co-sinusoidal signal (CS)) – a simplified but still real (not over simplified) version of the simplest band wide signal (SBLs). Co-sine wave is a SBLs consist with direct current (DC) component with zero amplitude and cosine component with non zero amplitude and usually with zero phase. The cosine wave has four parameters to reconstruct.

Decimation - incorrect term (nothing to do with the number 10), meaning “reducing of the sampling rate by calculations or omissions” especially during the signal reconstruction. (The decimation in the ancient Roman army is giving misleading, non technical and cruel historical background of the term).

Gibbs phenomenon – a non existing phenomenon in the engineering world. It is a mathematical phenomenon when a function with infinite slew rate (rate of change or first derivative) and/or ideal angles is approximated with Fourier series. The phenomenon is often illustrated with ideal (physically impossible) rectangular pulse and wrongly associated with the process of “ringing” due to inappropriate impedance loading. The real signal (RS) is always a “smooth function” and even if it is “truncated” it has: 1/ finite rate of change, 2/ rounded (not ideal, not broken) angles, 3/ finite number of spectral lines and 4/ finite energy in every moment. These basics properties of the real signals are making Gibbs phenomenon non-existing and misleading in the engineering world. Nevertheless it is implemented in the software packages used by engineers as Matlab.

Nyquist rate, Nyquist frequency – The term means several different things: 1. The highest frequency in the signal spectrum F_{smax} , 2. Twice the maximal frequency in the signal spectrum, 3. The sampling rate which is twice the maximal frequency in the signal spectrum, etc. This multi-definition is caused by the misleading interpretation is one of the proof that the classical SST is not accurate.

Delta function (or unit pulse) - unreal function used to construct the Dirac comb. No practical value in the sampling theory, because is leading to the model “take and forget”. In a real system the digital samples are always stored and used. The applicable model is always “take and memorize”.

Comb function or Dirac comb– non real function representing the sampling model “take and forget”, meaning that the sample is not memorized until the next sample came.

Petre Tzv Petrov is with Microengineering, Sofia, Bulgaria, emails: ppetre@caramail.com and ptzvp@yahoo.fr.

(Related to the “delta function”, “staircase function” and “trapezoidal function”)

Ideal rectangular pulse, ideal triangular pulse and ideal saw tooth pulses – Oversimplified models which do not respect the basic properties of the real signals. If they are applied they are leading to the Gibbs phenomenon and infinite Fourier series.

Noise – Misleading terms used mainly to represent: 1. Errors during the conversion process. 2. Unwanted signal added to the useful one. 3. Signal which cannot be used but is added to the useful signal. 4. Errors due to calculations.

Dirichlet conditions – conditions wrongly associated with real signals and Fourier series. It should be noted that every real signal is satisfying conditions more strongly than these conditions, and consequently the conditions are not applicable to the signal sampling theory. The Dirichlet conditions are way to say that the Fourier transform and Fourier series are applicable only to real signals, represented by mathematical function and not to all mathematical functions. Every physical signal is: 1. Satisfying the Dirichlet conditions (finite number of maximums, minimums and discontinuities in a given finite interval), 2. Integrable for the time of its existence and 3. Can be represented by a sum of the SBLs.

Dither – a method stating that adding noise to signal could be “good thing”. In fact adding noise is always a “bad thing” and the method is giving non reproducible results.

First order hold and zero order hold – Is it possible to deduce the definition of these terms? The terms “take and memorize (until the next sample come)”, “sample and hold” or “take and forget” are much clearer and self-explanatory.

Fourier series – oversimplified presentation of the real signals as a sum of sine and cosine waves with harmonic frequencies and with zero phases and zero DC components. Mathematically the sum could be infinite. In fact every real signal could be represented as a finite sum of SBLs with not obligatory harmonic sine and cosine components and with not obligatory zero phases and zero DC components.

Over sampling – sampling with frequency higher than Nyquist frequency and meaning to certain “redundancy” which is incorrect. Should be replaced with the terms “Signal sampling factor” (SSF) $N = F_s / F_d$ stating its value

Over sampling and averaging for additional bits of resolution – misleading method for “adding bits” to ADC (beyond its accuracy) with collection of a lot of samples and averaging them. In fact most of the “added bits” have random or not easy reproducible values. The “method” is requiring a lot of memory and computational power and is not efficient and not reliable. In fact the method is a kind of low pass filtering

Resolution – most often the total number of bits used to represent the signal or a function. All of these bits are not obligatory reproducible. In most of the cases the resolution is higher than accuracy and is more or less commercial (non technical and exact) parameter.

Reconstruction of the signal from zero samples - A misleading conception. Obviously there is no way to reconstruct a signal parameter if the information for that parameter is not carried by the samples or in another carrier.

Reconstruction filter – in most of the cases is associated wrongly only with low pass filter. In fact it could be also band pass filter, who is giving the possibility to reconstruct a sine signal even with SSF $N < 2$ in some cases. Also it could be any filter reconstructing the initial signal with the given accuracy in each parameter.

Sine wave (sinusoidal signal (SS)) – a simplified but still real (not over simplified) version of the SBLs. It has four parameters to reconstruct. Accepting that the phase and the direct current component are zeros do not suppress them from reconstruction.

Sin (x)/x - artificial function wrongly associated with sampling and reconstruction process of the analog signals. The function is one of the proofs that something artificial is used in the sampling and reconstruction of the signals.

Step function – too idealized transition. If tact should be replaced with transition with specified rate of change (slew rate) and defined rounded angles.

Staircase function – Idealized model of the process “take and memorize” with “idealized angles”.

Window – “limitation” of parameter. In some cases it is much clear to use terms “limit”/“limited” and stating the corresponding parameter.

White noise – noise with parameters impossible to generate. The amplitude, spectrum, power and number of spectral lines in the real noise are always limited and does not correspond to the definition of the white noise

III. NEW TERMS

New terms are introduced, defined and listed in alphabetical order. The given definition is self explanatory.

Absolute accuracy (of conversion) – the basic technical term describing the conversion process giving reproducible results. It should be compared with “resolution” and “precision” which are commercial terms and are giving not always repetitive results.

Angle of the first sample θ_0 is the angle between the beginning of the coordinate system ($x=y=0$ or $t=0$) of the signal and the moment of the first sample. It is measurable in degrees and is defined especially for a SS, CS and SBLs.

Angle of the maximal deviation from the maximal value of the SS, or the angle of the maximal amplitude error when a SS is sampled ($\theta_{E_{max}}$). $\theta_{E_{max}}$ for $N \Rightarrow 2$ is given with the equation below

$$\theta_{E_{max}} = 360 / (2N) = 180 / N \quad (1)$$

(Law of the) Average amplitude error during the conversion of SS (DC and phase components are zeros) is given with the equation below:

$$E_{max} = 1 - \cos(90 / N) \quad (2)$$

(Law of the) Average amplitude error during the conversion of CS (DC and phase components are zeros) given with the equation below:

$$E_{max} = 1 - \sin(90 / N) \quad (3)$$

Basic parameters of the sampling process – The three basic parameters of the idealized but still representative sampling process are: 1/ signal sampling factor (SSF) N , 2/ number of the bits of the converter n (the accuracy of the converter not its resolution) and 3/ angle of the first sample

φ_0 . The sampling process is fully defined by these three parameters:

Coefficient (factor) of the change of the frequency – K_{ch} is defined as follows:

$$K_{ch} = F_{it}/F_{rs}, \quad (4)$$

where F_{it} is the initial frequency (or a sine or co-sine wave) and F_{rs} is the resulting frequency. K_{ch} is used to show that the frequency of a sine or co-sine wave is changed (usually due to some non linear process and filtering).

Factor of the sample and hold circuits $F_{s/h}$. Term describing the effectiveness of adding a sample and hold circuit. It should be greater than 1 to show increasing performance. If it $F_{s/h} \leq 1$ there is no increasing the performance and in general the S/H should not be added.

$$F_{s/h} = T_{ap(s/h)}/T_{ap(adc)} \quad (5)$$

Where: $T_{ap(s/h)}$ is the aperture time of the sample and hold circuit and $T_{ap(adc)}$ is the aperture time of the converter

F_{s3db} or 3dB sampling frequency is the sampling frequency guaranteed maximal error E_{max} less than or equal to 3db. The corresponding equation is $F_{s3db} = 4 F_{max}$. Also is called the **frequency of 3dB modulation**.

F_{s100} is the main (first) frequency of 100% modulation. The term is intended to replace “the Nyquist frequency” or the “frequency of exact reconstruction”. The corresponding equation is $F_{s100} = 2 F_{max}$. **F_{s100}** is defined with SSF $N=2$ and with maximal amplitude error between 0 and 100% included.

(Law of the) Maximal amplitude error E_{ssmax} during the conversion of SS (DC and phase components are zeros) is given with the equation below:

$$E_{ssmax} = (1 - \sin(90 - 180/N)) = (1 - \cos(180/N)) \quad (6)$$

(Law of the) Maximal amplitude error E_{csmax} during the conversion of CS (DC and phase components are zeros) is given with the equation below:

$$E_{csmax} = (1 - \cos(90 - 180/N)) = (1 - \sin(180/N)) \quad (7)$$

(Law of the) minimal errors during the conversion of SS or CS (DC and phase components are zeros) is stating that SSF

$$N = 4 * k \quad (8)$$

($k=1,2,3,\dots$) is giving the opportunity to obtain zero amplitude, phase and frequency errors during the regular sampling and DC component error is always zero.

Non-reproducible bits (N_{nrb}) – bits which could not be reproduced in a repetitive way, e.g. the bits determining the resolution of (of a converter). N_{nrb} is the difference between the bits (e.g. of the converter) which is determining the resolution N_{res} (or the whole number of bits N_{all}) and the bits determining the accuracy or the reproducible bits (N_{ab}). N_{nrb} cannot be reproduced or predicted in all of the test cases. The equations below are clarifying the definition:

$$N_{nrb} = N_{all} - N_{ab} \quad (9)$$

$$N_{nrb} = N_{res} - N_{ab} \quad (10)$$

One dimensional sampling of SBLs – is the sampling of the signal given with the equation below:

$$X(t) = X_m \sin(\omega_x t + \varphi_x) + X_0 \quad (11)$$

During the one-dimensional sampling at least four samples are needed in order to calculate the four parameters of the signal.

Phase modulation during the sampling process – the change of the amplitude of the samples when the angle of the

first sample is changed. (The sampling and the sampled frequencies and the amplitude of the sampled SBLs are constants).

Postulate about basic properties of the real signals – the postulate which is stating that every real signal has the following basic properties: 1. Finite amplitude and peak to peak amplitude. 2. Finite power in every moment and during its existence. 3. Finite spectrum. 4. Finite number of spectral lines. 5. Finite slew rate, first derivative and every other derivative. 6. Could be represented as a finite sum of SBLs. 7. Is a smooth (uninterrupted) function.

Principle “One sample per parameter to reconstruct” is stating that the signals need at least one sample per parameter for parameters calculation and reconstruction.

Real signal – A signal which could be presented as a finite sum of the simplest band limited signals (SBLs) and with the following properties: 1. Finite slew rate (finite first and every other derivative). 2. Finite number of maximums and minimums. 3. Representing a continuous mathematical function. 4. Finite number of spectral lines 5. Finite energy (power) in each moment and during its finite existence.

Reproducible bits – bits which could be reproduced easily and repeatedly. These are determining the accuracy (e.g. of a converter).

Sampling angle θ_s is defined for a SS or CS signal with the equation below:

$$\theta_s = 360/N \quad (12)$$

It is measurable in degrees.

Angle of the maximum deviation from the maximum of the sine or cosine signal is the angle of the maximal amplitude error during the sampling:

$$\theta_{smax} = 180/N \quad (13)$$

It is measurable in degrees.

Sampling theorem for SS is stating that for the SS (with DC and phase components are zeros and SF $N \geq 2$) sampling factor N is given with the equation below when the maximal amplitude error E_{max} is given:

$$N = 180 / (90 - \arcsin(1 - E_{max})) \quad (14)$$

Sampling theorem for CS is stating that for the CS (with DC and phase components are zeros and SF $N \geq 2$) N is given with the equation below when the maximal amplitude error E_{max} is given:

$$N = 180 / (90 - \arccos(1 - E_{max})) \quad (15)$$

Sampling factor (SF) N or “signal sampling factor” (SSF) is given with the equation below

$$N = F_d / F_s = F_{max} / F_s \quad (16)$$

where F_d is the sampling frequency, F_s is the frequency of the sampled sinusoidal or co sinusoidal signal and F_{max} is the maximal frequency of the sampled band limited signal (BLS)

SBLs (the simplest band limited signal) is the simplest signal with two lines into its spectrum – one is a direct current (DC) and the other is a sine or cosine wave. The following two equations are applicable:

$$A = A_m \sin(2\pi f + \theta) + B \quad (17)$$

$$A = A_m \cos(2\pi f + \theta) + B \quad (18)$$

The SBLs is the simplest test signal with two lines into spectrum.

Trapezoidal staircase function with no rounded (ideal) angles – the function used to approximate the reconstructed

sampled signal. The finite slew rate is an advantage of that model compared to the rectangular staircase function but the idealized angles is making it too idealized and cannot be approximated with finite sum of SBLs. The trapezoidal function with rounded angles is the better solution.

Trapezoidal function with rounded angles (non interrupted or continuous trapezoidal function) – the only possible presentation of the reconstructed signal before filtering.

The principle of the limited values (finity) of the signal parameters is stating that every real signal has finite values of its parameters e.g. finite slew rate (SR), finite energy, finite spectrum, finite number of spectral lines, etc.

Reproducible bits (N_{rb})– the bits (e.g. of the converter) which is determining the accuracy and which could be reproduced under the testing conditions.

$$N_{rb} = N_{all} - N_{nr} \quad (19)$$

Errors of the direct reconstruction – the errors between the corresponding parameter of the input analog signal and the parameter of the reconstructed signal. The method of direct reconstruction with ADC and DAC with the same number of reproducible bits is used as a reference.

The sampling process is defined as process of conversion of an analog signal into staircase function with rounded angles.

The sampling rate F_s is the frequency of the taken and memorizing of the samples. It is related with the number on the parameters to reconstruct (k) and with the number of the spectral lines to reconstruct (p). The following two rules are respected: 1. At least one sample per parameter to reconstruct. 2. At least four samples per alternative current (SS/CS) spectral line. Applying the two rules simultaneously is guaranteeing the exact and predictable signal reconstruction. If we keep the band of the signal constant and if we are increasing the number of the spectral lines we will increase also the number of the samples required to reconstruct the parameters of the spectral lines in the complex signal.

Coefficient of changing of the sampling rate - is a term intended to replace the term “decimation” and an appropriate coefficient of changing should be defined:

$$K_{chs} = F_{is}/F_{os} \quad (20)$$

where F_{is} is the initial sampling frequency and F_{os} is the resulting (output) sampling frequency.

The following terms are much more self explanatory and representative that the terms “total harmonic distortion (THD) and “aliasing”:

In band added frequencies – sum of (the energies) of the added frequency components in the signal band due to nonlinear sampling (and reconstruction) process. The sum could be divided to the energy (amplitude, power) of the initial signal.

Out band added frequencies - sum of (the energies) of the added frequency components outside the initial signal band due to nonlinear sampling (and reconstruction) process. The sum could be divided to the energy of the initial signal.

Total added frequencies – sum of (the energies) of all added frequency components to signal due to nonlinear sampling (and reconstruction) process. Could be divided to the energy of the initial signal.

V. CONCLUSIONS

Basic terms in the signal sampling theory are misleading and needs of replacement. Some of the basic concepts and models should be reevaluated and replaced with models which are closed to the real signals. Repeating wrong terms does not make them useful and they should be replaced with more accurate terms which are self-explanatory. New terms are proposed and defined.

REFERENCES

- [1] The Scientist and Engineer's Guide to Digital Signal Processing, Second Edition by Steven W. Smith, 1997-1999 by California Technical Publishing, USA.
- [2] Cygnal Integrated Products, Inc. Improving ADC resolution by over sampling and averaging, An018-1.1, May 2001, USA.
- [3] James Potzick. Noise averaging and measurement resolution (or “A little noise is a good thing”). Review of scientific instruments. Vol. 70. No. 4. p. 2038. April 1999.
- [4] National Semiconductor Corp. Data Conversion / Acquisition Data book, 1984, USA. Chapter 5 and 7.
- [5] National Semiconductor Corp. National Analog and Interface Products Data book, 2002, USA. Chapter 6.
- [6] V A Kotelnikov, On the transmission capacity of the ‘ether’ and of cables in electrical communications. Proceedings of the first All-Union Conference on the technological reconstruction of the communications sector and the development of low-current engineering. Moscow, 1933.
- [7] C.E Shannon, Communication in the presence of noise. Proceedings IRE, Vol. 37, pp.10-21, Jan 1949.
- [8] National Instruments, AN092, Data Acquisition Specifications – a Glossary. 1997. USA.
- [9] A. Oppenheim, A. Willsky, I. Yong, Signals and Systems, Prentice Hall, Inc., 1983
- [10] Enhancing Data Acquisition with Intelligent Over sampling By Roger Lockhart DATAQ Instruments Originally Published In SENSORS June, 1997
- [11] Harper Collins Publishers, Collins Cobuild, English dictionary, 1995, Great Britain.
- [12] Penguin Group, Dictionary of Physics, Edited by Valerie Illingworth, second edition, 1991, ISBN 0-14- 051236-5, Printed in England.
- [13] Petre Tzv. Petrov, Sampling analog signals (Abstract with formulas, tables and figures), Sofia, 2004, Bulgaria, ISBN 954.438.385.9

SWOT Analysis of Method for Automatic Vectorization of Digital Photos Into 3D Model

Zoran G. Kotevski¹ and Igor I. Nedelkovski²

Abstract – Raster and vector are the two basic data structures for storing and manipulating images and graphics data on a computer. The conversion from vector to raster is easy and done automatically in seconds, but it is rather complicated to do an automatic conversion from raster to vector.

There has been extensive research efforts focused on this issue during the past decades.

This paper gives analysis of methods for creating 3D model out of digital photos, with emphasis on method of automatic vectorization and gives SWOT analysis for this method.

Keywords – Raster, rasterization, vector, vectorization.

I. INTRODUCTION

The two basic data structures for storing and manipulating images and graphics data on a computer are raster and vector. All of the major computer graphics software packages available today are primarily based on one of these two structures. They are either raster based or vector based, while they have some extended functions to support other data structures.

Raster images are presented in the form of bitmap (matrix) made from individual elements presenting the picture, where each individual element is defined by its position and color. These elements, which form the picture, are called pixels. In this case the file size is determined by the number of pixels forming the picture (resolution) and the number of bits used to define the color of each pixel. Raster data structures usually produce large file sizes.

Acquisition of raster images is easy and is done by using scanner or digital camera.

On the other hand, data structure of vector images comes in form of points and lines that are mathematically and geometrically associated. Points are stored using the coordinates in a two or three-dimensional space, and lines or curves are stored as a series of points that indicate line or curve.

In general vector data structure produce smaller file sizes than their raster equivalents.

Also topology among graphical objects is much easier to be represented using vector form instead of using raster form data structure.

Acquisition of images in vector data form is much more

difficult to be done than raster image acquisition, because of its abstract data structure, topology between objects and associated attributes. Acquisition of vector data structures of images today is done by process of vectorization.

II. WHAT IS VECTORIZATION AND WHAT IS ITS USE

Vectorization basically means acquisition of vector data. Raster image acquisition, as mentioned before, is easy to perform using scanner or digital camera, but vector acquisition is much harder to be done.

Vectorization today has wide area of implementation like:

- [1] Archaeology
- [2] Architecture and preservation
- [3] Accident reconstruction
- [4] Creating digital terrain maps
- [5] Film, Video, Animation
- [6] Plant and mechanical engineering etc.

Because of its wide area of use there has been extensive research efforts focused on this issue during the past decades, especially automation of the process and 3D vectorization.

III. METHODS FOR VECTORIZATION

A. Manual vectorization

Manual vectorization is method that is mostly used in cases where there are limitations of quality of the taken pictures as well as in the possibilities of taking pictures from different angles. The method uses raster image as backdrop directly in the software and the line tracing is done manually by the operator. During the manual tracing there is great flexibility in the process, and different kind of adjustments can be implemented and realized.

The workflow of this method includes:

- [1] Photographs acquisition
- [2] Line tracing
- [3] Creating the 3D model
- [4] Texturing the surfaces

This method produces good quality vector model as well as good precision and accuracy, but it requires well skilled operator and most often can be very time consuming.

B. Semi-automatic vectorization

This is more powerful vectorization method, which requires pictures of higher quality. The whole idea of the process is to replace rather boring and very time consuming manual line tracing. In this case the actual tracing is done automatically,

¹Zoran G. Kotevski is with the Faculty of Technical Sciences, I.L.Ribar bb, 7000 Bitola, Macedonia, E-mail: zoran.kotevski@uklo.edu.mk

¹Igor I. Nedelkovski is with the Faculty of Technical Sciences, I.L.Ribar bb, 7000 Bitola, Macedonia, E-mail: igor.nedelkovski@uklo.edu.mk

by the software that uses complex algorithms for line tracing, shape recognition, topology creation and attribute assignment.

After automated line tracing, the workflow is similar to the manual vectorization. The 3D model must be generated manually on the basis of traced images from different sides of the object; by extruding, revolving, sweeping, etc. traced 2D vector images.

This semi-automatic method produces 3D model with greater precision and is less time consuming than manual vectorization, but requires images of greater quality.

C. Automatic vectorization

Automatic vectorization is an efficient and effective method for modeling real world objects. 3DSOM's patented technology for model generation and sophisticated texturing technology allows 3D model to be created quickly and inexpensively while requiring low level of technical skill or expensive hardware platforms.

The workflow of this method is rather different from the previous methods. It requires larger amount of pictures (about 20) to be taken from different angles. The amount of photographs needed to create the 3D model is around 15 taken from lower angle and 3-7 taken from higher angle of horizontal centerline of the object, as well as some pictures from top and bottom perspective if needed. The quality of the photographs is the key element of this method so the photo session needs great deal of attention.



Fig.1 Laboratory for photo session



Fig.2 Position of the model for photo session

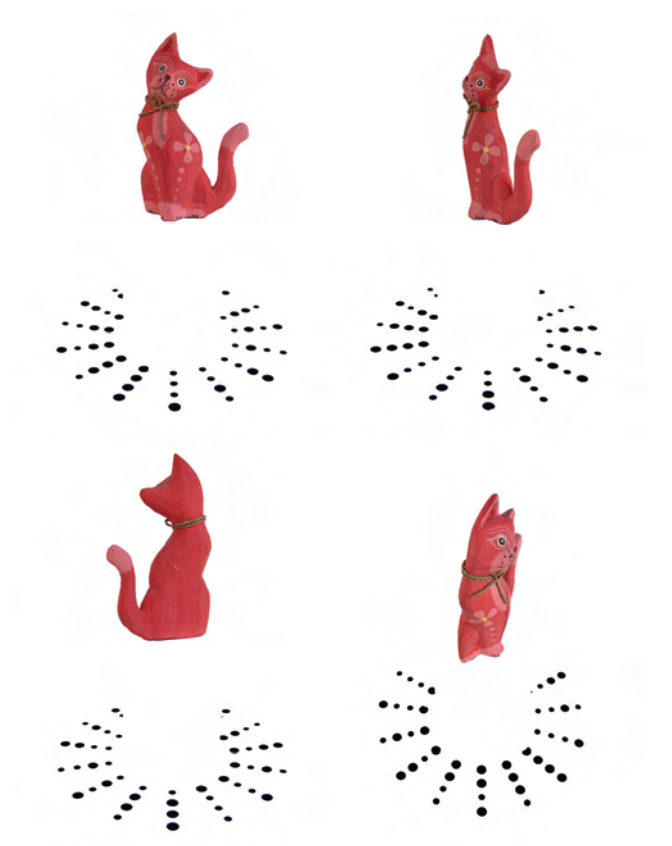


Fig. 3 Some of the total 19 taken pictures for vectorization of this model (toy – cat)

After the pictures are imported in the software the next step is automatic masking of the images what means cutting of the background. A mask is created to identify the outline or silhouette of the object, as seen from the camera's point of view.

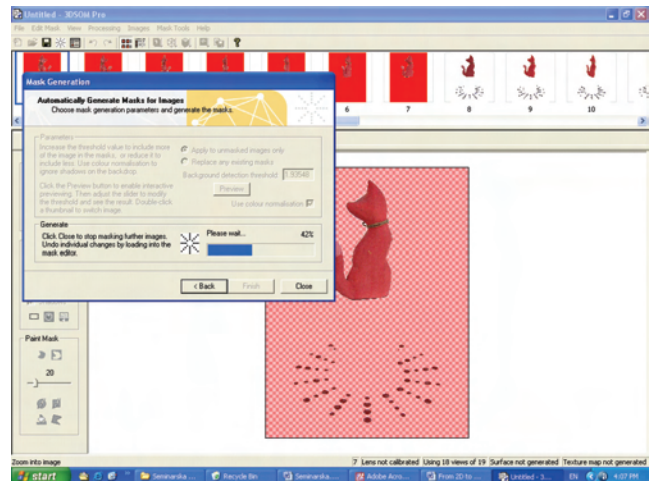


Fig. 4 Process of masking of imported pictures

The “Generate Wireframe” process that constructs the 3D model can be represented as a sculptor taking a block of clay and projecting each image mask onto it from the viewpoint of the camera. Wherever the projected mask appears on the clay, the clay is sliced away until the model’s silhouette matches

the masked silhouette obtained from the object's photo taken from that perspective.

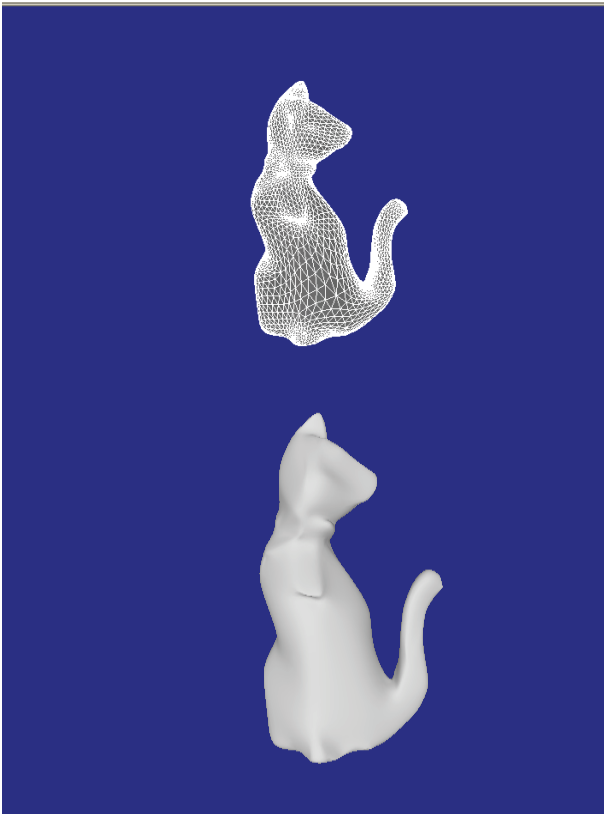


Fig. 5 Look of the model after applying techniques Generate Wireframe and Mesh Optimization

Mesh optimization and texturing are also done automatically in matter of seconds what puts this method ahead of previous two methods.



Fig. 6 Process of texturing surfaces of the model usually is performed by software automatically, but some surfaces sometime requires also manual texturing

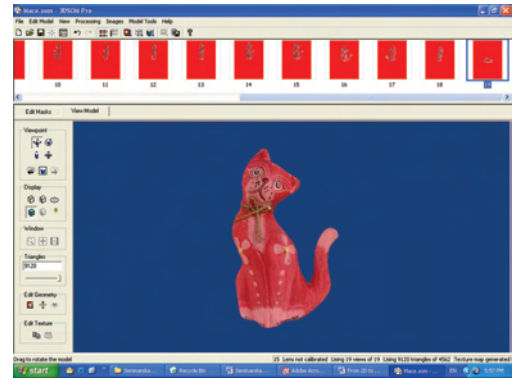


Fig.7 Final look of the 3D vector model after applying technique of texturing its surfaces

The limitations of this method are consisted in following: it can be used only for small size objects and it is complicated to vectorize transparent objects or objects with large holes like coffee cup.

IV. SWOT ANALYSIS

Table I – SWOT analysis of manual vectorization

Strengths	Weaknesses
<ul style="list-style-type: none"> - Good quality of the created 3D model - Line tracing flexibility - Greater control of the operator 	<ul style="list-style-type: none"> - Very time consuming - Medium level of accuracy and precision
Opportunities	Threats
<ul style="list-style-type: none"> - 3D model construction from low quality pictures - Unavailability of multiple photos from different angles 	<ul style="list-style-type: none"> - Automation of the process of vectorization - Complexity of the object being vectorized - Operators skills

Table II – SWOT analysis of semi-automatic vectorization

Strengths	Weaknesses
<ul style="list-style-type: none"> - Greater precision of the created model - Time consumption 	<ul style="list-style-type: none"> - Requires photos of greater quality
Opportunities	Threats
<ul style="list-style-type: none"> - Small amount of photos but 	<ul style="list-style-type: none"> - Automation of the process - Unavailability of photos from different angles - Manual optimization and texturing

Table III – SWOT analysis of automatic vectorization

Strengths	Weaknesses
<ul style="list-style-type: none"> - Great precision of the 3D model created - Exceptionally low time consuming - Low requirements regarding of operator skills 	<ul style="list-style-type: none"> - Requirement of greater number of high quality pictures - Large objects - Transparent objects and objects with larger holes (eg. coffee cup)
Opportunities	Threats
<ul style="list-style-type: none"> - Creating a model of complex real world objects 	<ul style="list-style-type: none"> - Unavailability of photos from different angles

V. CONCLUSION

From this analysis can be concluded that for vectorization of larger objects and objects that can not be easily photographed more convenient are the first two methods, but for smaller objects the more appropriate choice is the automatic vectorization which can be used mostly in the fields of preservation of historical and cultural heritage, as well as for 3D representation of real objects in animation industry.

REFERENCES

- [1] I. Nedelkovski, Z. Kotevski "Internet and Multimedia" Faculty of Technical Sciences - Bitola 2005
- [2] <http://www.3dsom.com/>
- [3] <http://www.ablesw.com/r2v/rasvect.html>
- [4] <http://animationartist.digitalmedianet.com/>
- [5] <http://www.architectureweek.com/>
- [6] <http://www.canoma.com/>
- [7] <http://en.wikipedia.org/wiki/SketchUp>
- [8] <http://www.sketchup.com/>
- [9] <http://imagemodeler.realviz.com/>
- [10] <http://www.maya.com/web/index.mtml>
- [11] <http://www.photo3d.com/eindex.html>
- [12] <http://www.strata.com/>
- [13] <http://www.vx.com/bundles.cfm>
- [14] <http://www10.mcadcafe.com/>
- [15] <http://www.mediamachines.com/>

SESSION ECST II

Electronic Components, Systems and Technologies
II

Monitoring System of Pulsation Processes in a Milking Machine

Anatolii. T. Aleksandrov¹ and Nikola D. Draganov²

Abstract – The paper treats alternative solutions for monitoring and control of the processes taking place in the milking bowl of a milking machine.

Observations have been conducted and experimental recordings have been made of the processes in the milking bowl of the milking equipment using a video camera placed in the milk chamber of the milking machine. Experimental results have also been obtained using an optic and a galvanomagnetic sensor.

On the basis of the results obtained a comparative analysis has been made and conclusions have been drawn about the operation of the milking machine.

Keywords - milking bowl, milk chamber, video camera, optic sensor, galvanomagnetic sensor

I. INTRODUCTION

Modern stockbreeding requires constant development and improvement of its automation tools. Milking machines are widely applied as tools for labour automation in stockbreeding, and they determine to a great extent the efficiency, as well as the cost and quality of the milk [2, 3, 4, 5]. It is interesting to study the processes taking part in the teat cup cluster of the milking machines and to establish the relationship between the operation of the pulsator and the position of the rubber teat cup.

The aim of the present paper is monitoring, study and control of the processes in the teat cup cluster of the milking machine. Its implementation creates conditions for improving the operating characteristics of the milking machines. [2-6]

II. INSTRUCTIONS FOR THE AUTHORS

To improve the operation and efficiency of milking machines, a good knowledge and description of the processes taking place in the teat cup cluster is necessary. To achieve this, alternative solutions for monitoring and control of these processes have to be developed.

Experiments have been conducted for observing the processes taking place in the milking chamber, using a video camera, model GV250, enabling transmission and processing of information on a PC [7].

The circuit of the test setting is shown in Fig. 1. The lens of the video camera (CCD matrix) 3 has been mounted in the artificial teat 2. LEDs 4 have been mounted around the video camera, which provide background light of the video camera. The control block 1 of the camera provides the connection to the personal computer 7 by means of a video cable 6. The video block created in this way is placed in the teat cup 8 of the teat cup cluster 9. Block 5 is composed of a LED and its function is to light the inside of the teat cup. The power supply of the test setting is provided by two stabilized rectifiers 10 and 11.

The video camera, model GV250, enables transmission and processing of information on a PC using the GeoCenter software. It has a resolution of 420 lines per frame. The video controller GV-600V2, operating on an NTSC video system, can have 4 video cameras connected to it. There is no strobbing input, but frame synchronization is possible by means of the

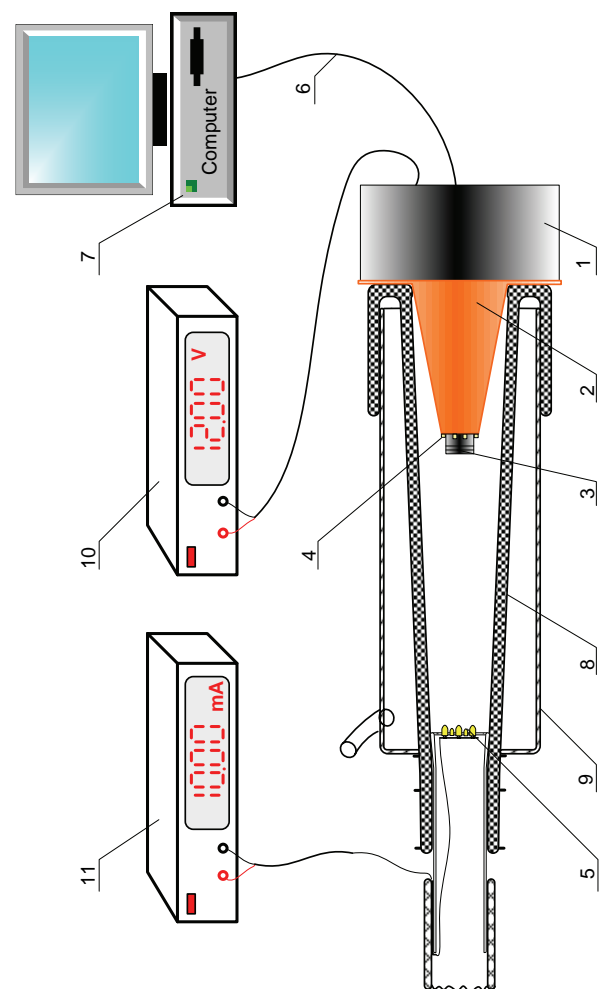


Fig. 1. Circuit of the test setting

¹ Anatolii T. Aleksandrov is with the Technical University, 4 H. Dimitar str. 5300 Gabrovo, Bulgaria, E-mail: alex@tugab.bg

² Nikola D. Draganov is with the Technical University, 4 H. Dimitar str. 5300 Gabrovo, Bulgaria, E-mail: nikola_draganov@mail.bg

camera illuminance.

The minimum configuration that the PC needs to have for the video controller and the camera to be installed is:

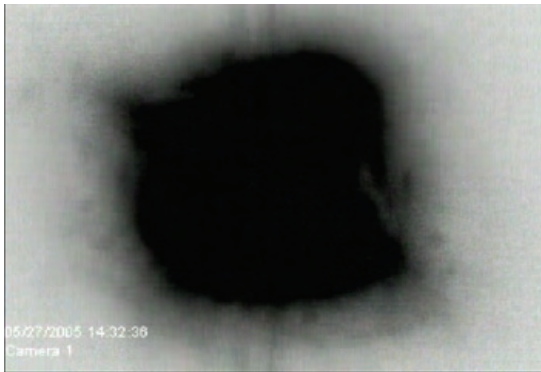


Fig. 2. Frame of the milking chamber from the first phase of the milking process – “squeeze” phase

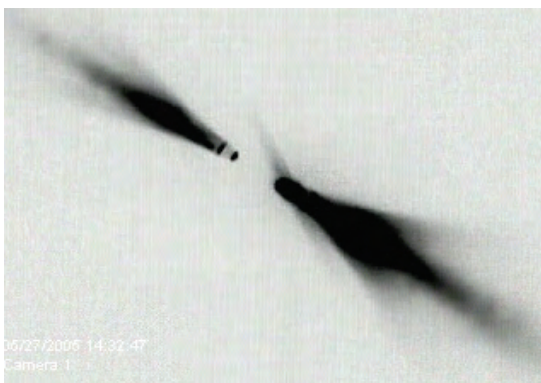


Fig. 3 Frame of the milking chamber from the second phase of the milking process “massage + stimulation”

Windows-98 operating system, CPU-Pentium II, 128MB RAM, 144MHz Bus speed, 16MB video controller, 15GB HDD. [7]

A film of any duration and extension *.avi can be recorded.

The test setting enables recording and monitoring of the processes in the teat cup cluster at different illuminance, with or without background light. The film can be broken into frames, the resolution being 25 frames per second using WirtualDibMod software product. Therefore, in addition to monitoring of the processes taking place in the teat cup cluster, photographs can be taken at specific moments, as well as qualitative and quantitative assessment of the shape of the milking chamber.

Fig. 2 and Fig. 3 show frames of the milking chamber from the first phase of the milking process – “squeeze” phase, and the second one – “massage + stimulation”.

The experiments that have been conducted give a good qualitative picture of the processes taking place in the teat cup cluster. By processing the resultant image using the MathCAD 2000 software package (Fig.4 and Fig.5), a quantitative assessment of the processes in the milking chamber can be obtained. The results are subject to further processing and analysis.

The processes in the milking chamber of the teat cup cluster have been studied experimentally using optical and

galvanomagnetic sensors as well [1, 6]. Fig.6 presents the flow chart, and Fig.7a and 7b– the conceptual electric circuits

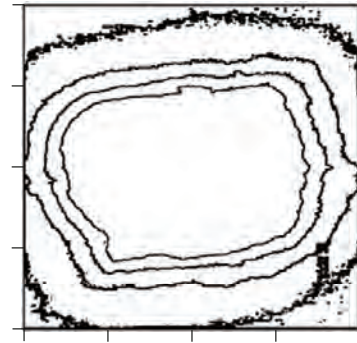


Fig. 4. Processing the resultant image using the MathCAD 2000

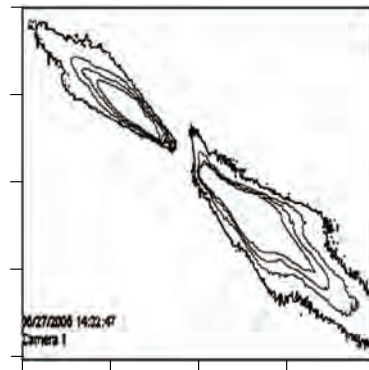


Fig. 5. Processing the resultant image using the MathCAD 2000

of the test settings. Both types of sensors provide information about the state of the rubber teat cup by means of double energy conversion.

In the circuit with the optical sensor the photosensitive element (phototransistor 3) has been mounted in the artificial teat 5 in place of the video camera. The milking chamber 8 is lit by means of LEDs 4. Under the action of the vacuum the teat cup 7 contracts and the luminous flux to the phototransistor is reduced, i.e. the position of the teat cup is converted into an equivalent light signal. The light signal is converted into an equivalent electrical signal in the phototransistor. [1, 6]

The galvanomagnetic sensor also gives indirect information about the contraction of the teat cup. This is achieved by sticking a magneto-sensitive element – Hall element 1 on the outer surface of the teat cup. A permanent magnet 2 is fixed against it. When the teat cup is loose, the distance between the magneto-sensitive element and the magnet is equal to the diameter of the teat cup in this area. In this case the Hall voltage measured by the voltmeter 12 will be the lowest. When the teat cup contracts as a result of the vacuum, the distance between the magnet and the Hall element is shortened. The generated Hall voltage will rise as the contraction of the teat cup increases [1].

The conversion characteristics measured experimentally $U_{CE}=f(L)$ (U_{CE} – voltage drop across the phototransistor; L – internal diameter of the teat cup) at $I_F=\text{const}$ (I_F – current

across the LCD) with the optical sensor are shown in Fig.8, and the conversion characteristics $U_H=f(L)$ show the change

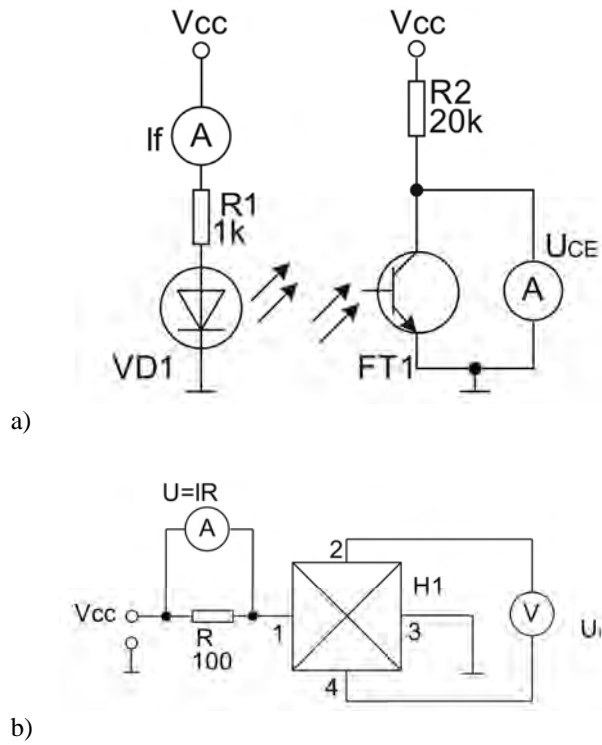


Fig. 7. Conceptual electric circuits of the test settings

in the diameter of the teat cup as a function of the Hall voltage (U_H – Hall voltage; L - internal diameter of the teat cup).

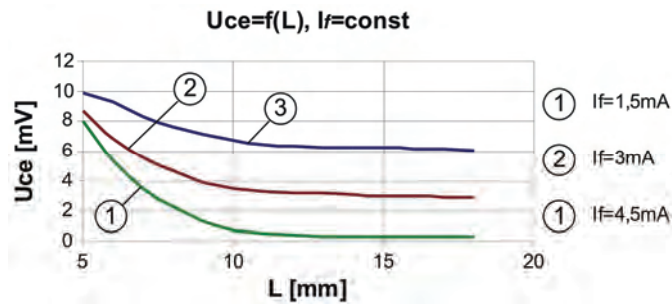


Fig.8. Conversion characteristics measured experimentally with optical sensor

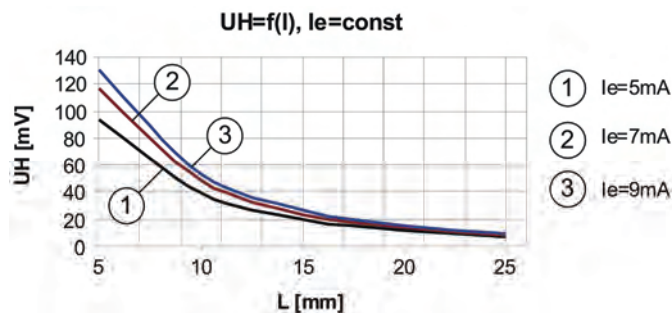


Fig. 9. Conversion characteristics measured experimentally with galvanomagnetic sensor

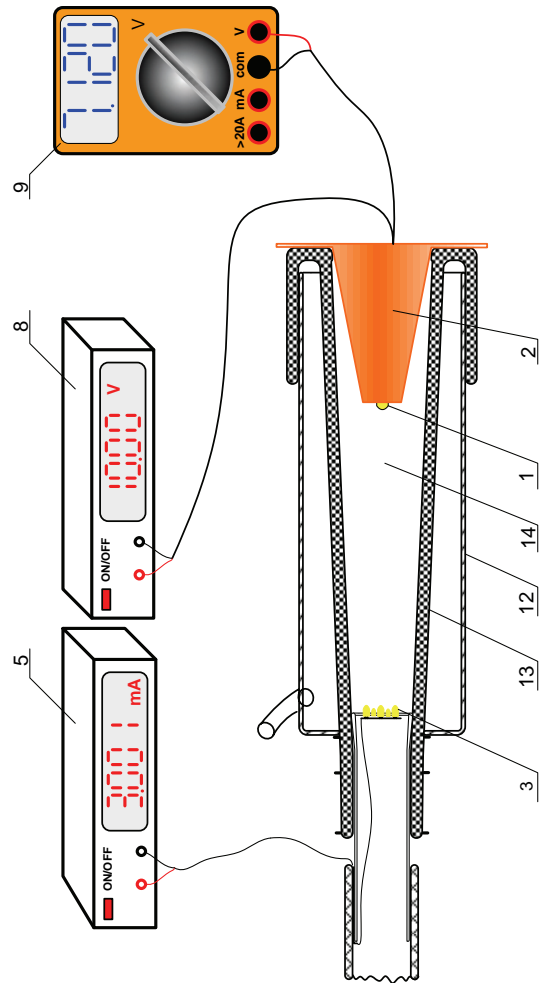


Fig. 6. Circuit of the test setting for optical and galvanomagnetic measurements

Both signals are information signals and can be used successfully for monitoring and control of the processes in the milking chamber.

The conversion characteristics measured experimentally enable indirect quantitative assessment of the degree of contraction of the teat cup through the value of the voltages measured (U_{CE} and U_H), depending on the sensor used.

Although the conversion characteristics are not linear, they can be used for control of the milking machine, since the two final states of the teat cup are important – squeezed and loose.

The conversion characteristics that exhibit the greatest conversion transconductance are the ones obtained for current across the LED $I_F=1,5mA$ and current across the Hall element $I_e=9mA$, which also determines higher sensitivity of the respective sensors in these operation modes [1,6].

III. CONCLUSION

Experimental studies have been conducted of the processes taking place in the teat cup cluster of the milking machine, using a video camera, model GV250, enabling

transmission and processing of information on a PC by means of GeoCenter software.

Circuits with an optical and a galvanomagnetic sensor have been proposed for studying the processes in the milking chamber. Experimental conversion characteristics have been obtained, and the voltage values U_{CE} and U_H that have been measured are used as a quantitative criterion for assessing the degree of contraction of the teat cup.

The video camera and the test setting for studies by means of an optical sensor can only be used in the simulation of the milking process, while the test setting with the galvanomagnetic sensor can find application under actual working conditions.

REFERENCES

- [1] Alexandrov, A. Discrete Semiconductor Elements, Gabrovo, Vasil Aprilov Publishing House, 2002 (in Bulgarian).
- [2] Banev B., V. Valashev, K. Peichev, Al. Blagoev. Study of pulsation camera of milking machine working with vibration-pulsator "Biopuls", periodical "Stock-science", 1987, 311-316.
- [3] Banev B., K. Peichev. Study of stress from of the rubber teat cup over false teat, SU Stara Zagora, 2003, p II, 286-288.
- [4] Banev B., B. Bonchev. Study of possibilities to use of pulse machine "POLANES" in milking machine for sheeps, periodical "Agricultural technics", 2004, №5, 33-37.
- [5] Valashev V., K. Peichev, B. Banev. Analysis of mechanical performance of rubber teat cup with different level of tighten, periodical "Agricultural technics" 2003, №3, 58-60.
- [6] Valkov S. A. Electronics and semiconductors elements and integrated circuit, Sofia, Technics, 1992
- [7] www.geocenter.com, from September 27.2005

A Method for Improvement Stability of a CMOS Voltage Controlled Ring Oscillators

Goran Jovanović¹ and Mile Stojčev²

Abstract – A CMOS voltage controlled ring oscillator based on N-stage single-ended chain of different inverter types is described in this paper. The proposal is characterized by increased frequency stability ($\Delta f/f < 2\%$) in term of power supply voltage variations in respect to standard solutions ($\Delta f/f > 4\%$). The presented results are obtained using HSpice simulation and CMOS library model, level 49, for 1.2 μ m technology.

Keywords – Voltage controlled oscillator, ring oscillator, CMOS, frequency stability

I. INTRODUCTION

A voltage controlled oscillator (VCO) is one of the most important basic building blocks in analog and digital circuits [1]-[6]. There are many different implementations of VCOs. One of them is a ring oscillator based VCO, which is commonly used in the clock generation subsystem. The main reason of ring oscillator popularity is a direct consequence of its easy integration. Due to their integrated nature, ring oscillators have become an essential building block in many digital and communication systems. They are used as voltage-controlled oscillators (VCO's) in applications such as clock recovery circuits for serial data communications [1], [2], disk-drive read channels [3], on-chip clock distribution [4], and integrated frequency synthesizers [5], [6]. The design of a ring oscillator involves many tradeoffs in terms of speed, power, area, and application domain. The problem of designing a ring oscillator is in focus of our interest in this paper. This paper proposes a suitable method for increasing frequency stability of a CMOS ring VCO.

The rest of the text is organized as follows. In Section 2, we give a brief review of voltage controlled ring oscillators, and define some crucial operating parameters. Hardware description of the proposed ring oscillator is presented in Section 3. In addition we present the simulation results which relate to frequency stability in terms of temperature and supply voltage variation. In Section 4, we define the terms of jitter and phase noise in ring oscillators, and present the appropriate simulation results. Finally, conclusions is given in Sections 5.

II. CMOS RING VCO – A REVIEW

A ring oscillator is comprised of a number of delay stages, with the output of the last stage fed back to the input of the first. To achieve oscillation, the ring must provide a phase shift of 2π and have unity voltage gain at the oscillation frequency. Each delay stage must provide a phase shift of π/N , where N is the number of delay stages. The remaining π phase shift is provided by a dc inversion [7]. This means that for an oscillator with single-ended delay stages, an odd number of stages are necessary for the dc inversion. If differential delay stages are used, the ring can have an even number of stages if the feedback lines are swapped. Examples of these two circuits are shown in Fig. 1.

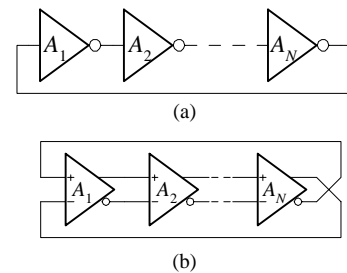


Fig. 1. Ring oscillator types: (a) single-ended and (b) differential

In order to determine a frequency of the ring oscillator we will use its linear model as is given in Fig. 2.

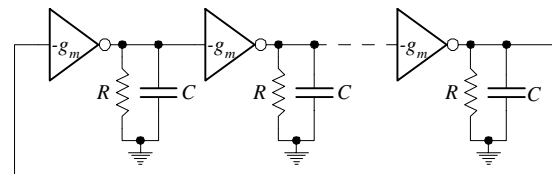


Fig. 2. Linear model of ring oscillators

We assume that all inverting stages are identical and that they can be modeled as a trans-conductance loaded by a parallel connection of resistor R and capacitor C . The gain of the inverting stage is defined as

$$A_1(j\omega) = A_2(j\omega) = \dots = A_N(j\omega) = \frac{-g_m R}{1 + j\omega RC} \quad (1)$$

According to Barkhausen criteria the ring oscillator is operative when the following conditions are satisfied

$$|A_1(j\omega) \cdot A_2(j\omega) \cdot \dots \cdot A_N(j\omega)| = 1, \text{ and}$$

¹Goran S. Jovanović is with the Faculty of Electronic Engineering, University of Niš, Aleksandra Medvedova 14, 18000 Niš, Serbia, Email: joga@elfak.ni.ac.yu

²Mile K. Stojčev is with the Faculty of Electronic Engineering, University of Niš, Aleksandra Medvedova 14, 18000 Niš, Serbia, Email: stojcev@elfak.ni.ac.yu

$$\angle A(j\omega) = \theta = \arctan \omega RC = \frac{2k\pi}{N}. \quad (2)$$

The frequency of oscillation is given by

$$\omega_0 = \frac{\tan \theta}{RC} \quad (3)$$

and the minimal single stage gain is

$$g_m R \geq \frac{1}{\cos \theta}. \quad (4)$$

Alternatively we can derive an equation for the frequency of oscillation if we assume that each stage provides a delay of t_d . The signal goes through each of the N delay stages once to provide the first π phase shift in a time of $N t_d$. Then, the signal must go through each stage a second time to obtain the remaining π phase shift, resulting in a total period of $2 N t_d$. Therefore, the frequency of oscillation is

$$f_0 = \frac{1}{2Nt_d}. \quad (5)$$

The difficulty in obtaining a value for the frequency arises when trying to determine t_d , mainly due to the nonlinearities and parasitics of the circuit. As is referred in [7] the delay per stage is defined as the change in output voltage at the midpoint of the transition, V_{sw} , divided by the slew rate, I_{ss}/C , resulting in a delay per stage of $C V_{sw}/I_{ss}$. Using definition (5), the oscillation frequency is given by

$$f_0 = \frac{I_{ss}}{2N V_{sw} C}. \quad (6)$$

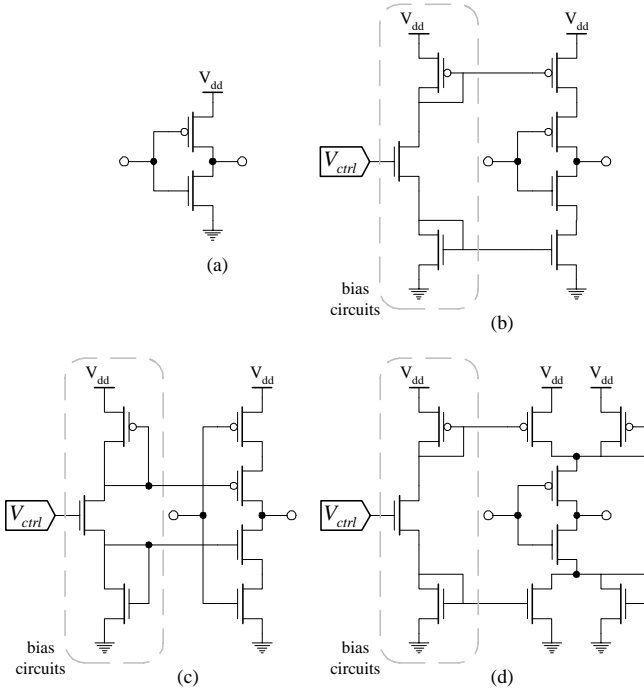


Fig. 3. Inverter: (a) basic type; (b) current starved with output-switching; (c) current starved with power-switching; (d) current starved with symmetrical load;

III. RING OSCILLATOR INVERTING STAGE

As we have already mentioned, the ring oscillators are realized with N inverter stages. There are numerous types of inverter stages by which a ring oscillator can be realized [8], [9]. Some of the standard solutions are pictured in Fig. 3.

Designs given in Fig. 3 (b), (c), (d) are of current starved type, for which the charging and discharging output capacitor current is limited by a bias circuit. [More details related to realization of this type of inverter stage can be found in References [8], [9].

Relative frequency deviations in term of temperature variations for 3-stages ring oscillators based on type of inverters stages presented in Fig. 3 are given in Fig. 4. In general all frequency deviations have similar behavior, but the basic type (Fig. 3a)) and current starved with symmetrical load (Fig. 3d)) inverters have the highest, while current starved with output-switching (Fig. 3b)) inverter has the lowest sensitivity. The ratio of relative frequency deviations between basic type (Fig. 3a)) and current starved with output-switching (Fig. 3b)) inverters is 5:1.

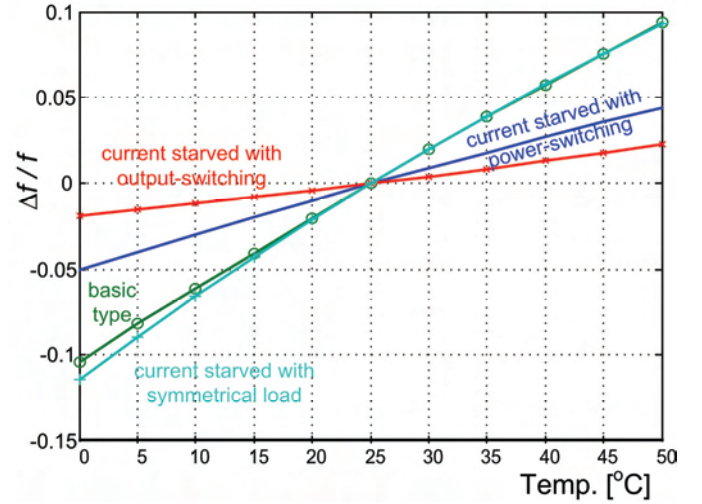


Fig. 4. Relative frequency deviation in term of temperature variation

Relative frequency deviations in term of power voltage supply variations for 3-stages ring oscillators based on type of inverters stages presented in Fig. 3 are given in Fig. 5. As can be seen from Fig. 5, the basic type (Fig. 3(a)) and current starved with symmetrical load (Fig. 3(d)) inverters have characteristics with negative slope, while current starved with output-switching (Fig. 3(b)) and current starved with power-switching (Fig. 3(c)) inverters have characteristics with positive slope. Absolute value of inverters sensitivity in function to power supply voltage variation is within a range of 10% excluding current starved inverter with power-switching (Fig. 3(c)) inverters which has sensitivity of 5%.

Taking into consideration the opposite slope characteristics of the relative frequency deviations in terms of power voltage supply variations of the mentioned inverters (Fig. 5), we can conclude that is reasonable to design a ring oscillator composed of cascade chain of inverters. For example, odd numbered inverters can have positive, while even numbered negative slope. In this way, the relative

frequency deviation in term of power voltage supply can be drastically reduced (more than 100%).

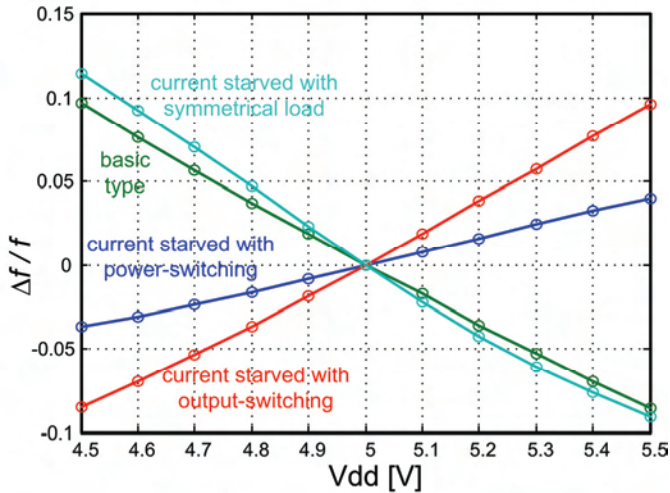


Fig. 5. Relative frequency deviation in term of power supply voltage variation

Several typical design solutions of 3-, 5- and 7- stages ring oscillators with reduced sensitivity are given in Fig. 6. a), b) and c), respectively. We call them as combined ring oscillators. Let note that in combined ring oscillators the odd numbered inverter stages are implemented with basic type, while even numbered as current starved with output-switching inverters.

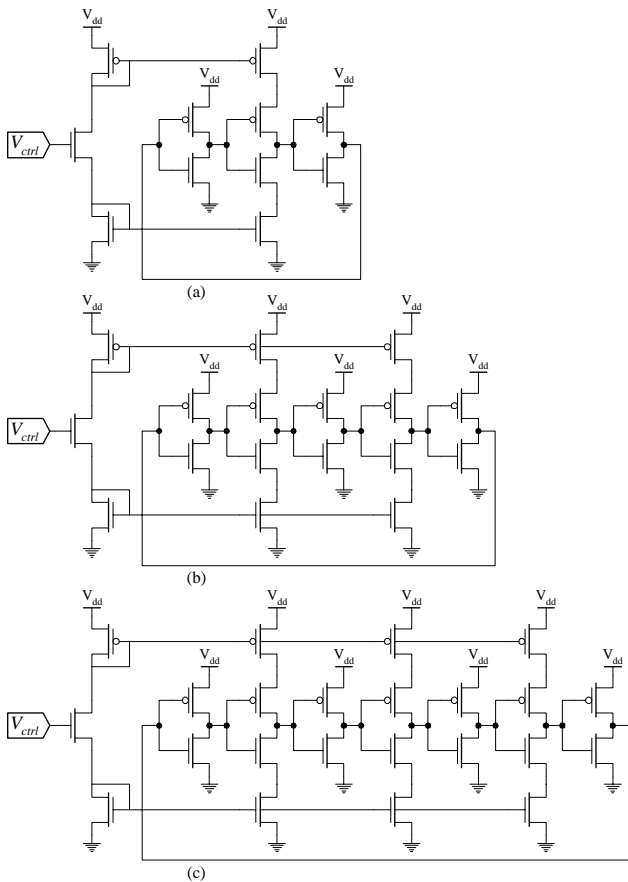


Fig. 6. Combined ring VCOs

The relative frequency deviations in term of power supply voltage for all three type of ring oscillators pictured in Fig. 6 are given in Fig. 7. By analyzing the results presented in Fig. 7 we can conclude the following: The relative sensitivity of the ring oscillator from Fig. 6 a) is less than 2%, while for those given in Fig. 6 b) and c) is less than 1%.

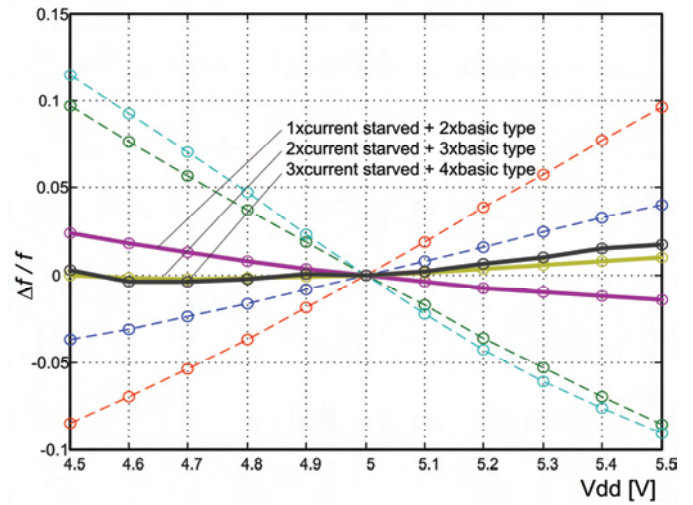


Fig. 7. Relative frequency deviation in term of power supply voltage variation for proposed ring VCOs

IV. JITTER AND PHASE NOISE IN RING OSCILLATORS

In general, CMOS circuits are sensitive both to power supply and temperature variations, as well as to noise generated in IC's building blocks (noise is inserted through power supply and the substrate). Due to these effects, the propagation delay, t_d , is variable [10], [11], [12]. As a consequence there are variations in t_d , in respect to its nominal value. This deviation is manifested as variation of the rising and falling pulse edges, and is referred as jitter (see Fig. 8).

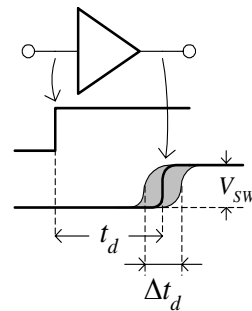


Fig. 8. Jitter effect

As can be seen from Fig. 8 the jitter for the rising edge is defined as a rms time error value, $\overline{\Delta t_d^2}$. The normalized jitter value is defined as a ratio between the effective time error and its nominal delay value, ie. $\frac{\Delta t_d \text{ rms}}{t_d}$.

Consider now a VCO with nominal period T_0 , and with a timing error accompanying each period that is Gaussian, with

zero mean and variance $\overline{\Delta t_{VCO}}^2$. If this timing error is expressed in terms of phase, $\Delta\phi=2\pi\Delta t/T_0$, then the variance of the phase error per cycle of oscillation is given by [10]

$$\sigma_\phi^2 = (2\pi)^2 \left(\frac{\Delta t_{VCO \text{ rms}}}{T_0} \right)^2. \quad (7)$$

The phase noise power spectral density expressed in terms of frequency is given by [10]

$$S_\phi(f) = \frac{f_0}{f^2} \left(\frac{\Delta t_{VCO \text{ rms}}}{T_0} \right)^2. \quad (8)$$

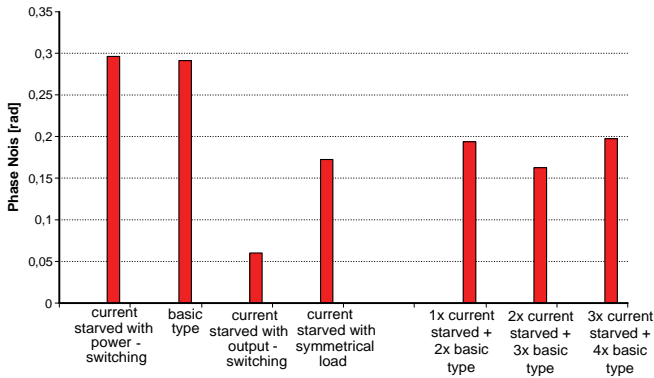


Fig. 9. Relative frequency deviation in term of power supply voltage variation for proposed ring VCOs

The amount of phase noise for all types of ring oscillators discussed in this paper is sketched in Fig. 9. By analyzing Fig. 9 we can conclude that the best performance (phase noise approx. 0.06 rad) have ring oscillators based on current starved inverters with output-switching, while the worst (phase noise approx. 0.3 rad) correspond to ring oscillators realized with basic type or current starved with power-switching inverters. Combined ring oscillators, composed of basic and current starved with output-switching inverters, have approximately phase noise within the range 0.16-0.2 rad.

V. CONCLUSION

Ring oscillators are basic building blocks of complex integrated circuits. They are mainly used as clock generating circuits. Many different types of ring oscillators are presented in literature [1]-[4]. They differ in respect to architectural, realization of inverters stages, number of inverter stages, etc. In this paper we have considered realization of ring oscillator based on four different types of single-ended inverters. The simulation was performed using HSpice Version 03.2006 and library model for 1.2 μ m CMOS technology. According to the obtained simulation results we can conclude:

- that for frequency stability in terms of temperature variations the best performance ($\Delta f/f < 2\%$) has current starved inverters with output-switching;
- that for frequency stability in terms of power supply voltage variations the best performance ($\Delta f/f < 4\%$) has current starved inverters with power-switching;
- by realizing combined types of ring oscillator the relative frequency deviation in terms of power supply voltage variations can be significantly decreased ($\Delta f/f < 2\%$) in respect to the best standard solutions ($\Delta f/f > 4\%$).
- in respect to phase noise, ring oscillators based on current starved inverters with output-switching have the best performance (phase noise approx. 0.06 rad).

REFERENCES

- [1] C. H. Park, O. Kim, B. Kim, "A 1.8-GHz self-calibrated phase locked loop with precise I/Q matching", *IEEE J. Solid-State Circuits*, vol. 36, pp. 777-783, May 2001.
- [2] L. Sun and T. A. Kwasniewski, "A 1.25-GHz 0.35- μ m monolithic CMOS PLL based on a multiphase ring oscillator", *IEEE J. Solid-State Circuits*, vol. 36, pp. 910-916, June 2001.
- [3] J. Savoj and B. Razavi, "A 10-Gb/s CMOS clock and data recovery circuit with a half-rate linear phase detector", *IEEE J. Solid-State Circuits*, vol. 36, pp. 761-767, May 2001.
- [4] C. K. K. Yang, R. Farjad-Rad, M. A. Horowitz, "A 0.5- μ m CMOS 4.0-Gbit/s serial link transceiver with data recovery using oversampling", *IEEE J. Solid-State Circuits*, vol. 33, pp. 713-722, May 1998.
- [5] M. Alioto, G. Palumbo, "Oscillation frequency in CML and ESCL ring oscillators", *IEEE Trans. Circuits Syst. I*, vol. 48, pp. 210-214, Feb. 2001.
- [6] B. Razavi, "A 2-GHz 1.6-mW phase-locked loop", *IEEE J. Solid-State Circuits*, vol. 32, pp. 730-735, May 1997.
- [7] S. Docking, M. Sachdev, "A Method to Derive an Equation for the Oscillation Frequency of a Ring Oscillator", *IEEE Trans. on Circuits and Systems - I: Fundamental Theory and Applications*, vol. 50, No. 2, pp. 259-264, February 2003.
- [8] G. Jovanović, M. Stojčev, "Current starved delay element with symmetric load", *International Journal of Electronics*, pp. 167-175, Vol. 93, No 3, March 2006.
- [9] O.-C. Chen, R. Sheen, "A Power-Efficient Wide-Range Phase-Locked Loop", *IEEE Journal of Solid State Circuits*, vol. 37, No. 1, pp. 51-, January 2002.
- [10] Todd Charles Weigandt, "Low-Phase-Noise, Low-Timing-Jitter Design Techniques for Delay Cell Based VCOs and Frequency Synthesizers", PhD dissertation, University of California, Berkeley, 1998.
- [11] S. Docking, and M. Sachdev, "An Analytical Equation for the Oscillation Frequency of High-Frequency Ring Oscillators", *IEEE Journal of Solid State Circuits*, vol. 39, No. 3, pp. 533-537, March 2004.
- [12] A. Hajimiri, S. Limotyrakis, T. Lee, "Jitter and Phase Noise in Ring Oscillators", *IEEE Journal of Solid State Circuits*, vol. 34, No. 6, pp. 790-804, June 1999.

Load Characteristics under Optimal Trajectory Control of Series Resonant DC/DC Converters Operating above Resonant Frequency

Nikolay D. Bankov¹ and Tsvetana Gr. Grigorova²

Abstract - In the paper resonant DC/DC converters optimal trajectory control method is examined. This control method allows the resonant tank energy is fully controlled with the tank energy, current and voltage, all staying well within bounds under all circumstance, including a short circuit across the converter output. The emphasis in this paper is on the obtained of steady-state equations, described DC/DC resonant converter operation above resonant frequency as a function of the diode trajectory radius, using as control parameter. Solving equations can be drawn an inverter family of load characteristics. Experimental results from the investigation of the DC/DC resonant converter are shown.

Keywords - resonant DC/DC converters, optimal trajectory control.

I. INTRODUCTION

The tank processes in series resonant DC/DC converters are fast dynamics and exchanges large amounts of pulsating energy with source and with the load in each half-cycle of operation converter. This optimal trajectory control method [1],[2] allows the resonant tank energy is fully controlled with the tank energy, current and voltage, all staying well within bounds under all circumstance, including a short circuit across the converter output and has many advantages over the existing methods [3-6].

The emphasis in this paper is on the obtained of steady-state equations, described DC/DC resonant converter operation above resonant frequency as a function of the diode trajectory radius, using as control parameter and corresponding normalized load characteristics, which are useful to design such converter.

II. ANALYSIS AND LOAD CHARACTERISTICS

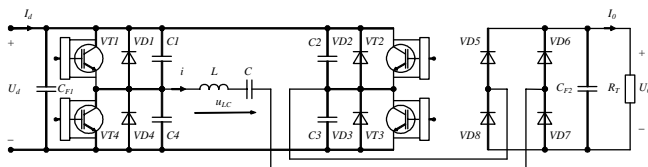


Fig.1 Full-bridge DC/DC resonant converter

¹ Nikolay Dimitrov Bankov is with the University of Food Technologies, 26 Maritza Blvd., 4002 Plovdiv, Bulgaria, E-mail: nikolay_bankov@yahoo.com

² Tsvetana Grigorova Grigorova is with the Technical University of Sofia, Branch Plovdiv, 61 Sankt Petersburg Blvd., 4000 Plovdiv, Bulgaria, E-mail: c_grigorova@abv.bg

Fig.1 shows proposed resonant DC/DC converter.

The analysis and design of such converter are presented in [2], [7]. The analysis is made under the following assumptions: the converter elements are ideal; the effect of snubber capacitors and the ripples of input and output voltages are neglected; the output capacitor is sufficiently large such that the output voltage U_o remains constant through a switching cycle.

The following common symbols are used:

- $\omega_0 = 1/\sqrt{LC}$ - angular resonant frequency; $Z_0 = \sqrt{L/C}$ - characteristic impedance;
- ω - switching frequency;
- $i'(0) = I'_{L0}$, $u'_c(0) = U'_{c0}$ - normalized initial values of the resonant link current and voltage across series capacitor for each stage of the converter operation;
- $\theta_Q = \omega_0 t_Q$ - transistors conduction angle; $\theta_D = \omega_0 t_D$ - diodes conduction angle;
- $U'_0 = \frac{U_o}{gU_d}$ - voltage ratio, where g is topology constant

($g=0.5$ for half-bridge topologies and $g=1$ for full-bridge topologies).

For unifying purposes all units are presented as relative ones: the voltages to the supply voltage U_d ; the currents to the current $I = U_d/Z_0$; the input power to the power $P = U_d^2/Z_0$.

Under optimal trajectory control of series resonant DC/DC converters operating above resonant frequency, the converter is analyzed with use of state plane. Fig. 2 shows one steady-state trajectory above resonant frequency.

In the $(u_c/U_d, i\sqrt{L/C}/U_d)$ state plane [2], the trajectory described by the operating point is arc of a circle with its center at the point of coordinates $(u_{LC}, 0)$ and drawn from representative point of the initial conditions $(u'_c(0), i'(0)\sqrt{L/C})$. The four centers are given by {Q1/Q3: $(1-U'_0, 0)$ }, {D1/D3: $(1+U'_0, 0)$ }, {Q2/Q4: $(-1+U'_0, 0)$ } and {D2/D4: $(-1-U'_0, 0)$ }. The optimal trajectory control, above resonant frequency utilizes the desired diode trajectory as the control law.

In the first half period, distance D (fig.2) of the state of the system from the center of trajectory located at $\{(-1-U'_0), 0\}$ is monitored. When this distance is smaller than radius value R_D , as set by the control system, transistors Q1/Q3 are turned on (segment M_1M_2). When distance D becomes equal to control input R_D at M_2 , transistors are turned off and diodes

D2/D4 are switched on (segment M_2M_3). At point M_3 diodes switch off, as resonant current reverses. Then transistors Q2/Q4 are turned on (segment M_3M_4). Distance D is once again monitored, this time as measured from the D1/D3 trajectory center $\{(1+U'_0, 0)\}$.

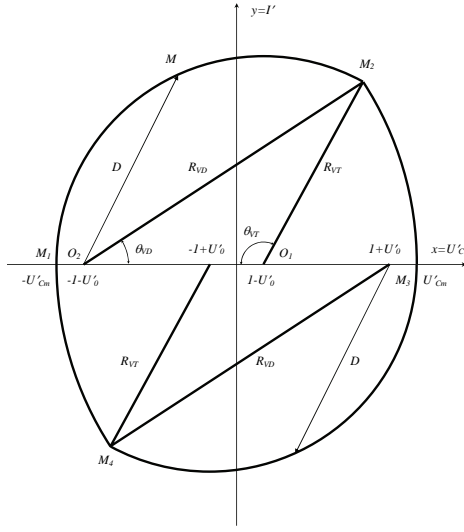


Fig.2 SRC steady-state trajectory above resonant frequency

From the triangle $O_1O_2 M_2$ (fig.2) the following equations for the diodes trajectory radius R_D and transistors trajectory radius R_Q are obtained

$$R_D = 1 + U'_0 + U'_{Cm} \quad (1)$$

$$R_Q = 1 - U'_0 + U'_{Cm} = R_D - 2U'_0. \quad (2)$$

For the radius R_D is evaluated

$$R_D = U'_0 + \sqrt{1 + (1 - U_0'^2) \cdot \text{tg}^2 \left(\frac{\theta_Q + \theta_D}{2} \right)} \quad (3)$$

In the base of equations (1)-(3) the expressions of base quantities characterizing converter operation get the form shown in table 1. The purpose is to obtain the expressions as a function of diode trajectory radius R_D , which is a base parameter for control under used method.

TABLE 1
RESULTS FROM ANALYSIS

Quantity	Expression
I'_{L0}	$R_{VD} \cdot \sin \left(\arccos \frac{1 - U'_0 \cdot R_{VD} + U_0'^2}{R_{VD} - 2 \cdot U'_0} \right)$ (4)
U'_{C0}	$U'_0 \cdot (R_{VD} - 1 - U'_0)$ (5)
U'_{Cm}	$R_{VD} - 1 - U'_0$ (6)
θ_{VT}	$\arccos \frac{1 - U'_0 \cdot R_{VD} + U_0'^2}{R_{VD} - 2 \cdot U'_0}$ (7)
θ_{VD}	$\arccos \frac{1 + U'_0 \cdot R_{VD} - U_0'^2}{R_{VD}}$ (8)
I'_0	$2 \cdot (I'_{VTAV} + I'_{VD,AV}) = \frac{(R_{VD} - 1 - U'_0)}{\arctg \sqrt{\frac{(R_{VD} - U'_0)^2 - 1}{1 - U_0'^2}}}$ (9)

$I'_d = P'_d$	$2 \cdot (I'_{VTAV} - I'_{VD,AV}) = \frac{U'_0 \cdot (R_{VD} - 1 - U'_0)}{\arctg \sqrt{\frac{(R_{VD} - U'_0)^2 - 1}{1 - U_0'^2}}}$ (10)
I'_{VTAV}	$\frac{(1 + U'_0) \cdot (R_{VD} - 1 - U'_0)}{4 \cdot \arctg \sqrt{\frac{(R_{VD} - U'_0)^2 - 1}{1 - U_0'^2}}}$ (11)
$I'_{VD,AV}$	$\frac{(1 - U'_0) \cdot (R_{VD} - 1 - U'_0)}{4 \cdot \arctg \sqrt{\frac{(R_{VD} - U'_0)^2 - 1}{1 - U_0'^2}}}$ (12)
I'_{VTm}	$R_{VD} - 2U'_0 \quad \theta_{VT} \geq \pi/2$ $(R_{VD} - 2U'_0) \cdot \sin \theta_{VT} \quad \theta_{VT} < \pi/2$ (13)

As a proof of the made analysis it is possible to define optimal control law, which is allowed transient processes with large amplitude, at same time converter stable operation (transistors and resonant tank) are ensured. The variable D is defined (fig.2) as the distance between the representative point of the system and the commuting center of the reference trajectories:

$$D = \sqrt{i'^2 + [u'_c + \text{sign}i'(1 + U'_0)]^2} \quad (14)$$

Transistors turn-off are realized when $D = R_D$. If $D > R_D$ transistors are turned on while $D = R_D$ or $\theta_Q = \pi$. Practically, to ensure transistors soft switching conditions (ZVS) it is necessary $\theta_Q < \pi$ and $I' > I'_{min}$.

Solving equations (4)-(13) can be drawn an inverter family of load characteristics. Those are the relationships of the converter main variables as a function of the voltage ratio U'_0 and radii R_D . The following relations can be of great interest: the converter output current $I'_0(U'_0, R_D)$, the input current $I'_d(U'_0, R_D)$, the transistors average current $I'_{Q,AV}(U'_0, R_D)$ and the freewheeling diodes average current $I'_{D,AV}(U'_0, R_D)$, the peak transistors current $I'_{Qm}(U'_0, R_D)$, the peak capacitor voltage $U'_{Cm}(U'_0, R_D)$. Figures 3 - 8 show corresponding graphs by $R_D = 1, 1, 1, 5; 2 \div 6$ in relative units.

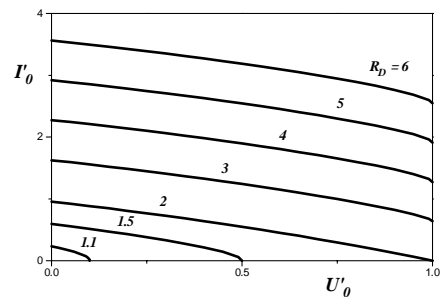


Fig. 3 Output characteristics for several values of R_D

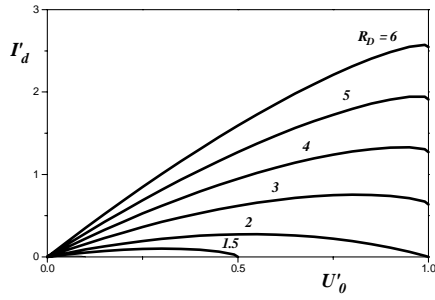


Fig.4 Normalized input current I'_d versus U'_0

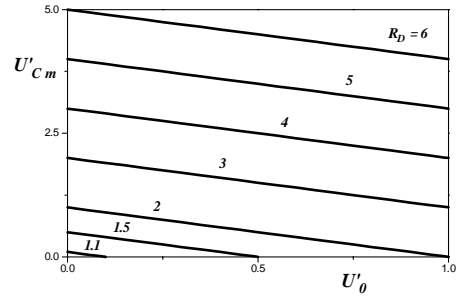


Fig.8. Normalized peak capacitor voltage U'_{Cm} vs U'_0

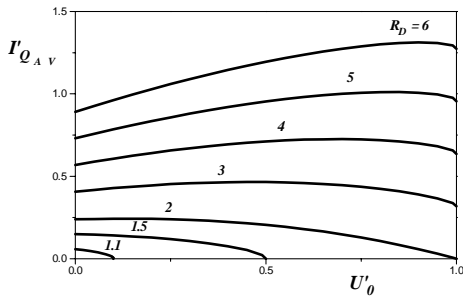


Fig.5 Normalized transistors average current $I'_{Q_{AV}}$ versus U'_0

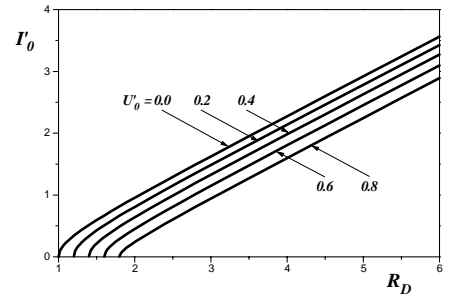


Fig. 9. Normalized output current vs normalized control input

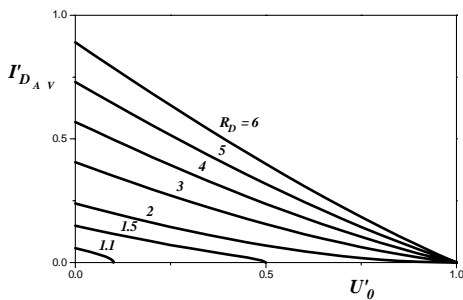


Fig.6 Normalized diodes average current $I'_{D_{AV}}$ versus U'_0

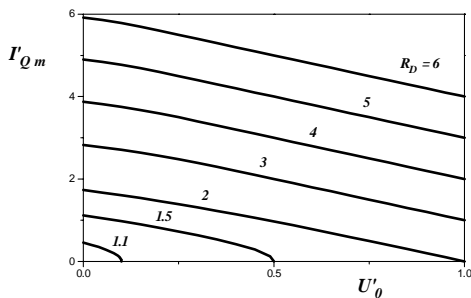


Fig.7. Normalized transistors peak current I'_{Q_m} vs U'_0

The relationships $I'_0(U'_0, R_D)$ (fig. 3) represent converter output characteristics. The converter can be considered as a current source, stable at short-circuit mode. Its operation near no-load running mode is limited from the transistors soft switching conditions (ZVS) [9]. The relationships $I'_0(R_D, U'_0)$ (fig.9) represent dc characteristics, which are useful in determining the control range for require output variation. Another important concern is whether by limiting the maximum value of the control input, a current- limited output can be obtained. It is important in determining the need of additional overcurrent protection circuit. A study of the characteristics shown in figs. 3 - 9 reveals that they can be used to calculate the circuits elements of the SRC – for example, the transistors average current $I'_{Q_{AV}}$ can be calculated from fig.5 for a selected values of U'_0 and R_D .

III. EXPERIMENTAL RESULTS

The experimental investigation of the resonant DC/DC converter designed under proposed analysis is made. The following conditions are used: power supply $U_j=300V$; switching frequency $f=125kHz$; output power $P=3kW$; and resonant link elements $L= 72,577\mu H$ and $C= 46,157nF$. During the experiment snubbers' value is $1nF$. Fig. 10 sows converter start-up optimal trajectory.

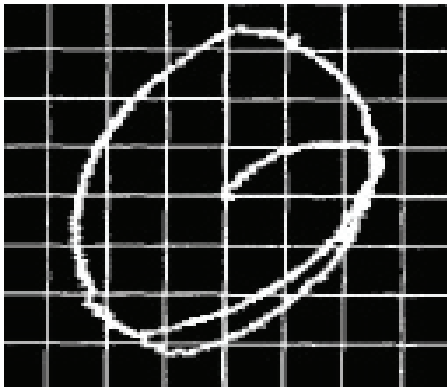


Fig.10 Start-up of the converter – x: u_C (200V/div) and y: i_{Ll} (5A/div).

IV. CONCLUSIONS

In this paper is obtained steady-state equations in optimal trajectory control, described DC/DC resonant converter operation above resonant frequency as a function of the diode trajectory radius and corresponding normalized load characteristics. They allow evaluating the behaviour of the considered converter when the load is changed strongly during the operation process. The converter experimental results are shown. The converters, operated under this control technique, are more suitable for electric arc welding devices, X-ray devices, lasers power supply etc., where for the supply source, characteristics of the current source are required.

REFERENCES

- [1] Oruganti R., F.C. Lee, Resonant Power Processor: Part II - Methods of control, Proc. IEEE-IAS'84 Ann. Meet., pp. 868-878, 1984.
- [2] Popov E.I., Antchev M. Hr. "A unified analysis and characteristics of a DC – DC converter operating above or below the resonance" International Scientific Conference ICEST'2004, Proceedings, June 2004, Bitola, Macedonia.
- [3] Sivakumar S., K. Natarajan, A.M. Sharaf, Optimal Trajectory Control of Series Resonant Converter using Modified Capacitor Voltage Control Technique, PESC'91, pp.752-759, 1991.
- [4] Natarajan, K., S. Sivakumar, Optimal trajectory control of constant frequency series resonant converter, Proc. IEEE-PESC '93, pp.215 – 221, 1993.
- [5] Rossetto L., A Simple Control Technique for Series Resonant Converter, IEEE Trans. on Power Electronics, vol.11, no.4, pp.554-560, 1996.
- [6] Kutkut N.H., C. Q. Lee, I. Batarseh, A Generalized Program for Extracting the Control Characteristics of Resonant Converters via the State-Plane Diagram, IEEE Trans. on Power Electronics, vol.13, no.1, pp.58-66, 1998.
- [7] Bankov N., Tsv. Grigorova, Investigation of a method for power control of a DC/DC transistor resonant converter, XXXIX ICEST'2004, Bitola, Macedonia, vol.1, pp.395-398, 2004.

Modeling of the Optimal Trajectory Control System of Resonant DC/DC Converters Operating Above Resonant Frequency

Nikolay D. Bankov¹ and Tsvetana Gr. Grigorova²

Abstract - The paper presents behavioral modeling of the control system of resonant DC/DC converters, operated above resonant frequency under “optimal trajectory control” technique. This method predicts the fastest response possible with minimum energy surge in the resonant tank. In this paper the investigations are extended and the specific variant of the series DC/DC converter controls system operated above resonant frequency is proposed.

Simulation and experimental results from the investigation of the converter are shown.

Keywords - resonant DC/DC converters, behavioral modeling, optimal trajectory control.

I. INTRODUCTION

The several control methods of series resonant DC/DC converters are widely discussed and compared in recent years [1-7]. Due to the presence of resonant circuit with its fast transient response, the control of resonant converters is considerably more complex than PWM converters [1].

The advantages of the optimal trajectory control method over the existing methods are reduced stress on the reactive and power semiconductor switching elements of the circuit and faster response in case of large variations of circuit operating conditions without affecting the global stability of the system [1], [8]. This method predicts the fastest response possible with minimum energy surge in the resonant tank.

In this paper the investigations are extended and the specific variant of the series resonant DC/DC converter controls system operated above resonant frequency is proposed. The control system is described using Analog Behavioral Modeling (ABM) [9].

II. BEHAVIORAL MODELING OF THE OPTIMAL TRAJECTORY CONTROL SYSTEM

The control system is described using Analog Behavioral Modeling (ABM). Fig.1 shows the simulation resonant DC/DC converter. The transistor individual control circuits are introduced [10].

¹ Nikolay Dimitrov Bankov is with the University of Food Technologies, 26 Maritza Blvd., 4002 Plovdiv, Bulgaria, E-mail: nikolay_bankov@yahoo.com

² Tsvetana Grigorova Grigorova is with the Technical University of Sofia, Branch Plovdiv, 61 Sankt Petersburg Blvd., 4000 Plovdiv, Bulgaria, E-mail: c_grigorova@abv.bg

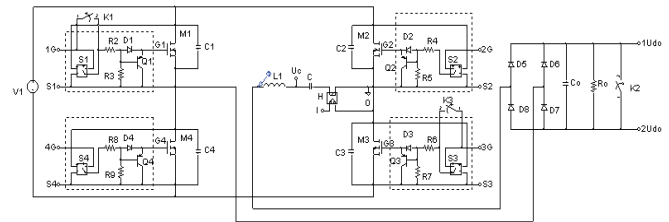


Fig.1. The simulation full-bridge resonant DC/DC converter

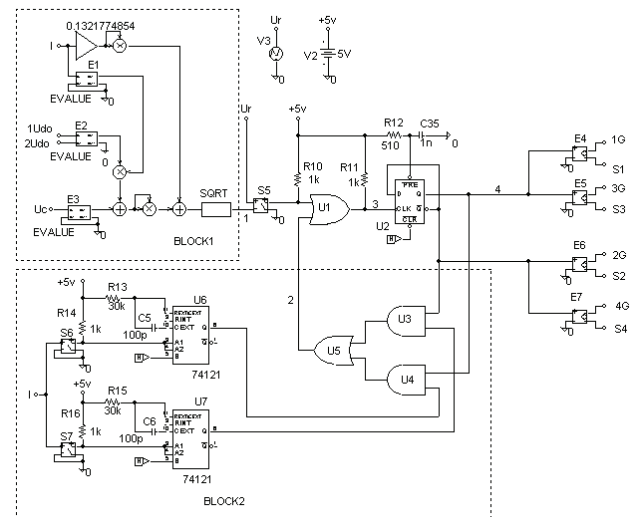


Fig. 2. Converter control system behavioral modeling

The proposed control system (CS) is shown in fig. 2 and in fig. 3 – the waveforms, which explain the system operation.

From the instantaneous values of i , u_C , U_0 and U_d , the control circuits compute the variable D [11] at every instant as given by BLOCK1, where

$$D = \sqrt{i'^2 + [u'_c + \text{sign}(1 + U'_0)]^2} \quad (1)$$

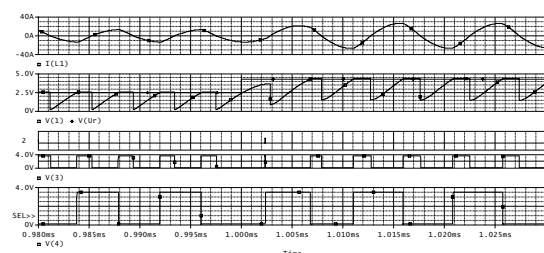


Fig. 3. Control system main waveforms

The dependent current control voltage source (CCVS) H senses the current trough the resonant tank. The signals for voltages U_0 and u_c are fed to the dependent voltage sources of EVALUE type (E2 and E3). The output of E1 (EVALUE) is the logical signal whose state (+1 or -1) is determined by the $signi'$. The dependent voltage source E1 realizes function:

$$SGN(V(\%IN+, \%IN-)) \tag{2}$$

in the EXPRESSION field of the EVALUE element.

The received value of D (v (1) in fig.2) is compared with control signal U_r .

The voltage controlled switches S6, S7, one-shot multivibrators 74121 and logical elements U3, U4, U5 ensure soft switching condition $\theta_Q < \pi$ and $I' > I'_{min}$. (BLOCK2).

The shaped pulses are fed to the flip-flop trigger U2. The pulse distributor U2 forms two channels of the control pulses, dephased at 180^0 . The dependent voltage control voltage sources (VCVS) E4÷E7, provide the required power, amplitudes and galvanic separation of the control signals.

As noted in [1,9], the maximum rate at which the tank energy can change in half a cycle is limited. Thus the system takes more than a half-cycle to reach the target trajectory. Fig. 4 shows the PSpice simulation results of the system response to large changes in control input. In fig.4a, when control input decrease, the tank energy is reduced by a series of successive diode conductions.

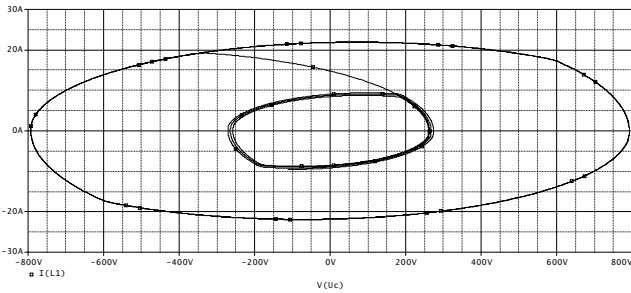


Fig.4-a. Response of optimal trajectory control for control decrease $R_{D1}=4,3 \rightarrow R_{D2}= 2,5$ ($t = 1980 \div 2030\mu s$)

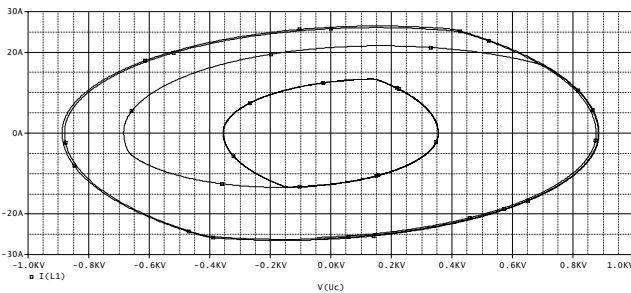


Fig.4-b. Response of optimal trajectory control for control increase $R_{D1}= 2,5 \rightarrow R_{D2}= 4,3$ ($t = 980 \div 1030\mu s$)

Likewise in fig.4b, when control input increase, the tank energy is built up a series of successive transistor conductions. Thus by utilizing the desired diode trajectory itself as the control low, the new steady state can be reached. In both cases, the system reaches the new equilibrium trajectory in the minimum possible time limited only by the intrinsic properties of the resonant converter.

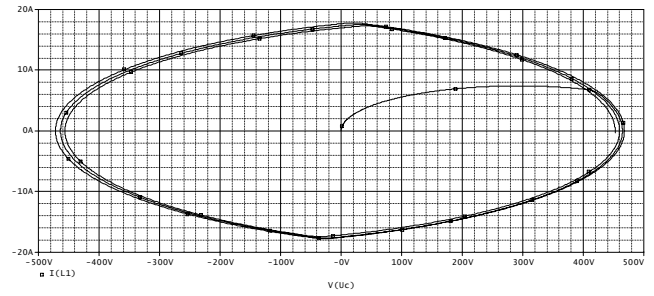


Fig.5-a. Transient under Converter start-up $R_D = 2,5$ ($t = 0 \div 30\mu s$)

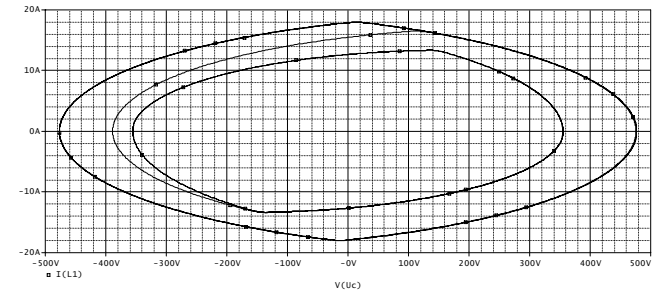


Fig.5-b. Transient under Load short circuit $R_D = 2,5$ ($t = 2980 \div 3030\mu s$)

Fig.5a shows PSpice simulation results of the system response at converter start-up. The performance of the method under short-circuit is also remarkable as shown in fig.5b. Within a short time, the system abruptly reaches another equilibrium trajectory at energy level only slightly greater than the earlier one. Thus optimal trajectory control fully exploits the potential of a converter to respond quickly to the demands of control and load.

III. EXPERIMENTAL RESULTS

The computer simulation and experimental results of the resonant DC/DC converter are given by the following conditions: power supply $U_I=300V$; switching frequency $f=125kHz$; output power $P=3kW$; and resonant link elements $L=72,577\mu H$ and $C= 46,157nF$. During the experiment snubbers' value is $1nF$.

Fig. 6 sows response of optimal trajectory control in the case for control increase.

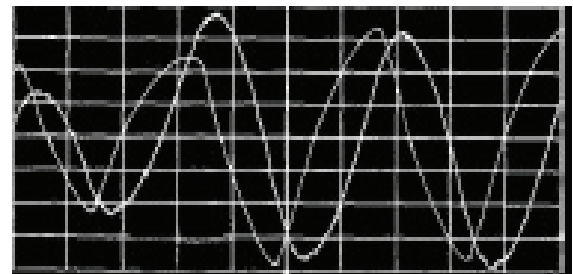


Fig.6-a. Response of optimal trajectory control for control increase Resonant current i_{L1} (5A/div) and capacitor voltage u_C (200V/div)

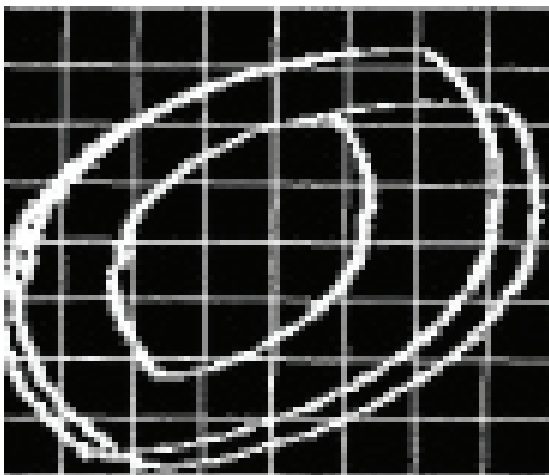


Fig.6-b. Response of optimal trajectory control for control increase
State plane -x: u_C (200V/div) and y: i_L (5A/div).

A very good agreement between simulation (fig.4b) and experimental results (fig.6) can be seen.

IV. CONCLUSIONS

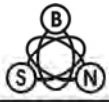
In the paper are presented the PSpice simulation results of the system response to large changes in control input. Showing different cases: when control input decrease, the tank energy is reduced by a series of successive diode conductions, likewise when control input increase the tank energy is built up a series of successive transistor conductions. Thus by utilizing the desired diode trajectory itself as the control low, the new steady state can be reached. In both cases, the system reaches the new equilibrium trajectory in the minimum possible time limited only by the intrinsic properties of the resonant converter.

PSpice simulation results of the system response at converter start-up are shown too. The performance of the method under short-circuit is also remarkable. Within a short time, the system abruptly reaches another equilibrium trajectory at energy level only slightly greater than the earlier one. Thus optimal trajectory control fully exploits the potential of a converter to respond quickly to the demands of control and load.

A very good agreement between simulation and experimental results can be seen.

REFERENCES

- [1] Oruganti R., F.C. Lee, Resonant Power Processor: Part II - Methods of control, Proc. IEEE-IAS'84 Ann. Meet., pp. 868-878, 1984.
- [2] Cheron Y., La commutation douce dans la conversion statique de l'energie electrique, Technique et Documentation - Lavoisier, 1989.
- [3] Sivakumar S., K. Natarajan, A.M. Sharaf, Optimal Trajectory Control of Series Resonant Converter using Modified Capacitor Voltage Control Technique, Proc. IEEE-PESC'91 Ann. Meet., Cambridge-Boston, pp.752-759, 1991.
- [4] Natarajan, K., S. Sivakumar, Optimal trajectory control of constant frequency series resonant converter, PESC '93, pp.215 - 221, 1993.
- [5] Rossetto L., A Simple Control Technique for Series Resonant Converter, IEEE Trans. on Power Electronics, vol.11, no.4, pp.554-560, 1996.
- [6] Kutkut N.H., C. Q. Lee, I. Batarseh, A Generalized Program for Extracting the Control Characteristics of Resonant Converters via the State-Plane Diagram, IEEE Trans. on Power Electronics, vol.13, no.1, pp.58-66, 1998.
- [7] Sendanyoye V., K. Al Haddad, V. Rajagopalan, Optimal Trajectory Control Strategy for Improved Dynamic Response of Series Resonant Converter, Proc. IEEE-IAS'90 Ann. Meet., Seattle, WA, pp. 1236-1242, 1990.
- [8] Al-Haddad K., Y. Cheron, H. Foch, V. Rajagopalan, Static and Dynamic Analysis of a Series Resonant Converter Operating above its Resonant Frequency, SATECH'86 Proceedings, Boston, pp. 55-68, 1986.
- [9] OrCAD PSpice A/D User's Guide, OrCAD Inc., USA, 1999.
- [10] Bankov N., Tsv. Grigorova, Modeling of a control system of a transistor resonant inverter, XXXIX ICEST'2004, Bitola, Macedonia, vol.1, pp.391-394, 2004.



This page intentionally left blank.

Comparison of Temperature Dependent Noise Models of Microwave FETs

Zlatica D. Marinković, Vera V. Marković and Olivera R. Pronić

Abstract – In this paper, a comparison of hybrid empirical-neural noise models of microwave FET transistors earlier-proposed by the authors is done. The models are compared from various aspects such as: model accuracy, model complexity, a number of measured data needed for a model development, etc. Moreover, the models are contrasted to the models based on neural networks only.

Keywords – Neural networks, microwave FET, noise.

I. INTRODUCTION

During the last decade, neural networks have found many applications in modelling in the microwave area, [1]-[7]. Since they have the ability to learn from the presented data, they are especially interesting for non-linear problems and for the problems not fully mathematically described. Considered as a fitting tool, they fit non-linear dependencies better than polynomials. Once trained, neural networks are able to predict outputs not only for the input values presented during training process (memorizing capability) but also for other input values (generalization capability). Neural networks have been applied in modelling of either active devices or passive components, in microwave circuit analysis and design, etc. They have been applied in microwave FET transistor signal and noise performance modelling as well, [3]-[7].

Accurate and reliable noise models of microwave transistors are required for analyses and design of microwave active circuits that are parts of modern communication systems, where it is very important to keep the noise at a low level. Transistor signal and noise performances depend on temperature, but most of the existing transistor signal, and especially noise models refer to a single temperature (usually, nominal temperature). Therefore, for further analyses involving various temperature conditions, it is necessary to develop models for each operating temperature point. Model development is basically an optimisation process, usually time-consuming. Furthermore, measured signal and noise data for each new operating point are necessary for model development. Since these measurements require complex equipment and procedures, measured data acquiring could take much effort and time.

Applying neural networks in the noise modeling can make modeling procedures more efficient and more accurate. Authors of this paper have proposed several temperature-dependent noise models of microwave transistors based on the neural networks. On the one side, there are hybrid-empirical models where neural networks are used for including the

temperature dependence into an existing empirical device noise model, [5]-[7]. On the other side, there are black-box models based on neural networks only, [5]. In this paper a detailed comparison of the proposed hybrid empirical-neural noise models is done. The models are compared from various aspects: model accuracy, model complexity, a number of measured data needed for a model development, etc. Furthermore, the models are contrasted to the models based on neural networks only. Additionally, several recommendations regarding applicability of the models and their development are given.

The paper is organized as follows: after Introduction, In Section II neural networks are shortly described. A brief review of the proposed neural models is given in Section III. Modelling example is presented in Section IV. Finally, in Section VI the main conclusions are reported.

II. MLP NEURAL NETWORK

A multilyer perceptron neural network (MLP), such has been used in this work, consists of neurons grouped into layers: one input layer, several hidden layers and one output layer, [1]. The network inputs are inputs of the first layer neurons. Each neuron from a layer is connected with all of the neurons from the next layer but there are no connections between the same layer neurons. The network outputs are outputs of the output layer neurons. Each neuron is characterized by an activation function and its bias, and each connection between two neurons by a weight factor. The neurons from the input and output layers have linear activation functions and hidden neurons have sigmoid activation function.

The neural network learns relationship among sets of input-output data (training set) by adjusting the network parameters (connection weights and biases of activation functions) using optimisation procedures, such as the backpropagation algorithm or its modification – the Levenberg-Marquardt algorithm, [1]. Once a neural network is trained its structure remains unchanged, and it is capable of predicting outputs for all inputs whether they have been used for the training or not.

For all networks trained for the purpose of work, a number of the hidden neurons was determined during the network training process. For each network structure, neural networks with different number of the hidden neurons were trained and the modelling ability of each network was tested. The network with the best modelling results was chosen as the model of the considered structure.

Authors are with the Faculty of Electronic Engineering
Aleksandra Medvedeva 14, 18000 Niš, Serbia,
E-mail: [zlatica, vera, oljap] @elfak.ni.ac.yu

III. TRANSISTOR NOISE MODELS BASED ON NEURAL NETWORKS

A microwave transistor, as a two-port noisy device can be characterized by a noise figure F , which is a measure of the degradation of the signal-to-noise ratio between input and output of the device. Noise characteristics of the device are usually treated in terms of four noise parameters: minimum noise figure F_{\min} , equivalent noise resistance R_n , and magnitude and angle of the optimum reflection coefficient, corresponding to the generator impedance resulting in minimum noise figure, $Mag(\Gamma_{\text{opt}})$ and $Ang(\Gamma_{\text{opt}})$.

In the text below, the proposed microwave transistor noise models based on neural networks are described. The first proposed model, a basic hybrid empirical-neural model, framed with a dotted line in Fig 1, consists of an existing empirical device noise model based on equivalent circuit representation and a neural network (NNet1) trained to model temperature dependence of equivalent circuit elements and parameters, (ECP), [5]. This network has one input neuron corresponding to the ambient temperature. The number of the neurons in the output layer corresponds to the number of transistor ECP (N in Fig. 1). The number of hidden neurons is optimised during the training.

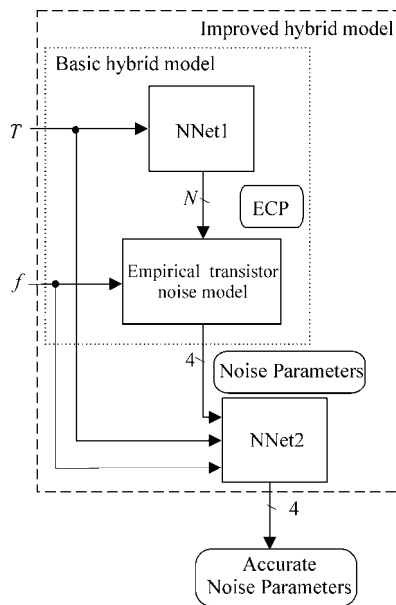


Fig. 1. Hybrid empirical-neural noise models

The model development starts from transistor signal and noise data measured at several temperature points. Using these measured values, ECP are extracted for each temperature. Further, the network training is done, and the trained network is assigned to the earlier-implemented device empirical model within a standard microwave simulator. The new model can be used as a user-defined library element, with the ambient temperature as the input, enabling the noise parameters' determination at each operating temperature, without need for noise parameters' measured values at that temperature and without additional optimizations.

A drawback of the basic hybrid empirical-neural model is that its accuracy can not be greater than the accuracy of the empirical model itself. Therefore, an alternative solution for improvement of the hybrid model enabling accuracy has been proposed in [7].

The mentioned improvement of the basic hybrid model is based on adding an additional neural network (NNet2) aimed to correct values of the noise parameters obtained by the basic hybrid model, Fig. 1. The inputs of the NNet2 network are temperature and frequency and the corresponding values obtained by the basic hybrid model. The training process of the NNet2 requires the basic hybrid model to be implemented previously, in order to obtain approximate values of the noise parameters for all combinations of the temperature and frequency used for the training. Since the measured values of the noise parameters are used as target output values for the NNet2, accuracy greater than the accuracy of the basic hybrid model can be achieved.

On the other hand, there is a black-box model, Fig 2, [5], consisting of a single neural network with two inputs corresponding to the temperature and frequency and four output neurons corresponding to the four noise parameters. The network is trained using the measured values of the noise parameters.

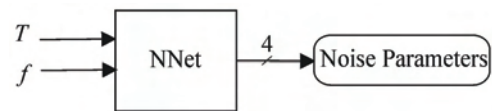


Fig. 2. Black-box neural noise model

IV. MODELING EXAMPLE

The above described models were applied to an HEMT device (type NE20283A) in a packaged form, in the temperature range $(-40 \div 60)^\circ\text{C}$. The measurements of the device noise parameters were performed by a research group with the University of Messina, by using an automated measurement system [8], [9]. The Pospieszalski's model, [10], is used for the transistor noise representation, Fig 3.

The intrinsic small-signal equivalent, framed with a broken line, includes two noise sources. The extrinsic circuit elements

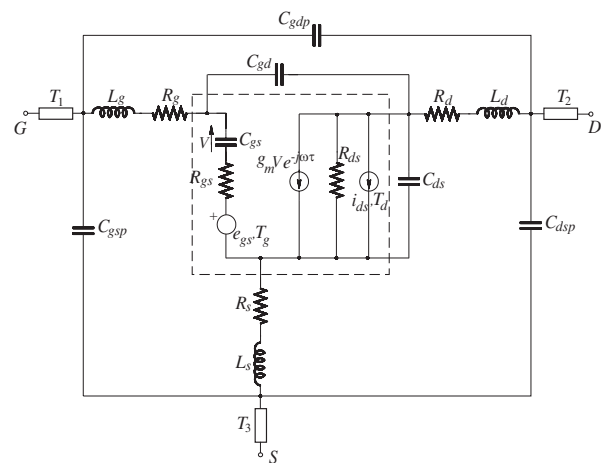


Fig. 3. Pospieszalski's transistor noise model

represent package effects and parasitic effects. Voltage noise source e_{gs} and current noise source i_{ds} represent the noise generated inside the device. The equivalent temperatures T_g and T_d are assigned to the voltage source e_{gs} and current source i_{ds} , respectively. The equivalent temperatures are empirical model parameters and are extracted from the measured device noise data through an optimisation process. The noise parameters related to the intrinsic circuit can be expressed as functions of equivalent circuit elements, two equivalent temperatures and frequency, [10]. Once four noise parameters of intrinsic circuit are determined, other model elements have to be added to the circuit with the aim to determine the noise parameters of the whole packaged device. The noise temperature of all resistances in the extrinsic circuit is assumed to be equal to the ambient temperature.

Therefore, the number of the ECP to be modelled is 20: 19 small-signal model elements and the equivalent drain noise temperature T_d . The equivalent gate noise temperature T_g is assumed to be equal to the ambient temperature. Firstly, the NNet1 was trained from the extracted values of the ECP for the mentioned temperatures. The network with 5 hidden neurons was chosen as the best, [5]. Then, the model was implemented in the ADS simulator, [11]. The noise parameters' values obtained by this new model at the temperatures: -40°C, 0°C, 20°C and 60°C and together with the corresponding measured noise parameters, were used for the NNet2 training. The best-obtained NNet2 has 10 hidden neurons, [7].

As an illustration, in Fig. 4 there is plot of the magnitude of optimum reflection coefficient in the frequency range (6-18) GHz. It is obvious that the values obtained by the improved hybrid model (solid line) are much closer to the reference (measured) values (squares) than the ones obtained by the basic hybrid model (dotted line). The modelling accuracy improvement is achieved not only at the training temperatures but also at the temperatures -20°C and 40°C, not used for the network training. The effects of the improvement are the most obvious at the boundaries of the temperature range.

The black-box neural noise model was developed using all of the available data, since training of the networks with a reduced set of the measured data did not give satisfactory modelling accuracy. The best-obtained NNet has two hidden layers each having 10 neurons. Compared to the basic hybrid model, this model provides better modelling accuracy, as can be confirmed by the scattering plots given in Figs. 5 and 6, showing the values of the magnitude of the optimum reflection coefficient versus the corresponding measured values for both of the models. There is less scattering from the ideal diagonal line $y=x$ in the case of the black-box neural modelling. On the other hand, the modelling accuracy of the black-box neural modelling is similar to the accuracy of the improved hybrid model, which can be observed by contrasting the corresponding scattering plots given in Figs. 6 and 7. As a further confirmation of the above-stated, in Fig. 8. there are values of the magnitude of the optimum reflection coefficient obtained by the black-box model (circles) matching very well to the corresponding ones obtained by the improved hybrid model (crosses).

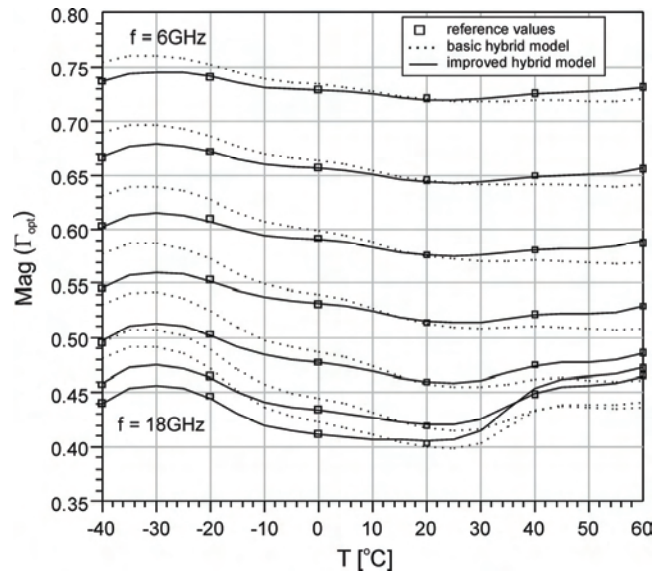


Fig. 4. Magnitude of optimum reflection coefficient

V. CONCLUSION

All of the proposed models, the hybrid empirical-neural ones and the black-box one, provide efficient noise modelling of microwave FET transistors. Contrary to the most of existing empirical models, where model development should be repeated for each operating temperature, once a neural model is developed, it is valid in the whole operating frequency and temperature range.

The advantage of the basic hybrid empirical-neural model is that the temperature dependence is included in the noise model but there are no improvements regarding the modelling accuracy.

Modelling accuracy can be enhanced by the improved hybrid empirical-neural model, which has an additional neural network aimed to correct values of the noise parameters. Since the correction network is trained using the measured noise data, the achieved modelling accuracy can be equal to the accuracy of the measured data. The previous is valid for the accuracy of the black-box neural model as well. In the both cases, all mechanisms of generating noise are included in the model.

The improved hybrid model has at its inputs additional knowledge about the noise parameters. Therefore, it requires less training data than the black box model and is suitable when there are no enough training data.

On the other hand, regarding the time needed for a model development and a number of necessary optimizations, the black-box model is the most efficient, since only the training of one neural network should be done and there are no optimizations in a circuit simulator. Hence, it is the best solution if there are enough measured data for the model development.

All of the proposed models can be easily implemented in standard microwave simulators.

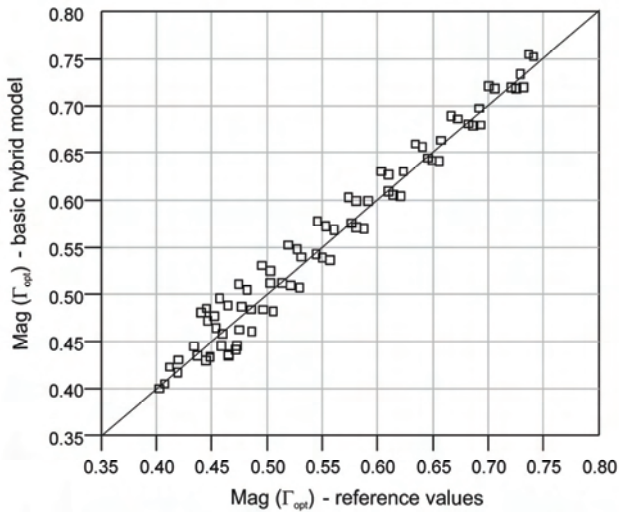


Fig. 5. Magnitude of optimum reflection coefficient Scatering plot: basic hybrid model vs. reference data

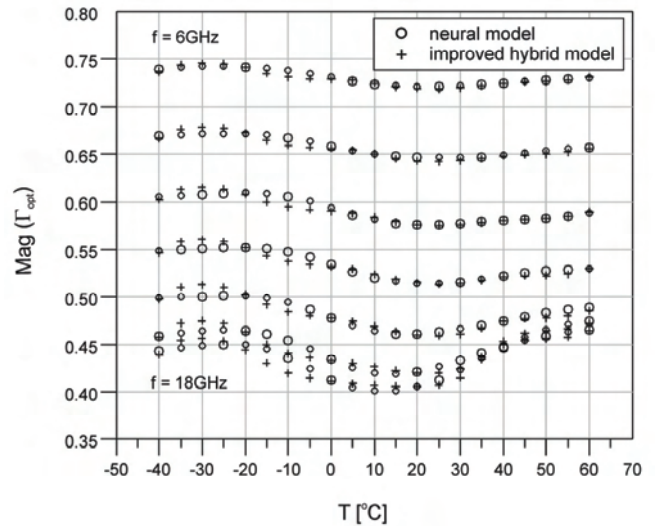


Fig. 8. Magnitude of optimum reflection coefficient Improved hybrid model contrasted to black-box model

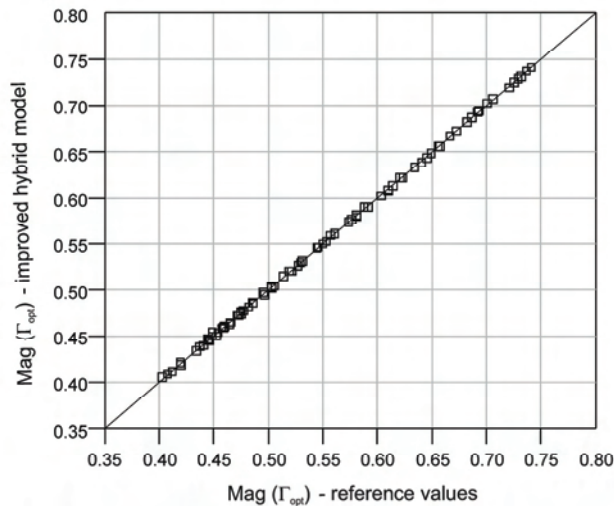


Fig. 6. Magnitude of optimum reflection coefficient Scatering plot: improved hybrid model vs. reference data

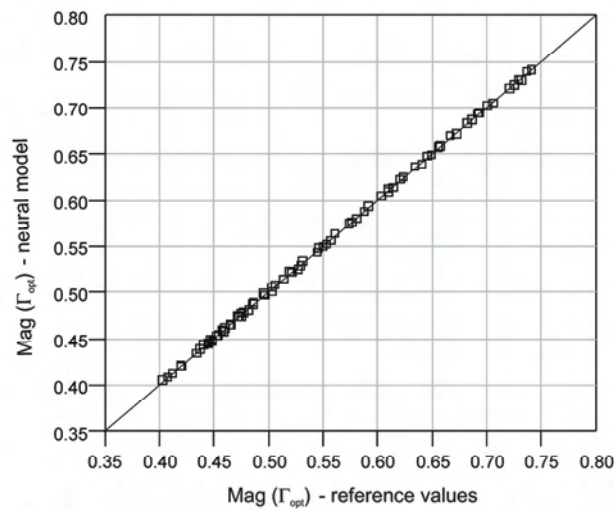


Fig. 7. Magnitude of optimum reflection coefficient Scatering plot: black-box neural model vs. reference data

REFERENCES

- [1] Q. J. Zhang, K. C. Gupta, *Neural networks for RF and microwave design*, Artech House, 2000
- [2] K.C.Gupta, "EM-ANN models for microwave and millimeter-wave components," *IEEE MTT-S Int. Microwave Symp. Workshop*, Denver, CO, June 1997, pp. 17-47.
- [3] F.Gunes, H.Torpi, F.Gurgen, "Multidimensional signal-noise neural network model", *IEE Proceedings on Circuits, Devices and Systems*, Vol.145, Iss.2, Apr 1998, pp. 111-117
- [4] P.M. Watson, M. Weatherspoon, L. Dunleavy; G.L. Creech, "Accurate and efficient small-signal modeling of active devices using artificial neural networks" *Proceedings of Gallium Arsenide Integrated Circuit Symposium, Technical Digest*, November 1998, pp. 95-98
- [5] Z. Marinković, V. Marković, "Temperature Dependent Models of Low-Noise Microwave Transistors Based on Neural Networks", *International Journal of RF and Microwave Computer-Aided Engineering*, vol.15, no. 6, pp.567-577, 2005.
- [6] Z. Marinković, O. Pronić, J. Radelović, V. Marković, "An Automated Procedure for MESFETs / HEMTs Noise Modeling Against Temperature", *ICEST2005*, June 2005, Niš, Serbia and Montenegro, pp. 89-92
- [7] Z. Marinković, V. Marković, "Accurate Temperature Dependent Noise Models of Microwave Transistors Based on Neural Networks", *Proceeding of European Microwave Week 2005 - 13th GAAS Symposium*, October 3-7, Paris, France, pp. 389-392
- [8] *NE20283A_temp.xls file*, internal communication with prof. A. Caddemi, University of Messina, Italy.
- [9] A. Caddemi, A. Di Paola, M. Sannino, "Determination of HEMT's Noise Parameters vs. Temperature using Two Measurement Methods", *IEEE Trans. on Instrumentation and Measurement*, Vol. IM-47, 1998, pp. 6-10.
- [10] M .W. Pospieszalski, "Modeling of noise parameters of MESFET's and MODFET's and their frequency and temperature dependence", *IEEE Trans. Microwave Theory Tech.*, Vol. 37, 1989, pp.1340-1350.
- [11] Advanced Design Systems-version 1.5, *Agilent EESof EDA*, 2000.

Power Losses and Applications of Nanocrystalline Magnetic Materials

Vencislav C. Valchev¹, Georgi T. Nikolov², Alex Van den Bossche³ and Dimitre D. Yudov⁴

Abstract – In this paper magnetic properties, power losses and applications of nanocrystalline magnetic materials are presented. It is figured out that because of their marvelous properties the nanocrystalline materials are very prospective in electronics. The loss comparison shows 2-3 times lower losses per unit weight of nanocrystalline compared to ferrites under both sine and square voltage measurements carried out.

Keywords – Nanocrystalline magnetic materials, losses

I. INTRODUCTION

Nanocrystalline alloys are firstly developed to obtain great permeability. The outcome of nanocrystalline manufacturing processes suggests an alternative about the use of other materials in power electronics applications. In nowadays power electronics applications, the nanocrystalline materials are concurrent to power ferrites and amorphous materials at high frequency devices.

The purpose of this paper is to presents the results of comparison of main parameters and application advantages of nanocrystalline soft magnetic materials and ferrites for Power Electronics Components.

II. NANOCRYSTALLINE ALLOYS PROPERTIES

The nanocrystalline alloys (FeSiBCuNb) are closely related to the amorphous soft magnetic materials. The precursor amorphous FeSiB alloy, containing small additions of Nb and Cu, is elaborated by very rapid solidification on ribbons 20µm thick (“Finemet” – HITACHI, “Vitoperm” – VACUUMSCHMELZE, “NanoPhY” – IMPHY). The material is annealed at medium temperature (500-550°C) to induce optimum crystallization and to develop the remarkable and unexpected magnetic properties of the nanocrystalline structure discovered at the end of the 80’s.

Due to their unique combination of favorable magnetic properties nanocrystalline cores are now well established in a wide field of applications. The major areas are: switched mode power supplies, digital telecommunications with

emphasis on ISDN systems, installation techniques at 50/60 Hz and since very recently applications in the automotive electronics. Additionally particle accelerators should be mentioned where cores with masses up to 50 kg or even more are needed for converters or resonators [1],[2].

A diagram, showing the comparison of typical properties of some Soft Magnetic Materials is shown in Fig. 1 [1].

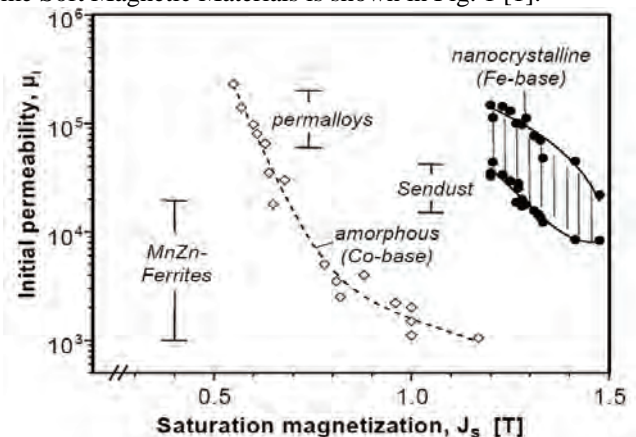


Fig. 1 Typical initial permeabilities and saturation inductions for soft magnetic materials

One of the great advantages that nanocrystalline magnetic materials offer is the ability to control their B-H curve, by applying a magnetic field during annealing. In Fig.2 three typical curves for FINEMET (Hitachi) cores are shown:

- 1) H type: a magnetic field is applied in a circumferential direction of the core plane during annealing.
- 2) M type: no magnetic field is applied during annealing.
- 3) L type: a magnetic field is applied vertically.

In manufacturer data sheets there is data about the losses under sine wave excitation. Comparison of losses under sine wave of typical magnetic materials is given in Fig.3 [1,3].

It must be emphasised that the comparison of only magnetic properties could not argue of an indisputable advantage of nanocrystalline compared to soft-ferrite materials [4]. So, integration capabilities of nanocrystalline materials must be analysed including power electronic specifications.

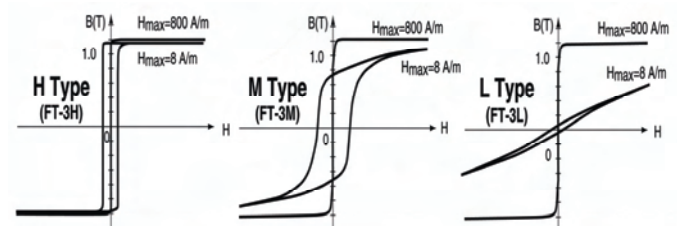


Fig. 2. Typical curves for FINEMET [5].

¹Vencislav C. Valchev - Technical University – Varna, Varna “Studentska” №1, Bulgaria, E-mail: vencilvalchev@hotmail.com

²Georgi T. Nikolov - Technical University – Varna, Varna “Studentska” №1, E-mail: nikolov_george@hotmail.com

³Prof. AlexVan den Bossche - EELAB EESA Firw08 UGENT, Sint-Pietersnieuwstraat 41, B 9000 Gent, Belgium

⁴Dimitre D. Yudov – Bourgas Free University, Bourgas, Bulgaria E-mail: yudov@bfu.bg

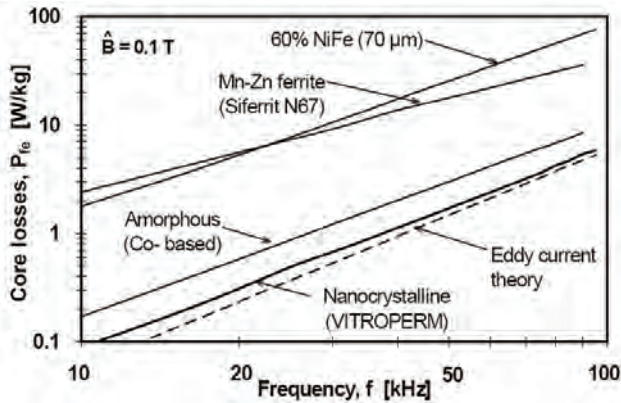


Fig. 3. Specific core losses of typical materials for power electronics under sine wave

Comparison of relative permeability μ_r of typical materials for power magnetic components is shown in Fig. 4 [5].

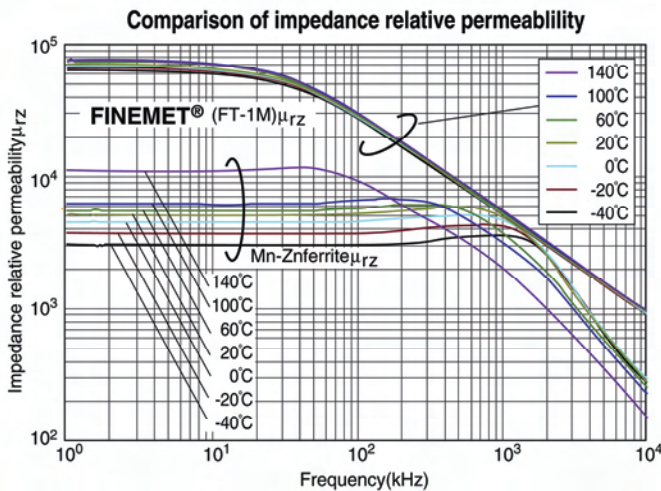


Fig. 4. Comparison of relative permeability μ_r of typical materials for power magnetic components.

III. POWER LOSSES IN NANOCRYSTALLINE MATERIALS FOR TYPICAL POWER ELECTRONICS WAVEFORMS

In power electronics sine waves are not very often used. Most frequently the voltage resemble a square wave or pulse wave with variable duty ratio. Thus, to carry out a comparison in respect to power electronics applications, we measured losses in nanocrystalline and a few ferrite materials.

A wide frequency loss model of nanocrystalline magnetic sheets including hysteresis effect is based on the theory of one-dimensional homogeneous transmission lines in the frequency domain [6]. The expressions for the complex impedances per unit length z_s and z_p result from the transmission line equations: $z_p = 1/(\sigma + j\omega\epsilon) \approx 1/\sigma$ with σ the conductivity. The effect of the permittivity ϵ is neglected so that z_p is real. The expression $z_s = j\omega\mu$ is combined with an impedance function in order to describe the hysteresis and the excess losses [7], represented by a constant loss angle δ_h (in radians):

$$z_s(j\omega) = j\omega\mu_h(j\omega) = \mu_{hr} \cdot (j\omega)^{1-2\delta_h/\pi} \quad (1)$$

Here, ω is the angular velocity and μ_{hr} a reference permeability. Thus, z_s represents a self inductance per unit length with a loss angle. Eq. (1) describes the magnetic behaviour of the material in the whole frequency range by only two parameters δ_h and μ_{hr} .

The measured material is VITROPERM 500F. The core shapes are all toroidal. Three different cores sizes are measured. The first coil (W435-04) is wound with four windings of 6 turns of 40 x 0,1 mm Litz wire in parallel. The secondary winding (0,25 mm double insulated) is used to measure the voltage and the flux. The number of turns is $N=6$. The second and third coil (W516-02 and W433-02) are wound with three windings of 5 turns of 40 x 0,1 mm Litz wire in parallel.

We measured the losses at variable duty ratios - D (from 50% to 5% with a 5% step), using a high-frequency test platform [8]. To be able to compare the data correctly, we used the specific volume losses. Experimental waveforms for duty ratio of 40% are shown in Fig.6.

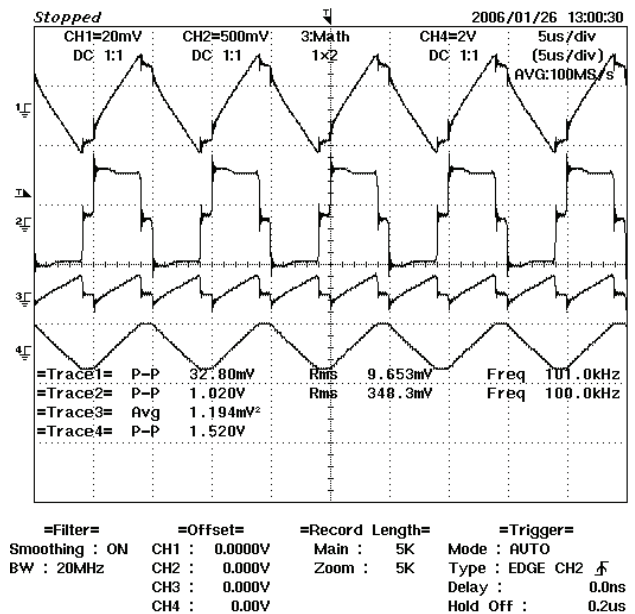


Fig. 5. VITROPERM 500F 63x50x25 core: W435-04 - Full Bridge, Square Wave, 100kHz, 25°C - 40% Duty Ratio

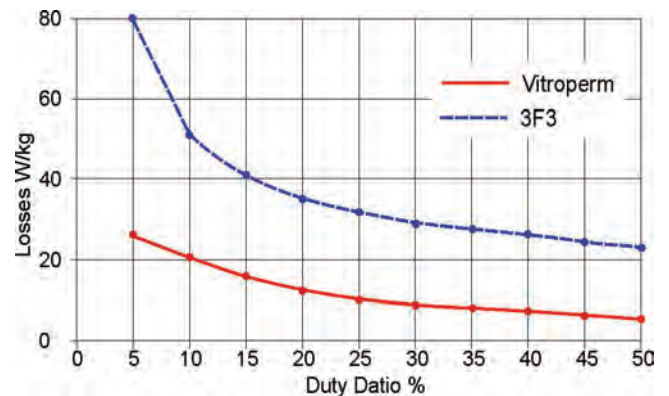


Fig. 6. Loss comparison for materials 3F3 and Vitroperm 500F, under square voltage, for variable duty ratio, from 50% to 5% with a 5% step, $f=100\text{kHz}$, $B_{\text{peak}}=0.1\text{T}$.

A comparison of the losses for materials 3F3 and Vitroperm 500, under square voltage, for variable duty ratio, from 50 % to 5 % with a 5 % step is shown in Fig.5 for $f=100$ kHz, $B_{peak}=0.1T$. As it is shown in the Figure 6, nanocrystalline materials exhibit significantly lower losses compared to the ferrites under typical power electronics waveforms.

IV. DESIGN SPECIFICS OF NANOCRYSTALLINE MATERIALS

Core shapes: With regard to core shapes, E-cores (for larger power even combinations of U- and I-cores) as well as toroidal cores are used.

Operating frequency range: A wide frequency range can be used at even high induction swing. Beside low core losses, the main inductance of a VITROPERM transformer will be dependent on frequency to a very small extent only, and as leakage inductances will be small due to the toroidal geometry and the low number of turns possible. This results in good magnetic coupling properties, and excess voltage peaks on switching transistors can be kept small. Moreover, there will be a low external leakage field.

The application temperature: The application temperatures of VITROPERM 500 F typically range from $-40^{\circ}C$ to $+120^{\circ}C$. This high maximum operating temperature provides a further volume advantage and is made possible by the large thermal stability of our materials and their properties. Core losses of most of nanocrystalline materials decrease up to 3-5% at $100^{\circ}C$, when compared to room temperature.

V. APPLICATIONS OF NANOCRYSTALLINE MATERIALS

Typical applications of nanocrystalline materials are:

- 1 telecommunications (telephone exchange power supplies, Base Stations);
 - 2 railways technology, mechanical handling equipment technology (battery charging devices);
 - 3 welding technology (switched mode Converters).
- In future, these will increasingly be extended to:
- 4 electric vehicles (battery charging devices, motor inverters);
 - 5 solar technology (inverters);
 - 6 induction heating.

The features of the nanocrystalline materials and the corresponding applications are summarized in Fig.7.

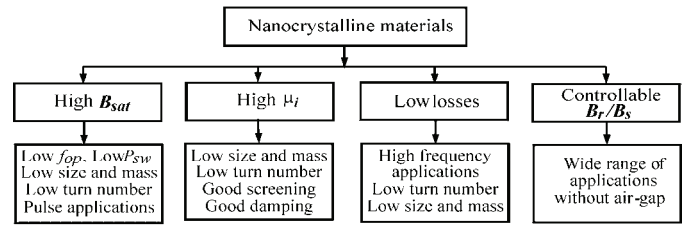


Fig.7 Features of nanocrystalline materials

Typical applications of nanocrystalline materials in Electronics and Power Electronics are shown in Fig.8. A useful comparison of properties and applications of most widely used soft magnetic materials in electronics is presented in Fig. 9.

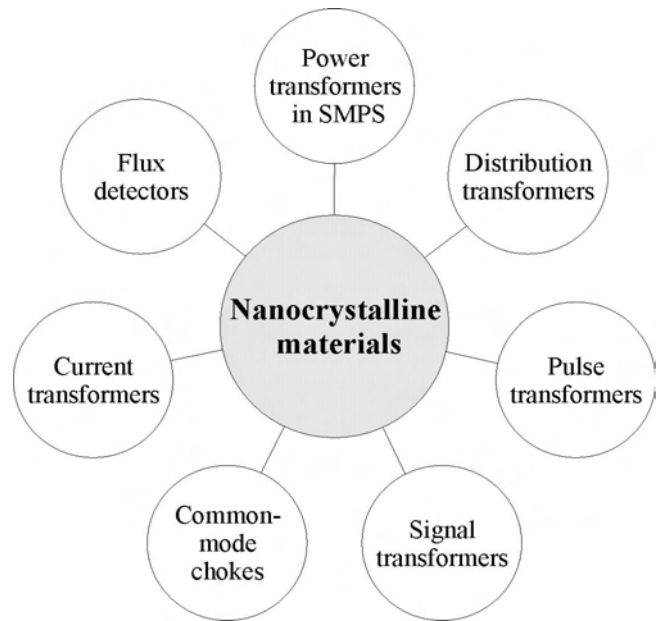


Fig.8. Typical applications of nanocrystalline magnetic materials in Electronics and Power Electronics.

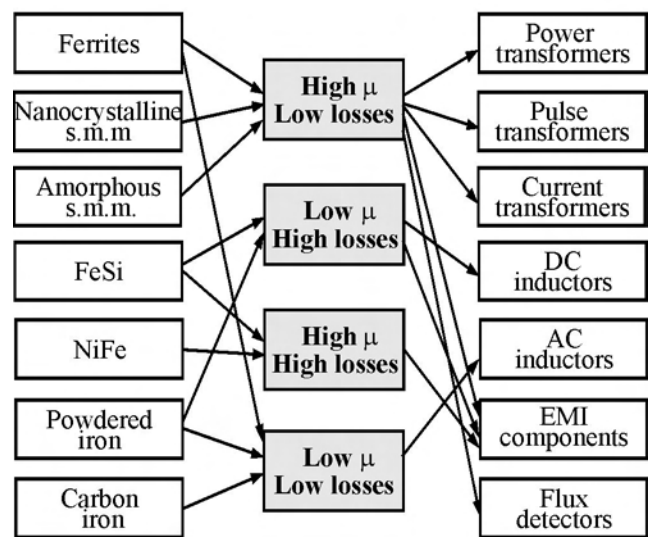


Fig.9. Comparison of the features and applications of soft magnetic materials in Electronics and Power electronics.

VI. CONCLUSION

In this paper magnetic properties, applications and global operating parameters of nanocrystalline magnetic materials are presented. The nanocrystalline materials combine high permeability of amorphous materials and low losses of ferrite materials, thus they are very promising in power electronics. Further advantage of the nanocrystalline materials is the possibility to control the B-H loop by applying magnetic field during annealing.

The loss comparison shows 2-3 times lower losses of nanocrystalline compared to ferrites under both sine and square voltages experiments and measurements carried out and depicted. A wide frequency loss model of nanocrystalline magnetic sheets including hysteresis effect is also discussed in the paper.

ACKNOWLEDGEMENT

The paper was developed in the frames of the NATO Research Program, Project RIG.981.482.

REFERENCES

- [1] Petzold J., "Advantages of softmagnetic nanocrystalline materials for modern electronic applications", *Journal of Magnetism and Magnetic Materials*, 242–245 (2002) 84-89
- [2] Vacuumschmelze GmbH & Co.KG., "Nanocrystalline VITROPERM - EMC Components", 2004
- [3] Herzer G., "Nanocrystalline soft magnetic alloys". in: K.H.L. Buschow (Ed.), *Handbook of Magnetic Materials*, Vol. 10, Elsevier, Amsterdam, 1997, pp. 415–462.
- [4] H. Chazal, J. Roudet, T. Chevalier, T. Waeckerle, H. Fraisse, "Comparative Study Of Nanocrystalline and Soft-Ferrite Transformer Using an Optimization Procedure", EPE 2003, Toulouse
- [5] Hitachi Metals, Ltd., "Nanocrystalline soft magnetic material "FINEMET®"", 2005
- [6] G. Bertotti, *Hysteresis in magnetism*, Academic Press, New York, (1998).
- [7] Van den Bossche, and V.C. Valchev, *Inductors and Transformers for Power Electronics*, CRC Press, Boca Ration, FL, USA (2005).
- [8] Van den Bossche A., T.A. Filchev, V.C. Valchev, D.D. Yudov, "Test Platform for resonant converters", 10th European Power Electronics and Applications Conference, EPE'03, Toulouse, France, 2-4 September 2003, CD-ROM

Multi level Electronic Transformer

Dimitre D. Yudov¹, Atanas Iv. Dimitrov², Vencislav C. Valchev³ and Dimitar M. Kovatchev³

Abstract – Serial connection of the rectifiers and parallel connection of the outputs of DCET are presented, providing reduced voltages of the components, as well as to increased battery charging current. Using the carried out investigations and experiments, useful relations are derived for dimensioning the components in the electronic transformer.

Keywords – AC/DC converter, DC/AC, DCET, battery charging

I. INTRODUCTION

The reduction of maximum static and dynamic voltage and current values of the converter components is achieved by using of multi-level converters. In [1] a three level converter operating on a common load and supply by a common source is presented. The operating high voltages require high voltage switching components and passive components .

The aim of the paper is introducing, analyzing and dimensioning of a “n” level converter, achieving considerable reduction of the voltages across the included converters. The converters are connected in series and their input and they are connected in parallel in their output (all the converters deliver energy to one and the same load).

II. BLOCK DIAGRAM

The block diagram of a “n” level converter is shown in fig.1. The block diagram includes n similar AC/DC converters, connected in series and “n” DC electronic transformers (DCET). The DCET operate on a common load. The choice of the number of the levels depends on the value of the supplying voltage and output voltage in order to obtain an optimal transformer ratio, n equal to 1 (n=1) [2].

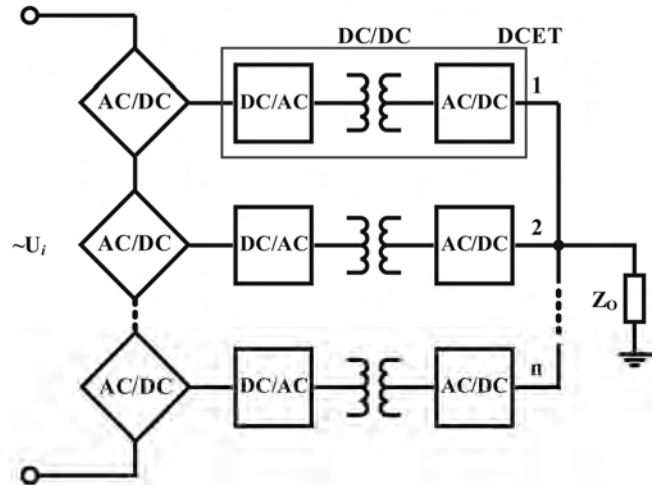


Fig. 1. Block diagram of a multilevel electronic transformer.

The realization of DCET can be achieved whit both one-switch or two-switch converters depending on the output power.

The power stage of one phase three level electronic transformer, suitable for battery charging, is shown in fig.2 Forward converter scheme is used to realize the levels of DCET. The new approach here is that the accumulated energy is transferred to the load by the windings w_m . This is obtainable because the load is almost purely capacitive [3,5,6]. The control of the power switches is realized by PWM controller, which is galvanically isolated in respect to the power stage [4].

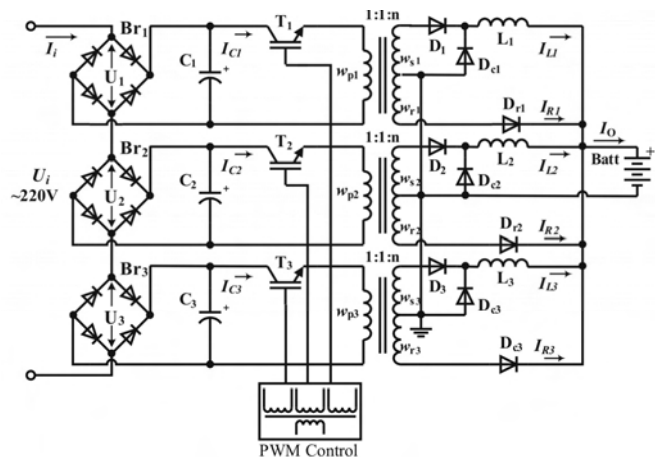


Fig. 2. Principle scheme of the power stage of a three level electronic transformer used for battery charging.

¹Dimitre D. Yudov is with the Centre of Informatics and Technical Sciences, Burgas Free University, 8000 Burgas, Bulgaria, E-mail: yudov@bfu.bg

²Atanas Iv. Dimitrov is with the Centre of Informatics and Technical Sciences, Burgas Free University, 8000 Burgas, Bulgaria E-mail: atanas@bfu.bg

³Vencislav Valchev and Dimitar M. Kovatchev are with the Faculty of Electronics, Technical University, 9000, Varna, Bulgaria

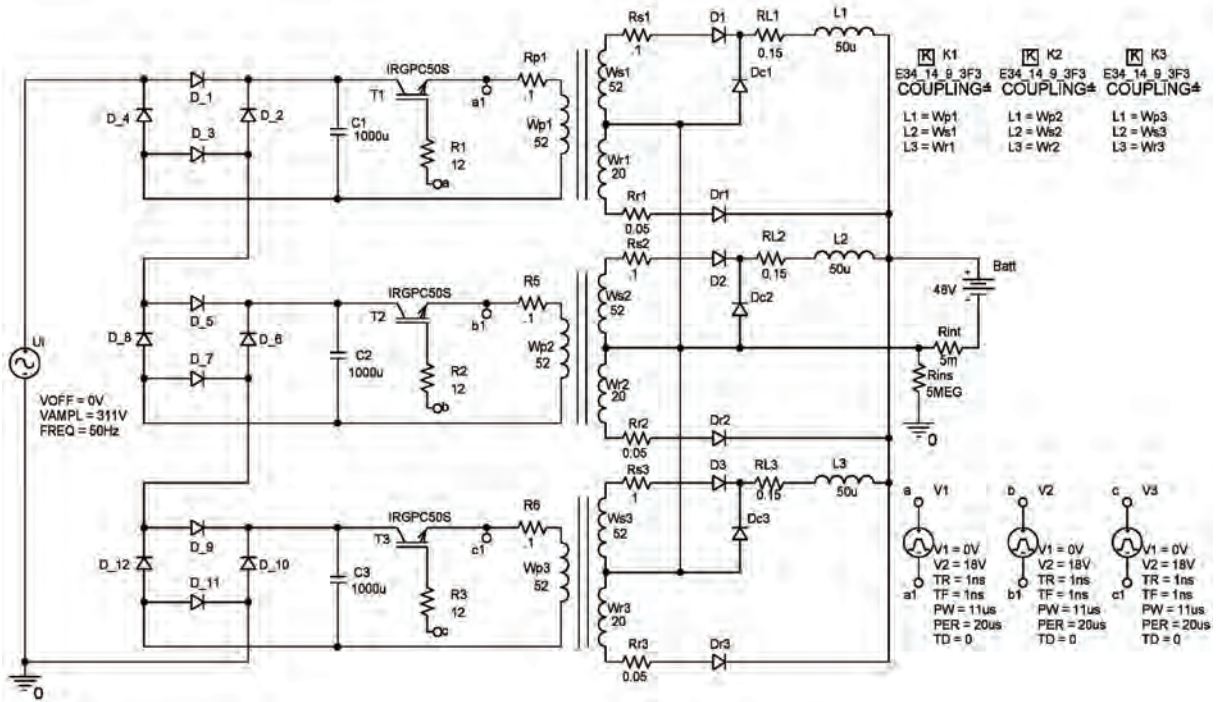


Fig. 3. PSpice model of the investigated three level electronic DCET for battery charging

A specific feature of the scheme is that the voltage across the diodes in the rectifier bridges is three times less than the power supply voltage, and the battery charging current is three times higher than the power transistor current. This advantage can be taken into account in investigation and dimensioning of the scheme.

In fig. 3 is shown the PSpice equivalent model of the circuit. Transformers of each of the levels are designed for $P_0=1000W$. A magnetic core model of PHILIPS is used with parameters $A_c=1,78cm^2$, saturation induction $B_{sat}=4900Gauss$ and $\mu_i=3000$ [3]. For the designed power, inductors with $L1=L2=L3=50\mu H$ are used.

In the equivalent model, the pulse-width modulator (PWM) is replaced by pulse generators V1, V2 and V3, which work synchronously without phase difference. The resistors $R_{p1}\div R_{p3}$, $R_{s1}\div R_{s3}$, $R_{r1}\div R_{r3}$ и $R_{L1}\div R_{L3}$ in the circuit represents the active resistance of the conductors of the windings. The resistor R_{ins} represents the isolation resistance of the transformers, and R_{int} the internal resistance of the battery.

In fig. 4 and fig. 5 are given the waveforms from PSpice simulations, showing the functionality of the chosen circuit.

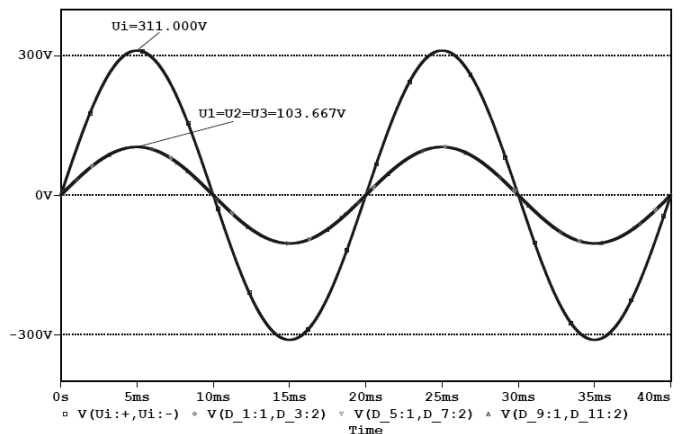


Fig. 4. Simulation waveforms of DCET

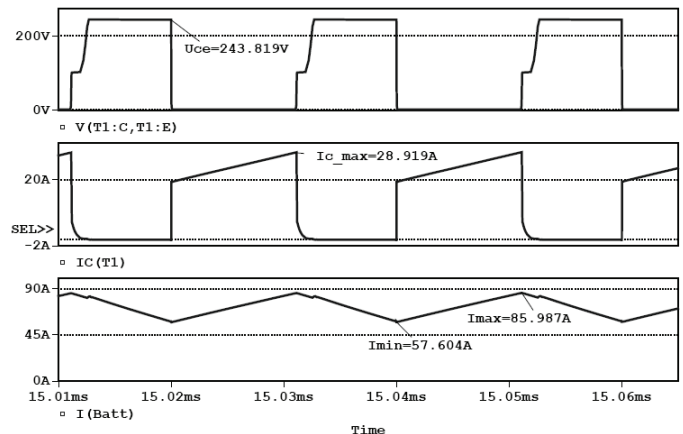


Fig. 5. Simulation waveforms of DCET, voltage and current of a power transistor and charge current of the battery

It can be noticed that:

- The input voltage of each stage ($U_1, U_2,$ and U_3) are equal, and three times less, than the input voltage (U_i)
- The voltage across transistors is in the admissible range ($U_{CE1}=2.4U_i$)
- The current through the transistors has small AC component and no real peak values.
- The charge current of the battery is three times more, than the current in each level, at transformation coefficient $k = 1$.

It is necessary to investigate the possibility of stabilization of the charge current, when the supply voltage and the battery voltage change. In fig. 6 is shown the control characteristics of the device under test, when the supply voltage changes. One can see that the current can be regulated in the range of $20 \div 60A$ when the supply voltage changes with $\Delta U_i = \pm 20\%$.

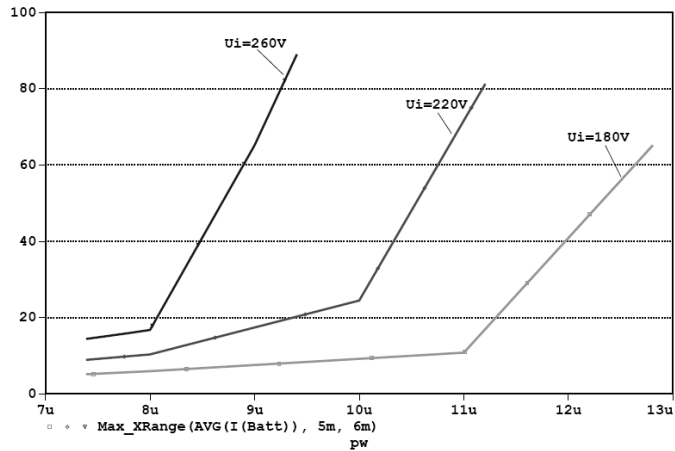


Fig. 6. Control characteristics of the circuit, when supply voltage changes

In fig.7 is shown the dependence of the charge current, on different values of the battery - $U(Batt)= 44, 48$ и $54V$.

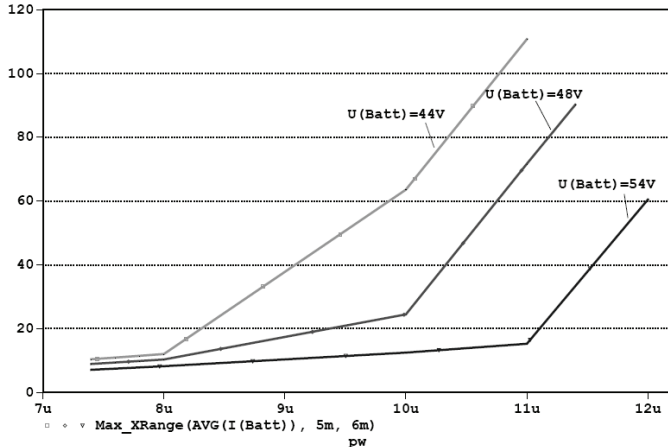


Fig. 7. Control characteristics of the circuit, when battery voltage changes

Two sections are clearly distinguished in fig.6 and fig. 7 are visible, characterized with different slopes. This is due to the discontinuous and continuous working mode of the converters. The discontinuous mode of the current through the

inductance is achieved at low values of duty ratio δ and the charge current depend less on δ .

The dependence of the maximum voltage across the power transistors upon the charge current with battery voltage changing ($U(Batt)= 44, 48$ and $54V$) is shown on fig. 8

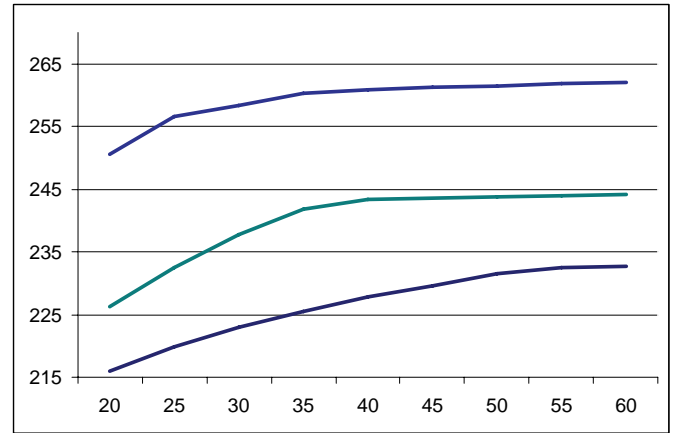


Fig. 8. Voltage across the power transistors versus the charge current

When the charge current changes according to the specifications ($20A \div 60A$), and the battery voltage is in the range $U_{batt}=(44\div 54)V$, the voltage across the power transistors does not change a lot $U_{CE}=(2.2 \div 2.6)U'$, where $U'=U_1=U_2=U_3$ is the supply voltage of each stage.

On the basis of the obtain waveforms and the dependences for the voltage and current of its components, several formulas can be derived to help dimensioning these components. The average value of the current through the power transistor is:

$$I_C = \frac{1}{T} \int_0^{t_n} k \cdot \frac{I_o}{n} dt = \frac{k \cdot \delta \cdot I_o}{n}, \quad (1)$$

where $k = \frac{w_s}{w_p}$ is the transformation coefficient of the power transformers;

n is number of levels (stages) of DCET.

The maximum value of the voltage across the transistors is:

$$U_{CE} = \frac{\gamma \cdot U_{im}}{n}, \quad (2)$$

where $\gamma=(2.2\div 3)$ is a coefficient giving voltage loading of the transistor.

The required value of the inductance in each level is determined by the admissible pulsations of the charge current:

$$L_n = \frac{n \cdot U_o \cdot (1 - \delta)}{a \cdot f \cdot I_o}, \quad (3)$$

where:

L_n is the inductance in each level;

a is the pulsations coefficient and $a \in [1.5 \div 3]$;

U_o is the output voltage;

f is the working frequency of the converters.

The choice of the number of levels depends on the supply voltage and the output voltage. In this way optimal structure of the transformer can be obtained with transformation coefficient $k=1$ [4].

CONCLUSION

Serial connection of the rectifiers and parallel connection of the outputs of DCET leads to reducing the working voltages of the transistors and the reactive elements, as well as to increasing the charging current of the battery.

When the supply voltage changes and/or battery voltage vary (according to the specifications), a constant value of the charging current is obtained by controlling the duty ratio δ .

Using the carried out investigations and experiments, useful relations are derived for dimensioning the components in the electronic transformer.

ACKNOWLEDGMENT

The paper was developed in the frames of the NATO Research Program, Project RIG.981.482.

REFERENCES

- [1] D. Yudov, At. Dimitrov, "Многозвонен понижаващ DC-DC преобразувател при работа на против Е.Д.Н.", Електроника'2006, София, България, 2006.
- [2] Van den Bossche, and V.C. Valchev, *Inductors and Transformers for Power Electronics*, CRC Press, Boca Ration, FL, USA (2005).
- [3] D. Yudov, At. Dimitrov, "A Step-Down Pulse Converter", ELECTRONICS ET2004, Conference Proceedings, pp. 21-27, book 4, Sozopol, Bulgaria, 2004.
- [4] Dimitar Kovachev, "BPSK randomization of PWM in dc-dc converters", Proc. of 5th International Conference TEHNONAV 2006, 19-21 MAY, 2006, Constanta, pp. 481-490.
- [5] Mi, N.; Sasic, B.; Marshall, J.; Tomaszewicz, S.A novel economical single stage battery charger with power factor correction, 2003. APEC apos;03. Eighteenth Annual IEEE Volume 2, Issue , 9-13 Feb. 2003 vol.2, Page(s): pp. 760 – 763.
- [6] Bojrup, M. Karlsson, P. Alakula, M. Simonsson, B. 'A dual purpose battery charger for electric vehicles' PESC 98 Record. 29th Annual IEEE 17-22 May, vol., p p. 565-570.

An Approach to Effectiveness Increasing of SPICE Macromodels

Elissaveta D. Gadjeva¹ Boryanka I. Mihova² and Vergil G. Manchev³

Abstract – In this paper transformed macromodels are proposed to effectiveness increasing of behavioral SPICE macromodels. The modifications of the *PSpice* library models allow to reduce the simulation time, the number of iterations and the order of the circuit matrix. The original and the modified models are compared and their effectiveness is evaluated.

Keywords – Behavioral models, Modified Nodal Analysis, OrCAD PSpice, Model Effectiveness

I. INTRODUCTION

Contemporary electronic devices are characterized with increasing complexity, a huge number of elements and high degree of integration. The standard electronic circuits contain hundreds, sometimes even thousands of elements. The effectiveness during the modeling of these circuits is of great importance. The circuit and the system simulators can run much faster today due to the availability of powerful computers and workstations. The circuits are more complex with each new generation of computers. This leads to huge computer resources assigned to circuit simulation in the design process in order to verify the circuit behavior [1,2,3].

The analysis of large electronic and electrical circuits and systems requires repeatedly solutions of sparse linear and nonlinear systems of equations. The sparsity can be used to accelerate circuit and system analysis. The nodal analysis equation have the form [4,5]:

$$[Y][V] = [J] \quad (1)$$

where $[Y]$ is the nodal admittance matrix; $[V]$ is the vector of unknown voltages; $[J]$ is the vector of the independent currents. The matrix $[Y]$ is sparse, because it contains a high proportion of zero-valued elements [1,2,3]. Every node is not connected to every other circuit node, and for nodal analysis nonzero-valued elements result only from direct connections. The dependence of the sparsity on the circuit size n is presented in Table I. It increases with circuit size and this can be used to reduce storage requirements and the number of floating point operations entailed in the solution of the circuit equations [1,2].

TABLE I
DEPENDENCE OF THE SPARSITY AND THE SIMULATION TIME ON THE MATRIX SIZE

n	% sparsity	Simulation time	Matrix type
10	50%	n^3	dense matrix
40	90%		
100	96%	$n^{1.5}$	sparse matrix
400	99%		
1000	99.9%	$n^{1.1}$	large sparse matrix

In order to increase the effectiveness, the modified nodal analysis (MNA) is used [1,2]. MNA allows to include all types of dependent and independent sources in the circuit matrix. The computer implementation of this procedure is easy, which is a substantial advantage for automated solution. According to the MNA, one equation is written for each of the circuit nodes and the equations for the voltage sources are included in the augmentation.

II. EFFECTIVENESS INCREASING

A. Effectiveness Increasing of Linear PSpice Operational Amplifier Behavioral Models

For the computer simulation of circuits containing operational amplifiers, macromodels of different complexity are used [1,7,8,9]. The linear macromodel of OpAmp is described by a voltage controlled voltage source (VCVS), which depends on the input signal. The frequency response of the output voltage is defined in the form:

$$V_{out}(f) = H(f) \cdot V_{in}(f), \quad (2)$$

where $V_{in}(f)$ is the input voltage. The open-loop gain $H(f)$ has the form:

$$H(f) = \frac{A_0}{1 + j \frac{f}{f_c}} \quad (3)$$

where A_0 is the DC open-loop gain, f_c is the cut-off frequency.

The standard linear macromodels of OpAmp are based on the equivalent circuit, shown in Fig. 1.

¹Elissaveta D. Gadjeva is with the Faculty of Electronics and Electronic Engineering, Technical University of Sofia, 1756 Sofia, Bulgaria, E-mail: egadjeva@tu-sofia.bg

²Boryanka I. Mihova is with the Faculty of Electronics and Electronic Engineering, Technical University of Sofia, 1756 Sofia, Bulgaria, E-mail: bobymih@abv.bg

³Vergil G. Manchev is with the English Language Department of Engineering, Technical University of Sofia, 1756 Sofia.

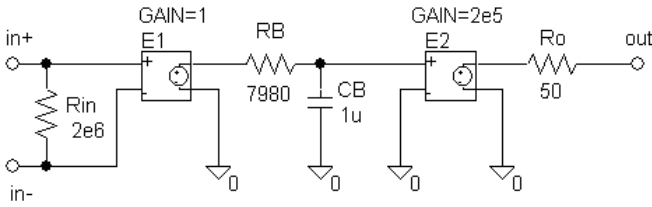


Fig. 1. Equivalent circuit of OpAmp macromodel

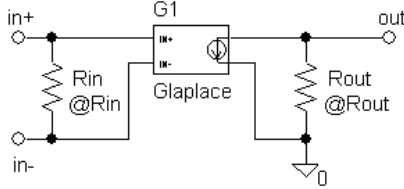


Fig. 2. Modified equivalent circuit of OpAmp macromodels

The frequency dependence of the OpAmp open-loop gain with one-pole approximation is modeled by a RC -circuit and dependent sources of **VCVS** type. The equivalent circuit of the macromodel adds internal nodes and each of the **VCVS**s extends the matrix order by 1. This leads to $\Delta n = 5$ additional rows and columns in the circuit matrix, for each OpAmp macromodel unit used in it.

The avoidance of these two dependent sources is the first step of the optimizing of the equivalent circuit. The macromodel can be realized more effectively by using of the analytical description of the frequency dependence of the open-loop gain $H(f)$. It is achieved in PSpice by the following expression, describing the OpAmp gain:

$$H(f) = \frac{A_0}{1 + \frac{s}{\omega_c}}, \quad (4)$$

$$s = j\omega = j2\pi f \quad (5)$$

Taking into account the equation (4), it is possible to described the OpAmp model by only one *Laplace* element of the **E** type, since it preserves all its characteristics. The simulation is also reliable, but significantly faster. An additional order reduction can be achieved by transforming the connected in series voltage source and resistance in current source and resistor, connected in parallel.

The modified equivalent circuit of the OpAmp is shown in Fig. 2. The resulting macromodel does not introduce any additional rows and columns to the circuit matrix.

B. Equivalent Transformations of More Complex PSpice Operational Amplifier Behavioral Models

In order to improve the effectiveness of the OpAmp macromodels, the elements that increase the order of the **Y** matrix should be replaced by other elements, which do not add additional nodes. The elements R , C , L , voltage controlled current source **VCCS** meet this requirement, while the elements without admittance matrix description (independent voltage source **E**, **VCVS**, current controlled voltage source

CCVS and current controlled current source **CCCS**) increase the matrix order, as shown in Table II.

TABLE II
MATRIX ORDER INCREASING FOR ELEMENTS
WITHOUT ADMITTANCE MATRIX DESCRIPTION

Type of source	E	VCVS	CCVS	CCCS
Δn	1	1	2	1

The improving the model by avoiding additional elements and nodes of the circuit, leads to a matrix of reduced order and to a decreased number of iterations made by the simulator. As a result, the simulation time is reduced and the effectiveness of the behavioral model is increased.

The dependent source **VCVS** can be converted to **VCCS** in the model and thus two additional rows and columns are eliminated from the original matrix (one from the **VCVS** and one from the extra node), as shown in Fig.3. If the voltage of the **VCVS** controls other electric voltage or current in the circuit, this transform cannot be applied. The voltage source E_{p2} and the resistance R_{p2} connected in series, are equivalently represented by the current source G_{p2} and resistor R_{p2} connected in parallel.

The macromodel of the HA-2500 [6] from the library HARRIS of the *OrCAD PSpice* is used as an example to illustrate the equivalent transformations.

The statements for EP2 and RP2 in the model section *Poles* are replaced by:

```
GP2 0 13 11 0 0.031407
RP2 0 13 3.184E+01
```

As a result, one node is skipped and one row and column are removed from the matrix due to the EP2 replacement. The voltage source EP1 in the original model can be transformed in **VCCS** in the similar way as shown in Fig. 3.

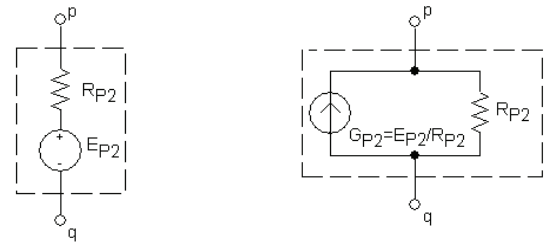


Fig. 3. Transformation of the VCVS into the VCCS

In this way, the statements describing the *Input Stage* in OpAmp HA-2500 model (current sources FP, FN, GC, GPP, GPN and IRX), the resistance RT and the statements of the *Poles* section describing EP1 and RP1, are replaced by the following statements:

```
FP1 11 0 VP 38.189
FN1 0 11 VN 38.189
GC1 0 11 8 0 5.127014E-10
GPP1 11 0 4 0 2.883069E-10
GPN1 11 0 5 0 5.127014E-10
IRX 0 11 -8.823707E-11
RP1 0 11 +1.0613E+02
```

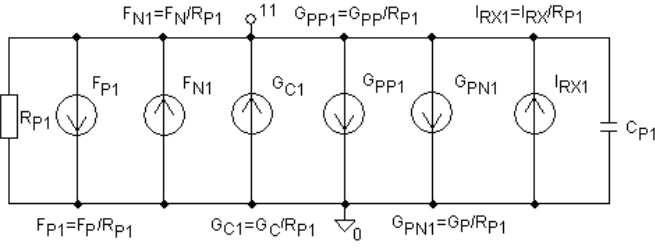


Fig. 4. Equivalent transformation in the OpAmp model

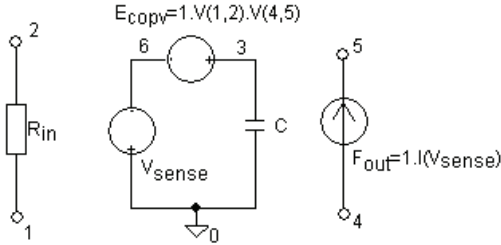


Fig. 5. Equivalent circuit of the variable admittance

The description of CP1 is not changed in the model. So nodes 9 and 10 are skipped and EP1 removed. The transformation is shown in Fig. 4.

The order of the \mathbf{Y} matrix for the modified model is reduced by $\Delta n = 5$ with comparison to the matrix order of the original mode – nodes 9, 10 and 12 are skipped and two VCVS are removed.

C. Effectiveness Increasing of PSpice Variable Admittance Behavioral Models

The equivalent circuit of the variable admittance is shown in Fig. 5. It contains dependent voltage source E_{copy} , short circuit V_{sense} and dependent current source F_{out} . $V(1,2)$ is the input voltage. $V(4,5)$ is the output voltage. Y_c is the reference admittance. The following equations are valid in this equivalent circuit:

$$I(V_{sense}) = Y_c \cdot V(1,2) \cdot V(4,5) \quad (6)$$

$$Y_{out} = I(V_{sense}) / V(4,5) = Y_c \cdot V(1,2) \quad (7)$$

The modified equivalent circuit is shown in Fig. 6. It realizes the same function $Y_{out} = Y_{ref} \cdot V_{control}$, as E_{copy} and V_{sense} are replaced by source V_1 and F_{out} is replaced by G_{out} .

The following equations are used in the modified equivalent circuit of the variable admittance:

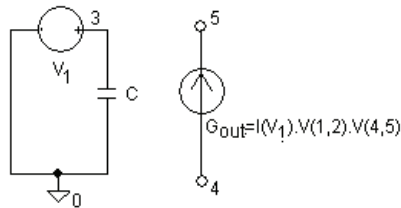


Fig. 6. Modified equivalent circuit of the variable admittance

$$I(V_1) = V_1 \cdot Y_c = 1 \cdot Y_c \quad (8)$$

$$I(4,5) = Y_c \cdot V(1,2) \cdot V(4,5) \quad (9)$$

$$Y_{out} = I(4,5) / V(4,5) = Y_c \cdot V(1,2) \quad (10)$$

The original matrix order for the standard model is $n_{st} = 8$, while the order of the modified one is $n_m = 6$ (source V_{sense} is removed).

D. Effectiveness Increasing of Behavioral PSpice Model of Sinusoidal Voltage Controlled Oscillator

The output voltage of the voltage controlled oscillator VCO-Sin is a sine wave, which frequency is controlled by a table voltage. The PSpice model has a form:

```
.subckt vco_sin in out Params: Fcenter=1k Frange=50
+ Vmin=1 Vmax=5 phase=0
Rin in 0 1G
Rtable table 0 1G
Etable table 0 Value {Table (V(in),Vmin,-1,Vmax,1)}
Esin out 0 Value{sin(6.28318*
+ (Fcenter*time+Frange*SDT(V(table))))+phase*
+ (3.14159/180))}
.ends
```

The dependent voltage source E_{table} is converted to the dependent source G_{table} of VCVS type. The \mathbf{Y} matrix is decreased by $\Delta n = 1$, because there is not resistance connected in parallel with the source E_{table} . The modified PSpice model of the VCO-Sin has the form:

```
.subckt vco_sin in out Params: Fcenter=1k Frange=50
+ Vmin=0 Vmax=5 phase=0
Rin in 0 1G
Rtable table 0 1
Gtable table 0 Value{Table (V(in),Vmin,-1,Vmax,1)}
Esin out 0 Value{sin(6.28318*(Fcenter*time+Frange*
+ SDT(V(table))))+phase*(3.14159/180))}
.ends
```

The original model matrix for one VCO-Sin unit is of order $n = 5$, while the order of the modified one is $n_m = 4$ (source E_{table} is removed).

E. Effectiveness Increasing of Behavioral PSpice Models of Square Voltage Controlled Oscillators

The output voltage of the voltage controlled oscillator VCO-Sqr is a square wave, which frequency is controlled by a table voltage. The PSpice model has the form:

```
.subckt vco_sqr in out Params: Fcenter=1k Frange=50
+ Vmin=1 Vmax=5 phase=0
Rin in 0 1G
Rtable table 0 1G
Etable table 0 Value{Table (V(in),Vmin,-1,Vmax,1)}
```

```

Esin sine 0 Value{sin(6.28318*(Fcenter*time+Frange*
+SDT(V(table)))+phase*(3.14159/180))}
Esqr out 0 table{V(sine)} (0,0) (1n,1)
.ends
    
```

The dependent voltage source E_{table} and E_{sin} are converted to the dependent source G_{table} and G_{sin} of VCCS type. The Y matrix order is decreased by $\Delta n = 2$. The modified *PSpice* model of the VCO-Sin has the form:

```

.subckt vco_sqr in out Params: Fcenter=1k Frange=50
+ Vmin=1 Vmax=5 phase=0
Rin in 0 1G
Rtable table 0 1
Gtable 0 table Value{Table (V(in),Vmin,-1,Vmax,1)}
Gsin 0 sine Value{sin(6.28318*(Fcenter*time+Frange*
+SDT(V(table)))+phase*(3.14159/180))}
Rsin 0 sine 1
Esqr out 0 table{V(sine)} (0,0) (1n,1)
.ends
    
```

The original model matrix (for one VCO-Sqr unit) is of order $n_{st} = 7$, while the order of the modified one is $n_m = 5$ (sources E_{table} and E_{sin} are removed).

III. SIMULATION RESULTS

The investigation of effectiveness is realized using the standard and modified *PSpice* OpAmp models. These models are included in test circuits. The simulation results using different OpAmp macromodels [7,8,9] are shown in Table III, where t_{st} is the simulation time using the standard model, t_m is the simulation time using the modified model, $\varepsilon_n, \%$ is the relative reduction of the matrix order using the modified macromodel. $\varepsilon_t, \%$ is the relative reduction of the simulation time using the modified macromodel.

The effectiveness of *PSpice* variable admittance model is investigated by comparison of the standard and modified models with respect to the simulation time and matrix order.

The simulation results are presented in Table IV. The simulation results for the standard and modified model of VCO-Sin and VCO-Sqr are shown in Table V.

TABLE III
SIMULATION RESULTS FOR THE ORIGINAL AND
MODIFIED OPAMP MODEL

OpAmp model	n_{st}	n_m	$\varepsilon_n, \%$	t_{st}, s	t_m, s	$\varepsilon_t, \%$
HA2500	82	67	18.3	23.75	21.67	8.8
HA2539	97	79	18.6	23.17	19.97	13.8
HA2541	211	160	24.2	39.75	36.52	8.1
HA5221	124	85	31.4	32.16	28.03	12.8

TABLE IV

SIMULATION RESULTS FOR THE ORIGINAL AND
MODIFIED MODEL OF VARIABLE ADMITTANCE

n_{st}	n_m	$\varepsilon_n, \%$	t_{st}, s	t_m, s	$\varepsilon_t, \%$
9	7	22.2	159.08	162.4	159

TABLE V

SIMULATION RESULTS FOR THE ORIGINAL AND
MODIFIED MODEL OF VCO

Type of model	n_{st}	n_m	$\varepsilon_n, \%$	t_{st}, s	t_m, s	$\varepsilon_t, \%$
VCO-Sin	11	97	18.2	1.81	1.77	2.2
VCO-Sqr	35	25	28.6	36.72	35.75	2.6

The OpAmp model HA-2500 is characterized by a reduction of the simulation time of about 8 %, the model HA-2539 - by 14 %, the model HA-2541 - by 8 % and the model HA-5221 - by 13 %.

IV. CONCLUSION

An approach has been proposed to effectiveness increasing of *PSpice* macromodels based on modified macromodels. They are characterized by a reduced order of the circuit matrix using modified nodal analysis approach. A number of modified macromodels are developed for operational amplifiers, variable admittance, as well as voltage controlled oscillators. The model description is presented in accordance with the input language of the *PSpice* simulator.

REFERENCES

- [1] J. Vlach, K. Singhal, "Computer Methods for Circuit Analysis and Design", Van Nostrand Reinhold, N.Y., 1994.
- [2] L. Raykovska, E. Gadjeva, "Automation of the Design in Electronics and Telecommunications" Part I, Sofia, Meridian 22, 2005.
- [3] S. Yordanova, E. Gadjeva, "Systems modeling and simulation", Sofia, Technical University of Sofia, 2003.
- [4] E. Gadjeva, T. Kouyoumdjiev, S. Farchy, "Computer Modeling and Simulation of Electronic and Electrical circuits using OrCAD PSpice", Sofia, 2001.
- [5] S. Farchy, S. Papisov, "Theoretical Electrical Engineering"-Part I, Sofia, Tehnika, 1998.
- [6] OrCAD PSpice and Basics. Circuit Analysis Software., OrCAD Inc., USA, 1998.
- [7] Huckabee, B., J. Cotreau, "HA-2539 Spice Operational Amplifier Macromodel", Intersil, December 2001.
- [8] Youngblood, D., "HA-2541 Spice Operational Amplifier Macromodel", Intersil, December 2001.
- [9] Riemer, D., "HA5221 Spice Operational Amplifier Macromodel", Intersil, December 2001.

POSTER SESSION – PO I

Signal Processing

Image Filtering and Scaling Algorithms

Slavy G. Mihov¹ and Georgy S. Zapryanov²

Abstract – Image filtering and resizing are essential for the purpose of correct image visualization. In this paper, parallel between different algorithms is made, and as basis for this comparison are used three methods: Mean Square Error (MSE), Peak Signal to Noise Ratio (PSNR) and Subjective Evaluation (SE). Here are given the results from the execution of the above algorithms.

Keywords – filtering, scaling, resizing, MSE, PSNR.

I. INTRODUCTION

Image resizing or scaling (magnification or reduction) is one of the main operations in image processing. It is done whenever resolution change has to be done. For example, for viewing images and video are used devices with fixed resolution, such as plasma panels and LCD displays. Digital resizing is also applied for scaling of video data of devices based on Digital Micromirror DeviceTM (DMDTM) technology, developed by Texas Instruments. DMD is in the core of Digital Light Processing (DLP) which is used in a large scale in the contemporary fully digital viewing systems. In the present moment such systems are produced in various forms: video projector, high definition displays, home theatre, standard TV etc. More and more popular become High Definition TV (HDTV) that also has fixed resolution, higher than that of DVD and films broadcasted at the TV channels. Also, when printing photographs taken by digital cameras, an adapting of the input resolution to that of the printer should be done. The quality of the image of the devices mentioned above tends to depend more and more on the resizing techniques used.

Image filtering is another main operation in image processing. It is used whenever is a necessity for removing artifacts from the image or adjusting some details in it. Image processing and especially image scaling comes at no cost. By using an algorithm for such a purpose, usually this introduces various artifacts in the image, some of which desirable and some – not. When in need of eliminating completely or lowering as much as possible these negative effects, the image is been processed by some filtering algorithms. Various types of them are widely used in practice. This paper concentrates primarily on the family of convolution filters.

The aim of the current paper is to create a methodology for comparison of some of the most common algorithms for

image filtering and interpolation. The interpolation methods are compared via executing those algorithms upon three types of images: synthetic (vector) and two types of real photographs. For noting the changes introduced in the processed image by each of the algorithms, we use two error metrics: the MSE and the PSNR in the RGB color space.

II. EVALUATION METHODS

A. General Issues

In the present paper is made a comparison between the following scaling algorithms: Box Algorithm (Nearest Neighbor - NN) [3, 5]; Simple (Pixel) Interpolation (SI), Bilinear Interpolation (BI) [3, 5]; Bicubic-Spline Interpolation (BSI) ($a = 0, -1/2, -1$) [1, 3]; Directional Interpolation (DI) [5]; Data Dependant Triangulation (DDT) [2]; “Marbella” [4] and Functional Interpolation (FI) [5] – sin and exp.

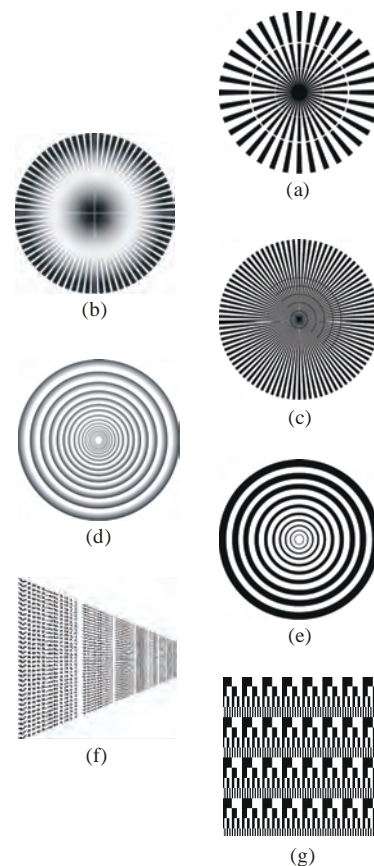


Fig. 1. Synthetic vector images (“miras”)

For the purpose of comparing the scaling algorithms were created 7 synthetic vector images (miras) (Fig. 1). These

¹Slavy G. Mihov is with the Technical University - Sofia, Bul. “Kl. Ohridsky” No. 8, 1100 Sofia, Bulgaria, E-mail: smihov@abv.bg

²Georgy S. Zapryanov is with the Technical University - Sofia, Bul. “Kl. Ohridsky” No. 8, 1100 Sofia, Bulgaria, E-mail: gszap@tu-sofia.bg

vector images are with four different resolutions: 256x256, 512x512, 800x800 and 1024x1024 pixels. For their creation is used the principle described in [3].

Images (a), (c), (e) and (g) are used for estimating the quality when transforming sharp edges; Images (a), (b) and (c) – for estimating the systematic sub pixel shift in different parts of the image; Images (b) and (d) – for estimating the transformation of low contrast details; Image (f) – for estimating the conversion of tiny details; The last image is the label “VirtLab1311”, repeated several times and displayed in perspective.

Except these 7 vector images, 14 photographs are tested too: 7 images from the Kodak test suite with resolution 768x512 pixels and 7 similar high quality photographs.

B. Image Scaling

The corresponding vector images are scaled up and down to suitable resolutions. The quality of the applied algorithm is estimated by comparing the result images with the original ones or with images got by third party algorithms (in the current case, for these purposes is used Photoshop 7.0 Bicubic algorithm – PB). Estimating the quality of the scaling process of the photographs is accomplished by following a strict succession of actions. These three steps are: scaling the image up or down using some of the tested algorithms, recovering the original resolution using the same methods and measuring MSE and PSNR between the original and the final image. There is no limitation for the value of the scaling coefficient, such as being integer. It can be even a floating point number. Furthermore, scaling down can be done with one algorithm, and scaling up – with another (for estimating the quality of combinations of algorithms).

When processing the selected image, for obtaining the final resolution is formed a so called “Frame”, comprising of four images: the original one, the intermediate one – obtained at the first step of the processing (reduction or magnification); the final one – obtained at the second step of the processing (for one-step image processing the intermediate and the final images are identical) and another one – represents the visual (RGB) difference between the original and the final images. In the software is realized the possibility for creating more than one frames, when processing an image (vector or raster), in order to study the variation of the algorithm’s quality, for different scaling coefficients.

C. Parallel Processing

The modern tendency in computer technique development is increasing the computing power by usage of more than one Central Processing Units (CPU) working cooperatively. Multiprocessor systems become more and more popular. Dual core processors and the preceding Hyper Threading Technology follow the same tendency, performing several physical or logical processors in one chip. The main principle of work is dispersing the computing load between the processors and thus each one processes a part of the common job, increasing the total performance.

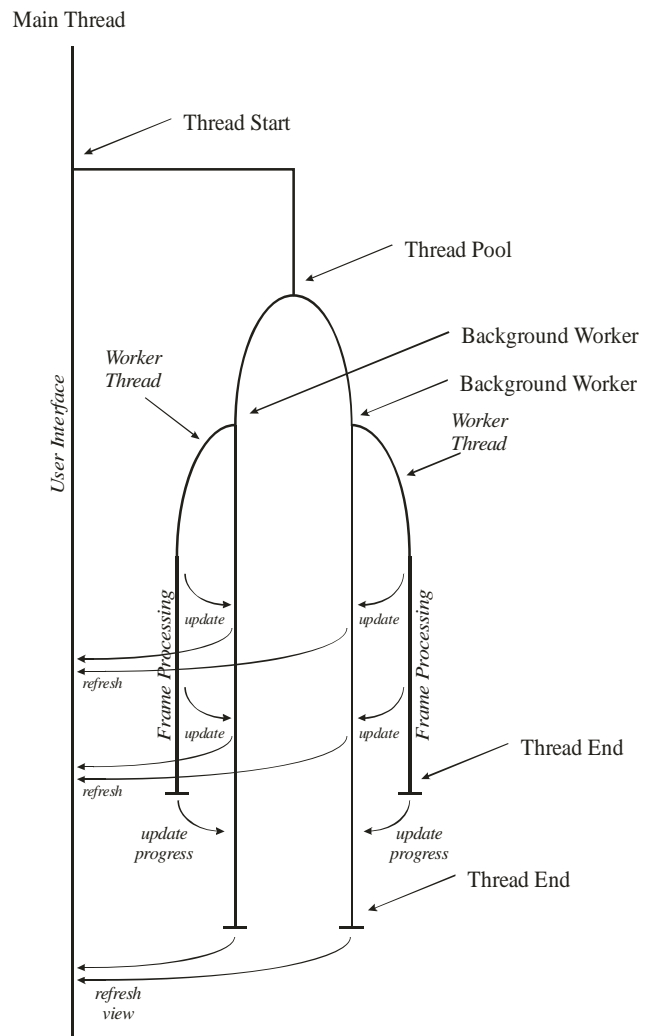


Fig. 2. Parallelism in image processing

For a program or just a mere computation procedure, to use the benefit of a multiprocessor system, is required to have a suitable structure. It should possess some sort of parallelism. Its algorithm should be organized in several autonomous linear sections. At runtime, these sections are meant for processing by different CPUs simultaneously and by this mean the whole computation load is dispersed among the available processing units. A proper dispersion of the computation load aims to balance the usage of all the CPUs equally and thus gives them equal portions of the entire task to complete.

In the case of image processing, image scaling and filtering tend to be the heaviest and most time consuming operations to be taken. The program flow is organized in such a way that effectively uses the capabilities of a computer system with two processors (this case includes systems with a single dual-core processor or a processor using Hyper Threading Technology). The independent work of both of the CPUs is organized in several threads running simultaneously. Fig. 2 illustrates the sequential flow of all the threads involved, the moments of their creation and synchronization.

As seen from Fig. 2, here are used three techniques for splitting the sequential program flow and creating new threads. The first one (Thread Start) is the simplest of all and

is known being thread-unsafe. It is used just to create a new thread and call it for execution. The newly started thread performs all the computation in image processing, while the main thread (the one it was created by) serves the user interface.

As mentioned above, the computation procedure is designed for processing by two CPUs (either physical or logical). The second technique for manipulating multiple threads (Thread Pool) implements this idea. The flow of the current thread is split into two identical threads, which differ only by their IDs (identification numbers). The operating system is responsible for the assignment of each of them being executed by one of the two processors. This is the stage where the computation load is dispersed and balanced among the CPUs. This technique tends to be thread-safe; in general case can involve more than two threads and thus is widely used in practice.

The next thing that follows is one and the same for all the working processors (the threads they execute are identical). The third technique used for manipulating threads is called Background Worker. It forms the current thread into two parallel ones. The first of them is the so called Worker Thread, that performs the heavy computation of image processing and the second one is its master thread responsible its control. Background Worker embeds numerous features for synchronization and communication between the threads it comprises. It is thread-safe and is extremely suitable for performing heavy computations in background regime.

Fig. 2 also shows the most important communications between the threads, by which they synchronize their work and exchange results. The parallel threads exist only until they complete their part of the common job, after which they terminate. Only the main thread remains and continues program's sequential flow.

D. Image Filtering

In the present project are used the following filtering algorithms: Mean Filter, Median Filter, Gaussian Smoothing, Conservative Smoothing, Laplacian Filter, Variance Filter, Laplacian of Gaussian (LoG Filter), Sharpening Filter and Custom (user-defined convolution) Filter. They are used to eliminate or partially decrease the presence of noise and various artifacts in images. Their usage can be combined with that of some scaling algorithms, as means to recover an image from the introduced artifacts by the preceding manipulation (usually a preceding resizing that had distorted the image in some way). Most of the filters mentioned above belong to the family of convolution filters. The mere filtering is done by convolving (performing the operation convolution) the image with a so called kernel. The kernel is a square two-dimensional integer matrix with resolution of 3x3, 5x5, 7x7 or 9x9. The size of the kernel should be an odd number. For practical purposes kernels larger than 9x9 aren't used. Even kernels with dimensions 9x9 are not very common.

The image and the kernel used in convolution are shown schematically on Fig. 3. The kernel shown is a non-square matrix with dimensions 2x3, which does not conflict with math theory in general. The image is represented as a

grayscale image by an integer matrix 6x9. The values I_{ij} of the matrix (values form 0 to 255) resemble the intensities of the individual pixels the image consists of. In case of a color image, (a 24-bit RGB image, for example) it is represented by several matrixes of the same kind, one for each channel.

I_{11}	I_{12}	I_{13}	I_{14}	I_{15}	I_{16}	I_{17}	I_{18}	I_{19}
I_{21}	I_{22}	I_{23}	I_{24}	I_{25}	I_{26}	I_{27}	I_{28}	I_{29}
I_{31}	I_{32}	I_{33}	I_{34}	I_{35}	I_{36}	I_{37}	I_{38}	I_{39}
I_{41}	I_{42}	I_{43}	I_{44}	I_{45}	I_{46}	I_{47}	I_{48}	I_{49}
I_{51}	I_{52}	I_{53}	I_{54}	I_{55}	I_{56}	I_{57}	I_{58}	I_{59}
I_{61}	I_{62}	I_{63}	I_{64}	I_{65}	I_{66}	I_{67}	I_{68}	I_{69}

K_{11}	K_{12}	K_{13}
K_{21}	K_{22}	K_{23}

Fig. 3. Image and kernel used in convolution

The values K_{ij} of the second matrix are the coefficients of the kernel. Eq. 1 shows the mere mathematical expression of operation convolution between the image and the kernel.

$$O(i, j) = \sum_{k=1}^m \sum_{l=1}^n I(i+k-1, j+l-1)K(k, l) \quad (1)$$

Here: $I(i, j)$ stands for the intensity of pixel (I_{ij}) with coordinates (i, j) from the image; $K(i, j)$ stands for the coefficient of the kernel K_{ij} ; $O(i, j)$ stands for the final value of pixel (i, j) , after completing the convolution.

E. Formal Metrics

For objective estimate of an algorithm's quality is used the main approach in digital image processing, based on computing the Mean Square Error (MSE) and Peak Signal to Noise Ratio (PSNR). MSE (Eq. 2) represents the average square error (difference) in the intensities [$I(i; j)$ and $I'(i; j)$] of a given color (channel) of the corresponding pixels from both of the images and it is dimensionless quantity. Because of its simplicity, it is the most common method for objective measurement of image quality, based on a reference image.

$$MSE = \frac{1}{m.n} \sum_{i=1, j=1}^{m,n} (I(i; j) - I'(i; j))^2 \quad (2)$$

PSNR (Eq. 3) represents the square of the ratio between the maximum of the signal (the maximal possible value of color's intensity (I_{max})) and the mean square error (difference) in the intensities [$I(i; j)$ and $I'(i; j)$] of a given color (channel) of the corresponding pixels from both of the images and is measured in decibels (dB).

$$PSNR = 10 \lg \frac{I_{max}^2 \cdot m.n}{\sum_{i=1, j=1}^{m,n} (I(i; j) - I'(i; j))^2} \quad [dB] \quad (3)$$

The estimate can be done by computing MSE and PSNR for every single color (Red, Green, Blue), as well as totally for the three of them.

III. RESULTS

For estimating the quality of each scaling algorithm, several experiments with different test images are competed. It is compared the results from execution of different algorithms upon one and the same image, as well as execution of one and the same algorithm upon different images. Combinations of algorithms executed upon one and the same image are tested too. The results got are compared in between and with pre-created images. Some of the images were resized, using Photoshop 7.0 Bicubic algorithm, and then compared with those got from the execution of this program.

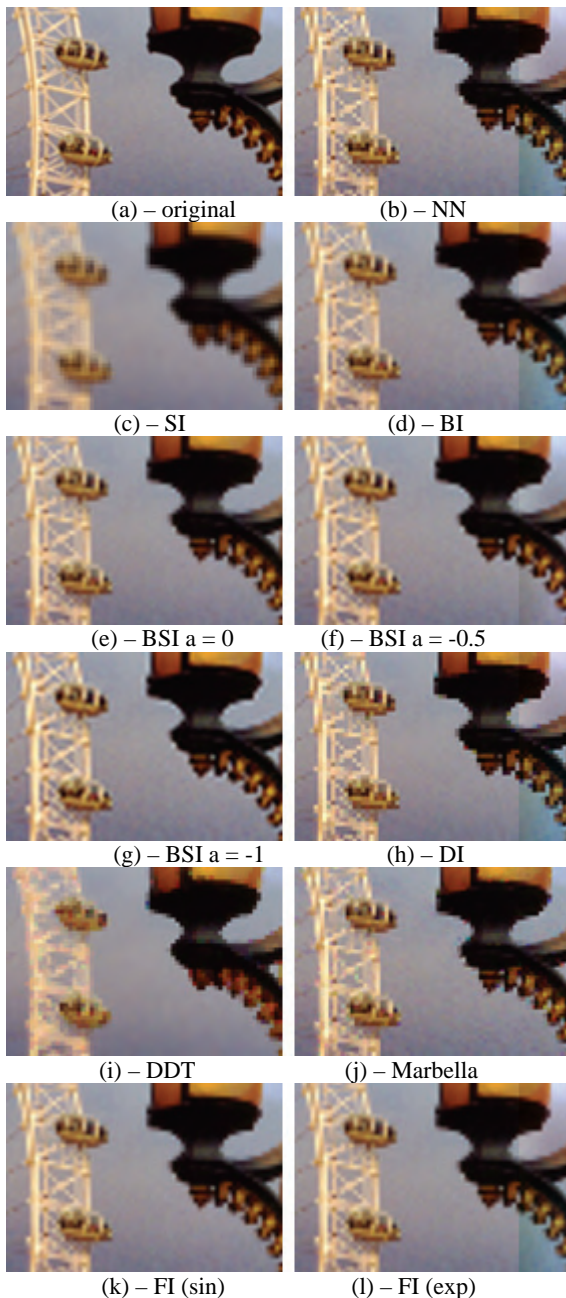


Fig. 4. ROI – algorithms' effects

The main artifacts in the images, that can be noted and determined as results of the scaling process, are:

1. Ringing – appearance of a single wave near a sharp edge in the image.
2. Overshooting – appearance of several such waves.
3. Sub-pixel shift – translation of the image to some direction. It is relevant to special features of the algorithm's realization. Sometimes it has no influence over the visual quality of the image, but has significant influence over the formal metrics.
4. Aliasing – so called “step effect” – irregularity of the sharp diagonal edges of the image. It emerges in the vector, as well as in the photographic images. It is most noticeable in Nearest Neighbor, DI, DDT and somewhat in Marbella.
5. Blurring – insignificant sharpness of the image after scaling. In fact it appears for all the interpolation algorithms, but is most distinctive for Simple Interpolation (SI). Boosting the sharpness increases the rest of the artifacts and vice versa – reducing the artifacts loses image's sharpness.

Some of these artifacts, regarded as negative effects, can be significantly reduced by applying some of the filtering procedures to that image. Various high-pass and low-pass filters (and combinations of them) are used to sharpen or smoothen different details in the image. This affects image quality and its total perception can be improved.

IV. CONCLUSION

The method for estimating the scaling algorithms offered in the paper is a convenient tool that allows implementing simple and efficient experiments with similar methods to be performed in order to improve their characteristics. This method is applicable for testing filtering algorithms too and even combinations of both types. The results achieved in this research, outline the directions for further tests and algorithm development.

For some methods, such as SI, DI and DDT it is not quite reasonable, attempts for improvements to be done, while for others (BSI-s, BI and FI) is recommended to be done efforts for improving the sharpness and the precision of the interpolation. Marbella also has potential for improving the quality. NN is suitable for image preview and for some specific applications.

REFERENCES

- [1] D. Lancaster, “Using Cubic Spline Basis Functions for Image Pixel Interpolation”, www.tinaja.com/glib/basis.pdf.
- [2] D. Su, P. Willis, “Image Interpolation by Pixel Level Data-Dependant Triangulation”, *Computer Graphics Forum*, No. 1, 2004.
- [3] D. Vatolin, S. Putilin, “Image scaling methods evaluation and comparative results between different methods”, *Proceedings of Graphicon-2003*, pp 202-207, Moscow, September 2003 (in Russian).
- [4] S. Battiato, “A new edge-adaptive zooming algorithm for digital images”, *Proceedings of Signal Processing and Communications SPC*, pp 144-149, Marbella, Spain, 2000.
- [5] <http://efg2.com/Lab/Library/ImageProcessing/Algorithms.htm>

System for Spectral Investigation of Signals

Stanyo V. Kolev, Irena V. Ivanova and Yuliyana S. Velchev

Abstract – The idea for realization of the concrete laboratory exercise is to help the students with investigation of the spectrum of basic types of signals. This is according to discipline “Signal and systems”. The goal is to build hardware and software for DSP and personal computer.

Keywords – Signal and systems, Spectral analysis, Digital signal processing.

I. INTRODUCTION

A software for spectral analysis for basic types of signals is build as well as hardware part for signal acquisition. The concept for this project is shown in figure 1.

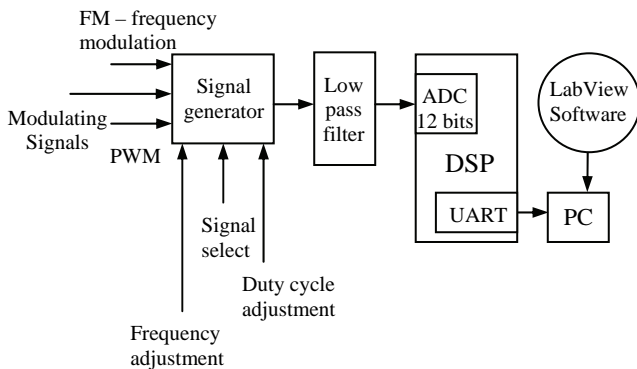


Fig. 1

The purpose of the signal generator is to provide the signal generator for further analysis. Some of the signal parameters can be adjusted or can be driven from additional generators in terms to achieve Frequency Modulation (FM) or Pulse Width modulation (PWM). The active Low-pass filter is implemented in order to make bandwidth limitation, before digitalization in 12-bit Analog to Digital Converter (ADC), which is built –in Digital Signal Processing (DSP). The Universal Asynchronous Receiver Transmitter (UART) realizes the communication with the PC.

II. FORMULATION OF THE PROBLEM

The purpose of the laboratory model is to make the student to become familiar with the spectral characteristics of basic

types of signals, discussed in the “Signals and Systems” discipline.

III. HARDWARE PART DISCRPTION

MAX038 is high frequency, precision, functional generator which can generate exact, sawtooth, triangle, sinusoidal and square signals. This can be done by minimal set of external components. The type of the signal can be chosen by setting of appropriate logic levels of the inputs A0 and A1 (figure 2) Duty cycle can be changed from 15% to 85% .

Sinusoidal, square or triangle signals can be set with appropriate code of two TTL pins. The low impedance output of the generator is possible to be loaded up to $\pm 20mA$ current. This chip is applicable for Precision Functional Generators (PFG); Voltage Controlled Oscillators (VCO); Frequency Modulators (FM); Pulse Modulators (PM) and Frequency Synthesizer.

Schematic diagram is shown in figure 2.

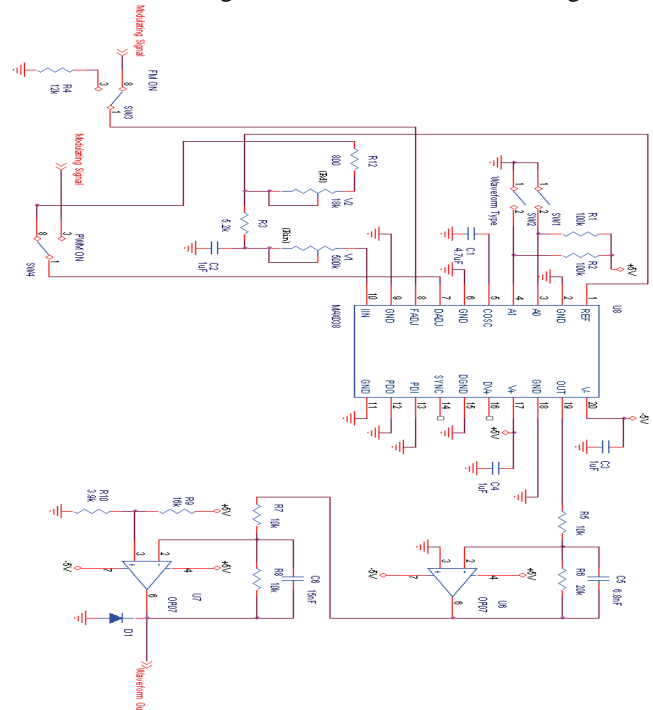


Fig.2

IV. DESCRIPTION OF THE WORK OF THE DIGITAL PART OF THE SCHEME

Figure 3 shows the schematic diagram for the part responsible for sending the digital signal into PC.

¹Stanyo V. Kolev is with the Faculty of Communication, TU – Sofia, Kl. Ohridsky str 8, Sofia, Bulgaria, E-mail: skolev77@mail.bg

²Irena V. Ivanova is with the Faculty of Communication, TU – Sofia, Kl. Ohridsky str 8, Sofia, Bulgaria, E-mail: irena_vl_iv@mail.bg

³Yuliyana S. Velchev is with the Faculty of Communication, TU – Sofia, Kl. Ohridsky str 8, Sofia, Bulgaria, E-mail: julian_velchev@abv.bg

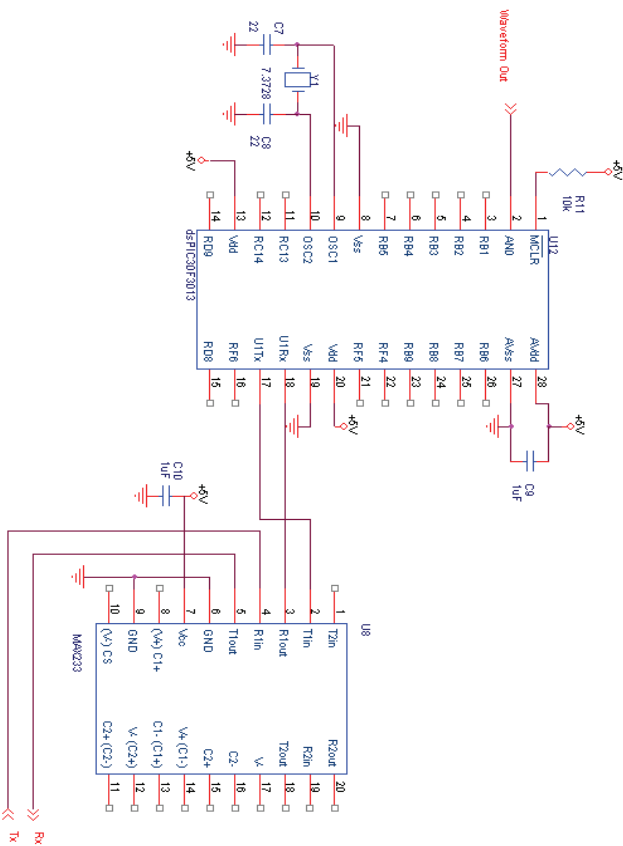


Fig.3.

This part consist DSP and level shifter for RS-232 standard. This DSP as well as ALU, RAM memory, Program memory has a lot of peripherals. In this case the built-in ADC is implemented. It can achieve 12-bit resolution. The type is SAR (succetive approximation register). This type of ADC is relatively fast but the limitation is the resolution (up to 13 and 14 bits). Only one analogue input is used (AN0) .

The DSP system clock is 7372800Hz. It is multiplied by 8 according to used PLL. The real system clock is $F_{OSC} * PLL/4$. The sampling frequency is chosen to be 8kHz so the overload number in the Timer3 is given by $(FCY/SAMPLING_RATE) + 1$. Timer3 is responsible for exact discretization .

The other used peripheral module is UART which is used to communicate with the PC. The concrete DSP makes signal processing in terms of decimation by factor 4. This is necessary to reduce the sampling rate as well as to use a relatively simple analogue filter with low order.

The decimation is always along with digital filtration. In this case the digital filter is FIR (Finite Impulse Response) type. This is because FIR has linear phase response and because it is always stable. Higher order of the filter makes long setting time. In our case the number of tabs is 128. The filter is build using Qedesign software.

The window functions is rectangular and the cut-off frequency is 995Hz. According to its Magnitude response is achieved attenuation of 75dB in stop band. The signal processing is in 1.15 format (fixed point).

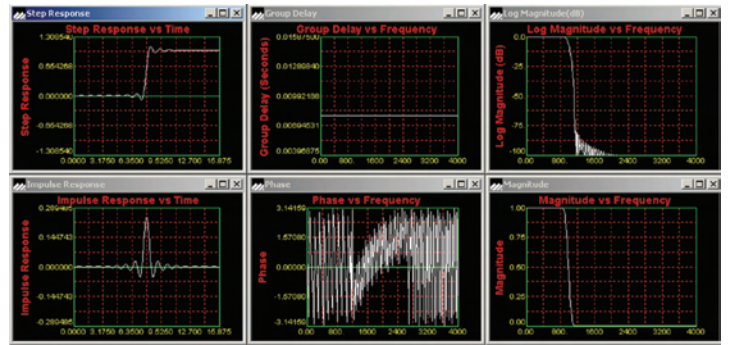


Fig.4.

V. EXPERIMENTAL RESULTS



Fig.5.

Figure 5 shows the amplitude and phase spectrum of rectangular pulses. This spectrum is calculated previously and the results are exactly matching.

CONCLUSIONS

A working laboratory model Spectral analysis was described in this paper. The future work will be concentrated in terms to achieve real time spectral analysis of signals with higher bandwidth and to improve throughput of the communication interface using USB instead RS 232 standard.

REFERENCES

- [1] Nenov , G. "Signals and Systems" , Sofia ,1999
- [2] Penev , R. "Handbook for Laboratory and Auditory Exercises for Signals and Systems " , Sofia, 2002
- [3] Koichev, K."Theory of Signals", Gabrovo, 1998
- [4] Openheim, A. "Signals and Systems"
- [5] dsPIC30F3013 Data Sheet, Microchip Technology Inc.,
- [6] MAX220/MAX222/MAX23A/MAX233A/MAX242/ MAX243: +5V -Powerd, Multichannel RS-232 Transceivers, Maxim Integrated Products, 2004 , www.maxim-ic.com/packages
- [7] Max038 High-Frequency Waveform Generator, Maxim Integrated Products, 2004

Design and Implementation of First Order Sigma-Delta Modulator

Snejana D. Terzieva¹, Georgi T. Tsenov², Peter I. Yakimov³ and Valeri M. Mladenov⁴

Abstract – The sigma-delta ADC offers several advantages over the other architectures, especially for high resolution, low frequency applications. First and foremost, the single bit sigma-delta ADC is inherently monotonic and requires no laser trimming. The sigma-delta ADC also lends itself to low cost foundry CMOS processes because of the digitally intensive nature of the architecture. As a result of this, they are widely used in different applications. In this paper an experimental electronic realisation of a first order sigma-delta modulator is presented. The implementation of 1-bit DAC circuit is proposed.

Keywords – A-D and D-A converters, sigma-delta modulator, circuit design, circuit analysis.

I. INTRODUCTION

Sigma-Delta Analog-Digital Converters (Σ - Δ ADCs) have been known for over thirty years, but only recently has the technology (high-density digital VLSI) existed to manufacture them as inexpensive monolithic integrated circuits. They are now used in many applications where a low-cost, low-bandwidth, low-power, high-resolution ADC is required. The name, sigma-delta, is a consequence of the integral, or summation over time (Σ), applied to the difference (Δ). Because sigma-delta converters latch on a high speed clock pulse, they do not require sample-and-hold circuits. Since the bit stream is a train of “ones” and “zeroes”, there are no missing codes. This type ADC contains very simple analog electronics (a comparator, voltage reference, a switch, and one or more integrators and analog summing circuits), and quite complex digital computational circuitry. The high proportion of digital circuitry makes the Σ - Δ ADCs excellent candidates for high yield manufacture in IC form. This circuitry acts as a filter (generally, but not invariably, a low pass filter). It is not necessary to know precisely how the filter works to appreciate what it does. To understand how a Σ - Δ ADC works, familiarity with the concepts of *over-sampling*, *quantization*

noise shaping, *digital filtering*, and *decimation* is required. The technique of over-sampling is explained with an analysis in the frequency domain. Where a *dc* conversion has a *quantization error* of up to $\frac{1}{2}$ LSB, a sampled data system has *quantization noise*.

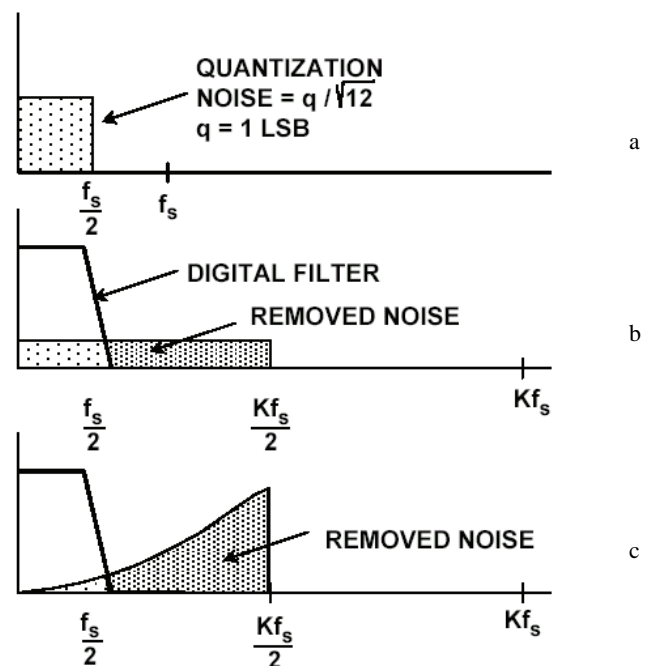


Fig. 1. Noise shaping

A perfect classical n -bit sampling ADC has a *rms* quantization noise of $q/\sqrt{12}$ uniformly distributed within the Nyquist band of *dc* to $f_s/2$ (where q is the value of an LSB and f_s is the sampling rate) as shown in Fig.1a. If the ADC is less than perfect, and its noise is greater than its theoretical minimum quantization noise, then its *effective* resolution (often known as its Effective Number of Bits or ENOB) will be less than n -bits. When a much higher sampling rate has been chosen, Kf_s (see Fig.1b), the *rms* quantization noise remains $q/\sqrt{12}$, but the noise is now distributed over a wider bandwidth *dc* to $Kf_s/2$. If then a digital low pass filter (LPF) is applied to the output, much of the quantization noise will be removed, but without affecting the wanted signal—so the ENOB is improved. Thus a high resolution A/D conversion has been accomplished with a low resolution ADC. The factor K is generally referred to as the *oversampling ratio*. It should be noted at this point that oversampling has an added benefit in that it relaxes the requirements on the analog antialiasing

¹Snejana D. Terzieva is with the Faculty of Automatics, Dept. of Theoretical Electrical Engineering, Technical University - Sofia, 1000 Sofia, Bulgaria, E-mail: ster19@tu-sofia.bg

²Georgi T. Tsenov is with the Faculty of Automatics, Dept. of Theoretical Electrical Engineering, Technical University - Sofia, 1000 Sofia, Bulgaria, E-mail: gogotzenov@tu-sofia.bg

³Peter I. Yakimov is with the Faculty of Electronic Engineering and Technologies, Dept. of Electronics, Technical University - Sofia, 1000 Sofia, Bulgaria, E-mail: pij@tu-sofia.bg

⁴Valeri M. Mladenov is with the Faculty of Automatics, Dept. of Theoretical Electrical Engineering, Technical University - Sofia, 1000 Sofia, Bulgaria, E-mail: valerim@tu-sofia.bg

filter. The Σ - Δ converter does not need such a high oversampling ratio because it not only limits the signal passband, but also shapes the quantization noise so that most of it falls outside this passband as shown in Fig.1c.

II. BASICS OF SIGMA-DELTA A/D CONVERTERS

The first-order Σ - Δ modulator as shown in Fig.2 is 1-bit ADC (generally known as a latched comparator), driven with the output of an integrator which is fed with an input signal summed with the output of a 1-bit DAC (two-level switched reference) controlled by the ADC output. To complete the ADC a digital low pass filter (LPF) and decimator at the digital output must be added. Σ - Δ modulator shapes the quantization noise so that it lies above the passband of the digital output filter, and the ENOB is therefore much larger than would otherwise be expected from the over-sampling ratio.

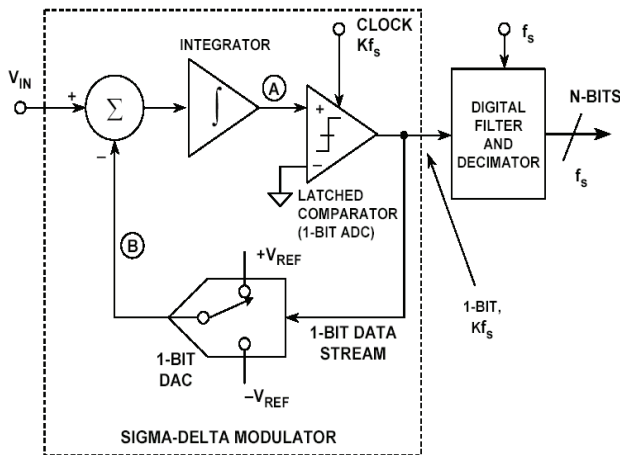


Fig. 2. Basic circuit of Σ - Δ modulator

Intuitively, a Σ - Δ ADC operates as follows. Assume a dc input at V_{IN} . The integrator is constantly ramping up or down at node A. The output of the comparator is fed back through a 1-bit DAC to the summing input at node B. The negative feedback loop from the comparator output through the 1-bit DAC back to the summing point will force the average dc voltage at node B to be equal to V_{IN} . This implies that the average DAC output voltage must equal the input voltage V_{IN} . The average DAC output voltage is controlled by the *ones-density* in the 1-bit data stream from the comparator output. As the input signal increases towards $+V_{REF}$, the number of "ones" in the serial bit stream increases, and the number of "zeros" decreases. Similarly, as the signal goes negative towards $-V_{REF}$, the number of "ones" in the serial bit stream decreases, and the number of "zeros" increases. From a very simplistic standpoint, this analysis shows that the average value of the input voltage is contained in the serial bit stream out of the comparator. The digital filter and decimator process the serial bit stream and produce the final output data.

For any given input value in a single sampling interval, the data from the 1-bit ADC is virtually meaningless. Only when

a large number of samples are averaged, the result will be with a meaningful value.

The sigma-delta ADC can also be viewed as a synchronous voltage-to-frequency converter followed by a counter (Fig. 3). If the number of "ones" in the output data stream is counted over a sufficient number of samples, the counter output will represent the digital value of the input. Obviously, this method of averaging will only work for dc or very slowly changing input signals. In addition, 2^n clock cycles must be counted in order to achieve n-bit effective resolution, thereby severely limiting the effective sampling rate.

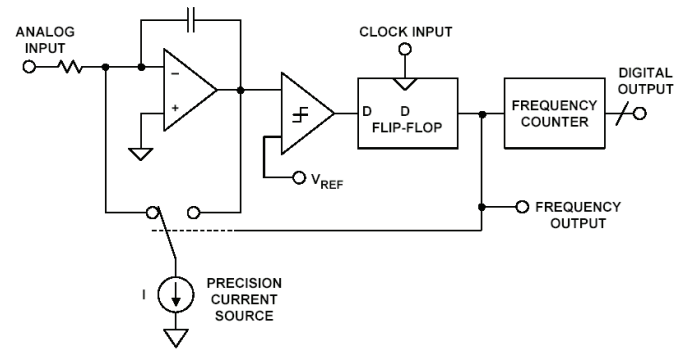


Fig. 3. Basic circuit of synchronous voltage-to-frequency converter

III. SIGMA-DELTA MODULATOR DESIGN

The Σ - Δ modulator is the basis of the contemporary oversampling analog-to-digital and digital-to-analog converters. This type of the circuit is very appropriate for high-resolution medium-to-low speed applications such as high quality digital audio, high-precision measurement devices, communication systems, etc. These devices utilize the only low cost conversion method, which provides both high dynamic range and flexibility in converting low-bandwidth input signal. This fact is the reason for the big interest among the microelectronic circuit designers in the operation and practical implementation of the sigma-delta modulators.

In this paper a proposal for sigma-delta modulator design is given on Fig. 4.

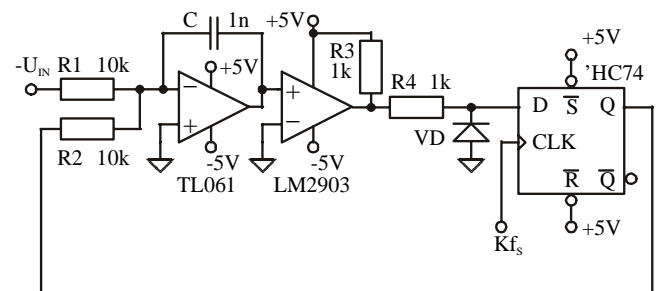


Fig. 4. Σ - Δ modulator design proposal

The circuit comprises of summing integrator, comparator and a D-type flip-flop. The j-FET low power operational amplifier TL061 is connected as a summing integrator, which integrates the difference between the input voltage U_{IN} and the

output product of the 1-bit DAC. The low power low offset voltage comparator with open collector output LM2903 is the next stage of the circuit. In order to be able to perform the wanted operation the D-type positive edge triggered flip-flop must have standard CMOS output (for example 74HC74).

The circuit is similar to the basic circuit of synchronous voltage-to-frequency converter. In contrary to the classical scheme of Σ - Δ modulator, the comparator is not latched. The 1-bit data stream is obtained from the flip-flop output. The statement of the comparator is latched in the Q output after the positive edge of the clock signal Kf_S .

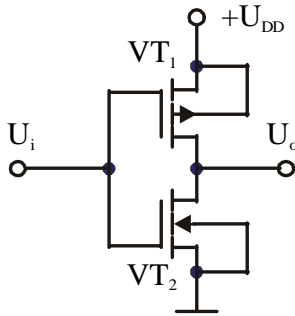


Fig. 5. CMOS output stage

The D-type flip-flop performs the function of the 1-bit DAC. Therefore its output stage must be standard CMOS inverter (Fig. 5). It comprises of two complementary MOSFET transistors (VT_1 -P-channel and VT_2 -N-channel). Because of their symmetry the logic "1" is equal to the value of U_{DD} and the logic "0" is equal to the ground. This ability of the CMOS output allows the D-type flip-flop 74HC74 to function as a two-level switched reference because it combines the functions of the memory cell and the two-level switch. So, when the statement of the comparator is high, voltage value equal to the 74HC74 supply voltage will be subtracted from the input voltage value. When the comparator statement is low the value of the subtracted voltage will be zero. To ensure a negative feedback the value of the input voltage of the Σ - Δ modulator must vary from ground to the negative supply. The additional components are with standard application. The resistor R_3 sets the voltage level in the open collector output of the comparator. The resistor R_4 and the diode VD prevent the negative voltage from the comparator output to break-down the input of the flip-flop.

IV. EXPERIMENTAL RESULTS

The experiments were carried out by PSpice simulation and laboratory set-up with testing and measurement instruments in order to integrate the processes of design, simulation, testing and measurement. The studying of these processes and their interaction gives the designer very useful information. To verify the design and simulation the measured values have been compared with the results obtained by PSpice simulation.

In the following figures the modulator's behaviour is depicted with probe.

The resulting output of the analog integrator in the PSpice realisation of the designed sigma-delta modulator is plotted in Fig. 6.

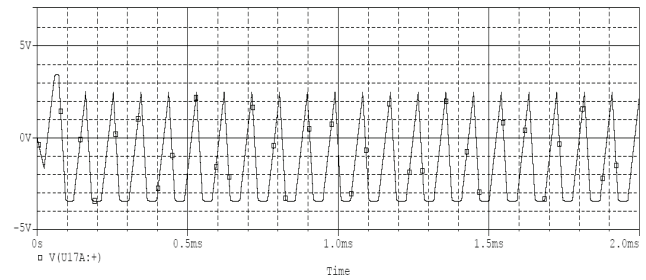


Fig. 6. Summing integrator output voltage

On Fig. 7 the resulting output the Q output of the flip-flop is given.

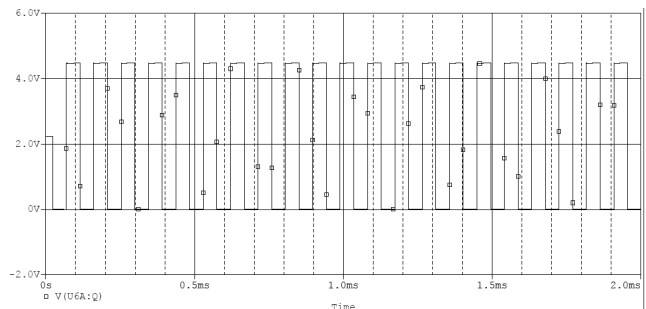


Fig. 7. Q output flip-flop waveforms

The feed from the digital clock impulse generator used for 74HC74 flip-flop is depicted in Fig. 8 while in Fig. 9 the resulting outputs of the 74HC74 (digital presentation of the signal) are shown.

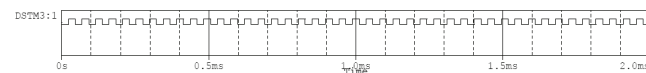


Fig. 8. Digital clock waveforms

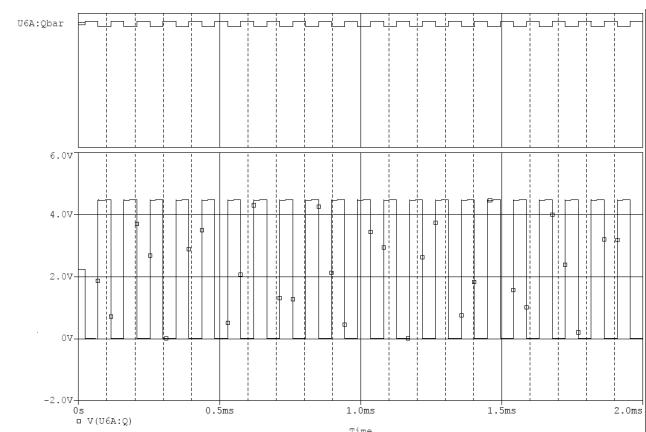


Fig. 9. 74HC74 outputs waveforms

After completing the measurements the obtained results were almost identical with the results obtained from PSpice simulations. The output of the analog integrator viewed on oscilloscope is given in Fig. 10 and the digital output signal observed on oscilloscope can be seen in Fig.11.

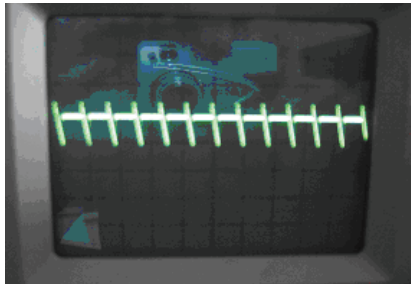


Fig. 10. Real summing integrator output voltage

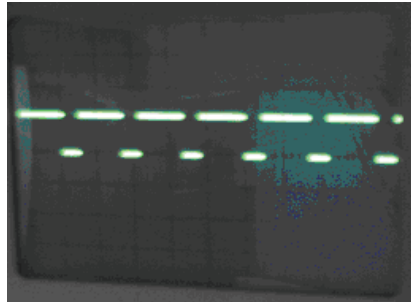


Fig. 11. Real digital output signal

V. CONCLUSION

With the aim of understanding the operation principle, it is especially useful to propose appropriate prototypes of first and higher order sigma-delta modulators. These prototypes should be quickly realisable and should allow easy and simple alteration of the circuit configuration, as well as of the circuit elements' parameters. This would make possible a fast and effective analysis of the designed circuit operation, and a control of the relation between the elements' parameters and the circuit's mode of operation.

The realisation of the designed first order sigma-delta modulator proved the simulation results which approbated it for future incorporation within the laboratory practice of Theoretical Electrical Engineering. Focus for some future experimental work will be the extension of modulator's model to higher order.

REFERENCES

- [1] Chapter 3 of Walt Kester, Editor, Analog - Digital Conversion, Analog Devices, 2004, ISBN: 0-916550-27-3, (Also available at <http://www.analog.com>).
- [2] Mihov G., Digital electronics, Sofia, Technical University, 2005, ISBN: 954-438-449-9 (in Bulgarian).
- [3] www.analog.com.
- [4] Paul Klonowski, Analog-to-Digital Conversion Using Voltage-to-Frequency Converters, Application Note AN-276, Analog Devices, Inc.
- [5] James M. Bryant, Voltage-to-Frequency Converters, Application Note AN-361, Analog Devices, Inc.
- [6] B. Boser and Bruce Wooley, The Design of Sigma-Delta Modulation Analog-to-Digital Converters, IEEE Journal of Solid-State Circuits, Vol. 23, No. 6, December 1988, pp. 1298-1308.
- [7] G. Tsenov, V. Mladenov, Modeling, simulation and implementation of sigma delta modulators, Proc. of the Fourth International Conference on Challenges in Higher Education and Research in the 21 Century, June 1-3, 2006, pp. 102-106, Sozopol, Bulgaria.
- [8] G. Tsenov, S. Terzieva, V. Mladenov, Modeling and implementation of first order sigma-delta modulator, Proceedings of the 15th International Scientific and Applied Science Conference "Electronics ET'2006", September 20-22, 2006, Sozopol, Bulgaria, book 1, pp. 47-52, ISBN: 954-438-564-9.
- [9] M. Tzanov, E. Manolov, F. Koparanov, A. Popov, Sigma-delta modulator prototyping using FPAA, Proceedings of the 15th International Scientific and Applied Science Conference "Electronics ET'2006", September 20-22, 2006, Sozopol, Bulgaria, book 1, pp. 65-70, ISBN: 954-438-564-9.

Recovering Optical Image Transferred Through Atmospheric Turbulence

Kalin L. Dimitrov¹

Abstract – In this paper we study model-based restoration of long exposure space-to-ground images. Such images may show strong degradation due to non-linear atmospheric turbulence effects and therefore, any efficient restoration method must take into account modeling of the turbulence. The paper deals with the restoration of one dimensional image with least squares methods applied to our turbulence model.

Keywords – Atmospheric turbulence, Least-squares methods, Restoration of images

I. INTRODUCTION

The resolution of images is determined by the processes of diffraction. Recently, practical algorithms have emerged that are capable of recovering spatial frequency detail that lies beyond the diffraction limit of an image sensor [1]. In this paper we will briefly review some application of our previous works [2,3]. We will present a least-squares method based algorithm that achieves reconstruction of diffraction-limited one dimensional images [4,5]. Examples of simulations of the algorithm will be given, along with a discussion of how the algorithm can be integrated in software applications.

II. SOLUTION OF THE INVERSE OBSERVING PROBLEM

A. Turbulence model

We will use as base analytical results for average optical intensity from our previous works [2,3]:

$$\langle I(x) \rangle = \langle I_0(x) \rangle \exp(-\gamma^2) + \frac{aL_m}{\sqrt{2f}} \times \sqrt{\frac{\frac{2}{\eta}}{1 + \frac{2}{\eta}(1+r^2)}} [1 - \exp(\gamma^2)] \times$$

$$\times \exp \left[-2 \frac{\frac{2}{\eta}(1+r^2)}{1 + \frac{2}{\eta}(1+r^2)} \frac{x^2}{x_0^2} \right] \quad (1)$$

where

$$\langle I_0(x) \rangle = \frac{aL_m}{\sqrt{2f}} \sqrt{\frac{1}{1+r^2}} \exp \left(-2 \frac{x^2}{x_0^2} \right) \quad (2)$$

and

$$r = \frac{2z}{kab}, \quad x_0 = \sqrt{1+r^2} x_b, \quad x_b = \frac{fb}{z}$$

a - aperture scale, b - investigation object scale, L_m - maximal brightness, f - focal length, z - distance to object.

In most of the cases $r^2 \ll 1$, so we assume

$$\sqrt{1/(1+r^2)} \approx 1 \quad (3)$$

Using (1), (2) and (3) and making some normalization we derive

$$\langle I(x) \rangle_n = \exp \left(-2 \frac{x^2}{x_0^2} \right) \exp(-\gamma^2) +$$

$$+ \sqrt{\frac{\frac{2}{\eta}}{1 + \frac{2}{\eta}}} [1 - \exp(\gamma^2)] \exp \left[-2 \frac{\frac{2}{\eta}}{1 + \frac{2}{\eta}} \frac{x^2}{x_0^2} \right] \quad (4)$$

We accept that we have information about atmospheric turbulence (for example from SODAR, SCIDAR [6] or LIDAR etc.). This mean that functions

$$\gamma = \sqrt{\pi} C_n^2 k^2 \langle l \rangle^{5/3} Z$$

and

$$\eta = \ln \left[\left(\exp(-\gamma^2) - 1 \right) \left(\exp(\gamma^2 / e^2) - 1 \right) \right] \text{ are known.}$$

¹Kalin L. Dimitrov is with the Technical University of Sofia, Faculty of Communication Technics and Technologies, Kl.Ohridski Blvd, 1756 Sofia, Bulgaria, E-mail: kld@tu-sofia.bg

B. Formulation of analysis

The formulation is shown on fig.1.

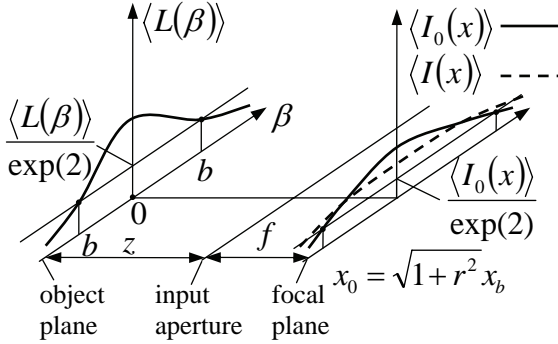


Fig. 1. Formulation of analysis

Our main goal is to find scale x_0 (see (4)). If we know x_0 we have possibility simply to calculate $\langle I_0 \rangle$ from (2) i.e. initial image distribution.

C. Least square solution

The method of least squares provides a means of estimating the values of coefficients in an equation. Typically, the estimates are based upon some sample of data. The idea of least squares is to minimize the total amount of error due to these estimates. Note that the technique of least squares is different from linear regression, though they have similar objectives [5].

We implement least squares method in way

$$\sum_i^n [y_i - \varphi(x_i; a)]^2 = \min \quad (5)$$

where y_i correspond to experimental data of $\langle I(x) \rangle_N$ (derived from n -sized CCD matrix for example); $\varphi(x_i; a)$ correspond to theoretical $\langle I(x) \rangle_N$ (see formula (4)); parameter a equivalent to x_0 .

Because we have only one parameter in minimization we use the first derivative case

$$\sum_i^n [y_i - \varphi(x_i; a)] \frac{\partial \varphi}{\partial a} \Big|_{x=x_i} = 0 \quad (6).$$

Now we derive the first derivative of (4)

$$\frac{\partial \varphi}{\partial a} = 4 \frac{c_1 x^2 \exp\left(-2 \frac{x^2}{a^2}\right)}{a^3} + \frac{4c_2 c_3 x^2 \exp\left(-2 \frac{c_3 x^2}{a^2}\right)}{a^3} \quad (7)$$

where c_1, c_2, c_3 are known constants (see (4)).

We put (7) and (4) in (6) and we derive the final equation to solve. The root of this equation is a (see (5) and (6)) respectively x_0 . We calculate this equation with numerical methods (not discussed here).

D. Numerical example

In our simulations we found that error is less than 1% in 100 points example in lack of noise.

III. ADDITIONAL REMARKS

This is first paper of solution of so called inverse restoration problem using previously developed turbulence model [1,2].

IV. CONCLUSION

In this paper we solve numerically the problem of restoration of turbulence degraded images using previously developed turbulence model. Next step is to investigate sum of signal with noise (for example Gaussian).

REFERENCES

- [1] M. Lemaitre, F. Mériaudeau, O. Laligant, J. Blanc-Talon, " Restoration of Images with Atmospheric Perturbation Simulation", Digital Image Computing: Techniques and Applications (DICTA'05), Conference Proceedings, p. 18, Nis, IEEE-Computer Society, 2005.
- [2] E. Ferdinandov, K. Dimitrov, Influence of the atmospheric turbulence over the images of cosmic objects, Optics Communications, Vol. 239, no. 1-3, pp. 1-6, 2004.
- [3] E. Ferdinandov, K. Dimitrov, Influence of the atmospheric turbulence over the optical cosmic investigations with ground based telescopes, ICEST, 2004.
- [4] E. Ferdinandov, B. Pachedjieva, *Probability and Statistics Methods in Communications*, Sofia, CIELA Press, 2005.
- [5] Madsen K., H.B. Nielsen, O. Tingleff, *Methods for non-linear least squares problems*, Informatics and Mathematical Modelling, TU-Denmark, 2004.
- [6] D. Garnier, D. Coburn and J. C. Dainty, "Single star SCIDAR for Cn2(h) profiling", Proc. SPIE 5891, 2005.

CATV systems - Volterra Kernels Identification

Oleg B. Panagiev¹ and Kalin L. Dimitrov²

Abstract – Nowadays, the most popular identification methods are those that allow the achievement of satisfactory results for the system with a minimum quantity of preliminary information or without any information about it. This is related to a certain universality of the models used. This universality allows the solution of many applicable tasks through these methods.

Keywords – CATV, identification, Volterra kernel, CSO, CTB.

I. INTRODUCTION

In the analysis of nonlinear systems whose model is described by Volterra series [1], [2], the basic problem consists in the possibility of identification of the non-linear operator $H_k(\omega)$ [3], [4]. In order to solve the task of identification, one needs to define the format of the mathematical system description (structural model). Then, the types of signals necessary for the identification have to be defined and an algorithm for restoring the model parameters according to the test results has to be developed. The identification success depends very much on the right choice of the model structure. There are two basic requirements to the model:

- The model should possess the sufficient precision to reflect the system properties for quite a wide range of signals compared to those used in the testing;
- The model form should not create great theoretical and calculative difficulties in the process of defining the system parameters.

The first requirement is usually hard to meet, because there is no sufficient preliminary information about the system. As a rule, we have to be content with the chosen model and its adequacy (correspondence) to the system [2]. After building the model, we test it by signals different from those used while building it. The system that is being examined is tested by the same signals (Fig.1), and then, the level of correspondence between the reactions of the system and the model is assessed.

Nowadays, the most popular identification methods are those that allow the achievement of satisfactory results for the system with a minimum quantity of preliminary information or without any information about it. This is related to a certain universality of the models used. This universality allows the solution of many applicable tasks through these methods [5], [6].

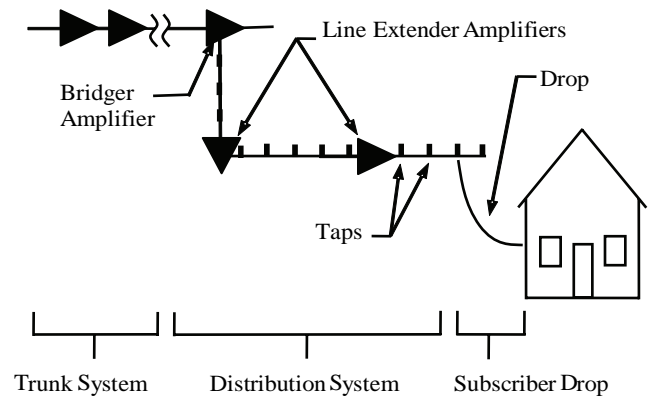


Fig.1. Scheme of the CATV system that is being examined

The problems of operator identification become more and more topical, due to the complication of the modern systems and the appearance of new technologies. Besides, the identification is also complicated by the existence of noise during the measurements. The noise causes some distortion of the useful signal. Therefore, in order to increase the precision of identification, we need to provide suppression of the noises and correction of the mistakes related to the distortion of the input signal.

II. IDENTIFICATION OF THE VOLTERRA KERNELS IN THE PRESENCE OF COMPOSITE INTERMODULATION PRODUCTS

Depending on the dynamic conditions of the active devices from the transmission medium, and even those from the high-frequency part of the subscriber equipment and the Head End, the Volterra kernels are analyzed in weak-signal regime. It is characteristic of these conditions that, due to many specific features, the non-linear distortions in the output reach the admissible norm with a very weak input signal (under 80 dB μ V), long before the non-linearity of the output characteristics starts taking effect [3], [5], [7].

Of the greatest interest to us, when calculating and measuring the amplitudes of the nonlinear products of intermodulation, are the Volterra kernels of second and third order. For initial data when defining the values of normal and normalized kernels, we will use the relationships between the composite distortion coefficients of the respective order and the signal transmission amplitudes, the system (amplifier) transfer coefficients and the Volterra kernels.

For the derivation of the expressions for the normal and the normalized kernels of second and third order, we will use the

¹Oleg B. Panagiev is with the Technical University of Sofia, Bulgaria, E-mail: olcomol@yahoo.com

²Kalin L. Dimitrov is with the Technical University of Sofia, Bulgaria, E-mail: kld@tu-sofia.bg

composite distortion formulae (CSO, CTB), which are derived in [8]. Below, you can see the expressions for the normal H_x and the normalized H_{xG} Volterra kernels after the anti-logarithm calculations and some other necessary mathematical operations related to them. During the derivation of the formulae, the following are taken into account: the data about the levels of the input A_{in} and the output A_{out} signals, the transfer coefficient G of the CATV system (amplifier) and the value of the composite distortions (CSO, CTB).

A. Second order Volterra kernels

$$H_2(f_i \pm f_j) = \frac{G^2}{A_{out}} \times 10^{-\frac{CSO}{20}} \quad (1)$$

$$H_{2G}(f_i \pm f_j) = \frac{G}{A_{out}} \times 10^{-\frac{CSO}{20}} \quad (2)$$

B. Third order Volterra kernels (three-component beat)

$$H_3(f_i \pm f_j \pm f_k) = \frac{2}{3} \times \frac{G^3}{A_{out}^2} \times 10^{-\frac{CTB}{20}}; \quad (3)$$

$$H_{3G}(f_i \pm f_j \pm f_k) = \frac{2}{3} \times \frac{G^2}{A_{out}} \times 10^{-\frac{CTB}{20}} \quad (4)$$

C. Third order Volterra kernels (two-component beat)

$$H_3(2f_i \pm f_j) = \frac{4}{3} \times \frac{G^3}{A_{out}^2} \times 10^{-\frac{CTB}{20}} \quad (5)$$

$$H_{3G}(2f_i \pm f_j) = \frac{4}{3} \times \frac{G^2}{A_{out}} \times 10^{-\frac{CTB}{20}} \quad (6)$$

In all the above-mentioned formulas $i \neq j \neq k = 1, 2, 3, \dots$; $A_{out} = A_{in} * G$ and f_i, f_j, f_k are the carrying frequencies of the image of the respective television channel from the CATV system.

III. RELATION BETWEEN THIRD VOLTERRA KERNELS WITH TWO-COMPONENT OR THREE-COMPONENT BEAT

When we compare (3), (4), and (5), (6), we can write down the following general formulae for Volterra kernels:

$$H_3(\omega_b) = \frac{2}{3} q \times \frac{G^3}{A_{out}^2} \times 10^{-\frac{CTB}{20}}; \quad (7)$$

$$H_{3G}(\omega_b) = \frac{2}{3} q \times \frac{G^2}{A_{out}} \times 10^{-\frac{CTB}{20}}, \quad (8)$$

where ω_b takes the values $2\pi(2f_i \pm f_j)$ or $2\pi(f_i \pm f_j \pm f_k)$.

The parameter q takes values according to Table 1, and the relation between the Volterra kernels with two-component and three-component beat is displayed by the expressions:

$$H_3(2f_i \pm f_j) = 2H_3(f_i \pm f_j \pm f_k); \quad (9)$$

$$H_{3G}(2f_i \pm f_j) = 2H_{3G}(f_i \pm f_j \pm f_k). \quad (10)$$

TABLE 1

Third order beat	q
$2f_i \pm f_j$	2
$f_i \pm f_j \pm f_k$	1

IV. CALCULATING VOLTERRA KERNELS FOR LINEAR (SUBTRUNK) AMPLIFIER IN THE PRESENCE OF INTERMODULATION

Here are the results of the theoretical identification Volterra kernels of the second and third order, characteristic of linear amplifier VX23A, produced by the German company WISI [9]. The drawing from Fig.2 is used for the definition of the composite distortion values. The derived data are written in Table 2, and the carrying frequencies of the image are chosen according to Appendix C of the European Standard CENELEC EN 50083-3. The frequency spectrum of the examined cable television system is from 49.75 MHz to 511.25 MHz, with the total number of the channels being 50.

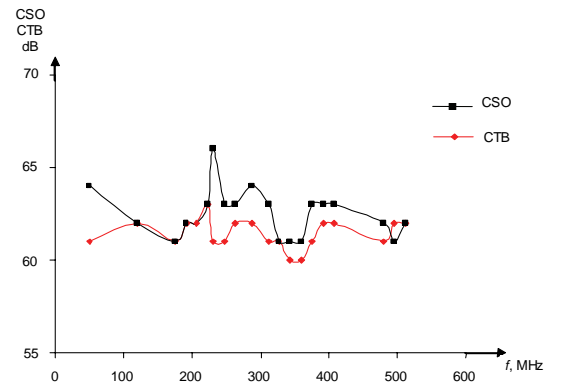


Fig.2. Graphic interdependency of the intermodulation composite distortions of the linear amplifier VX23A

TABLE 2

Frequency MHz	CTB dB	CSO dB
49.75	61	64
119.25	62	62
175.25	61	61
191.25	62	62
207.25	62	62
223.25	63	63
231.25	61	66
247.25	61	63
263.25	62	63
287.25	62	64
311.25	61	63
327.25	61	61
343.25	60	61
359.25	60	61
375.25	61	63
391.25	62	63
407.25	62	63
479.25	61	62
495.25	62	61
511.25	62	62

TABLE 3

Volterra kernels f MHz	Intermodulation			
	Second order		Third order	
	H_2	H_{2G}	H_3	H_{3G}
49,75	2,24E-06	3,98E-08	1,33E-10	2,37E-12
119,25	2,82E-06	5,01E-08	1,19E-10	2,11E-12
175,25	3,16E-06	5,62E-08	1,33E-10	2,37E-12
191,25	2,82E-06	5,01E-08	1,19E-10	2,11E-12
207,25	2,82E-06	5,01E-08	1,19E-10	2,11E-12
223,25	2,51E-06	4,47E-08	1,06E-10	1,88E-12
231,25	1,78E-06	3,16E-08	1,33E-10	2,37E-12
247,25	2,51E-06	4,47E-08	1,33E-10	2,37E-12
263,25	2,51E-06	4,47E-08	1,19E-10	2,11E-12
287,25	2,24E-06	3,98E-08	1,19E-10	2,11E-12
311,25	2,51E-06	4,47E-08	1,33E-10	2,37E-12
327,25	3,16E-06	5,62E-08	1,33E-10	2,37E-12
343,25	3,16E-06	5,62E-08	1,49E-10	2,65E-12
359,25	3,16E-06	5,62E-08	1,49E-10	2,65E-12
375,25	2,51E-06	4,47E-08	1,33E-10	2,37E-12
391,25	2,51E-06	4,47E-08	1,19E-10	2,11E-12
407,25	2,51E-06	4,47E-08	1,19E-10	2,11E-12
479,25	2,82E-06	5,01E-08	1,33E-10	2,37E-12
495,25	3,16E-06	5,62E-08	1,19E-10	2,11E-12
511,25	2,82E-06	5,01E-08	1,19E-10	2,11E-12

In Table3, the theoretical results about the Volterra kernels for a particular cable amplifier VX23A are presented. Their graphic interpretation is displayed on Fig.4 (normal kernels) and Fig.5 (normalized kernels).

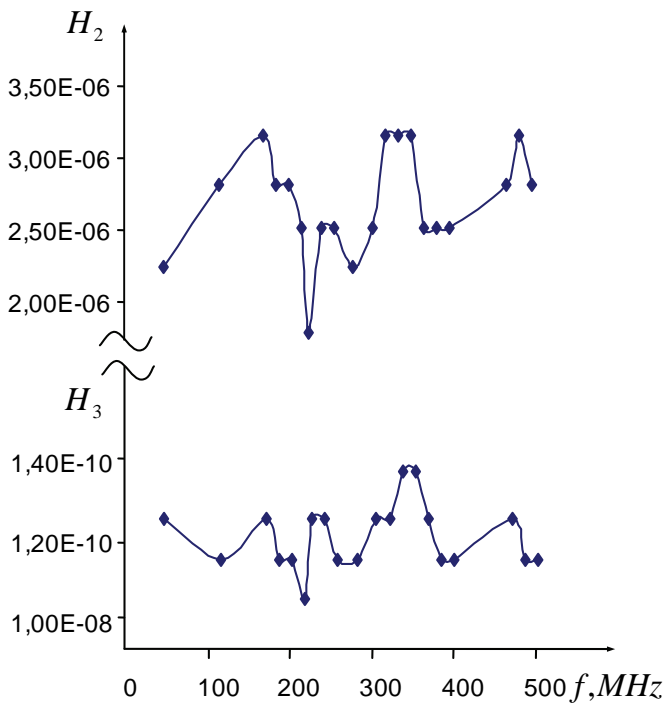


Fig.4. Normal Volterra kernels

V. CONCLUSION

The Volterra kernels can be derived by passing several successive signals to the input of the system (amplifier) and defining the reactions to them. The more test signals there are, the more precise the identification is, but the operations are more complex and longer. It is possible that the same non-linear system reactions occur with different input signals. The type and amplitude of the test signals is of a great importance to the precision of the identification and the convergence of the Volterra series.

The identification of kernels by this method is possible, if the power of the polynomial describing the system is known. Otherwise, it is necessary that an experiment for its definition be made. If the system is stationary, a sinusoidal signal with

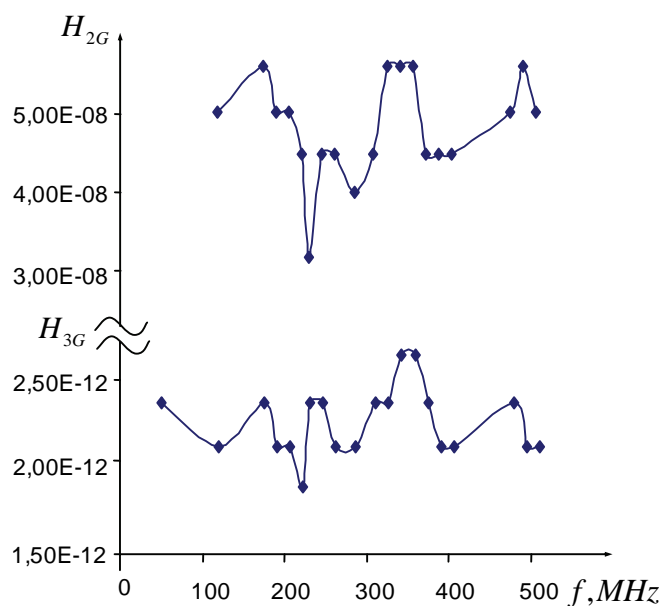


Fig.5. Normalized Volterra kernels

frequency ω is passed through its input, and then, a spectrum analysis of the output signal is done. The power of the polynomial is defined by the maximum multiple frequency present in the output signal.

In the theoretical research made, the Volterra kernels for a particular linear amplifier VX23A were identified. The derived results can be successfully used for the prediction, simulation and calculation of the nonlinear products in its output in whichever point of the cable distribution network, with the output/input signal being known.

REFERENCES

- [1] C. Evans, D. Rees, L. Jones and M. Weiss, "Periodic signals for measuring nonlinear Volterra kernel". IEEE Trans. Instrumentation and Measurement, vol.45, no.2, 1996.
- [2] O. B. Panagiev, "Non-linear distortions and methods of their limitation and reduction in the cable television systems". IX NSASC "Electronics'2000", Sozopol, 20 - 22 sept.2000.
- [3] L. V. Danylov, "Volterra-Picard series in the theory electric circuits", M, Radio and tie, 1987.
- [4] S. V. Levenec, *Nonlinear dynamic objects identification*, OGPU, Odessa, 1995.
- [5] P. H. Reischel, "Prediction of unsteady aerodynamic forces via nonlinear kernel identification". CEAS/AIAA/ICASE/NASA Langley International Forum on Aeroelasticity and Structural Dynamics, Williamsburg, June 22-25, 1999.
- [6] J. Schattschneider, U. Zolzer. "Discrete-time models for nonlinear audio systems", Proc. 2nd COST G-6 NTNU, Trondheim, Dec. 9-11, 1999.
- [7] C. Evans, D. Rees, L. Jones and M. Weiss. Periodic signals for measuring nonlinear Volterra kernels, IEEE Trans. on Instrumentation and Measurement, vol. 45, No. 2, April 1996.
- [8] O. B. Panagiev, Intermodulation composite distortions theoretically research in HFC networks, ICEST, Proc. of Papers, Ohrid, 24-27 June 2007.
- [9] WISI. A link to the future. Catalogue'2004.

Comments on the Method “Over Sampling and Averaging for Additional Bits of Resolution”

Petre Tzv. Petrov¹

Abstract - There is critical comments on the method “over sampling and averaging for additional bits of resolution”. The method is applied for “adding bits” to the analog to digital converter (ADC) and for “improving the ADC resolution”. It is shown that the results achieved by this method are unreliable, non-repetitive and the method “over sampling and averaging for additional bits” must be revised. The sampling theory is a victim of an oversimplification, overgeneralization and over sampling.

Keywords - over sampling and averaging for “additional bits”

I. INTRODUCTION

It is claimed in [1, 2] that with method “over sampling and averaging” (OA) additional bits of information are added to the bits generated from analog to digital converter (ADC). In order to clarify the situation a research was done as follows: 1. The method OA was studied and applied. The results were analyzed. 2. The terms “accuracy” and “resolution” were compared. 3. The application of these terms from different manufacturer was compared [3, 4]. 4. The maximal amplitude error was evaluated when the simplest band wide signal (SBLs) is sampled [5]. 5. The method was applied for external and internal ADC and digital to analog converters (DAC). 6. The conclusions were made.

In fact the method OA consists of two parts. The first part is an increasing the sampling rate (This is useful up to certain limit. In general the errors are reduced). The second part. is averaging of the samples. (This is equivalent of low pass filtering and of decreasing of the sampling rate. The advantages of the first part are reduced or even disappear.)

II. “OVER SAMPLING” VERSUS “SIGNAL SAMPLING FACTOR”

The term “over sampling” is used in term of “sampling at higher than “Nyquist rate” or “Shannon rate”[3, 4]. In fact that means “sampling with sampling factor greater than 2”. Generally the term “over sampling” means that certain “redundancies” are introduced into signal processing according to the Nyquist-Shannon-Kotelnikov sampling theorem. In fact this is not exact because the theorem does not give sufficient information for signal reconstruction [5].

The parameter “sampling factor” (SF) or “signal sampling factor” (SSF) is given with Eq. 1:

$$N = F_d/F_s = F_d/F_{max} \quad (1)$$

Where: F_d is the sampling frequency, F_s is the frequency of the sampled sinusoidal or co-sinusoidal signal, F_{max} is the maximal frequency of the sampled band limited signal (BLS). The SSF is more accurate than the term “over-sampling” because it gives the possibility to calculate the errors during the sampling process [5].

III. THE METHOD OVER SAMPLING AND AVERAGING

The method called “over sampling and averaging” (OA), described in [1,2] is based on the Eq.1:

$$F_{os} = 4^w F_{sn}, \quad (1)$$

Where: F_{os} is the “over sampling frequency”; w is the number of the “added bits” (“additional bits of resolution”); F_{sn} is the initial sampling frequency (“original sampling frequency” or “Nyquist frequency”).

Definition: The parameter “over sampling factor” (ratio) P is introduced with the equation below:

$$P = F_{os}/F_{sn}, \quad (2)$$

According to [1] the method OA is applicable if the noise added to the signal is “white noise”, but that type of noise is not reproducible and does not exist. Also [1] with 12-bits ADC and the method OA are obtained 16 bits of resolution or 4 more bits.. In total they have obtained “16-bits of useful data”. The Table I is based on the Eqs. 1 and 2. The question is “If in [1] there are 4 bits beyond the bits guaranteed by the accuracy of the converter are they always reproducible?” The answer is “No”. These additional bits are not always reproducible. They are filled with less or more unpredictable information. The comparison with higher accuracy measurement equipment shows that. In Table I a resume of the cases when 1 to 10 bits must be “added” to the existing accurate bits of the converter.

It is claimed [1] that the signal to noise ratio (SNR) of 12-bits ADC is incremented from the theoretical maximum of 74 dB (for 12 bits) up to 90 dB which are equivalent of 16 bits. The “gain” of 26 dB is obtained because of these 4 additional bits. Following the method OA Table I was made and tested with different signals. (w = “additional bits” = “gained bits of resolution” and P is the over sampling factor (ratio)). P is showing how many times the sampling frequency is higher than the frequency of 100% amplitude modulation (the frequency of SSF $N=2$).

The results from the experiments are as follows:

1. The additional calculated bits are not always predictable even when simple and stable sine wave or direct current (DC) signal is sampled.
2. The additional computational job for the

¹Petre Tzv. Petrov is with Micro Engineering-Sofia, Bulgaria. Emails: ppetre@caramail.com and ptzvp@yahoo.fr

processor is making the method OA non applicable to most of the small and multi-channel systems. 3. The required data memory is rapidly increasing with over sampling ratio. 4. The method is practically equivalent of low pass filtering. 5. The method is practically equivalent of sampling with high sampling rate and re-sampling with much lower sampling rate. 6. The histograms from the experiments show that the output digital codes do not correspond to the Gaussian distribution. 7. The noise from the converter and the equipment is individual and cannot be approximated with white noise. This is especially important for production purposes.

TABLE I.
SUPPOSED ADDED BITS TO THE ADC OR DAC WITH OA

w, bits	$P = F_{os}/F_{sn}$]	w, bits	$P = F_{os}/F_{sn}$
1	4	6	4096
2	16	7	16384
3	64	8	65536
4	256	9	262144
5	1024	10	1048576

IV. "ACCURACY" VERSUS "RESOLUTION"

The "accuracy" (or "total reproducible error" or "total reproducible bits") is the basic technical parameter of each conversion process. It is giving the absolute measurable error between the expected ideal code and the real code obtained from the converter. The accuracy is every time reproducible parameter and is always given by the manufacturer.. The accuracy is a price and application determining parameter.

The "resolution" (sometimes called "precision") is not an important technical parameter of the conversion process. In most of the cases it is a "commercial parameter" and cannot be used to compare reliably two products. The bits of "resolution" are not an every time reproducible parameter. They are is not a basic price and application determining parameter. For example if a converter has an 6 bit of accuracy and 8 bits of resolution in this case only 6 bits are guaranteed and reproducible and the bits 7 and 8 are nor guaranteed and reproducible during the test process. In many cases they are neglected, because no decision could be based on them.

An example with the popular series of 8-bits ADC08XX with one channel is given on Table II and examples for multi channels ADC are given in Table III.

Although the ADC from each of the tables are "pin to pin" compatible and with very similar characteristics they are not interchangeable. For example it is proven that ADC 0805 operating at 16 times higher frequency cannot replace ADC 0801, which has 4 times greater accuracy (+-0.25LSB against +- 1LSB). Both of them have the same number of bits and the same internal structure, but the LSB of ADC0805 is unstable. In fact if the clock frequency is increased from 100 kHz to 400 KHz or from 300KHz to 1200 kHz the conversion error is increased and not decreased. Moreover there is no way with averaging to reduce the error in a reproducible manner beyond the guaranteed accuracy of the converter. Consequently the method "over sampling and averaging for additional bits of resolution" is not a reliable method.

TABLE II
RESOLUTION (TOTAL BITS) AND ACCURACY (TOTAL ERROR)
OF THE ADC080X SERIES.

ADC	Total bits	Resolu- tion, bits	Total error, LSB	RP, bits
ADC0800	8	8	+ -2	6
ADC0801	8	8	+ -0.25	8
ADC0802	8	8	+ -0.5	8
ADC0803	8	8	+ -0.5	8
ADC0804	8	8	+ -1	7
ADC0805	8	8	+ -1	7

RP – reproducible bits = bits of the accuracy

TABLE III.
RESOLUTION (TOTAL BITS) AND ACCURACY (TOTAL ERROR)
OF THE ADC0808/9 MULTI CHANNEL ADC SERIES.

ADC	Total bits	Resolu- tion, bits	TUE	RP, bits
ADC0808	8	8	+ -0.5LSB	8
ADC0809	8	8	+ - 1LSB	7
ADC0816	8	8	+ -0.5LSB	8
ADC0817	8	8	+ - 1LSB	7

* TUE = Total unadjusted error = accuracy.

V. TESTING THE METHODS AND EXAMPLES

The methods "Over sampling and averaging" was tested with ADC with different word length connected to one microprocessor and sampling the same signal with same sampling rate and at the same moment. For example experiments with 6, 8, 10 and 12 bits ADC show clearly that there is no way with 6 bit ADC to replace 8, 10 or 12 bit ADC by simply increasing the sampling rate and averaging the samples. The accuracy of the converter depends from many design and production factors and cannot be overcome. Adding additional reproducible bits beyond the accuracy of the converter does not work.

Example 1: There is an "exception". For example an 8-bit ADC with 8-bit accuracy is used to sample a noisy DC signal (or a very low frequency AC signal) and only 6-bits are stable. In this case it is possible by increasing the sampling rate (if the parameters of the noise are known) and averaging the samples to obtain 7- or even 8-bit of accuracy (the samples are accurate and predictable) but thee is no way by increasing more the sampling rate to obtain more than 8 accurate bits. The conclusion is easy expanded and tested for any number of bits and for different converters. In fact this is low pass filtering.

Example 2: Many microcontrollers as PIC, MCS-51 derivatives, 68HC11 are with build in ADC with accuracy from 8 to 12 bits. Experiments show that there is no way (even after intensive computations) to obtain more accurate (predictable) bits that the bits guaranteed by the manufacturer. The bits added by computations are not always reproducible.

Example 3: With voltmeter with precision +-1% are done manually a lot of fast AC measurements and the samples are averaged but accuracy better than +-1% was not achieved. The "manual sampling rate" was varied but the additional

reproducible bits were not obtained. The results were compared against $\pm 0.2\%$ millimeter.

Example 4: A fast 8-bit ($\pm 0.2\%$) video ADC cannot replace a slow 12-bit ($\pm 0.0122\%$) industrial ADC. Four more bits cannot be gained according to the method “over sampling and averaging for adding bits”

Example 5: A comparator (e.g. LM311) could replace 1-bit ADC with two levels and with error $E_{adc} = \pm 25\%$ ($\pm 0.5 \cdot \text{LSB}$, $\text{LSB} = 50\% \cdot V_{fs}$. (V_{fs} is the full scale voltage of the converter). In order to apply the method OA a fast RISC PIC microcontroller was added and the output of the comparator was averaged. According to the method OA a converter with higher than one bit accuracy could be produced but this was not observable, because the accuracy (the predictable number of the produced bits) depends on many factors and not only from the averaged samples. The answer of the question “Is it possible with a simple comparator and processor to replace a multi bits ADC?” is “No”.

As a conclusion the incoming samples from n bit ADC can not be interpolated in a reproducible manner to samples from $n+1$, $n+2$, etc ADC. In order to achieve increased number of predictable and repetitive bits a lot of hardware conditions should be met (e.g. a better reference source and comparator) not only increasing the sampling rate and averaging the samples.

VI. THE METHOD OA AND THE DACS

If the method OA is really applicable to the ADC it should be applicable in clear and reproducible manner with the DAC. But there is no way to increase the accuracy or the resolution of the DAC by simply increasing of the frequency of the converted samples. In order to do that special hardware techniques should be used or simply DAC with more accurate bits should be used. But they are not part of the method AO.

VII. TESTING THE METHOD OA WITH THE SIMPLEST BAND WIDE TEST SIGNAL

Definition: The simplest band wide signal (SBLs) has two lines in its frequency spectrum. The first line is the direct current component (DC) and the second line is the alternative current (AC) component which is a sine or co-sine wave. Also is the simplest alternative current (AC) test signal (ACTS) which could be produced and very often is used as a basic test signal. SBLs was defined with the Eq. (3):

$$A = A_m \sin(\omega t + \theta) + A_{dc} = A_m \sin(2\pi f t + \theta) + A_{dc} \quad (3)$$

Where A is amplitude of the SBLs, ω is the angular frequency, f is the linear frequency, A_m amplitude of sine wave component and A_{dc} amplitude of the direct current component of BLS.

Sometimes graphically (or mechanically) SBLs is produced by circular movement of the vector with five components as follows: x and y are the coordinates of the center of the circle, ω is the frequency of rotation, r is the radius of the circle and θ is the starting position of the rotation of the vector.

Assumption $\theta=0$ and $A_{dc}=0$ (or $x=0$ and $y=0$) does not decrease the number of the parameters of the SS to

reconstruct. They are always at least four (and at least four samples for one period of the sine wave are needed for the reconstruction). We can simplify the Eq. 3 for analyzing it. We are obtaining the simplified formula (which is the formula of the simplest alternative current testing periodical signal) with zeroed phase and DC component:

$$A = A_m \sin(\omega t) = A_m \sin(2\pi f t) \quad (4)$$

We are introducing the principle “One sample per parameter to reproduce”. According to it at least four samples are required to reproduce all parameters of that signal (not two as the classical sampling theorem is stating).

VIII. BASIC AMPLITUDE ERRORS

When this signal is sampled with Analog to digital converter (ADC) with infinite (or sufficiently big) number of bits the deviation from the maximum of the sine wave component is called amplitude error. Here three amplitude errors are defined: maximal error (E_{max}), possible minimal error (E_{min}) and average (typical) error (E_{av}). The following equations are applicable and easy verifiable

$$E_{max} = 1 - \sin(90 - 180/N) = 1 - \cos(180/N) \quad (5)$$

$$E_{min} = 0 \quad (6)$$

$$E_{av} = 1 - \sin(90 - 180/(2N)) = 1 - \cos(90/N) \quad (7)$$

It is seen that if the sampling factor N is increased from zero to infinity neither of these errors is not following the rule “the error is decreasing twice if the sampling factor is increasing four times”. The dependency of the maximal amplitude error from the SSF from 2 to 37 is shown in Table IV.

According to [1] “If the sampling factor N is multiplied by four one more bit is added to the converter, or the resolution is multiplied by 2”. It is seen from the Table IV that if we increase the sampling factor four times we will not obtain one more bit (the maximal amplitude error will not decrease two times). The maximal amplitude error does not follow exponential law.

IX. FINAL COMMENTS ON THE METHOD “OVER SAMPLING AND AVERAGING”

The method OA was tested with direct current signal, sine wave and SBLs.

The “additional bits” obtain by the method OA sometimes could be added from generator of numbers with almost the same success.

The errors internal to the ADC cannot be overcome by the method OA because they are more or less individual and more than the guaranteed by the manufacturer bits cannot be achieved.

The increasing of the resolution (adding bits with OA) does not increase the accuracy of the measurement.

“Adding bits” with OA means that if we sample a DC with very high sampling rate and with very low accuracy ADC we will have the possibility to obtain a lot of bits of resolution but in practice a lot of not repeatable bits are obtained.

OA is useful as a kind of low pass filtering and is giving the possibility to use all accurate bits of the converter but cannot be used to go beyond the guaranteed accurate bits.

It seems that in general the method “over sampling and averaging for additional bits of resolution” has no theoretical and practical value. The “added bits” are not reproducible during the tests and are not useful.

If the frequency of the converter is increasing the conversion errors are increased too. Consequently there is a loss of data bits and there is no gain of additional bits.

The “delta sigma modulation” and the “over sampling and averaging” has nothing in common as a theory and practice. These are two different methods.

The theory of the “white noise” cannot be taken seriously because such a noise does not exist, cannot be generate and cannot be regulate effectively.

Charging a microcontroller with large among of data from the ADC in order to calculate non-reproducible bits is not effective technical task.

The errors during the conversion is closely related with the shape of the signal, the used hardware and software, the power supply and many application parameters and cannot be considered as “white noise”.

The “noise” is not a good thing. Adding noise (disturbing signal in that case) to the useful signal is not desirable from the point of view of the accuracy.

sample with supposed higher resolution or even accuracy (in this case the “gain” could be 2 bits), e.g. for $N=2$, $E_{\max} = 100\%$ and with $N=32$, $E_{\max}=0.482$ (Table IV). But this is not observed.

X. CONCLUSIONS ABOUT THE SIGNAL SAMPLING FACTOR

WithSSF $N=2$ the amplitude error of the digital copy of the sampled SS/CS could vary from 0 to 100%.

With SSF $N=4$ the amplitude error of the digital copy of the sampled SS/CS could vary from 0 to 29.3% (0 to 3 dB).

The CST based on Fourier series (oversimplified series) is uncompleted and cannot be used as a reference point during the signal sampling and reconstruction.

The SSF N divisible by 4 ($N = 4*k$, where $k = 1, 2, 3...$) is guarantying the possibility of zero DC error during the direct signal reconstruction and is giving the possibility to obtain zero amplitude errors because the signal could be sampled in its maximums, minimums and zero crossings.

Law of the limiting SSF was formulated: There is no sense to increase the SSF $N=F_d/F_s > 0$ higher the value limited by the accuracy and rapidity of the converter, because the obtained additional bits by calculations are nor reproducible.

Oversimplification, overgeneralization and over sampling did a lot of harm in the sampling theory.

The sampling rate of 20Hz to 20 kHz audio signal should be at least 80 kHz in order to guarantee always less than 3db maximal amplitude error.

TABLE IV
RELATION BETWEEN THE SAMPLING FACTOR N AND
 E_{\max} FOR N FROM 2 TO 37.

$N = F_d/F_s$	E_{\max} [%]	$N = F_d/F_s$	E_{\max} [%]
2	100	20	1.23
3	50	21	1.11
4	29.3	22	1.02
5	19.1	23	0.9314
6	13.4	24	0.856
7	9.9	25	0.789
8	7.61	26	0.729
9	6.09	27	0.676
10	4.89	28	0.629
11	4.05	29	0.586
12	3.40	30	0.548
13	2.91	31	0.513
14	2.51	32	0.482
15	2.18	33	0.453
16	1.92	34	0.427
17	1.70	35	0.403
18	1.51	36	0.381
19	1.36	37	0.360

The method OA is demanding exponential increase of the sampling rate and is producing non reproducible bits from the ADC. It is not applicable to DAC. The reverse over sampling and de-averaging for DAC does not work.

As mention before OA applied to the ADC means two things: 1/ Choosing the frequency of sampling much higher than SSF $N=2$. e.g.. $N=32$ is giving over sampling factor $P=32/2=16=4^2$. 2/ Adding and averaging each P samples (in this case sixteen consecutive samples) and producing only one

REFERENCES

- [1] Cygnal Integrated Products, Inc. Improving ADC resolution by over sampling and averaging, An018-1.1, May 2001, USA.
- [2] James Potzick. Noise averaging and measurement resolution (or “A little noise is a good thing”). Review of Scientific instruments. Vol. 70. No. 4. p. 2038. April 1999.
- [3] National Semiconductor Corp. Data Conversion /Acquisition Data book, 1984, USA. Chapter 5 and 7.
- [4] National Semiconductor Corp. National Analog and Interface Products Data book, 2002, USA. Chapter 6.
- [5] Petre Tzv. Petrov, Sampling analog signals (Abstract with formulas, tables and figures), Brochure printed in Technical University –Sofia, February 2004, Bulgaria, ISBN 954.438.385.9

POSTER SESSION – PO II

Electronic Components, Systems and Technologies

PSPICE Simulation of Optoelectronic Pulse Circuits

Elena N. Koleva¹ and Ivan S. Kolev²

Abstract – The pulse circuits simulated are own developments of the team. They present an autofluctuation multivibrator with photodiode optocouplers and a controllable combined generator of line altering voltage and square pulses (of fantastron type) with a phototransistor optocoupler. The circuits have been simulated by means of a PSPICE package. The circuits have been developed in practice.

Keywords – multivibrator, photodiode optocouplers, fantastron generator, phototransistor optocoupler

I. INTRODUCTION

The pulse circuits simulated are own developments of the team. They present an autofluctuation multivibrator with photodiode optocouplers and a controllable combined generator of line altering voltage and square pulses (of fantastron type) with a phototransistor optocoupler. The circuits have been simulated by means of a PSPICE package. Time diagrams of set points, as well as transfer characteristics are given. Equations for determining the basic parameters of generators such as frequency (period) and pulse duration have been worked out. The circuits have been realized in practice; the modeling results have been compared and the practical experiments have been theoretically calculated (the error does not exceed 5 %).

II. CONTROLLABLE AUTOFLUCTUATION MULTIVIBRATOR WITH PHOTODIODE OPTOCOUPLEDERS

A. A traditional circuit of a transistor autofluctuation multivibrator has been used, where the transistors have been replaced with phototransistor optocouplers in a photodiode mode, and the base time-setting resistors with optocoupler photodiodes – fig.1.

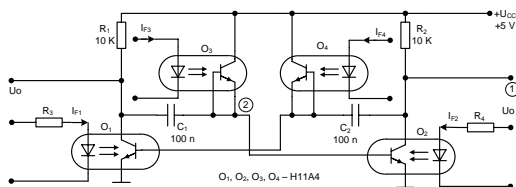


Fig. 1

B. The simulated time diagrams of the output voltage U_o (p. 1) and the voltage of one of the time-setting capacitor C_1 (p. 2) are shown in fig. 2.

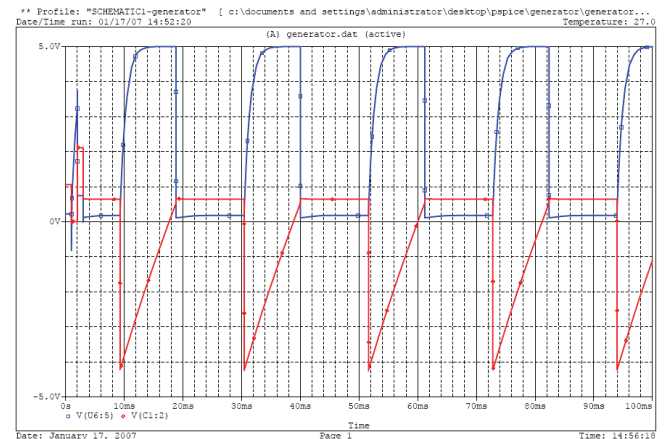


Fig. 2

The simulation refers to the following case:

$$I_{F3} = I_{F4} = 30 \text{ mA}, I_{F1} = I_{F2} = 0 \text{ mA}.$$

The reported simulated period of the generated pulses shown in fig. 2 is $T_C \approx 21\text{ms}$.

The equation for the period of the generated pulses, which has been theoretically worked out, is Eq. 1:

$$T \approx 0,7 \cdot C \left[R_{PD3} (I_{F3}) \cdot n_1 (I_{F2}) + R_{PD4} (I_{F4}) \cdot n_2 (I_{F1}) \right] \quad (1)$$

$C = C_1 = C_2$, $I_{F3} = I_{F4} = I_F$, R_{PD} – resistance of optocoupler photodiodes; n_1, n_2 – constants depending on the saturation degree of the phototransistors $n_1, n_2 = 1 \div 1,5$

When $I_{F3} = I_{F4} = 30 \text{ mA}$, $I_{F1} = I_{F2} = 0 \text{ mA}$, $n_1, n_2 = 1$, $T = 20 \text{ ms}$, $f = 50 \text{ Hz}$ from equation (1).

The error is Eq. 2:

$$\varepsilon = \frac{T_C - T_H}{T_C} \cdot 100\% = \frac{21 - 20}{20} \cdot 100\% = 5\% \quad (2)$$

When $I_{F3} = I_{F4} = 0,2 \text{ mA}$, $T_H = 0,98 \text{ ms}$, $f \approx 1 \text{ Hz}$ from equation (1), i.e. the frequency changes over approximately 50.

C. Using table I, a transfer characteristic of the controllable multivibrator has been worked out (see fig. 3).

It can be seen that the transfer characteristic is linear within the range $I_F = 5 \div 30 \text{ mA}$.

¹Elena N. Koleva is Ph. D. student, Department of Electronics, Technical University – Gabrovo, Street “Hadji Dimitar” No. 4, 5300 Gabrovo, Bulgaria, phone: +359 898 226 464, e-mail: elena_ndpt@yahoo.com

²Ivan S. Kolev is Assoc. Prof. Ph.D., Dr. Sci., Department of Electronics, Technical University – Gabrovo, Street “Hadji Dimitar” No. 4, 5300 Gabrovo, Bulgaria, phone: +359 898 634 633, e-mail: ipk_kolev@yahoo.com

TABLE I

I_F , mA	0,2	1	3	5	10
T, ms	960	185	87	64	42
F, Hz	1,04	5,41	11,5	15,6	23,8

I_F , mA	15	20	25	30
T, ms	31	25	21	18
F, Hz	32,3	40	48	55,6

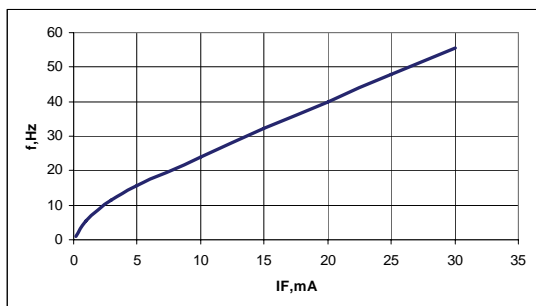


Fig. 3

II. OPTOELECTRONIC FANTASTRON GENERATOR – FIG. 4

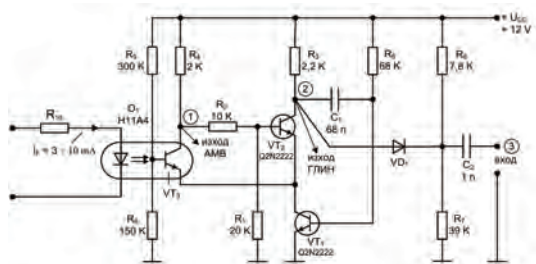


Fig. 4

It operates in a stand-by mode. The transistor fantastron generator has a collector coupling. The generator has an amplifier tracking coupling and contains a generator of line altering negative feedback voltage – Miller integrator with transistors VT₁ and VT₂. The transistors VT₂ and VT₃ form a trigger with an emitter coupling where the emitter resistor is replaced with the transistor VT₁ of the optocoupler O₁.

D. The circuit simulation is shown in fig. 5.

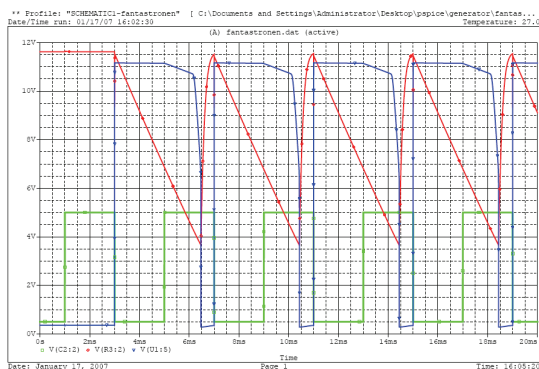


Fig. 5

Square pulses are taken at the output p.1 and line altering voltage at the output p.2. The circuit is set into motion at input p.3 by symmetric square pulses of 5 V amplitude and T = 4 ms (f = 250 Hz) period, where the T period of the generator of line altering voltage can be regulated within the range from 3,4 to 2,8 ms by changing the LED current from 3 ÷ 10 mA. The period of simulations is T_C = 4 ms when I_F = 3 mA (fig. 5).

Circuit application:

- Generator of line altering voltage
- Square pulse generator
- Pulse-width modulator
- Time-to-current (voltage) converter

The equations for the pulse duration (t_H), the pause between pulses (t_P), the non-linearity (K_H) and the period T of the generator are:

$$t_H = R_5 \cdot C_1 \frac{U_{CC} - U_{OL}}{U_{on}} = 68 \cdot 10^3 \cdot 68 \cdot 10^{-9} \frac{12 - 3}{11,5} = 3,62 \text{ ms} \quad (3)$$

$$t_P = R_3 \cdot C_1 \cdot \ln \frac{U_{CC}}{U_{CC} - U_Y} = 2,2 \cdot 10^3 \cdot 68 \cdot 10^{-9} \ln \frac{12}{12 - 10} = 0,268 \text{ ms} \quad (4)$$

$$U_Y = \frac{U_{CC}}{R_6 + R_7} \cdot R_7 = \frac{12}{7,8 + 39} \cdot 39 \approx 10 \text{ V} \quad (5)$$

$$T = t_P + t_H = 3,62 \text{ ms} + 0,268 \text{ ms} = 3,88 \text{ ms} \quad (6)$$

$$K_H = \frac{U_Y - U_{OL}}{U_{CC}} \cdot \frac{R_5}{R_3 \cdot h_{21E}} = \frac{10 - 3}{12} \cdot \frac{68}{2,2 \cdot 180} = 0,1 \quad (7)$$

The non-linearity of the generator of line altering voltage is K_H = 10 %.

The error, when T = 4 ms, is Eq. 8:

$$\varepsilon = \frac{T_C - T_H}{T_C} \cdot 100\% = \frac{4 - 3,88}{4} \cdot 100\% = 3\% \quad (8)$$

III. CONCLUSIONS

Two types of optoelectronic pulse circuits have been developed. They have been simulated by means of a PSPICE package. Methods for calculating the basic parameters have been elaborated. The circuits have been developed in practice. The simulation and calculation error has been determined – it does not exceed 5 %.

REFERENCES

- [1] Kolev, I. S. Optoelectronics. Gabrovo, University Publishing Hoise „V. Aprilov”, 2004.
- [2] Kolev, I. S. Infrared Optoelectronics. Gabrovo, University Publishing Hoise „V. Aprilov”, 2004.
- [3] Kolev, I. S. Development, research and modeling pulse, digital and logic circuits with optoisolators and digital optron integrated circuits. Thesis for a Doctor’s degree, 2006.
- [4] Kolev, I. S. and E. N. Koleva. Optoelectronics. S., Technique, 2007.

Temperature Profile of the Impulse Discharge

Iliycho P. Iliev¹ and Snezhana G. Gocheva-Ilieva²

Abstract – New analytical model for determining the gas temperature profile of the impulse discharge in the cross-section of copper-bromide laser is proposed. The model consists of heat conductivity equation subject to special nonlinear boundary conditions of third and fourth kind, which allow obtaining the gas temperature distribution as a function of the laser parameters, such as geometrical design, constructive materials, input electric power, etc. Numerical results in the case of natural convection are presented.

Keywords - impulse discharge, Copper-Bromide laser, temperature profile.

I. INTRODUCTION

The impulse discharge is very actively applied for exciting a range of impulse metal vapor lasers and its varieties with compounds, generated by self-restraint transitions from resonance to metastable levels (*r-m* lasers). These are copper vapor, gold vapor and manganese vapor lasers. Because of the physical nature of the laser level population processes, only this type of discharge induces an inversion population within the active laser levels and excites laser generation. Among the metal vapor lasers, the most investigated ones are lasers in which the active medium is modified by adding different halides of the working metal. More often hydrogen and hydrogen mixtures, such as HCl, HBr etc., are supplemented [1-2]. These modifications yield abatement of the operating medium temperature by 800-1000K and increase the frequency and energetic characteristics and laser radiation quality. Due to the above mentioned advantages this type of lasers are extensively used in modern of high-speed data recording systems, in material processing, in medicine, for atmosphere and world ocean investigation, in isotope splitting techniques, etc.

Among the metal vapor lasers the more perspective are the copper vapor lasers and copper compound vapor lasers. This type of lasers are the most powerful in the visible. Many papers are devoted to its investigation (see for instance [1-2] and quoted there literature). In order to enhance the laser characteristics and study the physical processes in the active laser medium different mathematical models and computer simulations of the kinetic processes have been developed [3-5]. The gas temperature is one of the most important thermodynamical characteristics of the active medium. This

determines the laser application term, laser generation deterioration, the distribution of the neutral atoms in the cross-section of the tube. The rise of the gas temperature produces a thermal population of the lower laser levels, which has influence on the laser power and laser beam mode composition. A higher temperature can provoke thermoionization gas discharge instability. Because of all this during the laser exploitation period and during the computer simulations, respectively, this parameter must be subject of detailed study. Two types of approach can be applied to determine the gas temperature – set the temperature on the tube walls [3-4] or choose some gas temperature distribution in the cross-section of the discharge tube, which do not change subsequently [5].

However, when multiple computer simulations are carried out, the geometrical design, tube constructive materials and thermal insulation the input electric power and working conditions often change. In this case the wall temperature is unknown. The stated initial temperature profile also changes. So without taking the correct gas temperature into account, the obtained results can be unreliable. Special attention to this problem is paid in [6].

In this paper a new analytical model is presented for more accurate determination of the gas temperature in the cross-section of the discharge in the copper-bromide vapor laser. The model is described by two-dimensional heat conductivity equation subject to nonlinear boundary conditions of the third and fourth kind, instead of the first kind boundary conditions, which were used till now. The model sets the air temperature (say $T_0 = 300K$) and takes into consideration the conduction and radiation processes in the heat exchange between the outside area of the laser tube and its surroundings. This approach allows obtaining the gas temperature and the wall temperature as a result of the solution of heat conductivity equation depending on the initial parameters, such as geometrical design, input electric power, etc.

II. DESCRIPTION OF THE MODEL

We study the impulse discharge in a copper-bromide vapor laser [7], operating at input electric power of 5KW and generating an output power of 120W. The geometrical design of the laser tube is shown in Fig. 1. The laser tube is manufactured of quartz, supplied with thermo-insulating glass wool, mineral wool or zirconium dioxide coating.

The following assumptions are imposed: 1) the temperature profile is sought in a quasistationary regime; 2) the gas

¹ Iliycho P. Iliev is with the Technical University Sofia - branch Plovdiv, 25 Tzanko Dushtabanov St, 4000 Plovdiv, Bulgaria

² Snezhana G. Gocheva-Ilieva is with the 'Paisii Hilendarski' University of Plovdiv, 24 Tzar Assen St, 4000 Plovdiv, Bulgaria, E-mail: snow@pu.acad.bg

temperature between the pulse-repetition rates does not change considerably; 3) the total amount of the input electric power is transformed to heat.

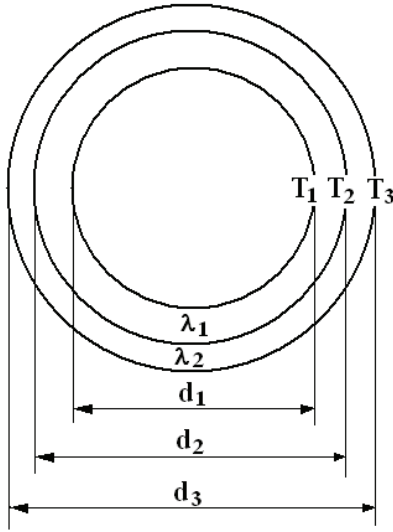


Fig. 1. Geometry of the cross-section of the laser tube:
 $d_1 = 56\text{mm}$, $d_2 = 60\text{mm}$, $d_3 = 70\text{mm}$.

Two-dimensional stationary heat conductivity equation in the cross-section of the discharge tube can be written in the form

$$\text{div}(\lambda_g \text{grad} T_g) + q_v = 0 \quad (1)$$

where λ_g is the heat conduction coefficient of the gas, q_v is the volume density of the internal heat source, and T_g is the temperature in the tube.

In order to solve equation (1) more often the boundary condition of the first kind is used. It means that the temperature T_2 of the outside area of the quartzous tube is supposed to be given. The value of λ_g is approximated in the form $\lambda_g = \lambda_0 T_g^m$. In this case equation (1) possesses the following explicit solution ([8])

$$T_g(r) = \left[T_2^{m+1} + \frac{q_v(m+1)}{4\lambda_0} (R^2 - r^2) \right]^{1/(m+1)}, \quad (2)$$

where R is the radius of the tube. Solution (2) is used for determination of the temperature profile of the copper-bromide vapor laser in [9], and for computer simulation of copper vapor laser in [4].

In our model we solve equation (1) under the following mixed boundary conditions of the third and fourth kind, which in cylindrical configuration take the form [10]

$$T_1 = T_2 + \frac{q_l \ln(d_2/d_1)}{2\pi\lambda_1}, \quad T_2 = T_3 + \frac{q_l \ln(d_3/d_2)}{2\pi\lambda_2}, \quad (3a)$$

$$Q = \alpha F_3 (T_3 - T_0) + F_3 \varepsilon c \left[(T_3/100)^4 - (T_0/100)^4 \right]. \quad (3b)$$

The boundary condition (3a) describes the continuity of the heat flow through the boundary between two walls. Here q_l is the power per unit length, $q_l = Q/l_a$, $l_a = 2m$ is the m -active length [7], λ_1, λ_2 are the heat conductivity coefficients of the quartzous tube and the thermal insulation, respectively, $d_j, j=1,2,3$ are the diameters of the inserted tubes (see Fig. 1). The boundary condition (3b) gives the way of heat exchange between the outside area of the laser tube and its surroundings. It consists of two terms. The first term at the right hand side of (3b) evolves from the Newton-Rihmann's law for heat exchange by convection. The second term gives the Stefan-Boltzmann law for heat exchange by radiation. The value of Q is equal to the overall heat flow and finds expression in the total consumed electric power, regarding the assumption 3, as it was stated above, α is the heat transfer coefficient, F_3 is the outside active area of the tube, ε is integral emissivity of the material, $c = 5.67\text{W}/(\text{m}^2\text{K}^4)$ is the black body radiation coefficient, $T_0 = 300\text{K}$ is the temperature of the air in the surroundings. In equation (3b) the values of α and T_3 are unknown. To find T_3 we need preliminarily to calculate the heat transfer coefficient α .

For all types of convection the Nusselt criterion hold [10]:

$$Nu = \alpha H / \lambda, \quad (4)$$

In the case of free convection the Grashoff criterion is given by the expression [10]:

$$Gr = g \beta H^3 (T_3 - T_0) / \nu^2, \quad (5)$$

For the horizontal tubes at natural convection the two upper criteria can be related by the equality [10]

$$Nu = 0.46 Gr^{0.25}, \quad (6)$$

which is valid if $700 < Gr < 7.10^7$. In the previous expressions (4)-(6) H is a characteristic dimension of the body, here $H = d_3$, g is the gravitational acceleration, β is the coefficient of cubical heat expansion of the gas, which for the air is $\beta_{air} = 3,41 \cdot 10^{-3}, \text{K}^{-1}$, ν is the kinematical viscosity, $\nu_{air} = 15,7 \cdot 10^{-6} \text{m}^2/\text{s}$, λ is the heat conduction coefficient, $\lambda_{air} = 0,0251 \text{W}/(\text{mK})$. These data are valid for the air temperature 300K [10].

By using (4)-(6) the heat conduction coefficient α can be expressed as

$$\alpha = 0.46\lambda_{air} \left[g\beta_{air}d_3^3(T_3 - T_0)/\nu_{air}^2 \right]^{0.25} / d_3. \quad (7)$$

The boundary condition (3b) represented with respect to power per unit length takes the form

$$q_l = 0.46\pi\lambda_{air} \left[g\beta_{air}d_3^3(T_3 - T_0)/\nu_{air}^2 \right]^{0.25} (T_3 - T_0) + \pi d_3 \varepsilon c \left[(T_3/100)^4 - (T_0/100)^4 \right], \quad (8)$$

Now, the outside temperature T_3 can be calculated by solving nonlinear equation (8). It is not difficult to establish that this equation possesses a unique real solution. Then by means of (3a) the temperatures T_2 and T_1 can be determined.

Finally, from (2) we obtain the following expression to calculate the gas temperatures in all internal points in the active discharge medium:

$$T_g(r) = \left[T_1^{m+1} + \frac{q_v(m+1)}{4\lambda_0} (R_1^2 - r^2) \right]^{1/(m+1)}, \quad (9)$$

where R_1 is the radius of the internal tube.

III. RESULTS AND DISCUSSION

In this section some numerical results for the temperature profile in the case of natural convection, obtained by our analytical model are presented. The values of the used physical constants are shown in Table 1.

Table 1. Data used in the calculation of the temperature profile. The lowest row shows the corresponding references.

Q, W	l_a, m	$q_v, W/cm^3$	$q_l, W/m$	$\lambda_g = \lambda_0 T^m, W/(mK)$	$\lambda_1, W/(mK)$	$\lambda_2, W/(mK)$	ε
5000	2	1.015	2500	$\lambda_0 = 5.8935 \cdot 10^{-5}$ $m = 1.091$ 15Torr Ne and 0.3Torr H ₂	1.96 ($T = 800 \div$ 1100K)	0.12 ($T = 800 \div$ 1100K) (mineral wool)	0.72
[7]	[7]			[9]	[11]	[10]	[11]

The equations (8), (3a) and (9) are solved consecutively. Curve 1 in Fig. 2 shows the obtained temperature distribution in the cross-section of the discharge tube. The corresponding values of the intermediate temperatures are: $T_3 = 662K$, $T_2 = 1174K$, and $T_1 = 1188K$, respectively, the temperature in the centre of the tube is $T(0) = T_{max} = 2200K$.

As it was mentioned above, the usually used technique in the literature required to give the outside surface temperature T_2 of the quartzous tube, which would be measured (for instance by a thermocouple). After that, assuming $T_2 = T_1$ in (2) one can calculate the internal temperature profile in the discharge tube [3, 7]. We found the absolute error in this case to be around $\Delta T = T_1 - T_2 = 14K$. As the temperature difference is small, this approach is practically admissible.

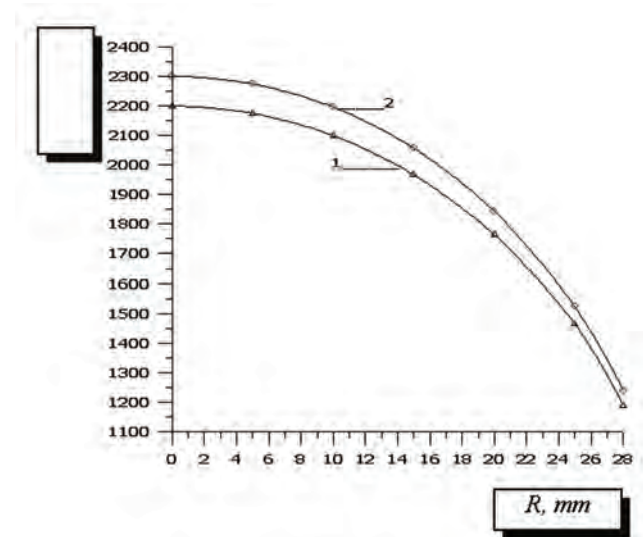


Fig. 2. Gas temperature distribution in the cross-section of the active discharge medium at natural convection: curve 1- at power $Q = 5000W$ and curve 2 - at power $Q = 5500W$.

By our model an “apriori” estimation of the possible temperature variation depending on the input electrical power can be obtained. As an example, an increase of 10% in the input electric power causes the increase of maximum temperature T_{\max} up to 100%, which is illustrated in Fig. 2. This type of results cannot be found using the above mentioned methods, while the temperature T_2 remains unknown.

Fig. 3 shows the relative change of the temperature $T(0)$ in the centre of the discharge with the change of the insulation coating thickness. The obtained results indicate a 8.7 % increase in the maximum temperature with an 11% increase in the thickness of the thermal insulation.

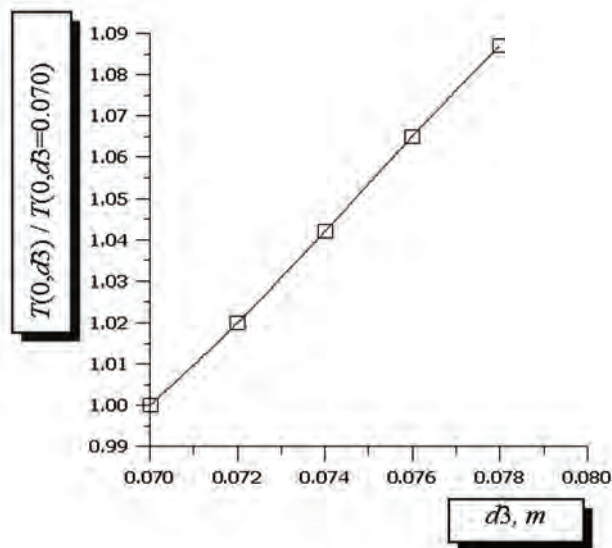


Fig. 3. Relative variation of the calculated temperature $T(0)$ in the centre of the tube, while increasing the thickness of the thermal insulation.

Another advantage of the presented model is that, at a given temperature T_3 , equation (8) allows analyzing the heat exchange behavior through the outside laser surface to the surroundings. For our data we obtain that the dominant heat exchange mechanism is heat radiation (66%) with the remainder being heat conduction (34%).

IV. CONCLUSION

A new approach in solving the heat conductivity equation for copper-bromide vapor laser is presented. Mixed boundary conditions of the third and fourth kind are introduced to describe more precisely the heat exchange between the laser tube and its surroundings.

The temperature profile of the discharge is calculated in the cross-section of the laser tube in the case of natural convection. It is established that the dominant heat exchange mechanism in this case is heat radiation. The proposed model allows carry out further computer simulations in order to optimize the working laser characteristics by changing geometric design, constructive materials, input electric power and other basic parameters.

ACKNOWLEDGEMENT

This work was supported by the Scientific Fund of the Bulgarian Ministry of Education and Science, Project VU-MI-205/2006 and NPD of Plovdiv University ‘Paisii Hilendarski’, Project 07M07.

REFERENCES

- [1] D. V. Shiyarov, V. B. Sukhanov, G. S. Evtushenko and O. S. Andrienko, “Experimental Investigation of the Effect of HBr Additions on the Lasing Characteristics of a CuBr Laser”, *Quant. Electronics*, vol. 34, no 7, pp. 625-629, 2004.
- [2] D. V. Shiyarov, G. S. Evtushenko, V. B. Sukhanov and V. F. Fedorov, “Effect of Gas Mixture Composition and Pump Conditions on the Parameters of the CuBr—Ne—H₂(HBr) Laser”, *Quant. Electronics*, vol. 37, no 1, pp. 49-52, 2007.
- [3] R. G. Carman, D. J. W. Brown and A. Piper, “A Self-Consistent Model for the Discharge Kinetics in a High-Repetition-Rate Copper-Vapor Laser”, *IEEE J. of Quant. Electr.*, vol. 30, no 8, pp. 1876-1895, 1994.
- [4] S. I. Yakovlenko, “Critical Electron Density in a Self-contained Copper Vapour Laser in the Restricted Pulse Repetition Rate”, *Quant. Electronics*, vol. 30, no 6, pp. 501-505, 2000.
- [5] A. M. Boichenko, G. S. Evtushenko, O. V. Zhdanev and S. I. Yakovlenko, “Theoretical Analysis of the Mechanisms of Influence of Hydrogen Additions on the Emission Parameters of a Copper Vapour Laser”, *Quant. Electronics*, vol. 33, no 12, pp. 1047-1058, 2003.
- [6] G. G. Petrash, “On the Simulation of a Copper Vapour Laser with Hydrogen Admixtures”, *Quant. Electronics*, vol. 35, no 6, pp. 576-577, 2005.
- [7] D. N. Astadjov, K. D. Dimitrov, D. R. Jones, V. K. Kirkov, C. E. Little, N. V. Sabotinov and N. K. Vuchkov, “Copper Bromide Laser of 120-W Average Output Power”, *IEEE J. of Quant. Electr.*, vol. 33, no 5, pp. 705-709, 1997.
- [8] M. J. Kushner and B. E. Warner, “Large-bore Copper-vapor Lasers: Kinetics and Scaling Issues”, *J. Appl. Phys.*, vol. 54, no 6, pp. 2970-2982, 1983.
- [9] D. N. Astadjov, N.K.Vuchkov and N.V. Sabotinov, “Parametric Study of the CuBr Laser with Hydrogen Additives”, *IEEE J. of Quant. Electr.*, vol. 24, no 9, pp. 1926-1935, 1988.
- [10] M. Oprel, S. G. Batov and D. Z. Uzunov, *Heat Technology*, Sofia, Technika, 1978.
- [11] *Physical Quantities*, Handbook, Moscow: Energotomizdat, 1991.

Simulation Investigation of Frequency Sensitive Digital Phase Detectors

Aleksandar H. Yordanov¹ and Georgy S. Mihov²

Abstract – In this paper a method for simulation of digital frequency sensitive phase detectors is examined. The main point is to create a simulation method to present phase - voltage response of analyzed schemes by using transient analysis. This can be done by setting to different frequencies to input pulse sequences which creates a linear increase of the phase difference. In that simulation the phase difference is equivalent to time with a predetermined phase step. The step can be changed when a different accuracy is desired and it is depend on input frequencies. In the paper are shown simulations of the most common digital frequency sensitive phase detector and a digital frequency sensitive phase detector working on both fronts of an input signal.

Keywords – Digital phase detector, Simulation of phase - voltage response, ICEST 2007,

I. SETTINGS FOR SIMULATION ANALYSIS OF PHASE DETECTORS

The main point of this paper is to crate a method of simulation analysis for digital frequency sensitive phase detectors and mainly their functional dependence. Frequency sensitive phase detectors have certain features which allow conveniently to present phase - voltage response by using transient analysis. This method can be used for analysis of many types of digital phase detectors and further more, it can be used with any kind of simulation programs with transient analysis.

The block diagram for simulation analysis of a phase detector is shown on Fig. 1.

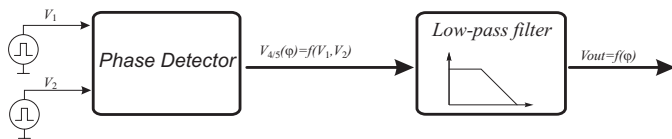


Fig. 1. Block diagram

The method uses two impulse generators with different frequencies.

In this simulation the low-pass filter which is used is active and inverts the input signal. To obtain the phase - voltage

response as it expected [1], it is take the leading signal to be v_2 . This is equal to take the second output as leading and respectively to invert the output signal, so the output voltage is expected to rise when phase difference is increasing.

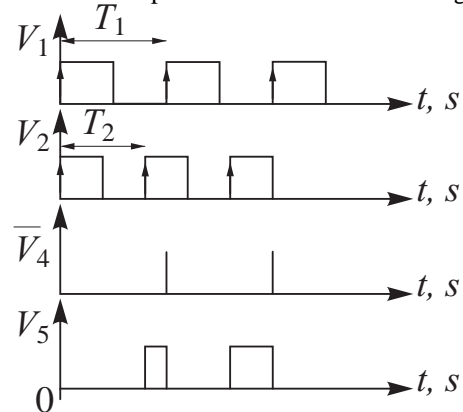


Fig. 2. Input/Output time diagrams

An example of input/output time diagrams is shown on Fig. 2. The signal v_5 is equal to the phase difference between signals v_1 and v_2 , respectively frequencies f_1 and f_2 .

$$V_1 = v_1(\varphi_1 + kT_1) \quad (1)$$

$$V_2 = v_2(\varphi_2 + kT_2) \quad (2)$$

where $k = 0, 1, 2, \dots$

$$v_1 = \begin{cases} 1, & \text{when } 0 \leq t \leq \frac{T_1}{2} \\ 0, & \text{when } t > \frac{T_1}{2} \end{cases} \quad (3)$$

$$v_2 = \begin{cases} 1, & \text{when } 0 \leq t \leq \frac{T_2}{2} \\ 0, & \text{when } t > \frac{T_2}{2} \end{cases} \quad (4)$$

φ_1 and φ_2 are starting phases, T_1 and T_2 are periods of both impulse sequences. If it is assumed, that φ_1 and φ_2 are 0 and

$$\Delta t = T_1 - T_2 \quad (5)$$

then

$$V_1 = v_1(kT_2 + k\Delta T_2) \quad (6)$$

¹Aleksandar H. Yordanov is with the Faculty of Electronic Engineering and Teshnologiess – Technical University of Sofia E-mail: yordanoval@abv.bg

²Georgy S. Mihov is with the Faculty of Electronic Engineering and Teshnologiess – Technical University of Sofia, E-mail: gsm@tu-sofia.bg

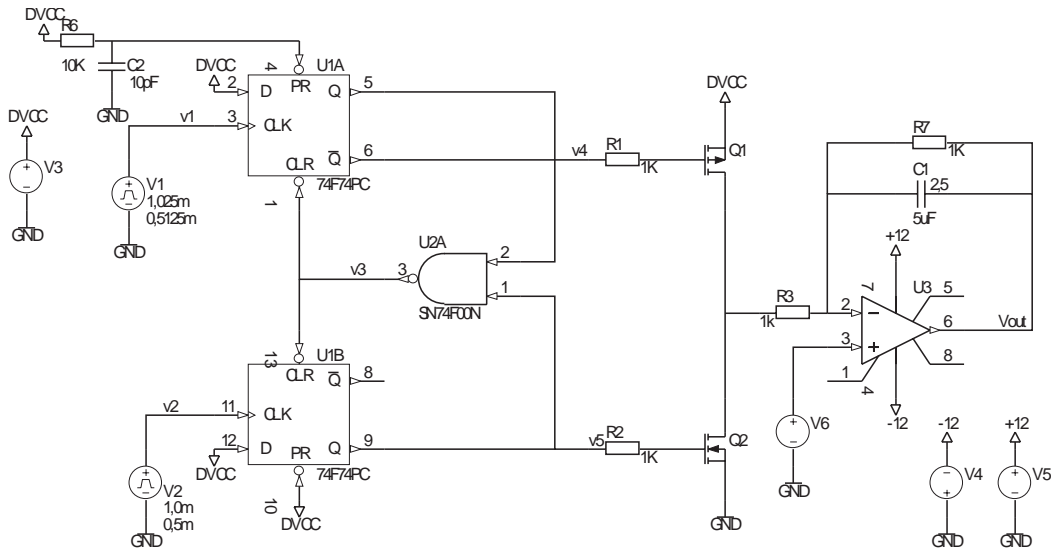


Fig. 3. Scheme of common phase detector

$$V_2 = v_2(kT_2) \quad (7)$$

Delay of signal v_1 towards signal v_2 for one period T_2 is Δt . Time delay Δt can be present as phase delay by using Eq. 5 and 6. To get the phase it is replaced

$$\varphi = q \cdot \Delta t \quad (8)$$

where q is coefficient with a dimension $\left[\frac{\text{rad}}{\text{s}} \right]$. If delay is equal to the repeating period T_2 then $2\pi = q \cdot T_2$ and

$$q = \frac{2\pi}{T_2} \quad (9)$$

It is replaced Eq. 9 in Eq. 8 and gets:

$$\Delta t = \frac{\varphi}{q} = \frac{\varphi \cdot T_2}{2\pi} \quad (10)$$

$$V_1 = v_1 \left(kT_2 + \frac{k \cdot \varphi \cdot T_2}{2\pi} \right) \quad (11)$$

The expression $\frac{k \cdot \varphi \cdot T_2}{2\pi}$ represents the phase difference between signals v_1 and v_2 , which is produced in output of the digital frequency sensitive phase detector. It is clear from Eq. 11, that the phase difference is proportional of period T_2 and the counts of periods k , which is passed. If

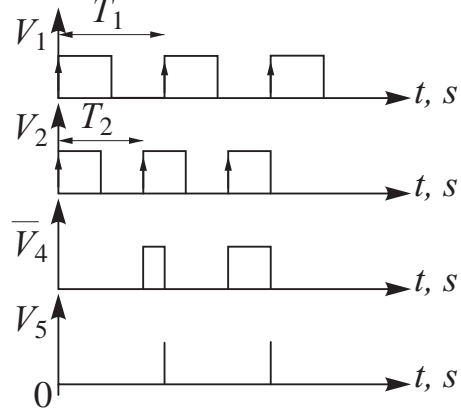
$$\frac{2\pi}{\varphi} = n \quad (12)$$

where n is integer, then when k is equal to n , the phase difference between two signals will be 0 or -2π , or $+2\pi$. The coefficient n represent the number of points, which describe phase - voltage response.

Example: If $\varphi = \frac{\pi}{4}$ then $n=8$, i.e. after 8 impulses the phase difference between v_1 and v_2 will be 2π .

Very important result for simulation is that the phase difference φ is linearly proportional of the time. This gives opportunity to change the time line of transient analysis with a phase line, i.e. x-axes is phase. The alteration step of this phase is different from the time step in transient analysis and is equal to coefficient n .

On Fig. 3 it is shown a scheme of a common digital frequency sensitive phase detector. This scheme is well known and studied and its phase - voltage response is varied from -2π to $+2\pi$. If two impulse generators are used with different frequencies this alteration will be only from 0 to $+2\pi$ or from 0 to -2π . This comes from the rotation direction of the phase which can be positive or negative. The full scale phase - voltage response can be produced if one of D-flip-flop is set to start from 1 as initial condition. In the scheme on Fig. 3 this is done by R6 and C2. This circuit hold on the D- flip-flop U1A at a logic level 1 for a time, which is much less then one period of the input signal v_1 but much more then the time of rising front. The initial condition sets an initial phase difference equal to -2π .


 Fig. 4. Input/Output time diagrams, when scheme is set to start whit phase difference $\varphi = -2\pi$ rad

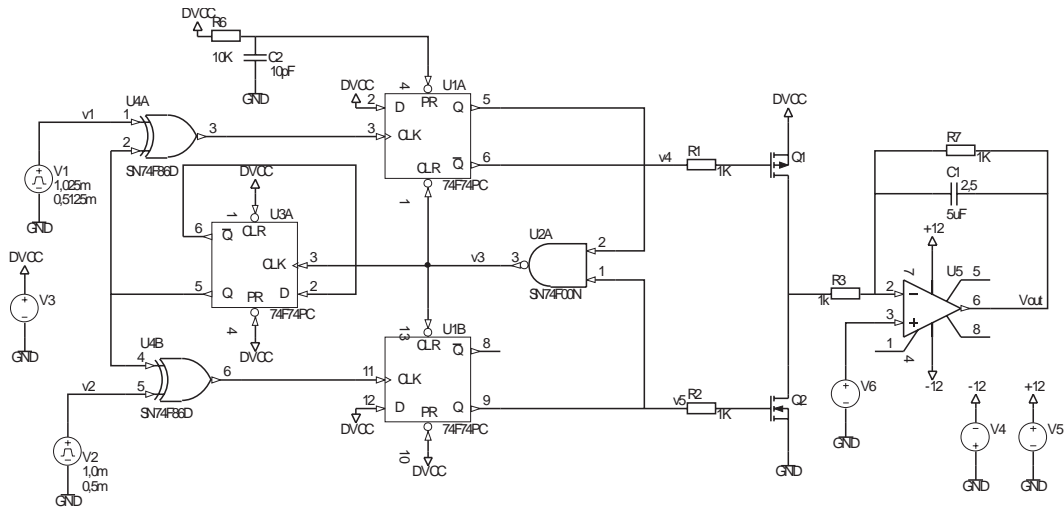


Fig. 6. Scheme of phase detector using both fronts of compared signals

Simulation parameters are:

- The time period of v_2 is 1 ms and the time of impulse is 0,5 ms (it is shown on Fig.3 near by the generator V2). This define a frequency of 1 kHz and a duty cycle of 50%
- The number of points of phase - voltage response in interval -2π to 0 is 40, i.e. $n=40$.
- From Eq. 12 and 11 for signal v_1 is calculated period 1,025 ms and the time of impulses is 0,5125 ms (it is shown on Fig.3 near the generator V1). This define frequency of 0,9756 kHz and a duty cycle of 50%.
- It is set as an initial condition on capacitor C1 voltage of 2,5 V. This is done because when the phase difference is equal to 0 (i.e. $\varphi=0$ rad), than the output voltage is $\frac{1}{2}$ of the whole voltage range (the power supply is 5 V). To skip the setting time of circuit it is recommended to set in simulation 2,5 V on capacitor C1.
- 2,5 voltage is set to not-inverting input of an operational amplifier by a generator V6.
- In transient analysis the time step is set at 10 μ s, the start time of the analysis is 0 s and the end time of the analysis is 80 ms.

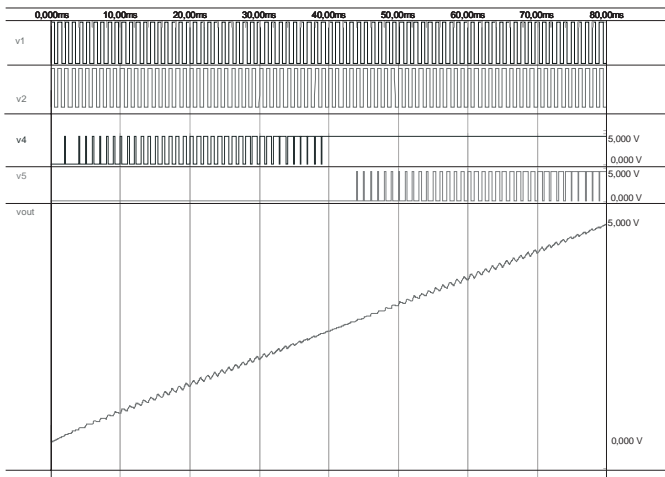


Fig. 5. Transient analysis of common phase detector

Fig. 5 shows a simulation transient analysis of the circuit from Fig. 3. Signals in points v_4 and v_5 give a phase difference between input impulses, which are changed from -2π to $+2\pi$. Output signal V_{out} is proportional of the phase difference which is changed on every period of the input sequence. The diagram of Fig. 5 can be assumed as a phase - voltage response of the scheme of Fig. 3 based on 80 points. It is important to note that this phase - voltage response is not only of the phase detector. It is a phase - voltage response of both the phase detector and the filter used.

II. DIGITAL PHASE DETECTOR USING BOTH FRONTS OF COMPARED SIGNALS

Digital frequency sensitive phase detector using both fronts of compared signals is based on a common scheme and it is shown on Fig. 5. Here input signals v_1 and v_2 are passed on logic elements XOR. These logic gates change working front depending on output signal v_4 and v_5 . The scheme of the digital frequency sensitive phase detector using both fronts of compared signals is shown of Fig. 5.

The simulation analysis method is similar to the previous one. Here it should be considered that the scheme works with both fronts of the input signals, i.e. in one period there is two output signals – one for the time of impulse and another one for the time of pause.

$$V_1 = v_1 \left(kT_2 + \frac{kT_2}{2\pi} (\varphi_{imp} + \varphi_{pause}) \right) \quad (13)$$

If the duty cycle is 0,5 then $\varphi_{imp} = \varphi_{pause} = \varphi$ and the Eq. 13 is:

$$V_1 = v_1 \left(kT_2 + \frac{k \cdot \varphi \cdot T_2}{\pi} \right) \quad (13a)$$

It is clear that the phase step in this case is twice then the one in previous example and the range is from $-\pi$ to $+\pi$.

The alteration of the front of comparison is done by a control D-trigger U3A on the scheme, shown on Fig. 6. When an output impulse is appeared, a control D-trigger changes its condition and respectively, changes the working front.

On Fig. 7 is shown the simulation analysis of the scheme on Fig. 6. Input parameters are the same as the those on previous example, but here for one period of input signal there are two output impulses. That is way the number of the phase steps is twice less, i.e. n is twice less (20) and the end time is twice less (40 ms).

Simulation parameters are:

- The time period of v_2 is 1 ms and the time of impulse is 0,5 ms (it is shown on Fig.6 near by the generator V2). This define frequency of 1 kHz and a duty cycle of 50%;
- The number of points of phase - voltage response in interval $-\pi$ to 0 is 20, i.e. $n=20$.
- From Eq. 13a for signal v_1 is calculated period 1,025 ms and the time of impulses is 0,5125 ms (it is shown on Fig.6 near by the generator V1). This define frequency of 0,9756 kHz and a duty cycle of 50%.

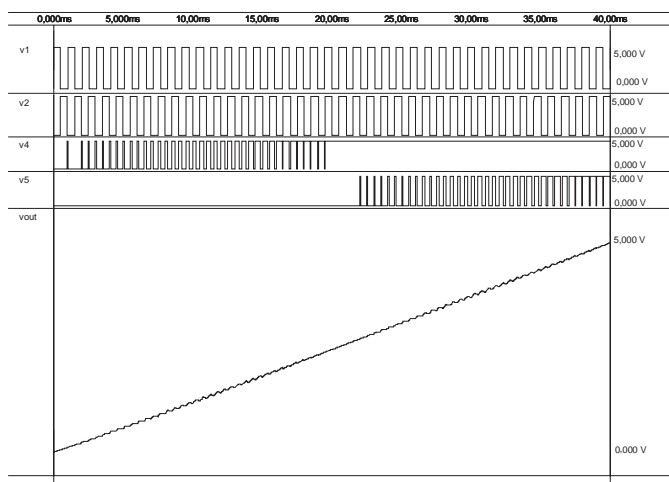


Fig. 7. Transient analysis of phase detector using both fronts of compared signals

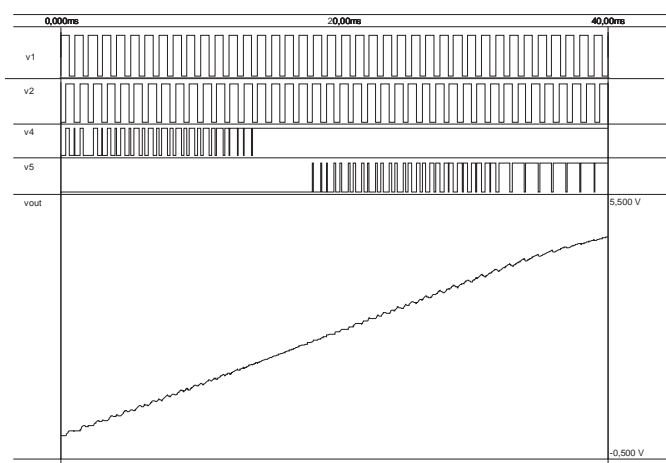


Fig. 8. Transient analysis of phase detector using both fronts of compared signals

On Fig. 8 is shown the simulation analysis of the scheme on Fig. 6. Input parameters are the same as the those on previous

example except the duty cycle of the both input sequences which, is 60% and the initial phase $\varphi = -0,79.\pi$.

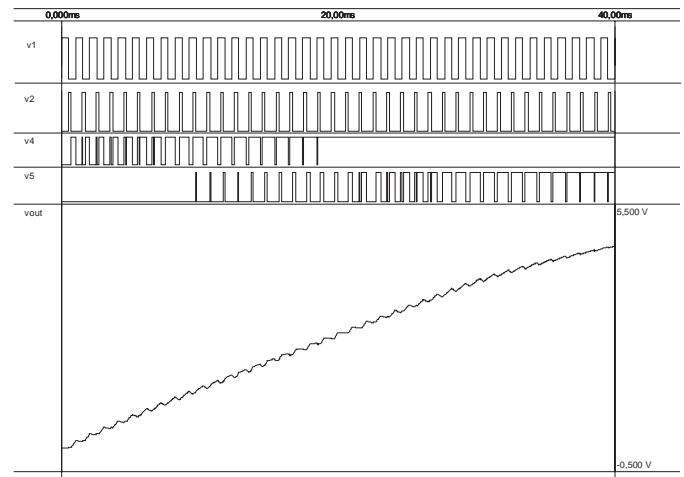


Fig.9. Transient analysis of phase detector using both fronts of compared signals

On Fig. 9 is shown the simulation analysis of the scheme on Fig. 6. Input parameters are the same as the those on previous example except the duty cycle of the input sequences, which is 50% for the signal v_1 and 10% for the signal v_2 . The initial phase is $-\pi$.

III. CONCLUSION

In this paper a method for simulation analysis of digital frequency sensitive phase detectors is presented. It is shown a simulation analysis of a common scheme of a digital phase detector and a simulation analysis of a scheme of digital frequency sensitive phase detector using both fronts of compared signals. The simulations of both schemes showed their specific features. The method gives correctly fundamental phase - voltage response of the examine detector and shows the basic features of the scheme.

Most of the common simulators do not give opportunity to set as an input parameter the phase difference between two generators. That is why to examine this kind of schemes is possible only if the phase is exchangeable with another parameter. The most convenient way is to use transient analysis and input generators with two different frequencies. This method gives a phase difference with constant step and linear constant change of input phase.

REFERENCES

- [1] Mihov G. A Digital Phase Synchronisation of Counters. The fifth National Scientific Conference ELECTRONICS '96. Bulgaria, Sozopol, 1996
- [2] Protel DXP 2004 Training Manual Design Explorer and Document Editor Basics, Altium Limited 2005.
- [3] Andrzej Przedpelski, "Phase-Locked Loop Design Articles", Electronic Design, 10 May 1978.
- [4] A. Willams "Designer's Handbook of Integrated Circuits. Mc Graw Hill" Inc., 1986.

Voltage-Scaling D/A Converters – Analysis and Practical Design Considerations

Dimitar P. Dimitrov¹

Abstract – The following article is an attempt to describe the basics of potentiometric D/A converters.

The analysis of one-stage and two-stage potentiometer-type D/A converters takes into account all the major factors that affect converters' performance. Practical design considerations are also discussed. To support the theoretical analysis, 10- and 12-bit D/A converters were designed and fabricated in 1.0 μm and 0.35 μm double-poly, double-metal CMOS processes. Experimental results are then analyzed. A good agreement between the theoretical analysis and practical results is observed. The D/A converters under discussion are included in a standard analogue cell library and are used in a successive approximation A/D converter as well.

Keywords – DAC, mixed-signal, CMOS

I. INTRODUCTION

Voltage-scaling (or potentiometer-type) Digital-to-Analog Converters (DACs) use resistors connected in series between the reference voltage V_{REF} and the ground node to selectively obtain voltages between these limits, Fig. 1

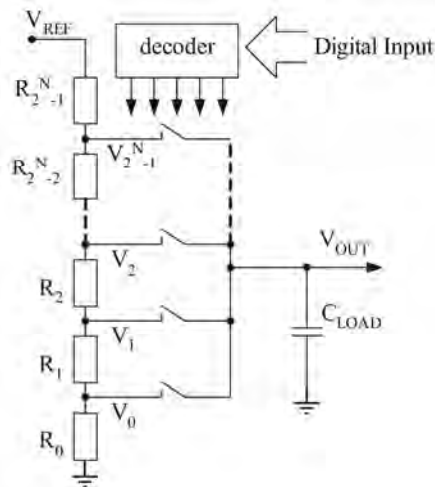


Fig. 1. The principle of operation of potentiometric DACs

With 2^N resistors 2^N reference signals are available and only one of them at a time is passed to the output depending on the digital input. An important advantage of the potentiometer-

type DAC is its inherent monotonicity, since the voltage at each tap cannot be lower than the voltage at the tap below it. The voltage-scaling converters are very suitable for current digital CMOS processes as they only need basic devices and have relaxed requirements for device matching.

In high-resolution applications the number of resistors increases exponentially and becomes too large. For example, a 10-bit DAC requires $2^{10}=1024$ resistors and 12-bit DAC would have $2^{12}=4096$ resistors. Such a big number of resistors occupies too much space; moreover, implementing big arrays of matched devices is difficult and impractical. To reduce the number of resistors required, two-stage structures are used, each of them usually having $2^{N/2}$ resistors, Fig. 2.

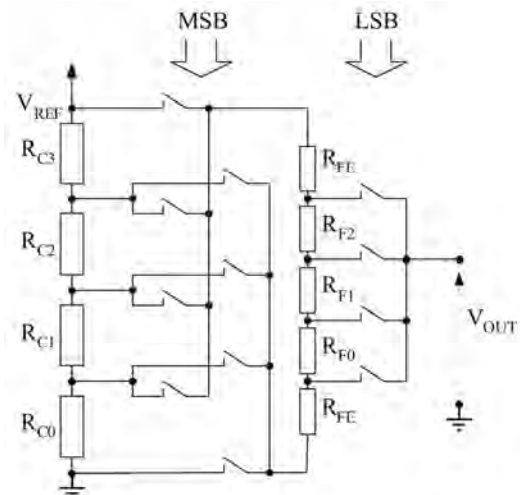


Fig. 2. Two-stage potentiometric DAC

The first stage divides the reference voltage into $2^{N/2}$ equal voltages which are then split into another $2^{N/2}$ levels. Thus the final resolution remains 2^N , since $2^{N/2} \times 2^{N/2} = 2^N$. However, the total number of resistors is $2 \times 2^{N/2}$ instead of 2^N . For example, a 10-bit two-stage DAC has 64 resistors and a 12-bit DAC has 128 resistors, which is much fewer than the one-stage architecture.

Since single-stage potentiometric DACs can only provide low resolution, the focus in this article is on the two-stage DACs. A good design compromise is to choose the number M of the most significant bits (MSB) that control the coarse divider to equal the number L of the least significant bits (LSB) that control the fine divider. A higher number of MSB would make it difficult to achieve the desired accuracy; fewer MSB would result in more resistors in the fine string and increased output impedance. For that reason and for the sake of simplicity of the equations, the preferred case with

¹Dimitar P. Dimitrov is with Melexis-Bulgaria Ltd, Samokovsko shose 2, Sofia 1138, Bulgaria

$M=L=N/2$ is considered, where N is the total number of bits. Nevertheless, all the expressions are valid if N and $N/2$ are replaced by the actual numbers M and L .

II. ERROR SOURCES IN THE TWO-STAGE POTENTIOMETRIC DACS

A. The influence of the fine resistor string on the coarse string

The straightforward approach to make the coarse resistor string independent of the fine string is to use buffer amplifiers between them, Fig. 2. Buffers, however, imply even more difficulties - true rail-to-rail operation is necessary and the offset voltage of the buffers adds to the total error of the converter. So a simplified topology was chosen instead, which does not need buffer amplifiers, providing some basic requirements are met. When the fine string is connected in parallel to any of the resistors in the coarse string, the actual resistance existing between the terminals of that coarse resistor changes:

$$R_C^{ACTUAL} = R_C \parallel (\sum R_F) = R_C \parallel (2^{N/2} R_F) \quad (1)$$

Hence the voltage drop across this coarse resistor also changes, the error being expressed as (intermediate steps are omitted for clarity):

$$\begin{aligned} \Delta V &= (V_{N+1} - V_N)_{ACTUAL} - (V_{N+1} - V_N)_{IDEAL} \\ &= \frac{V_{REF}}{2^{N/2}} \left(\frac{R_C}{R_C + 2^{N/2} R_F} \right) \end{aligned} \quad (2)$$

Two approaches are possible:

- keeping the error much smaller than 1 least significant bit (LSB)
- making the error exactly equal to 1 LSB

The first approach calls for $R_F \gg R_C$. This is not difficult to realize, but the resulting output impedance is high. The second approach needs

$$R_F = R_C \times \frac{2^N - 2^{N/2}}{2^N} \approx R_C \quad (3)$$

The fine resistors are smaller (less die area) and the output impedance is lower. However, the resistance of the MOS switches, which is added to the fine resistor string, introduces unacceptable errors. For this reason, the first approach is given preference, provided the load capacitance is low (approximately 1-5 pF)

B. Device mismatch

If $T_{(R_I, R_{II})}$ is the transfer function of a potentiometer,

$$T = V_{REF} \frac{R_I}{R_I + R_{II}} \quad (4)$$

then the absolute deviation of the output voltage due to resistor mismatch can be expressed as follows:

$$\Delta V_O = \frac{\partial T}{\partial R_I} \times \Delta R_I + \frac{\partial T}{\partial R_{II}} \times \Delta R_{II} \quad (5)$$

$$\begin{aligned} \Delta V_O &= V_{REF} \times \\ &\left\{ \frac{-R_I R_{II}}{(R_I + R_{II})^2} \times \frac{\Delta R_I}{R_I} + \frac{R_I R_{II}}{(R_I + R_{II})^2} \times \frac{\Delta R_{II}}{R_{II}} \right\} \end{aligned}$$

The maximum is reached when

$$\begin{aligned} R_I &= R_{II} = 2^{N/2} R \\ \frac{\Delta R_I}{R_I} &= -\frac{\Delta R_{II}}{R_{II}} = \delta R \\ \Rightarrow \frac{\Delta V_O^{MAX}}{V_{REF}} &= \frac{\delta R}{2} \end{aligned} \quad (6)$$

In the case of two-stage voltage-scaling DACs, the worst deviation from the ideal output is at mid-scale too. The corresponding output is:

$$\frac{\Delta V_O^{MAX}}{V_{REF}} = \frac{\delta R_C}{2} + \frac{\delta R_F}{2 \times 2^{N/2}} \quad (7)$$

The overall accuracy is actually determined by the coarse resistor string. The matching of two identically designed resistors can be described as [4]:

$$\sigma_R = \frac{A_R}{\sqrt{W_R \times L_R}} \quad (8)$$

where A_R is a process-dependent coefficient. In the case of an N -bit voltage-scaling DAC, R_I and R_{II} are composite resistors, each of them composed of 2^{N-1} unit resistors. Hence the mismatch of the composite resistors is

$$\delta R_I, \delta R_{II} = \frac{1}{\sqrt{2^{N-1}}} \times \delta R \quad (9)$$

Eq. 9 shows an important advantage of voltage-scaling DACs as opposed to binary-weighted architectures: for the same accuracy, matching does not need to be very high. More details on resistor matching are given in Section III – Experimental results.

C. Major carry transitions and differential nonlinearity

For most input codes the on-resistance of the switches has little impact on the device operation as R_{ON} is low compared to the total resistance of the fine resistor divider. There are, however, some codes where R_{ON} directly affects the converter's differential nonlinearity. These are the transitions at which the fine divider is first connected across nodes M and $M-1$ of the coarse divider with all fine bits "1s" and then the

fine divider is connected across nodes M and M+1 of the coarse divider with all fine bits "0s", Fig. 3.

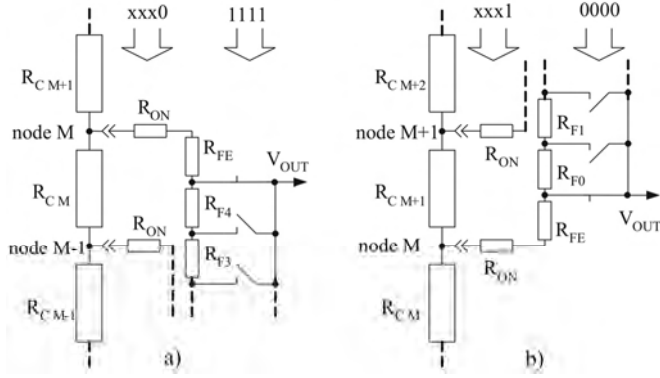


Fig. 3. Evaluating DNL

The voltage step for such a transition is:

$$\Delta V = \frac{V_{REF}}{2^{N/2}} \times \frac{R_C(1+\delta R)^2}{2^{N/2} R_L + R_C(1+\delta R)} + \frac{V_{REF}}{2^N} \times \frac{2(R_{ON} + R_{LE})}{R_L} \quad (10)$$

If we take into account that

$$(1+\delta R)^2 \approx 1+2\delta R \quad (11)$$

$$R_C \ll 2^{N/2} R_F$$

Eq. 10 can be simplified to:

$$\Delta V = \frac{V_{REF}}{2^N} \times \left(\frac{R_C(1+\delta R)}{R_F} + \frac{2(R_{ON} + R_{LE})}{R_F} \right) \quad (12)$$

And the Differential Nonlinearity (DNL) can be expressed in least-significant bits (LSB) as:

$$DNL = \frac{R_C(1+\delta R)}{R_F} + \frac{2(R_{ON} + R_{LE})}{R_F} - 1 \quad (13)$$

The first term of Eq. 13 represents the contribution to the total DNL of the coarse resistor divider. Its influence is negligible (Figs. 7 and 10), for $\delta R=0$ the first term becomes nothing but Eq. 3. The second term of Eq. 13 represents the influence of the switches. As R_{ON} cannot be made zero, the value of the R_{LE} resistors must be adapted to compensate for R_{ON} and keep DNL minimum:

$$R_{LE} = \frac{R_F - R_C}{2} - R_{ON} \quad (14)$$

D. Switch ON-resistance

The On-resistance of a closed MOS switch can be approximated as:

$$R_{ON} = \frac{I_D}{V_{DS}} \approx \mu \times C_{OX} \frac{W}{L} (V_{GS} - V_{TH}) \quad (15)$$

Due to the body effect, the threshold voltage is not constant but varies with the voltage at the switch terminals [3][5]:

$$V_{TH} = V_{T0} + \gamma \left(\sqrt{V_{SB} + |2\Phi_F|} - \sqrt{|2\Phi_F|} \right) \quad (16)$$

where V_{T0} is the threshold voltage for zero voltage at the source, the V_{SB} is the source-bulk voltage and γ is a process-dependant body-effect factor. As a result, the switch on-resistance is not constant but varies with the voltage at the switch terminals. To alleviate the influence of the body effect, P- and N-MOS transistors are connected in parallel to make a complementary switch. Nevertheless, the body effect cannot be fully compensated for (see also Fig. 8).

D. Output impedance and speed

The major limitation of speed is the output impedance of the D/A converter. In contrast to the R-2R ladders, the output impedance of the potentiometer-type DACs varies with the input code applied. The maximum is reached at mid-scale:

$$R_{OUT} = \frac{1}{4} \sum R_F + \frac{1}{4} \sum R_F = 2^{N/2-2} (R_C + R_F) \quad (17)$$

The on-resistance of the switches that select the fine output must be added to this value. Two output types are possible:

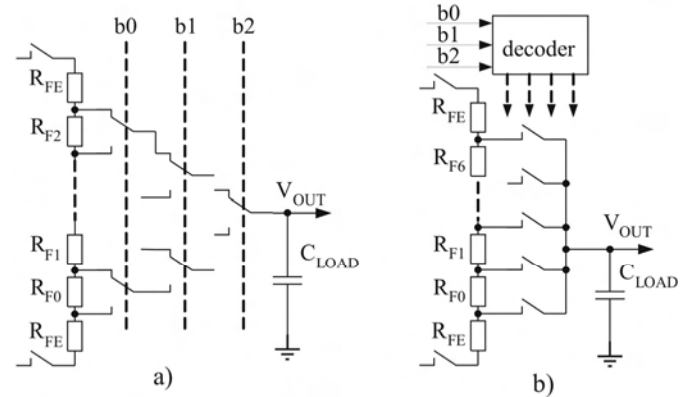


Fig. 4. LSB decoding

a) the binary-weighted tree (Fig. 4.a) does not need an LSB decoder; however, there are always $N/2$ switches connected in series and the total output impedance is:

$$R_{OUT} = 2^{N/2-2} (R_C + R_F) + \frac{N}{2} R_{ON} \quad (18)$$

b) The fully-decoded output (Fig.4.b) uses a decoder to control the switches that connect the output to the taps of the fine string. So the total impedance is:

$$R_{OUT} = 2^{N/2-2} (R_C + R_F) + R_{ON} \quad (19)$$

III. EXPERIMENTAL RESULTS

A family of 10 and 12-bit potentiometric DACs was developed for a standard cell analog library. The converters were fabricated in standard CMOS double-poly, double-metal 1.0 μ m, 0.6 μ m and 0.35 μ m processes. The die photograph of the 12-bit two-stage voltage-scaling DAC is shown in Fig. 4.

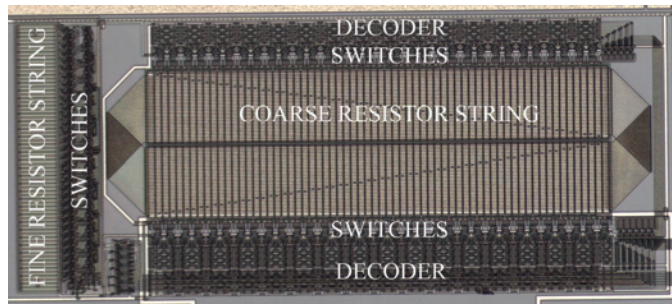


Fig. 5. 12-bit potentiometric DAC, die photograph

In Fig. 5 the matching results of 192 identical Poly1 resistors are shown. Using the same type of resistors, a 2-stage 12-bit potentiometric DAC was realized in a 1.0 μ m CMOS process. The INL and DNL of this converter are shown in Figs. 6 and 7. The coarse divider consists of 64 poly1 resistors and the fine divider consists of 63 poly2 resistors plus two smaller resistors at the ends of the string. The values of the smaller resistors were calculated according to Eq. 14 in order to compensate for the switch on-resistance. It is clearly seen that although the matching properties of the resistors used are not that good (approx. 1.04 % device mismatch), the INL of converter is much better – approx. 1.5 to 2.0 LSB. This is in agreement with the INL of 1.8 LSB predicted by Eqs. 7 and 9. The state-of-art layout that features common-centroid symmetry and equal wire lengths ensures pretty low nonlinearity. Along the DNL curves, the on-resistance of the switches used is shown versus the converter output. As predicted by Eqs. 7, 9 and 13, the overall INL is determined by the coarse resistor mismatch and the DNL is mainly determined by the variation of the switch-on-resistance along the output voltage.

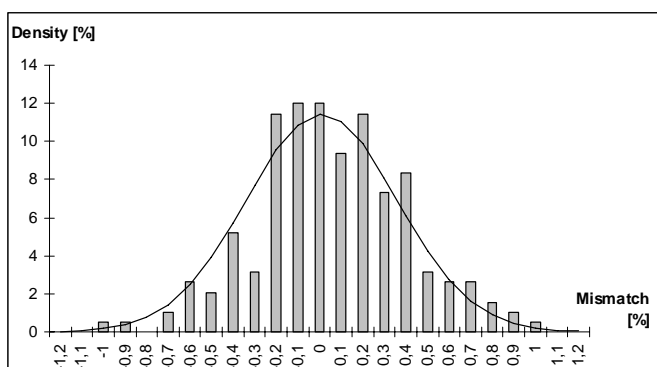


Fig. 6. Measured Poly1 resistor mismatch

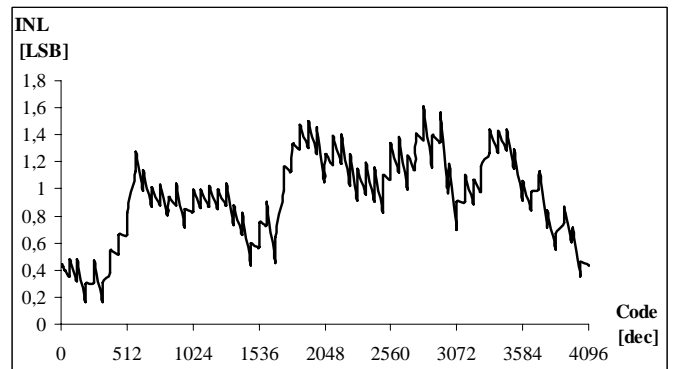


Fig. 7 INL of 12-bit voltage-scaling DAC

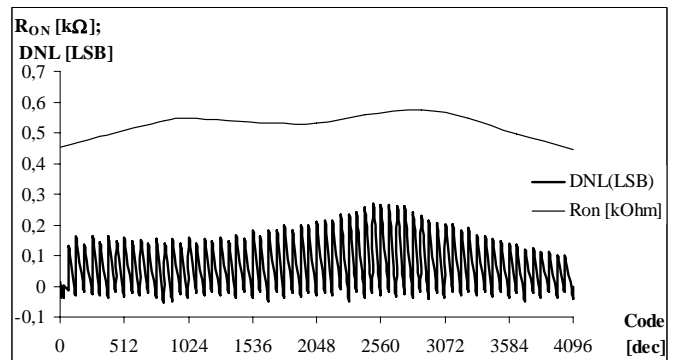


Fig. 8 DNL of 12-bit voltage-scaling DAC

IV. CONCLUSION

The potentiometer-type DAC is discussed in this article as a simple and effective way to guarantee monotonic D/A conversion. Two-stage topologies that circumvent the problems associated with buffer amplifiers are discussed in greater detail. The major sources of nonlinearities in potentiometric DACs are discussed. The derived expressions are proved by means of design experiments. Experimental results agree with the formulae derived in Section II. The developed D/A converters are very suitable for modern digital CMOS technologies.

REFERENCES

- [1] A. R. Hamade "A single-chip All CMOS 8-bit A/D Converter", IEEE JSSC, vol. 13, December 1978, pp. 785-791.
- [2] Mikael Gustavsson, J.Jacob Wikner, Nianxiang Nick Tan, "CMOS Data Converters for Communications" Kluwer Academic Publishers, 2002, pp. 64-79 .
- [3] David A. Johns, Ken Martin, "Analog Integrated Circuit Design", John Wiley & Sons, 1997, pp. 463-469
- [4] Marcel J. M. Pelgrom, AAD C. J Duijnmaijer, and Anton P.G. Welbers, "Matching Properties of MOS transistors" IEEE JSSC, vol. 24, October 1989, pp. 1433-40.
- [5] Paul R. Gray, Robert G. Meyer – "Analysis and Design of Analog Integrated Circuits" ", John Wiley & Sons, 1997, pp. 59-66.

Mechanical Properties of Thin Electrical Films

Silviya Letskovska¹ and Pavlik Rahnev²

Abstract – In this work the base mechanical properties of thin films are described. The attentions is paid of the type of stress state conditions in the system film/substrate, the possible fracture mechanisms. The date for mechanical properties of some commonly used thin films are given.

Key words – mechanical properties, thin film, testing methods.

I. INTRODUCTION

The digital revolution brought about by the development of integrated circuits over the last half century is one of the most astonishing achievements in human history. Most materials used in advanced microelectronic devices are in thin film form. In certain applications, thin films are used as components that carry mechanical loads.

In these applications, the mechanical behaviour behave of the thin-film material is the primary consideration in materials selection. In many other applications, thin films are selected primarily because of their unique electronic, magnetic, optical, or thermal properties. The mechanical characteristics of the materials of choice in such applications are, however, not unimportant because thin films are often subjected to large mechanical stresses during both the manufacturing process and normal operation of the devices.

II. MECHANICAL BEHAVIOR OF THIN FILMS

Generally, mechanical stresses in thin films can be divided into either the so-called intrinsic or growth stresses that develop during the deposition process, or the extrinsic stresses that are induced by external physical effects [1-4].

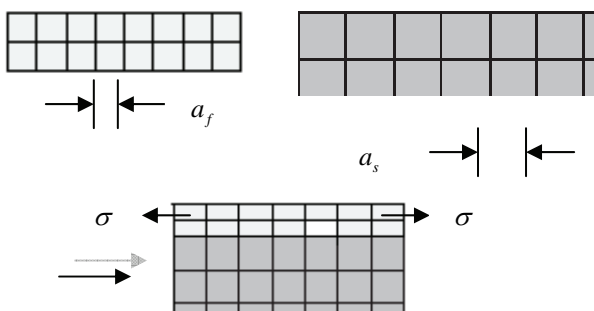


Fig. 1. Film on the substrate.

Thin-film materials are fabricated using very different processing methods than those for bulk materials, such as epitaxial growth and various vapour deposition techniques.

These processing methods often result in development of mechanical stresses in the films. For example - epitaxial stresses arise when films have perfectly coherent interfaces with their substrates (Fig. 1).

There have been many mechanisms proposed for the development of growth stresses, which depend sensitively on the materials systems, deposition technique, and process parameters [5]. These stresses arise because generally films are deposited under *non-equilibrium conditions*. In general, any redistribution of matter will result in film stresses, since the film is constrained by the substrate. Typical behaviour of the average film stress as a function of film thickness is shown in the following Fig. 2.

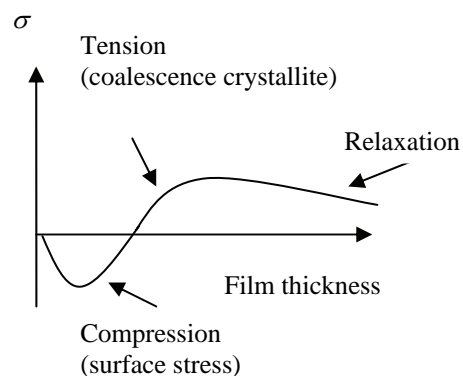


Fig. 2. Film stress as a function of the thickness.

The extrinsic stresses are induced by various physical effects after the film is grown. One of the most commonly encountered examples is the thermal mismatch stress due to the thermal expansion mismatch between a film and its substrate [1]. For an infinitely infinity substrate:

$$\sigma_T = M \Delta T \Delta \bar{\alpha} \quad (1)$$

where: $\Delta \bar{\alpha}$ average, differential thermal expansion; ΔT temperature difference; $M = E / (1 - \nu)$ - the biaxial modulus, for isotropic materials, E - Young's modulus, ν - Poisson's ratio.

The manufacturing process and normal operation of most thin-film based devices often involve large temperature cycles. Therefore, thermal mismatch stresses are inevitable and they can be very high if the thermal mismatch is large and the elastic modulus of the film is large, such as is the case for Cu films used in integrated circuits. Large mechanical stresses are unfavourable in most applications. For example, high

¹Silviya Letskovska is with of Burgas Free University, San Stefano 62, 8000 Burgas, Bulgaria, silvia@bfu.bg

²Pavlik Rahnev is with of Burgas Free University, San Stefano 62, 8000 Burgas, Bulgaria, rahnev@bfu.bg

levels of residual stress in shape memory alloy thin films may prevent a phase transformation from occurring and may lead to loss of the shape memory effect. For piezoelectric thin films, excessive deformations due to large stresses may also cause the material to behave differently from its ideal function. Even though the presence of large mechanical stresses may sometimes not significantly affect the functional properties of thin films, they may still cause a material to fail by promoting the formation of voids or cracks in the films or by delaminating the films from attached layers.

It is clear that the mechanical properties of thin films are very important. It has long been recognized that the mechanical properties of thin films can be very different from those of their bulk counterparts [1, 4, 6]. This phenomenon is generally referred to as a size effect. Some properties can be simply explained through extrapolation of bulk behaviour, but other properties depend sensitively on mechanisms that remain illusive [6]. The strength of thin films is a prime example - a substantial amount of experimental evidence has shown that thin metal films can support much higher stresses than the same material in bulk form. This strengthening has generally been attributed to dimensional and microstructural constraints on dislocation activity in thin films [7]. Dimensional constraints are imposed by the interfaces and the small dimensions typically encountered in thin films, while microstructural constraints arise from the very fine grains often found in thin films. In bulk materials, microstructural constraints dominate the plastic behaviour of the material. However, when material dimensions are comparable to microstructural length scales - as is typically the case for thin films - free surfaces and interfaces play an important role as well. For example, dislocations can exit the material through free surfaces, while strong interfaces can prevent them from doing so. Consequently, strong interfaces lead to a higher cumulative dislocation density in the film and result in a higher flow stress and a greater strain-hardening rate. This behaviour cannot be captured by classical plasticity theories and motivates a strong interest in developing new models to describe it. In addition to dimensional constraints, the microstructure of thin films also affects their mechanical properties. In summary, understanding the deformation mechanisms for thin films is not only important to take full advantage of the materials and improve device reliability, but also important expand to our knowledge of the processing-structure-property relationship, one of the basic tasks in materials science.

The traditional mechanical testing methods used for bulk materials cannot be applied directly to the study of thin films because of the thickness of these materials.

The techniques to characterize the mechanical behaviour of thin films can generally be divided into two main categories:

- Direct testing of thin films deposited on substrates, which involves minimum sample preparation. The film properties are, however, implicitly embedded in the experiment data, and significant post-processing effort is usually required in order to extract the intrinsic film properties;

- Mechanical characterization of freestanding films, which requires careful specimen processing and handling.

These techniques can yield explicit and accurate elastic-plastic properties of the films.

III. TECHNIQUES FOR STUDY

Several of the most widely used techniques in both categories.

3.1. Techniques for films on substrate: the substrate curvature and nanoindentation.

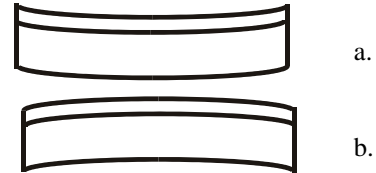


Fig. 3, a, b. Deformation of substrate and film.

Intrinsic stress results from the microstructure created in the film as atoms are deposited on the substrate. Tensile stress results from microvoids in the thin film, because of the attractive interaction of atoms across the voids. Tensile stress - film wants to be "smaller" than the substrate because it was "stretched" to fit. (Fig. 3a). Compressive stress, the film wants to be "larger" than the substrate, because it was "compressed" to fit (Fig. 3b).

In the substrate curvature measurement, strains are imposed by varying the temperature of the film/substrate system if the coefficients of thermal expansion (CTE) of the film and the substrate are different. The stress in the film causes the film/substrate system to bend, the curvature of which can be measured using optical methods. Since the curvature of the substrate may not be zero, it is necessary to measure the substrate curvature prior to film deposition. The change of the substrate curvature, Δk , can be related to the film stress, σ_f , through the Stoney equation [1]:

$$\Delta k = \frac{6\sigma_f h_f}{M_s h_s^2} \quad (2)$$

where: $M_s = E_s / (1 - \nu_s)$ is the biaxial modulus of the substrate, h_f , h_s - the film and substrate thicknesses, respectively. Given M_s , h_f and h_s the film stress can be readily determined as a function of temperature by measuring the curvature of the film/substrate system as a function of temperature. It should be noted that the imposed strain is equibiaxial if both the film and the substrate are thermally isotropic ($\sigma_{xx} = \sigma_{yy}$, $\sigma_{zz} = 0$). The technique is often used to study the thermal mechanical behaviour of metal films on ceramic substrates.

Proper interpretation of the experimental results is not easy because the mechanical response is complicated by the temperature change. Moreover, the strain level that can be imposed is limited by the difference of CTEs between the film and the substrate and the maximum temperature change. The

microstructure of the films may also change during the thermal cycles.

Nanoindentation [8] is a technique that can quickly probe the mechanical properties of various thin films deposited on substrates (fig. 4).

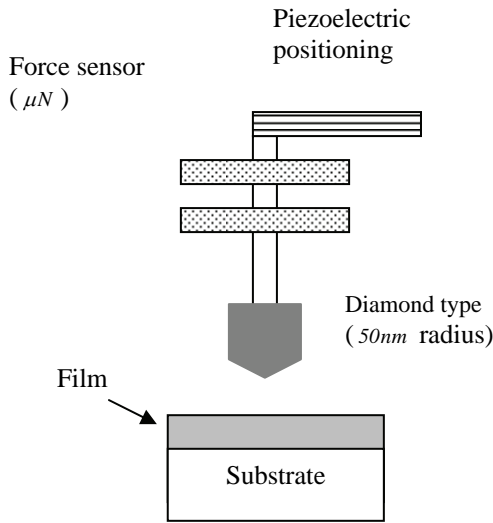


Fig. 4. Nanoindentation test method.

The hardness H is defined as the ratio between indentation load P and projected contact area A ($H = P/A$). The indentation modulus M can be extracted using the following equations:

$$S = (\gamma 2M \sqrt{A}) / \sqrt{\pi} \quad (3)$$

The contact stiffness S is obtained from the slope of the initial portion of the elastic unloading curve; γ is a correction factor for a specific indenter tip shape, e.g., 1.08 γ for a three-sided pyramidal indenter. The hardness, H , is proportional to the material yield stress. Nanoindentation on thin films has uncertainties due to well-known experimental limitations that make it difficult to interpret the experimental data accurately. Most notable among these are the effects due to presence of the substrate, densification of the film as a result of large hydrostatic stresses, issues with tip calibration, surface roughness, and size effects as a result of the non-homogenous strain field. Considerable effort has been devoted to understanding these issues and to relating nanoindentation results to intrinsic material properties [9]. The information that can be acquired from the nanoindentation is also limited. For example, nanoindentation is not suitable for measuring the work-hardening behaviour or the residual stress in the film.

In addition to the substrate curvature technique and nanoindentation, a number of dynamic techniques are available for determining the elastic properties of thin films on substrates. These techniques include surface acoustic wave spectroscopy (SAWS) and surface Brillouin scattering (SBS). These techniques typically require knowledge of the density of the film and only provide information on the elastic behaviour of the films.

3.2. Techniques for freestanding films: the microtensile test [10] and the bulge test [11].

These techniques require some sample preparation, but they can be readily applied to measure intrinsic film properties without any substrate effects, and to obtain thin film constitutive behaviour with relatively large applied strains.

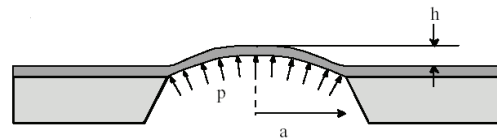


Fig. 5. Bulge test schematic.

The microtensile test is the analogy of its bulk counterpart. Due to difficulties associated with sample handling at the micron or submicron scale, microtensile testing often suffers from alignment and gripping problem, which often leads to inaccuracy in the strain measurement. Spaepen and colleagues [12] have developed a diffraction-based technique for measuring the local strains of a freestanding film by patterning a square array of photoresist islands on the film surface. There are still some uncertainties in the strain measurement due to transverse wrinkling of the freestanding film. Since the film needs to be removed from the substrate before mounting it on the testing stage, residual stresses in the film cannot be measured. The sample handling also limits the thickness of the film that can be tested. Alternatively, a thinner film can be tested by depositing the film on a compliant polymeric substrate and by stretching the film/substrate composite structure. The local stresses in individual grains in the film can also be measured by means of x-ray diffraction.

There is a variation of the microtensile test, the so-called membrane deflection experiment (MDE) that was developed by Espinosa and colleagues [13]. In this technique, a dogbane-shaped freestanding film stripe is micro fabricated with an enlarged contact area at its centre. A nanoindenter tip is used to apply line loading on this contact area and the load is continuously recorded. A nanoindenter tip is used to apply line loading on this contact area and the load is continuously recorded. The gauge section of the freestanding film undergoes a pure stretch and the displacement is measured by means of a full-field interferometric method. This technique involves less specimen handling and offers accurate strain measurement.

The bulge test (Fig. 5) is another powerful technique for measuring the mechanical behaviour of freestanding thin films. In this technique, freestanding thin films are obtained by opening a window in the substrate using micromachining techniques. The film is deflected by applying a uniform pressure to one side of the freestanding membrane. The mechanical properties of the film are determined from its pressure – deflection behaviour. Compared with microtensile testing, the bulge test technique has the unique advantage of precise sample fabrication and minimal sample handling. There are virtually no issues related to specimen alignment and film wrinkling due to Poisson’s effect since the film is supported by Si substrate at all edges. Moreover, the residual stress in the film can be measured. With some care,

freestanding films as thin as 50 nm can be prepared and tested. The results, derive after testing of mechanical properties some films are given in Table 1.

Table 1.

System	Yield σ_{ys} (MPa)	Modulus E (GPa)	Thick h (nm)	T ($^{\circ}C$)	G_c (J/m^2)
$Ta_2N / Al / Al_2O_3$	190	70	178	20	7
$Ta / Al - Cu / Al_2O_3$	298	70	500	20	5.6
$Ta_2N / Au / Al_2O_3$	517	80.8	200	20	1.4
Nb / Al_2O_3	2000	103	105	-	0.95
Ta_2N / Al_2O_3	-	-	100-6000	20	5.5-9.0
$Si_xN_y / SiO_2 / Si$	-	171	1000	20	1.5

Note: G_c - Adhesive Fracture energy.

CONCLUSION

Thin films are an essential component of all advanced electronic devices. Understanding of failure modes in these devices, especially interface delamination, requires a knowledge of the mechanical behavior of the films. Techniques for measuring the mechanical behavior of thin films are being developed and applied. Because the films are formed by condensation from the vapor phase, their microstructures, and hence their mechanical properties, are quite different from those of bulk materials of the same chemical composition. While the general principles of conventional mechanical testing are applicable to thin films, conventional test equipment and techniques are not. It is clear that the functional properties of thin films (single and multi layers) could be determinate using modern methods and devices to analyze the properties of the surface.

These methods allow to receive data for the Young's modulus, hardness, when very small (nanodimensional) volumes of material is used for investigation. The determination of these properties is of primary importance for creating new material structures and also for prediction of possible fracture mechanism.

REFERENCES

- [1] W. D. Nix, Mechanical properties of thin films, Metall. Trans, A 20, 2217 (1989).
- [2] J. Proost, F. Spaepen, Evolution of the growth stress, stiffness, and microstructure of alumina thin films during vapour deposition, J. Appl. Phys. 91, 204. (2002).
- [3] F. Spaepen, Interfaces and stresses in thin films, Acta Mater. 48, 31 (2000).
- [4] R. P. Vinci, J. J. Vlassak, Mechanical behaviour of thin films, Annu. Rev. Mater.Sci. 26, 431 (1996).
- [5] W. D. Nix, B. M. Clemens, Crystallite coalescence: A mechanism for intrinsic tensile stresses in thin films, J. Mater. Res. 14, 3467 (1999).
- [6] S. M. Spearing, Materials issues in micro electro mechanical systems (MEMS), Acta Mater., 48, 179 (2000).
- [7] E. Arzt, Size effects in materials due to microstructural and dimensional constraints, A comparative review, Acta Mater. 46,, 5611 (1998).
- [8] W. C. Oliver, G. M. Pharr, Measurement of hardness and elastic modulus by instrumented indentation, Advances in understanding and refinements to methodology, J. Mater. Res. 19, 3 (2004).
- [9] X. Chen, Y. Xiang, J. J. Vlassak,: A Novel Technique of Measuring the Mechanical Properties of Porous Materials by Nanoindentation with Application to Low-k Dielectric Thin Films, submitted (2005).
- [10] D. T. Read, Y.W. Cheng, R. R. Keller, J. D. Mc Colskey, Tensile properties of free - standing aluminium thin films, Scripta Mater. 45,, 583 (2001).
- [11] J. J. Vlassak, W. D. Nix, A new bulge test technique for the determination of Young's modulus and Poisson's ratio of thin films, J. Mater. Res, 7, 3242 (1992).
- [12] H. B. Huang, F. Spaepen, Tensile testing of free-standing Cu, Ag and Al thin films and Ag/Cu multilayers, Acta Mater. 48,, 3261 (2000).
- [13] H. D. Espinosa, B. C. Prorok, B. Peng, Plasticity size effects in free-standing submicron polycrystalline FCC films subjected to pure tension, J. Mech. Phys. Solids 52, 667 (2004).

An Improved IGBT Behavioral PSpice Macromodel

Tsvetana Gr. Grigorova¹ and Katya K. Asparuhova²

Abstract – The paper presents an improved IGBT behavioral macromodel suitable for OrCAD PSpice. In the new model, like real IGBTs the collector current slightly increases with the collector-emitter voltage. The developed IGBT behavioral model is parameterized and it is implemented as a subcircuit in the OrCad PSpice simulator. The static I-V characteristics offered by the behavioral model are shown. The tailing of the anode currents simulated by the behavioral model at a constant anode voltage-switching test are given. The model shows good agreement with measured results and built in PSpice simulator model.

Keywords – IGBT behavioral PSpice model.

I. INTRODUCTION

The IGBT was introduced into the family of power devices to overcome the high on-state loss while maintaining the simple gate drive requirements of power MOSFETs. The IGBT combines both bipolar and MOSFET structures and possesses the best features of both devices types. Because the IGBT has a low power gate drive requirement, a high current density capability and a high switching speed it is preferable to other devices in many power applications and a practical circuit model for IGBT is needed for simulation. Several analytical models have been implemented into circuit simulators (PSpice [1]-[4] and Saber [5]) in recent years. The IGBT models available in literature can be subdivided as either behavioral or physics-based. The physics-based IGBT models proposed to date, are not easily implemented in circuit simulators, require heavy numerical computations and the knowledge of process parameters, which are not easy to extract from electrical measurements. A significant part of existing behavioral macromodels [5] are physical, based on the internal device structure. The others, considering the semi-empirical relations between terminal voltages and currents, have a poor accuracy and their results are valid only in a narrow range of operating conditions.

However the model still presents some limitations in the saturation region at where the collector current is assumed flat. Real IGBTs show that the collector current slightly increases with the collector-emitter voltage. In this paper, an improvement to the behavioral macromodel, which is presented in [6],[7] is given to overcome this limitation.

¹ Tsvetana Gr. Grigorova is with the Technical University of Sofia, Branch Plovdiv, 61 Sankt Petersburg bul., 4000 Plovdiv, Bulgaria, e-mail: c_grigorova@abv.bg

² Katya K. Asparuhova is with the Department of Electronics and Electronics Technologies, Faculty of Electronic Engineering and Technologies, Technical University-Sofia, 8 Kliment Ohridski bul., 1000 Sofia, Bulgaria, e-mail: k_asparuhova@tu-sofia.bg

II. MODEL IMPROVEMENT

The behavioral macromodel, suitable for OrCAD PSpice, is shown in [6],[7]. In this paper the investigations are extended and an improvement made to the behavioral IGBT model is described.

The DC model is based on the empirical formulas for the IGBT collector current detailed described in [7]. It combines the equations that circumscribe the MOSFET in cut-off, the linear and saturation regions with the equations of a bipolar junction transistor operating in an active mode. The model accounts for high-level injection and the voltage drop in the extrinsic part of the IGBT. The next expressions give the collector current in all regions:

$$I_C = \begin{cases} 0, & \text{if } V_{GE} \leq V_{th} \text{ or } V_{CE} < V_D \\ k \cdot f_2 \left[\frac{(V_{GE} - V_{th})(f_1 V_{CE} - V_D) - (f_1 V_{CE} - V_D)^2}{2} \right], & \text{if } V_{CE} < V_{GE} + V_D - V_{th} \\ k \cdot f_2 \frac{(V_{GE} - V_{th})^2}{2}, & \text{if } V_{CE} > V_{GE} + V_D - V_{th} \end{cases} \quad (1)$$

where V_D is the voltage drop across the emitter-base junction, V_{th} is the threshold voltage of the MOSFET and k is the process transconductance parameter [2].

According to [2], [4] and [7] the correction function f_1 , dependent on gate-emitter voltage, is introduced in order to make the saturation voltage of MOSFET equal to the corresponding IGBT saturation voltage

$$f_1 V_{CEsat} = V_{GE} + V_D - V_{th} \quad (2)$$

The correction function is approximated with an appropriate polynomial. The degree of this polynomial depends on the number of the accounted points and required accuracy

$$f_1 = a_0 + a_1 V_{GE} + a_2 V_{GE}^2 \quad (3)$$

The output current in the saturation region is fitting using the correction function f_2 :

$$\frac{I_{Csat}}{f_2} = k \frac{(V_{GE} - V_{th})^2}{2} \quad (4)$$

where

$$f_2 = b_0 + b_1 V_{GE} + b_2 V_{GE}^2 \quad (5)$$

There has to be noticed that the correction functions f_1 and f_2 are equal to unity for the low level injection (it means for the

small values of V_{GE} , which case is not observed in the practice.

The polynomial coefficients a_i and b_i of f_1 and f_2 are determined from the I_C - V_{CE} curves. Record the coordinates of the saturation points (V_{CEsat} , I_{Csat}) for three given gate voltages V_{GE} . The value of V_{CEsat} is read at the point where the tangent in saturation region is separated from the curve. Using the systems' solutions the correction functions f_1 and f_2 can be calculated for each value of the gate voltage. The introduction of two-correction functions f_1 and f_2 allows the use of the more complex approach that relies on physical modeling.

From the Eqs.(1), it can be seen that the collector current of the behavioral model is saturated absolutely in the saturation region it is a constant with different collector-emitter voltages and just depends on the gate-emitter voltage only. However the collector current of the real IGBT will not be saturated absolutely in reality. So the behavior model is not accurate enough to describe the saturation characteristics and should be improved in the saturation region [8].

Based on the previous model, two assumptions are made: the first is that the collector current in the saturation region increases linearly with the V_{CE} . The second is that all the reverse extended lines of the collector current in the saturation region intersect the x-axis at the same voltage point V_{Early} [8] (Fig. 1).

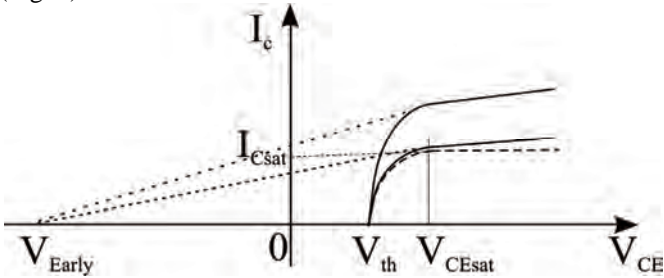


Fig.1. Static I-V characteristics of the improved model

This is similar to the Early voltage in the BJT. Based on these two assumptions, the collector current of the new IGBT model is modeled by adding a linear term to the original model when V_{CE} is greater than V_{th} . The dashed line in Fig.1 presents the original model and the linear term, the solid line presents the new model. From Eqs. (1) the new IGBT model can be written as:

$$I_C = \begin{cases} 0, & \text{if } V_{GE} \leq V_{th} \text{ or } V_{CE} < V_D \\ k.f_2 \left[\frac{(V_{GE} - V_{th})(f_1 V_{CE} - V_D) - (f_1 V_{CE} - V_D)^2}{2} \right], & \text{if } V_{CE} < V_{GE} + V_D - V_{th} \\ k.f_2 \frac{(V_{GE} - V_{th})^2}{2} - K(V_{GE}) \cdot (V_{CE} - V_{th}), & \text{if } V_{CE} > V_{GE} + V_D - V_{th} \end{cases} \quad (6)$$

where $K(V_{GE})$ represents the slope at a given gate – emitter voltage

$$K(V_{GE}) = \frac{I_{sat}(V_{GE})}{V_{Early} + V_{th}} \quad (7)$$

The voltage V_{Early} is determined in MATLAB through *polyfit* function using I_C vs $V_{CE}@V_{GE}$ data. The records are provided by device data sheets or by measurements.

III. IGBT PSpice MODEL IMPLEMENTATION

The behavioral model described above has been developed using ABM method and implemented in the OrCad PSpice simulator as a subcircuit. The DC part of the IGBT model includes the voltage control current sources GVALUE which implement Eqs. (6), using “IF-THEN-ELSE” operator in PSpice.

The dynamic part of the model is described in detail in [7] and is shown in Fig.2.

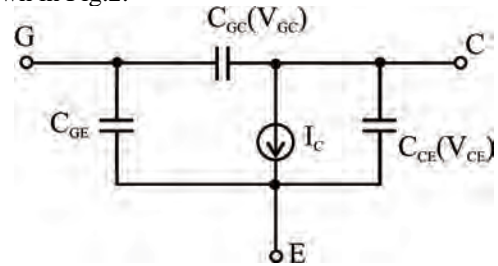


Fig.2 Dynamic behavioral model

From the datasheets, the following capacitance curves can be obtained:

$C_{ies} = C_{GE} + C_{GC}$, $C_{res} = C_{GC}$, $C_{oes} = C_{CE} + C_{GC}$, where C_{ies} is the input capacitance, C_{res} the reverse transfer capacitance, and C_{oes} the output capacitance. The values of the capacitors can be extracted from the dependence of the capacitance vs. V_{CE} for $V_{GE}=0$. To achieve an accurate description of IGBT's switching waveforms, it is necessary to develop a high precision voltage-controlled capacitance model that exhibit nonlinear variation of the corresponding voltages. The graphs from datasheet are digitizing using an appropriate program like GetData. In order to consider the dependence of the capacitors on the gate-emitter voltage their values are obtained by scaling on the fitting expression.

A voltage dependent capacitance, using in the dynamic part, can be specified by using a look-up table, or by using a polynomial. In this paper the look-up table in the ABM expression is used. The nonlinear capacitor in the model is replaced by a controlled current source G, which current is defined by

$$I = C(V)dV/dt \quad (4)$$

The time derivative $dV(t)/dt$ is modeled by using the DDT function in PSpice[9]. This table contains (voltage, capacitance) pairs picked from points on the curve. The voltage input is nonlinearly mapped from the voltage values in the table to the capacitance values. Linear interpolation is used between table values. This voltage dependent capacitance is the multiplied by the time derivative of the

voltage to obtain the output current.

The realization in Spice language is with GVALUE “look-up table” voltage control current source:

$$Table(V(\%IN+, \%IN-), voltage, capacitor)^* \quad (5)$$

$$DDT(V(\%IN+, \%IN-))$$

C_{GC} , C_{CE} and C_{GE} are modeled in this manner.

The process of the device switching is modeled using a voltage-controlled switch S with parameters:

$V_{on} = \{V_{th}\}$, $V_{off} < \{V_{th}\}$, $R_{on} = \{V_{CE(sat)}/I_C\}$ and R_{off} - a very big value corresponding on turn-off transistor.

An advantage of the proposed model is its parameterization. It allows easy implementations of the different IGBT types. A part of the preliminarily extracted parameters are included in PARAM operator – these are V_{th} , V_D , k . Other part is included in TABLE operator – these are the digitizing capacitance plot data. The parameters of the voltage-controlled switch are parameterized too.

IV. SIMULATION AND EXPERIMENTAL RESULTS

For the verification of the model the type CM600-24H IGBT is chosen. In the calculation it was assumed that $V_{th}=6V$, $k=102$. The simulations are made under following initiation conditions: $V_{CE} = 0 \div 12V$, $V_{GE} = 7 \div 12V$.

Fig. 3 shows the static I-V characteristics received from the implemented CM600-24H PSpice model and Fig. 4 shows these offered by the behavioral macromodel.

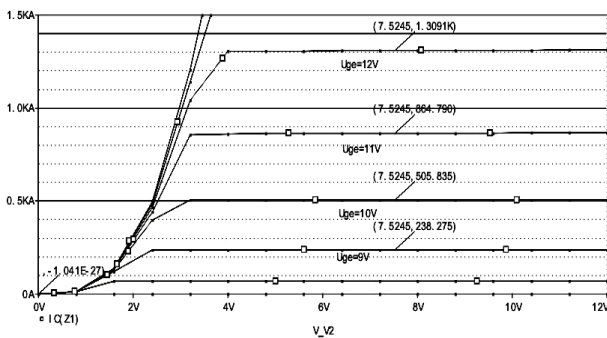


Fig.3. Implemented PSpice model simulated static I-V characteristics for the device CM600-24H

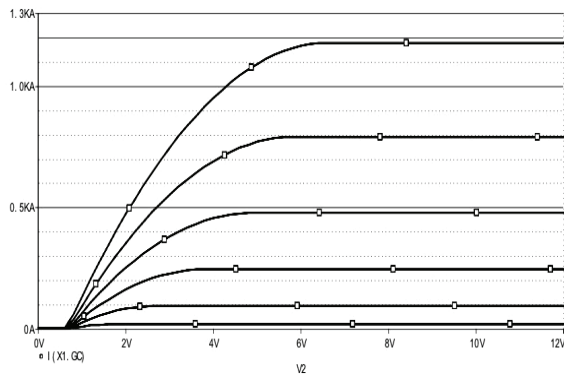


Fig.4. Behavioral macromodel simulated static I-V characteristics for the device CM600-24H

As can be seen in the saturation region the collector current is flat.

Using the Eqs.(6) the improved behavioral macromodel static I-V characteristics are simulated and are presented in Fig.5.

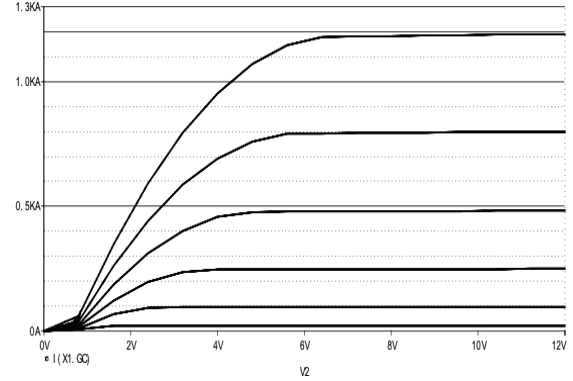


Fig.5. The improved behavioral macromodel simulated static I-V characteristics for the device CM600-24H

It is shown that in the new model, like real IGBTs the collector current slightly increases with the collector-emitter voltage. Fig.6 shows one of the transient test circuits at resistor and inductor load to verify the transient predictions of the proposed model.

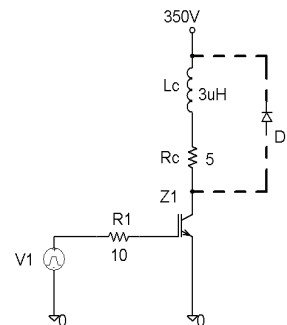


Fig.6. A test circuit at resistor and inductor load

The simulation results of the both models (implemented CM600-24H PSpice model and the proposed behavioral macromodel) are given in the Fig.7.

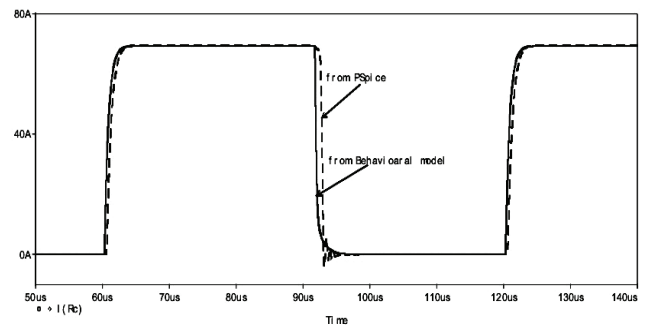


Fig.7 Simulated collector currents at a constant collector voltage-switching test

As seen a very good agreement between transient waveforms is achieved. The error is less than 2%.

On the basis of the proposed macromodel a PSpice behavioral model of IGBT type HGTD10N40F1S is created too [7]. The simulation and experimental results of the IGBT HGTD10N40F1S connected in the test circuit are presented in Fig.8 and Fig.9. The results are given by the following conditions: the supply voltage $V_{CC}=50V$; a load $R_C=10\Omega$ and $L_C=10\mu H$.

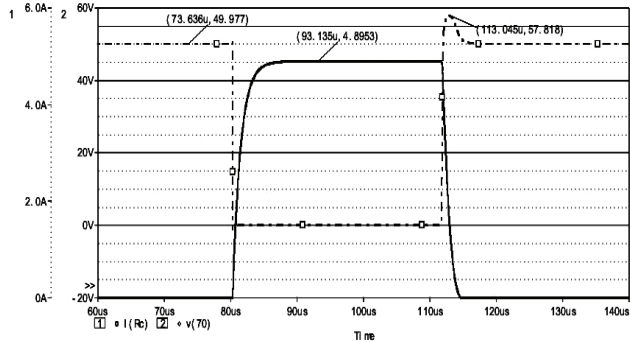


Fig. 8 Transient waveforms using inductive test circuit

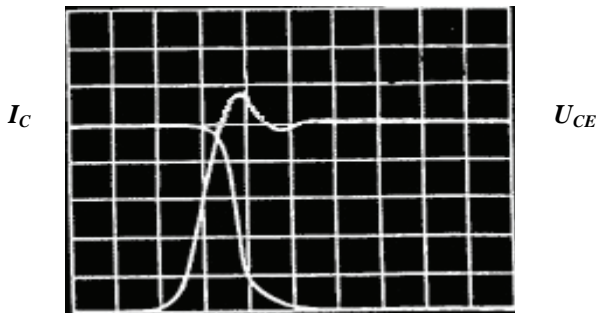


Fig. 9. Test circuit experimental results

The switching curves (U_{CE} and I_C) are given in Fig.9 at the resolution $U_{CE}=10V/div$ and $I_C=1A/div$. The average error between simulation and experimental results is around 3%.

V. CONCLUSION

The improved behavioral IGBT macromodel for OrCad PSpice simulator is presented. In the new model, like real IGBTs the collector current slightly increases with the collector-emitter voltage. The developed IGBT behavioral model is parameterized and it is implemented as a subcircuit in the OrCad PSpice simulator. The static I-V characteristics offered by the behavioral model are shown. The tailing of the anode currents simulated by the behavioral model at a constant anode voltage-switching test are given. The good agreement between the simulation and experimental results can be observed in the paper as the average error is around 3%.

REFERENCES

- [1] Z. Shen, T. P. Chow, "Modeling and characterization of the insulated gate bipolar transistor (IGBT) for SPICE simulation", IEEE Conf. Rec. 5th Int. Symp. Power Semiconductor Devices and IC's, pp. 165-170, 1993.
- [2] F. Mihalich et al., "IGBT SPICE model", IEEE Transactions on Industrial Electronics, vol.42, No1, pp. 98-105, Feb.1995.
- [3] A. Maxim, G. Maxim, "A novel analog behavioral IGBT Spice model", IEEE Trans. on Power Electron., pp. 364-369, 1999.
- [4] H. S. Oh, M. El Nokali, "A new IGBT behavioral model", Solid-State Electron., vol. 45, pp. 2069-2075, Nov. 2001.
- [5] A. R. Hefner, D. M. Diebolt, "An experimentally verified IGBT model implemented in the Saber circuit simulator", IEEE Transactions on Power Electronics, vol. 9, No 5 pp. 532-542, Sep., 1994.
- [6] K. Asparuhova, T. Grigorova, "IGBT Spice Behavioral Model Using the Hammerstein Configuration", 14th International Scientific and Applied Science Conference Electronics ET'2005, Sozopol, Bulgaria, b.1, pp 71-76, 2005
- [7] K. Asparuhova, Tsv. Grigorova, "IGBT behavioral PSpice model", Proceedings IEEE 25th International Conference on Microelectronics MIEL 2006, vol.1, pp. 215-218, Belgrad, Serbia and Montenegro, 14-17 May 2006,
- [8] M. Zhang, A. Courtney, Z. Yang, "An improved behavioral IGBT model and its characterization tool", Proceedings IEEE Electron Devices Meeting, 2000, pp.142-145, Hong Kong, June, 2000
- [9] Intersil Designer's Manual, 1999.

A Stochastic Model of Gamma-Ray Irradiation Effects on Threshold Voltage of MOS Transistors

Mihajlo T. Odalović¹ and Dragan M. Petković²

Abstract – In this paper a stochastic model of gamma-ray irradiation effects on density of charge in oxide of MOS transistors is explained. In this model the Monte Carlo method were used to develop an approach for estimating gamma-ray induced traps spatially distributed in oxide. The developed model enables the gamma-ray induced threshold voltage shift determination as a function on gamma-ray doses.

Keywords – MOS transistors, threshold voltage, gamma-ray irradiation, Monte Carlo method.

I. INTRODUCTION

The gamma radiation can degrade the electrical characteristics of MOS transistors and integrated circuits: threshold voltage, transconductance, leakage current and breakdown voltage [1] - [3]. However, the threshold voltage is considered to be the most radiation sensitive parameter. Also, the investigation of the radiation induced charge is very important for the gamma radiation dosimetry, which can be based on p-channel MOS (pMOS) dosimetric transistors [1]. The threshold voltage shift of gamma irradiated MOS transistors is caused by the change and incorporation of charges in oxide, i.e. introduction charges in SiO₂ (oxide charge) and by increasing the density of Si/SiO₂ traps (interface traps).

Experimentally determined dependences of the threshold voltage shift vs. absorbed dose are reported in many papers [1], [3] - [6]. But, regardless that, a model which is enable to describe the effects of irradiation on gate oxide and threshold voltage don't exist. The existing models very roughly take into account the physical mechanisms of gamma ray interaction with silicon dioxide, regardless that gamma ray absorption and ion formation in the oxide are a stochastic processes. Also, in the threshold voltage estimation, these models neglect the spatial distribution of positive charge in the oxide.

In this paper, we are evaluated an approach for estimating gamma-ray induced charge spatially distributed in oxide, based on Monte Carlo method. On the basis of this model and model of interface states, we are calculated the threshold voltage shift vs. absorbed dose dependencies, which are compared with our previously reported [4] - [6] experimental results.

II. THRESHOLD VOLTAGE OF IRRADIATED DEVICES

The change in threshold voltage of MOS transistor due to the irradiation was determined simply as:

$$\Delta V_T = V_T - V_{T0} \quad (1)$$

where V_{T0} denotes threshold voltage before devices where irradiated, and V_T is the threshold voltage after irradiation. The irradiation directly affects densities of oxide charge $q \cdot N_{ot}$ and interface states N_{it} , the change of threshold voltage caused by the effect of device irradiation can be expressed as:

$$\Delta V_T = \Delta V_{ot} + \Delta V_{it} = \pm \frac{q}{C_{ox}} \cdot \Delta N_{ot} + \frac{q}{C_{ox}} \cdot \Delta N_{it} \quad (2)$$

where C_{ox} is the gate oxide capacitance per unit area. The plus sign applies to pMOS transistors, and minus to nMOS devices. Consequently, in the case of pMOS transistors, the threshold voltage monotonously increased with absorbed dose. But, in the case of nMOS transistors, the threshold voltage decreased with absorbed dose up to certain doses (of about 200 Gy [4]), and then increased as result of rapid increase of negatively charged interface states.

In eq. (2) $q \cdot N_{ot}$ denote effective density of oxide charge on the Si/SiO₂ interface:

$$q \cdot \Delta N_{ot} = \frac{q}{d_{ox}} \cdot \int_0^{d_{ox}} n_{ox}(x) \cdot x \cdot dx \quad (3)$$

where $n_{ox}(x)$ is the concentration of long-term traps in oxide which are occupied by positive charge, i.e. $q \cdot n_{ox}(x)$ denote the concentration of spatially distributed charge towards the Si/SiO₂ interface, builds up in oxide.

Used one modification of a relation from [1] and [7], the density of interface traps charged due to the irradiation of dose D can be expressed as:

$$\Delta N_{it} = (\Delta N_{it})_{sat} \cdot \{1 - \exp[-\alpha_1 \cdot D + \alpha_2 \cdot \Delta N_{it}]\} \quad (4)$$

where $(\Delta N_{it})_{sat} = 3 \cdot 10^{12} \text{ cm}^{-2}$ is the maximal possible density of traps on the interface SiO₂/Si [9], [3]. Coefficients α_1 and α_2 are function on oxide characteristics. We are use the values $\alpha_1 = 1.43 \cdot 10^{-6} \text{ Gy}^{-1}$ and $\alpha_2 = 2 \cdot 10^{-13} \text{ cm}^{-2}$.

¹Mihajlo T. Odalović is with the Faculty of Science and mathematics, Knjaza Milosa 7, 38220 Kosovska Mitrovica, Serbia

²Dragan M. Petković is with the Faculty of Science and mathematics, Knjaza Milosa 7, 38220 Kosovska Mitrovica, Serbia, E-mail: petkovicd@bankerinter.net

III. MODEL OF OXIDE CHARGE CREATION

We assumed that only two mechanisms of gamma ray interaction with oxide are significant, i.e. absorption (dose decrease exponentially with distance) and ionization (with neglecting energy losses of gamma ray). Also, we are used simplified model of ion formation and electron transport across oxide [7], [8]. On this way, as the MOS devices are exposed to the gamma irradiation, the gate oxide becomes ionized by the dose it absorbs and electron-hole pairs are generated. The free electrons drift under the influence of the electric field that appears due to the work function difference between gate electrode and silicon. These electrons would be fairly benign if they drift out of the oxide and disappear, but a small fraction of them were to recombine by hole in the oxide. The fraction of holes remaining from recombination with electrons is subject to a transport mechanism through localized states in the oxide. The holes propagate towards the Si/SiO₂ interface and capture in long-term traps. After sufficient radiation dose, a large positive charge, spatially distributed towards the Si/SiO₂ interface, builds up in oxide. The density of oxide charge can be expressed as:

$$q \cdot n_{ox}(x) = q \cdot \alpha_{ox} \cdot f_y(E_{ef}) \cdot f_{ir}(E_{ef}) \cdot D \quad (5)$$

where α_{ox} is generation coefficient, f_y is the fraction of holes that are transported through localized states, f_{ir} is the fraction of holes that are captured in oxide, and E_{ef} is the effective electrical field in the oxide. The effective electrical field in the oxide is:

$$E_{ef} = E_x - E_{ox} \quad (6)$$

where E_x is the field caused by work function difference and:

$$E_{ox} = (q/\epsilon_{ox}) \cdot \Delta N_{ot} \quad (7)$$

is caused by spatially distributed holes.

Because the processes of gamma ray absorption and electron-hole pair's creation and recombination are stochastic processes, we are assumed that they are randomly occurred with certain probability. Therefore, we are assumed that the oxide is partitioned into number of layers and dose is dispensed on number of portions ΔD absorbed in oxide during time Δt , similar as in [8]. We are suppose that number of produced electron-hole pairs in each layer during the time Δt is Gaussian random variable. During the time Δt , holes migrate toward the Si/SiO₂ interface, and on the end of Δt they are captured in oxide. We are suppose that the electric field, hole mobility and time interval Δt are so small such that hole can move only in the neighbor layer for the time Δt . Also, we are using that number of migrated holes linearly dependent of the resultant electric field in the oxide. Due to this effect, trapped holes will be concentrated in few last layers, close to the Si/SiO₂ interface. Also, created electrons are moving in opposite direction of electric field and can recombine with previously generated and captured holes. We supposed that time required for finish of recombination process in each iteration is much smaller of time step Δt . So,

all created electrons are being recombined or they leave material in time much smaller than Δt . Also, we are assumed that the probability of electrons recombination depends directly on the concentration of previously captured holes.

Suppose that total depth of material is d_{ox} . We will divide whole material in n layers, each of the depth d_{ox}/n . Denote with G intensity of radiation at $x=0$ and with γ absorption coefficient. Then the intensity of radiation at depth x is:

$$g(x) = G \exp(-\gamma x) \quad (8)$$

Denote with α_k number of produced ions in k -th layer during the time Δt . For small ion concentrations, this number is independent of the concentration and for every time interval (of length Δt) is the same. We will suppose that α_k is Gaussian random variable, i.e. that holds:

$$\alpha_k : N(\bar{\alpha}_k, \sigma_\alpha) \quad (9)$$

where mean value:

$$\bar{\alpha}_k = \alpha \cdot g(x_k) \quad (10)$$

is directly proportional to the radiation intensity $g(x_k)$ in k -th layer. Denote with $\rho(x)$ charge density due to ionization.

In the small period of time, after creation, created ions act as holes and due to electrical field migrate in the direction of field. After this small period they become stationary and are not moving till the end of process. In our model we chose that period of time equal to Δt . So, new created ions are moving only in one iteration of our model. Due to this effect, produced ions will be concentrated in few last layers, close to the bound of material ($x=d_{ox}$). That concentration will produce electrical field in opposite direction. We will suppose that the field (and time interval Δt) is so small such that ions can move only in the neighbor layer ($k+1$ -th) for the time Δt . We will use that number of migrated ions $\Delta \alpha_k$ linearly dependent of the resultant field, i.e. that holds:

$$\Delta \alpha_k = \alpha_k \cdot s_1 \cdot [E - s_2 \cdot (\rho_{k+1} - \rho_k)] \quad (11)$$

where we denoted $\rho_k = \rho(x_k)$ and s_1 and s_2 are constants. If the ratio:

$$\frac{\Delta \alpha_k}{\alpha_k} > 1 \quad (12)$$

we will set:

$$\Delta \alpha_k = \alpha_k \quad (13)$$

This means that the field is sufficiently large, so all created ions will migrate to the neighbor layer.

We also included the recombination mechanism in our model. For each created ion we have also one electron created. Electrons are moving in opposite direction of field and can recombine previously generated ions. We supposed that time required for finish of recombination process in each iteration is much smaller of time step Δt (so all created

electrons are being recombined or they leave material in time much smaller than Δt). The probability that electron will be recombined, depends directly on the concentration of positive ions ρ . For the smaller values of ρ , we can approximate this dependence to linear. When ρ becomes large, this probability reaches the saturation. Denote with $\beta(\rho)$ this dependence. In our model we will use the following approximation:

$$\beta(\rho) = \begin{cases} \beta_0 \cdot \frac{\rho}{\rho_{crit}}, & \rho < \rho_{crit} \\ \beta_0, & \rho \geq \rho_{crit} \end{cases} \quad (14)$$

Where with ρ_{crit} we denoted the critical concentration of positive ions when saturation appears and β_0 is saturated probability.

In our model, electrons from the k -th layer can recombine ions from the layers $1, 2, \dots, k$ (because, the field direction does not change during the process). Denote with β_{ki} the number of electrons from k -th layer which enter the i -th layer and with $\Delta\beta_{ki}$ number of recombined electrons in the i -th layer. From previous consideration, we have that $\Delta\beta_{ki}$ is random variable with normal distribution:

$$\Delta\beta_{ki} : N(\overline{\Delta\beta_{ki}}, \sigma_\beta) \quad (15)$$

where mean value is:

$$\overline{\Delta\beta_{ki}} = \beta_{ki} \cdot \beta(\rho_i) \quad (16)$$

For the next entering number we have:

$$\beta_{k,i-1} = \beta_{ki} - \Delta\beta_{ki} \quad (17)$$

If we obtain $\beta_{k,i-1} < 0$, we set $\Delta\beta_{ki} = \beta_{ki}$ and recombination process from k -th layer is over.

IV. RESULTS OF OXIDE CHARGE DISTRIBUTION

This model has been developed through computer simulations using the Monte Carlo method. A clear advantage of such Monte Carlo computer simulations is that it is perhaps to quickly calculate new oxide charge distribution after each dose portion absorbed in oxide. To create Monte Carlo code for our computer simulations, we are employed programming language MATHEMATICA.

In presented calculation, we are accepted that oxide is divide in $n = 30$ layers as oxide thickness is $d_{ox} = 110 \text{ nm}$. In the cases of other oxide thickness, we accept the same ratio d_{ox}/n . Also, we are accepted that the portions of doses ΔD absorbed in oxide during time Δt , are $\Delta D = 1 \text{ Gy}$. On this way, the total absorbed dose is $D = N \cdot \Delta D$, or total time of irradiation is $T = N \cdot \Delta t$.

All of calculation are repeated hundred times with new generated random variable α_k and $\Delta\beta_{ki}$. Presented results are average values of all corresponding calculations.

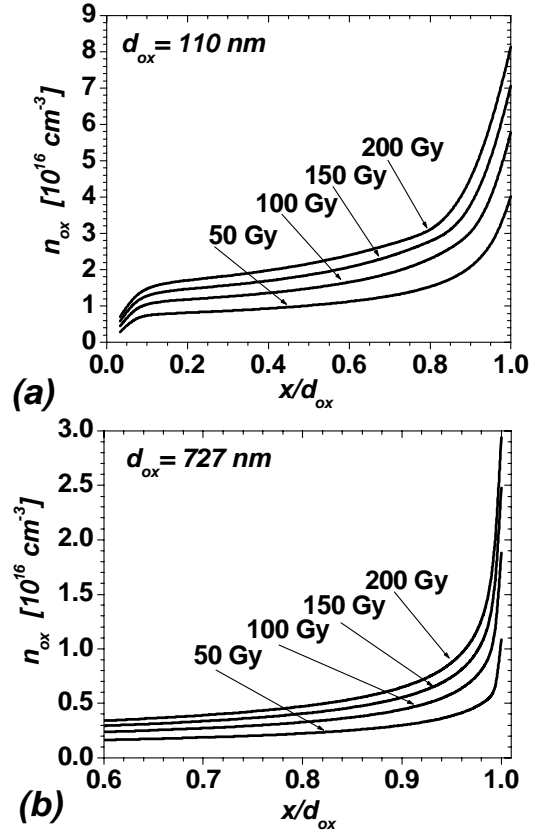


Fig 1. Spatial distribution of the oxide trapped holes induced by gamma ray for different doses of radiation and oxide thickness of 110 nm (a) and 727 nm (b).

On Fig. 1 it is shown spatial oxide charge distribution evaluated by predicted model. It was see that the oxide charges (i.e. trapped holes) are distributed near to the SiO₂/Si interface, but the spatial distribution of them is not negligible. For same doses, the density of trapped holes n_{ox} is lower as the oxide thickness is larger. The density of trapped holes is mainly uniform and has the values which are not negligible. Near the SiO₂/Si interface, the density of trapped hole rapidly increases. In all case, the slope of the holes distribution near the SiO₂/Si interface increases as both of irradiation doses and oxide thickness increases. Also, it was see that the most of trapped holes are distributed in narrow layer near to the SiO₂/Si interface. The thickness of this layer is about 20 nm, for all of irradiation doses and oxide thickness. The influence of irradiation dose on the trapped holes (i.e. oxide charge) density is approximately linear in the range of considered doses (up to 2000 Gy), in the area of uniformly distributed charge, as well as, in the area of rapid density increases.

V. RESULTS OF THRESHOLD VOLTAGE SHIFTS

Fig 2. shows the calculated threshold voltage change ΔV_{th} as a function of radiation dose (lines) and experimentally determined values (dots) for MOS transistors as reported in [4], [5]. In the case of nMOS transistors (fig. 2.a), ΔV_{th} vs. dose dependence show a turnaround (or 'rebound'). This can be explained by fact that at low absorbed doses (up to

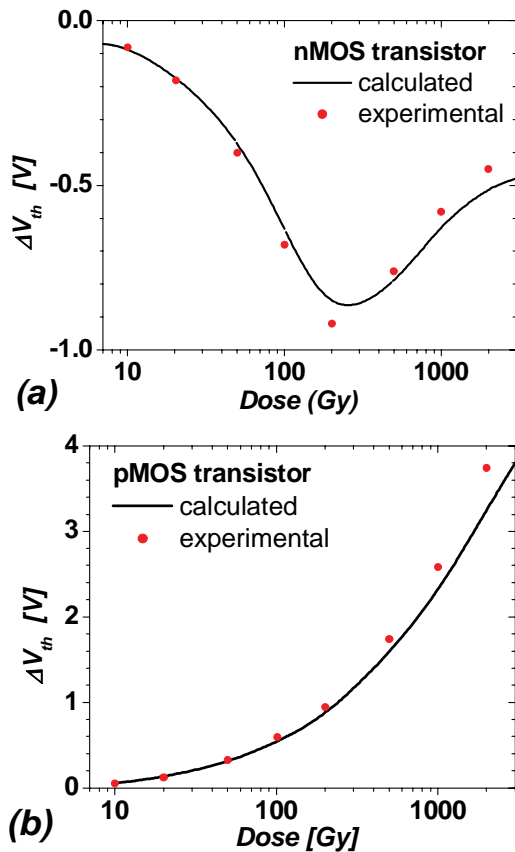


Fig 2. Calculated and experimentally determined threshold voltage shift vs. dose for nMOS (a) and pMOS (b) Al-gate transistor with 110 nm oxide thickness. Experimental results are previously reported in [4], [5].

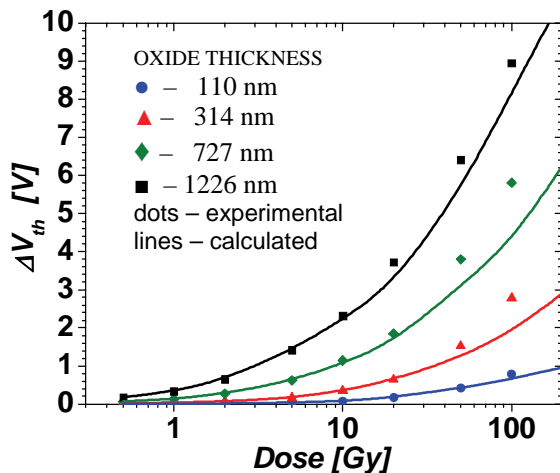


Fig 3. Threshold voltage shift vs. dose dependencies for different oxide thickness. Experimental results are previously reported in [6].

100 Gy) the contribution of trapped oxide charges dominates and results in a decrease of ΔV_{th} and above these doses the density of negatively charged acceptors at the SiO_2/Si interface is not negligible. In the case of pMOS transistors (fig. 2.b), it can be seen that ΔV_{th} increase continually with dose. The agreement of these dependencies with our previously reported [4], [5] experimental results obtained on nMOS and pMOS transistors with same layout and which are

made by same technology processes is good. Therefore, we can conclude that the method of N_{ot} and N_{it} calculation and relation (5) are valid. Also, dependencies on Fig 2 can be explained the fact that pMOS are most sensitive on irradiation than nMOS transistors.

On Fig 3. it is shown calculated and experimentally determined ΔV_{th} vs. dose dependencies for especially designed pMOS transistors with different oxide thickness. These transistors with very thick oxide layer are described in [6]. As it was seen, calculated and experimentally determined dependencies have satisfactory agreement.

VI. CONCLUSION

In this paper we explain a stochastic model based on Monte Carlo method for simulation distribution of charge trapped in SiO_2 gate layer of MOS transistor due to irradiation. This method is based on electron-hole generation model and it is able to calculate the threshold voltage shift ΔV_{th} vs. dose dependencies of irradiated MOS transistors. Calculated dependencies are compared with experiment and satisfactory agreements are shown. Also, we demonstrate that calculated values of effective density of holes trapped in oxide due to irradiation N_{ot} depend on irradiation dose but not depend on oxide thickness.

ACKNOWLEDGEMENT

This work has been supported by the Serbian by Ministry of Science and Environmental Protection (Project KM 141049Γ).

REFERENCES

- [1] A. Holmes-Siedle, L. Adams, *Handbook of Radiation Effects*, Oxford, Oxford University Press, 2002.
- [2] H. L. Hughes, J. M. Benedetto, "Radiation Effects and Hardening of MOS Technology: Devices and Circuits", *IEEE Trans. on Nuclear Science*, vol. 50, pp. 500-521, 2003.
- [3] T. R. Oldham, F. B. McLean, "Total Ionizing Dose Effects in MOS Oxides and Devices", *IEEE Trans. on Nuclear Science*, vol. 50, pp. 483-499, 2003.
- [4] M. Pejović, S. Golubović, G. Ristić, M. Ođalović, "Temperature and Gate Bias Effects on Gamma-Irradiated Al-Gate Metal-Oxid-Semiconductor Transistors", *Japan. J. Appl. Phys.* vol. 33, pp. 986-990, 1994.
- [5] M. Ođalović, B. Vučković, I. Manić, Z. Pavlović, "Investigation of Radiation Sensitivity and Postirradiation Thermal Sensitivity of MOS Transistor", *Proc. 21st International Conference on Microelectronics*, Vol. 1, pp. 357-360, Niš, Yugoslavia, 1997.
- [6] Z. Savić, D. Petković, "Razvoj MOS dozimetra za primenu u ličnoj dozimetriji", *Proc. 18th Yugoslav Symp. on Radiation Protection*, pp. 139-142, Beograd, Yugoslavia, 1993.
- [7] M. Ođalović, D. Petković, "A Model of Gamma-Ray Irradiation Effects in Silicon Dioxide Films and on Silicon Dioxide-Silicon Interface", *Materials Science Forum*, vol. 555, pp. 147-152, 2007.
- [8] M. de Almeida, M. Morales, "Monte Carlo Simulation of a Position Sensitive Gamma Ray Detector", *Brazil. J. of Physics*, vol. 35, pp. 741-743, 2005.

Some Geometrical Considerations Connected with the Planetary Movement of the Substrate During Sputtering

Stancho Pavlov¹ and Dimiter Parashkevov²

Abstract –Thin solid films produced by vacuum deposition have to be uniform in respect of their thickness. One has to pay attention to the geometrical arrangement of substrate and source in the vacuum chamber. Often rotation of the substrate holder around the evaporator is used for getting uniform films. In the present work we describe geometrically the rotation of the substrate plane around an arbitrary axis.

Key words – coordinate systems, rotation, transformation of coordinates, magnetron sputtering

I. INTRODUCTION

In modern vacuum machines great attention [1,2] is paid to the arrangement of all parts built in the vacuum chamber in order to get an uniform thickness distribution of the thin film over the substrates. In most cases the latter are plain: some are circular (Si wafers), other are rectangular (ceramics, glass). To develop a theoretical model of evaporation and afterwards a program for calculation the thickness of the film, one has to know the kind of evaporation source used and the configuration in the chamber. We can get the amount of condensed atoms (thickness of the film) in one certain point of the substrate if we know (in first approximation) for how long and under what flux of evaporated particles this point is exposed. The flux is determined by the space distribution of evaporation and the power of the source. These are technical characteristics of the source equipment.

The time of stay of a chosen point in the particle flux depends on the arrangement: source – substrate and the kind of motion the substrate performs. The substrate motion should ensure best thickness uniformity.

Every vacuum equipment is individual. We have a magnetron sputtering system consisting of 4 cathodes ordered in equal distances one from other and laying in one plane. The substrates are disposed on a plain plate (substrate holder). The target plain is motionless, while the substrate holder is rotating around its own axis and around the plain, where the targets lay. We need to know in every moment of this planetary movement of the substrate the position of every chosen point on it [3].

The aim of this work is to describe in geometrical terms the planetary movement of one plane around another.

¹ Stancho Pavlov, Mathematics Department, Bourgas Prof. Assen Zlatarov University, 1 Prof. Yakimov Str., Bourgas 8010, Bulgaria

² Dimiter Parashkevov, Physics Department, Bourgas Prof. Assen Zlatarov University, 1 Prof. Yakimov Str., Bourgas 8010, Bulgaria, E-mail: paraskhevov@abv.bg

II. ROTATION OF A PLANE AROUND AN ARBITRARY AXIS

We consider a rotation of a plain with a coordinate system bound to it around an axis of a fixed coordinate system.

Let's have the coordinate system $K(O,x,y,z)$. Around the Oz axis a plain σ is rotating. σ is in distance R from the point O has an angle α with the plane Oxy (Fig.1).

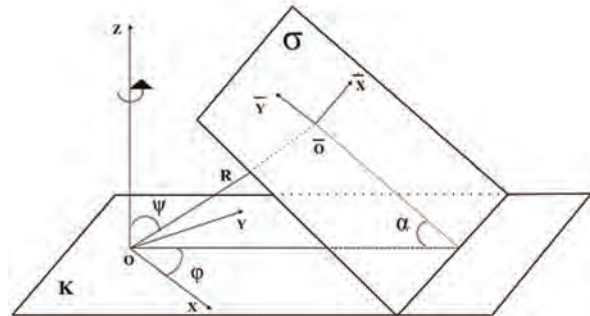


Fig. 1. Coordinate system K with a rotating plane σ

\bar{O} is the orthogonal projection of the point O in σ . We chose in the same plane σ a local coordinate system $\bar{K}(\bar{O}, \bar{x}, \bar{y}, \bar{z})$ with origin of coordinates point \bar{O} , so that \bar{x} is parallel to Oxy and $O\bar{y}$ lays in σ . We denote the fixed angle between Oz and $O\bar{O}$ with ψ , and the varied angle between Ox and the projection of $O\bar{O}$ in the Oxy plane with φ . Using these notations the \bar{O} coordinates in the coordinate system $K(O,x,y,z)$ are:

$$x = R \sin \psi \cdot \cos \varphi; \quad y = R \sin \psi \cdot \sin \varphi \quad (1); \quad z = R \cos \psi \quad (1)$$

If the angle velocity of σ around Oz is ω , it is obviously, that $\varphi = \omega \cdot t$. Let's have an arbitrary point S from σ with coordinates in $\bar{K} - \bar{x}, \bar{y}$ (Fig. 2).

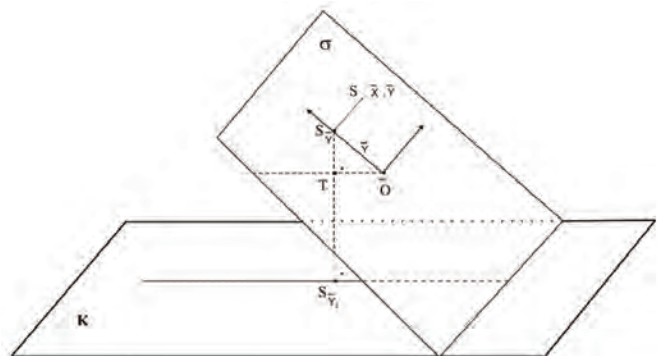


Fig. 2. Point S from σ and its projection in K

$S_{\bar{y}}$ is its projection on the axis $\bar{O}\bar{y}$. $S_{\bar{y}_1}$ is the projection of $S_{\bar{y}}$ in O,x,y plane. Let's T be a projection of \bar{O} over $S_{\bar{y}}$, then $\angle S_{\bar{y}}\bar{O}T = \alpha$ and $S_{\bar{y}}T = \bar{y} \cdot \sin \alpha$, $\bar{O}T = \bar{y} \cdot \cos \alpha$.

$Z_{S_{\bar{y}}} = Z_S$ because of that, that $S_{\bar{y}}S_{\bar{y}_1}$ is parallel to Oxy .

Besides that:

$$Z_{S_{\bar{y}_1}} = T S_{\bar{y}_1} + Z_{\bar{O}} + \bar{y} \cdot \sin \alpha = R \cos \psi + \bar{y} \cdot \sin \alpha \quad (2)$$

To find out S_x and S_y we project σ over the plane O,x,y . The projections of the different elements we denote with an additional index "1" (Fig.3).

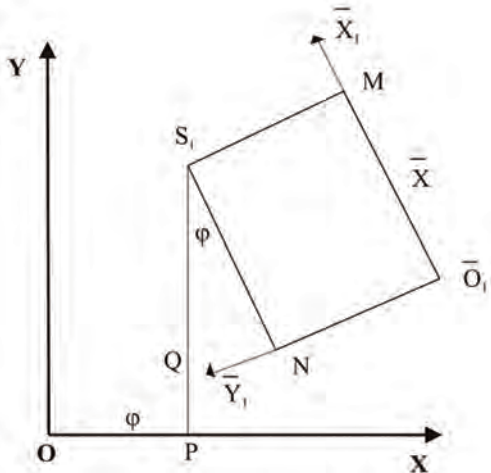


Fig. 3. Some points and segments in the plane O,x,y

Because $O\bar{O}$ is perpendicular to σ and $\bar{x} \parallel Oxy$ it follows, that $O\bar{O}_1 \perp \bar{O}_1\bar{x}_1$. From $\bar{O}\bar{y} \perp \bar{O}\bar{x}$ follows, that $\bar{O}_1\bar{y}_1 \perp \bar{O}_1\bar{x}_1$. We denote the projections of S_1 on the axes $\bar{O}_1\bar{x}_1$, $\bar{O}_1\bar{y}_1$ O,x with M, N and P respectively. From the fact, that $\bar{O}\bar{x}$ is parallel to O,x,y follows that, the distances along this axis remain the same when projected, this means $\bar{O}_1M = \bar{x}_s = \bar{x}$. From the other side $\angle NS_1P = \angle \bar{O}_1OP = \varphi$. The coordinated of S_1 we search are the lengths of the segments OP and S_1P . As can be seen from Fig.2 $\bar{O}_1N = \bar{y} \cdot \cos \alpha$. Further $S_1Q = \bar{x} / \cos \varphi$ and $NQ = \bar{x} \cdot \text{tg } \varphi$.

The projection of $O\bar{O}$ over Oxy is $O\bar{O}_1$ and has the length $R \sin \alpha$. From here follows:

$$OQ = O\bar{O}_1 - \bar{O}_1N - NQ = R \sin \alpha - \bar{y} \cdot \cos \alpha - \bar{x} \cdot \text{tg } \varphi \quad (3)$$

Therefore:

$$x_s = x_{s_1} = OP = OQ \cos \varphi = R \sin \alpha \cos \varphi - \bar{y} \cdot \cos \alpha \cos \varphi - \bar{x} \sin \varphi \quad (4)$$

$$y_s = y_{s_1} = S_1P = S_1Q + QP = \bar{x} / \cos \varphi + OQ \sin \varphi = \bar{x} / \cos \varphi + (R \sin \alpha - \bar{y} \cdot \cos \alpha - \bar{x} \cdot \text{tg } \varphi) \cdot \sin \varphi = \bar{x} \cos \varphi + R \sin \alpha \sin \varphi - \bar{y} \cdot \cos \alpha \sin \varphi \quad (5)$$

Finally, when we know the coordinates of S toward $\bar{K}(\bar{O}, \bar{x}, \bar{y}, \bar{z})$ in the plane σ , which has $\angle \alpha$ with Oxy ($\angle \psi = \angle \alpha$), the distance R from O with an angle φ between Ox and the projection $O\bar{O}$ in Oxy we get the following formulas for the coordinates of the point S in K:

$$x_s = R \sin \alpha \cos \varphi - \bar{y} \cos \alpha \cos \varphi - \bar{x} \sin \varphi = x_o - \bar{y} \cos \alpha \cos \varphi - \bar{x} \sin \alpha \quad (6)$$

$$y_s = R \sin \alpha \sin \varphi - \bar{y} \cdot \cos \alpha \sin \varphi + \bar{x} \cos \varphi = y_o - \bar{y} \cdot \cos \alpha \sin \varphi + \bar{x} \cos \varphi \quad (7)$$

$$z_s = R \cos \alpha + \bar{y} \sin \alpha = z_o + \bar{y} \sin \alpha \quad (8)$$

III. PLANETARY MOVEMENT OF THE SUBSTRATE PLANE

The planetary movement itself is a combination of two rotations of a body (plane): one rotation around its own axis and at the same time and independently from that around another central axis. The angular velocities of both rotations are in general different.

In our case (Fig. 4) the matter of interest is the rotation of σ , the plane, where the substrates are disposed (substrate plain) with an own angular velocity ϖ around an axis coincidental with the perpendicular R to σ and passing through \bar{O} . Besides that there is another independent movement around the Oz axis with an angular velocity ω .

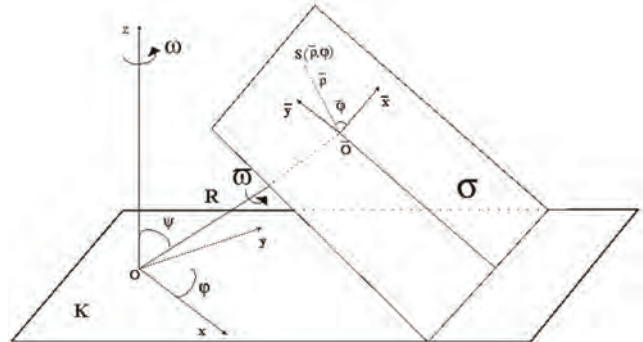


Fig. 4. Planetary rotation with two angle velocities ω and ϖ

The angle dependences by these two rotations are: $\dot{\varphi} = \omega \cdot t$ и $\dot{\varphi} = \omega \cdot t$. To describe the whole motion (planetary rotation) it is convenient in this case to use polar coordinates in the σ plane: $\sigma = \sigma(\rho, \sigma)$. Substituting in (6), (7) and (8) and having in mind, that R and α are parameters we can express x_s, y_s и z_s trough φ, ρ, σ .

These geometrical relationships give us in every moment the position of a chosen point of the substrate. This would be enough for creating the mathematical model of planetary rotation.

IV. CONCLUSIONS

We present in details a geometrical model for planetary rotation of a plane, consisting of a rotation around an arbitrary axis in the space and a rotation around another own axis. In the text there are schemes illustrating the transformations of coordinates of a chosen point from a moving coordinate system (substrate plane) to an fixed one.

The results will be used in a software program for predicting thickness distribution of the layer. The program will give an account not only to the particular geometrical conditions but also to the physical and technological parameters of our experimental equipment [4].

REFERENCES

- [1] Leon I. Maissel and Reinhard Glang, "Handbook of Thin Film Technology", McGRAW HILL COMPANY, 1970.
- [2] Lieberman, M. and Lichtenberg, A., "Principles of Plasma Discharge and Material Processing", Wiley Interscience (1994).
- [3] Stancho Pavlov, Dimiter D. Parashkevov, "Mathematical model for the motion of a substrate around the source for producing thin films", Science conference, 22-26 October 2006, Sliven, Bulgaria
- [4] D. Parashkevov, in preparation

This page intentionally left blank.

Program Calculation of Thin Film Thickness in Case of Parallel Arranged Target – Substrate

Dimitar D. Parashkevov¹

Abstract – It's important to forecast the characteristics of thin solid layers before doing experiments. Among them two quantities – film thickness and its uniformity – are very essential.

According to the arrangement of the magnetron sputtering system built in the vacuum chamber (parallel disposition between cathode and substrate) we predict the above mentioned parameters. Some mathematical models for sputtering from different kinds of targets are applied.

We calculate film thickness with software program MAPLE, but for special cases we developed and used our own one, based on the program language DELPHI.

Keywords – film thickness, magnetron sputtering, mathematical models, MAPLE, program language DELPHI.

I. INTRODUCTION

In the thin film technology the **thickness** d of the layer is of significant importance. This quality influences in most cases the electrical, optical, mechanical and other properties of the film [1,2,3]. In order to achieve the same quality of the film all over the substrate we need an equal **thickness uniformity**. The most useful quantity for us in this case would be not the absolute value of the film thickness d [nm] in a point at distance l from the center of the substrate, but the dimensionless ratio d/d_0 , where d_0 is the thickness of the film in the centre of the substrate ($l=0$) and where in most cases the thickness has the highest value.

We have a magnetron sputtering system consisting of 4 targets with $\phi=7,6$ cm each (Fig. 1) built in a vacuum chamber. Three of the cathodes maximum can operate simultaneously with constant power during the whole process. Here we introduce m_l - the mass of the sputtered material with density ρ , produced from one very little sputtered surface unit in one second, that is so to say the mass velocity (intensity) of sputtering.

The substrate holder ($\phi=30$ cm) contains 10 substrates (6.0 cm x 4.8 cm). It is motionless or rotates **parallel to the plane of the targets**. To calculate d or d/d_0 two main cases are considered (d_0 and d are here the thickness in the center and at distance l from the substrate center respectively):

1. Film deposition from **only one sputtered target** on a substrate holder, which center lies on the same vertical Z axis as the center of the first target (Fig. 1).

2. Film deposition from **one or two targets**. The substrate holder is again parallel to the targets, but its center projects on the connecting line between the centers of the two emitting sources. We'll name this case **removed substrate holder**.

We regard in both cases (1. and 2.) three different kinds of sputtered targets: thin *Ring*, *Ideal Disk* and *Real Disk*.

The first two cases are well described in the literature [], the last one gives an account of the different sputtered speed over the disk in our **real** experimental conditions [4].

Our aim is to make choice between different evaporation models and to predict thickness distribution of the film, in dependence of the distance target- substrate holder.

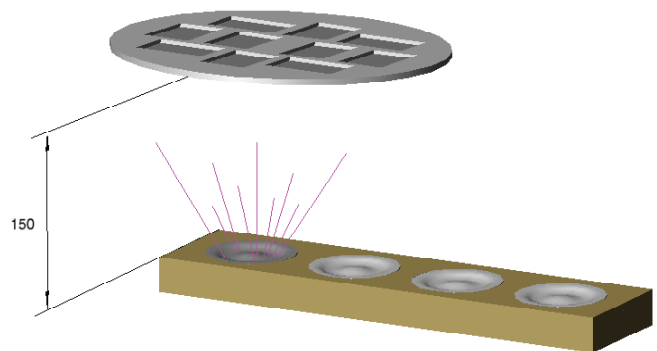


Fig.1: Drawing of the arrangement substrate: holder-sputtered target (150 mm distance between both of them)

II. ONE SPUTTERED TARGET. WORKING WITH MAPLE

The arrangement here is shown in Fig.1. The two centers – of substrate holder and of the sputtered target lay on one and the same perpendicular. Three parameters are important in the mathematical models below:

l - distance from substrate holder center to the considered point, h – height between target plane and the parallel to it substrate plane and s – radius of the sputtered ring ore disks.

For simplicity new arguments: $\frac{l}{h}$ - relative distance instead

of l and $\frac{s}{h}$ - relative radius of the ring (disk) instead of s

are introduced. Assuming a *plain substrate holder, motionless and parallel to the emitting surface (target- and substrate holder center lay on h)*, without more considerations we show the expressions which one need to

¹Dimitar D. Parashkevov, Physics Department, Bourgas Prof. Assen Zlatarov University, 1 Prof. Yakimov Str., Bourgas 8010, Bulgaria, E-mail: parashkevov@abv.bg

introduce in a software program in order to calculate d , d_0 and d/d_0 :

$$d = \frac{M_r}{\pi \rho h^2} \frac{1 + (l/h)^2 + (s/h)^2}{\left\{ \left[1 - (l/h)^2 + (s/h)^2 \right]^2 + 4(s/h)^2 \right\}^{3/2}},$$

$$d_0 = \frac{M_r}{\pi \rho h^2} \frac{1}{\left[1 + (s/h)^2 \right]^3} \quad - \quad (\text{Ring}) \quad (1)$$

$$d = \frac{M_d}{2\pi \rho s^2} \left\{ 1 - \frac{1 + \left(\frac{l}{h}\right)^2 - \left(\frac{s}{h}\right)^2}{\sqrt{\left[1 + \left(\frac{l}{h}\right)^2 + \left(\frac{s}{h}\right)^2 \right]^2 - 4\left(\frac{s}{h}\right)^2}} \right\},$$

$$d_0 = \frac{M_d}{2\pi \rho s^2} \cdot \frac{2 \cdot \left(\frac{s}{h}\right)^2}{1 + \left(\frac{s}{h}\right)^2} \quad - \quad (\text{Ideal Disk}) \quad (2)$$

$$d = \frac{2\tau}{\rho h^2} \int_{s=0}^{3.8} \frac{m_1(s) \cdot \left(1 + \left(\frac{l}{h}\right)^2 + \left(\frac{s}{h}\right)^2 \right)}{\left[\left(1 - \left(\frac{l}{h}\right)^2 + \left(\frac{s}{h}\right)^2 \right)^2 + 4 \cdot \left(\frac{l}{h}\right)^2 \right]^{3/2}} s \cdot ds$$

$$d_0 = \frac{2\tau}{\rho h^2} \int_{s=0}^{3.8} \frac{m_1(s) \cdot s}{\left[1 + \left(\frac{s}{h}\right)^2 \right]} ds \quad - \quad (\text{Real Disk}) \quad (3)$$

Here $M_r = 2\pi s \cdot ds \int_t m_1 dt = 2\pi s ds \tau$, and

$M_d = \pi s^2 \int_t m_1 dt = \pi s^2 m_1 \tau$ are the total amount of

sputtered material during the whole time of evaporation τ in the case of *Ring* and *Ideal Disk* evaporators.

In (1) and (2) we assume $m_1 = \text{const}(t)$ and $m_1 \neq m_1(s)$. In (3) $m_1 = m_1(s)$ and with $m_1(s) = (a + b \cdot s + c \cdot s^2 + d \cdot s^3 + e \cdot s^4)^{-1}$ we give an account of the different speeds of sputtering over the surface of the target in our experiments [1], so we have to integrate over s with respect to $m_1(s)$.

The above written expressions (1), (2) and (3) has to be solved numerically and presented graphically. An appropriate program for this purpose is the program **MAPLE**. The latter is a mathematical software for researches, teachers and students. It uses over 3500 commands, which are spread from the elementary arithmetic and algebra till calculations which include differential equations, program modules, Fourier

transformations and et. **MAPLE** offers good visualization possibilities.

Using **MAPLE** the problem was solved for each of the equations - (1), (2) and (3). We use a substrate holder with $R = l_{\text{max}} = 15$ cm. The upper limit of $\frac{l}{h}$ will vary with h .

So the range of the new argument $\frac{l}{h}$ will be $\left(0 \div \frac{R}{h} \right)$. For

our calculations the common used distances between target and substrate holder are $h = 2; 5; 7; 10; 15; 20$ and 40 cm. These are the standard values on the x axis when plotting only one

dependence $\frac{d}{d_0}$ on the graph. This gives for the upper limit

of $\frac{l}{h}$ the values - 7.5; 3; 2.14; 1.5; 1; 0.75 and 0.375

respectively. These are the standard values on the x axis when plotting only one dependence $\frac{d}{d_0}$ on the graph. By

plotting more than one on the graph the lower limit for x is chosen. By plotting more than one on the graph the lower limit for x is chosen.

Below we show also a graphic comparison ($h = 2$ cm.) performed by **MAPLE** for the above mentioned three cases.

Film Thickness from a Ring, Ideal and Real Disk Evaporator, $h = 2$ cm

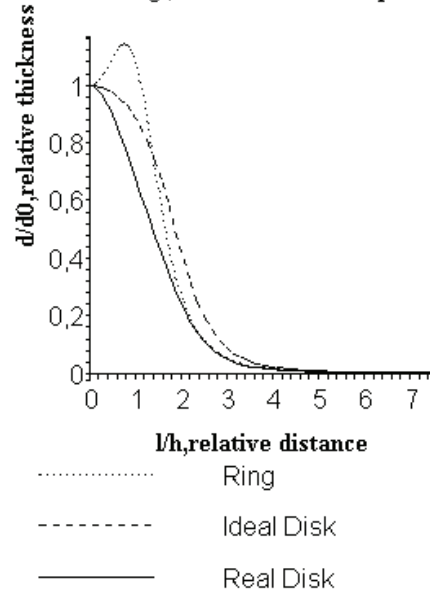


Fig. 2: Comparison : d/d_0 for the three evaporating models of evaporations by short distance h

Because of the *spherical symmetry* of the evaporating arrangement and if $m_1 \neq m_1(s)$ the results we will get for a motionless substrate holder will be the **same for a rotating** one .

III. REMOVED SUBSTRATE HOLDER. A DELPHI BASED PROGRAM

MAPLE is very convenient program for symbolic transformation, but it is not good for numerical calculations, which include sophisticated expressions. We can give an example on hand of equation (3) in the case of a removed substrate holder, that is when the centers of the sputtered target and the substrate holder **didn't** lay on one perpendicular to the parallel plains. The integral (3) is counted by **MAPLE** as **unsolvable** because of the complexity of

$$m_l(s) = (a + b \cdot s + c \cdot s^2 + c \cdot s^3 + c \cdot s^4)^{-1}, \text{ where} \quad (4)$$

$$a = -1,0284864, b = -1,715905, c = 0,0036083349$$

$$d = 4,3724109 \cdot \exp(-9), e = -4,3472891 \cdot \exp(-6)$$

By our new vacuum arrangements, according to the practice [5,6] we use one or two simultaneously emitting cathodes. In both cases the holder center project lays on the connection line of the two target centers (Fig. 3).

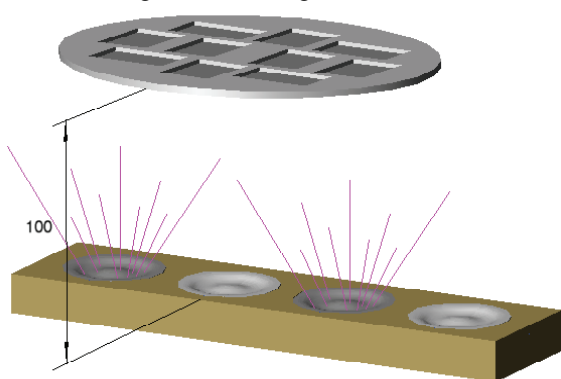


Fig. 3. Two emitting cathodes and a substrate holder above them in 100 mm. distance

The change in the experimental conditions (Fig.3) and the impossibility of **MAPLE** to give an account of them, forced us to develop our own program. The new experimental conditions complicate the development of an adequate theoretical model and appropriate applied program. Here one has to take in account the new technological parameters, such as the disposal between the targets and substrate holder, especially when targets are more than one and the substrates rotate. In this case the model is described with more sophisticated formulas than (1), (2) and (3).

For this purpose we chose the software language **DELPHI**.

DELPHI is based on the program language Pascal and is an environment for programming in Windows.

There are built in components in **DELPHI**, which save our efforts to create a convenient interface. **String Grid** is used for introducing input – and getting the output dates, not important if these are text, numbers or tables. The component **Image** is convenient for getting out graphics and images.

Fig. 4 represents the geometry, used in evaporation from 2 sources.

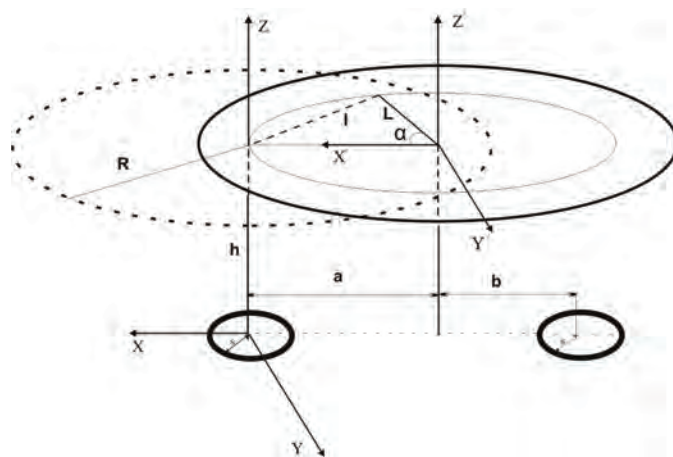


Fig. 4. Geometrical notations for evaporation from two sources, used for creating a theoretical model and a software program

In the component **StringGrid** (Fig. 5) we introduce the input data: height *h*, distance between center of rotation of substrate holder – *L*, the distances *a* and *b* between the cathode centers and the projection of the rotation center.

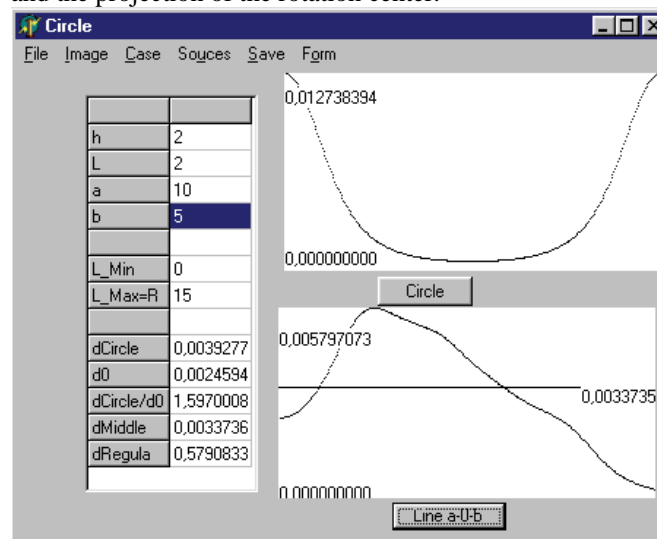


Fig. 4. Interface of the first form of the program

Case from the menu give us the possibility to change the kind of evaporation source: thin ring with radius *s* (**Ring**), ideal disk evaporator (**Ideal**) and a cathode from the experiments (**Real**) with the same radius.

With the option **Source** we can choose one or two identical sources and предлага izbor между един и два еднотипни изпарителя **Save** makes possible to save the results – in the form of tables or graphics.

Using the button **Circle** a graphic image of the thickness *d* over a circle with radius *L* is created. The average thickness value over the same circle is given in **dCircle**, and this in the centre of the holder in the row **d0**. The next row gives the ratio between the two values - **dCircle/d0**.

The button **Line a-0-b** creates a graphical presentation of the thickness d over the line, which connects the projects of the two evaporators on the holder's plane and passing through the centre of rotation O . $dMiddle$ represents the average value of thickness over the mentioned line.

As we already pointed out that a very important characteristic is the thickness uniformity of the layer. It is reported in the row $dRegula$, and is defined by

$$dRegula = \frac{p-s}{p+s}, \quad p = \int_0^{L_Ma} d(x)dx, \quad (5)$$

where

$$s = \frac{1}{2} \int_0^{L_Ma} abs(p/L_Max - d(x))dx.$$

The meanings of p and s from $dRegula$ is shown on Fig. 5.

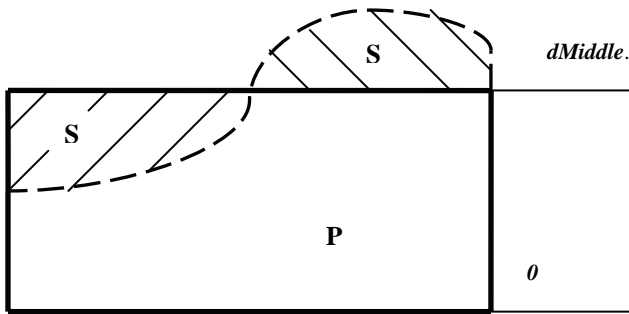


Fig.5. Geometric sense of p and s from $dRegula$

Using the option **Form** from the menu of the first form we go to the screen on Fig. 6.

The values of $C1*dRegula+C2*dMiddle$ for different h , a and b are shown here. The coefficients $C1$ and $C2$ are introduced in the lower part of the form and are responsible for the relative part of these two characteristics ($dRegula$ and $dMiddle$) in the produced layer.

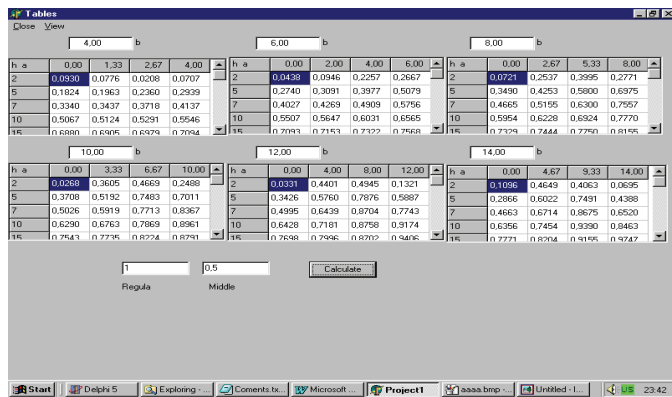


Fig.6. Interface of the second form of the program

Fig. 7 shows a quality picture of the thickness distribution over the substrate holder, which is produced by the same program. The darker parts of the picture corresponds to thicker parts of the film.

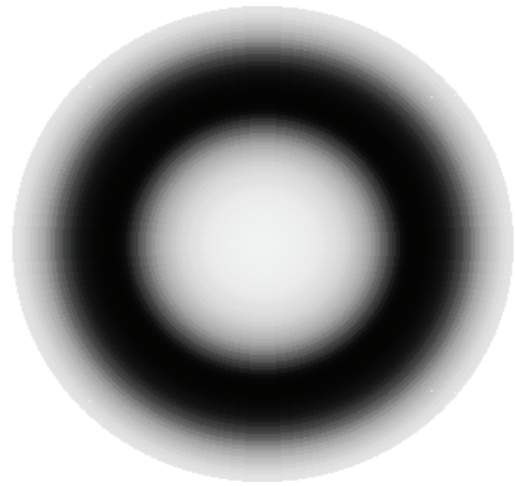


Fig.7. Thickness distribution over the substrate holder

IV. CONCLUSIONS

The problem, set in this work was to find the thickness distribution in a thin film produced by magnetron sputtering. Three different kind (*Thin Ring, Ideal Disk and Real Disk*) of targets were used in order to make a mathematical model of evaporation. The two varieties of one basic arrangement between the plain substrate holder and the target plane, namely parallel to each other need different software programs. In the first case we used a commercial one (**MAPLE**), in the second (*removed disk*) we had developed an **own program** on hand of the program language **DELPHI**.

The problem, announced at the beginning of the work has been solved, using the advantages of the two programs.

REFERENCES

- [1] Leon I. Maissel and Reinhard Glang, "Handbook of Thin Film Technology", McGRAW HILL COMPANY, 1970.
- [2] T. Riekkinen, et. "Reactive sputter deposition and properties of Ta_xN thin films", Microelectronic Engineering, Volume 64, Issues 1-4, October 2002, Pages 289-297
- [3] K.H.Berndt, "Thickness Uniformity on Rotating Substrates", Transaction of the Tenth National Vacuum Symposium of the AVS, 1963, pg. 379.
- [4] Dimiter D. Parashkevov, "Calculating the Thickness of Thin Films, Produced by Different Kinds of Evaporators", Proceedings of the 39th International Scientific Conference on Information, Communication and Energy Systems and Technologies – ICEST 2004, June 16-19, 2004, Bitola, Macedonia, pg. 48-51
- [5] S. Schiller et., "On the use of a multiple magnetron arrangement for metallization of electronic components at high productivity" Surface and Coatings Technology, Volume 36, Issues 3-4, 15 December 1988, Pages 879-892
- [6] Beensh-Marchwicka G., Prociów L., Posadowski W., "Preparation of thermosensitive magnetron sputtered thin films", Vacuum 53, 1999, pp.47-52

POSTER SESSION – PO III

Electronic Components, Systems and Technologies
& Industrial Electronics

Automatic Quality Classifiers of Food Products – Rate of the Speed Problems

Atanas S. Georgiev¹, Lena F. Kostadinova² and Radoslava N. Gabrova³

Abstract – The automatic quality classifiers (AQC) are a basic element of the modern systems for quality control of food products. Of the day direction of the development of these systems is providing traceability of quality in the chain “from the producer to the consumer”. This determines as a fundamental the “on-line” function of AQC, meaning high requirements to the rate of speed

Keywords – Quality of food, Automatic quality classifier, “On-line” quality assessment.

I. INTRODUCTION

The purpose of the investigation is to find out the possibilities for improving the rate of the speed of AQC sorting of food, especially of agricultural products (fruits and vegetables). As a base, some of the modifications of Bulgarian automatic sorting systems of the family AQS: ASM5.01, AQS 4PAP and AQS602, developed in the University of Food Technologies (UFT), Plovdiv, have been used. The general functional model of these systems is presented on Fig.1, where: FOMP is the module realizing the function “feeding the objects to the measuring position (MP)”; OET – “optic-electronically transformation”, formation of the “initial image” as an electrical signal, this is the sensor module (IS) of the system; PPII – “preliminary proceeding of the initial information”, operations as discretization, quantization, filtration, etc. The next functions are the functions that the automatic classifier of the system AQS performs: TIOSS means “transformation of the images of the objects into symptoms’ space”; SDC “standard description of the classes” of the products; RACP - “realization of the algorithm for classification of products” and EFDC “elaboration the final decision for the class of the products”, concerning applying to the proper class. It is evident, that the main element of the system is AQS and the basic directions for improving the rate of the speed of the system have to be searched for in its whole functioning. The last function of AQS, according in Fig. 1, is SP – “sorting products” by quality. Recourses suggested from modules FOMP and SP of the system are object of other investigations [1].

In this paper the possibilities for improving the rate of speed of AQS by more effective “transformation of the initial image” in the symptoms’ space. As an example, in Fig.2, the processed in FOMP image of a product (apple) from the abstract being classified is shown. This image is a result of transformation of the optical signal $\mathbf{E}(x, y)$ into electrical $\mathbf{s}(\xi, \eta)$ in the module OET. The optical signal presents “the light intensity” of the beam, radiated from the product to the module OET, as a result of its transmitting (T) and reflecting (R) ability after lightening with white light. This is the reason of using the indices T and R with \mathbf{s} , or $\mathbf{s}_{(T \cup R)}(\xi, \eta)$. This signal has been formed as an ratio of the transmitting and reflecting abilities at two different, informative for the products, wavelengths of electromagnetic radiance (EMR) – λ_1 and λ_2 . As a norm these wavelengths are in the visible and near infra red (NIR) range of the spectra. The signal $\mathbf{s}_{(T \cup R)}(\xi, \eta)$ formed in FOMP is a result of consecutive two-dimensional discretization.

$$|\mathbf{s}_{(T \cup R)}(i\Delta\xi, j\Delta\eta)| = \Phi_D[\mathbf{s}(\xi, \eta)] = \mathbf{s}(\xi, \eta) \cdot \text{comb}(i\Delta\xi, j\Delta\eta), \quad (1)$$

where Φ_D is an operator of discretization $\text{comb}(i\Delta\xi, j\Delta\eta)$, i.e. fenestration function of the type

$$\text{comb}(\alpha, \Delta\alpha) = \sum_{i=0}^{\infty} \delta(\alpha - i\Delta\alpha) = \begin{cases} \infty & \text{at } \alpha = i\Delta\alpha \\ 0 & \text{at } \alpha \neq i\Delta\alpha \end{cases} \quad (2)$$

and “quantization” (discretization by “level” with the operator Φ_k)

$$|\mathbf{s}_k(i\Delta\xi, j\Delta\eta, k\Delta z)| = \Phi_k[\mathbf{s}_{(T \cup R)}(i\Delta\xi, j\Delta\eta)] = 2^{-v} \text{ent} \frac{\mathbf{s}(i\Delta\xi, j\Delta\eta, k\Delta z) + 2^{-v-1}}{2^{-v}}, \quad (3)$$

where “ent” means operation “rounding”, “k” is a running index of the values by “level”(ordinate z), and for simplicity of writing the index (T ∪ R) has been skipped.

Each point of the image (3) from Fig.2 presents a vector $\mathbf{s}_k(\xi, \eta) \equiv \mathbf{s}_{(T \cup R)}(\xi, \eta) \equiv \mathbf{E}(x, y)$ in three-dimensional space, and the multitude of images of the products from one classified extract form linear vector space. In it each image is described by combination of matrices.

$$\{\mathbf{s}(i, j, k)\} = \{[\mathbf{s}_{ij}]^{(0)}, [\mathbf{s}_{ij}]^{(1)}, [\mathbf{s}_{ij}]^{(2)}, \dots, [\mathbf{s}_{ij}]^{(k)}, \dots, [\mathbf{s}_{ij}]^{(M-1)}\} \quad (4)$$

¹Atanas S. Georgiev from University of Food Technologies, 4000 Plovdiv, 26 Mariza bvd, Bulgaria, E-mail: asgeorg@yahoo.com

²Lena F. Kostadinova from University of Food Technologies, 4000 Plovdiv, 26 Mariza bvd, Bulgaria, E-mail: lenakostadinova@yahoo.com

³Radoslava N. Gabrova from University of Food Technologies, 4000 Plovdiv, 26 Mariza bvd, Bulgaria, E-mail: rgabrova@yahoo.com

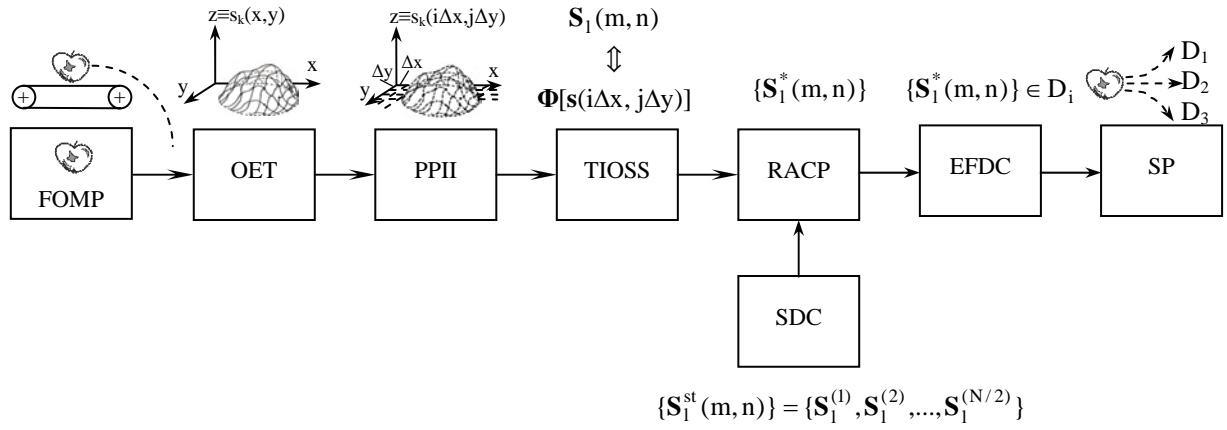


Fig. 1 General Functional Model of Automatic Sorting Systems AQS

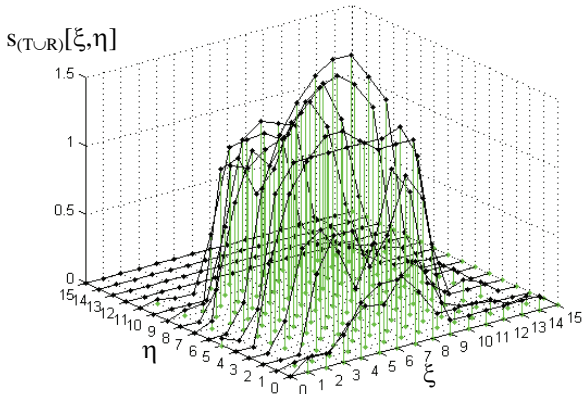


Fig. 2 Processed in FOPM Image of a Product (Apple)

When AQS works in “on-line” conditions (as it is in systems for quality “tracing”), the time for processing the information from the moment of the product entering in AQS, up to completing their sorting in the module SP, is of the rate parts of 1ms. This is determined from the requirements for “productivity” of the system. This is the reason for impossibility of using “initial images” of product (Fig.2), and the necessity of their transformation into new (symptoms’) space with the aim of sizable compression of data saving the value of the information of quality in them. Approaches for solving such tasks suggest “the general theory of signals”, in its part “approaches for harmonic and sequential analysis” of analog and discrete signals. In this way the images (4) from Fig.2 could be presented as equivalent in space with “basic”-functions of the type $\Psi[\xi, \eta; m, n]$, classical example for it could be “discrete exponential functions” (DEF), a base of the harmonic Fourier analysis:

$$\Psi[\xi, \eta; m, n] = \exp\left\{-j \frac{2\pi}{N} (m\xi + n\eta)\right\}. \quad (5)$$

Then $s_k(\xi, \eta)$ will be transformed to space $\{\xi, \eta, l\}$, where the signal will be described by no monotonously decreasing series of coefficients of Fourier decomposition

$$S_1(m, n) = \sum_{\xi=0}^{N-1} \sum_{\eta=0}^{N-1} s_k(\xi, \eta) \exp\left\{-j \frac{2\pi}{N} (m\xi + n\eta)\right\}, \quad (6)$$

where $\frac{2\pi}{N}\xi$ and $\frac{2\pi}{N}\eta$ are space frequencies.

Criteria for choosing a basis for transformation is the assessment of its abilities for using fast algorithms, especially when taking into account, that part of the functions Ψ allow “factorization” and as a result “fast transforms”.

II. RESULTS AND CONCLUSION

A lot of orthonormal transforms have been applied for transformation of the “initial image” in the symptoms’ space of space spectral components of the respective decomposition. The achieved acceleration of the algorithm of transformation will be illustrated with the example of ordinary “discrete” (DFT) and “fast Fourier transform” (FFT).

The space spectra of the product from Fig.2 is presented in Fig.3. If in the description of the “initial image” (3), Fig.2, each row is considered as one-dimensional discrete

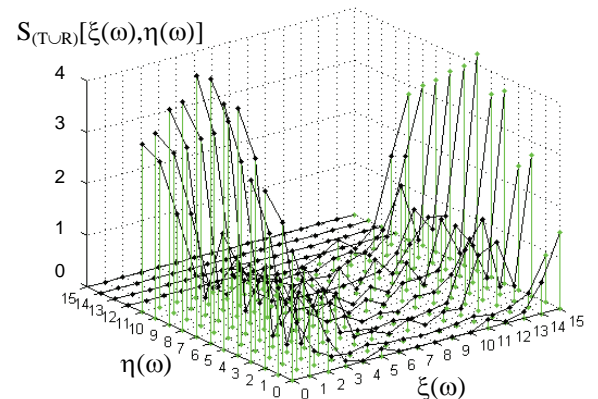


Fig. 3 Space Spectra of the Product from Fig.2

TABEL I

NUMBER OF NECESSARY OPERATIONS IN DFT AND SUGGESTED NEW ALGORITHM AT N=4, 8, 16 И 32

Algorithm	N	4	8	16	32
FDFT		4.1+2.1+8=1	4.3+2.3+24=4	4.17+2.17+64=164	4.49+2.49+160=45
(r.prod.+add.prod.+add.)*		4	2		4
New algorithm (addition)		8	24	100	356
Improved effectiveness, %		42,9	42,9	39	21,6

* real product +addition from products+additions

description of part of the object $s_k(\xi, \eta) = s_k(\xi, \eta = \text{const})$ then for it could be applied one-dimensional DFT

$$S_1(m) = \sum_{\xi=0}^{N-1} s_k(\xi) \exp\{-j \frac{2\pi}{N} m\xi\}, \quad \eta = \text{const} \quad (7)$$

and if DEF is indicated briefly as $W_N^{m\xi} = e^{-j \frac{2\pi}{N} m\xi}$

$$S_1(m) = \sum_{\xi=0}^{N-1} s_k(\xi) W_N^{m\xi}, \quad m = 0, 1, 2, \dots, N-1 \quad (8)$$

$$\xi = 0, 1, 2, \dots, N-1$$

and for all m, the system of equations is

$$\vec{S}_1(m) = \left| W_N^{m\xi} \right| \vec{s}_k(\xi) \quad (9)$$

where $\vec{S}_1(m)$ and $\vec{s}_k(\xi)$ are N-dimensional vectors, respectively of the transformed and the initial description of the products, and $\left| W_N^{m\xi} \right|$ is a matrices of the operator DFT.

At N=16 for realizing of (9) are necessary $N^2=256$ and $N(N-1)=240$ complex additions.

If some conditions, determined from the functions of AQS, are used: (1) because of the presence of great amount of equal values of addends in the system and preliminarily known values of DEF $W_N^{m\xi}$ and their loading in the memory of processor for previously processing of information (DSP); (2) taking into account the periodical character of $\left| W_N^{m\xi} \right|$ when increasing the exponent, the values of DEF repeat these from the first period N, i.e. $\left| W_N^{m\xi+pN} \right| = \left| W_N^{m\xi} \right|$ for p – positive integer, it is possible apriority in AQS to be organized a matrices of production

$$k \rightarrow \begin{matrix} 0 & 1 & 2 & \dots & M-1 & m\xi \end{matrix}$$

$$Q = \begin{matrix} W^0s(0) & W^0s(1) & W^0s(2) & \dots & W^0s(M-1) & 0 \\ W^1s(0) & W^1s(1) & W^1s(2) & \dots & W^1s(M-1) & 1 \\ W^2s(0) & W^2s(1) & W^2s(2) & \dots & W^2s(M-1) & 2 \\ \vdots & \vdots & \vdots & \dots & \vdots & \vdots \\ W^{N-1}s(0) & W^{N-1}s(1) & W^{N-1}s(2) & \dots & W^{N-1}s(M-1) & N-1 \end{matrix} \quad (10)$$

and at N-even number, the exponents decrease to N/2, i.e. the dimension of the matrices will be N/2xM.

Determined this way productions form the system for definition the symptoms:

$$S_1(0) = Q(0, m_{\xi_0}) + Q(0, m_{\xi_1}) + \dots + Q(0, m_{\xi_{N-1}})$$

$$S_1(1) = Q(0, m_{\xi_0}) + Q(1, m_{\xi_1}) + \dots + Q(N-1, m_{\xi_{N-1}}) \quad (11)$$

$$\dots \quad \dots \quad \dots \quad \dots$$

$$S_1(N-1) = Q(0, m_{\xi_0}) + Q(1, m_{\xi_1}) + \dots + Q(1, m_{\xi_{N-1}})$$

in such a way in the algorithm (9) all operations “production” are eliminated and only $N(N-1) \approx N^2$ complex additions are necessary.

In Table 1 are given data for the number of necessary calculations when using DFT, FFT and suggested new algorithm.

It is evident from the data the sizable increasing of the rate of the speed with the new fast algorithm, which has been tested with other orthonormal transformations - “cosine”, “sine”, Hartley, Wavelet etc.

REFERENCES

[1] L.Kostadinova, A. Manliev and A. Georgiev, “Determination the speed of the feeder – conveyer’s belt in case of objective recognition the quality and machine grading of fruits and vegetables”, VII International Conference of Electrical machines and drivers, Elma’93, Varna, 1993, pp.402-410.

[2] A. Georgiev, L. Kostadinova and R. Gabrova, “Problems of discremination and quantization of optic-electronic images of agricultural products in automatic quality classifiers” Scientific Works UFT, vol.XLIV, Iss. 3, pp.286-296.



This page intentionally left blank.

Computer-Aided Engineering with the help of OrCAD

Dimitar M. Kovatchev¹, Ekaterina Dimitrova² and Vencislav C. Valchev²

Abstract – The design of modern electronic appliances always requires some suite of tools to be used. This paper is dedicated to a methodology for design with the help of OrCAD. Some recommendations and more common rules about the whole process of design – from starting a new schematic project, through the circuit description, electrical analysis and simulation, printed circuit board development and fabricating, till the bill of materials and some additional documents, are given as well.

Keywords – OrCAD, PCD, CAE

I. INTRODUCTION

In order to design a modern electrical appliance there is always a need to use some complicated software tools that allow entering and simulating of the electrical circuits, as well as development and preparing to fabricate the corresponding printed circuit boards.

The computer-aided design includes activities from two partially overlapping areas [1] – the automated electrical engineering as well as the drafting and documents automation.

The automation of electrical engineering, often noted as Computer-Aided Engineering (CAE), includes:

- Circuit description – the process of the circuit entering – as text (some languages for hardware description are used, mostly ABEL, VHDL or Verilog) or graphical form (some tools for schematic design are used, there are many of them).
- Circuit analysis – most of all it is a computer-based simulation of the circuit behaviour that could be analog, digital or mixed (analog-digital).
- Technical documenting of the design – some bill of materials, manufacturing and debug reports, operation and repair instructions, etc.

The final result of CAE is an electrical circuit, fulfilling the all requirements of the assigned task.

Some of the activities, included in the drafting and documents automation, often noted as Computer-Aided Design (CAD) itself, are:

- Fitting and placement the elements as well as routing the wires on a common pcb, although in many cases the result could be a monolithic or programmable integrated

circuit (or even a system-on-a-chip).

- Some additional reports, intended for Computer-Aided Manufacture (some times noted as CAM), including so called Gerber files, drill files, mask files, etc.

Both activities are integrated in so called integrated CAE systems, or suits of tools, for example OrCAD, Protel, P-CAD, etc.

Next follows a brief discussion of the design flow with the help of OrCAD - one of widely used suits of tools for CAE. The presentation reflects the experience, collected in the Department of Electronics and Microelectronics, Technical University-Varna. OrCAD is selected mainly because of it is fully compatible with CADENCE – another well known integrated software system for computer-aided design of analog, digital and mixed integrated circuits.

II. PRESENTATION

Fig. 1 is a diagram of the OrCAD design workflow [2]. The left side shows the activities (electrical and/or mechanical), that have to be done when entering the design, in the middle is shown the printed circuit board design and the manufacture and documenting activities are shown in the right side of the

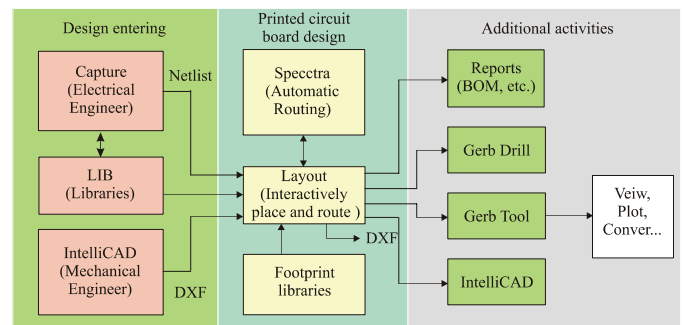


Fig. 1. Design workflow with OrCAD

figure.

The design process could be facilitated, as well as mistakes could be reduced, if the follow important steps are observed.

A. Preliminary activities

Before the beginning of a new project it could be helpful to do the next simple things, that allow better organizing of the design, facilitate its navigation, and make redesign (as well as errors fixing) easier:

- Define a simple and well organized structure of project folders [3]. OrCAD creates many files and holding them

¹Department of Electronics, Faculty of Electronics, Technical University - Varna, 9010 Varna, Studentska 1, Bulgaria, e-mail: dimiter_98@yahoo.com

²Department of Electronics, Faculty of Electronics, Technical University - Varna, 9010 Varna, Studentska 1, Bulgaria, e-mail: edimitrowa98@yahoo.com

in one folder quickly becomes very confusing. It is much better in the folder, which will keep the project, to create a hierarchy structure. Thus each type of files should be written in its subfolder, which allows much easy navigation and cross-probing, corrections, etc. The specific structure of subfolders depends on the design, for example it could contain subfolders for files of: schematics, libraries, boards, datasheets of used components, assembly related documents, etc.

- Setting up the environment of the schematic should be the first step, especially when a new project will be created [2, 4]. It is important to check (and to change, if needed) the Options menu, which Preferences will be remembered in .ini file and will be used with every new customer, as well as the Design Template, which templates are common for all the next new projects.

B. Creating a new schematic project

Only now did the structure and environment define, a new project may be created, having in mind following specialties:

- What kind of new project will be created – this defines the specific libraries to be used in the project by default [2, 4] since in different cases the components will have different properties. In any case it is possible to use some components from different (type of) libraries, but it supposes a very good knowledge of the OrCAD properties (not only Capture, but PSpice, Layout and Spectra as well).
- Creating a schematic parts (or so called symbols) local library (.olb), as well as a library for the corresponding footprints (.llb) [3]. Although OrCAD creates a cached copy of the part symbol in the design file (which makes schematic project portable), it is preferable to create separate libraries for symbols (and later for footprints). They must be saved in subfolder, especially intended for them. It is a good practice to edit parts always in the library, not in schematics, as this will break the synchronizing between design and the (local) library. It is better avoiding so called heterogeneous parts, however in very large parts (processors, for example) they may be acceptable. Last, even though some standard parts have power pins invisible, making them visible can save a lot of time and trouble later.

C. Real work on the project

Depending on the schematic (Capture) or printed circuit board (Layout) editor is used the main tasks can be divided into two groups [3, 5].

- Inside the schematic editor Capture.
 - ✓ It is good to name all nets, that later will be require special routing rules. This concerns especially the ground and power nets, as well as some specific signals (high impedance input signals, common clock signals, powerful output signals, etc.). The explicit naming of nets is very useful and can be much helpful in the layout process.

- ✓ A special attention must be paid to programmable logic devices, which behavior must be simulated inside the whole circuit. In some cases the PSpice model of the part can cause problem in Layout, which is possible to be fixed by deleting the model itself (the schematic property PSpice Template).

- ✓ The annotation is another important step in preparing the design to export to Layout. It must be done including the hierarchical structure of the circuit. If the circuit has blocks that will be reused in the Layout, the option Tools/Annotate/Layout Reuse must be used in annotation, too. For schematics with more than one sheet (circuit pages), the option Add Intersheet References must be used. The DRC (Design Rules Check) must be always done before the netlist generation of the schematics.

- ✓ It is a good practice to define in the circuit the most important properties that will be used later in the Layout. It concerns at least the PCBFootprint property, which can considerably facilitate the packaging of the circuit (i.e. the process of converting schematic symbolic parts to parts of the real world – like footprints of the elements). Although it is possible to do that in the Capture itself, for more complicated circuit is much easier to export them to Excel (Tools/Export Properties), make the all changes (Notepad will be useful, too), and import them back to Capture (Tools/Import Properties). Take in account that as the values of the elements are a separate property, it is important to have all elements with equal values with the same text notation in their value fields, else OrCAD will treat the elements with different text values (for example 100nF and 0.1uF) as completely different parts. This will complicate parts ordering and make part list (BOM) unreadable.

- Inside Layout (the printed circuit board editor).

- ✓ The first step (after or even before the board outline is drawn) should be defining all the layers that will be used in the design (so called Board Stackup). As the Gerber files are close coupled with the layers, it is a good practice to define them here, although it could be done later too.

- ✓ Next to define is the default padstack. The minimal size of the drill depends on the technology to be used, and must be entered into layers DRILL and DRLDWG. Each board shop has its requirements on the minimum annular ring size (the amount of metal beyond the size of the drill) based on the drill diameter, with a typical value of 20 mils (about 0.5 mm). If plane layers (POWER and GND) will be used a clearance around the drills must be defined, too. As a last thing, if a solder-mask is supposed to be used, it should be defined in layers SMTOP and SMBOT with a slightly large diameter (about 5 mils) than the annular rings. There is no need to define all the layers. As a common rule, the layers, that should be defined for thru-hole parts are: TOP, BOTTOM, INNER, PLANE, SMTOP, SMBOT, DRLDWG and DRILL; and for the surface mount parts they are: TOP, SMTOP and SPTOP. The default net properties should be checked in this point-the minimal width should correspond to the fabrication process to be used.

- ✓ After the board outline is defined is good to place the mounting holes first. If the boxes of their properties ‘Not in Netlist’, ‘Fixed’ and ‘Locked’ are not checked (which is a common mistake) the Layout will move them (or even delete) later.
- ✓ A common mistake is allowing Layout to do an automatic Place and Route, which could be acceptable vary rarely. The placement and routing of a board is much more an art than a science, and is best learnt by lots of practice. As the designer always knows how its circuit works, much better than any piece of software, the majority of manually placed and routed boards should be a higher quality than the automated. There are only a few cases (like memories board) when automatic place and route can do. Careful placement and routing can insure that the circuit board will perform to its fullest potential. The automatic placement and routing software tools have their place, but they should be used very carefully. Before the beginning of placement and routing it is good at least to specify which type is the board: a general analog, general purpose digital, high-performance analog, high-speed digital or radio frequency (RF). Of course most designs are a mix of the above board types, so the placement and routing strategies should be blended, too.
- ✓ Almost in any design the power and ground connections must be routed before anything else. It is a good idea to use as much as possible the interactively ways of routing (Edit Segment Mode as well as Add/Edit Route mode), but not the auto routing itself. For a successive interactive routing can be used the column Route Enabled from the Nets Spreadsheet, which allows enabling/disabling of the chosen net. A “good” ground means “low-impedance” of the ground (almost the same relates to the power connections). So the goal is to create a ground that has the lowest resistance at any frequency or board location. The ground plane is the best possible solution. Even if it is impossible to dedicate an entire layer to ground, large ground areas on both (top and bottom) sides of the board can come closer. In such cases the COPPER POUR option must be used. Active components which draw significant switching current should always be “bypassed”. The typical value for bypass capacitor is 100nF, but two, or even three different values capacitors can be used to bypass different

frequencies. When bypassing do not replace multiple capacitors with one single capacitor – it defeats the entire purpose of bypassing.

- ✓ Only after the ground and power nets are routed, is time to continue with the rest connections. For multi-layer responsible boards and the inner layer wires must be wider, than those of outside (top and bottom) layers. As a common rule, each track should be as short as possible. The clearance definitions must take in account requirements of the fabrication process, the layer position (internal or external), the voltages, the operational height of the board over above the sea level, etc. Table I allows roughly definition for the clearances.
- Final steps should be taken to finish the board and prepare for production.
 - ✓ The OrCAD suggests two possibilities – the ECO (Engineering Change Order) and Back Annotation. The first one is used from inside the Capture (so called forward annotation, i.e. when changes are made in schematics), and the second one is used for changes made during Layout. The renaming of components in the board is at least one example where is good to use back annotation. During debug on a larger board it could be very hard to find where a specific component is, because components seem to be named randomly. Using the Options/Components Renaming (and Right, Down in the rename directions) in Layout will be a good turn to the debug engineer.
 - ✓ The next step is to check for any spacing errors (DRC – Design Rule Check). Instead of trying to remove errors manually (one by one), the Auto-Remove Violations tool could be use, but this is not a good idea – it will actually rip-up offending traces and move parts, so a lot of cleanup and rerouting after using this tool should be done.
 - ✓ Cleaning up the design is a step before the final, which includes mitring the corners and exits from the pads, removing extra vias and drill size adjusting. The last means to adjust (consolidate) the drill sizes in accordance to the board shop limitations. It is a good practice to consolidate drills anyway (this will save money at least). Another good practice is to adjust the silkscreen layer - all text should be oriented in the same direction for readability and it cannot overlap pads or vias. A good documenting of the design helps both in manufacturing and debug. It is useful to add some useful text to the board, for example the names of some important nets and pins, as well as the initials of the person who designed it. In the special layer Drill Drawing should be added the Drill Chart and the board dimensions. It is good practice beneath the drill table to include the name, phone number and email of the designer. Because a separate Gerber file will be generated for each layer, outside the boundary of the board some text could be added, to indicate what layer this is.
 - ✓ The last step is creating and viewing the Gerber files that will be sent for fabrication. If they had been defined as was suggested in the beginning generation now is quite easy – just Auto-Run Post Processor must be selected.

TABLE I
CLEARANCES FOR ELECTRICAL WIRES

Voltage (DC or Peak AC)	Distance (clearance) between tracks		
	Internal layers	External layers	
		Sea level<3050m	Sea level>3050m
0-15V	0.05mm	0.1mm	0.1mm
16-30V	0.05mm	0.1mm	0.1mm
31-50V	0.1mm	0.6mm	0.6mm
51-100V	0.1mm	0.6mm	1.5mm
101-150V	0.2mm	0.6mm	3.2mm
151-170V	0.2mm	1.25mm	3.2mm
171-250V	0.2mm	1.25mm	6.4mm
251-300V	0.2mm	1.25mm	12.5mm
301-500V	0.25mm	2.5mm	12.5mm

OrCAD has a built-in Gerber viewer and editor called GerbTool. In fact, this is a very powerful program that allows viewing and editing of the Gerber files – it is often to catch mistakes in this program that are not seen in layout.

✓ To finish the work is good to cleanup the project folder – OrCAD generates a lot of files that can be deleted (if necessary, they can be generated again). The files that must be kept are: for Capture - project (.opj), design (.dsn) and library (.olb) files; for Layout – netlist (.mnl), library (.lib), template (.tpl) and the board (.max) files; for Gerber – all the layers files.

III. CONCLUSION

In this paper a concise review of some important activities of electrical appliances design methodology with the help of OrCAD are given. Following the shown consecution should lead to lower mistakes in the design process, better and more reliable printed circuit boards, as well as easier to debug, redesign and maintenance devices. Most of the given recommendations are applicable not only to OrCAD design, but to all designs that use some modern CAE systems.

ACKNOWLEDGEMENT

The paper was developed in the frames NATO Research Project EAP.RIG.981.482.

REFERENCES

- [1] Л. Райковска, Е. Гаджева – Автоматизация на проектирането в електрониката и комуникациите, част 1, Моделиране и симулация с OrCAD PSpice, Меридиан 22, София, 2005
- [2] OrCAD, v.10.5, Cadence Design System, Inc, 2005
- [3] An OrCAD Tutorial for ELEC 424, High Speed Systems Design, rev.1.0, 2002
- [4] Д.Ковачев, Е. Димитрова – Автоматизирано проектиране на електронна апаратура, Учебно пособие, ISBN-10: 954-20-0365-X, ISBN-13: 978-954-20-0365-6, ТУ-Варна, 2006
- [5] David L. Jones, PCB Design Tutorial, 2004, www.alternatezone.com
- [6] Jon Varteresian - Fabricating Printed Circuit Boards, 2002, Elsevier Science

Magnetron Dielectric Barrier Air Discharge at Low Frequency

Peter D. Dineff¹ and Dilyana N. Gospodinova²

Abstract – Dielectric barrier discharges that burn at atmospheric pressure and industrial frequency (50/60 Hz) are a good technological alternative to the RF- and glow discharges at low pressure (vacuum). The present investigation offers a new approach aiming at the creation of a new magnetron dielectric barrier discharge plasma system, intended for plasma-chemical treatment of low energy surface porous materials.

Keywords – atmospheric-pressure glow discharge, dielectric barrier discharge, high-pressure low-frequency dielectric barrier discharge, plasma-chemical surface modification.

I. INTRODUCTION

There are more than ten thousand (10,000) granted United States Patents which are related to the generation and applications of ozone. More than one hundred of these patents have been granted to innovative techniques of ozone generation, [2].

Ozone production is predominantly achieved by one of the following three groups of methods: electrical discharge methods, electrochemical methods, and ultraviolet (UV) radiation methods.

Electrical discharge methods, which are the commercial methods of widest use, have relatively low efficiencies (2 ÷ 10 %) and consume large amounts of electricity. The other two groups of methods (electrochemical and UV) are less cost-effective.

Because ozone is very reactive, it is also unstable. It cannot therefore be stored and has to be produced where and when it is needed. Ozone is produced from oxygen-containing gases in ozone generators by means of a dielectric barrier discharge (silent electrical discharge). All industrial-scale ozone generators make use of this method, [1, 2, 6, 7].

The dielectric barrier discharge (DBD) is an important type of alternating current (AC) glow discharge, operating at atmospheric pressure and in a lower frequency range (50 ÷ 60 Hz), where both electrodes, or at least one of them, are typically covered by a dielectric barrier, [6, 7].

As a result of applying an AC voltage to an electrode system with one or both electrodes covered by dielectric layer, a DBD appears in the gas gap. Such non-thermal or cold discharges are suitable for a wide range of applications, e. g. ozone generation, surface treatment and modification of plastic foils, textiles and even metals, pollution control,

sterilisation, ultraviolet and vacuum ultraviolet light sources for laser pumping, AC plasma displays, and others, [2].

Basic designs of plasma-chemical reactors using DBDs are given in Fig. 1. While the DBD in Fig. 1a is determined mainly by discharge columns in the gas gap and surface discharges on the dielectric, the arrangement with extended surface electrodes, Fig. 1b, leads only to surface discharges along the dielectric surface. The packed bed reactor with dielectric pellets, Fig. 1c, includes both types of DBDs.

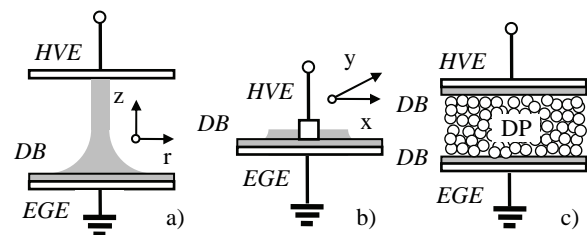


Fig. 1. Different types of DBDs arrangements: **a** - volume DBD plasma reactor, **b** - surface DBD plasma reactor and **c** - packed bed DBD plasma reactor.

HVE and EGE – high-voltage electrode and earth-grounding electrode; DB – dielectric barrier; DP – dielectric pellets.

In addition to applying an electric field (or difference of potentials) to a plasma reactor electrode system, a magnetic field can be also applied to a glow discharge. The most well-known discharge type with *crossed magnetic and electric fields* is the *magnetron discharge*. The electrons circulate in helices around magnetic field lines and give rise to more ionisation. Hence, magnetron discharges are typically operated at lower pressures and higher currents than conventional or normal and abnormal glow discharges, [1].

The theory of the *low-pressure magnetron glow discharge* was developed by R. Redhead, and the field of practical implementation is defined by the pressure; the discharge currents being 100 ÷ 200 mA/cm², [1].

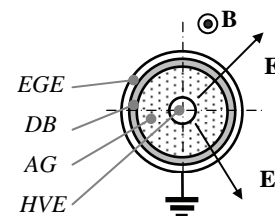


Fig. 2. Co-axial types (tube in tube) of a magnetron DBD plasma reactor with crossed magnetic **B** and radial electric fields **E**. HVE and EGE – high-voltage electrode and earth-grounding electrode; DB – dielectric barrier; AG – air (discharge) gap.

¹Peter D. Dineff is from the Faculty of Electrical Engineering of Technical University of Sofia, 1756 Sofia, Bulgaria, e-mail: dineff_pd@abv.bg

²Dilyana N. Gospodinova is from the Faculty of Electrical Engineering of Technical University of Sofia, 1756 Sofia, Bulgaria, e-mail: dilianang@abv.bg

The great concentration of gas particles at high pressure that determines the small average length of free path and high frequency of collisions between gas particles, does not speak of successful application of the *magnetron effect* to *DBDs*, i. e. for an atmospheric pressure glow discharge. An argument to this statement is the absence of concrete investigations in this field, despite of the great interest regarding *DBD* plasma technologies, [2].

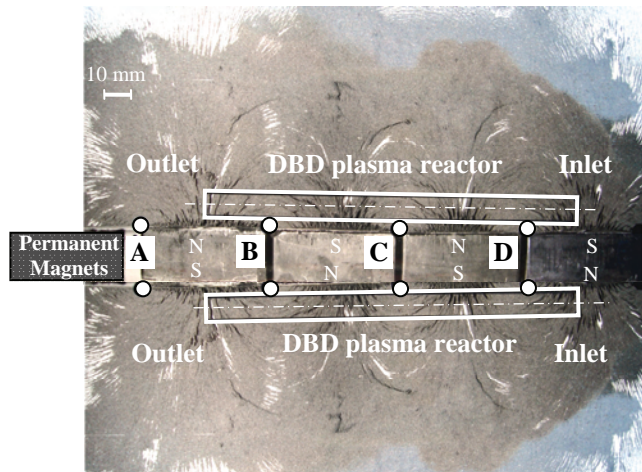


Fig. 3. *MDBD* plasma reactor with two co-axial discharge tube – graph of the magnetic flux density of an open magnetic system with four alternating permanent magnets poles arranged in line.

The TASK of the investigation presented consists in identifying the magnetron atmospheric pressure *DBD*, while observing the well-known definition of the magnetron effect with crossed magnetic and electrical fields.

The idea for realization of a *magnetron DBD (MDBD)* is demonstrated in Fig. 2: for the existing cylindrical symmetry of the electric field \mathbf{E} , the magnetic flux density \mathbf{B} should be directed along the electrode axis, i. e. Perpendicularly to the cross-section plane.

II. EXPERIMENTAL INVESTIGATIONS

Preliminary experimental investigations carried out on the selection of a source of permanent magnetic field and determination of the magnetic flux density \mathbf{B} , at which the magnetron effect exhibits itself, indicate that:

- the magnetron effect exhibits itself at relatively strong magnetic fields, i. e. at $B > 0.2$ T;
- the necessary geometry of the magnetic field can be structured by means of permanent magnets.
- it is not possible to create a permanent magnetic field ($B = \text{const}$) along the entire length of the discharge tube (of the plasma reactor).

For the purposes of the investigation, two types of devices having different structure of the permanent magnetic field have been created:

- *MDBD* reactor with an open magnetic system with alternating poles of the permanent magnets arranged unilaterally to the discharge tube in one or two layers, Figs. 3 and 4;

- *MDBD* reactor with an open magnetic system with alternating poles of the permanent magnets arranged to the discharge tube in one line, Fig. 5.

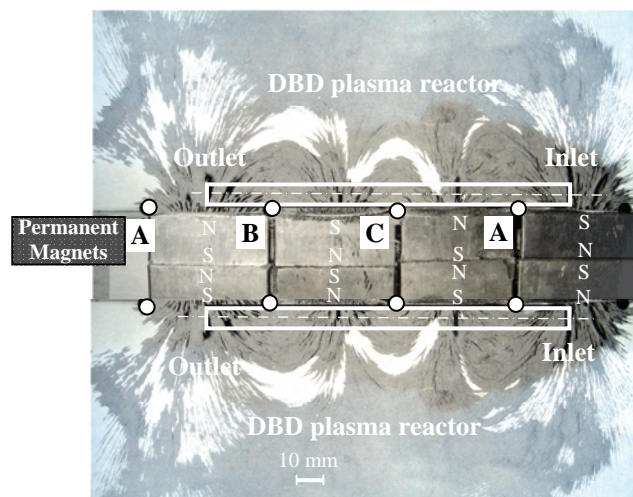


Fig. 4. *MDBD* plasma reactor with two co-axial discharge tube – graph of the magnetic flux density of an open magnetic system with four alternating poles of the permanent magnets arranged in two layers.

Technological magnetron *DBD* devices with permanent magnets represent a space structure consisting of anisotropic strontium permanent magnets Sf: 80 x 57 x 12 mm (*Magnit* Ltd., Permik, Bulgaria): $H_C \geq 224$ kA/m; $B_r = 0.37$ T; $(BH)_{\max} \geq 24$ kJ/m³; $\mu_r = 1.2$; $T_Q = 735$ K; $\rho_V = 10.6$ Ω m; $\delta = 4.5 \div 5.0$ g/cm³; $\delta l = (9 \div 15) 10^{-6}$; 55 HRC. They are suitable for making devices with an open magnetic system or with large air gaps.

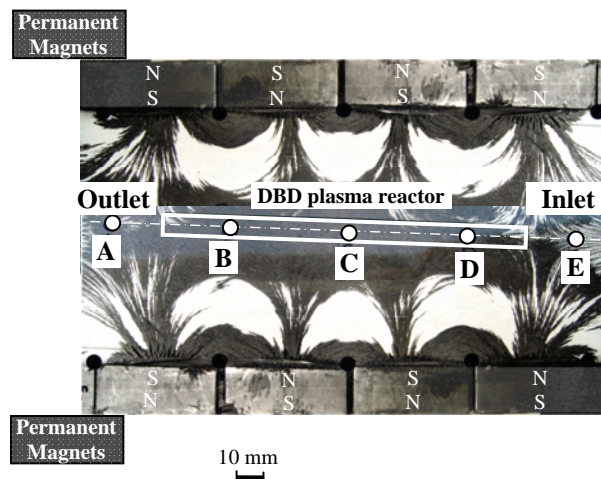


Fig. 5. *MDBD* plasma reactor with two co-axial discharge tube – graph of the magnetic flux density of an open magnetic system with alternating poles of the permanent magnets arranged bilaterally to the discharge tube in one layer.

Two design structures of magnetron *DBD* plasma reactors examined experimentally are shown schematically on the picture of the magnetic field obtained by means of fine ferromagnetic powder, Figs. 3, 4, and 5.

Figs. 3 and 4 show the same structure of an *MDBD* ozone generator – A55 and A75, their only difference being in the

double volume of the four pole groups, which increases the maximum value of magnetic flux density \mathbf{B} measured at designated points, namely A , B , C , and D . Measuring is carried out with a specialized instrument featuring an accuracy class of 0.5. In the first case, Fig. 3, the measured magnetic flux density is 55 mT, while doubling the magnetic mass of pole groups, Fig. 4, increases this value to 75 mT (i. e. by 36 %).

In the second examined structure of an *MDBD* ozone generator – B16, the arrangement of magnetic poles is realized in accordance with the so called quadrupled scheme that defines a maximally long sector with crossed magnetic and electric fields along the device’s central axis, Fig. 5. However, the value of the maximum magnetic flux density \mathbf{B} is lower, namely 16 mT.

Along the device there are periodically alternating areas, where the magnetic and electric fields cross each other.

The dielectric barrier is a quartz tube with internal diameter \varnothing 8 mm. A resistive wire of FeCrAl ($\rho = 1.35 \times 10^{-6} \Omega\text{m}$) having diameter \varnothing 0.20 mm is stretched along its axis. The second electrode is placed from outside by winding on the tube.

The elementary processes (impact dissociation, impact ionization, secondary electron emission from the cathode, chemical reactions) that are effected in the discharge gap play a different role as regards ozone generation: on one hand, O_2^* , O_2^+ , O_2^- , and O_2 help generating ozone, and on the other hand, N , N^* , NO_2 , and NO support its inhibition. In general, it is possible to form two modes of *DBD* burning: a mode of generating ozone and products of its decay, and a mode of generating nitrogen oxides NO_x , Fig. 6.

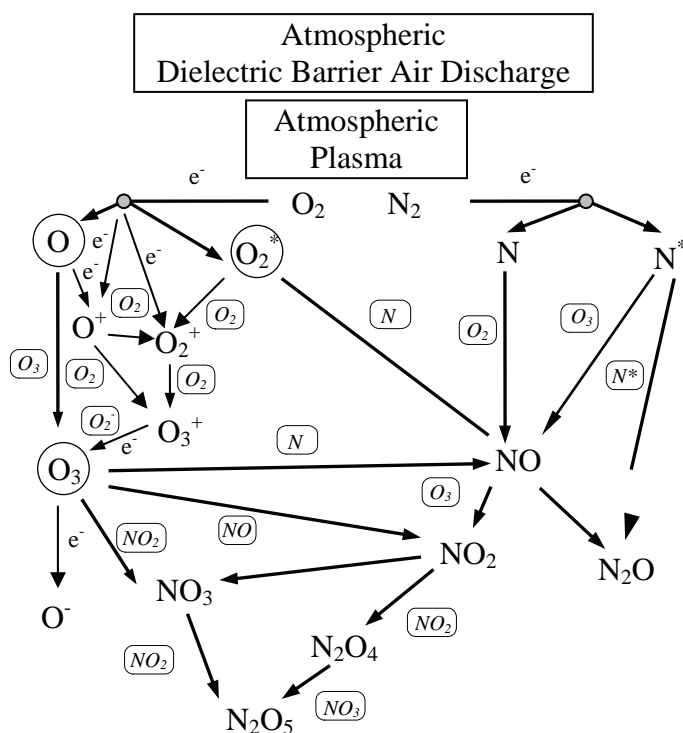


Fig. 6. Schematic presentation of the primary processes of impact electron ionization (e^-) and of the chemical transformations that on one hand generate ozone, and on the other hand inhibit it.

The external (volt-ampere) characteristic of *DBD*, presenting the relationship between the average value of discharge current I_{av} and the effective value of the voltage applied across the discharge gap U_{eff} , reflects the existence of two characteristic modes of *DBD* burning, Fig. 7, [3, 4, 5].

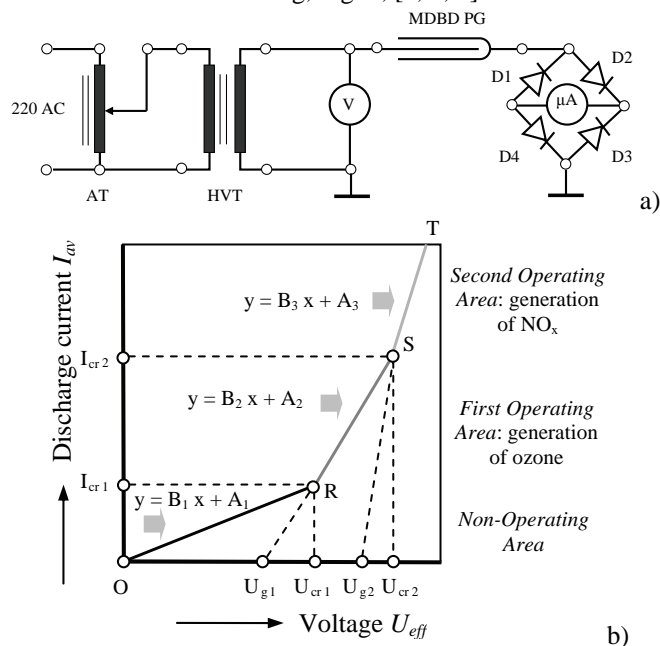


Fig. 7. Electric circuit of the experimental *MDBD* plasma generator (PG) (a) and volt-ampere characteristic (b).

AT – transformer for voltage regulation; *HVT* – step-up transformer; *D1*, *D2*, *D3* and *D4* – diodes allowing direct measurement of the average value of discharge current I_{av} .

III. RESULTS AND DISCUSSIONS

Experimentally plotted external characteristics of both discharges, *DBD* and *MDBD*, are shown in Figs. 8, 9 and 10 for each investigated structure of ozone generators.

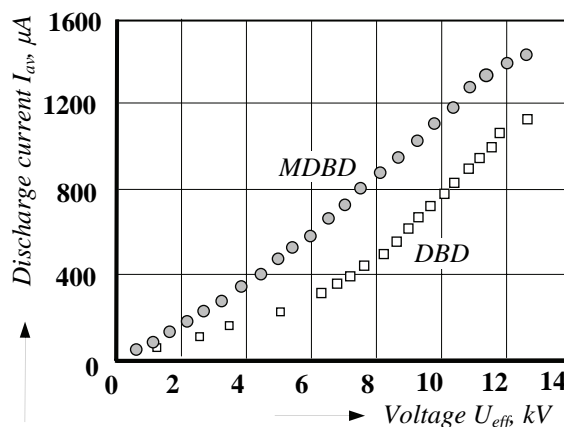


Fig. 8. Volt-ampere characteristics of *DB*- and *MDB*-discharges of the plasma generator A55.

Characteristics and a part of the critical parameters of the examined design structures of ozone generators A55, A75, and B16 are determined numerically and given in Table 1.

IV. CONCLUSION

Comparing the two realizations of the first design structure, A55 and A75, creates the impression of clearly expressed shifting of the volt-ampere characteristic to the left, i. e. to higher currents; the larger shifting being observed for the stronger magnetic field, and this being valid for both operating areas, Table 1.

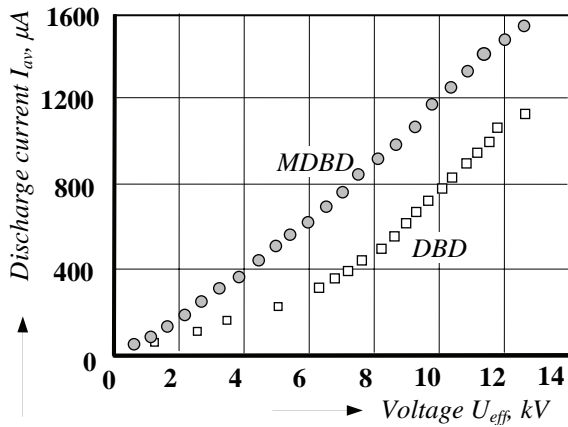


Fig. 9. Volt-ampere characteristics of DB- and MDB-discharges of the plasma generator A75.

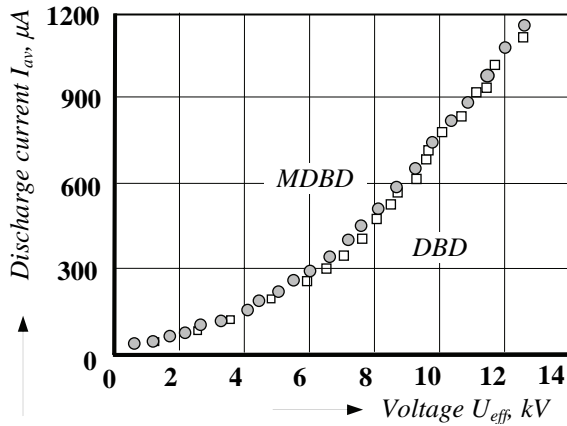


Fig. 9. Volt-ampere characteristics of DB- and MDB-discharges of the plasma generator B16.

TABLE I

Design Structure Type	DBD	MDBD A75	MDBD A55	MDBD B16
Correlation coefficient $r_{2,-}$	0.999	0.9986	0.9971	0.982
Correlation coefficient $r_{3,-}$	0.999	0.9962	0.9974	0.982
Critical voltage U_{cr1} , kV	2.237	6.269	4.2963	5.416
Critical current I_{cr1} , μ A	185.8	255.6	368.6	235.4
Burning Voltage U_b , kV	0.69	3.34	4.37	1.64
Slope B_2 , μ A/kV	84.3	41.6	87.0	4.7
Slope B_3 , μ A/kV	120.0	134.5	138.9	113.6
Intercept A_2 , μ A	-2.8	-5.5	-5.2	14.8
Intercept A_3 , μ A	-82.7	-587.6	-228.2	-379.6

The intensity of the permanent magnetic field exerts substantial influence on *MDBD* characteristics.

Based on the experimental investigations performed on various design structures of *MDBD* ozone generators, it is possible to derive the following main conclusions:

- the magnetron effect can be used in creating *MDBD* plasma technological systems;
- the impact of the magnetron effect is expressed by totally shifting the characteristic the left, while the critical ignition voltage of the discharge increases significantly, which also defines the high critical ignition current;
- using permanent magnets in the creation of *MDBD* plasma technological systems turns out to be a good solution that allows designing compact and efficient generators of ozone and cold plasma at atmospheric pressure;
- the developed magnetic system of the A type (A55 and A75) can be used not only in the considered case of volume *DBD* plasma reactor; it can also find an equally good application in the creation of surface *MDBD* plasma reactors;
- the combination of a magnetic system and two electrode systems can be considered a design module that is in position to produce complex *MDBD* plasma generators by repetition.

ACKNOWLEDGEMENT

The National Science Fund, Ministry of Education and Science of Bulgaria, is gratefully acknowledged for the financial support of research project VU-TN-205/2006.

REFERENCES

- [1] P. Dineff. Electrotechnology. *Introduction to Electrotechnology*. Technical University, Sofia, Bulgaria, 2000 (in Bulgarian).
- [2] G. Pietsch and V. Gibalov. Dielectric Barrier Discharges and Ozone Synthesis. *Pure & Applied Chemistry*, Vol. 70, No. 6, 1998, pp. 1169-1174.
- [3] P. Dineff and D. Gospodinova. Electric Characteristics of Barrier Discharge. XXXVI International Scientific Conference on Information, Communication and Energy Systems and Technologies "ICEST '2003". Sofia, Bulgaria, October 16-18, 2003. Proceedings, Heron Press. Ltd., 2003, pp. 442-445.
- [4] P. Dineff and D. Gospodinova. Electrical Characteristics of the No-load Regime of Electrical Barrier Discharge. 6th International Conference on Applied Electromagnetics "PES' 2003", June 1-3, 2003, Niš, Serbia and Montenegro. Proceedings, 2003, pp. 442-444.
- [5] P. Dineff and D. Gospodinova. Electrical Characteristics of Barrier Electrical Discharge. 38. International Scientific Conference on Information, Communication and Energy Systems and Technologies "ICEST 2003", October 16-19, 2003, Sofia, Bulgaria. Proceedings, 2003, pp. 442-445.
- [6] Kitayama, J. and M. Kuzumoto. Analysis of Ozone Generation from Air in Silent Discharge. *J. Phys. D: Appl. Phys.*, Vol. 32, 1999, pp. 3032.
- [7] Yagi, S. and M. Tanaka. Mechanism of Ozone Generation in Air-Fed Ozonisers. *J. Phys. D: Appl. Phys.*, Vol. 12, 1979, pp. 1509.

Application of the CFD Method for Heat Transfer Simulation

Anna V. Andonova¹ and Nadejda M. Kafadarova²

Abstract – Modern CFD codes now are used for microsystem heat transfer simulation. The outputs of these codes are 3D maps of temperature distributions. These codes can often predict a hot spot with good accuracy, but offer no diagnostic help in determining what to change for the next trial.

This paper proposes a set of diagnostic parameters that should be calculated for each critical component. From these parameters, it could be answer, during the heat transfer simulation process not only whether an overheating problem exists but what is the most likely cause.

Conjugate transient heat transfer from a sample carrier mounted microsystem component was numerically modeled using a CFD code dedicated to the thermal analysis of electronic system. It is used to evaluate the potential for improving module thermal design

Keywords – Computational Fluids Dynamics (CFD), Simulation, Heat transfer, Thermal management, Reliability, Virtual prototyping

I. INTRODUCTION

The need to reduce development cycle times and costs has lead to increased efforts to use virtual prototyping during the design phase in electronics microsystems. As the complexity of these systems rise, addressing thermal management issues has become increasingly important. The ultimate goal of system thermal design is not the prediction of component temperatures, but rather the reduction of thermally associated risk to the product [1]. Many tools exist to assist thermal design engineers during this process, including heat transfer correlations, Flow Network Modeling (FNM), Computational Fluid Dynamics (CFD), and experimental measurement techniques. The key to efficient and comprehensive thermal design is not, necessarily, the choice of the “best” tool for design, but rather the optimized integration of available tools.

The flow and heat transfer situations encountered in microelectronics cooling are very tricky .

There are many ways in which an “acceptable” thermal design can fail: inadequate or poor flow distribution, thermal

stratification (poor mixing), low heat transfer coefficient, or power dissipation higher than expected. Heat transfer simulation relies heavily on CFD codes that predict the flow and temperature distributions using more or less elegant turbulent flow models.

The applicability of CFD analysis to predict steady-state, single-component PCB heat transfer in free and forced convection has been well established [2].

The use of such CFD tools enable the following: 1) better prediction of component, board, and system temperature, 2) reduction in design-cycle time, 3) reduction in experimental testing, and 3) parametric materials investigation for a number of boundary conditions. This paper proposes diagnostic parameters that should be calculated for each critical component. From these parameters, it will be said not only whether an overheating problem exists but what is the most likely cause.

The design analysis was performed early in the module design process at a time when knowledge of the thermal characteristics of a module design is most useful. An example for a sample was demonstrate.

II. PRINCIPLE COMPUTATIONAL REQUIREMENT

A. Component level modeling

To create a good model of an entire microsystem, it is essential to develop accurate models of the components that are contained within the system. The underlying aim for this analysis approach is to create behavioral models based on the known characteristics of the component.

On the electrical side, an extensive library of component models for systems simulations has been created. These models are based on the electrical characteristics of the devices as supplied by the manufacturer or as determined through electrical testing. To develop thermal models of the system’s components, the devices are subjected to thorough testing during which the power dissipated and the temperatures attained are carefully monitored for various loading scenarios. This test data is then used to design a thermal model of the device that reflects the observed response as closely as possible over a broad range of electrical loading scenarios. This automated approach also allows the development of models that are highly accurate as well as computationally efficient.

Though a variety of microsystem layouts are possible, it will simplify the discussion to limit these considerations to a current standard system design.

¹ Department of Microelectronics, Technical University of Sofia, FETT, 8 Kl. Ohridski Str., 1797 Sofia, Bulgaria, E-mail: ava@ecad.tu-sofia.bg

² Technical University - Sofia, Plovdiv Branch, 25 Tsanko Diustabanov Str., 4000 Plovdiv, Bulgaria, E-mail: n_kafadarova@yahoo.com

Accurate prediction of components junction temperatures and the overall system temperature field is necessary to allow for adequate reliability and performance analysis in the design process. Ideally, computational fluid dynamics (CFD) simulations of the electronic microsystem, with detailed modeling of the components and conjugate heat transfer interactions, would be utilized to predict temperatures at the component and system level, but these simulations require significant computational resources. This computational expense is the result of large variability in length scales at the component and system level. In conventional discretization schemes, the smaller package length scales result in a larger number of control volumes in the surrounding fluid regions where fewer volumes might suffice. This is because the discretization required in the package translates into the fluid regions, and vice versa. System level compact thermal modeling attempts to eliminate the small length scales associated with modeling the details of the package by using models with length scales comparable to those required by the system level CFD simulation.

B. Diagnostic parameters for each critical component.

Table I summarizes the input data and results generated by the CFD and FE analyses of the commercial CFD software, FLOTHERM®. Geometry, grid and temperature information is passed from the CFD solver to the FE solver at the end of the CFD calculation. The outputs of these codes are “maps” of flow and temperature distribution. For identifying potential problems, these maps provide little or no guidance as to how to solve the problems they reveal.

TABLE I
INPUT DATA AND RESULTS

CFD Thermal Tool
<i>Data and Solution:</i>
· Fluid and Solid Regions
· Structured Mesh in Solid and Fluid Regions
· <i>Finite Volume Solver Results:</i>
· Fluid Velocities
· Temperatures
<i>Derived Quantities:</i>
· Fan Operating Point

It is hard to develop a systematic approach to problem solving where everything changes when anything changes. Classical theory for internal passage heat transfer uses a heat transfer coefficient based on the mean fluid temperature:

$$q_{conv} = h_m A (T_0 - T_m) \quad (1)$$

$$T_0 = T_m + q_{conv} / h_m A, \quad (2)$$

where A is the area, m^2 , h_m is the h based on $(T_o - T_{mean})$, $W/m^2 K$, h is the heat transfer coefficient, $W/m^2 K$, q_{conv} is the convective heat transfer rate, W .

Unfortunately, electronics cooling situations are characterized by abrupt changes in wall temperature, from one component to the next. Under those conditions, h_m can range between $+\infty$ and $-\infty$. The experimentally measured heat transfer coefficients presented in the electronics cooling literature are not values of h_m , they are referenced to the adiabatic temperature of the component, If those values are used in Eq.1, the actual temperature rise will be higher than the calculated one, sometimes by as much as 40%.

When h is defined in terms of the mean temperature (as it may be by a CFD code), then the value of h depends on the power distribution on the board and will change when the power distribution changes.

If it is introduced a more suitable definition of h for electronics cooling applications in [3]:

$$q_{conv} = h_m A_{ad} (T_0 - T_{ad}) \quad (3)$$

$$T_0 = T_{ad} + q_{conv} / h_{ad} A \quad (4)$$

where T_{ad} is the temperature the component attains with no power applied and with no radiation or conduction to it.

Thinking in terms of h_{ad} instead of h_m gives the designer more tools to work with. This can be seen by comparing Eq.2 and Eq. 5. Most importantly, however, h_{ad} is independent of the temperature distribution on the heated wall being determined by geometry and flow field alone. This allows the heat transfer engineer to deal with the overall temperature rise as the sum of a set of linearly independent temperature rise components that can be individually measured (or computed).

The four energy flows acting on a component are shown on Fig.1.

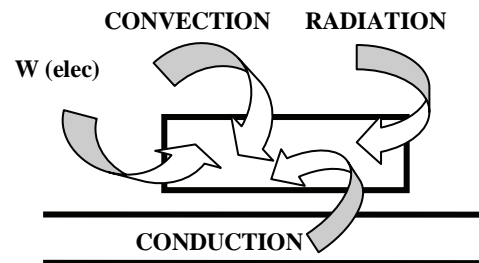


Fig. 1. Energy balance terms for an active component.

If the component is running too hot, it is important to know which of these four terms is causing the trouble. Starting from the energy balance equation, Eq. 6, the terms can be arranged into groups that represent the individual contributions to the component temperature:

$$q_{conv} + q_{rad} + q_{cond} + W_{elec} = 0 \quad (6)$$

Eq. 7 describes the four factors that affect the temperature rise of a component:

$$\Delta T_{overall} = (\Delta T_{ad} / \Delta T_m) \Delta T_m + \Delta T_{cond+rad} + \Delta T_{elec} \quad (7)$$

The CFD code calculates the operating temperature, T_o , in its normal mode of operation. The diagnostic benefit comes from

breaking up the total temperature rise at operating conditions to reveal these four factors, using Eq. 7 as a guide.

B. Example

Consider a microsystem consisting of regular array of components. Most are un-powered but in one region, a 10 watt component is installed immediately downstream of one dissipating 18 watts. Carrier spacing is 2.25 times the component height, and the inlet velocity (measured upwind of the first row of components) is 3.07 m/s. The CFD code predicts an operating temperature of 115 °C in a 20 °C ambient. The following information is needed for each component under normal operating conditions:

Intel Temperature – 20°C
Adiabatic temperature – 45,8°C
The mixed-mean coolant temperature – 24,7°C
The value of h_{ad} – 51W/m ² C
The pressure drop per row – 1,61 Pa
Operating temperature – 115 °C

The adiabatic temperature rise is 5.5 times the mixed-mean coolant rise. The coolant flow is badly stratified. If it were perfectly mixed, the operating temperature would drop by more than 20.

III. MODULE DESIGN PROCESS

To be most beneficial, thermal design analysis should be performed early in the module design cycle during component placement studies.

Electronic modules may be destined for use in a wide variety of applications and environments. Module operational times may be brief and therefore component package and local PCB/carrier heat capacitance effects may be dominant thermal concerns. In other cases, module operational time may be lengthy, in which case the proper design of heat conduction paths from the components to heat sinks may be paramount.

Frequently, active cooling systems are used, and temperature control is accomplished by direct immersion into a quiescent or circulating coolant. In low atmospheric pressure or space applications, radiation may be a significant factor as well. Thus, a very wide variety of applications are possible, each requirements was developed and translated into with varying modeling requirements. With these and other considerations in mind, a set of design analysis requirements for modeling in FLOTHERM.

The initial attempts, featured numerous internal plates and external walls, which led to many questions as to how the plates and walls would interact, and whether the whole process would prove too confusing for the module designer to use effectively. The following process allows an Auto Therm generated lib file to be analyzed within FLOTHERM using prescribed heat transfer coefficients in a conduction only mode. Auto Therm can generate a 3D model of a circuit board with components as shown in Figure 2. It consists of: a cuboid block representing the circuit board and a series of cuboid

blocks representing the components with non-conducting internal plates insulating the sides, and conducting plates setting the Θ_{j-c} and Θ_{j-t} values.

The principle of the approach is the translation of the resistance of the surface-fluid heat transfer coefficient into a thermal resistance created by an internal plate with a k , t combination through the relationship:

$$Q = hA\Delta T = kA\Delta T / t \text{ hence } h = k/t.$$

TABLE II
INPUT DATA AND RESULTS WITH HEAT SOURCE

Geometry Model	Type	X Position (m)	Y Position (m)	Z Position (m)	X Size (m)	Y Size (m)	Z Size (m)
Root Assembly	Assembly						
Structure	Assembly	0	0	0	0.25	0.075	0.3
Chassis	Enclosure	0	0	0	0.25	0.075	0.3
Low Y Plate	Perforated Plate	0.02	0	0.02	0.19	0	0.08
Low Z Plate	Perforated Plate	0.02	0.01	0.3	0.19	0.04	0
High Z Plate	Perforated Plate	0.02	0.01	0	0.19	0.04	0
Box Temperature	Monitor Point	0.125	0.0375	0.15	0	0	0
PSU	Assembly	0.145	0.01	0.235	0.075	0.04	0.05
PSU Heat	Source	0	0	0	0.075	0.04	0.05
PSU Temperature	Monitor Point	0.0375	0.02	0.025	0	0	0

TABLE III
INPUT DATA AND RESULTS WITHOUT HEAT SOURCE

Geometry Model	Type	X Position (m)	Y Position (m)	Z Position (m)	X Size (m)	Y Size (m)	Z Size (m)
Root Assembly	Assembly						
Structure	Assembly	0	0	0	0.25	0.075	0.3
Chassis	Enclosure	0	0	0	0.25	0.075	0.3
Low Y Plate	Perforated Plate	0.02	0	0.02	0.19	0	0.08
Low Z Plate	Perforated Plate	0.02	0.01	0.3	0.19	0.04	0
High Z Plate	Perforated Plate	0.02	0.01	0	0.19	0.04	0
Box Temperature	Monitor Point	0.125	0.0375	0.15	0	0	0
Electronics	Assembly	0	0	0	0.19	0.0016	0.21
PCB 1	PCB	0.02	0.01	0.23	0.19	0.0016	0.21
Component	PCB Component	0	0	0	0	0	0

The final stage of the process is to import the “plated” lib file into a pre-prepared project file consisting of: highly

conductive (hence isothermal) cuboid and a number of planar sources fixing the temperature of the cuboid to the “ambient” temperature (T_a).

With the assurance that the model making process was manageable, calculate the steady state temperature distribution

To illustrate the model making process a sample module was selected randomly as that described above, which had not been incorporated into the program to demonstrate calculation of the steady state temperature distribution. The data are shown in Table II and Table III with and without heat source respectively.

Arbitrary, typical thermal parameters were applied to each component. These features require editing in FLOTHERM if they are to be incorporated and thermal boundary conditions were applied. It was decided totally arbitrarily to calculate the steady state temperature distribution within a control volume for a high temperature free convection cooling case.

Fig. 2 shows the temperature distributions calculated for that case, and Fig. 3 shows the temperature profiles for the case with and without heat source respectively.

The design analysis can be performed early in the module design process at a time when knowledge of the thermal characteristics of a module design is most useful.

Thermal designers can participate closely in the overall process, by establishing and maintaining the component model databases and thermal parameter characterizations. These parameters would be predetermined to coincide with those manufacturing.

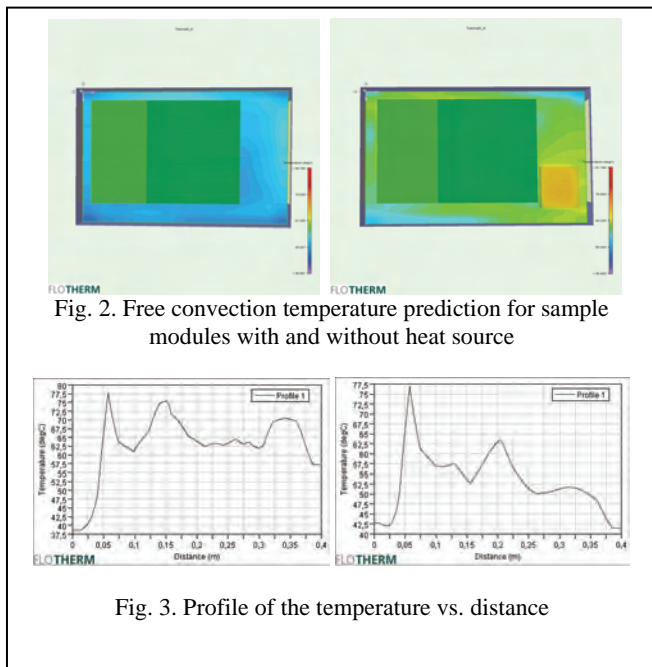


Fig. 2. Free convection temperature prediction for sample modules with and without heat source

Fig. 3. Profile of the temperature vs. distance

IV. CONCLUSION

Numerical methods have demonstrated their ability to produce useful and generally reliable estimates of the temperatures in electronic cooling situations.

These codes can often predict a hot spot with good accuracy, but offer no diagnostic help in determining what to change for the next trial.

This paper shows that the usefulness of a commercial code could be extended, and its value to the user greatly enhanced, paper shows that the usefulness of a commercial code could be extended, and its value to the user greatly enhanced, by equipping it to generate the diagnostic information needed by the heat transfer engineer.

The following information is needed for each component under normal operating conditions:

- Its operating temperature
- Its adiabatic temperature
- The mixed-mean coolant temperature approaching it
- Its net radiation and conduction inputs
- Its electrical power dissipation
- The value of h_{ad}
- The pressure drop per row in the vicinity

With these values known, the heat transfer engineer can diagnose the cause of overheating and more quickly arrive at an appropriate re-

The electronics cooling CFD package FLOTHERM is a computational fluid and heat transfer analysis and design package specifically for the analysis of electronic equipment. FLOTHERM makes use of the finite volume method to analyze three-dimensional geometries from chip level to system level.

These can all be obtained without undue effort either by integration of values already available over appropriate areas or by “freezing” the flow calculation and sequentially changing the power distribution (relying on the linearity of the energy equation and the fact that h_{ad} does not change when the temperature distribution changes).

ACKNOWLEDGEMENT

Research in this subject has recently commenced through a NIS TUS funded project, which started in 2007.

REFERENCES

- [1] J. H. Lienhard, *A Heat Transfer Textbook*, third edition, Phlogiston Press, Cambridge Massachusetts, 2006.
- [2] P. Gauche, “A Design Approach to Thermal Characterization of Forced Convection Systems Using Superposition in CFD” IMAPS, Conference Proceedings, pp. 18-22, Boston, USA, 2000.
- [3] D. E. Arvizu and R.J. Moffat, “The Use of Superposition in Calculating Cooling Requirements for Circuit-Board-Mounted Electronic Components” Proceedings of the 32nd Electronic Components Conference, pp. 133-144, San Diego, USA, 1982.
- [4] A. Andonova, N. Kafadarova, G. Pavlov, “Investigation of the Effective Thermal Conductivity of the PCB”, *Годишник на ТУ-София*, том 56, кн.1, стр. 120-125, 2006. G. Blad, D. Klepacki, J. Potencki, “Application of Electro-thermal Analogy for Complex Simulation of Hybrid Power Controllers”, ICEST, Conference Proceedings, pp. 262-265 Sofia, Bulgaria, 2006.

Laser Modeling In Q-switch Regime

Ivana Veselinovic¹, Milesa Sreckovic² and Biljana Veselinovic³

Abstract – A method which is often used to increase laser oscillator power and for obtaining short pulses consists of Q-switching (Q-spoiling method). The technique allows the production of laser pulses with extremely high (gigawatt) peak power. Some ways of laser cavity dumping by loss modulation (Q-switching) are analyzed in this paper. The chosen approach is performed used by numerical modeling.

Keywords – Q-switching, Q-spooling, Laser cavity, Loss modulation.

I. INTRODUCTION

We will analyze a mode of laser operation extensively employed for the generation of high pulse power which is known as Q-switching in this paper. The laser system should be designated to produce the adequate optical Q switch of the resonant cavity. The quality factor Q can be treated on various points of view. Generally speaking Q factor is defined as the ratio of the energy stored in the cavity to the energy loss per cycle.

In the technique of Q-switching, optical pumping energy is stored in the amplifying (active) medium while the Q factor is lowered to prevent the onset of laser emission. Although the energy stored and the gain in the active medium are high, the cavity losses are also high, lasing action is not possible. When a high Q is restored, the stored energy is suddenly released in the form of a very short pulse. Because of the high gain created by the stored energy in the active material, the excess excitation is discharged in an extremely short time. The peak power of the resulting pulse exceeds that obtainable from an ordinary long pulse by several orders of magnitude. Without Q modulation the dynamical lasing regime is in μs scale, (i.e. in free generation regime the spikes would be expressive). The theory of Q-switch regime is covered in numerous references [1-6], [9]. Some of them are based on five general laser equations. The principal facts are that the obtained pulses could be described by:

- triangle shape
- three characteristics zones.

Triangle shape for Q-switch pulse progress is presented in the Fig 1a.

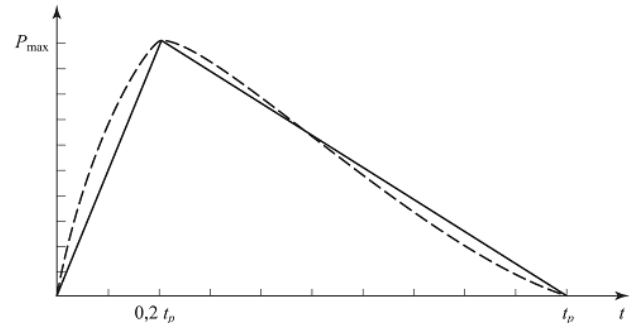


Fig. 1a. Triangle shape for Q-switch pulse progress

Three characteristic zones of pulse progress are shown in the Fig. 1b:

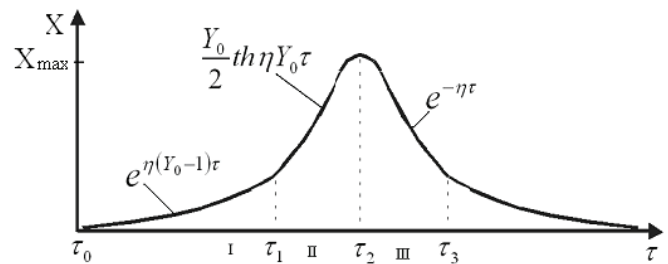


Fig. 1b. Three characteristics zones for Q-switch pulse progress

The most popular time cycle for Q-switching is shown in the Fig. 1c.

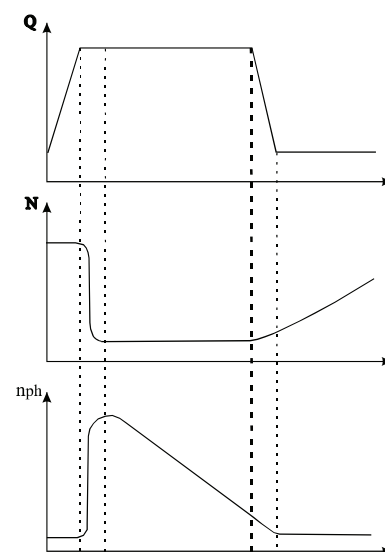


Fig. 1c. The most popular Q-switching cycle

¹Ivana Veselinović, 11000 Beograd, Serbia, E-mail: ivancica1301@yahoo.com

²Milesa Srećković, Belgrade University, Dept. Electric Engineering, Bulevar Kralja Aleksandra 73, 11001, Belgrade, Serbia, Email: Milesa@Tesla.rcub.bg.ac.yu

³Biljana Veselinović, Vinča Institute of Nuclear Sciences, Laboratory of computer sciences, P.O. Box 522, 11001, Belgrade, Serbia, Email: bilja@vin.bg.ac.yu

Output power may be written as:

$$P = \frac{h\nu n_f}{\tau_c}, \quad (1)$$

General approach to max output power may be evaluated as:

$$P = n_{f \max} \frac{h\nu}{\tau_c} = \begin{cases} \frac{N_0 h\nu}{2 t_c}, & \text{3-level-system} \\ N_0 \frac{h\nu}{\tau_c}, & \text{4-level-system} \end{cases} \quad (2)$$

where N_0 is linked to inversion population.

II. LASER CAVITY DUMPING BY LOSS MODULATION

Further, a method enabling to exceed the threshold carrier density in a laser will be described here. The method allows $n_{d0} \gg n_{threshold}$. Because of that, during an initial period, the cavity losses α_c are artificially increased to maintain cold cavity conditions. The density [1] of electrons which occupy level $|2\rangle$ is given by Eq. 3:

$$n_2(t) = R\tau_2(1 - e^{-t/\tau_2}) \quad (3)$$

The T_a is made enough large so that the most of available states $|2\rangle$ become occupied ($T_a \approx n/R$, where n is the total density of emission centres). The reflectivity of the exit mirror can be considerably reduced by means of a Pockels cell. As a result, the quality factor Q of the cavity can be modulated or Q-switched. The inversion population density $n_i \approx n$ (i for initial) in level $|2\rangle$ at the end of the first low-Q cycle is very large in comparison to the clamped inversion density $n_{threshold}$ during laser emission (Fig. 2).

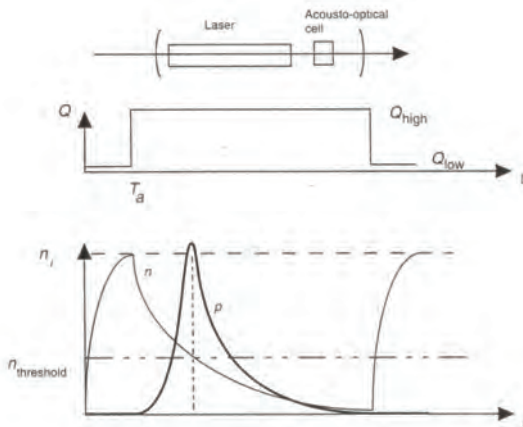


Fig. 2. Principle of laser cavity dumping by loss modulation (Q-switching)

In Fig. 2, between 0 and T_a , significant cavity losses are presented as a means of decreasing the Q factor of the cavity. That is achieved by using, acousto-optic, electrooptic and magneto-optic modulators or by mechanical modulation techniques.

While the Q of the cavity is artificially maintained at a value Q_{low} , the inversion population is built up to a value n_i exceeding the value of $n_{threshold}$ for the high- Q cavity. The Q -factor of the cavity is then restored to its original value of Q_{high} . The additional energy which is stored during the low- Q charging phase is released into a single giant pulse.

The same is true for the energy stored by the occupied states. The cavity is switched to a high- Q value, by restoring the high reflectivity of the mirrors, for example. Simplifying elementary equations for EM field [1], the energy stored in the cavity is released as:

$$\frac{d}{dt}Y = (X - 1)Y, \quad (4a)$$

$$\frac{d}{dt}X \approx -XY. \quad (4b)$$

To simplify, we will suppose that the lifetime of level $|2\rangle$ remains very large in comparison with the photon lifetime. The Eq. 4 may be written as:

$$\frac{d}{dt}Y = (X - 1)Y, \quad (5a)$$

$$\frac{d}{dt}X \approx u(X_0 - X) - XY. \quad (5b)$$

Dividing (5 a) with (5 b), we obtain:

$$\frac{dY}{dX} \approx \frac{1}{X} - 1, \quad (6)$$

which may be integrated and written as:

$$p = n_{threshold} \ln \frac{n_d}{n_i} - (n_d - n_i). \quad (7)$$

The photon density is at a maximum when $dp/dt = 0$ in Eq. 5, i.e. when $n = n_{threshold}$:

$$p_{\max} = n_i \left(1 + \frac{n_{threshold}}{n_i} \ln \frac{n_{threshold}}{n_i} - \frac{n_{threshold}}{n_i} \right) \approx n_i, \quad (8)$$

when $n_{threshold} \ll n_i$. That is often the case. We will now calculate the increase in maximum power of the laser relative

to its stationary operation. The number of photons available in the cavity (p_{cw} where CW refers to continuous wave) without Q-switching, may be written as:

$$p \approx p_{sat} \frac{n_{d0}}{n_{threshold}} = \frac{\tau_c}{\tau_{sat}} n_{d0} \approx \frac{\tau_c}{\tau_2} n_{d0} = R_2 \tau_c, \quad (9b)$$

or $p_{cw} = R \tau_c$, where τ_c is the photon lifetime in the high-Q cavity and R is the pump rate. The maximum photon density (p_{QS}) achieved by Q-switching is given by Eq. 8 or

$$p_{QS} = n_i = R T_a, \quad (9)$$

where $n_i \approx n$ is the total density of the emission centres. The time T_a is fairly close to the lifetime τ_2 . Then, the ratio of the CW exit power to the Q-switch power is (Fig.3.):

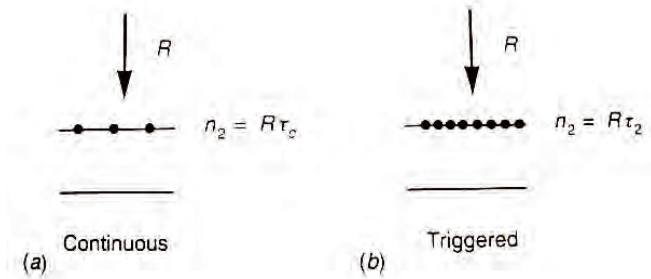


Fig. 3. Simplified comparison of the CW output power to the Q-switch power: (a) continuous (CW) mode, (b) Q-switched mode

In a laser operating in a continuous (CW) mode (a), the maximum density of electrons in the excited state is given by the threshold density value which is determined by photon lifetime in the cavity τ_c . In Q-switched mode (b), the maximum electron density is determined by carrier lifetime in the excited state τ_2 , and can be considerably larger than τ_c .

$$\frac{P_{QS}}{P_{CW}} = \frac{n_i}{n_{threshold}} \approx \frac{\tau_2}{\tau_c} \gg 1. \quad (10)$$

The lifetime τ_2 is generally of the order of 1 ms and τ_c is generally of the order of 1 ns. Because of that, we can conclude that the ratio given in Eq. 10 may become considerable. The peak output power of the pulse is precisely given by the product of half the internal photon density (we divide by two as only those photons moving in the direction of the exit mirror are to be considered) with and the transmittance T_s of the output mirror the cross-sectional area A of the laser cavity:

$$P_{QS} = h\nu \frac{c}{2} T_s A n_i. \quad (11)$$

The length of the laser pulse may be calculated by numerically integrating the non-linear differential Eq. (5).

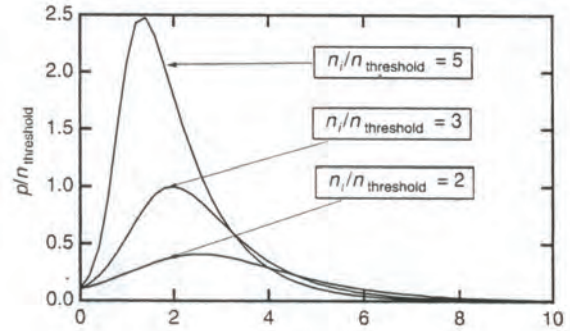


Fig. 4. $p/n_{threshold}$ in function t/τ_c in Q-switched laser mode for various values of $n_i/n_{threshold}$ above threshold

III. RESULTS OF PROGRAM P1

Analyzing references [1-9] we will present a program which allows to obtain dynamic behavior of a Q-switched laser, written for MATHEMATICA.

As the Eq. 5 has a zero photon density as an initial condition ($Y(0) = 0$), it enforces as acceptable solutions the time-independent inversion population $X(T) = X(0)$ and zero photon density $Y(T) = 0$. As shown in Fig. 4, we have had to put artificial initial conditions ($Y(0) = 0.1$) to simulate the effect of Q-switching. This points up the physical necessity of spontaneous emission in triggering laser oscillations. The program P1 allows calculation of the temporal response of a laser to modulated cavity loss. It is written assuming that $X(0) = 4$.

P1. Mathematica program which allows to obtain Q-switched laser dynamics

```

eq1 = y'[t] == y[t] (x[t] - 1);
eq2 = x'[t] == -x[t] y[t];
sol = NDSolve[{eq1, eq2, x[0] == 4, y[0] == 0.1},
  {x[t], y[t]}, {t, 0., 10}];
plot23 = Plot[Evaluate[y[t] /. sol],
  {t, 0, 10}, PlotStyle -> {RGBColor[0, 1, 1]},
  DisplayFunction -> Identity];
Show[plot23, DisplayFunction -> $DisplayFunction]
    
```

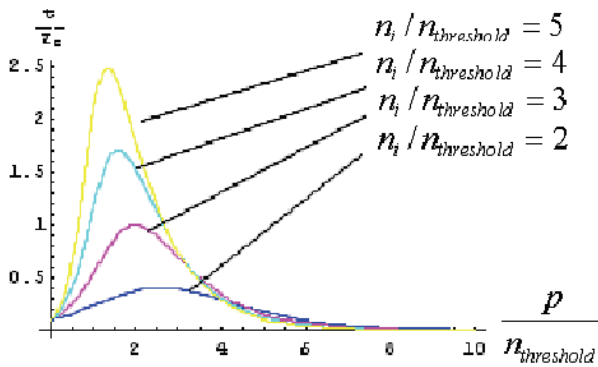


Fig. 5. Results of program P1

IV. ANALYSIS OF RESULTS

Fig. 5. gives four examples from which we conclude that the typical pulse lengths are of the order of a few photon lifetimes (a few τ_c), i.e. tens of nanoseconds for laser cavities [1] measuring a few centimeters in length. Loss modulation in the cavity can be achieved without external application of electrical pulses to an optical shutter, for instance. Beside mentioned electrooptics and mechanical ways, this can be achieved by placing a saturable absorber in the laser cavity, too. The introduction of such a passive element will result in spontaneous Q-switching of the cavity. At the beginning of the cycle, the absorbing characteristics of the material lower the Q factor of the cavity. During that time electrical energy is stored in the cavity by increasing the electron density in the excited level. When the medium saturates, the cavity losses are reduced and stimulated emission proceeds to liberate the stored energy in the carriers into the form of an optical pulse with high-power (giant pulse).

V. CONCLUSION

Some methods for pulse shortening by Q-switch methods are analyzed in this paper. Laser cavity dumping by loss modulation (Q-switching) was chosen for analyze in this paper. A program which allows to obtain dynamic behavior of a Q-switched laser has been written for MATHEMATICA. The results from reference are agreed with other references, and for given domains program works. We analyzed various approaches to Q - switch regime, qualitative description and variation of Lamb theory.

REFERENCES

- [1] E. Rosencher and B. Vinter, *Optoelectronics*, Cambridge University Press, Cambridge, 2002.
- [2] M. Young, *Optics and Lasers*, Springer – Verlag Berlin Heidelberg, New York, Tokyo, 1984.
- [3] F. Berstein, *Bases de l'électronique quantique*, Mir, Moskva, 1971.
- [4] W. Koechner, *Solid-State Laser Engineering*, Springer - Verlag, Berlin, 1976.
- [5] W. Demtröder, *Laser Spectroscopy: Basic Concepts and Instrumentation*, Electronic edition.
- [6] F. Gan, *Laser Materials*, Electronic edition.
- [7] I. Veselinović, M. Srećković, B. Veselinović, A. Đurđević, B. Stojković, "Non-linear Frequency Conversion Efficiency Analysis", YU INFO 2007. Kopaonik, Serbia.
- [8] B. Veselinović, M. Srećković, I. Veselinović, M. Vlačić, "Modeling of Semiconductor Laser Characteristics", YU INFO 2007. Kopaonik, Serbia.
- [9] W.E. Lamb, *Theory of Optical Maser*, Phys. Rev. 134, A1429-A1450, 1964.

Modeling of Quantum Generators and Amplifiers on Semiconductor Materials

Biljana Veselinović¹, Mileša Srećković², Ivana Veselinović³ and Milan Vlačić⁴

Abstract – Analysis of characteristics for quantum well laser diode are presented in this paper. The performed analysis had been based on analytical and numerical calculations. Some adequate program from literature are modified and executed for given calculator architecture. The variation of principal lasing parameters is performed.

Keywords – Quantum well lasers, p-n diode, Transparency threshold, Two-dimensional critical densities, Diode laser.

I. INTRODUCTION

Lasers and amplifiers on semiconductor materials more and more replace other type of lasers. We can see almost daily appearance of come new semiconductor lasers with different coloring (blue, yellow, ...). The output of the other laser types were obtained, either directly, with parameter changes, or by Raman's or some other processes (frequency coupling), but output from small active material (comparing with large ionic and other lasers) were far better. On the one hand, this is in context of the semiconductor technologies papers, and on the other hand, semiconductor lasers work on many possible pumping ways. They can also be used as pumps with the other laser types.

After the first laser diodes, double heterostructure lasers, a line of quantum well, quantum dot, quantum wire lasers appeared. There are also new types of VCSEL, VECSEL with a vertical resonators, etc. The main problems in all types are relations between laser characteristics: amplification, threshold, pump power, resonator configuration and efficiency. Efficiency is generally connected with pumping way, but here analysed type is type of active material that you should go theoretically and to approach high levels of efficiency. Beside the general approaches, like with the other types that have these parameters, there are also some peculiarities with every separate type. Transparency threshold was chosen as a problem in this paper.

II. TRANSPARENCY THRESHOLD

Fig. 1 shows the p-n diode which containing a single quantum well [1].

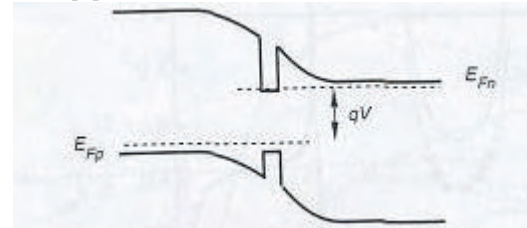


Fig. 1. A forward biased p-n diode containing a single quantum well.

Injected carriers accumulate in this well by forward biasing the diode. The carrier density per unit area n_s can be expressed as:

$$n_s = p_s = \frac{Jt_{tot}}{q} \quad (1)$$

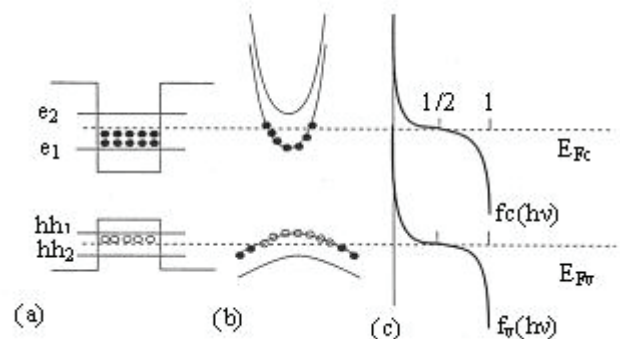


Fig. 2. Quantum well: a) band diagram; b) subband structure; c) associated Fermi-Dirac distributions;

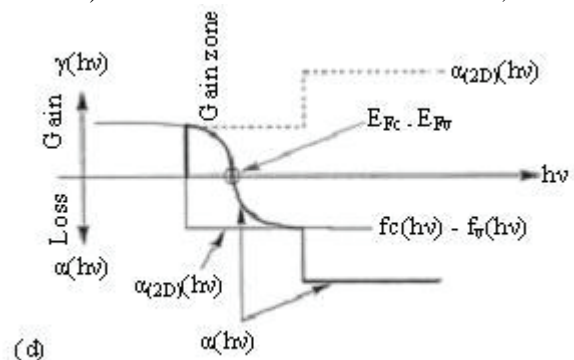


Fig. 2. Quantum well: d) gain curve

¹Biljana Veselinović, Vinča Institute of Nuclear Sciences, Laboratory of computer sciences, P.O. Box 522, 11001, Belgrade, Serbia, Email: bilja@vin.bg.ac.yu

²Mileša Srećković, Belgrade University, Dept. Electric Engineering, Bulevar Kralja Aleksandra 73, 11000, Belgrade, Serbia, Email: Mileša@Tesla.rcub.bg.ac.yu

³Ivana Veselinović, BIA, Belgrade, Serbia, Email: ivancica1301@yahoo.com

⁴Milan Vlačić, YUBC System A.D., Dimitrija Tucovića 6, 11000, Belgrade, Serbia, Email: holydud@teleport.co.yu

A population inversion which lead to transparency [4] in the quantum well (Fig. 2) can be obtained with a sufficiently elevated current densities. The quasi-Fermi levels begin to penetrate the subbands close to transparency. Only the $n=m=1$ subbands are involved. The gain can be expressed as:

$$\gamma(h\nu) = \alpha_{2D} [f_c^1(h\nu) - f_v^1(h\nu)] \theta(h\nu - E_g - e_1 - hh_1) \quad (2)$$

The absorption coefficient α_{2D} (cm^{-1}) represent the absorption for a quantum well with zero population [1].

The quasi-Fermi levels, E_{Fc} i E_{Fv} are given by the conditions:

$$n_s = \int_{-\infty}^{\infty} \rho_{2D,e}(E) f_c^1(E) dE, \quad (3)$$

$$n_s = \int_{-\infty}^{\infty} \rho_{2D,hh}(E) [1 - f_v^1(E)] dE. \quad (4)$$

These conditions can be calculated precisely if the state densities for electrons ($\rho_{2D,e}$) and holes ($\rho_{2D,hh}$) are known. For electrons, Eqs. (3) and (4) can be expressed as:

$$n_s = \rho_{2D,e} \int_{E_g+e_1}^{+\infty} \frac{1}{1 + \exp[(E - E_{Fc})/kT]} dE, \quad (5)$$

where the energy at the top of the valence band is taken to be zero. Setting $\exp((E - E_{Fc})/kT) = u$ and $\exp((E_g + e_1 - E_{Fc})/kT) = u_c$ Eq. (5) takes the form:

$$n_s = \rho_{2D,e} kT \int_{u_c}^{+\infty} \frac{1}{u(1+u)} du = \rho_{2D,e} kT \ln(1 + \frac{1}{u_c}), \quad (6)$$

so that:

$$n_s = n_c \ln \left[1 + \exp\left(\frac{E_{Fc} - E_g - e_1}{kT}\right) \right], \quad (7)$$

$$n_s = n_v \ln \left[1 + \exp\left(\frac{hh_1 - E_{Fv}}{kT}\right) \right], \quad (8)$$

where, n_c and n_v , are two-dimensional critical densities given by:

$$n_c = \rho_{2D,e} kT = \frac{m_e kT}{\pi \hbar^2}, \quad (9)$$

$$n_v = \rho_{2D,hh} kT = \frac{m_{hh} kT}{\pi \hbar^2}. \quad (10)$$

It will be shown that transparency and threshold densities can be expressed as a product of these two-dimensional critical densities by a factor close to 1, typical between 1 and 5.

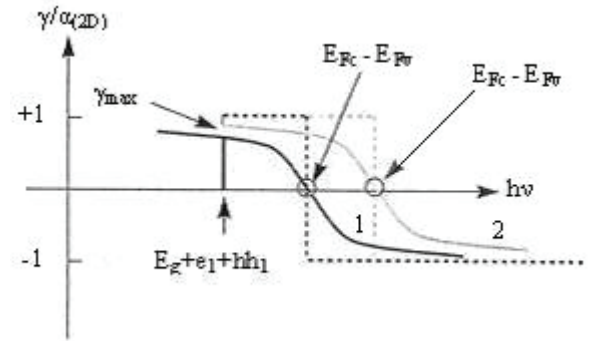


Fig. 3. Evolution of the gain curve for a quantum well laser for increasing pump currents.

The Fermi distributions in subbands n and m are given with:

$$f_c^n(h\nu) = \frac{1}{1 + \exp\{[E_c^n(h\nu) - E_{Fc}]/kT\}}, \quad (11)$$

$$E_c^n(h\nu) = E_g + e_n + \frac{m_r}{m_c} (h\nu - E_g - e_n), \quad (12)$$

$$f_c^m(h\nu) = \frac{1}{1 + \exp\{[E_v^m(h\nu) - E_{Fv}]/kT\}}, \quad (13)$$

$$E_v^m(h\nu) = -\frac{m_r}{m_v} (h\nu - E_g - hh_m). \quad (14)$$

We can calculate gain in this way: for a given current density J , calculate the carrier density (Eq. (1)), then quasi-Fermi levels (Eqs. (7) and (8)), and finally the gain with the help of (2) and Fermi functions (11-14). The gain curve as a function of photon energy for increasing carrier densities is presented in Fig. 3. The dotted curves show the gain values at zero temperature. The black curves (1) correspond to low pump current conditions. The grey curves (2) correspond to high pump current conditions. We note an abrupt increase in the gain for $h\nu > E_g + e_1 + hh_1$. The maximum gain

γ_{\max} is obtained when $h\nu = E_g + e_1 + hh_1$:

$$\gamma_{\max} = \alpha_{2D} [f_c^1(h\nu = E_g + e_1 + hh_1) -$$

$$-f_v^1(h\nu = E_g + e_1 + hh_1)]. \quad (15)$$

Eqs. (7), (8) and (11-14) allow to relate the value of the Fermi function to the carrier density n_s :

$$1 - e^{-n_s/n_c} = 1 - \frac{1}{1 + \exp[(E_{Fc} - E_g - e_1)/kT]} = f_c^1(E_g + e_1). \quad (16)$$

Similarly:

$$e^{-p_s/n_c} = f_v^1(hh_1). \quad (17)$$

The maximum gain can be written as:

$$\gamma_{\max} = \alpha_{2D}(1 - e^{-n_s/n_c} - e^{-n_s/R_{cv}n_c}), \quad (18)$$

where $R_{cv} = (m_{hh}/m_c)$ is the ratio of the effective masses for carriers in the conduction and valence bands.

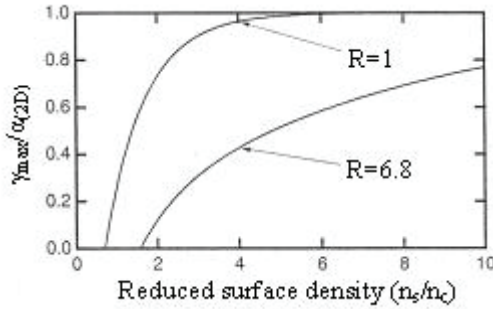


Fig. 4. Normalized gain as a function of normalized carrier surface density.

Fig. 4 shows the variation in maximum gain as a function of reduced carrier surface density n_s/n_c with $R=6.8$ (GaAs) and $R=1$. It is obvious that the gain increases rapidly once the transparency condition has been reached, but saturates quickly. This results from the form of the two-dimensional density of states. From (14) the maximum gain becomes positive when the transparency threshold is reached once. When the transparency threshold n_{tr} is reached:

$$e^{-n_{tr}/n_c} + e^{-n_{tr}/R_{cv}n_c} = 1. \quad (19)$$

For $R_{cv} = 1$, we have $n_{tr} = n_c \ln(2)$. The transparency current is always related to n_c by a numerical factor close to 1. It explains the importance of the concept of the two-dimensional density of states n_c . The transparency condition for different values of R_{cv} is presented in Fig. 4. We note that it is advantageous to have closely matched effective masses between the valence and conduction bands.

The variation in maximum gain γ_{\max} , as a function of carrier surface density is logarithmic:

$$\gamma_{\max} = \gamma_0 \ln\left(\frac{n}{n_{tr}}\right), \quad (20)$$

where the constant γ_0 depends only on the effective mass ratio R_{cv} . For values of n which approach the transparency threshold, the Eq. (20) leads to behaviours close to those predicted by (18).

III. RESULTS OF PROGRAM P1

In order to analyze ratio between Eqs. (18) and (20) a procedure has been modeled and modified in MATHEMATICA program, given in the reference [1]. Equality presentation has been done using P1.

P1: Equality presentation between (18) and (20).

```

f = 1 - Exp[-x] - Exp[-x/R];
R = 6.8;
plot1 = Plot[f, {x, .5, 5}];
plot1 = Plot[f, {x, .5, 5},
Frame -> True, FrameLabel -> {n/n_c, gamma/alpha_2D},
RotateLabel -> False];
FindRoot[f == 0, {x, 1}];
x0 = x /. %;
g = Log[x/x0];
plot2 = Plot[0.48 * g, {x, .5, 5},
Frame -> True, FrameLabel -> {n/n_c, gamma/alpha_2D},
RotateLabel -> False];
Show[plot1, plot2]
    
```

The graphics shown in Fig. 5 are the results of execution of the program P1.

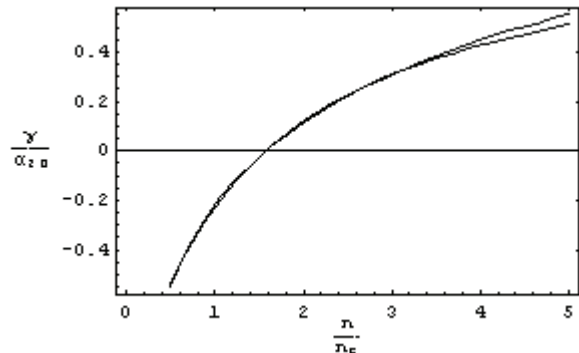


Fig. 5. Result of program P1

IV. ANALYSIS OF RESULTS

IV. CONCLUSION

Fig. 5 compares expressions (18) and (20). By fitting, we find that $\gamma_0 = 0.48\alpha_{2D}$.

For GaAs, the two-dimensional state densities are:

$$\rho_{2D,e} = m_c / \pi\hbar^2 = 2.8 \times 10^{13} \text{ cm}^{-2} \text{ eV}^{-1},$$

$$\rho_{2D,hh} = m_{hh} / \pi\hbar^2 = 1.9 \times 10^{14} \text{ cm}^{-2} \text{ eV}^{-1}.$$

The two-dimensional critical density in the conduction band is $n_c = \rho_{2D,e} kT$ or $2.8 \times 10^{13} \text{ cm}^{-2} \text{ eV}^{-1} \times 0.0259 \text{ eV} = 7.25 \times 10^{11} \text{ cm}^{-2}$. That is presented in Fig. 4. In GaAs, $n_{tr} = 1.6n_c = 1.16 \times 10^{12} \text{ cm}^{-2}$. In a 100\AA (10 nm) wide quantum well, this corresponds to a transparency threshold density of $1.16 \times 10^{18} \text{ cm}^{-3}$. The result is very close to that obtained for bulk material. The advantage of using quantum wells structures does not involve decreasing the threshold carrier densities, but rather in decreasing the transparency current densities and hence the threshold current densities.

We analyzed the appropriate theories [1-7] and lasing condition. For the chosen model, we analyzed existing programming. For selected lasing parameters, we calculated maximum gain. The results correspond to the literature and the program works in defined domains.

REFERENCES

- [1] E. Rosencher, B. Vinter, "Optoelectronics", Cambridge University Press, Cambridge, 2002.
- [2] http://www.iop.org/EJ/article/0268-1242/19/2/024/sst4_2_024.html
- [3] N. Andrejev, Advanced Electronic Technologies and Systems Based on Low-Dimensional Quantum Devices, Electronic edition.
- [4] E. Kapon, Semiconductor Lasers I, Electronic edition.
- [5] I. Veselinović, M. Srećković, B. Veselinović, A. Đurđević, B. Stojković, "Non-linear Frequency Conversion Efficiency Analysis", YU INFO 2007. Kopaonik.
- [6] B. Veselinović, M. Srećković, I. Veselinović, M. Vlajnić, "Modeling of Semiconductor Laser Characteristics", YU INFO 2007. Kopaonik.
- [7] A. Yariv, *Quantum Electronics*, Wiley, New York, 1989.

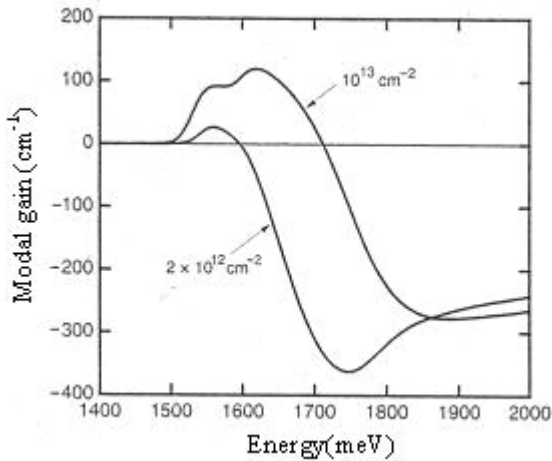


Fig. 6. Modal gain for a quantum well laser at two different carrier densities

The gain curve for a quantum-well laser is very complex. As the carrier densities increase in the wells, the electrons and holes populate higher energy states in the subbands and bring into play complex transitions: first the $e_1 - hh_1$ transitions, then $e_2 - hh_2$. Modal gain for a quantum well laser at two different carrier densities is presented in Fig. 6 shows. Both the $e_1 - hh_1$ and $e_2 - hh_2$ transitions can be observed under the higher current injection conditions.

Analysis of Electrical and Thermal Characteristics of Thermal Cutoffs

Aneta Prijić, Zoran Prijić, Biljana Pešić, Dragan Pantić and Stojan Ristić

Abstract – This paper presents the results of investigation of thermal cutoffs' characteristics in electrical and thermal domain by FEA. Radial S-type thermal cutoffs of two characteristic cutoff temperatures are simulated in steady state and transient regime. Dependences of rated functioning temperature, holding temperature, temperature rise and response time on different design parameters of cutoffs are analyzed. On the basis of the obtained simulation results optimization of geometry and dimensions of constitutive elements of thermal cutoffs is proposed.

Keywords – Thermal cutoffs, Electrical and thermal characteristics, FEA, Design optimization.

I. INTRODUCTION

Reliable operation of different home appliances, electric industrial and office automation equipment demands their protection from the overheating. For that purposes thermal cutoffs are utilized. They detect abnormal temperature rise in the device caused by conducting current above the rated value or by excess surrounding temperature and permanently open the electrical circuit. These are non-reset device type and act as the last protection components.

Functioning of thermal cutoffs is based on the property of low-melting alloy that fuses conducting parts to melt at the specified temperature (*cutoff temperature* - T_{CUTOFF}) thus breaking the connection between them. The basic classification of thermal cutoffs is by construction, rated functioning temperature and electrical ratings [1]-[3]. Construction of thermal cutoffs depends on the design of temperature sensing part (with special shrinking resin or spring), shape and dimensions of the leads (axial, radial or strip) and type of the packaging (ceramic, plastic or metal). Rated functioning temperature is defined by melting temperature of fusing alloy and ranges from 70°C to 240°C. Electrical ratings include different values of AC or DC current and voltage which determine cutoffs' operating conditions.

Thermal ratings of one type of cutoffs specify values of cutoff temperature, rated functioning temperature and holding temperature, as well as their tolerances. *Rated functioning temperature* - T_F is the temperature at which thermal cutoff changes its state of conductivity to open a circuit with detection current as the only load. Tolerances of this value are from -10°C to +0°C and it is usually for a constant value (dependent on the packaging) higher than the cutoff temperature.

Holding temperature - T_H is the maximum temperature at which thermal cutoff can be maintained while conducting rated current for 168 hours without functioning.

Beside thermal ratings which are crucial for appropriate implementation of thermal cutoffs, their quality and reliability are governed by performance data such as temperature rise due to *Joule* heating and response time [4]. Temperature rise is determined by properties of conducting parts and thermal properties of packaging. Response time is time for opening the cutoff after immersion into the silicon oil bath of specified temperature and is mainly dependent on thermal properties of constitutive elements.

Design and optimization of thermal cutoffs include determination of specified thermal and electrical ratings and performance data. For that purposes appropriate Finite Element Analysis (FEA) of electrical and thermal characteristics of cutoffs is employed.

In this paper results of electrical and thermal characteristics analysis of radial S-type thermal cutoffs by 3D numerical simulation are presented. Holding temperature and temperature rise for two types of cutoffs are determined by steady state simulation, while small displacement transient simulation is utilized for rated functioning temperature and response time investigations. Different geometries and dimensions of constitutive elements are considered. Optimization remarks from material consumption, manufacturing complexity and quality and reliability points of view are outlined.

II. CONSTRUCTION OF THERMAL CUTOFFS

Analyzed thermal cutoffs are with spring (S type) and radial leads, placed in plastic package. They are aimed for operation at rated current of 12 A and voltage of 250 V AC. Mechanical connection with the device under protection is made by classical soldering at free ends of the leads. Construction and main constitutive elements of considered cutoffs are shown in Fig. 1.

Active parts of the cutoff are soldering sheets made from low melting alloy which connect contact heads of the leads with conducting strip inside the package. Spring placed inside the package cap is compressed and it presses the strip. At normal operating temperatures there is an electrical conducting path between the leads. When cutoff temperature is reached alloy melts at the soldering sheets and the spring pushes the strip into the space above the leads. This space is filled by insulation fluid (in this case it is air), so conducting path is permanently cut off.

The authors are with the Department of Microelectronics and Microsystems, Faculty of Electrical Engineering, University of Niš, Aleksandra Medvedeva 14, 18000 Niš, Serbia, E-mail: aneta@elfak.ni.ac.yu

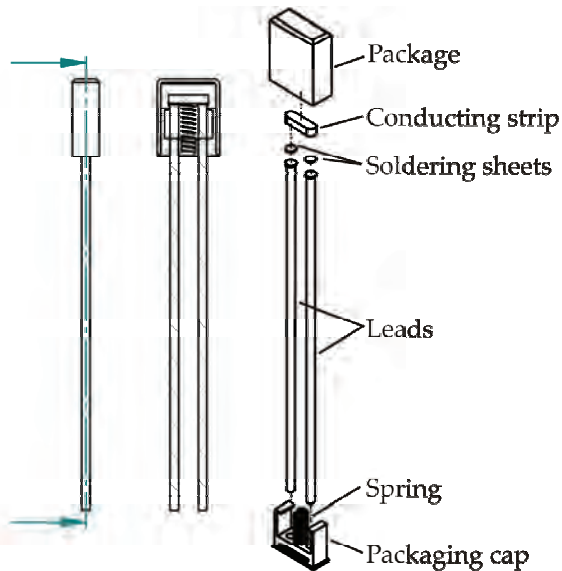


Fig. 1. Construction of thermal cutoffs

Values of characteristic dimensions of cutoff's elements, as well as materials they are made from, are listed in Table I.

TABLE I
CHARACTERISTIC DIMENSIONS AND MATERIALS OF
CUTOFF'S ELEMENTS

Element	Material	Characteristic dimension	Value (mm)
Lead	Copper	Length	57
		Diameter	1,2
		Contact head diameter	1,6
		Contact head thickness	0,25
Conducting strip	Copper	Length	5,6
		Width	1,6
		Thickness	0,6; 0,9; 1,2
Soldering sheet	Low melting alloy	Diameter	1,2; 1,6
		Thickness	0,15
Packaging	Makrolon (poly-carbonate)	Height	11
		Width	8,8
		Depth	3,8
		Cap height	4
		Wall thickness	0,5; 1
Spring	Steel	Diameter	1
		Length	3

Two low melting alloys are considered as the soldering sheet material. The first one is 42%Sn-58%Bi with melting point of 138°C. This is an eutectic alloy often used as Pb-free soldering material [5] and it is exploited in thermal cutoffs (S-138 type) for protection of power electric motors. The second is ternary eutectic alloy 52,5%Bi-15,5%Sn-32%Pb whose melting point is 95°C. Thermal cutoffs operating with this

alloy (S-95 type) are aimed for protection of water heating devices. Soldering sheets made from these alloys have microstructure with greater percentage of tin at the surface, which enables more efficient soldering of elements in cutoffs manufacturing processes [6].

Properties of cutoff elements' materials included in simulation incorporate their basic physical, electrical and thermal parameters [7], [8].

III. SIMULATION PROCEDURE

Simulation is performed with software that complex multiphysics problems solves numerically utilizing finite element analysis and multigrid approach [9]. It solves *Maxwell's* equations simultaneously with heat generation/transmission and elasticity equations. Through appropriate user interface geometry, dimensions and materials of cutoffs are given, load conditions are set and obtained solution is displayed graphically.

Load conditions define symmetry and degrees of freedom of cutoffs, values of conducting current, and method and areas of heat dissipation. Cutting plane from Fig. 1 presents symmetry boundary condition, while free ends of the leads are considered fixed. End of one lead is set to zero referent potential, while through second lead currents up to 15 A are applied. It is assumed that cutoffs are mounted in vertical position and heat exchange with bulk is by convection from free surfaces. Rated functioning temperatures, holding temperatures and temperature rise are determined for air as ambient fluid, while response time determination specifies silicon oil as surroundings. Values of convection coefficients in both cases are calculated according to [10] and assumed to depend on shape and orientation of the surface, thermal characteristics of the fluid and temperature difference between the surface and the bulk.

IV. RESULTS

Temperature of the soldering sheets under various operating conditions is of main interest in design and optimization processes of cutoffs. Its dependence on bulk temperature and applied current enables determination of rated functioning and holding temperatures important for cutoffs' implementation specifications. Distribution of temperature in S-138 cutoff at 12 A rated current and with bulk temperature 27°C is shown in Fig. 2. Vector presentation of current density distribution under the same condition is shown in Fig. 3. From these figures it is evident that maximum current density and consequently maximum temperature due to *Joule's* heating, exists at the boundary of conducting strip and soldering sheets. High thermal conductivity of leads, conducting strip and soldering sheets, as well as low thermal conductivity of package and air inside it, result that generated heat is mainly dissipated by convection from free surfaces of the leads. Also, range of temperature of conducting parts is only 1,5°C. The same qualitative distribution of temperature and current density exists in S-95 cutoffs, with slightly different maximum values [11].

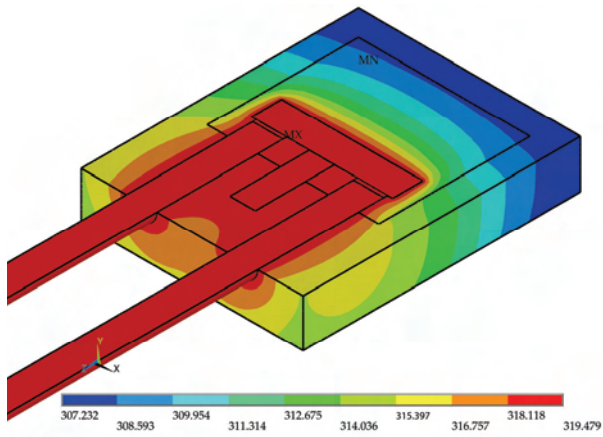


Fig. 2. Distribution of temperature (in K) in S-138 cutoff at rated current 12 A at bulk temperature of 27°C

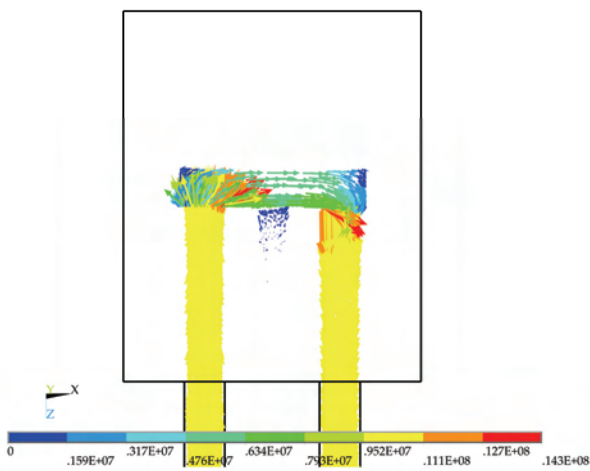


Fig. 3. Distribution of current density in S-138 cutoff at rated current 12 A at bulk temperature of 27°C

Temperature of soldering sheets in S-95 thermal cutoffs for different applied current at bulk temperature of 27°C is shown in Fig. 4. Temperature rise due to electro-thermal effects is less than 35°C even for currents 20% above rated 12 A. Simulation of S-138 thermal cutoffs gave similar dependence, with little lower temperature values due to higher conducting properties of applied alloy.

Dependence of soldering sheets temperature on bulk temperature for applied rated current of 12 A for S-95 thermal cutoff is shown in Fig. 5. From this figure holding temperature T_H is determined as the temperature of bulk at which cutoff temperature is reached and it is 78°C. Also, for S-138 thermal cutoffs this temperature is determined as 115°C.

For optimization purposes thermal cutoffs with different conducting strip thicknesses and changed contact heads of leads are simulated. Initial strip thickness value of 1,2 mm is decreased to 0,9 mm and 0,6 mm and dependencies of soldering sheets temperatures are analyzed. From Fig. 4 it is evident that decrease of strip thickness to 0,9 mm does not affect temperature rise, while for thickness of 0,6 mm it is slightly increased. Also, dependencies from Fig. 5 show that holding

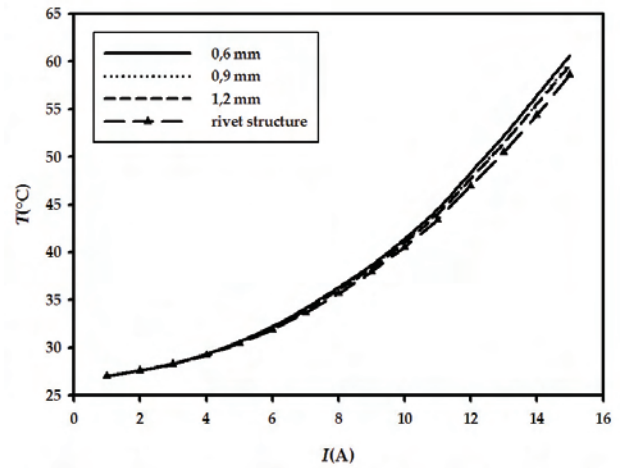


Fig. 4. Temperature rise in S-95 cutoff for different conducting strip thicknesses at bulk temperature of 27 °C

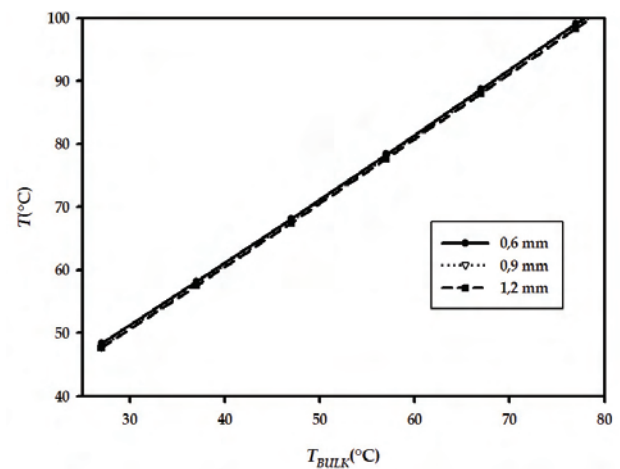


Fig. 5. Dependence of soldering sheets temperature on bulk temperature in S-95 cutoff with applied current 12 A for different conducting strip thicknesses

temperature remains unchanged in all cases. On the basis of the above considerations decrease of strip thickness to 0,9 mm is justified since thermal cutoffs performances remain unchanged, while better manufacturing capabilities and less material consumption are achieved.

In the second analysis contacting heads of leads are formed in rivet shape whose dimensions are listed in Table I and soldering sheets are adjusted appropriately. Riveted contact heads enable better mechanical characteristics of soldered joints. Considering electro-thermal characteristics, from Fig. 4 it is evident that temperature rise is decreased about 1°C for rated current value (for the second type of cutoffs it is about 0,5°C). These improvements are minimal and change of initial design is not justified since it involves additional manufacturing steps.

Rated functioning temperature and response time determination of thermal cutoffs demand transient analysis. Standards prescribe rated functioning temperature as the temperature at which cutoff is opened when operating in ambient whose temperature is set to 20°C bellow cutoff temperature and afterward gradually raised by 1°C/min. Simulation results for such boundary conditions of soldering sheets temperature in

time for both cutoff types are presented in Fig. 6. Rated functioning temperatures determined from this figure are 1°C above cutoff temperatures ($T_F=96^{\circ}\text{C}$ for S-95 and $T_F=139^{\circ}\text{C}$ for S-138 type), due to high thermal conductivity of cutoff's elements.

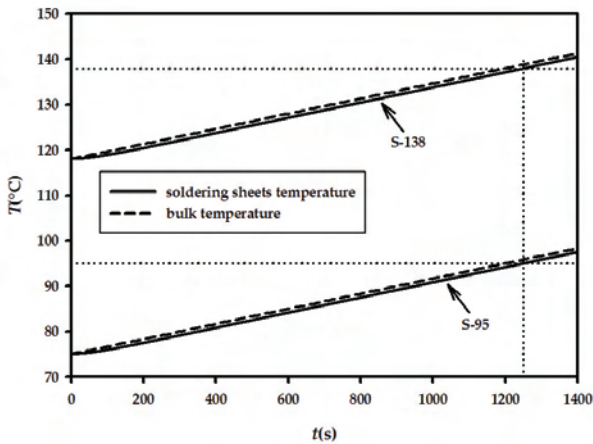


Fig. 6. Dependence of soldering sheets temperature for rated functioning temperature determination

Simulation results of soldering sheets temperature after immersion of S-95 cutoff maintained at 27°C into silicon oil bath whose temperature is ΔT above cutoff temperature is shown in Fig. 7. Similar dependencies are obtained for S-138 cutoff type. Response times determined on the basis of these curves for both types are plotted in Fig. 8 which could be used for quality verification of cutoffs with different constructions. It is evident that response time is strongly dependent on cutoff temperature and temperature of the silicon oil bath.

Also, cutoffs with reduced package wall thickness (0,5 mm) are investigated and no changes in rated functioning temperature and response time are observed. Therefore, since mechanical characteristics of cutoffs depend on this thickness, greater value is preferable.

V. CONCLUSION

On the basis of finite element analysis of electrical and thermal characteristics for two types thermal cutoffs, their rated functioning and holding temperatures are determined. Response time dependencies of thermal cutoffs for their quality specification are obtained. Change of conducting strip thickness is proposed as an optimization result, with minimization of material consumption and simplicity of manufacturing processes being design goals. On the other hand, it is concluded that rivet shape of contact heads of the leads introduces minor improvements into thermal characteristics of cutoffs and initial flat shape is optimal. Moreover, simulation showed that reduction of packaging wall thickness does not influence on time dependent parameters of cutoffs (rated functioning temperature and response time).

ACKNOWLEDGEMENT

This work was supported by grant of the Serbian Ministry of Science and Environmental Protection under contract No. TR6140.

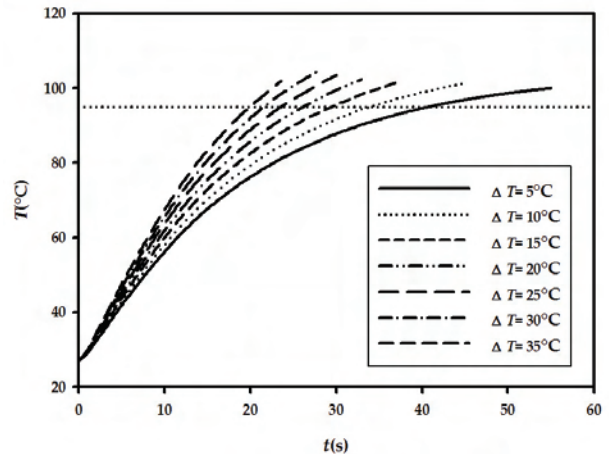


Fig. 7. Change of soldering sheets temperature with time in S-95 cutoff for different silicon oil temperatures

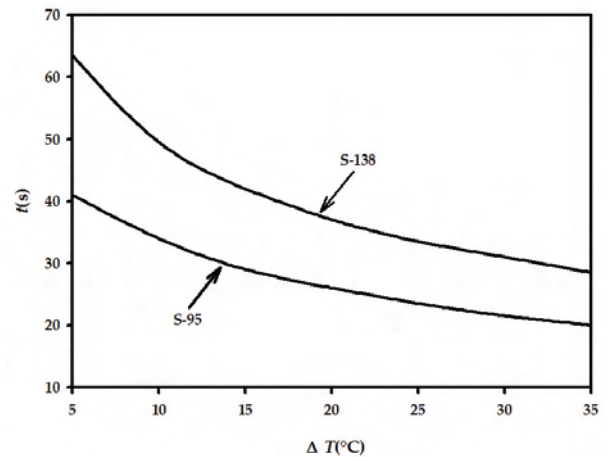


Fig. 8. Response time of cutoffs

REFERENCES

- [1] "Thermal cutoffs", World Thermo Corp., Taiwan, 1995.
- [2] <http://www.us-electronics.com/files/Thermalcutofffuses.pdf>.
- [3] PANASONIC-Thermal Cutoffs – Data sheet.
- [4] NEC-Thermal Cutoff SEFUSE – Data sheet, 1996.
- [5] F. Hua, Z. Mei, and J. Glazer, „Eutectic Sn-Bi as an Alternative to Pb-Free Solders“, in *Proc. of Electronic Component and Technology Conference*, pp. 277-283, 1998.
- [6] A. Prijić, B. Pešić, Z. Prijić, „Karakterizacija niskotopivih legura za primenu u termičkim prekidačima“, Zbornik radova L konferencije ETRAN, IV sveska, pp. 119-122, Beograd, Srbija i Crna Gora, Jun, 2006.
- [7] <http://www.indium.com/products/tableofalloys.xls>.
- [8] J. Rigdeon, *Macmillan Encyclopedia of Physics*. Simon & Schuster, 1996.
- [9] ANSYS 8.0 Inc.
- [10] C. Popiel, J. Wojtkowiak, „Experiments on free convective heat transfer from side walls of a vertical square cylinder in air“, *Experimental thermal and fluid science*, Vol. 29, No. 1, pp. 1-8, 2004.
- [11] A. Prijić, B. Pešić, Z. Prijić, D. Pantić, S. Ristić, „Analiza karakteristika termičkih prekidača 3-D numeričkom simulacijom“, Zbornik radova VI simpozijuma o industrijskoj elektronici INDEL 2006, pp. 48-52, Banja Luka, Republika Srpska, Novembar, 2006.

Macromodel for CMOS Analogue Switches Temperature Effects Sensing

Ivailo M. Pandiev¹

Abstract – This paper, is focused on an enhanced SPICE macromodel for CMOS analogue switches, which takes into account the second-order effects, such as the leakage current, the supply current and the on-resistance as a function of temperature. The simulation model is developed through modifying the basic macromodels employing the mechanism of controlled sources and subcircuits. Model parameters are extracted for the integrated analogue switches ADG411 and MAX4601 as examples. The accuracy of the models is demonstrated by comparison with the data sheet parameters of the real ICs.

Keywords – Analogue circuits, Temperature effects, CMOS analogue switches, SPICE, Modelling.

I. INTRODUCTION

Solid-state CMOS analogue switches have become an essential component in the design of electronic systems, which require the ability to control and select a specified transition path for the analogue signal. These analogue devices are used in a wide variety of applications including multi-channel data acquisition systems, process control, communication systems, etc. [1, 2].

The temperature effects of the leakage current I_{LKG} , the switch on-resistance R_{ON} and the positive (negative) supply current I_{VDD} (I_{VSS}) are important in many analogue circuits (as programmable amplifiers, filters and oscillators) and complex mixed (analogue-digital) circuits. However, temperature effects are not presented in the available SPICE macromodels of analogue switches. The majority of published SPICE analogue switch macromodels only attempt to model I_{LKG} at $T_{nom} = 27^\circ C$, usually by two ideal current sources connected between positive supply terminal (or ground) and input (or output) nodes [3, 4]. Also existing analogue switch macromodels simulate changing power supply current with output load current and input switching frequency but not accurately model temperature dependence of the supply current. Largely independent from various technically realized circuit structure known so far, an improved SPICE macromodel of analogue switches including temperature dependence of several parameters has been developed, which is based upon manufacturer's data. Macromodelling of temperature effects are based on those described in [5-8] and following the design procedure given in [9]. The equivalent circuit of the proposed model principally contains linear

passive elements and non-linear controlled current sources. The macromodel are implemented as subcircuit and the structure of its netlist confirm to the standard SPICE format.

A full description of the enhanced macromodel is given in Section II, including the computation of the model parameters for SPICE simulators. In Section III is presented comprehensive examples, describing the use of the enhanced model, as well as a comparison between data sheet parameters of the real IC and simulation results. Conclusions and further research are presented in Section IV.

II. SPICE MACROMODEL DEVELOPMENT

The schematic diagram of the proposed macromodel is shown in Fig.1. It's based on a previous analogue switch macromodels [3, 4] with the additional capability to model the temperature dependence of the leakage current, the supply current and the on-resistance. The existing macromodel is represented in Fig. 1 as black-box marked '*daswitch*' and the new elements and stages, added to the original circuit, are marked in grey.

Various temperature parameters have been modelled as follows.

A. Modelling the leakage current and the supply current as a function of temperature

The temperature dependence of the leakage current and the supply current is created by two temperature coefficients of the resistor model $TC1$ and $TC2$ provided by SPICE [10]. The relation between the resistance value at the certain temperature $R_T(T)$ and the value at nominal temperature $R(T_{nom})$ is controlled with equation:

$$R_T(T) = R(T_{nom}) \left[1 + TC1(T - T_{nom}) + TC2(T - T_{nom})^2 \right] \quad (1)$$

The temperature-sensitive resistor $R_T(T)$ is chosen with linear function ($TC2 = 0^\circ C^{-2}$) to simplify the calculations for the other components in the model. Since SPICE will give an error message if the resistor goes negative at any temperature, the value of the linear coefficient $TC1$ can be obtained by

$$TC1 \leq \frac{10^{-1}}{T_{nom} - T_{min}} \quad (2)$$

where T_{min} is the minimum temperature in the operating range of the real part.

In Fig. 1 the current I_T will flow through the temperature-sensitive resistor $R_T(T)$, towards the internal ground. In such

¹Ivailo M. Pandiev is with the Faculty of Electronics from Technical University of Sofia, Kliment Ohridski 8, 1000 Sofia, Bulgaria. E-mail: ipandiev@tu-sofia.bg

a way the voltage V_{100} will depend upon the temperature. The current source I_T is fixed at 1A and the resistor R_T is set to 1Ω such that to provide a voltage $V_{100} = 1V$ at $T_{nom} = 27^\circ C$. The low resistance value of 1Ω leads to minimization of the

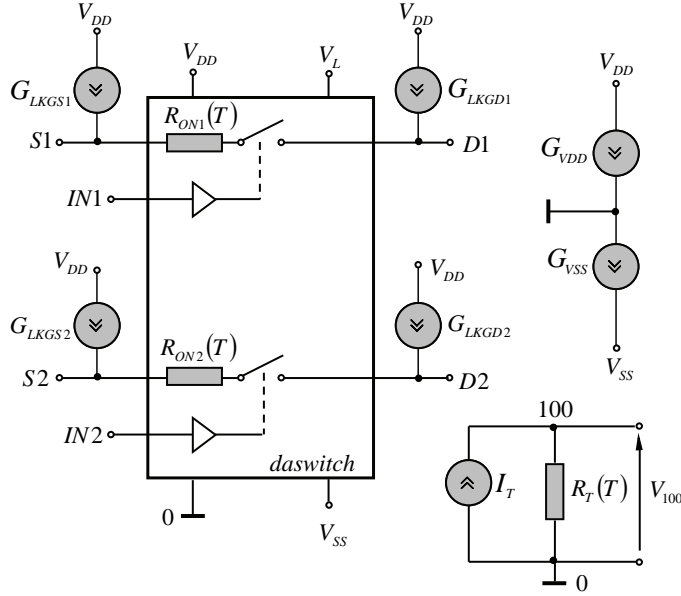


Fig. 1. Conceptual schematic of the proposed analogue switch macromodel improved with temperature effects.

generated thermal noise and to simplify the calculations for the other components in the macromodel. The voltage V_{100} works as a linear temperature-controlled input values for polynomial voltage-controlled current sources (VCCS) G_{LKGS1} (G_{LKGD1}) and G_{VDD} (G_{VSS}) in the model. As a result, both leakage current and supply current will be functions of temperature. The approximation to a non-linear behaviour is realized using appropriate polynomial coefficients of the controlled sources. A sufficient degree of accuracy for the purpose of modelling temperature dependence has been provided by choosing polynomial sources as six-order functions. The VCCS functions are given by

$$I(G_{LKGS1(2)}) = \sum_{i=0}^6 k_{i,LKGS1(2)} V_{100}^i \quad (3a)$$

and

$$I(G_{VDD(VSS)}) = \sum_{i=0}^6 k_{i,VDD(VSS)} V_{100}^i \quad (3b)$$

The polynomial coefficients $k_{i,VDD(VSS)}$ and $k_{i,LKGS1(2)}$ in equations (3a) and (3b) are calculated using Matlab. The advantage of this approach is that parameter extraction can be performed only from data sheet parameters, even for circuits whose internal structure is unknown.

B. Modelling the switch on-resistance as a function of temperature

The switch on-resistance is an important consideration in applying analogue switches within programmable amplifiers,

attenuators, etc. When the switch is closed (ON), dc performance is affected mainly by the on-resistance and leakage current. A resistive attenuator is created by the resistances of the generator, switch on-resistance and load which produce a gain error. The leakage current flows through the equivalent resistance of load in parallel with the sum of generator resistance and switch on-resistance. Not only can R_{ON} cause gain error, which can be calibrated using a system gain trim, but its variation with temperature and applied input signal (R_{ON} modulation) can introduce dc and ac distortion for which there is no calibration [1, 2]. The analogue switch macromodels described in [3, 4] only attempt to simulate on-resistance at $27^\circ C$, but not model its temperature effects. In response to this problem here is proposed a method for simulating temperature dependence of the on-resistance in the behaviour CMOS analogue switch macromodels.

The existing macromodels for analogue switches contains ideal voltage-controlled switches. The SPICE models of the ideal switches are a special kind of voltage-controlled resistors, where the resistance between switch terminals depends on the voltage between the controlling nodes. As it is the resistance varies continuously between the RON (on-resistance) and ROFF (off-resistance) model parameters [10]. The temperature effect of the RON is developed through modifying SPICE model form of the ideal switch and by utilizing the temperature-dependent resistor model $R_{ON1}(T)$ and $R_{ON2}(T)$, as shown in Figure 1. The temperature RON equation that fit a quadratic curve is given by

$$R_{ON}(T) = RON(0^\circ C) \left[1 + k_{LC} \cdot TEMP + k_{QC} \cdot TEMP^2 \right] \quad (4)$$

where $R_{ON}(0^\circ C)$ is the switch on-resistance at $0^\circ C$, $TEMP$ is the predefined parameter using the value of the control temperature option $TNOM$ in $^\circ C$, k_{LC} is the linear coefficient and k_{QC} is the quadratic coefficient. The equation (4) will fit a quadratic curve through three points in a temperature graph by solving three equations with three arguments.

The SPICE netlist for the temperature model form of an analogue switch is shown in Table 1. The numerical values of the model parameters are not specified, because they are determinate for an each CMOS analogue switch according to the manufacturer's data.

TABLE 1.
SPICE NETLIST FOR TEMPERATURE MODEL FORM
OF AN ANALOGUE SWITCH

```
.MODEL SMOD_RONT VSWITCH +
+ (RON={RON(0°C)(1+kLC*TEMP+kQC*TEMP*TEMP)}
ROFF=___ VON=___ VOFF=___)
.PARAM kQLC=___ kQLC=___
```

Therefore, the electronic circuits including analogue switches can be simulated at temperature other than default value $27^\circ C$ by changing the $TNOM$ option of the SPICE OPTIONS control card.

III. MACROMODEL PERFORMANCE

The verification of the enhanced model with additional elements, representing temperature effects of the leakage currents is carried out by comparing simulation results with data sheet parameters of the integrated IC ADG411 [11]. The analogue switch macromodel for the ADG411 [3] was used, with the I_{LKG} section removed and the new elements and temperature stage from Fig. 1, modelling the leakage current versus temperature, inserted between input/output and positive supply voltage terminal. The test circuit for simulation (Fig. 2), of a one analogue switch (X1.SW1) is created following the test conditions given in the manufacturer’s data. According to the data sheet of the selected IC the power supply voltage of the circuit are chosen $\pm 15V$ and logic supply voltage is set to $+5V$. For the testing of the analogue switch is

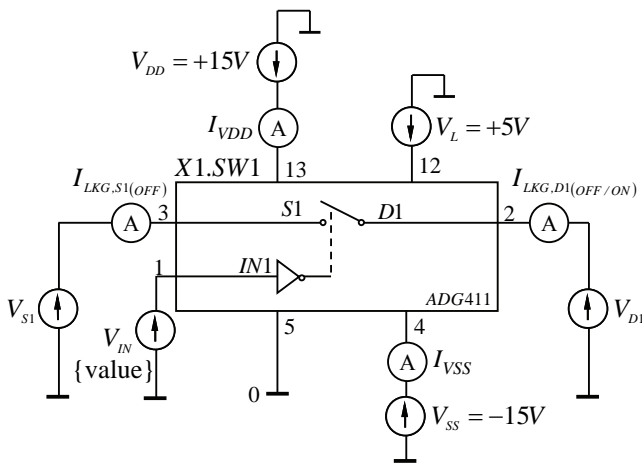


Fig. 2. Test circuit for simulation of leakage currents and supply currents

performed parametric dc sweep analysis with the following sweep parameters: start value $25^{\circ}C$, end value $85^{\circ}C$ and increment $1^{\circ}C$. The simulations are implemented in two modes of operation: (1) closed switch (ON) and (2) opened switch (OFF). The global parameter during simulation processes is the dc value of the logic control input voltage source V_{IN} . The logic levels of the V_{IN} , according to the data sheet of the IC steps from $0V$ (“ON” condition) to $3V$ (“OFF” condition). The dc voltage sources connected at the nodes 3 (S1) and 2 (D1) are set to $V_{S1} = -14,5V$ and $V_{D1} = +14,5V$. The simulation testing is implemented within OrCAD PSpice.

In Fig. 3a, Fig. 3b and Fig. 3c are presented simulation output, experimental results for the leakage currents and error in percents ($\delta = \left[\frac{I_{LKG,M} - I_{LKG,DS}}{I_{LKG,DS}} \right] 100\%$) versus temperature, where the solid lines show the behaviour of the SPICE macromodel. Notice that the simulated parameters closely match of the actual device ($\delta < 3\%$).

The verification of the enhanced model with additional elements, representing temperature effects of the supply current is carried out by comparing simulation results with data sheet parameters of the integrated MAX4601 CMOS analogue switch [12]. The analogue switch macromodel for the MAX4601 [4] was used, with the I_{VDD} (I_{VSS}) section remo-

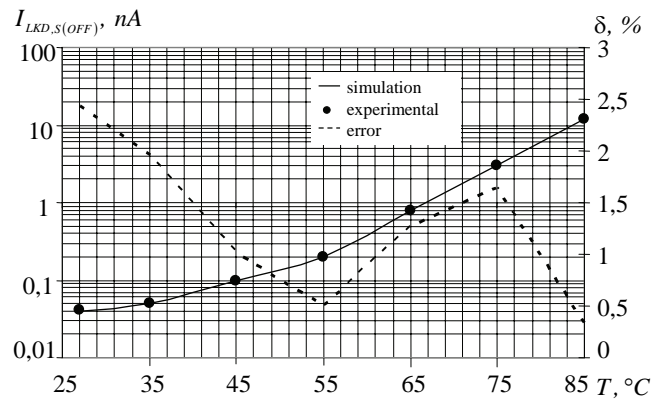


Fig. 3a. Source OFF leakage current as a function of temperature for ADG411

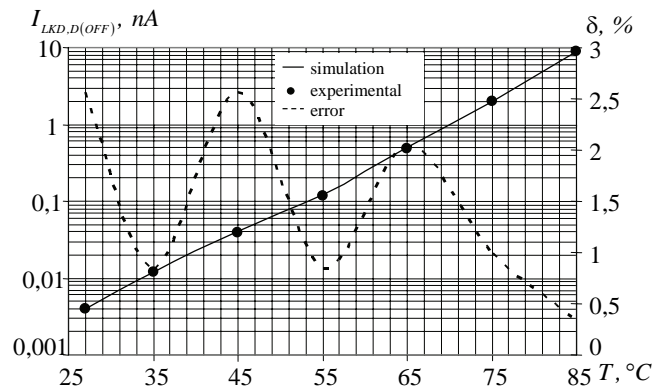


Fig. 3b. Drain OFF leakage current as a function of temperature for ADG411

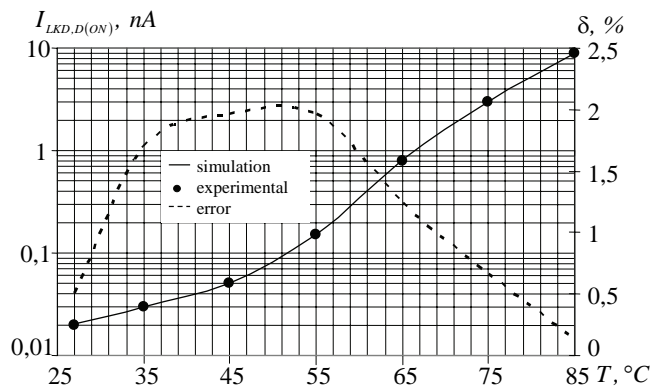


Fig. 3c. Drain ON leakage current as a function of temperature for ADG411

ved and the new elements and temperature stage from Fig. 1, modelling the supply current versus temperature, inserted between positive and negative supply terminals. The test circuit for simulation is presented in Fig. 2. During the process of simulation is specified and performed dc sweep analysis with the temperature range from $25^{\circ}C$ to $85^{\circ}C$. According to the manufacturer’s data the supply voltage is chosen $\pm 15V$ and logic supply voltage is set to $+5V$. In Fig. 4 is shown simulation output (solid lines) and experimental results (data pointed) for the positive and negative supply current. As shown in diagram (Fig. 4), the curves of the supply current versus temperature give a response close to that of the real

analogue switch. The resulting error between simulation and data sheet parameters is being not higher than 5%.

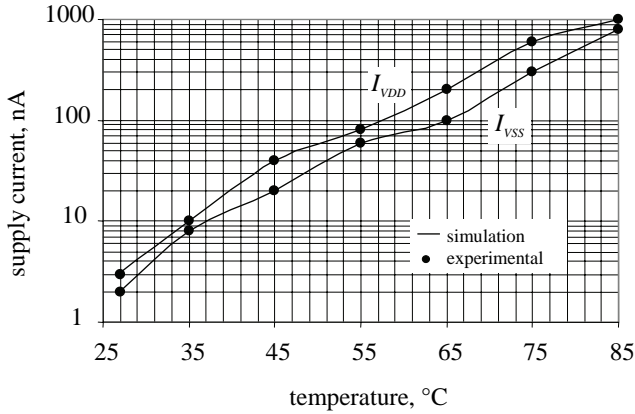


Fig. 4. Positive and negative supply current as a function of temperature for MAX4601

The verification check of the temperature effect for the on-resistance is performed by comparing simulation results with data sheet parameters of the MAX4601. The simulation testing is implemented following the test conditions given in the manufacture’s data. The single supply voltage for the circuit is chosen +12V, logic supply voltage is set to +5V and logic control input is fixed at +3V. The switch on-resistance is measured for the input voltage +6V. The simulation testing is performed within temperature range from -40°C to +85°C. In Fig. 5 is given simulation output, experimental results for the on-resistance and error in percents versus temperature. The solid line shows the behaviour of the SPICE macromodel, using the model parameters in the netlist of Table 2. The data points plotted shows temperature dependence of the on-resistance for the real-world device. As can be seen, the goal of a 2% match between the simulation model and the actual device is achieved.

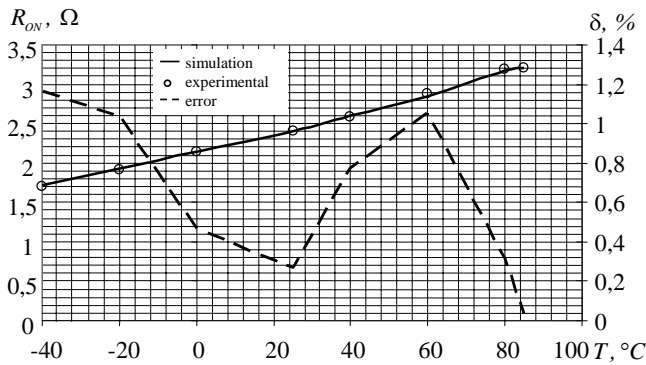


Fig. 5. Switch on-resistance as a function of temperature for MAX4601

TABLE 2.

SPICE NETLIST FOR TEMPERATURE MODEL FORM OF AN ANALOGUE SWITCH MAX4601

```
.MODEL SMOD_RONT VSWITCH
(ROn={2.11025641025641*(1+0.00524908869988*TEMP+
+ 9.720534628068047e-006*TEMP*TEMP)} ROFF=0.5E6
+ VON=0.8 VOFF=2.4)
```

IV. CONCLUSION

An improved SPICE macromodel for CMOS analogue switches that incorporates temperature effects of the leakage current, the power supply current and the on-resistance has been developed. It’s providing accurate model for dc, ac and transient analyses. The macromodel is independent from actual technical realizations and the model parameters can be obtained only from manufacturer’s data of the real IC. The efficiency of the model was proved by comparison of simulation results with data sheet parameters of the integrated CMOS analogue switches ADG411 and MAX4601. The maximum error between simulation and experimental results are not higher than 5%, which guarantee the sufficient degree of accuracy. Despite the addition all these new features, the macromodel’s simulation speed and computer resources needed are still equal to those of the SPICE standard libraries models. However, further research is required to develop appropriate macromodels with more complete temperature response.

ACKNOWLEDGEMENT

The author wish to thank Dr. G. Nikolov from the Automated measurement and testing laboratory, Technical University of Sofia, for the many valuable discussions.

REFERENCES

- [1] W. Kester, “Data converters”, Analog Devices, Norwood, MA, USA, pp. 7.62-7.66, 2005.
- [2] *Op Amp Applications*, Analog Devices, Norwood, MA, USA, pp. 6.128-6.129 and pp. 3.26-3.27, 2002.
- [3] “Switches/Multiplexers - SPICE Models”, Analog Devices 2005.
- [4] “Analog Switches and Multiplexers Macromodels”, Maxim Integrated Products 2005, <http://www.maxim-ic.com/tools/spice>.
- [5] H. Chenmin, D. Leach and Sh. Chan, “An improved macromodel for operational amplifiers,” *Int. J. Circ. Theory Appl.*, vol. 18, pp. 190-203, 1990.
- [6] U. Jörges, G. Jummel and G. Müller, “A macromodel of sample-and-hold circuits,” *Int. J. Circ. Theory Appl.*, vol. 25, pp. 483-502, 1997.
- [7] “Development of an extensive SPICE macromodel for current-feedback amplifiers,” National Semiconductor, Application Note AN 840, 1992.
- [8] M.E. Brinson and D.J. Faulkner, “SPICE macromodel for operational amplifier power supply current sensing,” *Electronics Letters*, Vol. 30, No. 23, pp. 1911-1912, 1994.
- [9] I.M. Pandiev, “Model building and testing procedure - An analogue multiplexer SPICE macromodel improved with temperature effects,” ICEST 2006, Bulgaria, Conference Proceedings, pp. 274-277.
- [10] *MicroSim PSpice A/D Reference Manual*, MicroSim, Irvine, California USA, Chapter 2, 1996.
- [11] “LC2MOS Precision Quad SPST Switch ADG411 - data sheet”, Analog Devices, Norwood, MA, USA, 2004.
- [12] “CMOS Analog Switch MAX4601 - data sheet”, Maxim Integrated Products, 2005.

Microstructure and Optical Properties of ITO Thin Films Investigated for Heat Mirrors in Solar Collectors

Georgy H. Dobrikov¹, Milka M. Rassovska², Stefan I. Boiadjiev², Kostadinka A. Gesheva³, Peter S. Sharlandjiev⁴ and Albena S. Koserkova⁴

Abstract – The aim of this work is preparation of RF sputtered ITO thin films for application as heat mirrors in solar thermal collectors. The alteration of optical properties and behaviour in IR spectra of additionally treated films was investigated. The films were deposited on silicon and glass substrates by RF sputtering on vacuum installation A-400 VL. For deposition of films were used targets with composition indium-tin 90:10 and 95:5 mol%. The films microstructure was studied by TEM and SEM. Optical and electrical properties as well as microstructure of the films change considerably after heat treatment.

The measurements in IR range of as-deposited ITO layers and heat treated ones were performed by Fourier transform infrared spectrophotometer Shimadzu Prestige 21. The as-deposited ITO films showed 45% in the Infrared, and after annealing at 500°C additional treatment, the films showed reflection in IR range not exceeding 60% at longer wavelengths. The films have high visible transmittance measured with CARY 5E – spectrophotometer.

Keywords – thin films, indium-tin oxide, IR properties, heat mirrors, solar energy conversion.

I. INTRODUCTION

ITO thin films have been studied extensively for optoelectronic device applications because of their unique transparent and conducting properties. ITO is a highly degenerated *n*-type wide band gap (3.3–4.3 eV) semiconductor with low electrical resistivity [1,3].

In many applications for effective use of solar energy the modern technology requires layers with high reflection in IR range and high transparency in the visible [4]. These coatings are usually deposited on the inside surface of the frontal window of solar collector and in combination with non-selective absorber this represents equivalent circuit of one selective absorber [5]. Expect for photothermal conversion the heat mirrors are widely used in modern buildings as low-emissive glass windows.

The heat mirrors have high transmittance in the solar

spectrum (0.3–2.5 μm) [6]. The investigation carried out confirms the relationship in the modern Materials Science between the composition, technological parameters and additional treatment, and microstructure and properties of the materials. The study tries to explain the obtained experimental results and to find the trends for improving them.

The purpose of this work is to obtain ITO thin films with high transparency in the visible (0.3–2.4 μm) and high reflection in the Infrared range (2.5–15 μm). We investigated the correlation of the films structure and optical properties of ITO thin films with the technological process parameters-target composition and annealing temperature.

II. EXPERIMENTAL

For deposition of ITO films the RF sputtering vacuum installation A-400 VL Leybold was used. The influence of technological factors as oxygen pressure, time of deposition and electrical parameters of the sputtering process were studied and strictly controlled. Two type targets with 90:10 and 95:5 mol % (In:Sn) were used. The films were deposited on glass substrates at room temperature. In our research the as-deposited amorphous ITO films were subjected to various annealing temperatures to obtain various degrees of the amorphous and crystalline phases of the ITO films.

The microstructure of the films was studied by TEM and selected area electron diffraction (SAED) using TEM-400, Philips transmission electron microscope. The surface of the layers was investigated by SEM. The substrates for RF sputtering deposition of non-annealed thin film samples for direct TEM observations were fresh fractured surfaces of NaCl crystals.

To identify the optical properties of films the methods of UV-VIS and IR spectrometry were used. The measurements in the Infrared of as-deposited ITO layers and heat treated ones were performed by Fourier transform infrared spectrophotometer Shimadzu Prestige 25. The transmittance in the visible range was measured with CARY 5E spectrophotometer.

III. RESULTS AND DISCUSSION

As it is seen in Fig.1a the TEM micrographs and SAED patterns show the initial amorphous structure of the investigated layer.

After “*in situ*” heat treatment of the films by electron beam in the microscope, where the temperature arises up to 270 –

¹ Georgy Dobrikov is with the Faculty of Electronic Technique and Technologies, Technical University, 8 “Kliment Ohridski” blvd., e-mail of corresponding author: georgy_ddobrikov@abv.bg Sofia, Bulgaria.

² Faculty of Electronic Technique and Technologies, Technical University, 8 “Kliment Ohridski” blvd., Sofia, Bulgaria.

³ Central Laboratory of Solar Energy and New Energy Sources, Bulgarian Academy of Sciences, 72 “Tzarigradsko chaussee” Blvd., 1784 Sofia, Bulgaria.

⁴ Central Laboratory of Optical Storage and Processing of Information, Acad. G. Bonchev str., bl. 109, 1113, Sofia, Bulgaria.

300 °C, structural evolution was observed and the formation of separated nano- and microcrystals (Fig. 1b) is followed by the appearance of polycrystalline structure (Fig. 1c).

As-deposited films have predominantly amorphous structure. After heat treatment at 250 °C and higher, the structure of ITO films was changed, a polycrystalline structure was observed.

The microstructure is strongly connected with the electrophysical properties of the films. It was established that the annealing of the ITO films influences their electrical and optical properties.

The transmittance and reflection in visible and near IR of as-deposited and heat treated films with different concentration of dopand (Sn) are showed on figures (2,3).

The investigated films have low sheet resistance ($25\Omega/\square$ for 90:10mol % and $20\Omega/\square$ for 95:5mol %). After heat treatment at 500 °C the sheet resistance of samples decreases, ($20\Omega/\square$ for 90:10mol % and $17\Omega/\square$ for 95:5mol % respectively). Similar results by other scientists, working with different targets and technologies of deposition and heat treatment at 600 °C were obtained [2,7]. Our results and the studied literature, show that the electrical parameters of ITO films can to be improved by using different dopands and treating methods of films.

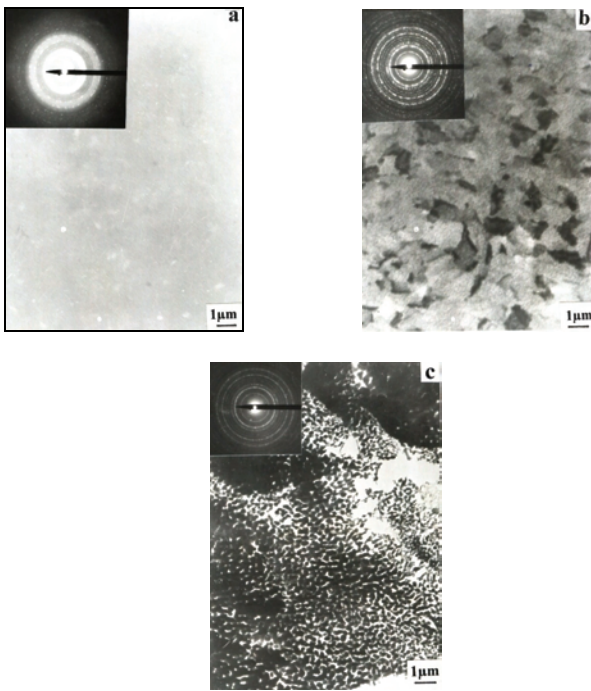


Fig. 1. TEM micrographs and SAED patterns of thin ITO films:

- a) amorphous structure before “*in situ*” electron beam heating;
- b) separated nano- and microcrystals obtained after the first steps of “*in situ*” electron beam heating;
- c) polycrystalline structure due to longer “*in situ*” electron beam heating of the film.

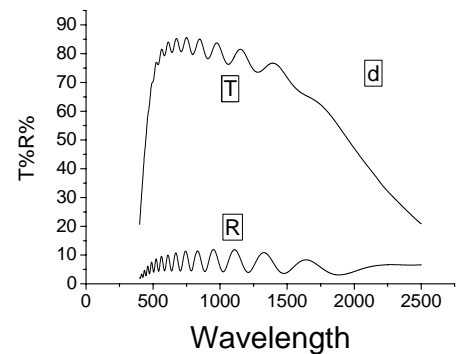
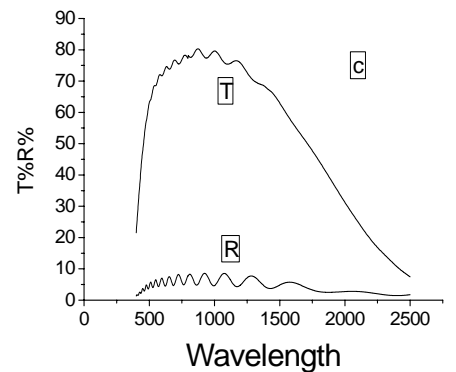
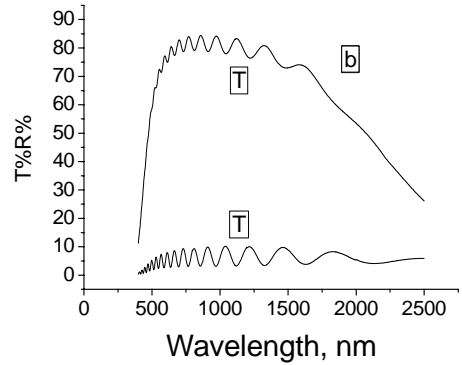
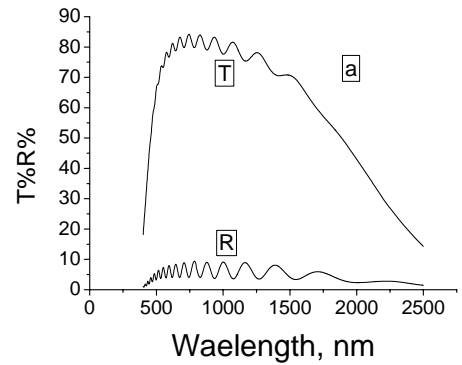


Fig.2. Transmition and reflection in visible and near IR range.

- a) as-deposition 90:10 mol % film;
- b) heat treated at 500 °C 90:10 mol % film;
- c) as-deposition 95:5 mol % film;
- d) heat treated at 500 °C 95:5 mol % film.

Fig. 2 shows that all investigated films independently of their dopands and their microstructure have high transparency in the visible range. But all efforts were directed to obtaining layers with high reflection in the infrared. The infrared reflectance of the investigated layers showed strong dependence on the content of dopands and on the microstructure of the films.

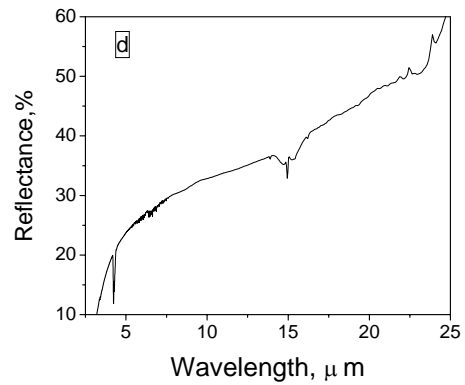
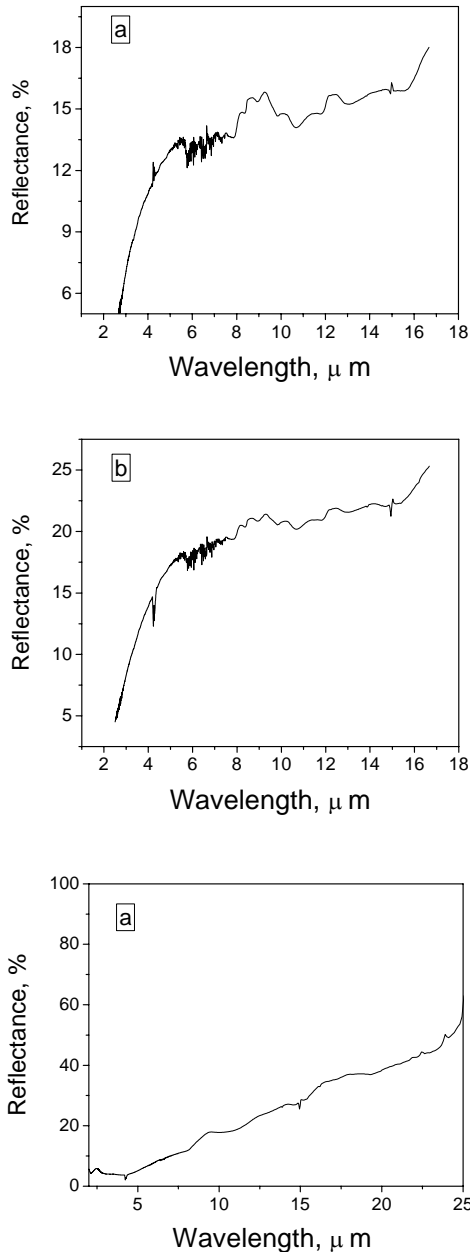


Fig.3. Reflection in IR range:
 a) as-deposition 90:10 mol % film;
 b) heat treated at 500 °C 90:10 mol % film;
 c) as-deposition 95:5 mol % film;
 d) heat treated at 500 °C 95:5 mol % film

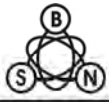
Fig. 3 shows that the obtained ITO films by target with composition 90:10 mol% (In:Sn) have low reflection in the IR range. All films were processed by heat-treatment with different temperatures. The films with composition 95:5 mol% (In:Sn) display dependence on heat-treatment at 500 °C. With that composition the reflection in IR range reached 60 % for the longer wavelengths.

IV. CONCLUSION

ITO films with increased reflection in the infrared were sputtered employing target 95:5 mol % and low sheet resistance. The obtained ITO thin films have high transparency in the visible, exceeding 80%. According to these optical and electrical parameters, films after proper optimization could find broad application in photothermal converters, display technique, etc.

REFERENCES

- [1] Y. Ohhata, F. Shinoki and S.Yoshida, "Optical Properties of r.f. Reactive Sputtered Tin-Doped In₂O₃ Films", *Thin Solid Films*, 59, pp. 255–261, 1979.
- [2] M. Buchanan, J. Webb and D. Williams, *Appl. Phys. Lett.*, 37, p. 213, 1980.
- [3] M. Just, N. Maintzer and I. Blech, "Stress in Transparent Conductive Sn-Doped Indium Oxide Thin Films", *Thin Solid Films*, 48, pp. L19-L20, 1978.
- [4] R. V. Kumar and A. Mansingh, "Effect of Target-Substrate Distance on the Growth and Properties of r.f. Sputtered Indium Tin Oxide Films", *J. Appl. Phys.*, 65 (3), pp. 1270–1280, 1989.
- [5] I. Adesida, D. G. Balleger, J. W. Seo, A. Katterson, H. Chang, K. Y. Cheng and T. Gessert, "Etching of Indium Tin Oxide in Methane/Hydrogen Plasmas", *Journal of Vacuum Science and Technology*, B9 (6), 1991, pp. 3551 – 3554.
- [6] V. Korobov, M. Leibovitch, Y. Shapira, Structure and conductance evolution of very thin indium oxide films, *J.Appl. Phys. Lett.*, 65, p. 2290, 1994.
- [7] T. Minami, T. Kakumu, Y. Takeda et al., Highly transparent and conductive ZnO-In₂O₃ thin films prepared by DC magnetron sputtering, *J.Thin Solid Films*, 1-5, pp. 290-291, 1996.



This page intentionally left blank.

POSTER SESSION – PO IV

Computer Systems and Internet Technologies

Automatic Weight Estimation Method for Multiple SVMs in Software Sensors Systems

Plamena Ts. Andreeva¹ and Svetla I. Vassileva²

Abstract – An automatic weight estimation method for multiple support vector machines (SVM) is considered, which takes advantage from the discriminative classification based on ROC analysis. The software sensors systems support the hardware systems and take benefit of the modelling process estimating the important variables. The achieved results are presented and future trends are given.

Keywords – Weight estimation, Prediction accuracy, Support Vector Machines, Software sensors systems.

I. INTRODUCTION

The machine learning (ML) technology provides systems with new tools able to improve process supervision. Thanks to Internet resources, a remote model can efficiently run a database diagnosis. An useful tool for processing information and analyzing feature relationships is data mining (DM) technique [1, 2]. The aim is to achieve fast and simple learning models that result in small rule bases, which can be interpreted easily. The wide used support vector [3, 4] machines (SVM) are effective tool for optimal classifier capacity tailored on the given task problem. In this particular study SVM are explored and evaluated by the test accuracy based on receiver operational characteristic (ROC) curve analysis. The automatic weight estimation method for multiple SVM is considered in order to conduct feasible classification and acquire accurate prediction in software sensors systems. For training the model easily the “one vs. all” strategy is used. This leads to improved initial accuracy.

Software sensor systems are applicable to linear and non-linear systems, when uncertainty or incomplete information is available. The main idea is that the efficiency of hardware sensors is complemented by software sensors [5] which combine the information from the sensor network with a process model in order to predict some key-process variables which are generally not available on-line.

The support vector machines [6] have been a promising tool for classification and regression. Its success depends on the tuning of several parameters which affect the generalization error. A popular approach is to approximate the error by a bound that is a function of parameters. Then, we search for

parameters so that this bound is minimized. In the context of medical diagnosis, the extraction of statistically independent components has been proposed as an objective of early sensory processing, finding the important attributes and primary dependencies.

II. PROBLEM STATEMENT

The automated acquisition of knowledge by machine learning approach is an active area of current research in Artificial Intelligence [7]. ML studies automatic techniques to make accurate predictions based on past observations. There are several multi-class classification techniques: Support Vector Machines (SVMs), decision trees, etc. [8, 9]. Nevertheless, building a highly accurate multi-class prediction is certainly a difficult task. Various systems of multiple classifiers have been proposed in the literature [10].

There is a scope of many diseases with the same symptoms, and also the degree or level of the symptoms is absent from the knowledge. To overcome the first problem, the knowledge engineer should design the knowledge base with more specific rules. For rules with identical symptoms, some sort of measures of coupling between the antecedent and the consequent clauses are to be devised. This measure may represent the likelihood of the disease among its competitive disease space. For example, if the diseases are seasonal, then the disease associated with the most appropriate season may be given a higher weight, which, in some ways should be reflected in the measure. The second problem, however, is more complex because the setting of the threshold level at the symptoms to represent their strength is difficult even for expert doctors. In fact, the doctors generally diagnose a disease from the relative strength of the symptoms but quantification of the relative levels remains unsolved.

The level or strength of the facts submitted may not conform to their actual strength, either due to media noise of the communicating sources of data or incapability of the sources to judge the correct level/ strength of the facts. Several mathematical models were developed in order to optimize the information provided by the sensor network for the studied process.

III. THEORETICAL BACKGROUND

The SVM can be used to learn highly accurate models from data. It is based on quadratic optimization [11] of convex function. This is realized by nonlinear mapping using so-

¹Plamena Ts. Andreeva is with the Department of Knowledge Based Systems at the Institute of Control and System Research, Bulgarian Academy of Sciences, 1113 Sofia, Bulgaria, E-mail: plamena@icsr.bas.bg

²Svetla I. Vassileva is the head of the Department of Knowledge Based Systems at the Institute of Control and System Research, Bulgarian Academy of Sciences, 1113 Sofia, Bulgaria, E-mail: vassileva@icsr.bas.bg

called kernel functions. Via normalizing any uniformly separating hyperplane can be defined by the property:

$$\begin{aligned} \mathbf{w}^T \mathbf{x} + b &\geq 1, \text{ when } \mathbf{x} \text{ is in } C_1 \text{ and} \\ \mathbf{w}^T \mathbf{x} + b &\leq -1 \text{ for } \mathbf{x} \in C_2 \end{aligned} \quad (1)$$

Given a separating hyperplane α which satisfies conditions (1), for the distances between α and the points \mathbf{x}_i , we have:

$$\text{dist}(\mathbf{x}, \alpha) = \frac{|\mathbf{w}^T \mathbf{x} + b|}{\|\mathbf{w}\|} \geq \frac{1}{\|\mathbf{w}\|} \quad (2)$$

and the optimal hyperplane is the one with maximal $1/\mathbf{w}$ that guaranties an optimal margin of width $2/\mathbf{w}$ because the equality in (2) is reached at least for one point in C_1 and at least one point in C_2 . By maximizing that distance we

minimize the following dot product $\frac{1}{2} \mathbf{w}^T \mathbf{w}$. This represents the quadratic constrained optimization problem.

A trained SVM can be used for classifying an unknown vector by applying the following criterion which depends on the sign of the expression:

$$f(x) = \sum_{i=1}^N \alpha_i y_i K(x_i, x) + b \quad (3)$$

In the sums above it holds $\alpha_i > 0$ only for the support vectors hence they play the main role during the usage phase. After calculating the α_i we can find the weight vector \mathbf{w} and the bias b we need by the formula:

$$\mathbf{w} = \sum_{i=1}^N \alpha_i y_i x_i \quad (4)$$

The loss functions can be incorporated into the SVM training problem. Unlike the naturally occurring high-dimensional measurements (as visual images), medical sensor's measurements are not easily interpretable by human observers. For a learning machine there is no fundamental difference between these types of data. In this domain, machine intelligence will prove to make sense out of the data.

Support vector machines are not preferred in applications requiring great classification speed, due to the large number of support vectors. To overcome this problem we devise a primal method with the following properties: a) the basis functions are not connected with the concept of support vectors; b) set of kernel basis functions with specified maximum size are found to approximate the SVM primal cost function well; c) it is efficient and roughly scales as $O(n \cdot d_{max}^2)$ where n is the number of training examples; and d) the number of basis functions for an accuracy close to the SVM accuracy is usually far less than the number of SVM support vectors.

A. Accurate prediction

We consider two measures for accurate prediction: test error numbers — the number of misclassifications on independent test samples, and the error numbers of 10-fold cross validation. The inference of diagnosis based on kernel function is equivalent to assigning a particular loss function to the errors: there are two types of error possible: of commission and errors of omission. The costs of making these two

types of error are not necessarily equal, and depend on the relative cost (used as weights) of an erroneous prediction compared to missing a interesting correct prediction. Generally we wish to make the decision which minimises the expected loss.

Classification can be tuned to find rules with different loss functions by changing the selection criteria in the validation set. An approach to improve accuracy involve fold prediction. When seeking to solve the constrained optimization problem, asking for small $\mathbf{w}^T \cdot \mathbf{w}$ is like "weight decay" in Neural Nets and like Ridge Regression parameters in Linear regression and like the use of Priors in Bayesian Regression—all are signed to smooth the function and reduce overfitting.

B. Precision measure

Nowadays it is accepted that there are no algorithms able to make exact classifications in a general domain. Local information is extracted from features associated to each local structure and provides information about its type of structure. Contextual information is incorporated by taking into account the relative spatial distribution of these local features. Finally global information is obtained as a result of considering the local features over wide neighborhoods embracing the whole feature set.

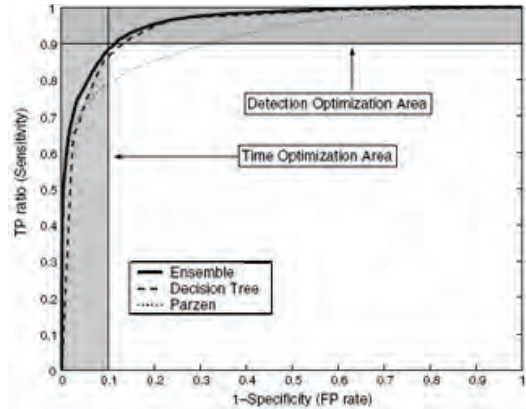


Figure 1. An illustrative example of specificity versus sensitivity plotted for the three different classifiers models.

The receiver operational characteristic (ROC) curves are used to optimize the trade-off between false positive and false negative rates. On Fig.1 are shown three classification curves with fault positive (FP) rates versus true positive (TP). We apply the use of ROC curves to evaluate several classifier models, including classifier ensembles. By simple classifiers examination our results shows that classifier ensemble methods have substantial advantages over simple classifiers. The ROC curves for all classifiers were calculated on the testing set. The ensemble with the largest area is plotted bold.

The curves plot on Fig. 1 shows the error tolerance on the X axis versus the percentage of points predicted within the tolerance on the Y-axis. The resulting curve estimates the cumulative distribution function of the error. In our medical experiments these curves provide a much more compelling presentation of regression results than tables of squared errors.

The shaded vertical stripe shows an example of a desirable time-optimization area. Its width denotes the maximum FP rate we are prepared to accept. Its height measures the amount

of accuracy we are prepared to sacrifice. A classifier performs well if the error curve climbs rapidly towards the upper left-hand corner. In our case, SVM was hand tuned based on testing information to estimate the best possible performance. Model parameters were selected using cross-validation.

IV. AUTOMATED WEIGHT ESTIMATION

The mechanism developed for the medical system (sensor system) diagnostic is based on the principles of multi-criteria decision making and takes into consideration input from training cases. Multiple criteria are used to describe the previous quality. In this paper we explore multiple SVMs in order to achieve optimal precision. Here the goal is to produce a model, which predicts target value of data instances in the testing set which are given only the attributes. The key idea in our approach is not primarily to define more complex functions, but to deal with more complex output spaces by extracting combined features over inputs and outputs. For a large class of structured models, we propose an automatic weight estimation to learn mappings involving complex structures in polynomial time despite an exponential number of possible output values. We empirically evaluate our approach for a specific problem: prediction of heart disease.

We select features with high F-scores and then apply SVM for training/prediction. The procedure is summarized below:

1. Calculate F-score of every feature.
2. Pick thresholds by human eye to cut low and high F-scores.
3. For each threshold, do the following:
 - a) Drop features with F-score below this threshold.
 - b) Randomly split the training data X_{train} / X_{valid} .
 - c) Let X_{train} be the new training data. Use the SVM in b) to obtain a predictor, then predict X_{valid} .
 - d) Repeat the steps above five times, and then calculate the average validation error.
4. Choose the threshold with the *min* average validation error.
5. Drop features with F-score below the selected threshold.

In the above procedure, possible thresholds are identified by human eye. For the examined data set, there is a quite clear gap between high and lower scores (see Figure 3). We can automate this step by gradually adding high-F-score features, until the validation accuracy decreases.

To test the above described method we conduct several experiments in Weka [12]. The distribution of experiments cuts down the time the experiments take. The setup of a selected classifier can be loaded and saved from and to XML. The multidimensional models [13] are also created and their associations are used in specific applications. This is rather useful for transferring a classifier setup from the Weka Explorer over to the Experimenter without having to setup the classifier from scratch. A robust alternative to the binary format is the XML format for Internet access [14].

V. EXPERIMENTAL RESULTS

In diagnosis applications the outcome may be the prediction of disease vs. normal or in prognosis applications. The input features may include clinical variables from medical

examinations, laboratory test results, or other measurements. In this study we have used a set of very well-known databases from UCI repository. Separating the classes with a large margin minimizes the bound on the expected generalization error. In the case of non-separable classes, it minimizes the number of misclassifications whilst maximizing the margin with respect to the correctly classified examples. On Fig. 2 the errors from the default SVM classifier with parameter $C=1$ are depicted. For the positive diagnosis there are 31 misclassifications out from the whole dataset (270 examples) which gives the 11,48% rate. After the automatic weight estimation the optimal classifier is obtained and the accuracy rises to 24 from the first class and 15 misclassification from the second. Unlike other algorithms, the method makes no assumptions about the relationships between a set of features (attributes) in a feature space. This allows us to identify and determine the most relevant features used in a model and their dependencies.

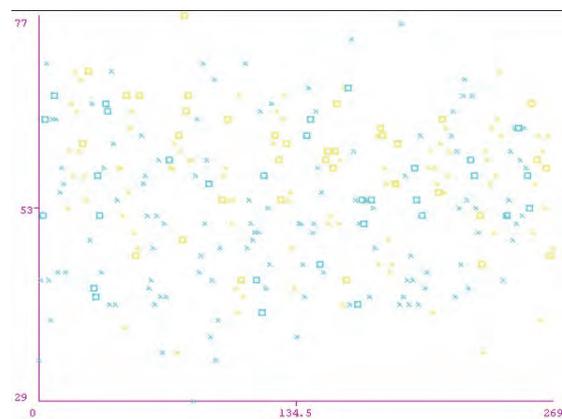


Figure 2. Error misclassifications results from the SVM classifier for the two diagnoses. The number of instances is on the X axis. The correct classified examples are depicted with cross and the misclassifications are given with squares – the yellow for negative diagnosis and the blue are for positive one.

In all our experiments, we train the algorithm, select parameters based on a validation set, and then report performance on an independent test set. SVM learning algorithm is performed on the data, generating a set of classifier models. Beyond the choice of model and loss function our method has only a single parameter to tune, namely the regularization parameter C . We train models with C ranging from 1 to 100, in powers of 2, all to precision 0.01. We then pick the best model based on the performance on the validation set, and report its performance on the test set.

Although the most regularized linear SVM is the best in this example, we notice the threshold 0,5 is determined by the two most extreme points in the two classes (see Fig. 3). For values larger than the initial value 0,1, the endpoint behavior depends on whether the classes are balanced or not. In either case, as α increases, the error converges to the estimated null error rate.

This same objection is often made at the other extreme of the optimal margin. Typically it involves more support points and tends to be more stable. Here the regularization forces more points to overlap the margin. We are able to implement our approach most easily with the “one vs all” strategy.

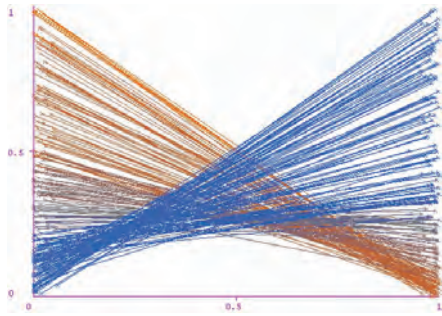


Figure 3. Threshold value around 0,5 and cost function for the tested binary classification. The blue are for the class "Yes".

The output results from Weka built model are given on Fig. 4. The correct classified instances are 231 (85,56%).

=== Detailed Accuracy By Class ===

TP Rate	FP Rate	Precision	Recall	F-Measure	Class
0.87	0.127	0.885	0.83	0.887	"yes"
0.873	0.17	0.845	0.873	0.859	"no"

Figure 4. Screen output results from Weka built model for the tested classifier on the heart dataset.

Automated, the optimized SVM classification can generate models based on a number of criteria including precision/recall, or correlation coefficient. In order to get statistically meaningful results, the default number of iterations is 10. The following results are generated. There are 30 result lines processed. In this experiment, each set of 10 cross-validation folds is averaged, producing one result line for each run. The percentage correct for each of the SVM schemes is shown in Fig. 4. The value at the beginning of the row represents the number of estimates that are used to calculate the standard deviation. The obtained model with weight estimation is given on Fig. 5. The positive diagnoses for class "Yes" are classified with precision of 0,885, and the negative are with lower precision which corresponds to the cost matrices. Our method enables the user to control the training time by choosing the number of basis functions to use.

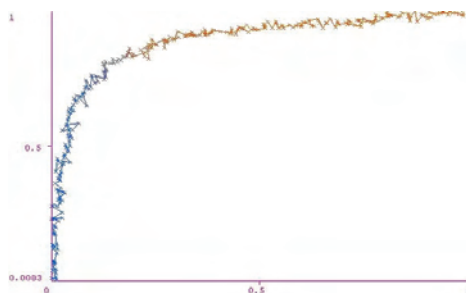


Figure 5. The ROC curve for the obtained optimal model with weight estimation.

The term statistical significance used in the previous section refers to the result of a pair-wise comparison of schemes using either a standard T-Test or the corrected resampled T-Test [2]. As the significance level is decreased, the confidence in the conclusion increases. In our experiment the resulting significance indicates the probability of positive diagnosis with attributes greater than selected. The accepted threshold is a significance level of 0.05. Such level is equivalent to requiring that the disparity would occur in no more than 1 in every 20 cases. The ranking test ranks the schemes according to the total number of significant wins and losses against the other schemes.

VI. CONCLUSION

The considered method applies multiple classifiers and on this basis makes the semi-automatic data analysis faster and easier. The advantages of this SVM method allow optimizing for different loss functions. The increased accuracy rate based on the automatic weight tuning method is a sure indicator of the importance of implementing DM systems. In our investigation we found that it is possible to build a flexible and accurate final model and present results to non-experts via ROC curves.

ACKNOWLEDGEMENT

This research is supported by the NSRF of the Bulgarian Ministry of Education and Science as part of the Project MI - № 1509/2005 and in part by a research grant I - № 1406/2004.

REFERENCES

- [1] P. Andreeva, "Data Modelling and Specific Rule Generation via Data Mining Techniques", Journal of E-learning and Knowledge Society, <http://www.je-lks.it>, 2007.
- [2] I. Witten, E. Frank, *Data Mining: Practical machine learning tools and techniques*. Morgan Kaufmann, San Francisco, 2005.
- [3] P. Bartlett, J. Sh-Taylor, "Generalization performance of support vector machines and other pattern classifiers", in: B. Schölkopf, C. Burges, and A. Smola, (Ed.): *Advances in Kernel Methods*, MIT Press, MA 43-54, 1999.
- [4] I. Steinwart, "On the influence of the kernel on the consistency of support vector machines", Journal of Machine Learning Research, 2:67-93, 2002.
- [5] S. Vassileva, X. Z. Wang, "Neural Network Systems and Their Applications in Software Sensor Systems for Chemical and Biotechnological Processes", in *Intelligence Systems: Technology and Applications*, Ed. C.T. Leondes, CRC Press, USA, pp.291-335, 2002.
- [6] T. Joachims, "Training linear SVMs in linear time", KDD'06, August 20-23, 2006, Philadelphia, Pennsylvania, USA. Results and analysis. ACM SIGKDD Newsletter, 12(2):95-108, 2006
- [7] S. Mark, *Introduction to Knowledge Systems*, Morgan Kaufmann, San Mateo, CA, Chapter 5, pp. 433-458, 1995.
- [8] S. Hadjitodorov, L. Kuncheva, L. Todorova, "Moderate diversity for better cluster ensembles", *Information Fusion*, 2006.
- [9] T. Joachims, "A support vector method for multivariate performance measures", in *International Conference on Machine Learning (ICML)*, 2005.
- [10] L. Kuncheva, *Combining Pattern Classifiers: Methods and Algorithms*, Wiley, 2004.
- [11] B. Schölkopf, Smola A.J., *Learning with Kernels: Support Vector Machines, Regularization, Optimization and Beyond*, MIT Press, Cambridge, 2002.
- [12] University of Waikato, ML Program WEKA, www.cs.waikato.ac.nz/ml/weka. 2007.
- [13] I. Valova, A. Goknil, "Applicability of the Object-Oriented Paradigm in Multidimensional Models", *Int. Scientific Conference Computer Science'06*, Oct. 12 - 15, Istanbul, Turkey, pp.190-195, 2006.
- [14] S. Vassileva, G. Georgiev, S. Mileva, "Knowledge-Based Control Systems via Internet", Part I. *Appl. in Biotechnology Bioautomation*, ISSN 1312-451X, pp. 37-48, 2005.

Improving Fairness for Pedestrian Users of CDMA-HDR Networks

Valentin P. Hristov¹

Abstract – In this paper an approach to improve throughput and fairness for pedestrian users of CDMA-HDR networks is given. The advantages of using more accurate estimation of the SINR combined with H-ARQ in Cellular Data Networks, and some simulation results obtained with an available online simulator are given, too.

Keywords – Cellular Data Networks, Fairness, SINR estimation, and Simulations.

I. INTRODUCTION

Improving throughput and fairness in Cellular Data Networks is a problem of present interest. In these networks, time is divided into many time slots and each wireless terminal-WT is transmitting packets (to a base station). WTs use one or more time slots to transmit their payload, but each time slot can only accommodate one WT. Multiple WTs are accommodated using the time division multiple access-TDMA technique. As a result, each WT can use the maximum power of the entire base station-BS. In the wireless mobile environment, the RF condition changes significantly with time. When the RF condition is good, little coding protection is needed and modulation with high constellation can be used, making it possible to transmit at a high data rate in a given timeslot. The data from each timeslot are scrambled and spreaded using a computer generated pseudo-random - sequence (chip) unique to the sector of cell, i.e. Code-Division Multiple Access- CDMA. Cellular Data Networks- CDNs combine the advantages of both techniques- TDMA and CDMA. This combination is well suited to the bursty nature of packet data, as well as has the advantage of being able to have frequency reuse in every sector.

CDNs as CDMA systems are known to be interference limited, which means that their capacity can be increased by reducing the minimum required (for stable reception of data at the receiver) energy of signal with a given Signal to Interference and Noise Ratio-SINR. The SINR is a function of several factors such as path loss, shadowing, fading, noise, and intercell interference.

Such CDNs, as CDMA-HDR (High Data Rate), 1xEVDO (1x Evolution for High-Speed Integrated Data and Voice) , and other systems realize procedures for power control [1]:

The WT measures the SINR of the received signal through the pilot channel and sends feedback to the BS; Based on the feedback from the WT, the BS adjusts its transmitted power level.

The Hybrid Automatic Repeat Request- H-ARQ (or more sophisticated Hybrid ARQ/FEC) is usually used to improve data throughput [4] and to allow for early packet termination. The general procedure of the H-ARQ is as follows: The packet is coded, interleaved, added CRC and formed into subpackets that are transmitted. The receiver decodes the packet and checks the CRC. If the CRC check passes/ does not pass, an acknowledgment /negative acknowledgment is sent back to the transmitter. Early packet termination refers to a successful reception of a packet before the nominal packet duration when the channel condition is good. In H-ARQ, the information bits are conveyed using several subpackets. If the packet can be decoded correctly before all the subpackets are transmitted, the packet transmission is terminated early and there is no need for additional transmissions. The repetition of the packet bits in the subpacket is accomplished by means of channel coding to obtain further coding gain. To allow time for the WT to process each subpacket and feed back the information to the base station, each subpacket is transmitted disjointly in time. In terms of energy, H-ARQ can be thought of as a scheme where additional energy for each subpacket is transmitted until the required SINR for the entire packet is reached [1- 4]. The effect of H-ARQ is quite similar to that of the fast power control technique since it minimizes the total interference to other WTs by controlling the power used to transmit packets. The H-ARQ is used to improve network performance in presence of inter-cell interference [5].

II. IMPROVING THROUGHPUT AND FAIRNESS

A. Background

The signal received by a WT over the forward link in a cellular data network contains interference from the neighboring base stations. In Fig. 1 is depicted WTs in some sectors of cell C receive inter-cell interference from corresponding sectors of cell C' and cell C''.

In [5], Mhatre et al. study the impact of network load in the neighboring sectors on the inter-cell interference in a cellular data network. The observation that signal received by a WT over the forward link contains interference from the neighboring base stations is used by the terminal to predict its SINR more accurately.

Also, It is shown that the SINR is function of signal amplitude-A, width of pulse- T_c (chip) , the channel gain from

¹Dr. Valentin P. Hristov is assoc. professor in Faculty of Mathematics and Natural Sciences, South West University, Ivan Mihailov str. 66 Blagoevgrad 2700, Bulgaria, E-mail: v_hristov@aix.swu.bg

the base station of the interfering sector to the terminal- G_i , and the probability that a time slot on the forward link of i -th sector is busy- ρ_i .

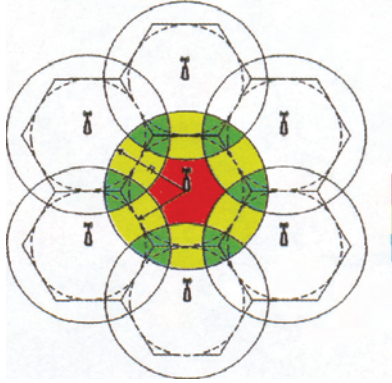


Fig. 1. Interference example.

Nowdays, in the actual implementation of CDMA-HDR [5], the BSs are GPS-synchronized and all the BSs transmit their pilot signal at the same time. Hence, the SINR measured by the terminals contains the worst case inter-cell interference, since the interfering signals are transmitted constantly during the measurement phase:

$$SINR' = \frac{G_0^2 A^2 T_c}{\frac{1}{3} A^2 T_c (G_1^2 + G_2^2) + 2N_0} \quad (1)$$

The SINR given by (1), is a function of G_i , and given by:

$$G_i^2 = cd_i^{-n} \cdot 10^{\xi_i/10} \cdot W_i^2 \quad (2)$$

In (2), the first term in the product is deterministic (for a fixed WT location), and corresponds to path loss, while the second term is a random variable corresponding to lognormal shadowing loss. Here, ξ_i is a Gaussian random variable with mean 0, and variance σ_G . Shadowing is correlated over each time slot depending on the speed of the WT as per Gudmundson model [6]. Last term- Rayleigh fading is accounted through W_i .

However, If the terminal has the information about the network loads in all the sectors that are in its active set, it can calculate the actual SINR''':

$$SINR'' = \frac{G_0^2 A^2 T_c}{\frac{1}{3} A^2 T_c (G_1^2 \rho_1 + G_2^2 \rho_2) + 2N_0} \quad (3)$$

Thus, using more accurate estimation of the SINR, WTs will be able to improve data throughput.

Moreover, H-ARQ also improves throughput, even in spite of initial conservative SINR estimates [5], because as mentioned above, H-ARQ adjusts to network loading in the adjacent sectors.

B. Fairness

The classical index of fairness displays level of satisfaction of each user/WT, respectively fair sharing of the network resources, and is given by:

$$Fairness = \left(\sum X_i \right)^2 / n \sum X_i^2 \quad (4)$$

So, Fairness =1 speaks of quite fairness sharing of the network resources between users, then and Fairness =0 corresponds to absolutely opposite situations [7]. The performance metric is based on data throughput (X_i).

It is expected that more accurate initial estimation of the SINR and H-ARQ can improve throughput and fairness. In next section it will be verified through simulations whether these improve the fairness.

III. SIMULATION RESULTS

We present simulation results of fairness when three WTs are served over the forward link, as run two sets of simulations. In the first set, all WTs use (1) in order to estimate SINR, and H-ARQ for early packet termination (Primary Scheme), while in the second set, all WTs use (3) to estimate SINR, and also use H-ARQ (Secondary. scheme).

Simulation parameters are listed in Table I, and have been taken from [5]. Each simulation is run for 20,000 time slots, and 600 independent simulations are run to gather WT throughputs within 90% confidence interval. The WT location is selected so that the terminal is equidistant from the two interfering base stations. The locations from the serving base station of WTs are selected to be $0.4R_0$, $0.7R_0$ and R_0 . The cell radius R is 1 Km. Simulations use ITU path loss models for pedestrian WTs with velocity- 3 kmph.

TABLE I
SIMULATION PARAMETERS

Carrier frequency, f_0	2000 MHz
Log-normal Shadowing variance, σ_G	10 dB
Shadow correlation distance	20.0 m
Noise spectral density, N_0	-174 dBm/Hz
A, amplitude of transmit waveform (base station transmit power of 15W)	5.48
Chip duration, T_c (1.25 Mcps)	0.8 us
Radius of the sector, R	1 Km
R_0 for 90% cell coverage	$0.95R = 0.95$ Km
Miscellaneous gains: antenna gains, body loss, cable loss	15.2 dB
Building penetration loss, (only for pedestrian WTs)	12 dB
Pedestrian path loss in dB, (f_0 in MHz, d in Km)	$30 \log_{10}(f_0) + 49 + 40 \log_{10}(d)$

In all our simulations, although the time-varying shadowing and fading, it is assumed that the WT location remains

unchanged during the course of the simulation. In all the simulations, for simplicity, it is assumed that the network loads in both the interfering sectors are the same, i.e., $\rho_1 = \rho_2$, and varied ρ to study the fairness of Primary ($\rho_1 = \rho_2 = 1$) and Secondary Schemes ($\rho_1 = \rho_2 = \rho$) for different network loads in the interfering sectors.

TABLE II
FAIRNESS OF PRIMARY SCHEME

ρ	X_1	X_2	X_3	Fairness
1.0	991	423	149	0.687252
0.9	999	428	151	0.689400
0.8	1007	432	153	0.690167
0.7	1012	436	155	0.691723
0.6	1018	439	158	0.693303
0.5	1023	442	160	0.694448
0.4	1027	445	162	0.695846
0.3	1034	450	165	0.697832

TABLE III
FAIRNESS OF SECONDARY SCHEME

ρ	X_1	X_2	X_3	Fairness
1.0	991	423	149	0.687252
0.9	992	432	156	0.696332
0.8	990	443	163	0.705844
0.7	987	453	172	0.716467
0.6	985	468	182	0.728971
0.5	980	480	193	0.741667
0.4	973	496	208	0.758444
0.3	963	517	228	0.780033

The tables 2 and 3 present the throughput (kbps) received by each WT as a function of the interfering network load under the both schemes for pedestrian model. Table 2 gives the indexes of throughput and fairness for standard CDMA-HDR networks (Primary Scheme). In columns titled as X_1 , X_2 , and X_3 are presented end to end throughput for WTs 1, 2, and 3. In the last column is calculated the indexes of fairness using (4). Simulation results for Secondary Scheme are given in table 3. Note that as the interfering network load decreases, both the schemes result in higher throughput for WTs 2 and 3. This is because both the schemes are designed to improve the throughput of a WT when the inter-cell interference is lower. However this benefit is especially more pronounced for WTs located near the cell boundary (WTs 2 and 3).

Figure 2 shows the fairness as a function of the interfering network load under Primary and Secondary Schemes for pedestrian users (See respectively table 2, and table 3).

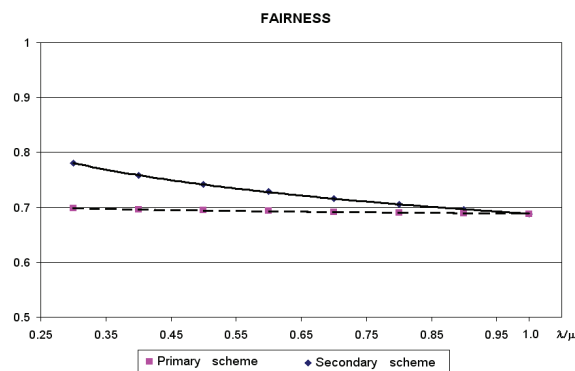


Fig. 2. Fairness of Primary and Secondary Schemes

Fairness of Primary Scheme is worse than Secondary Scheme. This can be explained with the fact that the Secondary Scheme benefits the WTs located far from the serving base station, as well as penalizes near located WTs. One can compare throughput received by WS1 in tables 2 and 3, and see that unlike Primary Scheme, where the throughput of WT 1 increases with decreasing network load, in Secondary Scheme, the throughput of WT 1 decreases with decreasing network load. As it has been shown above proposed mechanism (Secondary Scheme) is better than standard CDMA-HDR, taking into account throughput and fairness.

IV. CONCLUSION

In this paper the advantages of using more accurate estimation of the SINR combined with H-ARQ in Cellular Data Networks, as well as some simulation results obtained with an available online simulator [5] are given.

REFERENCES

- [1] Dimitrov, D. Communication systems in medicine, hand book, TU-Sofia, Bulgaria, 2005.
- [2] Dimitrov D., Georgieva V., A media system for telemedicine, Proceedings pp.83-84, 46 IWK 2001, TU-Ilmenau, Germany
- [3] Dimitrov D., Velchev Y., Communication Protocol for Medical Mobile Network, Proceedings of 48. Internationales Wissenschaftliches Kolloquium, September 22-25 2003, Ilmenau, Germany
- [4] Lee K. and Samuel C., Analysis of a Delay-Constrained Hybrid ARQ Wireless System, IEEE Transactions on Communications, Vol. 54, No. 11, November 2006, pp.2014- 2023
- [5] Mhatre V. et al., Impact of Network Load on Forward Link Inter-Cell Interference in Cellular Data Networks, IEEE Transactions on Wireless Communications, Vol. 5, No. 12, December 2006, pp. 3651-3661
- [6] ITU-MTR M.1225, Guidelines for Evaluation of Radio Transmission Technologies for IMT-2000, 2000.
- [7] Осипов Е.А., Проблемы реализации надежной передачи данных в самоорганизующихся и сенсорных сетях, ISSN 0013-5771. сп. "Электросвязь", № 6, 2006, с.29- 32.
- [8] Valentin Hristov, Dimiter Dimitrov, Distance learning system of low frequency magnetic field and beatdown problem, p.77-84, Proceedings of the Technical University –Sofia, v.52/2003
- [9] D.Dimitrov D., Georgieva V., Information system for telemedicine pp.343-347 Proceedings of 12th European EAEEIE conference May ,14-15, 2001, Nancy, France

This page intentionally left blank.

Web Application of Traveling Salesman Problem using Genetic Algorithms

Milena N. Karova¹, Julka Petkova² and Stoyan P. Penev³

Abstract – This paper introduces online method for finding a solution to the travelling salesman problem using a genetic algorithm. The travelling salesman problem comes up in different situations in our world. It is a special kind of optimisation problem. There had been many attempts to address this problem using classical methods, such as integer programming and graph theory algorithms with different success. The solution, which this paper offers, includes a genetic algorithm implementation in order to give a maximal approximation of the problem, modifying online a generated solution with genetic operators.

Keywords – genetic algorithms, TSP, travelling salesman problem, optimisation, selection, genetic operator, crossover, mutation.

I. INTRODUCTION

Genetic Algorithms are stochastic search methods that mimic the metaphor of natural biological evolution [1]. Genetic Algorithms (GAs) operate on a population of potential solutions applying the principal of survival of the fittest to produce better and better approximations to a solution. At each generation, a new set of approximations is created by the process of selecting individuals according to their level of fitness in the problem domain and breeding them together using operators from natural genetics [3]. This process leads to the evolution of populations of individuals that are better suited to their environment than the individuals that they were created from, just as in natural adaptation.

Gas model natural processes, such as selection, recombination, mutation, migration, locality and neighborhood

II. ONLINE SOLUTIONS OF TRAVEL SALESMAN PROBLEM

In the Internet world there are many web sites for solving Travel Salesman Problem (TSP). Usually the solutions are

Java applets [4]. It proposes random choice of city's number N (between 1 and 9). The city's distance represents matrix $N \times N$. The algorithm terminates in two ways: finding optimal distance or using definite number of iterations.

This algorithm contains two important disadvantages: small city's number and limit population size.

The Ga TSP solving in the University in Ohio offers to user defining city's location on the work area manually [5]. The population size is programming limited. If the city's number is big, the absence of automatically drawing of cities is disadvantage [6].

Generally the following actions are performed to compute the shortest path:

- Fitness function: the sum of distances between all cities
- Chromosomal Representation: sequence of numbers containing a permutation of the first n numbers represented as an array; e.g. 1-2-3-4-6-5
- Selection method: K-tournament selection
- Initialization: Random
- Genetic Model: Generate the next generation from the scratch
- Termination condition: The system is run for N generations and the best (or best k) solution is reported
- Operators: mutation, crossover, copy
- Operator application probabilities: crossover: 0% at generation 1; increase to 95% at generation N ; mutation: 95% at generation 1 is reduced to 0% at generation N ; copy: fixed at 5%
- Population size PS (e.g. 500)

III. GENETIC PARAMETERS AND GENETIC OPERATORS

A. Population

Population is a combination of chromosomes. In the program to present the population it uses array of 1002 chromosomes. The thousand and first chromosome stores the worst tour. The name of the array is population.

```
public static TChromosome population = new TChromosome[1001];
```

For each chromosome it calculates the length that is coded into it, actually this is the fitness of the tour [2]. It is stored in the next array:

¹Milena N. Karova is with the Department of Computer Science and Technologies, Technical University Varna, Studentska str. 1, 9010 Varna, Bulgaria, E-mail: mkarova@iee.bg

²Julka P.Petkova is with the Department of Computer Science and Technologies, Technical University Varna, Studentska str. 1 9010 Varna, E-mail: jppet@mbox.digsys.bg

³Stoyan P. Penev is with the Department of Computer Science and Technologies, Technical University Varna, Studentska str. 1, 9010 Varna, Bulgaria, E-mail: penev@engineer.bg

```
public static double[] popFitness=new double[1001];
```

Now it knows that the tour with index i has a fitness popFitness[i].

The maximum number of towns is 32. The current number is stored in the variable townCount. In the same way the number of populations – popCount. In the process of mutation, it uses the coefficient MutInd.

B. Genetic Operators for Recombination

Two of the main problems that occur were choosing proper methods of crossover and mutation. It has implemented two types of crossover – cycle crossover and a custom one [8]. The user can choose which one to use in the calculation. Let us take a closer look at the Cycle crossover.

First of all it fits perfectly to the way our tour is represented in the chromosome. For example if our tour is

```
Tour = 1234
```

This means that it goes from city 1 to city 2 to city 3 to city 4. Unlike other methods of crossover here it does not pick a crossover point at all. It chooses the first gene from one of the parent chromosome. If our parents are

```
parent1 = 12345678
```

```
parent2 = 85213647
```

say it picks 1 from parent 1,

```
child = 1*****
```

It must pick every element from one of the parents and place it in the position it was previously in. Since the first position is occupied by 1, the number 8 from parent2 cannot go there. So it must now pick the 8 from parent1.

```
child = 1*****8
```

This forces us to put the 7 in position 7 and 4 in position 4, as in parent1.

```
child = 1**4**78
```

Since the same set of position is occupied by 1,4,7,8 in parent1 and parent2, it finishes by filling in the blank positions with the elements of those positions in v2. Thus

```
child 1 = 15243678
```

and it get child2 from the complement of child1.

This type of crossover ensures that each new created chromosome is legal. A chromosome is legal if it is constructed according to the requirements of the salesman problem. In this crossover notice that it is possible for us to end up with the offspring being the same as the parents. This

is not a problem since it will usually occur if parents have high fitness, in which case, it could still be a good chance.

In the program it uses function TestCrossOver:

```
Public static TChromosome TestCrossOver (int indPar1, int indPar2);
```

where indPar1 and indPar2 are the parent's chromosomes.

If it want to solve this problem or other like not getting trapped in a local optimum we could use mutation. Due to the randomness of the process it will occasionally have chromosomes near a local optimum but none near the global optimum. Therefore the chromosomes near the local optimum will be chosen to crossover because they will have the better fitness and there will be very little chance of hiding the global optimum. So mutation is a completely random way of getting to possible solutions that would otherwise not be found.

Mutation is performed after crossover. In presented algorithm, there are 3 kinds of mutation: transposition, inversion and changing city's position. The mutation index (MutInd) must decide weather to perform mutation on this child chromosome or not. It then chooses a point to mutate and switch that point. For instance, in our example it had

```
child = 12345678
```

If we choose the mutation point to be gene three and 7, the child would become

```
child = 12745638
```

It simply switched the places of genes 3 and 7. Another mutation that takes place is inverting a subtour in our child chromosome. Let us have the chromosome

```
child = 12345678
```

and choose the same mutation points 3 and 7. The subtour between these two point is switched in reverse order

```
child = 12765438
```

After the mutation process the program makes a strict verification of the chromosome. If it is not legal then the chromosome is ignored.

In the program it uses function Mutate:

```
Public static TChromosome Mutate (TChromosome ch);
```

The idea of the traveling salesman problem is to find a tour of a given number of cities, visiting each city once and returning to the starting city where the length of this tour is minimized.

C. Fitness Function

The Purpose of the fitness function is to decide if a chromosome is good how good it is [4]. In the traveling salesman problem the criteria for good chromosome is it's

length. The longer the tour that is coded, the better the chromosome is. Calculation takes place during the creation of the chromosomes. Each chromosome is created and then its fitness function is calculated. The length of the chromosome is measured in pixels by the scheme of the tour.

$$fitness_chromosome = \sum_{i=1}^{towncount} t_i$$

where towncount is the number of cities in population, et ti is the distance between two cities.

D. Basic Functions used in this application

In this product were used 10 basic functions and procedures in order to create a completely working program:

- DrawCity
- ShowCities
- DrawChromosome
- GenerateTownSet
- CreateTown
- GetClick
- Mutate
- ClenUp
- Sort
- CreatePopulation
- TestCrossOver

IV. INTERFACE AND TEST RESULTS

The interface [Fig.1] is Web application, showing the current result at the moment they are calculated (the best and the worst chromosome). This screen offers determining cities, population, stop criteria (iteration number), crossover mode, mutation mode and mutation rate (coefficient of mutation). In this order tone of the stop criteria is that the user can terminate the calculations if he finds a feasible solution. The screen [Fig.2] shows the worst chromosome and the Fig. 3 – the best solution that is the chromosome with the smallest distance between cities.

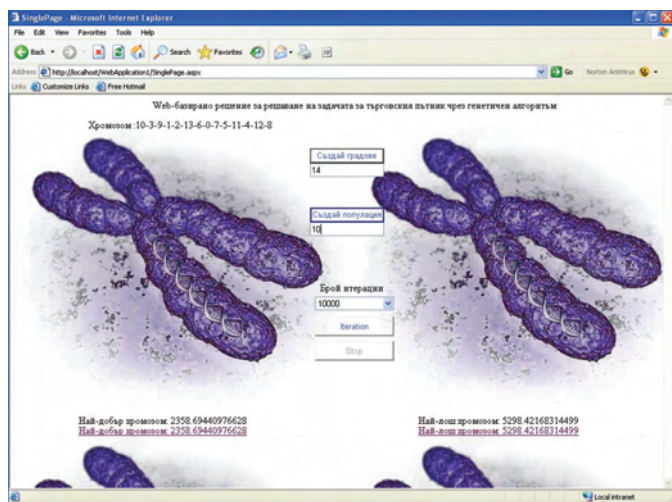


Fig. 1. The main page

Fig. 4 shows that algorithm needs the minimum iterations to obtain optimal solution (minimized cutie's tour) using mutation rate 3,5%.

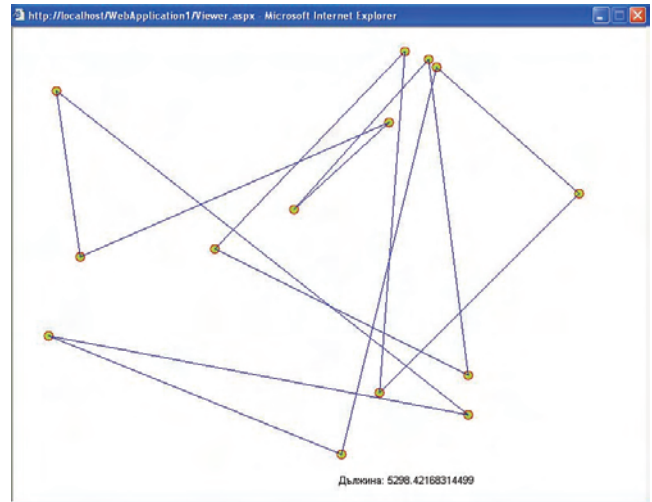


Fig. 2. The worst chromosome

The algorithm finds a good solution when there are 30 cities, when the coefficients of inversion and transposition have lower values. When there are less cities, coefficient's influence is smaller. When the distance between cities is constant, the dependences are the same [Fig.5, Fig.6].

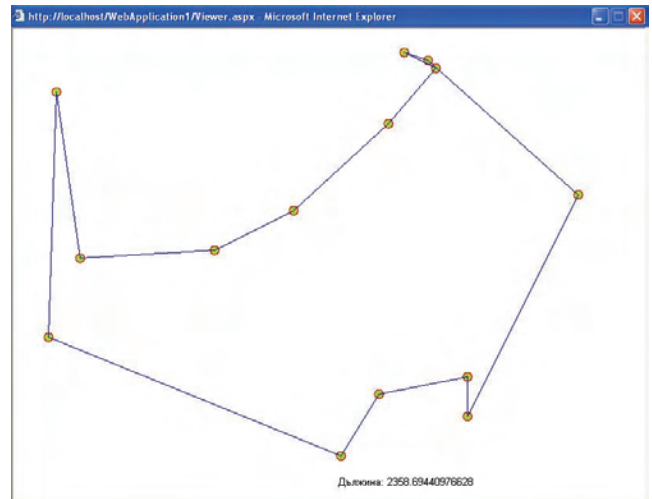


Fig. 3. The Best chromosome

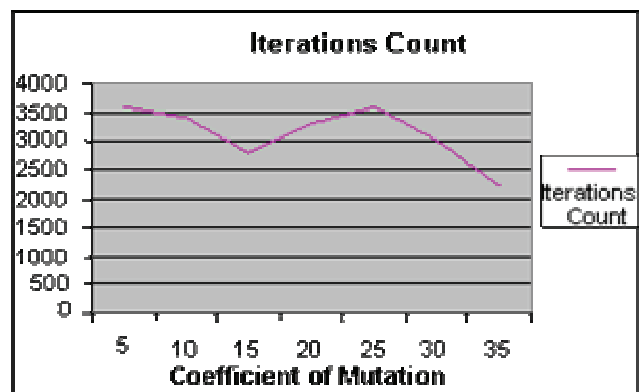


Fig.4 Coefficient of Mutation

V. CONCLUSION

Genetic algorithms appear to find good solutions for the traveling salesman problem, however it depends very much on the way the problem is encoded and which crossover and mutation methods are used. It seems that the methods that use heuristic information or encode the edges of the tour perform the best and give good indications for future work in this area.

Overall, it seems that genetic algorithms have proved suitable for solving the traveling salesman problem. As yet, genetic algorithms have not found a better solution to the traveling salesman problem that is already known, but many of the already known best solutions have been found by some genetic algorithm methods also.

It seems that the biggest problem with the genetic algorithm devised for the traveling salesman problem is that it is difficult to maintain structure from the parent chromosomes and still end up with a legal tour in the child chromosomes. Perhaps a better crossover or mutation routine that retains structure from the parent chromosomes would give a better solution that we have already found for some traveling salesman problems.

REFERENCES

- [1] Goldberg D, "Web Courses", <http://www.engr.uiuc.edu/OCEE>, 2000.
- [2] Engebretsen L., Karpinski M. Approximation hardness of TSP with bounded metrics, Proceedengs of 28th ICALP, LNCS 2076, Springer 2001
- [3] Mitchell M., "An Introduction to Genetic Algorithms", Massachusetts Institute of Technology, 1996
- [4] <http://students.ceid.upatras.gr/~papagel/project/tspprobl.htm>
- [5] <http://www.personal.kent.edu/~rmuhamma/Algorithms/AproxAlgor/TSP/tsp.htm>
- [6] <http://home.planet.nl/~onno.waalewijn/tsp.html>

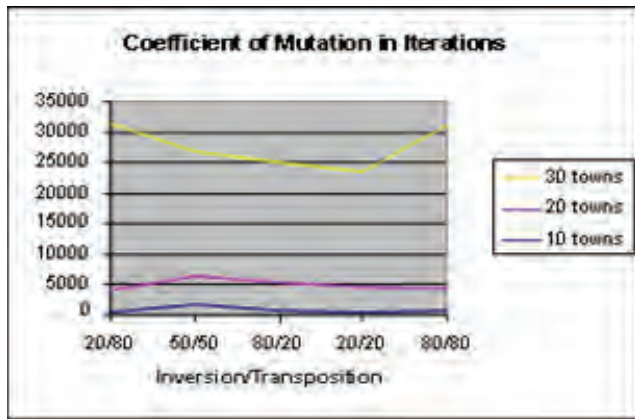


Fig. 5 Inversion/ Transposition

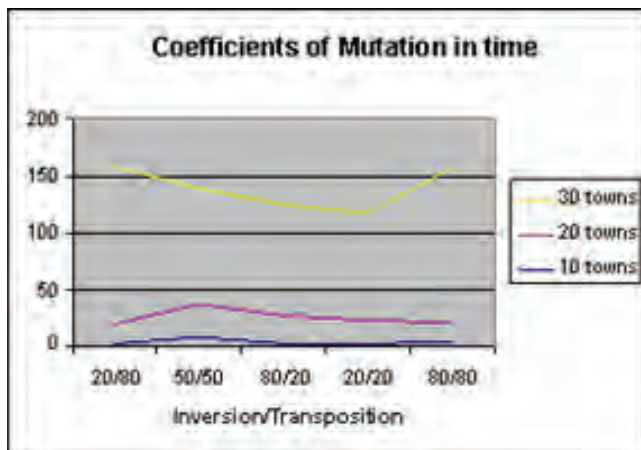


Fig. 6. Mutation Coefficients in time

A Performance Study of Run-time Systems for Distributed Time Warp Simulation

Hristo G. Valchanov¹, Nadezhda S. Ruskova² and Trifon I. Ruskov³

Abstract - Parallel discrete event simulation (PDES) is a basic approach for evaluation of complex systems. A PDES attempts to speed up the execution of a simulation by distributing the simulation's workload between multiple processors. A network of workstations is a widely available platform for PDES. The present article provides a comparative analysis of operational distributed simulation models based on the Time Warp algorithm. An operational model allowing for reduction of the simulation costs has been proposed based on an experimental evaluation.

Keywords – Distributed simulation, Time Warp, PDES.

I. INTRODUCTION

PDES allows acceleration of the simulation process through its distribution among a number of processor. The modeled system is represented as a set of components, simulated through simulation objects (SO). SO exchange timestamped messages, simulating the events occurring in a simulation model. The correctness of simulation (processing of events in their correct order of occurrence) is guaranteed by special synchronization protocols, with Time Warp being one of the most widely used nowadays [1].

The Time Warp protocol allows SO to process the events according to the order of their receiving – the so called “optimistic approach”. After processing of each event, SO moves up its own local time equal to the time of occurrence of the event. The approach allows processing of events in a sequence, different from that of their natural occurrence, which would result in a casualty error. Such an error occurs in case of receiving an event message (called *straggler*) with a timestamp lower than the current time of SO. The procedure of error correction requires SO to recover its state before the time of arrival of a straggler, and to cancel all messages sent up to that moment. For this purpose, each SO performs a periodic saving of its state. Canceling of all sent messages is effected through sending of corresponding anti-messages. The entire process of SO recovery is known as *rollback*.

An important feature of the discrete-event simulation is the so-called *granularity* [2]. Granularity is defined as the ratio between the individual event performance time and the

simulation total time. The direct real-to-simulation object mapping can result in events with very small granularity, i.e. the time for processing of a single event may turn out to be much smaller than the system time, spent for its simulation. The representation of many modeled components in a single SO may increase simulation granularity thus allowing for the internal communications in the simulation model to be implemented by means of a common memory. Within the SO cluster, formed in this way, the events can be processed by sequential simulation, based on a time-ordered event list – *cluster event list (CEL)*, whereas, for the communication between the clusters, the Time Warp protocol is used.

Each simulation cluster consists of two main components – simulation (SM) and communication modules (CM), through which distribution of cluster functionality is achieved. Both components can work in parallel, e.g. as threads executed in parallel. The SM processes the time-ordered queue of events from CEL. The CM ensures the exchange of messages between the clusters, executed on different processors. Such structure is common for the kernels of a number of software simulation packages, as WARPED, PARSEC, etc [3], [4]. A typical feature of their operational models is that the synchronization is performed within the code of the simulation module, in which the actions of message synchronization and message processing are sequential operations.

The usage of this operational model (called *BASE*) for simulation on distributed memory architectures, like network of workstations, can lead to undesirable effects, resulting in decrease of simulation performance. Due to the parallel work of SO, the asynchronous message exchange between them and the delays, typical of the network communications, a high probability for receiving of a straggler message exists. On the other hand, the parallel functioning of the modules allows receipt of the messages to be independent from their synchronization and processing. Thus, in case of receipt of a sequence of straggler- or anti-messages, these will be processed in different synchronization cycles of SM, with each cycle repeating the actions for state recovery and canceling of sent messages.

In the present paper, the process of simulation state recovery is discussed, and an operational model for simulation performance improvement is proposed.

II. THE BASE ROLLBACK MODEL

The simulation process can be represented as a sequence of simulation cycles, each one composed of synchronization (S_i) and processing (P_i) phases. Processing of a message, assigned

¹Hristo G. Valchanov is with the Computer Science & Engineering Department, Technical University of Varna, Bulgaria, E-mail: hristo@tu-varna.acad.bg

²Nadezhda S. Ruskova is with the Computer Science & Engineering Department, Technical University of Varna, Bulgaria, E-mail: ruskova@tu-varna.acad.bg

³Trifon I. Ruskov is with the Computer Science & Engineering Department, Technical University of Varna, Bulgaria, E-mail: ruskov@tu-varna.acad.bg

to SO, is performed without interruption, with checks for received stragglers and anti-messages being executed between two sequential event processing actions only.

The occurrence of a situation, in which a straggler or anti-message is received during processing phase P_i , will be defined as *violation of simulation correctness (VSC)*. In the present Chapter, we shall formulate *simulation effectiveness* with respect to simulation process recovery in the event of VSC.

Fig.1 shows a situation, in which single straggler or anti-message is received during the processing phase of the i^{th} simulation cycle.

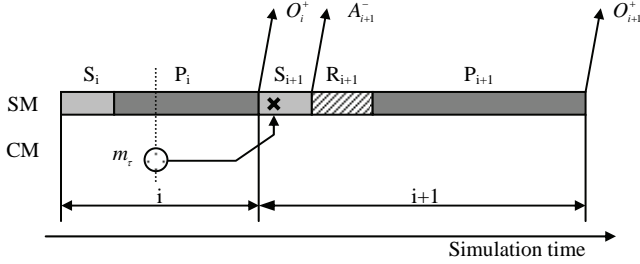


Fig.1. A single simulation correctness violation

Let m_i be a message for an event e_i , which is being processed in the i^{th} simulation cycle P_i . At the end of the P_i , the generated messages for the scheduled events within this cycle of the simulation - O_i^+ , will be sent out. Let m_τ be a violator-message with a timestamp lower than the *cluster virtual time* ($\tau < CVT$), received during the P_i phase. The actions for synchronization of this event will not be undertaken until the beginning of the next simulation cycle S_{i+1} . These will result in a rollback (R_{i+1}) to the correct state, corresponding to simulation time τ , and sending of canceling anti-messages:

$$A_{i+1}^- = O_i^- + O^-(k_{CVT,\tau}), \quad (1)$$

where O_i^- - number of anti-messages, necessary for canceling of the just sent normal O_i^+ messages;

$O^-(k_{CVT,\tau})$ - number of anti-messages, necessary for canceling of the normal messages sent out for all k events processed within the time interval between the current CVT and the violator-message timestamp τ . The number k defines the depth (in terms of number of events) of rollback for correct state recovery (R_{i+1}).

During the next simulation cycle P_{i+1} , all events in the recovered correct *CEL* (thanks to rollback R_{i+1}) will be processed. At the end of the cycle, normal messages will be sent again:

$$O_{i+1}^+ = O_i^+ + O^+(k_{CVT,\tau}) + O^+(\tau), \quad (2)$$

where O_i^+ - number of generated messages due to repeated event processing in the i^{th} simulation cycle;

$O^+(k_{CVT,\tau})$ - number of generated messages due to repeated event processing in the time interval (CVT, τ) due to rollback;

$O^+(\tau)$ - number of generated messages due to processing of message m_τ . (In case of m_τ is an anti-message, $O^+(\tau)=0$).

In the example presented, the VSC correction is done during a subsequent simulation cycle. This causes performance overhead, related to sending of normal messages, followed by cancellation and repeated sending of the same. At the same time, the repeated processing of event e_i must be pointed out.

Effectiveness is further decreased in case of subsequent straggler and anti-messages, following one by one (Fig.2).

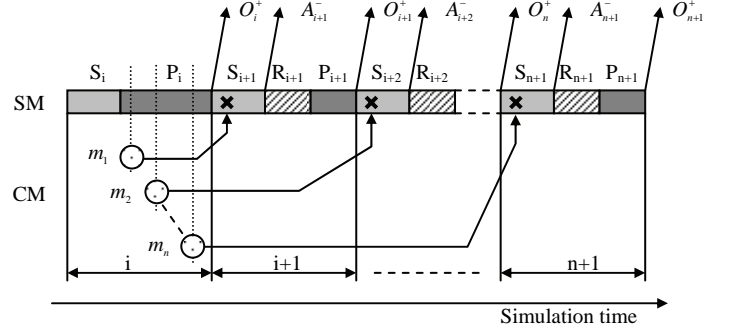


Fig.2. Multiple simulation correctness violation

Eqs. (1) and (2) can be derived for n violations, occurring in the i^{th} simulation cycle within a model time interval (τ, γ) , where $\tau, \gamma < CVT$ (τ is the timestamp of the first message m_i in the interval, γ is the timestamp of the last message m_n), as follows:

$$A_n^-(i) = n * A_{i+1}^- + \sum_{e=1}^{n-1} O_e^-(t_{\tau \leq t \leq \gamma}) + O^-(k_{\tau,\gamma}), \quad (3)$$

where $\sum_{e=1}^{n-1} O_e^-(t_{\tau \leq t \leq \gamma})$ - number of anti-messages, necessary for canceling of the normal messages sent after processing of the stragglers, included in *CEL* after state recovery;

$O^-(k_{\tau,\gamma})$ - number of anti-messages, necessary for canceling of the normal messages sent for all processed k events within the interval (τ, γ) , in case of $\gamma < \tau$.

Similarly,

$$O_n^+(i) = n * O_{i+1}^+ + \sum_{e=1}^n O_e^+(t_{\tau \leq t \leq \gamma}) + O^+(k_{\tau,\gamma}), \quad (4)$$

where $\sum_{e=1}^n O_e^+(t_{\tau \leq t \leq \gamma})$ is the number of generated messages due to the processing of violator-messages. If case of anti-messages, the value of this expression is zero;

$O^+(k_{\tau,\gamma})$ - number of messages generated by the repeated event processing within the interval (τ, γ) , in case of $\gamma < \tau$, due to rollback.

Based on Eqs. (3) and (4), the following conclusions for the effectiveness of this operational model with regard to VSC elimination can be drawn:

- On receipt of n straggler- or anti-messages during a simulation cycle, the simulation process will be recovered after n subsequent simulation cycles;

- Additional processor time is spent on event processing, after which rollback actions are necessary;
- The messages about scheduled events, generated after event processing by SO, will be delivered by the parallel running CM before the beginning of the next simulation cycle. During the VSC elimination actions, these messages will be generated and sent many times due to the repeated event processing;
- Cancellation of the previous actions will lead to multiple increase of the number of outgoing anti-messages, as well as to increase of the probability for cascade rollback.

As a result, there is an increased synchronization overhead, which will result in degradation of the simulation process performance.

III. THE COST REDUCTION MODELS (CRM)

In the present Chapter, an operational model, aimed at decreasing of VSC elimination overhead, is proposed. The basic concept of this model is reduction of the number of necessary recovery simulation cycles. This can be achieved by merging of the actions for synchronization of different violator-messages into one single synchronization cycle.

The model consists of three components: communication, synchronization and simulation modules, implemented as threads running in parallel within a simulation cluster. The purpose of the communication module is the same as that presented in Chapter I. A substantial difference is the separation of the synchronization operations in a standalone synchronization module (SYN), aimed at achievement of parallel execution of event synchronization and event processing.

Let's consider the i^{th} simulation cycle P_i , in which the event e_i is being processed (Figure 3).

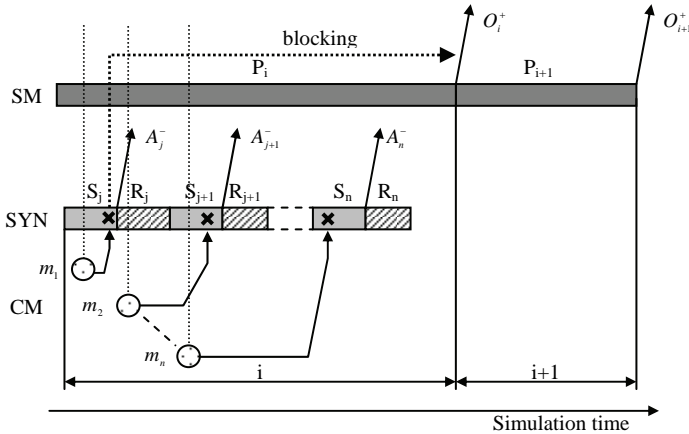


Fig.3. Multiple simulation correctness violation for CRM

Let m_i be a violator-message ($\tau < CVT$). Thanks to the parallel execution, SYN starts immediately a synchronization phase S_j . Meanwhile, the delivery of messages from SM to CM is blocked, which prevents sending of the messages through the communication network at the end of the processing phase. During S_j SYN starts rollback actions (R_j), resulting in recovery of the correct SO state.

Thus, in the i^{st} simulation cycle, the number of sent anti-messages will be:

$$A_i^- = O^-(k_{CVT,\tau}), \quad (5)$$

where $O^-(k_{CVT,\tau})$ - number of anti-messages, necessary for canceling of the sent normal messages for all k processed events within the interval between the current CVT and the time τ of the violator-message.

Within the current cycle, due to the blockage, no normal messages will be sent, i.e. $O_i^+ = 0$.

VSC elimination will be executed during the next $i+1^{\text{st}}$ simulation cycle, wherein the simulation process will continue with processing of the CEL, already recovered to its correct state. During this cycle, no anti-messages will be sent ($A_{i+1}^- = 0$), while the number of outgoing normal event messages will be:

$$O_{i+1}^+ = O_i^+ + O^+(k_{CVT,\tau}) + O^+(\tau), \quad (6)$$

where O_i^+ - number of messages generated due to processing of event e_i from the i^{th} simulation cycle;

$O^+(k_{CVT,\tau})$ - number of messages generated by the repeated event processing within the interval (CVT, τ) , due to rollback;

$O^+(\tau)$ - number of messages generated due to processing of message m_i . (In case of m_i is an anti-message, $O^+(\tau) = 0$).

Similarly, for n violations, having occurred during the i^{th} simulation cycle for a simulation time interval (τ, γ) , where $\tau, \gamma < CVT$, the number of anti- and normal messages sent out can be represented:

$$A_n^-(i) = O^-(k_{CVT,\tau}) + O^-(k_{\tau,\gamma}), \quad (7)$$

where $O^-(k_{CVT,\tau})$ - number of anti-messages, necessary for canceling of the normal messages sent out for all processed k events within the interval between the current CVT and the time τ of the violator-message.

$O^-(k_{\tau,\gamma})$ - number of anti-messages, necessary for canceling of the normal messages sent out for all processed k events within the interval (τ, γ) , in case of $\gamma < \tau$. In case of $\gamma \geq \tau$, this component has a value of zero,

and

$$O_n^+(i) = O_i^+ + \sum_{e=1}^n O_e^+(t_{\tau \leq t \leq \gamma}) + O^+(k_{\tau,\gamma}), \quad (8)$$

where O_i^+ - number of generated messages by processing of event e_i from the i^{th} simulation cycle;

$\sum_{e=1}^n O_e^+(t_{\tau \leq t \leq \gamma})$ - number of generated messages due to the processing of violator-messages within the interval (τ, γ) . In case of anti-message, the value of this expression is zero;

$O^+(k_{\tau,\gamma})$ - number of messages generated by the repeated event processing within the interval (τ, γ) , in case of $\gamma < \tau$, due to rollback.

Based on comparison of Eqs. (3)-(7) and (4)-(8), some conclusions about the positive results from application of this operational model can be drawn, mainly in the following directions:

- The proposed model allows VSC elimination for P_i to be done within one simulation cycle only, regardless of the number of violator-messages received during P_i ;
- Reduction of the number of anti-messages, transmitted over the network. In case of a rollback, since the possibility for sending of normal messages at the end of the simulation cycle is blocked, the necessity of sending corresponding canceling anti-messages is also eliminated;
- Reduction of the number of outgoing repeated normal event messages. Thanks to the blocking mechanism in the rollback case, the initial sending of such event messages is ignored;
- Reduction of the total elapsed simulation time.

IV. EXPERIMENTAL EVALUATION AND ANALYSIS

The experimental studies have been performed on the basis of the benchmark PHOLD [5] with increasing values of the number of SO and the events in the simulation model. PHOLD contains a fixed number N of simulation objects, connected through a 2D torus network and a set of tasks (messages) E , circulating among them. The increment of scheduled event's timestamps is determined by means of normal distribution. The destination of each newly generated scheduled event is chosen with equal probability among its four adjacent SO in the 2D topology.

The experiments have been carried out on a 100 Mb local area network of 900 MHz Pentium III PC workstations running Linux 2.6 operating system. A run-time system has been developed [6], consisting of simulation kernels performing the functions of simulation clusters. Each simulation kernel is executed as a standalone Linux-process on a separate workstation.

Fig. 4 shows the results, obtained within the study of the number of generated anti-messages

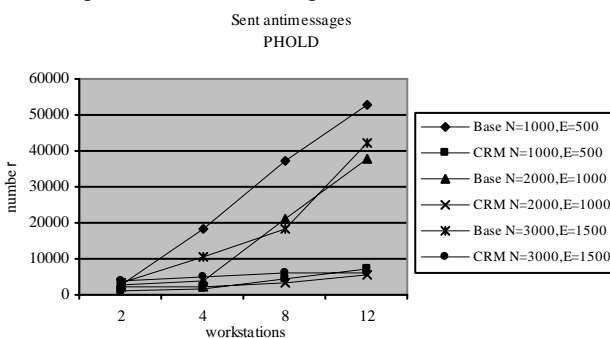


Fig.4. Sent anti-messages chart

A common tendency for both operational models studied (BASE and CRM) is the observed increase of the quantity of generated anti-messages proportional to the number of computational units. This is a normal consequence of the increased communication between the separate clusters wherein, because of message delivery delays, the potential probability of violator-message arrival, rollback and repeated

message sending also increases. The experiments show clearly the better effectiveness of the CRM model with respect to the number of generated anti-messages, expressed as a considerable reduction of the latter. This is a direct consequence of the parallelism of the event synchronization and event processing actions, wherein, for the rollback case, thanks to blocking of process-generated normal event outgoing messages, the necessity of subsequent outgoing anti-messages for their cancellation is also eliminated.

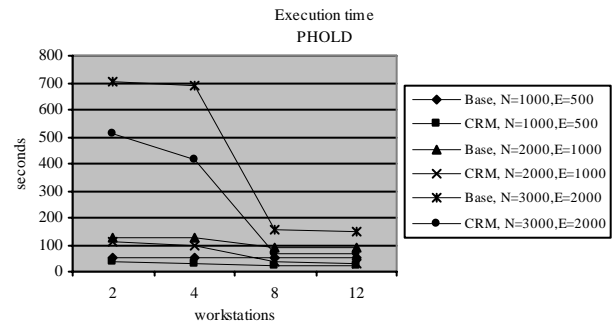


Fig.5. Execution time

Regarding the total elapsed simulation time, the CRM model demonstrates better features, as shown on Fig. 5. These better features are mainly due to the considerable reduction of the number of outgoing anti-messages, and the reduction of repeated event processing overhead, as well.

V. CONCLUSION

This paper presents a study of operational models for a Time Warp discrete-event simulation over a network of workstations. The experimental results show definitely the better features of the proposed CRM model regarding VSC elimination performance overheads. As a future goal for research work, improvement of the effectiveness of the proposed model with regard to reduction of performance overheads for recovery of previous correct simulation states should be pointed out first of all.

REFERENCES

- [1] Fujimoto R.M. Parallel Discrete Event Simulation. Communications of the ACM, vol.33, no.10, pp.41-52, 1990.
- [2] Nance R., Sargent R. Perspectives on the Evolution of Simulation. Operations Research, *INFORMS*, vol.50, no.1, pp.161-172, 2002.
- [3] Dale E., Wilsey P., Timothy J. WARPED Simulation Kernel Documentation, 1995.
- [4] Bagrodia, R., R. Meyer, Y. Chen. Parsec: a parallel simulation environment for complex systems, *IEEE Computer*, vol.10, pp.77-83, 1996.
- [5] Fujimoto R. Performance of TimeWarp under synthetic workloads. Proc. of the SCS, pp.23-28, 1990.
- [6] Valchanov H., Ruskova N., Ruskov T. Implementation of a Language for Distributed Simulation, Proc of the Computer Science Conference'05, Chalkidiki, Greece, vol.I, pp.208-213, 2005.

Genetic Algorithms in Solving Multi-objective Optimization Problems

Hristo I. Toshev¹ and Chavdar D. Korsemov²

Abstract: - The paper suggests discusses the development of the scientific research in the area of the genetic algorithms application in solving multi-objective optimization problems. Some of the most wide-spread algorithms, developed in the last years have been considered. The main directions, connected with the use of these algorithms, have been presented and the growth of the research work in this area (publications) during the last decade

Keywords – evolutionary multi-objective optimization, multi-objective evolutionary algorithms, genetic algorithms

I. INTRODUCTION

Genetic algorithms are a method for search based on the selection of the best species in the population in analogy to the theory of evolution of Ch. Darwin.

From the point of view of the information change, the evolutionary search is a sequential transformation of a single fuzzy (imprecise) set of some solutions into another one. The transform itself can be named a searching algorithm or a genetic algorithm (GA). The GA is not simply a random search, but an efficient usage of information in the evolutionary process [6], [11].

The main goal of GA-s is twofold:

- abstract and formal explanation of the adaptation processes in evolutionary systems;
- modelling natural evolutionary processes for efficient solution of determined class of optimization and other problems.

During the last years a new paradigm is applied to solve optimization problems GA-based and modifications of GA. GA realize searching a balance between efficiency and quality of solutions at the expense of selecting the strongest alternative solution from undetermined and fuzzy solutions [11].

Usually in the multi-objective optimization problems several criteria (objective functions) are optimized simultaneously in a set of feasible alternatives. In the general case there does not exist an alternative (solution), which is optimal for all the solutions. But there exists a set of alternatives (solutions), characterized by the following property: each improvement of the value of one of the criteria leads to the deterioration of the value of at least one of the other criteria. A set of alternative solutions is obtained, each of the alternatives in this set could be a solution of the multiobjective problem.

The notion of optimality was originally introduced by F. Edgeworth in 1881 and later generalized by V. Pareto in 1896. It is called Edgeworth-Pareto optimum or, simply, Pareto optimum. In words, this definition says that a solution to an MOP is Pareto optimal if there exists no other feasible solution which would decrease some criterion without causing a simultaneous increase in at least one other criterion. It should not be difficult to realize that the use of this concept almost always gives not a single solution but a set of them, which is called the Pareto optimal set. The vectors of the decision variables corresponding to the solutions included in the Pareto optimal set are called nondominated. The plot of the objective functions whose nondominated vectors are in the Pareto optimal set is called the Pareto front.

II. STARTING OF RESEARCH

The first to have designed an multi-objective evolutionary algorithm (MOEA) during the mid-1980s is D. Schaffer [27]. Schaffer's approach, called Vector Evaluated Genetic Algorithm (VEGA) consists of a simple genetic algorithm with a modified selection mechanism. At each generation, a number of sub-populations were generated by performing proportional selection according to each objective function in turn. These sub-populations would then be shuffled together to obtain a new population, on which the GA would apply the crossover and mutation operators in the usual way. VEGA had a number of problems, from which the main one had to do with its inability to retain solutions with acceptable performance, perhaps above average, but not outstanding for any of the objective functions. These solutions were perhaps good candidates for becoming nondominated solutions, but could not survive under the selection scheme of this approach.

Later researchers adopted for several years other naive approaches. The most popular were the linear aggregating functions, which consist in adding all the objective functions into a single value which is directly adopted as the fitness of an evolutionary algorithm [5]. Lexicographic ordering was another interesting choice. In this case, a single objective (which is considered the most important) is chosen and optimized without considering any of the others. Then, the second objective is optimized but without decreasing the quality of the solution obtained for the first objective. This process is repeated for all the remaining objectives [9].

Despite all these early efforts, the direct incorporation of the concept of Pareto optimality into an evolutionary algorithm was first hinted by David E. Goldberg in his book on genetic algorithms [10]. He suggested the use of nondominated ranking and selection to move a population toward the Pareto

¹Hristo I. Toshev and ²Chavdar D. Korsemov are with the Institute of Information Technologies, Bulgarian Academy of Sciences, Acad. G. Bonchev str., bl. 29A, 1113 Sofia, Bulgaria, E-mail: toshev@iinf.bas.bg, , chkorsemov@iinf.bas.bg

front in a multi-objective optimization problem. The basic idea is to find the set of solutions in the population that are Pareto nondominated by the rest of the population. These solutions are then assigned the highest rank and eliminated from further contention. Another set of Pareto nondominated solutions is determined from the remaining population and are assigned the next highest rank. This process continues until all the population is suitably ranked. Goldberg also suggested the use of some kind of niching technique to keep the GA from converging to a single point on the front.

For pity the author develops only theoretically his ideas and does not supply any real alteration of the procedures, described by him.

III. EXTENSION OF THE INVESTIGATIONS

In the previous study (section 2) it was pointed out that Goldberg does not provide a real execution of his procedures in multi-objective optimization (MOP), but in fact all the variants of this algorithm, later developed, are on the basis of his theory and are influenced by them.

3.1 Nondominated Sorting Genetic Algorithm (NSGA)

This algorithm is suggested by Srinivas and Deb [29]. The NSGA is based on several layers of classifications of the individuals as suggested by Goldberg [10]. Before selection is performed, the population is ranked on the basis of nondomination: all nondominated individuals are classified into one category (with a dummy fitness value, which is proportional to the population size, to provide an equal reproductive potential for these individuals). To maintain the diversity of the population, these classified individuals are shared with their dummy fitness values. Then this group of classified individuals is ignored and another layer of nondominated individuals is considered. The process continues until all individuals in the population are classified. Since individuals in the first front have the maximum fitness value, they always get more copies than the rest of the population. The algorithm of the NSGA is not very efficient, because Pareto ranking has to be repeated over and over again. Evidently, it is possible to achieve the same goal in a more efficient way.

3.2 Niche-Pareto Genetic Algorithm (NPGA)

This algorithm is suggested by Horn, Nafpliotis and Goldberg in [16]. The NPGA uses a tournament selection scheme based on Pareto dominance. The basic idea of the algorithm is quite clever: Two individuals are randomly chosen and compared against a subset from the entire population (typically, around 10% of the population). If one of them is dominated (by the individuals randomly chosen from the population) and the other is not, then the nondominated individual wins. All the other situations are considered a tie (i.e., both competitors are either dominated or nondominated). When there is a tie, the result of the tournament is decided through fitness sharing.

3.3 Multi-Objective Genetic Algorithm (MOGA)

This algorithm is suggested by Fonseca and Fleming in [7]. In MOGA, the rank of a certain individual corresponds to the number of chromosomes in the current population by which it is dominated. All nondominated individuals are

assigned the highest possible fitness value (all of them get the same fitness, such that they can be sampled at the same rate), while dominated ones are penalized according to the population density of the corresponding region to which they belong (i.e., fitness sharing is used to verify how crowded is the region surrounding each individual).

Making comparative analysis of the algorithms, above pointed, it is established with no doubt, that MOGA is excellent, followed by NPGA and NSGA. The investigations in that period are characterized by simplicity of the algorithms offered and the lack of any methodology for their testing [6].

The main conclusion about the implementations of this generation of GA is, that in order one MOEA to be successful, a good mechanism for the selection of the nondominated species has to be combined with a good mechanism for variety support, which will enable the generation of MOEA[6].

IV. ELITISM – THE STANDARD MECHANISM IN THE MOST RECENT EVOLUTIONARY ALGORITHMS

The wide development of MOEA in the recent years has begun after the works of Eckart Zitzler [32], due to it the elitism has become a standard mechanism in the development in this direction. In the context of multi-objective optimization, elitism usually (although not necessarily) refers to the use of an external population (also called secondary population) to retain the nondominated individuals found along the evolutionary process. The main motivation for this mechanism is the fact that a solution that is nondominated with respect to its current population is not necessarily nondominated with respect to all the populations that are produced by an evolutionary algorithm. Thus, what we need is a way of guaranteeing that the solutions that we will report to the user are nondominated with respect to every other solution that our algorithm has produced. Therefore, the most intuitive way of doing this is by storing in an external memory (or archive) all the nondominated solutions found. If a solution that wishes to enter the archive is dominated by its contents, then it is not allowed to enter. Conversely, if a solution dominates anyone stored in the file, the dominated solution must be deleted.

After the offered by Zitzler theory, most of researchers began to started to incorporate external populations in their MOEAs and the use of this mechanism (or an alternative form of elitism) became a common practice.

4.1 Strength Pareto Evolutionary Algorithm (SPEA)

This algorithm is introduced by Zitzler and Thiele in [32]. This approach was conceived as a way of integrating different MOEAs. SPEA uses an archive containing nondominated solutions previously found (the so-called external nondominated set). At each generation, nondominated individuals are copied to the external nondominated set. For each individual in this external set, a strength value is computed. This strength is similar to the ranking value of MOGA [7], since it is proportional to the number of solutions to which a certain individual dominates.

4.2 Strength Pareto Evolutionary Algorithm 2 (SPEA2)

This algorithm, introduced by Zitzler and Thiele in [31] has three main differences with respect to its predecessor:

(1) it incorporates a fine-grained fitness assignment strategy which takes into account for each individual the number of individuals that dominate it and the number of individuals by which it is dominated;

(2) it uses a nearest neighbor density estimation technique which guides the search more efficiently;

(3) it has an enhanced archive truncation method that guarantees the preservation of boundary solutions.

4.3. Pareto Archived Evolution Strategy (PAES)

This algorithm is introduced by Knowles and Corne in [21]. PAES consists of a (1 + 1) evolution strategy (i.e., a single parent that generates a single offspring) in combination with a historical archive that records the nondominated solutions previously found. This archive is used as a reference set against which each mutated individual is being compared. Such a historical archive is the elitist mechanism adopted in PAES. However, an interesting aspect of this algorithm is the procedure used to maintain diversity which consists of a crowding procedure that divides objective space in a recursive manner. Each solution is placed in a certain grid location based on the values of its objectives (which are used as its "coordinates" or "geographical location"). A map of such grid is maintained, indicating the number of solutions that reside in each grid location. Since the procedure is adaptive, no extra parameters are required (except for the number of divisions of the objective space). This adaptive grid (or variations of it) has been adopted by several modern MOEAs [4].

V. APPLICATIONS

The advance in the research of MOEA ensures them their widening application. In order to give a general fancy for the type of applications, they could be classified in four main directions [1], [2]: science, engineering, industry and various other directions (miscellaneous applications). Some specific areas inside any of these directions are discussed below.

- Scientific applications [1], [13], [17], [22], [23], [26]– of chemical, analysis of spectroscopy, medical image reconstruction [22], computer aided diagnosis, machine-learning in high-dimensional data, the analysis of promoters in biological sequences in the problem to deal with [26] and all.

- Engineering applications [1], [6], [12], [14] – electrical, hydraulic, structural, aeronautical, robotics and control and all.

- Industrial applications [1], [19], [24], [25] – design, manufacture, scheduling, management and all.

- Miscellaneous applications [1], [28], [15]– problem of attribute selection in data mining, decisions support system, finance, optimization a forecast model, forest management and all.

The strong interest for MOEA in so many different disciplines reinforces the idea that there will be new possibilities for solving still more real-life problems.

VI. CONCLUSIONS

After the attempt for a short survey it could be noted, that

the scientific research in the area considered are directed towards different aspects, but one of the major aspects is the efficiency, which is regarded at algorithmic level and at data structure level [2], [17], [20]. A variety of measures for implementation quality is suggested. It allow a quantitative (rather than only qualitative), comparison of results [30], [8], [32]. Zitzler et al. [30] stated that, when assessing performance of an MOEA, one was interested in measuring three things:

- Maximize the number of elements of the Pareto optimal set found.

- Minimize the distance of the Pareto front produced by our algorithm with respect to the global Pareto front (assuming we know its location).

- Maximize the spread of solutions found, so that we can have a distribution of vectors as smooth and uniform as possible.

- Concurrently with the research on performance measures, other researchers were designing test functions.

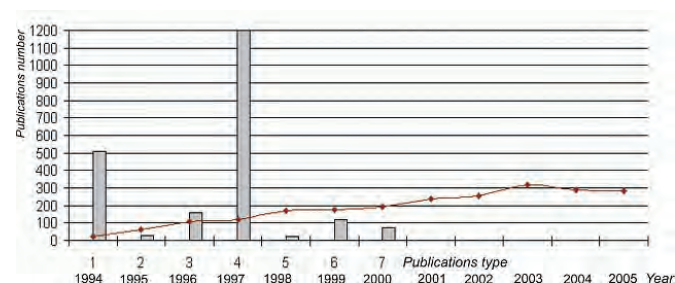


Fig.1 Distribution of the publications

For the enhancing development of the scientific investigations in thus direction (MOEA) the basic proof is the continuously increasing number of references and applications in the last ten years. In a paper of his Coello [3] represents approximate graphics of the publications according their type. Fig.1 represents the distribution of the publications, depending on the issue – 1-journal papers, 2 - books, 3- book chapters, 4- conference papers, 5- master's theses, 6- Ph.D. theses, 7 - technical reports and the distribution of the publications in years.

REFERENCES

- [1] C. A. Coello Coello and G. B. Lamont, "Applications of Objective Evolutionary Algorithms", Vol. 1, World Scientific, 2004, 761 pp. Hardcover, ISBN: 981-256-106-4.
- [2] C. A. Coell Coello, "Evolutionary Multi-Objective Optimization: A Historical View of the Field", IEEE Computational Intelligence Magazine, pp. 28-36, February 2006.
- [3] C.A. Coello Coello and N. Cruz Cortes, "Solving multiobjective optimization problems using an artificial immune system," Genetic Programming ,and Evolvable Machines. vol. 2, pp. 163-190, June 2005
- [4] K. Deb, A. Pratap, S. Agarwal, and T. Meyarivan, "A fast and elitist multiobjective genetic algorithm: NSGA-II," IEEE Transactions on Evolutionary Computation, vol. 6, no. 2, pp. 182-197. Apr. 2002.
- [5] N.H. Eklud and M.J. Embrechts, "GA-based multi-objective optimization of visible spectra for lamp design," In Cihan H.

- Dagli et al., editor. Smart Engineering System Design: Neural Networks, Fuzzy Logic, Evolutionary Programming, Data Mining and Complex Systems, pp. 451-456, New York, ASME Press, Nov. 1999.
- [6] V. V. Emelianov, V. M. Kureichik, V. V. Kureichik, "Theory and Practice of Evolutionary Modelling", Moscow, 2003. (in Russian)
- [7] C.M. Fonseca and P.J. Fleming. "Genetic algorithms for multiobjective Optimization: Formulation, discussion and generalization," in Stephanie Forrest, editor, Proceedings of the Fifth International Conference on Genetic Algorithms, pp. 416-423, San Mateo, California, University of Illinois at Urbana-Champaign, Morgan Kaufman Publishers, 1993.
- [8] C.M. Fonseca and P.J. Fleming, ".On the performance assessment and comparison of stochastic multiobjective optimizers," In Hans-Michael Voigt et al., editor. Parallel Problem Solving from Nature—PPSN IV, Lecture Notes in Computer Science, pp. 584- 593, Berlin, Germany, Springer Verlag, Sep. 1996.
- [9] L Gacogne. "Research of pareto set by genetic algorithm, application to multi criteria optimization of liizzy controller." In 5th Eurocaii Congress on intelligent Techniques and Soft Computing EUFIT'97, pp. 837-845, Aachen, Germany, Sep. 1997.
- [10] D.E. Goldberg, Genetic Algorithms in Search, Optimization and Machine Learning. Addison-Wesley Publishing Company, Reading, Massachusetts, 1989.
- [11] D. Goldberg, "Web Courses", <http://www.engr.uiuc.edu/OCCE>, 2000.
- [12] D. Greiner, G. Winter, J.M. Emperador, and B. Galvan, "Gray coding in evolutionary multicriteria optimization; Application in frame structural optimum design," In Carlos A. Coello Coello et al., editor. Evolutionary Multi-Criterion Optimization. Third international Conference, EMO 2005, pp. 576-591, Guanajuato, Mexico, Springer. Lecture Notes in Computer Science vol. 3410, Mar. 2005.
- [13] V. Guliashki, (2002) "Parallel Genetic Algorithm PGAmold, solving integer optimization problems", Proceedings of the International Scientific Conference on "Basic Technologies for E-Business'2002", September, 15-18, 2002, Albena, Bulgaria, pp. 272-277.
- [14] V. Guliashki, Burdick B., Mathis W., (2004) "Optimization of Test Signals for Analog Circuits", *Electronics*, ISSN 1450-5843, Vol. 8, № 1, May 2004, pp. 10-13.
- [15] T. Hanne and S. Nickel, "A multiobjective evolutionary algorithm for scheduling and inspection planning in software development projects." *European journal of Operational Research*, vol. 167, no. 3, pp. 663-678, Dec. 2005.
- [16] J. Horn, N. Nafpliotis, and al. f. Goldberg, "A niched pareto genetic algorithm for multiobjective optimization," In Proceedings of the First IEEE Conference on Evolutionary Computation, IEEE World Congress on Computational Intelligence, vol. I, pp. 82-87, Piscataway, New Jersey, IEEE Service Center, June 1994.
- [17] R.M. Hubley, E. Zitzler, and J.C. Roach, "Evolutionary algorithms for the selection of single nucleotide polymorphisms," *UMC Iliotfo: mattes*, vol. 4, no. 30, July 2003.
- [18] [26] M.T. Jensen, "Reducing the run-time complexity of multiobjective EAs: The NSGA-II and other algorithms," *IEEE Transactions on Evolutionary Computation*, vol. 7. no. 5. pp. 503-515. Oct. 2003.
- [19] T. Kipouros, D. Jaeggi. B. Danes, G. Parks, and M. Savill, "Multi-objective optimization of turbomachinery blades using tabu search." In Carlos A. Coello Coello et al., editor, Evolutionary Multi-Criterion Optimization. Third International Conference, EMO 2005. pp. 897-910. Guanajuato, Mexico. Springer. Lecture Notes in Computer Science Vol. 3410, Mar. 2005.
- [20] J. Knowles and E.J. Hughes, "Multiobjective optimization on a budget of 250 evaluations," In Carlos A. Coello Coello et al, editor. Evolutionary Multi-Criterion Optimization. Third International Conference. EMO 2005. pp. 176-190, Guanajuato, Mexico, Springer. Lecture Notes in Computer Science Vol. 3410. Mar. 2005.
- [21] J.D. Knowles and D.W. Corne, "Approximating the nondominated front using the pareto archived evolution strategy," *Evolutionary Computation*, vol. 8. no. 2. pp. 149-172, 2000.
- [22] M. Lahanas, "Application of multiobjective evolutionary optimization algorithms in medicine," In Carlos A. Coello Coello and Gary B. Lnmont, editors, Applications of Multi-Objective Evolutionary Algorithms, pp. 365-391. World Scientific. Singapore, 2004.
- [23] S. Manos, L. Poladian. P. Bentley, and M. Large, "Photonic device design using multiobjective evolutionary algorithms," In Carlos A. Coello Coello et al., editor. Evolutionary Multi-Criterion Optimization. Third International Conference, EMO 2005, pp. 636-650. Guanajuato. Mexico. Springer. Lecture Notes in Computer Science Vol. 3410. Mar. 2005.
- [24] A. Molina-Cristobal, LA. Griffin, P.J. Fleming, and D.H. Owens, "Multiobjective controller design: Optimising controller structure with genetic algorithms," In Proceedings of the 2005 IFAC World Congress on Automatic Control, Prague, Czech Republic, July 2005.
- [25] M. Nicolini, "A two-level evolutionary approach to multi-criterion optimization of water supply systems," In Carlos A. Coello Coello et al, editor, Evolutionary Multi-Criterion Optimization. Third International Conference, EMO 2005, pp. 736-751, Guanajuato, Mexico, Springer, Lecture Notes in Computer Science Vol. 3410, Mar. 2005.
- [26] R.S. Rosenberg. "Simulation of genetic populations with biochemical properties," Ph.D. thesis. University of Michigan, Ann Harbor, Michigan, 1967.
- [27] J. David Schaffer, "Multiple objective optimization with vector evaluated genetic algorithms." In Genetic Algorithms and their Applications: Proceedings of the First International Conference on Genetic Algorithms, pp. 93-100, Lawrence Erlbaum. 1985.
- [28] F. Schlottmann and D. Seese. "Financial applications of multi-objective evolutionary algorithms: Recent developments and future research directions." In Carlos A. Coello Coello and Gary B. Lamont, editors. Applications of Multi-Objective Evolutionary Algorithms, pp. 627-652. World Scientific, Singapore. 2004
- [29] N. Srinivas and K. Deb, "Multiobjective optimization using nondominated sorting in genetic algorithms." *Evolutionary Computation*, vol. 2, no. 3, pp. 221-248. Fall 1994
- [30] E. Zitzler. K. Deb, and L. Thiele. "Comparison of multiobjective evolutionary algorithms: Empirical results," *Evolutionary Computation*, vol. 8. no. 2, pp. 173-195. Summer 2000.
- [31] E. Zitzler, M. Laumanns, and L. Thiele, "SPEA2; Improving the strength pareto evolutionary algorithm." In K. Giannakoglou et al., editor. EUROGEN 2001. Evolutionary Methods for Design, Optimization and Control with Applications to Industrial Problems, pp. 95-100. Athens, Greece. 2002
- [32] E. Zitzler and L. Thiele, "Multiobjective evolutionary algorithms: A comparative case study and the strength pareto approach," *IEEE Transactions on Evolutionary Computation*, vol. 3. no. 4, pp. 257-271, Nov, 1999.

Applying Tabu - Search Heuristic for Software Clustering Problem

Violeta T. Bozhikova¹ and Mariana Ts. Stoeva²

Abstract – In the paper we present a Tabu-search software clustering algorithm. Unlike many other software clustering techniques, discussed in the literature, our approach evaluates the quality of a graph partition that represents a software clustering solution, considers the importance (weight) of cluster's components and satisfies a specific restrictive condition. We discuss the Tabu-Search features of our clustering algorithm. Next we present the full application of our algorithm over an open source object-oriented Java program. Finally we try to evaluate objectively our results, comparing them to those, produced by the algorithm of Spiros Xanthos [1].

Keywords – software reengineering, software-clustering algorithms, software representation.

I. INTRODUCTION

The software reengineering literature shows [1, 4-9] that the problem of clustering software structure is NP hard, so a hope for finding a general solution to this problem software is unlikely. Software clustering is used for decomposing the structure of software systems into cluster (subsystems), while satisfying a number of problem-specific constraints. Subsystems provide developers with structural information about the systems: their components, their interfaces, and their interconnections. Subsystems facilitate program understanding during the software maintenance by treating sets of source code resources as software abstractions. Software clustering is a very important approach when trying to decompose large and complex legacy systems into small parts in order to repair or to improve their structures. It is used also as a way to transfer software to new software or hardware platform.

A lot of heuristic approaches [1, 4-9] have been developed in order to effectively resolve this problem. In the paper we discuss our Tabu-Search algorithm that is an attempt to navigate through the search space of all possible graph partitions more effectively. Unlike many other software clustering techniques, our approach evaluates the quality of a graph partition that represents the software structure, considers the importance (weight) of cluster's components and satisfies a specific restrictive condition. Our clustering algorithm creates clusters by heuristically minimizing the value of a goal function, than maximizing the quality the

solution.

In the paper we present and discuss the application of our algorithm over an open source object-oriented Java program. We compare our clustering results to those, produced with the Spectral-Graph Partitioning algorithm, developed by Spiros Xanthos [1].

II. TABU-SEARCH TECHNIQUE

Tabu-Search is used for solving optimization problems. This is a heuristic procedure which tries to avoid falling into local optima by creating a special list of forbidden moves, called "tabu" list [3]. The work by Glover and Laguna 1997, gives a comprehensive description of the Tabu-Search technique [2].

In general, the criteria for classifying aspiring and forbidden moves are specific to the application. For example a move may be regarded as "tabu" simply because it was recent. Move may be also "tabu" is it could lead to a solution that is already been considered or has been repeated many times before [4]. On occasions, if we conceder a "tabu" move might lead to the best solution, that move might be allowed. Tabu-Search starts usually at a possible random point. The search space, or neighborhood, comprises a set of moves that lead to another solution when applied to the current one.

The general Tabu-Search algorithm can be summarized [4] as following:

1. Generate an initial random partition r_c
2. Loop
 - Define the neighborhood set of the current solution;
 - Identify the Tabu set (define a forbidden move);
 - Define an aspiring move;
 - Choose the best Move (Find the best neighbor r)
if r is found then $r_c = r$
- End Loop
(Exit when goal is satisfied or the stopping condition is reached)
3. r_c is the sub-optimal solution

III. OUR TABU-SEARCH APPROACH

Let describe how the key ingredients of the Tabu-search technique are realized in our algorithm:

- Define the initial solution;

It is important to have an easy and quick way of generating an initial solution. To get the best solution in a Tabu-Search implementation we simply use as initial solution the initial

¹Violeta T. Bozhikova is with the Department of Computer Science Varna Technical University, Bulgaria, E-mail: vbozhikova2000@yahoo.com

²Mariana Ts. Stoeva is with the Department of Computer Science Varna Technical University, Bulgaria, E-mail: mariana.stoeva@abv.bg

solution of our early created and experimentally evaluated heuristic clustering algorithms [8,9].

- Define a forbidden move.

For us, any solution which has been already selected is put into a “tabu” list so that it becomes ‘taboo’ (forbidden). This minimizes the chance of cycling in the same solution, and therefore creates more chances of improvement by moving into un-explored areas of the search space.

The space of all possible solutions is searched in a sequence of moves from one possible solution to the best available alternative taking in consideration the forbidden solutions saved in the “tabu” list.

- Define the neighborhood set of the current solution;

We define a partition r to be a neighbor of a partition r_c if the two partitions have at least one different element. Three types of operations are applied consecutively in order to find the best neighbor of a current partition (that minimize the goal function, satisfying a specific restrictive condition W_0). The result of the first operation is: merger of 2 clusters. The second operation is move. There are two types of moves: node move and block move. The third operation is swap of two nodes.

- Define an aspiring move;

The next move is best neighboring solution which is not in “tabu” list.

The goal of our software clustering process is to automatically partition the components of a system into clusters (subsystems) so that the resultant organization concurrently minimizes inter-connectivity (i.e., connections between the components of two distinct clusters) while maximizing intra-connectivity (i.e., connections between the components of the same cluster). We accomplish this task by treating clustering as an optimization problem where our goal is to minimize the goal function k (2) based on the relation between the inter-connectivity and intra-connectivity.

The six steps of our Tabu-Search algorithm are described below. We have to underline that we have developed this algorithm in order to improve the effectiveness (decreasing the number of the iterations in the iterative part) of our early developed clustering algorithm [8], than decreasing it's its computational complexity.

So, the general steps of our Tabu-Search clustering algorithm are:

1. Graph Structure Entry: $G = (X, U)$
2. Graph Structure Verification
3. Execute a sequential graph partition algorithm that creates the initial graph partition (Initial Solution - r_{apr}). Push r_{apr} into Tabu list. k_{apr} is the goal function of the graph partition r_{apr} .
4. Let $r_c = r_{apr}$, $k_c = k_{apr}$.
5. Get a set of solutions in neighborhood of r_{apr} executing a Tabu-search algorithm:
Repeat
Change=false;
Find the best neighboring partition r of a current partition r_c :
 - Execute Operation “Merge” (for clusters);
 - Execute Operation “Move” (for nodes, for clusters);

- Execute Operation “Swap” (for nodes).

If r is found (if $\exists r, k_r < k_c$) and r is not into Tabu list then

$r_c = r$;

Push r_c into Tabu list.

Change=True;

End if

Until not (Change);

6. Find r_c - the sub-optimal solution (k_c is value of the goal function).

Example

We have used for our experiments the graph representation of an open-source object oriented Java program. This graph representation is presented in [1]. We have used our described above clustering algorithm to partition the produced by Xanthos weighed graph that models just commented object oriented Java program.

In the paper we show the results of clustering this weighed graph using our Tabu-Search algorithm and compare our solution (figure 2) with the solution (figure 3) created with the spectral clustering algorithm of Xanthos [1].

Figure 1 show how the Java program is presented as a directed weighed graph $G = (X, U)$ by our clustering tool. The source code components (classes) of the Java program are modeled as set of N nodes X , and the source code dependencies (inherit, call, instantiated) are modeled as the set of graph's edges U .

In figure 2 is presented the sub-optimal clustering solution produced by applying our Tabu-Search algorithm.

Figure 3 shows the solution produced by the spectral clustering algorithm of Xanthos [1].

A goal function k (2) is used to evaluate the quality of each partition. “ k ” increases as the inter-edges (i.e., external edges that cross cluster boundaries) increase. In the case, “ k ” is designed so that a solution with a lower objective function value has a high quality and represents a better solution to the problem. Let x_i denote the node with index i and weight of w_i . Let M is the number of clusters in the current partition of G . A partition is clustering solution. It is a decomposition of the set of elements (i.e., all the nodes of the graph) into mutually disjoint clusters. The weight W_i (1) of each cluster “ i ” is the sum of the weights of all it's nodes. W_i must be less then W_0 , where W_0 is a user defined restrictive condition.

$$W_i \leq W_0 \quad (1)$$

The value of the objective function “ k ”, where k_{ij} is the number of inter-edges (i.e., external edges that cross cluster boundaries) between cluster “ i ” and cluster “ j ” is calculated as following (2) and must be minimal:

$$k = \frac{1}{2} \sum_{i=1}^M \sum_{j=1}^M k_{ij}, \quad \forall i \neq j \quad (2)$$

We can see and compare the results (figure 2) of the execution of our algorithm with this (figure 3) produced by the spectral clustering algorithm of Xanthos [1]. We realize

that our algorithm shows the same result (in quality of the decomposition solution – “k”).

Now that a lot of software clustering approaches exists, the validation of clustering results interests the Reverse Engineering research community. Similarity measurements enable the results of clustering algorithms to be compared to each other, and preferably to be compared to an agreed upon “benchmark” standard. We have to underline that the “benchmark” standard needn’t be the optimal solution in a theoretical sense. Rather, it is a solution that is perceived as being “good enough”. Using Precision/Recall similarity technique we have considered that the similarity between our solution (fig. 4) and the solution of Xanthos (fig. 3) is very good (>70%).

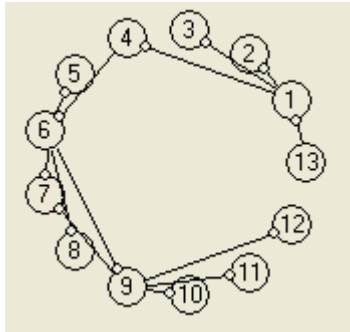


Fig. 1. The object oriented Java program, modeled as a graph $G=(X,U)$

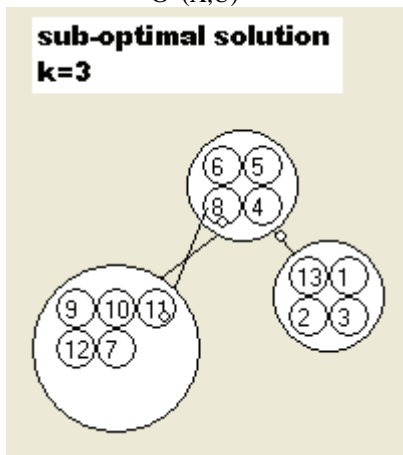


Fig. 2. The sub-optimal clustering solution produced by applying our Tabu-Search algorithm

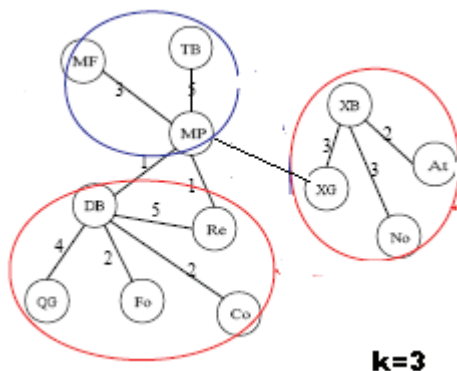


Fig. 3: The solution created by the spectral clustering algorithm of Spiros Xanthos [1].

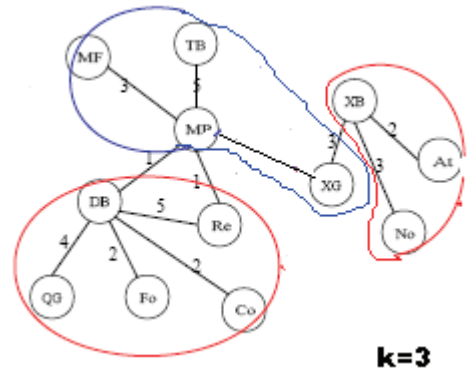


Fig. 4: Our sub-optimal clustering solution presented, using the presentation style of [1]

IV. CONCLUSION

Decomposing source code components and relations into subsystem clusters is an active area of research. Clustering methods and tools help software engineers understand and effectively maintain large and complex software systems is an active research area. Numerous clustering approaches have been proposed in the reverse engineering literature, each one using a different algorithm to identify subsystems than producing an architectural view [1,4-9].

The innovation of this paper is the use of Tabu Graph Partitioning Technique in the object oriented domain and the application of this technique for decomposing an object oriented system into smaller module, some of which might be used as reusable components.

The presented approach can be seen as a further improvement of our early developed heuristic software clustering algorithms [8,9]. Improving software clustering algorithms is one of the most important topics in the software clustering area. Our paper is about improving existing software clustering algorithms by applying new heuristics (in the case Tabu-Search) that take into consideration a restrictive condition and the weigh of nodes. We have observed that the most clustering tools don’t take into consideration some restrictive conditions. We find also that the existing clustering tools are not able to process graphs with weighted arcs or nodes because of the computational complexity of the clustering problem.

Our observation is that there is not enough experience in the field of clustering object-oriented software. That is because the existing clustering tools are not able to process large graphs. The problem is that even medium object-oriented programs produce such graphs because of polymorphism. In the paper we discuss the application of our Tabu-Search algorithm for clustering a small open source object oriented program. We have considered that the presented algorithm shows good results (in quality of the solution “k” and similarity between the produced partitions) for clustering this program. At the same time we must underline that extended research that confirms the correctness of this method for clustering object oriented software is needed. The problem is the lack of standard set of object-

oriented programs that can be used by the researchers in this field, to test and compare their algorithms. Our hope is to continue working in this field.

The results produced by the algorithm can have multiple uses:

- The modules that are found can be used as the starting point for the reverse engineering process of a software system.
- Each cluster can be viewed as a reusable component.
- The solution produced by our tool is in this case highly cohesive. Our algorithm minimizes the communication between the modules of the system, satisfying a restrictive condition (1) that guaranties the mutual equality of the weight of the clusters. Therefore, it can also be used to identify the modules that should be assigned in different machines, in a distributed environment.

REFERENCES

- [1] Spiros Xanthos "Clustering Object-Oriented Software Systems using Spectral Graph Partitioning"
- [2] Glover, F. (1990), Tabu-Search: A tutorial, *Interfaces* 20 (4), pp 74-94.
- [3] Reeves C. (1993), *Modern Heuristic Techniques for Combinatorial Problems*, Blackwell Scientific Publications, Oxford
- [4] Reformulating Software Engineering as a Search Problem, J. Clark, J. J. Dolado, M. Harman, R. Hierons, B. Jones, M. Lumkin, B. S. Mitchell, S. Mancoridis, K. Rees, M. Roper, M. Shepperd", In the Journal of IEE Proceedings - Software , 150(3): 161-175, 2003
- [5] Mitchell, Mancoridis, Traverso, " Search Based Reverse Engineering", In the ACM Proceedings of the 2002 International Conference on Software Engineering and Knowledge Engineering (SEKE'02), Ischia, Italy, July, 2002. pp. 431-438
- [6] Spiros Mancoridis, Brian Mitchell, C. Rorres, Y. Chen, and E. R. Gansner, Using Automatic Clustering to Produce High-Level System Organizations of Source Code, IEEE Proceedings of the 1998 International Workshop on Program Understanding (IWPC'98)
- [7] Derek Rayside, Steve Reuss, Erik Hedges, and Kostas Kontogiannis. The effect of call graph construction algorithms for object-oriented programs on automatic clustering. In Margaret-Anne Storey, Anneliese von Mayrhauser, and Harald Gall, editors, IWPC'00, pages 191–200, Limerick, Ireland, June 2000.
- [8] V. Bojikova, "Using decomposition to produce high-level system organization of software source code", ICEST'2003 Proceedings of papers, pp. 329-332, София, 15-17.10. 2003.
- [9] V. Bojikova, M. Karova "Using Genetic Algorithms to Solve Software Clustering problem", XXXIX Int'l Scientific Conference on Information, Communication and Energy Systems and Technologies, Proceedings of Papers - Vol.2, 16-19 June, 2004, Bitola, Macedonia, p. 763--765.

A New Approach to Symbol Description of the Spatial Location of Extended Objects in Spatial Databases

Mariana Stoeva¹ and Violeta Bozhikova²

Abstract – This paper presents our work in the area of image retrieval in Image Databases for images saved by spatial similarity of extended objects location. We propose a new approach to description of the spatial location of extended objects. The approach is based on a geometric approximation. By the development of the proposed approach we enrich our former efforts for creation of effective method for image storage and retrieval from SDB.

Keywords – Image databases, spatial databases, symbol description of spatial features, spatial query processing algorithms

I. INTRODUCTION

The aim of this paper is to achieve a new response to the raised requirements of different applications to Spatial Databases (SDB), namely attainment of invariance of query processing results with respect to arbitrary compositions of transformations. Our attention is directed to the object description methods by the spatial location of the extended objects contained in it. The image description in SDB is in conformity with the next image retrieval from it by spatial query.

In real-world database applications, the rotation invariance is a basic issue because each image is captured and stored in agreement with a viewpoint which is implicitly dependent on an outside viewer who establishes a fixed scanning direction. Any translation of this viewpoint and/or any rotation of the image affects the direction relations between each pair of objects. In the recent literature, several approaches can be found whose aim is to provide a solution to the rotation invariance of the conventional indexing methodologies based of symbolic projections [3], [4]. In [7], [8] and [5] are presented approaches for speeding-up the time responses in databases which uses Spatial Access Methods (SAMs) to treat image content in conjunction with two well known image matching methods, namely the editing distance on Attributed Relational Graphs (ARGs) and the Hungarian method for graph matching. It provides index support for the two most common types of similarity queries, referred to as range and nearest neighbor queries and has many desirable properties.

However, in real application, it would also to be able to find the images in the database that present a given pattern, even if it appears mirror reflected. In [6] is present an iconic indexing methodology which guarantees the rotation and reflection invariance of the image visual content, where it is described by direction relationships, which are view-based. This methodology does not recognize the similarity between two images when their corresponding symbolic descriptions (R-virtual images) have been extracted with respect to different rotation centers. In [9] we have proposed a geometric based structure which makes possible the extraction of spatial relations among domain objects that are invariant with respect to transformation such as translation, rotation, scaling, and now we are going to propose its further development.

By the proposed approach to spatial information description in an image we aim to achieve an effective storage of the image description information, effective query to SDB processing, and efficient invariant with respect of transformations image retrieval from SDB by spatial similarity. The difficulties that appear when creating an approach that satisfactory implements all defined requirements motivates the hard work on the task for image storage and retrieval from SDB by similarity of the spatial location of their extended objects.

By the development of the proposed approach for image spatial properties description we enrich our former efforts for creation of effective method for image storage and retrieval from SDB through “query by image example” that gives an account of the spatial location of image domain objects and is invariant with respect of transformation compositions. This method has to include the following basic components:

- An approach for determining the spatial attribute content that describes image spatial properties and the structure of its storage in SDB. It includes the well-grounded definition approximation named Minimum Area Rectangle (MAR). It is used to form the description of the spatial properties of domain objects;
- An approach for invariant determining of spatial relations built by the definition of the approximation Minimum object boundary Ring Sector (MRS), by the definition of spatial relations between objects, and by the definition of similarity between spatial relations;

Development of a mechanism for effective evaluation and processing of similarity spatial queries that recognize transformed images and sub-images, including definition of similarity distance, as well as an algorithm for its realization. The solution of the task for image storage and retrieval from SDB by spatial similarity lies on the following basic sub-solutions: consistency of original approximations of image

¹Mariana Stoeva is with the Department of Computer Science and Technologies, Varna Technical University, Bulgaria, E-mail: mariana_stoeva@abv.bg

²Violeta Bozhikova is with the Department of Computer Science and Technologies, Varna Technical University, Bulgaria, E-mail: vbozhikova2000@yahoo.com

objects area; determination of the spatial relations among domain objects, that are invariant with respect to transformations in images; determination of the similarity between spatial relations; determination of the measure of spatial similarity between two objects; spatial similarity algorithm whose results are determining for the spatial query processing. The solution uses two geometric of the extended objects by MRS, determined by concentrate circles. This second approximation is used for the determination of spatial relations between objects in a linear direction and in a specifically used circle direction.

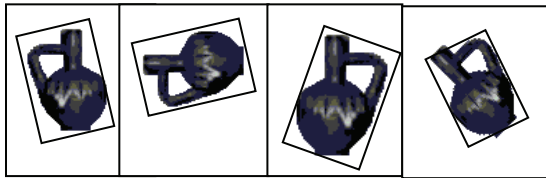


Fig. 1. Examples for determination of MAR of an object for its different transformation variants.

Invariance with respect to transformations in determining the atomic relations between two objects is provided by use of the circle direction properties, object centroid, (center of object weight) and image centroid. The paper is organized as follows: In Section 2 we propose the new approximation MAR and also an algorithm presented as MAR_{object} . In Section 3 we present the description used by us. In Section 4, for the purpose of similarity, we introduce descriptions of spatial relations, of spatial relation similarities, as well as similarity measure between two images. We publish a part of the experiments made and their results in Section 5. In Section 6 some conclusions are shown and further work aims are planned.

II. APPROXIMATION OF THE EXTENDED IMAGE OBJECT AREA

The requirement for storage and spatial investigation efficiency imposes the condition for minimal dimension of the shape description of extended image object area. The objects are two-dimensional areas and the search for their minimal description is as a description of their approximation with suitable for a following processing rectangle form. The requirements for invariance with respect to transformation impose the perceived approximation to be close to the object area, as well as to be simply determined with respect to transformations. This means that an object is approximated with rectangle, whose sides concur with the same points of its approximations of the image objects area. The first one defines the information that is stored as a symbol description for each image object and the second one gives ability for the spatial relations between image objects to be determined in such a way, that they stay invariant with respect to the transformations translation, rotation, scaling, reflection (symmetry), view point change, as well as arbitrary compositions of these transformations.

The basic idea of this method creation is that each image and its significant for the application objects will receive stored in SDB symbol description that includes symbol names of the

objects, as well as the coordinates of 5 typical for their area shape points. The determination of the typical for the object area points from the external contour is invariant with respect to different transformations. This stored for each object information enables the use of next shape approximation external contour, independently from the transformation the image in which it is located suffers.

Definition 1. From all rectangles that include the area of an image object MAR is the one whose area is minimal. If there are more than one such rectangles with minimal area, for approximating MAR is accepted this one, whose sides form smallest angle with the axis of area direction.

This definition insures that for the approximating MAR determination are taken the coordinates of the same points of the area external contour independently from the possible transformations. The points of the contour of the such determined approximating MAR of an object from an image keep their relative location towards its area centroid. Examples for approximation of an object that appears in different transformation variants of an image are illustrated at Fig.1. The such perceived approximation with MAR that encloses the object has minimal area and with removing the requirement: "its sides to be parallel to the corresponding coordinate axes" and adding another one: "the area of MAR to be minimal" several effects are achieved. MAR avoids the popular in the literature "diagonal imprecation" in two-dimensional area approximation by Minimal Boundary Rectangle (MBR). MAR is calculated by using object rotation around of its centroid. The MAR is computed by an ordinary algorithm. This algorithm has linear **time complexity** $O(n)$. The angle points of MAR determine 4 typical for the object shape, dimension and location points. The spatial data for each object include the absolute Decart coordinates of these 4 characterizing the object points (angle points of MAR) and of the object centroid, obtained from the points of its external contour.

III. IMAGE CONTENT DESCRIPTION

By image symbol description we avoid the need of their repeated understanding. The memory that is necessary for the storage of the performed symbol image is insignificant in comparison with its physical performance. The query processing for image retrieval from SDB uses only stored information for the image. The stored in SDB information for the domain objects of each image contains as attributes symbol object names and 5 pairs of Decart coordinates that describe the spatial data of the object. The first one is the pair of object centroid coordinates obtained from the coordinates of its area external contour. The next 4 are the coordinate pairs of the angle points of the approximating the object area MAR. The storage of absolute location of each object's centroid is indispensable due to the fact that the relative spatial location of the stored information for each object's area is preserved towards it. The image centroid towards which the image objects preserve their relative spatial location can be obtained from the stored centroids of an objects set from an image. An example of an image with 3 objects that

illustrates the way the spatial properties of an image are symbolically described, is performed at Fig. 2.

Object	centroid	Absolute coordinates
	(x ₀ ,y ₀)	(x,y) Objects MAR
Flower	(42, 80)	(39, 64) (25, 87) (42, 97) (56, 74)
Chair	(158, 134)	(142, 112) (142, 152) (174, 152) (174,112)
Table	(98, 114)	(68, 100) (68, 130) (128, 130) (128, 100)

Fig.2. An Example of Image Symbol Description

We accept that the domain objects describing symbol information is stored and arranged in alphabetic order of objects names. We accept that domain objects are named consistently through all images in DB and the images contain numerous examples of object type. The chosen SDB model is object-relational and results in a general structure with general type of relational diagrams of two relations: “Images” and “Image objects”.

The stored symbol information of an image occupies space O(N) that is linear towards N, where N is the number of objects in it, in difference with other similar methods that use quadratic space O(N²) [6]

IV. SPATIAL SIMILARITY IMAGE RETRIEVAL IN IMAGE DATABASE

A. Spatial Relations between Image Objects

This information that is saved for each object, allows us to use MRS determined by concentric circles for approximating the objects’ shape extent [9]. MRS of an object is obtained by the cross of concentric circles with center – the image centroid point, with passing through it strait lines. MRS minimally encloses the object area describing MAR and is determined by the minimums and maximums of its polar coordinates.

The spatial relations between each pair domain objects are determined in sense of conditions over the initial and final points of their MRS in two directions of a polar coordinate system [9]. By using this representation we analogically to the orthogonal models [1], [4] determine the well-known 13 relations in one linear direction and one specifically used circle direction.

We use a triple like (O_j γ O_i) that is called an atomic spatial relation, where O_j, O_i ∈ O_I are object names and γ ∈ {<, >, |, :, =, [, (,), /, \, %, #} is an operator. We use the notation (O_j γ_R O_i) to indicate that the pair of objects (O_j, O_i) belongs to relation γ in R-direction and (O_j γ_θ O_i) to indicate that the pair of objects (O_j, O_i) belongs to relation γ in θ-direction. The defining of binary spatial relations is identical to those in [1] adapted to a polar system and it is presented in [9]. Applied for both directions here arise generally 169 spatial relations between two objects in two dimensions, by which the spatial content can be suitably presented. We provide the

transformation invariance of determination the atomic relations between two objects by utilizing the properties of the object and image centroids

B. Spatial Similarity Image Retrieval

Similarity distance is defined on the number of objects from the query, the common for both images objects, as well as on the similarity of their corresponding atomic relations and equations. Its values are in the diapason [0,1], where 1 is valid for image that completely satisfies the query and the value is 0 if they have no common objects.

According to our understanding for similarity and our desire the method to be independent of subjective interpretation, we put forward a formula for similarity evaluation that assesses the similarity between the common for both images objects and their corresponding atomic relations.

Definition 2. Let the query image is Q and the Image Database image is I. We define the similarity distance $sim(Q,I)$ between Q and I by Eq.1 and $sim(Q,I) \in [0,1]$,

$$sim(Q,I) = \frac{1}{m} \left[C_o n + C_s \frac{1}{2n} \sum_j \sum_i (sim_{ji}(\gamma_R, \gamma_R') + \max \left\{ \begin{matrix} sim_{ji}(\gamma_\theta, \gamma_\theta') \\ sim_{ji}(\gamma_\theta^o, \gamma_\theta^o') \end{matrix} \right\}) \right] \text{ for } \forall n \neq 0 \quad (1)$$

$$sim(Q,I) = 0 \text{ for } \forall n = 0$$

where: $m = \|O_Q\|$ is the number of objects in the query image, $n = \|O_Q \cap O_I\|$ is the number of the common for both images objects,

$sim_{ji}(\gamma_R, \gamma_R')$ is the spatial similarity between the images Q and I for the object match (O_j, O_i) in R-direction, and

$sim_{ji}(\gamma_\theta, \gamma_\theta')$ is the spatial similarity between the images Q and I for the object match (O_j, O_i) in θ-direction.

$sim_{ji}(\gamma_\theta^o, \gamma_\theta^o')$ is similarity between the spatial relations of image I and reflection image of the query Q for the object match (O_j, O_i) in θ-direction;

and C_o, C_s are coefficients (C_o+C_s=1).

This definition is different of corresponding similarity distance from [9] by the including of the similarity between the spatial relations of image I and reflection image of the query Q in θ-direction ($sim_{ji}(\gamma_\theta^o, \gamma_\theta^o')$) and the coefficients (C_o, C_s). The processing of the image query to SDB includes a filter that detaches as candidates only those images from SDB that include objects from the query. The images – candidates are evaluated by spatial similarity for their proximity to the query by similarity algorithm SIM_{Rθ}. It is invariant with respect to transformations of a query image and transformation variants of its sub-images. The algorithm for image matching has **time complexity O(N+Mn2)**, where N is number of tuples in relation “Image Objects”, M (M << N) is the number of results of filter step, n - the number of objects that are common for both the query and databases images.

V. EXPERIMENTS

Experiments that investigate the efficiency of the method in 5 different aspects are executed. A collection of images in which terminal number of named objects is spatially situated

is created as insert data. The symbol descriptions of the spatial properties of each image are extracted. Each experiment consists in execution of the spatial similarity algorithm for each pair of images from the test group. The similarity distance between each image pair from the test group is evaluated. The experiments evaluate the method stability with respect to transformations, make comparison with other methods: - θR -stribg [2] and virtual image [6] by quantity evaluation of spatial similarity retrieval from SDB. They evaluate also the adaptability of the spatial similarity

algorithm and the way the similarity distance detects smaller and bigger spatial differences between images. The effectiveness and the efficiency of spatial similarity retrieval algorithm are evaluated by using an expert-provided rank ordering of a test collection with respect to a set of test queries using the R_{norm} measure from [2]. This measure evaluate similarity order using one expert similarity arrangement. The results are compared with related to the subject published results.

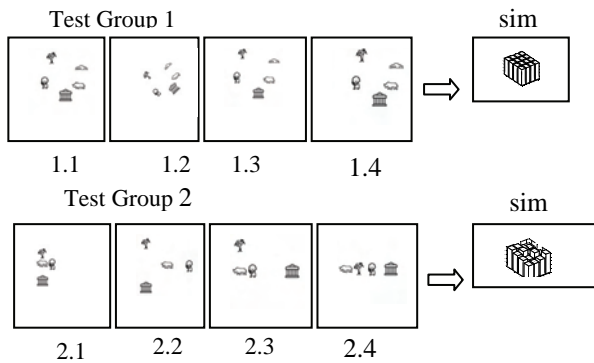


Fig. 3. Test images and spatial similarity measure (*sim*) on pairs of images of Group 1 and Group 2

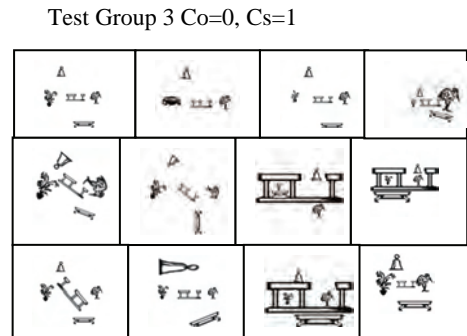


Fig. 4. Methods of Gudivada give images from Group 3 like spatially identical. Our approach gives measure $sim \in [0.6, 1]$ for the same images, that improves its sensitivity.

VI. CONCLUSION

The image spatial properties describing approach, proposed in this paper, implemented in a method for storage and retrieval of images from SDB by spatial similarity of their domain objects achieves stability with respect to arbitrary compositions of transformations, shows completeness, correctness and sensitivity of the results. The method achieves very good effectiveness of information storage in SDB and good efficiency of query processing. The experiments investigate it in details by use of various evaluations of the results and their comparison with other methods' results. The main contributions are:

- Utilization of new approximations MAR for extended objects shape representation in order to provide invariance with respect to transformations of spatial relationships extraction from the image.
- Representations of an algorithm for computing a new approximation MAR.

Definition of a similarity measure between two images with its components, that is invariant of the transformations: translation, scaling, rotation and reflection.

REFERENCES

- [1] J. F. Allen, "Maintaining Knowledge about temporal Intervals", *Comm. ACM*, vol. 26 pp.832-843, 1983
- [2] V. Gudivada, , V. Raghavan, "Design and Evaluation of Algorithms for Image Retrieval by Spatial Similarity", *ACM Trans. Information Systems*, vol. 13(1) pp. 115-144, 1995
- [3] F. Gudivada - θR -stribg: A geometry-based representation for efficient and Effective Retrieval of Images by Spatial Similarity, *IEEE Trans. Knowledge and data engineering*, vol. 10, no.3, pp.504-511, 1998
- [4] E. Jungert, "Rotation Invariance in Symbolic Slope Projection as a Means to Support Spatial Reasoning", *Proc. Third Int'l Conf. Automation, Robotics and Computer Vision "ICARCV'95"*, pp. 364-368, 1994
- [5] G. Kunev V.Antonova, P.Vladimirova, "System Modeling via Databases", *ICEST2004*, vol 2. pp. 277-278, Bitola, Macedonia, 2004
- [6] G Petraglia, G. Sebillio , M., Tucci G. Tortora, "Virtual Images for Similarity Retrieval in Image Databases", *IEEE Trans. on knowledge and data engineering* vol. 13(6) pp. 951-967, 2001
- [7] E.G.M. Petrakis, Fast Retrieval by Spatial Structure in Image Databases, *Journal of Visual Languages and Computing*, Vol. 13, No. 5, pp. 545-569, October 2002
- [8] E.G.M. Petrakis, "Content- Based Retrieval of Medical Images", *International Journal of Computer Research*, Volume 11, , pp. 171-182, Number 2, 2002
- [9] M. Stoeva, B. Rachev, "Retrieval by Spatial Similarity in Image Databases", *Proc. of 7th East European Conference, ADBIS 2003*, pp.48-59, Dresden, Germany, <http://www.adbis2003/September2003>

A Web-based Course for Development, Implementation and Administration of a Secure Portal within OracleAS Portal 10g

Valentina R. Antonova¹ and Petar T. Antonov²

Abstract – This paper focuses on the organization and contents of the Web-based course for designing and implementation of a secure portal within OracleAS Portal 10g, and also on the process of training in portal administration. The course is specially developed for students and specialists who want to acquire knowledge and skills for designing websites and web-based applications that meet the increased requirements for efficiency and security.

Keywords – Portal, security, website, web-based application.

I. INTRODUCTION

The rapid development of Internet technologies increases the necessity of well-trained specialists for developing and administering web-sites and web-based applications using the invented for those purpose newest technologies such as the environment of Oracle Application Server Portal 10g (OASP). This technology is notable for its efficiency and it can be used in various areas including support in solving problems with safety and reliability. Thus, the actuality and usefulness of the designed and presented in this article web-based course is proved, according to the methodological requirements of the distant e-learning. The course provides students and specialists with the opportunity to acquire the necessary knowledge in order to solve complex problems in designing databases within OASP, to provide access to the existing far databases and to design, build and administrate a secure portal.

II. COURSE DEVELOPMENT

A. Course purpose and tasks

The main purpose of the designed web-based course is to introduce the technology for development, implementation and administration of a secure portal within OASP. Here are the main tasks in developing the course:

- To differentiate a theoretical part for each course topic.
- To supply examples in order to illustrate the material for each topic.
- To provide practice on different topics.

B. Website organization

The site structure consists of for parts with strictly defined function and size. The top two parts contain the logo and the title of the site. On the left-hand side there is a navigational menu for selecting topics, which is a group of hyperlinks to HTML documents containing theoretical parts and examples. When clicked on there the dynamical menu is situated and provides a detailed description of topics. The information is visualized in the main section of the page. Buttons for navigation have been also designed to move to different pages.

C. Theoretical part

The academic material included in the course is topical and sufficient for forming a technology for development, implementation and administration of a secure portal within OracleAS Portal 10g, which includes concepts for professional managing of the information such as scaling, safety and defense, check of correctness and compatibility, planning problem situations, etc. [3], [4]. OASP is a multifunctional platform for designing websites and web-based applications that meet the increased requirements of the content management, application development and their integration by means of widening the traditional concepts in bases from data to web content [2].

The subject area on which the development and implementation of the database is built considers students' status during the time of their academic training. This area is also used for creating students' books in subjects studied in the Bachelor's degree programme in Computer Systems and Technologies specialty at the Technical University of Varna [5], [6] and in other designed multimedia courses [7] and environments [8].

The multimedia course contains the following topics [3]:

- Installing and Configuring OracleAS Portal 10g.
- Introducing the OracleAS Portal 10g Environment.
- Using the Navigator.
- Implementation of the database – tables, views, indexes, sequences, synonyms, procedures, functions, packages, triggers and others [1] (Fig. 1).
- Creating an access to an already existing remote database.

¹Valentina R. Antonova is with the Department of Computer Science and Engineering, Technical University of Varna, 1 Studentska str., 9010 Varna, Bulgaria, E-mail:valyvarna@yahoo.com

²Petar T. Antonov is with the Department of Computer Science and Engineering, Technical University of Varna, 1 Studentska str., 9010 Varna, Bulgaria, E-mail: peter.antonov@ieee.org

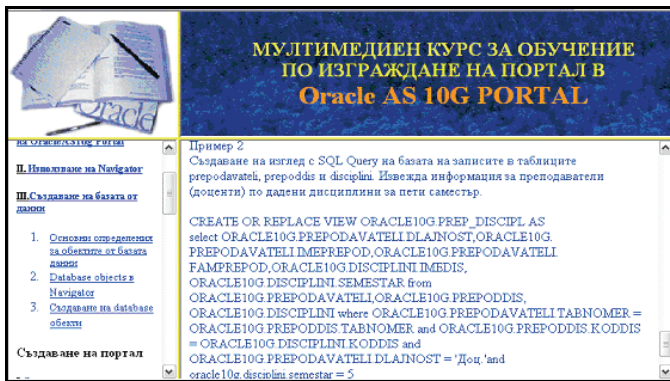


Fig. 1

- Building a Portal:
 - Introducing Portals and Portlets; Portlet management; framework services; runtime implementation.
 - Caching in OracleAS Portal 10g; types of caching – invalidation-based, validation-based, expiry-based; levels of caching.
 - Creating a Portal Page - working with regions; adding portlets; creating labels; customizing the page (Fig.2).

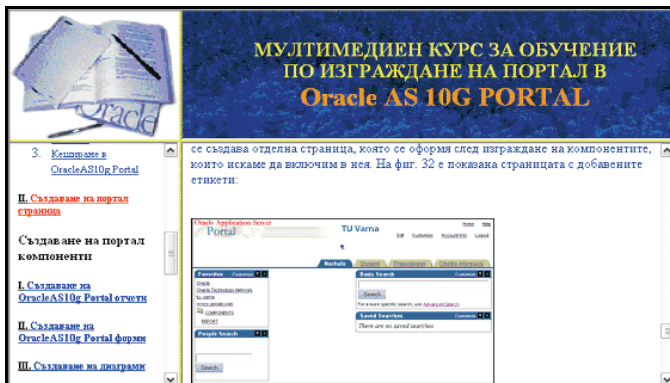


Fig. 2

- Building OracleAS Portal 10g components:
 - Reports – building a QBE report and creating a report with the Query Wizard; using SQL for specifying the source of report data, adding parameters to reports; using reports as portlets; calling reports directly (Fig. 3).



Fig. 3

- Forms – creating forms based on tables, on stored procedures and on a link between two tables – master-detail forms.
- Charts – creating charts with Query Wizard; creating charts based on a SQL statement; adding charts as a portlets.
- Calendars – building a calendar with Calendar Wizard.
- Hierarchies – building a hierarchy; navigating through a hierarchy.
- Dynamic Pages – working with HTML; using Frame Drivers.
- Building OracleAS Portal 10g Applications:
 - Working with Lists-of-Values –LOVs; building a static LOV object and a dynamic LOV object.
 - Creating Portal Menus.
 - Building compatibility in OracleAS Portal 10g web sites and applications.
 - Data validation with OracleAS Portal 10g: using JavaScript; testing JavaScript scripts (Fig.4).

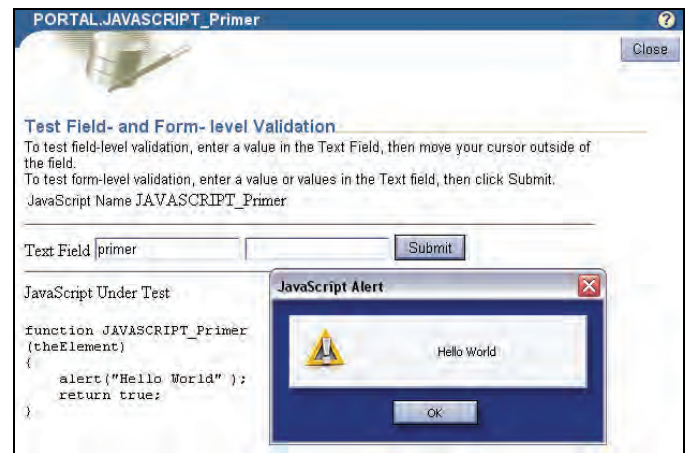


Fig. 4

- Using links to connect OracleAS Portal 10g objects.
- Integrating PL/SQL Logic.
- Administering OracleAS Portal 10g:
 - Administering Portal components.
 - Administering the OracleAS Portal 10g Environment.
 - OracleAS Portal 10g security:
 - Creating privileged accounts with Portal (Fig. 5).

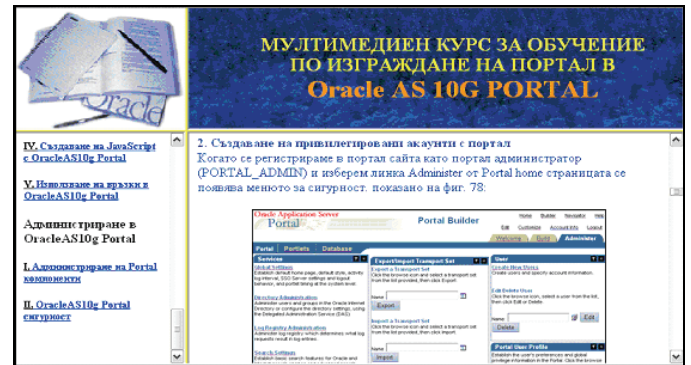


Fig. 5

- Creating groups and group privileges.
- Creating privileges on individual objects.
- Setting schema privileges.
- Using the Login Server.

The examples provided for each topic illustrate step by step the essence of the technology for designing, building and supporting a portal.

III. SECURITY IN ORACLEAS PORTAL 10G

Portal applications are no different from other browser-based applications or even classic client/server or terminal-based applications when it comes to the need for security. The database offers a very comprehensive set of security features that enables us to protect our data right at the source. In addition to the standard Oracle security features, the designers of Portal have provided some additional capabilities that help us deal with the stateless of the Internet. The resulting combination is a strong set of features that enable us to protect the data in our database from unauthorized access.

Oracle's database security is based on the concept of user names and passwords. Every Oracle database user is required to provide a user name and password to connect to a database. Database objects, such as tables, are owned by the user name that creates them. They are not normally accessible to other users unless specific access to these objects has been provided by use of the GRANT command [4].

If there are lots of objects and lots of users, it can become overly time-consuming to assign grants. Oracle provides support for roles - abstract users. By granting privileges to the role and then granting the role to the users, we can simplify the process of setting up the accounting group. Any change to the role is cascaded to the users automatically. You can create users, grant access to database objects, and define roles directly through the Portal interface.

There are five classes of portal users as defined by the various portal roles: Portal developers, Portal administrators, Portlet publishers, Database administrators (DBAs), Portal users (Fig. 6).

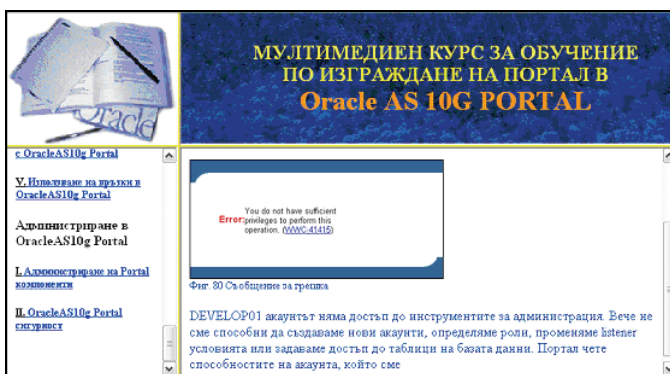


Fig. 6

The Portal security user interface is composed from the following three major functions: Users, Groups, Services.

With the release of 3.0, Oracle Portal uses the Oracle Login Server for authentication and authorization. Portal's user

accounts are stored as records within the Login Server. Portal automatically forwards authentication requests from the portal layer over to the Login Server [3].

There are four types of privileges (Built-in Group Privileges) that are conferred on user accounts through predefined groups as listed: DBA - to grant database administrator privileges to the user; PORTAL_ADMINISTRATORS - to grant the user portal administrator privileges; PORTAL_DEVELOPERS - to grant the user privileges to build applications with Oracle Portal; PORTLET_PUBLISHERS - to grant the user privileges to make Oracle Portal objects (folders, categories, application components, and pages) available as portlets.

Each Portal account is mapped to a physical Oracle database schema (a database user account). Portal accounts do not have direct access to the Oracle database. Portal accounts are lightweight database users as defined to the Login Server. Lightweight users are Oracle user accounts that are valid within Oracle Portal (and the Login Server), but do not exist in the Oracle database. The accounts that we define within the portal interface will only work with Oracle Portal.

We may choose to modify an existing account. There are three of object privileges that can be granted to a user on a global basis: Page Group; Portal DB Provider и Administration.

Every major object within the portal site, such as pages, reports, forms, charts, calendars, hierarchies and folders, can have individual permissions and grants associated with them. In order to simplify the process of granting lots of privileges to individual users, Portal provides the Object Privileges panel. Through this form, you can grant portal accounts super-user privileges to all four major functional areas of Oracle Portal.

Although Portal comes equipped with several predefined groups it is a simple matter to create our own groups.

Security configurations for end-user accounts generally require more individualized settings, because we do not give them free reign to access all of the data in our database. Oracle Portal makes the overall security process easier because we can restrict access to the database completely and only allow users to view data using specified application components.

When we attach users to a group, we combine users into categories that can then be managed as a group. In some cases, groups themselves confer privileges to users directly. In other cases, the setting of the group merely creates the logical grouping, without granting any specific privileges.

It is one thing for a group to be given access to an application or component. However, the schema that owns the application also needs to be given access to the underlying database objects (i.e., tables and views).

Physical database schemas act as the containers for applications. Although the source code for our applications is stored in the PORTAL schema—the generated database packages are stored in the application schema, which owns our application.

The Login Server manages the physical connections to the database and controls the authentication of individual users. The Login Server runs as a separate instance from the Portal

Server. When a portal user requests a page from the Portal Server, the portal engine checks for the presence of an application session cookie. If the user has not been authenticated already, the portal server forwards the request to the Login Server, which then prompts the user for a portal user name and password.

Portal's security mechanisms are built directly from the standards already in place within the Oracle database.

With Portal, user security is divided evenly between Portal privileges and schema privileges. Once we have implemented security settings for our portal, the next task is to monitor its performance by Oracle Portal's monitoring tools and reports.

IV. CONCLUSION

The web-based course presented in this article is used by students in the process of their training at the Technical University of Varna. It has given them a basic understanding of OracleAS Portal 10g, the various types of objects they can create with OracleAS Portal 10g, the basic structure of OracleAS Portal 10g and also OracleAS Portal 10g components and security features. That is why the observation of the used example database for students' status in different students' books and courses helps stating the links between different objects, components and mechanisms from the initial database building to the portal functioning.

The course development could be towards preparing assessment tests and test questions for each topic, that provide the user with the opportunity to estimate the level of his/her subject knowledge.

REFERENCES

- [1] К. Кълог, *Oracle8 Библия*. Прев. от англ. София, България: АлексСофт, 1999.
- [2] А. Одеуан, *Oracle Web приложения – PL/SQL въведение за разработчици*. O'Reilly. Прев. от англ. София, България: ЗестПрес, 2000.
- [3] R. Greenwald, J. Milbery, *Oracle9i AS Portal Bible*. New York, USA: Hungry Minds, 2001.
- [4] Р. Грийнвалд, Р. Стаковяк, Дж. Стърн, *Основи на Oracle - Oracle Database 10g*. O'Reilly. Прев. от англ. София, България: ЗестПрес, 2004.
- [5] Б. Рачев, В. Згурева (Антонова), Г. Кунев, Л. Калчев, *Бази от данни и информационни системи*. Варна, България: изд. ТУ Варна, 1997.
- [6] Б. Рачев, В. Згурева (Антонова), Г. Кунев, *Автоматизирани информационни и управляващи системи*. Варна, България: изд. ТУ Варна, 1994.
- [7] V. Antonova, G. Kunev, "Web-based Courses for Development, Implementation and Administration of Oracle Databases", *Computer Science'2004, Conference Proceedings*, pp.308-313, Sofia, Bulgaria, 2004.
- [8] V. Antonova, P. Antonov, "A Secure Web-based System for Administrative and Methodical Maintenance of Distance Learning", *Computer Science'2005, Conference Proceedings*, pp.230-235, Chalkidiki, Greece, 2005.

Models of e-business in Transportation

Dejan D. Marković¹, Bojan V. Stanivuković² and Momčilo J. Dobrodolac³

Abstract – In this paper, modern concepts of e-business and their usage in transportation are presented. The application of mobile business in association with actual problems in postal, road and railway transportation is specially described.

Keywords – Models of e-business, Mobile e-business, E-business in transportation

I. INTRODUCTION

Electronic technology, as combination of information and telecommunication technologies, is more and more in usage in modern business, i.e. the number of companies that have taken the concept of e-business is bigger every day in the world. Basic trend in development of e-business, especially in segment of business relations between the companies, is that Internet has become dominant channel for business relations. Main reason for that is about low costs that this way of business affects with combination of high efficient performance of business operations.

One of the trends in new e-business technology development is usage of mobile phones in e-business because they make an opportunity to implement entirely new services. That phenomenon brings us a new concept of modern business – Mobile Business. Because of its advantages and high spectrum of possibilities, there is belief that mobile phone, i.e. mobile technologies, will be significant channel for development of e-business in the future and there is a thinking that it will surpass Internet and take its position of dominant business channel away.

Modern concepts of e-business and their usage in transportation are presented in this paper. The application of mobile business in association with actual problems in postal, road and railway transportation is specially described.

II. MODELS OF E-BUSINESS

There is a question what business people, including small firms, corporation groups and managers on every level, should know in order to become a part of huge world of “e-business”. First of all, it is necessary that one should have a good knowledge about models of business on Internet. Making

¹ Dejan D. Markovic is with The Faculty of Transport and Traffic Engineering University of Belgrade, Vojvode Stepe 305, 11 000 Belgrade, Serbia, E-mail: mdejan@sf.bg.ac.yu

² Bojan V. Stanivukovic is with The Faculty of Transport and Traffic Engineering University of Belgrade, Vojvode Stepe 305, 11 000 Belgrade, Serbia, E-mail: stanivukovic@yahoo.com

³ Momcilo J. Dobrodolac is with The Faculty of Transport and Traffic Engineering University of Belgrade, Vojvode Stepe 305, 11000 Belgrade, Serbia, E-mail: m.dobrodolac@sf.bg.ac.yu

business on the new markets defines a type of e-business and also its model. Based on relations between parties, there are two basic models of e-business:

- Business to Business models – B2B models and
 - Business to Consumer models – B2C models,
- and also some derived models:
- Business to Employee – B2E;
 - Consumer to Consumer – C2C;
 - Consumer to Business – C2B;
 - Business to Business to Consumer – B2B2C;
 - Consumer to Business to Consumer – C2B2C;
 - People to People – P2P;
 - Intrabusiness;
 - Exchange to exchange – E2E;
 - M – commerce;
 - Government to citizens – G2C;
 - Government to government – G2G;
 - Government to Employee – G2E.

Two main e-business models are B2B and B2C. B2B market occupies the biggest part of on-line transactions. Transactions on that market bring between 80 and 85% of total e-commerce income.

A. Classification of Models Based on Basic Aim

There is no unique, universal and accepted classification of e-business models. Having in mind that problem, Centers for IBM e-business Innovations carried out the research analyzing 700 companies that were active on the Internet. On that basis, they determinate examples of on-line business models [1].

According to Centers for IBM e-business Innovations the following e-business classification models definition is given:

Offline facilitator – Those companies promotes their brands on-line, but they do not accept any form of orders by internet. They are trying to avoid any type of potential conflict (channel conflict).

Content provider – Those companies are known like related groups or content aggregators. Making business is special in experts way for certain fields and those companies are directed on specific value propositions. Their activity is based on subscriptions, advertisement or transaction fees.

Business destination – Their business is based first of all on direct sale channels. Their main activity is based on sale of good and services.

Online exchange – Their appearance, whether like auctioneers, finance transactions or market designers, brings customers and seller in connection and they help them to make business. The income is accomplished mostly by

transaction fees, but it may be supplemented by advertisement and subscribe taxes.

Gateway – There are several different tools: search engines, Internet service providers (ISP) and shopping agent. Those companies provide an easy way for users to find what they want on the Internet. As there is a case with the ones that appears the first time on the Internet, this on-line business brings the biggest income through advertisement.

Although many of companies can be ranked in these classes, anyway there are some hybrid models. The dynamic nature of digital economy demands permanent reevaluations and adoptions. For some companies it is enough to make a little progress in their own business model through new accomplishments.

III. EXAMPLES OF E-BUSINESS IN TRANSPORTATION

A. Postal Traffic

Today’s postal operators make business in environment that differs a lot from the period of postal originate. Postal customers have more and more specific demands, they have wide range of possible services to choose and they are much more demanding in respect to recent times. That forced postal operators to become aware of the fact that they must adjust their business in order to hold or make bigger their share in world communication market [2].

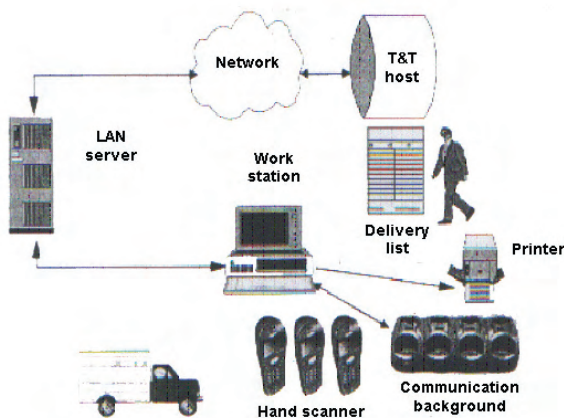


Fig.1. Track & Trace system with off-line PDT terminals

Question that is usually asked by postal service customers all over the world is position of their mail during the transportation. Customers want to know where is their mail in specific moment, why it is not yet consigned or who consigned it. System for track and trace of postal items is based on following elements: portable PDT terminal, T&T work station and T&T host computer. Architecture of Track & Trace system with off-line PDT terminals is shown on Figure 1.

Classic postal services – sending of all sort of mail, in the future will be digitally done. That means that kind of postal services will be under a new kind of measures that prevents

lost or migration of mail. These measures will be effected by adding identification to mail in digitally form. Based on that identification, it will be known where would be some specific postal item in every moment. That kind of data will be accessible to the person that sends the mail, postal workers that manipulate with that mail and also to recipient. A small RFID dice is incorporated in postal stamp sized like one business card. It includes all data about a person that sends



mail, about a person that receives a mail, about mail itself, its content and destination. As soon as that stamp is affixed, all data mentioned above is transferred in postal computer in form of identification tag. After that, moving of postal item can be tracked and traced over the Internet. Example of one postal stamp is shown on figure 2.

Fig.2. Postal stamp

B. Road Transportation

The most seen usage of e-business in road transportation is for track and trace of vehicles, for parking and toll rate payment. As tracking and tracing system for vehicles is concerned, it is implemented through information system that allows satellite observation of mobile objects under GPS and GSM/GPRS technology. Tracking the object is possible in every moment and data about status and vehicle position can be received by using SMS messages or Internet.

That kind of service provides:

- Tracking and displaying of vehicle status using SMS messages
- Signalizing the alarm to mobile phone
- Vehicle tracing in real time using Internet
- Vehicle tracing history using Internet
- Technical support 24 hours

System for tracking and tracing is specially useful in monitoring of business for big transportation companies and other systems that are in dispose of a huge rolling stock.

Besides tracking of vehicles in real-time and review of history of drives, this group of users finds particularly important to have route management feature: option to define various routes and perform off-line comparison between defined routes and real tracks. With a single click, user can get map with defined route and real tracks in different colors, so that any differences can be easily noticed.

Also, additional information could be very useful, such as mileage, total time vehicle usage time, maximal and average speed, etc.

Certus Autotrack information system, system that is developed in Serbia for tracking and tracing, fulfills a series of functions in fleet management:

Supervision:

- Exact positioning and status of vehicle in real time

- Control of drivers
- Coordination of vehicle usage

Operative:

- Improving of efficiency through vehicle usage coordination

Analytic:

- Statistic analyses can be made for specific vehicle in specific time period

Financial:

- Rationalization of costs is effectuated by better work discipline and better vehicle coordination

Demonstration of Certus Autotrack information system is given of Figure 3.



Fig.3. Elements of Certus Autotrack system

Advantages of Certus Autotrack information system are:

- Satellite monitoring through GPRS enables tracing huge number of vehicles in real time because all vehicles send data to IP address of server using Internet, while in standard GSM mode, number of vehicles that can be monitored in a moment is limited by number of GSM modems that are used by vehicles for connection.
- In case of GPRS, amount of transferred data is charged, but not period of line occupation (like it is case with GSM). This kind of system is much more cost effective.
- Calculation shows that for a price of one SMS message with position of vehicle, it can be transmitted 1000 messages using GPRS – if we assume that data are send every 30 seconds from vehicle and that there is 15 hours of vehicle usage on daily basis. This means that a price for GPRS monitoring do not overcome the price of two SMS messages.

One of the solutions of the problem with the lack of parking places in cities is division of city center into zones that characterize limited time of parking and tariff system for parking payment. System is totally automated and designed in way that driver can pay parking place in the least time period without any contact with some employee that make collection. Parking payment is doing in most modern way – by parking

tickets, parking machines, SMS messages of mobile phone network and using electronic dice cards.

Toll rate payment systems are based on “vehicle – road” communication technology, traditional microwave or infrared waves or recently used satellite technology (Global Positioning System – GPS), including Automatic Vehicle Identification – AVI and Automatic Vehicle Classification – AVC in order to enable electronic transfer of money between vehicle that passing toll rate gate and agency that organize system of payment.

Modern equipment for toll rate payment, in fact, takes job to workers that make payment in classic cabins. It allows the transactions be made at vehicle speed that is close to normal traveling speed. Some sorts of devices are designed in the way they can communicate with any reader. Agencies that organize system of payment are very interested in their further development and also in development of readers in order to improve the system.

C. Railway Transportation

Railway system has passed all technology and other changes and has found solutions for imposed mission of new age. The solution really is in following and implementation of modern scientific and competent knowledge and experience and that is the only way for it to subsist.

High speed trains, multimodal transport and synchronized railway time scheduling in international range demands new solutions in railway transportation. Having in mind that railway system has big competition in road and air transport, efficient communication is basic for unobstructed railway transportation flow with high level of safety.

Today, trains are equipped with up to six different navigational systems. Each is extremely costly and takes up space on-board. A train crossing from one European country to another must switch the operating standards as it crosses the border. All this adds to travel time and operational and maintenance costs. The solution of the problem is found in new system developed under the initiative of European Union authorities called ERTMS.

The European Rail Traffic Management System – ERTMS has been developed in recent ten years and its implementation is in process. GSM-R (Global System for Mobile Communication – Railways) is communication platform for ERTMS and it is developed on ETSI. GSR-R is an integral part of GSM. But GSR-R is much more that multifunctional wireless communication system – it actually provides general communication platform for control systems of trains in the future. ERTMS is digital system. It offers integrated services, has standardized open interfaces and it is made on modulus platform. Main components are ETCS and GSM-R. ETCS is the new control-command system and GSM-R is the new radio system for voice and data communication. Together, they form ERTMS, the new signaling and management system for Europe, enabling interoperability throughout the European Rail Network.

General ERTMS architecture consists of trackside equipment, trainborne equipment and GSM-R radio communications.

POSTER SESSION – PO V

Control Systems & Robotics

Application of Kalman Filtering Technique to Increase the Probability of Faults Detection in Test Equipment

Angel D. Tanev¹ and Antonio Vl. Andonov²

Abstract - One approach for application of Kalman filtering theory in test equipment has been considered. The main goal is to estimate the state (good or faulty) of this test equipment in case of failure in the measurement channel. We simulated this failure at given step of working of the channel. The covariance matrix $P(k|k)$ is shown when the failure has been occurred.

Keywords - Kalman filtering theory, covariance, failure model, precise test equipment.

I. INTRODUCTION

Let's consider the following measurement channel. This channel can be described by using state-space method [1]. It is also a linear discrete-time system with two equations describing the dynamics of the system Eq.(1.1) and the formation of the data accessible to the measurement Eq.(1.2):

$$\mathbf{x}(k+1) = \Phi(k+1, k)\mathbf{x}(k) + \mathbf{G}(k+1, k)\mathbf{w}(k) \quad (1.1)$$

$$\mathbf{y}(k) = \mathbf{H}(k)\mathbf{x}(k) + \mathbf{F}(k)\mathbf{v}(k), \quad (1.2)$$

where: k - time index,
 $\mathbf{w}(k)$ - zero-mean white noise(process noise),
 $\mathbf{x}(k)$ - internal state,
 $\mathbf{y}(k)$ - observed signal,
 $\mathbf{v}(k)$ - additive noise in observed signal.

Also $\Phi(k+1, k)$, $\mathbf{G}(k+1, k)$, $\mathbf{H}(k)$, $\mathbf{F}(k)$ are matrices regarding to $\mathbf{x}(k)$, $\mathbf{w}(k)$, $\mathbf{y}(k)$, $\mathbf{v}(k)$.

In this case we consider the following model of the system (shown in Fig.1).

II. PRESENTATION

Since the observed signal \mathbf{y} consists of additive noise \mathbf{v} , in test equipment it is used optimal estimation approach based on the theory of Kalman filtering in order to reduce the uncertainty in the measurement.

This estimation method is strong in several aspects- it can estimate previous, present and even future states of the system. The equation describing the estimated value $\hat{\mathbf{x}}(k/k)$ is obtained by the expression:

$$\begin{aligned} \hat{\mathbf{x}}(k/k) &= \Phi(k, k-1)\hat{\mathbf{x}}(k-1/k-1) + \\ &+ K(k)[\mathbf{y}(k) - H(k)\Phi(k, k-1) \times \\ &\times \hat{\mathbf{x}}(k-1/k-1)] = \\ &= \hat{\mathbf{x}}(k/k-1) + K(k)\hat{\mathbf{z}}(k/k-1) \end{aligned} \quad (2.1)$$

where: $K(k)$ - matrix coefficient of gain,
 $\hat{\mathbf{z}}(k/k-1)$ - innovation of the process,

$$\begin{aligned} K(k) &= P(k/k)H^T(k)R^{-1}(k) \\ &= P(k/k-1) \times H^T(k)[H(k) \times \\ &\times P(k/k-1)H^T(k) + R(k)]^{-1} \end{aligned} \quad (2.2)$$

The covariance matrix of the filtering error $P(k/k)$ consisting of the variances of different parameters is [2]:

$$\begin{aligned} P(k/k) &= P(k/k-1) - P(k/k-1)H^T(k) \times \\ &\times [H(k)P(k/k-1)H^T(k) + \\ &+ R(k)]^{-1} H(k)P(k/k-1). \end{aligned} \quad (2.3)$$

The main property of this filtering is that after each step of working the variance $P[k|k]$ of each parameter is going to reduce its initial value

$P[0|0]$ and the uncertainty tends to be zero. This is shown in Fig. 2. Also it is shown the state \mathbf{x} and the observed signal \mathbf{y} .

III. PRACTICAL CONSIDERATION AND APPLICATION

During normal functioning of the system (without failures), the variance $P(k|k)$ is minimum (after completing the transition processes).

We will consider the following important case in practice when the failure in the system is related to increasing of measurement noise $\mathbf{v}(k)$ in the equation of observation Eq.(1.2):

$$\mathbf{y}(k) = \mathbf{H}(k)\mathbf{x}(k) + \mathbf{F}(k)\mathbf{v}(k)$$

A failure event has been simulated at given step in order to show the real process. Then the covariance matrix of the filtering error $P(k/k)$ Eq.(2.3) consisting of the variances of different parameters will increase due to increasing of measurement noise $\mathbf{v}(k)$. It is shown in Fig. 3.

¹ Angel D. Tanev, Higher school of Transport, Bulgaria, Sofia, 158 Geo Milev Str. e-mail: ang_tanev@abv.bg

² Antonio Vl. Andonov, Higher school of Transport, Bulgaria, Sofia, 158 Geo Milev Str. e-mail:

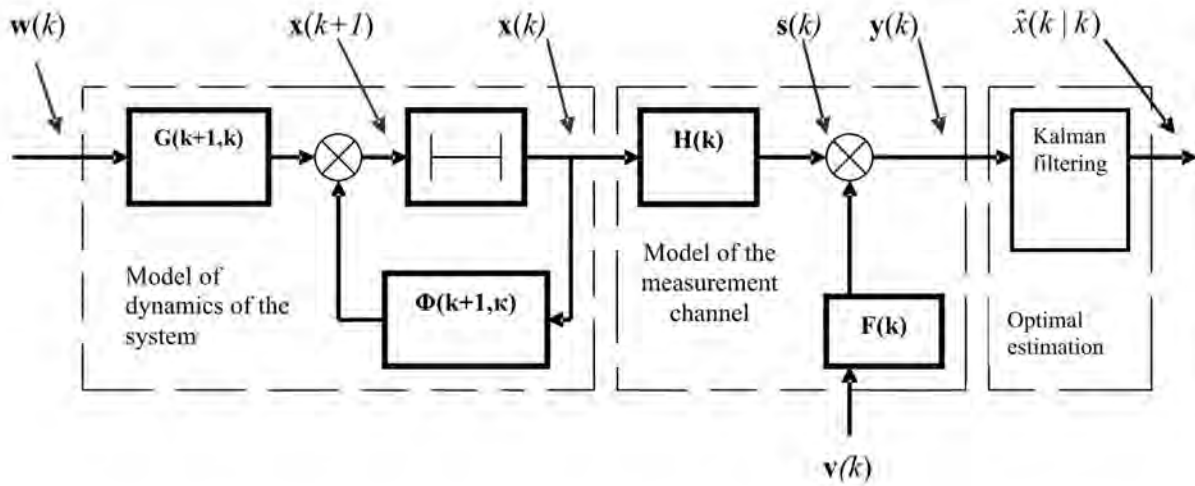


Fig. 1. Model of the dynamics of the system and model of measurement channel in “state-space” method

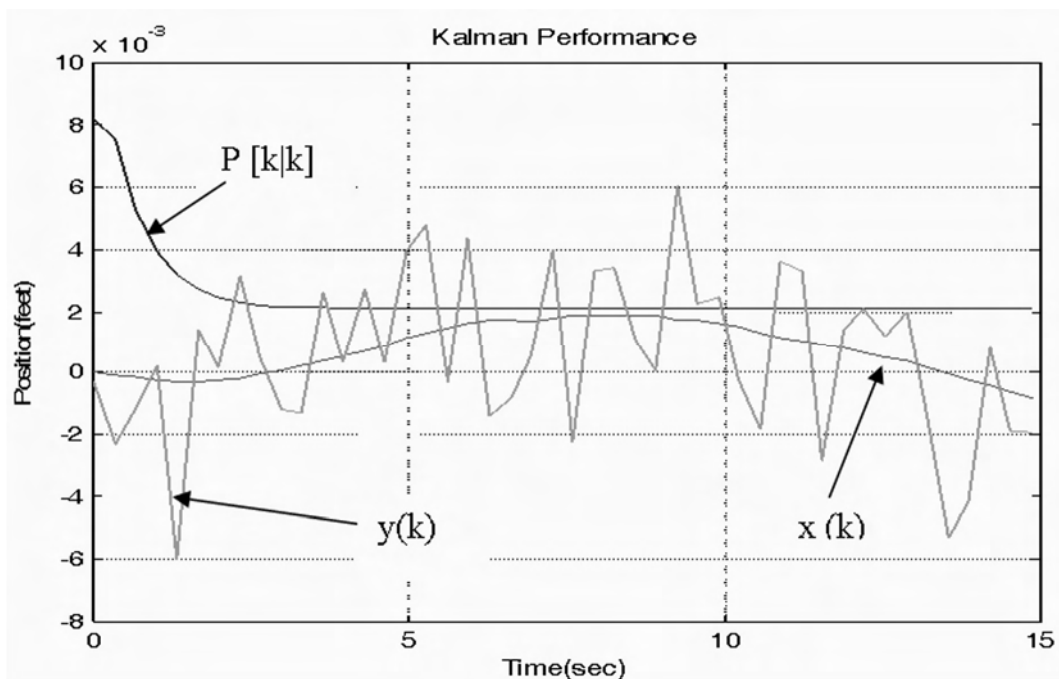


Fig. 2. The uncertainty estimation method based on Kalman filtering approach.

We can create algorithm for faults detection by using the covariance matrix of the filtering error $P(k/k)$ [3]. Thus, increasing of this error will be a sign for fault in the observed system. After creating the algorithm for faults detection at each step of working we can estimate the system when fault has been occurred.

In practice it is so important to take the right decision for failure because there are two errors:

- Error 1: α - when the object is working properly we take a decision for failure. It leads up to missed detection.
- Error 2: β - when the object is failed we take a decision for working properly. It leads up to false alarm.

There is a big difference between them. In practice error 1 is more important than error 2 (it is more dangerous).

Let's consider an information system with 100 parallel, independent working channels with probability of failure $Q = 1 - e^{-\lambda t}$, where: $\lambda = 10^{-3}$, $t = 10^3$ h (Fig.1). During their working we can not repair them. After completing the mission the system is subject to repair. We find the failed channels and after that the system starts working again with 100 channels. If during the maintenance we find all failed channels and after that we recover them, then mean value of channels working properly is N .

Let now during the maintenance the error 1 (missed detection) is $\alpha = 0,4$ [1]. Since the mean value of failed components for a time t from N independent working (parallel) channels is:

$$\bar{k} = N \cdot Q(t) \quad (3.1)$$

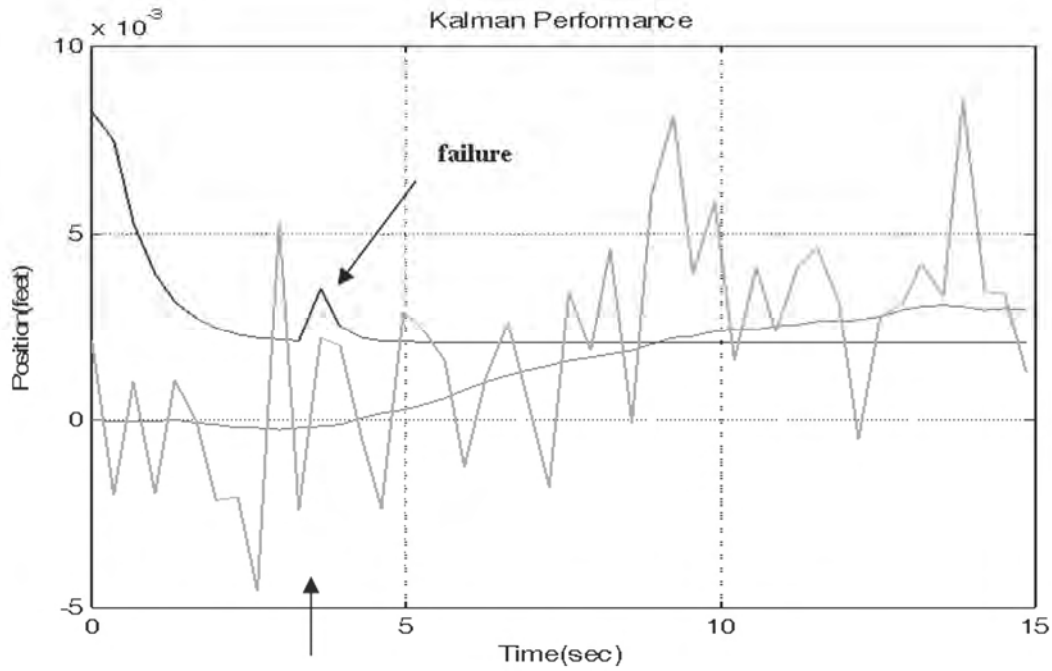


Fig. 3. Failure of the system at given step affecting on $P(k|k)$.

Then after the first cycle of maintenance we have:

$$\begin{aligned} \bar{k}_1(1000) &= 100.Q(1000) = \\ &= 100.(1 - e^{-1}) = 100.0,63 = 63 \end{aligned}$$

IV. CONCLUSIONS

Therefore, due to incorrect monitoring in test equipment the information system will work up to 70 % of its capacity.

In this case of 63 failed components the following ones can not be found: $63.0,4=25$.

After completing the second cycle of maintenance the failed components will be $\bar{k}_2 = 47$ and then total number failed channels will be $(47+25)=72$.

That is, the failed channels which will not be found are now: $72.0,4=29$ and the third cycle starts working with 71 channels. After completing the third cycle we will have 45 failed channels. The total number failed channels will be $(45+29)=74$ and finally we will have $74.0,4=30$ (not found channels).

The fourth cycle starts working with 70 channels in good state. This is the steady-state value of the channels working properly.

One approach for decision-making in case of faults detection has been proposed. This one includes estimation method based on Kalman filtering theory and it considers failure model related to increased value of noise in the observed signal. The main goal is to reduce the error 1: α because it is more dangerous in practice. The benefit is we will have more precise test equipment.

That is, in practice it is so important to use methods taking right decision in order to detect faults in the system. It is so actually in such systems as avionics, control systems related to technological processes, radiolocation systems, etc.

REFERENCES

- [1]. Gindev E., *An introduction of engineering reliability*, Part 1, "Marin Drinov" Academic publishing house, Sofia, 2000.
- [2]. Akashi, H., and H. Kumamoto, "Random Sampling Approach to State Estimation in Switching Environments", *Automatica*, Vol. 13, 1977.
- [3]. Anderson, B. D. O., and J.B. Moore, *Optimal Filtering*. Englewood Cliffs, NJ: Prentice Hall, 1979.

This page intentionally left blank.

Situational Control of RADAR

Ivan Evtimov Korobko

Abstract: The possibilities of adaptive control of RADAR in complex electromagnetic environment are considered. The adaptation and the control are executed by names of matrix antagonistic games continuously evaluating the control effectiveness.

Key words: RADAR, control, adaptation, theory of games

I. INTRODUCTION

The control task's general scheme is shown on fig. 1 [1]. It includes current situation description, its analysis, classification, correlation and impact on the object.

Current information description

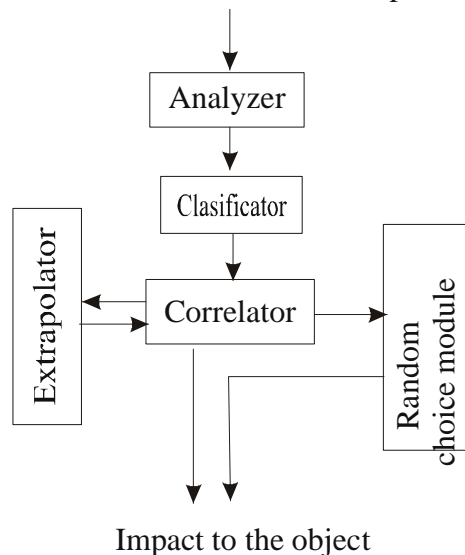


Fig 1

The current situation is understood as a data collection with information about its functionality at certain moment of time. The analyzer evaluates the message and it decides it is necessary to interfere in control system or not. The analyzer do not transmit the message further of there is no necessity of it. In the opposite case the message is to be passed to the classifier which classify the situation depending on single step solutions. This information is transmitted to the correlator. The correlator defines the rule which will be used for control. If several rules exist all of them have to be transmitted to the extrapolator. If the extrapolator also is not able to make a decision, an information supporting random choice of control impact is to be generated.

The above scheme is not working well enough for the radio location station due to the reason of presence of a man-operator who is performing the most part of operations. There is no good enough model created by the moment which could give adequate description of human behavior when working with radio location information. The main reason for that is the variety of the information, its perception and decision making. Another reason is that the operator works in a priori undetermined situation and with a priori undefined information.

II. TASK DEFINITION

In the most cases the radar's work can be considered as an interaction with the nature or with the opponent (enemy). We have a game with incomplete information taking in mind that the information at the moment of radio location signal detection in a priori undefined.

When we have a game with incomplete information the opponent's strategy and the profit's function are not known. Also it is not known are there any other players in the game. In this case the player (radar operation) makes subjective decision about random distribution of situations. The player has random evaluation about the game, about profit's function, opponent's strategy, about himself etc. He has information about different aspects of the game.

A game with incomplete information appears due to the technical imperfection of the equipment and systems or due to special actions of other participants in the conflict. At such type of games a series of mathematical difficulties appears in task definition and in its resolution.

One of the possibilities to eliminate the incomplete information is to create a system based on the ability to define appointments strategies and their parameters. Such a system must have an additional investigating receiver in its structure. Depending on the receiver's features the limitation of the decision making information absence will be eliminated. The target is to create a radar structure witch will allow adaptation to the electromagnetic situation with maximal effectiveness.

III. SYSTEM DESCRIPTION

The RADAR diagram of discussed type is shown on fig.2., where RLT is Receiver's Line Tract, IPU – Interference Protection Unit, TU – Threshold Unit, Tr – Transmitter with ability of frequency funning, AU – Adaptation Unit, QFM – Quality Factor Measuring unit, NA – Noise Analyzer, DF – Directed Deflector.

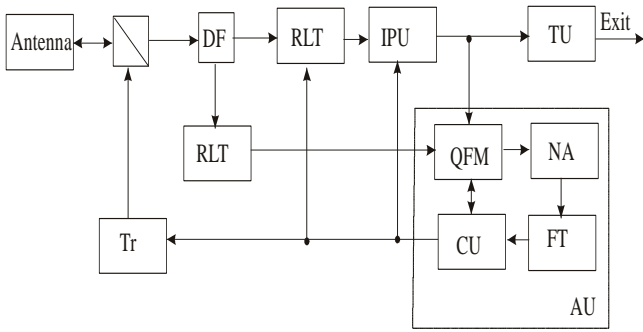


Fig.2

The shown RADAR differs from the standard known RADAR by presence of an additional receiver and of an Adaptation Unit, which improve quality factors of RADAR and they secure operation in situations where that factors are the best. As quality factors the ratio “signal/noise” or the difference between their powers could be used.

The purpose of the additional receiver is to analyze the electromagnetic situation and to define the appointment’s strategy. This information must be transmitted in real time to the information processing system and to the interference protection system. The real time is defined by the location rate. The adaptation unit is the main unit in the described RADAR. This unit measures the quality factor and analyses the noise using QFM and it defines the opponent’s strategy and it select/define the RADAR’ strategy using the functional transmitter(FT) and the control unit(CU). The choice of strategy is possible only if the RADAR structure is flexible. i.e. it allows parameters changing and possibilities of changes in hardware and software of the receiver, of the transmitter and of the antenna [2].

The purpose of the functional transformer Unit is to define RADAR strategies. This is possible using evaluation matrix (2). A sample evaluation matrix is shown on fig. 3, where FNN is filter of non synchronous noise, WLA – wideband amplifier – limiter – narrow band amplifier, WLF– wideband amplifier – limiter-matched filter, LFM – line frequency modulated signal, PCM – phase-code manipulation, CFAR-constant- false- alarm rate, MTI – moving targets indication, SL of AP – site lobe of antenna pattern. The evaluation is understood as quality factor of as a profit of use of some noise protection device. The noise protection device could be designed as hardware unit or software program. Some authors refer about 150 variants [3,4]. These devices define RADAR structure depending on its purpose. In the same time they define the level of RADAR noise protection. The changes in the electromagnetic situation case changes of the number of connected devices. The simplest way to do this is to select pure strategies. The opponent’s strategy recognition causes activation of one or another device, which gives the biggest effect. Using of pure strategies gives appointments to perform all actions in the real time by steps, adapting RADAR to the electromagnetic situation. If it is impossible to use pure strategy a mixed strategy has to be selected.

The matrix on fig.3. gives visual imagination about the size and the complexity of the solutions an about the difficulties in finding of optimal RADAR strategies. The optimal RADAR strategies do fine its structure. For this purpose it is necessary

to to find max min a_{ij} and all points which are members of the optimal strategies’ set. This set has to be convex, closed, limited and not empty. The line programming is used to overcome the complexity of finding of optimal mixed strategies.

Fig.3

	Aimed noise interference	Barrage noise interference	Passive interference	Chaotic interference	Wide band interference	Answering pulse interference	Max min a_{ij}
Tuning from view to view	100	0	0	100	100	100	0
Tuning with pause	100	1	1	100	100	100	1
Tuning from pulse to pulse	100	2	2	100	100	100	2
Adaptive tuning	200	4	4	200	200	200	4
PCM signal	13	13	3	13	10	1	1
LFM signal	30	30	0	30	20	1	0
Compressed noise signal	100	100	3	100	100	100	3
WLF	80	20	1	30	80	1	1
WLF + CFAR	160	40	2	60	160	2	2
FNN	10	10	10	80	10	0	0
FNN + CFAR	20	20	20	100	20	10	10
MTI	0	0	100	50	0	0	0
MTI + CFAR	2	2	200	100	2	0	0
Polarization selection	2	2	2	2	2	2	2
Compensation of SL of AP	80	80	0	80	80	80	0
Low SL of AP	1000	1000	0	1000	1000	1000	0
min max a_{ij}	1000	1000	200	1000	1000	1000	

The matrix solution (fig.3.) using line programming is as follows:

RADAR' optimal strategy:

- 1) MDS + CFAR with probability of 0.833;
- 2) Low side lobe of AP with probability of 0.167

Opponent's optimal strategy:

- 1) Passive interference with probability of 0.833;
- 2) Answering pulse interference with probability of 0.167.

The received game solutions show guaranteed profit for RADAR and as opponent loss. As it is shown here this solution demonstrate only weak points of RADAR which could be opposed by the opponent by certain strategies to minimize this loss. It has noted that RADAR trends towards to receive max $\min a_{ij}$. That means that in the proper column on fig.3. only minimal profit values are shown (on certain strategies), all other profits are bigger. i.e. all other game values are always bigger than received minimal values.

In this case maximums of minimums in order to their value and the optimal strategies define RADAR' structure.

The shown matrix gives complete imagination about the RADAR' structure, but it shows also that a précised appraised of different units' effectiveness is necessary. The decision about RADAR structure creation and RADAR control in dynamics will be more effective if the values of matrix members will be calculated with more accuracy. The dynamics in this case is defined by the abilities of the opponent and by the time for analysis of the opponent and by the time for analysis and decision making by the adaptation unit.

IV. CONCLUSION

The proposed radar's structure with additional receiver for electromagnetic environmental evaluation and with unit for adaptation to the electromagnetic environment works at the best quality factor. A specific feature of the radar is that it works with pure strategies which can give the biggest profit at antagonistic games. The analysis performed and the solutions received complete the synthesis of RADAR structure which is oriented to processing in complex dynamically changing electromagnetic environment.

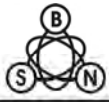
The usage of matrix antagonistic games prompts that optimal strategies finding helps not only to determine RADAR' structure but to select the strategy of maximal profit in dynamically changing electromagnetic environment. The changes of the electromagnetic environment is followed by continuous changes of RADAR' structure and parameters, by steps. Basically, only pure strategies are used as they can be executed easily in real time and always, at recognized situation, a strategy of maximal effect can be found. At least, of all possibilities are exchanged, a mixed strategy can be used. Unfortunately when mixed strategy is used the solution might be not optimal.

When using pure strategies an exact evaluation of the effect of different strategies usage is needed which means that they have to be played preliminary.

The performed calculations of detection parameters and their comparison with others shown certain advantages of the described RADAR. The presence of an adaptation shows significant improvement of the detection characteristics.

REFERENCES

- [1] Pospelov D.A. Situational Control. Theory and practice. M. Nauka, 1986.
- [2] Korobko I. E. Radio Technical Systems (System Design). S. Korvet press publ. Ltd, 144 p., 2003.
- [3] Johnson S. L. Radar Electronic Counter – countermeasures. IEEE Transactions on Aerospace and Electronic Systems. Vol. AES-14, Ni, 1978.
- [4] Radiointerferences Protection. Under ed. of M. V. Maximova., Sov. Radio,1976



This page intentionally left blank.

Control Systems with Frequency Converters save Energy in Food Industry

Lena F. Kostadinova¹, Radoslava N. Gabrova² and Atanas S. Georgiev³

Abstract – A possibility to meet carbon emission (Kyoto commitment) and energy conservation targets when using electric motors in food industry is discussed in this paper. Typical applications where savings could be confidently expected would include: pumps, compressors, fans, conveyors, mixers, refrigerators. Some of the most common applications of variable speed systems with frequency converters are discussed and worked examples showing the benefits that can be achieved are given.

Keywords – Energy conservation, Variable speed drives, Frequency converter

I. INTRODUCTION

Energy conservation has become an increasingly important feature in any solution selected today. More than 65% of industrial electrical energy consumed is by the electric motors, which in turn accounts for around 10% of a country's CO₂ emission. To meet carbon emission and energy conservation targets governments world wide are realizing the need to encourage more effective use of motors in all areas of industry. Savings have to be achieved in food industry as well. In typical applications (pumps, compressors, fans, conveyors) levels of utilization are approximately 50% with power losses estimated to be between 40% and 80% of the motor full load rating. The latest developments in microcomputer based technology present financially attractive opportunities to reduce these losses. There are three methods of improving energy efficiency by investment in: high efficiency motor; motor controller; variable speed system (VSS). High efficiency motors and motor controllers are options for constant speed motors. A decision tree for selection procedure in this case is discussed in [1]. The next opportunity for saving energy is using VSS. Historically, they were not installed for energy saving reasons but to satisfy process requirements. As a result, the degree of sophistication was determined by requirements of the process and usually meant that the particular speed needed was preselected and controlled manually from the range available. Today many more options exist and modern electronics helped by the

comparatively high cost of electricity, have brought about revolution in options. Infinitely variable and constantly changing speed can now be achieved at a relatively modest cost, determined mainly by the degree of flexibility required of the system. VSS have the objective to adjust the speed of the driven load in accordance with some measured parameter and they broadly fall into three categories: electronic variable speed systems; variable speed motors and electro-mechanical drives. The last two are not discussed in the paper. The electronic variable speed systems (EVSS) operate by electronically matching the speed of the motor, and the power input to it, to the requirements of the load. Hence the iron and other losses are reduced to minimum. EVSS could be separate to two main groups: DC and AC. Which solution is the right DC or AC EVSS, when choosing energy effective decision for control of electromechanical systems is discussed in [2].

Electronic variable speed systems (EVSS)

From the wide variety of AC EVSS frequency converters (FC) have become the most popular today. They convert the AC mains voltage to a DC voltage which is then inverted into a variable voltage, variable frequency AC supply. FC can be retrofitted to existing motors, but some derating of the motor (possibly by up to 10%) is necessary. They extend control down to zero speed and up to three-four times normal synchronous speed. The power factor of the supply current is normally high and relatively constant over the whole speed range. Since the output wave form is close to a pure sine wave there are few problems due to harmonics on the motor. The total efficiency of the VSS with FC as a drive control (Fig.1) depends on the losses in the motor and its control. Mechanical output power depends on the required torque (M) and rotating speed (ω). The presented results are based on the assessment of the total losses of a VSS with FC in two wide spread applications in food industry.

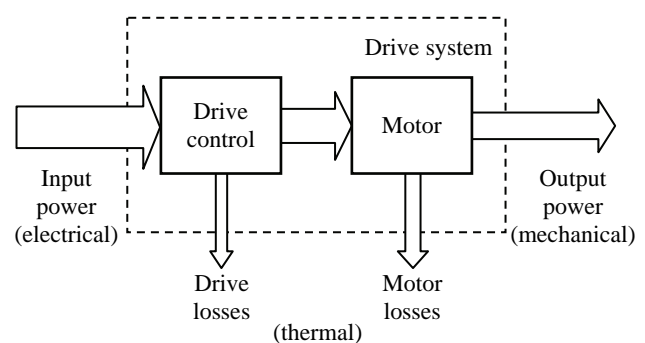


Fig. 1 The Efficiency of the Drive System

¹Lena F. Kostadinova from University of Food Technologies, 4000 Plovdiv, 26 Mariza bvd, Bulgaria, E-mail: lenakostadinova@yahoo.com

²Radoslava N. Gabrova from University of Food Technologies, 4000 Plovdiv, 26 Mariza bvd, Bulgaria, E-mail: rgabrova@yahoo.com

³Atanas S. Georgiev from University of Food Technologies, 4000 Plovdiv, 26 Mariza bvd, Bulgaria, E-mail: asgeorg@yahoo.com

Fans and Pumps

Fans and pumps are the worst offenders in the VSS efficiency. The need for flow rate control is widespread in food industry and the method selected has a significant bearing on the running cost. Pumps have much in common with fans and the laws governing their operation are similar. Head/flow and efficiency curves for a typical centrifugal pump operating at constant speed are shown in Fig.2. Pump's characteristic curve usually refers to certain specified speeds and densities of the medium being pumped. The design point

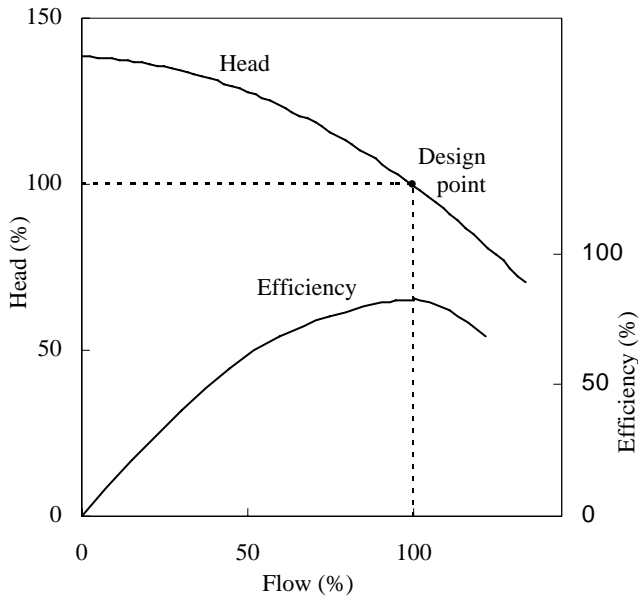


Fig. 2 Typical Centrifugal Pump Head/Flow Efficiency Curves for a Constant Speed Conditions

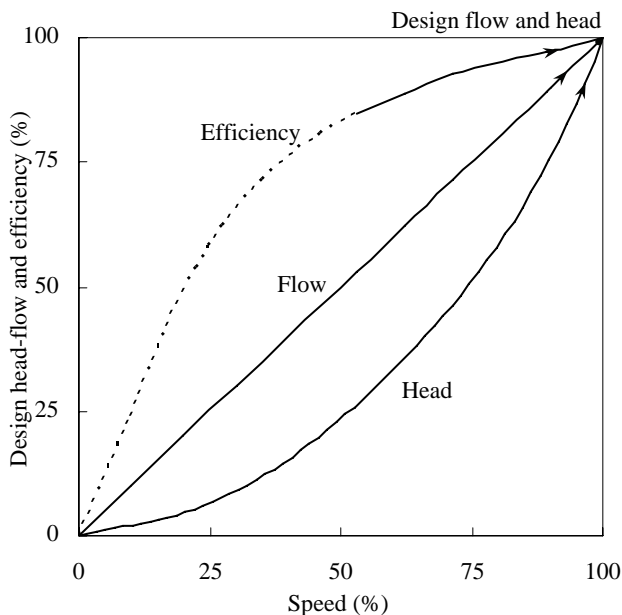


Fig. 3 Typical Centrifugal Pump Efficiency, Flow and Head Characteristics for Variable speed

in this example is selected so that maximum efficiency occurs at 100% flow. If the pump characteristics are examined when speed variation is introduced, the basic relationships which govern their operation are shown in Fig.3. The pump efficiency shows little reduction over the upper portion of the speed range, but rapidly decreases as the speed falls below 60% of the design value. Speed control of the pump (fan) is one method of changing the design point (Fig.4). The effect of

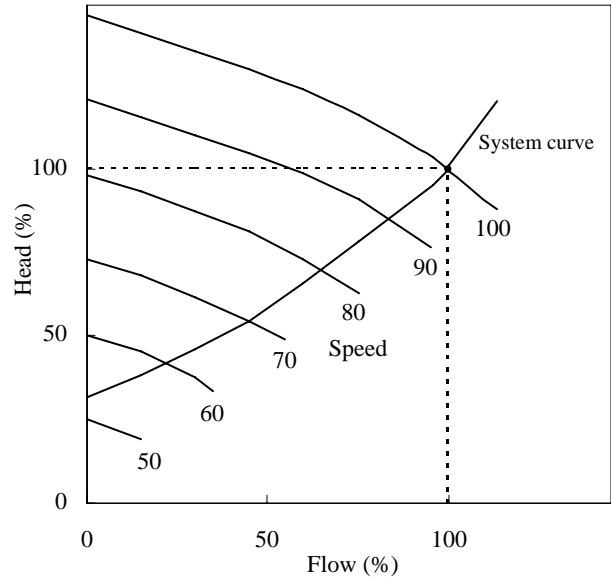


Fig. 4 Flow variation with Speed Reduction

speed control on the energy consumption of a centrifugal pump is evident from experimental results shown on Fig.5.

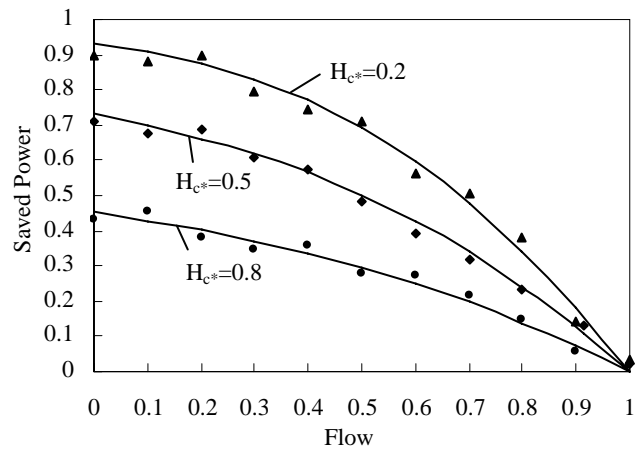


Fig. 5 Saved Power depending on Flow Rate at Static Delivery Head: $H_{c^*}=0.2; 0.5; 0.8$

The extra power consumption, when the control of flow is at a constant speed, using "throttling" by means of a control valve, compared to the power consumed when flow is controlled by the speed. The FC used for the experiment is of type Altivar 58HU18M2 of Schneider Electric [3]. The centrifugal pump has been examined at three static delivery heads (H_{c^*}). The extra power consumption is obtained by measuring the fixed speed power input and power input to drive. The results show

that changing the ‘throttling’ with VSS reduces the consumed power. Speed control is more effective when the static delivery head is smaller.

Conveyors

Almost all technological processes in food industry use different kinds of conveyors for processing, transporting and packaging. The productivity Q_* of the conveyor depends on the force F_{C*} needed to replace the useful load and the velocity v_* of movement. The equation in relative values is:

$$Q_* = F_{C*} v_* \quad (1)$$

When the conveyor is running at a constant speed $v_*=1=\text{const}$, the productivity is equal to the force $Q_* = F_{C*}$. The better way to control conveyors is to keep up the force constant at rated value ($F_{C*}=1=\text{const}$). In this case productivity will vary proportionally to the speed $Q_* = v_*$. Using VSS to control the productivity of conveyor gives a possibility for saving energy

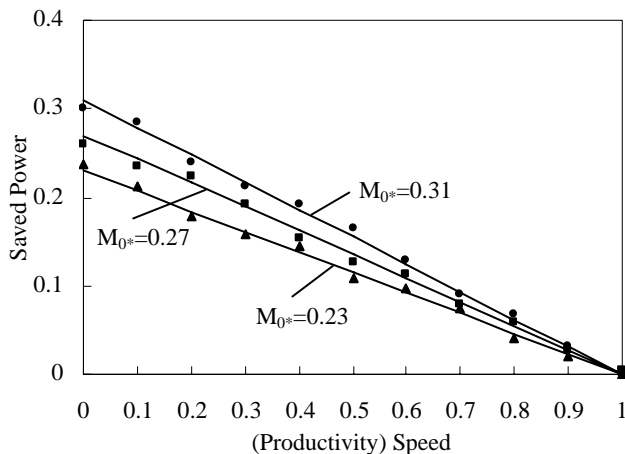


Fig. 6 Saved Power depending on Productivity at Ideal Running Torque $M_{0*}=0.23; 0.27; 0.31$

as compared to the constant speed work. The experimental data of saved power depending on productivity (speed) are presented in Fig. 6. The data are obtained from VSS with Lenze smd frequency converter ESM D251X3SFA [4]. The experiment has been made for three different values of the ideal running torque of motor ($M_{0*}=0.23; 0.27; 0.31$). It is evident from Fig. 6 that the saving effect from the speed control of productivity of the conveyor is as higher as bigger the torque M_{0*} is.

II. ADDITIONAL REMARKS

VSS with FC reduce energy wastage by changing the motor speed. This saves energy because the motor does not use more energy than required. There are several options for control the FC itself. FC Volt per Hertz is the control method of choice for applications where multiple motors are operated

simultaneously from one motor control. Closed Loop Vector operation of FC uses mounted encoder to precisely control motor torque and associated operating speed. Drive segregate motor current into components that produce torque from the current that produce motor heating. By minimizing the heating component of current and accurately controlling the torque component of applied current, the motor will behave very much like a DC motor but without the maintenance. Direct Torque Control (DTC) brings even more savings, often up to 30% according to ABB [5].

III. CONCLUSION

In this paper ways for saving energy by using VSS with FC in food industry are given.

Speed control methods of pumps are most appropriate where the friction losses dominate in the system characteristic. In cases where the static delivery head is principal component, speed control will show less benefit.

In addition to the energy cost reduction achievable, other benefits can arise from the use of VSS. These include the elimination of problems created by water hammer, the reduction of hydraulic loading, improved product quality and increased resistant index of the conveyor belts.

REFERENCES

- [1] L. Kostadinova, A. Georgiev and Ch. Damianov, "Saving Electric Energy in Food Production by Automation of the Electric Drives", Scientific Works HIFFL, vol. XLIII, Iss 3, pp. 321-326, 1998.
- [2] L. Kostadinova, P. Dimitrova, A. Kansazov and R. Tenchev, "DC or AC Drives when choosing Energy effective Decision for Control of Electromechanical systems", Scientific Works of UFT, vol. LIII, Iss. 2, pp.19-24, 2006
- [3] www.schneider-electric.com
- [4] www.Lenze.com
- [5] www.abb.com/motors&drives

This page intentionally left blank.

Multi-channel Wireless ECG System

Yuliyana S. Velchev¹

Abstract – In this paper a multi-channel wireless ECG system is present. According to the modern concept, the system is built as Wireless Personal Area Network (WPAN), formed by intelligent wireless ECG sensors and a coordinator – personal computer. The system is based on the Bluetooth™ standard for short range communication. This paper describes the overall system structure as well as the structure of the intelligent ECG sensor (signal conditioning and acquisition, signal processing and transmission over wireless link).

Keywords – Telemedicine, E-health, ECG

I. INTRODUCTION

The electrocardiogram (ECG) can be considered as simple but powerful non-invasive diagnostic tool in cardiology. The system shown in the paper introduces an improvement of classical ECG signal acquisition.

Nowadays the concept for transmitting medical data (particularly ECG) over short-range wireless link turns into forming a network from intelligent wireless sensors and personal computer. The main advantages of this concept are: increased patient mobility, simultaneously monitoring of more patient's ECG, possibility to make real-time analysis, possibility to store and forward the received ECG data using Internet, improved electrical safety of the patient. The described in this paper wireless ECG system utilizes the Bluetooth™ standard in order to form a wireless short-range personal network used to transmit the acquired ECG signal.

II. SYSTEM STRUCTURE

According to Figure 1, the system structure is based on intelligent sensors with wireless communication capabilities. The main part of each ECG sensor is Digital Signal Controller (DSC). The used signal controllers are dsPIC30f family, provided by Microchip Technology Inc. The built-in multi-channel ADC provides resolution of 12-bit. It samples the previously amplified and filtered ECG signal. The next stage is signal processing. In this project an adaptive filtering and decimation are used. DSC communicates with Bluetooth™ module via asynchronous serial interface. These modules along with PC (equipped with Bluetooth™ communication capability) form the so called Piconet, limited up to 7 devices. The PC application used to monitor the ECG signals is

developed using LabView™ software.

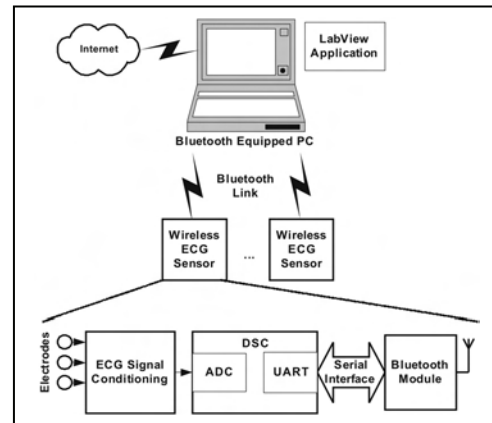


Fig. 1. System structure

One of the concepts in telemedicine known as “store and forward” is used in this project. So, this equipment is possible to be placed at patient's home and using Internet the ECG data can be forwarded to a hospital for further analysis and diagnosis by medical staff.

III. SIGNAL CONDITIONING AND ACQUISITION

Nowadays, the experts consider that ECG systems with 9, 12 or even 15 channels are suitable only for more complicated diagnosis, which is often a consequence from a relatively basic ECG diagnosis. The purpose of the described system is to help the doctor to track the patient's heart activity for a long period of time using only three ECG channels. As mentioned above, this can give enough information for medical staff.

The classic electrode placement is used (Figure 2), according to the well-known Enthoven's triangle.

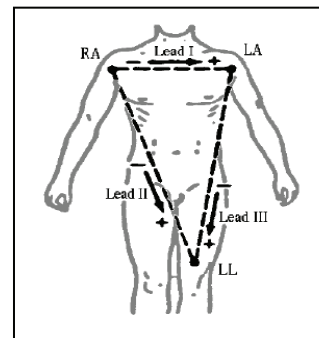


Fig. 2. ECG electrode placement

¹Yuliyana S. Velchev is with the Faculty of Communications and Communications Technologies, Technical University of Sofia, Address: 8, Kliment Ohridski St. Sofia-1000, BULGARIA, E-mail: julian_velchev@abv.bg

The spectrum of the ECG signal is concentrated from DC to about 120Hz. Peak to peak voltage can be considered of no more than 3mV. The ECG amplifier must be with high input impedance and very high CMRR (over 100dB). In order to met these strong requirements an instrumentation amplifier INA2126 or INA2128 (made by Texas Instruments) is used as first stage high CMRR amplifier. Figure 3 shows the simplified diagram for ECG signal conditioning. The gain of instrumentation amplifier is limited to 10mV/mV, because of possible amplifier saturation, which can be caused by electrodes polarization or power line noise. Power supply is $\pm 9V$ (made by DC-DC conversion from the battery power). To achieve better CMRR, a “right leg driven” circuit is implemented. The common mode signal is fed back to the patient’s body (right leg) to minimize the power line interference. Also this signal is used as reference input for adaptive filter, discussed in the next chapter, The DC component is removed by high-pass first-order passive filter. The overall gain is set to 1V/mV, so the next stage gain is 100mV/mV. In addition, this stage provides level shifting in order to match the voltage level requirements for ADC. The spectrum is limited to about 100Hz by low-pass active filter. The analog ECG signal is sampled by 12-bit ADC which is a peripheral part of the DSC. Sampling rate is chosen to be 1000Hz, thus the requirements for analogue low-pass filter is reduced. Also the setting time of adaptive filter is minimized significantly.

In future work the amplification will be made by Programmable Gain Amplifier (PGA), adjusted dynamically by DSC. In this case the gain can be increased when the power line noise is weak, so achieving better ADC resolution.

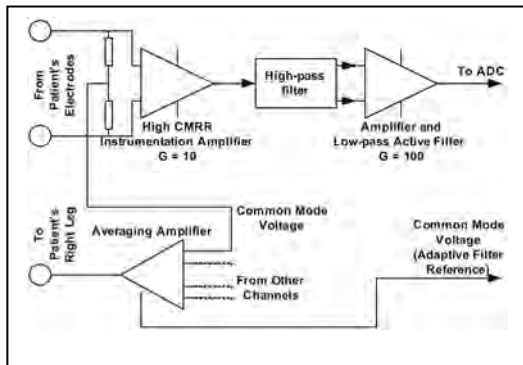


Fig. 3. ECG signal conditioning

IV. SIGNAL PROCESSING

Despite of high CMRR amplification and “right leg driven” circuit implementation, the power line interference is still significant. To remove this component without corrupting the ECG signal, an adaptive filter with 32 taps is used. According to Figure 4 a referent signal which is derived from common mode voltage is used as input signal in Normalized Least Mean Squares (nLMS) adaptive filter. Thus, the error signal is actually the ECG signal with removed uncorrelated power line interference.

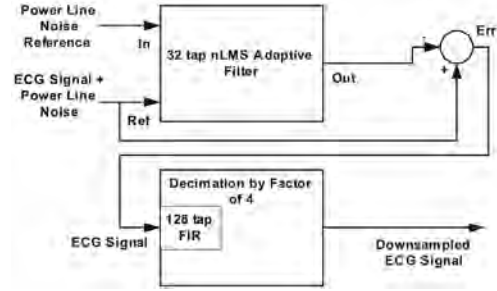


Fig. 4. ECG signal processing

The nLMS algorithm can be expressed as:

$$y[n] = \sum_{m=0}^{M-1} h[m] * x[n-m] \quad (1)$$

$$h(n+1)[m] = h(n)[m] + nu * e[n] * x[n-m] \quad (2)$$

$$e[n] = r[n] - y[n] \quad (3)$$

$$nu = \frac{mu}{mu * E[n]} \quad (4)$$

$$E[n] = E[n-1] + x^2[n] - x^2[n-M+1] \quad (5)$$

Where: $y[n]$ is the output signal (“Out” in this case), $x[n]$ is the input signal (“Ref” in this case), $r[n]$ is referent signal (“In” in this case), mu is adapting factor, $E[n]$ is estimated input signal energy, and $h(n)[m]$ are the filter coefficients in time “ n ”.

The parameters of power line noise can vary in time, so the adaptive filter is very suitable choice to track the eventually changes of these parameters. Some other types of adaptive filters are experimented such as Least Mean Squares (LMS) and adapting by error signal sign. Achieved results (in terms of setting time) are worse than nLMS algorithm. The setting time and Signal to Noise Ratio (SNR) are in conflict for adaptive filters. The adaptation factor “ mu ” is determined experimentally (in this case the best results are when it is equal to 8). Experimental results show that in order to simplify the circuit, a formed square wave signal from common mode voltage can be used as reference for adaptive filter. So, instead of additional analogue channel for reference an external interrupt input in DSC can be used. By this way the performance of the adaptive filter is reduced insignificantly. The sampling rate is 1000Hz, which is above the required minimum. So, decimation by factor of 4 is implemented to change the sampling rate down to 250Hz. A FIR type low-pass digital filter with 128 taps is used along with decimation. The cut-off frequency for this filter is 120Hz. All described above signal processing is in format 1.15 (fixed point data). The software is developed with MPLAB C30 compiler.

V. WIRELESS COMMUNICATION

In this project the Bluetooth™ v1.1 communication standard is met by using Class A modules, type F2M03C1 with chip antennas. Figure 5 shows the protocol layer model for these modules. As can be seen the upper layer is so called Wireless UART (WU, SPP), which means that the user is free to build complicated communication software. The communication is simple as organizing the link over rs-232 standard. In PC each module is associated as two virtual COMM ports (incoming and outgoing). The data encryption capabilities of Bluetooth™ standard are enabled in this project also.

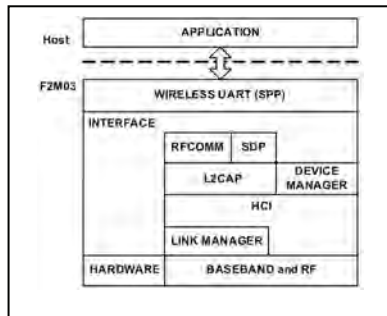


Fig. 5. F2M03C1 protocol layer model

Serial communication is organized with hardware handshaking (RTS/CTS) and two additional digital lines (first of them to initiate the connection and the second to inform the DSC whether the connection is available). The Bluetooth™ module connected to PC is standard USB dongle with Serial Port Profile (SPP) support.

VI. EXPERIMENTAL RESULTS

LabView™ based software is developed to communicate with ECG sensors and to display the received data. Figure 6 shows the process of ECG signal acquisition during the adaptation of nLMS filter.

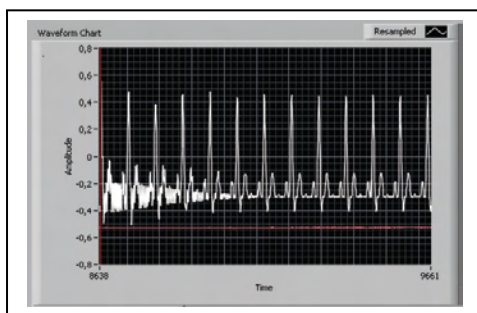


Fig. 6. ECG waveform during the nLMS filter adaptation

Figure 7 shows the same ECG signal after nLMS algorithm has been fully adapted to the power line interference.



Fig. 7. Acquired ECG waveform after nLMS filter has been fully adapted

The experiments have confirmed that the Bluetooth™ wireless communication is reliable in the range up to 30m indoor and up to 100m in outdoor conditions.

VII. CONCLUSION

In this paper a multi-channel wireless ECG system is described. As can be seen from above, the achieved experimental results are satisfying. The future work will be concentrated in terms to increase the number of nodes, which are now limited up to 7. By using next generation of DSC from Microchip (dsPIC33F, PIC24F) it will be possible to increase the number of channels and overall system performance, because of Direct Memory Access (DMA) capability. Also, it is obviously that the system needs to be developed by adding computer-based ECG analysis (QRS complex detection at next stage of development and more sophisticated methods in the future).

REFERENCES

- [1] D. Dimitrov, "Communication system in medicine", handbook, Sofia, 2005.
- [2] D. Dimitrov, Y. Velchev, "Communication Protocol for Medical Mobile Network", Proceedings of 48-th IWK, TU – Ilmenau, Germany, pp. 55-56, Ilmenau, Germany, 2003.
- [3] D. Dimitrov, D. Vasileva, "One Channel ECG System", Proceedings of 48-th International Scientific Conference of Information, Communication and Energy Systems and Technologies, ICEST '03, pp. 510-512, Sofia, Bulgaria, October 16-18, 2003.
- [4] D. Dimitrov, M. Nikolova, "Reconstruction of Periodical Impulse Sequence", Proceedings of Regular International Conference of Association of Computer Technique of USA on Computer Application – ACMBUL'92, p. 34-1, 34-5, 4-8 October, 1992, Varna, Bulgaria.
- [5] D. Dimitrov, Y. Velchev, "Distance Analysis of ECG", Proceedings of the Technical University-Sofia, Volume 52, p. 69-75, Sofia, Bulgaria, 2003.
- [6] D. Dimitrov, M. Nikolova, "Parameters Estimation in Computing Restoration Signals with Noise Spectrum", BAND 1, VORTRAGSREIHEN, 43 Internationales Wissenschaftliches Kolloquium, Technische Universitat, Ilmenau, Germany, p. 607-612, 21-24.09.1998, Ilmenau, Germany.

- [7] R. Paradiso, "Wearable Health Care System for Vital Signs Monitoring", Proceedings IEEE Int. Conf. Information Technology Applications in Biomedicine, pp. 283-286, 2003.
- [8] E. Jovanov, P. Gelabert, R. Adhami, B. Wheelock, R. Adams, "Real Time Holter Monitoring of Biomedical Signals", DSP Technology and Education Conference DSPS'99, August 4-6, 1999, Houston, Texas, 1999.
- [9] E. Jovanov, D. Raskovic, J. Price, A. Moore, J. Chappman, A. Krishnamurthy "Patient Monitoring Using Personal Area Networks of Wireless Intelligent Sensors", Biomedical Sciences Instrumentation, Vol. 37, pp. 373-378, 2001.
- [10] R. Ruiz, J. Perez, J. Sierra, S. Maguillo, "SCP-ECG Transmission by a Tele-medicine Home Care Device: an Implementation Approach", The 2nd Open ECG Workshop 1-3 April, 2004, Berlin, Germany, pp. 16-18, Berlin, Germany, 2004
- [11] Y. Jasemain, E. Toft, L. Arendt-Nielsen, "Real Time Remote Monitoring of Cardiac Patients at Distance, Integration of the ECG into the EHR & Interoperability of ECG Device Systems", The 2nd Open ECG Workshop 1-3 April, 2004, Berlin, Germany, pp. 48-50, Berlin, Germany, 2004.
- [12] T. Desel, T. Reichel, S. Rudischhauser, H. Hauer, "A CMOS Nine Channel ECG Measurement IC", ASIC, 1996. 2nd International Conference, October, 1996.

Heart Rate Measurement System

Yuliyana S. Velchev¹

Abstract – In this paper a portable heart rate measurement system is present. This system is low-cost and has low power consumption. It uses optical method by infrared light. Along with measurement capabilities the presented system can record the measured data as well as time, date and year for up to three days. The recorded data can be downloaded from personal computer for further analysis. Also a smart method for LED bias setting is introduced.

Keywords – Pulse oximetry, Heart rate, Telemedicine

I. INTRODUCTION

The pulse oximetry is a non invasive method for oxygen saturation measurement by sensing the infrared and red light absorption properties of deoxygenated and oxygenated hemoglobin. It is comprised of a sensing probe attached to a patient's earlobe, toe, or finger, which is connected to a data acquisition system for calculation and display of oxygen level, heart rate, and blood flow. Deoxygenated hemoglobin allows more infrared light to pass through and absorbs more red light. Highly oxygenated hemoglobin allows more red light to pass through and absorbs more infrared light.

Based on mentioned above method, the presented heart rate recorder uses infrared light to measure the period of AC component, sensed by light to voltage converter, caused by blood flow changing.

The system records the data into serial EEPROM with actual time, date and year.

II. SYSTEM STRUCTURE

According to Figure 1, the main part of the described system is Digital Signal Controller (DSC). The built-in 10-bit ADC samples the amplified pulses and by simple algorithm measures and averages its period. Also it is responsible for exact bias setting of the infrared LED ($\lambda = 940\text{nm}$) by driving the Digital to Analogue Converter (DAC). This DAC directly sets the LED current. It is necessary to set the correct bias in terms to achieve higher LED current (thus achieving strong signal for measurement) as well as to avoid amplifier saturation. This method is simple but efficient. The 4-bit current DAC is built using four resistors, each of them with resistance twice as resistance of previous (300Ω , 600Ω , 1200Ω and 2400Ω). So the maximum current can be about

20mA and the step is 1.4mA, considering 4.5V supply voltage. Experiments show that proper current is about 8-10mA. A feedback to the DSC, used for correct LED bias maintain is implemented as analogue comparator, which compares the DC level of the light to voltage converter output with a threshold. The threshold is set by divider to be a half of power supply voltage. No hysteresis is necessary for comparator, because it simply interrupts the DSC on achieving proper LED – photodiode bias. The used light to voltage converter is integrated photodiode with operational amplifier, type TSL250R. This concept simplifies the circuit, minimizes the size and reduces the price. The high-pass filter removes the DC component from the signal. Its cut-off frequency is set to 0.3Hz which corresponds to 20-30 beats per minute (lowest measured pulse). Because it is necessary to measure only the period of the waveform, a single supply operational amplifier with gain = 100, amplifies the positive half of signal. A low-pass filter removes high frequency components, thus ensuring correct ADC operation. A Real-Time Clock (RTC) with date and year maintain capability is implemented in DSC. The measured heart rate along with time/date is recorded into serial EEPROM, connected via SPI interface to the DSC. Later this recorded data can be downloaded from a PC through rs-232 interface. The measurement interval as well as time/date adjusting can be configured via rs-232 also.

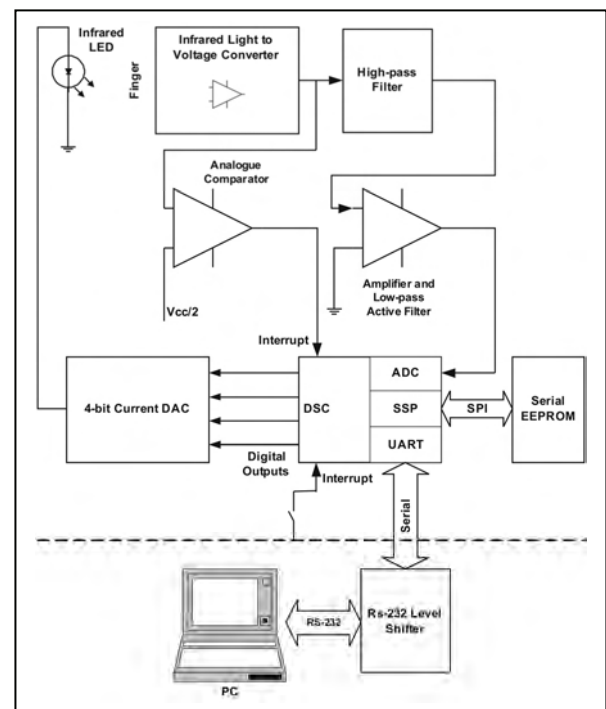


Fig. 1. System structure

¹Yuliyana S. Velchev is with the Faculty of Communications and Communications Technologies, Technical University of Sofia, Address: 8, Kliment Ohridski St. Sofia-1000, BULGARIA, E-mail: julian_velchev@abv.bg

In order to reduce the power consumption the LED is turned-on only in the process of measurement. The duration of this measurement is no more than 20s. The DSC uses SLEEP capability (low power mode). It wakes only on Real Time Clock update, or when the device is connected to the PC.

A serial 4kByte EEPROM with SPI interface is used to store the measured data. All data is in ASCII format, excepting the measured pulse which is recorded in one byte.

III. EXPERIMENTAL RESULTS

Figure 2 shows a chart of the sampled pulse waveform. As can be seen the period measurement can be made by zero-cross detection.

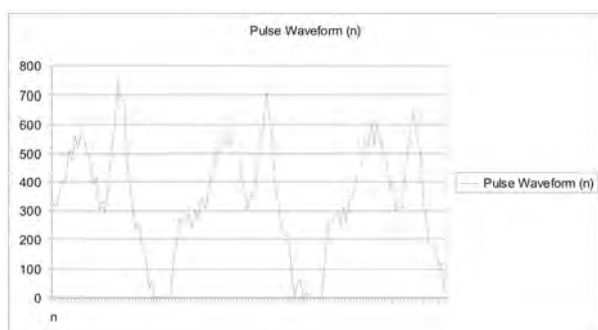


Fig. 2. Pulse waveform

A simple terminal program is used to configure the recorder and to read the recorded data. In figure 3 are shown downloaded sample results of heart rate measurement and recording. First column is year-month-date, the second is time and the third one is the recorded heart rate.

```

65535
2006-08-21      03:18:36  100
2006-08-21      03:18:48   96
2006-08-21      03:19:00   98
2006-08-21      03:19:12  100
2006-08-21      03:19:24   93
2006-08-21      03:19:36   97
2006-08-21      03:19:48   97
2006-08-21      03:20:00   96
2006-08-21      03:20:12  101
END

```

Fig. 3. Sample results of heart rate measurement

IV. CONCLUSION

In this paper a heart rate measurement system is described. As mentioned above, the system is low-cost and has low power consumption. The future work will be to minimize the influence of external light interference. By using DSC with more resources, it will be possible to achieve better results, if the period is measured not directly from the signal, but from previously calculated Auto Correlative Function (ACF). Despite of presented noise the ACF is still periodic with

period matching to the period of the investigated signal. By knowing the position of the absolute maximum of the ACF and finding the position of the second peak, measuring the period won't be difficult.

In addition a synchronous detection method can be very suitable for this system.

In other hand it will be useful to turn this system into pulse oximetry measuring and recording system just by adding a second red LED and red light sensor.

REFERENCES

- [1] D. Dimitrov, "Communication system in medicine", handbook, Sofia, 2005.
- [2] D. Dimitrov, Y. Velchev, "Communication Protocol for Medical Mobile Network", Proceedings of 48-th IWK, TU – Ilmenau, Germany, pp. 55-56, Ilmenau, Germany, 2003.
- [3] D. Dimitrov, D. Vasileva, "One Channel ECG System", Proceedings of 48-th International Scientific Conference of Information, Communication and Energy Systems and Technologies, ICEST '03, pp. 510-512, Sofia, Bulgaria, October 16-18, 2003.
- [4] D. Dimitrov, M. Nikolova, "Reconstruction of Periodical Impulse Sequence", Proceedings of Regular International Conference of Association of Computer Technique of USA on Computer Application – ACMBUL'92, p. 34-1, 34-5, 4-8 October, 1992, Varna, Bulgaria.
- [5] D. Dimitrov, Y. Velchev, "Distance Analysis of ECG", Proceedings of the Technical University-Sofia, Volume 52, p. 69-75, Sofia, Bulgaria, 2003.
- [6] Y. Velchev, Tz. Dimitrova "Wireless Module for Distance Temperature Control", CSICE Conference, Sofia, Bulgaria, October, 2005.
- [7] E. Jovanov, D. Raskovic, R. Hormigo, "Thermistor-Based Breathing Sensor for Circadian Rhythm Evaluation", Biomedical Sciences Instrumentation, Vol. 37, pp. 493-497, 2001.
- [8] E. Jovanov, D. Raskovic, J. Price, A. Moore, J. Chapman, A. Krishnamurthy "Patient Monitoring Using Personal Area Networks of Wireless Intelligent Sensors", Biomedical Sciences Instrumentation, Vol. 37, pp. 373-378, 2001.
- [9] E. Jovanov, A. Milenkovic, S. Basham, D. Clark, D. Kelley, "Reconfigurable Intelligent Sensor for Health Monitoring: A Case Study of Pulse Oximeter Sensor", Proceedings of the 26th Annual International Conference of the IEEE Engineering in Medicine and Biology Society, San Francisco, pp. 4759-4762, September 2004, 2005.

Robust Estimators Based on the Two-Stage Method for Closed-Loop Identification

Nasko R. Atanasov¹

Abstract - This paper discusses closed-loop robust identification using the joint input-output approach in the case of additive output noise with outliers. To calculate robust estimates of unknown parameters, the recursive robust S, H and W algorithms are applied here. Test investigations with simulation data are applied.

Keywords - Closed-loop identification, joint input-output approach, robust GM-estimates, outliers.

I. STATEMENT OF THE PROBLEM

Assume that a control system to be observed is linear and time-invariant with one input $u(k)$, $k=1,2,\dots$ and one output $y(k)$, $k=1,2,\dots$ and given by the equations

$$\begin{aligned} y(k) &= G_o(q, \theta)u(k) + v(k), \\ v(k) &= H_o(q, \varphi)\xi(k), \end{aligned} \quad (1)$$

that consist a process model $G_o(q, \theta)$ and a noise one $H_o(q, \varphi)$.

Here θ and φ are unknown parameter vectors, q is the time-shift operator (i.e., $q^{-1}u(k) = u(k-1)$), the initial signal $\xi(k)$, $k=1,2,\dots$ used to generate unmeasurable noise $v(k)$, $k=1,2,\dots$ is assumed to be statistically independent and stationary with

$$\begin{aligned} E\{\xi(k)\} &= 0, \\ E\{\xi(k)\xi(k+\tau)\} &= \sigma_\xi^2 \delta(\tau). \end{aligned} \quad (2)$$

The input $u(k)$, $k=1,2,\dots$ is given by

$$u(k) = \Psi(k, y_k, u_{k-1}, r(k)), \quad (3)$$

where $y_k = [y(1), \dots, y(k)]$, $u_{k-1} = [u(1), \dots, u(k-1)]$. The reference signal $r(k)$, $k=1,2,\dots$ is a quasi-stationary signal, independent of the stochastic disturbance $v(k)$, $k=1,2,\dots$, and Ψ is a given deterministic function such that the closed-loop system from Eqs. (1) and (2) with the controller $G_r(q, \alpha)$ (see Fig. 1), which is designed for disturbance $v(k)$, $k=1,2,\dots$ by minimizing a quadratic performance function

$$J = \lim_{N \rightarrow \infty} E \left\{ \frac{1}{N} \sum_{k=0}^{N-1} y^2(k) + \rho u^2(k) \right\}, \quad (4)$$

is exponentially stable [2], [6]. Here α is the parameter vector of the controller, the factor $0 < \rho \leq 1$.

The basis of identification is the data set

$$Z^N = \{r(1), \dots, r(N), u(1), \dots, u(N)\}, \quad (5)$$

when the regulator $G_r(q, \alpha)$ is known, and the data set

$$Z^N = \{r(1), \dots, r(N), u(1), \dots, u(N), y(1), \dots, y(N)\}, \quad (6)$$

in the opposite case. The data sets consist of measured observations of the reference signal $r(k)$, $k=1,2,\dots,N$, the input $u(k)$, $k=1,2,\dots,N$ and the noisy output $y(k)$, $k=1,2,\dots,N$.

The aim of the given paper is to investigate robust estimators based on the two-stage method, which belongs to the joint input-output approach, when assumption from Eqs. (2) is not satisfied because of occasionally appearing outliers in an unmeasurable noise signal $v(k)$, $k=1,2,\dots$, acting on the output of the system to be identified.

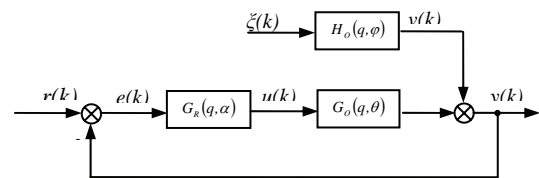


Fig. 1. A closed-loop system to be observed

II. THE TWO-STAGE METHOD FOR THE PREDICTION ERROR MODEL

The input signal $u(k)$ and the output signal $y(k)$, $k=1,2,\dots$ of the closed-loop system given in Fig. 1 are determined according to

$$u(k) = [r(k) - y(k)]G_r(q, \alpha) \quad (7)$$

and

$$y(k) = G_o(q, \theta)u(k) + H_o(q, \varphi)\xi(k), \quad (8)$$

respectively. By combining Eqs. (7) and (8) are obtained the closed-loop relations

$$y(k) = \Phi_o(q, \beta)G_o(q)G_r(q)r(k) + \Phi_o(q, \beta)H_o(q)\xi(k), \quad (9)$$

$$u(k) = W_o(q, \beta)G_r(q)r(k) - W_o(q, \beta)G_r(q)H_o(q)\xi(k), \quad (10)$$

with the output and input sensitivity functions

$$\Phi_o(q, \beta) = [1 + G_o(q, \theta)G_r(q, \alpha)]^{-1}, \quad (11)$$

$$W_o(q, \beta) = [1 + G_r(q, \alpha)G_o(q, \theta)]^{-1}, \quad (12)$$

correspondingly. Rewriting Eq. (10) in such a form

$$u(k) = W_o(q, \beta)G_r(q, \alpha)[r(k) - H_o(q, \varphi)\xi(k)], \quad (13)$$

can get

$$r(k) = C(q, c)u(k) + H_o(q, \varphi)\xi(k), \quad (14)$$

where

$$C(q, c) = W_o^{-1}(q, \beta)G_r^{-1}(q, \alpha) = G_r^{-1}(q, \alpha) + G_o(q, \theta). \quad (15)$$

The system, corresponding to Eq. (14), is presented in Fig. 2 [6].

Introducing

¹ Nasko R. Atanasov is with the Faculty of Computer System and Automation, Technical University, 1 "Studentska", 9010 Varna, Bulgaria, E-mail: nratanasov@yahoo.com.

$$\begin{aligned} G_R(q, \alpha) &= \frac{g_0 + g_1 q^{-1} + \dots + g_v q^{-v}}{r_0 + r_1 q^{-1} + \dots + r_v q^{-v}}, \\ G_O(q, \theta) &= \frac{b_0 + b_1 q^{-1} + \dots + b_m q^{-m}}{1 + a_1 q^{-1} + \dots + a_m q^{-m}}, \end{aligned} \quad (16)$$

Eq. (15) can be rewritten in such an extended form

$$\begin{aligned} C(q, c) &= \frac{r_0 + r_1 q^{-1} + \dots + r_v q^{-v}}{g_0 + g_1 q^{-1} + \dots + g_v q^{-v}} + \frac{b_0 + b_1 q^{-1} + \dots + b_m q^{-m}}{1 + a_1 q^{-1} + \dots + a_m q^{-m}} = \\ &= \frac{p_0 + p_1 q^{-1} + \dots + p_n q^{-n}}{d_0 + d_1 q^{-1} + \dots + d_w q^{-w}} = \frac{P(q, p)}{D(q, d)}. \end{aligned} \quad (17)$$

The estimate

$$\hat{c}(N) = [\hat{d}_0(N), \hat{d}_1(N), \dots, \hat{d}_w(N), \hat{p}_0(N), \hat{p}_1(N), \dots, \hat{p}_n(N)]^T \quad (18)$$

of the vector of parameters of system with the transfer function $C(q, c)$, shown in Fig. 3, could be found as follows

$$\hat{c}_N = \arg \min_{c \in \Omega} Q_N(c), \quad (19)$$

by minimizing the criterion

$$Q_N(c) = \frac{1}{N} \sum_{k=1}^N \varepsilon^2(k, c). \quad (20)$$

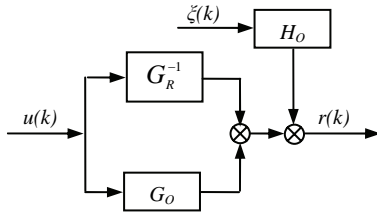


Fig.2 The block scheme of the system, when the regulator is known

Here

$$\varepsilon(k, c) = D(q, d)r(k) - P(q, p)u(k) \quad (21)$$

is a prediction error, Ω is the area of permissible parameter values, restricted by the stability conditions of the respective linear difference equation.

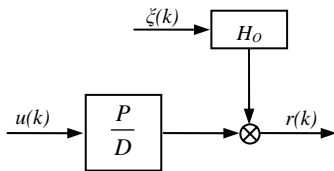


Fig.3 The block scheme of the system, when the regulator is unknown

Let introduce the optimal solution

$$c^* = [d^*, p^*]^T = [d_0^*, d_1^*, \dots, d_w^*, p_0^*, p_1^*, \dots, p_n^*]^T, \quad (22)$$

consists of the true values of the parameters. Then

$$\varepsilon(k, c^*) = D(q, d^*)r(k) - P(q, p^*)u(k) = \xi(k) \quad (23)$$

and

$$Q_N(c^*) = \frac{1}{N} \sum_{k=1}^N \varepsilon^2(k, c^*) = \sigma_\xi^2, \quad (24)$$

respectively, if and only if

$$H_O(q, \varphi) = D^{-1}(q, d^*). \quad (25)$$

In such a case, the prediction error from Eq. (23) has zero mean $E\{\varepsilon(k, c^*)\} = 0$ and its correlation function could be expressed by the formula

$$K_{\varepsilon\varepsilon}(\tau) = \sigma_\xi^2 \delta(\tau), \quad \delta(\tau) = \begin{cases} 1 & \text{npu } \tau = 0 \\ 0 & \text{npu } |\tau| \neq 0 \end{cases}. \quad (26)$$

It follows, that the prediction error model gives the minimal value of criterion Eq. (24) for $c = c^*$ when $H_O(q, \varphi)$ is of the form Eq. (25). It also means that the stochastic disturbance $v(k)$, $k=1, 2, \dots$ is an autoregressive (AR) process that is generated by filtering a white noise sequence $\xi(k)$, $k=1, 2, \dots$ and its correlation function could be expressed by the formula by a filter of the form Eq. (25) [6].

III. THE RECURSIVE ESTIMATION PROCEDURE

For the estimation of unknown parameters, the ordinary prediction error method, based on the RLS of the form

$$\hat{c}(k) = \hat{c}(k-1) + \frac{P(k-1)z(k)}{1 + z^T(k)P(k-1)z(k)} \hat{\varepsilon}(k), \quad (27)$$

$$P(k) = P(k-1) - \frac{P(k-1)z(k)z^T(k)P(k-1)}{1 + z^T(k)P(k-1)z(k)}, \quad (28)$$

could be used with the vector of observations

$$z^T(k) = [-r(k-1), \dots, -r(k-w), u(k-1), \dots, u(k-n)] \quad (29)$$

and some initial values of the vector $\hat{c}(0)$ and covariance matrix $P(0)$.

Here

$$\hat{\varepsilon}(k) = r(k) - z^T(k)\hat{c}(k-1) \quad (30)$$

is the current k -th value of the prediction error and $\hat{c}(k)$ is a current estimate of the parameter vector

$$c = [d_1, d_2, \dots, d_w, p_0, p_1, \dots, p_n]^T, \quad (31)$$

assuming that $d_0 = 1$. The next step is to calculate the current k -th value of the auxiliary input according to the formula

$$\hat{u}(k) = C^{-1}(q, \hat{c}(k))r(k), \quad (32)$$

assuming that $C(q, \hat{c}(k))$ is inversely stable on each k -th iteration. Then the current estimates of the parameters vector

$$\theta = [a_1, a_2, \dots, a_m, b_0, b_1, \dots, b_m]^T \quad (33)$$

could be determined by the RLS with the vector of observations

$$\tilde{z}^T(k) = [-y(k-1), \dots, -y(k-m), \hat{u}(k-1), \dots, \hat{u}(k-m)] \quad (34)$$

and a current k -th value of the prediction error

$$\hat{\varepsilon}_1(k) = y(k) - \tilde{z}^T(k)\hat{\theta}(k-1). \quad (35)$$

In the case of the known regulator the system is acting according to the scheme shown in the Fig. 2. Then the estimation procedure is completely simplified, because the problem is only in determining the parameters $\theta = [a_1, a_2, \dots, a_m, b_0, b_1, \dots, b_m]^T$, using the RLS with the vector of observations

$$\tilde{z}^T(k) = [-r^*(k-1), \dots, -r^*(k-m), u(k-1), \dots, u(k-m)], \quad (36)$$

where

$$r^*(k) = r(k) - G_R^{-1}(q, \alpha)u(k) \quad (37)$$

and a current k -th value of the prediction error

$$\hat{\varepsilon}_2(k) = r^*(k) - \bar{z}^T(k)\hat{\theta}(k-1). \quad (38)$$

IV. THE TWO-STAGE METHOD IN A PRESENCE OF OUTLIERS IN OBSERVATIONS

Assume now that the white noise $\xi(k)$, $k=1,2,\dots$ really is a sequence of independent identically distributed variables with an ε_f -contaminated distribution of the form [3]

$$f(\xi(k)) = (1 - \varepsilon_f)N(0, \sigma_\mu^2) + \varepsilon_f N(0, \sigma_\zeta^2) \quad (39)$$

and the variance

$$\sigma_\xi^2 = (1 - \varepsilon_f)\sigma_\mu^2 + \varepsilon_f\sigma_\zeta^2. \quad (40)$$

Here $f(\xi(k))$ is the probability density distribution of the sequence $\xi(k)$, $k=1,2,\dots$;

$$\xi(k) = (1 - \gamma_k)\mu_k + \gamma_k\zeta_k \quad (41)$$

is the value of $\xi(k)$, $k=1,2,\dots$ at a time moment k ; γ is a random variable, taking values 0 or 1 with probabilities $p(\gamma_k = 0) = 1 - \varepsilon_f$, $p(\gamma_k = 1) = \varepsilon_f$; μ_k and ζ_k are sequences of independent Gaussian variables with zero means and variances $\sigma_\mu^2, \sigma_\zeta^2$, respectively; besides $\sigma_\mu < \sigma_\zeta$; $0 \leq \varepsilon_f \leq 1$ is the unknown fraction of contamination [2].

Given the model Eq. (14) and measured data Eq. (5) and assuming that $\xi(k)$, $k=1,2,\dots$ is a process of the form Eqs. (39), (40) and (41), is determined the robust M-estimate, based on prediction error Eq. (21), of the parameter vector Eq. (31) by minimizing

$$\hat{c}_N = \arg \min_{c \in D_M} \frac{1}{N} \sum_{k=1}^N \rho \left[\frac{\varepsilon(k, \theta, \alpha, \varphi)}{s} \right], \quad (42)$$

or by solving the equation in the vector form

$$\sum_{k=1}^N z(k) \psi \left(\frac{r(k) - z^T(k)\hat{c}(k-1)}{s} \right) = 0. \quad (43)$$

Here \hat{c}_N is the estimate, determined by processing N pairs of the reference signal and input samples; s is the robust scale estimate of prediction errors; ρ is a symmetric, positive-definite contrast function with unique minimum at zero and is chosen to be less increasing than square; the influence function $\psi = \rho'$ measures the influence of data on the value of the parameter estimate [1].

It is known that in both such cases, i.e. $\varepsilon_f \neq 0$ and $H_o(q, \varphi) = D^{-1}(q, d)$ [5], current M-estimate of unknown parameters can be calculated using three robust techniques:

- the S-algorithm

$$\hat{c}(k) = \hat{c}(k-1) + \frac{P(k-1)z(k)}{\{\psi'[\alpha(k)]\}^{-1} + z^T(k)P(k-1)z(k)} \beta(k), \quad (44)$$

$$P(k) = P(k-1) - \frac{P(k-1)z(k)z^T(k)P(k-1)}{\{\psi'[\alpha(k)]\}^{-1} + z^T(k)P(k-1)z(k)}, \quad (45)$$

If $\psi'(x) = 0$ than $\psi'(x)$ have to be replaced with $x^{-1}\psi(x)$.

- the H-algorithm

$$\hat{c}(k) = \hat{c}(k-1) + \frac{P(k-1)z(k)}{1 + z^T(k)P(k-1)z(k)} \beta(k), \quad (46)$$

$$P(k) = P(k-1) - \frac{P(k-1)z(k)z^T(k)P(k-1)}{1 + z^T(k)P(k-1)z(k)}, \quad (47)$$

- the W-algorithm

$$\hat{c}(k) = \hat{c}(k-1) + \frac{P(k-1)z(k)}{[w(k)]^{-1} + z^T(k)P(k-1)z(k)} s\alpha(k), \quad (48)$$

$$P(k) = P(k-1) - \frac{P(k-1)z(k)z^T(k)P(k-1)}{[w(k)]^{-1} + z^T(k)P(k-1)z(k)}. \quad (49)$$

On the base on the prediction error from Eq. (30) in the last equations are introduced symbols

$$\alpha(k) = \frac{\hat{\varepsilon}(k)}{s}; \quad (50)$$

$$\beta(k) = s\psi[\alpha(k)]; \quad (51)$$

$$w(k) = \begin{cases} \psi[\alpha(k)]/\alpha(k) & \text{if } \alpha(k) \neq 0 \\ 1 & \text{if } \alpha(k) = 0 \end{cases}. \quad (52)$$

The S-algorithm represents a version of the algorithm proposed by Polyak and Cypkin for an on-line robust identification of parameters of the linear dynamic model [5], [6]. The robusting of the ordinary RLS follows by substituting the “winsorization” step of the residuals in Eq. (27) and by modification in computing of the covariance matrix in Eqs. (27) and (28). The recursive H-algorithm is obtained only by inserting the winsorization” step in Eq. (27). The W-algorithm is obtained by inserting different weights from Eq. (52) in respect to the influence function into the already existing ordinary RLS.

The mostly used influence function is [3]

$$\psi(x) = \begin{cases} x, & |x| \leq c_H \\ c_H \operatorname{sign} x & |x| > c_H \end{cases}, \quad (53)$$

with given robust factor $1 < c_H < 2$. In this case modifications in computing of the covariance matrix are equivalent for S-algorithm and W-algorithm. Consequently, the S-algorithm combines robust performances of the other two algorithms.

These algorithms are based on robust M-estimators of Huber which reduce influence of observations only if corresponding residuals are big. GM-estimators downweight “vertical” outliers and “leverage points” [1], [4].

For defining GM estimators in this paper are changed Eqs. (51) and (52) with

$$\beta(k) = s w_{z1} \psi \left[\frac{\alpha(k)}{w_{z2}} \right], \quad (54)$$

$$w(k) = \begin{cases} w_{z1} \psi[\alpha(k)/w_{z2}] / [\alpha(k)/w_{z2}] & \text{if } \alpha(k) \neq 0 \\ w_{z1} & \text{if } \alpha(k) = 0 \end{cases}, \quad (55)$$

correspondingly. Here w_{z1} and w_{z2} are additional weights of observations to one’s choice estimator’s type:

- Huber’s M-estimator (MHUB)

$$w_{z1} = w_{z2} = 1; \quad (56)$$

- Mallows' GM-estimator (GMM)

$$\begin{cases} w_{z1} = w_z[h(k)], \\ w_{z2} = 1 \end{cases}; \quad (57)$$

- Schweppe's GM-estimator (GMS)

$$w_{z1} = w_{z2} = w_z[h(k)]. \quad (58)$$

Here $w_z[h(k)] = \sqrt{1-h(k)}$ and $h(k)$ is k -th diagonal element of the hat matrix H [1]

$$H = Z(Z^T Z)^{-1} Z^T. \quad (59)$$

The current k -th diagonal element can be calculated according to the formula [1]

$$h(k) = z^T(k)P(k)z(k). \quad (60)$$

There is the prediction error based on the estimates from the previous iteration in Eqs. (27) and (50). The prediction accuracy can be increased if the prediction error based on the estimates from the new iteration is used

$$\hat{\varepsilon}_{new}(k) = r(k) - z^T(k)\hat{c}(k), \quad (61)$$

The current k -th value of this error can be calculated according to the formula [1]

$$\hat{\varepsilon}_{new}(k) = [1 - h(k)]\hat{\varepsilon}(k). \quad (62)$$

V. NUMERICAL SIMULATION

The closed-loop system to be simulated is described by linear difference equations of the form [6]

$$\begin{cases} y(k) = 0.75u(k-1) + 0.985y(k-1) + v(k) \\ u(k) = e(k) + 0.1005u(k-1) - 0.1016u(k-2) \\ v(k) = 0.985v(k-1) + \xi(k) \\ e(k) = r(k) - y(k) \end{cases}. \quad (63)$$

where $\xi(k)$, $k=1,2,\dots$ is a process described by Eqs. (39), (40) and (41).

Eqs. (63) determine model structure and true values of the parameters to be estimated on the first and second stage

$$C(q,c) = \frac{1 - 0.3355q^{-1} + 0.2006q^{-2} - 0.1001q^{-3}}{1 - 0.985q^{-1}}, \quad (64)$$

$$G_0(q,\theta) = \frac{0.75q^{-1}}{1 - 0.985q^{-1}}, \quad (65)$$

correspondingly.

The sequences, including that kind of noise $\xi(k)$, $k=1,2,\dots,200$ with different parameters, are generated using MATLAB. The respective experiments are shortly described by abbreviation $J_{i1;i2;i3}$. Here subscripts denote: i_1 is the noise

contamination part ε_f in Eq. (39) in [%]; $i_2 = \frac{\sigma_\xi}{\sigma_\mu}$ in Eq. (40);

$i_3 = \frac{\sigma_\xi}{\sigma_{y_0}}$ in [%] (y_0 is y in the absence of additive noise).

The basis of identification are data sets Eq. (6) with $N=200$. The first 20 pairs of signals are processed by non recursive robust estimators in order to obtain the initial off-line estimates of the vectors c and θ .

Afterwards, the recursive estimation is performed. Four estimators are applied: RLS (1); Huber's M-estimator based on S-algorithm (2); Mallows' GM-estimator based on S-algorithm (3); Schweppe's GM-estimator based on S-algorithm (4).

Bar-diagrams of relative mean-squared errors for the estimated parameters relative to the true parameters of the last iteration are shown at the Figs. 4 and 5.

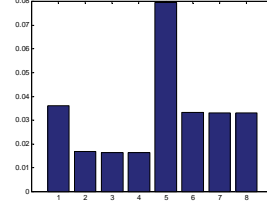


Fig. 4. Bar-diagram ($J_{5;10;10}$)

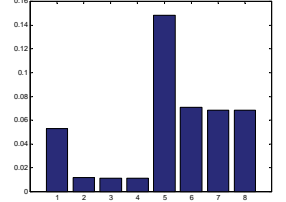


Fig. 5. Bar-diagram ($J_{10;10;10}$)

First four columns correspond with estimates of parameters of $C(q,c)$ shown in Eq. (64) as the number of described above estimators correspond with the number of column. Second four columns correspond with estimates of parameters of $G_0(q,\theta)$ shown in Eq. (65) as the number of described above estimators are retained from 5 to 8.

VI. CONCLUSION

The outliers have a strong influence over the quality of parameter estimates in closed-loop identification.

The joint input-output approach regards the input and output both together as the output of some augmented system excited by some extra input or a set-point signal and noise.

In the case of an additive correlated noise with outliers, the accuracy of all represent robust estimators is bigger than the RLS accuracy.

The S-algorithm combines robust performances of the H and W algorithms if the influence function is Huber's one.

When the contamination increases the accuracy of GM-estimators is bigger than the accuracy of M-estimators, because of a presentation of well known from the regression theory leverage points.

REFERENCES

- [1] Н. Атанасов, Робастно оценяване в системи за автоматично управление, Дисертация за получаване на ОНС "доктор", Варна, 2005.
- [2] Н. Атанасов, Д. Генов и Р. Пупейкис, Робастни М- и GM-оценители при косвена идентификация в затворен контур за управление, „А&Г'06”, София, 2006.
- [3] П. Хьюбер, Робастность в статистике, Москва, Мир, 1984.
- [4] А. Лукас, A brief introduction to robust statistics, www.staff.feweb.vu.nl/alucas/thesis.
- [5] J. Novovicova, Recursive computation of M-estimates for the parameters of the linear dynamical systems, Problems of Control and Information Theory, 16(1), 4-59, 1987.
- [6] R. Pupeikis, On system identification using the closed-loop observations, INFORMATICA, 2001, Vol. 12, №3, 439-454, Vilnius.

Scalable Modular Control Architecture For Walking Machines

Mladen M. Milushev¹ Nikolay V. Krantov² and Volker Zerbe³

Abstract – The development of a new generation of flexible robots is based on implementing principle movements as observed in nature, i.e. peristaltic ones or such featured by insects. The creation of a modular architecture for control and processing of information related to the mentioned robot type, which in the viewed case means the creation of a basic module, is the point of the presented paper. Final objective of the suggested approach is the building of architecture by way of generating a multitude of instances of the basic module and completing an interaction among them in higher level of hierarchy in order to secure a rapid adaptation to various configurations of independent multistage structures for the robot's actuating.

Keywords – mechatronics, mechatronic system, biomechanics, peristaltic, actuator, sensor, functional decomposition, programmable logical devices, VHDL model, schematic design entry, Y-diagram

I. INTRODUCTION

In recent years intensive research and development in the field of moving robots are heavily influenced by biological species. A persisting tendency towards the development of crawling (Fig.1) and walking robots (Fig.2) is on the way.

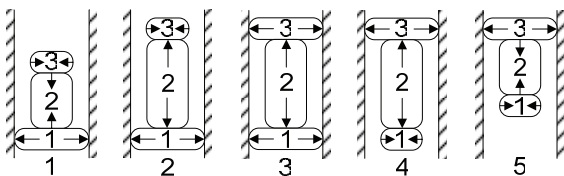


Fig. 1 Movement principle which is constructed from three segments - two holding (1 and 3) and one pushing (2)

Initially for setting robots into motion predominantly electrical motors (converted from the existing robotic engineering) were used. They transferred moments over gears, belts and levers. Disadvantage of such actuators is the lack of passive air-cushioning ability as found in biological muscles. Consequently, researches lean more and more towards fluidic muscles performing peristaltic movements – shortening and extension – mirroring those of living organisms.

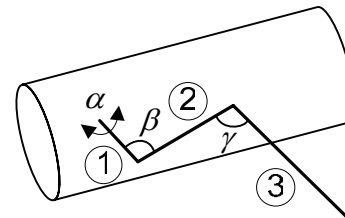


Fig. 2 Six feet structure with three joints

II. CONTROL ARCHITECTURE CHOICE

Depend upon the way they are presented throughout scientific literary sources [1],[2],[3], control concepts for mobile robots can be classified as:

- Analytical description;
- Rule-based control
- Behavior-oriented control
- Neural network-based control

Currently the approach towards mobile robots with behavior-oriented control is domineering. In turn behavior-oriented control concepts can be represented through reactive, deliberative or hybrid control. *Reactive* control systems put direct connection between sensor information and commands to the actuators, which allow robots to react immediately to environment changes. With *deliberative* systems the robot is capable of using the complete existing and current sensor information to plan its behavior, which is a rather complex one. *Hybrid* systems attempt to unite the benefits of both reactive and deliberate systems.

The hereby-suggested architecture (Fig.3) for a mobile robot control roots in the hybrid principle, which means to define the elementary behavior types along with the ways of combining them in order to achieve complex control architecture. The latter consists of four levels: joint/segment, leg/module, body and moving robot. Each level contents intelligent units for interpretation of sensor information and for providing backup actions to the upper level.

The least functional unit is the joint/segment. A control task on this level involves the managing of the pressure and force of the actuator working in antagonistic mode. Since the only alternating variable in the control loop is the fluid flowing in and out of the muscle, the valve takes up 3 positions: fill in-close up- let out. Integrating the reflexive entity on that level proves to be purposeful in regard of the contact force on the surface.

¹Mladen S. Milushev is from the Faculty of Mechanical Engineering, TU-Sofia, Kliment Ohridsky blvd. 8, 1756 Sofia, Bulgaria, e-mail: mcm@tu-sofia.bg

²Nikolay V. Krantov is from the Faculty of Mechanical Engineering, TU-Sofia, Kliment Ohridsky blvd. 8, 1756 Sofia, Bulgaria, e-mail: n_krantov@tu-sofia.bg

³Volker Zerbe is from the Faculty of Informatics and Automation, TU-Ilmenau, D-98684 Ilmenau, Germany, e-mail: volker.zerbe@tu-ilmenau.de

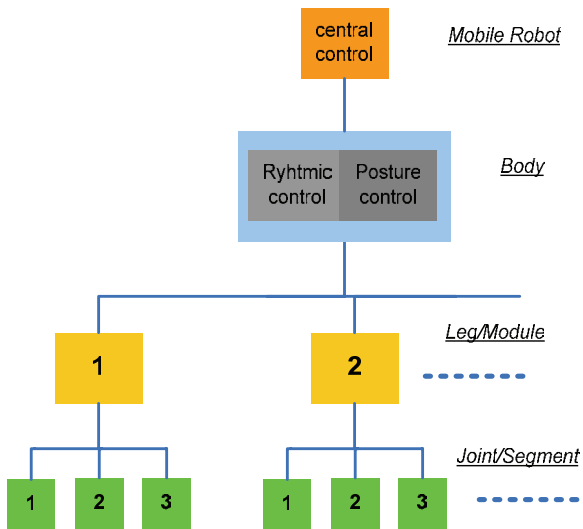


Fig. 3 Six feet structure with three joints

Next functional level is the leg/module that displays a combination of the three joints/segments. Control solutions here are focused on the originating and proceeding of information concerning the leg/module along with providing backup actions for the higher level and thus allowing the leg/module to be viewed as an independent entity. The accompanying integration of a reflexive unit would be appropriate with reference to the force of contact or collision alongside the movement direction. At this point proceeds the regulation of a communication link between the controllers for the leg and those for the body.

The body level is in charge of coordinating the legs in a way granting a static stability of different walking modes, e. g. tripod or tetrapod. Depending on the walk velocity the phase and speed for each of the legs are chosen (Rhythmic Control). Additional function on this level is the control of body alterations (Posture Control). All data required to control horizontal changes and body velocities are calculated using the valid joints/segments angles dimensions or are valued on base of additional body sensor information.

The moving-robot-level performs the highest level of moving systems control. It accounts for the motion's trajectory set up and for body changes as the main control algorithm – coordinating sub-levels. The moving-robot-level should provide for a data exchange in order to:

- Obtain commands, e. g. move to a premeditated position through detection by the own sensors, or ;
- Communicate data about the robot's status quo.

III. HARDWARE PLATFORM CHOICE

There are many approaches for implementation of digital systems design: microprocessor and microcontroller based (or software), dedicated ASICs and FPGA-based solutions. Maximum flexibility can be reached with software specifications of the full system; however for highly parallel systems microprocessor based solutions are not suitable. Dedicated ASICs is the best solution for achieving good performance but prototype development makes no sense for

using ASICs. At the same time such an approach dramatically reduces the adaptability of the system. FPGA based systems provide both higher performance for parallel computation than software solutions, enhanced flexibility and low development cost compared to ASICs. Moreover it is possible to reduce execution time by implementing intensive computational parts of the algorithm in hardware.

Hardware implementation of electronic systems requires the extensive use of verification stages throughout the design process to guarantee correct functionality of the final product. The use of high-level VHDL for modeling and simulation is especially appealing since it provides a formal description of the system and allows the use of specific description styles to cover the different abstraction levels used in the design (architectural, algorithmic, RTL and logic level as is shown in the wide-spread Y-diagram).

IV. JOINT BLOCK ARCHITECTURE

In the present paper the whole logic design is hierarchical which means that the top-level design file is a VHDL based including component instances that refer to schematic based one.

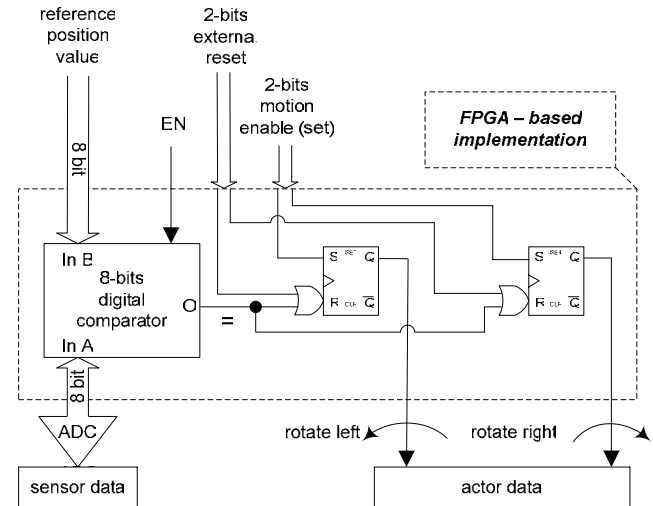


Fig. 4 Block diagram for implementing a joint control

Register transfer level architecture of the joint block follows the logic shown on the figure 4. The main unit in the design is an 8-bits digital comparator and two RS Flip-Flops. The comparator gives us a relation between the predefined value which is set up externally and the current position of the joint achieved from external sensor also with 8 bits of resolution. Equation event between two values activate an output of the comparator which is used in conjunction with two external signals to act as reset for flip-flops. For setting purposes of the logic blocks is used also a 2 bits external signal for motion control. Outputs of the flip-flops are used respectively for enable the action of external actors for left or right rotation movement of the joint as can be seen from the figure. There is included a global enable signal for the digital comparator which enable the entire joint block. So until the current position values of joint reach the predefined position value the actors for rotation and linear movement are active.

V. IMPLEMENTATION

For development was used integrated synthesis environment (ISE) WebPACK which is the ideal solution for FPGA and CPLD design. It offers HDL synthesis and simulation, implementation, device fitting, and JTAG programming. This ISE allows convenient productivity by providing a design solution that is always up-to-date and provides features and functionality at no cost.

The digital architecture of the joint control was entered by using schematic editor which is integrated into ISE. With ready to use library elements translation of the control idea into synthesizable form is very straight forward process similar to conventional CAD tools such as Protel and OrCAD. The ready joint architecture is shown on the following figure.

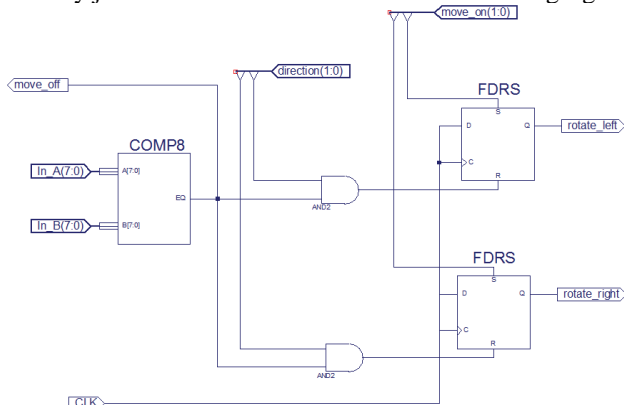


Fig. 5 Joint architecture schematic

Instantiating of the joint module at higher level of the logic design is possible through the VHDL source code shown on the figure 6.

```

34 COMPONENT Joint
35   GENERIC(width : natural := 8);
36   PORT( reset_ext : IN STD_LOGIC_VECTOR (1 DOWNTO 0);
37         move_en : IN STD_LOGIC_VECTOR (1 DOWNTO 0);
38         GCLK : IN STD_LOGIC;
39         angle_control : OUT STD_LOGIC;
40         position_control : OUT STD_LOGIC;
41         In_A : IN STD_LOGIC_VECTOR (width-1 DOWNTO 0);
42         In_B : IN STD_LOGIC_VECTOR (width-1 DOWNTO 0);
43   END COMPONENT;
44
45 Joint_1: Joint PORT MAP(
46   reset_ext => ,
47   move_en => ,
48   GCLK => ,
49   angle_control => ,
50   position_control => ,
51   In_A => ,
52   In_B =>
53 );

```

Fig. 6 Piece of code identifying joint instance

Adding component declaration at the beginning of the top architecture gives us ability to instantiate this component in the body of the architecture infinite times. Also with generics which are especially powerful where there is a reuse policy in mind, we can easily create parameterized in width ADC interface depending on the one in use.

As final step there was examined simulation of the described system using third-party simulator from Cadence – ModelSIM (Fig. 7). The results show generation of control signals for rotating at two directions as was mentioned earlier.



Fig. 7 Logical design simulation

VI. CONCLUSION

The presented paper offers a structure intended at significant enhancement in the modularity of control for mobile robots, which use the principle of peristaltic motion through antagonistically functioning muscles. The suggested reflexive control mechanisms can be applied to overcome a wide range of obstacles without modelling the latter. The described reflexes can be considered as a first-time application in those systems. The system opens a possibility to widen the presence of reflexes during experiments, to combine them on different levels with reflex chains. For that, types of elementary behavior modes have to be defined as well as models for their combination.

There was shown the full top-down design cycle for implementing digital behavior. Using schematic entry at the lower level is very straightforward approach to describe basic functionality. VHDL at higher level allow flexibility and adaptability of the full body system. Description language also minimizes time for verification and post-processing stages and reduces significantly implementing of fully functional logic system. Trade-off between price and achieved functionality is obvious.

ACKNOWLEDGEMENT

Every research this paper is accounting for has been done under the assignment of Contract BY – TH – 201/2006 entitled “Research of a Modular Architecture for the Control of Mechatronic Elastic Multi-Link Devices”

REFERENCES

- [1] O. Matsumoto, W. Ilg, K. Berns and R. Dillmann. Dynamically stable control of the fourleggedwalking machine BISAM in trot motion using foot force sensors. In proceedings of the International Conference of Intelligent Autonomous Systems (IAS 6), p. 301-306. Venice, July 2000
- [2] H. Miura and I. Shimoyama. Dynamic Walking of a biped, International Journal of Robotics Research, 3(2):60-74, 1984
- [3] Marc H. Raibert, Legged Robots That Balance. MIT Press Cambridge, MA, 1986
- [4] M. Vukobratovic, B. Borovac, D. Surla and D. Stokic. Biped Locomotion. Springer-Verlag, Heidelberg, Berlin, New York, 1990
- [5] Armstrong J. R., F. G. Gray: "Structured Logic Design with VHDL", Prentice Hall, Englewood Cliffs, 1993
- [6] Selz, M., "Untersuchungen zur synthesesgerechten Verhaltensbeschreibung mit VHDL", Dissertation am LRS, Universität Erlangen-Nürnberg, 1994
- [7] Burriel, R., "Industrial Use of VHDL in ASIC-Design", EURO-VHDL, Hamburg, 1992
- [8] Darringer, J., F. Ramming, "Computer Hardware Description Languages and their Applications", North Holland, Amsterdam, 1990D
- [9] Cohen, B., "VHDL coding styles and methodologies", Second. Boston, MA: Kluwer Academic Publishers, 1999. – ISBN 0-7923-8474-1

This page intentionally left blank.

Evaluation of Fluidic Muscles for a Walking Machine Driver

Mladen S. Milushev¹ Dimitar I. Diakov²,
Vania K. Georgieva³ and Nenad T. Pavlovic⁴

Abstract – The paper outlines the research on and choice of pneumatic muscles for setting walking robots in motion. Typical for walking robots is the need for appropriate correlation between weight and performance power. Presented are the results from simulation and experimental investigations of pneumatic muscles developed by the FESTO Company. A choice based on pre-given parameters for the creation of leg prototypes for a 6-leg-robot is made. In order to reduce weight and meet requirements two muscle types are investigated. Shown are the simulation and experimental investigations.

Keywords - walking robots, actors, fluid muscles, mechatronics.

I. INTRODUCTION

Most research works described in the literature and dealing with walking mobile robots use electric motors as drivers. In recent years efforts in the field of designing such robots are focused on achieving a maximal proximity with the biomechanics of living species. In literature, 3 kinds of artificial muscles have been described: electrochemical, fluid [3] and mechanical [4]. Many researches dealing with biologically motivated robots are based on the *Carausius Morosus* (stick insect). Efforts are aimed at a maximal resemblance with the nature's model. Presently the application of fluid muscles provides for achieving elastics similar to that of biological muscles and power matching the one of electric drivers. Further, it allows the setting of a configuration whose geometry and proportions are in conformity with the natural specimen and in favor of achieving a maximum reproduction. These ideas are implied in order to create the model of a walking mobile robot driven by fluid muscles.

II. MODEL DESCRIPTION

During the model's development and since fluid muscles

¹Mladen S. Milushev – Technical University of Sofia, Kl. Ohridski Bld., 8, 1000 Sofia, Bulgaria, E-mail: mcm@tu-sofia.bg

²Dimitar I. Diakov – Technical University of Sofia, Kl. Ohridski Bld., 8, 1000 Sofia, Bulgaria, E-mail: diakov@tu-sofia.bg

³Vania K. Georgieva – Technical University Sofia, Kl. Ohridski Bld., 8, 1000 Sofia, Bulgaria, E-mail: vgeorgieva@tu-sofia.bg

⁴Nenad T. Pavlovic – University of Nis, Mechanical Engineering Faculty, Aleksandra Medvedeva 14, 18000 Niš, Serbia and Montenegro, E-mail: pnenad@masfak.ni.ac.yu

can generate only one-dimensional forces, for the motioning of one segment were used two muscles, following the principal of antagonism – the force of the concentric contraction (constricting) always opposes the force of the eccentric contraction (extension). While a muscle contracts and rotates the joint, the other expands and thus the necessary position of the segment is settled. The leg-model created in conformity with the above principle is built of three segments (Fig. 1).

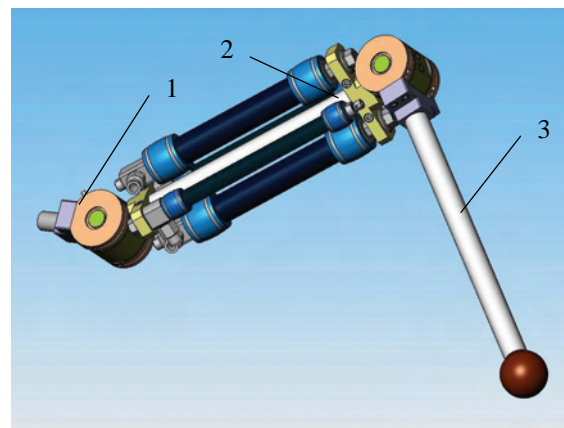


Fig.1 Model leg for a six-legged mobile robot

Based on afore planned weight and geometrical parameters, following parameters are determined: 2 – maximal load = 600N and step $S = 13$ mm, while for segments 1 and 3 the maximum load = 210N, the step $S = 13$ mm.

III. SETTING THE PARAMETERS FOR THE FLUID MUSCLE

In order to define sizes for the pneumatic muscles, which would satisfy the above mentioned requirements the simulation program developed by FESTO and known as MuscleSim-2.0.1.6. is applied.

The first task of the simulation was to fix a minimal size for the muscle under provision of the necessary load and step. For this it was purposeful to use the following muscle types: DMSP 20 for segment 2 and DMSP 10 for segments 1 and 3.

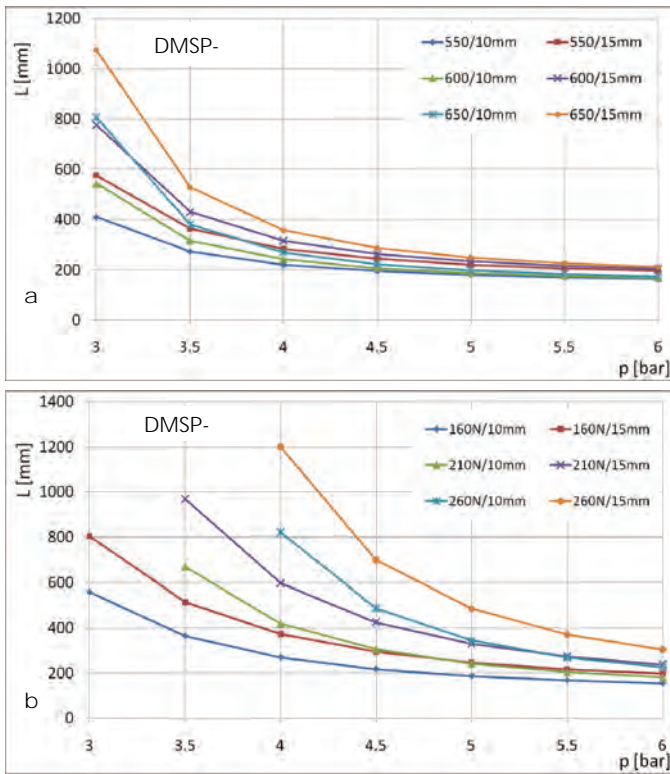


Fig. 2 Simulation results with FESTO –MuscleSim-2.0.1. a- muscle type DMSP 20, b-muscle type DMSP 10.

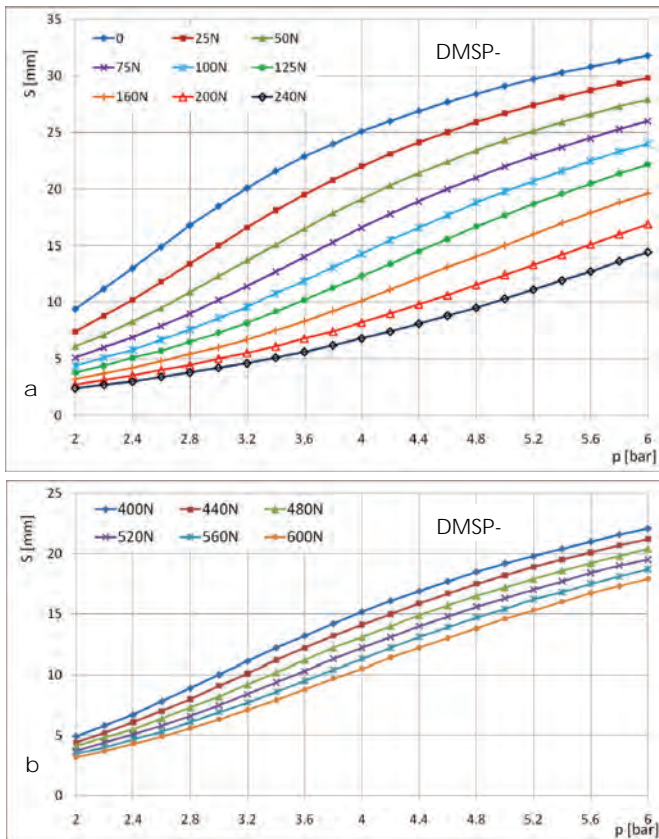


Fig. 3 Simulation results with FESTO –MuscleSim-2.0.1. a-muscle type DMSP 10, b-muscle type DMSP 20.

The results obtained for both muscle types can be seen on Fig. 2. From the curves describing muscle types DMSP 20 (Fig.2a) and DMSP 10 (Fig. 2b) becomes obvious that in the case of work pressures ranging from 4 to 6 bar the optimal length L is between 200 and 250 mm.

Based on the obtained results and in accordance with the fixed proportion the muscles chosen to bring the three segments in motion have a length $L = 210$ mm.

With the second task a definition of the working range and the motion reserves of the selected muscles aligned with the given loads and pressures were sought. The preformed simulation studied the case of a constantly charged muscle, which functioning mode came at closest to the principle of the antagonistic muscle couple. During research the pressure was set at $p = 2 \dots 6$ bar and loads were in the range from 0 to 240N for muscle DMSP 10 (Fig. 3a) and from 400 to 600N for muscle DMSP 20 (Fig. 3b). The loads for muscle DMSP 10 start at “zero” in order to make a comparison with the experimental research. The resulting graphs prove that the chosen muscles cover the intended step of 13 mm within the zone of working loads and pressures.



Fig. 4 Experimental test-rig

IV. EXPERIMENTAL RESEARCH

To validate the muscles parameters achieved through simulation an experimental research was conducted. The practical test-rig is shown on Fig. 4.

Object of the experiment was a muscle of the type DMSP10 with a 210mm length, which was functioning under constant load. The research was done both in static and dynamic modes. The static mode in fact repeated the simulation conditions. The background of the experiments granted possibilities for changing the loads in the range 0 to 125N. In the dynamic mode equal loads were applied and provisions for a cyclic contracting of the muscle with a 1Hz frequency were made. The dynamic mode experiment had to check the carrying out of intended motions in circumstances matching the even pace of a walking robot. The test results in a static

mode are shown on Fig. 5 and those in dynamic mode – on Fig. 6.

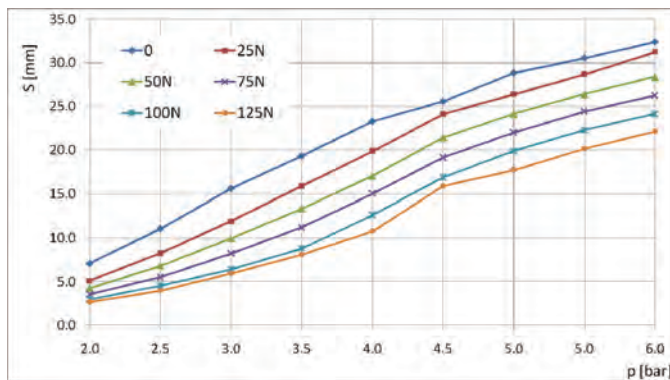


Fig. 5 Experimental results-static mode

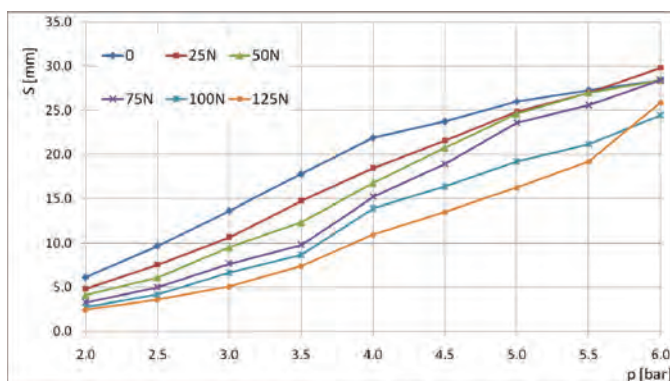


Fig. 6 Experimental results-dynamic mode

CONCLUSION

The paper offers an approach towards the choice of fluidic muscles with predetermined parameters aimed at setting in motion a mobile walking robot. This choice requires the solving of two major problems:

- A preliminary determination of the minimal muscle size with respect to the necessary load and pace – the test provided as a result sizes in the range from 200 mm to 250 mm for both muscle types (DMSP 10 and DMSP 20)
- Definition of the working zone and the motion reserves of muscles with lengths for both muscle types matching the intended loads and pressures.

Both the simulation and tests were done with regard to the specifics of the fluidic muscle's antagonistic function mode. The experimental results confirm the correlation types provided by the simulation with value differences regarded as negligible. The experiment executed in dynamic mode where the fluidic muscle features didn't change significantly give a solid reason to believe that the chosen muscles will be functional in the intended antagonistic operation mode.

ACKNOWLEDGEMENT

Every research this paper is accounting for has been done under the assignment of Contract BY – TH – 201/2006 entitled "Research of a Modular Architecture for the Control of Mechatronic Elastic Multi-Link Devices"

REFERENCES

- [1] H.-J. Weidemann, F. Pfeiffer, J. Eltze: The six-legged TUM walking robot., *Intelligent Robots and Systems (IROS)*, 2004, Vol. 2, 1026 -1033.
- [2] T. Kerscher, J. Albiez, K. Berns, Joint control of the six-legged robot AirBug driven by fluidic muscles. *Proceedings of the Third International Workshop on Robot Motion and Control*, Poland, 2002.
- [3] K. Berns, J. Albiez, V. Keppelin, C. Hillenbrand: Airbug - Insect-like Machine Actuated by Fluidic Muscle. *4th International Conference on Climbing and Walking Robots*, 2001, 237-244
- [4] A. Hildebrandt, O. Sawodny, R. Neumann, A. Hartmann, A Flatness Based Design for Tracking Control of Pneumatic Muscle Actuators, *Seventh international Conference on Control, Automation, Robotics And Vision (ICARCV'02)*, 2002.
- [5] R.W. Colbrunn, G.M. Nelson, R.D. Quinn: Design and ontroll of a Robotic Leg with braided Pneumatic Actuators *International Conference on Intelligent Robots and Systems*, 2001, Vol. 2 ,992-998
- [6] K. Berns, F. Grimminger, U. Hochholdinger, T. Kerscher, J. Albiez: Design and Control of a Leg for the Running Machine PANTER. *11th International Conference on Advanced Robotics*, 2003, 1737-1742

This page intentionally left blank.

AUTHOR INDEX

- A**
Acevski, N., 599,
Aćimović-R.V., 27, 177, 245,
Acović, M., 471,
Aleksandrov, A., 711,
Aleksić, S., 227,
Aleksieva, V., 621,
Altimirski, E., 329,
Anastasov, J., 189,
Andonov, A., 879,
Andonova, A., 815,
Andreeva, P., 841,
Angelov, K. N., 329,
Angelov, K., 287, 421, 425,
Angelovski, I., 445,
Antić, D., 557,
Antolović, I., 403,
Antonov, P., 43, 869,
Antonova, V., 43, 869,
Antovski, Lj., 155,
Arapinoski, B., 683,
Arnaudov, R., 333,
Arsov, G., 645,
Arsov, Lj., 121,
Asparuhova, K., 785,
Atamian, D., 303,
Atanasković, A., 231, 391,
Atanasov, I., 241, 387,
Atanasov, N., 897,
Atanasovski, M., 587,
Attea, G., 61,
- B**
Babić, Z., 403,
Baev, S., 83,
Balabanova, I., 111,
Bankov, N., 719, 723,
Bedzhev, B., 51,
Bekiariski, A., 355,
Bellanger, M., 39,
Bilkiewicz, J., 467,
Blagojević, D., 295,
Blanuša, B., 679,
Bogdanov, M., 511,
Bogdanova, S., 381,
Boiadžiev, S., 835,
Bonev, B., 203,
Borovska, P., 395, 399,
Boumbarov, O., 521,
Bozhikova, V., 861, 865,
Bungurova-Kaziovska, Z., 173,
- C**
Cârstea I., 579, 583,
Cârstea, D., 579, 583,
Chantov, D., 549,
Cundeva-Blajer, M., 121,
Curcivska, D., 151,
Cvetković, N., 91,
Cvetković, S., 503, 697,
- D**
Damyanov, D., 495,
Danković, B., 557,
Despotović, V., 629,
Diakov, D., 905,
Dimcev, V., 125, 103,
Dimić, G., 623,
Dimitrijević, A., 261,
Dimitrijević, B., 97, 441,
Dimitrijević, T., 219,
Dimitrov, A., 735,
Dimitrov, D. P., 777,
Dimitrov, D. Tz., 455, 459,
Dimitrov, K., 755, 757,
Dimitrov, V., 411,
Dimitrova, E., 807,
Dimitrova, V., 481,
Dineff, P., 667, 811,
Dizdarević, F., 185,
Djokić, B., 543,
Djordjević, N., 527,
Djordjević-Kajan, S., 403,
Djordjević, G., 135,
Djordjević-Kozarov, J., 691,
Dobrev, D., 279, 417,
Dobrikov, G., 835,
Dobrodolac, M., 873,
Dodov, N., 81, 215,
Dončov, N., 223, 391,
Dontschewa, M., 373, 377, 407, 693,
Dostanić, A., 471,
Dotsinsky, I., 633,
Drača, D., 275,
Draganov, I., 477,
Draganov, N., 711,
Draganov, V., 641,
- E**
Eferica, P., 403,
Efnusev, I., 165,
- F**
Fetaji, B., 609, 613, 617,
Fetaji, M., 609, 613, 617,
Filev, Ts., 517,
- G**
Gabrova, R., 803, 887,
Gadjeva, E., 739,
Gajda, J., 13,
Ganev, G., 671,
Gavrilovska, L., 445,
Gavrovski, C., 103,
Georgiev, A., 803, 887,
Georgiev, G., 437,
Georgieva, V. K., 905,
Georgieva, V. M., 689,
Gesheva, K., 835,
Gluhchev, G., 521,
Gmitrović, M., 309,
Gocheva-Ilieva, S., 769,
Gocić, M., 265,
- Golev, K., 303,
Goleva, M., 303,
Goleva, R., 303,
Gorvits, Y., 605,
Gospodinova, D., 811,
Gradinarova, B., 605,
Grigorova, Ts., 719, 723, 785,
Guliashki, V., 39, 249,
Gusev, M., 151, 155,**
- H**
Hristov, G., 181,
Hristov, V., 845,
Hussein, K., 61,
- I**
Idzkowski, A., 469,
Ilić, S., 227,
Iliev, B., 3,
Iliev, G., 47, 347,
Iliev, I. G., 199, 531,
Iliev, I. P., 769,
Iliev, M., 181,
Iliev, T., 31, 35,
Ilievski, B., 539,
Iontchev, E., 113,
Ivanova, I., 749,
Ivanova, K., 483,
Ivanović, Ž., 679,
- J**
Janevski, T., 165, 169, 173,
Janković, D., 691,
Janković, N., 653,
Joković, J., 219,
Jordanova, L., 279, 417, 429,
Jovanović, G., 715,
Jovanović, Z., 557,
Jović, M., 691,
- K**
Kafadarova, N., 815,
Kapacinović, N., 185,
Karailiev, H., 637,
Karakehayov, Z., 131,
Karakehayova, L., 161,
Karapenev, B., 341,
Karatepe, E., 291,
Karova, M., 361, 849,
Kempter, G., 693,
Koceska, N., 561,
Koceski, S., 561,
Koitchchev, K., 287, 421, 425, 433,
Kokolanski, Z., 103,
Kolev, I., 767,
Kolev, S., 749,
Kolev, V., 675,
Koleva, E., 767,
Korobko, I., 883,
Korsemov, Ch., 857,
Kosanović, M., 143,
Koserkova, A., 835,
Kosev, J., 645,
- Kostadinova, L., 803, 887,
Kostić-Ljubisavljević, A., 177,
Kostov, M., 511,
Kostov, N., 23, 107,
Kotevski, Z., 705,
Kountchev, R., 351, 365, 369,
Kountcheva, R., 351, 365,
Kovatchev, D., 735, 807,
Krantov, N., 901,
Krasowski, A., 469,
Krasov, M., 215,
Krstić, D., 185, 649,
Kuk, K., 623,
Kunev, G., 487,
Künz, A., 407,**
- L**
Latzoski, P., 539,
Lazarova, M., 395,
Letskovska, S., 101, 781,
Levchev, Ch., 73, 77,
Loskovska, S., 613,
Lutskanov, K., 553,
- M**
Maier, E., 693,
Makal, J., 467, 469,
Males-Ilić, N., 231,
Manchev, V., 739,
Mančić, Ž., 227,
Manoilov, P. G., 399,
Manoilov, P. K., 451, 463,
Marinković, Z., 727,
Marinov, E., 553,
Marinova, G. I., 39,
Marinova, G. K., 23, 107,
Marković, D., 873,
Marković, G., 27,
Marković, V., 727,
Matić, P., 679,
Matoruga, H., 591,
Meijer, G., 3,
Mekić, E., 185,
Mezei, I., 359, 499,
Mihajlović, V., 261, 403,
Mihov, G. S., 633, 773,
Mihov, S. G., 745,
Mihova, B., 739,
Miletiev, R., 113, 333,
Milić, Z., 649,
Milijić, M., 235,
Milivojević, D., 629,
Milivojević, S., 507,
Milivojević, Z., 507,
Milojković, M., 557,
Milosavljević, A., 261,
Milosavljević, Č., 565,
Milošević, B., 623,
Milovanović, B., 219, 223, 231, 235, 391,
Milović, D., 275,
Milushev, M., 901, 905,
Mir, N., 283,
Mirčevski, J., 543,

Mirchev, V., 369,
Mironov, R., 369,
Mirtchev, S., 193,
Mitić, A., 295, 299,
Mitrevski, P., 151, 155,
Mitrovski, C., 511, 657,
Mladenov, V., 751,
Mladenović, S., 535,
Mladenovski, Z., 645,
Monov, Z., 161,
Mulalić, E., 503,
Musa, S., 211, 283,

N

Najdenkoski, K., 125,
Naumović, M., 573,
Nazarkiewicz, A., 467,
Nedelchev, I., 313,
Nedelchev, M., 199, 531,
Nedelkovski, I., 705,
Nemigenchev, I., 313, 341,
Nenkov, J., 429,
Nenov, C., 487,
Nikolić, P., 649,
Nikolić, S., 503, 697,
Nikolić, T., 135,
Nikolić, V., 169,
Nikolić, Z., 441,
Nikolov, G., 731,
Nikolov, T., 253, 269,
Nikolova, N., 81,
Nikolova, Z., 491,
Nikolova-Jahn, I., 117,

O

Odalović, M., 789,
Ognjanović, V., 265,
Osmani, S., 609,
Ovtcharov, M., 47,

P

Pachamanov, R., 139,
Palović, B., 189,
Panagiev, O., 321, 325, 757,
Panajotović, A., 275,
Pandiev, I., 831,
Pankov, I., 517,
Pankov, J., 517,
Pantić, D., 653, 827,
Paraliev, M., 663,

Parashkevov, D., 793, 797,
Pavlov, M., 629,
Pavlov, S., 793,
Pavlović, N., 905,
Pencheva, E., 387,
Penev, S., 849,
Pešić, B., 827,
Pesić, T., 653,
Petkov, P., 81,
Petkova, J., 361, 849,
Petković, D., 789,
Petkovski, M., 657,
Petrov, D., 55,
Petrov, P. Tz., 701, 761,
Petrov, P., 569,
Petrova, P., 55,
Peulić, A., 471,
Pleshkova-Bekiarska, S., 495,
Popnikolova R., M., 683,
Popova, A., 477,
Popović, H., 299,
Popović, N., 543,
Popovski, B., 539,
Poulkov, V., 47,
Predić, B., 403,
Prijić, A., 827,
Prijić, Z., 827,
Pronić, O., 727,

R

Radev, D., 31, 147,
Radojičić, V., 177,
Radonjić, V., 245,
Raev, R., 257,
Raeva, I., 257,
Rahnev, P., 101, 781,
Rajković, P., 507,
Rančić, D., 261, 403, 527,
Rančić, M., 337,
Rančić, P., 91, 337,
Randelović, M., 391,
Randić, S., 471,
Rankovska, V., 637,
Rashkova, E., 147,
Rassovska, M., 835,
Ristić, S., 827,
Ruskov, T., 853,
Ruskova, N., 853,

S

Sadiku, M., 211,
Sadinov, S., 287, 421, 433,
Sarevska, M., 235,
Savov, M., 521,
Savov, S., 69,
Shaalan, A., 61,
Sharlandjiev, P., 835,
Simić, M., 97,
Sirakov, E., 317,
Smarkov, V., 361,
Sokolović, M., 649,
Sokullu, R., 291,
Spalević, P., 623,
Spasić, J., 381, 441
Spirovski, M., 599,
Srbinovska, M., 103,
Srečković, M., 543, 819, 823
Sroka, R., 13,
Stanchev, Z. D., 641,
Stanimir, V., 295,
Stanivuković, B. V., 873,
Stanković, Z., 235,
Stankovski, D., 147, 257,
Statev, S., 193,
Stefanov, M., 65,
Stefanova, I., 207,
Stefanović, D., 295, 299,
Stefanović, I., 299,
Stefanović, M., 185, 189, 275,
Stoeva, M., 861, 865,
Stoilkov, V., 125,
Stojčev, M., 135, 143, 715,
Stošić, B., 309,
Stoyanov, G., 483,
Stoyanov, N., 73, 77, 437,
Struharik, R., 359, 499,
Sturn, T., 373,

T

Tanchev, I., 641,
Tanev, A., 879,
Tashev, T., 51,
Tasheva, Z., 51,
Tasić, V., 629,
Taskovski, D., 381,
Temelkovski, I., 189,
Terzieva, S., 751,
Todorov, G., 671,
Todorov, V., 351, 365,

Todorova, M., 595,
Toshev, A., 87,
Toshev, H., 857,
Toshkova, D., 569,
Traikovski, G., 433,
Trpezanovski, Lj., 587,
Tsankov, B., 139,
Tsenov, A., 253,
Tsenov, G., 751,
Tsenov, Tz., 675,
Tzeneva, R., 667,
Tzvetkova, S., 675,

V

Valchanov, H., 853,
Valchev, V., 731, 735, 807,
Van den Bossche, A., 731,
Varbanov, G., 487,
Varbanova, N., 425,
Vasileva, M., 595,
Vassileva, S., 841,
Vassileva, V., 69,
Velchev, Y., 749, 891, 895,
Veličković, V., 189,
Velikov, N., 23,
Veselić, B., 565,
Veselinović, B., 819, 823,
Veselinović, I., 819, 823,
Vesković, S., 535,
Vlajnić, M., 823,
Vukosavić, S., 679,

W

Weber, H., 407,

Y

Yakimov, P., 751,
Yordanov, A., 773,
Yordanova, S., 23, 107,
Yudov, D., 731, 735,

Z

Zaharieva-Stoyanova, E., 523,
Zapryanov, G., 745,
Zerbe, V., 901,
Zhekov, Z. S., 553,
Zildžo, H., 591,
Zu-yao Chang Xiujun Li, 3,